Experimental Study of Shadow Region Imaging Algorithm with Multiple Scattered Waves for UWB Radars

Shouhei Kidera[1], Takuya Sakamoto[2], and Toru Sato[2]

[1]Department of Electronic Engineering, University of Electro-Communications, Japan
[2]Graduate School of Informatics, Kyoto University, Japan

Abstract— Ultra-wide band (UWB) radar is capable of high range resolution near field sensing, and is thus applicable to security systems designed to identify a human body even when invisible. Although Synthetic Aperture Radar (SAR) creates a stable and accurate target image for such applications, it often suffers from increased shadow regions in the case of complex or multiple targets. On the contrary, a multiple scattered wave has the potential to enlarge a visible range on target surfaces because it propagates a path which differs from that of a single scattered wave. While various algorithms based on time-reversal processing with multiple scattered waves have been developed, these require a priori information of the surroundings or a target model. This paper proposes a shadow region imaging algorithm based on the aperture synthesis of multiple scattered waves. While the proposed algorithm only synthesizes a double scattered wave according to its propagation path, it can directly increase the visible area and is applicable to arbitrary target shapes. The results from the numerical simulation and experiment verify that the proposed algorithm directly makes a shadow region visible without a preliminary observation.

1. INTRODUCTION

UWB pulse radar is promising as a near field sensing technique with high range resolution, and is applicable to non-contact measurement of reflector antennae or aircraft bodies that have precise and specular surfaces. It is also applicable to a collision avoidance for automobile under the low visibility. For such applications, various imaging algorithms have been published, as the SEABED accomplishes real-time imaging by using a reversible transform BST [1], and the Envelope + SOC reconstructs the target surface to an accuracy on the order of 1/100 wavelength [2]. The SAR algorithm remains promising, in providing a stable and accurate image by using the full information of the received signals [3]. However, in the case of complex or multiple targets, any of the algorithms suffers from increased shadow regions because they use only the single scattered wave for imaging. On the contrary, except for an edge diffraction wave, a multiple scattered wave passes through a path, different from that of a single scattered wave, which means that the multiple scattered echo has the potential to enhance the visible range. Although the time reversal algorithms with multiple scattered waves have been proposed when focusing on reliable target detection or accurate positioning in cluttered situations [4–6], they require target modeling or a priori information of the surrounding environment like the walls. To expand the applicability of these methods, this paper proposes a non-parametric imaging algorithm based on the aperture synthesis of multiple scattered signals. The results obtained from numerical simulations and an experiment verify the effectiveness of the proposed method which is applicable to arbitrary target shapes, and directly enlarges the visible range of the target surface.

2. CONVENTIONAL ALGORITHM

Figure 1 shows the system model. It assumes that the target has an arbitrary shape with a clear boundary, and high conductivity like metallic objects. The propagation speed of the radio wave c is assumed to be a known constant. A mono-cycle pulse is used as the transmitting current, and the space is normalized by λ as the center wavelength of the pulse. The omni-directional antenna is scanned in the plane $z = 0$. The real space in which the target and antenna are located is expressed by the parameter $r = (x, y, z)$. $z > 0$ is assumed for simplicity. $s(X, Y, Z)$ is defined as the output of the Wiener filter at the antenna location at $(x, y, z) = (X, Y, 0)$, where $Z = ct/(2\lambda)$ is expressed as a function of the time t.

As a spatial measurement in the near field, the SAR algorithm has an ability to create a stable and accurate image by using the UWB signal. The distribution image $I_1(r)$ obtained by the SAR is formulated as

$$I_1(r) = \int_{q \in \Gamma} s\left(q, d_1(r, q)/2\right) \mathrm{d}X \mathrm{d}Y \tag{1}$$

where $q = (X, Y)$ and Γ is the scanning range of the antenna. $d_1(r, q)$ is the round-trip distance between the point r and the antenna location as $(X, Y, 0)$. The target boundary can be extracted from its focused image $I_1(r)$. This algorithm has an advantage that it can produce a stable and accurate image for various target shapes. An example of this method follows. The target shown in Fig. 1 is assumed. The received signals are observed for $-2.5 \leq X, Y \leq 2.5$ at 51 locations in each axis. The left hand side of Fig. 2 shows the image viewed at $x = 0$ with the conventional method. This figure shows that the image expresses only the bottom part of the target boundary, and the greater part of the triangular boundary falls into shadow regions. This is because the distinguishable echo from this area cannot be observed at any antenna location, since the inclination of the triangle boundary is too large. This is an inherent problem in the conventional algorithms [1, 2] that only use single scattered echoes for a target reconstruction.

3. PROPOSED ALGORITHM

To overcome the problem described above, this paper proposes a shadow region imaging algorithm based on the aperture synthesis of double scattered signals. A double scattered wave propagates a different path from that of a single scattered one, except for an edge diffraction wave, which often provides significant information from two scattering centers on the target boundaries. The proposed method calculates the distribution image $I_2(r)$ synthesized by the double scattering waves as

$$I_2(r) = - \int_{q \in \Gamma} \int_{r' \in R} I_1(r') s\left(q, d_2(r, r', q)/2\right) F(r, r'q) \ dx' dy' dz' dX dY \tag{2}$$

where $r' = (x', y', z')$, R denotes the region of the real space. $d_2(r, r', q)$ is the peripheral distance of the triangle whose apexes are located at r, r' and the antenna location. The weight function $F(r, r', q)$ is defined as

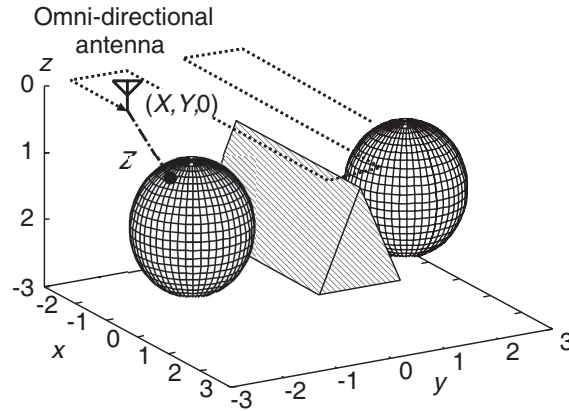$$F(r, r', q) = 1 - \exp\left[-\frac{\{d_2(r, r', q) - d_1(r, q)\}^2}{2\sigma_{\mathrm{FZ}}^2}\right], \tag{3}$$
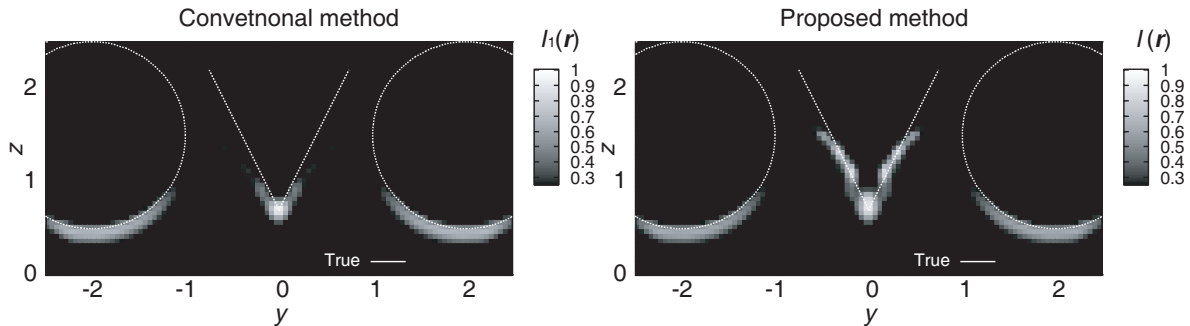

Figure 1: System model.

Figure 2: Estimated images with the conventional (left) and the proposed method (right).

where σ_{FZ} is determined empirically. $F(r, r', q)$ suppress the weight for the region included in the Fresnel zone, which is determined by the initial image $I_1(r)$. The minus sign in Eq. (2) creates a positive image focused by the double scattered waves, that have an inverse phase relationship from that of single scattered wave. Eq. (2) expresses the aperture synthesis of the received signals by considering only a double scattered path.

Here, we assume that only the positive images of $I_1(r)$ and $I_2(r)$ are necessary for the target boundary extraction. Then, the proposed method determines the final image $I(r)$ as,

$$I(r) = I_1(r)H(I_1(r)) + I_2(r)H(I_2(r)), \tag{4}$$

where $H(x)$ is defined as

$$H(x) = \begin{cases} 1 & (x \geq 0), \\ 0 & (x < 0). \end{cases} \tag{5}$$

The proposed method uses only the initial image $I_1(r)$ and directly emphasizes the target regions which double scattered waves passed through. The right hand side of Fig. 2 shows the example of the proposed method viewed at $y = 0$, when the same data in the left side hand of Fig. 2 is used. $\sigma_{\mathrm{FZ}} = 0.5\lambda$ is set. This result verifies that the proposed method enlarges the region of the target that can be reconstructed, and the area around the triangular side becomes visible. This is because the double scattered waves are focused on the triangular side by using Eq. (2).

4. PERFORMANCE EVALUATION IN EXPERIMENT

This section shows the experimental investigation of the proposed algorithm. Fig. 3 shows the experimental setup with both cylindrical and rectangular targets. The UWB pulse with a 10 dB-bandwidth of 3.0 GHz and a center wavelength λ of 93.75 mm is used. The pair of the transmitting and receiving antennas is scanned on the $z = 0.0\lambda$ plane, for $-3.0\lambda \leq x \leq 3.0\lambda$ and $-1.0\lambda \leq y \leq 1.0\lambda$, with each sampling interval set to 0.1λ. Each antenna has an elliptic polarization, and the major polarimetric axis is along the y-axis. The data is coherently averaged by 1024 times. The direct scattered signal from the trapezoidal target can be obtained by eliminating the received signal without a target.

Figure 4 shows the output of the Wiener filter viewed at $Y = 0$ in the experiment. The S/N of the double scattered wave is around 25 dB. The left hand side of Fig. 5 shows the estimated image at $y = 0$ with the conventional method. This figure shows that only bottom part of the rectangular target is reconstructed, and the target shape is hardly identified. The right hand side of Fig. 5 shows the estimated image with the proposed method, where the bi-static extension is applied. In comparison, this image reconstructs the side of the rectangular target, and offers significant information for identifying the target shape. This result verifies that the proposed method is effective in enhancing the visible area of the target surfaces even in a real environment. Moreover, this method does not require target modeling or a priori information of the surroundings, yet is a substantial improvement from the conventional approaches [4–6]. However, the calculation time to
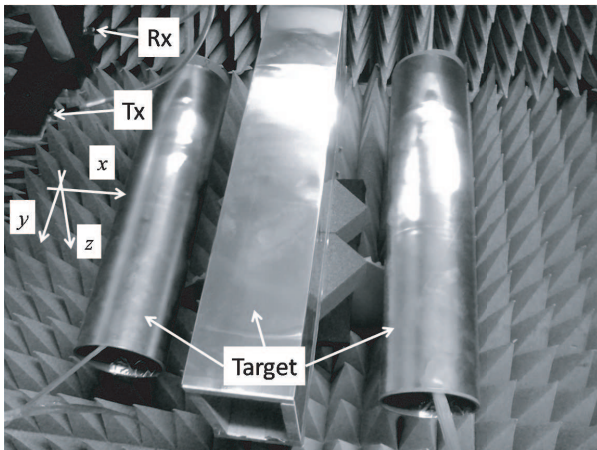

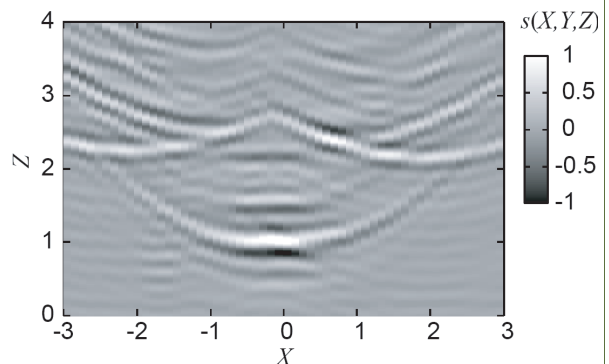Figure 3: Arrangement of the antenna and the multiple targets in the experiment.

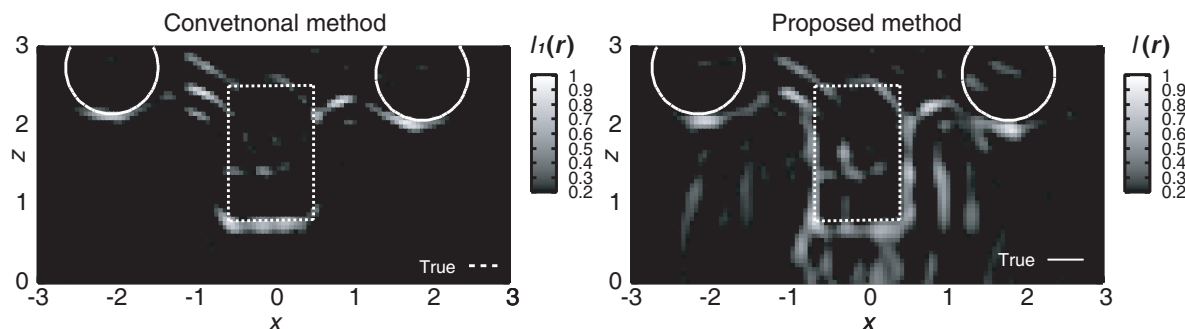Figure 4: Output of the wiener filter in the experiment at $Y = 0$.

Figure 5: Estimated images with the conventional method (left) and proposed method (right) in the experiment ($y = 0$).

obtain each cross-section image, requires around 100 minutes with a single Xeon 2.8 GHz processor. Thus, the acceleration of the imaging speed becomes our future work.

5. CONCLUSION

This paper proposes a direct shadow region imaging algorithm based on aperture synthesis for double scattered waves. In the conventional SAR, the greater part of a complex target or multiple targets falls into a shadow region because it uses only a single scattered wave. To overcome this problem, we extended the SAR algorithm to use double scattered waves. The results from the numerical simulation and an experiment verify that the proposed algorithm can enhance the visible region and offers a significant image to identify the target shape, even in a real environment. In addition, a substantial advantage of the proposed method is that it does not require information about surroundings or target models. Although the proposed method requires a great deal of calculation, this algorithm can expand the application range of the near field radar in cluttered situations.

REFERENCES

1. Sakamoto, T., "A fast algorithm for 3-dimensional imaging with UWB pulse radar systems," *IEICE Trans. Commun.*, Vol. E90-B, No. 3, 636–644, 2007.
2. Kidera, S., T. Sakamoto, and T. Sato, "High-resolution and real-time 3-D imaging algorithm with envelope of spheres for UWB radars," *IEEE Trans. Geosci. Remote Sens.*, Vol. 46, No. 11, 3503–3513, Oct. 2009.
3. Mensa, D. L., G. Heidbreder, and G. Wade, "Aperture synthesis by object rotation in coherent imaging," *IEEE Trans. Nuclear Science.*, Vol. 27, No. 2, 989–998, Apr. 1980.
4. Lehmanm, S. K. and A. J. Devaney, "Transmission mode time-reversal super-resolution imaging," *Acoust. Soc. Am.*, Vol. 113, No. 5, May 2003.
5. Moura, J. M. F. and Y. Jin, "Detection by time reversal: Single antenna," *IEEE Trans. on Signal Process.*, Vol. 55, No. 1, 187–201, Jan. 2007.
6. Kitamura, T., T. Sakamoto, and T. Sato, "Imaging method for UWB radars with a single antenna by using multipath waves in an unknown room," *IEICE General Conference*, C-1-10, Mar. 2009 (in Japanese).

Monitoring Surface Deformations over Siberian Gas Deposit Areas Using ALOS PALSAR Interferometry

**Makoto Maruya[1], Seiji Yoshimoto[1], Masanori Miyawaki[2], Shino Yamaguchi[2],
Evgeniy Kiselevskiy[3], Peter Korviakov[4], Dmitry Sergeev[4], Yuriy Baranov[5],
Goro Ando[6], and Masaki Kawai[6]**

[1]NEC Corporation, Japan
[2]NEC Aerospace Systems, Japan
[3]Gazprom, Russia
[4]Gazprom Space Systems, Russia
[5]Gazprom VNIIGAZ, Russia
[6]ERSDAC, Japan

Abstract— Japan and Russia cooperated in performing a study to monitor ground surface deformations over gas deposit areas in Siberia using the phased array type L-band synthetic aperture radar (PALSAR) of the Advanced Land Observing Satellite (ALOS). The studied areas had permafrost and surface subsidence due to gas extraction, both of which would affect gas facilities and infrastructure. The observation sites were located in a tundra that had widespread permafrost, bogs, and a thin layer of mosses and lichens. Differential interferometry analysis was conducted independently by both NEC and GASPROM Space Systems using PALSAR data. The results clearly showed widespread ground subsidence with block structures over the past two years. Also, small hills and dips apparently formed by permafrost were detected by high spatial resolution (25 m) interferometry analysis. This study demonstrates that L-band SAR observation using a satellite provides a wide area instrumental technique for gathering information to support field and pipeline operation and for observing the resulting impact on the environment. The results also show the technical and economic efficiency of surveying and performing geodesic monitoring of gas field areas using ALOS PALSAR.

1. INTRODUCTION

Major gas and oil deposit areas in Russia are located in the polar climate zone, and the polar gas and oil fields have permafrost and surface subsidence due to gas extraction, both of which would affect gas facilities and infrastructure. Therefore, monitoring ground surface deformations is important to support field and pipeline operation and for observing the resulting impact on the environment. However, the natural and climatic conditions of the areas severely limit the applicability of ground surveying, and many of the areas are covered by clouds most of the year that obstruct satellite optical sensor observations.

Synthetic aperture radar (SAR), especially L-band SAR, is suitable for observing these areas, because it is less affected by vegetation, snow, and atmospheric conditions than C-Band or X-band radars [1–6]. Therefore, by using the phased array type L-band synthetic aperture radar (PALSAR) of the Advanced Land Observing Satellite (ALOS), Japan and Russia have cooperated in performing a study to monitor ground surface deformations over gas deposit areas in Siberia based on the application of space-based radars.

The observation sites are located in a tundra near the Obi river delta that has widespread permafrost, bogs, and a thin layer of mosses and lichens. The purpose of the study is to demonstrate that L-band SAR observation using a satellite can provide a wide area instrumental technique for gathering information to support field and pipeline operation and for observing the resulting impact on the environment. For this demonstration, an interferometry analysis with higher horizontal resolution such as 25 m was tried in this polar climate area.

2. OBSERVATION BY ALOS PALSAR

ALOS is an earth-observation satellite developed by Japan Aerospace Exploration Agency (JAXA) and built by NEC Corporation, which was the system contractor. ALOS is in sun synchronous orbit around the earth at an altitude of 690 km and an inclination of 98 degrees, and has a 46 day repeat cycle. ALOS carries two optical sensors and a radar sensor, PALSAR developed by METI and JAXA. The PALSAR is a high resolution active microwave sensor that has an L-band frequency intended for applications such as building DEMs and extracting topography data via

interferometry. PALSAR has three observation modes: fine, ScanSAR, and Polarimetric, and the fine mode includes fine beam single polarization (FBS) mode and fine beam dual polarization (FBD) mode. The main characteristics of PALSAR are summarized in Table 1 [7].

Table 1: Main PALSAR characteristics.

Mode	Fine		ScanSAR	Polarimetric
Center Frequency	1270 MHz (L-band)			
Bandwidth	28 MHz	14 MHz	14, 28 MHz	14 MHz
Polarization	HH or VV	HH + HV or VV + VH	HH or VV	HH + HV + VH + VV
Incidence angle	8 to 60°	8 to 60°	18 to 43°	8 to 30°
Range Resolution	7 to 44 m	14 to 88 m	100 m	24 to 89 m
Swath	40 to 70 km	40 to 70 km	250 to 350 km	20 to 65 km
Quantization	5 bits	5 bits	5 bits	3 or 5 bits
Data rate	240 Mbps	240 Mbps	120 Mbps, 240 Mbps	240 Mbps

ERSDAC (the Earth Remote Sensing Data Analysis Center), one of the data production and research agencies for PALSAR, requested the intensive observation of the studied gas deposit areas near the Obi river delta in 2008. ALOS started PALSAR observation in the middle of 2006 and about sixty PALSAR scenes covering the studied area were available by the end of 2008 in the ERSDAC PALSAR Archive [8]. After several attempts to correlate on various data sets by NEC and GASPROM Space Systems, the following two scene pairs were selected for DEM generation and interferometry analysis (Table 2).

Table 2: PALSAR scenes used in this study.

PALSAR scene pair	Date of scene1	Date of scene 2	Observation interval	Perpendicular baseline (m)	Off nadir angle (degrees)	Observation mode	Orbit heading
A (DEM generation)	June 9, 2006	June 25, 2006	2 months	1,783	41.5	FBS (HH)	Ascending
B (2-year defomation)	June 9, 2006	September 14, 2008	2 years	1,500	41.5	FBS (HH)	Ascending

3. INTERFEROMETRY ANALYSIS

To measure the location and amplitude of surface deformations over the past two years, three-pass differential interferometry (DInSAR) analysis was conducted independently by NEC (using its proprietary software) and GASPROM Space Systems (using SARSCAPE). As shown in Figure 1, pair A was used to generate the DEM, and pair B was used to extract information about surface deformations over the past two years. The analysis results of the two companies were almost the same even though they used different software. The generated PALSAR DEM was compared with a DEM built from a 1/200000 Russian map, and they showed good agreement with a 6 meter standard deviation [1].

Processing results are shown in Figures 2(a) to (f). The ALOS PALSAR FBS data amplitude image has high spatial resolution (7 m at best), and major gas-field facilities such as buildings, roads, and pipelines are well identified in (b). An interferogram of pair B that has a 25 meter spatial resolution is shown in (c). In spite of a two-year observation time interval, the high spatial resolution interferogram was obtained for almost all area of the scene. This result demonstrates the advantage of L-band DInSAR over C-band DInSAR for high resolution land subsidence detection with a long-term observation interval.

A coherence histogram, computed with eight looks (two looks for the range direction, and four looks for the azimuth direction), is shown in (e). Surface deformation results obtained from the
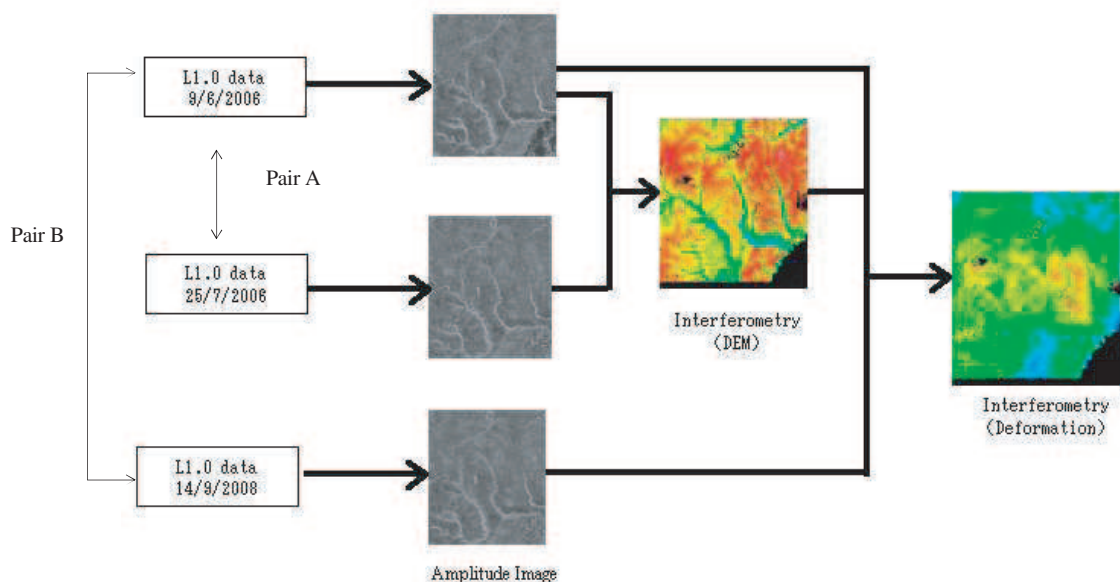
Figure 1: Three-pass DInSAR processing flow.

interferogram by phase unwrapping are shown in (f). Because PALSAR has high spatial resolution, unwrapping was performed well. GCP data was used to fix the absolute scale. The result indicates that the maximum subsidence in two years reached 5 to 8 cm. This result will be quantitatively validated during the next study phase.

4. DISCUSSION OF USEFULNESS OF PALSAR INTERFEROMETRY FOR MONITORING IN POLAR GAS DEPOSIT AREAS

The PALSAR interferometry analysis results were reviewed and discussed by the joint team from the viewpoint of the industrial application of ALOS PALSAR interferometry. The most important roles indentified for monitoring in polar gas deposit areas are summarized below.

4.1. Providing a High Resolution Overall Image of Widespread Ground Subsidence in large Polar Gas Fields

Wide area ground subsidence (20 km east-west, 50 km north-south), thought to be caused by gas extraction, is clearly revealed to be nearly in line with the gas field facilities by PALSAR interferometry analysis. The PALSAR FBS mode data has high resolution (7 m) and a wide swath width (70 km). Therefore, analysis using this data provides a high resolution overall image of surface subsidence caused by gas extraction in a large gas field.

The natural and climatic conditions of polar gas deposit areas severely limit the applicability of remote sensing by even ground instrumentation using GPS receivers. It is not technically feasible to create a network of GPS sensors, for example, due to the large and hardly accessible territory and very low temperatures down to minus 50 degrees C in winter. Under such conditions, it is difficult to provide the power supply for the GPS sensors and acquiring their data. Therefore, ALOS PALSAR DInSAR analysis is the most practical remote sensing method that can provide a high resolution overview of the widespread ground subsidence in large polar gas fields.

4.2. Detection of Block Structures for Geological Structure Analysis

Careful observation of the high resolution interferometry analysis results revealed that the ground subsidence occurred in several blocks as shown in Figure 2(f). The distribution and shape of each subsidence block provides a clue for analyzing the complex geological structure of this area, and is important information for supporting the operation and management of the gas field. The boundary areas of the blocks would not be suitable for building major facilities.

4.3. Detection of Permafrost Activities

Small hills and dips form as a result of seasonal permafrost activities (melting in summer and freezing in winter) in tundra areas. These natural ground deformations were also detected by high resolution (25 m) interferometry analysis (Figure 3). The horizontal size of the hills and dips

(a) Amplitude image on June 9, 2006

(b) Enlargement of part of image (a)

(c) Interferogram of pair B

(d) Coherence map of pair B

(e) Coherence histogram of pair B
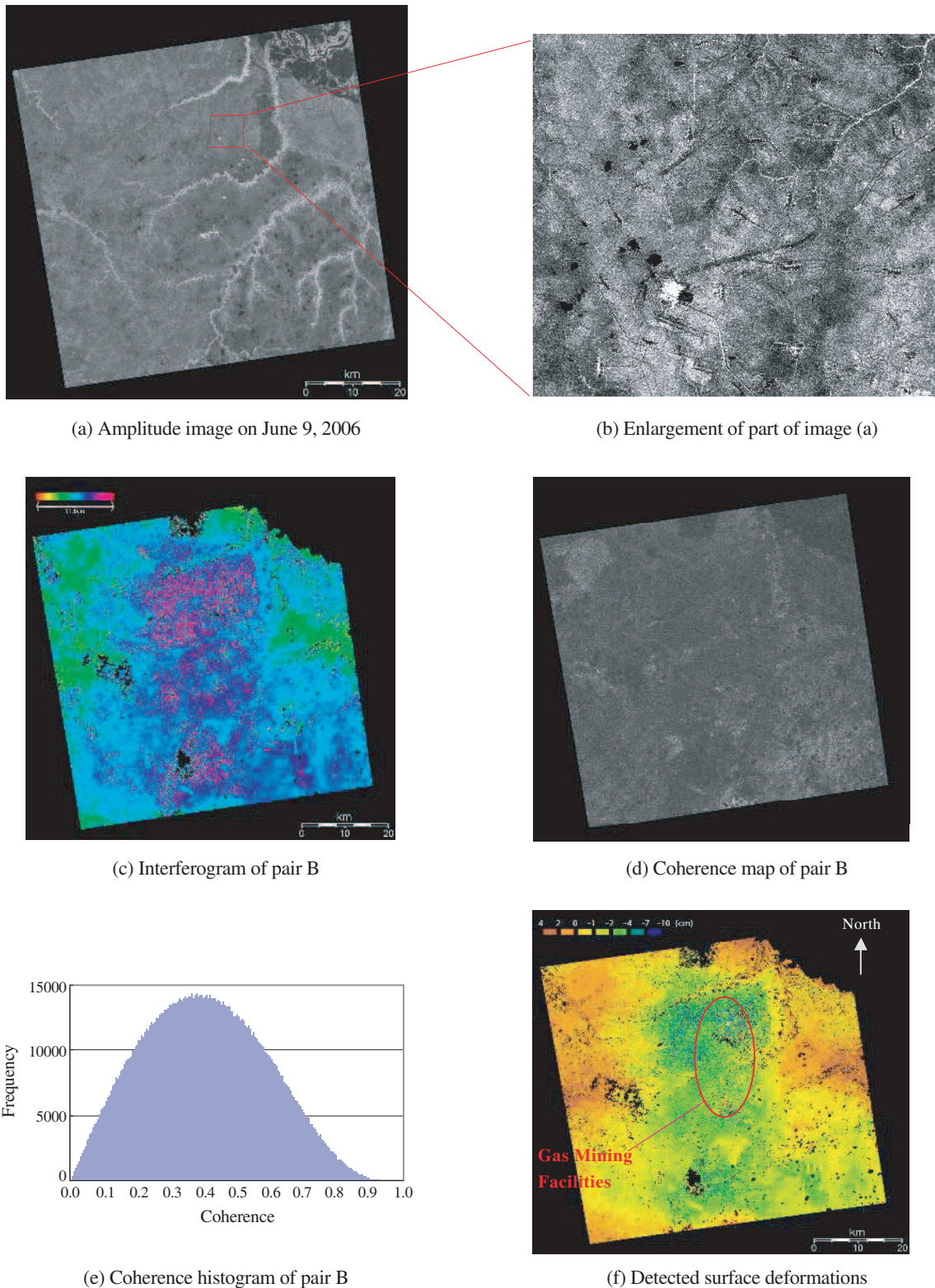
(f) Detected surface deformations

Figure 2: Results of interferometry analysis.

were from dozens of meters to several hundred meters. These natural ground deformations might damage roads, pipelines, and other gas field facilities. PALSAR interferometry analysis provides useful information for monitoring permafrost changes around facilities and for controlling potential damage to them.
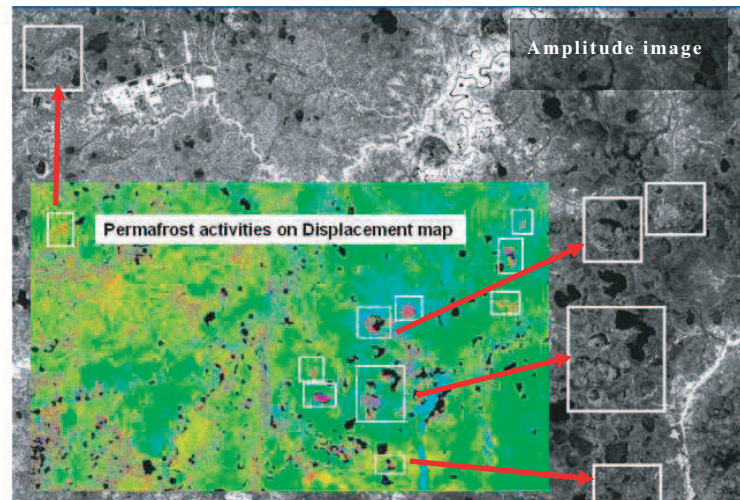
Figure 3: Detected permafrost activities.

5. CONCLUSION

This study demonstrated that L-band SAR observation can provide a wide area instrumental technique for gathering information to support field and pipeline operation and for observing the resulting impact on the environment. The results also show the technical and economic efficiency of surveying and performing geodesic monitoring of gas field areas using ALOS PALSAR. Future study will concentrate on the quantitative validation of the surface deformation based the ground truth.

ACKNOWLEDGMENT

REFERENCES

1. Sevastiyanov, D., N. Sevastiyanov, P. Korviakov, D. Sergeev, E. Kiselevskiy, Y. Baranov, S. Yoshimoto, M. Maruya, M. Miyawaki, S. Yamaguchi, G. Ando, and M. Kawai, "Application of ALOS PALSAR for building a DEM and monitoring deformations on the surface of polar pad deposit areas," *Proceedings of International Conference, III International Conference Remote Sensing — The Synergy of High Technologies*, 2009.
2. Strozzi, T., U. Wegmuller, C. L. Werner, A. Wiesmann, and V. Spreckels, "JERS SAR interferometry for land subsidence monitoring," *IEEE Transactions on Geoscience and Remote Sensing*, Vol. 41, No. 7, 2003.
3. Wang, C., H. Zhang, Z. Liu, S. Cheng, and G. Lu, "ERS difference SAR intereferometry for urban subsidence monitoring of Suzhou, Eastern China," *IGARSS*, 2001.
4. Takeuchi, S., S. Yamada, and C. Yonezawa, "Comparison of InSAR capability for land subsidence detection between C-band and L-band SAR," *IGARSS*, 2002.
5. Ng, A. H., H. Chang, L. Ge, C. Rizos, and M. Omura, "Radar interferometry for ground subsidence monitoring using ALOS PALSAR data," *Proceedings of The XXI Congress, The International Society for Photogrammetry and Remote Sensing*, 2008.
6. Deguchi, T., M. Kato, H. Akcin, and H. S. Kutoglu, "Monitoring of mining induced land subsidence using L- and C-band SAR interferometry," *IGARSS*, 2007.
7. http://www.palsar.ersdac.or.jp/e/about/sensor.html.
8. https://ims1d.palsar.ersdac.or.jp/palsar_ims1_public/ims1/pub/en/.

Over the Horizon Sky-wave Radar: Coordinate Registration by Sea-land Transitions Identification

F. Cuccoli[1], **L. Facheris**[2], **D. Giuli**[2], **and F. Sermi**[1]

[1]U.O. CNIT, c/o Dipartimento di Elettronica e Telecomunicazioni, Università di Firenze
Via di Santa Marta, 3, 50139 Firenze, Italy
[2]Dipartimento di Elettronica e Telecomunicazioni, Università di Firenze
via di Santa Marta, 3, 50139 Firenze, Italy

Abstract— In this paper, we propose an approach to the problem of real time coordinate registration for Over the Horizon Sky Wave signals. The approach is based on the *a priori* knowledge of the displacement of the sea-land transitions within the radar coverage area, namely, takes advantage of the geo-morphological structure of the surveillance area, employing it to build a binary mask to be used as a geographic reference for the received radar echo. The georeferencing algorithm, based on the maximization of the cross-correlation between the received radar echo and the binary clutter signatures, is outlined in order to point out the minimum requirements in terms of received signal-to-noise ratio and differential sea-land backscattering coefficient.

1. INTRODUCTION

Despite it is based on a well known technology, the Over The Horizon Sky Wave Radar (OTHR-SW), developed during World War II and largely employed during the "Cold War", is attracting today much interest, thanks to the great steps forward made in the last years by the signal processing and data storage techniques.

OTHR systems are HF-band sensors that, via surface propagation (Ground-Wave) or ionospheric reflection (Sky-Wave), cover an area that is located well beyond the horizon line, that is the natural operational limit for most ground-based radars.

In particular, OTHR-SW are the only ground-based sensors with a surveillance area comparable in surface with that of satellite constellations or airborne radar networks. This is achieved by exploiting the propagation characteristics of the Ionosphere (see Fig. 1 for a simplified sketch, where are also defined some parameters used in the following).

Nevertheless, the employment of the Ionosphere as part of the Tx-Rx channel implies a substantial uncertainty in the actual ray path. In fact, the non-homogeneous structure and time-dependent behavior of the Ionosphere has an important impact on the OTHR-SW Coordinate Registration (CR) procedures of current common use. The consequent uncertainty propagates to every radar measurement and the estimated position of an eventually detected target may result heavily inaccurate.

So far, several different approaches to the CR task for OTHR-SW systems have been developed. Most of them require external sources of information arranged within the surveillance area, such as ionosonde networks [1, 2], beacons or transponders [3], passive receivers [4], additional radar systems [5], etc.

Often, the employment of these methods in an operative radar context is limited by one of the following factors:

- the construction/maintenance costs growth due to the introduction of external systems;
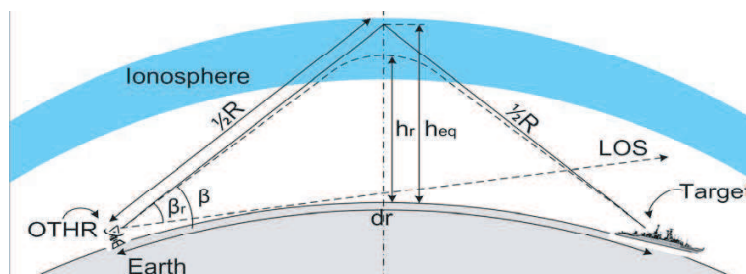

Figure 1: OTHR simplified operative scenario scheme.

- the need to arrange those systems within the surveillance area, that generally is a restricted access zone;
- the sporadic nature of additional information availability.

The OTHR-SW real time CR approach proposed in this paper does not ask for any information source external to the radar, but exploits the *a priori* knowledge of the geo-morphological structure of the surveillance area in order to georeference in real time the received echoes.

In the following sections we describe the CR method we developed together with the main hypotheses on the OTHR-SW simplified scenario and with some relevant simulation results.

2. THE PROPOSED REAL TIME CR METHOD

Although the OTHR transmission channel is non-homogeneous and time-dependent and therefore extremely hard to model (eventually requiring continuous ionospheric soundings), the geo-morphological structure of the surveillance area can be easily and profitably employed as static geographic reference.

An *ad hoc* procedure (not described here) to generate a static Binary Clutter Mask (*BCM*) must be applied before starting the real time echo processing, with the objective to mark the sea-land transitions within the radar coverage area.

When the radar is gathering data pertinent to a given azimuth θ, the corresponding binary clutter profile is extracted from the *BCM*. An ensemble of equivalent ionospheric heights is then defined and for each of them the corresponding radar footprint projection is evaluated. Such ensemble is centered around a first guess value of the equivalent ionospheric height as well as provided by seasonal ionospheric statistics over the geographic areas under test. The projections of the radar footprints on the binary clutter profile provide a set of binary clutter signatures (*BCS*). Every *BCS* is cross-correlated with the received radar echo and the maximum (the "best match") is then selected (dashed line in the example of Fig. 4). The chosen *BCS* unambiguously[1] corresponds to a certain value of the elevation vector. This value is selected to be the estimate of the actual ionospheric equivalent reflection height (h_{eq}) and consequently of the radar footprint position relative to the received echo.

3. MODEL HYPOTHESES AND SIMULATION SCENARIOS

In order to prove the reliability of the method and to determine possible restrictions to its employment in an operative radar system schedule, we designed a simplified model of the complex OTHR-SW scenario. In this section, we outline the most significant hypotheses assumed for this purpose, explaining how they affect the CR procedure applicability in an actual radar context.
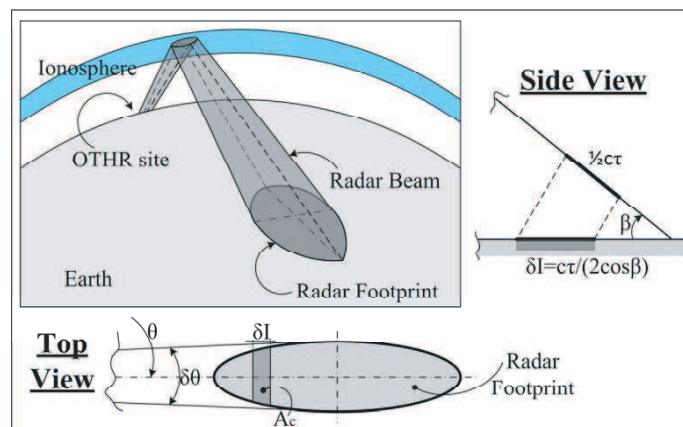

Figure 2: Radar footprint and clutter area (radar patch). c = light speed; τ = pulse length; β = take-off angle; δI = pulse projection; θ = azimuthal angle; $\delta\theta$ = radar beam azimuthal span angle; Ac = clutter area.

The radar system on which the proposed CR method is developed is a monostatic OTHR-SW that transmits a vertically polarized unmodulated pulse of length τ, with a take-off angle β and a beam azimuthal span angle $\delta\theta$, as shown in Fig. 2.

---

[1]In order to avoid the possibility of similar clutter signatures on the same azimuth, it is necessary to employ the proposed CR procedure on favourable (in terms of sea-land transitions dislocation) binary clutter profiles.

The Earth magnetic field effects on ray propagation are neglected, while the spherical geometry of the planet and the ionospheric layers is substituted by its projection on parallel planes. Note that, since for a given radar position the former aspect appears time-independent and the latter is just geometric, they can both be taken into account by a constant multiplicative coefficient.

The propagation path (that includes the ionospheric reflection) is the scenario's aspect that requires more restrictive assumptions in order to fit in a simplified geometrical model. It's assumed that a stable single-hop ionospheric path is available (hypothesis that appears to be correct at Europeans latitudes) with mirror ray reflection, identical for transmitted signal and received echo. At this stage the iono-scattering effect is neglected[2], i.e., the Ionosphere is modeled as a stratified medium, with no geographic gradient.
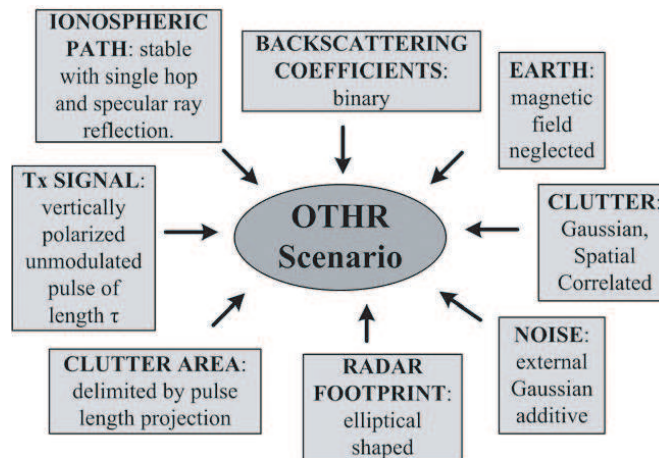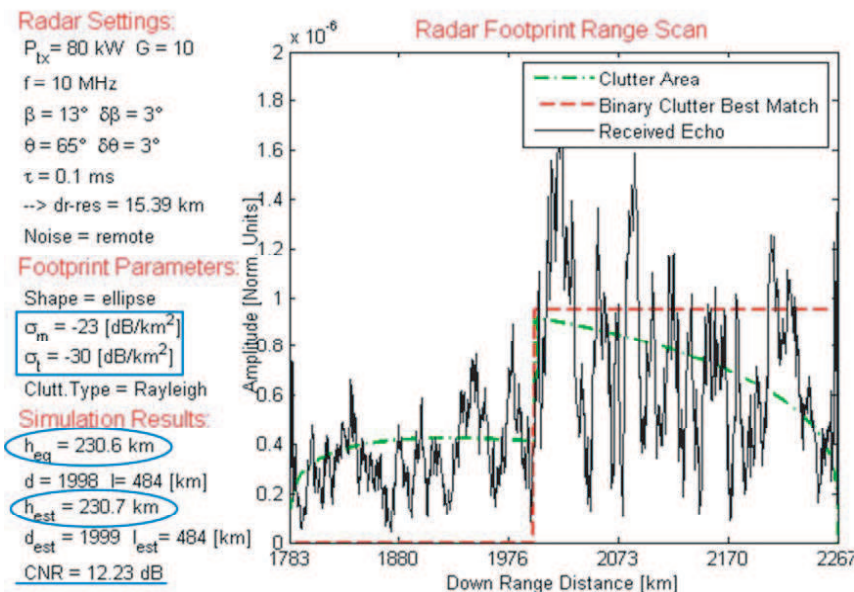

Figure 3: OTHR simulated scenario hypotheses.

Figure 4: Snapshot of a simulation result. On the left, the main radar parameters: sea & land backscattering coefficients (σ_m and σ_t); actual & estimated ionospheric reflection height (h_{eq} and h_{est}); clutter-to-noise ratio (CNR). On the right, plot of amplitude versus down range (echo pertinent to a single radar pulse).

The surface clutter is considered binary (that implies sharp-cut sea-land transitions). Such hypothesis is confirmed by the marked difference between sea and land backscattering coefficients σ_m and σ_t [8, 9]. A spatially correlated Gaussian clutter is assumed [6, 7].

---

[2] Generally multipath distorts the surface backscattered signature by superimposing signals scattered at different ground ranges in one radar range bin [2]. This effect has not yet been taken into account in the model.

The system noise for an OTHR-SW originates predominantly from the external, divided into three main components: atmospheric, cosmic and man-made. We represented the overall noise as an additive Gaussian process with assigned (in accordance with the radar site location) mean value, statistically independent from clutter.

The radar footprint, intersection between an elliptical base cone (the radar beam) and an oblate spheroid (the Earth surface), is geometrically approximated with an ellipse, while we suppose the clutter area limited in range by the radar pulse length projection on the Earth surface (see Fig. 2). Fig. 3 summarizes schematically the assumptions made for the basic scenario components.

4. RESULTS AND CONCLUSIONS

Simulations have been performed under different geographic contexts, in terms of number and relative location within the radar footprint of sea-land transitions, intensity of backscattering coefficients, size of the clutter area, etc. In the following, we discuss the most significant results providing a performance analysis of the proposed CR method.

Figure 4 shows a simulation result carried out under the hypotheses outlined in the previous section, with a plot of normalized amplitude versus down-range distance of the received radar echo (continuous line), the selected (cross-correlation maxima) binary clutter profile (dashed line) and the clutter area profile during the radar footprint scan (dash-dot line).

The results of simulation trials in different scenarios suggest that in case of Clutter-to-Noise Ratio (CNR) higher than $3\,\mathrm{dB}$ (CNR $= 12.23\,\mathrm{dB}$ in this test) a minimum differential sea-land backscattering coefficient ($\Delta\sigma = \sigma_m - \sigma_t$) of $7\,\mathrm{dB/km}^2$ is required to guarantee an error smaller than $3\,\mathrm{km}$ in the estimate of the actual ionospheric equivalent reflection height (h_{eq}).

Such requirement is promising for the feasibility of the proposed CR method. In fact, even if the bibliography about real HF sea-land backscattering coefficients is scarce, in [9] we find the following statement: "Extensive observations [. . .] indicated that, averaged over a wide area, sea clutter power levels were about an order of magnitude higher than those from an area of similar size in the central United States.".

Note that in the proposed simulation a ionospheric reflection height bias of hundred meters leads to an error in the radar footprint range position estimation of about one kilometer. This value is quite satisfactory if compared with the OTHR-SW down-range resolution (dr-res) that, with a pulse length $\tau = 0.1\,\mathrm{s}$ and a take-off angle $\beta = 13°$, corresponds to about $15.4\,\mathrm{km}$.

In conclusion, the simulation results we presented here suggest that the proposed method, based on a priori knowledge of the sea-land transition dislocation within the surveillance area, can be actually exploited for CR procedures in an OTHR-SW operative context.

The next step in this OTH radar context is the development of a specific simulation tool allowing an easier management of the simplified scenario hypotheses and of the radar parameters. It will be possible to improve the overall model with more complex and realistic hypotheses, in order to test the CR method in scenarios closer to the real ones. In particular we are interested in the development of a complete ionospheric model accounting of non uniform space-time structure.

ACKNOWLEDGMENT

REFERENCES

1. Krolik, J. L. and R. H. Anderson, "Maximum likelihood coordinate registration for Over-The-Horizon Radar," *IEEE Transactions on Signal Processing*, Vol. 45, No. 4, 945–959, 1997.
2. Wheadon, N. S., J. C. Whitehouse, J. D. Milson, and R. N. Herring, "Ionospheric modelling and target coordinate registration for HF Sky-Wave Radars," *Sixth International Conference on HF Radio Systems and Techniques*, 258–266, Jul. 1994.
3. Weijers, B. and D. Choi, "OTH-B coordinate registration experiment using an HF beacon," *IEEE International Radar Conference*, 49–52, 1993.
4. Frazer, G. J., "Forward-based receiver augmentation for OTHR," *IEEE Radar Conference*, 373–378, Apr. 2007.
5. Torrez, W. C. and W. J. Yssel, "Over-The-Horizon Radar surveillance sensor fusion for enhanced coordinate registration," *IEEE Proceedings on Information, Decision and Control*, 227–230, Feb. 1999.
6. Ward, K. D., R. J. A. Tough, and S. Watts, "Sea clutter: Scattering, the K distribution and radar performance," *The Institution of Engineering and Technology*, 2006.

7. Khan, R. H., "Ocean-clutter model for high-frequency radar," *IEEE Journal of Oceanic Engineering*, Vol. 16, No. 2, 181–188, 1991.
8. Barrick, D. E., "Remote sensing of sea state by radar," *OCEANS*, Vol. 4, 186–192, Sep. 1972.
9. Skolnik, M., *Radar Handbook*, 2nd Edition, Chap. 24, McGraw-Hill, 1990.

Infrared Signature Studies of Aircraft and Helicopters

S. P. Mahulikar, **G. A. Rao**, **H. R. Sonawane**, and **H. S. S. Prasad**

Department of Aerospace Engineering, Indian Institute of Technology, Bombay, India

Abstract— The infrared (IR) seekers have exploited techniques to passively acquire and intercept airborne targets, by detecting their IR energy [1]. The basic principle of IR detection is the discrimination of target's IR radiance in the detector's wavelength band with the background IR radiance (atmospheric emission/solar radiation) [2]. In an aircraft, the internal sources include plume and surface emissions; and power-plant is the major and reliable source. The aircraft rear fuselage skin of a typical military aircraft is heated by the flow of hot combustion products in the embedded engine [12]. The solid angle subtended by the rear fuselage skin is an order of magnitude larger than that of the tailpipe [9]. Therefore, its contribution is significant especially in the 8–12 micron band; in which, IR-detection is possible also due to external sources, e.g., earthshine and skyshine reflection [19].

Unlike surfaces of solids, gases emit and absorb radiation only at discrete wavelengths associated with specific rotational and vibrational frequencies. These frequencies depend on the particular type of molecule, temperature, pressure, and molecular concentration of radiation participating species [13]. The atmosphere limits the use of the IR spectrum to specific bands called as *atmospheric windows*; and has a crucial role, which includes that of transmission and background radiance [8]. For reducing detection by IR-guided missiles, aircraft and helicopters use IR Signature Suppression (IRSS) techniques. A well-designed IRSS system can drastically reduce IRSL by restricting the visibility of hot parts and by matching the visible radiance with the background [22]. Their effect in reducing target's susceptibility (P_{H}) can be gauged by models that relate *the two*. Due to significant advancements in the performance of IR-detectors, modern missiles are generally constrained by their burnout range rather than their lock-on range. The 'lethal range' is a function of target's lock-on range, target's velocity, missile velocity, missile burnout range, missile's guidance logic and blast kill radius; and it is a superior estimate of P_{H} [23].

1. INTRODUCTION

The tactical advantages of passive detection and tracking by infrared (IR) signature seeking missiles pose a great threat to the survivability of aircraft and helicopters. The requirements of Radar Cross-Section (RCS) reduction are much more stringent as compared to IR Signature Level (IRSL), due to much higher sensitivity of IRSL relative to RCS, to detection range. The IR seekers have exploited techniques to passively acquire and intercept airborne targets, by detecting their IR energy [1]. Developments in IR detection and tracking have increased the effectiveness of IR guided missiles, which are now portable (e.g., MANPADS) and have proliferated world-wide [2]. The atmosphere limits the use of the IR spectrum to specific bands, e.g., 3–5 μm and 8–12 μm, called as *atmospheric windows* [3]; which are used for target detection and tracking. Enhanced IR-detection capabilities are enabled by cooled tri-metal photon detectors (e.g., HgCdTe), and advanced manufacturing and Charge-Coupled Device read-out technologies. The rapid advances in VLSI processor and IR detector array technology have led to enhanced sensitivity, low noise, multi-spectral, and smart detection capabilities [4, 5]. Smart sensors have sensing and signal processing capabilities that enhance the target signal-to-noise ratio by background clutter suppression [6]. The basic principle of IR detection is the discrimination of target's IR radiance in the detector's wavelength band with the background IR radiance (atmospheric emission/solar radiation).

2. IRSL SOURCES AND THEIR ESTIMATION

The sources of IRSL in an aircraft and their classification is in Fig. 1, and Fig. 2 illustrates the input parameters needed for predicting IRSL of an aircraft as seen by IR-detector. The internal IR-sources include plume emission and surface emissions from the following: (a) engine hot parts (tail-pipe), (b) airframe skin heated by the engine (rear fuselage), and (c) airframe skin heated by aerodynamic heating especially at high Mach numbers (forward stagnation region of nose, wing leading edges, and air intakes). Power-plant is the major and reliable source of IRSL because of the large amount of heat produced by combustion inside the gas turbine engine. The aircraft rear fuselage skin of a typical military aircraft is heated by the flow of hot combustion products in the embedded engine. Though the spectral radiance of rear-fuselage is less than that of tailpipe, IR emission from the
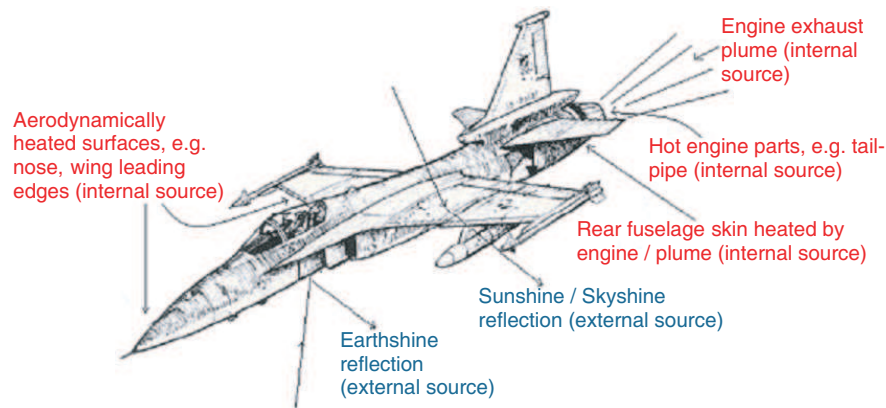
Figure 1: Sources of IR radiance from aircraft and their classification [2].
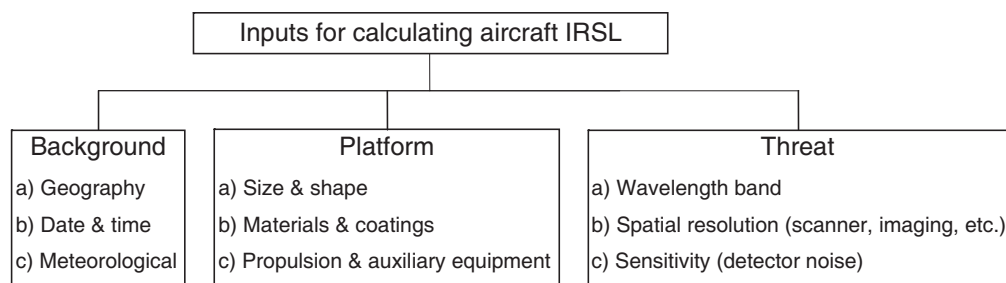

Figure 2: Classification of inputs for calculating IRSL on detector [7].

rear-fuselage is important especially in 8–12 μm band [8]. Also, the solid angle subtended by the rear fuselage skin is an order of magnitude larger than the tailpipe [9]. The spectral reflectance and emissivity (ε) of the aircraft surface depends on the applied coatings/paintings. Mahulikar et al. [10] discussed that it is desirable to treat different regions of the airframe with coatings of different emissivities. Mahulikar et al. [11, 12] developed a model incorporating the radiation interchange in engine layout, to compute the temperature distribution of rear-fuselage skin for given engine operating conditions. Unlike surfaces of solids, gases emit and absorb radiation only at discrete wavelengths (λ) associated with specific rotational and vibrational frequencies. These frequencies depend on the particular type of molecule, temperature, pressure, and molecular concentration of radiation participating species. Gases with asymmetrical molecular structures such as H_2O (vap.), CO_2, and CO are responsible for the emission of IR radiation from the plume in 3–5 μm band. Mahulikar et al. [13] concluded that IRSL from non-afterburning plume is much less significant than from tailpipe and rear fuselage skin, especially in 8–12 μm band.

The atmosphere has a crucial role in the estimation of IRSL, which includes that of atmospheric transmission and background radiance. Examples of atmospheric propagation models are: (i) LOWTRAN (Low-resolution atmospheric Transmission), (ii) MODTRAN (Moderate-resolution atmospheric Transmission), and (iii) HITRAN (High-resolution atmospheric Transmission). Versions after LOWTRAN-4 included atmospheric radiance (with scattered solar/lunar radiance) and direct solar/lunar radiance, in addition to atmospheric transmission. Since IRSL of aircraft on the detector is determined by its contrast with the background (sky) that it replaces, sky IR radiance at different altitudes (h) is needed.

The LOWTRAN estimates sky radiance at different h in specified wavelength band in a particular direction, thereby providing directional spectral emissivity $\varepsilon(\lambda, \theta)$. Fig. 3 shows the directional spectral radiance per unit solid angle (ω) of clear sky ($B_{\lambda\omega}$) obtained using LOWTRAN code for different θ, for mid-latitude summer atmosphere. The predictions of LOWTRAN code qualitatively match with the data of Berdahl & Fromberg [14], except in 16–20 μm band (not of interest for IRSL studies). Their experimental data [14] was obtained with radiometer instrumentation for the same conditions. For estimating the skyshine at a specific h, hemispherical spectral emissivity averaged over the entire hemispherical range is needed. Berger's empirical-based model [15] estimates background/sky/atmospheric radiance (hemispherical spectral emissivity) on the ground, but not at

different h. It uses ground and dew point temperatures as inputs, and estimates sky radiance with reasonable accuracy using less computational time. Berger & Bathiebo [16] and Berger et al. [17] respectively estimated the total emissivity of sky from the hemispherical spectral emissivity of sky and total sky radiation, at different h. The estimation of directional spectral emissivity of Berger & Bathiebo [18] can be used for obtaining the total spectral emissivity. From Fig. 3, it is seen that for $\theta \to 90°$, the spectral sky radiance is almost like blackbody radiation at the base altitude temperature. Fig. 4 [19] shows the hemispherical spectral irradiance of average skyshine at different h using LOWTRAN-7, for mid-latitude summer conditions. For $h = 0$ km, it matches with the predictions of the model of Berger [15] in quality and quantity. It is inferred from Fig. 4 that the skyshine is high for 8–12 μm band as compared to 3–5 μm band, especially for low h. Further, from the earth's surface up to $h = 3$ km, the atmosphere itself is responsible for the background IR radiance in the atmospheric windows.

The role of earthshine is important for low-flying aircraft and helicopter in 8–12 μm band [10]. It consists of emission from the ground and reflection of solar radiation during the day (of lesser importance in 8–12 μm band). The emission from Earth's surface is a function of several parameters; e.g., vegetation, temperature, humidity, type of soil and rock. Other than vegetation, most surfaces characterizing earth are predominantly diffuse and behave as grey bodies with high ε.
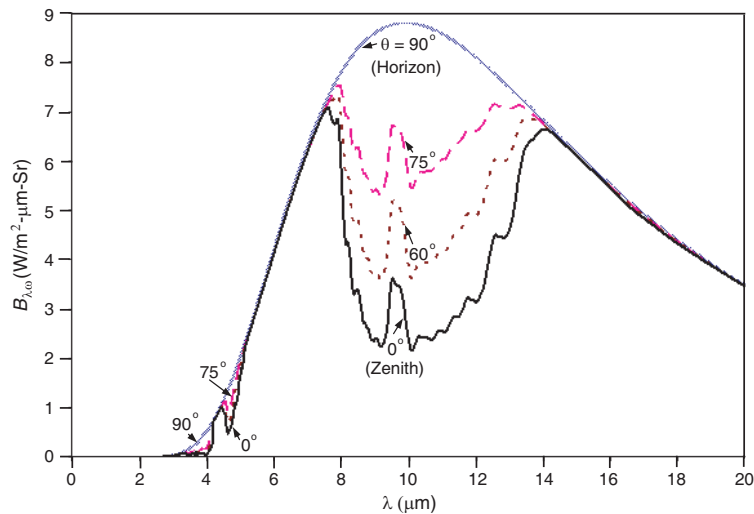

Figure 3: Directional spectral radiance of clear sky for mid-latitude summer atmosphere.
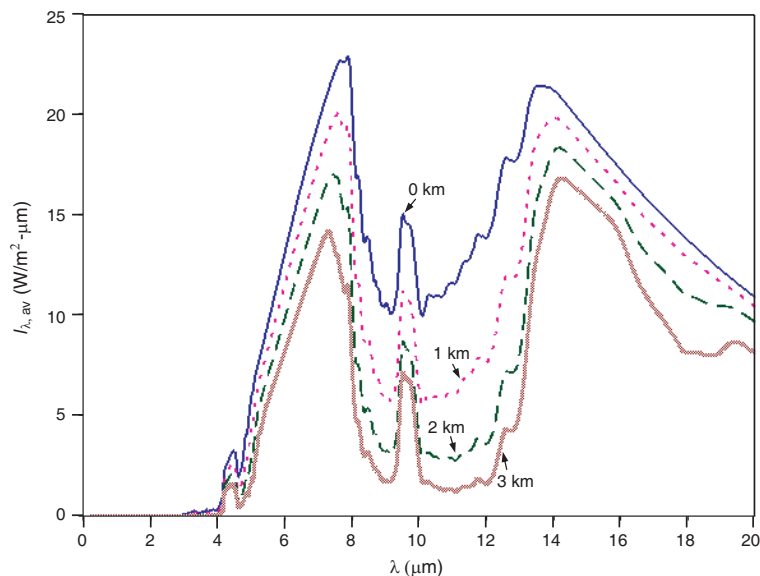

Figure 4: Hemispherical irradiance of clear sky for mid-latitude summer atmosphere [19].

Most agricultural plants have $\varepsilon \sim 0.95$ and soil surface has $\varepsilon \sim 0.93$ [20]. Atmospheric transmission decreases with increasing h; therefore, in 8–12 μm band, earthshine is important especially for low altitude missions and is dominant relative to skyshine and sunshine. Above a particular h (~ 5 km), the change in irradiance is insignificant. The effect of earthshine decreases with increase in ε_{ac}, because of a decrease in surface reflectivity.

The amount of solar radiation received on the earth's day-side surface is determined by the sun angle, state of the atmosphere, and altitude. The solar radiation outside the atmosphere is given by the solar constant, which consists of the entire spectrum of solar radiation (including IR). The solar constant is the amount of incoming solar radiation per unit area on the outer surface of the Earth's atmosphere, in a plane perpendicular to the sun-rays. It is measured by satellite to be approximately 1366 W/m^2, and can also be estimated from the temperature of the sun and the solid angle subtended by the earth at the sun. The spectral distribution of sunshine reflection from aircraft resembles that of the solar blackbody radiation at 6000 K. However, it is modified by the following factors: (i) atmospheric transmission; (ii) angle between sun, aircraft, and observer; (iii) shape of the reflecting surfaces; (iv) type of reflection (BRDF) and surface reflectivity. The knowledge of solar irradiance at different altitudes in the atmosphere is needed to compute solar heating of aircraft surface, sunshine, and earthshine. The temperature increase due to solar heating on the sun-side of the aircraft is typically $5°$C [21], which is not considered in NIRATAM. Solar heating of the upper surface of aircraft can reduce the IR-contrast when viewed from top; for which, the earth's surface at higher temperature is the background.

3. IRSL SUPPRESSION

For reducing detection by IR-guided missiles, aircraft and helicopters use IR Signature Suppression (IRSS) techniques (Ref. e.g., [22]). A well-designed IRSS system can drastically reduce IRSL by restricting the visibility of hot parts and by matching the visible radiance with the background. Their effect in reducing target's susceptibility (P_H) can be gauged by models that relate the two [23].

4. IR SUSCEPTIBILITY

The locus of points around a target where the IR seeker locks-on, i.e., the missile tracks the target automatically is the lock-on envelop; which depends only on target's IRSL and seeker's performance. Conventionally, the lock-on envelope was considered to evaluate P_H; but based on an Essential Element Analysis, it is found to fail in providing a comprehensive assessment of P_H. Due to advancements in the performance of IR-detectors, modern missiles are generally constrained by their burnout range rather than their lock-on range. The 'lethal envelope' is the locus of points around the target in which if the missile is launched, there is a high probability of the missile hitting it or detonating sufficiently close to it to cause unserviceable damage. The 'lethal envelope' is a function of target's lock-on envelop, missile's burn-out range, missile's velocity, target's velocity, missile's guidance logic and blast kill radius; and it is a superior estimate of P_H [23]. As the ratio of target's lock-on range to missile's burnout range decreases, the 'lethal envelope' tends to 'lock-on envelope'; hence, 'lock-on envelope' gives an assessment of P_H for older generation missiles.

REFERENCES

1. Rao, G. A. and S. P. Mahulikar, "Integrated review of stealth technology and its role in airpower," *The Aeronautical Journal*, Vol. 106, No. 1066, 629–641, 2002.
2. Mahulikar, S. P., H. R. Sonawane, and G. A. Rao, "Infrared signature studies of aerospace vehicles," *Progress in Aerospace Sciences*, Vol. 43, No. 7–8, 218–245, 2007.
3. Gebbie, H. A., W. R. Harding, C. Hilsum, A. W. Pryce, and V. Roberts, "Atmospheric transmission in the 1 to 14 μm region," *Proceedings of the Royal Society (London) Series A*, Vol. 206, No. 1084, 87–10, 1951.
4. Anderson, N. C., "Target-to-background performance of various detectors for a wide range of operating conditions," *Infrared Physics*, Vol. 4, No. 3, 149–156, 1964.
5. Stillwell, P. F. T. C., "Thermal imaging," *Journal of Physics E: Scientific Instruments*, Vol. 14, No. 10, 1113–1118, 1981.
6. Corsi, C., "Smart sensors," *Infrared Physics & Technology*, Vol. 49, No. 3, 192–197, 2007.
7. Davis, W. R. and J. Thompson, "Developing an IR signature specification for military platforms using modern simulation techniques," *Annual SMI Pursuit of Stealth Conference*, London, 2002.

8. Rao, G. A. and S. P. Mahulikar, "Effect of atmospheric transmission and radiance on aircraft infrared signatures," *Journal of Aircraft*, Vol. 42, No. 4, 1046–1054, 2005.

9. Mahulikar, S. P., S. K. Potnuru, and P. S. Kolhe, "Analytical estimation of solid angle subtended by complex well-resolved surfaces for infrared detection studies," *Applied Optics*, Vol. 46, No. 22, 4991–4998, 2007.

10. Mahulikar, S. P., G. A. Rao, and P. S. Kolhe, "Infrared signatures of low flying aircraft and their rear fuselage skin's emissivity optimisation," *Journal of Aircraft*, Vol. 43, No. 1, 226–232, 2006.

11. Mahulikar, S. P., S. K. Sane, U. N. Gaitonde, and A. G. Marathe, "Numerical studies of infrared signature levels of complete aircraft," *The Aeronautical Journal*, Vol. 105, No. 1046, 185–192, 2001.

12. Mahulikar, S. P., P. S. Kolhe, and G. A. Rao, "Skin temperature prediction of aircraft rear fuselage with multimode thermal model," *Journal of Thermophysics and Heat Transfer*, Vol. 19, No. 1, 114–124, 2005.

13. Mahulikar, S. P., G. A. Rao, S. K. Sane, and A. G. Marathe, "Aircraft plume infrared signature in nonafterburning mode," *Journal of Thermophysics and Heat Transfer*, Vol. 19, No. 3, 413–415, 2005.

14. Berdahl, P. and R. Fromberg, "The thermal radiance of clear skies," *Solar Energy*, Vol. 29, No. 4, 299–314, 1982.

15. Berger, X. A., "Simple model for computing the spectral radiance of clear skies," *Solar Energy*, Vol. 40, No. 4, 321–333, 1988.

16. Berger, X. and J. Bathiebo, "From spectral clear sky emissivity to total clear sky emissivity," *Solar & Wind Technology*, Vol. 6, No. 5, 551–556, 1989.

17. Berger, X., J. Bathiebo, F. Kieno, and C. N. Awanou, "Clear sky radiation as a function of altitude," *Renewable Energy*, Vol. 2, No. 2, 139–157, 1992.

18. Berger, X. and J. Bathiebo, "Directional spectral emissivities of clear skies," *Renewable Energy*, Vol. 28, No. 12, 1925–1933, 2003.

19. Mahulikar, S. P., S. K. Potnuru, and G. A. Rao, "Study of sunshine, skyshine, and earthshine for aircraft infrared detection," *Journal of Optics A: Pure & Applied Optics*, Vol. 11, No. 4, Art. No. 045703, 10, 2009.

20. Hipps, L. E., "The infrared emissivities of soil and artemisia tridentate and subsequent temperature correction in a shrub-steppe ecosystem," *Remote Sensing of Environment*, Vol. 27, No. 3, 337–342, 1989.

21. Beier, K., "Infrared radiation model for aircraft and re-entry vehicle," *Proceedings of the SPIE — The International Society for Optical Engineering: Infrared Technology XIV*, Vol. 972, 363–374, International Society for Optical Engineering, Bellingham, WA, USA, 1988.

22. Mahulikar, S. P., H. S. S. Prasad, and S. K. Potnuru, "Infrared signature suppression of helicopter engine duct based on 'conceal and camouflage," *Journal of Propulsion & Power*, Vol. 24, No. 3, 613–618, 2008.

23. Rao, G. A. and S. P. Mahulikar, "New criterion for aircraft susceptibility to infrared homing missiles," *Aerospace Science & Technology*, Vol. 9, No. 8, 701–712, 2005.

An Analytic Method for Computing the Time-Dependent Electromagnetic Fields in Anisotropic Crystals

V. G. Yakhno[1] and T. M. Yakhno[2]

[1]Electrical and Electronics Engineering Department, Dokuz Eylul University, Turkey
[2]Computer Engineering Department, Izmir University, Turkey

Abstract— A homogeneous non-dispersive anisotropic crystal, characterized by a symmetric positive definite permittivity tensor and a positive constant permeability, is considered. An analytic method for deriving the time-dependent electric and magnetic fields in this anisotropic crystal is suggested in the paper. This method is based on explicit formulae for electric and magnetic fields which are solutions of initial value problems for Maxwell's equations describing the wave propagation in the anisotropic crystal. The suggested method consists in several steps: Maxwell's equations are written in the second-order form in terms of the Fourier modes with respect to space variables; explicit formulae for the Fourier modes of electric and magnetic fields are derived using the matrix transformations and the technique of ordinary differential equations; finally, the inverse Fourier transform is applied to obtained formulae for the Fourier modes.

1. INTRODUCTION

Many technically important materials (media) and crystals which become popular in new technologies are anisotropic. For example, the widely used substrate material sapphire and the lithium niobate ($LiNbO_3$), which is used in the design of integrated optics devices, are anisotropic [1, 2]. The physical properties of homogeneous isotropic crystals do not depend on the direction and the position inside the medium. At the same time physical properties of anisotropic crystals essentially depend on orientation and position. An anisotropic crystal is called homogeneous when its physical properties depend on orientation and do not depend on position.

Crystals react to applied electromagnetic fields in a variety of ways. For example, if a point pulse source is located in an optical homogeneous isotropic crystal, then fronts of electric and magnetic waves have spherical shapes. The shapes of the fronts in anisotropic crystals are not spherical and have very peculiar forms. The simulation of invisible electromagnetic wave phenomena is a very important issue of modern inter-discipline engineering areas.

The observations of electric and magnetic fields in different anisotropic crystals generated by electric currents give an information about the dependence of electromagnetic field behavior and the structure of crystals. These observations allow engineers to study properties of known anisotropic crystals and design new crystals with the certain response to electric and magnetic fields for given source. Nowadays real experiments and measurements are successfully combined with computer modeling and simulation. Thus most of electromagnetic scattering problems, initial value and initial boundary value problems have been solved by numerical methods, in particular, finite elements method, boundary elements methods, finite difference method, nodal method (see, for example, works [3–5] and their references).

The time-dependent electric and magnetic fields in homogeneous non-dispersive crystals are governed by the following Maxwell's system (see [6–8])

$$\nabla \times \mathbf{H} = \varepsilon_0 \bar{\bar{\varepsilon}} \frac{\partial \mathbf{E}}{\partial t} + \mathbf{j}, \quad \nabla \times \mathbf{E} = -\mu_0 \frac{\partial \mathbf{H}}{\partial t}, \qquad \nabla \cdot (\mu_0 \mathbf{H}) = 0, \quad \nabla \cdot (\mu_0 \bar{\bar{\varepsilon}} \mathbf{E}) = \rho, \qquad (1)$$

where $x = (x_1, x_2, x_3)$ is a space variable from R^3, t is a time variable from R, $\mathbf{E} = (E_1, E_2, E_3)$, $\mathbf{H} = (H_1, H_2, H_3)$ are electric and magnetic fields, $E_k = E_k(x, t)$, $H_k = H_k(x, t)$, $k = 1, 2, 3$; $\mathbf{j} = (j_1, j_2, j_3)$ is the density of the electric current, $j_k = j_k(x, t)$, $k = 1, 2, 3$; ε_0 and μ_0 are the permittivity and permeability of the free space respectively, $\bar{\bar{\varepsilon}} = (\varepsilon_{ij})_{3\times3}$ is the 3×3 matrix; ρ is the density of electric charges. The electric charges and current are sources of electromagnetic waves. We assume these sources are given. It follows from (1) that electric charges and current have to satisfy the conservation law of charges

$$\frac{\partial \rho}{\partial t} + \nabla \cdot \mathbf{j} = 0. \qquad (2)$$

In this paper we suppose that

$$\mathbf{E} = 0, \quad \mathbf{H} = 0, \quad \mathbf{j}, \quad \rho = 0, \quad \text{for} \quad t \le 0. \tag{3}$$

Remark 1. The first two equations of (1) under conditions (3) imply the last two equalities of (1) (we assume here that (2) is satisfied).

Remark 2. By combining the first two Equation (1), under conditions (3) we obtain the second-order forms of the Maxwell's equations with initial data (see, for example [5], pages 4–5)

$$\varepsilon_0\mu_0\bar{\bar{\varepsilon}}\frac{\partial^2\mathbf{E}}{\partial t^2} + \nabla \times \nabla \times \mathbf{E} = -\mu_0\frac{\partial\mathbf{j}}{\partial t}, \quad \mathbf{E}|_{t\le0} = 0, \quad \left.\frac{\partial\mathbf{E}}{\partial t}\right|_{t\le0} = 0, \tag{4}$$

$$\varepsilon_0\mu_0\frac{\partial^2\mathbf{H}}{\partial t^2} + \nabla \times \bar{\bar{\varepsilon}}^{-1}\nabla \times \mathbf{H} = \nabla \times (\bar{\bar{\varepsilon}}^{-1}\mathbf{j}), \quad \mathbf{H}|_{t\le0} = 0, \quad \left.\frac{\partial\mathbf{H}}{\partial t}\right|_{t\le0} = 0, \tag{5}$$

where $\bar{\bar{\varepsilon}}^{-1}$ is the inverse matrix to $\bar{\bar{\varepsilon}}$.

The Cauchy problem for the system of crystal optics (system (4), where $\bar{\bar{\varepsilon}}$ is a diagonal matrix with different positive elements with smooth data and an exact solution of this problem has been described by Courant and Hilbert in [9] (see pages 603–612). Burridge and Qian in [10] have used a 'plane wave' approach to obtain an explicit formula for a fundamental solution of the same system of crystal optics. This formula has been expressed in terms of real loop integrals according to Herglotz-Petrovskii formula. Using this formula the numerical computation of the fundamental solution has been obtained. Nowadays computers can perform very complicated symbolic computations and this opens up new possibilities. Symbolic computations can be considered as useful tools for analytical methods that can provide exact solutions of problems. So, for example, Yakhno in [11] has used matrix symbolic computations for constructing an explicit formula for a fundamental solution (the Green's function) for the system of crystal optics (system (4), where $\bar{\bar{\varepsilon}}$ is a symmetric positive definite matrix with constant elements). The approach of the paper [11] has been successfully used in [12–14] for simulations of waves in homogeneous anisotropic dielectrics.

In the present paper, arbitrary positive definite matrice $\bar{\bar{\varepsilon}}$ with constant elements is considered. The main objects of the paper are the following initial value problems of the radiation from the electric current in anisotropic crystals.

Problem 1. Let $\mathbf{j}(x,t)$ be a given vector-function such that $\mathbf{j}|_{t<0} = 0$. Find a vector function $\mathbf{E}(x,t)$ satisfying (4).

Problem 2. Let $\mathbf{j}(x,t)$ be a given vector-function and $\mathbf{j}|_{t<0} = 0$. Find a vector function $\mathbf{H}(x,t)$ satisfying (5).

In the present paper, new explicit formulae for solutions of Problem 1 and Problem 2 are obtained.

The paper is organized as follows. In Section 2 Problem 1 is written in terms of the Fourier transform with respect to space variables and the explicit formula for the electric field is derived. In Section 3 Problem 2 is written in terms of the Fourier mode and the explicit formula for magnetic field is obtained. Section 4 concludes the paper.

2. DERIVING AN EXPLICIT FORMULA FOR ELECTRIC FIELD

Let $\tilde{\mathbf{E}}(\nu,t)$, $\tilde{\mathbf{j}}(\nu,t)$ be the Fourier transform images of the electric field $\mathbf{E}(x,t)$ and current $\mathbf{j}(x,t)$ respectively with respect to $x = (x_1, x_2, x_3) \in R^3$, i.e.,

$$\tilde{\mathbf{E}}(\nu,t) = \mathcal{F}_x[\mathbf{E}](\nu,t), \quad \tilde{\mathbf{j}}(\nu,t) = \mathcal{F}_x[\mathbf{j}](\nu,t), \quad \nu = (\nu_1, \nu_2, \nu_3),$$

$$\mathcal{F}_x[\mathbf{E}](\nu,t) = \int_{-\infty}^{+\infty} \int_{-\infty}^{+\infty} \int_{-\infty}^{+\infty} \mathbf{E}(x,t)e^{i\nu x}dx_1dx_2dx_3, \quad x\nu = x_1\nu_1 + x_2\nu_2 + x_3\nu_3, \quad i^2 = -1.$$

The problem (4) can be written in the term of the Fourier image $\tilde{\mathbf{E}}(\nu,t)$ as follows

$$\bar{\bar{\varepsilon}}\frac{\partial^2\tilde{\mathbf{E}}}{\partial t^2} + c^2\mathcal{A}_1(\nu)\tilde{\mathbf{E}} = -\frac{1}{\varepsilon_0}\frac{\partial\tilde{\mathbf{j}}}{\partial t}, \quad \left.\tilde{\mathbf{E}}\right|_{t\le0} = 0, \quad \left.\frac{\partial\mathbf{E}}{\partial t}\right|_{t\le0} = 0, \quad \nu \in R^3, \tag{6}$$

where $\tilde{\mathbf{j}} = \mathcal{F}_x[\mathbf{j}](\nu,t)$, $\mathcal{A}_1(\nu)\tilde{\mathbf{E}}(\nu,t) = \mathcal{F}_x[\nabla \times \nabla \times \mathbf{E}](\nu,t)$. Using properties of the Fourier transform we find that $\mathcal{A}_1(\nu)$ is the symmetric positive semi-definite matrix whose elements are defined by

$$A_{11}^1 = \nu_2^2 + \nu_3^2, \qquad A_{22}^1 = \nu_1^2 + \nu_3^2, \qquad A_{33}^1 = \nu_1^2 + \nu_2^2,$$
$$A_{12}^1 = A_{21}^1 = -\nu_1\nu_2, \quad A_{13}^1 = A_{31}^1 = -\nu_1\nu_3, \quad A_{23}^1 = A_{32}^1 = -\nu_2\nu_3.$$

The construction of an exact solution of (6) consists of several steps. In the first step, using the matrix formalism for given symmetric positive semi-definite matrix $\mathcal{A}_1(\nu)$ and the symmetric positive definite matrix $\bar{\bar{\varepsilon}}$ we construct a non-singular matrix $\bar{\bar{T}}$ and a diagonal matrix $\bar{\bar{D}}(\nu) = \mathrm{diag}(d_1(\nu), d_2(\nu), d_3(\nu),)$ with non-negative elements such that

$$\bar{\bar{T}}^T(\nu)\bar{\bar{\varepsilon}}\bar{\bar{T}}(\nu) = \bar{\bar{I}}, \qquad \bar{\bar{T}}^T(\nu)\mathcal{A}_1(\nu)\bar{\bar{T}}(\nu) = \bar{\bar{D}}(\nu), \tag{7}$$

where $\bar{\bar{I}}$ is the identity matrix, $\bar{\bar{T}}^T(\nu)$ is the transposed matrix to $\bar{\bar{T}}(\nu)$.

Remark 3. Computing $\bar{\bar{D}}(\nu)$ and $\bar{\bar{T}}(\nu)$ can be made explicitly by using $\bar{\bar{\varepsilon}}^{-1/2}$. We note that for the given diagonal matrix $\bar{\bar{\varepsilon}} = \mathrm{diag}(\varepsilon_{11}, \varepsilon_{22}, \varepsilon_{33})$ with positive elements on the diagonal the matrix $\bar{\bar{\varepsilon}}^{-1/2}$ is given by $\bar{\bar{\varepsilon}}^{-1/2} = \mathrm{diag}\left(\frac{1}{\sqrt{\varepsilon_{11}}}, \frac{1}{\sqrt{\varepsilon_{22}}}, \frac{1}{\sqrt{\varepsilon_{33}}}\right)$. For the given positive definite non-diagonal matrix $\bar{\bar{\varepsilon}}$ we construct an orthogonal matrix $\bar{\bar{R}}$ by eigenvectors of $\bar{\bar{\varepsilon}}$ such that $\bar{\bar{R}}^T\bar{\bar{\varepsilon}}\bar{\bar{R}} = \bar{\bar{L}} \equiv \mathrm{diag}(\lambda_1, \lambda_2, \lambda_3)$, where $\bar{\bar{R}}^T$ is the transpose matrix to $\bar{\bar{R}}$ and $\lambda_k > 0$, $k = 1, 2, 3$ are eigenvalues of $\bar{\bar{\varepsilon}}$ (see, for example [15]). Then $\bar{\bar{\varepsilon}}^{1/2}$ is defined by $\bar{\bar{\varepsilon}}^{1/2} = \bar{\bar{R}}\bar{\bar{L}}^{1/2}\bar{\bar{R}}^T$, where $\bar{\bar{L}}^{1/2} = \mathrm{diag}(\sqrt{\lambda_1}, \sqrt{\lambda_2}, \sqrt{\lambda_3})$. The matrix $\bar{\bar{\varepsilon}}^{-1/2}$ is the inverse to $\bar{\bar{\varepsilon}}^{1/2}$. Let us take the given positive semi-definite matrix $\mathcal{A}_1(\nu)$ and the matrix $\bar{\bar{\varepsilon}}^{-1/2}$ which assumed to be found. Let us consider the matrix $\bar{\bar{\varepsilon}}^{-1/2}\mathcal{A}_1(\nu)\bar{\bar{\varepsilon}}^{-1/2}$ which is symmetric positive semi-definite. The diagonal matrix $\bar{\bar{D}}(\nu) = \mathrm{diag}(d_1(\nu), d_2(\nu), d_3(\nu))$ is constructed by eigenvalues of $\bar{\bar{\varepsilon}}^{-1/2}\mathcal{A}_1(\nu)\bar{\bar{\varepsilon}}^{-1/2}$. The columns of the orthogonal matrix $\bar{\bar{Q}}(\nu)$ are formed by normalized orthogonal eigenvectors of $\bar{\bar{\varepsilon}}^{-1/2}\mathcal{A}_1(\nu)\bar{\bar{\varepsilon}}^{-1/2}$ corresponding to eigenvalues $d_k(\nu)$, $k = 1, 2, 3$ (see, for example [15]). The matrix $\mathcal{T}(\nu)$ is defined by the formula $\bar{\bar{T}}(\nu) = \bar{\bar{\varepsilon}}^{-1/2}\bar{\bar{Q}}(\nu)$. Using symbolic transformations in MATLAB we have computed the explicit formulae for $\bar{\bar{D}}(\nu)$, $\bar{\bar{T}}(\nu)$ and $\bar{\bar{T}}^T(\nu)$.

In the second step we are looking for the solution of (7) in the form $\tilde{\mathbf{E}}(\nu, t) = \bar{\bar{T}}(\nu)\mathbf{Y}(\nu, t)$, where the matrix $\bar{\bar{T}}(\nu)$ is constructed in the first step and a vector function $\mathbf{Y}(\nu, t)$ is unknown. Substituting $\tilde{\mathbf{E}}(\nu, t) = \bar{\bar{T}}(\nu)\mathbf{Y}(\nu, t)$ into (6) and then multiplying the obtained differential equation by $\bar{\bar{T}}(\nu)^T(\nu)$ and using (7) we find

$$\frac{d^2\mathbf{Y}}{dt^2} + c^2\bar{\bar{D}}(\nu)\mathbf{Y} = -\frac{1}{\varepsilon_0}\bar{\bar{T}}(\nu)^T(\nu)\frac{\partial\tilde{\mathbf{j}}}{\partial t}, \qquad \tilde{\mathbf{Y}}\Big|_{t\leq 0} = 0, \quad \frac{\partial\mathbf{Y}}{\partial t}\Big|_{t\leq 0} = 0, \quad \nu \in R^3, \tag{8}$$

where $c = 1/(\varepsilon_0\mu_0)$ is the light velocity.

In the third step of the method, using the ordinary differential equations technique (see for example [16]), a solution of the initial value problem (8) is given by

$$\mathbf{Y}(\nu, t) = -\frac{1}{\varepsilon_0}\int_0^t \cos\left[c\sqrt{\bar{\bar{D}}}(t - \tau)\right]\bar{\bar{T}}(\nu)^T(\nu)\tilde{\mathbf{j}}(\nu, \tau)d\tau, \quad t > 0, \tag{9}$$

where $\cos\left[c\sqrt{\bar{\bar{D}}}t\right]$ is the diagonal matrix whose diagonal elements are $\cos(c\sqrt{d_n(\nu)}t)$, $n = 1, 2, 3$.

In the last step the electric field $\mathbf{E}(x, t)$ is determined by the inverse Fourier transform $\mathcal{F}_\nu^{-1}$ to the constructed Fourier image of the electric field $\tilde{\mathbf{E}}(\nu, t) = \bar{\bar{T}}(\nu)\mathbf{Y}(\nu, t)$, $\nu = (\nu_1, \nu_2, \nu_3) \in R^3$, $t > 0$.

3. DERIVING AN EXPLICIT FORMULA FOR MAGNETIC FIELD

Let $\tilde{\mathbf{H}}(\nu, t) = \mathcal{F}_x[\mathbf{H}](\nu, t)$. The problem (5) can be written in terms of $\tilde{\mathbf{H}}(\nu, t)$ as follows

$$\frac{\partial^2\tilde{\mathbf{H}}}{\partial t^2} + c^2\mathcal{A}_2(\nu)\tilde{\mathbf{H}} = -ic^2[\nu \times \bar{\bar{\varepsilon}}^{-1}\tilde{\mathbf{j}}], \qquad \tilde{\mathbf{H}}\Big|_{t\leq 0} = 0, \quad \frac{\partial\mathbf{H}}{\partial t}\Big|_{t\leq 0} = 0, \quad \nu \in R^3, \tag{10}$$

where $\tilde{\mathbf{j}} = \mathcal{F}_x[\mathbf{j}](\nu, t)$, $\mathcal{A}_2(\nu)\tilde{\mathbf{H}}(\nu, t) = \mathcal{F}_x[\nabla \times \bar{\bar{\varepsilon}}^{-1}\nabla \times \mathbf{H}](\nu, t)$.

Using properties of the Fourier transform we derive the following relation

$$\mathcal{A}_2(\nu) = -\mathcal{S}(\nu)\bar{\bar{\varepsilon}}^{-1}\mathcal{S}(\nu), \quad \mathcal{S}(\nu) = \begin{pmatrix} 0 & -\nu_3 & \nu_2 \\ \nu_3 & 0 & -\nu_1 \\ -\nu_2 & \nu_1 & 0 \end{pmatrix}. \tag{11}$$

We note that the inverse matrix $\bar{\bar{\varepsilon}}^{-1} = (m_{ij})_{3\times 3}$ to $\bar{\bar{\varepsilon}} = (\varepsilon_{ij})_{3\times 3}$ is symmetric and positive definite. Using (11), we find that elements of the matrix $\mathcal{A}_2(\nu) = (A_{ij}^2)_{3\times 3}$ are given by the following formulae

$$A_{11}^2(\nu) = m_{33}\nu_2^2 + m_{22}\nu_3^2 - 2m_{23}\nu_2\nu_3, \quad A_{22}^2(\nu) = m_{33}\nu_1^2 + m_{11}\nu_3^2 - 2m_{13}\nu_1\nu_3,$$

$$A_{33}^2(\nu) = m_{22}\nu_1^2 + m_{11}\nu_2^2 - 2m_{12}\nu_1\nu_2, \quad A_{12}^2(\nu) = A_{21}^2(\nu) = -m_{33}\nu_1\nu_2 - m_{12}\nu_3^2 + m_{23}\nu_1\nu_3 + m_{13}\nu_2\nu_3,$$

$$A_{23}^2(\nu) = A_{32}^2(\nu) = -m_{11}\nu_2\nu_3 - m_{23}\nu_1^2 + m_{13}\nu_1\nu_2 + m_{12}\nu_1\nu_3,$$

$$A_{13}^2(\nu) = A_{31}^2(\nu) = -A_{22}^2\nu_1\nu_3 - m_{13}\nu_2^2 + m_{23}\nu_1\nu_2 + m_{12}\nu_2\nu_3.$$

This means that $\mathcal{A}_2(\nu)$ is the symmetric matrix. Let $\mathcal{S}^T(\nu)$ be the transpose matrix to $\mathcal{S}(\nu)$. The equality $\mathcal{S}^T(\nu) = -\mathcal{S}(\nu)$ follows from (11). Using this equality we find the chain of equalities $< \mathcal{A}_2(\nu)\eta, \eta > = < -\mathcal{S}(\nu)\bar{\bar{\varepsilon}}^{-1}\mathcal{S}(\nu)\eta, \eta > = < \bar{\bar{\varepsilon}}^{-1}\mathcal{S}(\nu)\eta, \mathcal{S}(\nu)\eta >$ for any $\eta = (\eta_1, \eta_2, \eta_3) \in R^3$ and any $\nu = (\nu_1, \nu_2, \nu_3) \in R^3$. Here $< \cdot, \cdot >$ means the inner product in R^3, i.e., $< \xi, \eta > = \xi_1\eta_1 + \xi_2\eta_2 + \xi_3\eta_3$ for points $\xi = (\xi_1, \xi_2, \xi_3) \in R^3$ and $\eta = (\eta_1, \eta_2, \eta_3) \in R^3$. Since $\bar{\bar{\varepsilon}}^{-1}$ is positive definite then we have $< \bar{\bar{\varepsilon}}^{-1}\mathcal{S}(\nu)\eta, \mathcal{S}(\nu)\eta > \geq 0$ for arbitrary points $\eta = (\eta_1, \eta_2, \eta_3) \in R^3$ and $\nu = (\nu_1, \nu_2, \nu_3) \in R^3$. The positive semi-definiteness of $\mathcal{A}_2(\nu)$ follows from the above mentioned chain equalities and the last inequality.

The construction of an exact solution of (10) consists of four steps. In the first step, using the symbolic transformations in MATLAB for the given symmetric positive semi-definite matrix $\mathcal{A}_2(\nu)$ we construct an orthogonal matrix $\bar{\bar{P}}$ and a diagonal matrix $\bar{\bar{K}}(\nu) = \mathrm{diag}(k_1(\nu), k_2(\nu), k_3(\nu),)$ with non-negative elements such that

$$\bar{\bar{P}}^T(\nu)\bar{\bar{P}}(\nu) = \bar{\bar{I}}, \qquad \bar{\bar{P}}^T(\nu)\mathcal{A}_2(\nu)\bar{\bar{P}}(\nu) = \bar{\bar{K}}(\nu), \tag{12}$$

where $\bar{\bar{I}}$ is the identity matrix, $\bar{\bar{P}}^T(\nu)$ is the transposed matrix to $\bar{\bar{P}}(\nu)$.

In the second step we are looking for the solution of (10) in the form $\tilde{\mathbf{H}}(\nu, t) = \bar{\bar{P}}(\nu)\mathbf{Z}(\nu, t)$, where the matrix $\bar{\bar{P}}(\nu)$ is constructed in the first step and a vector function $\mathbf{Z}(\nu, t)$ is unknown. Substituting $\tilde{\mathbf{H}}(\nu, t) = \bar{\bar{T}}(\nu)\mathbf{Z}(\nu, t)$ into (10) and then multiplying the obtained differential equation by $\bar{\bar{P}}(\nu)^T(\nu)$ and using (12) we find

$$\frac{d^2\mathbf{Z}}{dt^2} + c^2\bar{\bar{K}}(\nu)\mathbf{Z} = -ic^2\bar{\bar{P}}(\nu)^T(\nu)[\nu \times \bar{\bar{\varepsilon}}^{-1}\tilde{\mathbf{j}}], \qquad \tilde{\mathbf{Z}}\Big|_{t\leq 0} = 0, \quad \frac{\partial\mathbf{Z}}{\partial t}\Big|_{t\leq 0} = 0, \quad \nu \in R^3. \tag{13}$$

In the third step of the method, using the ordinary differential equations technique (see, for example [16]), a solution of the initial value problem (13) is given by

$$\mathbf{Z}(\nu, t) = -ic \int_0^t \bar{\bar{K}}^{-1/2}(\nu) \sin\left[c\sqrt{\bar{\bar{K}}}(t - \tau)\right] \bar{\bar{P}}(\nu)^T(\nu)\left[\nu \times \bar{\bar{\varepsilon}}^{-1}\tilde{\mathbf{j}}(\nu, \tau)\right] d\tau, \quad t > 0, \tag{14}$$

where $\sin\left[c\sqrt{\bar{\bar{K}}}t\right]$ is the diagonal matrix whose diagonal elements are $\sin(c\sqrt{k_n(\nu)}t)$ and $\bar{\bar{K}}^{-1/2}(\nu)$ is the diagonal matrix whose diagonal elements are $1/\sqrt{k_n(\nu)}$, $n = 1, 2, 3$.

In the last step the electric field $\mathbf{H}(x, t)$ is determined by the inverse Fourier transform $\mathcal{F}_\nu^{-1}$ to the constructed Fourier image of the electric field $\tilde{\mathbf{H}}(\nu, t) = \bar{\bar{P}}(\nu)\mathbf{Z}(\nu, t)$, $\nu = (\nu_1, \nu_2, \nu_3) \in R^3$, $t > 0$.

4. CONCLUSION

In the paper a novel efficient method of constructing new explicit formulae for electric and magnetic fields arising from a given electric current in anisotropic homogeneous non-dispersive crystals is described. This method is based on matrix symbolic computations and the inverse Fourier transform which is done numerically. The robustness of our method is based on the modern achievements of computational algebra which allow us to make symbolic transformations of cumbersome formulae and matrices. This method combines in a rational way analytical techniques and numerical computations. Using this method we have generated images of electric and magnetic fields components which are a result of the electromagnetic radiations arising from a pulse dipole with a fixed polarization in different anisotropic crystals.

ACKNOWLEDGMENT

REFERENCES
1. Dolgaev, S. I., A. A. Lyalin, et al., "Fast etching of sapphire by a visible range quasi-cw laser radiation," *Applied Surface Scince*, Vol. 96–98, 491–496, 1996.
2. Yim, Y.-S. and S.-Y. Shin, "Lithium niobate integrated-optic voltage sensor with variabl sensing ranges," *Optics Communications*, Vol. 152, 225–228, 1998.
3. Yee, K. S., "Numerical solution of initial boundary value problems involving Maxwell's equations in isotropic media," *IEEE Transactions on Antennas and Propagation*, Vol. 14, No. 3, 302–307, 1966.
4. Monk, P., *Finite Element Methods for Maxwell's Equations*, Clarendon Press, Oxford, 2003.
5. Cohen, G. C., *Higher-order Numerical Methods for Transient Wave Equations*, Springer Verlag, Berlin, 2002.
6. Ramo, S., J. R. Whinnery, and T. Duzer, *Fields and Waves in Communication Electronics*, John Wiley and Sons, New York, 1994.
7. Kong, K. J., *Electromagnetic Wave Theory*, John Wiley and Sons, New York, 1986.
8. Eom, H. J., *Electromagnetic Wave Theory for Boundary-value Problems*, Springer, Berlin, 2004.
9. Courant, R. and D. Hilbert, *Methods of Mathematical Physics*, Vol. 2, Interscience, New York, 1962.
10. Burridge, R. and J. Qian, "The fundamental solution of the time-dependent system of crystal optics," *European Journal of Applied Mathematics*, Vol. 17, 63–94, 2006.
11. Yakhno, V. G., "Constracting Green's function for time-depending Maxwell system in anisotropic dielectrics," *Journal of Physics A: Mathematical and General*, Vol. 38, 2277–2287, 2005.
12. Yakhno, V. G., T. M. Yakhno, and M. Kasap, "A novel approach for modelling and simulation of electromagnetic waves in anisotropic dielectrics," *International Journal of Solids and Structures*, Vol. 43, 6261–6276, 2006.
13. Yakhno, V. G. and T. M. Yakhno, "Modelling and simulation of electric and magnetic fields in homogeneous non-dispersive anisotropic materials," *Computers and Structures*, Vol. 85, 1623–1634, 2007.
14. Yakhno, V. G., "Computing and simulation of time-dependent electromagnetic fields in homogeneous anisotropic materials," *International Journal of Engineering Science*, Vol. 46, 411–426, 2008.
15. Goldberg, J. L., *Matrix Theory With Applications*, McGraw-Hill, New York, 1992.
16. Boyce, W. E. and R. C. DiPrima, *Elementary Differential Equations and Boundary Value Problems*, Wiley, New York, 1992.

Design of Wide Band Tunable Birefringent Filters with Liquid Crystals

Ofir Aharon and I. Abdulhalim

Department of Electro Optic Engineering, Ben Gurion University, Beer Sheva 84105, Israel

Abstract— We demonstrate LC tunable filters designed for integration into biomedical optical imaging systems and can be utilized to many other areas. Two types of tunable filters with wide dynamic range are presented based on a stack of birefringent plates similar to Lyot based configuration. Modification of sets of Lyot filters controlled by different sets of external electric field allowed us to eliminate unwanted orders. In a different approach integration of an additional thin liquid crystal cell (retarder) between crossed polarizers to eliminate one order of the Lyot filter. Another configuration proposed uses a sequence of retarders each between crossed polarizers but with increasing thickness following an arithmetic sequence.

1. INTRODUCTION

Liquid crystal tunable filters (LCTFs) belong to a class of optical components that selectively transmit or reflect certain wavelength bands of light. They are based on various material configurations and are opening up new pathways for efficient, low-cost optical components and integrated systems. Birefringence filters are usually composed of a number of birefringent plates such as liquid crystal retarders (LCRs) which can be controlled and tuned with a small voltage. Tunable filters are most commonly used for optical telecommunication [1–4] but lately also for biomedical spectral imaging [5, 6] such as Raman chemical imaging [7, 8] and fluorescence microscopy applications. The basic design rule of an optical filter [9–15] is against two major parameters, the bandwidth defined by the full width at half maximum (FWHM) of its main output peak and the free spectral range (FSR) or the dynamic range. These two parameters are very desirable for wavelength filtering and tuning. In cases when a very narrow bandwidth is needed for highly selective filters, the throughput power is usually degraded due to a multiple usage of LCRs and polarizers. For the majority of biomedical applications the bandwidth requirement is moderate, for example for fluorescence and Hyper Spectral Imaging (HSI) [16–18], 20 nm FWHM is adequate. The Lyot and Šolc based LCTFs use the retardation to create constructive and destructive interference between two orthogonal polarizations, to pass a narrow passband of light. LCTFs have the advantages of not just miniaturization of the designed system but also tuning the centre wavelength with no mechanical movements and the capability of rapid wavelength selection within millisecond to microsecond tuning speeds. The dynamic spectral range obtained by using these filters can be as large as few hundreds of nanometers, thus covering the whole visible and near infrared ranges.

2. CONCEPT AND DESIGN

Lyot filter consists of N birefringent plates (retarders) each between parallel polarizers oriented such that the polarizer axis makes an angle of 45 degs to the optic axis (Figure 1(a)). The thickness d of the thinnest plate is such that it satisfies the full wave condition: $d = m\lambda/\Delta n$ where $\Delta n = n_e - n_o$ is the birefringence and m is a positive integer. The thickness of the jth plate is $2^{j-1}d$. The transfer function of the jth birefringent plate between parallel polarizers has the form: $T_j = \cos^2(2^{j-2}\Gamma)$ where $\Gamma = 2\pi d\Delta n/\lambda$ is the phase retardation accumulated in passing through the thinnest retarder. The transfer function for the N plates is:

$$T = \prod_{j=1}^{N} \cos^2(2^{j-2}\Gamma) = \left(\frac{\sin 2^{N-1}\Gamma}{2^N \sin \Gamma/2} \right)^2 \tag{1}$$

This transfer function gives peak wavelengths, FWHM and FSR given by:

$$\lambda_{peak} = \frac{d(n_e - n_o)}{m}; \quad \text{FWHM} = \frac{\lambda_{peak}}{2^N m}; \quad \text{FSR} = \frac{\lambda_{peak}}{(m+1)} \tag{2}$$

where $m = 1, 2, 3, \ldots$, and λ_{peak} is the peak wavelength. The angular field of view is given by: $n_o(\text{FWHM}/\lambda_{peak})^{0.5}$ defined as the angle of incidence when the peak shifts by half the width.

The concept of a two stage Lyot filter is shown in Figures 1(a) and 1(c), where d is the first retarder thickness and $2d$ is for the 2nd, both between parallel polarizers having extinction ratio of 1000. Transmission spectra for the 1st (dotted, $d = 8000\,\text{nm}$) and 2nd (dashed) retarders within the Lyot filter as well as their multiplication output (bold) are shown in Figure 1(c). The width and dynamic range of the Lyot filter are determined mainly by the first retarder following Equation (2). The spectral bandwidth can be decreased by increasing the number of retarders N, however the dynamic range does not change. In working with the first order peak one can get wide dynamic range, however the FWHM is larger by factor of 4 than the 2nd order. For example taking $\lambda_{peak} = 900\,\text{nm}$, the FSR for $m = 1$ using Equation (2) is 450 nm however the FWHM will be 225 nm if two stages ($N = 2$) are used. Working with the 2nd order peak $m = 2$ yields FSR $= 300\,\text{nm}$ and FWHM $= 125\,\text{nm}$. Adding more Lyot stages means adding retarders with thicknesses of $4d$, $8d$ or more which makes the tuning speed very slow and increases the attenuation due to the additional interfaces and polarizers. In our design we overcome this problem by working with higher order peaks to get smaller spectral width and eliminating the nearby orders to get wider dynamic range. The additional retarder between crossed polarizers shown in Figure 1(b) is designed so that it eliminates the 3rd order peak as shown in Figure 1(d).

For designing the filter we relied on the properties of Nematic LC materials of the E-series of Merck. Specifically we used the 4-pentyl-4'-cyanobiphenyl (E44) purchased from Merck. With strong anchoring where the LC molecules orientations on the surfaces are fixed the LC director profile is nonuniform along the normal to substrates z when a voltage V is applied. The total retardation [2] should then be calculated by the integral over

$$\delta = \frac{2\pi}{\lambda} \int_0^d [n_e(z, V) - n_o]dz \tag{3}$$

where λ is the wavelength in vacuum, z is the coordinate normal to the substrates, V is the applied voltage, n_e is the extraordinary index of refraction which depends on the LC molecules tilt angle θ, no is the ordinary index of refraction, and d is the LC layer thickness. The tilt angle profile $\theta(z)$ depends on the external voltage and on the surface anchoring conditions. In reality the angle of the LC molecules is governed by a nonlinear differential equation [2] which results in a larger angle at the middle of the LC layer compared to the facets at $z = 0$ and $z = d$.
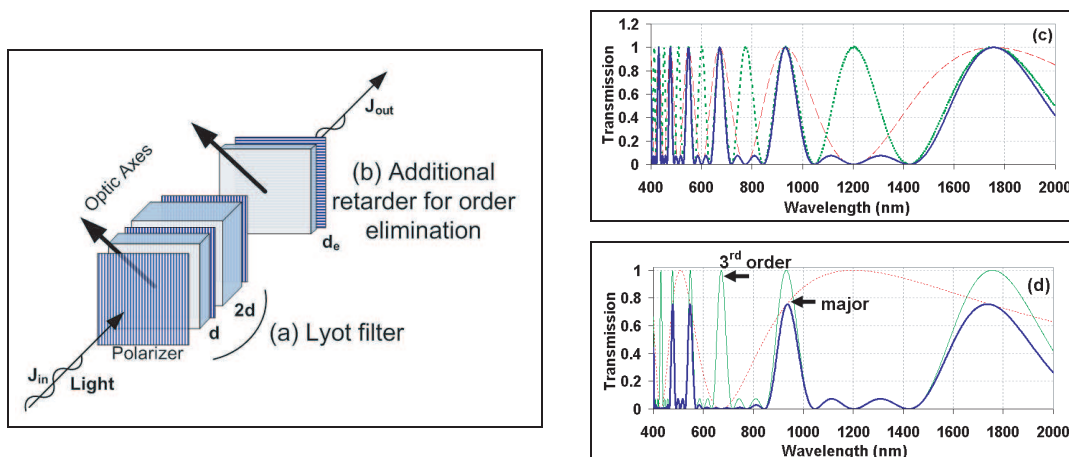

Figure 1. (a) Liquid crystal Lyot filter composed of two stages, d is the first retarder thickness, (b) the additional eliminator retarder between crossed polarizers. (c) Transmission spectra for the 1st (dotted, $d = 8000\,\text{nm}$) and 2nd (dashed) retarders within the Lyot filter as well as their multiplication which gives the Lyot filter output (bold). (d) The output of the additional retarder (order eliminator) between crossed polarizers with thickness $de = 2666\,\text{nm}$ (dashed), the Lyot output (dotted) and their multiplication spectrum (bold) showing the elimination of the 3rd order peak of Lyot filter, resulting in FSR at this particular case of almost 500 nm.

The design algorithm composed of determining the set of retardations $\{\delta_j\}$ with $j = 1, 2, 3, \ldots,$ N where j is the retarder number in the filter structure and N is the total number of retarders. Once this set of retardations is found for each wavelength, the LC dynamic equation is solved and the retardation integral in Equation (3) is calculated as a function of the applied voltage in order to determine the corresponding set of voltages $\{V_j\}$. The dispersion of the LC refractive indices calculated based on the Sellmieir type relations [19], which for E44 the constants are given as follows when the wavelength is in nm: $A_o = 9.8468 \times 10^{-5}\,\text{nm}^{-2}$; $B_o = 4.3937 \times 10^{-5}\,\text{nm}^{-2}$; $A_{||} = 6.7553 \times 10^{-5}\,\text{nm}^{-2}$; $B_{||} = 2.3057 \times 10^{-5}\,\text{nm}^{-2}$.

3. FILTER TRANSFER FUNCTION

The transfer function for an LCR between two parallel polarizers with the optic axis oriented at 45° with respect to the polarizer axis is $\cos^2(\delta/2)$. Similarly, when it is between crossed polarizers the transfer function is $\sin^2(\delta/2)$. The filter proposed is composed of Lyot filter followed by a collection of additional retarders each between crossed polarizers oriented by 45 degrees with respect to the polarizer axis. This latter configuration was found by itself to act as a filter with FSR when the retarders thicknesses are d, $3d$, $5d$, $(2j-1)d$, with d being the thickness of thinnest retarder. We found that adding this odd sequence width to the Lyot filter can eliminate the third order as well as any odd order of the Lyot filter and by that widening the FSR. The combined filter transfer function for the general case is then:

$$T = \left(\frac{\sin 2^{N-1}\Gamma}{2^N \sin \Gamma/2} \right)^2 \cdot \left[\prod_{j=1}^{N} \sin^2((2j-1)\delta_e/2) \right] \tag{4}$$

where δ_e is the phase retardation for the first eliminator retarder, the left brackets are the transmission of the Lyot filter and the right brackets are the transmission of what we call **Jump** filter. For the system of two LCRs between parallel polarizers and the additional LCR between crossed polarizers (third LCR) we get the transmission function:

$$T_{out} = \left(\cos\left(\frac{\delta_1}{2} \right)^2 \cdot \cos\left(\frac{\delta_2}{2} \right)^2 \right) \cdot \left[\sin\left(\frac{\delta_3}{2} \right)^2 \right] \tag{5}$$

where δ_j with $j = 1, 2, 3$, for LCR j corresponds to the retardation calculated using the integral in Equation (3) with the corresponding thickness for each LCR. The expression in left brackets describes the transfer function for a two stage Lyot filter (the first two LCRs) and the right brackets are for the Jump filter with one stage. Additional retarders will only narrow the FWHM of the peaks without prominent effect on the FSR.

The question now is how the multiplication by the transfer function of the Jump filter or even one retarder of its sequence as the third LCR-δ_3, improves the FSR? The basic idea is to design this third retarder (the eliminator) so that its minima coincide with the 3rd order peak of the Lyot filter. We are looking for a mathematical condition when $\sin^2(\delta_3/2) = 0$ for the eliminator retarder (Figure 1(b)) and $\cos^2(\delta_1/2) = 1$ for the first Lyot's retarder. The latest condition gives: $\delta_1 = 2\pi m$, which imposes the condition on the eliminator LCR: $\delta_3 = 2\pi l$ where l is another positive integer. Assuming we want to eliminate the mth peak of the Lyot filter then using: $\lambda_m = d\Delta n_1/m$ we get the following condition:

$$\frac{d_3 \Delta n_3}{l} = \frac{d_1 \Delta n_1}{m} \tag{6}$$

where here $d_3 = d_e$ is the thickness of the eliminator retarder and Δn_3 is its total birefringence. As discussed before, the set of voltages that we find for each wavelength should assure that this equation holds, meaning that the total effective birefringence values Δn_j, $j = 1, 3$ should be found numerically corresponding to the voltage values V_j, $j = 1, 3$ where Δn_j is calculated from the integral over the whole LC retarder as in Equation (3) without the $2\pi/\lambda$ term.

4. EXPERIMENTAL AND RESULTS

First option of eliminating an order and broadening the FSR is given in Figure 1(d), which shows the Lyot filter (Figure 1(a)) with the additional retarder (Figure 1(b)), of thickness $de = 2666\,\text{nm}$.

The first minimum of its transfer function coincides with the third order peak of the Lyot filter output, thus improving the FSR without damaging the second order severely (around ~ 970 nm in Figure 1(d)). The first order peak tuning can also be considered if one is interested in the IR range. The order eliminator minima can then be situated at the second order peak and the FSR will increase to 1000 nm. In this case the order eliminator will have a thickness of 4 µm and can be tuned to get the elimination of the second, third, and the forth orders as necessary depending on the spectral range of interest. The experimental filter outputs shown in Figure 2 closely resemble the designed filter especially in the visible regime since our polarizers have good extinction ratio in the range from 450 nm to 850 nm. The retarders thicknesses we built were $d_1 = 8899$ nm, $d_2 = 16043$ nm for the first and the second retarders of the Lyot filter, and the thickness of the additional retarder as the order eliminator was $de = 2600$ nm. The thicknesses d_1 and d_2 are not at the nominal values of 8000 nm and 16000 nm, yet we were able to construct the transmission spectrum according to the design by having the flexibility in driving each LCR at different voltage. The second LCR with $d_2 = 16043$ nm was actually made of two retarders each of thickness nearly 8000 nm. Although this has the disadvantage of increasing the number of glass interfaces, its advantage is in keeping fast switching speed. The slowest switching time depends on the thickness of 8000 nm and can be computed to be between 25 msec to 65 msec for voltages between 1.9 V to 3 V [2, 16]. An improvement in spectrum shape as well as the FSR can be done by adding an additional two retarders to the Jump filter (see Figure 3). The construction of the Jump filter was made by retarders with thickness of 2500 nm, 7000 nm and 12700 nm to simulate nominal thicknesses of 2200 nm, 6600 nm and 11000 nm. The Jump filter retarders were calibrated and controlled by using our LabView code with a function generator PCMCIA card.
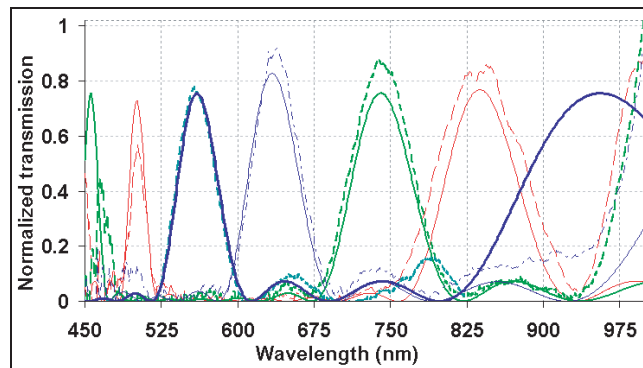

Figure 2. Four examples of measured spectra (dashed lines) and the theoretical fits (solid lines), for the 2nd order peak of the Lyot filter at 838 nm, 740 nm, 634 nm and 560 nm when the sets of voltages for the first and the second Lyot's retarders as well as for the additional eliminator retarder were: {2.23 V, 2 V, 2.16 V}, {2.492 V, 2.28 V, 2.455 V}, {2.785 V, 2.61 V, 2.79 V}, {3.0625 V, 2.915 V, 3.105 V} correspondingly.
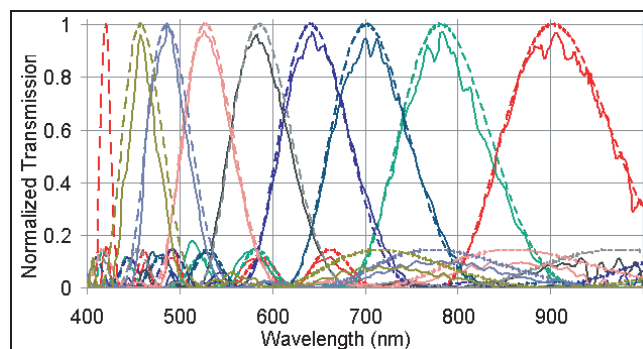

Figure 3. Output of the designed Jump filter (dashed) and the measured spectra (line). The thicknesses of the LCRs are 2500 nm, 7000 nm and 12700 nm.

The voltages sets are summarized below:

Wavelength (nm)	FWHM (nm)	$V_1(V_{ms})$	$V_2(V_{ms})$	$V_3(V_{ms})$
903	134	1.03	0.26	1.21
782	109	1.3	1.45	1.4
702	95	1.43	1.59	1.53
641	83	1.47	1.74	1.63
586	69	1.65	1.86	1.77
528	57	1.85	1.99	1.93
487	54	2	2.16	2.08
459	47	2.1	2.26	2.22

5. CONCLUSION

We demonstrated novel tunable filtering concepts with an improved FSR by adding one retarder between crossed polarizers or using a sequence of LC retarders between crossed polarizer with increasing thicknesses in odd arithmetic incrimination. Reasonable agreement is found between the simulated and measured outputs of the filter. To compensate for small variations in the retarders thicknesses, multichannel voltage supply was provided so that each retarder is under different voltage. The same concept can be applied to obtain narrow band high dynamic range tunable filtering by simply increasing the number of the Jump filter stages. Presently the integration of the Jump filter demonstrated in this article is going on within a skin spectral imaging system in our lab. For this particular application the spectral width of few tens of nm is adequate to enable under skin imaging of abnormalities [20].

ACKNOWLEDGMENT

REFERENCES

1. Yariv, A. and P. Yeh, *Optical Wave in Crystals*, John Wiley, New York, 1984.
2. Eldadaa, L., "Optical communication components," *Rev. Sci. Instrum.*, Vol. 75, No. 3, 2004.
3. Sneh, A. and K. M. Johnson, "High speed continuously tunable liquid crystal filter for WDM networks," *J. Lightwave. Technol.*, Vol. 14, No. 6, 1067, 1996.
4. Abdulhalim, I., G. Moddel, and K. M. Johnson, "High speed analog spatial light modulator using an a-Si: H photosensor and an electroclinic liquid crystal," *Appl. Phys. Lett.*, Vol. 55, No. 16, 1603, 1989.
5. Chaudhari, A. J., F. Darvas, J. R. Bading, R. A. Moats, P. S. Conti, D. J. Smith, S. R. Cherry, and R. M. Leahy, "Hyperspectral and multispectral bioluminescence optical tomography for small animal imaging," *Phys. Med. Biol.*, Vol. 50, 5421–5441, 2005.
6. Gat, N., "Imaging spectroscopy using tunable filters: A review," *Proc. SPIE*, Vol. 4056, 50–64, 2000.
7. Miller, P. J. and C. C. Hoyt, "Multispectral imaging with a liquid crystal tunable filter," *Proc. SPIE*, Vol. 2345, 354–65, 1995.
8. Morris, R. H., C. C. Hoyt, P. Miller, J. P. Treado, and J. Patrick, "Liquid crystal tunable filter Raman chemical imaging," *Appl. Spect.*, Vol. 50, No. 6, 697–819, 1996.
9. Saeed, S., P. J. Bos, and Z. Li, "A method of generating full color in a liquid crystal display using birefringent filters," *Jpn. J. Appl. Phys.*, Vol. 40, 3266–3271, 2001.
10. Hamdi, R., B. E. Benkelfat, Q. Zou, and Y. Gottesman, "Bandwidth tuning of hybrid liquid-crystal solc filters based on an optical cancelling technique," *Opt. Com.*, Vol. 269, No. 1, 64–68, 2007.
11. Stockley, J. E. and G. D. Sharp, "Fabry-Perot etalon with polymer cholesteric liquid-crystal mirrors," *Opt. Lett.*, Vol. 24, No. 1, 1999.
12. Zhuang, Z., Y. J. Kim, and J. S. Patel, "Behavior of the cholesteric liquid-crystal fabry-perot cavity in the bragg reflection band," *Phys. Rev. Lett.*, Vol. 84, No. 6, 2000.
13. Masterson, H. J., G. D. Sharp, and K. M. Johnson, "Ferroelectric liquid-crystal tunable filter," *Opt. Lett.*, Vol. 14, No. 22, 1249–1251, 1989.

14. Sharp, G. D. and K. M. Johnson, "A new RGB tunable filter technology," *Proc. SPIE*, Vol. 12, No. 2650, 98–105, 1996.

15. Sharp, G. D., K. M. Johnson, and D. Doroski, "Continuously tunable smectic A* liquid-crystal color filter," *Opt. Lett.*, Vol. 15, No. 10, 523–525, 1990.

16. Gal, S., E. Eidinger, Z. Zalevsky, D. Mendlovic, and E. Marom, "Tunable birefringent filters-optimal iterative design," *Opt. Exp.*, Vol. 10, No. 26, 1534–1541, 2002.

17. Saeed, S. and P. Bos, "Multispectrum, spatially addressable polarization interference filter," *J. Opt. Soc. Am. A*, Vol. 19, 2301–12, 2002.

18. Hardeberg, J. Y., F. Schmitt, and H. Brettel, "Multispectral color image capture using a liquid crystal tunable filter," *Opt. Eng.*, Vol. 41, 48–2532, 2002.

19. Abdulhalim, I., "Dispersion relations for liquid crystals using the anisotropic Lorentz model with geometrical effects," *Liq. Cryst.*, Vol. 33, 1027–1041, 2006.

20. Aharon, O., A. Safrani, R. Moses, and I. Abdulhalim, "Liquid crystal tunable filters and polarization controllers for biomedical optical imaging," *Proc. SPIE*, Vol. 7050, 70500P, 2008.

Design of Composite Electromagnetic Wave Absorber Made of Fine Aluminum Particles Dispersed in Polystyrene Resin by Controlling Permeability

K. Sakai, **Y. Wada**, **Y. Sato**, **and S. Yoshikado**

Department of Electronics, Doshisha University, Japan

Abstract— The ability to control the relative complex permeability μ_r^* of composites made of fine aluminum particles dispersed in polystyrene resin was investigated for the purpose of designing electromagnetic wave absorbers with good absorption properties at frequencies above 1 GHz. The volume mixture ratio V and particle size of aluminum were varied and the frequency dependences of μ_r^*, the relative complex permittivity ε_r^*, and the return loss were measured. Theoretical values of μ_r^* for the composites were also calculated using Maxwell's equations. The measured value of μ_r', the real part of μ_r^*, was found to decrease with increasing frequency in the low frequency range. However, at high frequencies, μ_r' was almost independent of frequency and decreased proportionately with V. In addition, the measured value of μ_r'' was found to be proportional to V and inversely proportional to the aluminum particle size. These results showed good agreement with the calculated values of μ_r' and μ_r''. An electromagnetic wave absorber with a flexible design was proposed based on the ability to control μ_r' and μ_r'' independently by adjusting V and the aluminum particle size.

1. INTRODUCTION

Electromagnetic waves with frequencies higher than 1 GHz are being increasingly used for telecommunication devices such as wireless local area network (LAN), and the frequencies used by these devices is expected shift to values above 10 GHz in the future. For this reason, attempts have been made to develop an electromagnetic wave absorber suitable for these frequency bands [1]. To design such an absorber, control of the frequency dependence of the relative complex permeability μ_r^* and the relative complex permittivity ε_r^* is important because the absorption of electromagnetic waves is determined by these parameters. In particular, μ_r', the real part of μ_r^*, must be less than unity to satisfy the non-reflective condition at frequencies above 10 GHz. The design of such an absorber using metamaterials, in which μ_r^* and ε_r^* can be artificially controlled, has also been reported [2, 3]. Moreover, materials used for absorbers should be low-cost and abundant in order to avoid the depletion of global resources. Composites made from aluminum and polystyrene resin satisfy both of these requirements. The mass density of aluminum and polystyrene is small and they are low-cost materials. Moreover, when an electromagnetic wave of high frequency enters an aluminum particle, an eddy current flows on the particle surface and a reverse magnetic moment is generated. Thus, μ_r' becomes less than unity, and the non-reflective condition is satisfied in the high frequency range. Consequently, the energy of the electromagnetic wave is converted into thermal energy by the eddy current [4].

In this study, the frequency dependences of μ_r^*, ε_r^* and the absorption characteristics of composite electromagnetic wave absorbers made from fine aluminum particles dispersed in polystyrene resin were investigated in the frequency range from 1 MHz to 40 GHz. In addition, μ_r' and μ_r'', the real and imaginary components of μ_r^*, were theoretically calculated and were compared with the measured values in order to control these parameters artificially. In the calculations, the eddy currents which flow inside the aluminum particles, were calculated using Maxwell's equations and used to determine μ_r' and μ_r''.

2. EXPERIMENTS

Commercially available aluminum particles, with average diameters of approximately 8 to 50 μm, were used in this study. Chips of polystyrene resin were dissolved in acetone and the particles were mixed in until they were uniformly dispersed within the resin. Aluminum particle volume ratios of 16.4, 33.8 and 50 vol% were used for each particle size. The mixture was then heated to melt the polystyrene resin and was hot-pressed at a pressure of 5 MPa to form a pellet. This was allowed to cool naturally to room temperature and was processed into a toroidal-core shape (outer diameter of approximately 7 mm, inner diameter of approximately 3 mm) for use in a 7 mm

coaxial line in the frequency range 1 MHz to 12.4 GHz, or into a rectangular shape (P-band: 12.4–18 GHz, 15.80 mm × 7.90 mm, K-band: 18–26.5 GHz, 10.67 mm × 4.32 mm, R-band: 26.5–40 GHz, 7.11 mm × 3.56 mm) for use in a waveguide. The sample was mounted inside the coaxial line or waveguide using silver past to ensure that no gap existed between the sample and the walls of the line/waveguide. The complex scattering matrix elements S_{11}^* (reflection coefficient) and S_{21}^* (transmission coefficient) for the TEM mode (coaxial line) or TE$_{10}$ mode (rectangular waveguide) were measured using a vector network analyzer (Agilent Technology, 8722ES) by the full-two-port method in the frequency range from 1 to 40 GHz. The values of μ_r^* ($\mu_r^* = \mu_r' - j\mu_r''$, $j = \sqrt{-1}$) and ε_r^* ($\varepsilon_r^{*;} = \varepsilon_r' - j\varepsilon_r''$) were calculated from the data of both S_{11}^* and S_{21}^*. In the frequency range from 1 MHz to 1 GHz, the values of μ_r^* and ε_r^* were calculated from the data of the impedance measured by an impedance analyzer (Agilent Technology, 4291A). The complex reflection coefficient Γ^* for a metal-backed single layer absorber was then determined from the values of μ_r^* and ε_r^*. The return loss R for each sample thickness was calculated from Γ^* using the relation $R = 20\log_{10}|\Gamma^*|$. R was calculated at 0.1 mm intervals in the sample thickness range 0.1 to 30 mm.

3. THEORETICAL CALCULATION OF RELATIVE COMPLEX PERMEABILITY

We have previously reported that μ_r' and μ_r'' for a composite composed of aluminum particles dispersed in polystyrene resin are as given below [4].

$$1 - \mu_r' = V \tag{1}$$
$$\mu_r'' = 2V\delta/a \tag{2}$$

Here, V is the volume mixture ratio of aluminum particles in the composite, δ is the skin depth, and a is the radius of the aluminum particle. The skin depth δ in aluminum for an electromagnetic wave is

$$\delta = \sqrt{\frac{2}{\omega\sigma\mu_0\mu_{Mr}'}}. \tag{3}$$

Here, ω is the angular frequency of the electromagnetic wave, σ is the electrical conductivity of aluminum, μ_0 is the permeability in free space and μ_{Mr}' is the real part of the relative complex permeability of the aluminum (μ_{Mr}' is almost 1). However, the measured values of μ_r' and μ_r'' did not agree with the values calculated from Equations (1) and (2) in the low frequency range, where δ is almost the same as the radius of the aluminum particles. This discrepancy is due to the fact that eddy currents, which flow to a depth of more than δ, were neglected. Therefore, in this section, the eddy currents flowing inside the aluminum particles are calculated from Maxwell's equations, and μ_r' and μ_r'' are subsequently determined.

To simplify the discussion, the shape of an aluminum particle is approximated as a cylinder of radius a and length $2a$, as shown in Fig. 1(a). For an incident magnetic field strength of H_0 parallel to the central axis of the cylinder, the eddy current density $J_\varphi(x)$ [A/m^2] may be defined as

$$J_\varphi(x) = Ae^{\left(-\frac{a-x}{\delta}\right)} \tag{4}$$

Here, A is the proportional coefficient and x is the distance from the center of the cylinder. It is assumed that a uniform magnetic field vector $\vec{H}'$ parallel to the central axis of the cylinder is
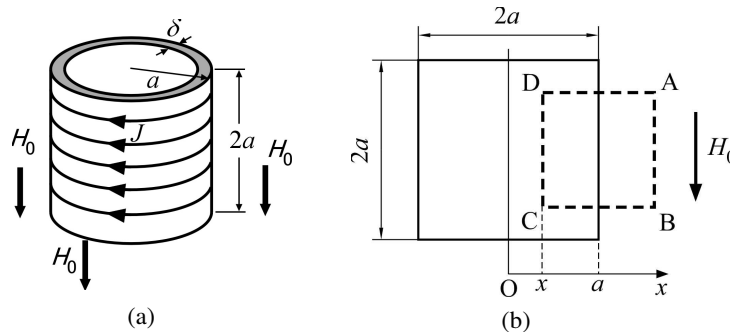

Figure 1: Model of thin metallic cylindrical shell used for calculation of μ_r'. (a) Metallic cylindrical shell. (b) Sectional drawing.

generated by $J_\varphi(x)$. When Ampere's circuital law is applied to the integral route of ABCD shown in Fig. 1(b), the following equation is obtained, because $\vec{H}'$ is $\vec{0}$ along the route AB, $\vec{H}' \perp$ BC and $\vec{H}' \perp$ AD.

$$\oint_{\text{ABCD}} \vec{H}' \cdot d\vec{s} = H'(x)\overline{\text{DC}} = \int_x^a J_\varphi(x)\,dx\,\overline{\text{DC}} \tag{5}$$

Therefore, $H'(x)$ is obtained from Equations (4) and (5).

$$H'(x) = \int_x^a A e^{\left(-\frac{a-x}{\delta}\right)}dx = A e^{-\frac{a}{\delta}}\delta\left(e^{\frac{a}{\delta}} - e^{\frac{x}{\delta}}\right) \tag{6}$$

For an electric field vector $\vec{E}$ and a magnetic flux density vector $\vec{B}$, Maxwell's equation and Stokes' theorem give the following equations.

$$\iint_S (\vec{\nabla} \times \vec{E}) \cdot d\vec{S} = -\frac{\partial}{\partial t}\iint_S \vec{B} \cdot d\vec{S} \tag{7}$$

$$\iint_S (\vec{\nabla} \times \vec{E}) \cdot d\vec{S} = \oint_C \vec{E} \cdot d\vec{s} \tag{8}$$

Here, C is a circle of radius x, whose center is O, and S is the area inside the integral route C. When the radius of C is a ($x = a$), the integral in the right side of Equation (7) is given by

$$\iint_S \vec{B} \cdot d\vec{S} = \iint_S (\vec{B}_0 + \vec{B}') \cdot d\vec{S} = \pi a^2 \mu_0 H_0 + \iint_S \vec{B}' \cdot d\vec{S} \tag{9}$$

$$\iint_S \vec{B}' \cdot d\vec{S} = \int_0^a 2\pi x B'(x)dx$$

$$= 2\pi\mu_0 \int_0^a xH'(x)dx = 2\pi\mu_0 \int_0^a A e^{-\frac{a}{\delta}}\delta x \left(e^{\frac{a}{\delta}} - e^{\frac{x}{\delta}}\right)dx$$

$$= 2\pi\mu_0 A\delta\left(\frac{1}{2}a^2 + \delta^2 - \delta^2 e^{-\frac{a}{\delta}} - \delta a\right) \tag{10}$$

Here, $\vec{B}_0$ is the external magnetic flux density vector and $\vec{B}'$ is the magnetic flux density vector generated by $J_\varphi(x)$. Also, the integral in the right side of Equation (8) is given by

$$\oint_C \vec{E} \cdot d\vec{s} = \oint_C E_\varphi(x)ds = 2\pi a E_\varphi(a) = \frac{2\pi a J_\varphi(a)}{\sigma} = \frac{2\pi a A}{\sigma}. \tag{11}$$

Here, $E_\varphi(x)$ ($= J_\varphi(x)/\sigma$) is the electric field at the circumference of the cylinder. Thus, the following equation is obtained from Equations (9), (10) and (11).

$$\frac{2\pi a A}{\sigma} = -\frac{\partial}{\partial t}\left[\pi a^2 \mu_0 H_0 + 2\pi\mu_0 A\delta\left(\frac{1}{2}a^2 + \delta^2 - \delta^2 e^{-\frac{a}{\delta}} - \delta a\right)\right]$$

$$= -j\omega\left[\pi a^2 \mu_0 H_0 + 2\pi\mu_0 A\delta\left(\frac{1}{2}a^2 + \delta^2 - \delta^2 e^{-\frac{a}{\delta}} - \delta a\right)\right] \tag{12}$$

A is obtained from Equation (12).

$$A = \frac{-j\omega a\mu_0\sigma/2}{1 + j\omega\mu_0\delta\frac{\sigma}{a}\left(\frac{1}{2}a^2 + \delta^2 - \delta^2 e^{-\frac{a}{\delta}} - \delta a\right)}H_0 = \frac{-j\omega\alpha}{1 + j\omega\beta}H_0 \tag{13}$$

Here, α and β are given by

$$\alpha = \frac{a\mu_0\sigma}{2} \tag{14}$$

$$\beta = \mu_0\delta\frac{\sigma}{a}\left(\frac{1}{2}a^2 + \delta^2 - \delta^2 e^{-\frac{a}{\delta}} - \delta a\right). \tag{15}$$

When $a \gg \delta$, β becomes

$$\beta = \mu_0 \delta \frac{\sigma}{a} \frac{1}{2} a^2 = \frac{\mu_0}{2} \delta \sigma a. \tag{16}$$

Therefore, $J_\varphi(x)$ is obtained from Equations (4) and (13).

$$J_\varphi(x) = Re\left(\frac{-j\omega\alpha}{1+j\omega\beta}\right) e^{(-\frac{a-x}{\delta})} H_0 = -\frac{\omega^2\alpha\beta}{1+\omega^2\beta^2} e^{(-\frac{a-x}{\delta})} H_0 = A' e^{(-\frac{a-x}{\delta})} H_0. \tag{17}$$

Here, A' is given by

$$A' = -\frac{\omega^2\alpha\beta}{1+\omega^2\beta^2}. \tag{18}$$

The magnetic moment m generated by $J_\varphi(x)$ is given by

$$m = 2a \int_0^a \pi x^2 J_\varphi(x)\, dx = -\frac{2\pi a\omega^2\alpha\beta}{1+\omega^2\beta^2} e^{-\frac{a}{\delta}} H_0 \int_0^a x^2 e^{\frac{x}{\delta}}\, dx. \tag{19}$$

If $2a$ is constant, the number N of cylindrical particles per unit volume of the composite is given by

$$N = V/2\pi a^3. \tag{20}$$

Here, V is the volume mixture ratio of the particles in the composite. If it is assumed that the direction of all magnetic moments is the same and that the eddy current loss is zero, the magnetization M is given by

$$M = Nm = -\frac{V\sigma\mu_0\omega^2\beta K_0 e^{-\frac{a}{\delta}}}{2a(1+\omega^2\beta^2)} H_0. \tag{21}$$

Here,

$$K_0 = \int_0^a x^2 e^{\frac{x}{\delta}}\, dx = \delta(2\delta^2 - 2a\delta + a^2)(e^{\frac{a}{\delta}} - 1) - a\delta(2\delta - a). \tag{22}$$

Also, the following relation holds between the average magnetic flux density B and the magnetization M in the composite when M is assumed to be proportional to H_0.

$$M = B/\mu_0 - H_0 = (\mu_r^* - 1)H_0 = (\mu_r' - 1 - j\mu_r'')H_0 \tag{23}$$

Therefore, the following equation is obtained from Equations (21) and (23).

$$1 - \mu_r' = \frac{\sigma\mu_0\omega^2 V\beta e^{-\frac{a}{\delta}}}{2a(1+\omega^2\beta^2)} \left[\delta(2\delta^2 - 2a\delta + a^2)(e^{\frac{a}{\delta}} - 1) - a\delta(2\delta - a)\right] \tag{24}$$

The Joule loss P, caused by the eddy current loss, per unit volume of the composite is

$$P = N\frac{1}{2} 2a \int_0^a 2\pi x \frac{J_\varphi(x)^2}{\sigma}\, dx. \tag{25}$$

Because $J_\varphi(x)$ is given by Equation (17), P is given by

$$P = \frac{V A'^2 e^{-2\frac{a}{\delta}}}{\sigma a^2} \left[-\frac{\delta^2}{4}\left(e^{2\frac{a}{\delta}} - 1\right) + \frac{a\delta}{2} e^{2\frac{a}{\delta}}\right] H_0^2 \tag{26}$$

μ_r'' is defined as the ratio of the magnetic energy lost in one cycle and the magnetic energy accumulated in the cylinder. Therefore, μ_r'' is given by

$$\mu_r'' = \mu_r' \frac{P}{\frac{\omega}{2}\mu_r'\mu_0 \iiint H^2 dv}. \tag{27}$$

Here, H is the magnetic field in the cylinder. The integral in the denominator of Equation (27) is obtained as follow.

$$
\begin{aligned}
\frac{\omega}{2}\mu'_r\mu_0 \iiint H^2 dv &= \frac{\omega}{2}\mu'_r\mu_0 \iiint_{\substack{outside \\ cylinder}} H_0^2 dv + \frac{\omega}{2}\mu'_r\mu_0 N \iiint_{\substack{inside \\ cylinder}} \left(H_0 + H'(x)\right)^2 dv \\
&= \frac{\omega}{2}\mu'_r\mu_0(1-V)H_0^2 + \frac{\omega}{2}\mu'_r\mu_0 N \int_0^a 2a \cdot 2\pi x \left(H_0^2 + 2H_0 H'(x) + H'(x)^2\right) \\
&= \frac{\omega}{2}\mu'_r\mu_0(1-V)H_0^2 + \frac{\omega\mu'_r\mu_0 V}{a^2}\left[\frac{1}{2}a^2 H_0^2 + 2A'\delta\left(\frac{1}{2}a^2 - \delta a + \delta^2 - \delta^2 e^{-\frac{a}{\delta}}\right)H_0^2\right] \\
&\quad + \frac{\omega\mu'_r\mu_0 V A'^2\delta^2}{a^2}\left(\frac{1}{2}a^2 - \frac{3}{2}\delta a + \frac{7}{4}\delta^2 - 2\delta^2 e^{-\frac{a}{\delta}} + \frac{1}{4}e^{-2\frac{a}{\delta}}\delta^2\right)H_0^2 \qquad (28)
\end{aligned}
$$

It is found from Equation (24) that $1-\mu'_r$ is proportional to V and depends on a and δ in the low frequency range. It is also found from Equation (27) that μ''_r depends not only on V and a but also on δ. Meanwhile, in the high frequency range, the values of $1-\mu'_r$ and μ''_r approach the values calculated from Equations (1) and (2).

The above qualitative results may also be applicable to spherical aluminum particles. In the calculation of μ'_r and μ''_r using Equations (24) and (27), a was modified by $\sqrt[3]{2/3}a$ assuming that the volumes of cylindrical and spherical particles are the same.

4. RESULTS AND DISCUSSION

4.1. Measured and Calculated Values of $1-\mu'_r$ and μ''_r for a Composite Composed of Aluminum Particles Dispersed in Polystyrene Resin

The frequency dependence of $1-\mu'_r$ for the composites containing aluminum particles with sizes of $8\,\mu m$ and $50\,\mu m$ is shown in Fig. 2. The data points show the measured values and lines represent the values calculated using Equation (24). As seen in Fig. 2(a), the measured values of $1-\mu'_r$ for the composite with $8\,\mu m$ aluminum particles increased gradually with increasing frequency. This is in qualitative agreement with the calculated curves, with also increase with frequency. The measured values of $1-\mu'_r$ for the composite with $50\,\mu m$ aluminum particles were almost constant at frequencies above $1\,GHz$ and roughly agreed with the calculated values in the frequency range from $10\,MHz$ to $40\,GHz$, as shown in Fig. 2(b).

At low frequency, the measured values of $1-\mu'_r$ for the composite with $8\,\mu m$ particles were lower than those for the composite with $50\,\mu m$ particles when V was the same. The reason for this difference is as follows. When the particle size is small, the frequency f' at which the radius of the particle is equal to δ is high. f' is obtained from Equation (3).

$$
f' = \frac{1}{a^2\pi\sigma\mu'} \qquad (29)
$$

For example, f' for 50 and $8\,\mu m$ aluminum particles is approximately 11 and $420\,MHz$, respectively. Therefore, the frequency at which the effect of the magnetic moment generated by the eddy current
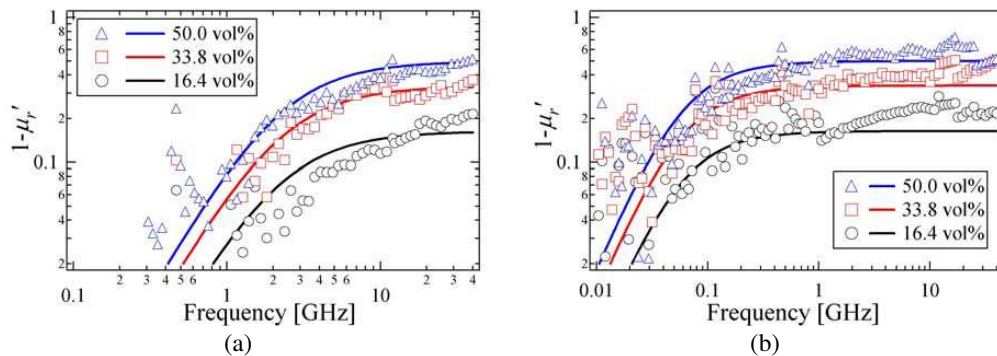

Figure 2: Frequency dependence of $1-\mu'_r$ for composites made of polystyrene resin and aluminum particles with sizes of (a) $8\,\mu m$ and (b) $50\,\mu m$. The aluminum volume mixture ratios are 16.4, 33.8 and 50.0 vol%. Lines show values calculated using Equation (24).
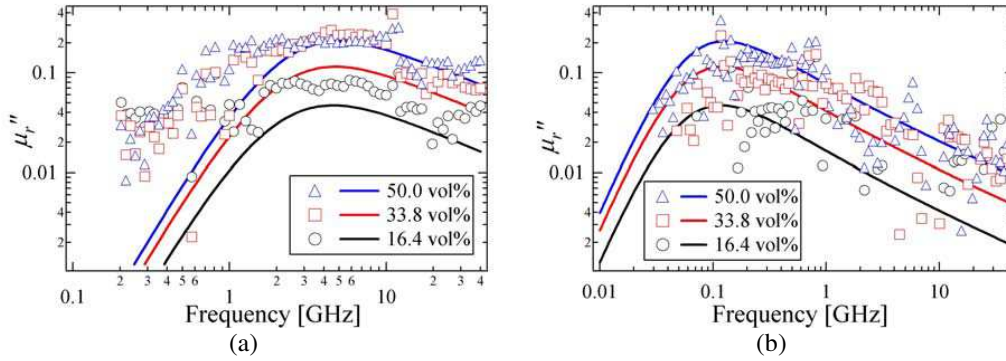
Figure 3: Frequency dependence of μ_r'' for composites made of polystyrene resin and aluminum particles with sizes of (a) $8\,\mu m$ and (b) $50\,\mu m$. The aluminum volume mixture ratios are 16.4, 33.8 and 50.0 vol%. Lines show values calculated using Equation (27).

becomes apparent increases with decreasing particle size. Consequently, at low frequencies, the value of $1 - \mu_r'$ depends on the particle size, as shown in Figs. 2(a) and(b). The calculated values also showed a particle size dependence and qualitatively agreed with the measured values. Thus, Equation (24) can be used to determine the values of $1 - \mu_r'$ in the low frequency range.

On the other hand, at high frequencies where δ is much smaller than the particle size, it was found from Figs. 2(a) and (b) that the measured values of $1 - \mu_r'$ depend on V, and are independent of frequency and particle size. This result almost agrees with the values calculated from Equation (24). Therefore, it can be concluded that μ_r' can be controlled by simply changing the value of V in the high frequency range.

Figure 3 shows the frequency dependence of μ_r'' for the composites containing aluminum particles with sizes of $8\,\mu m$ and $50\,\mu m$. Again, the solid lines show the theoretical values, in this case calculated using Equation (27). The measured μ_r'' value for the composite with $8\,\mu m$ aluminum particles was found to increase at frequencies above $100\,MHz$, reach a maximum around $5\,GHz$, and decrease with increasing frequency. By contrast, for the $50\,\mu m$ case, μ_r'' was found to decrease with increasing frequency at frequencies above $100\,MHz$. In both cases, these results are in qualitative agreement with the calculated curves, indicating that the frequency dependence of μ_r'' can be correctly determined using Equation (27). Moreover, since μ_r'' is proportional to V and inversely proportional to a at high frequencies, it can be controlled by a suitable choice of V and a.

From these results, it can be concluded that the frequency dependence of μ_r' and μ_r'' can be predicted using Equations (24) and (27). However, the calculated values did not agree quantitatively with the measured values, as seen in Figs. 2 and 3. One reason for this is believed to be the distribution of aluminum particle sizes around the average size. In addition, the low purity of the aluminum must be considered, since the conductivity of aluminum depends on its purity.

4.2. Frequency Dependences of ε_r', ε_r'' and Return Loss

The measured values of ε_r' and ε_r'' were found to be fairly independent of frequency and increased with increasing V. For a $8\,\mu m$ particle size, the values of ε_r' measured at $10\,GHz$ for composites with 16.4, 33.8 and 50 vol%-aluminum particles were 6, 13 and 31, and for a $50\,\mu m$ particle size were 7, 14 and 47, respectively. For particle sizes of both 8 and $50\,\mu m$, the measured values of ε_r'' for the composite made with 16.4 and 33.8 vol%-aluminum particles were less than 1 and for the composite made with 50.0 vol%-aluminum particles were approximately 4.

The frequency dependence of the return loss in free space was calculated from the measured values of μ_r^* and ε_r^* for all samples. The absorber used for the calculation was a metal-backed single layer absorber and the incident electromagnetic wave was perpendicular to the surface. As shown in Fig. 4, good absorption characteristics were obtained for the composite with 16.4 vol%-aluminum and 33.8 vol%-aluminum, in both cases with a $8\,\mu m$ particle size. The percentages shown in the graphs represent the normalized $-20\,dB$ bandwidth (the bandwidth Δf corresponding to a return loss of less than $-20\,dB$ divided by the absorption center frequency f_0). A value of $-20\,dB$ corresponds to the absorption of 99% of the electromagnetic wave power. The return loss was found to be less than $-20\,dB$ for several frequencies in the range 4 to $40\,GHz$ for both samples. However, a return loss of less than $-20\,dB$ could be achieved for thinner samples in the case of the 33.8 vol%-aluminum composite. Moreover, the normalized $-20\,dB$ bandwidth of the composite made with
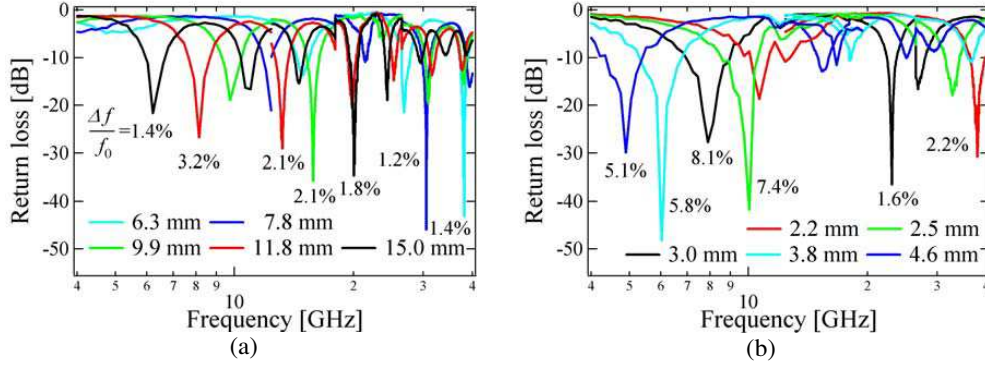
Figure 4: Frequency dependence of return loss for composites made of polystyrene resin and 8 μm aluminum particles. The aluminum volume mixture ratios are (a) 16.4 vol% and (b) 33.8 vol%.
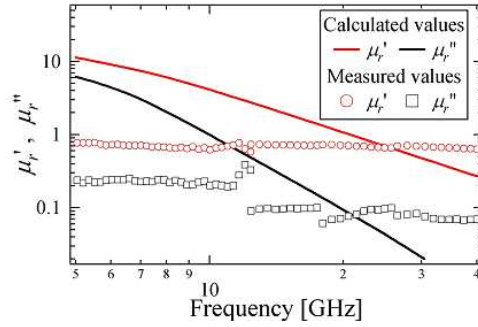

Figure 5: Measured values of μ_r' and μ_r'' for the composite made of polystyrene resin and 8 μm aluminum particles with a volume mixture ratio of 33.8 vol%. Lines show values calculated using Equation (30).

33.8 vol%-aluminum was larger than that of the composite made with 16.4 vol%-aluminum. These results indicate that practical high frequency absorbers can be realized by a suitable combination of aluminum volume mixture ratio and particle size.

4.3. Control of Absorption Characteristics by Adjusting μ_r' and μ_r''

To investigate the possibility of controlling the absorption characteristics, the values of μ_r' and μ_r'' that satisfy the non-reflective condition given by Equation (30) [5] were calculated using the least squares method.

$$\sqrt{\mu_r^*/\varepsilon_r^*} \tanh\left(\gamma_0 d\sqrt{\mu_r^*\varepsilon_r^*}\right) = 1 \tag{30}$$

Here, γ_0 is the propagation constant in free space and d is the sample thickness. The values of ε_r' and ε_r'' used for the calculation are independent of frequency and are the same as the measured values ($\varepsilon_r' = 13$, $\varepsilon_r'' = 0.5$). The sample thickness used was 3 mm. Fig. 5 shows the measured values of μ_r^* and those calculated by Equation (28). As shown in Fig. 5, an intersection occurs between the measured and calculated values of μ_r' near 25 GHz and between the measured and calculated values of μ_r'' near 21 GHz. This result indicates that the measured values of μ_r' and μ_r'' were close to the values that satisfy Equation (30) in the frequency range from 20 to 30 GHz, and a large amount of electromagnetic power was absorbed at approximately 23 GHz, as shown in Fig. 4(b).

As discussed in Section 4.1, μ_r' depends only on V in the high frequency range where δ is much smaller than the radius of the aluminum particles. Meanwhile, μ_r'' depends on V and a at high frequencies, as given by Equation (27). Thus, μ_r' and μ_r'' can be controlled independently by adjusting V and a. This result suggests that the frequency at which the absorption of electromagnetic waves occurs can be selected by changing V and a, although the resulting increase or decrease of ε_r^* should be considered. Moreover, it can be expected that absorption at frequencies above 40 GHz is possible by modifying the values of V and a.

It is found from Fig. 5 that the values of μ_r' and μ_r'' calculated from Equation (30) decrease with increasing frequency. If these frequency dependences could be obtained, wide-bandwidth absorption is expected because Equation (30) is satisfied over a wide frequency range. As shown in Fig. 4(b), the normalized −20 dB bandwidth of the composite made with 33.8 vol% aluminum is large at

frequencies below 10 GHz. This is thought to be because the value of μ_r' for the composite with 8 μm particles decreases in this frequency range at a rate similar to that calculated from Equation (30). On the other hand, the normalized -20 dB bandwidth is small at higher frequencies since μ_r' and μ_r'' are almost independent of frequency in this region, as shown in Fig. 5. However, μ_r' begins to decrease when δ becomes smaller than the radius of the aluminum particles, and the frequency at which this occurs can be increased by reducing the aluminum particle size, as follows from Equation (29). Therefore, by using small aluminum particles the frequency where μ_r' begins to decrease can be pushed to very high values and μ_r' can satisfy Equation (30) over a wide frequency range. This result suggests the possibility of a high frequency, wide bandwidth absorber.

5. CONCLUSIONS

Composites made from aluminum particles dispersed in polystyrene resin were found to exhibit a return loss of less than -20 dB in the frequency range from 4 to 40 GHz when a suitable volume mixture ratio and aluminum particle size were selected. The relative complex permeability for the composite was calculated using Maxwell's equations. The calculated values qualitatively agreed with the measured values of μ_r' and μ_r'', and the calculation results also explained the particle size dependence of μ_r' and μ_r'' at low frequencies. At high frequencies, μ_r' was found to depend only on the volume mixture ratio of aluminum, whereas μ_r'' was determined by both the volume mixture ratio and the aluminum particle size. It is proposed that the absorption characteristics of such composite materials can be tailored by independently controlling μ_r' and μ_r''.

REFERENCES

1. Liu, J. R., M. Itoh, T. Horikawa, E. Taguchi, H. Mori, and K. Machida, "Iron based carbon nanocomposites for electromagnetic wave absorber with wide bandwidth in GHz range," *Appl. Phys. A*, Vol. 82, 509–513, 2006.
2. Kotsuka, Y. and C. Kawamura, "Novel computer controllable metamaterial beyond conventional configurations and its microwave absorber application," *IEEE MTT-S Int. Microwave Symp. Dig.*, 4264159, 1627–1630, 2007.
3. Landy, N. I., S. Sajuyigbe, J. J. Mock, D. R. Smith, and W. J. Padilla, "Perfect metamaterial absorber," *Phys. Rev. Lett.*, Vol. 100, No. 20, 207402, 2008.
4. Wada, Y., N. Asano, K. Sakai, and S. Yoshikado, "Preparation and evaluation of composite electromagnetic wave absorbers made of fine aluminum particles dispersed in polystyrene medium," *PIERS Online*, Vol. 4, No. 8, 838–845, 2008.
5. Naito, Y. and K. Suetake, "Application of ferrite to electromagnetic wave absorber and its characteristics," *IEEE Trans. Microwave Theory Tech.*, Vol. 19, No. 1, 65–72, 1971.

Investigation of Coupling of EMC Disturbances in Doubly Fed Induction Generators

S. Schulz, R. Doebbelin, and A. Lindemann

Institute of Electric Power Systems, Otto-von-Guericke-University Magdeburg, Germany

Abstract— In renewable power generation doubly fed induction generators (DFIG) are used, in which the stator of the generator is directly connected to mains, while the converter for the rotor is rated only for slip power. Due to the interaction of rotor and stator windings in a DFIG, the high-frequency harmonics caused by the pulsed output of rotor power converters are transmitted into the stator current and cause conducted emissions. These high-frequency harmonics have to be considered, taking into account that harmonics — which can be limited by filters — will also be transmitted into the stator.

1. INTRODUCTION

In recent years the exploitation of renewable energy has significantly increased with a major contribution of wind and water energy. One intent of energy production is high yield as achievable by variable speed operation. This requires the use of a converter. However, the high-frequency and fast changing output voltage of the converter can cause conducted emissions and system perturbation.

2. GRID COUPLING

2.1. Possibilities of Grid Coupling

In power plants (especially in water-power plants and wind farms) turbines are based on synchronous or induction generators. To supply the energy of the generators into the grid it is common to use a power converter [1]. There are two possibilities:

- power converter for the full rated power, cf. the topologies in Figures 1(a), (c), (d))

- power converter for the rotor of a DFIG — only to be rated for slip power, cf. 1(b))
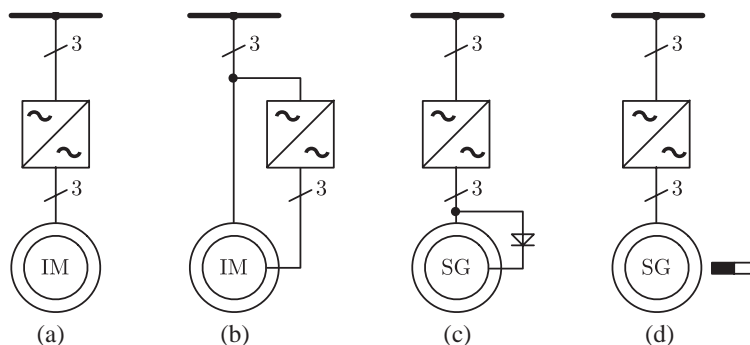
Figure 1: Possibilities of grid coupling in power plants.

Generally speaking, care must be taken to comply with the EMC regulations for grid connection. Filters may be used to compensate harmonics; however they reach a considerable size and cause considerable cost at high power ratings of the converter.

2.2. Doubly Fed Induction Machine

Using doubly fed induction generators (DFIG), in which the stator of the generator is directly connected to the mains, whereas the rotor of the machine is supplied by a converter. The converter for the rotor is only rated for slip power which is about 30% of the nominal power of the DFIG. Thus, this topology can inherently decrease the EMI level because of the lower power rating of the rotor converter compared to a converter for full rated power in conventional systems. This kind of system according to Figure 2 allows a large speed range of about 70% to 130% of the nominal rotor speed for optimized power generation [2].

3. SYSTEM PERTURBATION OF DFIG

3.1. EMI Sources

In DFIG the applied rotor converters are designed as indirect power converter with DC link or as cycloconverters. Electromagnetic compatibility aspects concerning system perturbation (up to 2 kHz) and conducted emissions (9 kHz to 30 MHz) of power converters are regulated in grid connection regulations of the transmission system operator [3], and furthermore in EN 61000 [4, 5], EN 61800-3 [6] and EN 50160 [7]. The emission limits given by these standards correspond with limits of the fundamental EMC standard EN 55011 [8]. System perturbation and conducted emissions are generally determined in the usually non-regulated (2 kHz to 9 kHz) range of the switching frequency of rotor converters. The harmonics and conducted emissions produced by the rotor converter are compensated by an input filter of the converter. Figure 2 shows several possibilities for the emergence and propagation of conducted emissions in the considered system: High-frequency pulsed rotor voltages cause harmonics of the rotor currents (A) which are transferred to the stator current (B); considering the slip of the generator, interharmonics will occur. The stator current supplies the transformer, thus the harmonics and interharmonics will proceed to the grid (C). The implemented EMC filter is mostly intended to reduce the additional conducted emissions of the rotor converter (E) on transformer side (D). Emissions of the stator current are hardly affected by this filter.

3.2. Simulation

3.2.1. Model of the Power System

Figure 3 shows the configuration of the simulated power system. The stator shall feed a power of 12 kW into the line sources (u_{e1}, u_{e2}, u_{e3}). The rotor current i_r of the DFIG is supplied by a converter. It is nearly sinusoidal but will include harmonics given by the modulation of the rotor converter. Mechanically, the rotor is driven by a torque of 76 Nm; it rotates with 1527 1/min. Note that the relatively low power level has been chosen to facilitate comparison with experimental results according to Section 3.4.2.
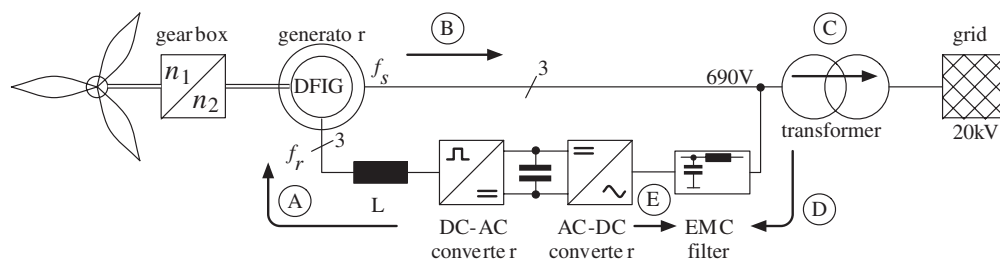
Figure 2: Doubly fed induction generator for wind power generation (DFIG).
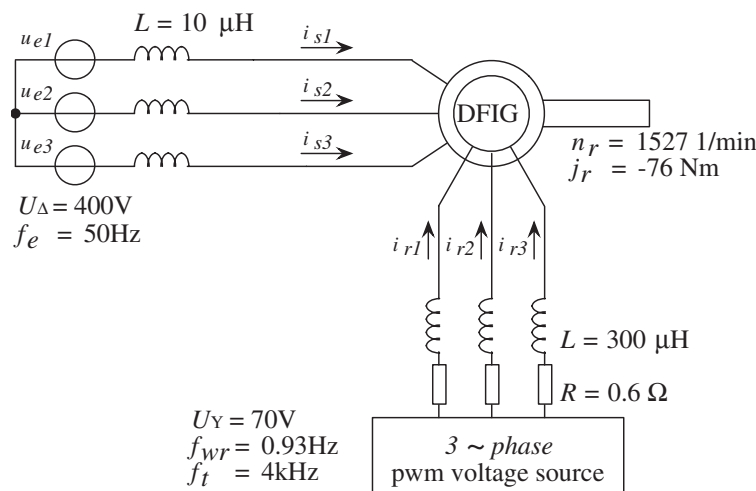
Figure 3: Simulation model of doubly fed induction generator (DFIG).

3.2.2. Simulation Results of the Power System

The simulation results correspond excellently to the theoretically expected waveforms. The three-phase rotor current and stator current are nearly sinusoidal. While stator frequency corresponds to mains frequency of 50 Hz, rotor frequency is low. The detailed simulation results are shown in Figure 4(a). The harmonics generated by the 4 kHz pulsed rotor converter appear in the rotor current i_r as well as in the stator current i_s. This result illustrates that the harmonics are transmitted by the magnetic field, i.e., the waveform of simulated stator current i_s shows the transmitted harmonics into the stator windings. FFT analysis in Figure 4(b) again shows the harmonics caused by pulsed rotor converter.

3.2.3. Model of Driving a Doubly Fed Induction Machine

To verify this effect it is possible to consider the inverse method of operation of the power system. Figure 5 shows the configuration of the simulation of an existing experimental setup. Here, the stator of the 11 kW DFIG is supplied by an AC-DC-AC power converter with a switching frequency of 4 kHz, while the wound rotor is short-circuited. The only filter elements are line inductors ($L = 810\,\mu\text{H}$) between converter and stator windings.
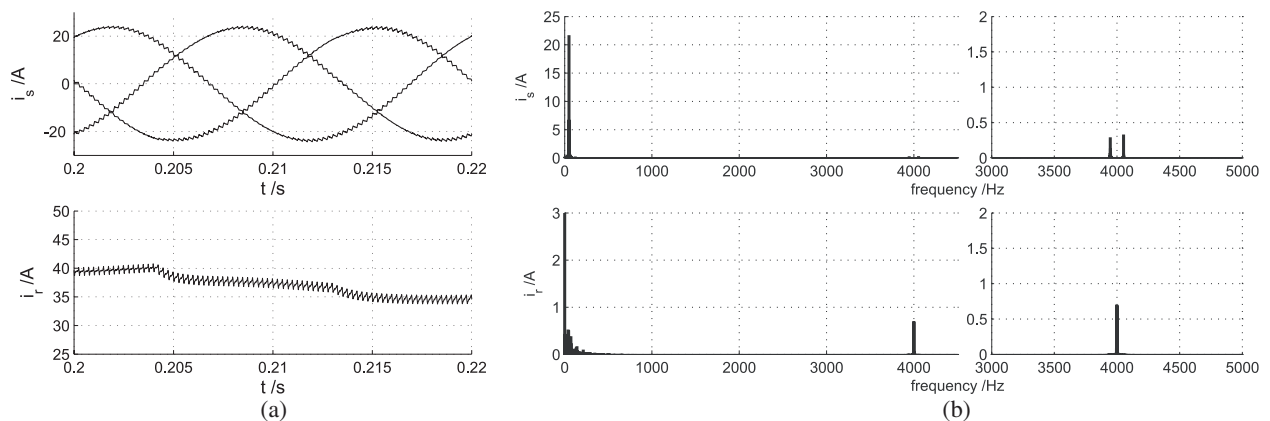
Figure 4: Simulation of (a) stator current i_s, rotor current i_r, (b) FFT of the simulated stator current i_s, rotor current i_r.
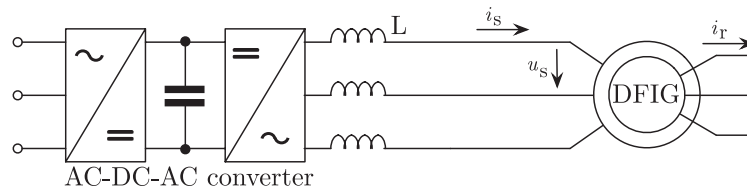
Figure 5: Simulation and experimental setup for driving a DFIG.
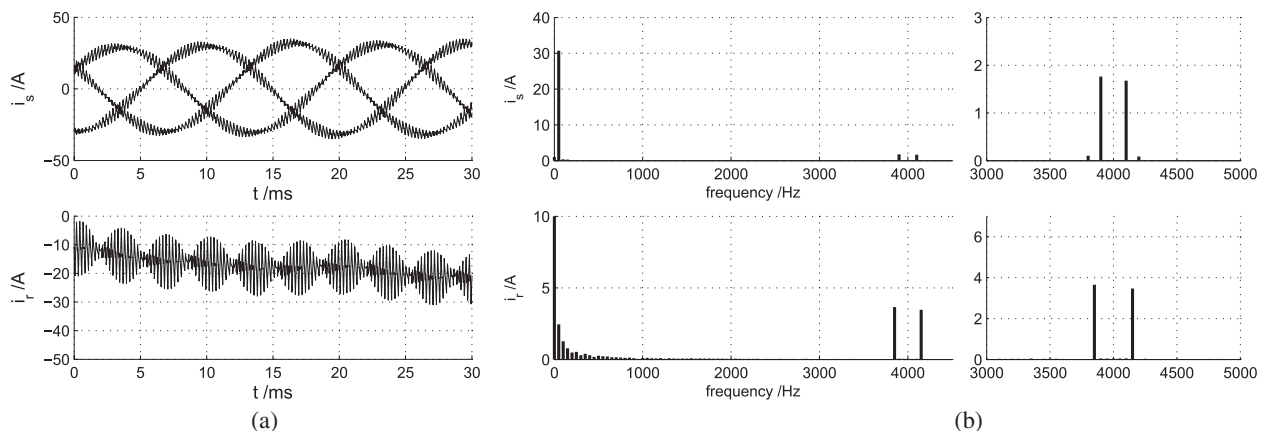
Figure 6: Simulation of (a) stator current i_s, rotor current i_r, (b) FFT of the simulated stator current i_s, rotor current i_r.

3.2.4. Simulation Results of Driving a Doubly Fed Induction Machine

The simulation results are in very good coincidence with the theoretically expected waveforms. The three-phase stator current is a superposition of a sinusoidal current (50 Hz mains frequency) with high-frequency harmonics caused by the switching frequency of 4 kHz of the converter. According to the preceding considerations, harmonics in the stator currents should cause harmonics in the rotor currents as well. Figure 6 illustrates that harmonics of all three stator currents — caused by their pulsed supply voltage — can be found in rotor currents.

3.3. Circuit Theory — Equivalent Circuit of a Doubly Fed Wound Rotor Induction Machine

The reason for this behavior can be found in the single-phase equivalent circuit of a doubly fed induction machine which corresponds to the equivalent circuit of a transformer (Figure 7), where the equations of Faraday's law of induction apply:

$$u_s = i_s \cdot (R_1 + j\omega_1 L_{1\sigma}) + u_\mu \tag{1}$$

$$\frac{u'_r}{s} = i'_r \cdot \left(\frac{R'_2}{s} + j\omega_1 L'_{2\sigma}\right) + u_\mu \tag{2}$$

$$u_s = i_s \cdot (R_1 + j\omega_1 L_{1\sigma}) - i'_r \cdot \left(\frac{R'_2}{s} + j\omega_1 L'_{2\sigma}\right) + \frac{u'_r}{s} \tag{3}$$

Harmonics in rotor voltage u_r/s caused by the converter will produce harmonics in rotor and stator currents. Therefore, mains current of the DFIG is a superposition of a sinusoidal current with high-frequency harmonics. The conducted emissions and harmonics depend on the pulse pattern of the rotor converter, frequency, the rotor filter and the line filter of the system.
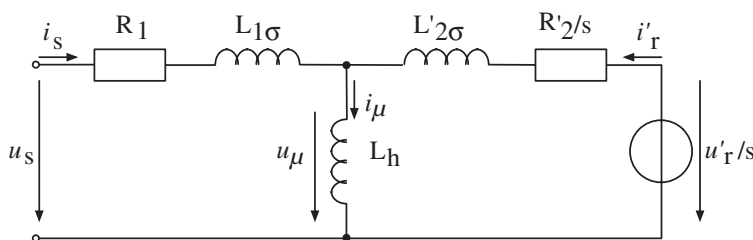
Figure 7: One phase equivalent circuit of a DFIG [9, 10].

(a)   (b)
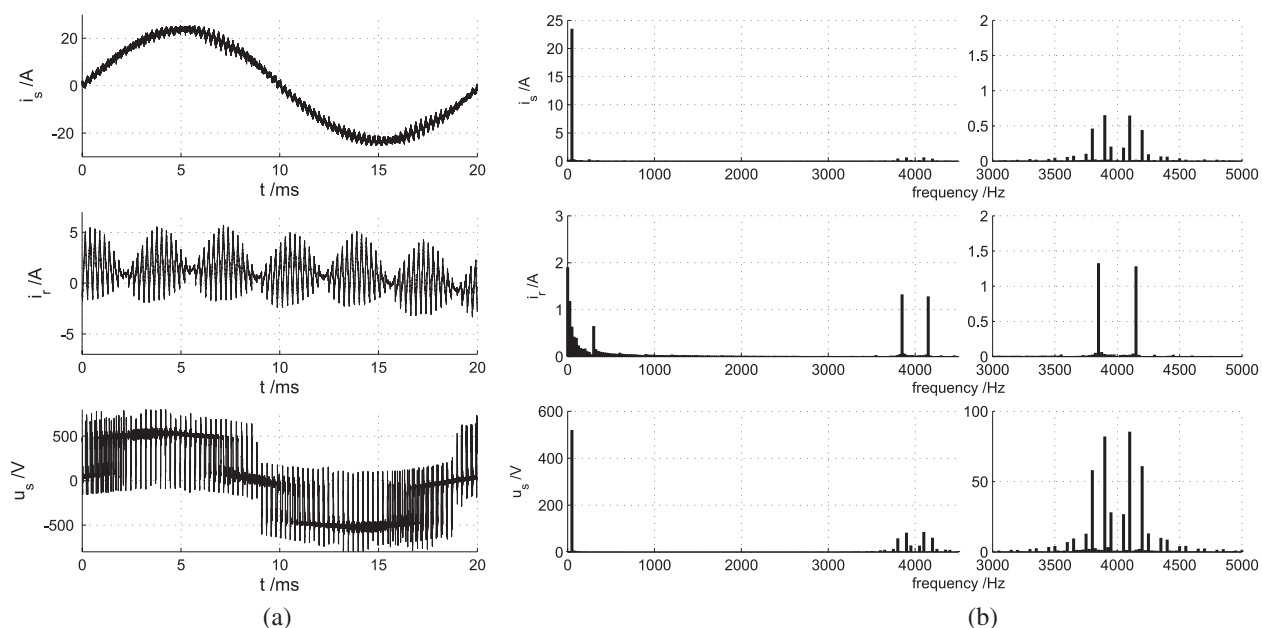
Figure 8: Measurement of (a) stator current i_s, rotor current i_r, stator voltage u_s, (b) FFT of the measured stator current i_s, rotor current i_r, stator voltage u_s.
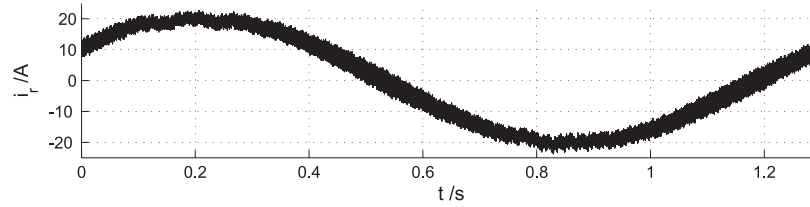
Figure 9: Measurement of rotor current i_r with superimposed pulses of the power converter.

3.4. Experiment

3.4.1. Experimental Setup

To investigate the effect of the transmitted high frequency harmonics, an existing experimental setup according to Figure 5 has been used: Here, the stator of the 11 kW DFIG is supplied by an AC-DC-AC power converter with a switching frequency of 4 kHz, while the wound rotor is short-circuited. The only filter elements are line inductors ($L = 200\,\mu\text{H}$) between converter and stator windings.

3.4.2. Experimental Results

According to the preceding considerations, harmonics in the stator currents of the experimental setup should cause harmonics in the rotor currents as well. The detailed view in Figure 8 — with waveforms over time and results of FFT analysis — illustrates that harmonics of all three stator currents — caused by their pulsed supply voltage — can be found in rotor current.

4. CONCLUSION

With the increase of power plants with DFIG without line filters of the rotor circuit or system filters also EMC disturbances increase. These high frequency harmonics influence the mains, transformers and line filters of other systems connected to the mains. As a consequence malfunction and damage of electronic equipment can occur. This paper deals with the interaction of rotor and stator winding in a doubly fed induction generator [12]. High frequency harmonics caused by the pulsed output of rotor power converters are transmitted into the stator current and cause conducted emissions. It is possible to reduce them with filters in the rotor circuit, thus requiring a rating of only 30% of the nominal power.

REFERENCES

1. Kimura, N., T. Morizane, K. Taniguchi, and T. Hamada, "Inverter excited induction machine for high performance wind power generation system," *European Power Electronics and Drives Association (EPE)*, Aalborg, 2007.
2. Toufik, B., M. Machmoum, and F. Poitiers, "Doubly fed induction generator with active filtering function for wind energy conversion system," *European Power Electronics and Drives Association (EPE)*, Dresden, 2005.
3. E.ON Netz GmbH, *Grid Connection Regulations for High and Extra High Voltage*, Bayreuth, 2006.
4. Electromagnetic compatibility (EMC) — Part 3-2: Limits for harmonic current emissions (equipment input current ≤ 16 A per phase) (IEC 61000-3-2:2005); German version EN 61000-3-2:2006.
5. Electromagnetic compatibility (EMC) — Part 6-4: Generic standards Emission standard for industrial environments (IEC 61000-6-4:2006), German version EN 61000-6-4:2007.
6. Adjustable speed electrical power drive systems — Part 3: EMC requirements and specific test methods (IEC 61800-3:2004); German version EN 61800-3:2004.
7. Voltage characteristics of electricity supplied by public distribution networks, German version EN 50160:2007.
8. Industrial scientific and medical (ISM) radio-frequency equipment Electromagnetic disturbance characteristics — Limits and methods of measurement (IEC/CISPR 11:2003 + A1:2004, modified + A2:2006); German version EN 55011:2007 + A2:2007.
9. Sinelnikova, E., *Design und optimale Betriebsfuehrung doppelt gespeister Asynchrongeneratoren fuer die regenerative Energieerzeugung*, Dissertation, Fakultaet fuer Elektrotechnik und Informationstechnik der Technischen Universitaet Chemnitz, 2004.

10. Schroeder, D., *Elektrische Antriebe Regelung von Antriebssystemen*, Springer Verlag, 2001.
11. Giesecke, J. and E. Mosonyi, *Wasserkraftanlagen Planung, Bau und Betrieb*, Springer Verlag, 2005.
12. Schulz, S. and A. Lindemann, "Investigation of coupling of EMC disturbances in wind generators with DFIG," *4th PhD Seminar on Wind Energy in Europe*, Magdeburg, 2008.

Inductive Coupling between Wires in Cables with a Grounded Conductor

Bernd W. Jaekel

Siemens AG, Sector Industry, EMC-Center, Germany

Abstract— The arrangement of conductors in a multi-core power cable leads to a situation where various conductor loops are built up. One or several loops are formed by the phase and neutral conductors with the operational current flowing in these conductors. A further loop is built up by the protective earth conductor which is connected to the equipotential bonding system at several locations. The area of this loop is essentially arranged outside of the power cable. The inductive coupling from the phase conductor loops into that loop causes common mode voltages in the protective earth system with consequent common mode currents. It can be demonstrated that this effect takes place even in case of balanced phase currents in the cable. Numerical simulations and parameter studies were carried out in order to describe this effect quantitatively and to investigate the influence of different cable parameters onto the resulting common mode voltages.

1. INTRODUCTION

Power cables represent components of an entire power supply network which can be carried out in different types. If an earthed system is required, i.e., a system which is connected to the local reference earth, mainly two types of supply networks can be distinguished: TN-C and TN-S. From the point of view of electromagnetic compatibility (EMC) a TN-S power network should definitely be preferred [1]. In this type of network the neutral and protective earth (PE) conductors are strictly separated except at one net point where both conductors are connected, normally at the transformer or the switchgear. This type of installation prevents flowing of any operational currents outside of the phase and neutral conductors. There should be no net currents and therefore the equipotential bonding system is generally assumed to be free of any operational currents. But when looking at this type of network and the physical structure of power cables in more detail some physical mechanisms can be identified which nevertheless lead to generation of common mode voltages and common mode currents even in the case of balanced loaded TN-S power net systems.

2. LOW VOLTAGE POWER CABLES

Multi-core low voltage power cables consist of the phase conductors and — depending on the grounding arrangement of the power supply network — of a neutral conductor and/or a PE conductor. Each of the conductors as well as the entire conductor arrangement are covered by an insulation, for which material is chosen depending on the specific requirements and fields of applications [2].

The n individual insulated conductors are twisted together and each conductor can be represented by a helical line. An appropriate cylindrical coordinate system for describing the spatial arrangement of a conductor is shown in Fig. 1 together with the relevant parameters such as a as the radius of the helical line with respect to the centre line of the cable and the pitch distance p as the twist length of the cable, i.e., the length of the cable per rotation of the conductors. For simplicity reasons only one conductor is shown. The further $n-1$ conductors can be represented as similar lines and they are rotated by an angle $\Phi = 360/n$ with respect to that one shown in Fig. 1.

3. COMMON MODE VOLTAGES IN POWER CABLES

The magnetic flux density $\mathbf{B}$ caused by the currents in the individual conductors can be calculated by means of the Biot-Savart law, as long as the situation at the power frequency range is considered:

$$\mathbf{B} = \frac{\mu_0 \mathbf{I}}{4\pi} \int_C \frac{d\mathbf{r}' \times (\mathbf{r} - \mathbf{r}')}{r^3} \tag{1}$$

$\mathbf{I}$ represents the phasor of the exciting alternating current, $\mathbf{r}$ with its cylindrical coordinates r, Φ, z denotes the observation point and $\mathbf{r}'$ with its cylindrical coordinates r', Φ, z' means a variable point on the line current. Though this expression can be easily solved in the case of straight wires,
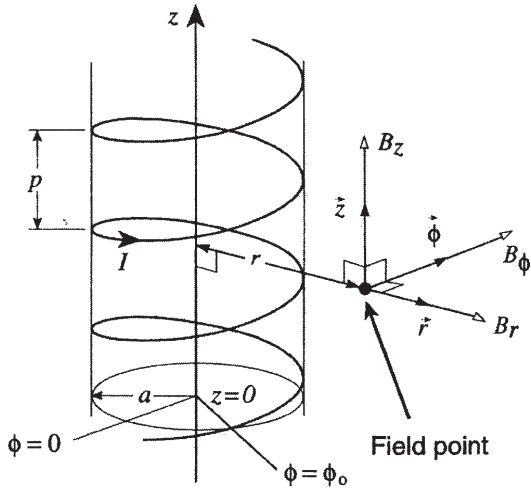
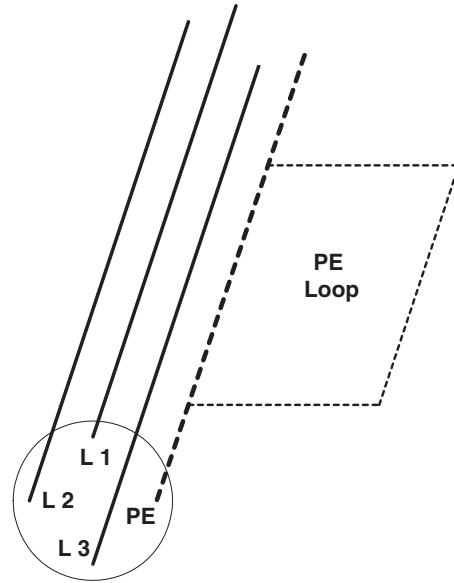Figure 1: A twisted conductor (helical line) in a cylindrical coordinate system [3].

Figure 2: Mechanism for generation of common mode voltages.

the situation is relatively complex in case of power cables where various conductors are twisted and each conductor can be represented by a helical solenoid (see Fig. 1).

In power cables where a protective earth (PE) conductor is twisted along with the phase conductors inductive coupling exists between the phase conductor loops and a loop built up by the PE-conductor and its connecting structures to the equipotential bonding system. This effect can be explained by means of a schematic sketch of a 4-conductor cable as shown in Fig. 2. For reasons of clarity twisting of the conductors is not shown in the figure.

The conductors L_1, L_2 for example form a spatial loop in which the phase current I_{L_1-L2} flows. Corresponding loops are built up by the arrangement of conductors $L_1 - L_3$ and $L_2 - L_3$ with the loop currents $I_{L_1-L_3}$ and $I_{L_2-L_3}$, respectively. A further loop results from the PE conductor which is connected to the equipotential bonding system by conductive structures. This loop is shown as PE-Loop in Fig. 2.

The induced voltage U_{PE} in the PE-Loop can be derived by means of the mutual inductances between the various phase conductor loops and the PE-Loop or accordingly by the mutual inductance between the current carrying phase conductors and the PE-Loop:

$$U_{\mathrm{PE}} = \omega \left(I_{L_1} M_{L_1-PE} + I_{L_2} M_{L_2-PE} + I_{L_3} M_{L_3-PE} \right) \tag{2}$$

with the mutual inductances M_{L_i-PE} $(I = 1, 2, 3)$ to be derived by

$$M_{L_i-PE} = \frac{\int\limits_{S} \mathbf{B}_{L_i} \cdot dS}{I_i} \tag{3}$$

$\mathbf{B}_{L_i}$ represents the magnetic flux density caused by the current I_i in conductor L_i $(i = 1, 2, 3)$ and $\mathbf{S}$ the area of the PE-Loop [4]. Fig. 2 shows the situation for a four-conductor cable. It can be seen from the cross-section of the entire cable configuration that there is no total symmetry in the three mutual inductances between the phase conductors and the PE loop. Hence a net mutual inductance results leading to a net induced common mode voltage and a common mode current in the case of a closed loop, respectively.

The Biot-Savart integral (1) needed in order to determine $\mathbf{B}_{L_i}$, however, cannot be calculated analytically for a current in a helical conductor arrangement. The magnetic vector potential has to be used and a series expansion of the reciprocal distance between the observation point and a variable point on the conductor has to be introduced. Using some well-known trigonometric theorems together with Bessel functions, the following equations for the different components of the magnetic flux density vector can be derived for observation points outside $(r > a)$ the helical

arrangement [5]:

$$B_r = -\frac{\mu_0 I}{\pi} a \, \Omega^2 \quad \sum_{n=1}^{\infty} n I_n'(an\Omega) K_n'(rn\Omega) \cdot \sin(n(\phi_0 - \phi + \Omega z)) \tag{4}$$

$$B_r = \frac{\mu_0 I}{2\pi \, r} + \frac{\mu_0 I}{\pi} \frac{a}{r} \, \Omega \cdot \quad \sum_{n=1}^{\infty} n I_n'(an\Omega) K_n(rn\Omega) \cdot \cos(n(\phi_0 - \phi + \Omega z)) \tag{5}$$

$$B_z = -\frac{\mu_0 I}{\pi} a \, \Omega^2 \cdot \sum_{n=1}^{\infty} n I_n'(an\Omega) K_n(rn\Omega) \cdot \cos(n(\phi_0 - \phi + \Omega z)) \tag{6}$$

with

$\Omega = 2\pi/p$:   the coordinate of the point where the helix intersects the plane
$I_n(x), K_n(x)$: modified Bessel functions of first and second kind of order n ($I_n'(x), K_n'(x)$: their derivatives)

In [5], the corresponding investigations are expanded to the situation of a twisted three-phase arrangement. Furthermore an approximation is given there to estimate the field strength versus distance to the twisted phase conductor arrangement. There are different possibilities to determine the amplitude of the induced voltage U_{PE}:

- by analytically performed integration techniques
- by numerical simulations or
- by measurements.

The integration of the magnetic flux density across the area of the PE loop results in the total magnetic flux and subsequently in the induced voltage. This approach, however, represents a very complex task, because on one hand the expressions (4), (5) and (6) with the Bessel functions have to be integrated and on the other side these equations valid for observation points outside the cable as well as corresponding equations which describe the situation inside the power cable have to be considered [5]. No analytical results or approximate procedures were found in the technical literature offering solutions.

4. NUMERICAL SIMULATIONS

Within the frame of numerical simulations the twisted conductors as well as the generated PE-loop have to be modeled spatially. A schematic representation of the physical model of a twisted power cable is given in Fig. 3. For the simulations the geometrical data of a cable of type $4 \times 25 \, \mathrm{mm}^2$ are used where a twist length (pitch) of $0.4\,\mathrm{m}$ was considered. The PE-conductor of the cable is connected to conductive structures (of equipotential bonding system) and a closed loop results. The dimensions of the loop are length L and width W.

The simulations were performed by means of the computer program CONCEPT which bases on the Method of Moments [6]. This method and program allow modeling of all the conductive structures of the arrangement under consideration. The phase conductors are excited by means of a three phase voltage source and all the voltages and currents induced in any conductive element of the model can be calculated.

The amplitude of the induced common mode voltage depends on the actual cable parameters and the cable installation condition. As a first step the dependency on the phase current amplitudes and the phase current frequencies in the range from several Hz to several hundreds of Hz, i.e., in the electrically low frequency range, were investigated. In both cases a linear correlation between induced voltage and current and frequency, respectively, could be found. This clearly indicates that the physical mechanism which causes the induced voltage is an inductive coupling between the current carrying phase conductors and the PE-loop.

Next the voltage induced into the PE-loop was calculated for varying lengths of the loops, i.e., for varying longitudinal dimensions of the resulting loop built up by the PE-conductor of the power cable and the equipotential bonding system. The results are given in Fig. 4.

The induced voltage linearly increases with increasing longitudinal length L of the loop. This behavior can be expected due to the resulting conductor configuration where the arrangement of the PE conductor is constant with respect to the phase conductors. Hence the PE-loop is exposed
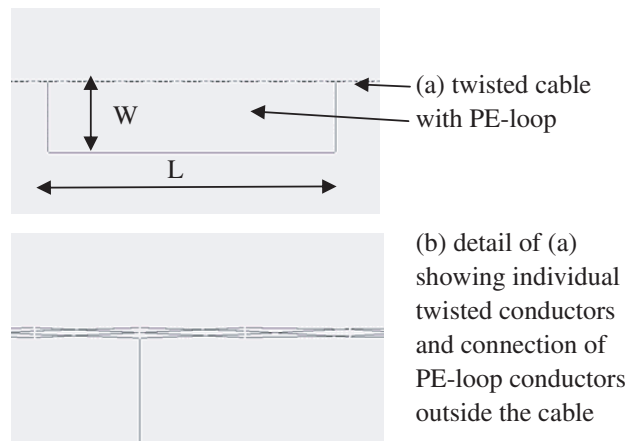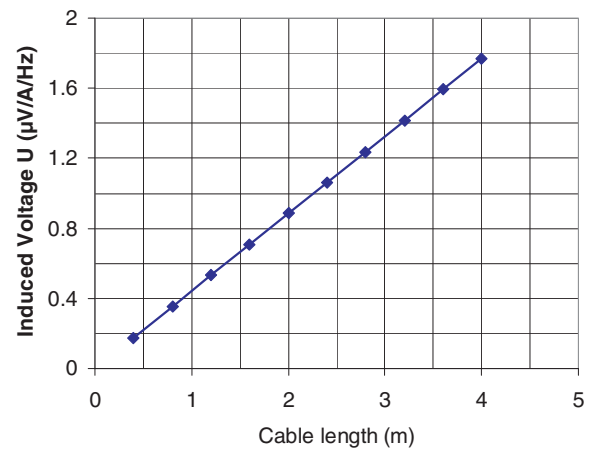
(a) twisted cable with PE-loop

(b) detail of (a) showing individual twisted conductors and connection of PE-loop conductors outside the cable

Figure 3: Spatial model of a power cable.

Figure 4: Induced voltage versus length L of the PE-loop.

to constant magnetic fields along the cable length resulting in a constant induced voltage per length unit. This behavior was also verified by means of experimental investigations [7]. From the slope of the line a coefficient can be derived which expresses the induced voltage per cable/loop length and which is about $0.44\,\mu\text{V/A/m/Hz}$.

In the case of a balanced three phase system with phase current **I,** taking into account the phase relationship, Equation (2) can be simplified in order to de-scribe the relation between the induced voltage U_{PE}, the frequency f of the currents and their amplitudes:

$$U_{\text{PE}} = 2\pi f I M_{NET} \tag{7}$$

with M_{NET} as the net mutual inductance derived from the superposition of the individual mutual inductances. According to this relation a mutual inductance $M'_{NET} = 70\,\text{nH}$ per meter length results when the induced voltage U_{PE} is considered as derived above. The mutual inductance is expected to depend on several cable parameters. Corresponding investigations concerning the amplitudes of the induced voltage U_{PE} were performed for various cable parameters and cable configurations [8]. It can be derived from those results that there is nearly no dependency on the twist length (pitch) of the power cable conductors, at least for practical twist lengths of more than about 40 cm. Furthermore, there is only a small impact of the helical radius of the power cable conductors. This fact was found also by means of measurements where the results of a $4 \times 95\,\text{mm}^2$ power cable are nearly the same as in the present case of a $4 \times 25\,\text{mm}^2$ power cable [7, 8].

5. CONCLUSIONS

In power cables with twisted PE conductors a common mode voltage is induced by currents in the phase conductors. This is valid even in the case of balanced currents and to the fact that the PE conductor has a certain asymmetry with respect to the phase conductors resulting in a net magnetic flux through the loop built up by the PE conductor and structures of the equipotential bonding system. The amplitude of the induced voltage depends strongly on the loop length but only slightly on the loop width and on cable parameters such as twist length or conductor cross-section. Hence a mutual inductance per unit length can be derived to express the induced voltage. It is in the range of about 70–100 nH/m and can be used to estimate induced common mode currents.

It shall be mentioned that this phenomenon takes place for cables with twisted PE conductors only. It does not exist in the case of cables with concentric PE conductors which therefore should preferably be used when low magnetic stray fields are required.

REFERENCES

1. IEC 60364-4-44: Electrical installations of buildings — Part 4–44: Protection for safety — Protection against voltage disturbances and electromagnetic disturbances, 2001-08.

2. Heinhold, L., *Power Cables and Their Application*, Siemens Aktiengesellschaft, Berlin and Munich, 1990.

3. Petterson, P. and N. Schonborg, "Predicting the magnetic field from twisted three-phase arrangement," *IEEE 1997 International Symposium on Electromagnetic Compatibility*, 513–17, Austin, TX, USA, 1997.

4. Tesche, F. M., M. V. Ianoz, and T. Karlsson, *EMC Analysis Methods and Computational Models*, John Wiley & Sons, Inc., New York, 1997.

5. Hagel, R., L. Gong, and R. Unbehauen, "On the magnetic field of an infinitely long helical line current," *IEEE Transactions on Magnetics*, Vol. 30, No. 1, 80–84, Jan. 1994.

6. Mader, T. and H.-D. Brüns, "EFIE analysis of arbitrary metallic structures in the area of EMC," *9th Int. Zurich Symposium and Technical Exhibition on EMC*, Zurich, Switzerland, Paper 87M2, 1991.

7. Messer, R., "Investigation of low frequency magnetic stray fields of power cables and their coupling to grounding loops," Project report, University of York, UK, 1994.

8. Jaekel, B., "Investigations on induced common mode voltages in power cables," *17th International Wroclaw Symposium and Exhibition on Electromagnetic Compatibility*, 182–187, Wroclaw, Poland, 2004.

Measurement of Corona Characteristics and Electromagnetic Environment of ±800 kV HVDC Transmission Lines under High Altitude Condition

Zheng Zhang, **Rong Zeng**, **and Zhanqing Yu**

State Key Lab of Control and Simulation of Power Systems and Generation Equipments
Department of Electrical Engineering, Tsinghua University, Haidian District, Beijing 100084, China

Abstract— Measurement of corona characteristics was carried out on newly constructed ±800 kV HVDC test lines located in Kunming, China, with an altitude of 2100 m. Radio interference, audible noise, resultant electric field and ion current density at ground level were measured and compared with the calculated results. All these corona characteristics were also measured at other voltage levels for the purpose of comparison. The measured result show some difference with those acquired above sea level and is significant for further studies of corona mechanism under high altitude condition.

1. INTRODUCTION

Corona of power transmission lines refers to the discharge phenomenon accompanied with light emission, produced by the ionization of air around the conductors, when the conductor surface potential gradient exceeds a critical value, namely, the corona onset gradient [1]. The corona characteristics of DC transmission lines are different from those of AC lines mainly because of the magnitude of environmental space charge arisen from ionization in the space between the two conductors of the lines and between each conductor and ground [2]. The corona effect would not only cause corona loss (CL) but also influence the environment, which includes electric field effect, radio interference (RI) and audible noise (AN), etc. Due to the existence of space charge caused by corona, the electric field under HVDC transmission lines is actually the resultant electric field formed by electric charges on the conductors and in the space together. Parameters used to describe the electric field effect include resultant electric field (Es) and ion current density (Js) at ground level, etc. Corona performance is an important consideration in the design and operation of HVDC transmission lines.

From the 1970s, many countries such as USA and Canada have carried out experimental researches on the electromagnetic environment of HVDC lines [3, 4] and brought forward many empirical formulae for the calculation of CL, RI, AN, etc. However, most of these researches were carried out under lower voltage levels and altitudes.

In recent years, the rapid economic development in China has called for great needs in electricity. Under such circumstances, the ultra HVDC power transmission technique, which could realize power delivery in larger capacity and longer distance, is developing rapidly in accordance with the nation's energy policy. The construction of a brand new power test base and ±800 kV HVDC test lines has recently been completed in Kunming, a famous tourist city in southwest China with an altitude of 2100 m. The corona performance of the lines with the voltage level above 800 kV and under an altitude of more than 2000 m has never been researched and is a brand new and scholarly worthy field to study.

2. MEASUREMENT FIELD, EQUIPMENT AND METHOD

The test line has 4 towers and a length of 800 m (Figure 1). The length of the segment between the two towers in the middle is 410 m and the other two segments at each side are 195 m respectively. The distance between the two poles is 22 m and the minimum height of the lines at mid-span is 18 m. The type of the mounted bundle is $6 \times$ LGJ-630/45, with a diameter of 3.36 cm of a single conductor and a distance of 45 cm between nearby sub-conductors in the bundle.

RI is measured using an ETS-Lindgren6507 loop antenna and a Schaffner SCR3502 radio receiver. The pedestal of the antenna is 1.5 m high. The section of the antenna is rotated parallel to the lines in order to get the maximum readings, which are represented as quasi-peak values. AN is measured using a TES1353 sound level meter held at 1.5 m high and the result is represented as equivalent A-level. This frequency weighed network can best simulate the average response of human ear to pure sound. Es is measured using a rotating voltage meter which has been calibrated

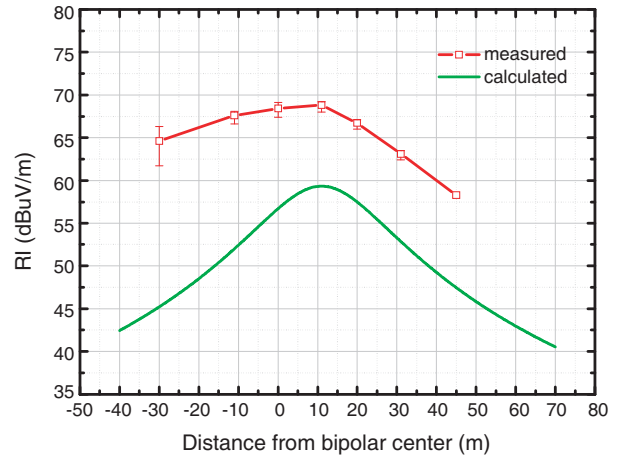Figure 1: Picture of the test lines and measurement field.

Figure 2: Lateral profile of RI at ±800 kV.

before measurement, while Js is acquired with a $0.6\,\text{m} \times 0.6\,\text{m}$ metal plate for receiving the ion current flowing down to the ground. Js data is read in voltage unit from a voltage meter and then converted into current density by dividing the resistance inside the meter and the area of the plate.

All the corona characteristics are measured point by point at predetermined location perpendicular to the lines. The data at each point should be read several times and the measurement result is expressed as average values as well as maximum and minimum errors.

3. CORONA CHARACERISTICS AT NOMINAL VOLTAGE LEVEL

3.1. RI

Both measured and calculated results of the lateral profile of RI at ±800 kV are shown in Figure 2. The calculation is based on the Special International Committee on Radio Interference (CISPR) empirical formula for RI, which is internationally recognized:

$$\text{RI} = 38 + 1.6(g_{\max} - 24) + 46\log(r) + 5\log(N) + \Delta E_f + 33\log\left(\tfrac{20}{D}\right) + \Delta E_w$$
$$\Delta E_f = 5\left[1 - 2\left(\log(10f)\right)^2\right] \tag{1}$$

In the formula, $g_{\max}$ represents the maximum bundle gradient (kV/cm), r is the radius of the sub-conductor (cm), N is the number of sub-conductors in a bundle, D is the distance of the calculated point from the positive pole (m), ΔE_w is a meteorological correction term with an addition of 3.3 dB per 1000 m with a benchmark of 500 m, ΔE_f is a frequency correction term, and f represents the frequency needed.

In Figure 2, the zero point of the abscissa represents the center of the two lines and the positive direction represents the direction towards the positive pole. The frequency under test is 0.5 MHz and the corresponding environmental RI is 53.8 dB. According to the figure, the measured RI attains maximum beneath the positive pole and declines to either side. The maximum value is 68.8 dB. The RI at 20 m from the positive pole is 63.1 dB. The calculated maximum and RI at 20 m from the positive pole are 59.3 dB and 52.9 dB respectively. The calculated RI profile is in accordance with the measured profile under and beyond the positive pole, and is 9 to 10 dB lower. However, calculated RI attenuates faster along the negative side than the measured. This is probably due to the difference of corona mechanism between higher altitude and above sea level. The inner causation needs further investigation.

3.2. Es

The measured result of Es at ±800 kV is shown in Figure 3. The calculated resultant electric field as well as the nominal electric field without space charge using the Electric Power Research Institute (EPRI) semi-empirical formula [6] is also illustrated in the figure. It shows that measurements carried out at different time vary in a range, which is mainly due to the variation of weather parameters such as temperature, humidity, wind velocity and air pressure. The average value at the maximum Es position near the positive pole is about 35 kV/m, while the minimum value

near the negative pole is about $-40\,\mathrm{kV/m}$. The calculated result is generally accordant with the measured one and the resultant field is 2 to 3 times of the nominal field, which manifests that the presence of the space charge increases the electric field at ground level.

3.3. Js

The measured result as well as the calculated result using EPRI semi-empirical formula [6] for Js at $\pm 800\,\mathrm{kV}$ is illustrated in Figure 4. Measured results at different time fluctuate intensely for the reason that the space charge is very keen to weather conditions especially the wind, and the wind velocity could reach a maximum of $10\,\mathrm{m/s}$ at the test base. Thus, the moments when the instant wind velocity is less than $2\,\mathrm{m/s}$ are chosen to record the Js data. The calculated result near the positive pole is well consistent with the measured, but the absolute value of calculated result near the negative pole is significantly higher than the measured counterpart. It is generally recognized that the mobility of negative ions is larger than that of the positive and thus leads to higher Js in absolute value under the negative pole. The measured result doesn't reflect the difference possibly because the wind may influence the Js profile and high altitude condition may affect the ion mobility. The internal mechanism has to been further investigated.
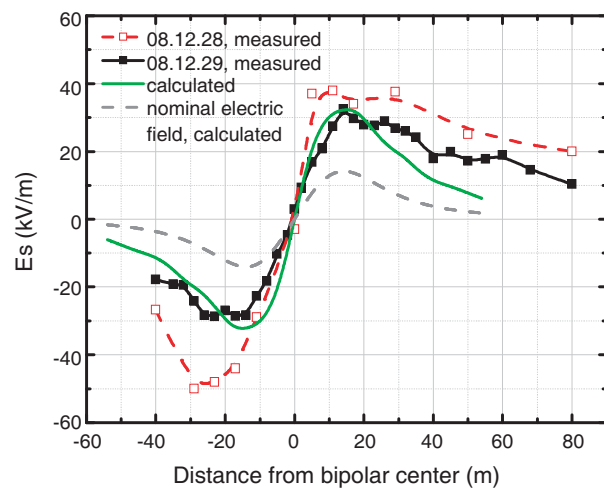
Figure 3: Lateral profile of Es at $\pm 800\,\mathrm{kV}$.
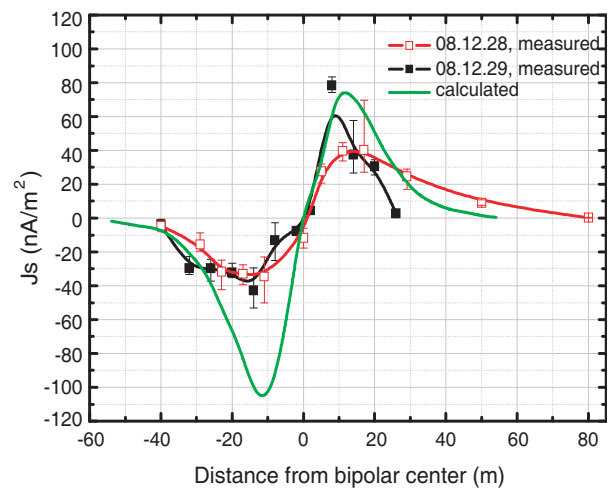
Figure 4: Lateral profile of Js at $\pm 800\,\mathrm{kV}$.
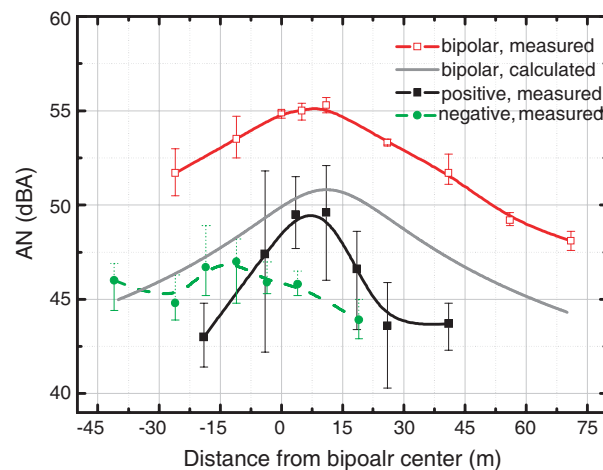
Figure 5: Lateral profile of AN at $950\,\mathrm{kV}$.

4. CORONA CHARACERISTICS AT DIFFERENT VOLTAGE LEVELS

Measurement of corona characteristics is also carried out under other three voltage levels: $\pm 500\,\mathrm{kV}$, $\pm 600\,\mathrm{kV}$ and $\pm 950\,\mathrm{kV}$. The result of AN, Es and Js are illustrated below.

Since the construction of the test base has not been completed, the vehicles onsite and airplanes frequently passing by has introduced irregular ambient noise comparable with AN produced by the lines at intervals, which makes it difficult to obtain proper AN data at any time. Bipolar, positive and negative AN profile at the voltage level of 950 kV are available and illustrated in Figure 5. At that time the ambient noise with the poles unenergized is 42 dB and has kept quite steadily in the whole measuring process. Corona produced AN can be easily distinguished. The calculated bipolar AN using the Bonneville Power Agency (BPA) empirical formula [5] as below is also illustrated in the figure.

$$
\begin{aligned}
\text{AN} &= -133.4 + 86 \cdot \lg g_{\max} + 40 \cdot \lg d_{eq} - 11.4 \cdot \lg D \\
d_{eq} &= 6.6 \cdot n^{0.64} \cdot d
\end{aligned}
\tag{2}
$$

In the formula, d is the diameter of the sub-conductor (cm), n is the number of sub-conductors in a bundle, and $g_{\max}$ and D have the same meaning as in Equation (1). Bipolar AN is obviously higher than monopolar AN, so as the positive AN than the negative AN. The result supports that the positive corona is the main source of AN in HVDC lines. The maximum bipolar AN is about 55 dB under the positive pole. The calculated AN profile is in accordance with the measured, but is holistically 4 dB lower than the measured result, which is possibly due to the increase of altitude. The altitude of the test base is 2100 m. The benchmark of the formula is 500 m. It can be deduced from the comparison that the altitude correction factor for AN is 2.5 dB per 1000 m.

Figures 6 and 7 show the measured Es and Js profiles at different voltage levels respectively. The profile of the other three voltages is consistent with the ± 800 kV result. The lines almost do not generate corona at 500 kV, so there is hardly any space charge and ion current under the lines, and the Es contains the nominal component only. As the voltage increases, the corona becomes more intense and the value of both Es and Js increases.
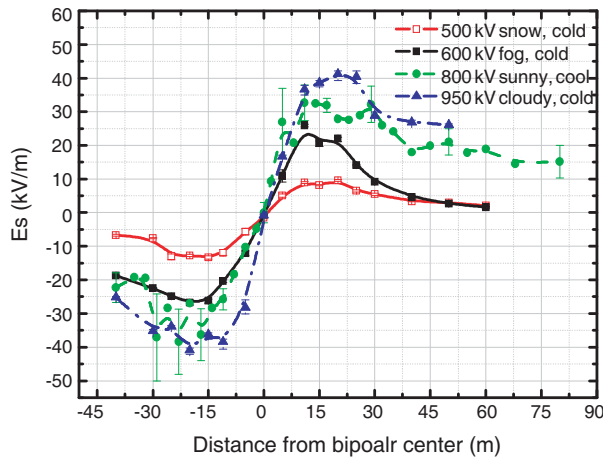

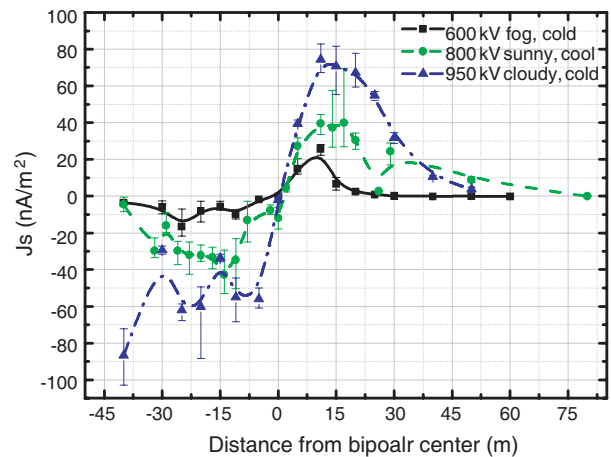Figure 6: Lateral profile of Es at different voltage levels.

Figure 7: Lateral profile of Js at different voltage levels.

5. CONCLUSION

A thorough measurement study of the corona characteristics of HVDC transmission lines with the nominal voltage of ± 800 kV was carried out. The result shows that positive corona is the main source of RI and AN. Tests at the nominal voltage show that measured RI is 9 to 10 dB higher than the calculated result under and beyond the positive pole along the profile vertical to the lines, and attenuates more slowly than the calculated profile along the negative side. The measured Es is well in accordance with the calculated result, whereas the measured Js is lower than the calculated in absolute value under the negative pole. AN measured at ± 950 kV is 4 dB higher than the calculated result along the profile and an altitude correction factor of 2.5 dB per 1000 m was deduced. Measurements at different voltage levels reveal that all the corona characteristics increase with the voltage and the profiles are similar.

Differences between measured results and calculated results using empirical formulae can be concluded into two major reasons: the first is that all the corona characteristics are sensitive to

weather conditions, therefore long-term measurement is needed to acquire profiles expressed in cumulative distributions; and the second is probably due to the difference in corona mechanism under high altitude and thin air condition, which requires further investigations.

REFERENCES

1. Maruvada, P. S., *Corona Performance of High-voltage Transmission Lines*, Research Studies Press Ltd, Baldock, Herfordshire, England, April 2000.
2. *HVDC Transmission Line Reference Book*, Published by EPRI, Palo Alto, California, USA, 1993.
3. *Transmission Line Reference Book HVDC to* $\pm 600\,kV$, Published by EPRI, Palo Alto, California, USA, 1977.
4. Maruvada, P. S., et al., *EPRI Report EL-1170, Bipolar HVDC Transmission System Study Between* $\pm 600\,kV$ *and* $\pm 1200\,kV$*: Corona Studies, Phase I*, Published by EPRI, Palo Alto, California, USA, 1979.
5. Zhao, W., *HVDC Engineering Technology*, China Electric Power Press, Beijing, China, May 2005.
6. *EPRI Report EL-2257, Conductor Development*, Published by EPRI, Palo Alto, California, USA, February 1982.

No Maxwell Electromagnetic Wavefield Excited inside Cloaked Concealment and Broadband GL Cloaks

Jianhua Li, **Ganquan Xie**, **Lee Xie**, **and Feng Xie**

GL Geophysical Laboratory, USA

Abstract— The simulations of the electromagnetic (EM) wave field excited from the point source inside the cloak device is presented in this paper. By using the GL modeling simulation, we found a phenomenon that there exists no Maxwell EM wave field can be excited by nonzero sources inside of the single layer cloaked concealment with normal materials. The theoretical proof of the phenomenon by GL method is proposed in this paper. The GL method is fully different from the conventional methods. We propose a broadband GL cloak. The GL method has double abilities of the theoretical analysis and numerical simulations to research the physical process and cloak metamaterial properties that is exhibited in this paper.

1. INTRODUCTION

For the point source located outside of the cloak, the 3D Global and Local field (GL) EM modeling method [1–3] has been used to simulate the 3D full EM wave field propagation through the cloaks. Our simulations and theoretical analysis verify the cloak functions from the exterior EM field. The EM wave field propagation outside of cloak does not penetrate into the concealment and never be disturbed by the cloaks [4]. The cloak simulation of the point sources and the local sources inside of the cloak is lack in the published papers. The GL modeling simulations of the EM wave field through cloak and excited by the nonzero local sources inside of the cloak is presented in this paper. Moreover, the point source inside the concealment, the GL EM method simulations meet divergent and chaos difficulty. The many failing simulation results remind and motivate us to suspect the claim in [4] "no field may escape from the region". We discover a phenomenon that there is no Maxwell EM wave field can be excited by nonzero local sources inside the cloaked concealment [5]. The phenomenon is proved by the GL method theoretical analysis and the EM integral equation [1–3]. For overcoming the weakness and difficulty of the single layer cloak, we propose a novel GL double layer EM cloak [6]. Finding and exploration is inverse problem; Hiding and cloaking is other inverse problem. They have close relationship. A double layer cloth phenomenon to prevent the GILD inversion [7–9] detection has been observed in [10] in 2001 which is published in SEG online: The double cloth anti detection is obvious around the fly in Figure 11 and around the bar in Figure 2 in [10]. After that year, we chose a computational physical simulation approach to study the metamaterial and photonic crystals etc. new materials. We developed a novel and effective Global and Local field (GL) modeling and inversion to study and simulate the metamaterials, periodic photonic crystals and condense nanometer materials etc. wide physical sciences. 3D GL EM modeling and inversion [11] and computational mirage [12] have been presented in PIERS 2005 and published in the proceeding of PIERS 2005 in Hangzhou in Piers web. Metamaterial of the novel GL double layer cloak is proposed and simulated in this paper and eprint papers [6].

To study the EM wave excited from local sources inside of the cloaked concealment is in a few papers. Authors of [13] and [14], studied the effect on invisibility of active devices inside the cloaked region. Author in [14] stated that "when these conditions are over-determined, finite energy solutions typically do not exist". Our statement is that: "There exists no Maxwell EM wave field that can be excited by nonzero local sources inside of the single layer cloaked concealment with normal materials [5]. The phenomenon without EM wave excited in the cloaked concealment may make the concealment to be complete dark hole, Moreover, it may cause that the excited EM field in the concealment is divorced from Maxwell governing and becomes an irregular chaos radiation, the high frequency chaos radiation interferes the EM devices and equipments and hurt the health of human working in the cloaked concealment. The single layer cloak is unsafe and insufficient. We propose a broadband GL cloak. Our GL double layer EM cloak overcomes the weakness and difficulty of the single layer cloak.

Our GL modeling and inversion method is fully different from conventional methods for cloak and physical and science simulations. It has advantages over the conventional methods. The GL method consistent combines the theoretical analytical and numerical method together. In the GL modeling, there is no big matrix equation to solve and no absorption condition on artificial

boundary to truncate infinite domain. The method is a significant physical scattering process. The finite inhomogeneous domain is divided into a set of small sub domains. The interaction between the global field and anomalous material polarization field in the sub domain causes a local scattering wave field. The local scattering wave field updates the global wave field by an integral equation. Once all sub domains are scattered, the wave field in the inhomogeneous anomalous materials will be obtained. Therefore, the GL method can be used to both of theoretical analysis and numerical simulation for physical and chemical phenomena and process.

The description arrangement of the paper is as follows. The introduction is described in Section 1. The Global and Local EM field modeling is proposed in Section 2. The phenomenon that there is no the Maxwell EM wave field can be excited by the local sources inside of the concealment is proved in Section 3. The GL modeling simulations of the EM wave field propagation through the cloaks are presented in Section 4. The frequency broadband GL cloak is presented in Section 5. We make discussion and conclusions in Section 6.

2. 3D GLOBAL AND LOCAL EM FIELD MODELING

2.1. The 3D EM Integral Equations

The 3D EM integral equation in frequency domain has been proposed in authors' papers [1] and [2]. In this paper, we proposed the EM integral equation in time domain as follows:

$$
\begin{bmatrix} E(r,t) \\ H(r,t) \end{bmatrix} = \begin{bmatrix} E_b(r,t) \\ H_b(r,t) \end{bmatrix} + \int_\Omega G_{E,H}^{J,M}(r',r,t) *_t \delta[D(r')] \begin{bmatrix} E_b(r',t) \\ H_b(r',t) \end{bmatrix} dr',
\tag{1}
$$

The detailed EM integral equation is proposed in [6].

2.2. 3D GL EM Modeling

We propose the GL EM modeling based on the EM integral equations (1) and (2) [6] in the time space domain. The detailed GL method in time domain is presented in the eprint [6]. The GL EM modeling in the space frequency domain is proposed in the paper [1, 2], we call the GL modeling in frequency domain as GLF method.

3. NO MAXWELL ELECTROMAGNETIC WAVE FIELD CAN BE EXCITED INSIDE CLOAKED CONCEALMENT

3.1. There Exists No Maxwell EM Wavefield Can Be Excited By Nonzero Local Sources inside of the Single Layered Cloaked Concealment with Normal Materials

Statement: Suppose that a 3D anisotropic inhomogeneous single layered cloak domain separates the whole 3D space into three sub domains, one is the single layered cloak domain Ω_{clk} with the cloak material; the second one is the cloaked concealment domain Ω_{conl} with normal EM materials; other one is the free space outside of the cloak. If the Maxwell EM wavefield excited by a point source or local sources outside of the concealment Ω_{conl} is vanished inside of the concealment Ω_{conl}, then there is no Maxwell EM wave field can be excited by the local sources inside of the cloaked concealment Ω_{conl}.

The statement is proved by the GL method in author's paper [5]. The Maxwell EM wavefield is the EM wave field which satisfies the Maxwell equation and continuous interface boundary conditions. We call the Maxwell EM wavefield as the EM wavefield and use inverse process to prove the *statement* 2 as follows: Suppose that there exists Maxwell EM wavefield excited by the local sources inside the concealment with the normal materials, the wavefield satisfies the Maxwell equation in the 3D whole space R^3 which includes the anisotropic inhomogeneous cloak domain Ω_{clk} and concealment Ω_{conl}, and satisfies the continuous interface conditions on the interface boundary surface S_1 and S_2. The S_1 is the interface boundary surface between the cloak domain Ω_{clk} and the concealment Ω_{conl}, it also is the inner boundary surface of the cloak domain Ω_{clk}. The S_2 is the interface boundary surface between the cloak domain Ω_{clk} and the free space, it also is the outer boundary surface of the cloak domain Ω_{clk}.

Let $R_c = R^3 - \Omega_{clk} \bigcup \Omega_{conl}$, $R_d = R^3 - \Omega_{conl}$, and by the EM integral equation (1), the EM wave field satisfies

$$
\begin{bmatrix} E(r,t) \\ H(r,t) \end{bmatrix} = \begin{bmatrix} E_b(r,t) \\ H_b(r,t) \end{bmatrix} + \int_{\Omega_{clk} \bigcup \Omega_{conl}} G_{E,H}^{J,M}(r',r,t) *_t \delta[D] \begin{bmatrix} E_b(r',t) \\ H_b(r',t) \end{bmatrix} dr',
\tag{2}
$$

where $G_{E,H}^{J,M}(r',r,t)$ is the EM Green's tensor, its components E^J, H^J, E^M, and $H^M(r',r,t)$ are the EM Green's function on $\Omega_{clk} \bigcup \Omega_{conl} \bigcup R_c$, excited by the point impulse sources outside of the concealment, $r \in R_d$. By the assumptions, $G_{E,H}^{J,M}(r',r,t)$ exists on $\Omega_{clk} \bigcup \Omega_{conl} \bigcup R_c$ and when $r' \in \Omega_{conl}$, $G_{E,H}^{J,M}(r',r,t) = 0$. The integral equation (2) becomes to

$$\left[\begin{array}{c} E\,(r,t) \\ H\,(r,t) \end{array}\right] = \left[\begin{array}{c} E_b\,(r,t) \\ H_b\,(r,t) \end{array}\right] + \int\limits_{\Omega_{clk}} G_{E,H}^{J,M}\,(r',r,t) *_t \delta\,[D] \left[\begin{array}{c} E_b\,(r',t) \\ H_b\,(r',t) \end{array}\right] dr'. \tag{3}$$

We consider the Maxwell equation in R_d, the virtual source is located r, $r \in R_d$ and the point source is located r_s, $r_s \in \Omega_{conl}$ and $r_s \notin R_d$, we have

$$\left[\begin{array}{cc} & \nabla\times \\ -\nabla\times & \end{array}\right] G_{E,H}^{J,M}\,(r',r,t) = [D]\,G_{E,H}^{J,M}\,(r',r,t) + I\delta(r',r)\delta(t), \tag{4}$$

and

$$\left[\begin{array}{cc} & \nabla\times \\ -\nabla\times & \end{array}\right] \left[\begin{array}{c} E_b \\ H_b \end{array}\right](r',r_s,t) = [D_b] \left[\begin{array}{c} E_b \\ H_b \end{array}\right](r',r_s,t), \tag{5}$$

By using $[E_b(r,t), H_b(r,t)]$ to convolute (4), and $G_{E,H}^{J,M}(r',r,t)$ to convolute (5), to subtract the second result equation from the first result equation and make their integral in R_d, and use integral by part and make some manipulations, we can prove

$$\left[\begin{array}{c} E_b\,(r,t) \\ H_b\,(r,t) \end{array}\right] + \int\limits_{\Omega_{clk}} G_{E,H}^{J,M}\,(r',r,t) *_t \delta\,[D] \left[\begin{array}{c} E_b\,(r',t) \\ H_b\,(r',t) \end{array}\right] dr' = \oint\limits_{S_1} G_{E,H}^{J,M}\,(r',r,t) \otimes_t \left[\begin{array}{c} E_b\,(r',t) \\ H_b\,(r',t) \end{array}\right] d\vec{S}, \tag{6}$$

where $\otimes_t$ is cross convolution. From the assumption of the *statement* that "the Maxwell EM wavefield excited by a point source or local sources outside of the concealment Ω_{conl} is vanished in inside of the concealment Ω_{conl}", and virtual source r is located outside of the concealment, $r \in R_d$, if $r' \in \Omega_{conl}$, $G_{E,H}^{J,M}(r',r,t) = 0$. By continuity, when $r' \in S_1$, we have $G_{E,H}^{J,M}(r',r,t) = 0$. By continuous interface conditions of $G_{E,H}^{J,M}(r',r,t)$, the term in right hand side of (6) is vanished, we have

$$\left[\begin{array}{c} E_b\,(r,t) \\ H_b\,(r,t) \end{array}\right] + \int\limits_{\Omega_{clk}} G_{E,H,b}^{J,M}\,(r',r,t) *_t \delta\,[D] \left[\begin{array}{c} E\,(r',t) \\ H\,(r',t) \end{array}\right] dr' = 0. \tag{7}$$

Upon substituting integral equation (7) into the integral equation (3), we have

$$\left[\begin{array}{c} E\,(r,t) \\ H\,(r,t) \end{array}\right] = 0. \tag{8}$$

From the continuous property of the EM wave field, we obtain the following over vanish boundary condition on the boundary S_1 of the concealment Ω_{conl}, we have

$$\left.\left[\begin{array}{c} E\,(r,r_s,t) \\ H\,(r,r_s,t) \end{array}\right]\right|_{S_1} = 0, \tag{9}$$

where r_s denotes point source location inside of the concealment, r is EM field receiver point, $r \in S_1$. The (9) is the over vanished boundary condition. In the paper [5] and [6]. we proved that there exists no EM wavefield satisfies the Maxwell equation and the over vanished boundary condition (9). Therefore, we proved the *Statement* that there exists no Maxwell EM wavefield can be excited by the nonzero local sources inside of the single layered cloaked concealment with normal materials.

For overcoming the weakness and difficulty of the single layer cloak, we propose a novel GL double layer EM cloak [6, 19]. Our GL double layer cloak consists of the outer layer and inner layer. The outer layer has invisibility function, it cloaks the Local concealment from the Global exterior EM wavefield excited in the free space. The Global exterior wavefield in free space never be disturbed by the outer layer. The inner layer has absorption function, it cloak the Global exterior or free space region from the inner EM wavefield excited in the concealment. The inner EM wave field never be disturbed by the inner cloak.

We discovered a single negative metamaterial [19] and fill it in the sphere concealment which is cloaked by the sphere annular single layer cloak, for example the cloak by Pendry [4]. The GL modeling simulation show that the EM wave excited in the concealment propagates go out to the free space through the Pendry single layer cloak. That means the single layer cloak loss the invisibility for the special metamaterial in the concealment. Therefore, our GL double layer cloak is necessary. Also, by the statement, the EM field excited in the concealment is divorced from the Maxwell equation, it may be an irregular EM chaos propagation in this region, and interferes the EM devices and equipments working inside of the concealment, the high frequency irregular EM chaos radiation will hurt the health of the human, the single layer cloak is unsafe. Our GL double layer cloak is safe and robust cloak.

4. SIMULATION OF THE EM WAVE FIELD THROUGH THE CLOAKS BY GL METHOD

Simulation for the EM wave field excited by the point source, in particular, the source located inside of cloak, $r_s \in \Omega_c$, or inside of concealment $r_s \in \Omega_d$ is lack.

4.1. The Simulation Model of The GL Double Layered Cloak

The simulation model: the 3D domain is $[-0.5\,\text{m}, 0.5\,\text{m}] \times [-0.5\,\text{m}, 0.5\,\text{m}] \times [-0.5\,\text{m}, 0.5\,\text{m}]$, the mesh number is $201 \times 201 \times 201$, the mesh size is $0.005\,\text{m}$. The electric current point source is defined as

$$\delta(r - r_s)\delta(t)\vec{e}, \tag{10}$$

where the r_s denotes the location of the point source, the unit vector $\vec{e}$ is the polarization direction, the time step $dt = 0.3333 \times 10^{-10}$ second, the frequency band is from $0.05\,\text{GHz}$ to $15\,\text{GHz}$, the largest frequency $f = 15\,\text{GHz}$, the shortest wave length is $0.02\,\text{m}$. The EM GL double layered cloak $\Omega_{GL} = \Omega_{GLI} \bigcup \Omega_{GLO}$ is consist of the double spherical annular Ω_{GLI} and Ω_{GLO} with the center in the origin and interior radius $R_1 = 0.22\,\text{m}$, meddle radius $R_2 = 0.3\,\text{m}$. and exterior radius $R_3 = 0.35\,\text{m}$. The cloak is divided into $90 \times 180 \times 90$ cells. The spherical coordinate is used in the sphere $r \leq R_3$, the Cartesian rectangular coordinate is used in outside Ω_{GL} to mesh the domain.

4.2. The Point Source in the Concealment and Other Point Source in the Free Space

The two point sources are used to excite the EM wave propagation through the GL double layered cloak. The first point current source is located inside of the center sphere concealment at $(-0.12\,\text{m}, -0.12\text{m}, 0.0)$, by which the excited EM wave $E_{xx,1}$ is named *First electric wave*. The second current point source is located in free space at $(0.518\,\text{m}, 0.518\,\text{m}, 0.0)$ where is the right and

Figure 1: (color online) At time step $98dt$, front of *Second EM wave*, $E_{xx,2}$ inside of the outer layer of GL cloak $R_2 \leq r \leq R_3$ propagates more faster than light speed. The wave front of the *First electric wave*, $E_{xx,1}$, propagates inside the inner layer, $R_1 \leq r \leq R_2$.
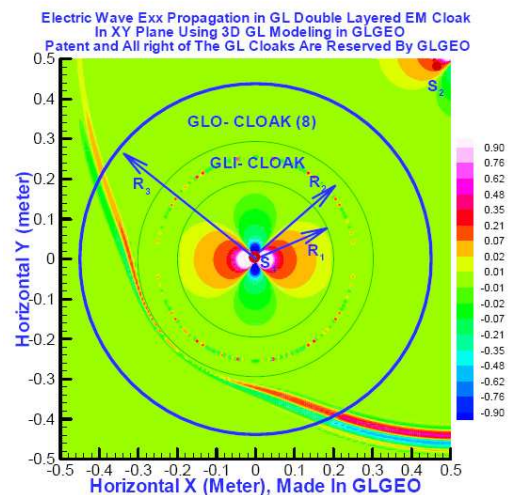
Figure 2: (color online) At time step $98dt$, front of *Second EM wave*, $E_{xx,2}$ inside of the outer layer of GL cloak $R_2 \leq r \leq R_3$ propagates a little faster than light speed. It is slower than $E_{xx,2}$ in Figure 1. The wave front of the $E_{xx,1}$, propagates inside the inner layer, $R_1 \leq r \leq R_2$.
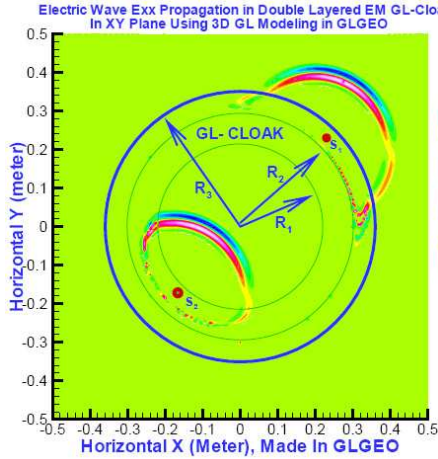
Figure 3: (color online) At the time step $21dt$, the Exx excited inside outer and inner layer cloaks propagate through cloaks.
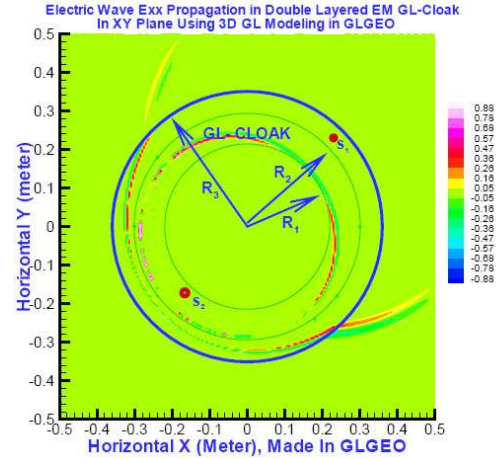

Figure 4: (color online) At the time step $48dt$, the Exx excited inside outer and inner layer cloaks are propagating through the cloak.

top corner outside of the whole GL double layered cloak. The EM wave $E_{xx,2}$, is named *Second electric wave*. The GL modeling simulations of the EM wave excited by above two point sources propagation through the GL double layered cloak are presented in the Figures 1–2. In the Figure 1, at time step $98dt$, front of the *Second electric wave*, $E_{xx,2}$, inside the outer layer cloak, $R_2 \leq r \leq R_3$, propagates more faster than the light speed. The *First electric wave*, $E_{xx,1}$, is propagating inside of the inner layer of the GL double layer cloak, $R_1 \leq r \leq R_2$. In the Figure 2, at time step $98dt$, front of the *Second electric wave*, $E_{xx,2}$, inside the outer layer cloak, $R_2 \leq r \leq R_3$, propagates only a little faster than the light speed. It is shower than $E_{xx,2}$ in the Figure 1. The *First electric wave*, $E_{xx,1}$, is propagating inside of the inner layer of the GL double layer cloak, $R_1 \leq r \leq R_2$. The outer layer cloak material in Figure 2 has more frequency broadband than the cloak in Figure 1.

4.3. The Point Source in the Inner Layer Ω_{GLI} and Other Point Source in the Outer Layer Ω_{GLO}

The 3D EM full wave excited by the point source in the inner layer and other point source in the outer layer of GL double Layered cloak are simulated by using GL EM modeling. The two point sources are used to excite the EM wave propagation through the GL double layered cloak. The first point current source is located inside of the inner layer of the GL cloak at $(-0.165\,\mathrm{m},\ -0.165\,\mathrm{m},\ 0.0)$, by which the excited EM wave is named *First electric wave*. The second current point source is located in outer layer GL cloak at $(0.23\,\mathrm{m},\ 0.23\,\mathrm{m},\ 0.0)$. The EM wave by the second source is named as *Second electric wave*. In the Figure 3, at moment $21dt$, one part of the front of the *First electric wave*, $E_{xx,1}$, propagates enter to the concealment; other part of the front is still propagating inside of inner layer, $R_1 \leq r \leq R_2$. One part of front of *Second electric wave*, $E_{xx,2}$, reaches the middle interface boundary $r = R_2$; other part of the front has propagated outside of the whole cloak and in free space with disturbance. At the time step $48dt$, the *First electric wave*, $E_{xx,1}$, has propagated through the concealment and whole front is inside of the inner layer of the GL cloak $R_1 \leq r \leq R_2$, its speed is smaller than the light speed. The *Second electric wave* never propagates into the inner layer of GL cloak. The part of the front of *Second electric wave*, $E_{xx,2}$, is inside of outer layer of the GL double layered cloak, $R_2 \leq r \leq R_3$, and being forward bending with speed lager than the light speed. Other part of the front has been propagating in free space with disturbance. The EM wave propagation image is presented in Figure 4.

5. FREQUENCY BROADBAND

5.1. The Inner Layer Material Has Frequency Broadband

The inner layer material of the GL double layer cloak [6] has frequency broadband. The EM wavefield speed in the inner material is slower than the light speed.

5.2. A Outer Layer Cloak Material Has Frequency Broadband

We proposed a new #8 outer layer material for the GL double layer cloak [19]. By comparison between the electric wavefield E_{xx} propagation in Figure 2 and Figure 1 by the same source and in same configuration, it is obvious that the #8 outer cloak material has much more broadband than #2 cloak material. In Figure 1, at $98dt$ time step, the E_{xx} in the #2 outer layer cloak propagates more faster than light speed, while in Figure 2, at $98dt$ time step the E_{xx} in the #8 outer layer cloak propagates shower than it does in Figure 1. The E_{xx} in the #8 outer layer cloak propagates only a little faster than the light speed. Therefore, #8 outer layer cloak material has frequency broadband.

6. CONCLUSIONS

The GL method is suitable to simulate the invisibility of the sphere and arbitrary cloaks. Statement that "there excites no Maxwell EM wave field can be excited by the nonzero local sources inside single layer cloaked concealment with normal materials" is discovered and proved by the GL method. The single layer cloak is unsafe and insufficient. Our GL double layer EM cloak overcomes the weakness and difficulty of the single layer cloak. The GL double layer cloak is robust, safe, complete and sufficient cloak which is necessary for cloak design and fabrication. The GL EM method consistent combines the analytical and numerical approaches together. The GL method has double capabilities of the theoretical analysis and numerical simulations to study the cloak metamaterials and wide material and field scattering in physical sciences.

The 3D and 2D GL parallel software is made and patented by GLGEO. The GL modeling can be extended to GL EM quantum field modeling to solve quantization scattering problem of the electromagnetic field in the dispersive and loss metamaterials, cloaks and more wide anisotropic materials.

REFERENCES

1. Xie, G., F. Xie, L. Xie, and J. Li, "New GL method and its advantages for resolving historical diffculties," *Progress In Electromagnetics Research*, PIER 63, 141–152, 2006.
2. Xie, G., J. Li, L. Xie, and F. Xie, "GL method for solving equation in math-physics and engineering," *Acta Mathematicae Application Sinica*, Vol. 23, No. 2, 391–404, 2008.
3. Xie, G., J. Li, L. Xie, and F. Xie, "GL metro carlo EM inversion," *Journal of Electromagnetic Waves and Applications*, Vol. 20, No. 14, 1991–2000, 2006.
4. Pendry, J. B., D. Schurig, and D. R. Smith, "Controlling electromagnetic field," *Science Express*, Vol. 312, 1780, 2006.
5. Xie, G., J. Li, F. Xie, and L. Xie, "An electromagnetic GL double layered cloak," arXiv:0904.3168, 2009.
6. Li, J., G. Xie, F. Xie, and L. Xie, "No Maxwell electromagnetic wave field excited in cloaked concealment," arXiv:0904.3040, 2009.
7. Xie, G., J. Li, D. Zhuo, M. Enrest, and M. Oristaglio, "3-D electromagnetic modeling and nonlinear inversion," *Geophysics*, Vol. 65, No. 3, 804–822, 2000.
8. Xie, G. and J. Li, "New parallel SGILD modeling and inversion," *Physics D*, Vol. 133, 477–487, 1999.
9. Xie, G., "A new iterative method for solving the coefficient inverse problem of wave equation," *Comm. on Pure and Applied Math.*, Vol. 39, 307–322, 1986.
10. Li, J., G. Xie, C. Lin, and J. Liu, "2.5 dimensional GILD electromagnetic modeling and application," *SEG, Expanded Abstracts*, Vol. 21, No. 1, 692–695, 2002. http://www.segdl.org/journals/doc/SEGLIBhome/dci/searchDCI.jsp.
11. Xie, G., J. Li, and F. Xie, "New global and local electromagnetic field modeling," *Progress In Electromagnetics Research Symposium Abstracts*, 68, Hangzhou, China, August 24–28, 2005. [ISBN: 1-933077-06-9], http://piers.mit.edu/piersproceedings/piers2k5Proc.php.

12. Xie, F. and L. Xie, "New computational Mirage," *Progress In Electromagnetics Research Symposium Abstract*, 296, Hangzhou, China, August 24–28, 2005. [ISBN: 1-933077-06-9], http://piers.mit.edu/piersproceedings/piers2k5Proc.php.
13. Zhang, B., H. Chen, B. I. Wu, and J. Kong, "Extraordinary surface voltage effect in the invisibility cloak with an active device inside," *PRL*, Vol. 100, 063904-1 4, 2008.
14. Greenleaf, A., Y. Kurylev, M. Lassas, and G. Uhlmann, "Full-wave invisibility of active devices at all frequencies," *Communication Math. Phys.*, Vol. 275, 749–789, 2007.
15. Xie, G., "The 3-D finite element method in the elastic structure," *Mathematical Practice and Knowledge*, Vol. 1, 28–41, 1975 (Chinese).
16. Xie, G., J. H. Li, L. Xie, and F. Xie, "A new broadband invisible GL double layer EM cloak," *Technology Report of GL Geophysical Lab.*, Vol. 9, 11–28, 2009.
17. Brandts, J. and M. Krizek, "History and futures of superconvergence in three dimensional finite element method," *Mathematical Sciences and Applications*, Vol. 15, 24–35, 2001.

Surface Waves Suppression in a Biaxially Anisotropic Metamaterial Grounded Slab

Salma Mirhadi and Manoochehr Kamyab Hessari

Department of Electrical Engineering, K. N. Toosi University of Technology, Tehran, Iran

Abstract— In this paper, we have investigated specific conditions for suppression of transverse electric (TE) and transverse magnetic (TM) surface waves in a biaxially anisotropic metamaterial grounded slab. Ordinary and evanescent surface waves, which evanescent only in the air and both in the air and inside the slab respectively, are considered for TE and TM polarizations. On the basis of the graphical solution of dispersion equations, we have presented conditions which surface waves are eliminated. Consequently, this structure may be useful as a substrate for planar antennas.

1. INTRODUCTION

Recently, there has been a remarkable attention in properties and applications of materials which have either negative permittivity or negative permeability [1–9]. Materials with simultaneously negative permittivity and permeability, which referred to as left-handed materials (LHM) or double negative (DNG), were first studied by Veselago in 1968 [1]. There exist vast investigations on wave propagation through isotropic LHM [2, 3], but the LHM that have been made are actually dispersive and anisotropic and realization of 3D isotropic artificial left handed (LH) structures may be difficult [4, 5]. Some recent publications have dealt with the surface wave suppression in an isotropic metamaterial grounded slab for improvement planar antenna performance [6–8]. In this paper, according to the simple graphical analysis, we intend to derive sufficient conditions for suppression of surface waves in a biaxially anisotropic metamaterial grounded slab. We have shown that the suppression of surface waves in this structure is greatly dependent on the tensor components of the constitutive parameters, height of slab and operating frequency.

2. SURFACE WAVE MODES

The geometry under study is shown in Fig. 1. Region 1 is assumed to be a biaxially anisotropic metamaterial slab placed on a perfectly conducting ground plane and with relative permittivity and relative permeability as $\overline{\overline{\varepsilon_r}} = \varepsilon_x \hat{x}\hat{x} + \varepsilon_y \hat{y}\hat{y} + \varepsilon_z \hat{z}\hat{z}$ and $\overline{\overline{\mu_r}} = \mu_x \hat{x}\hat{x} + \mu_y \hat{y}\hat{y} + \mu_z \hat{z}\hat{z}$ respectively that part or all of components can be negative. Region 0 is considered to be a free space with permittivity ε_o and permeability μ_o. The guidance condition for ordinary TE surface waves with the real transverse wavenumber (k_{z1}) inside the slab and imaginary transverse wavenumber in the air (α_{z0}) can be written as [9]

$$\alpha_{z0} = -\frac{1}{\mu_x} (k_{z1}d) \cot (k_{z1}d) \tag{1}$$

Dispersion relations in Region 0 and 1 are respectively

$$(k_x d)^2 - (\alpha_{z0}d)^2 = (k_o d)^2 \tag{2}$$

$$(k_x d)^2 + \frac{\mu_z}{\mu_x} (k_{z1}d)^2 = (k_o d)^2 \varepsilon_y \mu_z \tag{3}$$

where k_x is the wavenumber in the x-direction and k_o is the free space wavenumber. Eqs. (2) and (3) can be combined as

$$(\alpha_{z0}d)^2 + \frac{\mu_z}{\mu_x} (k_{z1}d)^2 = (\varepsilon_y \mu_z - 1) (k_o d)^2 \tag{4}$$

For the evanescent TE surface waves, the transverse wavenumber inside the slab is imaginary $(k_{z1} = j\alpha_{z1})$ and we can obtain

$$\alpha_{z0}d = -\frac{1}{\mu_x} (\alpha_{z1}d) \coth (\alpha_{z1}d) \tag{5}$$

$$(\alpha_{z0}d)^2 - \frac{\mu_z}{\mu_x} (\alpha_{z1}d)^2 = (\varepsilon_y \mu_z - 1) (k_o d)^2 \tag{6}$$
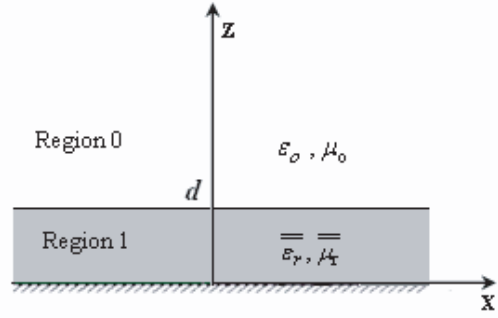
Figure 1: Geometry of biaxially anisotropic grounded slab waveguide with thickness d.

Similarly for ordinary TM surface waves, these equations may be expressed as

$$\alpha_{z0}d = \frac{1}{\varepsilon_x}(k_{z1}d)\tan(k_{z1}d) \tag{7}$$

$$(\alpha_{z0}d)^2 + \frac{\varepsilon_z}{\varepsilon_x}(k_{z1}d)^2 = (\mu_y\varepsilon_z - 1)(k_od)^2 \tag{8}$$

and for evanescent TM surface waves we can write

$$\alpha_{z0}d = -\frac{1}{\varepsilon_x}(\alpha_{z1}d)\tanh(\alpha_{z1}d) \tag{9}$$

$$(\alpha_{z0}d)^2 - \frac{\varepsilon_z}{\varepsilon_x}(\alpha_{z1}d)^2 = (\mu_y\varepsilon_z - 1)(k_od)^2 \tag{10}$$

3. GRAPHICAL SOLUTION OF DISPRSION EQUATIONS

3.1. Ordinary TE Surface Waves

Ordinary TE surface waves will be considered first. By combining Eqs. (1) and (4), we can obtain

$$\tan(k_{z1}d) = -\frac{1}{\mu_x} \times \frac{k_{z1}d}{\sqrt{(\varepsilon_y\mu_z - 1)(k_od)^2 - \frac{\mu_z}{\mu_x}(k_{z1}d)^2}} \tag{11}$$

and may be expressed as:

$$\tan(\zeta) = \frac{-\zeta}{\mu_x\sqrt{t_1 - t_2\zeta^2}} = f_{\text{ord}}^{\text{TE}}(\zeta) \tag{12}$$

where $\zeta = k_{z1}d$, $t_1 = (\varepsilon_y\mu_z - 1)(k_od)^2$ and $t_2 = \mu_z/\mu_x$. Studying of surface waves can be achieved graphically by finding the intersections between the tangent function at the left hand side of Eq. (12) and the function $f_{\text{ord}}^{\text{TE}}(\zeta)$ at the right hand side of the same equation as which employed in Ref. [6] for isotropic metamaterial grounded slab. As we can see, $f_{\text{ord}}^{\text{TE}}(\zeta)$ is dependent on μ_x, t_1 and t_2; therefore, we shall make our discussions based on the sign of them. The condition $t_1 < 0$, $t_2 > 0$ will not be studied because the function $f_{\text{ord}}^{\text{TE}}(\zeta)$ for $\zeta > 0$ is indefinite and ordinary TE surface waves cannot exist.

A) $\mu_x > 0$

A-1) $t_1 > 0$, $t_2 > 0$, The function $f_{\text{ord}}^{\text{TE}}(\zeta)$ is defined for $\zeta < \sqrt{t_1/t_2}$ and has negative value. Furthermore, it is monotonically decreasing in interval $[0, \sqrt{t_1/t_2})$, is zero at $\zeta = 0$ and tends to minus infinity for $\zeta \to \sqrt{t_1/t_2}^-$. By observing Fig. 2, we can find the conditions for avoiding intersection between $\tan(\zeta)$ and $f_{\text{ord}}^{\text{TE}}(\zeta)$ is

$$\sqrt{t_1/t_2} < \pi/2 \tag{13}$$

A-2) $t_1 > 0$, $t_2 < 0$, As we can see in Fig. 3, $f_{\text{ord}}^{\text{TE}}(\zeta)$ is defined for $\zeta > 0$, is monotonically decreasing, is zero at $\zeta = 0$ and tends to $-1/\mu_x\sqrt{|t_2|}$ for $\zeta \to \infty^+$. An interesting phenomenon

occurs that infinite ordinary TE surface modes can be supported by the grounded slab on account of the fact that infinite intersections between $f_{\mathrm{ord}}^{\mathrm{TE}}(\zeta)$ and the branches of $\tan(\zeta)$ exist so, suppression is impossible.

A-3) $t_1 < 0$, $t_2 < 0$, The function $f_{\mathrm{ord}}^{\mathrm{TE}}(\zeta)$ is defined for $\sqrt{|t_1/t_2|} < \zeta$, tends to $-\infty$ for $\zeta \to \sqrt{|t_1/t_2|}^+$ and tends to $-1/\mu_x\sqrt{|t_2|}$ for $\zeta \to \infty^+$. In addition, it is monotonically increasing. From Fig. 4, it is clear that the intersections between the branches of $\tan(\zeta)$ and $f_{\mathrm{ord}}^{\mathrm{TE}}(\zeta)$ always occur and surface waves suppression is impossible.

B) $\mu_x < 0$

B-1) $t_1 > 0$, $t_2 > 0$, In this condition, the function $f_{\mathrm{ord}}^{\mathrm{TE}}(\zeta)$ is defined for $\zeta < \sqrt{t_1/t_2}$ and is monotonically increasing in interval $[0, \sqrt{t_1/t_2})$, is zero at $\zeta = 0$ and tends to plus infinity for $\zeta \to \sqrt{t_1/t_2}^-$. It can be seen from Fig. 5 that there exists two cases for suppression of surface waves.

B-1-I) $\sqrt{t_1/t_2} < \pi/2$, as shown in Fig. 5 in the dashed line. In such a case, a straight line $r_1(\zeta) = c_1\zeta$ must be existed such that $\tan(\zeta)$ lies below it and $f_{\mathrm{ord}}^{\mathrm{TE}}(\zeta)$ lies above it. We choose $c_1 = 1/|\mu_x|\sqrt{t_1}$ which corresponds to derivative of $f_{\mathrm{ord}}^{\mathrm{TE}}(\zeta)$ at $\zeta = 0$ and must be more than the derivative of $\tan(\zeta)$ at $\zeta = 0$. Furthermore, $\tan(\sqrt{t_1/t_2})$ has to be less than $r_1(\sqrt{t_1/t_2})$. These conditions lead to

$$|\mu_x|\sqrt{t_1} < 1, \quad \sqrt{t_1/t_2} < \pi/2 \qquad \tan\left(\sqrt{t_1/t_2}\right) < 1/|\mu_x|\sqrt{t_2} \tag{14}$$

B-1-II) If $\pi/2 < \sqrt{t_1/t_2} < \pi$, as we can see in Fig. 5 in dash-dotted line, a straight line $r_2(\zeta) = c_2\zeta$ must be existed such that $\tan(\zeta)$ lies above it and $f_{\mathrm{ord}}^{\mathrm{TE}}(\zeta)$ lies below it. In this case, c_2 is equal to the derivative of $\tan(\zeta)$ at $\zeta = 0$ and must be more than the derivative of $f_{\mathrm{ord}}^{\mathrm{TE}}(\zeta)$ at $\zeta = 0$. Moreover, $f_{\mathrm{ord}}^{\mathrm{TE}}(\pi/2)$ has to be less than $r_2(\pi/2)$. We may write these conditions as:

$$\pi/2 < \sqrt{t_1/t_2} < \pi \qquad |\mu_x|\sqrt{t_1 - t_2(\pi/2)^2} > 1 \tag{15}$$

B-2) $t_1 > 0$, $t_2 < 0$, $f_{\mathrm{ord}}^{\mathrm{TE}}(\zeta)$ is defined for $\zeta > 0$, convex and monotonically increasing, is zero at $\zeta = 0$ and tends to $1/\mu_x|\sqrt{|t_2|}$ for $\zeta \to \infty^+$ as we can see in Fig. 6. Suppression of surface waves cannot occur since infinite intersections between the $f_{\mathrm{ord}}^{\mathrm{TE}}(\zeta)$ and the branches of $\tan(\zeta)$.

B-3) $t_1 < 0$, $t_2 < 0$, In this case, The function $f_{\mathrm{ord}}^{\mathrm{TE}}(\zeta)$ is defined for $\sqrt{|t_1/t_2|} < \zeta$, tends to $+\infty$ for $\zeta \to \sqrt{|t_1/t_2|}^+$ and tends to $1/|\mu_x|\sqrt{|t_2|}$ for $\zeta \to \infty^+$. In addition, it is monotonically decreasing as shown in Fig. 7. Infinite ordinary TE modes can propagate in the structure since there exist infinite intersections between two curves.
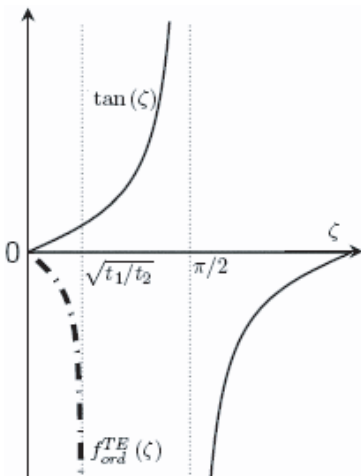

Figure 2: Graphical solution of Eq. (12) for ordinary TE surface waves in case $\mu_x > 0$, $t_1 > 0$, $t_2 > 0$ (A-1).
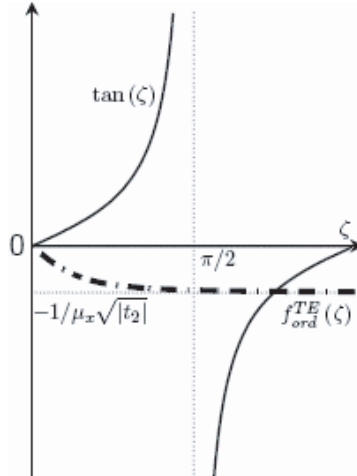
Figure 3: Graphical solution of Eq. (12) for ordinary TE surface waves in case $\mu_x > 0$, $t_1 > 0$, $t_2 < 0$ (A-2).
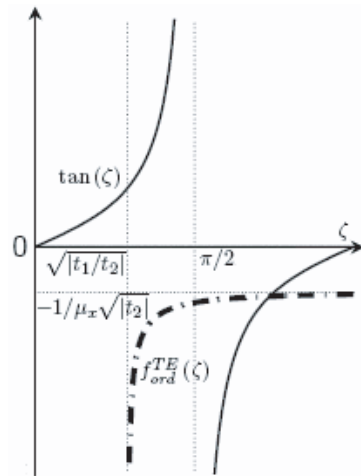
Figure 4: Graphical solution of Eq. (12) for ordinary TE surface waves in case $\mu_x > 0$, $t_1 < 0$, $t_2 < 0$ (A-3).
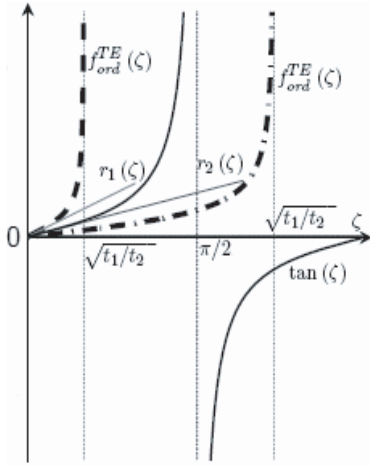
Figure 5: Graphical solution of Eq. (12) for ordinary TE surface waves in case $\mu_x < 0$, $t_1 > 0$, $t_2 > 0$ (B-1).
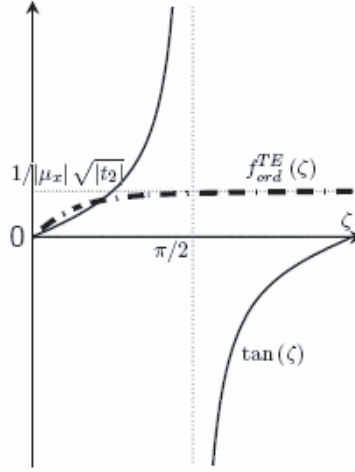
Figure 6: Graphical solution of Eq. (12) for ordinary TE surface waves in case $\mu_x < 0$, $t_1 > 0$, $t_2 < 0$ (B-2).
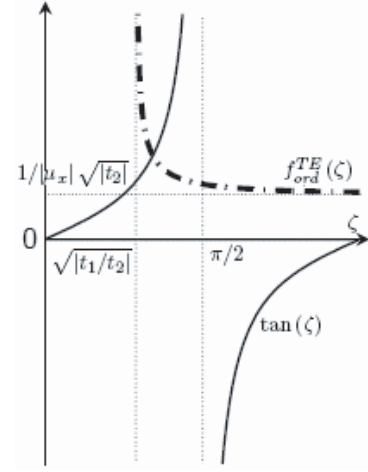
Figure 7: Graphical solution of Eq. (12) for ordinary TE surface waves in case $\mu_x < 0$, $t_1 < 0$, $t_2 < 0$ (B-3).

3.2. Evanescent TE Surface Waves

Combination of Eqs. (5) and (6) leads to

$$\tanh(\xi) = -\frac{1}{\mu_x} \frac{\xi}{\sqrt{t_1 + t_2 \xi^2}} = f_{ev}^{\mathrm{TE}}(\xi) \tag{16}$$

where $\xi = \alpha_{z1} d$. Evanescent TE surface waves cannot exist in case $t_1 < 0$, $t_2 < 0$ and is not considered here.

A) $\mu_x > 0$

A-1) $t_1 > 0$, $t_2 > 0$, the function $f_{ev}^{\mathrm{TE}}(\xi)$ is shown in the dash-dotted line in Fig. 8. This function is zero at $\xi = 0$, monotonically decreasing and tends to $-1/\mu_x \sqrt{t_2}$ for $\xi \to \infty^+$. Intersection between it and $\tanh(\xi)$ will not occur; therefore, Evanescent TE surface waves cannot exist.

A-2) $t_1 > 0$, $t_2 < 0$, the function $f_{ev}^{\mathrm{TE}}(\xi)$ is also depicted in dashed line in Fig. 8. It is defined for $\xi < \sqrt{|t_1/t_2|}$, is zero at $\xi = 0$, monotonically decreasing and tends to $-\infty$ for $\xi \to \sqrt{|t_1/t_2|}^-$. Evanescent TE surface waves cannot propagate in the structure in this case since no intersections between $\tanh(\xi)$ and $f_{ev}^{\mathrm{TE}}(\xi)$ occur.

A-3) $t_1 < 0$, $t_2 > 0$, the $f_{ev}^{\mathrm{TE}}(\xi)$ is represented with dotted line in Fig. 8. As we can see in this case, $f_{ev}^{\mathrm{TE}}(\xi)$ is defined for $\sqrt{|t_1/t_2|} < \xi$, tends to $-\infty$ for $\xi \to \sqrt{|t_1/t_2|}^+$ and tends to $-1/\mu_x \sqrt{t_2}$ for $\xi \to \infty^+$. Intersections never exist; consequently, Evanescent TE surface waves cannot be found in this case.

B) $\mu_x < 0$

B-1) $t_1 > 0$, $t_2 > 0$, $f_{ev}^{\mathrm{TE}}(\xi)$ is defined for every ξ, convex, monotonically increasing, is zero at $\xi = 0$ and tends to $1/|\mu_x|\sqrt{t_2}$ for $\xi \to \infty^+$. Two cases may be possible for evanescent TE surface waves suppression.

B-1-I) The horizontal asymptote of $f_{ev}^{\mathrm{TE}}(\xi)$ lies above the horizontal asymptote of $\tanh(\xi)$, as we can see in Fig. 9 in the dashed line. In this case, a straight line $r_1(\xi) = c_1\xi$ must be existed such that $\tanh(\xi)$ lies below it and $f_{ev}^{\mathrm{TE}}(\xi)$ lies above it, as far as $f_{ev}^{\mathrm{TE}}(\xi)$ lies below the horizontal asymptote of $\tanh(\xi)$. We choose $c_1 = 1$ which equals to derivative of $\tanh(\xi)$ at $\xi = 0$. These conditions may be express as

$$\frac{1}{|\mu_x|\sqrt{t_2}} > 1$$
$$\sqrt{(1/\mu_x)^2 - t_2} > \sqrt{t_1} \tag{17}$$

B-1-II) the horizontal asymptote of $f_{ev}^{\mathrm{TE}}(\xi)$ lies below the horizontal asymptote of $\tanh(\xi)$, as illustrated in dash-dotted line in Fig. 9. In this case, a straight line $r_2(\xi) = c_2\xi$ must be existed
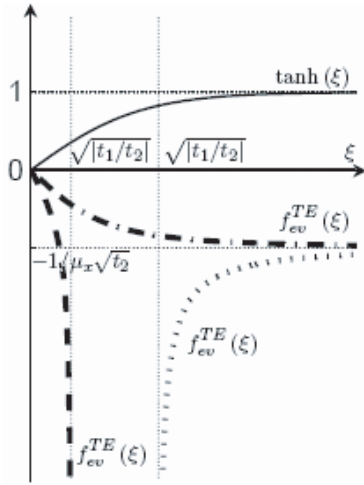
Figure 8: Graphical solution of Eq. (16) for evanescent TE surface waves in case $\mu_x > 0$, (A-1,2,3).
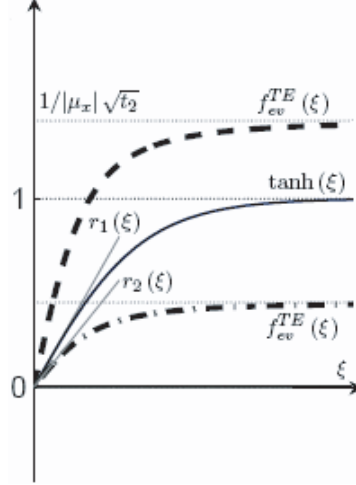
Figure 9: Graphical solution of Eq. (16) for evanescent TE surface waves in case $\mu_x < 0$, $t_1 > 0$, $t_2 > 0$ (B-1).
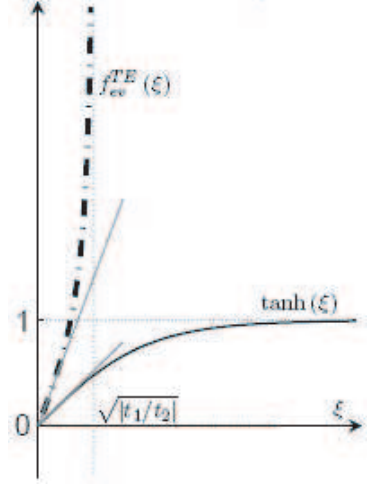
Figure 10: Graphical solution of Eq. (16) for evanescent TE surface waves in case $\mu_x < 0$, $t_1 > 0$, $t_2 < 0$ (B-2).

such that $\tanh(\xi)$ lies above it and $f_{ev}^{\mathrm{TE}}(\xi)$ lies below it, as far as $\tanh(\xi)$ lies below the horizontal asymptote of $f_{ev}^{\mathrm{TE}}(\xi)$. We can choose $c_2 = 1/|\mu_x|\sqrt{t_1}$ which corresponds to derivative of $f_{ev}^{\mathrm{TE}}(\xi)$ at $\xi = 0$. These conditions lead to

$$\frac{1}{|\mu_x|\sqrt{t_2}} < 1$$

$$\sqrt{t_1/t_2} > \tanh^{-1}\left(\frac{1}{|\mu_x|\sqrt{t_2}}\right)$$

(18)

B-2) $t_1 > 0$, $t_2 < 0$, the function $f_{ev}^{\mathrm{TE}}(\xi)$ is shown in Fig. 10 in dash-dotted line. It is defined for $\xi < \sqrt{|t_1/t_2|}$, concave and monotonically increasing, tends to $+\infty$ for $\xi \to \sqrt{|t_1/t_2|}^{-}$. It is clear from Fig. 8 that sufficient condition for suppressing evanescent TE waves in this case is, the derivative of $\tanh(\xi)$ at $\xi = 0$ is less than the derivative of $f_{ev}^{\mathrm{TE}}(\xi)$ at $\xi = 0$ which can be expressed as

$$|\mu_x|\sqrt{t_1} < 1$$

(19)

Table 1: Summary of conditions for suppression of surface waves. ($\times$) represents that the surface wave suppression is impossible and ($-$) represents that the propagation of surface waves does not exist.

TE modes		$t_1 > 0, t_2 > 0$	$t_1 > 0, t_2 < 0$	$t_1 < 0, t_2 > 0$	$t_1 < 0, t_2 < 0$
$\mu_x > 0$	Ordinary	Eq. (13)	$\times$	$-$	$\times$
	Evanescent	$-$	$-$	$-$	$-$
$\mu_x < 0$	Ordinary	Eq. (14) or (15)	$\times$	$-$	$\times$
	Evanescent	Eq. (17) or (18)	Eq. (19)	Eq. (20)	$-$
TM modes		$s_1 > 0, s_2 > 0$	$s_1 > 0, s_2 < 0$	$s_1 < 0, s_2 > 0$	$s_1 < 0, s_2 < 0$
$\varepsilon_x > 0$	Ordinary	$\times$	$\times$	$-$	$\times$
	Evanescent	$-$	$-$	$-$	$-$
$\varepsilon_x < 0$	Ordinary	$\sqrt{s_1/s_2} < \pi/2$	$\times$	$-$	$\times$
	Evanescent	$\|\varepsilon_x\|\sqrt{s_2} < 1$	$\times$	$\|\varepsilon_x\|\sqrt{s_2} < 1$ $\mathrm{arctanh}\left(\|\varepsilon_x\|\sqrt{s_2}\right) < \sqrt{\|s_1/s_2\|}$	$-$

B-3) $t_1 < 0$, $t_2 > 0$, in this case, $f_{ev}^{\mathrm{TE}}(\xi)$ is defined for $\sqrt{|t_1/t_2|} < \xi$, is monotonically decreasing, tends to $1/|\mu_x|\sqrt{t_2}$ for $\xi \to \infty^+$ and tends to $+\infty$ for $\xi \to \sqrt{|t_1/t_2|}^+$, as depicted in Fig. 11. If the horizontal asymptote of $f_{ev}^{\mathrm{TE}}(\xi)$ lies above the horizontal asymptote of $\tanh(\xi)$, suppression of surface waves can be occurred. This can easily be expressed as

$$|\mu_x|\sqrt{t_2} < 1 \tag{20}$$

Specific conditions for suppression of TM modes can be extracted similarly and are not repeated here. Conditions for avoiding of propagation both TE and TM surface waves in the biaxially anisotropic grounded slab are summarized in Table 1. The parameters s_1 and s_2 are defined as $s_1 = (k_o d)^2 (\mu_y \varepsilon_z - 1)$ and $s_2 = \varepsilon_z/\varepsilon_x$. The cross sign represents that the surface wave suppression is impossible and the dash sign represents that the propagation of surface waves does not exist. By examining Table 1, we can conclude that the propagation of evanescent surface waves is not possible for $\varepsilon_x > 0$ and $\mu_x > 0$. Moreover, the suppression of entire surface waves can achieve only in the metamaterial slab.

4. CONCLUSION

In conclusion, we have studied conditions that ensure the absence of surface modes in a biaxially anisotropic grounded slab and shown that the suppression of entire surface modes can occur only in the anisotropic metamaterial grounded slab.

REFERENCES

1. Veselago, V. G., "The electrodynamics of substances with simultaneously negative values of ε and μ," *Soviet Physics USPEKHI*, Vol. 10, No. 4, 509–514, 1968.

2. Grzegorczyk, T. M. and J. A. Kong, "Review of left-handed metamaterials: Evolution from theoretical and numerical studies to potential applications," *Journal of Electromagnetic Waves and Applications*, Vol. 20, No. 14, 2053–2064, 2006.

3. Pacheco, J., T. M. Grzegorczyk, B. I. Wu, Y. Zhang, and J. A. Kong, "Wave propagation in homogeneous isotropic frequency-dispersive left-handed media," *Phys. Rev. Lett.*, Vol. 89, No. 25, 257401-257404, Dec. 2002.

4. Chen, H., B. I. Wu, and J. A. Kong, "Review of electromagnetic theory in left-handed materials," *Journal of Electromagnetic Waves and Applications*, Vol. 20, No. 15, 2137-2151, 2006.

5. Hudlicka, M., J. Machac, and I. S. Nefedov, "A triple wire medium as an isotropic negative permittivity metamaterial," *Progress In Electromagnetics Research*, PIER 65, 233–246, 2006.

6. Baccarelli, P., P. Burghignoli, F. Frezza, A. Galli, P. Lampariello, G. Lovat, and S. Paulotto, "Fundamental modal properties of surface waves on metamaterial grounded slabs," *IEEE Trans. Microwave Theory Tech.*, Vol. 53, No. 4, 1431–1442, 2005.

7. Baccarelli, P., P. Burghignoli, G. Lovat, and S. Paulotto, "Surface-wave suppression in a double-negative metamaterial grounded slab," *IEEE Antennas Wireless Propag. Lett.*, Vol. 2, No. 19, 269–272, 2003.

8. Baccarelli, P., P. Burghignoli, F. Frezza, A. Galli, P. Lampariello, G. Lovat, and S. Paullotto, "New dispersion characteristics and surface-wave suppression in double-negative metamaterial grounded slabs," *URSI Int. Electromagnetic Theory Symp.*, Vol. 1, 379–381, Pisa, Italy, May 23–27, 2004.

9. Songhua, L., C. Liang, and L. Changhong, "Guided modes in a grounded slab waveguide of uniaxially anisotropic left-handed material," *Microwave and Optical Technology Lett.*, Vol. 49, No. 7, Jul. 2007.

Almost Complete Absorption of Light in Nanostructured Metallic Coatings: Blackbody Behavior

V. G. Kravets, **F. Schedin**, and **A. N. Grigorenko**

Department of Physics, University of Manchester, M13 9PL, Manchester, UK

Abstract— We have experimentally demonstrated blackbody-like behavior in a thin nanostructured metallic layer shaped in the form of a composite deep diffraction grating. This behavior is recorded over a wide optical wavelength range (240–550 nm) and for a broad range of angles of light incidence (0–75°) for samples with metal thickness of just 90 nm. The strong absorption at a level of 97–99% is observed for one light polarization and is attributed to excitation of localized plasmons coupled to incident light waves. An effective-medium approach provides a satisfactory qualitative description of the reflection and transmission spectra in our samples and confirms their blackbody behavior.

1. INTRODUCTION

By Kirchhoff's definition, the blackbody is an object that absorbs all light that falls on it. Perfect blackbody absorbs electromagnetic radiation of any wavelength and does not produce reflected or transmitted light under any kind of illumination. Blackbody surfaces are of increasing importance in many fields of science and modern technologies. One of the most promising applications of the blackbody coatings is in the field of photothermal and photoelectrical conversion of the solar energy, where they could considerably increase the effectiveness of solar cells [1, 2].

The promising candidates for a design of robust "blackbody" absorbing layers are plasmonic photonic crystal structures. While smooth metal surfaces reflect most of incident visible light and cannot be used as "blackbody" surfaces, the optical properties of a metallic film can be significantly altered by its nanostructuring that allows one to "manufacture" a desired index of refraction and achieve extraordinary optical properties. Collective electronic excitations called plasmons, both propagating and localized, are the main physical mechanisms for achieving strong absorption of light in periodic metallic structures [3–5].

In this work we experimentally demonstrate plasmonic "blackbody" based on deep diffraction gratings made of extremely thin (90 nm) and robust gold films deposited on Poly-methyl-methacrylate (PMMA) nanostripes. By "blackbody" in this paper we imply an object which strongly absorbs light in a wide spectral and angle range demonstrating blackbody-like behavior. We measure reflectance, transmittance and ellipsometry spectra for the samples of two orientations (gold stripes perpendicular plane of incidence and gold stripes parallel to the plane of incidence) and for two light polarizations (p-polarized and s-polarized light). We show that optical spectra of our structures can be tuned by adjusting the geometry of the gratings. For gold nanostructures, 97%–99% of light absorption is observed in a wavelength range of 240–550 nm for the large range of the incident angles (0–75°) for the light with electric field vector perpendicular to the grating stripes.

2. EXPERIMENTAL DETAILS

Deep gold composite diffraction gratings were fabricated on glass slides by electron beam lithography and metal evaporation. Poly-methyl-methacrylate (PMMA) of the total thickness of 120 nm was spun on the substrate and baked. The nanostripe arrays were exposed by electron beam lithography and the samples were developed resulting in 1D array of PMMA stripes of width b with the array constant $a = 320$ nm. Thermal evaporation has been used to deposit 5 nm Cr and 90 nm of Au onto the developed structures. The whole sample has size of 200 μm × 200 μm.

The ellipsometric spectra and polarized reflection spectra of the gold stripes have been measured by the focused beam M-2000F spectroscopic ellipsometer (J. A. Woollam, Inc.) which provides a small measurement spot (down to 30 μm). We recorded a pair of ellipsometric parameters Ψ and Δ in the wavelength range from 250 to 1000 nm. The ellipsometric parameters have been measured for incidence polar angles θ ranging from 45° to 74°. The samples were rotated along the vertical axis to provide the azimuth angle ϕ variations. Two configurations of the azimuth angle, $\phi = 0°$ and $\phi = 90°$, will be discussed for which the plane of incidence is oriented either along stripes arrays or perpendicular to them, respectively. The reflectivity spectra were also performed for the

same two values of ϕ and two polarizations of incident light: p-polarization (electric field in the plane of incidence) and s-polarization (electric field perpendicular to the plane of incidence).

Optical transmission spectra were collected with a visible — near infrared Ocean Optics USB2000 spectrometer (400–830 nm). The transmitted light was collected using an optical fiber coupled to the spectrometer (200 μm core). The angle of incidence was varied from 0° to 60°. The transmission spectra were also measured for both p- and s-polarized illumination.

3. RESULTS AND DISCUSSION

Figures 1(a) and (b) illustrate p- and s-polarized reflectivity spectra measured at different incident angles ($45° \leq \theta \leq 74°$ in steps of 4°) for gold stripes of width $b \sim 150$ nm, the grating constant $a = 320$ nm and the azimuth angle $\phi = 90°$. For all incident angles the reflectivity is close to zero for p-polarized light at the wavelength range of 240–550 nm. These spectra reach a maximum in the region $\lambda \sim 550$–650 nm, and after that $R_p(\lambda)$ slowly decrease with increasing wavelength (Fig. 1(a)). The s-polarization spectra $R_s(\lambda)$ do not show significant changes for examined structure and look like the reflection spectra observed for homogeneous thick gold films (Fig. 1(b)). Inset of Fig. 1(b) shows the reflection spectra for p- and s-polarized light measured at the normal angle of incidence ($\theta = 0°$) using reflection spectrometer. Figs. 1(c) and (d) show the transmission spectra of the gold nanostripes for p- and s-polarized light, respectively, for the same azimuth angle $\phi = 90°$. There are negligible changes in the intensity of transmission light for all spectral region and spectra for both polarizations are similar. The optical transmission for both polarizations leads to an extremely low value less than 0.5%. Small broad peaks in transmission occur at $\lambda \sim 500$ nm for the normal angle of incidence (Figs. 1(c) and (d)).

For all angles of incidence ($0° \leq \theta \leq 75°$) we observed pronounced reflectivity plateau with values of $R_p(\lambda)$ as low as 1–3% in the spectral range 240–550 nm. Transmission experiments revealed that within plateau only 0.5% of the incident light is transmitted through the gold stripes. Using the Kirchhoff's rule (the sum of the transmittance $T(\lambda)$, reflectance $R_p(\lambda)$ and absorbance $A(\lambda)$ should equal 1 in the absence of scattering and diffraction), we conclude that the coefficient of absorption for the studied grating was about 97% in the frequency range of 240–550 nm. Therefore, the gold nanostripes behave as an effective broadband absorbing coating mimicking the behavior of a blackbody in a wide spectral range that covers a large portion of visible spectra important for the operation of solar cells and in a wide range of incident angles.

The inset of Fig. 1 shows the polarization-contrast microscopy images our samples, which confirm the blackness of our object. In experiment the electric field of the white-light was set to be either perpendicular to the stripes, TM mode of the polarization, or parallel to the stripes, TE mode of polarization. The light transmitted or reflected from the gold nanostripes was collected by an objective and send to a CCD camera. These polarization-contrast optical images provided a simple and quick way to assess the blackness of the gold nanostripes observed in the TM illumination.

We utilize the effective medium approximation (EMA) and assign a complex effective index of refraction to our structure. For sub-wavelength diffraction gratings this refractive index can be calculated by using, e.g., Maxwell-Garnett approach [6, 7]. The values of gold permittivity, $\varepsilon(\omega)$, have been extracted from ellipsometric data measured on a flat 90 nm thick gold deposited at the same conditions as the studied samples. We determined the effective complex refraction index $n_{eff}^{\parallel} + ik_{eff}^{\parallel}$ and $n_{eff}^{\perp} + ik_{eff}^{\perp}$ (along stripes arrays or perpendicular to them) which have been used to calculate the optical response of the samples with the help of Fresnel coefficients for the EMA model. Fig. 2(a) shows the spectral dependence of the effective optical constants $n_{eff}^{\perp}$ and $k_{eff}^{\perp}$. The dispersion observed for $n_{eff}^{\perp}$ and $k_{eff}^{\perp}$ is different from that of the bulk gold. We note that $n_{eff}^{\perp}$ and $k_{eff}^{\perp}$ demonstrate nearly flat bands in the wavelength range (240–500 nm).

The reflectance and transmittance curves were calculated using the Fresnel equations for the three-layer system: air, uniform layer of nanostripes (effective medium), and thick gold (90 nm). Fig. 2(b) shows the polarized reflection spectra for the case of $\phi = 90°$, which are in a good qualitative agreement with our experimental data shown in Figs. 1(a) and (b). For p-polarized light there are two regions. In first region 250–550 nm, the magnitude of $R_p(\lambda)$ is close to zero, and second region 650–1000 nm where the magnitude of $R_p(\lambda)$ tends to one.

Physically, the origin of the blackbody-like behavior (total absorption) comes from excitation of localized plasmons in an isolated gold stripe. Due to the negative real part of the dielectric constant of gold $\mathrm{Re}(\varepsilon(\omega))$ incident light excites localized plasmon resonances. These resonances can occur at discrete frequencies and are strongly localized in skin surface layer of stripes. Due to dipole-

dipole interaction between ensemble of stripes and strong coupling between localized plasmon these resonances tend to broadening and producing tight bound bands. The existence of plasmon bands is a necessary condition for creating plasmonic blackbody. Sufficient condition for appearance of almost 100% absorption is adjusting the structure parameters of stripes. We have shown both experimentally and theoretically that composite deep metallic gratings are promising structures for absorptive coatings working in a wide spectral range and for a wide range of incident angles.
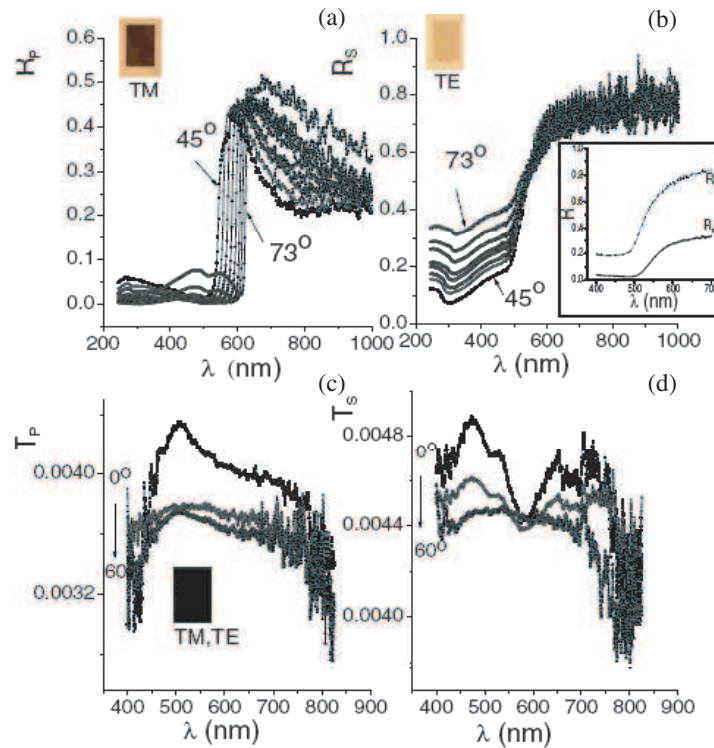
Figure 1: The reflection (transmission) spectra for the light of (a), (c) p-polarization and (b), (d) s-polarization. (Insets: the polarization-contrast optical microscopy images for reflected (a), (b) and transmitted (c) light; the reflection spectra for p- and s-polarized light at normal incidence).
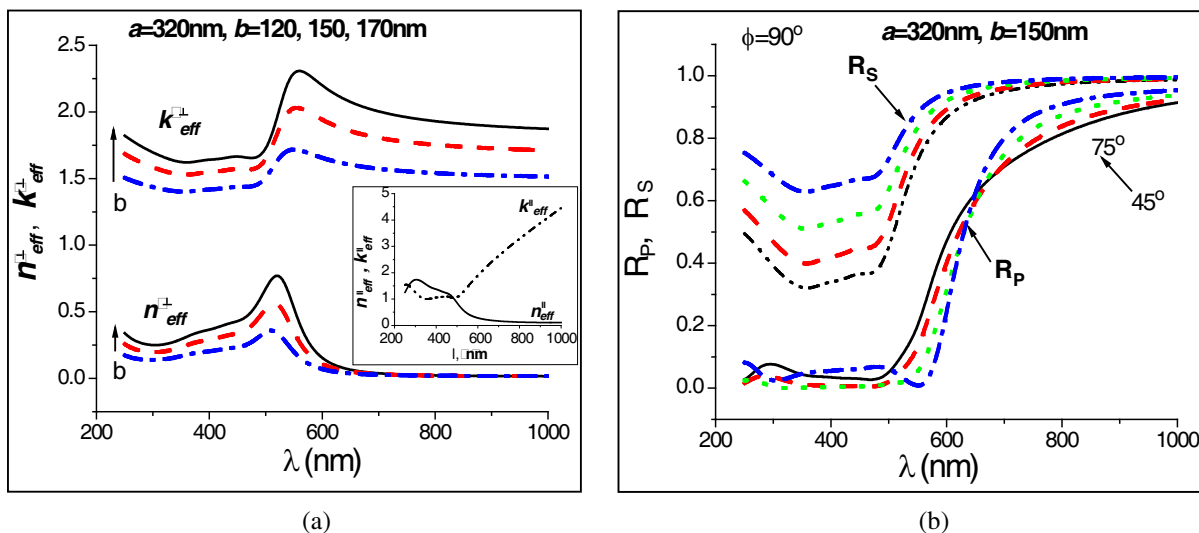
Figure 2: (a) The effective refractive index for the light with the electric field perpendicular (inset: parallel) to the stripes. (b) The theoretical reflection spectra for p- and s-polarized light for gold nanostripes ($\phi = 90°$).

REFERENCES

1. Schaadt, D. M., B. Feng, and E. T. Yu, *Appl. Phys. Lett.*, Vol. 86, 063106, 2005.
2. Panoiu, N. C. and R. M. Osgood, *Opt. Lett.*, Vol. 32, 2825, 2007.
3. Grigorenko, A. N., A. K. Geim, H. F. Gleeson, Y. Zhang, A. A. Firsov, I. Y. Khrushchev, and J. Petrovic, *Nature*, Vol. 438, 335, London, 2005.
4. Zayats, A. V. and I. I. Smolyaninov, *J. Opt. A: Pure Appl. Opt.*, Vol. 5, S16, 2003.
5. Tan, W.-C., J. R. Sambles, and T. W. Preist, *Phys. Rev. B*, Vol. 61, 13177, 2000.
6. Garcia-Vidal, F. J., J. M. Pitarke, and J. B. Pendry, *Phys. Rev. Lett.*, Vol. 78, 4289, 1997.
7. Kravets, V. G., F. Schedin, and A. N. Grigorenko, *Phys. Rev. B*, Vol. 78, 205405, 2008.

Effects of Array Dimensions on the Resonance Characteristics of SRR Type Metamaterial Arrays with Small Sizes: Simulations and Experiments

E. Ekmekci[1, 2]**, K. Topalli**[1]**, T. Akin**[1]**, and G. Turhan-Sayan**[1]

[1]Department of Electrical and Electronics Engineering
Middle East Technical University, Ankara, Turkey
[2]Department of Electronics and Communication Engineering
Suleyman Demirel University, Isparta, Turkey

Abstract— It has been discussed in various studies that two dimensional periodical arrays of SRRs with large array sizes have wider stop bandwidths and lower transmission magnitudes around their resonance frequencies as compared to the single SRR unit cell. In this paper, effects of array dimensions on the transmission characteristics of SRR arrays are investigated in more detail especially for small sized arrays in a comparative manner. For this purpose, various SRR arrays with small array sizes are fabricated and their transmission characteristics are measured by Agilent 8720D network analyzer. The measurement results are verified by the full-wave electromagnetic simulation results obtained from Ansoft's HFSS software. In conclusion, it is demonstrated that increasing array dimensions increases the depth of the transmission minimum and widens the stop bandwidth, as expected. Furthermore, interestingly observed that resonance frequency of the SRR array shifts either towards the lower frequencies or towards the higher frequencies depending upon the dimension at which the number of array elements is increased. This behavior is interpreted as a result of different coupling effects in two different dimensions due to the inherent asymmetry of the two-dimensional SRR arrays implemented in this study.

1. INTRODUCTION

Split ring resonator (SRR) is a well-known metamaterial structure that is commonly used in microwave and antenna applications. The SRR pattern is printed on a dielectric substrate in the form of conducting strip lines made of good conductors such as copper or gold. An SRR array can provide highly positive or highly negative effective permeability values over some definite frequency bands [1]. These negative valued permeabilities, in particular, enable us to realize left-handed metamaterials which were theoretically proposed by V. G. Veselago, in 1968 [2, 3].

A schematic view of a typical square shaped SRR structure is given in Figure 1(a). A time-varying magnetic field applied perpendicularly to the plane of the structure induces currents over the inner and outer rings. These induced currents and the splits in the structure cause polarizations which occur along each split ring. As a result of a total capacitance effect (C) due to these polarizations and a total inductance effect (L) due to the conducting strip lines, the SRR unit cell behaves like a magnetic resonator with the angular resonance frequency of $w_o = 1/(LC)^{1/2}$ [4].

In literature, there are various studies which investigate the SRR arrays having large number of unit cells. For example, in 2002, Bayindir et al. experimentally investigated the transmission characteristics of composite metamaterials which consist of SRRs and conducting wires in free space [5]. Again in 2002, Markos et al. investigated the transmission characteristics of both individual SRR arrays and the left-handed structures composed of SRR arrays, numerically [6]. Also Gay-Balmaz et al. investigated the coupling between two or more SRR structures for different geometrical arrangements [7]. In 2006, Aydin et al. investigated the transmission characteristics of an SRR unit cell and two dimensional SRR arrays with large number of elements in microwave region. They also investigated the effects of electrical coupling on magnetic resonance by exciting the SRR unit cells with different alignments and observing their transmission characteristics [8]. In 2008, Penciu et al. investigated the interactions between SRR structures with single gaps or multiple gaps in the SRR plane.

In this study, transmission characteristics of an SRR unit cell and various two dimensional SRR arrays with varying array sizes are first measured and then these results are verified by electromagnetic full-wave simulations. As being different from the studies reported in literature, these arrays are designed with small array sizes such that they consist of only 2, 3, 4 or 6 elements. As the two dimensional SRR array has an inherent asymmetry, it is aimed to investigate the effects

of array size in each array dimension on the transmission characteristics and hence on the resonance frequency. Besides those small-sized arrays, a two dimensional array of 100 elements and a three dimensional array of 300 elements are also designed and fabricated to investigate their transmission characteristics experimentally.

2. DESIGN

The schematic view and the parameters of the investigated SRR unit cell are given in Figure 1(a). This square shaped SRR structure is fabricated with golden strip lines having the thickness of $t_{gold} = 1$ micron and the side-length of $l = 2.8$ mm. All the remaining conducting line parameters (g, w, s) are 0.3 mm. The structure is printed over a glass substrate with the dielectric constant of $\varepsilon_r = 4.6$, dielectric loss-tangent of $\tan \delta_c = 0.01$, and the dielectric thickness of 0.5 mm. A picture of the fabricated unit cell is given in Figure 1(b).

(a)   (b)
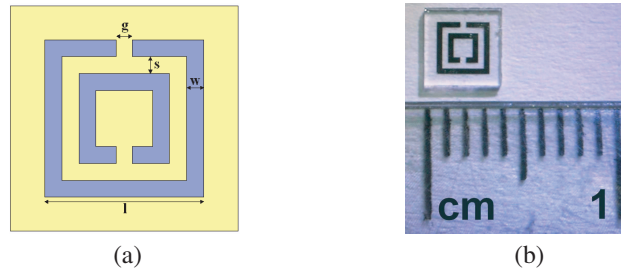
Figure 1: SRR unit cell: (a) Schematic view. (b) A picture of fabricated SRR.

To observe the effects of array size on the transmission characteristics, some small sized arrays are designed using the above mentioned SRR unit cell in one or two dimensions with 4 mm periodicity. These newly designed array structures are given in Figures 2 and 3. Herein, the small array given in Figure 2(a) is named as the $2 \times 1 \times 1$ array due to the fact that it is composed of 2 unit cells in x direction, 1 unit cell in y direction and also 1 unit cell in y direction. Similarly, in Figure 2(b) a $3 \times 1 \times 1$ array, in Figure 2(c) a $1 \times 2 \times 1$ array, in Figure 2(d) a $2 \times 2 \times 1$ array, in figure 2(e) a $3 \times 2 \times 1$ array, and finally, in figure 3 a $10 \times 10 \times 1$ array are shown.

The SRR unit cell and the SRR arrays used in experiments are fabricated at METU MEMS Center Fabrication Facilities with 100 Å/0.5 µm Ti/Au patterned with lithography on a 4″ glass substrate having a thickness of 500 µm and relative permittivity of 4.6 with a loss tangent of 0.01.

3. SIMULATION AND EXPERIMENTS

In this study, the experimental results for the structures given in Figures 1 and 2 are obtained by Agilent 8720D network analyzer using TRL calibration. The structure under investigation is placed in an X-band waveguide with the length of 12.8 mm and its scattering parameters are measured. Herein, $|S_{21}|$ provides us enough information about the resonance frequencies of the structures. (There is no special reason for choosing a waveguide with the length of 12.8 mm.)

The structure given in Figure 3 is too large to be placed in an X-band waveguide, thus its transmission characteristics are measured by placing it between two horn antennas.

In this study, the experimental results are validated by HFSS simulations with the simulation setup is given in Figure 4. This simulation setup is in fact nothing but the imitation of the experimental setup for a realistic comparison. While the experimental setup is imitated, the walls perpendicular to y and z axes are modeled to be PEC. The walls perpendicular to x axes are modeled to be the input/output ports. The resonator structure to be tested is placed in the waveguide and excited by an electromagnetic wave with propagation vector $(\vec{k})$ along the x direction, electric filed vector $(\vec{E})$ along the y direction and magnetic field vector $(\vec{H})$ along the z direction.

4. RESULTS

The transmission characteristics of the unit cell structure obtained by simulations (dashed line with triangle marker) and experiments (solid line with square marker) are given in Figure 5. This figure shows that the unit cell structure resonates around 9.49 GHz. It is also obvious that experimental results and simulation results are in very good agreement.
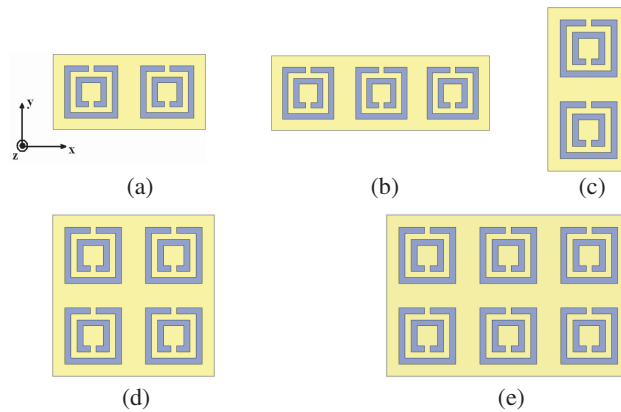
Figure 2: SRR arrays with various small sizes: (a) $2 \times 1 \times 1$, (b) $3 \times 1 \times 1$, (c) $1 \times 2 \times 1$, (d) $2 \times 2 \times 1$, (e) $3 \times 2 \times 1$.
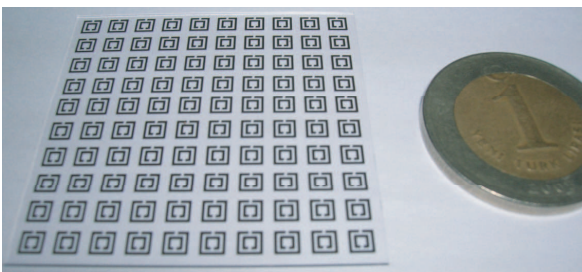

Figure 3: The SRR array with 100 unit cells ($10 \times 10 \times 1$).
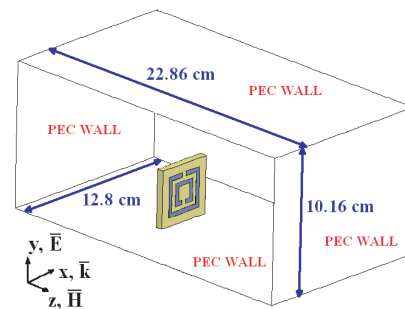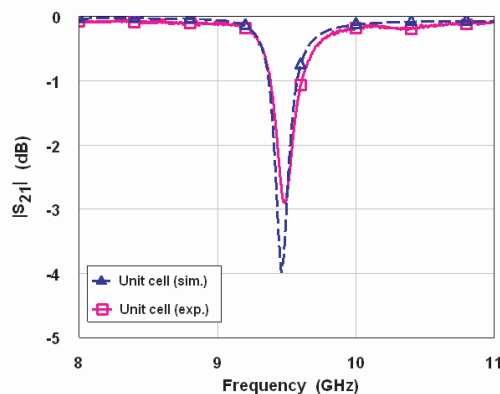

Figure 4: Simulation and experimental setup.

Figure 5: Transmission (i.e., $|S_{21}|$) characteristics of SRR unit cell obtained by simulation and experiment.
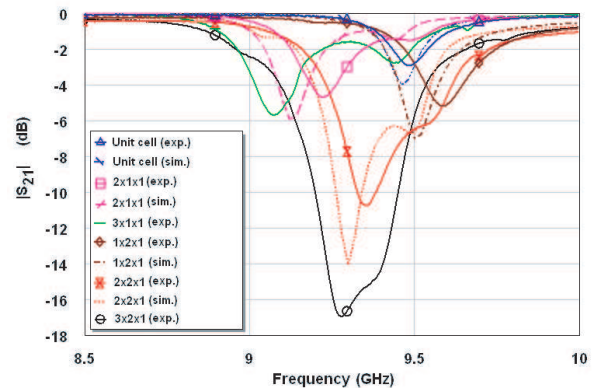

Figure 6: Transmission characteristics of small sized SRR arrays obtained by simulations and experiments.

In Figure 6, there are $|S_{21}|$ characteristics plotted for the SRR arrays with various small array sizes. Simulations and experimental results show that, increasing the array size in x direction (i.e., $2 \times 1 \times 1$ and $3 \times 1 \times 1$ arrays) lowers the resonance frequency with respect to unit cell structure (i.e., $1 \times 1 \times 1$). Besides, increasing the array size in y direction (i.e., the $1 \times 2 \times 1$ array) increases the resonance frequency with respect to unit cell. On the other hand, the transmission characteristics of the $2 \times 2 \times 1$ array displays the behavior observed both in the $2 \times 1 \times 1$ array and in the $1 \times 2 \times 1$ array, resulting in a stop-bandwidth that widens towards both lower and upper frequencies. A similar transmission behavior is observed for the $3 \times 2 \times 1$ array, which in fact can be considered as the combination of the $3 \times 1 \times 1$ array and the $1 \times 2 \times 1$ array and it inherits their characteristics. Moreover, Figure 6 shows that increasing the number of elements in array formation, increases the depth of the transmission minimum.

Lastly, we investigate the transmission characteristics of a two dimensional array of size $10 \times 10 \times 1$ and a three dimensional array of size $10 \times 10 \times 3$, experimentally. These results are given in Figure 7.

For the $10 \times 10 \times 3$ array, the distance between the adjacent elements in z direction is chosen to be $d_z = 4$ mm. Therefore in all dimensions the repetition intervals become the same. It is clear from Figure 7 that, increasing the array size and hence the number of elements, increases the depth of the transmission minimum and widens the stop-bandwidth.
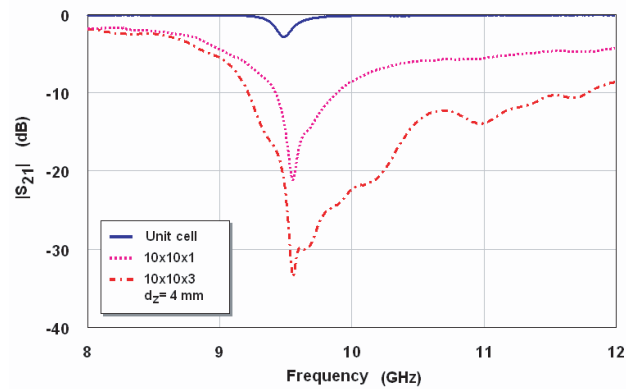

Figure 7: Transmission characteristics of SRR unit cell, $10 \times 10 \times 1$ array and $10 \times 10 \times 3$ array obtained by experiments.

5. CONCLUSION

In this study, an SRR based unit cell and SRR based array structures with various sizes have been designed and fabricated in order to investigate the effects of array sizes on the transmission characteristics. Transmission characteristics were obtained by both simulations and experiments. Results have shown that increasing array size increases the depth of the transmission minimum at the resonance frequency and also widens the stop-bandwidth, in general. Also, the resonance frequency of the array is shifted either towards the lower frequencies or towards the higher frequencies depending upon the array dimension at which the number of array elements is increased. Coupling effects between the SRR unit cells in x and y directions are different due to the built-in asymmetry of a given SRR array and this problem will be investigated by means of the equivalent circuit models as a future study.

REFERENCES

1. Pendry, J. B., A. J. Holden, D. J. Robbins, and W. J. Stewart, "Magnetism from conductors and enhanced nonlinear phenomena," *IEEE Trans. Microw. Theory Tech.*, Vol. 47, No. 11, 2075–2084, 1999.
2. Veselago, V. G., "The electrodynamics of substances with simultaneously negative values of ε and μ," *Soviet Phys. Uspekhi*, Vol. 10, No. 4, 509–514, 1968.
3. Shelby, R. A., D. R. Smith, and S. Schultz, "Experimental verification of a negative index of refraction," *Science*, Vol. 292, 77–79, 2001.
4. Smith, D. R., W. J. Padilla, D. C. Vier, S. C. Nemat Nasser, and S. Schultz, "Composite medium with simultaneously negative permeability and permittivity," *Phys. Rev. Lett.*, Vol. 84, No. 18, 4184–4187, 2000.
5. Bayindir, M., K. Aydin, E. Ozbay, P. Markos, and C. M. Soukoulis, "Transmission properties of composite metamaterials in free space," *Appl. Phys. Lett.*, Vol. 81, No. 1, 120–122, 2002.
6. Markos, P. and C. M. Soukoulis, "Numerical studies on left-handed materials and arrays of split ring resonators," *Phys. Rev. E*, Vol. 65, 036622-1–036622-8, 2002.
7. Gay-Balmaz, P. and O. J. F. Martin, "Electromagnetic resonances in individual and coupled split-ring resonators," *J. Appl. Phys.*, Vol. 92, No. 5, 2929–2936, 2002.
8. Aydin, K. and E. Ozbay, "Identifying magnetic response of split-ring resonators at microwave frequencies," *Opto-Electronics Rev.*, Vol. 14, No. 3, 193–199, 2006.
9. Penciu, R. S., K. Aydin, M. Kafesaki, T. Koschny, E. Ozbay, E. N. Economou, and C. M. Soukoulis, "Multi-gap individual and coupled split-ring resonator structures," *Opt. Express*, Vol. 16, No. 22, 18131–18144, 2008.

A Novel Dual-band Metamaterial Structure

E. Ekmekci[1,2] **and G. Turhan-Sayan**[1]

[1]Department of Electrical and Electronics Engineering
Middle East Technical University, Ankara, Turkey
[2]Department of Electronics and Communication Engineering
Suleyman Demirel University, Isparta, Turkey

Abstract— In this study, we propose a novel metamaterial structure having magnetic resonances at two different frequencies and hence providing negative effective permeability values over two separate bandwidths. The introduced metamaterial unit cell topology in this paper is made of a single loop of conducting strip printed over a dielectric substrate with a special winding geometry. Transmission and reflection spectra of this unit cell are simulated using the Ansoft's HFSS software to observe its resonance frequencies. Then, the effective permeability (μ_{eff}) and effective permittivity (ε_{eff}) curves are retrieved from the already computed complex S-parameters to demonstrate the presence of two distinct negative permeability bandwidths. The results clearly show that this novel structure can be a very useful alternative to the ordinary SRR and spiral resonator (SR) structures especially when a dual band operation is needed.

1. INTRODUCTION

Left-handed metamaterials are artificial materials that show simultaneously negative values of permittivity and permeability over a finite frequency band [1]. Such an artificial medium can be realized with the combination of periodical arrays of split ring resonators (SRRs) and thin wires. Herein, SRRs are used to obtain negative values of permeability, whereas thin wires are used to obtain negative values of permittivity [2–4]. However, the SRR is not a unique structure to obtain negative values of permeability. In literature, there are many examples demonstrating the usage of spiral resonators (SR) [5], S-shaped resonators [6–8], Ω-type resonators [8], and V-shaped resonators [9] in left-handed metamaterial applications.

Dual-band metamerials have attracted the interest of the scientists, especially in the terahertz regime, recently [10, 11]. In this study, we introduce a novel dual-band magnetic resonator structure for metamaterial applications, so called single loop resonator (SLR), which can be useful in both microwave and terahertz regimes. As the name implies, the suggested unit cell structure is made of a single loop of a conducting strip printed over a dielectric substrate with the special winding geometry shown in Figure 1. We have simulated this SLR unit cell topology using Ansoft's HFSS software to compute its complex scattering parameters. These parameters are used for estimating the resonance frequencies of this novel structure and also for the retrieval of the associated effective medium parameters μ_{eff} and ε_{eff}.

2. DESIGN

The schematic view and the design parameters of the proposed SLR unit cell are given in Figure 1. This square shaped SLR structure is designed with copper strip lines having the thickness (t_{copper}) of 0.03 mm, the side-length of (l) 4 mm, the gap width (g) of 0.3 mm, the line width (w) of 0.1 mm, and the separation distance between two adjacent copper lines (s) of 0.1 mm. The structure is printed over a square shaped *Rogers RO3003(tm)* substrate with the dielectric constant (ε_r) of 3, the dielectric loss-tangent ($\tan \delta_c$) of 0.0013, the side length (L) of 5 mm, and the thickness of 0.5 mm.

3. SIMULATION

The HFSS simulation setup used in this study is shown in Figure 2. The resonator structure to be tested is placed in the waveguide and excited by an electromagnetic wave with propagation vector ($\vec{k}$) along the x direction, electric filed vector ($\vec{E}$) along the y direction and magnetic field vector ($\vec{H}$) along the z direction. Herein, the walls perpendicular to y axes are modeled to be PEC boundaries, the walls perpendicular to z axes are modeled to be PMC boundaries, and lastly the walls perpendicular to x axes are modeled to be the input/output ports.
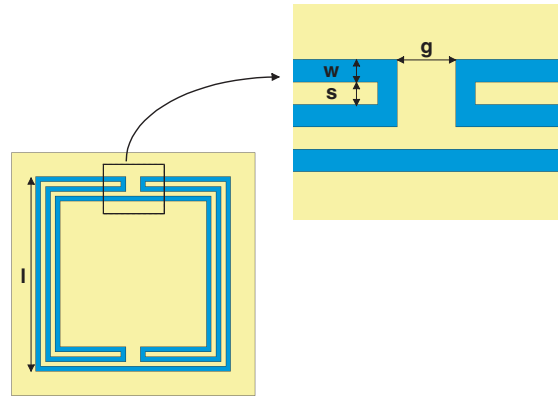
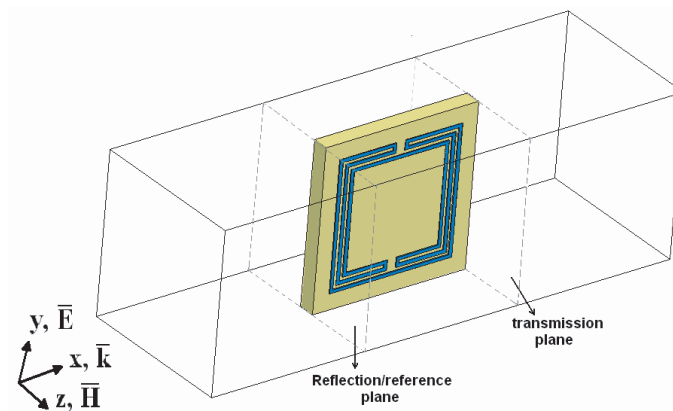Figure 1: Schematic view of the SLR unit cell.

Figure 2: HFSS Simulation setup.

4. RESULTS

The simulated spectra for transmission (S_{21}) and reflection (S_{11}) characteristics of the proposed SLR structure are given in Figure 3. In Figure 3(a) blue-solid and red-dashed lines indicate the magnitudes of S_{21} and S_{11}, respectively. It is clear from the Figure that the structure resonates at three different frequencies, which are 7.72 GHz, 8.60 GHz, and 9.86 GHz. Similarly Figure 3(b) shows the phase spectra of S_{21} and S_{11}. Moreover, Figure 4 shows the current distribution on the SLR unit cell structure around its first resonance at 7.72 GHz. Unlike the SRR and SR structures, the current flows in opposite directions in the inner and outer rings, because of the special winding geometry.

(a)

(b)
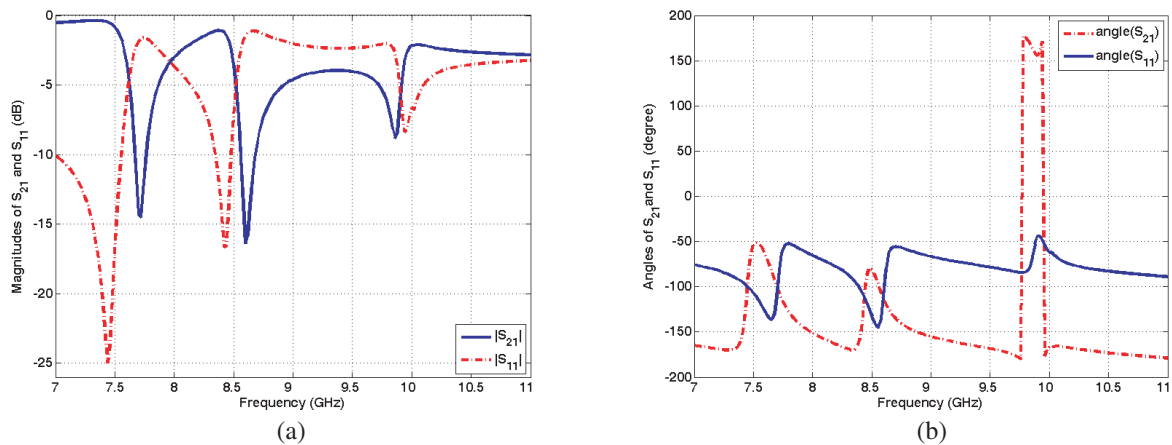
Figure 3: (a) Magnitude spectra of S_{21} and S_{11}. (b) Phase spectra of S_{21} and S_{11}.

Using the procedure given in [12], the effective medium parameters, μ_{eff} and ε_{eff}, are extracted from the simulated complex S_{21} and S_{11} parameters and the results are given in Figure 5. Figure 5(a) shows that the SLR structure has two bands with negative real effective permeability, which are from 7.64 to 7.88 GHz and from 8.53 to 8.84 GHz. Whereas, the real part of effective permittivity never goes below zero, however it fluctuates around 3, which is the relative permittivity of the dielectric substrate *RO3003(tm)*. These results clearly show that the SLR structure can be an alternative to the well known SRR and SR structures to be used in the design of composite left-handed metamaterials especially when a dual-band magnetic resonator operation is needed. Realization of negative permeability over two different frequency bands may also be useful in broadband metamaterial applications.
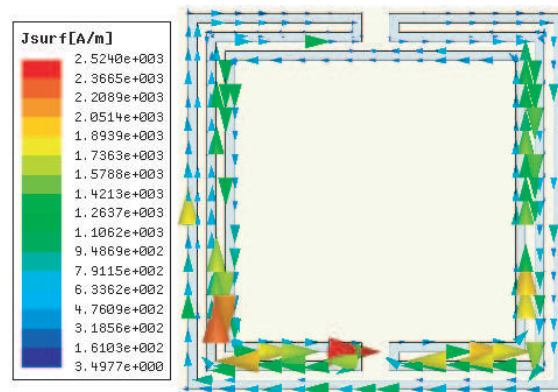
Figure 4: Current distribution on SLR structure around the first resonance at 7.52 GHz.
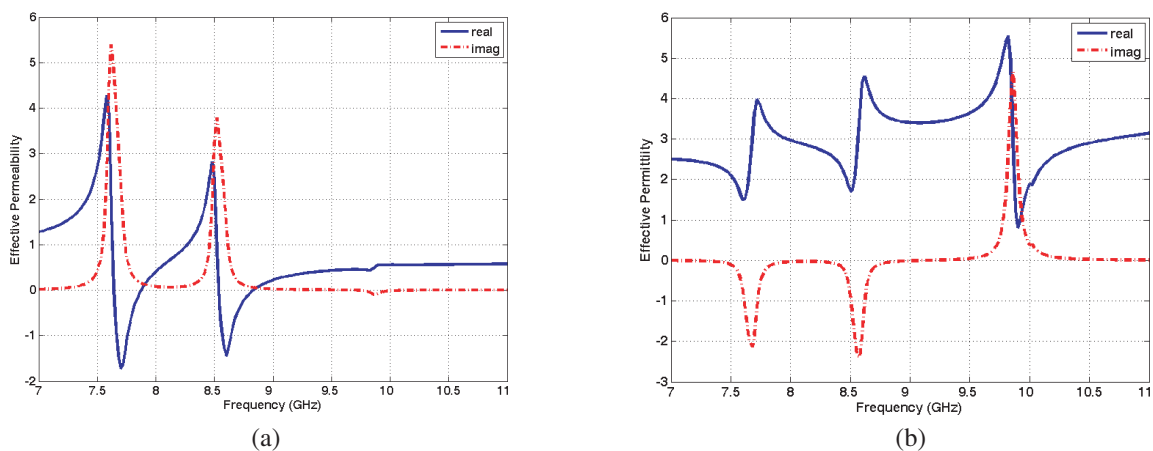
Figure 5: (a) Effective permeability versus frequency. (b) Effective permittivity versus frequency.

5. CONCLUSION

In this study we proposed a novel metamaterial structure, which is called the *single loop resonator*, SLR. Simulation results show that the suggested structure resonates at three different frequencies, which are 7.72 GHz, 8.60 GHz, and 9.86 GHz. Moreover, extraction of the effective medium parameters, μ_{eff}, ε_{eff}, shows that this structure has two regions with negative values of real permittivity; one from 7.64 to 7.88 GHz and the other from 8.53 to 8.84 GHz. However, the real part of effective permittivity never extends beyond zero.

These results show that, the proposed SLR structure can be a useful candidate for multi-frequency or broadband left-handed metamaterial applications.

REFERENCES

1. Veselago, V. G., "The electrodynamics of substances with simultaneously negative values of ε and μ," *Soviet Phys. Uspekhi*, Vol. 10, No. 4, 509–514, 1968.

2. Pendry, J. B., A. J. Holden, D. J. Robbins, and W. J. Stewart, "Low frequency plasmons in thin-wire structures," *J. Phys.: Condens. Matter*, Vol. 10, 4785–4809, 1998.

3. Pendry, J. B., A. J. Holden, D. J. Robbins, and W. J. Stewart, "Magnetism from conductors and enhanced nonlinear phenomena," *IEEE Trans. Microw. Theoty Tech.*, Vol. 47, No. 11, 2075–2084, 1999.

4. Smith, D. R., W. J. Padilla, D. C. Vier, S. C. Nemat Nasser, and S. Schultz, "Composite medium with simultaneously negative permeability and permittivity," *Phys. Rev. Lett.*, Vol. 84, No. 18, 4184–4187, 2000.

5. Baena, J. D., R. Marqués, F. Medina, and J. Martel, "Artificial magnetic metamaterial design by using spiral resonators," *Phys. Rev. B*, Vol. 69, 014402(1)–(5), 2004.

6. Chen, H., L. Ran, J. Huangfu, X. Zhang, and K. Chen, "Left-handed materials composed of only S-shaped resonators," *Phys. Rev. E*, Vol. 70, 057605(1)–(4), 2004.

7. Wang, D., L. Ran, H. Chen, M. Mu, J. A. Kong, and B.-I. Wu, "Experimental validation of negative refraction of metamaterial composed of single side paired S-ring resonators," *Appl. Phys. Lett.*, Vol. 90, 254103(1)–(3), 2007.

8. Wu, B.-I, W. Wang, J. Pacheco, X. Chen, T. Grzegorczyk, and J. A. Kong, "A study of using metamaterials as antenna substrate to enhance gain," *Progress In Electromagnetics Research*, PIER 51, 295–328, 2005.

9. Ekmekci, E. and G. Turhan-Sayan, "Investigation of permittivity and permeability for a novel V-shaped metamaterial using simulated S-parameters," *Proceedings of 5th International Conference on Electrical and Electronics Engineering*, Bursa, Turkey, December 2007.

10. Kwon, D.-H., D. H. Werner, A. V. Kildishev, and V. M. Schalev, "Near-infrared materials with dual-band negative-index characteristics," *Opt. Express*, Vol. 15, No. 4, 1647–1652, 2007.

11. Yuan, Y, C. Bingham, T. Tyler, S. Palit, T. H. Hand, W. J. Padilla, D. R. Smith, N. M. Jokerst, and S. A. Cummer, "Dual-band planar electric metamaterial in the terahertz regime," *Opt. Express*, Vol. 16, No. 13, 9746–9752, 2008.

12. Ghodgaonkar, D. K., V. V. Varadan, and V. K. Varadan, "Free-space measurement of complex permittivity and complex permeability of magnetic materials at microwave frequencies," *IEEE Trans. Instrum. Meas.*, Vol. 39, No. 2, 387–394, 1990.

The Effect of TEM in Generation of Earthquake Associated with Geological Engineering

Alireza Bayat[1], **H. Ghafori Fard**[2], **and Abolfazl Taherpour**[3]

[1]Communication Eng. Department, Imam Khomeini International University, Iran
[2]Electrical Eng. Department, Imam Khomeini International University, Iran
[3]International Institute of Earthquake Engineering and Seismology, Iran

Abstract— In this paper, the authors is explaining a new method of phenomena of earth quick; due to creation of electromagnetic fields which is owing to the strong negative charged clouds near the surface of earth that in turn form a closed loop circuit with volume charge density of earth. Critical angles & Brewster angles should also be taken into account [1]. The effect of vertical polarization regarding to the geology engineering and sounds in the fault which is indicative of earthquake, should be considered as well.

The connection between clouds and earthquake faded from view after 1985. Zhanglao has predicted earthquake since June 20, 1990, when he observed a long line shaped cloud with a tail pointing in the North West direction, 18 hours later, a magnitude 7.7 Richter earthquakes struck Iran and killed and injured so many people [2]. One of the authors observed some dark clouds very close to the surface of the earth about 8 to 10 hour before occurrence of the earthquakes at the Alamut zone in 2004 in Iran, which has been occurred. About 8 to 10 hours before the earthquake on Alamut area, there was emission of TEM waves; which was due to the interaction of earth magnet and charged cloud near the surface of earth. Authors believed according to data collected, that some relations between the emissions of TEM waves and created sound in the inner layers of the earths and space exists. Of course, in earthquake the created sounds and fault depends on the permeability and permittivity of the earth. So with different angle of emission of TEM waves critical angles will be created. Gathering of highly charged clouds near the surface of earth and transferring energy in to earth a closed loop of magnetic flux density will be formed, so changing the behavior of animals before occurring earthquake (8 to 10 hours before occurrence of earthquake). Therefore created TEM waves will polarize the animals blood, and some eventuation can be taken in to account that existence of TEM waves will irritate animals prior to Earthquake.

1. INTRODUCTION

In this theory it is possible to obtain expressions for the electric and magnetic field strengths in terms of charge and current density, ρ and J respectively, of course such a derivation is, in general, somewhat difficult. So that, in the study of the electrostatic field and steady magnetic field, it is found possible, and often simpler, first to set up potentials in terms of the charges or current and then to obtain the electric or magnetic fields from potentials. In electrostatics a scalar potential V is set up, related to electric charge distribution through

$$V(r) = \frac{1}{4\pi\varepsilon} \int_{v'} \frac{\rho(r')}{R} dv' \tag{1}$$

From this potential the electric field is obtained.

Nothing that the sources of electromagnetic field are current and charge $(\nabla \cdot H = J + D)$, distributions that vary with time, so it is reasonable to try these same potentials, generalized for time, variations. That is, it is expected to be able to write

$$A(r, t) = \frac{\propto}{4\pi} \int \frac{j(r', t)}{R} dv' \tag{2}$$

$$V(r, t) = \frac{1}{4\pi\varepsilon} \int \frac{\rho(r', t)}{R} dV' \tag{3}$$

As it is obvious the strength of these potentials varies instantaneously with the strength of the sources. It is logical that the potentials from which the fields are to be derived, and should also display finite propagation time. Now we should say due to revolution of earth core some energy will

be transmitted to the particles of outer layer, as it is known stationary and moving electric charges produce forces on other stationary and moving electric charges. When charges are stationary, the resulting force field is an electric field or an electrostatic field, whereas charges moving with constant velocity give rise to a magnetic field that is called a magneto static field. As it is known accelerated charges produce an electromagnetic field that consists of related time-varying electric and magnetic fields.

Hass showed that water at $300°$C boils at a pressure of 86 atmospheres [3], it is possible that underground water at temperatures of $300°$ to $1500°$C boils at great depths, where friction acts prior to an earthquake. In fact, the vapor has actually been observed before [4] and after earthquakes [5]. The tremendous pressure of the vapor forces the surface through pores and crakes the ground, "but the authors believe that vapor is created by TEM waves". The effect of the superheated steam has been observed at the surface on numerous occasions. "Water spouts erupted from as high as 115 feet above the valley floor at an estimated 400 cubic feet per second during the 7.3 Borah Peak, Idaho earthquakes on October 28, 1983 [6] and "Petroleum erupted about 20 meters high" from a well eleven days before the Tang Shan earthquake [7]. Furthermore, the pressure in certain oil level sharply rose 20 to 50 atm. about a month before the Tang Shan earthquake [8].

2. SPACE WAVES AND SURFACE WAVES

Sommerfeld (J) stated that it was possible to divide the ground wave field strength in two to parts, a space wave and surface wave. The space wave predominates at large distance above the earth, whereas the surface wave is larger near the earth surface. The expressions for the electric field of an electric dipole above the surface of a finitely conducting plane earth are in a form that clearly shows this separation in to space and surface waves. At large distances from the dipole, such that the terms containing the higher order of $1/R_1$ and $1/R_2$ may be neglected, the expressions for the vertical dipole above a finitely conducting plane reth reduce to

$$E_z = j30\beta Idl \left[\cos^2 \Psi \left(e^{-j\beta r_1}/R_1 + R_v\, e^{-j\beta R_2}/R_2 \right) + (1 - R_v)\left(1 - u^2 + u^4 \cos^2 \Psi\right) F\, e^{-j\beta R_2}/R_2 \right]$$

$$E_p = j30\beta Idl \left[\begin{array}{l} \sin \psi \cos \psi \left(e^{-j\beta R_1}/R_1 + R_v\, e^{-j\beta R_2}/R_2 \right) \\ - \cos \Psi (1 - R_v) u\sqrt{1 - u^2 \cos^2 \psi}\, F\, e^{-j\beta R_2}/R_2 \left(1 + \sin^2 \psi/2\right) \end{array} \right]$$

In this expression, E_z is the Z component of electric field and E_p is radial component and R_1 and R_2 are distances from the dipoles. As it is known the space wave predominates at large distance above the earth, whereas the surface wave is larger near the earth surface (Jordan). A vertically polarized wave at the surface of the earth will have a forward tilt, the magnitude of which depends upon the conductivity ($\sigma = -\propto_e \rho$) of the earth.

The slight tilt forward of the electric field strength is responsible for a small vertically downward component of the pointing vector ($E \cdot H$), sufficient to furnish the power dissipated in the earth over which the wave is passing, as it is known, the component of electric field strength parallel to the earth will not be in phase with component perpendicular to it, so the electric field just above the surface of the earth will be elliptically polarized, eventually the more destruction may occur and eventuate the faults in inner layers of earth and also critical angel may be existed, therefore, critical wave lengths, so critical deformation will exist in that zone. Brewster angle of Particular interest is the possibility in this equation:

$$\frac{E_r}{E_i} = \frac{(\varepsilon_2/\varepsilon_1) \cos \theta_1 - \sqrt{(\varepsilon_2/\varepsilon_1) - \sin^2 \theta_1}}{(\varepsilon_2/\varepsilon_1) \cos \theta_1 + \sqrt{(\varepsilon_2/\varepsilon_1) - \sin^2 \theta_1}}$$

Of particular interest is the possibility in above equation of obtaining no reflection at a particular angle. This occurs when the numerator is zero. For this case

$$\tan \theta_1 = \sqrt{\frac{\varepsilon_2}{\varepsilon_1}}$$

As it is known at this angle, which is called the Brewster angle, there is no reflected wave when the incident wave is parallel polarized. As we know that if the incident wave is not entirely parallel polarized, there will be some reflection, but the reflected wave will be entirely perpendicular (or horizontal) polarization. The final form of the expression for the reflection factor for the horizontal

polarization is

$$R_h = \frac{\sin\psi - \sqrt{(\varepsilon_r - jx) - \cos^2\psi}}{\sin\psi + \sqrt{(\varepsilon_r - jx) - \cos^2\psi}}$$

The reflection factor for parallel or vertical polarization is obtained from Equation (1). It is evident from Equation (2)

$$R_v = \frac{(\varepsilon_r - jx)\sin\psi - \sqrt{(\varepsilon_r - jx) - \cos^2\psi}}{(\varepsilon_r - jx)\sin\psi + \sqrt{(\varepsilon_r - jx) - \cos^2\psi}}$$

As it is known the two above equations that the reflection factors are complex and that the reflected wave will differ both in magnitude and phase from the incident wave. The manner in which the reflection factors vary with angle of incidence is shown in Figs. 1 and 2. The various curves are for different frequencies.

Study of this figures yield some interesting information. When the incident wave is horizontally polarized, so E is perpendicular to the plan of incident and parallel to the reflecting surface, the phase of the reflected wave differs from that of the incident wave by nearly 180 degrees for all angles incident. For angles of incident near grazing ($\psi = 0$), the reflected wave is equal in magnitude but 180 degrees out of phase with the incident wave for all frequencies and all ground conductivities. As it is expected the angle of incident is increased, both the magnitude and phase of reflection factor change, but not to any large extent. The change is greater for the higher frequencies and lower ground conductivities. The curves of Fig. 1 are drawn for an earth having a "good" conductivity and can be used for a range of frequencies from 0.5 to 100 MGH. However, as the angle ψ increase from zero, the magnitude and phase of reflected wave decreases rapidly. The magnitude reaches a minimum and the phase goes through -90 degrees at an angle known as the Brewster angle. For lower frequencies and higher conductivities the Brewster angle is less, approaching zero as $x = \frac{\sigma}{\omega\varepsilon_v}$ becomes much larger than ε_r.

3. EFFECT OF THE EARTH'S MAGNETIC FIELD IN UPPER ATMOSPHERE AND INNER LAYER OF THE EARTH'S

As it is known Surface of earth is formed of hard shell with the average thickness about 100 km, which the beneath of that is plastic formation. Due to non continuity hardness of Surface (Shell) and softness of inner layer (plastic layer) the surface layer will be teared and constitute plates. These plates are sliding on plastic zone, so relative situation and boundary condition between them is usually varying slowly so this slows Motion of plate's cause energy storage in the earth plates, and due to sudden release of energy and propagation of TEM. Earthquake may occur.

It is necessary to briefly touch upon mechanomagnetic conversions in the crust. The four known mechanisms of magnetic field generation by seismic waves are associated with the induction, piezomagnetic, deformational, and inertial effects, respectively [Guglielmi, 1999; Tsegmed et al., 2000]. Theoretically, the Love wave generates the magnetic field at the Earth's surface via the inertial mechanism alone. The magnetic field is excited due to forced vibrations of fluids in pores
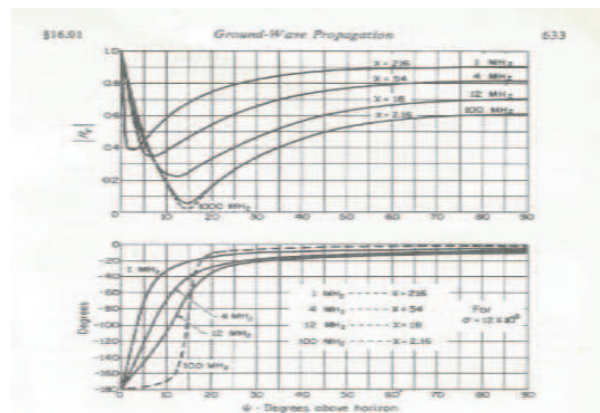

Figure 1. Magnitude and phase of the plane-wave reflection coefficient for vertical polarization.
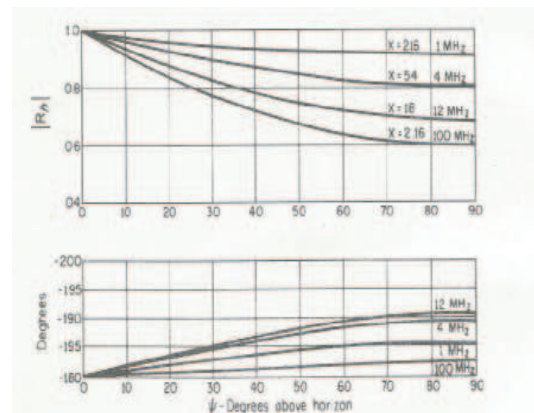
Figure 2. Magnitude and phase of the plane-wave reflection coefficient for **horizontal polarization**.

and cracks produced by the inertial force during Love wave propagation. In a homogeneous uniform isotropic model of the medium, the equation of generation has the form

$$\frac{\partial B}{\partial t} = \alpha \nabla \cdot A + \beta \nabla^2 B$$

Here, A is the acceleration of rocks, B is the magnetic flux density, α is the coefficient of mechano-magnetic conversion, and β is the diffusion coefficient of the magnetic field. The coefficients α and β are proportional to the electro kinetic coefficient K and the electrical resistivity of the rocks ρ, respectively. Information on ρ can be gained from magneto telluric sounding data. The basic idea of seism magnetic sounding is that, at a known value of ρ, the interpretation parameter $\xi = B/A$ contains information on the coefficient K, characterizing the electro kinetic properties of rocks. The fundamental and practical difficulties involved in the realization of the seism magnetic sounding method are covered in the review [9].

On these basis the Authors believe that not only the above theorem is not only sufficient for creation of earthquake, but also TEM waves propagation is needed to have a closed loop energy in to the ground and space;

$$B = \nabla \cdot A$$
$$A = \frac{\propto_0 j}{4\pi} \oint_C \frac{dl'}{R}$$

So electrons and ions in the ionosphere are influenced not only by the fields of passing electromagnetic wave but also by the earth's magnetic field which causes the charged particles to move in circular or spiral paths. It will be shown that the effects of the earth's magnetic field may be taken in to account by a suitable modification in the permeability. Now as it is known by variation of charges in the inner layers of earth, due to created volume charge density (Strain) of the earth. Negatively charges of the inner layers of earth owing to earth core energy and charged cloud near the surface of earth, eventuate the creation of an electromagnetic force field from upper atmosphere to inner layer of earth's which is propagated in circular polarization and moved in Z direction, which is perpendicular to direction of propagation. Of course the destruction of the zone which is depends upon the critical angle.

Since power of epicenter is propagating through inner and outer layers, it will share its energy to the concerned particles of that area, so eventuate strain of the concerned particles therefore fault may occur, of course this fault is not depend upon only the strain of the media but also depends upon the stress of inner layers too, such as permittivity, permeability, conductivity and angle of incident of inner layers. While the stress and strain in inner layers is reaching to maximum of the values, then, may pass from the plastic zone, then, fracture may occur in layers. Considering continuity of the alternate layer's fracture, fault will be made.

ALGORITHM OF EARTHQUAKE
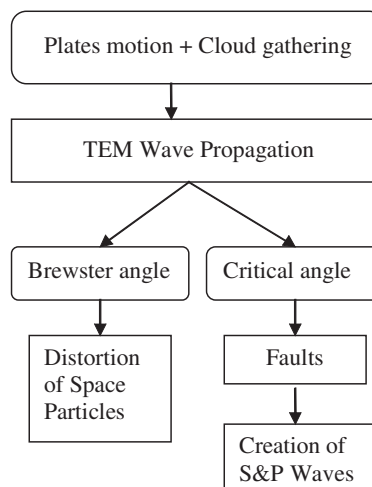
4. SUMMERY AND CONCLUSION

In this paper authors is tried to develop some theory according to some real phenomena which happened in Bam 2004, Alamut 1999 and Roudbar 1990 earthquake in Iran and other places such as China, Japan, and tsunami in Indonesia too. Authors also try to explain a new method of phenomena of earth quick; due to creation of electromagnetic field (TEM wave) with initiative of special clouds near the surface of earth and emission of the TEM with effecting of critical angle and Brewster angle respectively. Brewster angle affects space flights and Critical angle tilt the wave on the surface of earth so producing elliptical polarization with respect to geology engineering, which was indicative of impendent earthquake as well. According to this theory, passing TEM wave through underground water will make the water vapor.

The Figs. 1 and 2 shows the manner in which the reflection factor R_v for vertical polarization varies with angle of incidence.

REFERENCES

1. Jordan, E. C. and K. G. Balmain, *Electromagnetic Waves and Radiating Systems*, Prentice-Hall, 1968.
2. Li, D. J., *Earthquake Clouds*, 148–150, Xue Lin Public Store, Shanghhai, China, 1982.
3. Hass,Jr., J. L., "The effect of salinity on the maximum thermal gradient of a hydrothermal system at hydrostatic pressure," *Eco. Geol.*, Vol. 66, 940–946, 1971.
4. Glowacka, E. and F. A. Nava, "Mafor earthquakes in Mexicali Valley, Mexico, and fluid extraction at Cerro Prieto geothermal field," *Bulletin of the Seismological Society of America*, Vol. 86, No. 1A, 93–105, 1996.
5. Chandrasekharam, D., "Ateam emanation due to seismic pumping," *Geol. Surv. Ind. Spl. Pub.*, No. 1A, 93–105, Mahashratra, 1995.
6. Lane, T. and C. Waag, *Ground-water Eruption in Chilly Butters Area*, Special Publication, Vol. 91, No. 19, Central Idaho, 1985.
7. Shi, H. X. and Z. H. Cai, "Case examples of peculiar phenomena of subsurface fluid behavior observed in China preceding earthquakes," *Acta Seismologica Sinica*, Vol. 5, No. 4, 425–429, 1980.
8. Zhang, D. Y. and G. M. Zhao, "Anomalous variatipns in iol ills distributed in the Bohai bay oil field before and after the Tangshan earthquake of 1976," *Acta Sismologica Sinica*, Vol. 5, No. 3, 360–369, 1983.
9. Guglielmi, A. V., B. Tsegmed, A. S. Potapov, J. Kultima, and T. Raita, "Seismomagnetic signals from the strong sumatra earthquake," *Izvestiya Physics of the Solid Earth*, Vol. 42, No. 11, 921–927, 2006.

Improving the Absorbing Boundary Condition in a 3D Maxwell's Equation Solver

F. Assous

Ariel University Center, Ariel 40700, Israel

Abstract— Solving the time-dependent Maxwell equations in an unbounded domain requires the introduction of artificial absorbing boundary conditions (*ABCs*) to close the computational domain. In this paper, we first introduce an *ABC* proposed by Joly et al.. Then we explain how to include it in order to improve the *ABCs* in a 3D Maxwell solver based on a finite element method. Numerical results show the feasibility of the approach.

1. INTRODUCTION

The numerical solution of time-dependent Maxwell's equations in a unbounded domain requires the introduction of artificial absorbing boundary conditions (*ABCs*) designed to minimize the amplitude of the parasitic waves reflected by the artificial frontier of the domain of computation. In [2], a P^1-conforming finite element method for the time-dependent three dimensional Maxwell equations was proposed. Particular attention was paid on a correct account of the divergence constraints on the electric and magnetic fields, in view of coupling this method with a particle approximation of the Vlasov equation. The applications we had in mind dealt with electron beam propagation, hyperfrequency vacuum devices, etc.... However, the method proved to be also worthwhile in pure electromagnetic wave propagation problems like radar problems. Nevertheless, the *ABC* implemented in the code was of the first order. So, there was a need in improving it in order to apply the code in pure electromagnetic context.

To construct *ABCs* which lead to a well-posed problem (from a mathematical point of view), and to a stable algorithm (from a numerical point of view), there is a need to a rigourous mathematical and numerical analysis. In a previous study, Joly et al. [12] have proposed a new second order *ABC* for the Maxwell's equation in dimension 3, that is particularly well-adapted to a finite element formulation. In some extend, this can be viewed as an alternative to the famous Bérenger condition [6].

The aim of this paper is to present how to apply this second-order *ABC* in the framework of our finite element method. It will be necessary to derive a new variational formulation. Afterwards, the problem of the implemetation in a finite element 3D code, based on a Hood-Taylor method of approximation, will be adressed.

Our paper will be organised as follows. After a brief recall of the Maxwell equations and their mixed second order formulation, we will introduce the Joly-Mercier *ABC*. Then, we will show a way to include it in a finite element approach. Finally, numerical results will be shown to illustrate the feasibility and the accuracy of this method.

2. THE MAXWELL EQUATIONS

We consider here the time-dependent Maxwell equations written in the vacuum

$$\frac{1}{c^2}\frac{\partial E}{\partial t} - \nabla \times B = -\mu_0 J \,, \quad \nabla \cdot E = \frac{\rho}{\varepsilon_0} \,, \tag{1}$$

$$\frac{\partial B}{\partial t} + \nabla \times E = 0 \,, \qquad \nabla \cdot B = 0 \,, \tag{2}$$

where E denotes the electric field and B the magnetic induction. The constants ε_0, μ_0 are respectively the dielectric permittivity and the magnetic permeability in the vacuum. c is the speed of the light and satisfies $\varepsilon_0\mu_0 c^2 = 1$. The right-hand sides ρ and J are respectively the charge and the current densities, which are given functions in the domain Ω.

Then, a wave equation formulation is introduced, because its discretization allows a better control of the oscillations of the solution than the first order one (1)–(2) (see [2]). For instance for the electric field, differentiating Ampere equation with respect to t and using Faraday equation, we

eliminate B in Equation (1) to obtain E as a solution of:

$$\frac{\partial^2 E}{\partial t^2} + c^2 \, \nabla \times (\nabla \times E) = -\frac{1}{\varepsilon_0} \frac{\partial J}{\partial t},$$ (3)

$$\nabla \cdot E = \frac{\rho}{\varepsilon_0},$$ (4)

Similarly for the magnetic induction, we get:

$$\frac{\partial^2 B}{\partial t^2} + c^2 \, \nabla \times (\nabla \times B) = \frac{1}{\varepsilon_0} \nabla \times J,$$ (5)

$$\nabla \cdot B = 0$$ (6)

As these equations are of the same nature, we will concentrate in the sequel of this paper on one of them, namely the electric field formulation (3)–(4).

It is well known that the divergence constraints (4) and (6) are satisfied as soon as they are satisfied at initial time $t = 0$ and that the continuity equation

$$\frac{\partial \rho}{\partial t} + \nabla \cdot J = 0.$$ (7)

is fulfilled. However, after discretization, these properties may very well be violated, either because the continuity equation is not exactly satisfied (due to numerical errors), or because the discrete divergence and curl operators do not satisfy exactly the compatibility condition $\nabla \cdot (\nabla \times \cdot) = 0$. In the discrete case when such circumstances occur, the associated Cauchy problem is then ill-posed, even if the initial data do satisfy the divergence constraint. In [2], we have developed a numerical method which guarantees that at each time step, both divergence constraints are exactly satisfied. In the present paper, we are interested to continue this work in the case of Joly-Mercier second order ABC. We shall follow the ideas of [2] and introduce a constrained formulation of the second-order Maxwell equations involving Lagrange multipliers (denoted by Φ for the electric field) of the divergence constraints, which guarantee the well-posedness of the problem.

For the electric field, such a formulation in the vacuum is written:

$$\frac{\partial^2 E}{\partial t^2} + c^2 \, \nabla \times (\nabla \times E) - \nabla \Phi = -\frac{1}{\varepsilon_0} \frac{\partial J}{\partial t},$$ (8)

$$\nabla \cdot E = \frac{\rho}{\varepsilon_0},$$ (9)

We may impose homogeneous Dirichlet boundary condition on Φ. Obviously, Φ is identically zero (however, they will not remain zero after discretization) if ρ and J satisfy the continuity Equation (7). Hence the system we solve is an equivalent formulation of the classical Maxwell equations.

3. IMPROVING THE ABSORBING BOUNDARY CONDITION

Let us deal now with the boundary conditions. We assume that the boundary Γ of the domain Ω consists of two parts. A conducting boundary part denoted Γ_C, on which we prescribe the perfect conductor condition

$$E \times \mathbf{n} = 0, \quad B \cdot \mathbf{n} = 0 \text{ on } \Gamma_C,$$ (10)

and an artificial boundary part Γ_A on which we have to prescribe absorbing boundary conditions. In [2], we have implemented a first order absorbing condition written in the following time derivative form

$$\frac{\partial}{\partial t}[(E \times \mathbf{n}) \times \mathbf{n}] - c(\mathbf{curl}\, E) \times \mathbf{n} = 0 \quad \text{on } \Gamma_A,$$ (11)

to be well-suited to the wave equation expression of the Maxwell equations.

In this paper, we propose to improve the 3D Maxwell solver by introducing a well-adapted second order ABC, without rewrite the whole method. For that, we use the second order absorbing condition proposed by Joly et al. in [12] that reads (the absorbing plane is $x_3 = $ constante)

$$\left(\frac{\partial}{\partial t} + \frac{\partial}{\partial x_3}\right) \left(\begin{array}{c} E_1 \\ E_2 \end{array}\right) - \frac{1}{2} \left(\begin{array}{cc} \frac{\partial}{\partial x_1} & \frac{\partial}{\partial x_2} \\ \frac{\partial}{\partial x_2} & -\frac{\partial}{\partial x_1} \end{array}\right) \left(\begin{array}{c} E_3 \\ B_3 \end{array}\right) = 0.$$ (12)

Remark 1. *Even if we consider a wave-like expression of the Maxwell equations, we can not use the classical absorbing boundary conditions derived in the framework of the wave equations (see for instance [5, 8]). This is essentially due to the fact that the second-order 3D Maxwell's Equations (3)–(4) are not equivalent to 3D wave equations. One can easily illustrate this point with the formula*

$$\nabla \times (\nabla \times E) = \nabla (\nabla \cdot E) - \mathbf{\Delta} E \quad in \ \mathbb{R}^3,$$

which shows that both formulations can be equivalent only if the divergence vanishes.

As it was emphasized in [3], expression (12) can be written in an intrinsec way as

$$\left(\frac{\partial}{\partial t} + c\frac{\partial}{\partial \mathbf{n}}\right)(\mathbf{n} \times (E \times \mathbf{n})) - \frac{1}{2}\,c\,\mathrm{grad}_\Gamma(E \cdot \mathbf{n}) - \frac{1}{2}\,c^2 curl\,_\Gamma(B \cdot \mathbf{n}) = 0, \tag{13}$$

where grad_Γ and $curl\,_\Gamma$ denote respectively the tangential gradient and rotational. Now, to derive the second order ABC well adapted to our formulation, we eliminate the normal derivative $\frac{\partial}{\partial \mathbf{n}}$ by using the relation

$$\frac{\partial}{\partial \mathbf{n}}(\mathbf{n} \times (E \times \mathbf{n})) = (\nabla \times E) \times \mathbf{n}) + \mathrm{grad}_\Gamma(E \cdot \mathbf{n}).$$

Then one obtains for the ABC

$$\frac{\partial}{\partial t}(\mathbf{n} \times (E \times \mathbf{n})) + c(\nabla \times E) \times \mathbf{n}) + \frac{c}{2}\,\mathrm{grad}_\Gamma(E \cdot \mathbf{n}) - \frac{c^2}{2} curl\,_\Gamma(B \cdot \mathbf{n}) = 0. \tag{14}$$

The same process can be performed to get a condition well adapted to the wave equation in B.

4. A FINITE ELEMENT APPROXIMATION

The finite element discretization starts with a variational formulation of problem (8)–(9) together with the second-order absorbing boundary condition (14). Recall first the definitions of some functional spaces. The spaces $H(curl, \Omega)$, $H(div, \Omega)$ are defined in the usual way [10]:

$$H(curl, \Omega) = \left\{F \in L^2(\Omega)^3, \nabla \times F \in L^2(\Omega)^3\right\},$$
$$H(div, \Omega) = \left\{F \in L^2(\Omega)^3, \nabla \cdot F \in L^2(\Omega)\right\},$$

and we set

$$X = H(curl, \Omega) \cap H(div, \Omega),$$
$$X_0 = \{F \in X, \ F \times \mathbf{n} = 0 \text{ on } \Gamma_C\}.$$

The symbol $(E, F)_\Omega$ stands for the $L^2(\Omega)$ inner product of the two vector fields E and F, namely

$$(E, F)_\Omega = \int_\Omega E \cdot F\, d\omega,$$

where $\cdot$ stands for the usual inner product of vectors in $\mathbb{R}^3$. In these conditions, the augmented variational formulation for the constrained wave equation of the electric field on the whole domain reads
Find $(E, \Phi) \in X_0 \times L^2(\Omega)$ such that

$$\frac{d^2}{dt^2}(E, F)_\Omega + c\frac{d}{dt}(E \times \mathbf{n}, F \times \mathbf{n})_{\Gamma_A} + c^2(\nabla \times E, \nabla \times F)_\Omega + c^2(\nabla \cdot E, \nabla \cdot F)_\Omega + (\Phi, \nabla \cdot F)_\Omega$$

$$+\frac{c^2}{2}(\mathrm{grad}_\Gamma(E \cdot \mathbf{n}), F)_{\Gamma_A} + \frac{c}{2}(curl\,_\Gamma(B \cdot \mathbf{n}), F)_{\Gamma_A} = -\frac{1}{\varepsilon_0}\frac{d}{dt}(J, F)_\Omega + c^2(\rho, \nabla \cdot F)_\Omega, \ \forall F \in X_0, \tag{15}$$

$$(\nabla \cdot E, \psi)_\Omega = \frac{1}{\varepsilon_0}(\rho, \psi)_\Omega, \qquad\qquad\qquad\qquad \forall \psi \in L^2(\Omega). \tag{16}$$

The variational formulation (15)–(16) is of mixed type. Its well-posedness is guaranteed by the so-called "inf-sup" condition [4, 7] which holds in the present case between the spaces X and $L^2(\Omega)$. Furthermore, it can be proved that the solutions of this formulation are such that $\Phi = 0$. If E

is regular, for instance in $H^1(\Omega)^3$, the bilinear form $(\nabla \times E, \nabla \times F)_\Omega + (\nabla \cdot E, \nabla \cdot F)_\Omega$ could be replaced by

$$(\nabla E : \nabla F)_\Omega + \sum_{\alpha=1}^{3} (\nabla E_\alpha \times \mathbf{n}, u_\alpha \times F)_\Gamma,$$

where the symbol: stands for the contracted product of tensors on $\mathbb{R}^3$ and $(E, F)_\Gamma$, for the $L^2(\Gamma)$ inner product of vector fields defined on the boundary Γ of Ω. Finally, u_α is the α-th vector of the canonical basis of $\mathbb{R}^3$, E_α is the α-th component of E.

Remark 2. *It should be pointed out that, when the field is not regular enough, the two variational formulations are not equivalent, and in particular, the Lagrange multiplier Φ can no more be proved to be 0. This instance occur at reentrant edges and corners, where the exact fields are singular. We refer the reader to [1] for more details.*

We now turn to the finite element discretization of the variational formulations (15)–(16) by means of the Hood-Taylor method. The main step is the choice of the finite dimensional spaces V^h and L^{2h} which contain the approximations of the functions of X and $L^2(\Omega)$, where h stands for a generic index measuring the size of the mesh. The mathematical analysis shows that for the method to be convergent, the "inf-sup" condition must be satisfied independently of h as $h \to 0$. This means that the approximation spaces V^h and L^{2h} cannot be chosen independently. The requirement that the "inf-sup" condition be fulfilled is very restrictive and leads to a very limited set of possible approximation spaces, which have been quite exhaustively studied in computational fluid dynamics (see e.g., [10]). Among the possible options, we have chosen the Hood-Taylor element, for reasons that are detailed in [2].

The Hood-Taylor element relies on the definition of two levels of tetrahedrizations, the finer one being deduced from the coarser one by dividing each tetrahedron into 8 sub-tetrahedra. The degrees of freedom are the values of E at the nodes of the finer tetrahedrization and the values of Φ at the nodes of the coarser one. Both E and Φ are chosen continuous over the domain: E is P^1 conforming on the finer mesh while Φ is P^1 conforming on the coarser one.

Having defined the finite dimensional spaces where we look for a solution, we can introduce the matrices associated to the different terms in the variational formulation. We denote by $\mathbb{M}$ the lumped mass matrix for vectors on the finer mesh and by $\mathbb{L}$ the matrix corresponding to $(\nabla \cdot E, \psi)$. We also introduce the matrix $\mathbb{M}^{\Gamma_A}$ defined on the boundary Γ_A, that is the boundary mass matrix constructed from $(E \times \mathbf{n}, F \times \mathbf{n})_{\Gamma_A}$. Moreover for any matrix $\mathbb{A}$, $\mathbb{A}^T$ denotes the transpose of $\mathbb{A}$. With these notations one can derive the problem discretized in space for the electric field. Recall that the Hood-Taylor finite element is particularly interesting in our context, as it leads to a diagonal mass matrix $\mathbb{M}$ without any loss of precision. This property associated with a centered, second-order finite differences time discretization (a leap-frog scheme) leads to an explicit scheme without inverting any linear system at each time step. In order to enforce the constraints numerically the Lagrange multipliers are defined at the most advanced time steps which yields the following matrix problem, which needs to be solved at each time step:

$$\left(\mathbb{M} + c\frac{\Delta t}{2} \mathbb{M}^{\Gamma_A} \right) E_h^{n+1} + \mathbb{L}^T \Phi_{2h}^{n+1} = F^n,$$

$$\mathbb{L} E_h^{n+1} = G^n,$$

where F^n and G^n contain all the terms being known at the time step $n+1$. Then the linear system to be solved has the form (with $\widetilde{\mathbb{M}} = \mathbb{M} + c\frac{\Delta t}{2} \mathbb{M}^{\Gamma_A}$)

$$\begin{pmatrix} \widetilde{\mathbb{M}} & \mathbb{L}^T \\ \mathbb{L} & 0 \end{pmatrix} \begin{pmatrix} E_h^{n+1} \\ \Phi_{2h}^{n+1} \end{pmatrix} = \begin{pmatrix} F^n \\ G^n \end{pmatrix}.$$

An efficient way to solve such a linear system is to use the Uzawa algorithm [9]. Noticing that we can eliminate the unknown E_h^{n+1} in the system to get

$$\mathbb{L}\widetilde{\mathbb{M}}^{-1}\mathbb{L}^T \Phi_{2h}^{n+1} = \mathbb{L}\mathbb{M}^{-1}F^n - G^n,$$

the Uzawa algorithm amounts to using a conjugate gradient algorithm on this latter system. Its resolution involves the inversion of $\mathbb{M}$ which is straightforward since the mass matrix $\mathbb{M}$ is a diagonal one.

5. NUMERICAL RESULTS

We give now a numerical example to illustrate the feasibility of the method. We consider the propagation of the transverse electric (TE) mode in a cubic waveguide, which is of interest because an analytic expression of the solution is known (see for instance [11]). The guide (discretized by irregular tetrahedra) is then illuminated by ingoing plane waves which enter from the bottom plane $x_3 = 0$. On the top face, we impose in a first run of the code the first order ABC (11), then the Joly-Mercier ABC (14) in a second run. On the other faces of the cube, we impose a perfect conductor boundary condition. We have implemented a mode $TE_{1,0}$ with an angle of incidence (with the x_3-axis) θ approximatively equal to $\theta = 25°$. Indeed, as the first order ABC is exact for normal incidence, we have to choose a non-normal incidence to see a better absorption from the Joly-Mercier condition. We summarized in the Table 1 the range of the relative error between the exact and the computed field in each case (0% is the total absorption).

Table 1: Error at the absorbing boundary compared with the exact solution.

Electric field	Error (%)
1st order ABC	7–8%
2nd order ABC	1.5–2%

6. CONCLUSION

In this paper, we presented how to apply the second order ABC introduced by Joly-Mercier in the framework of finite element methods. Variational formulations were derived, and an implementation in a finite element 3D approach, based on a Hood-Taylor method of approximation was given. This shows that the improved ABC is easy to implement in this context, and does not require rewriting the whole method. Numerical results were presented to illustrate the good behavior of the method, in comparison with the first-order absorbing boundary condition.

REFERENCES

1. Assous, F., P. Ciarlet, Jr., and E. Sonnendrücker, "Resolution of the Maxwell equations in a domain with reentrant corners," *Modél. Math. Anal. Numér.*, Vol. 32, 359–389, 1998.
2. Assous, F., P. Degond, E. Heintze, P. A. Raviart, and J. Segré, "On a finite-element method for solving the three-dimensional maxwell equations," *J. Comput. Phys.*, Vol. 109, 222, 1993.
3. Assous, F. and E. Sonnedrücker, "Joly-Mercier boundary condition for the finite element solution of 3D Maxwell equations," accepted to *Math. and Comput. Model.*.
4. Babuska, I., "The finite element method with Lagrange multipliers," *Numer. Math.*, Vol. 20, 179–192, 1973.
5. Bayliss, A. and E. Turkel, "Radiation boundary conditions for wave-like equations," *Comm. Pure. Appl. Math.*, Vol. 33, 707–725, 1980.
6. Bérenger, J.-P., "A perfectly matched layer for the absorption of electromagnetic waves," *J. Comput. Phys.*, Vol. 114, 185–200, 1994.
7. Brezzi, F., "On the existence, uniqueness and approximation of saddle point problems arising from Lagrange multipliers," *RAIRO Anal. Numér.*, 129–151, 1974.
8. Engquist, B. and A. Majda, "Absorbing boundary conditions for acoustic and elastic wave equations," *Math. Comput.*, Vol. 31, 629–651, 1977.
9. Fortin, M. and R. Glowinski, *Augmented Lagrangian Methods*, Springer Series in Computational Mathematics, 5, 1986.
10. Girault, V. and P. A. Raviart, *Finite Element Methods for Navier-Stokes Equations*, Series in Computational Mathematics, Vol. 5, Springer-Verlag, Berlin, 1986.
11. Jackson, J. D., *Classical Electrodynamics*, John Wiley & Sons, New York, 1975.
12. Joly, P. and B. Mercier, "A new second order absorbing boundary condition for Maxwell's equations in dimension 3," *INRIA Res. Report*, Vol. 1047, 1989.

Parallel Power Grid Analysis Using Sensitivities

A. Korobkov, **W. Au**, **L. Yang**, **and V. Subramanian**

Sun Microsystems Inc., USA

Abstract— Design and analysis of on-chip power distribution network are extremely important to ensure the reliable and fully functional product. Growing chip size and complexity makes power network analysis a challenging task, where the traditional methods such as parasitic level time domain circuit simulation of the entire design does not work. In this paper, we propose an efficient power network simulation method for extremely large scale processor design with tens of millions devices. We present a new technique designed to partition power distribution network into the smaller clusters, and to determine current locality shell size for each cluster using sensitivity analysis, such that each shell can be simulated independently in multiple threads by taking advantage of the modern *CMT* (Chip Multi-Threading) processor architecture. The method is scalable with the number of parallel threads, and we have demonstrated an impressive performance improvement over the conventional single thread transient simulation, when applied to the *UltraSparc* power network design.

1. INTRODUCTION

With the increasing chip design complexity and shrinking feature size, design and analysis of power distribution network become a very challenging task, which demands both high computational efficiency and accuracy for analysis tools. For that purpose, the power distribution network (typically referred as *power grid*) is traditionally represented by large-scale linear system, while time-domain circuit simulation techniques are applied to such system, to identify IR drop, electromigration and noise failures.

Several techniques [1–9] has been developed to address power grid simulation efficiency problem. Efficient sparse linear systems solution techniques were proposed in [1], along with initial matrix factors reuse methods when fixed simulation time step is applied, and Cholesky factorization [2] being used to exploit the sparsity of linear system associated with the power grid topology. However there is still a serious network size limitation imposed by this approach. Approximate sparse vector techniques were proposed in [3], to gain speed at the expense of accuracy, by skipping some operations in forward or backward substitution. To overcome capacity limitation, hierarchical analysis technique using macromodels was presented in [4], and the hierarchical random-walk algorithms were discussed in [5]. However, since power grid design may not have a hierarchy, fast and reliable methods for the flat design simulation are still in demand. In [6–8] algebraic multigrid approach widely used for partial differential equations was applied to power grid analysis. Although the runtime improvement is significant, it is difficult to use these techniques for irregular grid. Also accuracy degradation becomes an issue. A natural partitioning approach using overlapping power grid shells based on the current sources locality effect was discussed in [9]. With a minor loss of accuracy and the runtime dramatically reduced over the full chip simulation, this method however is practical for DC operating point analysis only.

Parallel circuit simulation, as an alternative solution to overcome design complexity problem, was a subject of research for a long time. Several techniques were proposed in [10–14], most of them are based on *divide-and-conquer* approach when original circuit is partitioned into the subcircuits, and every subcircuit simulation is performed in parallel with different processes or threads. Parallel domain decomposition has been discussed in [15], with respect to the power grid application. However, with the complex partitioning scheme, large number of connections and strong DC couplings among partitions, it is quite difficult to achieve significant performance gain over conventional methods, while accuracy loss is imminent. Parallel transient simulation through the waveform pipelining scheme has been proposed in [16], but it can be used with the variable step size simulation methods only, which limits power grid analysis performance.

2. BACKGROUND

The power grid with resistors and capacitors connected to ground is represented for the purpose of transient analysis as a set of first order ordinary differential equations, according to the Nodal Analysis:

$$G \times \overline{x}(t) + C \times \frac{d\overline{x}(t)}{dt} = \overline{j}(t) \tag{1}$$

where $\overline{x}(t)$ is n-dimensional vector of unknown node voltages, G is $n \times n$ conductance matrix, C is $n \times n$ capacitance matrix, $\overline{j}(t)$ is n-dimensional vector of current sources.

By applying the backward Euler method to (1), we obtain the set of linear equations representing original system discretized at the time t, h is simulation time step:

$$\left(G + \frac{C}{h}\right) \times \overline{x}(t+h) = \overline{j}(t+h) + \frac{C}{h} \times \overline{x}(t) \tag{2}$$

Since $G + \frac{C}{h}$ is a sparse symmetric positively definitive matrix, it is beneficial to use Cholesky sparse linear solver to solve the Equation (2) repeatedly for every simulation time step. When simulation time step h is fixed, matrix $G + \frac{C}{h}$ does not change during the transient analysis, therefore matrix factorization can be performed one time. Then matrix factors can be reused at every simulation time, which reduces computational cost significantly [1]. It is easy to observe, that in this case the major performance problem is due to the forward and backward substitution, which is performed as many times as the number of simulation steps, for the entire set of unknown circuit variables. Taking into account that small time step $\sim 1\,\mathrm{ps}$ is typically desired to obtain decent simulation accuracy, the number of forward/backward substitutions is normally between 1000 and 10000. With the number of unknown circuit variables growing beyond tens of millions, the total full chip power grid simulation cost increases dramatically.

One solution would be to partition the entire power grid into subcircuits, and simulate them independently, similar to the approach widely used by transistor level fast circuit simulators [15]. However, due to the specifics of power grid topology, it is important to perform partitioning along natural boundaries, to preserve accuracy as much as possible in presence of strong DC couplings between subcircuits. It was observed that current drawn from the power delivery bumps affects the closest area of the power grid only, which can be considered a *locality shell* [9]. Every shell associated with one or more current sources or sinks can be simulated independently with parallel processes or threads. However the question how much area has to be taken around current sources and how to estimate locality variations during the transient analysis, to provide a reasonable tradeoff between performance gain and simulation accuracy, still remains open.

3. PARTITIONING STRATEGY

In this paper, we consider flat full chip power grid design, where current drawn from the grid into the blocks is represented by piecewise linear current sources arbitrary distributed over the entire grid area, as demonstrated on Fig. 1. For simplicity, it is assumed that all existing voltage sources representing power delivery points are set to zero, for both supply and ground networks. For the voltage supply network, it is easy to derive the actual voltage drop by simple addition of supply voltage value to the simulation results. Our goal is to calculate time domain voltage waveforms across all power grid nodes, to identify areas where voltage drop violates design requirements.

It was observed from the experiments that one Cholesky factorization performed before transient simulation normally takes $\sim 15\%$ of the total simulation time when implemented using one of the efficient matrix reordering schemes. Therefore in order to reduce the memory overhead and simplify implementation we perform Cholesky factorization for the entire matrix representing power grid, and then we apply a partitioning scheme for the forward and backward substitution only. We cut the entire sparse vector of current sources $\overline{j}(t+h)$ into the set of subvectors $\{\overline{j}_1, \overline{j}_2, \ldots, \overline{j}_N\}$ according to the order created by linear solver, then we identify a locality shell associated with the set of current sources correspondent to each subvector, and perform forward and backward substitution for every shell independently in parallel. For that purpose, we mask state variables outside of the given shell, such that these variables do not participate in substitution. For the overlapping part, the results are accumulated from all overlapping shells.
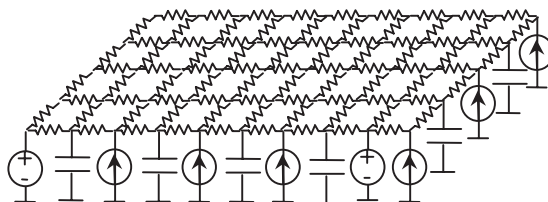

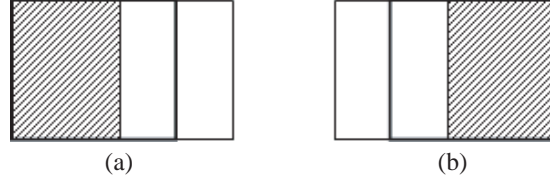Figure 1: Full chip power grid representation.

Figure 2: Example with two partitions. (a) Partition 1, (b) partition 2.

The example with two partitions is demonstrated on Fig. 2. First, we apply Cholesky decomposition to the matrix $G + \frac{C}{h}$ from (2), as a result we have lower L and upper U triangular matrices, where U is a transpose of L: $U = L^T$. After we partition the sparse vector of current sources into the set of subvectors, the Equation (2) can be expressed as follows:

$$L \times U \times \overline{x}\,(t+h) = \overline{\overline{j_1}}(t+h) + \overline{\overline{j_2}}(t+h) + \ldots + \frac{C}{h} \times \overline{x}(t) \tag{3}$$

Then for every subvector $1, 2, \ldots, N$ we perform the forward and backward substitution independently for each equation:

$$L \times U \times \overline{x}_1(t+h) = \overline{j}_1(t+h) + \frac{C}{h} \times \overline{x}_1(t)$$

$$L \times U \times \overline{x}_2(t+h) = \overline{j}_2(t+h) + \frac{C}{h} \times \overline{x}_2(t) \tag{4}$$

$$\ldots$$

$$L \times U \times \overline{x}_N(t+h) = \overline{j}_N(t+h) + \frac{C}{h} \times \overline{x}_N(t)$$

where $\overline{x}(t+h) = \overline{x}_1(t+h) + \overline{x}_1(t+h) + \ldots + x_N(t+h)$ and $\overline{x}_1, \overline{x}_2, \ldots, \overline{x}_N$ are formed according to the locality shell of the current sources associated with the partition. Let us replace the right-hand side of arbitrary equation k from (4) by $\overline{b}_k$:

$$L \times U \times \overline{x}_k = \overline{b}_k \tag{5}$$

In order to solve (5), a standard forward and backward substitution is employed [17]. We have a subvector $\overline{y}_k = U \times \overline{x}_k$, which is the solution of forward substitution in the equation $\overline{y}_k = L^{-1} \times \overline{b}_k$. Please note $\overline{b}_k$ is a sparse subvector and we do not need to solve n equations to obtain $\overline{y}$ [18]. For that purpose, we build a dependency graph using a symbolic representation of matrix L, vector $\overline{b}_k$ to predict the non-zero pattern of $\overline{y}_k$. The dependency graph does not change during the transient analysis, therefore it can be built one time before simulation. For the backward substitution, we calculate a subvector $\overline{x}_k$ correspondent to the nodes inside the shell of the given partition k.

4. SHELL SIZE DETERMINATION

In order to determine a shell associated with the current sources in the given partition, we use worst-case node voltage sensitivities with respect to the current sources. Nodes with small sensitivity are considered outside of the shell, because the voltage at these nodes is not strongly affected by current sources associated with the given partition. By applying differentiation rules to both parts of an arbitrary system of equations k in (4), we have sensitivity equation:

$$L \times U \times \frac{d\overline{x}_k(t+h)}{d\overline{j}_l} = \frac{d\overline{j}_k(t+h)}{d\overline{j}_l} + \frac{C}{h} \times \frac{d\overline{x}_k(t)}{d\overline{j}_l} \tag{6}$$

The vector $\frac{d\overline{j}_k(t+h)}{d\overline{j}_l}$ has 1 at the entry where current source of interest is located, and 0 at all other entries. In order to calculate worst case sensitivities, we combine the impact of all current sources into one analysis, therefore we set 1 at each entry where current source is connected. $\frac{d\overline{x}_k(t)}{d\overline{j}_l}$ is a vector of state variables sensitivities at the previous time step, which actually has a recursive dependency on all time steps occurred before. This is obviously a part of the equation responsible

for the locality shell size variation during the transient analysis. However if the value of time step h is sufficiently large compared to the power grid capacitors, then the part $\frac{C}{h} \times \frac{d\overline{x}_k(t)}{d\overline{j}_l}$ can be ignored. Typically, the maximum value of power grid capacitors is small enough, at least 10^4 times less than normally used time step value of 1 ps. For sensitivity analysis, we use Cholesky factors calculated before for the entire matrix. We perform one forward and one backward substitution to solve sensitivity equations for the entire system, and one forward and backward substitution to solve the Equation (6) for each partition in parallel. For every node, the sensitivity value with respect to the subset of current sources associated with the given partition is compared against the total sensitivity value calculated for the entire system. If contribution is not significant, then this particular node is considered out of the shell. In most cases, power grid nodes with sensitivity less than 0.1% of the maximum node voltage variation can be ignored with the loss of accuracy $\sim 0.1\%$.

5. COMPLEXITY ANALYSIS

The proposed technique reduces complexity of forward and backward substitution only. Approximate minimum degree ordering scheme [18] is used in our implementation to reduce fill-ins in the factorization process. We estimate that the entire process complexity is $O(N^{1.5})$ where N is the number of nodes. The estimated complexity for the forward and backward substitution is $O(m \times l \times N)$, where m is the number of transient analysis steps, $1000 < m < 10000$, l is the average number of entries per column in factor matrix L, in our case ~ 8. If there are K partitions, and every partition shell size is extended by A nodes, the cost of substitution for one partition is $O(m \times l \times (\frac{N}{K} + A))$. For example, if we consider power grid with 20 M nodes, the original substitution complexity is 1.6×10^{12}, but with the number of partitions $K = 8$ and every partition shell extended by 1 M nodes the cost to process one partition is reduced down to 2.8×10^{11} which overall delivers $> 5.7X$ improvement taking into account that partitions are processed in parallel.

6. RESULTS

Simulation results for a set of representative *UltraSparc* design blocks of different complexity are demonstrated on Fig. 3, with each block size shown in Table 1. The total CPU time is reported, with different number of threads executed in parallel. Apparently, there is a clear performance scaling trend as the number of threads increases, however scaling degradation is evident when the number of parallel threads is growing beyond two. One important reason is that the Cholesky decomposition is still performed using one thread. Accumulation of the node voltages calculated within different parallel threads imposes an additional performance overhead. Also, shell size primarily depends on the number of current sources and their strength within the associated partition and does not scale with the number of threads at the same rate as partition size. As a result, the growing size of overlapped regions makes its contribution into the scaling degradation.
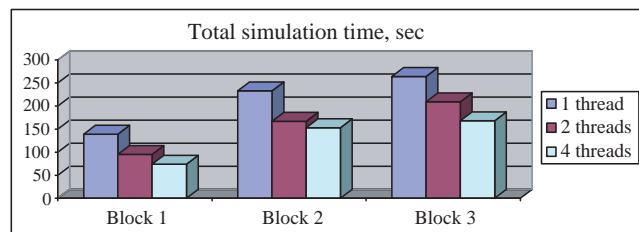
Figure 3: Power grid simulation results.

Table 1: Number of nodes and devices for each benchmark.

Benchmark	Number of nodes	Number of devices
Block 1	189 K	268 K
Block 2	11 M	16 M
Block 3	10 M	17 M

7. CONCLUSIONS

The paper describes an efficient power grid simulation method for very large scale applications, such as high performance processor design. The method proposes power grid partitioning based on the sparse vector decomposition and current locality effect, applicable to the transient analysis with the fixed time step. Simulation results indicates up to $2X$ performance improvement over the conventional one-thread run, when executed with 2 to 4 parallel threads, with a negligible accuracy loss.

REFERENCES

1. Dharchoudhury, A., R. Panda, D. Blaauw, R. Vaidyanathan, B. Tutuianu, and D. Bearden, "Design and analysis of power distribution networks in power PC microprocessors," *Proc. ACM/IEEE DAC*, 738–743, 1998.
2. Golub, G. H. and C. F. Loan, *Matrix Computations*, Johns Hopkins University Press, Baltimore, MD, 1984.
3. Bacher, R., G. C. Ejebe, and W. F. Tinney, "Approximate sparse vector techniques for power network solutions," *IEEE Trans. on Power Systems*, Vol. 6, No. 1, 420–426, Feb. 1991.
4. Zhao, M., R. V. Panda, S. S. Sapatnekar, and D. Blaauw, "Hierarchical analysis of power distribution networks," *IEEE Trans. on CAD*, Vol. 21, No. 2, 159–168, Feb. 2002.
5. Qian, H. and S. S. Sapatnekar, "Hierarchical random-walk algorithms for power grid analysis," *Proc. of the 2004 Conf. on ASP DAC*, 499–504, 2004.
6. Zhu, Z., B. Yao, and C.-K. Cheng, "Power network analysis using an adaptive algebraic multi-grid approach," *Proc. of the 40th DAC*, 105–108, 2003.
7. Su, H., E. Acar, and S. R. Nassif, "Power grid reduction analysis based on algebraic multigrid principles," *Proc. of the 40th DAC*, 109–112, 2003.
8. Zhuo, C., J. Hu, and K. Chen, "An improved AMG-based method for fast power grid analysis," *Proc. of the 7th ISQED*, 290–295, 2006.
9. Chiprout, E., "Fast flip-chip power grid analysis via locality and grid shells," *Proc. of the 2004 IEEE/ACM ICCAD*, 485–488, 2004.
10. Maekawa, Y., K. Nakano, M. Takai, and H. Kasahara, "Near fine grain parallel processing of circuit simulation using direct method," *Proc. of IEEE Pacific Rim Conf.*, 272–276, 1995.
11. Klinger, V., "DiPaCS: A new concept for parallel circuit simulation," *28th Annual Simulation Symp.*, 32–41, 1995.
12. Wever, U. and Q. Zheng, "Parallel transient analysis for circuit simulation," *Proc. of the 29th Annual Hawaii International Conference on System Sciences*, 442–447, 1996.
13. Hachiya, K., T. Saito, T. Nakata, and N. Tanabe, "Enhancement of parallelism for tearing-based circuit simulation," *Proc. of ASP-DAC*, 493–498, 1997.
14. Frolich, N., B. M. Riess, U. A. Wever, and Q. Zheng, "A new approach for parallel simulation of VLSI circuits on a transistor level," *IEEE Trans. on Circuits and Systems*, Vol. 45, No. 6, Jun. 1998.
15. Sun, K., Q. Zhou, K. Mohanram, and D. Sorensen, "Parallel domain decomposition simulation for large-scale power grid," *Proc. of 2007 IEEE/ACM ICCAD*, 54–59, 2007.
16. Dong, W., P. Li, and X. Ye, "WavePipe: Parallel transient simulation of analog and digital circuits on multi-core shared memory machines," *Proc. of the 2008 DAC*, 238–243, 2008.
17. Trefethen, L. N. and D. Bau, "Numerical linear algebra," *SIAM*, 1997.
18. Davis, T. A., "Direct methods for sparse linear systems," *SIAM*, 2006.

Nonlinear Time Series Analysis of the Ionospheric Measurements

Victor A. Eremenko and Natalia I. Manaenkova

Institute of Terrestrial Magnetism, Ionosphere and Radio Wave Propagation (IZMIRAN)
Troitsk 142190, Moscow Region, Russia

Abstract— The application of the tools of nonlinear time-series analysis to measurements, obtained by digital ionosonde is considered. Time series of the observables of reflected HF radio waves, corresponding to not perturbed day ionogram are examined. Reliability of the estimations of the value of correlation dimension D_2 by standard correlation algorithm was confirmed by applying to data sets the test of time-separation. Calculation of the largest Liapounov exponent, analysis of the surrogate data were employed. Successful prediction results also show the low-dimensional, deterministic features of our time series.

1. INTRODUCTION

The application of fractal geometry provides convenient tool to describe naturally occurring rough structures, that is why, there are numerous papers devoted to fractal analysis of the so complex dynamic systems as magnetosphere, ionosphere. The recent years, a new approach, so-called "non-linear time series analysis", has been developed for the study of data sets of physical observables, whose dynamics exhibit irregular or chaotic behavior. For forced, dissipative systems the low-dimensional chaotic dynamics is often associated with the presence of a strange attractor in the system phase space. The various methods provide estimates of properties of the attractor such as the fractal (Hausdorff-Besicovich) dimension D, correlation dimension D_2 [1], the estimation of Kolmogorov entropy — K_2 [2], the spectrum of Lyapunov exponents [3].

We use the tools of nonlinear time-series analysis in order to determine the number of effective degrees of freedom, or dimension of the system ionosonde-ionosphere [4, 5]. But the well-known algorithm of Grassberger and Procaccia for estimating the dimension one must apply with extreme care, before claiming, that the dynamics of the certain system is purely deterministic, low dimensional. It is necessary to use J. Theiler's modification of standard algorithm, recommendations, regarding the number of data points N, choice of value of time delay [6, 7]. For low-dimensional deterministic system it is possible to forecast future states not knowing the law of evolution, only on the base of corresponding time-series [9].

We apply the techniques of nonlinear time-series analysis to measurements, obtained by digital ionosonde "PARUS", created at IZMIRAN.

2. DATA ANALYSIS AND METHODS

We examine small-scaled structure of the electron density Ne at F-region of ionosphere by exploring observables of reflected HF radio wave (amplitude, phase). The transmitted frequency F was selected 3–6 MHz, i.e., the wavelength (50–100 m) is comparable the size of roughness of reflection surface. High resolution of digital ionosonde permit us to measure the amplitude and the phase of received signal with precision $\sim 0.1\%$.

The receiver output is digitized in a quadrature method. Time series were formed as consequence of quadrature samples $X(t_i)$ and $Y(t_i)$, $i = 1, \ldots, N$ of received signal for the fixed value of the virtual height h and transmitting frequency f. Consider one of these sets, starting 20-12-04 at $12 : 31 : 13$ (it conforms to ionogram obtained by ionosonde 20-12-04 at $12 : 36 : 48$) corresponding to frequency $f = 4444$ kHz and value of virtual height $h = 237$ km (reflection of the ordinary component of radio wave). The main quasiperiodic process is formed by general ionosphere motion: up or down. In addition we see something like noise — this is the effect, inducing by small-scaled inhomogeneities (Figure 1).

It is well-known, that if the time series of the single variable is measured, we are able by the method of time delays reconstruct the n-dimensional orbit, representing the time evolution of the system. For finite amounts of noisy data it is very important the choice of value of time delay. For these ionosphere measurements sampling time $\Delta t = 20$ ms, this value of Δt is relevant to quick fluctuation of electron density Ne. Reliability of the estimation of the correlation dimension D_2 was achieved by application of correlation algorithms to sufficiently long sets of measurements $X(t_i)$, corresponding to not perturbed ionosphere, $N = 16000$. Of course, no statistics of a time series is
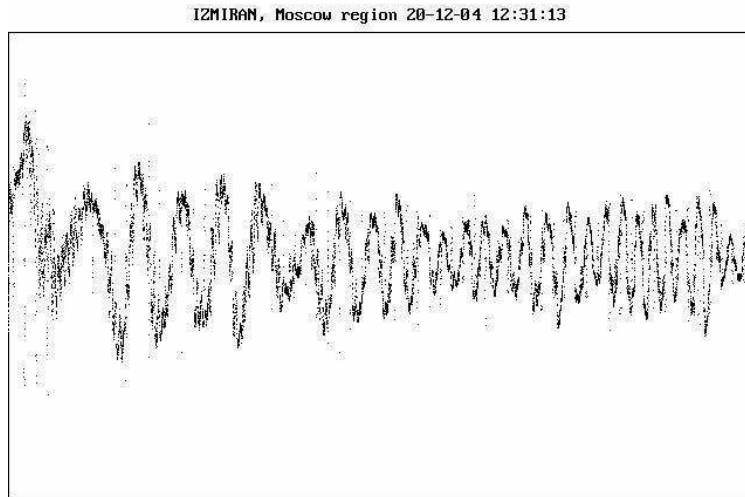
Figure 1: Quadrature samples $X(t)$ of received signal, corresponding to ionogram, obtained by ionosonde 20-12-04 at $12 : 36 : 48$. The transmitter frequency $f = 4444\,\text{kHz}$, virtual height $h = 237\,\text{km}$, value of time interval was fixed, $\Delta t = 20\,\text{ms}$, $N = 16000$.

reliable, unless the process we are studying is stationary. That is why we exclude first 4000 points and study next 10000 points, where the mean and variance are relatively stationary.

Further, we recall the standard correlation algorithm, proposed by Grassberger and Procaccia for computing correlation dimension of strange attractors. Given a scalar time series $X(t_i)$ the first step is an embedding procedure to reconstruct a pseudo phase space for the system considered. A common way to obtain a reconstruction space is to use time-embedding procedure [4], in this case the vector time series is defined as $\mathbf{X} = \{X(t), \ldots, X(t + (n - 1)\tau)\}$, τ is an appropriate time delay multiple of the sampling time Δt, n is the dimension of the vector $\mathbf{X}$. Given vector time series $\mathbf{X}$, one defines the correlation integral $C_n(r)$. The correlation integral is expected to scale as a power of the radius r. This relationship is generally true over a range of r called the scaling region of the correlation integral. From the correlation integral one estimates the correlation dimension $D_2(n) = \Delta \log C_n(r)/\Delta \log r$, e.g., the change of $\log C_n(r)$ versus the change of $\log r$. One may show [5], that at sufficiently large n, $D_2(n) \Rightarrow D_2$. D_2 gives lower estimation of the fractal dimension D.

3. RESULTS

At first, we calculate correlation dimension D_2 by the usual Grassberger and Procaccia method [1]. What we observe at log-log plot of the correlation function vs. radius r (Figure 2(a)) is, that there seems to be the tendency of the curves to achieve a definite slope over a scaling region. At Figure 2(b), there is the plot of the numerical derivatives of the curves of Figure 2(a) versus $\log r$. $D_2 \approx 4.25$. Regarding the number N of data points, used in these calculations, we point out that, according to a formula, proposed by Nerenberg and Essex [6], $N > N_{\min}$, with $N_{\min} = 10^{2+0.4D}$, where D is the fractal dimension. In our case, $N = 10000$ is large enough.

Further, in order to avoid the spuriously low estimate of dimension we have examined data sets more properly, using J. Theiler's modification of standard algorithm [7]. It is recommended, that the good choice for so-called "cutoff" parameter W is provided by the value $W > \text{tau}(2/N)^{2/n}$, where tau — the autocorrelation time. For our case, when $N = 10000$, $n = 15$, tau $= 205$ we choose the value $W = 68$. Small scaling region, poor convergence of slopes, all this indicate, that our time series is not completely deterministic. The fact, that there is noise in our data, is confirmed by applying to our series the test of signal differentiation [8]: our data fail to pass this test.

In order to distinguish low-dimensional dynamics from stochastic processes, it is useful to consider the stochastic surrogate signals obtained by inverting a power spectrum exactly equal to that of the signal under study and random, independent and uniformly distributed Fourier phases. The invariance of the correlation dimension estimates under phase randomization strongly implies that these estimates are not indicative of low-dimensional dynamics. In our case correlation integral for the phase-randomized signal does not saturate, it differ from the behavior of the original set

(a)

(b)
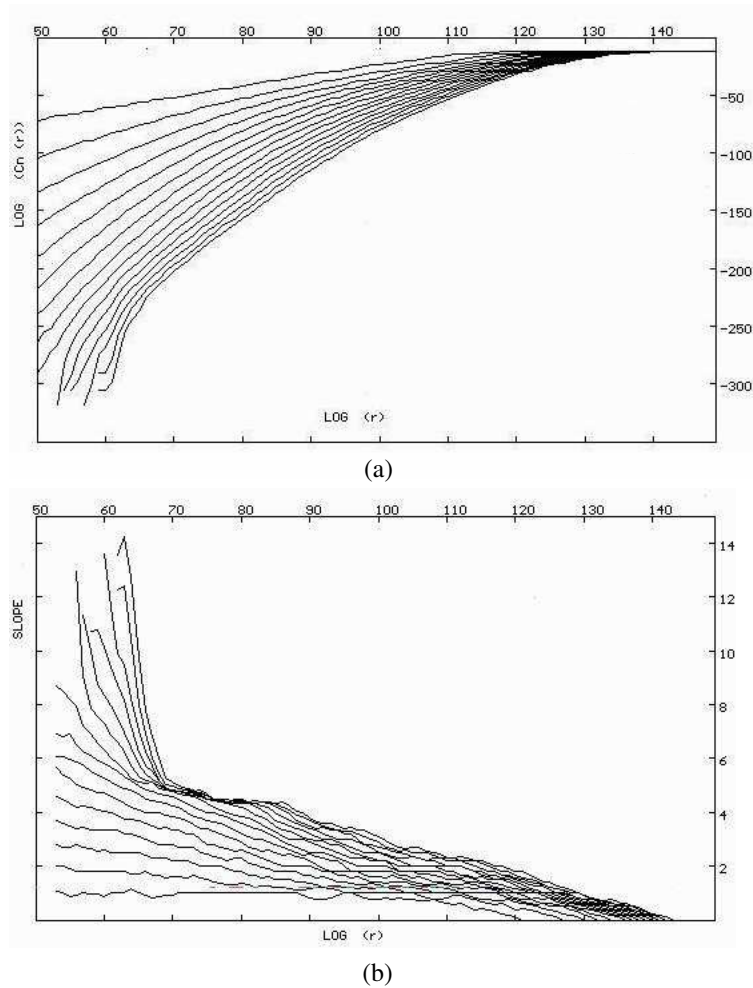
Figure 2: (a) Log-log plot of the correlation function vs radius r for the time-series with $N = 10000$, for $n = 1$ to 15. (b) Numerical calculation of the slope of the curves of a Figure 2. (a) Note the convergence of slopes with increasing n to $D_2 = 4.25$.

significantly. It is clearly, that our dynamic system is quite different from stochastic one.

Further, we turn to the calculation of the largest Liapounov exponent of our time series, i.e., the largest rate of divergence of initially nearby trajectories under time evolution in a n-dimensional embedding space. It is well-known, that $\lambda_{\max} \approx K_2$. We have used the algorithm of Wolf, Swift, Swinney [3]. A positive $\lambda_{\max}$ does not constitute, by itself, convincing evidence of low-dimensional chaos, since random signals are also known to yield $\lambda_{\max} > 0$. $\lambda_{\max}$ for a deterministic system is expected to increase, when the dimensionality of the embedding space is reduced, as the attractor occupies a larger "portion" of available space. For our time series: $\lambda_{\max} \approx 0.008$ for $n > 15$; for $n = 7$, $\lambda_{\max} = 0.016$ and for $n = 3$, $\lambda_{\max} = 0.029$. This behavior is quite distinct from what is observed for a random signal.

The strongest test for distinguishing between low-dimensional chaos and random behavior is the ability to forecast successfully. We used the method of constructing short-term predictors of Farmer and Sidorowich [9]. To predict $X(t + T)$ for time series $\{X(t_i)\}$, $i = 1, \ldots, N$, we make local first-order linear approximation, using only K neighboring points. Working in n-dimensional reconstructed phase space, it is expected for chaotic time series, that the normalized predictor error $E = \sigma_\Delta(T)/\sigma_x$ will suddenly decrease to a value close to zero as n is increasing to the correct minimal embedding dimension $n_{pr} > D_2$, and remain close to zero for values of n above n_{pr}. Here $\sigma_\Delta(T)$ — root-mean-square error:

$$\sigma_\Delta(T) \quad = \left\langle [X_{pred}(t, T) - X(t, T)]^2 \right\rangle^{1/2}, \ \sigma_x \text{ --- rms deviation of the data: } \sigma_x = \left\langle (X - \langle X \rangle)^2 \right\rangle^{1/2}$$

We estimate normalized error E for different values of embedding demension. Naturally, E

decrease with increasing of value n, $E \ll 1$, but as a whole, this non-linear predictor is not so good for our time-series, because of high level of noise in the measurements.

4. CONCLUSIONS

As a results, we may say, that estimation of low-dimension for our time-series is caused not by long autocorrelation time, but by the dynamics of the systems. Nonlinear time series analysis demonstrate, that our set is not completely deterministic, since it contains a significant "random noise". But the presence of noise don't renders this analysis obsolete, because the last one, nevertheless, clear up, that the main deterministic features of not perturbed ionosphere's dynamics are governed by the interaction of only few fundamental variables. As soon as the nonlinear forecasting is the useful diagnostic tool to investigate deterministic chaos, successful prediction results also shows the low-dimensional, deterministic features of our time series.

For low-dimensional chaos there are well-known numerical techniques for constructing nonlinear predictive model directly from time series. For example, there is the method of nearest neighbors, mentioned above. But simple formulae $T_{max} = 1/K_2 \ln(1/\varepsilon)$ clear up, that time T of reliable prediction of investigated parameter is limited: $T \ll T_{max}$. T_{max} is defined by the value of $K_2(D_2)$ and the accuracy ε of data measurements or computations of the corresponding ionosphere parameters.

Even for high resolution of our digital ionosonde "Parus", precision of measurements of received signal $\varepsilon \sim 0.1\%$. Knowing that $\lambda_{max} \approx K_2$, we may approximately estimate T_{max} — the maximum number of sampling time Δt. For $T > T_{max}$ inaccuracy of prediction of considered parameter increases to 100%. For our data sets, when time delay $\tau = \Delta t$, $T_{max} \approx 1000\Delta t$. It means, that for $\Delta t = 20\,\text{ms}$, $T_{max} \approx 20\,\text{s}$. So restricted time of reliable prediction of investigated ionosphere parameter is quite natural. Because it is distinctive feature of any low-dimensional, chaotic dynamic system.

REFERENCES

1. Grassberger, P. and I. Procaccia, "Measuring the strangeres of strange attractors," *Physica D*, Vol. 9, No. 1–2, 189–208, 1983.
2. Grassberger, P. and I. Procaccia, "Estimation of Kolmogorov entropy from a chaotic signal," *Phys. Rev. A*, Vol. 28, 2592–2593, 1983.
3. Wolf, A., J. B. Swift, H. L. Swinney, and J. Vastano, "Determing Lyapounov exponents from a time series," *Physica D*, Vol. 16, 285–317, 1985.
4. Takens, F., "Detecting strange attractors in turbulence," *Lect. Notes in Math.*, Vol. 898, 366–381, Berlin Heidelberg, NY, 1981.
5. Eckman, J.-P. and D. Ruelle, "Ergodic theory of chaos and strange attractors," *Rev. Mod. Phys.*, Vol. 57, 617–656,1985.
6. Nerenberg, M. A. and C. Essex, "Correlation dimension and systematic geometric effects," *Phys. Rev. A*, Vol. 42, 1986.
7. Theiler, J., "Spurious dimension from correlation algotithms applied to limited time-series data," *Phys. Rev. A*, Vol. 34, 2427, 1986.
8. Provenzale, A., L. A. Smith, R. Vio, and G. Murante, "Distinguish low-dimensional dynamics and randomness in measured time series," *Physica D*, Vol. 58, 31–49, 1992.
9. Farmer, J. D. and G. G. Sidorowich, "Predicting chaotic time series," *Phys. Rev. Lett.*, Vol. 59, 845, 1987.

Born-Infeld Non-linear Electrodynamics and String Theory

S. V. Ketov

Tokyo Metropolitan University, Japan

Abstract— Born-Infeld electrodynamics is the particular non-linear generalization of Maxwell electrodynamics. The well known remarkable features of the Born-Infeld electrodynamics include (i) its invariance under (Dirac) electric-magnetic duality, (ii) absence of dichroism, and (iii) existence of solitonic solutions. In addition, the Born-Infeld electrodynamics arises as the low-energy effective action of open strings, and as part of the world-volume effective action of D3-branes (string solitons). I describe an $N = 1$ supersymmetric generalization of the Born-Infeld action, and emphasize its physical interpretation as the Nambu-Goldstone-type action associated with spontaneous partial supersymmetry breaking, $N = 2$ to $N = 1$, in a 4-dimensional spacetime.

1. INTRODUCTION

Born-Infeld (BI) non-linear electrodynamics [1] in flat spacetime (vacuum) is defined by

$$\mathcal{L}_{\text{BI}}(F) = \frac{1}{b^2}\left\{1 - \sqrt{-\det(\eta_{\mu\nu} + bF_{\mu\nu})}\right\}, \tag{1}$$

where $F_{\mu\nu} = \partial_\mu A_\nu - \partial_\nu A_\mu$, $\mu, \nu = 0, 1, 2, 3$, and b is the dimensional coupling constant ($b = 1$ in what follows). The BI theory gives rise to the famous taming of Coulomb self-energy of a point-like electric charge [1], while it shares with the Maxwell theory electric-magnetic self-duality [2] and physical propagation (no shock waves, or no dichroism) [3, 4]. A generic non-linear electrodynamics is defined by the field equations

$$\nabla \times \vec{E} = -\frac{\partial \vec{B}}{\partial t}, \quad \nabla \cdot \vec{B} = 0, \quad \nabla \times \vec{H} = +\frac{\partial \vec{D}}{\partial t}, \quad \nabla \cdot \vec{D} = 0. \tag{2}$$

If there exists a Lagrangian $\mathcal{L}(\vec{E}, \vec{B})$ for them, we have

$$\vec{H} = -\frac{\partial \mathcal{L}}{\partial \vec{B}} \quad \text{and} \quad \vec{D} = +\frac{\partial \mathcal{L}}{\partial \vec{E}}. \tag{3}$$

Lorentz invariance in four spacetime dimensions implies further restrictions,

$$\mathcal{L} = \mathcal{L}(\alpha, \beta), \quad \text{where} \quad \alpha = \tfrac{1}{2}\left(\vec{B}^2 - \vec{E}^2\right) \quad \text{and} \quad \beta = \vec{E} \cdot \vec{B}. \tag{4}$$

The electric-magnetic self-duality of the non-linear electrodynamics (2) under rigid rotations,

$$\vec{E} + i\vec{H} \to e^{i\theta}\left(\vec{E} + i\vec{H}\right) \quad \text{and} \quad \vec{D} + i\vec{B} \to e^{i\theta}\left(\vec{D} + i\vec{B}\right), \tag{5}$$

together with Eq. (3) gives rise to a non-linear constraint [2],

$$\vec{E} \cdot \vec{B} = \vec{D} \cdot \vec{H}. \tag{6}$$

In the manifestly Lorentz-covariant setting with $\mathcal{L}(F_{\mu\nu})$, it is natural to deal with the equations of motion and the Bianchi identities having the same form,

$$\partial^\nu \tilde{G}_{\mu\nu} = 0 \quad \text{and} \quad \partial^\nu \tilde{F}_{\mu\nu} = 0, \tag{7}$$

respectively, where we have defined

$$\tilde{G}_{\mu\nu}(F) = \tfrac{1}{2}\varepsilon_{\mu\nu\lambda\rho}G^{\lambda\rho}(F) = 2\frac{\partial \mathcal{L}(F)}{\partial F^{\mu\nu}}, \quad \tilde{F}_{\mu\nu} = \tfrac{1}{2}\varepsilon_{\mu\nu\lambda\rho}F^{\lambda\rho}. \tag{8}$$

Eq. (6) then amounts to the non-linear constraint [2]

$$G^{\mu\nu}\tilde{G}_{\mu\nu} + F^{\mu\nu}\tilde{F}_{\mu\nu} = 0. \tag{9}$$

Causal propagation in a classical field theory follows from the dominant energy condition on the energy-momentum tensor $T_{\mu\nu}$ (Hawking theorem),

$$T_{00} \geq T_{\mu\nu} \quad \text{for all} \quad \mu \text{ and } \nu. \tag{10}$$

It is straightforward to verify that the BI theory (1) obeys both Eqs. (9) and (10). The absence of shock waves (no dichroism) essentially means that the phase speed is phase-independent.

The BI theory possesses even more magical properties, such as the built-in upper bound for the electro-magnetic field-strength and the existence of exact soliton-like solutions (called BIons) of finite total energy, $\int d^3x \, T_{00} < \infty$. The existence of the maximal electromagnetic field strength is obvious from the form of the dual Hamiltonian density of the BI theory,

$$\mathcal{H}_{\text{dual}} = 1 - \sqrt{1 - \vec{H}^2 - \vec{E}^2 + \left(\vec{H} \times \vec{E}\right)^2}. \tag{11}$$

The BIon solution of electric charge Q to the field equation

$$\nabla \cdot \vec{D} = 4\pi Q \delta(\vec{r}) \tag{12}$$

is given by

$$\vec{D} = \frac{Q}{r^2} \, \vec{e}_r, \qquad \vec{E} = \frac{\vec{D}}{\sqrt{1 + \vec{D}^2}} = \frac{Q}{\sqrt{r^4 + Q^2}} \, \vec{e}_r, \tag{13}$$

so that the electric field singularity of the Maxwell theory is not present in the BI theory, while the *effective* electric density $\rho_{\text{eff.}}$ of a point-like electric charge Q,

$$\rho_{\text{eff.}} = \frac{1}{4\pi} \nabla \cdot \vec{E}, \tag{14}$$

has a finite non-vanishing radius (of order $\sqrt{b}$). The total BI electric field energy is also finite,

$$\int d^3r \, \mathcal{H}_{\text{BI}} \equiv \int d^3r \left(\vec{E} \cdot \vec{D} - \mathcal{L}_{\text{BI}}\right) \propto \int_0^\infty dy \left(\sqrt{1 + y^4} - y^2\right) < \infty \tag{15}$$

In string theory, when a *constant* Kalb-Ramond background $B_{\mu\nu}$ is turned on, $F_{\mu\nu} \to F_{\mu\nu} + B_{\mu\nu}$, the BI theory in the limit $b = 2\pi\alpha' \to 0$ appears to be equivalent to a non-commutative $U(1)$ gauge field theory in flat spacetime with $[x^\mu, x^\nu] = iB^{\mu\nu}$, via the Seiberg-Witten map [5]. The Lorentz invariance is broken in this case. The BI Lagrangian (1) in Euclidean spacetime interpolates between the Maxwell Lagrangian $\frac{1}{4}F^2$ for small F, and the topological density $\frac{1}{4}F\tilde{F}$ for large F, because of the identity

$$\sqrt{\det(F_{\mu\nu})} = \frac{1}{4} \left| F\tilde{F} \right|. \tag{16}$$

The (Euclidean) BI Lagrangian in the $b \to 0$ limit reads

$$\frac{F^2}{\left| F\tilde{F} \right|}, \tag{17}$$

where we have used the relations

$$\sqrt{\det(\varepsilon^{1/2} + F)} \to \sqrt{\varepsilon^2 + \tfrac{\varepsilon}{2}F^2 + \tfrac{1}{16}(F\tilde{F})^2} \xrightarrow{\varepsilon \to 0} \tfrac{1}{4}\left| F\tilde{F} \right| + \varepsilon \frac{F^2}{\left| F\tilde{F} \right|}. \tag{18}$$

The first term on the right-hand-side of this equation is a total derivative, so that one arrives at Eq. (17) after rescaling Eq. (18) by a factor of ε^{-1}.

The BI Lagrangian (1) in Euclidean spacetime obeys the BPS bound

$$\mathcal{L}_{\text{BI}} = \sqrt{\left(1 + \tfrac{1}{4}F\tilde{F}\right)^2 + \tfrac{1}{4}\left(F - \tilde{F}\right)^2} - 1 \geq \tfrac{1}{4}\left| F\tilde{F} \right| \tag{19}$$

It becomes saturated for *self-dual* field configurations, $F = \tilde{F}$, like that in the Maxwell case.

2. SUPERSYMMETRIC BORN-INFELD THEORY

The standard technology of constructing supersymmetric extensions of a bosonic field action is provided by superspace — see e.g., [5]. Manifest supersymmetry does not respect the standard form (determinant) of the BI Lagrangian (1). Moreover, Eq. (1) is not even the most elegant form of the BI theory! The complex bosonic variable, having the most natural $N = 1$ supersymmetric extention (with linearly or manifestly realized $N = 1$ supersymmetry), is given by

$$\omega = \alpha + i\beta, \qquad \alpha = \frac{1}{4}F^{\mu\nu}F_{\mu\nu} \equiv \frac{1}{4}F^2, \quad \beta = \frac{1}{4}F^{\mu\nu}\tilde{F}_{\mu\nu} \equiv \frac{1}{4}F\tilde{F}. \tag{20}$$

The BI Lagrangian (1) can be rewritten to the form ($b = 1$)

$$\mathcal{L}_{\mathrm{BI}}(\omega, \bar{\omega}) = 1 - \sqrt{1 + (\omega + \bar{\omega}) + \tfrac{1}{4}(\omega - \bar{\omega})^2}, \tag{21}$$

or, equivalently,

$$\mathcal{L}_{\mathrm{BI}}(\omega, \bar{\omega}) = \mathcal{L}_{\text{ free}} + \mathcal{L}_{\text{ int.}} \equiv -\tfrac{1}{2}(\omega + \bar{\omega}) + \omega\bar{\omega}\mathcal{Y}(\omega, \bar{\omega}), \tag{22}$$

whose structure function is given by

$$\mathcal{Y}(\omega, \bar{\omega}) \equiv \frac{1}{1 + \frac{1}{2}(\omega + \bar{\omega}) + \sqrt{1 + (\omega + \bar{\omega}) + \frac{1}{4}(\omega - \bar{\omega})^2}}. \tag{23}$$

A remarkably compact form of the BI action [5],

$$\mathcal{L}_{\mathrm{BI}}(\omega, \bar{\omega}) = -\frac{1}{2}(\chi + \bar{\chi}) = -\operatorname{Re}\chi, \tag{24}$$

arises as the iterative solution to the simple non-linear (sigma-model-like) constraint [6]

$$\chi = -\tfrac{1}{2}\chi\bar{\chi} + \omega. \tag{25}$$

Such *Non-Linear Sigma-Model* (NLSM) form of the bosonic BI theory is quite natural from the viewpoint of *Partial Spontaneous (Super)symmetry Breaking* (PSSB) [5]. Indeed, to spontaneously break a rigid symmetry, one can start with a free action that is invariant under the linearly realized symmetry, and then impose an invariant non-linear (algebraic) constraint that gives rise to the NLSM whose solutions break the symmetry.

The bosonic BI theory in the NLSM form is mostly convenient for a direct supersymmetrization in $N = 1$ superspace. One simply replaces the abelian bosonic field strength $F_{\mu\nu}$ by the abelian $N = 1$ chiral spinor superfield strength W_α obeying the standard off-shell $N = 1$ superspace Bianchi identities

$$\bar{D}_{\dot{\alpha}}W_\alpha = 0, \qquad D^\alpha W_\alpha - \bar{D}_{\dot{\alpha}}\bar{W}^{\dot{\alpha}} = 0, \qquad \alpha = 1, 2. \tag{26}$$

In the chiral basis the $N = 1$ superfield W_α reads

$$W^\alpha(x, \theta) = \psi^\alpha(x) + \theta^\beta\left[(\sigma^{\mu\nu})_\beta{}^\alpha F_{\mu\nu}(x) + i\delta_\beta{}^\alpha D(x)\right] + \theta^2 i\partial^{\alpha\dot{\beta}}\bar{\psi}_{\dot{\beta}}(x), \tag{27}$$

where $\psi_\alpha(x)$ is the fermionic superpartner (Goldstone fermion) of the BI vector field, and D is the real auxiliary field. The $N = 1$ superextension of ω is simply given by $\frac{1}{2}D^2W^2$, where $W^2 \equiv W^\alpha W_\alpha$ and $D^2 = D^\alpha D_\alpha$. The $N = 1$ manifestly supersymmetric abelian BI action in the NLSM form is just given by [6]

$$S_{1\mathrm{BI}} = \int d^4x d^2\theta\, X + \text{h.c.}, \tag{28}$$

where the $N = 1$ chiral superfield Lagrangian X obeys the non-linear constraint [6]

$$X = \frac{1}{2}X\bar{D}^2\bar{X} + \frac{1}{2}W^\alpha W_\alpha. \tag{29}$$

The iterative solution to Eq. (29) gives rise to the superfield action

$$S_{1\text{BI}} = \tfrac{1}{2} \left(\int d^4x d^2\theta \, W^2 + \text{h.c.} \right) + \int d^4x d^4\theta \, \mathcal{Y}(\tfrac{1}{2}D^2W^2, \tfrac{1}{2}\bar{D}^2\bar{W}^2) W^2 \bar{W}^2 \tag{30}$$

with *the same* structure function (23) as in the bosonic BI case.

The NLSM form (28) and (29) of the $N = 1$ BI action is also most useful in proving its invariance under the *second* (non-linearly realized and spontaneously broken) $N = 1$ supersymmetry with the rigid spinor parameter η^α [6], [1]

$$\delta_2 X = \eta^\alpha W_\alpha, \quad \delta_2 W_\alpha = \eta_\alpha \left(1 - \frac{1}{2}\bar{D}^2\bar{X} \right) + i\bar{\eta}^{\dot{\alpha}} \partial_{\alpha\dot{\alpha}} X, \tag{31}$$

and its $N = 1$ supersymmetric electric-magnetic self-duality as well. The latter amounts to a verification of the non-local constraint [7]

$$\int d^4x d^2\theta \left(W^2 + M^2 \right) = \int d^4x d^2\bar{\theta} \left(\bar{W}^2 + \bar{M}^2 \right), \quad \text{where} \quad \frac{i}{2} M_\alpha = \frac{\delta S_{1\text{BI}}}{\delta W^\alpha}, \tag{32}$$

which is just the $N = 1$ supersymmetric extension of Eq. (9).

The $N = 1$ supersymmetric BI action can be put into the $N = 1$ *superconformal* form by inserting a conformal compensator ($N = 1$ chiral superfield) Φ into the non-linear constraint (29) as follows [7]:

$$X = \frac{X}{2\Phi^2}\bar{D}^2\left(\frac{\bar{X}}{\bar{\Phi}^2} \right) + \frac{1}{2}W^\alpha W_\alpha. \tag{33}$$

Eq. (29) is recovered from Eq. (33) in the gauge $\Phi = 1$. Varying the new action (28) with respect to Φ yields $W_\alpha = 0$ and, hence, $\omega = 0$ that, in turn, implies $F^2 = F\tilde{F} = 0$. Thus we arrive at the $N = 1$ superconformal extension of the ultra-BI (conformal) bosonic theory.

3. CONCLUSION

The $N = 1$ supersymmetric extension of the abelian (Maxwell) BI action in four spacetime dimensions is the *Nambu-Goldstone* action associated with *Partial Spontaneous Supersymmetry Breaking* (PSSB) of $N = 2$ supersymmetry to to $N = 1$, whose Goldstone fields belong to a Maxwell (vector) supermultiplet with respect to the unbroken $N = 1$ supersymmetry.

REFERENCES

1. Born, M. and L. Infeld, "Foundations of the new field theory," *Proc. Roy. Soc. Lond.*, Vol. A144, 425–451, 1934.
2. Gaillard, M. K. and B. Zumino, "Non-linear electromagnetic self-duality and Legendre transformations," *Proceedings of Newton Institute Euroconference on Duality*, 33–48, Cambridge, UK, April 1997.
3. Plebanski, J., "Nordita lectures on non-linear electrodynamics," *Niels Bohr Institute Preprint*, Copenhagen, Denmark, 1968 (unpublished).
4. Bialynicka-Birula, Z. and I. Bialynicki-Birula, "Non-linear effects in quantum electrodynamics," *Phys. Rev.*, Vol. D2, 2341–2345, 1970.
5. Ketov, S. V., *Quantum Non-linear Sigma-models*, Springer-Verlag, Berlin, Heidelberg, 2000.
6. Bagger, J. and A. A. Galperin, "A New Goldstone multiplet for partially broken supersymmetry," *Phys. Rev.*, Vol. D55, 1091–1098, 1997.
7. Kuzenko, S. M. and S. Theisen, "Nonlinear selfduality and supersymmetry," *Fortschr. Phys.*, Vol. 49, 273–309, 2001.

---

[1]In this case, a spontaneously broken supercharge does not exist, though a supercurrent does.

Computer System to Assist Selecting Models, Methods and Solution Algorithms for Problems in Electrodynamics

A. S. Samokhina and E. A. Trahtengerz

Institute of Control Sciences, Moscow, Russia

Abstract— Major steps while solving electromagnetic problems: To describe the problem (to construct the physical model); to formulate the problem (to construct the mathematical model); to write down the problem in differential or integral equations; to determine boundary conditions for differential equations; to estimate parameters of the mathematical model and criterions for choosing optimal solution; to solve electromagnetic problem by using analytical or numerical methods; to analyze the solution. Thus the construction of computer system to support choosing the models, methods and algorithms of solving mathematical physics problems, incl. electromagnetic problems, is of dire importance.

1. INTRODUCTION

The present evidence clearly indicates the need in computer support to correctly formulate electrodynamics problems and select right solution methods. Computer support and selection management system presents the new perspective in the art of making decisions in mathematical physics, including electrodynamics, per se it is the skill of using computational means, combining the output (estimations and solutions) of mathematical models with subjective assumptions, that are based on the personal experience, knowledge and intuition of a scientist or engineer.

Basic steps of solving a problem in electrodynamics may be represented as following: To formulate the problem with formalized fundamental terms (build up a physical model); to formulate the problem mathematically (build up a mathematical model); to formulate the problem with differential and integral equations; to define value boundary conditions for differential equations; to evaluate parameters of mathematical model and selection criteria for optimal solution; to solve electrodynamics problem with the assistance of analytical and numerical methods (possibly with mathematical software packets); to select analogues; verification of the solution; analysis of the solution.

The issue of selecting rises at the each step of solving the problem, be it locating the correct and optimal physical and mathematical model or choosing numerical versus analytical solution's method and algorithm. Computer support and selection management system for models, methods and algorithms of solving mathematical physics problems, incl. electrodynamics problems, could manage the issue of selecting. The above-mentioned system should be based on the knowledgebase composed be the experts, be able to calculate a vast amount of possibilities and function on-line for the user.

2. GENERAL FORMULATING OF THE PROBLEM

In general case the problem of mathematical physics may be represented as value boundary problem of determining the solution $u(x)$ for the equation

$$(Lu)(x) = f(x), \quad x \in D, \tag{1}$$

where variables $x = (x_1, \ldots, x_n)$ belong to the field D and $u(x)$ satisfy at the boundary S of this field (or of its part) the following boundary conditions:

$$(Bu)(y) = \varphi(y), \quad y \in S. \tag{2}$$

Boundary value problem is correctly formulated if the solution exists, is unique and continuously depends on the input data of the problem. Correctness of the problem's formulating is connected with the type of the operator L, the form of the boundary S and the operator of boundary conditions B. Operators B and L may be written down as algebra functions. These values may be formalized and computed by the Computer System with the help of qualified mathematicians brought in to classify problems of mathematical physics while building up the System's knowledgebase, so that later in while formulating the concrete problem the user could be assisted to correctly construct and write down the mathematical description of the problem.

For many problems also applies the alternate formulation in integral equations. In this case boundary conditions are considered in the core of integral equation.

3. SELECTING THE CORRECT FORMULATION OF THE PROBLEM IN ELECTRODYNAMICS AND ITS ACCURACY CHECK

We shall name the initial problem (1) formalized in mathematical terms as Q; it is the boundary value problem for differential equation for it is natural initial formulation. Concrete problem in mathematical physics, for example for 2-dimensional differential equation in partial derivatives may be formulated as following:

$$a_{11}(x_1, x_2)\frac{\partial^2 u}{\partial x_1^2} + 2a_{12}(x_1, x_2)\frac{\partial^2 u}{\partial x_1 \partial x_2} + a_{22}(x_1, x_2)\frac{\partial^2 u}{\partial x_2^2} + b_1(x_1, x_2)\frac{\partial u}{\partial x_1} + b_2(x_1, x_2)\frac{\partial u}{\partial x_2} + c_0 u = f(x_1, x_2).$$

Here $u = u(x_1, x_2)$ is the unknown function, $f(x_1, x_2)$ is the given coordinates' function. The above stated equation is elliptic in the field D of the 2-Dimensional volume E_2 (D may be equal to E_2), if for any point $x = (x_1, x_2)$, $x \in D$, following equation holds true:

$$\Phi(x, p) = \left| a_{11}(x)p_1^2 + 2a_{12}(x)p_1^2 p_2^2 + a_{22}(x)p_2^2 \right| \neq 0,$$

for each p_1, p_2, p_3, $p_1^2 + p_2^2 + p_3^2 = 1$.

To correctly formulate the problem, it is necessary to define additional conditions at the boundary of the field D for the function u.

Initial problem Q may be always represented as integral equation, generally written down as:

$$a(x)u(x) + \int_D K(x, y)b(y)u(y)dy = f(x),$$

where x — is a period in the 2- or 3-dimensional volume $x = (x_1, x_2)$ or $x = (x_1 + x_2 + x_3)$, D — is the integration domain, 2-dimensional surface of 3-dimensional volume; $a(x)$, $b(x)$ — scalar or vector (in case of a vector number of dimensions l is stated): $K(x, y)$ — core of integral equation, may be scalar or matrix (for the case of matrix its number of dimensions will be $l \times l$.) Shape of the core of integral equation $K(x, y)$ is given by the user. Following cases are possible:

1. $K(x, y)$ — limited coordinates' function in the field D.
2. $K(x, y) = \frac{M(x,y)}{R^\beta}$, where $M(x, y)$ — is a limited coordinates' function in the field D, R^β — is interval between periods x and y, $\beta > 0$ — is given by the user; $R = \sqrt{(x_1 - y_1)^2 + (x_2 - y_2)^2}$ — for 2-Dimensional volume, $R = \sqrt{(x_1 - y_1)^2 + (x_2 - y_2)^2 + (x_3 - y_3)^2}$ — for 3-Dimensional volume.
3. $K(x, y) = \frac{M(x-y)}{R^\beta}$.

In the knowledgebase or references the user may find corresponding value β for different classes of the problems.

At the step of defining functions $a(x), b(x)$ and $K(x, y)$ Computer system checks the correctness of problem's formulating; and issues following possible outcome: The problem is formulated correctly, the problem is formulated incorrectly, the system issues guidelines for possible changes in formulating; the problem is formulated conventionally correct; the system points on what is most important for numerical solving.

4. SELECTING THE PHYSICAL MODEL OF THE PROBLEM

To select the physical model, it is necessary to evaluate the model's correspondence to the initial fundamental problem, therefore experts' appliance is advisable, especially for important problems.

We shall examine the element of experts' approving of the physical model. At first objects to be approved are defined. As objects could be considered:

1. Objectives — as common representation of the problem, mission-global goals.
2. Strategies — approaches and means of achieving the stated objective. There is a connection with the idea of utility — impact of solving subgoals upon solving the problem as a whole. Pigu-Dalatin principle states that utility transfer from object i to object j increases (or dos not decrease) the summary utility, if the utility of object i exceeds utility of object j before and after the transfer. The principle should be heavily relied upon while choosing the concrete strategy.

Given the objective that could be realized by n independent strategies. For each strategy functional dependence of costs $S_i(\tau_i)$ from the duration of strategy's execution τ_i is given; there is a limit of total costs $\sum_{i=1}^{n} S_i(\tau_i) \leq S$. We need to define the optimal time of realization of all strategies to minimize losses C_i per unit time.

It is stated that non-execution of some strategies is a possibility, losses from non-execution of strategy i are d_i. We need to find multitude of strategies Q, to be executed with minimal losses and duration of these strategies, with limitation $\sum_{i \in Q} S_i(\tau_i) \leq S$. In this case, losses will equal

$$\Phi(\tau_i, Q) = \sum_{i \in Q} C_i \tau_i + \sum_{i \notin Q} d_i, \text{ because } \sum_{i \notin Q} d_i = \sum_{i=1}^{n} d_i - \sum_{i \in Q} d_i, \ \Phi(\tau, Q) = \sum_{i \in Q} (C_i \tau_i - d_i) + \sum_{i=1}^{n} d_i.$$

In case of discrete dependence we face a problem of choosing optimal multitude of executed strategies Q such that $\sum_{i \in Q} (C_i \tau_i - d_i) \to \min$ with limitation of $\sum_{i \in Q} S_i(\tau_i) \leq S$.

Hence, we see that for this case the objective is minimization of total losses while solving the problem.

3. Criteria — are indictors that specify the stated objective. For mathematical physics problems as criteria could be considered both rather accurate numerical values such as number of operations needed for solving the problem, amount of computer memory needed, and diffused estimations, such as adequacy of solution, correctness etc.

Criteria, their values and importance, are used to range objectives and strategies.

5. SELECTING MATHEMATICAL MODEL OF THE PROBLEM

Formulating with Maxwell differential equations:

$$\text{rot}\vec{H} = -i\omega\hat{\varepsilon}\vec{E} + \vec{J}_E^0, \quad \text{rot}\vec{E} = -i\omega\hat{\mu}\vec{H} + \vec{J}_H^0. \tag{3}$$

We consider 3 problems:

1. Electromagnetic dispersion on the limited dielectric objects in the free space. In this case, Maxwell equations' solution must satisfy the condition at infinity.
2. Electromagnetic dispersion on the limited super-conducting body or surface. In this case, we add to the two conditions of the previous problem a following condition: Tangential component of electromagnetic field on the surface of ideal superconductor must equal null.
3. Electromagnetic dispersion on dielectric objects that are confined into ideal superconducting surface. For this case, there is no condition at infinity due to limited area of the given problem. Boundary conditions are the same as for the second problem — Tangential component of electromagnetic field on the surface of ideal superconductor must equal null.

For integral equations, the emanation conditions are present in the core of integral equations (which is not the case for differential equations) thus the solution is searched only in relation to the field's value in the dispersion area of the object.

Alternate formulating of the problem with integral equations:

1. For the first problem the volume's integral equation is written down as follows:

$$\vec{E}(x) = \vec{E}^0(x) + k_0^2 \int_Q \left(\hat{\varepsilon}_r - \hat{I}\right)\vec{E}(y)G(R)dy + \text{grad div} \int_Q \left(\hat{\varepsilon}_r - \hat{I}\right)\vec{E}(y)G(R)dy.$$

2. For the second problem, the surface's integral equation is written down as follows:

$$\vec{J}(x) + 2\left[\vec{n}(x), \int_S (\vec{J}(y), \text{grad}G(R))dS_y\right] = 2\left[\vec{n}(x), \vec{H}^0(x)\right], \ x \in S.$$

3. In general case, it is impossible to write down integral equation for the third problem.

We consider numerical criteria of numerical methods to solve differential and integral equations: T — number of arithmetical operation needed to implement algorithm and M is the memory's size needed. We note that $T \approx LT_A$, where L — is the number of iterations, T_A — number of arithmetical operations of multiplying matrix to vector.

The first 2 problems, written down in differential equations, are under condition at infinity, for numerical solution this condition is changed to the condition of emitting on the surface far distanced from the object. In this case, matrix SLAE matrix is sparse matrix (number of non-zero element per row ≈ 10), such matrix is easily multiplied; numerical $T_A \approx 10N_D$, where N_D — is the number of unknowns in the limited area. The needed memory size is of the N exponent part. There are no troubles with the memory size for solving differential equations.

For the first problem, written down in integral equations, SLAE is fully fulfilled (as it is true for all integral equations) and thus we have numerical criteria $T_A \approx N_l LOG(N_l)$, where N_l — number of unknowns in dispersive object, LOG — is integer logarithm, which is the sum of all prime multipliers of the number (for example, for 10^6 $LOG = 42$). We define LOG as:

$$LOG(N) = \sum_{i=1}^{m} N_i, \quad N = \prod_{i=1}^{m} N_i,$$

where N_i — prime multipliers of the number N, m — number of unknowns. The memory size for saving matrix SLAE is proportional to the number of unknowns $M \approx N_l$.

For the second problem written down in integral equations, $T_A \approx N_l^2$, where N_l — number of unknowns in dispersive object. Number of unknowns for integral equations is at least a thousand times less than the number of unknowns needed to solve the same problem but formulated in differential equations. $N_l \ll N_D$, where N_D — is the number of unknowns for differential problem, due to the fact the for integrally formulated problem the solution is being searched inside the object, and for the differentially formulated problem the solution is being searched in the area, that greatly exceeds the object's size.

6. CONCLUSION

Summarizing the above stated, we conclude that: For the first problem, it is better to use integral equations, for the second problem in some cases, it is better to use differential equations, in some-integral equations. The third problem is always to be solved through differential equations.

The Virtual Resonator in Embedding Method of Horn Array Antennas

P. V. Filonov and V. L. Kuznetsov

Moscow State Technical University of Civil Aviation, Russia

Abstract— The problem of virtual resonator in embedding method more complexity requirements to accuracy to solution of basic subproblem — diffraction of bar lattice. In this work new method for this problem proposed. Some results of numerical experiments are considered. The possibility of application new method to virtual resonator problem is shown.

1. INTRODUCTION

In our publication in PIERS in Beijing 2007 [1] we considered the application of embedding method to problem of computing the transparency and reflection coefficients of horn area antenna (HAA). The embedding equations basics on the virtual resonator with "semitransparent" mirror could be written down [2, 3]:

$$
\begin{aligned}
T_{n+1} &= t_{n+1} M_n^{-1} T_n \\
R_{n+1} &= r_{n+1} + t_{n+1} M_n^{-1} R_n t_{n+1} \\
M_n &= I - R_n r_{n+1}
\end{aligned}
\tag{1}
$$

here T_n, R_n — transparency and reflection matrices of HAA, t_n, r_n — transparency and reflection matrices of "semitransparent" elemental layer, M_n^{-1} — matrix which describe the virtual resonator. It could be easily shown what elementary layer could be consider as grating lattice consist of ideal conductive rectangle section skids with small height. As we are using the iteration procedure to compute the solution, to good accuracy we must produce high requirements to computing of t_n and r_n.

In classical solution of diffraction problem on skids lattice (considered in Shestopalov's works [4–6]) we have to distribute the fields by two different basises with different periods. Such kind of procedure must be done because usually the equations on metal and on slot are considering separately [4]. And they exist only on a part of the period. In this work we use method which allow us to consider both equations as a one and distribute the fields on all period of lattice. Such approach allows to connect filed in feeding waveguides with filed in free space.

2. DIFFRACTION ON IDEAL CONDUCTIVE BARS. FULL PERIODIC BASISES

Geometry of scattering surface presented in Fig. 1.

Let's write down representation of field in following form:

$$
E_{in} = e^{i(q_0 y - \kappa_0 z)}, \quad E_r = \sum_n a_n e^{i(q_n y + \kappa_n z)}
$$

$$
E_{inner} = \sum_n a_n e^{i(q_n y - \kappa_n(z+h))}
$$

$$
E_t = \sum_{k=1}^{\infty} \left(c_k e^{-i\sigma_k z} + d_k e^{i\sigma_k(z+h)} \right) \sin\left(\frac{\pi k}{d} y\right)
\tag{2}
$$
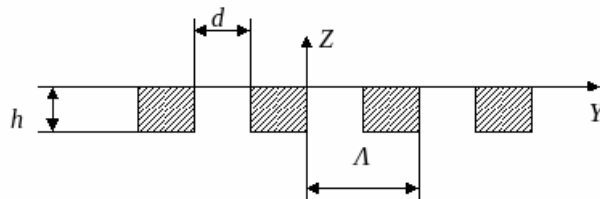
Figure 1: Bars lattice.

here $q_n = \frac{2\pi}{\Lambda} n + q_0$, $\kappa_n = \sqrt{k^2 - q_n^2}$, $\sigma_k = \sqrt{k^2 - \left(\frac{\pi k}{d}\right)^2}$.

For continuity conditions we could write down following system of equations:

$$e^{-iq_0 y} + \sum_n a_n e^{iq_n y} = \begin{cases} \sum\limits_{k=1}^{\infty} \left(c_k d_k e^{i\sigma_k h}\right) \sin\left(\frac{\pi k}{d} y\right) & , \quad y \in \tilde{D}_0 \\ 0 & , \quad y \in \tilde{D}_1 \end{cases}, \tag{3}$$

Here $\tilde{D}_0 = [0, d]$, $\tilde{D}_1 = [d, \Lambda - d]$. By multiply (3) on $e^{-iq_0 y}$ we bring left part of equation to Λ — periodic function. In this way right part of (3) must also be Λ — periodic. Further we distribute (3) by Λ — periodic basis to get equation for a_n

$$a_n = -\delta_{n0} + \frac{1}{\Lambda} \sum_{k=1}^{\infty} \left[c_k + d_k e^{i\sigma_k h}\right] A_{nk} \tag{4}$$

For derivative continuity conditions let's apply same technique

$$-\kappa_0 e^{iq_0 y} + \sum_n a_n \kappa_n e^{iq_n y} - \sum_{k=1}^{\infty} \sigma_k \left(d_k e^{i\sigma_k h} - c_k\right) \sin\left(\frac{\pi k}{d} y\right) = \begin{cases} 0, & y \in \tilde{D}_0 \\ g(y), & y \in \tilde{D}_1 \end{cases} \tag{5}$$

In this case the unknown function $g(y)$ (derivative "hop") doesn't allow us to get independence system. So we will use following artificial technique. We will multiply (5) with following "mask": $\Pi(y; \Lambda) = \Theta(y + \Lambda p) - \Theta(y - d + \Lambda p)$, $p \in Z$, here $\Theta(y)$ — Heaviside function,

$$\left(-\kappa_0 + \sum_n a_n \kappa_n e^{i\frac{2\pi}{\Lambda} n y}\right) \Pi(y; \Lambda) = \sum_{k=1}^{\infty} \sigma_k \left(d_k e^{i\sigma_k h} - c_k\right) \sin\left(\frac{\pi k}{d} y\right) e^{-iq_0 n} \Pi(y; \Lambda) \tag{6}$$

Distributing system (6) by Λ — periodic basis and using equations for a_n (4)

$$-2\kappa_0 B_{n0} + \frac{1}{\Lambda} \sum_p \kappa_p \left[\sum_{k=1}^{\infty} \left(c_k + d_k e^{i\sigma_k}\right) A_{pk}\right] B_{np} = \sum_{k=1}^{\infty} \sigma_k \left(d_k e^{i\sigma_k h} - c_k\right) A_{pk} \tag{7}$$

For conditions on lower bound we can do the same. From continuity of filed we find out:

$$b_n = \frac{1}{\Lambda} \sum_{k=1}^{\infty} \left[c_k e^{i\sigma_k h} + d_k\right] A_{nk}, \tag{8}$$

And from derivative continuity condition:

$$\sum_p \kappa_p \left[\sum_{k=1}^{\infty} \left(d_k + c_k e^{i\sigma_k}\right) A_{pk}\right] B_{np} = \sum_{k=1}^{\infty} \sigma_k \left(c_k e^{i\sigma_k h} - d_k\right) A_{pk} \tag{9}$$

After replacing variables $x_k = c_k + d_k$, $y_k = d_k - c_k$ and some modifications we could write down following system:

$$\begin{cases} -2\kappa_0 B_{n0} + \frac{1}{\Lambda} \sum_p \kappa_p \left[\sum_{k=1}^{\infty} x_k \left(1 + e^{i\sigma_k}\right) A_{pk}\right] B_{np} = \sum_{k=1}^{\infty} \sigma_k x_k \left(e^{i\sigma_k h} - 1\right) A_{pk} \\ -2\kappa_0 B_{n0} + \frac{1}{\Lambda} \sum_p \kappa_p \left[\sum_{k=1}^{\infty} y_k \left(e^{i\sigma_k} - 1\right) A_{pk}\right] B_{np} = \sum_{k=1}^{\infty} \sigma_k y_k \left(e^{i\sigma_k h} - 1\right) A_{pk} \end{cases} \tag{10}$$

Let's represent system (10) in matrix view with new notations:

$$\begin{cases} \left(\frac{1}{\Lambda} M (I + E) + \sigma A (I - E)\right) x = F \\ \left(\frac{1}{\Lambda} M (I - E) + \sigma A (I + E)\right) y = -F \end{cases} \tag{11}$$

here $I_{ij} = \delta_{ij}$, $\kappa_{ij} = \delta_{ij} \kappa_i$, $E_{ij} = \delta_{ij} e^{i\sigma_i h}$, $\sigma_{ij} = \delta_{ij} \sigma_i$, $M = B\kappa A$, $F_i = 2\kappa_o B_{i0}$.
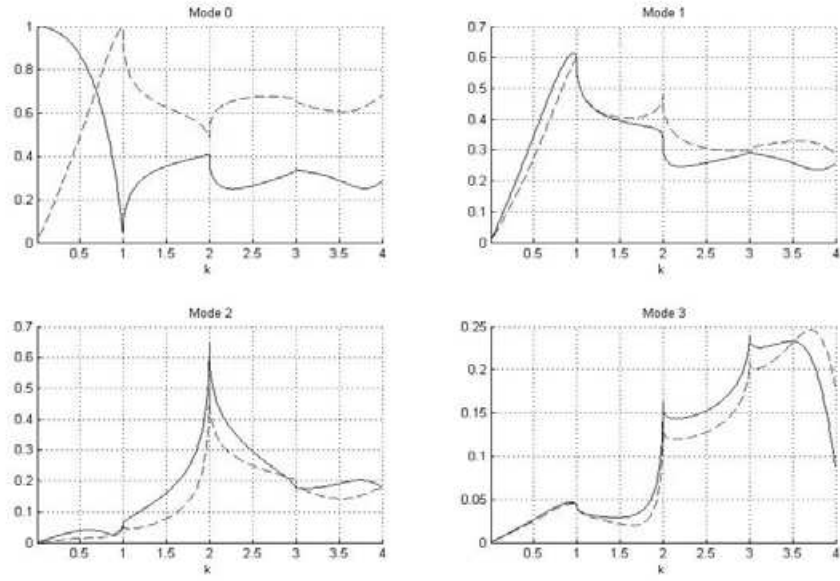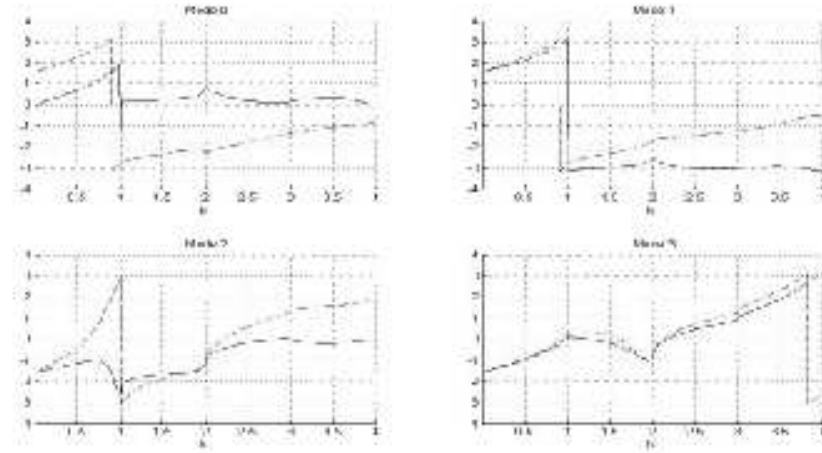
Figure 2: Amplitudes (a) and phases (b) of scattering filed ($q_0 = 0$).
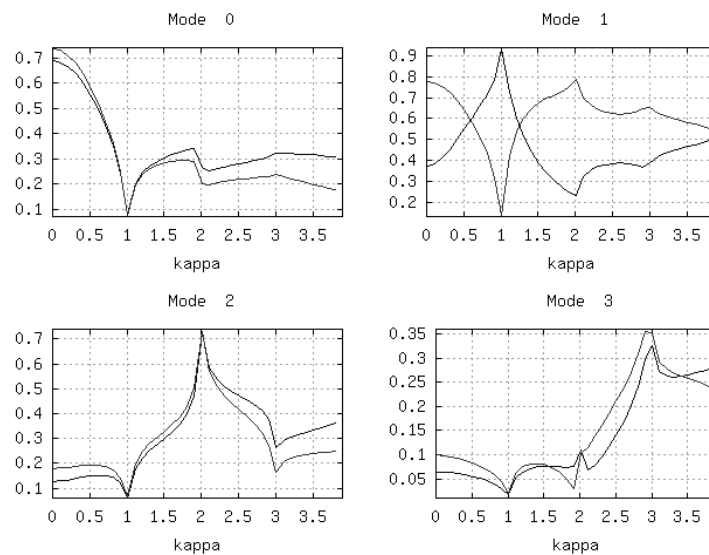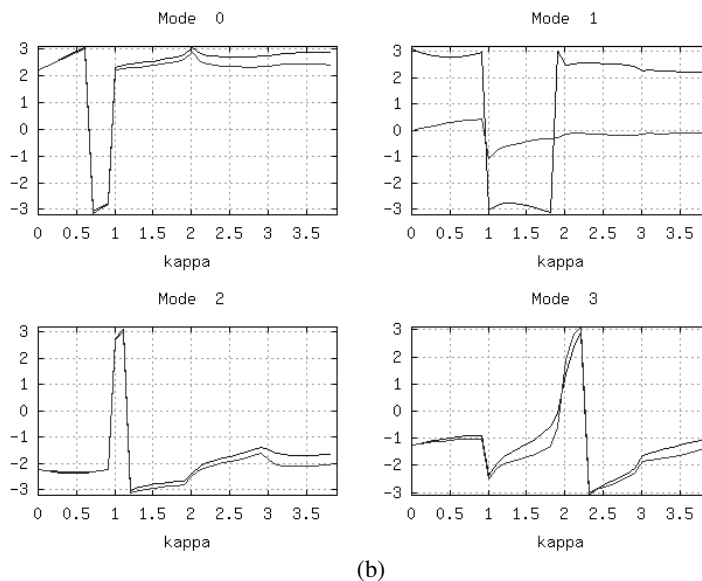
Figure 3: Amplitudes (a) and phases (b) of scattering filed ($q_0 = 1$).

3. RESULTS OF NUMERICAL EXPERIMENTS

Equations (11) were calculated numerically and showed good correspondence to results of works [4–6] with different values of lattice parameters. New approach makes more accuracy on Poiting's theorem. The specific of calculation is that with increasing number of modes we reduce conditional number of system. System still could be solved by straight numerical methods with number of modes less than 81. For more completive solution the additional regularization methods should be used.

On figures we have shown some solutions of (11) with following values of parameters $\Lambda = 2\pi, d = 0.7\Lambda, h = 0.03\Lambda$ with number of modes $n = 21$. On Fig. 2 the solution for normal scattering ($q_0 = 0$) shown and on Fig. 3 the scattering of inhomogeneous (in range of $kappa \in [0, 1)$) wave shown. The points of resonances well seen on integer values of $kappa$. This points describes process of transformation from inhomogeneous wave to homogeneous.

4. CONCLUSION

The new solution for diffraction problem on bar lattice proposed with using full periodic basises. Numerical experiments show good corresponding to classical solutions and more good accuracy. This method will be used for embedding Equation (1) to solve the problem of nanosecond radiolocation.

REFERENCES

1. Filonov, P. V. and V. L. Kuznetsov, "The new approach of computing transparency of horn layer of linear antenna lattice," *Progress In Electromagnetics Research Symposium Abstracts*, Beijing, China, March 26–30, 2007.
2. Bakhrakh, L. D., V. L. Kuznetsov, and I. I. Vizgina, "The theory of HAA (embedding method)," *Telecommunications and Radio Engineering*, No. 8–9, 2004.
3. Bakhrakh, L. D., A. I. Kozlov, and V. L. Kuznetsov, "Ideology of embedding method in theory of HAA-antennas," *Telecommunications and Radio Engineering*, No. 2, 48, 2001.
4. Shestopalov, V. P., S. A. Masalov, and I. E. Tarapov, "Diffraction of electromagnetic waves on space periodical lattice of bars," *Radio Techniques and Electronics*, Vol. 9, 1964.
5. Shestopalov, V. P., A. A. Kirilenko, S. A. Masalov, and U. K. Sirenko, "Resonance scattering of waves. Diffraction lattices," Vol. 1, Kiev, 1986.
6. Shestopalov, V. P., A. A. Kirilenko, S. A. Masalov, and V. G. Sologub, "Diffraction of waves on lattices," Harkov, 1973.

Numerical Calculation of Diffracted Field by a Circular Disk of Perfect Conductor Using Multiple Precision Arithmetic

Takashi Kuroki[1], **Toshihiko Shibazaki**[1], **and Teruhiro Kinoshita**[2]

[1]Tokyo Metropolitan College of Industrial Technology, Japan
[2]Tokyo Polytechnic University, Japan

Abstract— The electromagnetic diffraction by a circular disk of a perfect conductor has been analyzed rigorously by Nomura and Katsura. Numerical data of the diffracted field using their analysis method have been reported in the case that the radius of the disk is smaller than 3 wavelengths. The reason is to learn why the numerical error increases, as the radius of the disk becomes larger. From our investigation, one of the reasons for the numerical error is the cancellation error in the calculation process. The purpose of this study is to obtain numerical data of the current distribution on the disk with the radius larger than 3 wavelengths using multiple precision arithmetic and to calculate the diffracted field. As a result of comparing data of multiple precision arithmetic with data of double precision(or ordinary precision), sufficient accuracy is not obtained with ordinary precision calculation and we can confirm the necessity of multiple precision arithmetic.

1. INTRODUCTION

As the shape of a circular disk coincides with a separable coordinate system of the oblate spheroid, a diffracted field is usually expressed by the oblate spheroidal functions [1]. Another analytical technique not using spheroidal functions has been developed by Nomura and Katsura [2, 3]. They used hyper-geometric polynomials, and have derived a rigorous solution. Numerical data of the diffracted field using their analysis method has been reported in the case that the radius of the disk is smaller than 3 wavelengths [2]. The convergence property of numerical calculation becomes poor and the numerical error increases, as the radius of the disk becomes larger. One of the reasons for the calculation error is the cancellation error in the calculation process [5]. For such a problem, multiple precision arithmetic libraries of numerical computation that can be calculated with more than double precision or quadruple precision have been utilizable in recent years.

The purpose of this study is to obtain numerical data of the current distribution on the disk with the radius larger than some wavelengths using multiple precision arithmetic and to discuss the characteristics of the diffracted field.

In numerical calculations, we use GMP (GNU Multiple Precision Arithmetic Library) [6] and MPFR (Multiple Precision Floating-Point Reliable Library) [7] that are multiple precision calculation libraries.

2. FORMULATION OF PROBLEM

In the following section, we use $e^{j\omega t}$ for the time factor (is omitted throughout), ε for permeability and μ for magnetic permeability and $k(=\omega\sqrt{\mu\varepsilon})$ for wave number, $\lambda(=2\pi/k)$ for wavelength.

We consider calculating the diffracted field in the case of putting a circular disk of a perfect conductor and adding a plane wave from a long distance. In Fig. 1(a), the rectangular coordinate system with the origin at the center of the disk (radius a) is chosen and the disk lies in x-y plane ($z = 0$).

In Fig. 1(b), an incident wave comes from the direction of α to the origin, where α is the angle measured from z axis inside x-z plane. The wave number vector of the incident wave is expressed by

$$\boldsymbol{k}^{(i)} = k(\sin\alpha, 0, -\cos\alpha).$$

An electric Hertz vector $\boldsymbol{\Pi}^{(i)}$ of the incident wave can be expressed by

$$\boldsymbol{\Pi}^{(i)} = \left(\Pi_x^{(i)}, \Pi_y^{(i)}, 0\right) e^{-j\boldsymbol{k}^{(i)}\cdot\boldsymbol{r}}, \tag{1}$$
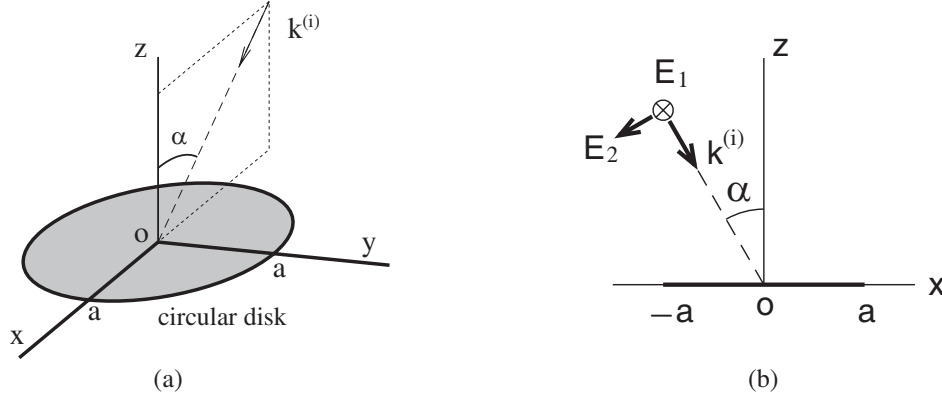
Figure 1: A Coordinate system of a conductive disk and an incident plate wave. (a) Conductive disk (radius a, thickness 0), (b) Coordinate system of incident plane wave.

where $\boldsymbol{r} = (x, y, z)$. Here, the induced current on the circular disk does not have z component. Therefore, the diffracted field is expressed by an electric Hertz vector that has only x and y components. Scatter field $\boldsymbol{E}^{(s)}$, $\boldsymbol{H}^{(s)}$ caused by the induced current is expressed by

$$\boldsymbol{E}^{(s)} = \nabla(\nabla \cdot \boldsymbol{\Pi}) + k^2 \boldsymbol{\Pi} \tag{2}$$

$$\boldsymbol{H}^{(s)} = j\omega\varepsilon\nabla \times \boldsymbol{\Pi}. \tag{3}$$

$\boldsymbol{\Pi}$ can be expanded as follows [1]:

$$\Pi_x = \sum_{n=0}^{\infty}\sum_{m=0}^{\infty} \epsilon_n S_m^n(r, z) \left\{ A_m^n \cos n\varphi + B_m^n \sin n\varphi \right\}, \tag{4}$$

$$\Pi_y = \sum_{n=0}^{\infty}\sum_{m=0}^{\infty} \epsilon_n S_m^n(r, z) \left\{ C_m^n \cos n\varphi + D_m^n \sin n\varphi \right\}, \tag{5}$$

$$\Pi_z = 0, \tag{6}$$

where ϵ_n is either 1 (if $n = 0$) or 2 (if $n \neq 0$).

$$S_m^n(r, z) = \int_0^{\infty} \frac{\sqrt{\xi} J_n(r\xi/a) J_{n+m+\frac{1}{2}}(\xi)}{\sqrt{\xi^2 - (ka)^2}} \exp\left[-\sqrt{\xi^2 - (ka)^2}\frac{|z|}{a} \right] d\xi \tag{7}$$

is an eigen function of a wave equation [2] and is continuous except for the surface of the circular disk of a conductor. A_m^n, B_m^n, C_m^n, D_m^n are expansion coefficients and the unknown parameters that are determined from a boundary condition and so on.

The determination of the expansion coefficients requires that a boundary condition and an edge condition be satisfied. The expansion coefficients can analytically be determined by the introduction of an arbitrary scalar function and an expression of a wave equation with cylindrical coordinates. The Hertz vector of scattered field $\boldsymbol{\Pi}$ is separated into two terms as follows:

$$\boldsymbol{\Pi} = \boldsymbol{\Pi}_1 + \boldsymbol{\Pi}_2, \tag{8}$$

where, $\boldsymbol{\Pi}_1$ cancels the tangential component of the incident electric field, and $\boldsymbol{\Pi}_2$ makes null the electric field on the disk. By expanding (4) and (5), using functions related to Jacobi's polynomial

$$u_m^n(t) = t^{-n/2} \int_0^{\infty} \frac{J_n(\xi\sqrt{t}) J_{n+2m+\frac{1}{2}}(\xi)}{\sqrt{\xi}} d\xi, \tag{9}$$

the infinite dimensional matrix equation for the expansion coefficients of $\boldsymbol{\Pi}_1$ is obtained, where $t = (r/a)^2$. After truncating the infinite series of the unknown coefficient, and inverting the matrix, the expansion coefficients are determined. We will show only the required equation according to the procedure of the numerical calculation in the following section.

3. FLOW OF NUMERICAL CALCULATION

By choosing the ratio a/λ of radius a of a circular disk to wavelength λ as a parameter, we can calculate the expansion coefficients $n = 0, 1, 2, \ldots$. The procedure of the calculation is as follows:

1. Calculating $[A_{1m}^n]$, $[B_{1m}^n]$, $[C_{1m}^n]$, $[D_{1m}^n]$, $[f_{1m}^n]$. Matrix equations for the expansion coefficients are as follows:

$$\left[G_{\ell,m}^n\right]\left[A_{1m}^n\right] = \left[\Pi_x^{(e)}{}_\ell^n\right] \tag{10}$$

$$\left[G_{\ell,m}^n\right]\left[B_{1m}^n\right] = \left[\Pi_x^{(o)}{}_\ell^n\right] \tag{11}$$

$$\left[G_{\ell,m}^n\right]\left[C_{1m}^n\right] = \left[\Pi_y^{(e)}{}_\ell^n\right] \tag{12}$$

$$\left[G_{\ell,m}^n\right]\left[D_{1m}^n\right] = \left[\Pi_y^{(o)}{}_\ell^n\right] \tag{13}$$

$$\left[G_{\ell,m}^n\right]\left[f_{1m}^n\right] = \left[f_\ell^n\right]. \tag{14}$$

The elements of the matrix equations are as follows:

$$G_{\ell,m}^n = \int_0^\infty \frac{\sqrt{\xi} J_{n+2m+\frac{1}{2}}(\xi)}{\sqrt{\xi^2 - \gamma^2}} \left\{ \int_0^1 \frac{t^{n/2} J_n(\xi\sqrt{t})}{\sqrt{1-t}} \times u_\ell^n(t)\,dt \right\} d\xi \tag{15}$$

$$= \frac{\Gamma(n+\ell+\frac{1}{2})\Gamma(\ell+\frac{1}{2})}{\Gamma(n+\ell+1)\Gamma(\ell+1)} \left\{ g_1(n+m+\ell, |m-\ell|) - j g_2(m+n+\ell, |m-\ell|) \right\}, \tag{16}$$

$$g_1(p,q) = \frac{\sqrt{\pi}}{2} \sum_{b=q}^\infty \frac{(-1)^b}{b!} \frac{\Gamma(p-b+\frac{1}{2})\Gamma(2b+1)\left(\frac{\gamma}{2}\right)^{2b}}{\Gamma(\frac{1}{2}-b)\Gamma(p+b+\frac{3}{2})\Gamma(b+q+1)\Gamma(b-q+1)}, \tag{17}$$

$$g_2(p,q) = \frac{\sqrt{\pi}}{2} \sum_{b=0}^\infty \frac{(-1)^b}{b!} \frac{\Gamma(p+b+1)\Gamma(2p+2b+2)\left(\frac{\gamma}{2}\right)^{2p+2b+1}}{\Gamma(2p+b+2)\Gamma(p+b+q+\frac{3}{2})} \frac{1}{\Gamma(p+b-q+\frac{3}{2})\Gamma(p+b+\frac{3}{2})}. \tag{18}$$

$\Pi_{x,y}^{(e,o)}$ are the equations of the incident wave and can be expressed by

$$\Pi_x^{(e)}{}_\ell^n = \frac{(-j)^n E_2}{k^2 \cos\alpha} \int_0^1 \frac{t^{n/2}}{\sqrt{1-t}} u_\ell^n(t) J_n(\sqrt{t}\gamma \sin\alpha)\,dt$$

$$= \frac{(-j)^n E_2}{\sqrt{2}k^2 \cos\alpha} \frac{\Gamma(\ell+\frac{1}{2})\Gamma(n+\ell+\frac{1}{2})}{\Gamma(\ell+1)\Gamma(n+\ell+1)} \sum_{\nu=0}^\infty \frac{(-1)^\nu \left(\frac{1}{2}\gamma\sin\alpha\right)^{n+2\ell+2\nu}}{\Gamma(\nu+1)\Gamma(\nu+n+2\ell+\frac{3}{2})}, \tag{19}$$

$$\Pi_y^{(e)}{}_\ell^n = -\frac{(-j)^n E_1}{\sqrt{2}k^2} \frac{\Gamma(\ell+\frac{1}{2})\Gamma(n+\ell+\frac{1}{2})}{\Gamma(\ell+1)\Gamma(n+\ell+1)} \sum_{\nu=0}^\infty \frac{(-1)^\nu \left(\frac{1}{2}\gamma\sin\alpha\right)^{n+2\ell+2\nu}}{\Gamma(\nu+1)\Gamma(\nu+n+2\ell+\frac{3}{2})}, \tag{20}$$

$$\Pi_x^{(o)}{}_\ell^n = \Pi_y^{(o)}{}_\ell^n = 0. \tag{21}$$

2. Satisfying an edge condition, calculate correction coefficients using (22)–(24).

$$kU_0^{(e)} = \frac{\displaystyle\sum_{m=0}^\infty (-1)^m \left(A_{1m}^1 + D_{1m}^1\right)}{\displaystyle\sum_{m=0}^\infty (-1)^m f_{1m}^1}, \tag{22}$$

$$kU_n^{(e)} = -\frac{\displaystyle\sum_{m=0}^\infty (-1)^m \left[A_{1m}^{n-1} + A_{1m}^{n+1} - D_{1m}^{n-1} + D_{1m}^{n+1}\right]}{\displaystyle\sum_{m=0}^\infty (-1)^m \left[f_{1m}^{n-1} - f_{1m}^{n+1}\right]}, \qquad (n \geq 1) \tag{23}$$

$$kU_n^{(o)} = -\frac{\sum\limits_{m=0}^{\infty}(-1)^m \left[B_{1m}^{n-1} + B_{1m}^{n+1} + C_{1m}^{n-1} - C_{1m}^{n+1}\right]}{\sum\limits_{n=0}^{\infty}(-1)^m \left[f_{1m}^{n-1} - f_{1m}^{n+1}\right]}, \qquad (n \geq 1) \tag{24}$$

where $B_{1m}^0 = D_{1m}^0 = 0$.

3. Calculate the expansion coefficients of the Hertz vector in the diffracted (quadratic) field using (25)–(28).

$$[A_m^n] = [A_{1m}^n] + \frac{k}{2}\left(U_{n+1}^{(e)} - U_{n-1}^{(e)}\right)[f_{1m}^n], \tag{25}$$

$$[B_m^n] = [B_{1m}^n] + \frac{k}{2}\left(U_{n+1}^{(o)} - U_{n-1}^{(o)}\right)[f_{1m}^n], \tag{26}$$

$$[C_m^n] = [C_{1m}^n] + \frac{k}{2}\left(U_{n+1}^{(o)} + U_{n-1}^{(o)}\right)[f_{1m}^n], \tag{27}$$

$$[D_m^n] = [D_{1m}^n] - \frac{k}{2}\left(U_{n+1}^{(e)} + U_{n-1}^{(e)}\right)[f_{1m}^n]. \tag{28}$$

4. Calculate the current distribution by the following process.

$$H_x = H_x^{(i)} - j\omega\varepsilon\frac{\partial \Pi_y}{\partial z}, \tag{29}$$

$$H_y = H_y^{(i)} + j\omega\varepsilon\frac{\partial \Pi_x}{\partial z}, \tag{30}$$

the current $\boldsymbol{J}$ on the surface of the circular disk is expressed by

$$J_x = -H_y = -H_y^{(i)} - j\omega\varepsilon\frac{\partial \Pi_x}{\partial z}, \tag{31}$$

$$J_y = H_x = H_x^{(i)} - j\omega\varepsilon\frac{\partial \Pi_y}{\partial z}, \tag{32}$$

$$J_r = J_x\cos\varphi + J_y\sin\varphi = -H_\varphi^{(i)} - j\omega\varepsilon\left\{\cos\varphi\frac{\partial \Pi_x}{\partial z} + \sin\varphi\frac{\partial \Pi_y}{\partial z}\right\}, \tag{33}$$

$$J_\varphi = -J_x\sin\varphi + J_y\cos\varphi = H_r^{(i)} - j\omega\varepsilon\left\{-\sin\varphi\frac{\partial \Pi_x}{\partial z} + \cos\varphi\frac{\partial \Pi_y}{\partial z}\right\}. \tag{34}$$

$\frac{\partial \Pi_x}{\partial z}$ and $\frac{\partial \Pi_y}{\partial z}$ are expressed by

$$\frac{\partial \Pi_x}{\partial z} = \sum_{n=0}^{\infty}\sum_{m=0}^{\infty}\epsilon_n\frac{\partial S_m^n(r,z)}{\partial z}\left\{A_m^n\cos n\varphi + B_m^n\sin n\varphi\right\} \tag{35}$$

$$\frac{\partial \Pi_y}{\partial z} = \sum_{n=0}^{\infty}\sum_{m=0}^{\infty}\epsilon_n\frac{\partial S_m^n(r,z)}{\partial z}\left\{C_m^n\cos n\varphi + D_m^n\sin n\varphi\right\} \tag{36}$$

From (7) at $z = 0$,

$$\frac{\partial}{\partial z}S_m^n(r,\pm 0) = \mp\frac{1}{a}\int_0^{\infty}\sqrt{\xi}J_n(r\xi/a)J_{n+2m+\frac{1}{2}}(\xi)\,d\xi$$

$$= \mp\frac{1}{a}\frac{\sqrt{2}t^{n/2}\Gamma(m+n+1)}{\Gamma(n+1)\Gamma(m+\frac{1}{2})}F\left(m+n+1, -m+\frac{1}{2}, n+1; t\right), \tag{37}$$

where F is a function related to a Gauss' hyper-geometric function [2].

5. Calculate the Hertz vector of the scatter field using (38)–(39).

$$\Pi_x \simeq \sqrt{\frac{2}{\pi}}a\sum_{n=0}^{\infty}\sum_{m=0}^{\infty}\epsilon_n j^n j_{n+2m}(\gamma\sin\theta)\left\{A_m^n\cos n\varphi + B_m^n\sin n\varphi\right\}\frac{e^{-jkR}}{R} \tag{38}$$

$$\Pi_y \simeq \sqrt{\frac{2}{\pi}}a\sum_{n=0}^{\infty}\sum_{m=0}^{\infty}\epsilon_n j^n j_{n+2m}(\gamma\sin\theta)\left\{C_m^n\cos n\varphi + D_m^n\sin n\varphi\right\}\frac{e^{-jkR}}{R}, \quad (kR \gg 1) \tag{39}$$

4. NUMERICAL CALCULATION

In this section, we calculate the current distribution. We calculate for the case that the incident wave is the plane wave that hits the disk surface vertically ($\alpha = 0$). The electric field of the incident wave has only a y component.

Figure 2 shows the energy error based on the optical theorem with double precision. The horizontal axis indicates the radius of the disk a normalized by the wavelength λ. The vertical axis indicates the relative energy error. After approximately $a/\lambda = 3.0$, an unstable large error occurs, as a increases. The error of the series calculation in (17) and (18) is considered to be the major cause. From this result, there is a necessity to calculate the current distribution with a more precise calculation for a large circular disk.
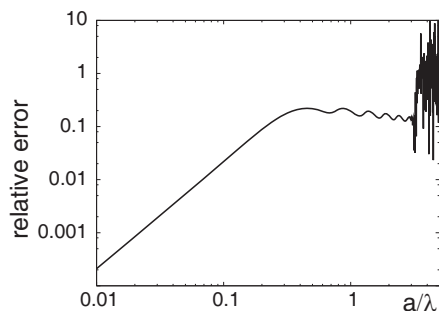
Figure 2: Energy error with double precision.
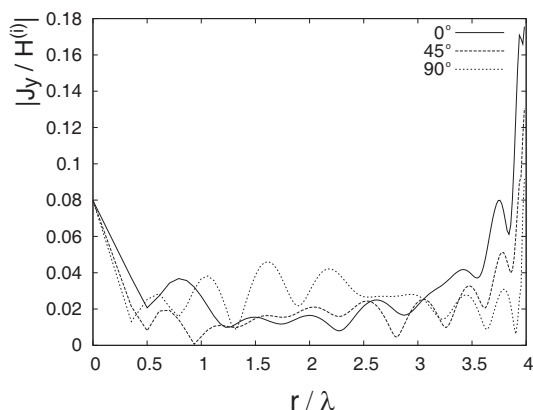
Figure 3: Current distribution at $a/\lambda = 4.0$ with double precision using the FORTRAN code.
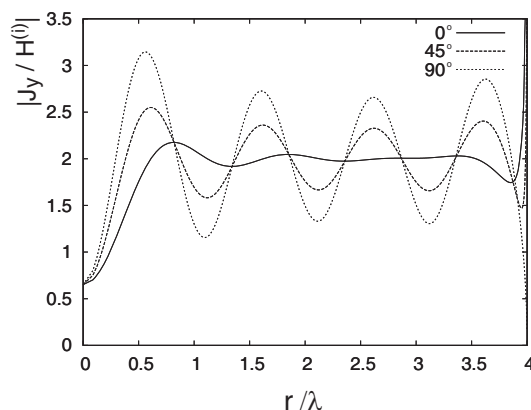
Figure 4: Current distribution at $a/\lambda = 4.0$ with 128-bit precision.
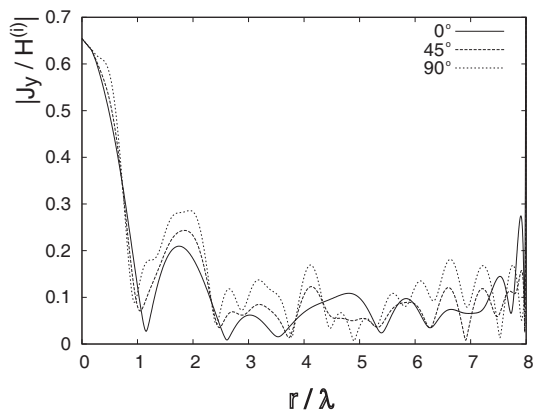
Figure 5: Current distribution at $a/\lambda = 8.0$ with the calculation precision 128-bit.
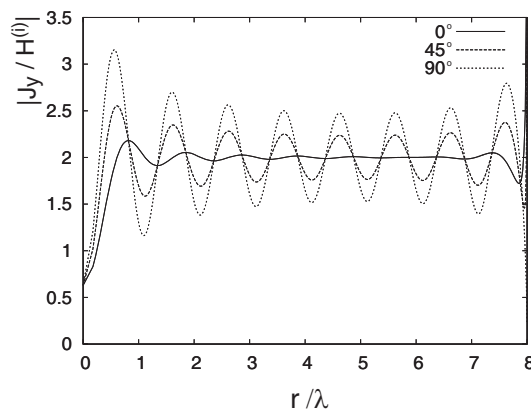
Figure 6: Current distribution at $a/\lambda = 8.0$ with the calculation precision 256-bit.

Figure 3 and Figure 4 show the current distribution in the case with double precision using the FORTRAN code and with 128-bit precision using multiple precision arithmetic. Parameter φ is the angle from the x axis to the observer. The horizontal axis indicates the distance r normalized by the wavelength λ from the center of the disk to the observer. The vertical axis indicates the amplitude of the y component of the current normalized by the incident magnetic field $\boldsymbol{H}^{(i)}$. In Fig. 3, the expected result is not obtained. However, a good result is obtained in Fig. 4.

Figures 5 and 6 show the current distribution in the case $a/\lambda = 8.0$ with 128-bit and 256-bit precision. As the radius of the circular disk is increasing, the required precision is increasing.

5. CONCLUSION

The purpose of this study was to obtain numerical data of the current distribution on the disk with the radius larger than 3 wavelengths using multiple precision arithmetic.

An unstable large error occurred, as the radius of the disk increased, while calculating with double precision arithmetic. It was shown that the current distribution can be calculated more accurately by using multiple precision arithmetic when the circular disk has a radius larger than 3.0 wavelengths.

Based on the above discussion, we will calculate the diffracted field hereafter.

REFERENCES

1. Bowman, J. J., et. al, *Electromagnetic and Acoustic Scattering by Simple Shapes*, Chapter 14, Hemisphere Publishing Corporation, New York, 1987.
2. Nomura, Y. and S. Katsura, "Diffraction of electromagnetic waves by circular plate and circular hole," *Journal of the Physical Society of Japan*, Vol. 10, No. 4, 285–304, 1955.
3. Hongo, K. and Q. A. Naqvi, "Diffraction of electromagnetic wave by disk and circular hole in a perfectly conducting plane," *Progress In Electromagnetics Research*, PIER 68, 113–150, 2007.
4. Ando, M., T. Murasaki, and T. Kinoshita, "Elimination of false singularities in GTD equivalent edge currents," *Proc. IEEE*, Vol. 138, No. 4, 289–296, 1991.
5. Kuroki, T., T. Kinoshita, and T. Shibazaki, "Calculation technic of diffracted electromagnetic waves by a circular disk of perfect conductor using multiple precision arithmetic", *PIERS Proceedings*, 603–609, Cambridge, USA, July 2–6, 2008.
6. "GNU MP-the GNU multiple precision arithmetic library," Edition 4.2.1, 2006.
7. "MPFR-the multiple precision floating-point reliable library," Edition 2.2.0, 2005.

Fourier Solution of the 2D Dirichlet Problem for the Helmholtz Equation

D. Caratelli[1], **P. Natalini**[2], **and P. E. Ricci**[3]

[1]Delft University of Technology, The Netherlands
[2]Roma Tre University, Italy
[3]Sapienza University of Rome, Italy

Abstract— The interior and exterior Dirichlet problems for the Helmholtz equation in star-like planar domains are addressed by using a suitable Fourier series technique. Attention is in particular focused on normal-polar domains whose boundaries are defined by the so called "superformula" introduced by J. Gielis.

1. INTRODUCTION

In recent papers [1–3], the classical Fourier method for solving the Dirichlet problem for the Laplace equation in canonical domains has been extended in order to address the same differential problem in a starlike domain, i.e., a domain $\mathcal{D}$ which is normal with respect to a suitable polar co-ordinate system, so that $\partial\mathcal{D}$ can be interpreted as an *anisotropically stretched unit circle*, centered at the origin.

In this contribution, a suitable technique useful to compute the coefficients of Fourier-type expansions representing solutions of boundary-value problems (*BVPs*) for the classical Helmholtz equation in complex planar domains is presented. In particular, the boundaries of the considered domains are defined by the so called "superformula" introduced by J. Gielis [4].

In order to verify and validate the relevant technique, a suitable numerical procedure based on the computer algebra system Mathematica© has been developed. By using such procedure, a point-wise convergence of the Fourier-series representation of the solution in regular points of the boundary, with Gibbs-like phenomena potentially occurring in singular points, has been observed. The obtained numerical results are in good agreement with theoretical findings by L. Carlson [5].

2. THE LAPLACIAN IN STRETCHED POLAR CO-ORDINATES

We introduce in the x, y plane the usual polar co-ordinate system:

$$x = \rho\cos\vartheta, \ y = \rho\sin\vartheta, \tag{1}$$

and the polar equation of $\partial\mathcal{D}$

$$\rho = R(\vartheta), \ (0 \leq \vartheta \leq 2\pi), \tag{2}$$

where $R(\vartheta)$ is a piece-wise C^2 function in $[0, 2\pi]$. We suppose the domain $\mathcal{D}$ satisfies

$$0 \leq \rho \leq R(\vartheta), \tag{3}$$

and $\min_{\vartheta\in[0,\,2\pi]} R(\vartheta) > 0$. We introduce the auxiliary function

$$\Upsilon := \Upsilon(\vartheta) := \frac{1}{R(\vartheta)}, \ (0 \leq \vartheta \leq 2\pi), \tag{4}$$

and the stretched radius ϱ^* such that

$$\rho = \frac{\varrho^*}{\Upsilon(\vartheta)}. \tag{5}$$

So, the following curvilinear (i.e., stretched) co-ordinates ϱ^*, ϑ

$$x = \frac{\varrho^*}{\Upsilon(\vartheta)}\cos\vartheta, \ y = \frac{\varrho^*}{\Upsilon(\vartheta)}\sin\vartheta, \tag{6}$$

can be usefully adopted in the x, y plane. In this way, $\mathcal{D}$ is obtained assuming $0 \leq \vartheta \leq 2\pi$, $0 \leq \varrho^* \leq 1$.

Remark 1. — *Note that, in the stretched co-ordinate system the original domain $\mathcal{D}$ is transformed into the unit circle, so that in this system we can use for the transformed Helmholtz equation all the classical techniques, including separation of variables.*

We consider a $L^2(\mathcal{D})$ function $v(x, y) = v(\rho \cos \vartheta, \rho \sin \vartheta) = u(\rho, \vartheta)$ and the Laplace operator in polar co-ordinates

$$\Delta u = \frac{\partial^2 u}{\partial \rho^2} + \frac{1}{\rho} \frac{\partial u}{\partial \rho} + \frac{1}{\rho^2} \frac{\partial^2 u}{\partial \vartheta^2}. \tag{7}$$

We start representing this operator in the new stretched co-ordinate system ϱ^*, ϑ. Setting

$$U(\varrho^*, \vartheta) = u\left(\frac{\varrho^*}{\Upsilon(\vartheta)}, \vartheta\right), \tag{8}$$

we find (denoting for shortness $\Upsilon(\vartheta) := \Upsilon$)

$$\Delta u = (\Upsilon^2 + \Upsilon'^2)\frac{\partial^2 U}{\partial \varrho^{*2}} + \frac{\Upsilon^2 + \Upsilon\Upsilon''}{\varrho^*} \frac{\partial U}{\partial \varrho^*} + \frac{2\Upsilon\Upsilon'}{\varrho^*} \frac{\partial^2 U}{\partial \varrho^* \partial \vartheta} + \frac{\Upsilon^2}{\varrho^{*2}} \frac{\partial^2 U}{\partial \vartheta^2}. \tag{9}$$

For $\varrho^* = \rho$, $\Upsilon(\vartheta) \equiv 1$, we recover the Laplacian in polar co-ordinates.

3. THE DIRICHLET PROBLEM FOR THE HELMHOLTZ EQUATION

Let us consider the interior Dirichlet problem for the Helmholtz equation in a starlike domain $\mathcal{D}$, whose boundary is described by the polar equation $\rho = R(\vartheta)$,

$$\begin{cases} \Delta v(x, y) + k^2 v(x, y) = 0, & (x, y) \in \mathring{\mathcal{D}}, \\ v(x, y) = f(x, y), & (x, y) \in \partial\mathcal{D}. \end{cases} \tag{10}$$

where $k > 0$ denotes the propagation constant. The following theorem holds true.

Theorem 1. — *let*

$$f(R(\vartheta)\cos\vartheta, R(\vartheta)\sin\vartheta) = F(\vartheta) = \sum_{m=0}^{+\infty} (\alpha_m \cos m\vartheta + \beta_m \sin m\vartheta), \tag{11}$$

where

$$\left\{ \begin{matrix} \alpha_m \\ \beta_m \end{matrix} \right\} = \frac{\epsilon_m}{2\pi} \int_0^{2\pi} F(\vartheta) \left\{ \begin{matrix} \cos m\vartheta \\ \sin m\vartheta \end{matrix} \right\} d\vartheta, \tag{12}$$

$\epsilon_m = \begin{cases} 1, & m = 0 \\ 2, & m \neq 0 \end{cases}$ *being the Neumann's symbol. Then, the interior boundary-value problem for the Helmholtz Equation (10) admits a solution*

$$v(x, y) \in L^2(\mathcal{D}) \tag{13}$$

such that the following Fourier-Bessel series expansion holds

$$v(\varrho^* R(\vartheta)\cos\vartheta, \varrho^* R(\vartheta)\sin\vartheta) = U(\varrho^*, \vartheta)$$
$$= \sum_{m=0}^{+\infty} J_m(k\varrho^* R(\vartheta))(A_m \cos m\vartheta + B_m \sin m\vartheta). \tag{14}$$

The coefficients A_m, B_m in (14) can be determined by solving the infinite linear system

$$\sum_{m=0}^{+\infty} \begin{bmatrix} X_{n,m}^+ & Y_{n,m}^+ \\ X_{n,m}^- & Y_{n,m}^- \end{bmatrix} \cdot \begin{bmatrix} A_m \\ B_m \end{bmatrix} = \begin{bmatrix} \alpha_n \\ \beta_n \end{bmatrix}, \tag{15}$$

where

$$X_{n,m}^\pm = \frac{\epsilon_n}{2\pi} \int_0^{2\pi} J_m(kR(\vartheta)) \cos m\vartheta \left\{ \begin{matrix} \cos n\vartheta \\ \sin n\vartheta \end{matrix} \right\} d\vartheta, \tag{16}$$

$$Y_{n,m}^\pm = \frac{\epsilon_n}{2\pi} \int_0^{2\pi} J_m(kR(\vartheta)) \sin m\vartheta \left\{ \begin{matrix} \cos n\vartheta \\ \sin n\vartheta \end{matrix} \right\} d\vartheta, \tag{17}$$

with $m, n \in \mathbb{N}_0$.

Remark 2. — *It is worth noting that an approximate solution of the infinite linear system (15) can be obtained by solving the corresponding finite system with $m, n = 0, 1, \ldots, N$. Such solution is convergent as N approaches infinity since it is related to the solution of a vectorial integral equation corresponding to a compact operator with an L^2 kernel [6]. In fact, substituting in (15) the discrete index m with a continuous parameter μ and, consequently, putting $A_m = A(\mu)$, $B_m = B(\mu)$, $\underline{\zeta}(\mu) = [A(\mu), B(\mu)]^T$, $\underline{\Sigma}(\mu\vartheta) = [\cos(\mu\vartheta), \sin(\mu\vartheta)]^T$, yields*

$$\int_0^{+\infty} J_\mu(kR(\vartheta))\underline{\Sigma}(\mu\vartheta) \cdot \underline{\zeta}(\mu)d\mu = F(\vartheta). \tag{18}$$

Let $M_R := \max_{\vartheta \in [0, 2\pi]} R(\vartheta)$. Then, we can estimate

$$\int_0^{+\infty}\int_0^{2\pi} \|J_\mu(kR(\vartheta))\underline{\Sigma}(\mu\vartheta)\|^2 d\vartheta d\mu = \int_0^{+\infty}\int_0^{2\pi} J_\mu(kR(\vartheta))^2 d\vartheta d\mu$$

$$\le \int_0^{+\infty}\int_0^{2\pi} \left\{\frac{[\frac{1}{2}kR(\vartheta)]^\mu}{\Gamma(\mu+1)}\right\}^2 d\vartheta d\mu \le 2\pi \int_0^{+\infty}(\frac{ekM_R}{2\mu})^{2\mu}d\mu < +\infty, \tag{19}$$

for all $M_R \in \mathbb{R}^+$. This confirms that the kernel of the integral Equation (18) is in L^2.

In a similar way, the exterior Dirichlet problem

$$\begin{cases} \Delta v(x, y) + k^2 v(x, y) = 0, & (x, y) \in \mathbb{R}^2 \setminus \mathcal{D}, \\ v(x, y) = f(x, y), & (x, y) \in \partial\mathcal{D}, \end{cases} \tag{20}$$

subject to the Sommerfeld radiation condition

$$\lim_{\rho \to +\infty} \sqrt{\rho}\left(\frac{\partial}{\partial_\rho} - ik\right) v(x, y) = 0, \tag{21}$$

may be addressed. In particular, the following theorem can be easily proved.

Theorem 2. — *Under the hypotheses of the previous theorem, the exterior boundary-value problem for the Helmholtz Equations (20)–(21) admits a solution*

$$v(x, y) \in L^2(\mathbb{R}^2 \setminus \mathcal{D}) \tag{22}$$

such that the following Fourier-Bessel series expansion holds

$$v(\varrho^* R(\vartheta)\cos\vartheta, \varrho^* R(\vartheta)\sin\vartheta) = U(\varrho^*, \vartheta)$$

$$= \sum_{m=0}^{+\infty} H_m^{(1)}(k\varrho^* R(\vartheta))(A_m \cos m\vartheta + B_m \sin m\vartheta), \tag{23}$$

where $H_m^{(1)}(\cdot)$ denotes the Hankel function of first kind and order m. The coefficients A_m, B_m in (23) are the solution of the infinite linear system

$$\sum_{m=0}^{+\infty}\begin{bmatrix} X_{n,m}^+ & Y_{n,m}^+ \\ X_{n,m}^- & Y_{n,m}^- \end{bmatrix} \cdot \begin{bmatrix} A_m \\ B_m \end{bmatrix} = \begin{bmatrix} \alpha_n \\ \beta_n \end{bmatrix}, \tag{24}$$

where

$$X_{n,m}^\pm = \frac{\epsilon_n}{2\pi}\int_0^{2\pi} H_m^{(1)}(kR(\vartheta))\cos m\vartheta \left\{\begin{matrix} \cos n\vartheta \\ \sin n\vartheta \end{matrix}\right\} d\vartheta, \tag{25}$$

$$Y_{n,m}^\pm = \frac{\epsilon_n}{2\pi}\int_0^{2\pi} H_m^{(1)}(kR(\vartheta))\sin m\vartheta \left\{\begin{matrix} \cos n\vartheta \\ \sin n\vartheta \end{matrix}\right\} d\vartheta, \tag{26}$$

with $m, n \in \mathbb{N}_0$.

Remark 3. — *Note that the above formulas still holds under the assumption that the function $R(\vartheta)$ is a piecewise continuous function, and the boundary data are described by square integrable functions, not necessarily continuous, so that the relevant Fourier coefficients α_m, β_m in Equation (12) are finite quantities.*

4. NUMERICAL EXAMPLE

In the following numerical example, we assume for the boundary $\partial\mathcal{D}$ a general polar equation of the type

$$R(\vartheta) = \left(\left| \frac{\cos \frac{p\vartheta}{4}}{\gamma_1} \right|^{\nu_1} + \left| \frac{\sin \frac{q\vartheta}{4}}{\gamma_2} \right|^{\nu_2} \right)^{-1/\nu_0}, \tag{27}$$

as introduced by J. Gielis in [4]. Very different shapes of the considered domain, including ellipses, Lame curves (also called *Superellipses*), ovals, and m-fold symmetric figures can be obtained by assuming suitable values of the parameters p, q, γ_1, γ_2, ν_0, ν_1, ν_2 in (27). It was noticed in [4] that many characteristic geometries occuring in Nature (starfish, equisetum, raspberry, etc.) can be approximated in such a way. We emphasize that almost all two-dimensional normal-polar domains are described (or at least approximated in a close way) by the above mentioned curves.

To assess the performance of the proposed algorithm in terms of numerical accuracy and convergence rate, the relative boundary error has been evaluated as follows

$$e_N = \|U_N(1,\vartheta) - F(\vartheta)\| / \|F(\vartheta)\|, \tag{28}$$

$\| \cdot \|$ denoting the usual $L^2\ (\partial\mathcal{D})$ norm, and $U_N(\varrho^*, \vartheta)$ the partial sum of order N relevant to the Fourier-type series expansion representing the solution of the specific boundary-value problem for the Helmholtz equation, namely

$$U_N(\varrho^*, \vartheta) = \sum_{m=0}^{N} Z_m(k\varrho^* R(\vartheta))(A_m \cos m\vartheta + B_m \sin m\vartheta), \tag{29}$$
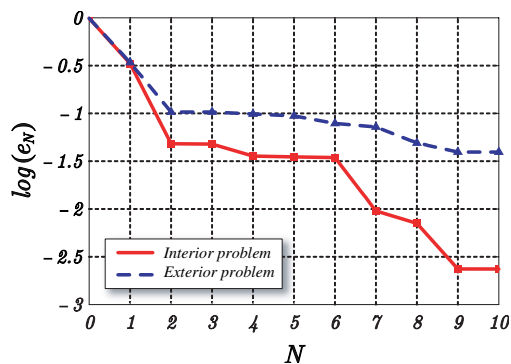
Figure 1: Relative boundary error e_N as function of the number N of terms in the expansion (29). The relevant domain $\mathcal{D}$ is described by the polar Equation (27) with $\gamma_1 = \gamma_2 = 3/4$, $p = q = 7$, $\nu_0 = 10$, $\nu_1 = \nu_2 = 6$.

(a)

(b)
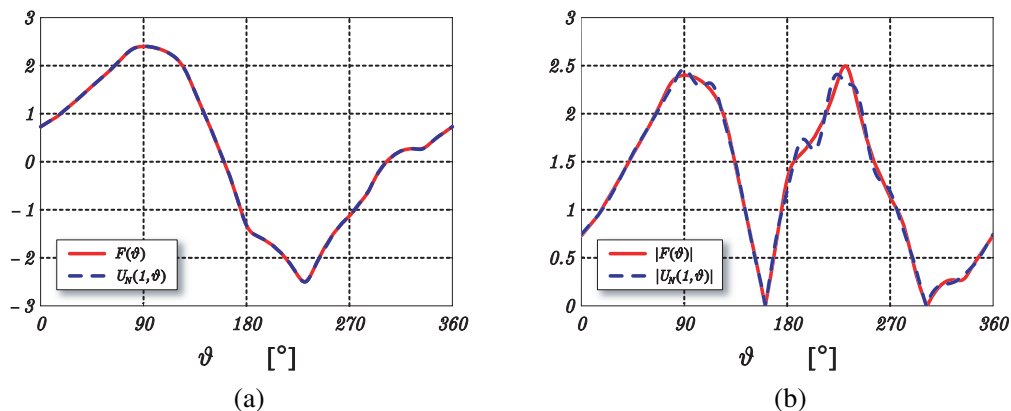
Figure 2: Angular behavior of the partial sum $U_N(1,\vartheta)$ of order $N = 10$ representing the solution of the (a) interior and (b) exterior problem for the Helmholtz equation. The relevant domain $\mathcal{D}$ is described by the polar Equation (27) with $\gamma_1 = \gamma_2 = 3/4$, $p = q = 7$, $\nu_0 = 10$, $\nu_1 = \nu_2 = 6$.
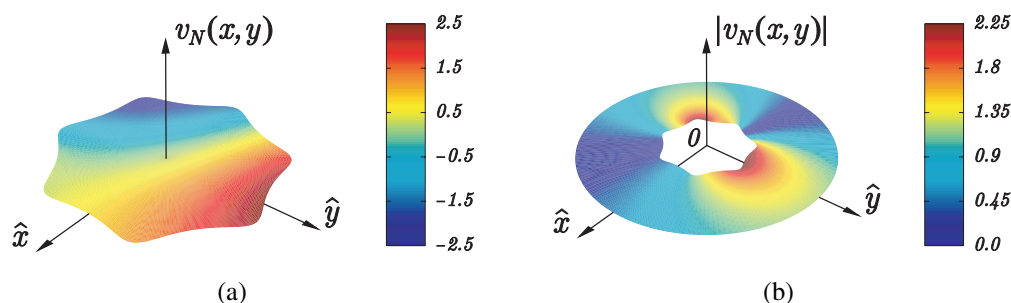
Figure 3: Spatial distribution of the partial sum $\nu_N(x, y)$ of order $N = 10$ representing the solution of the (a) interior and (b) exterior problem for the Helmholtz equation. The relevant domain $\mathcal{D}$ is described by the polar Equation (27) with $\gamma_1 = \gamma_2 = 3/4$, $p = q = 7$, $\nu_0 = 10$, $\nu_1 = \nu_2 = 6$.

where $Z_m(\cdot)$ are Bessel or Hankel functions of the first kind.

By assuming in (27) $\gamma_1 = \gamma_2 = 3/4$, $p = q = 7$, $\nu_0 = 10$, $\nu_1 = \nu_2 = 6$, and $\vartheta \in [0, 2\pi]$, the domain $\mathcal{D}$ features an equisetum-like shape. Let $f(x, y) = x + 2y + \cos(2x + y)$ be the function describing the boundary data. Then, under the hypothesis of normalized propagation constant $k = 1$, the relative boundary error e_N as function of the number N of terms in the series expansion (29) exhibits the behavior shown in Fig. 1. As it appears from Fig. 2, the selection of the expansion order $N = 10$ leads to a very accurate Fourier representation of the solution, whose approximate spatial distribution is shown in Fig. 3.

5. CONCLUSION

The use of stretched co-ordinate systems, reducing a starlike domain to a unit circle, allows the application of the classical Fourier method to a wide set of differential problems in complex two-dimensional normal-polar domains. In this way, closed-form solutions can be obtained by using suitable quadrature rules, so avoiding cumbersome numerical techniques such as finite-difference or finite-element methods.

ACKNOWLEDGMENT

REFERENCES

1. Caratelli, D. and P. E. Ricci, "The Dirichlet problem for the Laplace equation in a starlike domain," *Proceedings of 2008 International Conference on Scientific Computing*, Las Vegas, Nevada, 160–166, Jul. 2008.
2. Caratelli, D., B. Germano, M. X. He, and P. E. Ricci, "Solution of the Dirichlet problem for the Laplace equation in a general cylinder," (submitted).
3. Caratelli, D., P. Natalini and P. E. Ricci, "The Dirichlet problem for the helmholtz equation in a starlike planar domain," (submitted).
4. Gielis, J., "A generic geometric transformation that unifies a wide range of natural and abstract shapes," *Amer. J. Botany*, Vol. 90, 333–338, 2003.
5. Carleson, L., "On convergence and growth of partial sums of fourier series," *Acta Math.*, Vol. 116, 135–157, 1966.
6. Riesz, F., *L*es systèmes d'équations linéaires à une infinité d'inconnues, Gauthier Villars, Paris, 1952.

Rigorous Electromagnetic Analysis of Domestic Induction Heating Appliances

G. Cerri, S. A. Kovyryalov, V. Mariani Primiani, and P. Russo

Università Politecnica Delle Marche — DIBET, Via Brecce Bianche, Ancona 60100, Italy

Abstract— In this paper the developed analytical electromagnetic model of induction heating system is presented. The model was built up assuming equivalent electric and magnetic currents flowing in each planar element of the typical structure used for an induction heating system: the load disk represents the pan steel bottom, the copper inductor, and ferrite flux conveyor. A system of integral equations system was then obtained enforcing the boundary conditions on each element of the structure for the electric and magnetic fields, produced by the equivalent currents. The numerical solution of the system is a matrix equation with a known voltage vector in the left-hand side, and product of impedance coefficients matrix and unknown electric and magnetic currents vector in the right-hand side. Since the feeding voltage is known, and impedance coefficients are calculated using of geometry and material parameters, currents vector can be also calculated. Thus, the whole model is solved and it gives a detailed picture of currents distribution in the system, which in its turn allows to analyze heating process in the load. Each step of developing of the model was verified by appropriate experimental measurements. Achieved results give a possibility to analyze and develop improvements to increase efficiency, safety and to reduce the cost.

1. INTRODUCTION

Domestic induction cookers become more and more popular because of their high efficiency, safety and ease in use. Due to the state-of-the-art a present-day induction heating applicator consists of inductor, some ferrite bars below the coil screened by aluminum and the load (pot) above the coil (see Fig. 1). Inductor of the induction system is a spiral planar coil which is fed by a medium-frequency (20–100 kHz) power source. According to Faraday's law the alternating magnetic field induces eddy currents in the metal pan and, additionally, in ferromagnetic materials produces magnetic hysteresis. Both phenomena heat up the pan. Ferrite is located under the coil as a shielding to protect the electronic control system which is usually placed under applicator.

There are different methods of analyzing and calculating some parameters of induction system which are widely described in existing literature. Most of them are numerical and based on finite elements method (FEM) and similar [1]. There are also some methods used for inductor impedance calculation such as the interpolation method [2] and squared-field-derivative for computation of losses [3]. More than that, since inductors of modern induction cooking systems are winded using multistrand wire with helix transposition of the strands — Litz-wire, there are some works dedicated to investigation of inductor impedance and its internal resistances according to peculiarities of construction of Litz-wire [4, 5].

The objective of the present work is to develop a rigorous analytical electromagnetic model of induction heating applicator which allows to analyze the magnetic coupling between system elements, their influence on the system operation and also to calculate circulating currents in each part of the system. Currents distribution in the load and their amplitudes give a possibility to value the heating efficiency.

2. ANALYTICAL MODEL

The key point of the system is the electromagnetic coupling among the source winding (inductor), the ferromagnetic pot bottom (load) and the flux conveyor (ferrite). Therefore, we focus the attention on the simplified geometry reported in Fig. 2. The model was built up assuming equivalent electric and magnetic currents flowing in each planar element of the structure (Fig. 4). The expressions for magnetic (J_m) and electric (J) current densities can be obtained from the Maxwell field equations in free space:

$$\begin{cases} \bar{J}_m = j\omega\mu_0(\mu_r - 1)\bar{H} \\ \bar{J} = \sigma\bar{E} + j\omega\varepsilon_0(\varepsilon_r - 1)\bar{E} \end{cases} \tag{1}$$
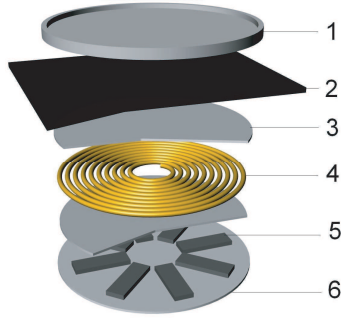
Figure 1: Induction system structure: (1) pot, (2) cooking surface, (3) electric insulation, (4) winding, (5) flux conveyor and (6) shielding.
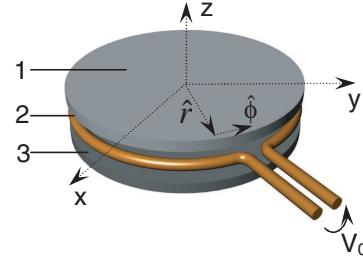
Figure 2: Model structure: (1) load, (2) source turn, (3) ferrite.

Applying these expressions for each element of the model with appropriate parameters of its material they can be written as follows:

$$\begin{cases} \bar{J}_S = \sigma_S \bar{E} & [\sigma_S \gg j\omega\varepsilon_0(\varepsilon_{rS} - 1)] \\ \bar{J}_{mS} = j\omega\mu_0(\mu_{rS} - 1)\bar{H} \\ \bar{J}_C = \sigma_C \bar{E} & [\sigma_C \gg j\omega\varepsilon_0(\varepsilon_{rC} - 1)] \\ \bar{J}_{mC} = 0 & [\mu_{rC=1}] \\ \bar{J}_F = \sigma_F \bar{E} + j\omega\varepsilon_0(\varepsilon_{rF} - 1)\bar{E} \\ \bar{J}_{mF} = j\omega\mu_0(\mu_{rF} - 1)\bar{H} \end{cases} \tag{2}$$

where J_S, J_{mS}, J_C, J_{mC}, J_F, J_{mF} are electric and magnetic current densities in steel (load), copper (source) and ferrite (flux conveyor) respectively; σ_S, σ_C, σ_F are conductivities of steel, copper and ferrite respectively; μ_{rS}, μ_{rC}, μ_{rF} are relative magnetic permeabilities, σ_0 and μ_0 are conductivity and magnetic permeability of free space; E and H are electric and magnetic fields respectively. So, the solution of the problem is to find unknown currents in each planar element of modeled system.

Let E_0 the incident electric field induced by feeding voltage V_0. After enforcing the boundary conditions for the electric and magnetic field on each element of the structure, the system of equations which is the analytical description of electromagnetic model can be written as follows:

$$\begin{cases} 0 + \bar{E}\left(\bar{J}_C\right) + \bar{E}\left(\bar{J}_S\right) + \bar{E}\left(\bar{J}_{mS}\right) + \bar{E}\left(\bar{J}_{mF}\right) = \dfrac{\bar{J}_S}{\sigma_S}; \\[2mm] \bar{E}_0 + \bar{E}\left(\bar{J}_C\right) + \bar{E}\left(\bar{J}_S\right) + \bar{E}\left(\bar{J}_{mS}\right) + \bar{E}\left(\bar{J}_{mF}\right) = \dfrac{\bar{J}_C}{\sigma_C}; \\[2mm] 0 + \bar{H}\left(\bar{J}_C\right) + \bar{H}\left(\bar{J}_S\right) + \bar{H}\left(\bar{J}_{mS}\right) + \bar{H}\left(\bar{J}_{mF}\right) = \dfrac{\bar{J}_{mS}}{j\omega\mu_0\left(\mu_{rS} - 1\right)}; \\[2mm] 0 + \bar{E}\left(\bar{J}_C\right) + \bar{E}\left(\bar{J}_S\right) + \bar{E}\left(\bar{J}_{mS}\right) + \bar{E}\left(\bar{J}_{mF}\right) = \dfrac{\bar{J}_F}{\sigma_F + j\omega\varepsilon_0\left(\varepsilon_{rF} - 1\right)}; \\[2mm] 0 + \bar{H}\left(\bar{J}_C\right) + \bar{H}\left(\bar{J}_S\right) + \bar{H}\left(\bar{J}_{mS}\right) + \bar{H}\left(\bar{J}_{mF}\right) = \dfrac{\bar{J}_{mF}}{j\omega\mu_0\left(\mu_{rF} - 1\right)}. \end{cases} \tag{3}$$

We also assume that all currents flow uniformly along the wire and across its cross-section. As for directions electric currents flows along wire curve, but magnetic currents have two components — normal and radial:

$$\left\{\bar{J}_S = J_S\hat{\phi}; \quad \bar{J}_C = J_C\hat{\phi}; \quad \bar{J}_F = J_F\hat{\phi} \right. \quad \left\{ \begin{array}{l} \bar{J}_{mS} = J_{mS\rho}\hat{\rho} + J_{mSz}\hat{z} \\ \bar{J}_{mF} = J_{mF\rho}\hat{\rho} + J_{mFz}\hat{z} \end{array} \right. \tag{4}$$

After applying (4) in (3) the system (3) can be rewritten with detailed description considering direction of current densities vectors. Each field element of every equation is calculated using basic definitions of vector potential and magnetic vector potential.

3. NUMERICAL SOLUTION

Taking advantage from cylindrical symmetry we can represent the disk as a set of concentrical current paths (Figs. 3 and 4). Thus, each elementary current path should be considered as separate element which counteracts with the whole system: either with neighbor elementary paths or source turn or equivalent paths on ferrite disk.

The numerical solution of the analytical system of Equation (3) is the solving of linear matrix equation. The matrix Equation (5) includes all self- and mutual impedance coefficients which in its turn was grouped in matrixes M and Z, vector of fed voltage V_0 and column of unknown currents. Solving the Equation (5) gives us all currents known which allows to analyze its distribution in the load disk (Figs. 5 and 6).

$$
\begin{vmatrix} V_0 \\ 0 \\ \vdots \\ 0 \\ 0 \\ 0 \\ 0 \end{vmatrix} = \begin{vmatrix} Z_{11(1,1)} & M_{12(1,Na)} & M_{13(1,Na)} & M_{14(1,Na)} & M_{15(1,Nf)} & M_{16(1,Nf)} & M_{17(1,Nf)} \\ M_{21(Na,1)} & Z_{22(Na,Na)} & M_{23(Na,Na)} & M_{24(Na,Na)} & M_{25(Na,Nf)} & M_{26(Na,Nf)} & M_{27(Na,Nf)} \\ M_{31(Na,1)} & 0 & Z_{33(Na,Na)} & 0 & M_{35(Na,Nf)} & M_{36(Na,Nf)} & M_{37(Na,Nf)} \\ M_{41(Na,1)} & M_{42(Na,Na)} & 0 & Z_{44(Na,Na)} & M_{45(Na,Nf)} & M_{46(Na,Nf)} & M_{47(Na,Nf)} \\ M_{51(Nf,1)} & M_{52(Nf,Na)} & M_{53(Nf,Na)} & M_{54(Nf,Na)} & Z_{55(Nf,Nf)} & M_{56(Nf,Nf)} & M_{57(Nf,Nf)} \\ M_{61(Nf,1)} & M_{62(Nf,Na)} & M_{63(Nf,Na)} & M_{64(Nf,Na)} & 0 & Z_{66(Nf,Nf)} & 0 \\ M_{71(Nf,1)} & M_{72(Nf,Na)} & M_{73(Nf,Na)} & M_{74(Nf,Na)} & M_{75(Nf,Nf)} & 0 & Z_{77(Nf,Nf)} \end{vmatrix} \cdot \begin{vmatrix} I_{cu(1,1)} \\ I_{a(Na,1)} \\ I_{map(Na,1)} \\ I_{maz(Na,1)} \\ I_{f(Nf,1)} \\ I_{mfp(Nf,1)} \\ I_{mfz(Nf,1)} \end{vmatrix}
$$

$$[V]_{(1,\,1+3Na+3Nf)} = [M]_{(1+3Na+3Nf,\,1+3Na+3Nf)} \ \ [I]_{(1+3Na+3Nf,\,1)}$$

$$
M_{23(N_a,N_a)} = \begin{bmatrix} R_{ilS3(1,1)} & \cdots & R_{ilS3(1,N_a)} \\ \vdots & \ddots & \vdots \\ R_{ilS3(N_a,1)} & \cdots & R_{ilS3(N_a,N_a)} \end{bmatrix}
\tag{5}
$$

$$
R_{ilS3(i,j)} = -\frac{1}{4\pi} \int_{L_{Si}} \int_{L_{Sj}} \frac{e^{-jk|R_{0jk}|}}{|R_{0jk}|^3} t \left(\hat{\phi} \cdot \hat{\phi}' \right) dl dl'
$$

where $R_{ilS3(i,j)}$ is mutual impedance of the i-th and j-th elementary currents, R_{0jk} is the distance between active and passive points of integration (see vector potential definition), N_a and N_f are numbers of elementary current paths in load and ferrite disks respectively.

4. EXPERIMENTAL VALIDATION

For the experimental model a copper ring was taken of diameter Ø15 cm and diameter of cross-section Ø1 mm as a simple inductor. For the load and flux conveyor two iron disks were taken with external diameter Ø20 cm and internal Ø10 cm, thickness 1.4 mm ($\delta = 0.05$ mm skin-depth).
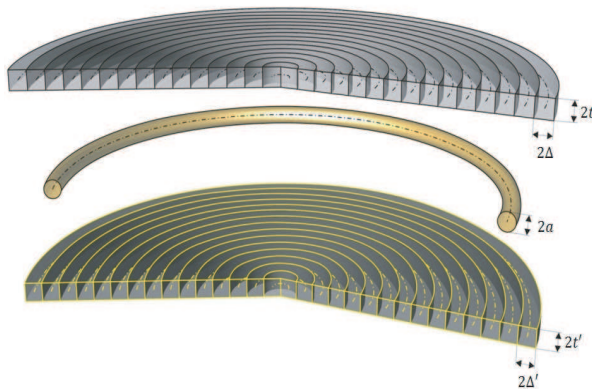
Figure 3: Model structure with elementary concentrical current paths.
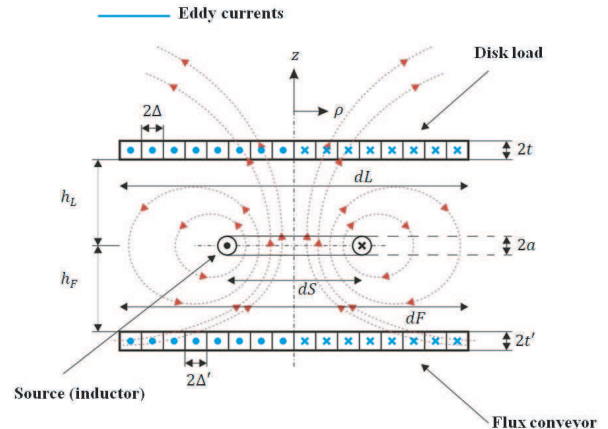
Figure 4: Schematic representation of the modeled system operation.
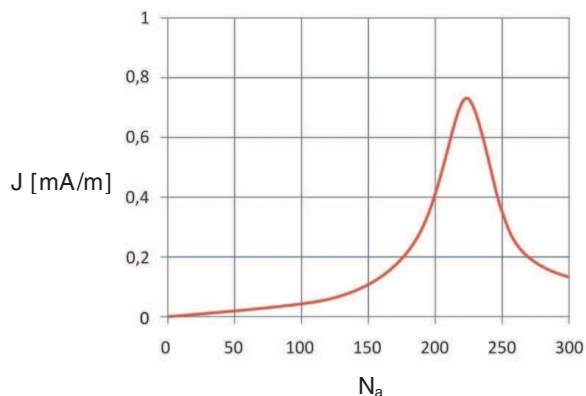
Figure 5: Electric current density distribution in the load disk (iron, $\mu_r = 150$).
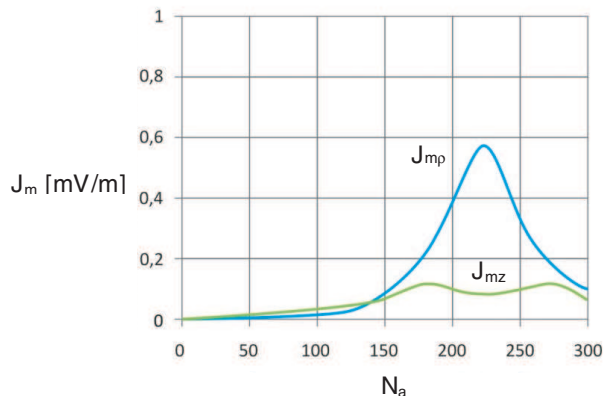
Figure 6: Magnetic current density distribution in the load disk (iron, $\mu_r = 150$).

Table 1: Measured and calculated results.

Configuration	Measured		Calculated	
	$\mathbf{R}$ (Ω)	$\mathbf{X}$ (Ω)	$\mathbf{R}$ (Ω)	$\mathbf{X}$ (Ω)
Single source turn (Ø15 cm)	0.01533	0.24183	0.01313	0.24508
Single source turn (Ø15 cm) + ring ($\varnothing_{ext}$20 cm, $\varnothing_{int}$10 cm)	0.04129	0.17358	0.04317	0.17232
Single source turn (Ø15 cm) + 2 ring ($\varnothing_{ext}$20 cm, $\varnothing_{int}$10 cm)	0.03139	0.16315	0.03326	0.16204

Figure 7: Measurement set-up.

The main parameter of verification was input impedance which was measured using HP LCR-meter at frequency 75 kHz and feeding voltage $V_0 = 1$ V (Fig. 7). The ring was connected to the instrument and input impedance was measured in three cases: 1) single source turn; 2) single source turn with the load iron ring placed above it at the distance 5 mm; 3) single source turn with both the load and flux conveyor iron rings placed above and under copper turn at the distance 5 mm. The measured and calculated results are presented in Table 1.

5. CONCLUSIONS

An analytical electromagnetic model to analyze induction heating applicator is presented. The system was described with potential balance equation based on electric and magnetic currents definition. The numerical solution was derived as the matrix equation based on equivalent circuit method. In order to compute self- and mutual impedance coefficients, a calculation of electric and magnetic fields is required. For this purpose basic definitions of vector potential and magnetic vector potential are used. Thus, when fed voltage and impedance matrixes are known, the currents are computed. The obtained values of currents and impedance give a possibility to analyze of induction system operation. The theoretical results were tested and verified experimentally. Measured and simulated results exhibit a good agreement.

ACKNOWLEDGMENT

REFERENCES

1. Egan, L. R. and E. P. Furlani, "A computer simulation of an induction heating system," *IEEE Trans. Magn.*, Vol. 27, No. 5, 4343–4354, 1991.
2. Imai, T., K. Sakiyama, I. Hirota, and H. Omori, "A study of impedance analysis for an induction heating deviceby applying a new interpolation method," *IEEE Trans. Magn.*, Vol. 33, No. 2, 1991.
3. Hernandez, P., F. Monterde, J. M. Burdio, J. R. Garcia, and S. Lorente, "Power losses distribution in the litz-wire winding of an inductor for an induction cooking appliance," *IECON 02 (Annual Conference of the Industrial Electronics Society)*, IEEE, 2002.
4. Acero, J., R. Alonso, J. M. Burdio, L. A. Barragan, and D. Puyal, "Analytical equivalent impedance for a planar circular induction heating system," *IEEE Trans. Magn.*, Vol. 42, No. 1, 2006.
5. Acero, J., R. Alonso, J. Burdio, L. A. Barragan, and D. Puyal, "Frequency-dependent resistance in litz-wire planar windings for domestic heating appliances," *IEEE Trans. Power Electron.*, Vol. 21, No. 4, 2006.

Vibrations of Electrically Polar Structures in Biosystems Give Rise to Electromagnetic Field: Theories and Experiments

M. Cifra[1, 2], **J. Pokorný**[2], **F. Jelínek**[2], **and O. Kučera**[2, 3]

[1]Department of Electromagnetic Field, FEE, Czech Technical University in Prague, Czech Republic
[2]Institute of Photonics and Electronics, Academy of Sciences of the Czech Republic, Czech Republic
[3]Department of Circuit Theory, FEE, Czech Technical University in Prague, Czech Republic

Abstract— Mechanical vibrations of electrically polar structures are fundamental mechanism of generation of the electromagnetic field (EMF) in living cells. Overview of the experiments showing existence of the vibrations on the cellular level by measurements with various techniques is given; some of the recent theoretical and experimental achievements of the authors' group are also presented.

1. INTRODUCTION

Electromagnetic field (EMF) in living cells can be generated by various mechanisms. Mechanical vibrations of electrically polar cellular structures are probably the most important for broad range of frequencies from several hundred of Hz to THz. Vibrations on the cellular level have been proved by experiments using various techniques: Vibrations of the cell membrane have been measured up to tens of Hz by optical techniques, measurement of kHz membrane oscillations have been performed by AFM by some authors. Other authors also attempted to measure coherent THz oscillations of living cells by Raman spectroscopy. Some crucial points of the success and failures of this kind of experiments are elucidated.

2. PREMISE

The relation of nanomechanical oscillations of cellular structures to the generation of the EMF is following. Many intracellular structures have polar properties. The majority of proteins are electrically polar molecules [1]. Vibrations may be excited in the protein structures provided that energy is supplied. The spectrum of vibrations may span from low kHz up to GHz region [2–4] and likely also to THz [5].

The most likely candidate for the generation of EMF in a cell is cytoskeleton. Heterodimer of alpha and beta tubulin, which microtubules, one of three cytoskeleton elements, consist of, is a strong electric dipole with dipole moment about 10^{-26} cm [6]. Energy is supplied to the cytoskeleton from three possible sources: Hydrolysis of GTP (guanosine triphosphate) after polymerization of microtubules, motor protein movement and flow of wasted energy from mitochondria [7]. Other possible candidates for EMF generation are proteins in a cellular membrane which are in nonlinear regime due to the electric field created by membrane potential (in human cells up to -100 mV) which is realized on extremely short size of membrane thickness (about 10 nm). It is more then probable, that mechanical oscillations of microtubules and cell membrane generate EMF and it is supposed, that this field plays role in cell physiology [8] and participate in the controlling of the organization of living matter [9]. A few crucial experiments dealing with electromagnetic activity of living cells will be cited.

3. CELLULAR ELECTROMAGNETISM

Characteristics of the electrostatic and current field, causes of the membrane potential and action potential respectively, are widely known [10, 11]. Measurement of the electric component of the field generated is widely used in medical diagnostics (ECG, EEG, EMG e.g.,).

Attraction of small dielectric particles to the surface of the living cell as a result of the dielectrophoretic effect was observed by Pohl [12, 13]. The number of attracted particles was dependent on cell cycle and was greatest during the beginning of the M-phase, when the microtubules show extraordinary dynamic instability and form the mitotic spindle.

Electric vibrations of yeast cell membrane in kilohertz range were measured by Pohl et al. and Pokorný et al. [7, 14]. Electromagnetic oscillations in megahertz range were measured by Pokorný et al. [15] ($8 \div 9$ MHz) and by Hölzel and Lamprecht [16] ($1 \div 100$ MHz). Grundler and Keilmann [17, 18] observed nonthermal resonant effects of 42 GHz microwaves on the growth rate of

yeasts. One of the explanations was that external EMF resonantly interacts with cellular vibrational system, thus the cellular electrically polar vibrations could be of comparable frequency. Nevertheless, direct measurement of the electromagnetic activity in the mm wave region by Jelínek et al. [19] has not confirmed the hypothesis. Vos et al. [20] measured coherent spectral lines in stimulated emission from membrane proteins in the sub-millimeter and far infra-red (IR) range of spectra using femtosecond laser spectroscopy. Albrecht-Buehler [21] described the ability of cells to interact in the red or near infra-red range. Biological photon emission in visible and ultra-violet (UV) range is widely accepted and was described and measured e.g., in [22, 23].

4. THEORIES

There are several theories which have been postulated regarding the generation of EMF in biological systems and its possible organizational role. One of the most influential hypothesis connected with transformation of random thermal vibrations to coherent vibrations has been postulated by Fröhlich [24]. Nonlinear conditions allowing this transformation have been assumed. Fröhlich assumed that nonlinearity may be caused by high electric field in the cellular membrane and conjectured therefore that transmembrane proteins are the vibrational centres which transform the thermal energy to coherent. Only recent experimental findings [25] show that there is a high static electric field inside a cell due to protons diffusing from mitochondria. Microtubules are in a strong electric field since mitochondria are aligned near them. Mitochondria are also source of thermal energy and radiation released in the course of citric acid cycle. It is very likely that mitochondrial activity provides necessary conditions for the nonlinear behavior and energy transformation in the cytoskeleton.

5. MECHANICAL VIBRATIONS OF CELLS AND SUBCELLULAR STRUCTURES

We briefly overview published experimental observation of mechanical oscillations and vibrational modes of cellular structures from low to high frequencies in this section.

Nanoscale structure and low frequency (minutes period) dynamics associated with live red blood cells membrane displacements are measured using quantitative phase images provided by Fourier phase microscopy [26]. He et al. [27] observed periodic motion of native human cancer cells on sub-hertz frequencies. Piga et al. [28] revealed nanometre-scale vibrations (up to 30 Hz) of live cells (rat pheochromocytoma line PC12) by the Scanning Near-field Optical Microscope (SNOM). Levin, Korenstein et al. [29] observed nonlinear nano-scale oscillations (at frequencies 0.2–30 Hz) of human erythrocytes membrane with point dark field microscopy and linked them to MgATP-dependent dynamic assembly of the sub-membrane skeleton. The oscillations were also observed in monocytes, lymphocytes, 3T6 fibroblasts, cardiomyocytes and murine lymphoma B and T cell lines [30]. The amplitude of oscillations was of the order of magnitude of tens to few hundreds of nm's depending on the cell type.

Group of Kamimura showed with phase-contrast microscopy [31] and modified atomic force microscopy [32] that axoneme[1] generate vibrations of 300 Hz in presence of MgATP.

Pelling et al. [33, 34] demonstrated a local nanomechanical motion of the cell wall of yeast *Saccharomyces cerevisiæ* under physiological conditions using atomic force microscopy (AFM). Oscillatory signal observed with average amplitude of 3.0 ± 0.5 nm was characteristic for about 70% measurements performed. Fourier transforming of signal measured disclosed temperature dependent prominent peak of 0.9 kHz at $22°$C to 1.6 kHz at $30°$C. Oscillatory character of the motion disappeared after treating the cells with metabolic inhibitor sodium azide. Authors concluded the metabolic origin of the motion with special attention to concerted activity of motor proteins. Measurement of such oscillations was reproduced by Pokorný et al. [7].

Mosbacher et al. [35] reported membrane mechanical motions of HEK293 cells using AFM when AC voltage was applied through voltage clamps. These movements of several nm's amplitude tracked the voltage at frequencies >1 kHz with a phase lead of 60–120$°$, as expected for a displacement current.

Edwards reported direct coupling of microwave field to acoustic modes of DNA probed by dielectric spectroscopy [36], which was manifested by resonant response of absorption coefficient. The connection between result obtained and microwave coupling was criticized by Foster [37].

Recent advances in THz spectroscopy show existence of THz modes in various biopolymers and biomolecules [38], in DNA, albumin, collagen [39], benzoic acid, aspirin [40], tryptophan [41].

---

[1]Axoneme is a core of whip-like cilia or eukaryotic flagella, in, e.g., sperm. The building block of axonemes are microtubules and various protein complexes including motor proteins dyneins.

Experiments with classical Raman spectroscopy [42–44] found that the certain vibrational modes ($\sim$ THz) in *E. coli B* can be nonthermally excited. Although the results weren't accepted and were attributed to fluorescence artifacts by e.g., [45, 46], del Giudice et al. [47, 48] strongly argued for the validity of above interpretation.

Coherent vibrations of proteins were experimentally investigated using femtosecond laser spectroscopy [20, 49–51]. Coherent vibrational nuclear motion in submilimeter band[2] have been detected in membranes of bacteria (e.g., of *Rhodobacter capsulatus*) with genetically modified photosynthetic systems. Coherent nuclear dynamics in bacterial reaction centers was observed even at room temperature [50].

6. DISCUSSION

There are several technical prerequisites for the measurement setup which is aimed to probe cellular vibrations. One of them was pointed out by Korenstein et al. [29]. They found that the low frequency membrane mechanical oscillations (up to 30 Hz) could only be resolved when measuring from area $0.25\,\mu m^2$ or less. It may be expected that the spatial resolution for detection of high frequency vibrations might be of the order of magnitude of tens or units of nanometers if successful measurement is to be performed. Regarding the possibility of detection of nonthermal excitations of living cells with classical Raman spectroscopy it needs to be noted that there is a fundamental incompatibility of the measured objects with the measurement technique itself. Principally, measurement of ratio of anti Stokes and Stokes line intensities is the most straightforward method to determine the above thermal excitations. The appearance of the anti Stokes lines may also depend on the cell cycle. But there is a principal obstacle to detect far IR biological signals of the Raman systems as far as they are based on macroscopic volume detection. The intracellular processes are based on molecular nanostructures and this property determines requirement for detection systems. One needs new types of Raman spectroscopy which provide sufficient amplification of the signal and point measurement to show if there are coherent vibrations in biological systems in spectral region suitable for Raman spectroscopy. Modification of surface enhanced Raman spectroscopy [52] or Coherent anti-Stokes Raman spectroscopy may fulfill these conditions. Wavelength of excitation laser is preferred to lie in infrared region rather than in visible to minimize possibility of fluorescence and disruption of cells.

Brillouin spectroscopy, fulfilling similar prerequisites as those mentioned above for Raman spectroscopy, may be suitable for the measurement of vibrational modes in microwave region.

7. CONCLUSION

A brief overview of theories and experiments dealing with vibrations of electrically polar structures in biosystems was given. These vibrations are supposed to generate an endogenous biological EMF the existence of which may have deep consequences in organization of biological processes and structures and possible interaction with exogenous EMF.

Comprehensive review of the issue presented is being prepared and will be published soon.

REFERENCES

1. Wada, A. and H. Nakamura, "Nature of the charge distribution in proteins," *Nature*, Vol. 293, 757–758, 1981.
2. Pokorný, J., F. Jelínek, V. Trkal, I. Lamprecht, and R. Hölzel, "Vibrations in microtubules," *Journal of Biological Physics*, Vol. 23, 171–179, 1997.
3. Pokorný, J., "Conditions for coherent vibrations in cytoskeleton," *Bioelectrochemistry and Bioenergetics*, Vol. 48, No. 2, 267–271, 1999.
4. Wang, C., C. Ru, and A. Mioduchowski, "Vibration of microtubules as orthotropic elastic shells," *Physica E: Low-dimensional Systems and Nanostructures*, Vol. 35, No. 1, 48–56, 2006.
5. Fröhlich, H., "The biological effects of microwaves and related questions," *Advances in Electronics and Electron Physics*, Vol. 53, 85–152, 1980.

---

[2]under $300\,cm^{-1}$, which corresponds to frequencies of the order of units of or lower than THz.

6. Tuszyński, J. A., J. A. Brown, E. J. Carpenter, E. Crawford, and M. N. A. Nip, "Electrostatic properties of tubulin and microtubules," *Proceedings of ESA Conference*, June 2002.

7. Pokorný, J., J. Hašek, J. Vaniš, and F. Jelínek, "Biophysical aspects of cancer — Electromagnetic mechanism," *Indian Journal of Experimental Biology*, Vol. 46, 310–321, May 2008.

8. Pokorný, J., J. Hašek, F. Jelínek, J. Šaroch, and B. Palán, "Electromagnetic activity of yeast cells in the M phase," *Electro- and Magnetobiology*, Vol. 20, No. 1, 371–396, 2001.

9. Pokorný, J., J. Hašek, and F. Jelínek, "Endogenous electric field and organization of living matter," *Electromag. Biol. Med.*, Vol. 24, 185–197, 2005.

10. Guyton, A. and J. Hall, *Textbook of Medical Physiology*, Elsevier Inc., 2006.

11. Hodgkin, A. and A. Huxley, "Quantitative description of membrane current and its application to conduction and excitation in nerve," *J. Physiol.*, 117–500, 1952.

12. Pohl, H., "Oscilating fields about growing cells," *Int. J. Quant. Chem., Quant. Biol. Symp.*, 411–431, 1980.

13. Pohl, H. A., T. Braden, S. Robinson, J. Piclardi, and D. G. Pohl, "Life cycle alterations of the micro-dielectrophoretic effects of cells," *Journal of Biological Physics*, Vol. 9, 1981.

14. Pohl, H. A., *Interactions between Electromagnetic Fields and Cells*, Ch. AC Field effects of and by Living Cells, 437–458, Plenum Press, New York and London, 1985.

15. Pokorný, J., J. Hašek, F. Jelínek, J. Šaroch, and B. Palán, "Electromagnetic activity of yeast cells in the M phase," *Electro- and Magnetobiology*, Vol. 20, No. 3, 371–396, 2001.

16. Hölzel, R. and I. Lamprecht, "Electromagnetic fields around biological cells," *Neural Netwrok World*, Vol. 3, 327–337, 1994.

17. Grundler, W., F. Keilmann, V. Putterlik, L. Santo, D. Strube, and I. Zimmermann, "Nonthermal resonant effects of 42 GHz microwaves on the growth of yeast cells," *Coherent Excitation in Biological Systems*, Ed. by H. Fröhlich and F. Kremer, 21–37, 1983.

18. Grundler, W. and F. Keilmann, "Sharp resonances in yeast growth prove nonthermal sensitivity to microwaves," *Phys. Rev.*, Vol. 51, No. 13, 1214–1216, 1983.

19. Jelínek, F., J. Šaroch, O. Kučera, J. Hašek, J. Pokorný, N. Jarezic-Renault, and L. Ponsonnet, "Measurement of electromagnetic activity of yeast cells at 42 GHz," *Radioengineering*, Vol. 16, 39–39, April 2007.

20. Vos, M. H., F. Rappaport, J. C. Lambry, J. Breton, and J.-L. Martin, "Visualization of coherent nuclear motion in a membrane protein by femtosecond spectroscopy," *Nature*, Vol. 363, 320–325, 1993.

21. Albrecht-Buehler, G., "Rudimentary form of cellular 'vision'," *Proceedings of the National Academy of Sciences of the USA*, Vol. 89, 8288–8293, 1992.

22. Beloussov, L., F. Popp, V. Voiekov, and R. V. Wijk, *Biophotonics and Coherent Systems*, Moscow University Press, 2000.

23. Shen, X. and R. V. Wijk, *Biophotonics — Optical Science and Engineering of 21st Century*, Springer, 2005.

24. Fröhlich, H., "Quantum mechanical concepts in biology," *Theoretical Physics and Biology*, 13–22, North Holland, Amsterdam, 1969; *Proc. 1st Intern. Conf. on Theoretical Physics and Biology*, Versailles, 1967.

25. Tyner, K. M., R. Kopelman, and M. A. Philbert, ""Nano-sized voltmeter" enables cellular-wide electric field mapping," *Biophysical Journal*, Vol. 93, 1163–1174, 2007.

26. Popescu, G., K. Badizadegan, R. R. Dasari, and M. S. Feld, "Coherence properties of red blood cell membrane motions," *Journal of Biomedical Optics Letters*, Vol. 11, No. 4, 040503, 2006.

27. He, H., S. Kong, and K. Chan, "First optical observation of periodic motion of native human cancer cells," *Quantum Electronics and Laser Science Conference, QELS 2008*, 1–2, 2008.

28. Piga, R. R. Micheletto, and Y. Kawakami, "Acoustical nanometre-scale vibrations of live cells detected by a near-field optical setup," *Opt. Express*, Vol. 15, No. 9, 5589–5594, 2007.

29. Tuvia, S., S. Levin, and R. Korenstein, "Oxygenation-deoxygenation cycle of erythrocytes modulates submicron cell membrane fluctuations," *Biophysical Journal*, Vol. 60, 733–737, 1992.

30. Krol, A. Y., M. G. Grinfeldt, S. V. Levin, and A. D. Smilgavichus, "Local mechanical oscillations of the cell surface within the range 0.2–30 Hz," *European Biophysics Journal*, Vol. 19, No. 2, 93–99, 1990.

31. Kamimura, S. and R. Kamiya, "High-frequency vibration in agellar axonemes with amplitudes reflecting the size of tubulin," *Journal of Cell Biology*, Vol. 116, No. 6, 1443–1454, 1992.

32. Sakakibara, H. M., Y. Kunioka, T. Yamada, and S. Kamimura, "Diameter oscillation of axonemes in sea-urchin sperm flagella," *Biophysical Journal*, Vol. 86, No. 1, 346–352, 2004.

33. Pelling, A. E., S. Sehati, E. B. Gralla, J. S. Valentine, and J. K. Gimzewski, "Local nanomechanical motion of the cell wall of saccharomyces cerevisiae," *Science*, Vol. 305, 1147–1150, 2004.

34. Pelling, A. E., S. Sehati, E. B. Gralla, and J. K. Gimzewski, "Time dependence of the frequency and amplitude of the local nanomechanical motion of yeast," *Nanomedicine: Nanotechnol. Biol. Med.*, Vol. 1, 178–183, 2005.

35. Mosbacher, J., M. Langer, J. Horber, and F. Sachs, "Voltage-dependent membrane displacements measured by atomic force microscopy," *J. Gen. Physiol.*, Vol. 111, No. 1, 65–74, 1998.

36. Edwards, G. S., C. C. Davis, J. D. Saer, and M. L. Swicord, "Microwave-field-driven acoustic modes in DNA," *Biophysical Journal*, Vol. 47, 799–807, 1985.

37. Foster, K. R., B. R. Epstein, and M. A. Gealt, "'Resonances' in the dielectric absorption of DNA," *Biophysical Journal*, Vol. 52, 421–425, 1987.

38. Beard, M. C., G. M. Turner, and C. A. Schmuttenmaer, "Terahertz spectroscopy," *The Journal of Physical Chemistry B*, Vol. 106, No. 29, 7146–7159, 2002.

39. Markelz, A. G., A. Roitberg, and E. J. Heilweil, "Pulsed terahertz spectroscopy of dna, bovine serum albumin and collagen between 0.1 and 2.0 THz," *Chemical Physics Letters*, Vol. 320, No. 1–2, 42–48, 2000.

40. Walther, M., P. Plochocka, B. Fischer, H. Helm, and P. U. Jepsen, "Collective vibrational modes in biological molecules investigated by terahertz time-domain spectroscopy," *Biopolymers*, Vol. 67, 310–313, 2002.

41. Yu, B., F. Zeng, Y. Yang, Q. Xing, A. Chechin, I. Xin, X. Zeylikovich, and R. R. Alfano, "Torsional vibrational modes of tryptophan studied by terahertz time-domain spectroscopy," *Biophysical Journal*, Vol. 86, 1649–1654, 2004.

42. Webb, S. J., M. E. Stoneham, and H. Fröhlich, "Evidence for non-thermal excitation of energy levels in active biological systems," *Physics Letters A*, Vol. 63, 407–408, 1977.

43. Webb, S. J., "Laser-raman spectroscopy of living cells," *Physics Reports*, Vol. 60, No. 4, 201–224, 1980.

44. Drissler, F. and L. Santo, *Coherent Excitations in Biological Systems*, Ch. Coherent Excitation and Raman Effect, 6–8, Springer, Berlin, Heidelberg, New York, 1983.

45. Layne, S. P. and I. J. Bigio, "Raman spectroscopy of bacillus megatherium using an optical multi-channel analyzer," *Physica Scripta*, Vol. 33, 91–96, 1986.

46. Layne, S. P., I. J. Bigio, A. C. Scott, and P. S. Lomdahl, "Transient uorescence in synchronously dividing Escherichia coli," *Proceedings of the National Academy of Sciences of the United States of America*, Vol. 82, No. 22, 7599–7603, 1985.

47. Giudice, E. Del, S. Doglia, M. Milani, C. W. Smith, and S. Webb, "Presence of lines in raman spectra of living cells," *Physics Letters A*, Vol. 107, No. 2, 98–100, 1985.

48. Giudice, E. Del, S. Doglia, M. Milani, and S. Webb, "A time consistent feature seen in the raman spectra of metabolically active cells," *Physics Letters A*, Vol. 91, No. 5, 257–259, 1982.

49. Vos, M. H., J. C. Lambry, S. J. Robles, D. C. Youvan, J. Breton, and J.-L. Martin, "Direct observation of vibrational coherence in bacterial reaction centers using femtosecond absorption spectroscopy," *Proc. Natl. Acad. Sci.*, Vol. 88, 8885–8889, USA, 1991.

50. Vos, M. H., M. R. Jones, C. N. Hunter, J. Breton, and J.-L. Martin, "Coherent nuclear-dynamics at room temperature in bacterial reaction centers," *Proc. Natl. Acad. Sci.*, Vol. 91, 12701–12705, USA, 1994.

51. Rischel, C., D. Spiedel, J. P. Ridge, M. R. Jones, J. Breton, J.-C. Lambry, J.-L. Martin, and M. H. Vos, "Low frequency vibrational modes in proteins: Changes induced by point-mutations in the protein-cofactor matrix of bacterial reaction centers," *Proc. Natl. Acad. Sci.*, Vol. 95, 12306–12311, USA, 1998.

52. Kneipp, K., "Surface-enhanced raman scattering," *Physics Today*, Vol. 60, 40–47, 2007.

A Value-added Method to Design a Compact and Low Cost Hairpin Line Microstrip Bandpass Filter for Communication Systems

Jagdish Shivhare[1] and S. B. Jain[2]

[1]Department of Electronics and Communication, Institute of Technology and Management
Sector-23 A, Gurgaon, Haryana, India
[2]Department of Electronics and Communication
Indira Gandhi Institute of Technology, Indraprashth University Campus, Delhi, India

Abstract— A value-added design method has been discussed for a multi-section Hairpin line microstrip bandpass filter at microwave frequencies. The design method may be used from a few hundred MHz to 10 GHz to serve the very basic purpose of reducing the overall size of the hairpin line band pass filters. Hairpin line resonator filters are relatively simple to design and build and are compact and low in cost. Two hairpin line microstrip band pass filters have been designed by using this value-added method. Simulation and optimization have been done by using Agilent-make software ADS 2005. These hairpin line filters have been fabricatyed by using very low cost metallized ABS-plastic substrate in place of very high cost RT-Duroid substrates. Finally these hairpin line bandpass filters have been tested on Vector Network Analyzer HP8510 (HP-make).

1. INTRODUCTION

Microstrip is one of the most widely used transmission media planar structure for microwave devices. Because of its open ended configuration discrete and monolithic components are readily mounted on microstrip substrate for ease of production, assembly and tuning. The basic microstrip circuits, consist of a single dielectric substrate, coated with a conductive material transmission line on one side and a metal gound plate on the other side. In the microstrip the electric field extends into the dielectric material as well as the air around, hence called Quasi-TEM [1, 4, 7, 9, 15, 21].

Since the fields are passing through two different mediums, then the relative dielectric constant, Er, no longer remain constant but becomes a function of W/H ratio. This results in a new parameter called effective dielectric constant (E_{eff}), which takes into account the fields between the air and the substrate. The effective dielectric constant will always be lower than the relative dielectric constant. Some substrates have dielectric constants as low as 2 or 3 while the constants of others may be around 10 (ten) depending on the designers choice [2, 3, 5, 6, 8, 11].

Some companies like Rogers Corp. Trans-Tech, Bell, Murata, Compositech, Keen Corp. etc. are manufacturing the substrates. The manufa-cturers are now looking at the requirements for the finished products to design a board/substrate for an exact application rather than designing a variety of boards/substrates for engineers to pick and choose from [4–6].

Microstrip filters fabricated from the newer materials are finding uses in areas such as avionics, communication products, consumer electronics, automotive electronics, GPS, tracking systems etc. PTFE is still an important board and substrate material in the RF fields. However, other materials, have a lot to offer the designing engineers provided they make the right choice [3].

2. DESIGN OF HAIRPIN LINE FILTERS

A microstrip transmission line consists of a strip conductor and a ground plate separated by a dielectric medium. The dielectric material serves as a structural substrate upon which the thin film
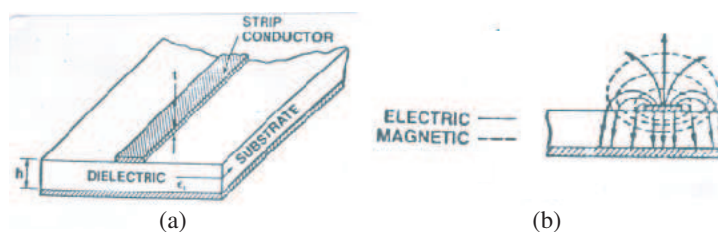
Figure 1: Electric and Magnetic fields in Microstrip.

metal conductor (copper) is deposited. No ground connections are required. Coupling between resonators caused by electromagnetic fields fringing. The coupling can be represented electrically as capacitors between adjacent resonators and ground planes [1, 4, 5, 9, 14, 18, 22].

Required parameters:

Center frequency (f_o) of the filter.
Ripple in the pass band.
Band width in passband w r t f_o.
Band width in stopband w r t f_o.
Lower side attenuation.
Upper side attenuation.
Input/output impedance.
Dielectric constant and thickness of Substrate.
Filling factor of substrate material velocity of light in free space.
Thickness of copper coating on substrate.

Parameters to be calculated:

Wavelenght in dielectric (λ_d).
Effective dielectric constant (E_{eff}).
Microstrip impedence (Z_o).
Width of transmission line (W/h) for known impedence effective dielectric constant (E_{eff}).
Coefficient of coupling $\mathbf{K_{n,n+1} = (k_{n,n+1})BW_{3\,dB}/f_o}$.
Separation between adjacent resonators $\mathbf{S_{12}}$, $\mathbf{S_{23}}$ by using nomograph $\mathbf{(S_{n,n+1})/h}$ v/s $\mathbf{K_{n,n+1}}$.
Input/output tapping locations by using nomogram $Q_{sh}Z_o/R$ v/s l/L for hairpin line structure.

Design Procedure:

Step-1: To know the number of sections: Here Response form factor (R) = [B.W. in stop band]/[B.W. in pass band]. Mark the pass band and stop band attenuation on the respective scales. Draw a line joining the two points. Draw a line parallel to the X-axis. The intersect point of this line and response form factor, nearest to the curve, may be taken as the number of sections.

Step-2: To know 3 dB bandwidth: For known number of sections the ratio of specified band width (let it 1 dB) and 3 dB bandwidth can be calculated from the nomogram. Hence $\mathbf{BW_{3dB} = BW_{1dB}/0.85}$. X-axis: Response form factor.

Step-3: To know the effective dielectric constant by using formula; $\mathbf{E_{eff} = [1 + q(E - 1)]}$.

Step-4: To know the wavelength in dielectric material by using equation $\mathbf{\lambda_d = \lambda_0/(E_{eff})^{1/2} = C/f_o(E_{eff})^{1/2}}$.

Step-5: To know W/h from the graph, for known value of input/output impedence and E_{eff} For Example, W/h ratio for glass epoxy ($E_r = 4.8$) is 1.8. Thickness of substrate may be chosen as per requir ment of the design.

Step-6: To calculate the microstrip impedence Z_o. By using the graph, Z_o v/s W/h, the resonator strip width may be calculated for the value, E_{eff}

$Z_o = 60/(E_{eff})^{1/2}$ loge$[8h/W + 0.25W/h]$ when $W/h < 1$

$Z_o = 120 \times 3.14/(E_{eff})^{1/2}$ $[W/h + 1.397 + 0.667$loge$(W/h + 1.444)]$ when $W/h > 1$.

Step-7: To calculate the separation (s_{12}, s_{23}) between adjacent resonators (hairpin line structure) with the help of $K_{n,n+1}$ vs $(S_{n,n+1})/h$ graph. Where h is the thickness of the substrate.

Step-8: The final step is to calculate the input and output tape point locations (l/L) from the graph Q_{sh}/RZ_o v/s l/L where $Q_{sh} = q(f_o/BW_{3dB})$, where q — filling factor of the substrate, R — impedance of generator, Z_o — internal impedance of filter and $\mathbf{L_1}$ and $\mathbf{L_2}$ are length of resonator-tapping tapping position. For hairpin line structure, to get 16 dB coupling, the gap between two arms of hairpin resonator is kept 2.54 mm, when the substrate used is RT durioid # 5880 (Th. 0.082 inch, Er = 2.22) while 1.16 mm, in case of RT duroid # 6010.5 (Th. 050, Er = 10.5) [2, 4, 6].
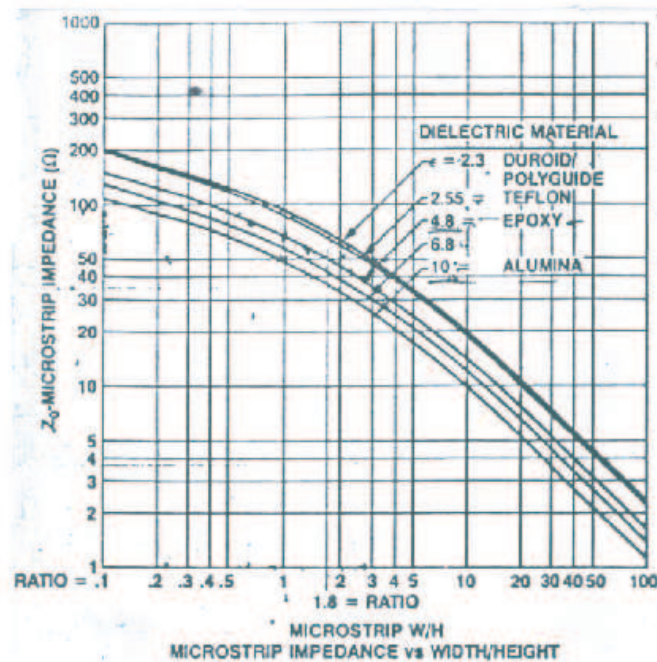
Figure 2: Impedance v/s Width/Height ratio.

3. TUNING PROCEDURE

The center frequency can be shifted by increasing/decreasing lengths of resonators. All resonators to be trimmed-off equally to reduce ripple in the pass band. The bandwidth and pass band ripples are determined by the spacing between the adjacent resonators. Copper foils may be used for optimization. The return loss may be optimized by changing the tapping positions along the first and last resonators.

In our experiments, we used the microstrip filter fabricated on ABS plastic substrate by using positive/negative of RT-Duroid based filters. The centers of response were achieved at lower frequencies than that of RT-Duroid. The filters were optimized by trimming-out the resonator lengths. The band widths with respect to centerfrequencies were not similar to RT-Duroid based filters in both cases.

Two hairpin line microstrip band pass filters have been designed, simulated and optimized by using Agilent-make software ADS 2005 and tested on Network Analyzers HP8754 A and HP8510.

The performance of two hairpin line filters at 1537.5 MHZ and 1575.42 MHZ have been verified over temperature range of — 10 deg.C to 60 deg.C. Some exact graphs such as impedance vs W/H, (width of strip/thickness of substrate) coefficient of coupling vs S/H (space between resonators/thickness of substrate) loaded Q vs l/L (tapping positions) are yet to be generated for ABS plastic substrate to support design calculations as in the case of RT-Duroid substrate.
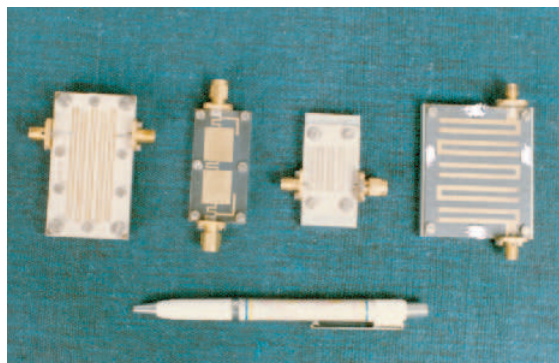
Figure 3: Five-section hairpin line filter.

The resonator lengths, practically found at 1537.5 MHZ and 1575.42 MH have been verified the correctness of measured ε_{eff} of ABS plastic substrate. The correctness of measurement method is

Table 1: Measurement of effective dielectric constant (ε_{eff}) on net analyzer HP 8510.

Frequency of measurement in MHz	RT.DUROID # 5880				ABS-PLASTIC # AP78 EP			
	Measured Electrical length in (mm) for		ε eff	ε eff	Measured Electrical length in (mm) for		ε eff	ε eff
	150mm physical length of 50 Ohm line	50mm physical length of 50 Ohm line			150mm physical length of 50 Ohm line	50mm physical length of 50 Ohm line		
45.0	230.76	96.26	1.345	1.81	231.22	93.82	1.374	1.89
650.0	232.18	96.18	1.360	1.85	233.15	95.35	1.378	1.90
1500.0	234.49	97.79	1.367	1.87	234.61	95.71	1.389	1.93
2500.0	235.82	97.62	1.382	1.91	235.70	95.40	1.403	1.97
4500.0	236.75	97.15	1.396	1.95	237.14	96.14	1.410	1.99
7000.0	242.11	97.91	1.442	2.08	250.32	108.22	1.421	2.0
10000.0	251.43	106.53	1.449	2.10	263.07	117.47	1.456	2.1
From DATA sheet of ROGERS CORP, USA. Er = 2.22 ± 0.02, up to 10GHz. ε eff=1.89 for 50 ohm line. Dissipation factor: 0.0009. Measured ε eff is approximately equal to actual ε eff (1.89). Which verifies correctness or our test method of measurement. (Table 2)					From DATA sheet by ABSTRON Er = (2.8 – 3.3) at 1MHz. ε eff (measure) =1.89 – 2.12 for 50 ohm line from 45MHz to 10GHz. Dissipation factor: 0.0024 at 9.0GHz. Measured by wave guide method with 19x19x3 mm³ sheet of ABS plastic.			

$$\text{eff})^{1/2} = \frac{\text{Difference of electrical length i.e., (EL150-EL50)}}{\text{Difference of physical length i.e., (150-50)}}$$
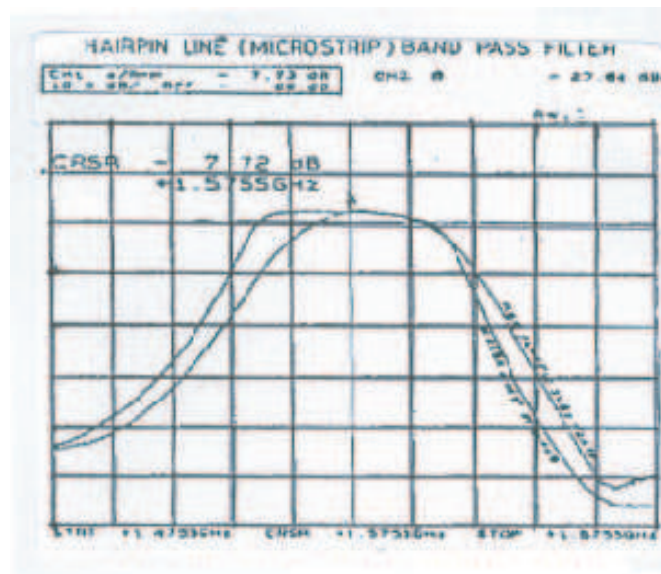
Figure 4: Simulated and measured test results of hairpin line filters at centre frequency 1537.5 MHz.

also verified with the help of value of ε_{eff}, measured and available in the data sheet of # 5880, RT-Duroid, supplied by Rogers Corp. USA. We have measured ε_{eff} for ABS plastic and RT-Duroid, having electrical lengths of 150 and 50 mm of 50 ohms microstrip line of each substrate material (Table 1).

So, if the insertion loss and band width are not critical, low cost microstrip filters can be developed by using ABS-plastic substrate as an alternative to RT-Duroid substrate.

4. ADVANTAGES

The compact, smaller size and light weight, microstrip filters can be developed by choosing the high dielectric constant substrate with high temperature stability (instant 400 deg.C, continuous > 150 deg.C) and high power handling capacity upto 400 W instantly and > 120 W continuously. The bandwidth upto 50% of centre frequency and insertion loss, < 0.5 dB, may be achieved. Moderate to high attenuation is possible by choosing proper structures. Grounded ends and underground configuration reduce the problems posed by ground connections at higher frequencies. Centre frequency and input/output return loss may be optimised due to the accessibility. Devices fabricated from PTEE substrates are rugged and have high mechanical stability [7, 8].

5. APPLICATIONS

The microstrip filters are used in place of Helical, Lumped and Mechanical cavity filters in communication subsystem, up and down converters of receiver and transmitters, space applications Military/commercial/consumer application.

6. CAD/SOFTWARES FOR DESIGN

Miniaturization is on the top of every ones list of recent trends. The smaller is better philosophy holds true for substrate and boards as well. By using ceramic materials the size of the circuit may be reduced up to 1/10 effectively. By using the commercially available CAD/Softwares the design, simulation and optimization work has become easier and faster.

Table 2: Verification of correctness of our test method.

S.No.	For RT-DUROID # 5880 T MAKE-ROGERS CORP. USA	For ABB-PLASTIC # AP78EP MAKD-ABSTRON INDIA
01.	Thickness of substrate: 1-6 mm	Chosen thickness for filters: 1-6 mm
02.	As per DATA sheet: ε eff = 1.89 for 50 ohm line upto 10 GHz	Measured on Network Analyzer HP 8510 : ε eff =1.89 to 2.12 from 45 MHz – 10 GHz
03.	Length of resonator ($\frac{\lambda}{4}$) at 1537.5 MHz & 1575.42 MHz $$\frac{\lambda}{4} = \frac{3 \times 10^{11}}{4 \times 1537.5 \times 10^{6} \sqrt{1.89}}$$ = 35.628 at 1537.5 MHz $\frac{\lambda}{4}$ = 34.483 at 1575.42 MHz	Practically (found) lengths of hairpin line resonators are 31.0mm and 32.0mm at center frequencies 1537.5 & 1575.42 respectively. Therefore, $$\sqrt{eeff} = \frac{3 \times 10^{11}}{4 \times 1537.5 \times 10^{6} \times (\frac{\lambda}{4})}$$ = 1.96 at 1537.5 MHz and 1.94 at 1575.42 MHz.
04.	By our test method, ε eff =1.87 at 1500 MHz and varies form 1.89 to 2.12 for 45 MHz to 10 GHz. Thus the measured values of ε eff are very close to the actual ε eff (1.89 for 50 ohm line), which verifies the correctness of our test method.	By the same test method, ε eff =1.93 (Table 1) for which is very close to the values found practically, ε eff=1.94 & 1.96 at 1537.5 MHz & 1575.42 MHz. This also provides the proof of the correctness of our method adopted for measurements of ε eff.
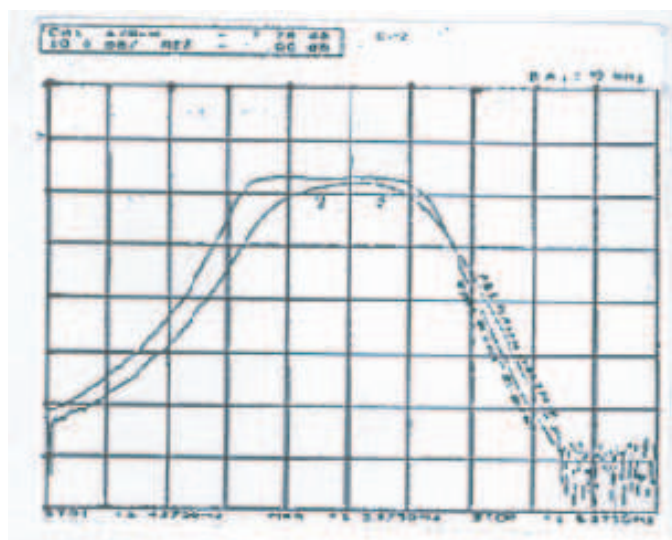
Figure 5: Simulated and measured test results of hairpin line filters at centre frequency 1575.5 MHz.

7. CONCLUSION

In this paper, We have reported the value added design procedure only. The simulation and optimization of filters can be carried out by using MATLAB, Ansoft, Essoff, Sonnet softwares. The Results of the simulation/optimization will be based on the design equations that are present in the paper.

REFERENCES

1. Zerev, A. I., *A Handbook of Filter-synthesis*, John-Wiley, New York, 1967.
2. Bahl, I. J. and D. K. Trivedi, "A designers guide to Microstrip lines," *Microwaves*, May 1977.
3. Tam, A., "Principles of mictrostrip design," *RF Design*, June 1985.
4. Matthaei, G. L., L. Young, and E. M. T. John, *Microwave Filters, Impedence Matching Networks and Coupling Structures*, Arctech House, Norwood, MA, 1988.
5. Pozar, D. M., *Microwave Engineering*, 2nd Edition, John-Wiley, New York, 1998.
6. Zhu, L., H. Bu, and K. Wu, "A compact multi-Pole microstrip band pass filter," *Proc. Inst. Elect. Engg.*, 71–77, February 2002.
7. Tsai, C.-M., S.-Y. Lee, and H.-M. Lee, "Transmission line filter with capacitively coupled lines," *IEEE Trans. Microw. Theory and Tech.*, Vol. 51, No. 15, 2003.
8. Kuo, J. T. and E. Shih, "Microstrip resonator bandpass filter with an extended optimal rejection and width," *IEEE Trans. MTTS*, Vol. 51, 1154–59, 2003.
9. Hong, J. S. and M. J. Lancaster, "Microstrip filters for RF/microwave application," *A Wiely-Inter Science Publications*, Canada, 2004.
10. Wang, H. and L. Zhu, "Microstrip resonator with ultra-broad rejection bandwidth," *Electronic Lett.*, Vol. 40, No. 9, 1188–1189, September 2004.
11. Pozar, D., *Microwave Engineering*, 416–438, 3rd Edition, Wiley, 2005.
12. TasiKuo, J., M.-J. Maaand, and P.-H. Lu, "Microstrip filter with compact miniaturized hairpin line resonators," *IEEE Microwave Theory and Guided Letters*, Vol. 10, No. 3, 94–95, March 2005.
13. Jovanovic, S. and A. Nesic, "Microstrip bandpass filters with capacitive coupled resonators," *Electronic Lett.*, Vol. 41, No. 112–13, 2005.
14. Chung, M.-S., I.-S. Kim, and S.-W. Yun, "Hairpin Line bandpass filter with attenuation poles," Presented at *APMC*, 2005.
15. Chung, W., et al., "Miniaturized passband microstrip filters," *IEEE Trans. MTT*, February 2005.
16. Kinayman, N. and M. I. Akush, *Modern Microwave Circuits*, Artech House, Boston, London, 2005.
17. Xiao, J.-K., S. P. Li, and Y. Li, "Novel planar bandpass filters using single patch resonators," *Journal of Electromagnetic Waves and Applications*, Vol. 20, No. 11, 1493, 2006.

18. Deng, P. H., Y. S. Lin, C. H. Wang, and C. H. Chen, "Compact microstrip bandpass filters with good selectivity and stopband rejection," *IEEE Transaction MTTS*, Vol. 54, No. 2, 533–539, February 2006.
19. Kazerooni, M. and A. Cheldavi, "Simulation, analysis, Design and applications of microstrip structure filters using multistrip method," *Progerss In Electromagnetics Research*, PIER 63, 193–207, 2006.
20. Zhu, Y. Z., Y. J. Xie, and H. Feng, "Novel microstrip bandpass filters with transmission zeros," *Progress In Electromagnetics Research*, PIER 77, 29–41, 2007.
21. Wang, Y. X., B. Z. Wangand, and J. wang, "A compact dualmode bandpass filters with widestopband," *Progress In Electromagnetics Research*, PIRE 77, 67–73, 2007.
22. Xio, J. K., "Novel microstrip bandpass filters using patch resonators," *Journal of Electromagneric Waves and Applications*, Vol. 21, No. 10, 1341–1351, 2007.
23. Zhu, Y.-Z., Y.-J. Xie, and H. Feng, "Novel microstrip Bandpass filters with transmission zeros," *Progress In Electromagnetics Research*, PIER 78, 419, 2008.
24. Agilent Technologies, Inc., Information at www.agilent.com.
25. Sonnet Software, Information at www.sonnetusa.com.
26. Ansoft-HFSS-3D for Electromagnetic modeling: www.ansoft.com.
27. Zealand IE 3D Software for design, simulation and optimization of planar-structured microstrip filtersat: www.zealand.com.

Influence of Weak Combined Static and Low-frequency Alternating Magnetic Fields on Tumor Growth of Ehrlich Ascites Carcinoma in Mice

V. V. Novikov, **G. V. Novikov**, **V. O. Ponomarev**,
V. V. Kuvichkin, **and E. E. Fesenko**

Institute of Cell Biophysics, Russian Academy of Sciences
Pushchino, Moscow region 142290, Russia

Abstract— The parameters of the ultralow-frequency (1, 4.4, 16.5, Hz or the sum of these frequencies) extremely weak (300, 100, 150–300 nT, according to frequencies) alternating component of combined magnetic fields (MFs) have been found at which it has a marked antitumor activity — inhibits or suppresses the growth of Ehrlich ascites carcinoma (EAC) in mice. Effect realize in increasing of longevity tumor bearing animals and enhancement of damaged tumor cells. The necrosis was prevailing type of cell death.

1. INTRODUCTION

Most experiments devoted to the effect of weak combined alternating (AC) and static (DC) magnetic fields (MFs) on biosystems have been performed using fields with the amplitude of the AC component of tens of microteslas against the background of the static MF of comparable strength. However, there is substantial evidence indicating that very weak alternating MFs of the nanotesla range are also capable of inducing marked biological effects [1–12]. It should be noted that in the majority of cases, the experiments with very weak AC MFs were conducted against the background of the geomagnetic field whose magnetic induction is $\sim 50\,\mu\text{T}$. The present study deals with the effect of combined MFs consisting of a static component comparable with the geomagnetic field and an alternating component with an intensity of tens and hundreds of nanoteslas, which is parallel to the constant component. The AC field in this case has a frequency of 0.5–16.5 Hz, i.e., is an extremely weak ultralow-frequency field.

One of the most striking and interesting findings in basic and applied bioelectromagnetic investigations is the antitumor effect of weak and extremely weak MFs and electromagnetic radiations, which has been found by several investigators in different ranges of field frequency and intensity [4, 9, 13, 14]. Previously we have revealed that weak combined DC/AC MFs adjusted to the cyclotron resonance of ions of amino acids have the antitumor activity [4, 9, 11, 15].

Preliminary experiments with monofrequency AC components of MFs showed that the pronounced antitumor effect is registered only at a frequency of 16.5 Hz, which formally corresponds to the cyclotron frequency of K^+ (DC 42 μT), at an intensity of AC MF 80 nT. With regard to the choice of frequency, this result coincides with the data of A. Liboff on the antitumor activity of combined MF adjusted to the cyclotron resonance of potassium ions [16]. Then it was shown that the two-frequency signal generated by adding the modulating frequency of 0.5 Hz (experimentally found optimal value) to the frequency of 16.5 Hz (carrier frequency corresponding to the potassium ion cyclotron resonance) produced a much more pronounced antitumor effect [11].

Thus, we determined the optimal frequency ranges for the AC component of MF: 0.25–1 Hz; 4–5 Hz, and 15.5–17.5 that had a pronounced antitumor activity (inhibited or suppressed the growth of EAC in mice) at superlow intensities (amplitude of about a hundred nT) in the presence of a collinear geomagnetic field (42 μT). However, until this work, the amplitude dependences of the antitumor effect of weak combined MFs with monofrequency AC components have not been determined experimentally. It remained unclear why the multifrequency magnetic signal is biologically more effective than the monofrequency field.

2. MATERIALS AND METHODS

2.1. Object

BALB/c male mice weighing 22–26 g with intraperitoneally transplanted EAS cells were used. The choice of this model was dictated by the fact that the ascitic form of EAC was found to be more sensitive to weak MF compared with the solid form of this tumor [11]. Animals were taken from the nursery of the Shemyakin-Ovchinnikov Institute of Bioorganic Chemistry, Russian Academy of

Sciences. The National Research Council criteria for the care and use of the laboratory animals in research were carefully followed.

EAC was inoculated by intraperitoneal injection of tumor cells ($1 * 10^6$ in $0.5\,$ml of isotonic solution) to animals. Tumor cells were always inoculated to all animals of a series and only after this, the animals were divided into groups (experimental and control). With this amount of EAC cells, tumors were formed in mice not exposed to MF (control groups) in 100% of cases. Visual signs of tumor formation were noted by day 6–7 after the inoculation of tumor cells from an increase in the abdominal perimeter caused by the accumulation of ascitic fluid in the abdomen. By day 13–18, the animals of the control group died.

2.2. Characterization of MFs and the Methods of Their Formation

The device for the exposure of tumor-bearing animals consisted of two pairs of coaxially arranged Helmholtz coils oriented along the vector of the geomagnetic field (GMF). The local GMF partially compensated to $42 \pm 0.1\,\mu$T using one pair of Helmholtz coils served as a DC component of MF. The alternating component collinear to the DC field was formed using the second pair of Helmholtz coils.

Several series of experiments were conducted at a frequency of the AC component of $16.5\,$Hz (this frequency corresponds to the cyclotron frequency of potassium ions at the induction of the DC component of MF $42\,\mu$T) in two variants: in the presence of the modulating frequency and at a monofrequency. The following intensities were used: 40, 80, 150, 200, 250, 300, 350, 400, and $500\,$nT. In the case of a two-frequency signal, the modulating frequency was $0.5\,$Hz. The next series of experiments were conducted at the frequencies of the AC component of 0.5 and $1\,$Hz separately.

Then series of experiments at a frequency of the AC component of $4.4\,$Hz (this frequency corresponds to the cyclotron frequency of the glutamic amino acid at the induction of the DC component of MF $42\,\mu$T) have been conducted. The following intensities of the AC component of MF were used: 40, 65, 80, 100, 140, 200, 250, and $300\,$nT.

The next series of experiments was devoted to the effect of a complex magnetic signal, which represented the sum of three frequencies (1, 4.4, and $16.5\,$Hz) at the previously found optimal intensities of individual frequencies.

Each experiment was performed in triplicate. The number of animals in a group was 10. The intensity of working fields was controlled by direct measurements using a Mag-03 MS 100 Bartington magnetometer (Oxford, Great Britain). The intensity of background industrial magnetic fields ($50\,$Hz) was 10–$50\,$nT. Animals were exposed to MF beginning from the first day after the inoculation of tumor cells. The duration of one séance was $1\,$h a day (every day), for 12 days. Exposures were carried out in the daytime between 10 and $17\,$h at room temperature (18–$22°$C) under conditions of natural illumination.

Animals of the control group were located in a GMF with the DC component of $\sim 42\,\mu$T and the same values of background industrial magnetic fields as in the case of experimental groups.

2.3. Estimation of Efficiency of Action of MFs on Tumor Growth

The antitumor effect of MFs was estimated by registering the life span after the injection of tumor cells. In some cases, the results were presented as the percent of animals that survived within a month of observation after the injection of tumor cells. In addition, a cytological analysis of EAC cells isolated from the abdomen of tumor-bearing mice was performed. The state of tumor cells was estimated by the method of light microscopy. Preliminarily smears were fixed by ethyl ester and stained by hematoxylin and eosin. After a visual analysis, the ratio of damaged tumor cells to healthy cells (total number of cells 1000) was determined.

2.4. Statistical Analysis

Statistical analysis was performed using the Student t-test. The value $P < 0.05$ was considered to be statistically significant.

3. RESULTS

The study showed that the magnitude of the antitumor effect of weak combined MFs depends on the amplitude of their AC component (carrier frequency $16.5\,$Hz and modulating frequency $0.5\,$Hz). As the amplitude was increased in the range of 40–$300\,$nT, the effect enhanced; however, further increase in amplitude caused a decrease in the effect (Fig. 1). A maximum effect was achieved at an amplitude of the AC component of $300\,$nT.

At the next stage we determined the dependence of the antitumor effect on the amplitude of the monofrequency magnetic signal separately at a carrier frequency of 16 Hz and a modulating frequency of 0.5 Hz. The data obtained at a frequency of 16.5 Hz are presented in Fig. 2. It is evident from the figure that the antitumor activity of the MF in this case is somewhat less pronounced than in previous experiments. It is also seen that the magnitude of the effect remains approximately constant in the amplitude range of 150–300 nT. Therefore, we assumed that the maximum effect at 300 nT in the case of the two-frequency signal with the modulating frequency of 0.5 Hz is related to the presence of this very frequency. Further experiments confirmed this suggestion.
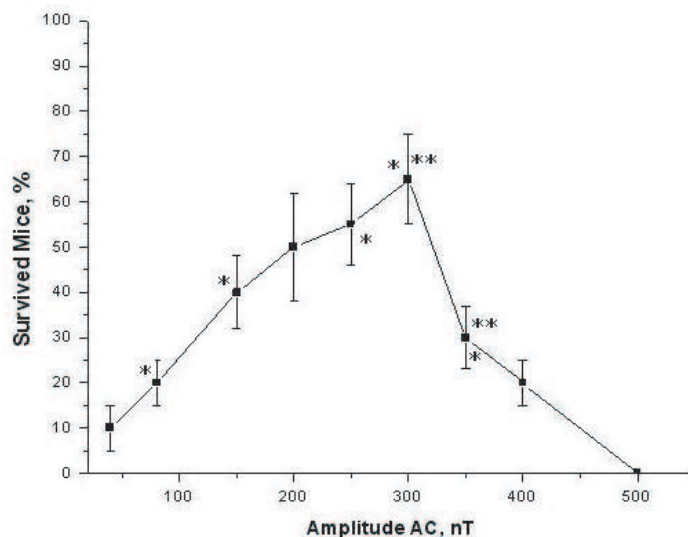
Figure 1: Dependence of the antitumor activity of weak combined collinear magnetic fields (DC field 42 μT) on the amplitude of the AC component at a modulating frequency of 0.5 Hz and carrier frequency of 16.5 Hz. The percentage of survived animals 1 month after the inoculation of tumor cells is given. In control groups, all animals died by this term. The data are the means ± standard deviation ($n = 3$). $^*P < 0.05$ statistical difference between the experimental groups.
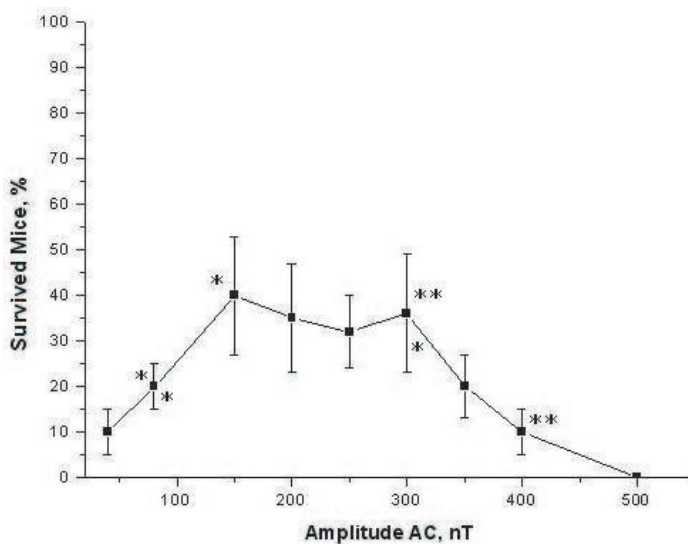
Figure 2: Dependence of the antitumor activity of weak combined collinear magnetic fields (DC field 42 μT) on the amplitude of the AC component at a frequency of 16.5 Hz. The percentage of survived animals 1 month after the inoculation of tumor cells is given. The data are the means ± standard deviation ($n = 3$). $^*P < 0.05$ statistical difference between the experimental groups.

Two frequencies in the range of effective modulating frequencies were taken, 0.5 and 1 Hz, and the amplitude dependence of the effect at each frequency was examined. It was found that both

induce a marked effect at amplitudes of 250–350 nT (Fig. 3). This leads to the conclusion that the higher biological activity of the two-frequency signal is due to the overall effect of separate frequencies, in this case 16.5 and 0.5 (or 1) Hz.

Then we examined the amplitude dependence of the antitumor effect at a frequency of 4.4 Hz (the cyclotron frequency of the ionic form of glutamic acid at the induction of the DC component of MF 42 μT). The choice of this frequency was made on the basis of the results of previous experiments, which showed that combined MFs have a pronounced antitumor activity at the cyclotron frequencies of the ionic forms of amino acid molecules [4, 9]. It is evident from Fig. 4 that the maximum activity of a extremely weak AC MF at a frequency of 4.4 Hz occurs at 100 nT.
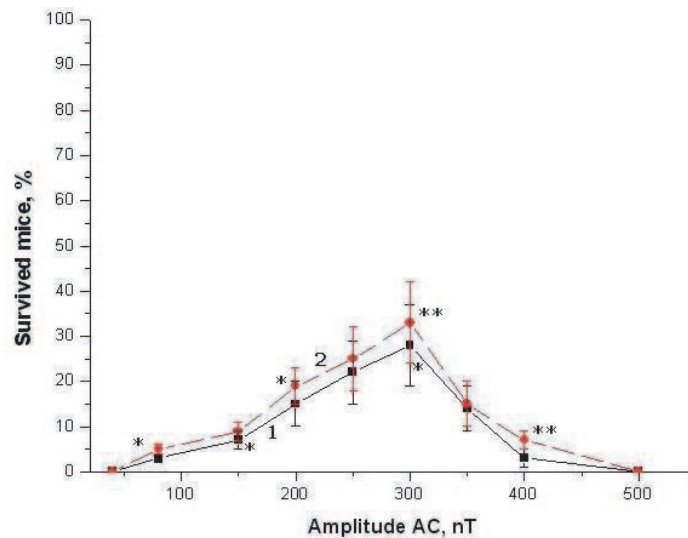
Figure 3: Dependence of the antitumor activity of weak combined collinear magnetic fields (DC field 42 μT) on the amplitude of the AC component at a frequency of 0.5 and 1 Hz. 1 — 0.5 Hz; 2 — 1 Hz. The percentage of survived animals 1 month after the inoculation of tumor cells is given. The data are the means ± standard deviation ($n = 3$). *$P < 0.05$ statistical difference between the experimental groups.
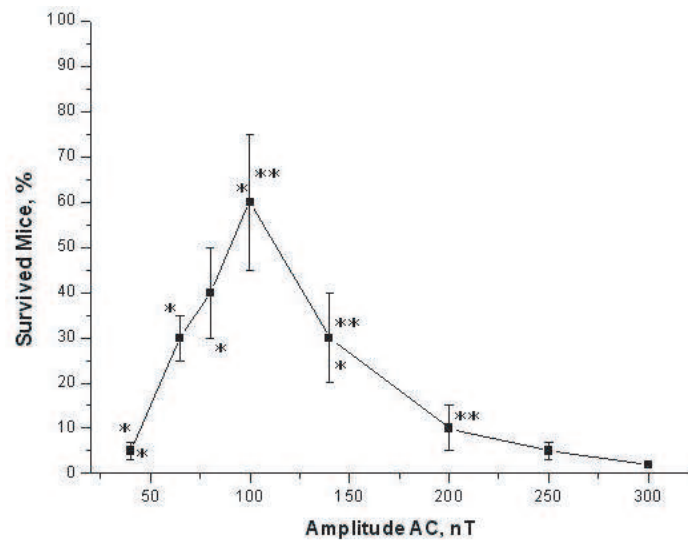
Figure 4: Dependence of the antitumor activity of weak combined collinear magnetic fields (DC field 42 μT) on the amplitude of the AC component at a frequency of 4.4 Hz. The percentage of survived animals 1 month after the inoculation of tumor cells is given. The data are the means ± standard deviation ($n = 3$). *$P < 0.05$ statistical difference between the experimental groups.

Thus, we determined optimal ranges of amplitudes at different effective frequencies of the extremely weak AC component of combined MFs. In the case of 16.5-Hz frequency, effective ampli-
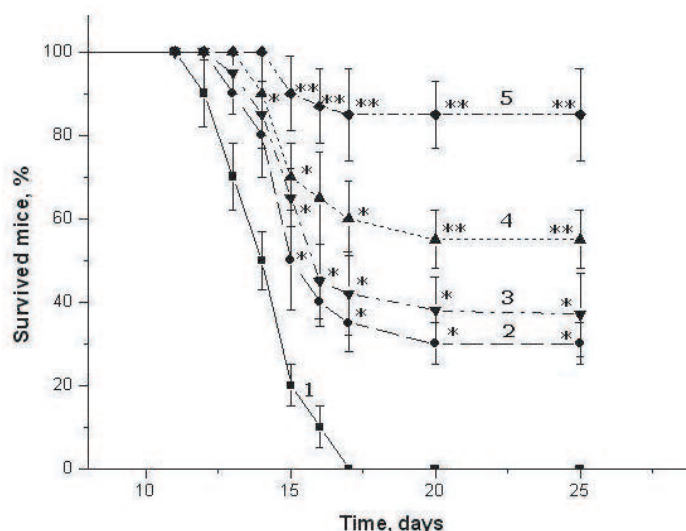
Figure 5: Life spans of tumor-bearing animals at different frequencies and amplitudes of the AC component (DC field 42 μT). On the abscissa is the period of observation of animals in groups after tumor inoculation. 1 — control; 2 — 1 Hz, 300 nT; 3 — 16.5 Hz, 150 nT; 4 — 4.4 Hz, 100 nT; 5 — the sum of frequencies (1 Hz, 300 nT; 4.4 Hz, 100 nT; 16,5 Hz, 150 nT). The data are the means ± standard deviation ($n = 5$). *$P < 0.01$ relative to the control. **$P < 0.01$ statistical difference between the experimental groups and between the experimental groups and the control.

Table 1: Dependence of the state of EAC cells on the parameters of the extremely weak AC MF at DC MF of 42 μT.

Parameters of exposure	EAC cells, degenerative forms, %			
	Day 3	Day 7	Day 10	Day 12
Control group	2.2 ± 0.2	3.1 ± 0.3	5.2 ± 0.4	10.4 ± 1.2
1 Hz, 300 nT	$8.6 \pm 0.8^*$	$15.6 \pm 1.5^*$	$36.4 \pm 3.1^*$	$72.2 \pm 6.9^*$
4.4 Hz, 100 nT	$9.4 \pm 1.6^*$	$26.4 \pm 2.9^*$	$62.2 \pm 6.4^{**}$	$81.0 \pm 6.5^*$
16.5 Hz, 150 nT	$7.4 \pm 0.6^*$	$21.4 \pm 2.6^*$	$43.2 \pm 4.2^*$	$68.4 \pm 5.1^*$
Sum of frequencies	$15.4 \pm 1.5^{**}$	$36.3 \pm 4.5^{**}$	$83.5 \pm 7.4^{**}$	$94.6 \pm 5.3^{**}$

Average values ± standard deviation are given ($n = 5$).

*$P < 0.01$ relative to the control.

**$P < 0.01$ relative to the control and other experimental groups.

tudes lie in the range of 150–300 nT; at 0.5 and 1 Hz, the maximum effect occurs at 300 nT; and at a frequency of 4.4 Hz, the highest activity of MF is observed at 100 nT.

In the next series of experiments, we examined the biological activity of a multifrequency signal involving the sum of all three frequencies (1, 4.4, and 16.5 Hz) at the optimal amplitude values (300, 100, and 150 nT, respectively) found. It is evident from Fig. 5 that the multifrequency signal with the experimentally found effective amplitudes has a higher activity compared with separate monofrequency signals at these amplitudes.

A cytological analysis of the contents of the abdomen of tumor-bearing animals showed that MFs produced a damaging action on EAC cells. Among experimental EAC cells from animals exposed to weak MFs, there was a great number of degenerative cell forms (Table 1). A quantitative analysis of EAC cells revealed differences in the degree of damage induced by different types of the magnetic signals used. The highest percent of damaged EAC cells was registered in mice exposed to the multifrequency signal (sum of effective frequencies at their corresponding effective amplitudes). It is seen that the level of degeneration in EAC cells directly correlates with the percent of survival of mice in groups (Table 1, Fig. 5). These results suggest that the cytological analysis of the contents of the abdomen is an adequate method for express estimation of the state of tumor-bearing animals.

Further experiments were performed using the most effective parameters of combined MFs with the AC component that represented the sum of effective frequencies at their corresponding effective amplitudes.

4. DISCUSSION

In the experiments, optimal or close to optimal parameters of the ultralow-frequency (1, 4.4, and 16.5 Hz, or the sum of these frequencies) extremely weak (300, 100, and 150–300 nT, according to frequency) AC component of combined MFs were found at which it has a marked antitumor activity against the background of the static field of $42\,\mu T$ (the intensity of the DC component corresponds to the region of GMF).

It was shown that, after the exposure to weak MFs, a great number of degenerative cell forms are present among EAC cells as distinct from the control group. Probably, the degradation of the tumor tissue is initiated by autolytic enzymes, which are released from lysosomes upon the damage to membrane; as a result, tumor cells swell and are lysed. It is likely that the exposure to MFs with the parameters specified in this study sharply activates the mechanism of the natural degradation of tumor cells.

It is worth noting that the antitumor activity of weak MFs was detected at different frequencies: 0.5, 1.0, 4.4, and 16.5 Hz. In this work, we did not examine the antitumor effect at other frequencies of AC MF that are close to frequencies used in these experiments. However, we have previously shown that, at an intensity of AC of $\sim 100\,nT$ in two frequency ranges: 4.2–5.2 Hz and 15.5–17.5 Hz, the effect nonlinearly depends on frequency at an intensity of the DC magnetic component of $42\,\mu T$ [11].

This finding suggests the universality of the effector mechanism triggering the damage to tumors by the action of weak MFs. We previously reported that the whole-body exposure to weak MFs activates the system of antitumor immunity; in particular, it stimulates the production of the tumor necrosis factor (TNF) by the macrophages of the abdomen in mice [17]. It is known that the mechanism of the damaging effect of TNF on tumor cells involves the generation of reactive oxygen species (ROS) [18]. In our opinion, the most probable candidates for the role of damaging agents for tumor cells in the case of the treatment with weak MFs are ROS that are produced and operate immediately in the cells of the immune system (macrophages) and/or in the tumor tissue. In favor of this assumption are the earlier detected effects of weak MFs, namely, the weakening of the protein defense of chromatin DNA against DNase I [19] and the activation of hydrolysis of proteins and peptides in aqueous medium [20]. These effects may be caused by ROS, in particular hydrogen peroxide [21]. It is tempting to suppose that weak MFs can increase local concentrations of ROS, thereby producing the antitumor action.

Presumably, the difference in the responses of immune and tumor tissues to superweak AC is due to the features of the metabolism of macrophages and tumor cells. It is known that, in tumor cells, anaerobic processes, in particular glycolysis, prevail. In cells of the immune system, the oxidative phosphorylation processes predominate. It is likely that it is the difference in the type of their metabolism that determines the difference in their responses to AC. It would be tempting to suggest that, if this is the case, then the stimulation of ROS production by the action of superweak AC MF with the characteristics specified in our study may lead to the activation of the cells of the immune system and simultaneously to the disturbance of the metabolism in tumor cells.

REFERENCES

1. Juutilainen, J., E. Laara, and K. Saali, "Relationship between strength and abnormal development in chick embryos exposed to 50 Hz magnetic field," *International Journal Radiation Biology & Relative Studies on Physical Chemistry Medicine*, Vol. 52, 787–793, 1987.

2. Berman, E., L. Chacon, D. House, B. A. Koch, W. E. Koch, J. Leal, S. Løvtrup, E. Mantiply, A. H. Martin, G. I. Martucci, K. H. Mild, J. C. Monaham, M. Sandstrom, K. Shamsaifar, R. Tell, M. A. Trillo, A. Ubeda, and P. Wagner, "Development of chicken embryos in a pulsed magnetic field," *Bioelectromagnetics*, Vol. 11, 169–187, 1990.

3. Liburdy, R. P., T. R. Sloma, R. Sokolic, and P. Yaswen, "EMF magnetic fields, breast cancer, and melatonin: 60 Hz field block melatonin's oncostatic action of ER+ breast cancer cell proliferation," *Journal Pineal Research*, Vol. 14, 89–97, 1993.

4. Novikov, V. V., N. I. Novikova, and A. K. Kachan, "Cooperative effects by the action of weak magnetic fields on the tumor growth in vivo," *Biofizika*, Vol. 41, 934–938, 1996.

5. Persinger, M. A., L. L. Cook, and S. A. Koren, "Suppression of experimental allergic encephalomyelitis in rats exposed nocturnally to magnetic fields," *International Journal of Neuroscience*, Vol. 100, 107–116, 1999.

6. Blackman, C. F., S. G. Benane, and D. E. House, "The influence of $1.2 \mu T$, $60 Hz$ magnetic field on melatonin — and tamoxifen — induced inhibition of MCF-7 cell growth," *Bioelectromagnetics*, Vol. 22, 122–128, 2001.

7. Belova, N. A., O. N. Ermakova, A. M. Ermakov, Z. Ye. Rojdestvenskaya, and V. V. Lednev, "The bioeffects of ext emely weak power-frequency alternating magnetic fields," *Environmentalist*, Vol. 27, 411–416, 2007.

8. Belova, N. A. and V. V. Lednev, "Effects of extremely weak alternating magnetic fields on the gravitropism of plants," *Biofizika*, Vol. 46, 122–125, 2001.

9. Novikov, V. V., "Antitumor effects of weak and ultraweak magnetic field," *Biophysics*, Vol. 49, S43–S47, 2004.

10. Bobkova, N. V., V. V. Novikov, N. I. Medvinskaya, I. Yu. Aleksandrova, and E. E. Fesenko, "Reduction in the β-amyloid level in the brain under the action of weak combined magnetic fields in a model of sporadic Alzheimer's disease," *Biophysics*, Vol. 50, S2–S7, 2005.

11. Novikov, V. V., V. O. Ponomarev, and E. E. Fesenko, "Analysis of the biological activity of two-frequency magnetic signal and single-frequency variable components during exposure to weak and extremely weak combined constant and low-frequency variable magnetic fields on the growth of grafted tumors in vice," *Biophysics*, Vol. 50, S110–S115, 2005.

12. Novikov, V. V., I. M. Sheiman, and E. E. Fesenko, "Effect of weak static and low-frequency alternating magnetic fields on the fission and regeneration of the planarian dugesia (Girardia) tigrina," *Bioelectromagnetics*, Vol. 29, 387–393, 2008.

13. Akoev, I. G., A. F. Kozhakaru, V. M. Mel'nikov, and A. V. Usachev, "Effect of prolonged low-intensity radiofrequency radiation of the centimeter range on the subcutaneously grafted Ehrlich adenocarcinoma," *Radiation Biology. Radioekologiya*, Vol. 35, 23–27, 1995.

14. Muzalevskaya, N. I. and V. M. Uritskii, "Antitumor effect of weak extremely low-frequency stochastic magnetic field with the spectrum 1/f," *Biofizika*, Vol. 42, 961–970, 1997.

15. Novikova, N. I., V. V. Novikov, and V. E. Kurakovskaya, "Combined action of weak static and alternating magnetic fields adjusted to the cyclotron resonance of ions of amino acids on the development of Ehrlich ascites carcinoma in mice," *Biofizika*, Vol. 43, 772–774, 1998.

16. Liboff, A. R., B. R. McLeod, and S. D. Smith, "Method and apparatus for the treatment of cancer," US Patent 5045050, 1991.

17. Novoselova, E. G., V. B. Ogai, O. V. Sorokina, V. V. Novikov, and E. E. Fesenko, "Effect of electromagnetic waves of the centimeter range and combined magnetic field on the production of the tumor necrosis factor in cells of mice with experimental tumors," *Biofizika*, Vol. 46, 131–135, 2001.

18. Zenkov, N. K., V. Z. Lankin, and E. B. Men'shikova, "Oxidative stress: Biochemical and pathophysiological aspects," *MAIK Nauka/Interperiodika*, 343, Moscow, 2001.

19. Novikov, V. V., Yu. P. Shvetsov, E. E. Fesenko, and N. I. Novikova, "Molecular organisms of the biological action of weak magnetic fields. I. Restistance of chromatin of Ehrlich ascites carcinoma cells and mouse brain to Dnase I by the combined action of weak static and low-frequency alternating magnetic fields adjusted to the cyclotron resonance of the ions of polar amino acids," *Biofizika*, Vol. 42, 733–737, 1997.

20. Novikov, V. V. and E. E. Fesenko, "Hydrolysis of some peptides and proteins in weak combined static and low-frequency alternating magnetic fields," *Biofizika*, Vol. 46, 235–241, 2001.

21. Burlakova, E. B., A. A. Kondradov, E. L. Mal'tseva, "Superweak effects of chemical compounds and physical factors on biological systems," *Biofizika*, Vol. 49, 551–564, 2004.

Merger of Two Different Dosimetry Rationales

S. Perov[1], Q. Balzano[2], and N. Kuster[3]

[1]RAMS Research Institute of Occupational Health, Moscow, Russia
[2]Department of Electrical and Computer Engineering, University of Maryland, Maryland, USA
[3]Foundation for Research on Information Technologies in Society, Zurich, Switzerland

Abstract— At the present time there are two basic scientific rationalizations of radiofrequency dosimetry. Finding the possible correlations between the measured parameters of the two different scientific approaches is one of the main obstacles to global safety (hygienic) standard harmonization. One approach is based on the measure or estimate of specific absorption rate which is the power absorbed per unit weight of an object. The other relies on the measure of the time integrated radiofrequency power density incident on an object. Development of a common science-based dosimetric approach may be possible by taking into account the exposure time. Time is the "key" factor, which is used both in the specific absorption rate and the power density definitions. Finding the correlations between the specific absorption rate and the power density of an exposure depending on time duration might make possible the creation of a common estimate of electromagnetic field biological action. It can help to find the correlation between power density and specific abortion rate for near and far field of radiofrequency sources.

Safety standard harmonization is much more complicated than just harmonizing dosimetric criteria. Safety standard setting involves the mediation of various concerns and interests, such as political, economic, technological, etc. However, a necessary common ground is one dosimetric approach with accurate substantiation of measurement methodologies. It will consist in finding a homogeneous bioeffect data base for the two current science-based dosimetric approaches.

1. INTRODUCTION

During the last twenty years the existence of substantially different safety standards has become a major problem. This problem is limiting the growth of the international trade and of the rapid diffusion of wireless products. We consider the harmonization of these standards an issue needing urgent attention. Safety standard harmonization is much more complicated than just harmonizing dosimetric criteria. Safety standard setting involves the mediation of various concerns and interests, such as political, economic, technological, etc. However, a necessary common ground is one dosimetric approach with accurate substantiation of measurement methodologies. The first step towards the solution of the harmonization problem is the definition of a common science-based dosimetric approach. At the present time there are two basic scientific rationalizations of radiofrequency (RF) dosimetry. Finding the possible correlations between the measured parameters of the two different current science-based dosimetric approaches is one of the main obstacles to global safety (hygienic) standard harmonization.

2. ICNIRP EXPOSURE ASSESSMENT AND DOSIMETRY

The history of RF human exposure limitation begun in the 50th and 60th year of the last century. The stimulus to establish an electromagnetic energy safety standard was the USA research program under the direction of H. Schwan. The result of this research was the approval of the first national safety EMF standard [1]. At present, there is the International Commission on Non-Ionizing Radiation Protection (ICNIRP). ICNIRP is developing science-based electromagnetic exposure guidelines, measurement and dosimetry recommendations. The exposure metrics of the ICNIRP require the measurement of electric (E), magnetic (H) field strength and power density (PD). In the frequency band 100 kHz–10 GHz, the ICNIRP basic restrictions [2] hinge on the concept of specific absorption rate (SAR) which is defined as

$$\text{SAR} = \frac{\sigma E^2}{\rho} = c_i \frac{dT}{dt} \tag{1}$$

where E is the RMS value of the electric field in tissue, σ and ρ are the tissue conductivity and mass density. In establishing the national standard in the USA, scientists proceeded only from reproducible thermal mechanisms and the safety levels were based mainly on effects of acute, single exposures. Therefore, initially, SAR measurements were used to pinpoint thermal gradients of RF exposures. In (1) also, c_i and $\frac{dT}{dt}$ are the specific heat of tissue and the time derivative of the

temperature at the onset of the RF exposure. With much improved instrumentation, now SAR levels can be evaluated for non thermal exposures also. SAR measures the rate of EMF energy absorption in the unit of weight of an exposed object. SAR is used to quantify tissue exposure from EMF in the far and the near field of RF sources, where PD might not be defined or even definable. The SAR basic restrictions of ICNIRP are time independent because the rate of energy absorption is limited, not its total amount.

Also ICNIRP guidelines have a specific energy absorption (SA) in joule per kilogram (J/kg). This parameter is not as commonly applied as SAR, but it is used in the scientific literature and experimental reports.

The ICNIRP approach requires SAR measurements on simulated humans (phantoms). The phantoms used in the measurements do not simulate the details of the human anatomy (fine multi-layered structures, blood vessels, innervations). On the positive side, it is possible to measure SAR in the near and far field of RF sources. SAR maps the distribution of the EMF absorption in tissue, with the peak value ("hot spot") locations. The SAR distribution helps in pinpointing interaction sites, valuable information when assessing the cause of a detected biological effect in animals.

3. RUSSIAN EXPOSURE ASSESSMENT AND DOSIMETRY

The history of Russian first hygienic rules and norms (national safety standard) started at the same time as in USA, and the head of this research program was Z. Gordon. In the USSR, and now in the Russian Federation exposure limits are founded on chronic biological effects caused by non thermal EMF exposures; the effects were investigated using behavioral, electrophysiological, hematological and biochemical methods.

The safety levels of the first national standards in USA and USSR differed by more than three orders of magnitude. It clearly expressed a basic difference of scientific views of that time for mechanisms of biological effects. Now, these safety levels have moved closer but they still are very different.

The Russian approach to exposure assessment and dosimetry has two main differences from those of ICNIRP. First, the concept of SAR was never adopted, because near field measurements were not required until recently. The near field evaluation is performed by computations extrapolating the far field measurement values using theoretical equations. Second, the dosimetry is based on the parameter "power exposition" (PE) which is a dynamic estimate of the EMF biological effects from the exposure. This parameter differentiates the exposure dose during a given time interval. In other words, the Russian exposure limitations consider cumulative the biological effects of RF EMF. PE values depend on time, field level and frequency range using the formulas:

$$PE_E = E^2 \cdot t \quad PE_H = H^2 \cdot t \quad \text{(for 300 kHz–300 MHz)} \tag{2}$$

and

$$PE_{PD} = PD \cdot t \quad \text{(for 0.3 kHz–300 MHz)} \tag{3}$$

The values of PE_E, PE_H, PE_{PD}, and t are given in [2].

The Russian exposure limitation approach and its dosimetry aim to avoid any unfavorable biological effects caused by chronic exposure. This approach defines a dose-dependent biological action of RF EMF and, so, a dependence of time and intensity of the safe RF exposure.

The Russian dosimetry has a major weakness in the evaluation of the near field exposure. With few exceptions, near E and H-field values cannot be reconstructed from far field measurements, because the same far field patterns can be supported by RF sources with very different near fields. The Russian approach has not adopted a dosimetric parameter like SAR; so the "hot spot" of an exposure object are undetected. However, the Russian approach has a dose-dependent science-based exposure safety criterion in PE, which is based on PD measurements and exposure time. PD is a measure of RF EMF exposure for both standards. However, PE is more useful in survey situations than PD, since it does not require further exposure evaluations using phantoms. The safety determination of far field exposures is immediate.

4. MERGER OF TWO DIFFERENT DOSIMETRY APPROACHES

Merging two different dosimetry approaches requires the use of different methods such as numerical simulation, phantom measurement and the detection of predefined biological effects from cell culture to whole organisms.

Undoubtedly SAR is one of the most useful tools for the assessment of RF EMF distribution during exposure. Therefore SAR should be the fundamental dosimetric parameter in the harmonization process and the first dosimetric parameter in common approach. The PD is one characteristic of EMF.

One approach is based on the measure or estimate of SAR which is the power absorbed per unit weight of an object. The other relies on the measure of the time integrated radiofrequency PD incident on an object. The PD measurements do not exclude SAR. SAR is the additional and important dosimetry criterion. Development of a common science-based dosimetric approach may be possible by taking into account the exposure time. Time is the "key" factor, which is used both in the specific absorption rate and the power density definitions. Therefore SA and PE are closer parameter than SAR and PD and have common parameter-time. A definite correlation between SA and PE during a period of time gives interconnection SAR and PD in far and near field. With its present definition, PE is not an accurate parameter, because it does not measure the absorbed energy in the exposed objects, however PE has linear relationship to PD. The application of "dose" approach has restrictions connected with the general biological law of nonlinear dependence on the levels of an agent. With reference to microwave effects, it is established that the simple time-intensity dependence $PD \cdot T = const$ remains valid only in the range from 0.05 to $1 \, mW/cm^2$. At the high levels of exposure, increased general biological effects demand the introduction of correction factors: at PD 1–$5 \, mW/cm^2$–1.3; at PD 5–$10 \, mW/cm^2$–2; at PD 10–$25 \, mW/cm^2$–3; at PD 25–$50 \, mW/cm^2$–5 [4].

Modified PE criteria might be a key to the correlation between biological effects and the two different approaches of dosimetry. Exposure depending on time duration might make possible the creation of a common estimate of electromagnetic field biological action. The basis of EMF biological efficiency assessment may be the proposed Russian scale of biological effects in the last century [4, 5]. The biological effects of EMF exposure (depending of reaction intensity) can be divided into several categories: perception, adaptation, compensation, reparative regeneration, pathology. Each step of reaction can be characterized by its own threshold EM values of intensity and development times. The magnitude of an effect grows not only with the exposure intensity but also with the exposure time. Progressing through stages of reactions to EMF exposure of various intensities, it is possible to define a range of outcomes. This range can be divided into some areas. In the ideal case, transitions between areas represent thresholds of action of the exposure (see Fig. 1).

The biological effects of RF exposures are not always harmful. Threshold events should be defined statistically. Significant transitions are considered those changes whose occurrence in experiments exceeds 95% ($p < 0.05$). However, not all significant changes registered in exposed organism are necessarily to be regarded as harmful, especially when it concerns the establishment

Figure 1: Scale of biological effects depending on different EM exposure.

of threshold EMF levels.

According to the accepted criteria, are considered threshold only the minimum EMF levels which cause changes in an organism. These changes are characterized by one of following signs:

a) Significant changes ($p < 0.05$) from the controls which fall outside the limits ($> 2\sigma$) of the physiological fluctuations of an indicator for the given kind of animals and for the given season (σ is a standard deviation of the evaluated parameter).

b) Significant changes ($p < 0.05$) in comparison with the control are not present. Latent unbalance with the environment (narrowing of adaptation possibilities) are observed. In particular, they are revealed by means of functional changes of vital parameters (behavioral, blood, immune, etc.) and extreme loadings (reactions fall outside the limits $\pm 2\sigma$ corresponding norm).

c) Significant changes ($p < 0.05$) from the control. They are at the limits of physiological normality, but persist over time (in experimental animals — more than 1 month).

It is possible to find a correlation of these thresholds for far field and near field exposures using the more convenient dosimetric parameter and calculating the other.

5. CONCLUSION

Definition of similar unequivocal interrelation between SAR and PD will allow the development of more adequate approaches to dosimetry harmonization. A synthesis of the positive features of the two existing dosimetric approaches in a uniform concept will create a base for a new step to safety standard harmonization.

Using single approach to assessment of EMF biological effects exposure will give science-based foundation not only to Russian and international safety standard harmonization, but it will allow to develop single international RF EMF approach. But undoubtedly, modern dosimetry approach, EMF biological effect studies on laboratory animals and epidemiological investigations are the basis for developing more advanced international safety standard.

REFERENCES

1. American Standards Association, "Safety levels of electromagnetic radiation with respect to personnel," USASI standard C95.1-1966.
2. ICNIRP Guidelines, "Guidelines for limiting exposure to time-varying electric, magnetic and electromagnetic fields (up to 300 GHz)," *Health Physics*, Vol. 74, No. 4, 494–522, 1998.
3. SanPiN 2.2.4.1191-03 Sanitary norms and rules, "Electromagnetic fields in occupational conditions," Moscow, 2003 (in Russian).
4. Savin, B. M., "Hygienic rationing of non-ionizing radiation," *Hygienic Rationing Factors of Occupational Condition and Labor Process*, Medicine, Moscow, 115–146, 1986 (in Russian).
5. Savin, B. M., "Hygienic electromagnetic rationing problem at modern," *Methodical Questions of Hygienic Rationing*, NII GT I PZ AMN SSSR, Moscow, 12–42, 1979 (in Russian).

Microwave Effect on Proteins in Solution — Fluorescence Polarization Studies

I. Barak, **M. Golosovsky**, and **D. Davidov**

The Racah Institute of Physics, The Hebrew University of Jerusalem
Jerusalem 91904, Israel

Abstract— We studied the fluorescence emission of the Enhanced Green Fluorescent Protein (EGFP) in aqueous solution under continuous microwave irradiation with a well-defined field pattern (a TE_{011} microwave cavity operating at 9.5 GHz). We focused on polarization of the emitted light and measured the spectrum of the fluorescence emission anisotropy. We found that in the spectral range 500–540 nm the microwave-induced effect can be reduced to heating, while in the spectral range 540–560 nm, the microwave-induced effect differs from that resulting from conventional heating.

1. INTRODUCTION

Whether or not microwave irradiation can exert a non thermal effect on biomolecules is a controversial issue [1, 2]. Calculations showed that the resonant excitation of a molecule in aqueous solutions, as well as the thermal gradient between the molecule and its surroundings, is negligibly small at microwave frequencies [3, 4], in such a way that the non thermal effect of microwave fields on proteins may be discernible only at extremely high electric field $> 10^7$ V/m [5, 6]. The empirical evidence for the non thermal microwave effect on biomolecules is inconclusive. The X-ray studies of the microwave effect on the protein conformation in the crystalline form [7]; fluorescence studies of organic fluorophores [8]; the functioning of ion channels in living cells under microwave irradiation [9] did not reveal non thermal microwave effects. Several other studies [10–13] reported a specific microwave effect which cannot be reduced entirely to macroscopic heating.

The possible pathways by which microwaves could affect chemical and biochemical processes include orientational effects [1, 2] although only a few works [8–10, 14] addressed these issues so far. In this study we apply the microwave field with a well-defined geometry and focus on such microwave-induced protein response that carries information about protein orientation. This could be the polarization of the fluorescence emission which is characterized by the fluorescence anisotropy:

$$r = \frac{I_s - GI_p}{I_s + 2GI_p}. \tag{1}$$

Here I_s, I_p are the intensities of the emitted light with the s- and p-polarizations and G is a calibration factor [15]. The maximum value of the fluorescence anisotropy, achieved for polarized light excitation in the ensemble of immobile molecules with parallel absorption and emission transition moments, is $r_0 = 0.4$. The partial loss of the fluorescence anisotropy, due to random fluorophore rotation in liquid, is described by the Perrin equation

$$r = \frac{r_0}{1 + \tau_F/\tau_D} \tag{2}$$

where τ_F is the fluorescence lifetime, $\tau_D = \eta V/k_B T$ is the rotational correlation time, η is the solvent viscosity and V is the hydrodynamic volume of the fluorescent molecule.

We compared the fluorescence emission spectra $I_s(\lambda), I_p(\lambda)$ of the aqueous solution of the Enhanced Green Fluorescent Protein (EGFP) under continuous microwave irradiation and under conventional heating. The EGFP [16] has $\tau_D = 13$–18 nsec, $\tau_F = 2.6$–3 nsec [17–19], and $r_0 = 0.38$–0.39 [15].

Figure 1 shows our optical setup. A glass pipette with an inner diameter of 1.2 mm and an outer diameter of 1.5 mm contained $\sim$ 5 μl of the 0.84-mg/ml solution of EGFP in Tris buffer with pH 8.0 [11]. The pipette was mounted in the center of a TE_{011} microwave cavity operating at 9.5 GHz and made of 5-mm thick brass (Fig. 2). The fluorescence was excited by a linearly polarized 488-nm Argon laser and was measured by a photomultiplier followed by a photon counter. To determine calibration factor G in Eq. (1) (it takes into account different sensitivities of the detector channel
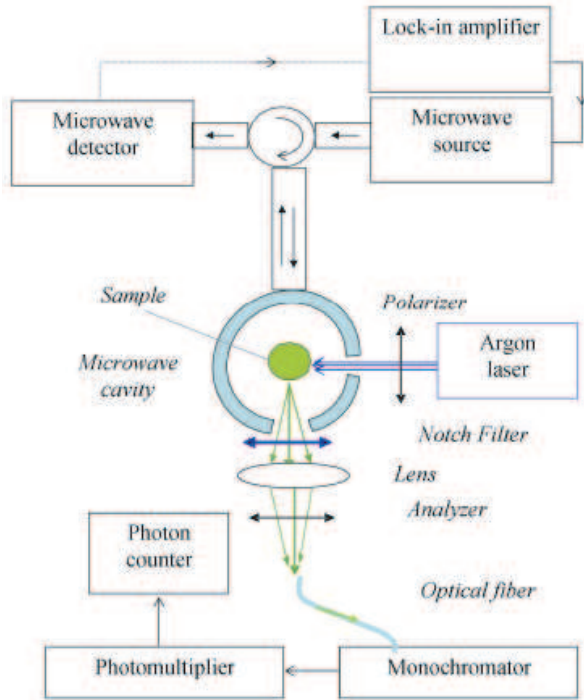
Figure 1: Experimental setup to measure the fluorescence anisotropy of solutions under microwave irradiation. The sample is mounted in the center of the TE_{011} cylindrical microwave cavity (top view). A vertically polarized laser beam passes through a small hole in the cavity wall and excites fluorescence of the sample. Fluorescence emission is measured at 90° to the incident beam using a microscope objective lens coupled to a monochromator via an optical fiber and polarization analyzer. The notch filter blocks scattered laser light. The microwave energy is supplied from the HP-83623A synthesizer through the circulator. The microwave frequency is locked to the resonant frequency of the cavity. Microwave reflection from the cavity is monitored by the microwave detector and lock-in amplifier.
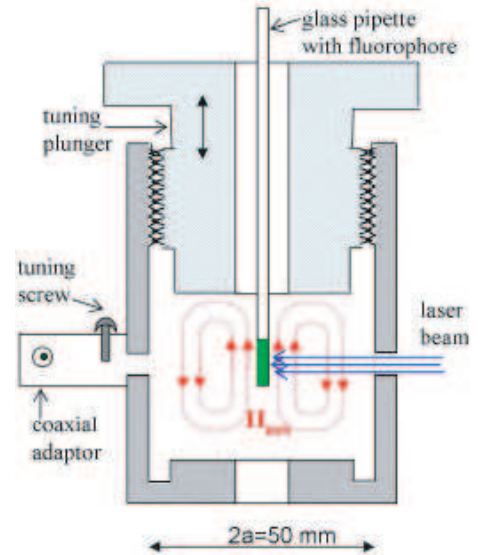
Figure 2: The TE_{011} cylindrical cavity resonator has an inner diameter $2a = 50$ mm and variable height ($d = 20$ to 30 mm). The resonant frequency is 9.5 GHz and it is adjusted by the tuning plunger. The microwave energy is supplied through the coaxial adaptor via the coupling hole equipped with a tuning screw. The glass pipette with a fluorophore is mounted in the center of the cavity. Two small holes of 2-mm diameter in the cavity sidewalls allow optical access to the sample.

with respect to s- and p-polarization) we used a 1 mM solution of Rhodamine 6G (Rh6G) that consists of small molecules and is characterized by a negligible fluorescence anisotropy.

The microwave electric field at the sample location is solenoidal (Fig. 3, inset). This minimizes the field perturbation introduced by a high-ϵ sample and eliminates the problem of interfacial polarization since there is no electric field component perpendicular to the liquid-glass or liquid-air interface. Using analytical expression for the fields of the TE_{011} cylindrical cavity [20] we obtained the components of the microwave electric field in the cavity center

$$E_R = 0, E_z = 0, E_\phi \approx \frac{26.9R}{a} \left(\frac{P_{in}Q}{\omega \epsilon_0 V_c} \right)^{0.5} \tag{3}$$

where R is the radial coordinate, a is the cavity radius, $V_c = \pi a^2 d$ is the cavity volume, ω is the resonance frequency, Q is the Q-factor, P_{in} is the incident microwave power, and ϵ_0 is the dielectric permittivity of free space.

The resonance frequency of our cavity was tuned to 9.5 GHz by adjusting the cavity height, d. The Q-factor in the absence and the presence of the sample was $Q_u \approx 3000$ and $Q_L \approx 1000$, correspondingly. To estimate the fields at the sample location we substituted into Eq. (3): $Q_L = 1000, P_{in} = 250$ mW, $V_c = 48$ cm^3, $a = 25$ mm, $R = 0.6$ mm and obtained $E_{max} = 2027$ V/m.

The bulk heat production rate resulting from the microwave absorption in the sample, $q = \omega \epsilon_0 \epsilon_r'' E^2 / 2$, has a circular spatial pattern, $q \propto R^2$, whereas the maximum q is achieved at the sample periphery. We substituted there $\epsilon_r = 60 - i30$ and obtained the total absorbed power,

$P_{abs} = \int q dV = 162\,\text{mW}$ (this corresponds to the specific absorption rate of SAR $= 3.2 \times 10^4\,\text{W/kg}$). Most part of the heat is carried away due to effective convective cooling ensured by the openings in the cavity top and bottom (Fig. 2).

The temperature gradient across the sample was found by approximating it by an infinitely long cylinder of radius R and height $h \gg R$ which is held at constant surface temperature. The Poisson equation for heat transfer, $\frac{d^2T}{dR^2} + \frac{1}{R}\frac{dT}{dR} + \frac{q}{\kappa} = 0$, yields $\Delta T(R) = \Delta T_0 - P_{abs}R^4/6\pi h\kappa R_0^4$ where κ is the thermal conductivity of the sample, and ΔT_0 is the difference between the temperature in the center and the periphery. For $h = 5\,\text{mm}$, $R_0 = 0.6\,\text{mm}$, $\kappa = 0.6\,\text{W/mK}$ and $P_{abs} = 162\,\text{mW}$ the above equation yields $\Delta T = 2.9\,\text{K}$. For our convectively cooled sample we can not reliably calculate ΔT_0 from the thermal model, so we found it experimentally: $\Delta T_0 = 9.7\text{–}12.5\,\text{K}$.

2. EXPERIMENTAL

2.1. Experimental Procedure

We introduced the glass pipette with the fluorescent solution into the microwave cavity, tuned the microwave source to match the resonant frequency of the cavity, and tuned the screw coupler to achieve critical coupling. The microwave power was then switched off and we measured the fluorescence spectrum for s- and for p-polarizations (~ 1 minute per spectrum). The microwave power was then switched on, we waited for several minutes until the fluorescence intensity arrived to a steady-state, and measured the fluorescence spectrum under continuous microwave irradiation. Then we switched the microwave off, waited for several minutes and measured the fluorescence spectrum once again. Fig. 3 shows reversible decrease of the EGFP fluorescence intensity under microwave irradiation by 16%. We found that this percentage linearly depended on microwave power. In all subsequent experiments we operated at the highest available incident power of 250 mW.

To estimate the microwave-induced temperature rise in solution we performed the same set of experiments with another fluorophore, Rhodamine 6G. The fluorescence of the Rh6G solution in water is unpolarized, and we expected that in this case the microwave irradiation effect is reduced to heating. By comparing the fluorescence intensity of the Rh6G solution under conventional and microwave heating we found that the effect of 250 mW microwave irradiation is to rise the temperature of the 5 µl sample by 9.7–12.5 K.

To perform experiments under conventional heating we used the same sample and sample holder
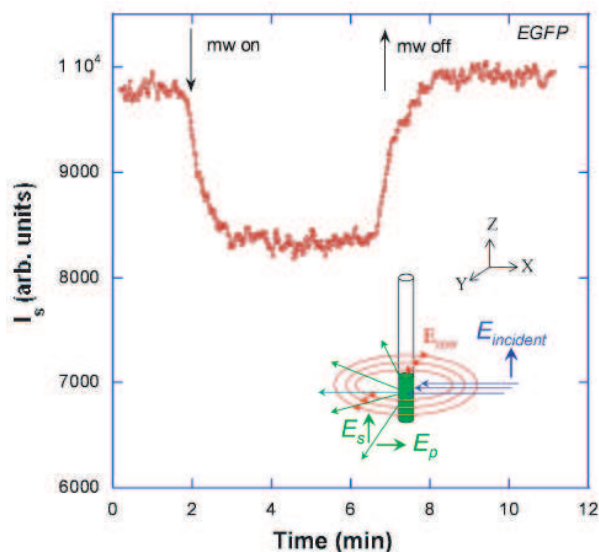
Figure 3: Time dependence of the EGFP fluorescence intensity under continuous 250 mw microwave irradiation. The inset shows orientation of the microwave and optical electric fields. The microwave electric field forms a circular pattern confined in the x-y plane. The electric field of the optical excitation is $E_{incident}\|z$, while $E_{mw}^z = 0$.
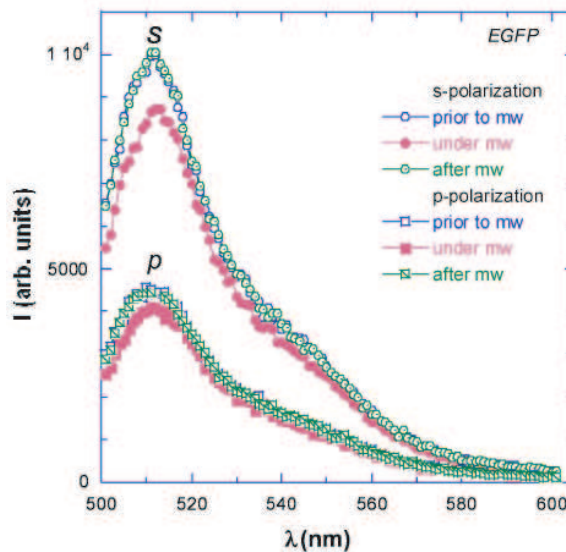
Figure 4: Microwave effect on the EGFP fluorescence spectrum. The open/solid/crossed symbols denote the fluorescence prior to/under/after microwave irradiation, correspondingly. The microwave power is 250 mW and the frequency is 9.5 GHz. Under microwave irradiation, the fluorescence intensity decreases and the spectrum is red-shifted.

but replaced the microwave cavity with the water bath that was heated externally by a hot plate. The fluorescence spectrum of the pipette immersed in the water bath was measured at several fixed temperatures (measured by thermocouple immersed in the bath) and the temperature dependence of the fluorescence intensity was determined.

2.2. Experimental Results

Figure 4 shows the fluorescence emission spectrum of the EGFP solution. The spectrum exhibits a main peak at 510 nm and a vibronic satellite at 540 nm [21]. Under continuous microwave irradiation the fluorescence intensity decreases and the spectrum is red-shifted. These changes are roughly consistent with the microwave-induced temperature rise of 9.7–12.5 K found in our experiments with Rh6G.

Figure 5 compares the EGFP fluorescence emission anisotropy spectra at two different temperatures. The temperature rise results in overall decrease of the fluorescence anisotropy whereas the r-spectra at different temperatures are quite similar: r slightly decreases at long wavelengths. A similar spectral dependence was observed earlier [22] and it could result from the superposition of fluorescence emissions with different lifetimes [23, 24].

Figure 6 compares the EGFP fluorescence emission anisotropy spectrum with and without microwave irradiation. The overall decrease of the fluorescence anisotropy under microwave irradiation can be attributed to the temperature rise resulting from the microwave heating of solution, and to associated reduction of the water viscosity (Eq. (2)). However, the spectra of r^{nomw} and r^{mw} slightly differ — note the bump in the r^{mw} at 540–560 nm. This difference is emphasized when we plotted the microwave-induced change, $\Delta r^{mw} = r^{nomw} - r^{mw}$. Whereas the temperature-induced
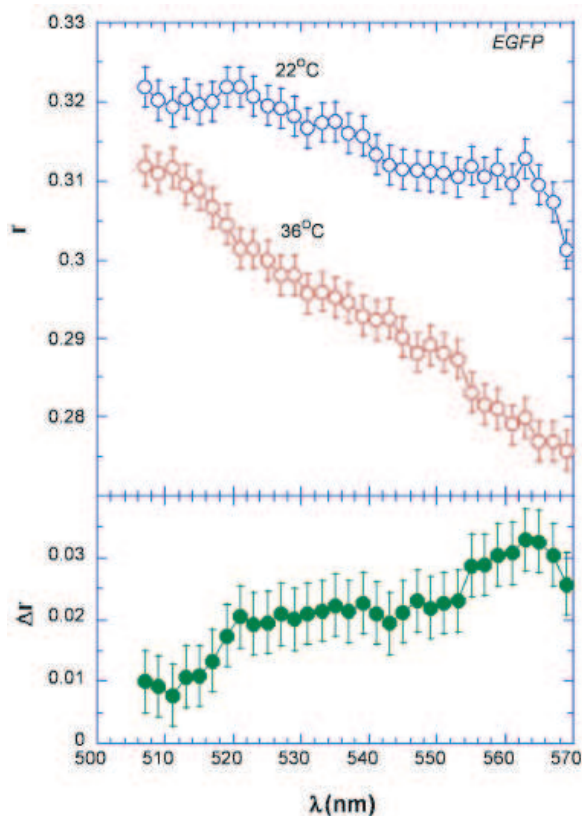
Figure 5: Fluorescence emission anisotropy spectrum of the EGFP solution at two different temperatures. The lower panel shows the temperature-induced fluorescence anisotropy variation under 14 K temperature rise, $\Delta r^T = r(22°C) - r(36°C)$. The fluorescence anisotropy decreases upon heating due to reduced solvent viscosity.
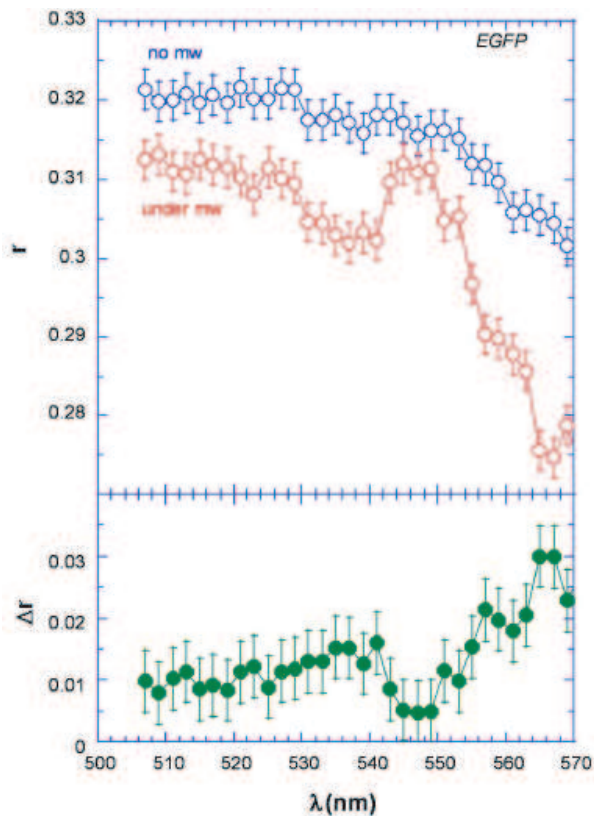
Figure 6: Fluorescence emission anisotropy spectrum of EGFP under continuous 250 mW microwave irradiation. The lower panel shows the microwave-induced fluorescence anisotropy variation, $\Delta r^{mw} = r^{nomw} - r^{mw}$. Under microwave irradiation, the fluorescence anisotropy decreases mostly owing to heating by 9.7–12.5 K. However, the spectrum of Δr^{mw} is not identical to Δr^T (Fig. 5), in particular, note a dip at 540–560 nm.

$\Delta r^T = r(T) - r(T + \Delta T)$ does not exhibit spectral features, the microwave-induced Δr^{mw} displays a dip at 540–560 nm. This experiment was performed four times and three times out of four we observed the spectral feature at 540–560 nm.

3. DISCUSSION

The dominant microwave irradiation effect on the EGFP fluorescence anisotropy is the temperature rise associated with microwave heating. This affects the water viscosity ($\Delta \eta / \eta = -5.4\%/$ K) and the EGFP fluorescence lifetime ($\Delta \tau_F / \tau_F = -1.1\%/$ K [25]) and results in the wavelength-independent reduction of r. The Δr^T under conventional heating is indeed almost wavelength-independent. However, the microwave-induced reduction of the fluorescence anisotropy has a spectral feature at 540–560 nm. Although this feature is small and only slightly exceeds the measurement error, it can not be discarded.

It could look as if the microwave radiation induces some preferential alignment of the EGFP emitting dipoles. However, the absorption and emission dipole moments of EGFP are nearly parallel ($r_0 \sim r_0^{\max} = 0.4$), therefore the microwave electric field can hardly align them better. Note however, that the alleged microwave effect appears in the vicinity of the vibronic transition at 540 nm and r_0 for vibronic transitions can be different from 0.4 [26].

The microwave dielectrophoretic effect is not very probable since the microwave period of 0.1 nsec is much shorter than the rotational diffusion time of EGFP, $\tau_D = 13$–18 nsec. While molecular orientation in the electric field of 10^5–10^6 V/m can produce an appreciable effect on the fluorescence anisotropy of biomolecules with a permanent dipole moment [6, 27] the EGFP molecules do not have such dipole moment [28], hence this mechanism is improbable here. The proton transfer that in principle could be affected by the microwave electric field, is also improbable since EGFP consists mostly of deprotonated forms [23, 24].

Enhanced fluorescence anisotropy in the spectral range 540–560 nm could imply microwave-induced fluorescence lifetime reduction (see Eq. (2)). However, the microwave electric field in our experiments is too small to expect such electric field quenching [6].

In summary, microwave irradiation affects polarization of the EGFP fluorescence. The fluorescence anisotropy of the main 510 nm fluorescence peak is reduced owing to microwave heating. However, microwave effect on the EGFP fluorescence anisotropy in the spectral range 540–560 nm (that corresponds to vibronic transition) is not reduced to heating. No satisfactory explanation of this small effect has been found. This calls for further studies, including different microwave or optical excitation schemes, such as fluorescence excitation anisotropy spectrum, time-resolved measurements, etc. The main limitation of our present study is that although the microwave field is always perpendicular to the optical electric field, it does not have definite orientation in the plane. It would be preferable to use in such studies a linearly polarized microwave electric field. However, this is associated with numerous side effects and requires a very different microwave setup.

ACKNOWLEDGMENT

REFERENCES

1. De la Hoz, A., A. Diaz-Ortiz, and A. Moreno, "Microwaves in organic synthesis. Thermal and non-thermal microwave effects," *Chem. Soc. Rev.*, Vol. 34, 164–178, 2005.

2. Kappe, C. O. and A. Stadler, *Microwaves in Organic and Medicinal Chemistry*, Wiley-VCH, Weinheim, 2005.

3. Adair, R. K., "Biophysical limits on athermal effects of RF and microwave radiation," *Bioelectromagnetics*, Vol. 24, 39–48, 2003.

4. Foster, K. R., "Thermal and nonthermal mechanisms of interaction of radio-frequency energy with biological systems," *IEEE Trans. Plasma Science*, Vol. 28, 15–23, 2000.

5. Suydam, I. T., C. D. Snow, V. S. Pande, and S. G. Boxer, "Electric fields at the active site of an enzyme: Direct comparison of experiment with theory," *Science*, Vol. 313, 200–204, 2006.

6. Nakabayashi, T., M. Kinjo, and N. Ohta, "Electric field effects on fluorescence of the green fluorescent protein," *Chem. Phys. Lett.*, Vol. 457, 408–412, 2008.

7. Weissenborn, R., K. Diederichs, W. Welte, G. Maret, and T. Gisler, "Non-thermal microwave effects on protein dynamics? An X-ray diffraction study on tetragonal lysozyme crystals," *Acta Cryst. B*, Vol. 61, 163–172, 2005.

8. Aslan, K. and C. D. Geddes, "Microwave-accelerated metal-enhanced fluorescence: Platform technology for ultrafast and ultrabright assays," *Anal. Chem.*, Vol. 77, 8057–8067, 2005.

9. Olapinski, M., S. Manus, N. Fertig, and F. C. Simmel, "Probing whole cell currents in high-frequency electrical fields: Identification of thermal effects," *Biosensors & Bioelectronics*, Vol. 23, 872–878, 2008.

10. Bohr, H. and J. Bohr, "Microwave-enhanced folding and denaturation of globular proteins," *Phys. Rev. E*, Vol. 61, 4310–4314, 2000.

11. Copty, A. B., Y. Neve-Oz, I. Barak, M. Golosovsky, and D. Davidov, "Evidence for a specific microwave radiation effect on the green fluorescent protein," *Biophys. J.*, Vol. 91, 1413–1423, 2006.

12. George, D. F., M. M. Bilek, and D. R. McKenzie, "Non-thermal effects in the microwave induced unfolding of proteins observed by chaperone binding," *Bioelectromagnetics*, Vol. 29, 324–330, 2008.

13. Hamad-Schifferli, K., J. J. Schwartz, A. T. Santos, S. G. Zhang, and J. M. Jacobson, "Remote electronic control of DNA hybridization through inductive coupling to an attached metal nanocrystal antenna," *Nature*, Vol. 415, 152–155, 2002.

14. Previte, M. J. R. and C. D. Geddes, "Fluorescence microscopy in a microwave cavity," *Optics Express*, Vol. 15, 11640–11649, 2007.

15. Lakowicz, J. R., *Principles of Fluorescence Spectroscopy*, Kluwer, N.Y., 1999.

16. Zimmer, M., "Green fluorescent protein (GFP): Applications, structure, and related photophysical behavior," *Chem. Rev.*, Vol. 102, 759–781, 2002.

17. Hess, S. T., E. D. Sheets, A. Wagenknecht-Wiesner, and A. A. Heikal, "Quantitative analysis of the fluorescence properties of intrinsically fluorescent proteins in living cells," *Biophys. J.*, Vol. 85, 2566–2580, 2003.

18. Uskova, M. A., et al., "Fluorescence dynamics of green fluorescent protein in AOT reversed micelles," *Biophys. Chem.*, Vol. 87, 73–84, 2000.

19. Suhling, K., D. M. Davis, and D. Phillips, "The influence of solvent viscosity on the fluorescence decay and time-resolved anisotropy of green fluorescent protein," *J. Fluorescence*, Vol. 12, 91–95, 2002.

20. Poole, C. P., *Electron Spin Resonance*, Wiley, N.Y., 1983.

21. S. S. Stavrov, K. M. Solntsev, L. M. Tolbert, and D. Huppert, "Probing the decay coordinate of the green fluorescent protein: Arrest of cis-trans isomerization by the protein significantly narrows the fluorescence spectra," *J. Am. Chem. Soc.*, Vol. 128, 1540-1546, 2006.

22. Haldar, S. and A. Chattopadhyay, "Dipolar relaxation within the protein matrix of the green fluorescent protein: A red edge excitation shift study," *J. Phys. Chem. B*, Vol. 111, 14436–14439, 2007.

23. Heikal, A. A., S. T. Hess, and W. W. Webb, "Multiphoton molecular spectroscopy and excited-state dynamics of enhanced green fluorescent protein (EGFP): Acid-base specificity," *Chem. Phys.*, Vol. 274, 37–55, 2001.

24. Cotlet, M., et al., "Excited-state dynamics in the enhanced green fluorescent protein mutant probed by picosecond time-resolved single photon counting spectroscopy," *J. Phys. Chem. B*, Vol. 105, 4999–5006, 2001.

25. Pepperkok, R., A. Squire, S. Geley, and P. I. H. Bastiaens, "Simultaneous detection of multiple green fluorescent proteins in live cells by fluorescence lifetime imaging microscopy," *Current Biology*, Vol. 9, 269–272, 1999.

26. Zondervan, R., F. Kulzer, H. van der Meer, J. A. J. M. Disselhorst, and M. Orrit, "Laser-driven microsecond temperature cycles analyzed by fluorescence polarization microscopy," *Biophys. J.*, Vol. 90, 2958–2969, 2006.

27. Suzuki, S., T. Yamanashi, S. Tazawa, O. Kurosawa, and M. Washizu, "Quantitative analysis of DNA orientation in stationary AC electric fields using fluorescence anisotropy," *IEEE Trans. Industry Appl.*, Vol. 34, 75–83, 1998.

28. Wallace, P. M., D. R. B. Sluss, L. R. Dalton, B. H. Robinson, and P. J. Reid, "Single-molecule microscopy studies of electric-field poling in chromophore-polymer composite materials," *J. Phys. Chem. B*, Vol. 110, 75–82, 2006.

Ion Cyclotron Bioresonance in Regenerative Medicine

Alberto Foletti[1] and Settimio Grimaldi[2]

[1]BITitalia, Milan, Italy
[2]Institute of Neurobiology and Molecular Medicine, CNR, Rome, Italy

Abstract— The prometheus myth, is a fitting model for regenerative medicine. As punishment for giving fire to humanity, Zeus ordered Prometheus chained to a rock and sent an eagle to eat his liver each day. However, Prometheus' liver was able to regenerate itself daily, enabling him to survive. Today we hope to make the legendary concept of regeneration into reality by developing therapies to restore lost, damaged, or aging cells and tissues in the human body. Electromagnetic therapy is a treatment method in which an electromagnetic or magnetic stimulus is used to achieve physiological changes in the body. The specific aim of the present work concerns the effectiveness of low frequency electromagnetic fields treatment (tuned at Calcium cyclotron energy resonance) to modify biochemical properties and trigger cells differentiation in a pituitary cells line (AtT20). Cells were exposed to a 7 Hz electromagnetic field (B_o field 9.2 µT) a commercially available wave generator (Vega Select 719), the cyclotron frequency were calculated by the following equation $f_c = \frac{q}{2\pi m} B_o$, where f_c is the cyclotron frequency, q and m are the charge and mass of the ion, and B_o is the vector of the geomagnetic field (DC field) parallel to the component of the applied electromagnetic field ($B \sin$). In our case since the geomagnetic component (B_o) parallel to the applied $B \sin$ is 9.2 µT, the calculated f_c for calcium is 7 Hz. Here, we report that 50 Hz 2 mT ELF-EMF on rat anterior pituitary derived AtT20 D16V cells produces a sudden increase in the intracellular calcium level, followed by the reorganization of the cytoskeletal network via the polymerization of the actin and the differentiation of the proteins expression. These findings demonstrate that exposure to cyclotron resonance can transfer biological information on pituitary cells, supporting the relevance of low frequency electro-magnetic field as a therapeutic agent, thus suggesting the potential use of cyclotron resonance in nerve regeneratrion.

1. INTRODUCTION

The aim of this work is the study of the effect of electromagnetic radiations (ELF-EMF) at a frequency of 7 Hz on the differentiation process of pituitary corticotrope-derived AtT20 D16V cells. These cells respond to nerve growth factor (NGF) [1] by extending neurite-like processes and differentiating into neurosecretory-like cells. To establish whether exposure to the field could influence the molecular biology of the pituitary gland; a corticotrope-derived cells line (AtT20 D16V) was exposed to ELF-EMF at a frequency of 7 Hz, and a magnetic flux density of 20 micro Tesla (µT).

2. MATERIALS AND METHODS

2.1. Cell Culture

AtT20 D16V cells (American Type Culture Collection, Rockville, MD) were grown in monolayer culture on thin (00) glass cover slips (Corning Glass Works, Corning, NY) coated with poly-L-lysine, or in plastic culture flasks, in Dulbecco's Modified Eagle's Medium (DMEM) supplemented with 5% fetal calf serum, 1.0 unit/ml penicillin, and 1.0 mg/ml streptomycin (Sigma Chemical Company, St. Louis, MO) at 37°C a humidified incubator in 95% air and 5% CO_2. Cells were plated at 250,000/ml.

2.2. ELF-EMF Exposure Systems

Cells were continuously exposed in a small solenoid placed in a cells incubator the field were supplied by a commercial signal generator (Vega select 719).

2.3. Electrophoresis

SDS-polyacrylamide gel electrophoresis (SDS-Page) was carried out according to Laemmli, 1970. After exposure to Calcium ICR electromagnetic fields, equal amount of cell proteins from control and exposed cells, measured by Lowry test, were loaded for each line, after lysis in sample buffer. The samples were boiled for 5 minutes. Electrophoresis was carried on 7.5% SDS polyacrilamide gel at 30 mA for about 2 hours. Gel was subsequently transferred on nitrocellulose membrane (Biorad) at 200 mA for 3 hours, and membrane, after blocking in 3% not dried fat milk for 1 hours at room temperature, was incubated NF-200 antibody (Sigma) at a dilution of 1:100 as suggested by manufacturer and revealed by ECL (Amersham).

Three different sets of experiments were performed.

3. RESULTS

In Fig. 1 is reported the effect of 7 Hz continuous exposure on AtT20cells (right panel) compare with control non exposed cells (left panel). Arrows indicate the formation of neurite like protrusion between cells.

In Fig. 2 is a western blot electrophoresis of the protein extract from 7 Hz cultured and control AtT20 cells. Clearly exposure induces synthesis of the neurite protein NF-200 in the exposed cells, while the NF-200 is almost non present in a control culture.
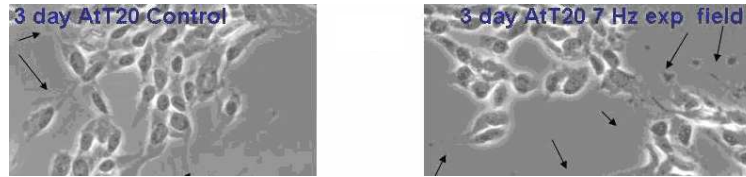
Figure 1: Phase contrast microscopy of 7 Hz exposed AtT20 cells.
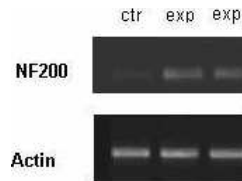
Figure 2: Western blot analysis of control and 7Hz exposed AtT20 cells.

4. CONCLUSIONS

AtT20 D16V is an interesting cell line because it expresses all enzymes required for polysialylation of neural cell adhesion molecule (NCAM). Additionally, the AtT20 D16V clone D16V, is known, to spontaneously develop, after 5 days of culture, long neurite-like processes in the growth cones where ACTH secretory granules accumulate.The findings that in exposed samples, cells more rapidly exhibit properties typical of peptidergic neuronal cells (Fig. 2) is further supported both by the synthesis and accumulation of the neuronal protein NF-200. Our results suggests that exposure to 7 Hz EMF can be used as a tool to initiate differentiation in AtT20 D16V cells.

REFERENCES

1. Lisi, A., M. Ledda, E. Rosola, D. Pozzi, E. D'Emilia, L. Giuliani, A. Foletti, A. Modesti, S. J. Morris, and S. Grimaldi, "Extremely low frequency electromagnetic field exposure promotes differentiation of pituitary corticotrope-derived AtT20 D16V cells," *Bioelectromagnetics*, Vol. 27, No. 8, 641–651, 2006.

2. Foletti, A., A. Lisi, M. Ledda, F. De Carlo, and S. Grimaldi, "Cellular ELF signals as a possibile tool in informative medicine," *Electromagn. Biol. Med.*, Vol. 28, No. 1, 71–79, 2009.

3. Liboff, A. R., "Toward an electromagnetic paradigm for biology and medicine," *J. Altern. Complement. Med.*, Vol. 10, No. 1, 41–47, Review, 2004.

4. Lisi, A., S. Rieti, A. Cricenti, A. Flori, R. Generosi, M. Luce, P. Perfetti, A. Foletti, M. Ledda, E. Rosola, L. Giuliani, and S. Grimaldi, "ELF non ionizing radiation changes the distribution of the inner chemical functional groups in human epitelial cell (HaCaT) culture," *Electromagnetic Biology and Medicine*, Vol. 25, 281–289, 2006.

5. Lisi, A., M. Ledda, F. De Carlo, D. Pozzi, E. Messina, R. Gaetani, I. Chimenti, L. Barile, A. Giacomello, E. D'Emilia, L. Giuliani, A. Foletti, A. Patti, A. Vulcano, and S. Grimaldi, "Ion cyclotron resonance as a tool in regenerative medicine," *Electromagnetic Biology and Medicine*, Vol. 27, No. 2, 127–133, 2008.

6. Lisi, A., M. Ledda, F. De Carlo, A. Foletti, L. Giuliani, E. D'Emilia, and S. Grimaldi, "Ion Cyclotron Resonance (ICR) transfers information to living systems: Effects on human epithelial cell differentiation," *Electromagnetic Biology and Medicine*, Vol. 27, No. 3, 230–240, 2008.

7. Lisi, A., A. Foletti, M. Ledda, E. Rosola, L. Giuliani, E. D'Emilia, and S. Grimaldi, "Extremely low frequency 7 Hz 100 µT electromagnetic radiation promotes differentiation in the human epitelial cell line HaCaT," *Electromagnetic Biology and Medicine*, Vol. 25, 269–280, 2006.

A Definition of Thermophysiological Parameters of SAM Materials for Temperature Rise Calculation in the Head of Cellular Handset User

S. I. Al-Mously[1] and M. M. Abousetta[2]

[1]Department of Electrical and Computer Engineering
School of Applied Sciences and Engineering, Academy of Graduate Studies, Tripoli, Libya
[2]Department of Electrical and Electronics Engineering, Faculty of Engineering
Al-Fateh University, Tripoli, Libya

Abstract— A definition of thermophysiological parameters of the Specific Anthropomorphic Mannequin (SAM) CAD model material is proposed in this paper to calculate the temperature-rise in the head of cellular handset users. The SAM materials have the electrical and thermal parameters based on the averaged properties of a heterogeneous High-Resolution European Female Head (HR-EFH) with twenty five different tissues. The specific absorption rate (SAR) and the temperature-rise in the SAM because of the exposure to radiation of different handset models, i.e., candy-bar with external antenna and candy-bar with internal antenna, are calculated in the GSM900 and GSM1800 using a FDTD-based platform. The computations were also carried out applying HR-EFH for comparison.

1. INTRODUCTION

Since the biological hazards due to RF exposure in cellular communications are caused mainly by a temperature-rise in tissue, calculations of temperature may be preferable to calculations of SAR because of the more direct relationship between temperature and safety. Thus, the effect of localized SAR for portable telephones should also be related to the temperature-rise in the human head.

The temperature increase in the anatomically based human head models due to handset antennas has been calculated in quite a few works, as in [1–3]. In those works, the handset is simulated using either dipole antenna or monopole over a rectangular metal box (dielectric covered or none-covered) or a simple metal chassis with shorted-patch antenna. None of the previous work has considered a realistic or semi-realistic handset models in evaluating their thermal effect on tissues, as considered in this paper.

In this paper, the bioheat equation is solved using a Finite-Difference Time-Domain (FDTD)-based Electromagnetic (EM) solver, *SEMCAD X* [4], to compute the temperature-rise in both anatomically based human head and SAM as related to, first, the antenna radiated power of 0.6 W at 900 MHz and 0.125 W at 1800 MHz, second, safety SAR limits [5, 6].

2. PENNES BIOHEAT EQUATION (BHE)

Temperature ($T = T(x, y, z, t)$ [°C]) was modeled in the head with a finite difference implementation of bioheat transfer equation (BHE), developed by Pennes in 1948 [7]:

$$\rho c \frac{\partial T}{\partial t} = \nabla \cdot (k \nabla T) + \rho Q_{met} + \rho(\text{SAR}) - B(T - T_{blood}) \tag{1}$$

$$B = \rho_{blood} c_{blood} \rho \omega \tag{2}$$

where the ρ [kg/m^3] is the material density, c [J/(kg·°C)] is the specific heat capacity, k [W/(m·°C)] is the thermal conductivity, Q_{met} [W/kg] is the metabolic heat generation rate, B [W/(m^3·°C)] is the blood perfusion coefficient, ω [L/(s·kg)] is the blood perfusion rate, and T_{blood} is blood temperature. In (1), the term on the left represents the rate of change in the stored internal energy of the tissue, the term $\nabla \cdot (k \nabla T) = k \nabla^2 T$ is the heat transfer due to thermal conduction, and the last term relates convection heat loss associated with blood flow. The heat is distributed through the simulation domain by diffusion. It is generated by metabolic body processes and by the deposited radiation energy. A homogeneous 'heat-sink' term has a cooling effect and models the heat removal due to blood circulation.

Heat exchange at the tissue interface with the surrounding environment is modeled by imposing the continuity of heat flow perpendicular to the skin surface as the boundary condition. Various

boundary conditions are commonly applied: the Dirichlet $(T = T_a)$, the Neumann $(k\partial T/\partial n = q)$ and the mixed boundary condition which is used and expressed as;

$$k\frac{\partial T}{\partial n}(x, y, z) = -H_a (T_{skin} - T_a) \left[\frac{\text{W}}{\text{m}^2}\right] \tag{3}$$

where n is the normal to the skin surface and the right hand expression models the heat losses from surface of the skin due to convection and radiation which are proportional to the difference between the skin temperature (T_{skin}) and external environment (ambient) temperature (T_a), H_a is the convection coefficient for heat exchange with the external temperature. In this study, the heating due to RF absorption is very small; therefore, the neglecting of sweating does not make any difference.

3. TEMPERATURE-RISE CALCULATION IN HETEROGENEOUS HEAD MODEL

The temperature-rise in HR-EFH due to handheld set model-A (candy-bar type with external top-loaded short whip antenna) and Model-B (candy-bar type with internal short patch antenna) [8] while in use has been computed at 900 and 1800 MHz. Figure 1 shows both handset models with realistic hand-holding and close to head (HR-EFH and SAM) at *cheek*-position. The tissues electrical properties given in [8] and the thermal properties given in Table 1 are used.

Solving the BHE using the conformal-FDTD method to compute the temperature-rise in handset user's head due to the SAR deposition needs accomplishing two simulations; first, the EM-simulation to compute the deposited SAR in tissue, second, thermo-simulation to compute the temperature-rise in tissue. In the EM-simulation achieved in this paper, the FDTD-grid for each handset setup has a minimum spatial resolution of $0.5 \times 0.5 \times 0.5 \text{ mm}^3$ and maximum resolution of $10 \times 10 \times 10 \text{ mm}^3$ in the x, y, and z directions with grading ratio of 1.2. The absorbing boundary conditions (ABCs) are set as U-PML mode with 10 layers thickness [4]. This FDTD-grid setting is also applied in thermo-simulation. A mixed boundary condition given in (3) involving skin plus ears is used with convection coefficient $(H_a = 2.7 \text{ W}/(\text{m}^2 \, ^\circ\text{C}))$ and ambient temperature $(T_a = 25^\circ\text{C})$. The core temperature is $(T_{blood} = 37^\circ\text{C})$. The heat exchanged through the neck and the other remaining parts of the body has been approximated by means of setting the neck boundary temperature as the blood temperature.

It should be noticed that the results based on experiments involving animals are used for most of the thermal parameters required in the human-head model [2]. Since no solid relations describing the thermal parameters dependency on the minor expected temperature-rise in head of the handset user; in this paper, blood perfusion coefficient is modeled to be linearly temperature dependent as based on the temperature distribution and blood perfusion response in rat brain during selective brain cooling presented by Diao and Zhu in [9]. Although the heat dissipation in the skin of rats differs from that of in the human skin, the experiment results presented in [9] are used to approximate per 1°C blood perfusion in brain, skin and ears tissue at a rate value of 13%, while computing the temperature-rise in the head of handset user.

Table 2 depicts the number of generated voxels, the computed SAR(1g) induced in HR-EFH
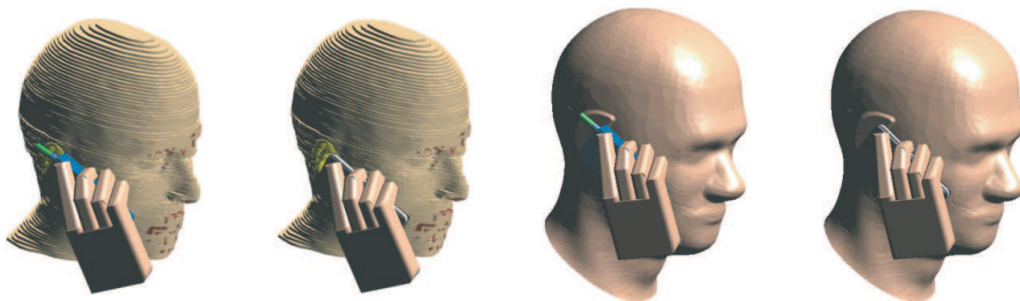
Figure 1: Handset models-A and B setups for temperature-rise computation in HR-EFH as well as in SAM. (a) Handheld set model-A at *check*-position with HREFH. (b) Handheld set model-B at *cheek*-position with HREFH. (c) Handheld set model-A at *check*-position with SAM. (d) Handheld set model-B at *check*-position with SAM.

Table 1: Mass, mass density and thermal properties assumed for the various HR-EFH tissues [1–3].

HR-EFH Tissue	Mass	ρ [kg/m^3]	c [J/(kg·°C)]	k W/(m·°C)]	Q_{met} [W/kg]	B [W/(m^3·°C)]
1. Air	0.000	1.16	1006	0.0263	0	0
2. Blood Vessel	0.005	1050	3553	0.46	1.52	1000
3. Bone	0.030	1990	1300	0.4	0.15	1000
4. Brain /grey matter	0.871	1039	3700	0.57	9.7	35000
5. Brain /white matter	0.367	1043	3600	0.5	9.7	35000
6. Cerebellum	0.125	1040	4200	0.58	9.7	35000
7. CSF	0.256	1007	4000	0.6	0	0
8. Ear (cartilage)	0.011	1100	3400	0.45	0.2	9100
9. Eye-cornea	0.002	1032	4200	0.58	0.0	0.0
10. Eye-lens	0.002	1090	3000	0.4	0.0	0.0
11. Eye-vitreous body	0.010	1009	4200	0.6	0.34	0
12. Fat	0.032	916	2500	0.25	0.15	520
13. Jaw bone	0.243	1990	1300	0.4	0.15	1000
14. Mastoid cells	0.027	980	2700	0.22	5.82	32000
15. Mid-brain	0.026	1039	3700	0.57	9.7	35000
16. Muscles	0.940	1041	3600	0.5	0.67	2700
17. Nasal cavity	0.063	1050	3300	0.43	1.523	9000
18. Parotid Gland	0.020	1050	3700	0.53	9.7	25000
19. Skin/dermis	0.760	1100	3500	0.42	1.07	9100
20. Skull	0.744	1645	1300	0.4	0.15	1000
21. Spinal cord	0.007	1038	3500	0.46	9.7	35000
22. Spine	0.120	1990	1300	0.4	0.15	1000
23. Thalamus	0.015	1039	3700	0.57	9.7	35000
24. Tongue	0.035	1041	3300	0.42	0.461	13000
25. Ventricles (brain)	0.005	1007	4200	0.6	0	0

Table 2: Number of the generated voxels, peak SAR (1 g) induced in whole HR-EFH and in brain, and the corresponding peak temperature-rise after 60 min of using the handheld set models-A and B with antenna output power of 600 mW at 900 MHz and 125 mW at 1800 MHz.

900 MHz	Position	No. of Voxels	SAR$_{1g}$ in Head (W/kg)	SAR$_{1g}$ in Brain (W/kg)	Max. T in Head (°C)	Max. T in Brain (°C)
Model-A	Cheek	23409725	4.70	2.08	37.43	37.28
	Tilt	22581248	3.70	1.85	37.35	37.25
Model-B	Cheek	24175264	3.88	0.82	37.45	37.26
	Tilt	24226455	2.26	0.62	37.34	37.19
1800 MHz	Position	No. of Voxels	SAR$_{1g}$ in Head (W/kg)	SAR$_{1g}$ in Brain (W/kg)	Max. T in Head (°C)	Max. T in Brain (°C)
Model-A	Cheek	23955708	1.63	0.51	37.31	37.20
	Tilt	24147585	1.62	0.61	37.32	37.21
Model-B	Cheek	24420000	1.60	0.24	37.30	37.14
	Tilt	24680656	1.39	0.23	37.28	37.13

tissues and in brain, i.e., ventricles, thalamus, spinal cord, mid-brain, cerebro spinal fluid, cerebellum, grey matter and white matter, and their corresponding steady-state temperature after 60 min of using the handheld set models-A and B and normalized to antenna radiated power of 600 mW at

900 MHz and 125 mW at 1800 MHz. The 600 mW antenna radiated power is for the analogue phone, whereas, the radiated power of digital generation of GSM mobile phone is 250 mW at 900 MHz. That is because the main aim of the study is to calculate the maximum temperature-rise in human head due to the possible maximum RF emission for the purpose of comparison with previously published works on this subject.

Although the IEEE [5] and FCC [6] standards apply the SAR limit for the extremities to the normal pinnae, and since the used MRI-based head model (HR-EFH) has pressed pinnae; in this paper, the pinnae are subject to the same exposure limit, for peak spatial SAR, as the head. It has been observed that there are no substantial differences between the computed SAR values for the head with and without pressed pinnae, where the peak spatial SAR location is not at the pinna, instead the peak shift to region near the pinna.

The results show that the global maximum field position of both SAR and its corresponding temperature are not identical; while the peak SAR occurs outsid the pinna or skin surfaces depending on the handset position, the peak temperature occurs inside the head tissues and mostly in cheek muscle. Moreover, the handset position plays an important role in convection. For the same SAR values, the handset at *cheek*-position induces more temperature in head than handset at *tilt*-position, and this behavior increased while using handheld set model-B, as compared with handheld set model-A. Positioning the handset close to head at *cheek*-position, first, moves the peak SAR position from the pinna to cheek skin, second, blocks the convective heat exchange between the skin layers and air, causing temperature rises in the tissues around the contact zone.

The computed possible temperature-rise in head and brain (using HR-EFH) for the SAR prescribed in the safety IEEE [5] and FCC [6] standards are 0.3 ± 0.02 and 0.16 ± 0.02, respectively, for the different handset models in different conditions. These results are coinciding with that given in [2].

Simulating the heated-handset with a temperature of 39°C, which measured practically for different commercial cellular handsets, temperatures of 38.36°C and 38.48°C are noticed in the ear tissue for the handset model-A at *cheek* and *tilt*-position, respectively, whereas, temperatures of 38.86°C and 38.85°C are noticed in the ear tissue for the handset model-B at *cheek* and *tilt*-position, respectively, but without any considerable temperature increase in the brain tissue. These results are agreed with that given in [1].

Table 3: The proposed dielectric and thermal parameters of the SAM phantom materials computed using (4). Mass density of the shell = 1100 kg/m^3 and mass density of inside-material = 1000 kg/m^3.

SAM material	Frequency	ε_r	σ [S/m]	c [J/(kg·°C)]	k [W/(m·°C)]	Q_{met} [W/kg]	B [W/(m^3·°C)]
Shell	900 MHz	41.41	0.87	3500	0.42	1.07	9100
	1800 MHz	38.87	1.18				
Inside	900 MHz	41.30	0.79	2982.7	0.49	3.79	14050
	1800 MHz	39.60	1.13				
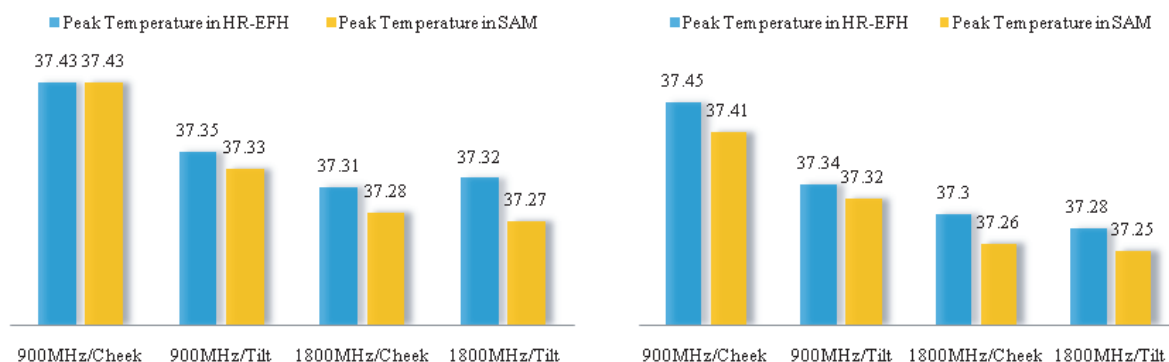
Figure 2: Peak temperature values (°C) corresponding to the spatial peak SAR(1g) values induced in HR-EFH and SAM whole phantom given in Tables 2 and 3 due to; (a) Handheld set model-A and (b) Handheld set model-B, in different conditions.

4. TEMPERATURE-RISE CALCULATION IN SAM

It is essential to have a standard phantom with standard thermophysiological parameters to simulate the temperature-rise in the entire head of cellular handset users, as many anatomically correct head models are available for different sexes, ages, resolutions and number of tissues; with different parameters, which as a result give different temperature-rise induced by cellular handsets [2].

Both pinnae are a part of the shell in the SAM phantom and are not tissue-simulating materials. In order to simulate a real pressed ear, which may play an important role in simulating the temperature-rise in human head due to the RF emission of mobile phone, a definition of thermophysiological parameters of SAM CAD-phantom materials is proposed as follows; the entire shell has the electrical and thermal properties similar to that of HR-EFH skin-tissue, whereas, the lossy inside-material has the electrical and thermal parameters based on the averaged properties of the HR-EFH tissues (excluding skin and cartilage tissues). The electrical and thermal parameters of the 23 different HR-EFH tissues are averaged using the following equation, and considered as the SAM inside-material parameters, Table 3.

$$SAM\ Parameter(n) = \sum_{i=1}^{23} parameter(n)\ of\ \text{HR-EFH}\ tissue(i) \cdot \frac{Mass\ of\ tissue\,(i)}{Head\ total\ mass} \qquad (4)$$

Parameter ($n = 1, 2, 3, 4, 5$ and 6) $\equiv \varepsilon_r, \sigma, c, k, Q_{met}$ and B, respectively. ε_r and σ are frequency dependent.

Using the thermophysiological parameters given in Table 3, the steady-state temperature in SAM materials due to handheld set models-A and B are computed in different conditions, Figure 2.

5. CONCLUSION

The definition of the thermophysiological parameters of the SAM material proposed in this paper show a temperature-rise in head due to the cellular handset comparable to that calculated using an MRI-based heterogeneous head model. Thus, these parameters definition may be applied numerically using SAM phantom to standardize the temperature-rise simulation in the head of cellular handset users.

REFERENCES

1. Bernardi, P., M. Cavagnaro, S. Pisa, and E. Piuzzi, "Power absorption and temperature elevations induced in the human head by a dual-band monopole-helix antenna phone," *IEEE Transaction on Microwave Theory and Techniques*, Vol. 49, No. 12, 1118–1126, Dec. 2001.
2. Hirata, A. and T. Shiozawa, "Correlation of maximum temperature increase and peak SAR in the human head due to handset antennas," *IEEE Transaction on Microwave theory and Techniques*, Vol. 51, No. 7, 1834–1841, Jul. 2003.
3. Fujimoto, M., A. Hirata, J. Wang, O. Fujiwara, and T. Shiozawa, "FDTD-derived correlation of maximum temperature increase and peak SAR in child and adult head models due to dipole antenna," *IEEE Transactions on Electromagnetic Compatibility*, Vol. 48, No. 1, 240–247, Feb. 2006.
4. SEMCAD, X, "Reference manual for the SEMCAD simulation platform for electromagnetic compatibility, antenna design and dosimetry," *SPEAG-Schmid & Partner Engineering AG*, http://www.semcad.com.
5. "Standard for Safety levels with respect to human exposure to radiofrequency electromagnetic fields, 3 kHz to 300 GHz, *IEEE Standards Coordinating Committee*, 28.4, 2006.
6. "Evaluating compliance with FCC guidelines for human exposure to radio frequency electromagnetic field, supplement C to OET bulletin 65, *Federal Communications Commission*, Edition 9701, Washington, DC, USA, 1997.
7. Pennes, H. H., "Analysis of tissue and arterial blood temperature in resting forearm," *J. Appl. Phys.*, Vol. 1, 93–122, 1948.
8. Al-Mously, S. I. and M. M. Abousetta, "Anticipated impact of hand-hold position on the electromagnetic interaction of different antenna types/positions and a human in cellular communications," *International Journal of Antennas and Propagation*, Vol. 2008, Article ID 102759, 22, 2008.
9. Diao, C. and L. Zhu, "Temperture distribution and blood perfusion response in rat brain during selective brain cooling," *Med. Phys.*, Vol. 33, No. 7, 2565–2573, Jul. 2006.

Experimental Investigations of Adaptive Reactance Parasitic Antenna Dipole Array

M. O. Shuralev[1, 2]**, A. L. Umnov**[1, 2]**, A. Mainwaring**[3]**,**
M. A. Sokolov[1, 2]**, and A. U. Eltsov**[1, 2]

[1]Nizhny Novgorod State University, Nizhny Novgorod 603950, Russia
[2]Intel Corporation, Nizhny Novgorod, Russia
[3]Intel Research Laboratory at Berkeley, CA 94704, USA

Abstract— This work describes a simple, low-cost electrically steerable antenna system suitable for long-distance point-to-point links based on WiFi technology. The antenna consists of a tunable mirror, assembled as an array of closely spaced passive dipoles (scatterers) illuminated by one driven element. The scatterers are arranged in multiple layers that contribute overlapping ranges of phase shift. While collectively providing full 360 degrees of phase range, this approach enables individual scatterers to provide greater amplitude response across narrower phase bands. Smoothness of phase composition is guaranteed by the small spacing between layers ($< 0.15\lambda$). Results show that with careful design given the amplitude-phase characteristics of the scatterers, both individually and in aggregates, the antenna can form highly directional beam patterns that are controllable in azimuth and elevation. Experiments demonstrate that an antenna with 500 scatterers, with a $100\,\text{cm} \times 65\,\text{cm}$ aperture, achieves 19–22 dBi of gain across 120 degrees of azimuth and 20 degrees of elevation.

1. INTRODUCTION

Many contemporary information and communication technology (ICT) activities around the world are using low-cost, off-the-shelf radios with directional antennas for long-distance point-to-point wireless links. The antennas provide additional gain that compensate for the low powers ($< 1\,\text{W}$) of the typically unlicensed radios. The use of directional antennas with narrow beams requires that antennas at each endpoint of a link be precisely aligned during installation. Moreover, because some antennas drift out of alignment over time, performance may gradually suffer until a complete outage requires costly and time-consuming on-site maintenance visits. Simple, low-cost electrically steerable antennas have the potential to simplify and reduce the costs of these networks.

High antenna gain can be achieved by using electrically large parabolic reflector, but steering the pattern of such an antenna is non trivial. One possible solution is to move the whole antenna mechanically, but this has disadvantages. Large mechanically steerable antennas require significant hardware power, and they are difficult to adjust either quickly or precisely. Ruze [1] demonstrated that the principal beam direction can be changed slightly by moving the feed position in the focal plane. Such a movement, however, substantially degrades the antenna gain, as the feed point is no longer at the focus. Winter [2] proposed an electrically steerable antenna consisting of a tunable reflective surface illuminated by an active element. This work received its continuation when Durnan [3] used a switched parasitic antenna located at the focus as the feed. Two parasitic elements are displaced vertically from the driven element and have a diode switch located at their center. The vertical polar pattern is controlled electronically by changing the impedance state of the diode. The technique of beam steering by shifting bias voltages has been used in various antennas [4] and relectarrays [5, 6].

The main idea of the antenna system presented in [7] is shown in Figure 1. It uses discrete passive dipoles as an element of the mirror excited by the active RF element. The distance between scatterers in each layer is chosen to be much less than the wavelength in order to minimize power losses due to energy leaking though the layers (the mirror) while providing a wide range of steerability. Another significant feature of its construction is the use of a multi-layered structure. Many efforts focus on extending the phase deviation range of the reemitted or radiated field, and in this regard, are archiving up to 360 degrees range or more, but at the same time there can be significant amplitude deviations, e.g., as in [8] which corresponded to the resonant properties of the elements. The key points with large phase offsets may also have small reemitted/radiated field amplitudes.

The layering of the antenna structure allows operation within other bands of the phase-amplitude response of a scatterer. If one layer antenna assembled of scatterers has the possibility to vary phase
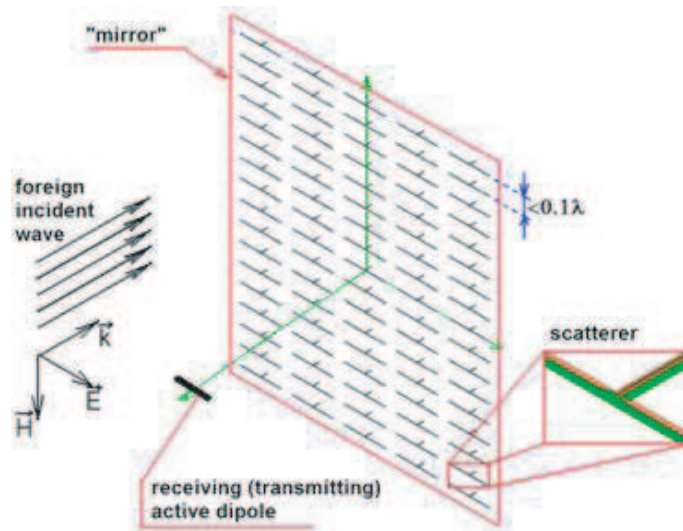
Figure 1: Scheme of the antenna.

of the reemitted field in the range of 360 deg divided by N (where N is the number of layers), then there's a solution to use the same layers located in space by D further from the RF element, it will produce shifting of phase range by doubled D divided by wavelength and multiplied by 360 degrees. Collectively, the N layers provide full (360 degrees) phase range. This construction allows scatterers to have near uniform reemitted field amplitude characteristic, because they use portions of the amplitude and phase characteristics from the resonant point at each layer.

Discrete passive dipoles, which are mounted orthogonally to the face of the array, additionally help the layered construction because of each layer is RF-transparent at some points where reemitted amplitude of custom layer can be set to minimum, and there are no other obstacles to propagation like ground substrates [9].

The work is dedicated to explain experimental analysis and optimization of the work presented in [7]. There are five stages of the investigation: Section 2 presents the scatterers amplitude-phase characteristics précising. Section 3 presents the multilayer structure and construction. Section 4 presents a bandwidth investigation. Section 5 presents the pattern diagrams and optimization. And Section 6 concludes with preliminary field tests.

2. SCATTERER CHARACTERISTICS ANALISIS

The scatterers (Figure 2) were modeled as dipoles printed on the surface of common printed circuit board material (FR4) loaded with varactor diodes through impedance transformers (slot lines). The dipole and slot line geometries (length and width of the dipole, and the gap, length and width of the slot line) were determined from models optimized with HFSS, FEKO and Microwave Office, given the FR4 board thickness (1.57 mm), dielectric permittivity (4.9), and dissipation factor (0.018). The models were based on the voltage-capacitance response of the MA4ST-1240 diodes supplied by the vendor, and were then optimized given the experimentally measured characteristics of the diode, as well as the amplitude and phase of reemitted field by actual prototype scatterers.

The amplitude and phase characteristics of the varactors were in the antenna chamber using the following approach. A circular assembly of scatterers was made (Figure 3, $R = 300$ mm) with an active dipole in the center for transmitting and receiving. The signal from center propagated the same distance (R) to each scatterer along the circumference, and the reflections arrived back at the center. By uniformly changing the capacitances of all diodes in unison, the reflections arrived back at the center in phase, and it was possible to obtain the amplitude and phase characteristics of the reemitted field, which take into account the now uniform mutual coupling and interactions among the scatterers as a first approximation. It is also possible to vary the radius of the assembly, which allows the strengths of those interactions to be examined. The numerically predicted and experimentally measured characteristics are shown in Figure 4, showing the close match of phases and amplitudes.
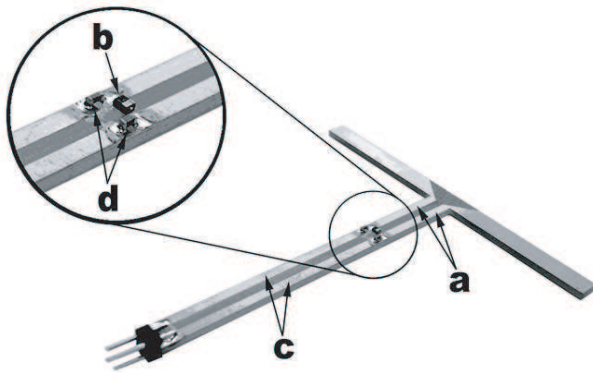
Figure 2: Scatterer: (a) slot line — impedance transformer, (b) tunable varactor diode, (c) control lines, (d) radio frequency chokes.
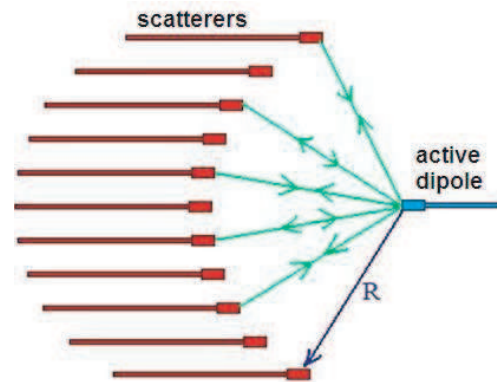
Figure 3: Circular assembly of scatterers for reemitted field amplitude and phase measurements.
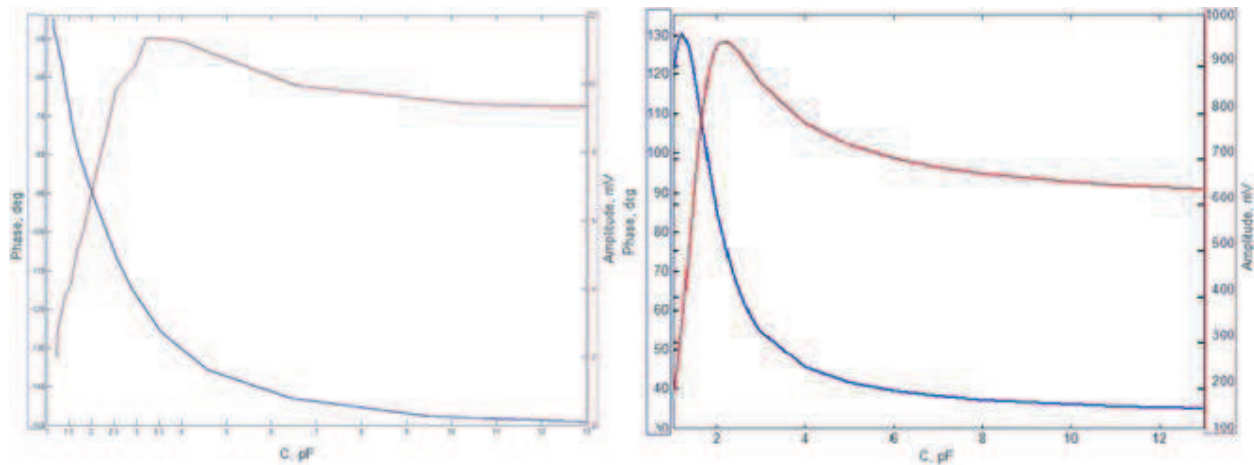
Figure 4: Experimental (left) and numerical (right) amplitude-capacitance (red) and phase-capacitance (blue) of scatterers.

3. MULTILAYER STRUCTURES INVESTIGATION

Each row of scatterers in the antenna has a controller consisting of an FPGA (Field Programmable Gate Array), which provided 100 channels with operational amplifiers. The controller produces diode bias voltages in the range of 0 V to 15 V. Up to five controllers can be interfaced by a high speed serial bus to host computer that carries out multivariate optimization processes, e.g., genetic algorithms. The optimization process searches for the best distribution of bias voltages (equivalently diode capacitances or elemental phase shifts) in term of forming the necessary phase front for specific wave propagation situation and in terms of forming maxima or minima of antenna directivity diagram. The active receiving/transmitting element from a 24 dBi parabolic grid antenna was reused for this work. This exciter was placed as the same focal distance in front of the array as for the dish. Experiments were carried out in the antenna chamber of the N.I. Lobachevsky State University of Nizhni Novgorod. Images of the antenna in the antenna chamber and experimental plant are presented in Figure 5. Agilent Network Analyzers were used to measure the S_{12} characteristics.

Within this framework, several additional experiments were carried out to refine the multilayer structure. The first step was to determine the optimal horizontal spacing between scatterers in a layer in order to maximize gain. For this, a subset of the complete antenna array assembly was used, which consisted of one row and one layer. An adjustable mechanism for holding the individual elements was made, and spacing was varied from 1 cm to 12 cm in 1 cm increments (note the operational wavelength was 12.5 cm). The 3 cm spacing corresponded to a maximum achievable gain of the subassembly of 10.5 dBi. The second step was to determine the optimal spacing between layers also in order to maximize gain. For this, a different subset of the complete antenna array
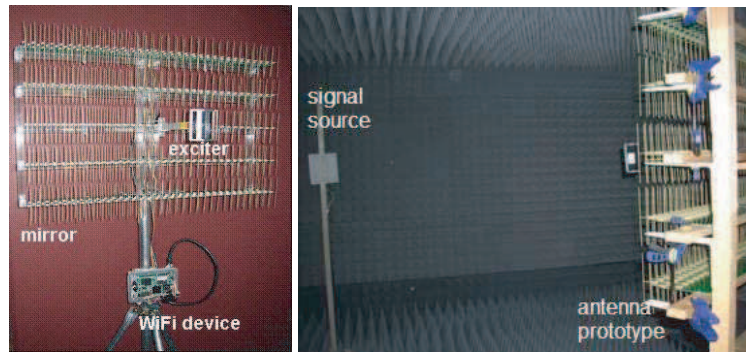
Figure 5: Antenna prototype (left) and experimental setup in the antenna chamber (right).

assembly was used, which consisted of one row with two layers with the 3 cm spacing between the scatterers in each layer. Another adjustable mechanism for holding the individual elements was made, and spacing between layers was varied from 15 mm up to 59 mm in 2 mm increments. The 27 mm spacing corresponded to a maximum achievable gain for the subassembly of 13.5 dBi. Subsequently, a 3 layer subassembly was produced, distances were varied, the optimal spacing was 21 mm, and the optimal gain for the sub-assembly was found to be 14 dBi. The final step was the assembly of multiple rows. The maximum achievable gain depends on the array aperture, which is turn depends on the length of a row and the number of rows stacked one on top of another: 2 rows achieved 16.2 dBi, 3 rows achieved 18.9 dBi, 4 rows achieved 20 dBi, and 5 rows achieved 21.2 dBi.

The final array assembly has five rows of 100 elements. The aperture was 100 cm by 60 cm, which is the same as for 24 dBi parabolic grid antennas. Each row had three offset layers of scatterers with a horizontal spacing of 3 cm and a separation between layers of 21 mm. The vertical separation between rows was found experimentally with the ideal separation of 96% of the wavelength, in this case 120 mm.

4. ANTENNA BANDWIDTH INVESTIGATION

An important consideration for the antenna system was that it should be possible to produce beam patterns with sufficient bandwidth for transmitting WiFi signals, which are nominally 22 MHz wide. While it would be desirable for a given pattern to exhibit constant or minimal variation in bandwidth, e.g., of 1 dB or less, across the entire frequency band used by 802.11b/g signals, optimizing channel-specific patterns remains viable.

Figure 6 shows the bandwidth characteristics of the antenna. The top (orange) curve shows the gain for a pattern optimized for a center frequency of 2.415 GHz to the direction (azimuth = 0 deg, elevation = 0 deg). The bandwidth is 47 MHz wide defined by the −1 dB level. The green curve (bottom) shows the gain for a pattern optimized for a center frequency of 2.415 GHz to the direction (azimuth = 30 deg, elevation = 0 deg). The band is 45 MHz wide. Significant variation in gain is observed for frequencies out of 50 MHz band, where maximum distortion for the first direction (0/0) is −3.5 dB, and for the second direction (30/0) is −4.5 dB. (We believe that a modified pattern optimization process that simultaneously optimizes the pattern gain at multiple frequencies with the 802.11b, for example, could find alternative vectors of varactor bias voltage that would correspond to highly directive patterns with correspondingly wider bandwidths.)
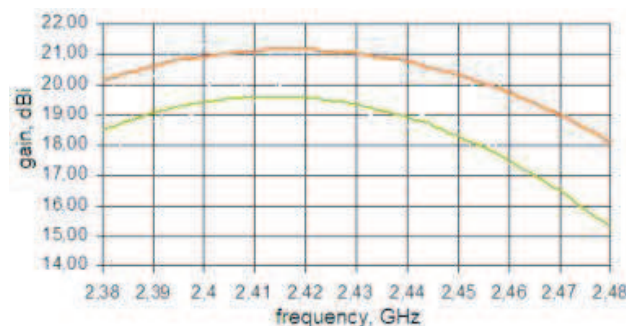
Figure 6: Antenna pattern bandwidth characteristics.

5. DIRECTIVITY DIAGRAM FORMING

The next step of adaptive antenna investigation is to create table of bias voltages distributions for different beam orientations. These patterns form a lookup table that can be used to retrieve the bias voltage vectors associated with a particular pattern. Experiments were provided in antenna chamber by rotating the antenna in azimuth and elevation planes, and then executing external optimization algorithms to maximize the gain. Figure 7 shows several directivity diagrams for patterns with different orientations in azimuth and elevation.

Figure 8 shows graphs of the maximum gains across a range of beam orientations. They show the experimental results (blue) and predicted diminution (red) of the effective antenna aperture (COS-diminution). In general, the experiments track predictions well. An experimental artifact of the antenna chamber, specifically imperfections around the access door, is believed to be responsible for the divergence approaching the −60 degree angle. The maximum gain was 22.5 dB, when using a genetic algorithm for optimizing the varactor loads.
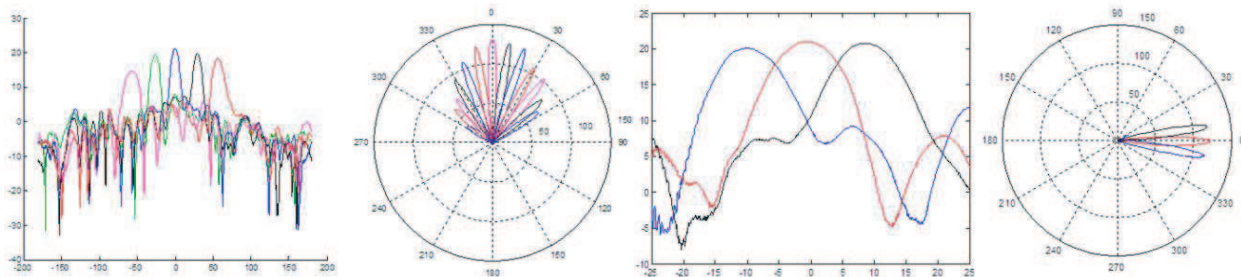
Figure 7: Azimuth (right) and elevation (left) planes customizability (rectangular coordinate system: ordinate — gain [dBi], abscissa — direction [deg]; polar coordinate system: radial — gain [times]).
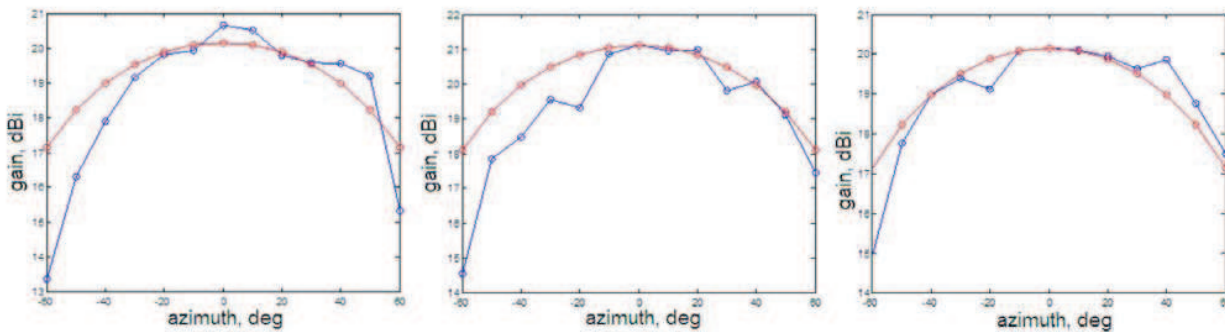
Figure 8: Maximum reachable gain (left — elevation +10 deg; center — elevation 0 deg; right — elevation −10 deg).
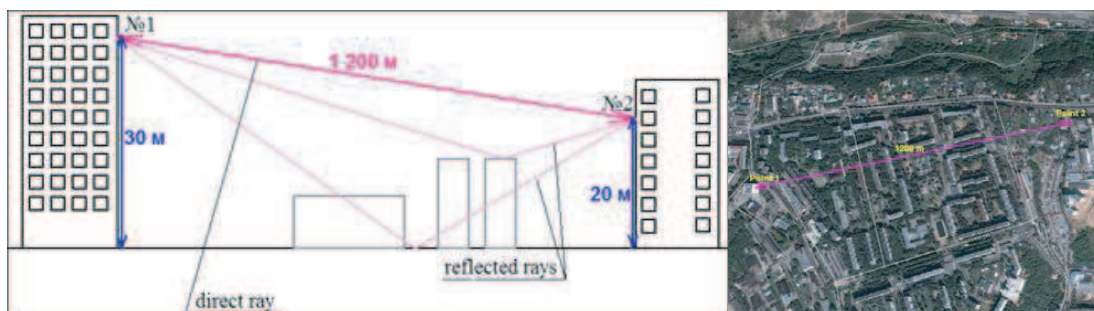
Figure 9: Scheme of the field tests.

6. OUTDOOR FIELD TESTS

Preliminary field trials were done as shown in Figure 9. The antenna was placed on the 9th floor of one office building approximately 30 meters above ground level. A standard parabolic dish antenna with 18 dBi of gain was placed on the 6th flour of a second office building approximately 20 meters above ground level. The distance between the two antennas was approximately 1200 meters.

Each antenna was connected to a Gateworks Avila Network Processing System (GW2348-4) with one 600 mW Ubiquity XR2 802.11bg network adaptor. The systems utilized a wireless stack with TDMA MAC extensions. A single 802.11b point to point link was established between the systems. The sustained performance of TCP transfers of 10 MB files was observed to range from 6.17–7.53 Mbps, which corresponds to similar measurements reported in [10] but with the possibility of beam steering.

7. CONCLUSIONS

This work demonstrates the potential of using multi-layer structures of passive tunable scatterers in highly directional antenna arrays with near uniform gain across a wide range of steerability. The careful optimization of the amplitude-phase characteristics of the scatterers, in isolation and in multilayer structures, is essential given the strong mutual coupling of the elements and the desire to maximize gain and steerability simultaneously. Investigations show the array had sufficient bandwidth to accommodate WiFi channels. Pattern measurements show well formed, high gain patterns that are controllable in azimuth and elevation. Preliminary outdoor experiments demonstrate these antennas in operation in point-to-point links based on WiFi technologies.

ACKNOWLEDGMENT

REFERENCES

1. Ruze, J., "Lateral feed displacement in a paraboloid," *IEEE Transactions on Antennas and Propagation*, Vol. 13, 660–665, 1965.
2. Winter, C. H., "Phase-scanning experiments with two-reflector antenna systems," *Proceedings of the IEEE*, Vol. 56, No. 11, 1984–1999, 1968.
3. Duran, G. J., D. V. Thiel, and G. O'Keefe, "Switched parasitic feeds for parabolic antenna angle diversity," *Microwawe and Optical Tech. Letters*, Vol. 23, No. 4, 200–203, 1999.
4. Thiel, D. V. and S. Smith, *Switched Parasitic Antennas for Cellular Communications*, Norwood, MA, Artech House, 2002.
5. Sievenpiper, D. F., J. H. Schaffner, H. J. Song, R. Y. Loo, and G. Tangonan, "Two-dimensional beam steering using an electrically tunable impedance surface," *IEEE Transactions on Antennas and Propagation*, Vol. 51, 2713–2722, 2003.
6. Hum, S. V., M. Okoniewski, and R. J. Davies, "Realizing an electronically tunable reflectarray using varactor diode-tuned elements," *IEEE Microwave and Wireless Components Letters*, Vol. 15, No. 6, 442–424, 2005.
7. Mainwaring, A., A. L. Umnov, V. A. Filimonov, I. S. Shishalov, and M. O. Shuralev, "Theoretical and experimental investigations of adaptive reactance parasitic antenna array," *Proceedings of Mobile and Wireless Communications Summit, 2007. 16th IST*, 1–4, July 1–5, 2007.
8. Vendik, O. G. and M. Parnes, "A phase shifter with one tunable component for a reflectarray antenna," *IEEE Transactions on Antennas and Propagation*, Vol. 50, No. 4, 53–65, 2008.
9. Sievenpiper, D. F., J. H. Schaffner, H. J. Song, R. Y. Loo, and G. Tangonan, "Two-dimensional beam steering using an electrically tunable impedance surface," *IEEE Transactions on Antennas and Propagation*, Vol. 51, No. 10, Part 1, 2713–2722, Oct. 2003.
10. Chebrolu, K., B. Raman, and S. Sen, "Long distance 802.11b links: Performance measurements and experience," *MobiCom'06*, Los Angeles, California, USA, Sep. 23–26, 2006.

Planar Array Antenna with Parasitic Elements for Beam Steering Control

M. T. Ali[1], **T. A. Rahman**[2], **M. R. Kamarudin**[2],
M. N. Md Tan[1], **and R. Sauleau**[3]

[1]Faculty of Electrical Engineering, Universiti Teknologi Mara (UiTM)
Shah Alam, Selangor, Malaysia
[2]Wireless Communication Center (WCC), Universiti Teknologi Malaysia
81310 UTM Skudai, Johor, Malaysia
[3]Institut d'électronique et de télécommunications de Rennes, (IETR)
UMR CNRS 6164, University of Rennes 1, France

Abstract— A new antenna structure is formed by combining the concept of a reconfigurable planar array antenna with the parasitic elements technique to improve the beam steering. The integration of PIN diode switches to the antenna enables one to steer the antenna beams in the desired direction. This can be done by changing the switch state to either *on* or *off* mode. In this work, a number of reflectors have been proposed, namely parasitic elements, and were placed between the patches to increase the beam steering angle. With such a configuration, the main beam radiated by the array can be tilted due to the effect of mutual coupling between the driven elements and the parasitic elements (reflectors). The unique property of this antenna design is that instead of fabricating all together in the same plane, the antenna's feeding network is separated from the antenna radiating elements (the patches) by an air gap distance. This allows reducing spurious effects from the feed line. The optimization results for the resonant frequencies of the antennas with variable air gap heights were also studied. Comparisons of the antenna performance with and without parasitic elements have been also investigated. The simulations results will be compared to measurements at $5.8\,\mathrm{GHz}$. Experimental results are presented to demonstrate the excellent performance of this antenna.

1. INTRODUCTION

The development of wireless communication has had a good impact on the field of the antenna design. When considering on adding new features to existing antennas, question arises about the benefits and applications of doing so. Reconfigurable antenna will be an attractive feature in the modern wireless communication system because it enables to provide a single antenna to be used for multiple systems. In the reconfigurable antenna, the structure of the antenna can be changed by integrated with Radio Frequency (RF) switches [1–3]. Most of these approaches were able to alter the fundamental characteristics such as operating frequency, bandwidth, polarization and radiation pattern [4].

One of the applications of the reconfigurable antenna is that, it can desirably steering the beam pattern into many directions. The reconfigurable antennas have attracted much attention in wireless communication systems such as cellular-radio system, smart weapons protection and point to point propagation. In [5], the authors presented reconfigurable antennas, which were radiated at different beam patterns by adjusting the apertures and maintaining their operating frequencies. The antenna presented in [6], describes a dual band dipole antenna integrated with series MEMS switches. However, this method typically used a dual operating frequency to reconfigure a beam pattern. In array application, mutual coupling effect is often considered undesirable, since it reduce the antenna gain, raises the sidelobe level. However, in the case of microstrip antenna, the mutual coupling between the driven elements and the parasitic elements can be used to direct the beam so that its peak can be tilted to the desired direction. For example, the Yagi antenna uses parasitic elements in combination with at active element to control the direction of a beam [7–9]. The amount of mutual coupling depends on the separation between antenna elements, and it will increase if the antennas are closer to each other.

In this paper, a combination of the reconfigurable 4×4 rectangular microstrip planar array antenna and the parasitic elements technique is presented. The integration of PIN Diode switch in feed line was investigated to steer the beam by changing the switches to *on* or *off* mode. There are three possible of configurations, the first being to switch *on* all the switches. The second and third configuration requires only two sets of switches (S_1 and S_3 or S_2 and S_4) in *off* mode condition.

The comparison results between antenna with and without parasitic elements were investigated in this paper. The proposed antenna is then simulated by using Computer Simulation Technology (CST) Studio Suite 2008.

2. STRUCTURE OF PLANAR ARRAY ANTENNA

The fabrication and assembly of the antenna array with separated feed network using the air gap technique is described here. The basic structure of the proposed antenna is constructed using multiple 2×2 sub-array modules with its "H" shape printed feed line, as shown in Figure 1. In this structure, the antenna is fed by a 50 Ohm coaxial probe. The size of each patch is $16 \, \text{mm} \times 11.15 \, \text{mm}$ and their inter-element spacing is approximately $\lambda_o/2$. The feed network is conventional [11].

The 16-element array comprises four sub-arrays of 4-elements. Figure 6 shows the structure of the separated feed antenna was proposed in this paper. The input ports on the antenna board are labeled as P_1 to P_4. The top antennas are fed by a vertical coaxial probe connecting the feed network to feed sub-array. The gap height h_1 has been optimized to achieve a good return loss at $5.8 \, \text{GHz}$.
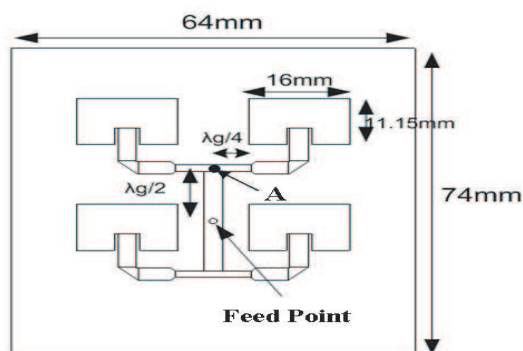
Figure 1: Schematic diagram of the 2×2 sub-array antenna.

| (a) | (b) | (c) |
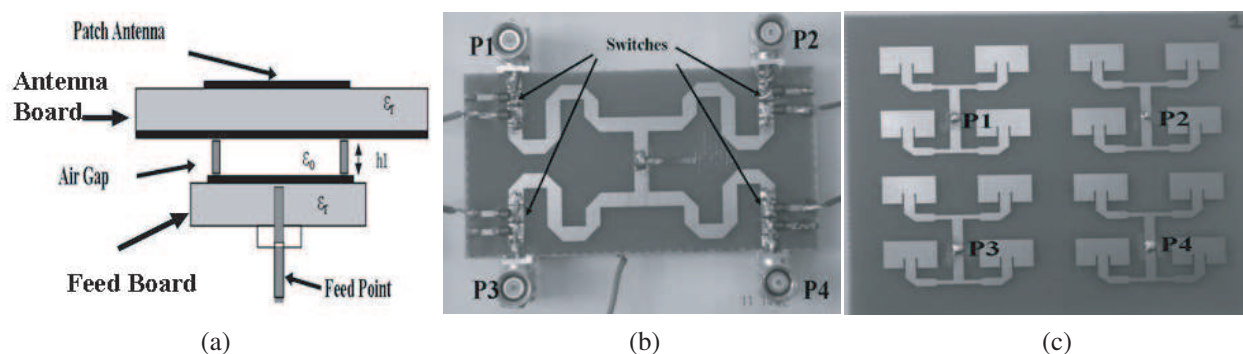
Figure 2: Separated feed antenna through an air gap structures. (a) Antenna Structure, (b) active feed board, (c) antenna board.

Table 1: Return loss and resonant frequency variation depending on the air gap height.

Cases	Air Gap (h_1) mm	Resonant Freq. (GHz)	Return Loss S_{11} (dB)
1	15.65	5.49	-16
2	13.25	5.58	-18.86
3	11.55	5.65	-19.96
4	8.89	5.7	-21.2
5	7.99	5.8	-23.93
6	7.55	5.81	-25.3

The influence of h_1 on the antenna return loss is illustrated in Figure 3. This figure shows that increasing the air gap height induces a decrease of the resonant frequency. The best result providing a good impedance matching at 5.8 GHz is obtained for $h_1 = 7.99$ mm. Hence, this height has been chosen in the final design.

3. MEASUREMENT AND RESULT DISCUSSION

3.1. "Result 1": Antenna Structure without Parasitic Elements

To demonstrate the flexibility of the design approach, several cases have been presented to realize a beam steering reconfigurable. According to the simulated and measured results, the radiation pattern characteristic of the antenna forming has been tuned efficiently; the pattern obtained is directed to three directions as shown in Figure 4. It is seen that by changing the mode of the PIN Diode, the beam can be steered in three directions. The simulated beam diversity angles of $-3°$, $0°$ and $+2°$, compared with the measured diversity angles of $-6°$, $0°$, and $+5°$.

As a result, the structure of the antenna is not perfectly developed to produce the large beam diversity angles. It is therefore assumed that this technique could be expanded to allow a large number of directions than described. But good agreements can be observed from the results that the arrangement of the antenna structure effected by a beam pattern. Other alternative approach for increasing the angle of steering beam is presented. Parasitic elements have been used in microstrip patch antennas in order to improve the angle of steering beam.

3.2. "Result 2": Antenna Structure with Parasitic Elements and Smaller Spacing

The beam diversity of the reconfigurable microstrip planar array antenna can be increased by placed in a parasitic elements and reducing spacing between the patch elements [10]. Based on
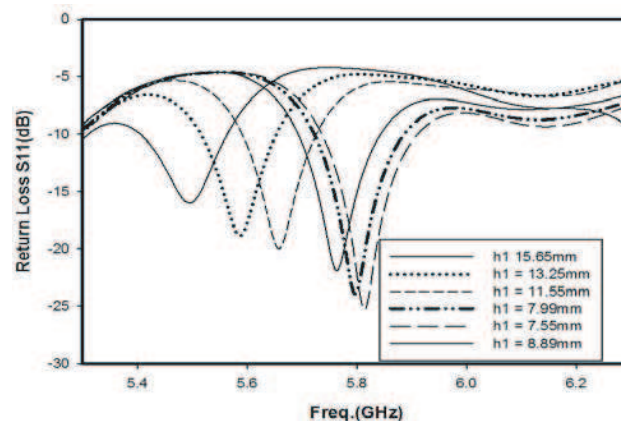
Figure 3: Simulated results of return loss with different the air gap height.
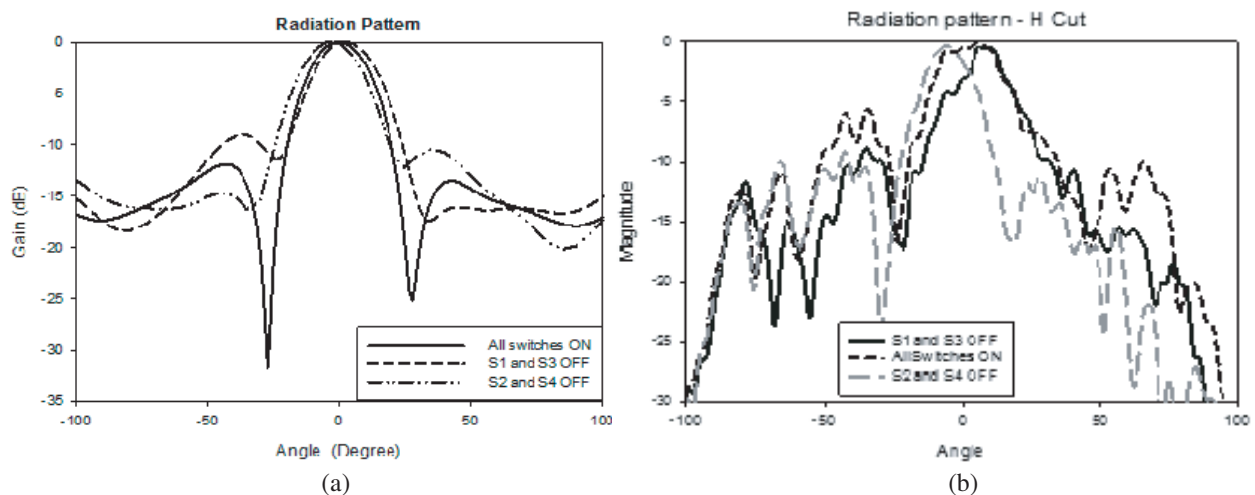
Figure 4: Results of radiation pattern at different switches configuration. (a) Simulated, (b) measured.

(a) (b) (c)
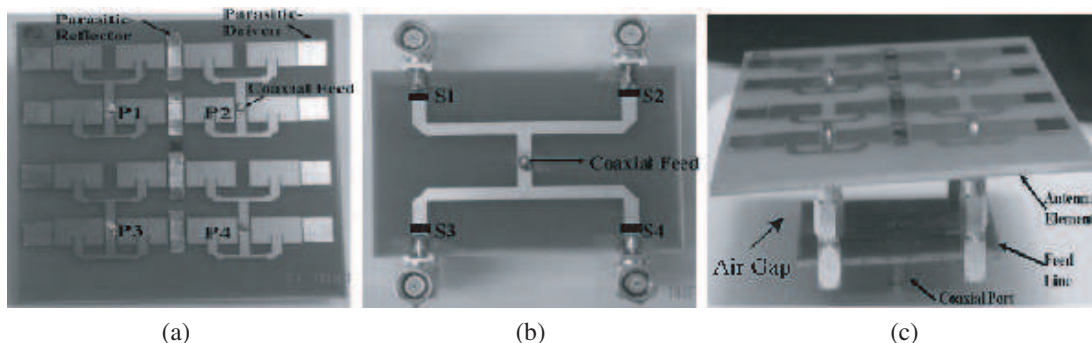
Figure 5: Prototype of array antenna with parasitic elements. (a) Top view, (b) overall antenna structure, (c) feed board.

(a) (b)
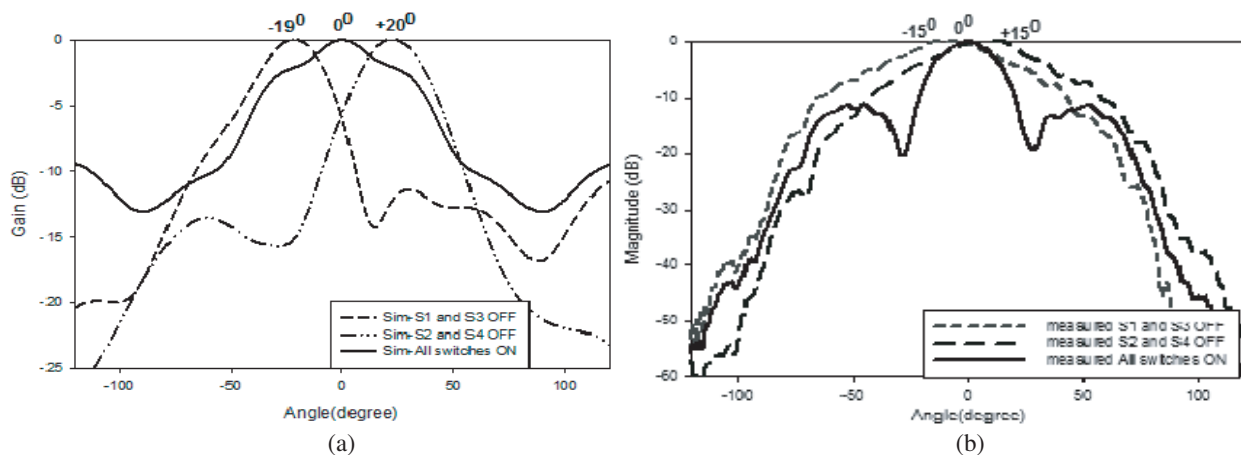
Figure 6: Results of radiation pattern at different switches configuration. (a) Simulated, (b) measured.

Table 2: Comparison results of proposed antenna both with and without parasitic element.

Switch Conf.	Simulated				Measured			
	"Result 1"		"Result 2"		"Result 1"		"Result 2"	
	Angle	S_{11} (dB)	Angle	S_{11} (dB)	Angle	S_{11} (dB)	Angle	S_{11} (dB)
All switches ON	0°	−31.9	0°	−10.5	2°	−21.12	0°	−17.41
S_2 and S_4 OFF	+2°	−23.19	+20°	−25.01	+5°	−19.98	+15°	−16.0
S_1 and S_3 OFF	−3°	−21.35	−19°	−23.08	−6°	−18.01	−15°	−18.03

the simulation analysis, the optimum spacing between active elements and the parasitic elements for the largest steering beam is about 1.2 mm. The dimension ration of the parasitic element to the active patches element should be around 1.1 to 1.3. When a parasitic element is added in the antenna structure, as shown in Figure 5(a), the pattern shows some improvement in term of steering angle compared to antenna without parasitic elements. In this case, the PIN Diode switch is represented as a small gap with black colour as in Figure 5(b). When the switch are in the *off* state condition, the gap between feed line occur and no current flowing through the gap. So, three set of feed boards are needed to achieve the configurations.

Figure 6 shows that the angles of radiation pattern were steered to three directions, +20°, 0°, and −19°, compared with the measured results of −15°, 0°, and +15°. The comparison of simulated and measured results of the beam diversity and return loss for "Result 1" and "Result 2" are listed in Table 2.

4. CONCLUSION

In this paper, simulated and measured data is demonstrated the concepts of reconfigurable planar array antenna that produced steering beam pattern characteristic. The reconfigurable radiation

beam antenna presented in this paper can be steered in three directions, $+15°$, $-0°$, and $-15°$, respectively at frequencies across the entire 5.8 GHz band, with excellent transmission matching for all configuration mode. The antenna designs with various radiation patterns have great potential for wireless communication systems, such as point to point applications.

REFERENCES

1. Peroulis, D., K. Sarabandi, and L. P. B. Katehi, "Design of reconfigurable slot antennas," *IEEE Transactions on Antennas and Propagation*, Vol. 53, 645–654, 2005.
2. Mak, A. C. K., C. R. Rowell, R. D. Murch, and C. L. Mak, "Reconfigurable multiband antenna designs for wireless communication devices," *IEEE Transactions on Antennas and Propagation*, Vol. 55, 1919–1928, 2007.
3. Panagamuwa, C. J., A. Chauraya, and J. C. Vardaxoglou, "Frequency and beam reconfigurable antenna using photoconducting switches," *IEEE Transactions on Antennas and Propagation*, Vol. 54, 449–454, 2006.
4. Cetiner, B. A., H. Jafarkhani, Q. Jiang-Yuan, Y. Hui Jae, A. Grau, and F. De Flaviis, "Multi-functional reconfigurable MEMS integrated antennas for adaptive MIMO systems," *Communications Magazine, IEEE*, Vol. 42, 62–70, 2004.
5. Pringle, L. N., P. G. Friederich, S. P. Blalock, G. N. Kiesel, P. H. Harms, D. R. Denison, E. J. Kuster, T. L. Fountain, and G. S. Smith, "GTRI reconfigurable aperture design," *Antennas and Propagation Society International Symposium, IEEE*, Vol. 1, 473-476, 2002.
6. Schaffner, J. H., R. Y. Loo, D. F. Sievenpiper, F. A. Dolezal, G. L. Tangonan, J. S. Colburn, J. J. Lynch, J. J. Lee, S. W. Livingston, R. J. Broas, and M. Wu, "Reconfigurable aperture antennas using RF MEMS switches for multi-octave tunability and beam steering," *Antennas and Propagation Society International Symposium, IEEE*, Vol. 1, 321–324, 2000.
7. Thiel, D. V., S. O'Keefe, and W. L. Jun, "Electronic beam steering in wire and patch antenna systems using switched parasitic elements," *Antennas and Propagation Society International Symposium, AP-S. Digest*, Vol. 1, 534–537, 1996.
8. Gray, D., L. J. Wei, and D. V. Thiel, "Electronically steerable Yagi-Uda microstrip patch antenna array," *IEEE Transactions on Antennas and Propagation*, Vol. 46, 605–608, 1998.
9. Mori, K., K. Uchida, and H. Arai, "Active antenna using parasitic elements," *Antennas and Propagation Society International Symposium, IEEE*, Vol. 3, 1636–1639, 1998.
10. Zhang, S., G. H. Huff, J. Feng, and J. T. Bernhard, "A pattern reconfigurable microstrip parasitic array," *IEEE Transactions on Antennas and Propagation*, Vol. 52, 2773–2776, 2004.
11. Shuch, H. P., "Multiband reconfigurable synthetic aperture radar antenna," *ESTC 2004 Proceedings (CD)*, Paper B1P1, Palo Alto CA, June 2004.

Multiband MIMO Antenna with a Band Stop Matching Circuit for Next Generation Mobile Applications

Min-Seok Han and Jaehoon Choi

Division of Electrical and Computer Engineering, Hanyang University
17 Haengdang-dong, Seongdong-gu, Seoul 133-791, Korea

Abstract— A compact multiband MIMO antenna with a band stop matching circuit for next generation mobile applications is proposed. The proposed multiband MIMO antenna consists of two dual-band PIFAs which provide wideband characteristics. In order to improve the isolation characteristic at the LTE band, a band stop matching circuit was inserted at the corner of each antenna element. The proposed MIMO antenna has the isolation of approximately 15 dB at the LTE band and higher than 20 dB at the upper band. In addition, the band stop matching circuit has minimal effect on the upper band performance. This property makes the design of a multiband MIMO antenna easy. Design considerations and experimental results of the multiband MIMO antenna with a band stop matching circuit are presented.

1. INTRODUCTION

Next generation mobile systems have to satisfy the requirements of high data rates and flexible interfaces for different communication system standards. MIMO (Multiple Input Multiple Output) technology has been regarded as one of practical approaches to accommodate such requirements by increasing wireless channel capacity and reliability [1, 2]. However, it is usually a big challenge to place multiple antennas within a small and slim mobile handset while maintaining the good isolation between antenna elements since the antennas are strongly coupled with each other and even with the ground plane by sharing the surface currents distributed on it. So far, many researchers have been trying to find new techniques for isolation improvement between antenna elements inside mobile handsets. Although several techniques have been reported for high isolation characteristics by employing small N-section resonators in the form of slots on the ground plane [3], two identical antennas that have current paths orthogonal to each other [4] and a T-shaped and dual inverted L-shaped ground branches [5], it is still quite difficult for antennas closely located within the limited space in a mobile handset to have good isolation at long term evolution (LTE) bands.

In this paper, a multiband MIMO antenna with a band stop matching circuit for next generation mobile applications is proposed. The proposed multiband MIMO antenna consists of two dual-band PIFAs which provide wideband characteristics. In order to improve the isolation characteristic at the LTE band, a band stop matching circuit was inserted at the corner of each antenna element. The inserted band stop matching circuit is to suppress the surface currents at the specific frequency band and to generate two additional resonances at 760 MHz LTE and 860 MHz GSM850 bands. In addition, the band stop matching circuit has minimal effect on the upper band performance. The proposed MIMO antenna can cover LTE, GSM850, GSM900, GSM1800, GSM1900, WCDMA and M-WiMAX services, simultaneously. Details of the design considerations and experimental results of the multiband MIMO antenna with a band stop matching circuit are presented and discussed.

2. MIMO ANTENNA DESIGN

The geometry of the proposed multiband MIMO antenna for next generation mobile applications is shown in Figure 1. A wide folded patch structure along with the strong coupling between feeding and shorting lines through the slit (slit1) reduce the size of antenna as well as widen the bandwidth in low frequency band near 800 MHz. The antenna area is maximized by adopting the folded structure for high radiation efficiency. The bandwidth near 2 GHz is mainly controlled by a slit (slit2) between main patch and shorting line. The dimension of slit2 controls the high resonance frequencies without any effect on low resonance frequency. This fact provides the flexibility to MIMO antenna design. The overall size of the radiating element is 36 mm × 12 mm × 6.2 mm. Two same elements are placed at the top and bottom sides of a FR4 ($\varepsilon_r = 4.4$) substrate having volume of 48 mm × 108 mm × 0.8 mm, which simulates the ground plane of a practical bar type mobile handset. In order to improve the isolation characteristic at the LTE band, a band stop matching circuit was inserted at the corner of each antenna element. The band stop matching circuit is used to suppress the surface currents at the specific frequency band and to generate two

(a)   (b)

(c)
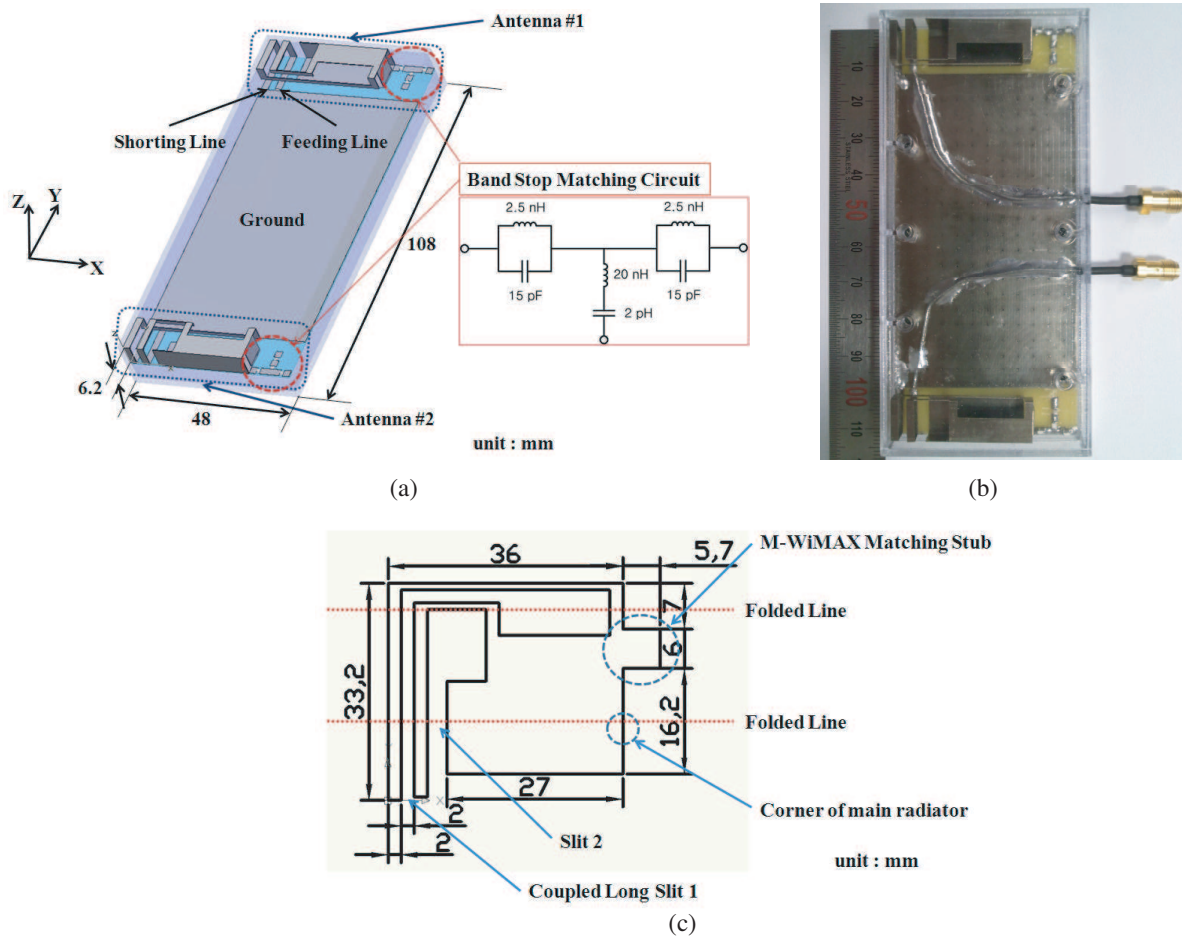
Figure 1: Geometry of the proposed multiband MIMO antenna: (a) 3D view, (b) fabricated MIMO antenna, (c) structure of radiating element.

additional resonances near 760 MHz LTE band and near 860 MHz GSM850 operation. By inserting a band stop matching circuit having the central frequency of about 810 MHz with 3-dB band stop bandwidth of around 190 MHz, the proposed MIMO antenna has dual-resonance characteristics at the lower band. Consequently, wide bandwidth covering LTE/GSM850/GSM900 is obtained.

3. RESULTS AND DISCUSSIONS

The S-parameter characteristics with and without inserted band stop matching circuit are given in Figure 2. It is shown that the simulated s-parameter characteristics are similar to those of measurement. From the measured results, the 6-dB return loss impedance bandwidth is 31.2% (from 700 MHz to 960 MHz) for LTE, GSM850 and GSM900 bands. For the upper band, the MIMO antenna has sufficient bandwidth to cover GSM1800, GSM1900, WCDMA, and M-WiMAX bands. Without band stop matching circuit, the MIMO antenna has the isolation of about 7 dB at LTE band and over 20 dB at M-WiMAX band. When band stop matching circuit is added, the simulated isolation characteristic at LTE band is increased to 15 dB as shown in Figure 2. Simulation was carried out using MWS [6] to optimize the geometric parameters of the proposed antenna.

The measured radiation patterns of the designed MIMO antenna at 780, 1920, and 2550 MHz are plotted in Figure 3. Although MIMO antenna elements usually have different directivity for each element, the radiation patterns of the designed antennas resemble to each other. From the H (xz)-plane patterns, it is confirmed that the antenna has patterns close to omni-directional in all frequency bands. The simulated and measured gains are shown in Table 1. The measured peak gains of two antenna elements are -0.37 dBi and -0.86 dBi at the LTE band, 1.19 dBi and 2.81 dBi at the WCDMA band and 0.81 dBi and 0.2 dBi at the M-WiMAX band, respectively.
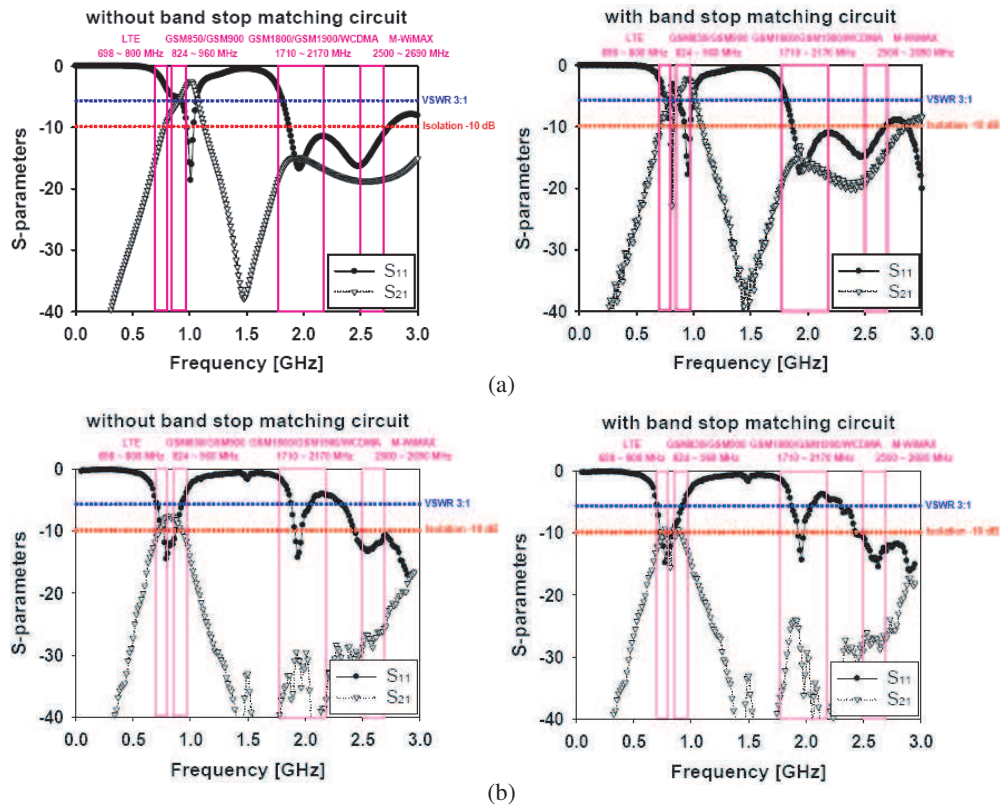
Figure 2: *S*-parameter characteristics without and with band stop matching circuit: (a) Simulated *S*-parameter characteristics, (b) measured *S*-parameter characteristics.
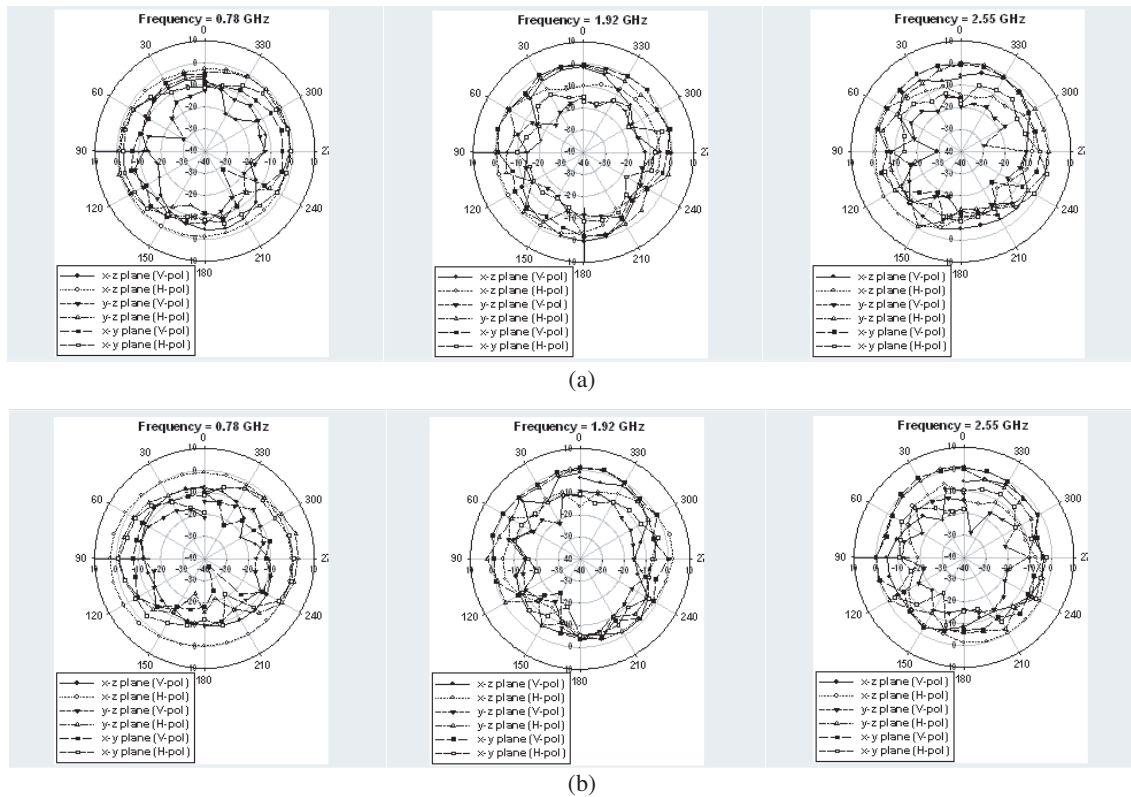
Figure 3: Measured radiation patterns of the proposed multiband MIMO antennas: (a) Antenna #1, (b) antenna #2.

Table 1: Simulated and measured antenna gains.

Simulated Antenna Gains (dBi)	$f = 0.78\,\text{GHz}$	$f = 1.92\,\text{GHz}$	$f = 2.55\,\text{GHz}$
Antenna #1	−1.02	2.16	2.23
Antenna #2	−0.65	2.38	2.04
Measured Antenna Gains (dBi)	$f = 0.78\,\text{GHz}$	$f = 1.92\,\text{GHz}$	$f = 2.55\,\text{GHz}$
Antenna #1	−0.37	1.19	0.81
Antenna #2	−0.86	2.81	0.2

4. CONCLUSION

In this paper, an internal multiband MIMO antenna with a band stop matching circuit for LTE/GS-M850/GSM900/GMS1800/GSM1900/WCDMA/M-WiMAX applications was proposed. A band stop matching circuit is added at the corner of each radiating elements in order to enhance the isolation characteristic at LTE band. The fabricated antenna has the isolation of about 15 dB at the lower band and higher than 20 dB at the upper band. The measured peak gains of two antenna elements are −0.37 dBi and −0.86 dBi at the LTE band, 1.19 dBi and 2.81 dBi at the WCDMA band and 0.81 dBi and 0.2 dBi at the M-WiMAX band, respectively.

ACKNOWLEDGMENT

REFERENCES

1. Foschini, G. J. and M. J. Gans, "On limits of wireless communications in a fading environment when using multiple antennas," *Wireless Personal Comm.*, Vol. 6, No. 3, 311–335, Mar. 1998.
2. Shiu, D. S., G. J. Foschini, M. J. Gans, and J. M. Kahn, "Fading correlation and its effect on the capacity of multi element antenna systems," *IEEE Trans. on Comm.*, Vol. 48, No. 3, 502–513, Mar. 2000.
3. Kim, K.-J. and K.-H. Ahn, "The high isolation dual-band inverted F antenna diversity system with the small N-section resonators on the ground plane," *IEEE Microwave and Optical Technology Letters*, Vol. 49, No. 3, 731–734, 2007.
4. Mak, K.-M., H. Wong, and K.-M. Luk, "A shorted bowtie patch antenna with a cross dipole for dual polarization," *IEEE Antennas and Wireless Propagation Letters*, Vol. 6, 126–129, 2007.
5. Cai, Y., Z. Du, and K. Gong, "A novel wideband diversity antenna for mobile handsets," *IEEE Microwave and Optical Technology Letters*, Vol. 51, No. 1, 218–222, 2009.
6. Computer Simulation Technology (CST) Microwave Studio Suite, 2008, http://www.cst.com.

Directional GPS Antenna for Indoor Positioning Applications

Kerem Özsoy[1, 2] and Ibrahim Tekin[1]

[1]Electronics Engineering, Sabancı University, Istanbul, Turkey
[2]Vestek Electronic Research & Development Corp., Istanbul, Turkey

Abstract— In this paper, a directional GPS antenna for L1 frequency — 1575 MHz — with RHCP and a high directive gain is proposed for indoor positioning applications. The proposed antenna is made of a standard off the shelf GPS patch antenna with an additional conical reflector to enhance the gain and the beamwidth of the antenna. The angle of the cone reflector is optimized by HFSS 11 software. Finally, the cone is fabricated, integrated with the patch antenna and measured. The measurement results show that the antenna with the reflector has a 9 dBi gain and a beamwidth of 60 degrees with an axial ratio of 1 dB which agrees well with simulation results.

1. INTRODUCTION

Civil Global Positioning System (GPS) has become very popular in recent years and it has wide usage in many areas. With the latest technological advances such as Differential GPS (DGPS), Assisted GPS (AGPS), civil GPS receivers are able to locate themselves with an error of 1–3 meters outdoors [1]. Although GPS is very successful in outdoor areas, it is hard to decode GPS signals indoors due to the additional signal loss caused by the buildings. GPS signals are transmitted from the satellites orbiting around 20.000 km in the sky. When these signals reach the earth surface, the strength of the signals is very low due to free space loss. For indoors, signals go through additional loss of 10–30 dB [2], in which case, signal levels are too low for an off-the shelf GPS receiver to detect the satellite signals. In order to solve indoor coverage problem, we plan to build an indoor positioning system that uses the GPS infrastructure. This indoor positioning system consists of GPS pseudo-satellites (pseudolite) and a GPS receiver with improved positioning algorithms. A GPS pseudolite works like an RF repeater, i.e., it picks up a satellite signal, amplifies and then retransmits into the building in which there is no GPS signal coverage. It is crucial to have directional receive and transmit antennas for our indoor positioning system. A pseudolite should be able to pick up the satellite signal only from a given direction in the sky and transmit the amplified signals to an indoor area. There are several ways to design directional antennas such as Yagi-Uda, horn, log periodic, reflector and parabolic antenna or phased array systems [3]. Along these antennas, we choose the reflector antenna type since it is simple to manufacture, and also compact and robust in performance and low cost.

In this paper, we propose a directional GPS antenna for L1 frequency — 1575 MHz — with RHCP and a high directive gain. A standard off the shelf GPS patch antenna is used in the design, and the directivity increase is achieved through the use of a conical reflector. The cone is fabricated and integrated with the standard GPS patch antenna and finally directional GPS antenna is measured. The organization of the rest of the paper will be as follows: in Section 2, the design procedure of the antenna is given. In Section 3, measurement results will be presented, and finally the paper will be concluded.

2. ANTENNA DESIGN

The proposed antenna is comprised of a standard of the shelf GPS antenna and a conical reflector as illustrated in Figure 1. Standard GPS antenna is a circularly polarized patch antenna operating at the frequency of 1575 MHz. The circular polarization is provided by truncation of the two diagonal corners and feeding the antenna asymmetrically with a coaxial probe under the patch [3]. The dimensions of the GPS patch antenna — 25 mm × 25 mm — are kept small by using high electrical permittivity ($e_r = 25$). Microstrip patch antennas are medium gain antennas. In order to further increase the directivity of the patch antenna, either a phased array system consisting of multiple radiating elements or a parasitic reflector system can be utilized. In our approach, we choose a simple reflector system over other directional antennas. The conical reflector is simple, compact, robust in performance and low cost. Most importantly, as opposed to phase array antenna, reflector antenna does not need a beam forming network which decreases the received power and increases
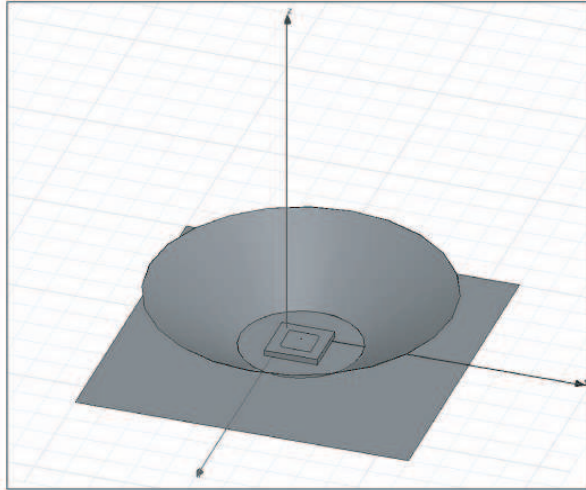
Figure 1: GPS patch antenna with the conical reflector.
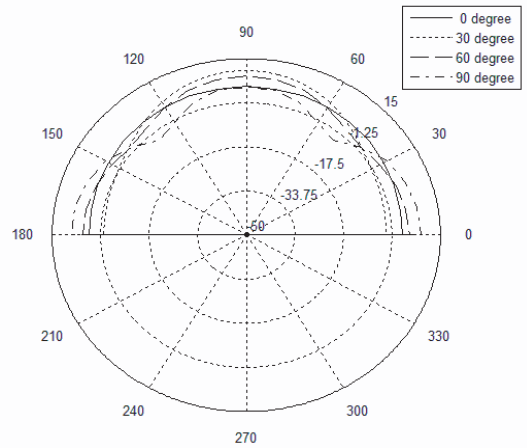
Figure 2: Radiation patterns with different cone angles.

the noise figure of the overall system. Therefore, a reflector is designed to increase the directivity of the antenna.

The design of conical reflector together with the patch antenna is performed using Ansoft's High Frequency Structure Simulator (HFSS). First, off the shelf GPS patch antenna is simulated and parameters of the antenna are adjusted such that the specifications in the datasheet are obtained with good accuracy. Then, the GPS patch antenna is placed in the middle of cone reflector. The reflector is left as floating reflector, i.e., it is not grounded. Optimizations are done iteratively by the simulation tool and more emphasis is given to three parameters of the conical reflector namely height of the cone, angle between the cone and the ground plane and the distance of cone to the patch antenna. The distance between the cone and the standard patch antenna basically affects the all parameters. However, most importantly, it affects the return loss of the antenna. The height of the cone changes the beamwidth and the gain of the antenna. The cone angle mostly affects the radiation pattern of the antenna. In Figure 2, one can observe the effect of the cone angle to the radiation pattern of the antenna with the other parameters set to optimum values.

After simulation results, thickness of the conical reflector is chosen as 1 mm, the two of the three parameters are fixed with the best results acquired in simulations and the other parameters are optimized. The summary of the dimensions of the proposed antenna after the optimizations are given in Table 1.

Table 1: Optimized parameters.

Distance of the cone to the standard patch antenna	4 cm
Height of the cone	4 cm
Angle between the cone and the ground plane	30°

3. SIMULATION AND MEASUREMENT RESULTS

Simulation results of the stand alone GPS patch antenna shows that the antenna has 4 dBi maximum directive gain and 120° half power beam width. Antenna is matched at GPS L1 frequency. These simulation results agree with the datasheet of the GPS patch antenna. After the design of the cone and the integration of the cone with the GPS patch antenna, measurements are done in an anechoic chamber. The results show that the gain of the antenna is increased and the center resonant frequency of the overall system slightly changed which does not affect the overall performance. The simulated and the measured return loss of the directional antenna with the measured return loss of the stand alone GPS patch antenna can be seen in Figure 3. As seen in the figure, cone changes the

input impedance slightly. However, directional antenna still matches at GPS L1 frequency. The measured and simulated radiation pattern of the directional antenna can be seen in Figures 4 and 5 with the phi angles 0 and 90 degree respectively. The beamwidth of the directional GPS antenna is 60 degrees. Decrease in the beamwidth angle can be seen in Figure 6 in which the measured radiation pattern of the directional antenna and the simulated radiation pattern of the GPS patch antenna are shown. Measured radiation patterns of the two orthogonal phi angles can be seen in Figure 7. As seen in the figure, axial ratio of the directional antenna is 1 dB which indicates that the antenna is circularly polarized. Simulated directional gain of the antenna is 10 dB and the measured maximum directional gain of the overall system is 9 dB. Cone brings an additional 5 dB gain to the patch antenna. The measurement results of the return loss, gain and the radiation patterns fit well with the simulation results.
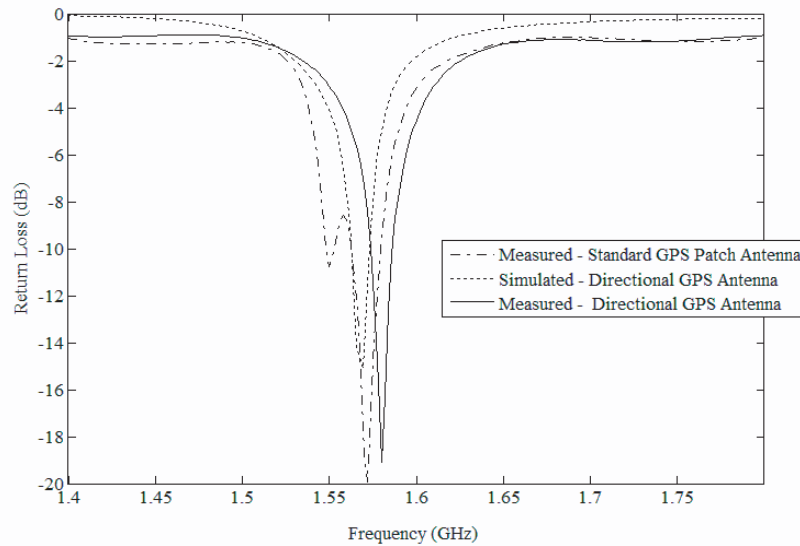
Figure 3: Measured return loss of the standard GPS patch antenna and directional antenna. Simulated return loss of the directional antenna.
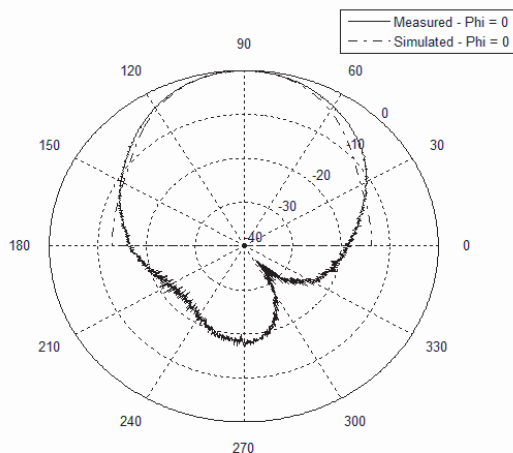
Figure 4: Measured and simulated radiation patterns $\phi = 0°$.
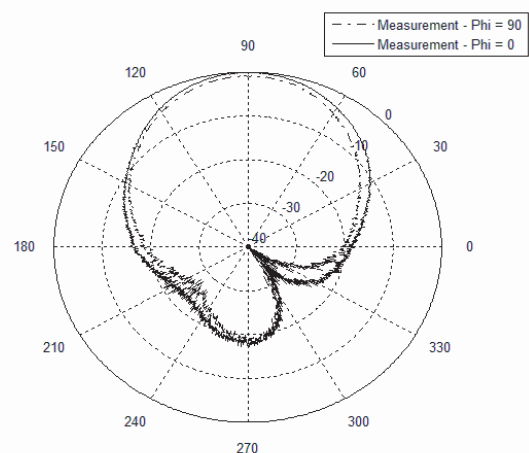
Figure 5: Measured radiation patterns at $\phi = 0°$ and $\phi = 90°$.
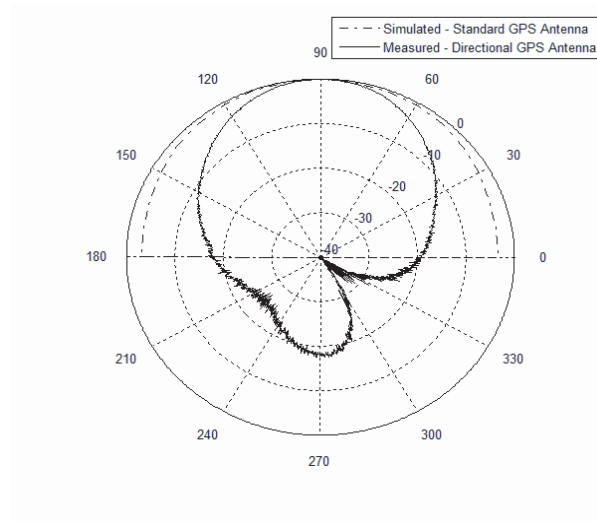
Figure 6: Measured and simulated radiation patterns $\phi = 0°$
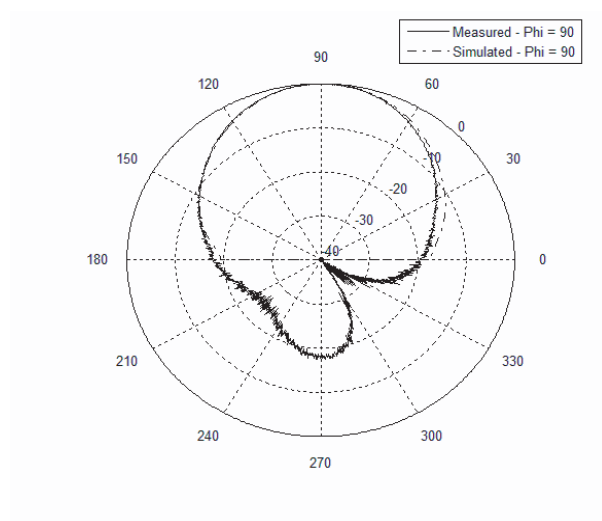
Figure 7: Measured and simulated radiation patterns at $\phi = 90°$.

4. CONCLUSION

In the proposed paper, a directional GPS L1 frequency antenna is designed for indoor GPS applications and repeaters by using an off the shelf GPS patch antenna and a conical reflector. Directionality is achieved through the conical reflector. The measurement results show that the overall gain of the antenna is 9 dB and the beam width of the antenna is 60 degree which is highly satisfactory results. The conical reflector is optimized with the simulator tool and the optimization results are demonstrated in the paper. Our design shows that conical reflector can be used to increase the directivity and decrease the beam widths of the patch antennas. In different applications same method can be used to simply increase directivity of the antenna for different aims.

REFERENCES

1. Liu, H., H. Darabi, P. Banerjee, and J. Liu, "Survey of wireless indoor positioning techniques and systems," *IEEE Transaction on Systems, Man, and Cybernetics*, Vol. 37, No. 6, 1067–1077, November 2007.
2. Peterson, B. B., D. Bruckner, and S. Heye, "Measuring GPS signals indoors," *Proceedings of the Institute of Navigation's ION GPS-2001*, September 2001.
3. Balanis, C. A., *Antenna Theory, Analysis and Design*, 2nd edition, Wiley, New York, 1997.

Printed Dipole Array Fed with Parallel Stripline for Ku-band Applications

M. Dogan[1, 3]**, K. Özsoy**[1, 2]**, and I. Tekin**[1]

[1]Electronics Engineering, Sabanci University, Istanbul, Turkey
[2]Vestek Electronic Research & Development Corp., Istanbul, Turkey
[3]TUBITAK, UEKAE, Kocaeli, Turkey

Abstract— This paper presents the design procedure of a printed dipole antenna and 1D array configurations of the single dipole element in the Ku-Band with its metallic reflector plane parallel to the array plane. The proposed antenna has a natural beam tilt which is useful for some specific applications. Several array configurations in 1D are simulated and tested. The effect of mutual coupling among each array elements is also investigated. Required modifications on the individual array element and the feed structures due to the effect of mutual coupling are examined. The single dipole and array of dipole has measured VSWR values smaller than 2 in the Ku-Band with simulated gains of 5.7 dBi and 12 dBi, respectively. All the simulations are performed with ADS-2006A software and measurements are performed in an anechoic chamber.

1. INTRODUCTION

Recent studies are highly focused on antenna design in Ku-Band. Since the Ku-band has enough available bandwidth for satellite links, these systems are widely used in satellite communications, especially in the mobile antenna systems used in vehicles. There are also other application areas of Ku-band systems such as weather radars and fire detection radars. These systems need highly directive antennas with a very wide frequency band covering the entire Ku-Band to transmit signals to the receiver with equal power in the whole frequency range and an automatic tracking system to capture the maximum power incident from the satellite while the time and place of the receiver changed. In order to provide good tracking system, one can use digital phase shifter technology or mechanical systems to tilt the beam of the receiver both in azimuth and elevation to the specified direction which will increase the cost of the system or decrease the accuracy of the tracking system respectively [1]. In this paper, printed dipole antenna configurations which operate in the Ku-Band with different gains and tilted beam positions are proposed. Since the proposed antennas have tilted beams in elevation, they can be used in mobile satellite communication systems to eliminate the mechanical hardware or digital circuit needs at least in one direction to tilt the beam of the system [2]. Also, arrays of these printed dipoles will be investigated and the gain of the arrays will be both simulated and measured.

2. KU BAND SYSTEMS AND DIPOLE ANTENNAS

Most of the mobile antenna systems used in vehicles operates in Ku-band for satellite communications. The communication link works properly as the beam of the transmitter antenna (satellite) and the receiver antenna (mobile antenna o) see each other. During the journey of the moving vehicle, as the location and the time vary, the ground station cannot control the transmitter, thus the only way to prevent disconnection is to track the best incoming signal level from the satellite. Majority of the commercial mobile communication systems use either mechanical tracking systems or digital phase shifters to capture the maximum power incident from the satellite. Mechanical systems provide the coverage by rotating both in the azimuth and in the elevation planes which may not be that accurate and fast enough for signal tracking in [1, 3]. Digital/Analog phase shifters overcome the disadvantages of the mechanical systems by simply orienting the main beam of the antenna to the desired direction by adjusting the phase and amplitude of the array elements electronically without rotating the antenna. Unfortunately, this technology is too expensive to be used in civil applications. Digital/Analog phase shifters mostly used in military systems.

In this paper, a dipole antenna system is proposed which can provide full coverage by simply rotating the antenna system only 180 degrees in azimuth direction. In this system, there is no need for rotating the antennas in the elevation angle due to the images of the electric dipoles over perfect infinite conductor (PEC). The dipole itself and image of the dipole can be modeled as a two element array system. The array factor of the two element system directly depends on the

distance between the dipole and its image. As the distance between the dipole and the PEC is varied, the array factor changes. Therefore, one can simply tilt the beam of the mobile antenna system by adjusting the height of the antenna from the vehicle which was studied for 1.5 GHz MSAT application in [2]. In addition to tilt of the main beam of the antenna, grating lobes (or scalloping of the main beam) are generated with the increased height between the dipole antennas and the ground plane [4]. Here, it is assumed that the vehicle body is the ground plane of the dipole antennas. Thus, we eliminate mechanical rotation in elevation requirement by introducing the dipole antennas over the ground plane, and forming two beams through the proper design of the dipole arrays in the azimuth direction, only 180 degrees rotation is sufficient for the coverage of the entire 360 degree azimuth plane.

3. SIMULATION AND MEASUREMENT RESULTS

In this section, simulation and measurement results of the three dipole antenna array configurations will be given, the antennas are single dipole element and 1×2 and 1×8 dipoles over PEC as shown in Figure 1. The distance between the antennas and the ground plane is 13 mm. The dipole element lengths are designed by considering the mutual couplings between the elements.

The antenna elements are simulated using the ADS-2006A Momentum simulation tool. The input return loss results are given in Figure 2. The single dipole element has S_{11} values less than -10 dB between 10.7 GHz–13.1 GHz, while the 1×2 dipole antenna array has S_{11} values less than -10 dB between 10.4 GHz–12.2 GHz.
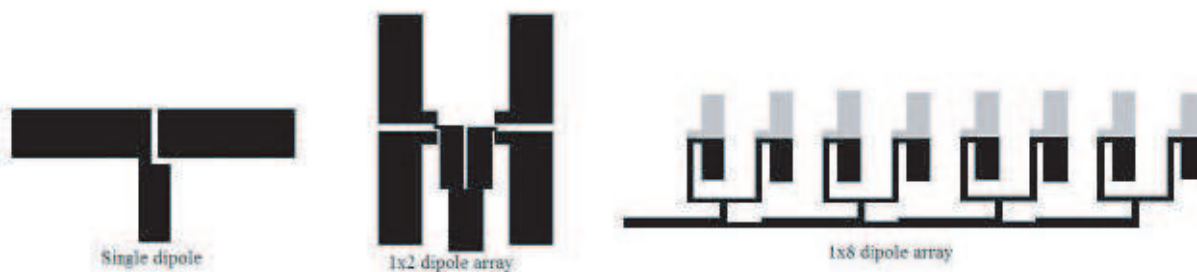
Figure 1: Single dipole, 1×2 dipole, 1×8 dipole arrays (element length $= 15$ mm).
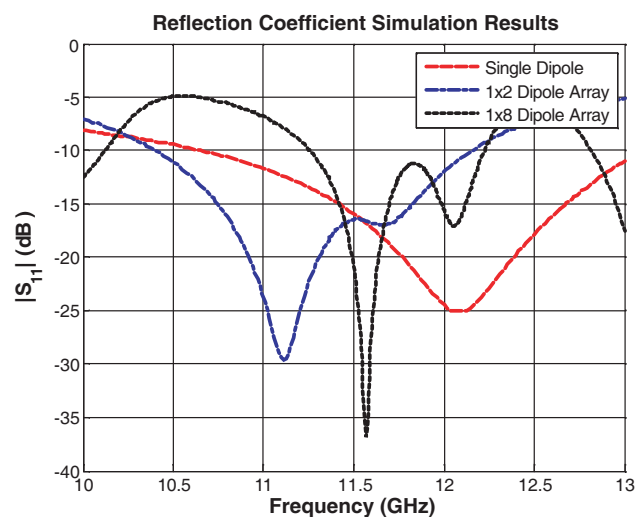
Figure 2: The simulated return loss of single dipole, 1×2 dipole and 1×8 dipole arrays.
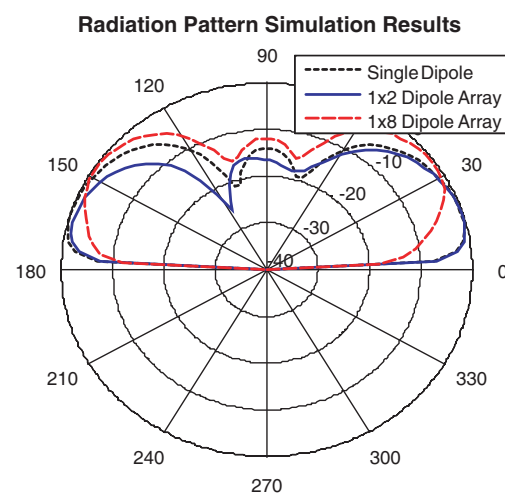
Figure 3: The simulated radiation patterns of single dipole, 1×2 dipole and 1×8 dipole arrays.

The 1×8 dipole antenna array has S_{11} of less than -10 dB between 11.3–12.3 GHz frequency range, and -5 dB return loss point is between 10 GHz and 13 GHz. As the more antenna elements

are added, it is expected to have a narrower bandwidth operation, however, the antennas can still be used with a small return loss in the entire Ku bandwidth.

After obtaining the input impedance results, antennas are simulated for the radiation pattern, and the simulated radiation patterns of the dipole antennas (E-plane) are obtained as shown in Figure 3. As the antenna height changes over the ground plane, the main beam of the antennas are tilted closer to the direction of the array. In Figure 3, for a specific antenna height of 13 mm from the PEC, the radiation patterns are plotted, and it can be seen that the pattern can be tilted even to 20 degrees with the direction of the array. Note that without the presence of the ground plane, the antennas would be radiating in their maximum direction of 90 degrees.

After simulations, the antennas are manufactured and S_{11} measurements are performed using Agilent Network Analyzer 8720ES for the three different antenna arrays without the presence of the ground plane. The single dipole antenna element has less than -15 dB return loss in 10.7–12.7 GHz band, the 1×2 dipole antenna has measured return loss of less than -10 dB in the 10.7–12.7 GHz frequency band, and 1×8 array has less than -12.7 dB return loss in the 10.7–12.7 GHz frequency band. We have simulated the radiation patterns in ADS 2006A, and simulated gain changes between 10–12 dBi in the band of interest for the 1×8 dipole array.
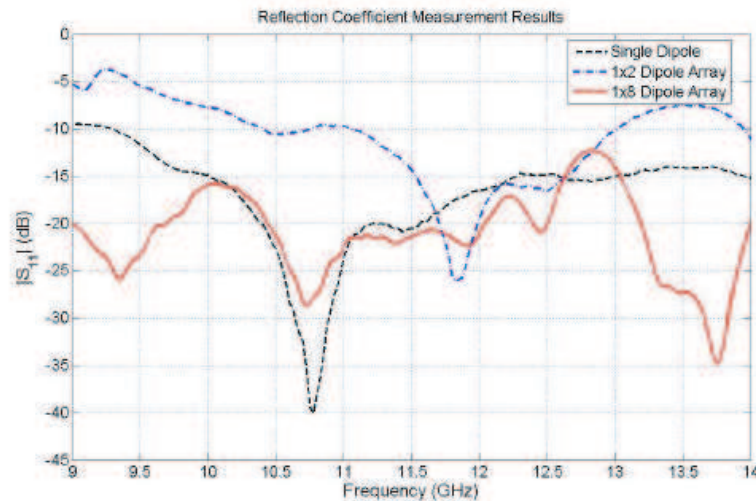
Figure 4: The measured return loss of single dipole, 1×2 dipole and 1×8 dipole arrays.

4. CONCLUSION

Dipole antenna arrays with a beam tilt in elevation plane are proposed to be used in Ku band mobile communication systems. Due to ground plane, antenna beams are tilted, and the requirement for rotation in elevation is eliminated by adjusting the height between the antenna and the ground plane. Three antennas; single dipole, 1×2 dipole array and 1×8 dipole arrays are simulated and measured. Simulation and measurement results show that the return loss of the antennas are less than -10 dB in 10.7–12.7 GHz band. The beam is tilted from the broadside direction such that only azimuth rotation is necessary for a mobile antenna system. Patterns are measured without the presence of the ground plane, as a future work, the antenna gains and radiation patterns will be measured with the ground plane.

REFERENCES

1. Diaz, L. M. and M. S. Smith, "Parabolic torus transreflector antenna," *IEE Proceedings, Part H — Microwaves Optics and Antennas*, Vol. 131, 359–364, December 1984.
2. Huang, J. and A. C. Densmore, "Microstrip yagi array antenna for mobile satellite vehicle application," *IEEE Trans. Antennas and Prop.*, Vol. 39, No. 7, July 1991.
3. Park, U. H., H. S. Noh, S. H. Son, K. H. Lee, and S. I. Jeon, "A novel mobile antenna for Ku-band satellite communications," *ETRI Journal*, Vol. 27, No. 3, June 2005.
4. Balanis, C. A., *Antenna Theory, Analysis and Design*, 2nd Edition, Wiley, New York, 1997.

Using High Impedance Ground Plane for Improving Radiation in Monopole Antenna and Its Unusual Reflection Phase Properties

S. M. Abootorabi, **M. Kaboli**, **S. A. Mirtaheri**, **and M. S. Abrishamian**

K. N. Toosi University of Technology, Iran

Abstract— This paper introduces High Impedance Electromagnetic Surfaces and investigates the performance of monopole antenna embedded on a High Impedance Ground plane. The HIS has an obvious surface wave Band Gap. Suppression of surface wave is used to improve antennas radiation pattern and Back lobe level reduces. For producing HIS we use periodic structures. Simulation and measurement results have good agreement.

1. INTRODUCTION

When natural or synthetic periodic structures interact with electromagnetic waves fascinating phenomena is observable. For example characteristic such as frequency band gap can be identified [1, 2]. These periodic structures operate in the high frequency and microwave frequency range. Within the Band Gap, surface waves which are present in many situations will not support. This property is very useful in antennas. We can replace metal normal ground plane with this surface to reduce undesirable backward radiation. These periodic structures are referred to HIS (High Impedance Surface), EBG (Electromagnetic Band Gap), HIGP (High Impedance Ground Plane) and other designations.

2. EBG DESIGN

The basic High Impedance Surface is shown in Figure 1. It consists of a flat metal sheet covered with an array of metal protrusions on a dielectric substrate which are connected to the lower conducting surface by metal plated vias [3].

To adjust the optimal design to the required frequency, the size of the squared EBG unit cell is designed as follows: $t = 2.4\,\text{mm}$, $d = 0.6\,\text{mm}$, $a = 7.2\,\text{mm}$, $g = 1.2\,\text{mm}$ and $\varepsilon_r = 2.55$. According to our knowledge there is no accurate formula to calculate frequencies of the Stop Band. One procedure is extracting the dispersion diagram. The dispersion diagram or $\beta\text{-}f$ can be calculated from the unit cell and applying a periodic boundary condition on the sides of the unit cell to follow a periodic structure extending to infinity and PML boundary condition on the top wall as shown in Figure 2(b). Two dimensional eigen mode solutions for Maxwell's equations are solved for the Brillouin zone [4, 5]. In the present work, a commercially available simulation tool based on finite element method has been used. Figure 2(a) shows the simulated dispersion diagram. A complete band gap between first mode and the second mode, from frequency 4.6 GHz to 7.9 GHz can be seen.
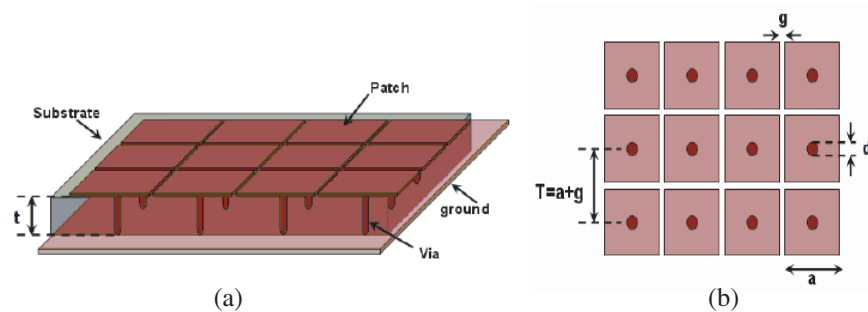
Figure 1: Geometry of EBG structure (a) perspective view (b) top view.

3. REFLECTION PHASE

One of the attractive properties of EBG structures is the reflection phase, which is of special interest. The reflection phase is defined as the phase of reflected electric field at the reflecting surface. It is normalized to the phase of the incident electric field at the reflecting surface. Unlike

(a)   (b)
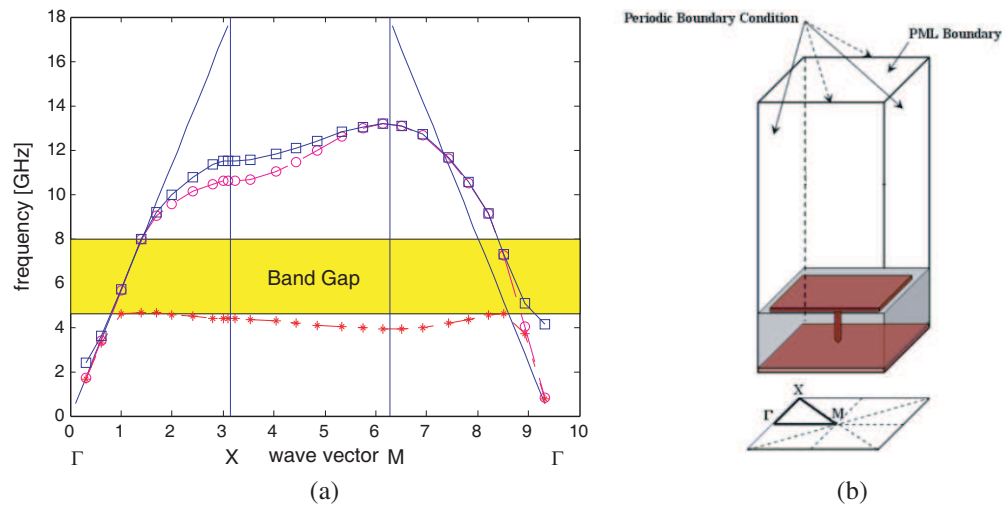
Figure 2: Dispersion diagram of the EBG structure having 7.2-mm square patches with a substrate of $\varepsilon_r = 2.55$ and height of 2.4-mm (b) unit cell of the EBG structure.

(a)   (b)
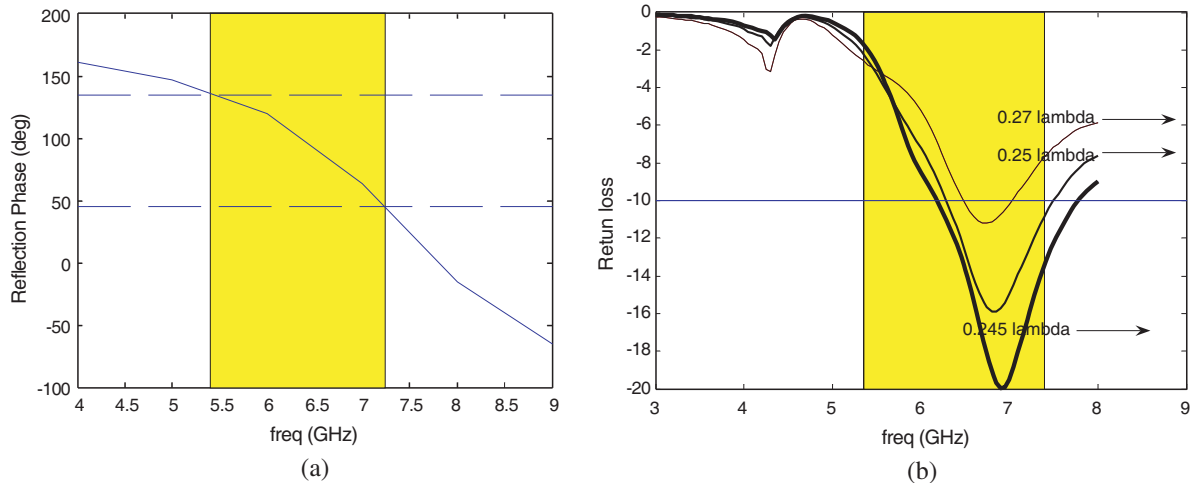
Figure 3: Reflection phase of the EBG structure (b) return loss of monopole when its length is 0.245λ, 0.25λ and 0.27λ.

perfect electric conductors which have 180° reflection phase and perfect magnetic conductors which have 0° reflection phase for normal incident plane wave, the reflection phase of these structures changes continuously from +180° to −180° versus frequency [6]. By modelling a unit cell with periodic boundary condition on side walls and running a parametric sweep using an incident wave excitation at different frequencies the reflection phase can be calculated from field results in HFSS. Due to the procedure and formulas which are used in reference [7], reflection phase of the EBG structure with the same parameters of preceding session was obtained with HFSS and it is observed in Figure 3(a).

Now one question arises: where is the suitable frequency band? For this purpose, instead of normal metal ground plane, the EBG structure has been used for a monopole antenna. The length of monopole antenna has been changed from 0.245λ to 0.27λ and each time return loss of the antenna was obtained (the frequency of simulation is 5 GHz). With a deeper look in reflection phase diagram and return loss we can guess the suitable frequency band for monopole antenna. As we seen from Figures 3(a) and 3(b), the suitable frequency band is overlap of input match frequency and where the reflection phase has a quantity between 90° ± 45°.

4. MONOPOLE ANTENNA

Monopole antenna is one of the beneficial antennas in communication, it is established on a ground plane which is always finite and its edges make undesired effect on radiation pattern. In addition

to space waves the antenna generates surface waves in the ground plane which radiate when they reach edges and corners [8]. Combination of radiation from the wire and the edges of ground plane causes a multipath nulls and lobes at various angles. In this manner thus, the monopole antenna was examined on normal ground plane and also on high impedance surface of the same size. Dimension of the ground plane was $2\lambda \times 2\lambda$. Simulation and measurement results will be seen ahead. In Figure 4 radiation pattern of monopole antenna over normal metal ground plane for 6 GHz frequency can be observed.

As we see from radiation pattern of the figure, there are ripples in forward direction and a significant amount of power is wasted in back lobes. There are good agreements with measurement and simulation results as shown in Figure 4. Now if normal metal ground plane is replaced with high impedance ground plane of the same size (Figure 5), good results will be obtained. Dimensions of the EBG structure are as before, except that in this case, height of the substrate is 1.58 mm. As we know driven currents can exist on any reflective surface, they don't propagate on high impedance ground plane. All the induced currents are restricted to a region around antenna and they don't reach edges of the ground [9].

Surface current density in the case of normal metal ground plane and high impedance ground plane was obtained by HFSS and the results are shown in Figure 6. So absence of multipath interference leads to a smoother radiation pattern and less wasted power in back lobes. In Figure 7(a), we can see the measurement results for return loss of monopole antenna on normal metal ground plane and high impedance ground plane. Comparison of patterns on normal metal ground plane and HIGP in 6 GHz frequency which are obtained by HFSS simulation could be seen in Figure 7(b).

As we see, due to suppression of surface waves in the band gap, a significant amount of power that is wasted in back lobes reduces about 8 dB, also radiation power in forward direction increases about $10 \sim 25$ dB in some directions. There are good agreements with measurement and simulation
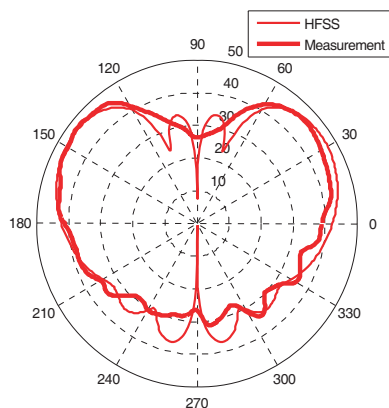
Figure 4: Comparison of simulation and measurement results for radiation pattern of monopole on normal plane at 6 GHz frequency.
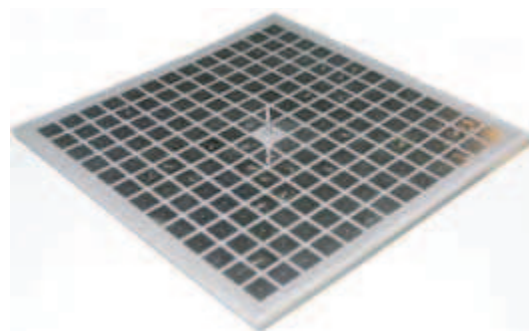
Figure 5: Monopole antenna above HIGP.

(a)   (b)
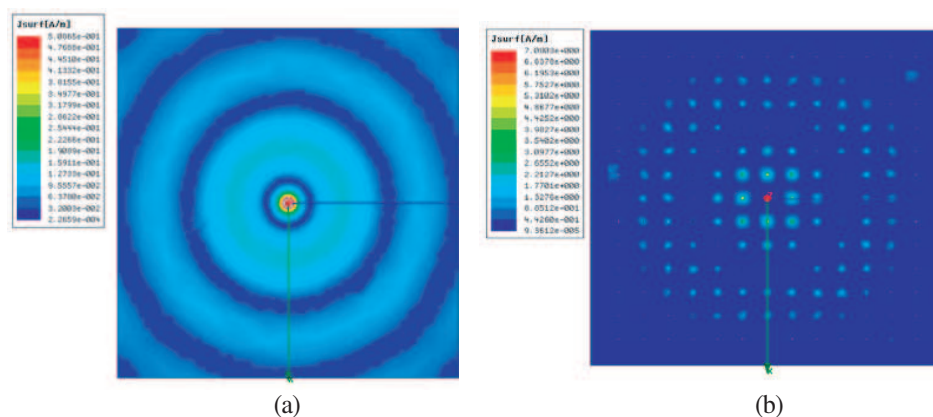
Figure 6: Surface current density (a) normal ground plane (b) HIGP.

results in the case of high impedance ground plane in 6 GHz frequency as shown in Figure 7(c).

The band gap for this EBG structure was obtained from 5.09 to 7.9 GHz. Now if operational frequency of the antenna is outside of the band gap, high impedance ground plane acts like normal metal ground plane. Radiation pattern of monopole antenna on normal metal ground plane and high impedance surface at 8 GHz frequency is observed in Figure 8(a). Due to existence of surface
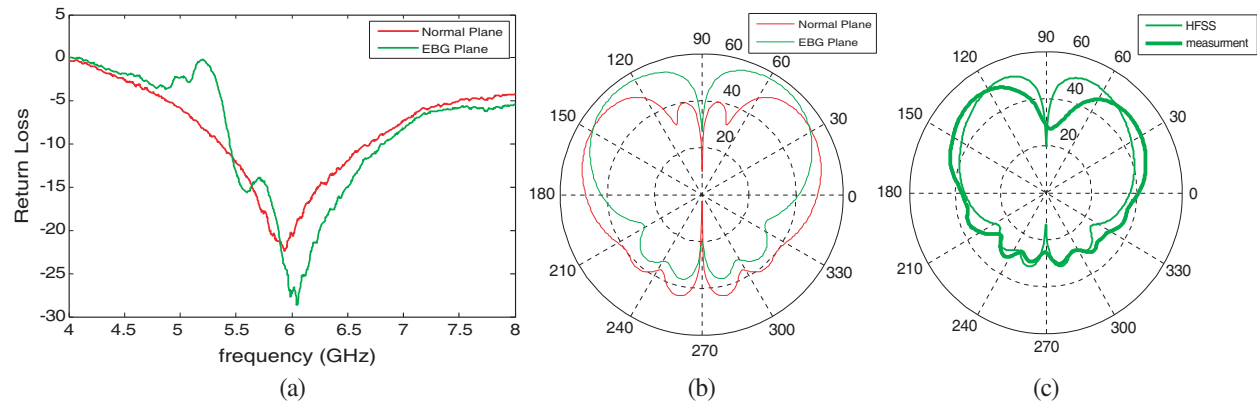
Figure 7: (a) measurement results for return loss of monopole antenna on normal plane and HIGP (b) comparison of patterns on normal metal ground plane and HIGP in 6 GHz frequency (c) measurement and simulation results in the case of high impedance ground plane.
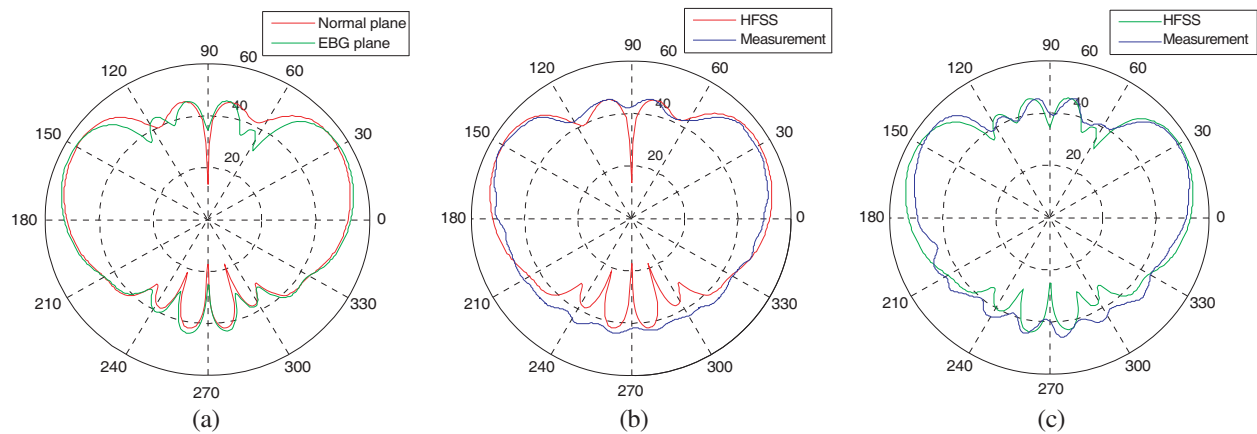
Figure 8: (a) Comparison of patterns on normal metal ground plane and HIGP in 8 GHz frequency (b) comparisons of simulation and measurement results on normal plane (c) comparisons of simulation and measurement results on HIGP.
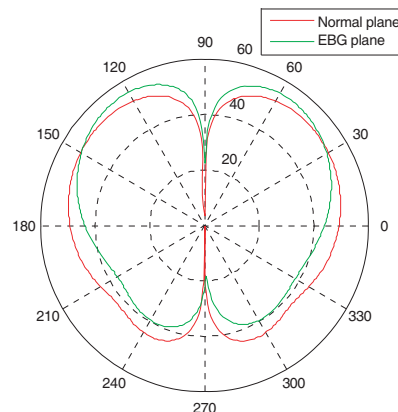
Figure 9: Simulation results for radiation patterns of monopole antenna on normal ground and HIGPP at 6 GHz frequency dimension of the ground plane is taken $1\lambda \times 1\lambda$.

waves outside of the band gap, high impedance ground plane has no effect. In Figures 8(b) and 8(c) comparisons of simulation and measurement results for radiation pattern of monopole antenna on normal metal ground plane and HIGP at 8 GHz frequency are observed.

Effects of the ground plane dimension and number of square patches have also been investigated. This time, dimension of the ground plane is taken $1\lambda \times 1\lambda$. Simulation results for radiation patterns of monopole antenna on normal ground and HIGPP at 6 GHz frequency are compared in Figure 9. As we see smaller ground plane and fewer numbers of square patches will have less effect of improving radiation pattern.

5. CONCLUSION

As was shown in this study, the EBG structure can be used as a ground plane for monopole antenna. Radiation power in forward direction increases about $10 \sim 25$ dB and the power wasted in back lobes reduces about 8 dB. Simulation and measurement results have good agreement with each other. Reflection phase of these structures has a unique property. It is changing continuously from $+180°$ to $-180°$ with frequency. It has been observed that where the reflection phase has a quantity between $90° \pm 45°$ is very close to input match frequency band. Effect of HIGP dimension and the number of square patches have also been investigated and we saw that more number of square patches will have a better effect of improving radiation pattern.

ACKNOWLEDGMENT

REFERENCES

1. Xu, H.-J., Y.-H. Zhang, and Y. Fan, "Analysis of the connector section between K connector and microstrip with Electromagnetic Band Gap (EBG) structure," *Progress In Electromagnetics Research*, PIER 73, 239–247, 2007.
2. Pirhadi, A. and M. Hakkak, "Using electromagnetic band gap superstrate to enhance the bandwidth of probefed Microstrip antenna," *Progress In Electromagnetics Research*, PIER 61, 215–230, 2006.
3. Mohajer-Iravani, B., S. Shahparnia, and O. M. Rahami, "Coupling reduction in enclosures and cavitiesusing electromagnetic band Gap structures," *IEEE Transactions on Electromagnetic Compatibility*, Vol. 48, No. 2, May 2006.
4. Mahmoudian, A. and J. Rashed-Mohassel, "Reduction of EMI and mutual coupling in array antennas by using DGS and AMC structures," *PIERS Online*, Vol. 4, No. 1, 2008.
5. Mahmoudian, A. and K. Forooragi, "A novel planar leaky wave antenna for wireless applications," *Journal of Electromagnetic Waves and Applications*, Vol. 22, No. 2, 313–324, 2008.
6. Yang, F. and Y. Rahmat-Samii, "Reflection phase characterizations of the EBG ground plane for low profile wire antenna applications," *IEEE Transactions on Antennas and Propagations*, Vol. 51, No. 10, October 2003.
7. Remski, R., "Analysis of photonic band gap surfaces using ansoft HFSS," *Microwave Journal*, September 2000.
8. Sievenpiper, D., L. Zhang, R. F. J. Broas, N. G. Alexopolous, and E. Yablonovitch, "High-impedance electromagnetic surfaces with a forbidden frequency band," *IEEE Transactions on Microwave Theory and Technique*, Vol. 47, No. 11, November 1999.
9. Sievenpiper, D., "High-impedance electromagnetic surfaces," Ph.D. Dissertation, UCLA, 1999.

The Impact of New Feeder Arrangement on RDRA Radiation Characteristics

A. S. Elkorany, **A. A. Sharshar**, **and S. M. Elhalafawy**

Department of Electronics and Electrical Comm., Faculty of Electronics Eng.
Menoufia University, Menouf, Menoufia 32952, Egypt

Abstract— In this paper, a new feeder arrangement for rectangular dielectric resonator antenna (RDRA) is proposed for ultra wideband applications A short metallic patch is introduced in the air gap between the dielectric and the ground plane and attached to the coaxial probe that excites the RDRA. The patch dimensions have been varied to obtain the widest antenna impedance bandwidth (VSWR $\leq$ 2). An impedance bandwidth of about 4 : 1 between 10 GHz and 40 GHz is obtained The proposed antenna has been examined using Finite Element Method (FEM) and Finite Integration Technique (FIT). Excellent agreement between both results is obtained.

1. INTRODUCTION

Dielectric resonator antennas (DRAs) have been extensively investigated after the first paper published by Long et al. [1]. Recently one of the major topics in DRA research is to widen the impedance bandwidth [2]. The techniques that have been used include, inserting air gap between the dielectric and the ground plane [3, 4], different dielectric geometries [5–7], strip fed [8], hybrid configuration [9], and multi-segment configuration [10].

Rectangular dielectric resonator antenna with an air gap that inserted between the dielectric and ground plane was previously investigated, and an achievement in the impedance bandwidth in the order of 31% in the C band has been obtained [3].

In this work, a further development in the antenna structure has been suggested to get an improvement in the antenna impedance bandwidth. A new feeder arrangement has been proposed and its effect on the antenna impedance bandwidth has been recorded. This is done by inserting a small rectangular metallic patch within the air gap. The metallic patch is connected to the inner conductor of the coaxial probe feeder. This technique was used successfully in a previous work with microstrip patch antenna, in which two metallic patches with different shapes were inserted between the patch and ground plane [11].

In the present research, the dimensions of inserted metallic patch have been changed and the impact of that on the antenna impedance bandwidth has been examined. An impedance bandwidth of about 4 : 1 between 10 GHz and 40 GHz is obtained when the patch dimensions were $L = 9$ mm, and $W = 3$ mm. The proposed antenna has been examined using two different techniques, FEM which is operated in frequency domain through the usage of HFSS, and FIT that is operated in time domain through the usage of CST Microwave Studio. Excellent agreement between both results is obtained.

2. ANTENNA STRUCTURE

The structure of the proposed antenna is shown in Fig. 1. The dielectric that is used is FR4 with $\varepsilon_r = 4.5$, and its dimensions are 20 mm $\times$ 12 mm $\times$ 5 mm, and it is placed at a distance of 1.5 mm above the ground plane. The probe diameter is 1.25 mm, and its height is 2.5 mm. The inserted patch height is 1 mm from the ground plane. All the antenna parameters are held constant in all cases except the patch dimensions that are varied to obtain the widest impedance bandwidth.

3. RESULTS AND DISCUSSION

Many trials have been done to obtain the best patch dimensions and position that produce the widest impedance bandwidth. The entire structure without the inserted metallic patch has been first examined and the obtained return loss S_{11} is shown in Fig. 2. Good agreement between FIT and FEM results has been obtained. From figure, the impedance bandwidth is depicted to be about 61.7% between 11.2 GHz and 21.2 GHz. When the patch was inserted unexpected ultrawide impedance bandwidth has been obtained. The best results only are recorded here to show the effect of this new arrangement on the antenna impedance bandwidth.

In the beginning, the inserted patch height from ground plane is optimized, results not shown, but the best obtained results were at 1 mm height, then the patch dimensions was optimized. Fig. 3
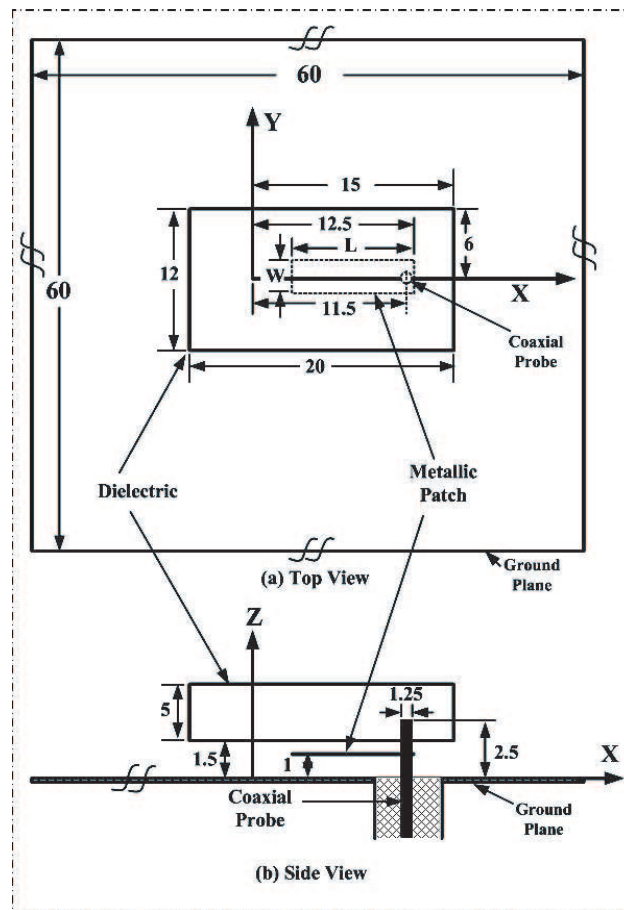
Figure 1: Proposed RDRA structure (all dimensions are in mm).
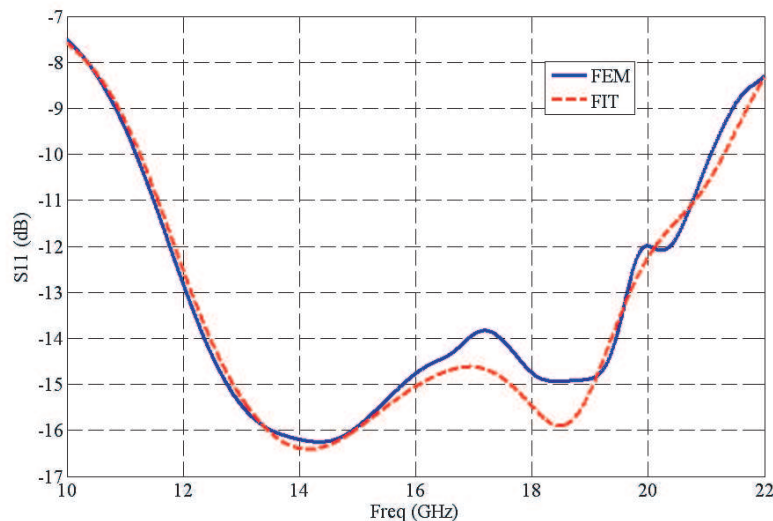
Figure 2: The return loss versus frequency for the entire structure without the inserted metallic patch.

shows the return loss versus the operating frequency for a patch width of $W = 2$ mm and different values of patch length (L). From figure, a bandwidth of 2.9 : 1 is obtained from 10 GHz up to 29 GHz when $L = 9$ mm. FIT was used to obtain all the results otherwise indicated.

Also Figs. 4 and 5 show the case for a patch width of $W = 3$ mm and $W = 4$ mm respectively, and for different values of patch length (L). As shown in Fig. 4, an impedance bandwidth of about 4 : 1 from 10 GHz up to beyond 40 GHz is obtained when $L = 9$ mm. Also a bandwidth of about 2.77 : 1 is obtained from 9.5 GHz up to 26.3 GHz when $L = 10$ mm, as shown in Fig. 5. Fig. 6 shows
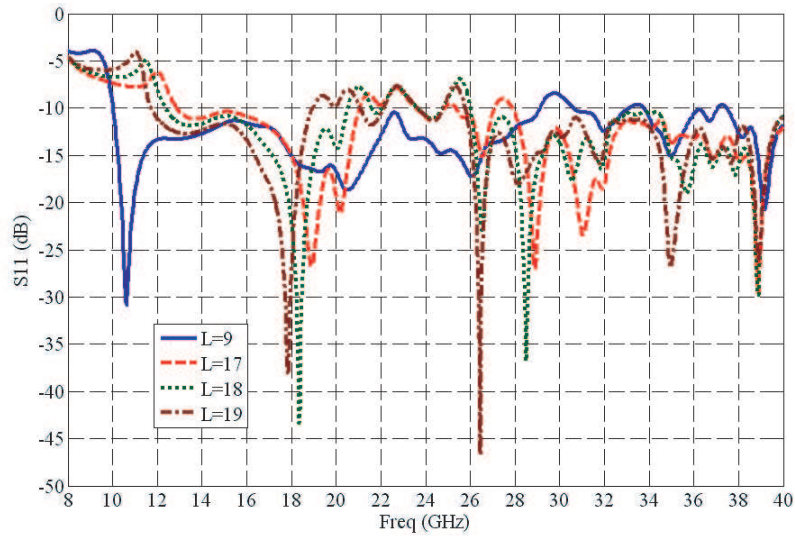
Figure 3: The return loss versus frequency for $W = 2$ (all dimensions are in mm).
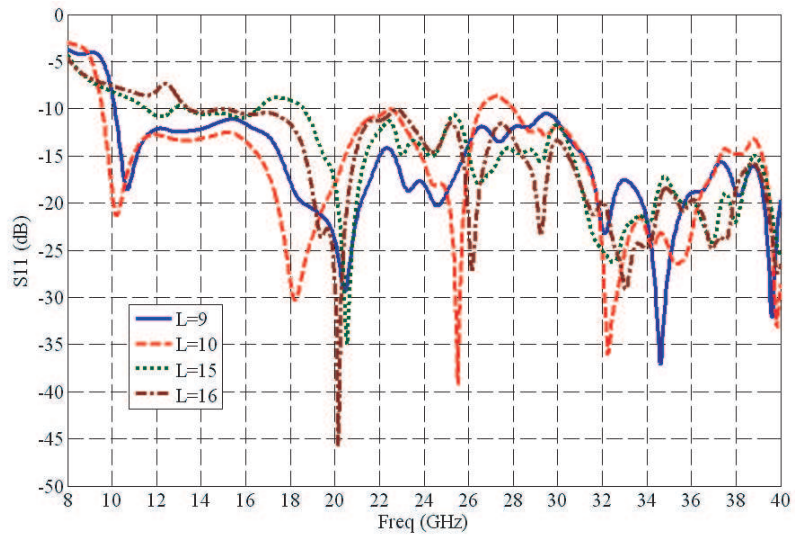
Figure 4: The return loss versus frequency for $W = 3$ (all dimensions are in mm).
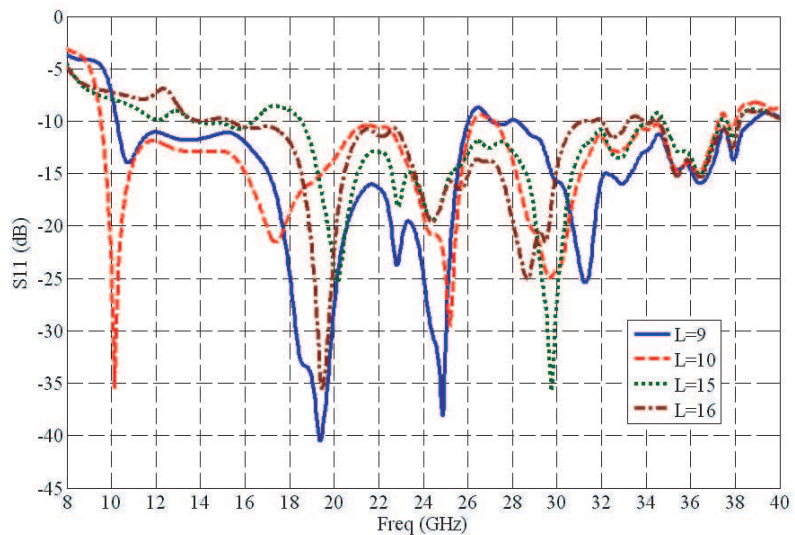
Figure 5: The return loss versus frequency for $W = 4$ (all dimensions are in mm).
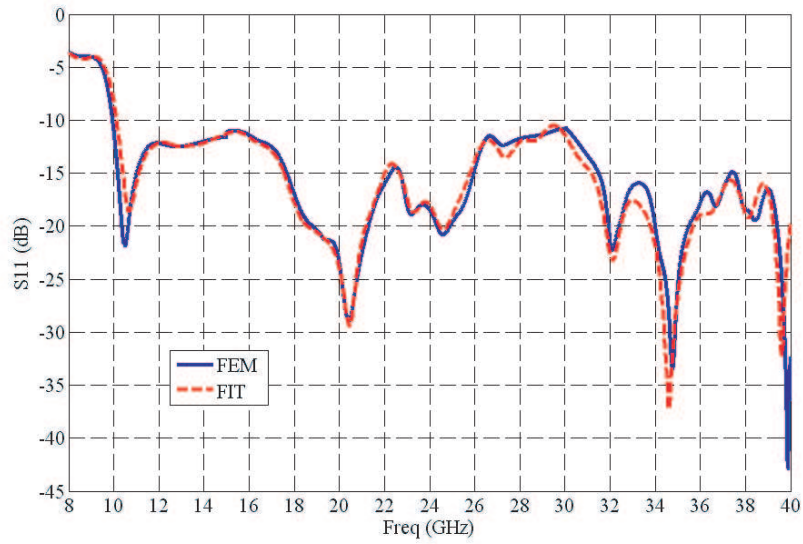
Figure 6: Comparison between FIT and FEM return loss results for $L = 9\,\text{mm}$ and $W = 3\,\text{mm}$.

(a)

(b)
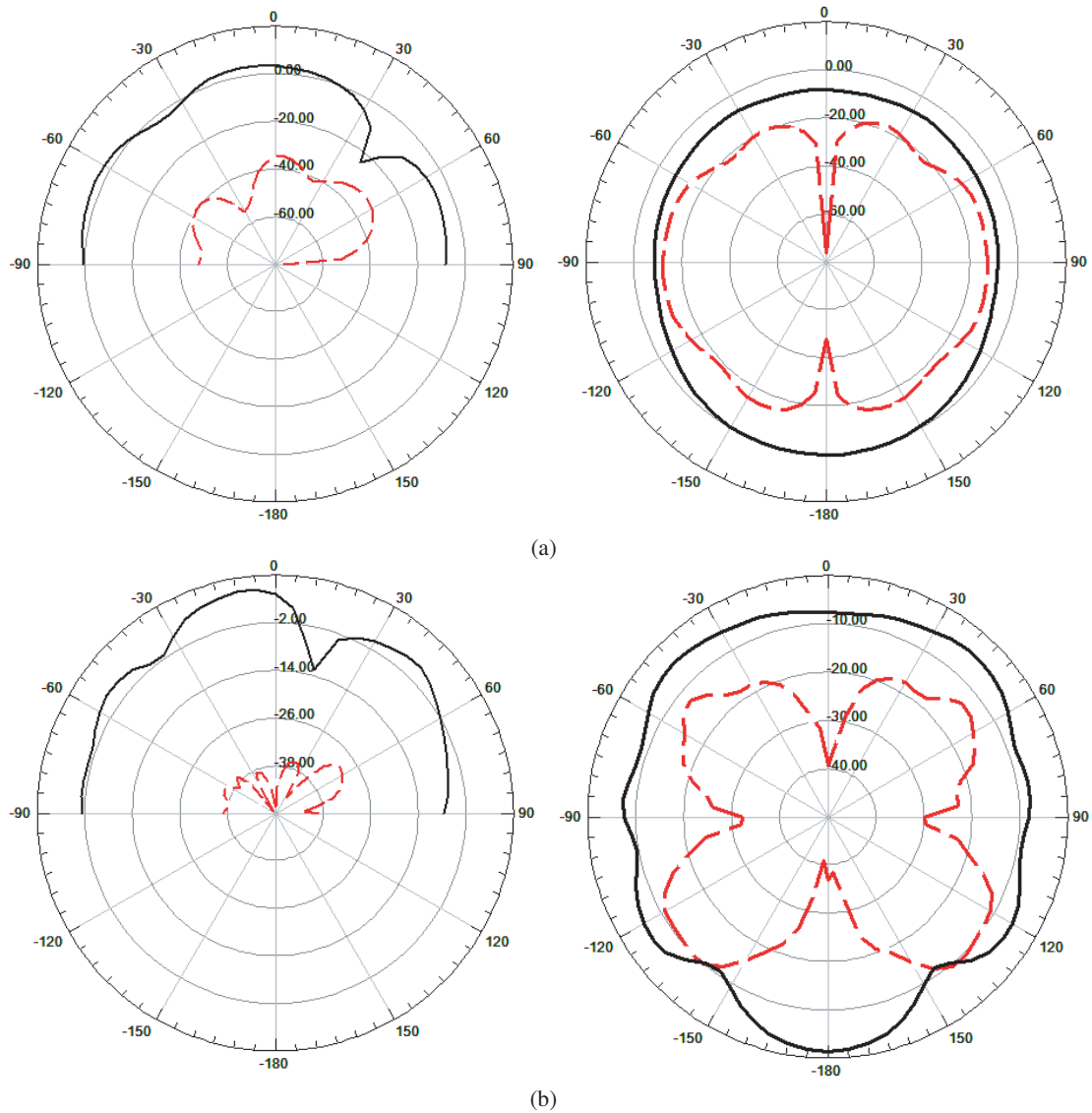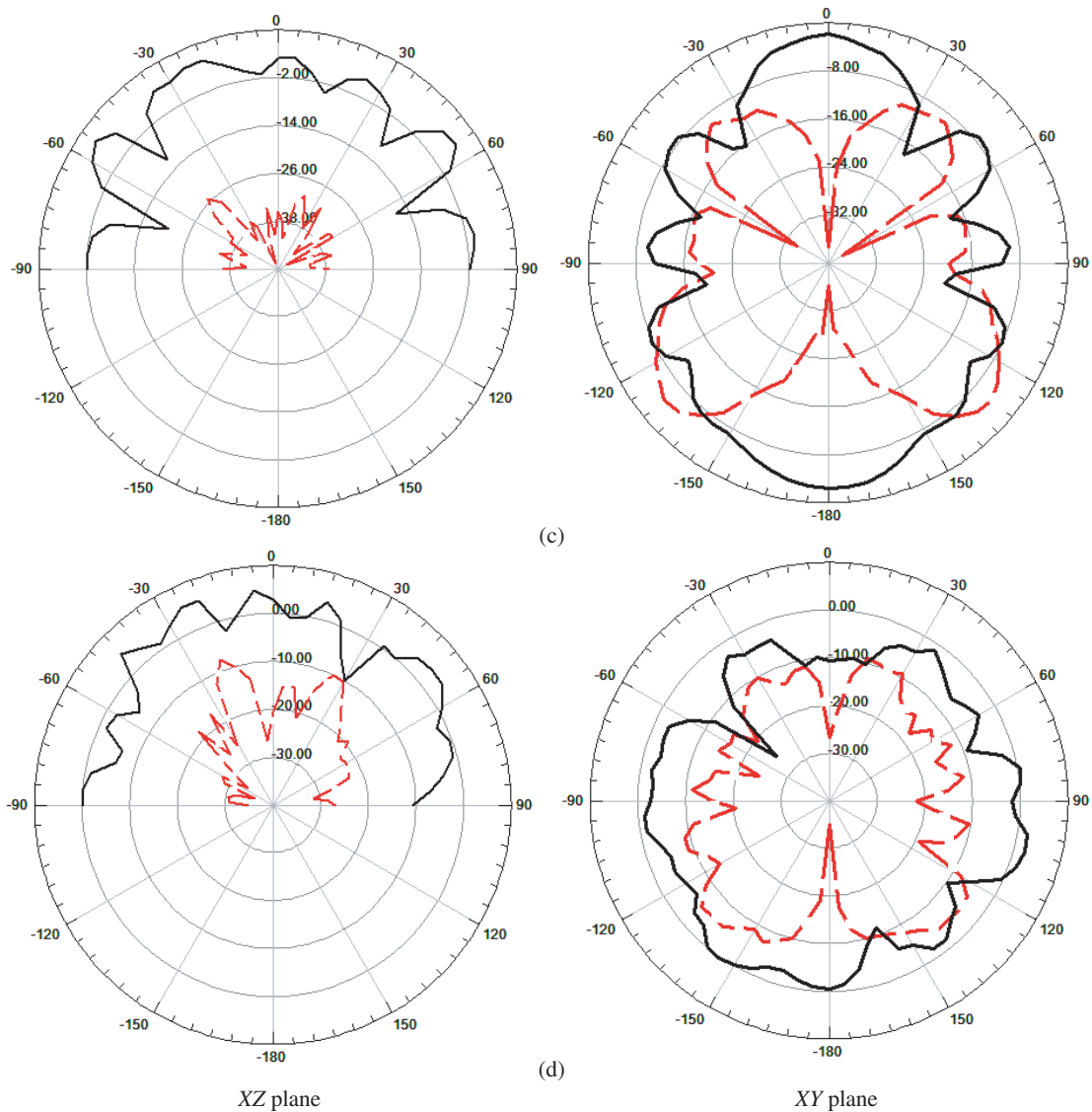
Figure 7: The radiation pattern for the Antenna with $W = 3\,\text{mm}$, and $L = 9\,\text{mm}$ (E_θ (solid) and E_ϕ (dashed)). (a) Freq = 10.5 GHz, (b) Freq = 20.5 GHz, (c) Freq = 34.8 GHz, (d) Freq = 40 GHz.

a comparison between FIT and FEM results for the widest impedance bandwidth case, $W = 3\,\text{mm}$, $L = 9\,\text{mm}$. Excellent agreement between both results is obtained.

Figure 7 shows the radiation pattern for the proposed antenna with $W = 3\,\text{mm}$ and $L = 9\,\text{mm}$ at 10.5 GHz, 20.5 GHz, 34.8 GHz, and 40 GHz. Generally, there is no significance change in the radiation pattern at theses frequencies, with maximum radiation in the broadside direction.

4. CONCLUSION

In this paper, a new feeder arrangement has been proposed, and its effect on the antenna impedance bandwidth has been checked. An extensive wideband in the order of $4 : 1$ between 10 GHz up to beyond 40 GHz has been obtained. This may be investigated due to the mutual effect between the inserted patch and the dielectric resonator, so that a behavior of hybrid antenna has been resulted. There is no significance change in the radiation pattern at the specified frequencies, with maximum radiation in the broadside direction.

REFERENCES

1. Long, S. A., M. W. McAllister, and L. C. Shen, "The resonant cylindrical cavity antenna," *IEEE Trans. Antennas Propag.*, Vol. 31, 206–412, 1983.
2. Petosa, A., *Dielectric Resonator Antenna Handbook*, Artech House, INC., 2007.

3. Elkorany, A. S., S. M. El-Halafawy, and H. A. Sharshar, "FDTD analysis of a new wideband inserted RDRA," *Minufiya Journal of Electronic Engineering Research (MJEER)*, Vol. 7, No. 2, July 2007.

4. Cooper, M., "Investigation of current and novel rectangular dielectric resonator antennas for broadband applications at L-band frequencies," M.Sc. Thesis, Carleton University, 1997.

5. Kishk, A. A., Y. Yin, and A. W. Glisson, "Conical dielectric resonator antennas for wide-band applications," *IEEE Trans. Antennas Propag.*, Vol. 50, No. 4, 469–474, April 2002.

6. Kishk, A. A., "Wide-band truncated tetrahedron dielectric resonator antenna excited by a coaxial probe," *IEEE Trans. Antennas Propag.*, Vol. 51, No. 10, 2913–2917, October 2003.

7. Guha, D. and Y. M. M. Antar, "New half-hemispherical dielectric resonator antenna for broadband monopole-type radiation," *IEEE Trans. Antennas Propag.*, Vol. 54, No. 12, 3621–3628, December 2006.

8. Li, B. and K. W. Leung, "Strip-fed rectangular dielectric resonator antennas with/without a parasitic patch," *IEEE Trans. Antennas Propag.*, Vol. 53, No. 7, 2200–2207, July 2005.

9. Lapierre, M., Y. M. M. Antar, and A. Petosa, "Ultra wideband monopole/dielectric resonator antenna," *IEEE Microwave and Wireless Components Letters*, Vol. 15, No. 1, 7–9, January 2005.

10. Petosa, A., N. Simons, R. Siushansian, A. Ittipiboon, and M. Cuhaci, "Design and analysis of multisegment dielectric resonator antennas," *IEEE Trans. Antennas Propag.*, Vol. 48, No. 5, 738–742, May 2000.

11. Ang, I. and B. L. Ooi, "A broad band stacked microstrip patch antenna," *Asia-Pacific Microwave Conference, APMC 2005*, Vol. 2, December 4–7, 2005.

Vector Diffraction Integrals for Solving Inverse Problems of Radio-holographic Sensing of the Earth's Surface and Atmosphere

A. G. Pavelyev

IRE RAS, Moscow Region 141120, Russia

Abstract— Vector relationships between the fields on a certain surface confining an inhomogeneous three-dimensional volume and the fields inside this volume were obtained by the Stratton-Chu method developed for the case of homogeneous media. The vector relationships allow one to solve the direct and inverse problems of determining the fields inside an inhomogeneous medium given the field on its boundary. It is shown that the Green's function of the scalar wave equation in an inhomogeneous medium should be used as the reference signal for solving the inverse problem of the radio-occultation (RO) monitoring. This validates the method of radio-holographic focused synthetic aperture method (RHFSA) previously used for high-accuracy retrieval of the vertical refractive-index profiles in the ionosphere and atmosphere. Zverev's diffractive integral is used to compare the canonical transform (CT), back propagation (BP), and RFSA methods. For comparison, a general inverse operator (GIO) is introduced. The CT and BP transforms can be obtained by application of the GIO transform to Zverev's diffractive integral. The CT method can resolve physical rays in multipath situations under an assumption of the global spherical symmetry of the atmosphere and ionosphere. The obtained equations can be used for the high-accuracy solving of inverse problems of remote sensing of the Earth's atmosphere and surface by highly-stabilized signals of radio-navigational satellites.

1. INTRODUCTION

The digital methods for remote sensing (the earth- and space- based radiotomographic investigation, radio occultation sounding in the satellite-to-satellite communication link etc.) use the diffractive integrals connecting electromagnetic fields on the some interface or curve in the space (for example, the orbital trajectory of a low earth orbit (LEO) satellite) with the field in the space between the transmitter and receiver [1–4]. Below the application of the diffractive integrals to the radio occultation remote sensing technique is discussed. Radio occultation (RO) investigations of the earth's atmosphere are possible by using two satellites, one transmitting radio signals and the other one receiving them. As the satellites move, the ray trajectory of radio waves passes through different portions of the atmosphere. The phase and amplitude variation profiles are recorded onboard the receiver of low earth orbital (LEO) satellites. These profiles provide information about the refractive properties of the earths atmosphere [3–5]. This information is important for global real-time monitoring of the troposphere, stratosphere, and ionosphere, and for estimating conditions for telecommunication in trans-atmospheric satellite-to-satellite links. In recent years new radio-holographic techniques based on combination of the RO amplitude and phase data have been considered, such as back-propagation [6, 7], synthetic aperture method [8], radio-holographic focused synthetic aperture (RHFSA) [4], canonical transform [9], and the Full Spectrum Inversion (FSI) method [10]. These studies improved the vertical resolution and accuracy in retrieving of physical parameters of the atmosphere and broadened the applicability domain of RO method. The aim of this paper consists in the presentation of the diffractive vector integrals for bistatic radio holographic remote sensing of the terrestrial surface and atmosphere, substantiating the RFSA method, introducing a simple way to obtain the CT and BP transforms and establishing their limitations using a GIO.

2. DIFFRACTIVE INTEGRALS

Scheme of the RO remote sensing is shown in Fig. 1. The centre of the earth is located at point O (Fig. 1). GPS transmitter is located in the plane POG at point G and a receiver is installed onboard a Low Earth Orbital satellite (LEO) at point P (Fig. 1). SP is the trajectory of LEO satellite. Let us chose the two parallel planes S_1, S_2 from opposite sides of the atmosphere and ionosphere (Fig. 1). The surfaces S_1, S_2 are located in free space These planes are perpendicular to plane POG (Fig. 1). The inhomogeneous part of medium between the transmitter and receiver

occupies the volume V. The diffractive vector integrals have been obtained in the form [4]:

$$\mathbf{E}_{d,b}(A) = -(4\pi)^{-1} \int_{s1,s2} \left\{ i\omega\mu/c[\mathbf{n} \times \mathbf{H}]\Phi^{\pm} + [\mathbf{n} \times \mathbf{E}] \times \nabla\Phi^{\pm} + (\mathbf{n} \cdot \mathbf{E})\nabla\Phi^{\pm} \right\} da + \mathbf{E}_{vd,b}(A) \quad (1)$$

$$\mathbf{E}_{vd,b}(A) = -(4\pi)^{-1} \int_{v} (\mathbf{E} \cdot \nabla \ln \varepsilon)\nabla\Phi^{\pm} da \quad (2)$$

$$\mathbf{H}_{d,b}(A) = (4\pi)^{-1} \int_{s1,s2} \left\{ i\omega\varepsilon/c[\mathbf{n} \times \mathbf{E}]\Phi^{\pm} - [\mathbf{n} \times \mathbf{H}] \times \nabla\Phi^{\pm} - (\mathbf{n} \cdot \mathbf{H})\nabla\Phi^{\pm} \right\} da + \mathbf{H}_{vd,b}(A) \quad (3)$$

$$\mathbf{H}_{vd,b}(A) = (4\pi)^{-1} \int_{v} (\mathbf{E} \cdot \nabla \ln \varepsilon)\nabla\Phi^{\pm} da \quad (4)$$

where ε is the electric permittivity, μ is the magnetic permeability of the medium. The electric and magnetic vectors $\mathbf{H}, \mathbf{E}$ contain the time only as a factor $\exp(-i\omega t)$. In Equations (1)–(4) indexes "d" and "b" and the signs "+" and "−" are relevant to the direct and back propagating radio waves. The volume integrals (2) and (4) introduce the appending contribution to the fields. In the case of radio occultation experiments the medium under investigation is spherical symmetric, and the volume contribution introduces only the changes in the orientation of the electric and magnetic vectors because of the refraction of the transverse electromagnetic waves in the layered medium. For example, the volume integral (2) is equal to zero if the electric vector $\mathbf{E}$ is oriented normally to the gradient of the electric permittivity ε. The Green function $\Phi^{\pm}$ in Equations (1)–(4) should be found as a solution of the wave equation:

$$\Delta\Phi^{\pm} + k^2\Phi^{\pm} = -4\pi\delta(\mathbf{r} - \mathbf{r}') \quad (5)$$

where $\delta(\mathbf{r}-\mathbf{r}')$ is delta-function, $\mathbf{r}, \mathbf{r}'$ are vectors describing the positions of the element of integration at (x, y, z) and the point of observation A at (x', y', z') inside volume V. Distance $|\mathbf{r} - \mathbf{r}'| = r$ is measured from the element at (x, y, z) to the point of observation at A: $r = [(x - x')^2 + (y - y')^2 + (z - z')^2]^{1/2}$. In general case this solution is accounting for refraction, multibeam propagation, diffraction, scattering effects and may have a very complex form. The Equations (1)–(5) with Green function Φ^+ give solution of direct problem. This function can describe one ray and multi-path propagation (lines GBP, GMP), reflection from the earth's surface (ray GDP) (Fig. 1), and other propagation effects. From the Green function one can obtain the refraction angles of radio-waves $\xi(p)$ as function of the impact parameter p, if the trajectory data: the distances R_1, R_2, the central angle θ, and the impact parameter ps corresponding to the line of sight GLP are known (Fig. 1). To find the field at any point A (x', y', z') (Fig. 1) it is necessary to know the field distribution in the plane S_1 according to Equation (1) or (3) and to estimate the volume contribution from (2) or (4). It follows from Equations (1)–(5) that for precise retrieving of the fields in the space between the transmitter and receiver it is necessary to have accurate solution Φ^- of the scalar Equation (5). This can be made accurately for the case of layered spherical symmetric structures
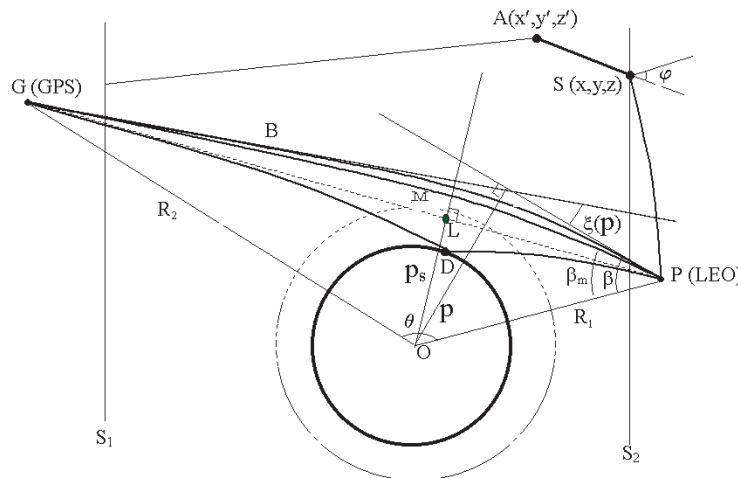
Figure 1: Scheme of the radio-holographic RO remote sensing.

when the volume integrals contribution (2) and (4) may be neglected. The Green function Φ^- in this case can be found by approximate methods (for example, WKB method). For accurate retrieving of the irregular structures it is necessary to estimate the volume integrals in (2) and (4). In the cases when the volume integrals can be neglected (1) and (3) present 3-D radio holographic equations to restore the radio fields between the transmitter and receiver using known radio fields at the surface S_2. As shown in [4]. In the case of the 2-D homogeneous medium the next equations for the fields $\mathbf{H}, \mathbf{E}$ have been obtained [4]:

$$\mathbf{E}_b(A) = 0.5[k_0/(2\pi)]^{1/2} \int_{SP} \{-\mu[\mathbf{n} \times \mathbf{H}] + [\mathbf{n} \times \mathbf{E}]\tau + (\mathbf{n}\mathbf{E})\tau\} \exp(i\pi/4 - ikr)/r^{1/2} dl \quad (6)$$

$$\mathbf{H}_b(A) = 0.5[k_0/(2\pi)]^{1/2} \int_{SP} \{\varepsilon[\mathbf{n} \times \mathbf{E}] + [\mathbf{n} \times \mathbf{H}] \times \tau + (\mathbf{n} \cdot \mathbf{H})\tau\} \exp(i\pi/4 - ikr)/r^{1/2} dl \quad (7)$$

where k_0 is the wave number corresponding to propagation of radio waves in a vacuum, and τ is the unit vector parallel to the direction on the current integration element from the observation point.

According [6, 7], the back-propagated field $u(x, y, z)$ is calculated using the diffractive integral:

$$u(x, y, z) = \sqrt{\frac{k}{2\pi}} \int ds \, |\mathbf{r} - \mathbf{y}|^{-1/2} \cos\varphi \exp(i\pi/4 - ik |\mathbf{r} - \mathbf{y}|) u_0(s) \quad (8)$$

where $\mathbf{r}$, $\mathbf{y}$ correspond to coordinates of the observation point A and the current point of integration on the curve SP along the LEO orbit; φ is the angle between vector $\mathbf{r} - \mathbf{y}$ and normal to the curve SP (Fig. 1) at the current integration (5), (6), and Equation (7) consists of the polarization terms in the right sides. Thus the known 2-D scalar equation applied for the solution of the inverse radio occultation problem is a partial case of the diffractive vector integrals for 3-D inhomogeneous medium. Distinction between the equations for 3-D and 2-D cases consists of different form of the Green functions. In Equations (6)–(8) the Green function corresponding to propagation in free space is used. The Green function determines the form of the reference signal in radio-holographic RHFSA and FSI methods.

3. GIO, CT AND BP METHODS

The diffraction integrals (1)–(8) use the Green functions corresponding to a point source. There are, however, another way for obtaining the diffractive integrals by use of the plane waves which are solutions of the wave equation in free space. For example, we consider the Canonical Transform (CT) and Back Propagation methods (BP). To reveal connections between CT and BP methods we apply the Zverev's transform [8], connecting the field $E(y, z)$ and its angular spectrum $A(u)$

$$E(y, z) = \int du A(u) \exp\{ik[\Phi(u, y, z) - \Phi_j(u)]\},$$

$$\Phi(u, y, z) = z\sqrt{1 - u^2} + yu; \quad \Phi_j(u) = \Phi(u, y_j, z_j) \quad (9)$$

$$A(u) = \frac{k}{2\pi} \int dy E(y, z = z_j) \exp(-ikyu) \quad (10)$$

where $\Phi(u, y, z)$, $\Phi_j(u)$, y_j, z_j are the phase function, initial phase, and initial co-ordinates of the j-th physical ray, u is the projection of the unit wave vector of a plane wave on the direction
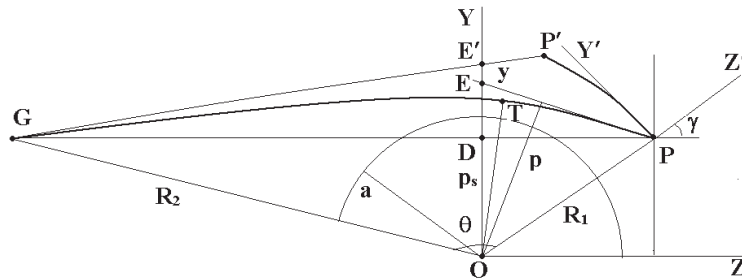
Figure 2: Geometrical parameters for GIO, RFSA, CT and BP methods.

OY. The centre of co-ordinate system y, z coincides with point O and axis OY is perpendicular to direction GP (Fig. 2). The angular spectrum $A(u)$ can be determined as a Fourier transform of the field along the straight line $z = z_j$. To connect the Zverev's transform woth the LEO trajectory let us introduce the new co-ordinate system y', z' with centre at point P and oriented at angle γ relative to the co-ordinate system y, z (Fig. 2). The coordinate y' is reckoned from point P along the tangent to orbital trajectory of LEO satellite:

$$y = y_p + y' \cos \gamma + z' \sin \gamma; \ \ z = z_p + z' \cos \gamma - y' \sin \gamma \tag{11}$$

where y_p, z_p are the co-ordinates of the point P (Fig. 2) in the co-ordinate system ZOY (Fig. 2). We introduce GIO transform as a Fourier operator $I(p)$:

$$E(p) = I(p)E(y, z) = \int d\eta B(\eta) \exp\{i\kappa[pf(\eta) - d(\eta)]\} I_1(\eta) \tag{12}$$

$$I_1(\eta) = \frac{k}{2\pi} \int ds \exp(-ik\eta s) E[y(s), z(s)] \tag{13}$$

where $I_1(\eta)$ is the internal Fourier-operator, $B(\eta)$ is the amplitude function, $d(\eta)$ is the auxiliary phase function, $f(\eta)$ is the impact function, p is the parameter, having different physical interpretation depending on $f(\eta)$, s is the path of integration along the orbital trajectory of the LEO satellite.

Below we suppose that the orbital trajectory during RO measurements can be approximated by a straight line and integration on s can be changed by integration on the variable y' in the operator $I_1(\eta)$ (13). After substitution (9), (11), and (13) into (12) and changing the order of the integration one can perform integration on y' letting $z' = 0$:

$$I_1(\eta) = \frac{k}{2\pi} \int dy' \exp(-ik\eta y') \int du A(u) \exp\{ik[y' \sin(\alpha - \gamma)$$
$$+ (z_p - z_j) \cos \alpha + (y_p - y_j) \sin \alpha]\}, \quad u = \sin \alpha, \ \sqrt{1 - u^2} = \cos \alpha \tag{14}$$

After changing of integration order on y' and u in (14) one can obtain:

$$\delta[\eta - \sin(\alpha - \gamma)] = \frac{k}{2\pi} \int dy' \exp\{iky'[\sin(\alpha - \gamma) - \eta]\} \tag{15}$$

$$I_1(\eta) = \int du A(u) \delta[\eta - \sin(\alpha - \gamma)] \exp\left\{ik\left[(z_p - z_j)\sqrt{1 - u^2} + (y_p - y_j)u\right]\right\} \tag{16}$$

Substitution of (16) into (12) gives after integration on η the next result:

$$E(p) = \int du A(u) B(\eta) \exp\{ik[pf(\eta) - d(\eta) + (z_p - z_j) \cos \alpha + (y_p - y_j) \sin \alpha]\}$$
$$\eta = \sin(\alpha - \gamma) \tag{17}$$

The left part of (17) is the field $E(p)$ transformed by the operator $I(p)$ from the RO signal. The function $d(\eta)$ in (17) is arbitrary, and one can chose $d(\eta)$ to simplify the GIO transform:

$$d(\eta) = (z_p - z_0) \cos\left(\gamma + \sin^{-1} \eta\right) + y_p \sin\left(\gamma + \sin^{-1} \eta\right) \tag{18}$$

where z_0 is a parameter determining the location of a straight line where the field should be retrieved. If the origin of the co-ordinate system y', z' is disposed at the OZ axis and $\gamma = 0$, $y_p = 0$, then the function $d(\eta)$ is equal to $d(\eta) = (z_p - z_0)(1 - \eta^2)^{1/2}$ and coincides with the phase of the transfer function for free space introduced early [1]. The BP case can be obtained from (17) by choosing $B(\eta) = 1$, and $f(\eta) = \sin(\gamma + \sin^{-1} \eta) = \sin \alpha$ in the GIO transform (12). In this case the right part of the first equation in (17) coincides with (9), if $z = z_0$, and, as a consequence, p has a geometrical sense of the co-ordinate y (Fig. 2). The second important partial case is

$$f(\eta) = \gamma + \sin^{-1} \eta, \ d(\eta) = z_p \cos(\gamma + \sin^{-1} \eta) + y_p \sin\left(\gamma + \sin^{-1} \eta\right) \tag{19}$$

For the case $\gamma = 0$ this function has been found early by the CT method [9]. Equation (19) generalized the CT method for any values $\gamma \neq 0$. For this case stationary phase method gives a connection between the angle α_j and parameter p

$$p = -z_j \sin \alpha + y_j \cos \alpha. \tag{20}$$

Equation (20) defines p as the distance between the j-th physical ray and the centre of the coordinate system — point O (Fig. 2). If the centre of global spherical symmetry of the medium coincides with point O, p is the impact parameter of the j-th ray. The SP method gives the next formula for the transformed field

$$E(p, \gamma) = E_a(p, \alpha) \exp[ik\Phi_a(p, \alpha)], \quad \Phi_a(p, \alpha) = p\alpha - z_j \cos \alpha - y_j \sin \alpha \tag{21}$$

where $E_a(p, \alpha)$ is the coefficient describing contribution of the stationary point corresponding to j-th physical ray. When the modified refraction index $M(r)$ is a monotonic function, only one physical ray can correspond to the impact parameter p. A possibility of the multi-path effect corresponding to monotonic $M(r)$ profiles has been shown earlier in [16]. In this case the GIO can disentangle the multi-path rays expressing the ray direction angle α as a single-valued function of the impact parameter p. The CT method has the same capability as a partial case of the GIO transform. The ray direction angle α can be determined from (21) by differentiating the phase of the field $E(p, \gamma)$:

$$d\Phi_a(p, \alpha)/dp = \alpha(p) \tag{22}$$

Note, that in this case the BP method can be a subject of multi-path distortion. In reality only the centres of the local spherical symmetry are existing for different parts of the ray trajectories in the ionosphere and atmosphere. In this case the phase of the field transformed by the GIO, CT and BP methods can contain distortion connected with horizontal gradients in multi-path situation [9].

4. CONCLUSION

The diffractive integrals are important tool for RO remote sensing of the atmosphere and ionosphere. Analysis of 3-D diffractive vector integrals indicate that the volume scattering contribution caused by intense irregular or turbulent structures can introduce interference when solving inverse RO problem. The volume scattering may be neglected in the case of layered locally spherical symmetric structures. In this case the RO inverse problem solution can be obtained by different presentation of diffractive integrals based on the Green function corresponding to a point source or on the plane wave presentation of the field in free space.

REFERENCES

1. Zverev, V. A., *Radio Optics*, Soviet Radio, Moscow, 1975.
2. Kunitsyn, V. E. and E. D. Tereshchenko, *Ionospheric Tomography*, Springer-Verlag, Berlin, 2003.
3. Melbourne, W. G., "Radio occultations using earth satellites: A wave theory treatment," *Jet Propulsion Laboratory California Institute of Technology, Monograph 6*, Deep space communications and navigation series, 2004.
4. Pavelyev, A. G., Y. A. Liou, and J. Wickert, "Diffractive vector and scalar integrals for bistatic radio-holographic remote sensing," *Radio Sci.*, Vol. 39, No. 4, RS4011, 1–16, 2004.
5. Yakovlev, O. I., *Space Radio Science*, Taylor and Francis, London, 2003.
6. Gorbunov, M. E. and L. Bengtson, "Advanced algorithms of inversion of GPS/MET satellite data and their application to reconstruction of temperature and humidity," *Tech. Rep. Report No. 211*, Max Planck Institute for Meteorology, Hamburg, 1996.
7. Hinson, D. P., F. M. Flasar, A. Schinder, J. D. Twicken, and R. G. Herrera, "Jupiter's Ionosphere: Results from the first Galileo radio occultation experiment," *Geophys Res. Lett.*, Vol. 24, No. 18, 2107–2110, 1997.
8. Pavelyev, A., "On the possibility of radio holographic investigation on communication link satellite-to-satellite," *Journal of Communications Technology and Electronics*, Vol. 43, No. 8, 126–131, 1998.
9. Gorbunov, M. E., "Canonical transform method for processing gps radio occultation data in lower troposphere," *Radio Sci.*, Vol. 37, No. 5, 9-1–9-10, doi:10.1029/2000RS002592, 2002.
10. Jensen, A. S., M. S. Lohmann, H.-H. Benzon, and A. S. Nielsen, "Full spectrum inversion of radio occultation signals," *Radio Sci.*, Vol. 38, No. 3, doi:10.1029/2002RS002763, 2003.

Identification and Localization of Layers in the Atmosphere and Ionosphere Based on Observing Variations in the Phase and Amplitude of Radio Waves along the Satellite-to-satellite Path

A. G. Pavelyev[1], **Y. A. Liou**[2], **J. Wickert**[3], **and A. A. Pavelyev**[1]

[1]IRE RAS, Moscow, Russia
[2]CSRSR, NCU, Chung-Li 320, Taiwan
[3]GFZ-Potsdam, Potsdam, Germany

Abstract— The phase acceleration of radio waves is fundamentally important to the analysis of radio occultations (RO) data and plays the same role as the Doppler frequency and phase path excess. Phase acceleration technique allows one to convert the phase path excess or Doppler frequency changes measured in RO experiments into the refraction attenuation variations. From these derived refraction attenuation and amplitude data one can estimate the integral absorption of radio waves. It is important also that the contribution in RO signal from layered structures in the atmosphere and ionosphere can be separated from that one of the irregularities and turbulence by comparison and/or correlation of the refraction attenuations found from the phase and amplitude data. The advantages of the phase acceleration/intensity technique are validated by analyzing the RO data from the Challenging Minisatellite Payload (CHAMP) mission. The technique was verified by measuring the turning point on the ray trajectory in a neutral gas in the atmosphere. The position for inclined plasma layers was determined and the electron density distribution was found for the considered radio occultation sessions.

1. INTRODUCTION

The radio occultation RO method is an effective tool for the investigation of the earth atmosphere and ionosphere at different altitudes with global coverage [1]. In the ionospheric investigation the RO method may be considered as an additional global tool as compared with the global earth-based radio tomography [2]. For many years measurements of the integral absorption by use of the RO amplitude data have been not conducted. As described in detail in [3], there exist significant difficulties to measure from RO data the atmospheric absorption of radio waves by Full Spectrum Inversion (FSI) analysis and other radio-holographic methods using Fourier integral operators. A new and important connection between the phase acceleration, Doppler shift, phase and intensity variations of RO signals has been discovered by theoretical considerations and experimental analysis of radio-holograms registered during CHAMP and FORMOSAT-3 RO low orbital satellites missions [4, 5]. This relationship gives a simple way to convert the phase acceleration (or time derivative of Doppler shift) into the refraction attenuation. This is useful for estimating the integral absorption of radio waves in the atmospheric communication links. It is important also that a contribution in RO signal from layered structures in the atmosphere and ionosphere can be separated from that one of the irregularities and turbulence by comparison and/or correlation of the refraction attenuations found from the phase and amplitude data. In this paper, the phase acceleration/intensity technique is validated by use of CHAMP GPS RO data, and a method for identification of layered structures in the atmosphere and ionosphere is presented. A possibility to measure the integral absorption of radio waves is considered.

2. IDENTIFICATION OF LAYERED STRUCTURES

The geometry of the GPS radio occultation experiment is shown in Figure 1. The radio waves emitted by a GPS satellite (point G) arrive at a receiver on board the LEO satellite (point L) along the ray trajectory GTL, where T is the ray perigee. The projection of point T on the surface of the earth determines the geographical coordinates of the RO region. A connection between the phase excess $\Phi(p)$ (eikonal) acceleration and refraction attenuation of radio waves has been detected in [4, 5] and presented in the form:

$$1 - X(t) = ma = mdF_d/dt = md^2\Phi(p)/dt^2; \quad m = q/(dp_s/dt)^2; \quad q = d_{1s}d_{2s}/R_0 \tag{1}$$

Formula (1) connects the refraction attenuation $X(t)$, derivative of the Doppler frequency F_d on time and the phase acceleration $a = dF_d(t)/dt = d^2\Phi(p)/dt^2$ via a relationship similar to classical
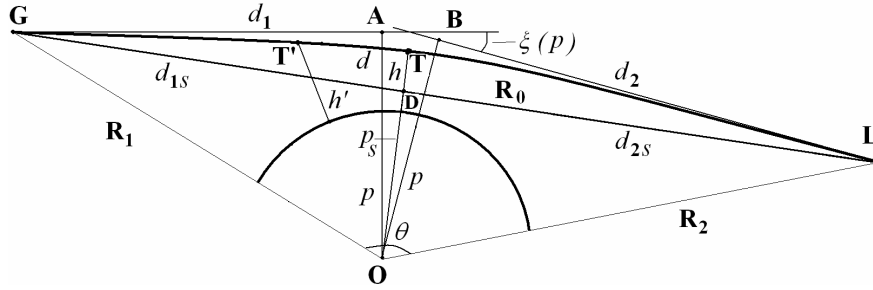
Figure 1: Scheme of trans-atmospheric link satellite-to-satellite.
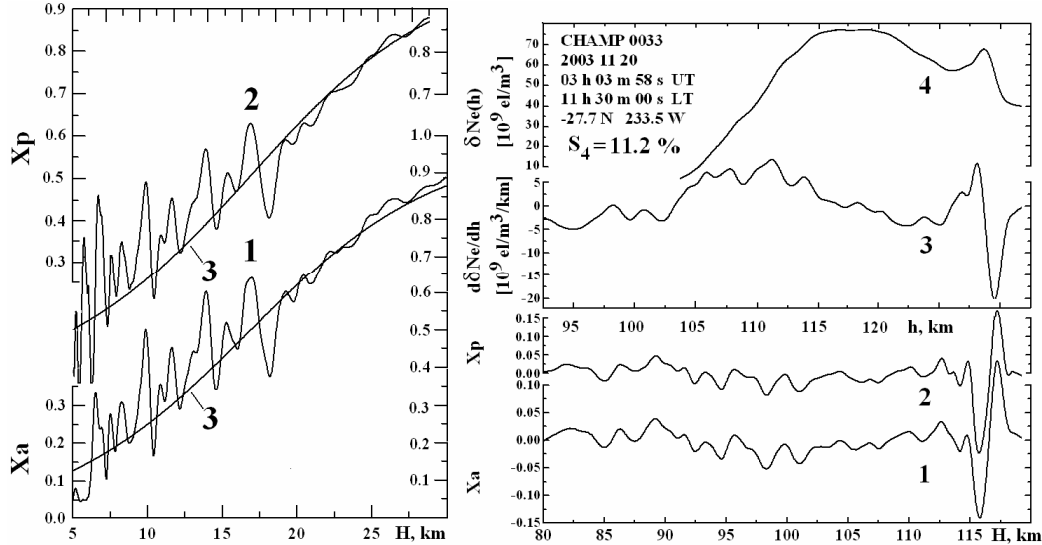
Figure 2: Refraction attenuations $X_p(t)$, $X_a(t)$ recalculated from the amplitude and phase data at the first GPS frequency.

dynamics equation. Equation (1) indicate equivalence between the variations of the phase path excess (eikonal) acceleration a, derivative of the Doppler shift $F_d(t)$ on time, and refraction attenuation $X(t)$. Parameters m and dp_s/dt may be accurately evaluated from the orbital data. The distance d_{2s} can be evaluated from the relationship:

$$d_{2s} = 2R_0\beta[1 + 2\beta(1 - w/v) + (1 - 4\beta w/v)^{1/2}]^{-1}, \quad \beta = mv^2/R_0, \quad m = [1 - X(t)]/a \qquad (2)$$

where w, v are the velocity components of the GPS and LEO satellites, respectively, which are perpendicular to the straight line GL in the plane GOL. The components w, v are positive when orienting in direction to the point O and are negative in the opposite case. Analysis of the CHAMP GPS RO data indicates correctness of relationships (1). Variations of the refraction attenuations X_a and X_p (curves 1 and 2) in the altitude intervals 5–30 km and 75–125 km are shown in details for GPS RO event $\mathcal{N}\underline{o}$. 0033 in Figure 2, left and right panel, respectively. To convert the phase data the phase acceleration a has been estimated numerically by double differentiation over a fixed time interval Δt. The value of Δt was equal to 0.42 s. The standard dependence of the combined atmospheric refraction attenuation and absorption is indicated in Figure 2, right panel, by curves 3. The refraction attenuations X_a and X_p change in strikingly similar manners in the stratosphere (Figure 2, left panel) and in the lower ionosphere (Figure 2, right panel). This identifies a common origin of the phase and amplitude variations of GPS RO signal as corresponding to layered structures in the atmosphere and ionosphere. As a further identification step it may be examined a possibility to locate layers in the atmosphere and/or in the ionosphere. If parameter m will be estimated from the experimental data by use of Equation (2), it is possible to find the new value of distance $T'L \approx d'_{2s}$ and to determine the displacement of new tangent point T' and location of a layer relative to the point T (Figure 1):

$$d = d'_2 - d_{2s} = d'_{2s} - \left(R_2^2 - p_s^2\right)^{1/2} \qquad (3)$$

Results of determination of parameter m, displacement d, and corrected layer height h are given in Tables 1 and 2 as function of the altitude H of ray perigee T. Data indicated in Tables 1 and 2 correspond to CHAMP GPS RO event $\mathcal{N}$о. 0033. The refraction attenuations X_a, X_p calculated from the amplitude and phase data and estimated values of parameter m are indicated in the second, third, and sixth columns in Table 1 as functions of the ray perigee height H in the interval of 9.14–9.34 km. These refraction attenuations correspond to curves 1 and 2 shown in Figure 2 (left panel). The displacement d and an estimated value of the layers altitude h are indicated in the forth and fifth columns of Table 1, respectively. The displacement d is changing in the −6-km to +40-km interval and corresponding corrections to the altitude H are about 0.1–0.2 km in average. These results confirm location of layer in the ray perigee T (Figure 1).

Table 1: Displacement d in the neutral atmosphere.

H, Km	X_p	X_a	d, km	h, km	$\delta°$	m, s^2/m
9.36	0.32461	0.29659	−5.35	9.36	−0.046	0.43083
9.35	0.32266	0.29152	4.98	9.35	0.044	0.43308
9.33	0.32062	0.28662	14.4	9.35	0.128	0.43515
9.32	0.31833	0.28197	22.3	9.36	0.200	0.43687
9.31	0.31594	0.27761	29.0	9.37	0.258	0.43831
9.30	0.31341	0.27354	34.2	9.39	0.306	0.43945
9.28	0.31069	0.26984	37.7	9.40	0.338	0.44021
9.27	0.30773	0.26645	39.6	9.40	0.354	0.44060
9.26	0.30407	0.26334	38.5	9.38	0.344	0.44035

Table 2: Location of an ionospheric layer.

H, km	$X_p - 1$	$X_a - 1$	d, km	h, km	$\delta°$	m, s^2/m
117.34	0.13934	0.16763	330.1	125.8	2.94	0.60984
117.30	0.14184	0.17263	352.3	127.0	3.14	0.61692
117.26	0.14338	0.17647	373.9	128.1	3.34	0.62383
117.22	0.14384	0.17896	394.9	129.4	3.52	0.63057
117.19	0.14305	0.17996	416.6	130.7	3.72	0.63758
117.15	0.14090	0.17929	439.1	132.2	3.92	0.64485
117.11	0.13757	0.17674	458.1	133.5	4.10	0.65102
117.07	0.13301	0.17214	472.7	134.5	4.22	0.65577
117.04	0.12761	0.16547	476.5	134.7	4.26	0.65697
117.00	0.12093	0.15663	474.3	134.5	4.24	0.65621

High correspondence between the refraction attenuations X_a and X_p is seen also in the ionospheric part of their altitude profiles in the interval of 78–120 km (Figure 2, right panel, curves 1 and 2, respectively). Significant variations of the refraction attenuations X_a and X_p in the 78- to 90-km altitude interval of the ray perigee T, in which the expected contributions from the neutral gas or the electron density in the RO signal changes are negligible at both GPS frequencies, may be caused by horizontal gradients in the ionosphere associated with inclined plasma layers [5, 6]. A new phase acceleration/intensity ratio technique seems to be effective for determination of the height and inclination of layered plasma structures (including sporadic E_s layers) in the ionosphere. Results of determination of the displacement d, inclination δ, layer altitude h, and parameter m are given in Table 2 as function of the altitude H of the ray perigee T. Also, variations of the refraction attenuations $X_p - 1$ and $X_a - 1$ are given in Table 2. The displacement d as seen from the forth column of the Table 2 is changing in the 277-km to 476-km interval and corresponding corrections

to the altitude H are about 12 km in average. Therefore results in Table 2 confirm location of main part of sporadic E_s layer at the height 130 km with displacement $d \approx 420$ km from ray perigee T in the direction TG and inclination about of 2–4°. Results shown in Figures 2 and 3 and in Tables 1 and 2 give evidence of practical importance of proposed method for identification of layers in the atmosphere and ionosphere. Identification of the sporadic E_s layer justifies application of the Abel' transform for solving the inverse problem. Advantage of using phase acceleration/intensity technique consists in excluding a linear trend in the phase path excess caused by the upper ionosphere. The results of retrieving the variations $\delta Ne(h')$ in the electron density and its gradient $d\delta Ne(h')/dh'$ are shown in Figure 2 (right panel) for RO session 0033. Variations in the refraction attenuations X_a and X_p are shown by curves 1 and 2 as function of the altitude of the ray perigee H. Curves 3 and 4 describe the retrieved variations $d\delta Ne(h')/dh$ and $\delta Ne(h)$ as functions of the adjusted altitude h. Curves 1 and 2 agree well. Actually, it is another example of the fulfillment of Equation (1) for the case of the sporadic E_s layer. According to the curve 3, Figure 2, right panel, the magnitude of $d\delta Ne(h)/dh$ is slowly changing in the interval $\pm 5 \cdot 10^9$ el/m^3 /km at the altitudes h between 92.5 and 125 km. Sharp variations in the vertical gradient $d\delta Ne(h)/dh$ caused by sporadic E_s layer are observed at the altitudes 126–129 km. Integration of the vertical gradient $d\delta Ne(h)/dh$ allows one to obtain the variations in the electron density $\delta Ne(h)$. The results of estimation of the vertical profile of $\delta Ne(h)$ are shown by curve 4 in Figure 2, right panel. The arbitrary integration constant has been chosen to be equal to $40 \cdot 10^9$ el/m^3. The function $\delta Ne(h)$ has two maximums at the altitudes 118 and 128 km. The first maximum is broad and corresponds to a smooth behavior of the electron density in the ionospheric E-layer. The second maximum is caused by the sharp sporadic E_s-layer located between altitudes 126 and 129 km. This maximum is difficult to observe from the earth based tools because it is located at the higher altitude than the first maximum. This demonstrates the advantage of the phase acceleration/intensity technique for observation of the E-layer of the lower ionosphere. Although the analysis provided is preliminary, it reveals a possibility of establishing in some instances the actual location, height, and inclination of sporadic E_s structures in the ionosphere from a single RO vertical profile.

3. DETERMINATION OF INTEGRAL ABSORPTION

The relationships (1) widen an applicability domain of the RO method. Equation (1) give a possibility to convert the phase acceleration a and/or Doppler frequency F_d to the refraction attenuation X_a. This is useful for estimation of the integral absorption in the atmosphere. The refraction attenuation X_a is determined from the amplitude data as a ratio of intensity of radio signal propagating through the atmosphere $I_a(t)$ to its intensity in free space I_s:

$$X_a(t) = I_a(t)/I_s \tag{4}$$
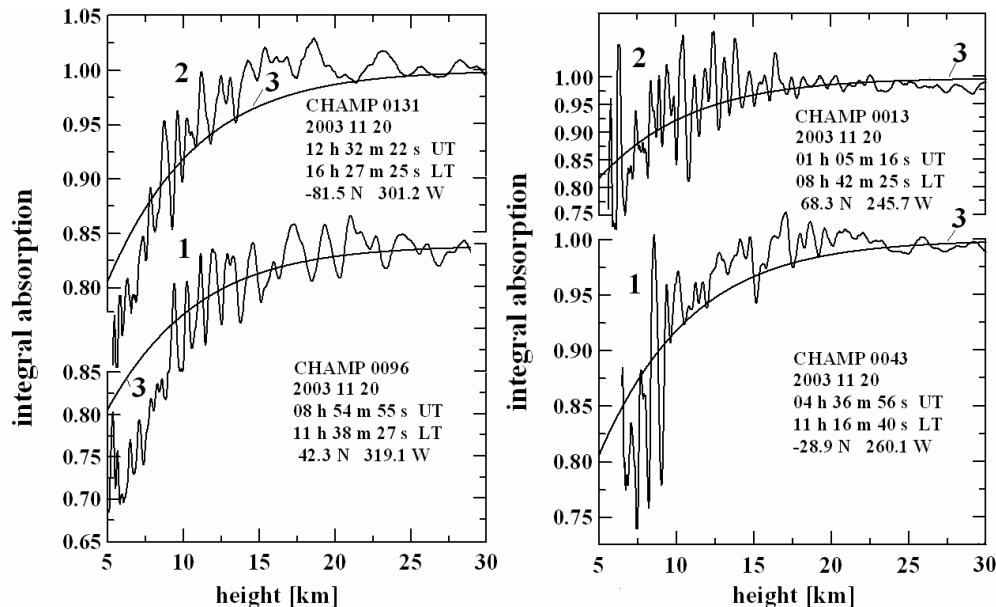
Figure 3: Integral absorption in the atmosphere recalculated as a ratio $X_a(t)/X_p(t)$.

The value X_a is the product of the refractive and absorption contributions. The phase acceleration depends on the refraction effect only. One can determine the integral absorption $Y(t)$ as a ratio:

$$Y(t) = X_a(t)/X_p(t), \quad X_p(t) = 1 - ma = 1 - mdF_d(t)/dt \tag{5}$$

where $X_p(t)$ is the refraction attenuation of radio waves recalculated from the phase data. Vertical profiles of the integral absorption of radio waves in the atmosphere are shown in Figure 3, left and right panel, for four CHAMP RO measurement sessions conducted in November 20, 2003. Three sessions — $\mathcal{N}$o. 0013, $\mathcal{N}$o. 0096, and $\mathcal{N}$o. 0131 — correspond to polar and moderate latitude areas in the northern and southern hemispheres, one session — 0043 — is relevant to a tropical region (Figure 3, right panel). Therefore these measurements represent conditions of radio wave propagation in practically all regions of the earth. The integral absorption recalculated by use of Equation (5) are demonstrated in Figure 3 by curves 1 and 2. Smooth curves 3 correspond to the integral absorption due to atmospheric oxygen calculated according to technique described in [7]. Theoretically, influence of the atmospheric oxygen can be seen below 30 km. Experimental data support this theoretical suggestion with accuracy of about $\pm 20\%$. Below about 8 km altitude the experimental data indicate additional attenuation down by nearly 10% compared to what was used in the theoretical dependence (Figure 3). Preliminary results revealed good correspondence with theoretical values of attenuation described in [7]. Magnitude of the average integral atmospheric attenuation measured during bistatic radio location of sea surface at wavelength 32 cm [8], which was estimated as about of 0.0096 ± 0.0024 dB/km, coincides with experimental values of the integral attenuation indicated in Figure 3. As follows from our analysis comparison of the refraction attenuations restored from the amplitude and phase variations is very useful also for identification of layers in the atmosphere.

4. CONCLUSION

A new important connection between the phase acceleration, Doppler frequency and intensity variations of RO signal has been discovered and validated by means of the theoretical consideration and experimental analysis of the radio-holograms registered during CHAMP, FORMOSAT-3 and other low orbital satellites missions. The discovered connection gives a possibility to convert the phase acceleration (or time derivative of Doppler frequency) into the refraction attenuation and allows one to measure the integral absorption of radio waves in the atmosphere. The examples of the measurements of the integral absorption indicate effectiveness of proposed technique. Advantages of the phase acceleration/intensity technique are validated by means of analysis of the CHAMP GPS RO data.

REFERENCES

1. Yakovlev, O. I., *Space Radio Science*, Taylor and Francis, London, 2003.
2. Kunitsyn, V. E. and E. D. Tereshchenko, *Ionospheric Tomography*, Springer-Verlag, Berlin, 2003.
3. Lohman, M. S., A. S. Jensen, H. H. Benson, and A. S. Nielsen, "Radio Occultation retrieval of Atmospheric Absorption based on FSI Report 03-22," Danish Meteorological Institute, Copenhagen, 2003.
4. Liou, Y. A. and A. G. Pavelyev, "Simultaneous observations of radio wave phase and intensity variations for locating the plasma layers in the ionosphere," *Geophys. Res. Lett.*, Vol. 33, No. 23, L23102, 1–5, 2006.
5. Pavelyev, A. G., Y. A. Liou, J. Wickert, T. Schmidt, A. A. Pavelyev, and S. F. Liu, "Effects of the ionosphere and solar activity on radio occultation signals: Application to CHAllenging Minisatellite Payloadsatellite observations," *J Geophys. Res.*, Vol. 112, No. A06326, 1–14, 2007.
6. Wickert, J., A. G. Pavelyev, Y. A. Liou, et al., "Amplitude scintillations in GPS signals as a possible indicator of ionospheric structures," *Geophys. Res. Lett.*, Vol. 31, No. 24, L24801, 1–4, 2004.

7. Kislyakov, A. G. and K. S. Stankevich, "Absorption of radio waves in the atmosphere," *Izv. Vyssh. Uchebn. Zaved. Radiophyz*, Vol. 10, No. 9–10, 1244–1270, 1967.
8. Pavelyev, A. G., A. V. Volkov, A. I. Zakharov, S. A. Krutikh, and A. I. Kucherjavenkov, "Bistatic radar as a tool for earth investigation using small satellites," *Acta Astronoutica*, Vol. 39, No. 9–12, 721–730, 1996.

Peculiarities and Perspectives of Network Digital Ionospheric Station "PARUS"

Alexander L. Karpenko, **Ljudmila N. Leshchenko**, **and Natalia I. Manaenkova**

Institute of Terrestrial Magnetism, Ionosphere and Radio Wave Propagation (IZMIRAN)
Troitsk, Moscow Region 142190, Russia

Abstract— The Digital Ionosonde "Parus", created at IZMIRAN, is modern high-precision ionospheric network station, oriented to sounding of the ionosphere at the different rates: vertical-incidence, oblique-incident, backscatter and trans-ionosphere sounding. Program package for radiophisical measurements holds some components intended for sounding: resident program, realizing standard regime of ionosphere station; fast continuous sounding program etc. Ionosonde is accompanied by special software — "Integrated multiwindow Data Processor", directing data proceeding, including actions with data base of measurements, generating accounts; generating archive of row and processed ionograms, graphic editor producing interactive scaling of ionogram; The measurements are used to make HF radio wave propagation forecasts, ionosphere monitoring, scientific and applied investigations.

1. INTRODUCTION

The commonly used method of remote diagnostic of the space distribution and the time behavior of so complex media as ionosphere is based on the using of special devices — so called ionosondes. Sounding process consists of sending of radio pulses on a set of frequencies and registration of reflected signals. Registered parameters of signals may be: time delay, amplitude, phase, Doppler shift, envelope, wave polarization and the angle of arrival of the reflected radio signal. The process of ionosphere sounding produces relatively large amount of digital information, including "useful" radio signals reflected of ionosphere as well as noise signals of different genesis. Ordinary ionogram can contain in "raw" digital presentation up to 10 Mbytes of information. Meanwhile essential information is only small part of all.

The Digital Ionosonde "Parus", first created at IZMIRAN (http://www.izmiran.ru) almost twenty years ago, is developing successfully [1] and now it is advanced modern high-precision inexpensive instrument. It makes availability to recreate Russian ionosphere network.

There are some Web-pages, devoted to full description of Version 3.0 and Version 4.0 of Ionosonde "Parus": http://www.izmiran.ru/ionosphere/parus. Unfortunately, information is only partly in English.

2. SECTION 1

The developed in IZMIRAN digital ionosonde "Parus" is constructed on two-processor basis: IBM PC + DSP ADSP2189. Signal processor performs the most complicated part of calculations with incoming data stream: signal accumulation, analysis, extraction from noise, digital conversion of signal in the case of using pseudo-random modulation. Signal processor module is fulfilled as PCI slot.

PC processor controls the total sounding process: radio receiving/transmitting, time synchronization. It performs final data storing, dynamic graphical presentation of results, interaction with operator.

Ionosonde includes digital frequency synthesizer and 2-channel receiver for the frequency range from 0.5 to 40 MHz. It may be completed by transistor 1 kW wideband transmitter with the pulse width up to 800 μsec or it may be 20 kW wideband tube power amplifier with the pulse width 200 μsec. In the ranges from 0.5 to 25 MHz amplifiers have the uniform characteristics.

It is foreseen in the Ionosonde "PARUS":

- software, setting of the multiplicity of sounding pulse emissions for each transmitted frequency;
- operation with complex, phase coding signals;
- usage of the same antennas for transmitting and receiving of sounding pulses;
- computer control and management of ionosonde power supply.

Ionosonde "PARUS" provides standard regime of ionospheric station with the possibility of self-acting every 5, 15, 30 minute. Minimum time of ionogram registration is near 6 seconds (the number of transmitted frequencies equals 500).

Trans-ionosphere sounding can be putted into effect in joint work with artificial satellites. The Table 1 summarizes all above:

3. SECTION 2

The measurements, obtained by digital ionosonde are time-series of the observables of reflected HF radio wave. In order to use these measurements and make ionosphere monitoring, HF radio wave propagation forecasts and other scientific investigations [2] it is necessary to create suitable interface.

All the ionosonde data processing, recording and visualization of measurements are realized on the base of microcomputer IBM PC. Ionogram (Figure 1), as usual, includes 500 frequencies evenly distributed in necessary frequency range, but it is possible to change number of frequencies and its distribution law.

Program package for radiophisical measurements holds some components intended for sounding: resident program, realizing standard regime of ionosphere station; fast continuous sounding program; sounding program including Doppler measurements on any given frequency set; some programs provided measurements of absorption in ionosphere on a sliding frequency; programs for special measurements of effects, produced by small-scaled inhomogeneities.

Ionosonde "Parus" is accompanied by special software — "Integrated multiwindow Data Processor". Wide capabilities of this Data Processor allow to direct data proceeding, including actions

Table 1: Main specifications of the ionosonde "PARUS".

Frequency sweep	1–20 MHz.
Pulse peak power of the tube amplifier	15 kW.
Pulse width, (programmable)	50–200 mksec.
Pulse repetition rate (normal)	50 Hz.
Frequency increment (normal)	1 Hz
Receiver sensitivity (S/N 10 dB)	10 mkv.
Receiver bandwidth	18 kHz.
Minimal height increment (programmable)	0.75 km.
Total dimensions	$0.46 * 0.43 * 0.65$ m.
Weight	30 kg.
Power consumption	600 W.
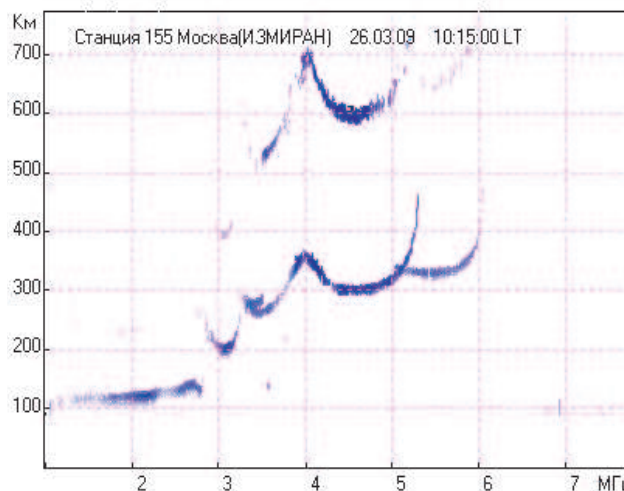
Figure 1: An example of "raw" ionogram, produced by Ionosonde "Parus".

with data base of measurements; generation of day F-H — graphics and month accounts; generation of archive of row and processed ionograms. Data Processor includes component of transformation of ionogram data to electron density profile N(h). So-called Graphic Editor produces interactive scaling of ionogram. As a result of processing of row ionogram by "Graphic Editor" it is possible to receive all ionospheric parameters and characteristics, corresponding URSI standard, to digitize any ionosphere layer, to generate output file in SAO-format.

Web-site http://www.izmiran.ru/ionosphere/parus contains full description of Hardware and Software of Ionosonde "Parus" (Version 3.0 and Version 4.0).

Ionosonde PARUS's Europe and Asia Locations Map is available at Figure 2 and web-page: http://top.izmiran.troitsk.ru/parus/parusmap.html.

The view of current ionogram, produced by Ionosonde "Parus" is available at web-page: http://www.izmiran.ru/ionosphere/parus/ViewLastIonSrc.html.

Special illustrations, concerning capabilities of "Integrated multiwindow Data Processor" are available at numerous Web-Pages. There are some examples:

1) http://www.izmiran.ru/ionosphere/parus/IonProRaw.html

It is demonstrated the high quality of the raw ionograms, produced by Ionosonde "Parus".

2) http://www.izmiran.ru/ionosphere/parus/IonProArchSrch.html

It is shown that Search for ionogram in Archive Data Base is realized.

3) http://www.izmiran.ru/ionosphere/parus/IonProEdt.html

There is the illustration of processing of row ionogram by so-called "Graphic Editor". It is possible to digitize any ionosphere layers, main ionospheric parameters and characteristics, corresponding URSI standard; to convert output file in SAO-format.

4) http://www.izmiran.ru/ionosphere/parus/IonProProc.html

An example of some processed ionogram is demonstrated.

5) http://www.izmiran.ru/ionosphere/parus/IonProFHGraf.html

Digital variant of standard F-H daily graphic of some processed ionogram is represented.

Data Base of processed ionograms is accumulated at IZMIRAN during period 2002–2009 years.

4. SECTION 3

The best way to get conditions of HF propagations is to use available Data Base of measurements of either an ionospheric and geophysical parameters. Short-term prediction typically involves all these parameters and then they are applied to an empirical model or algorithm. Long-term predictions

Current supplied PARUS Ionosondes

Map location #	City	Country	Devices	Customer
1	Moscow	Russia	2	IZMIRAN Russian Academy of Sciences
2	Rostov	Russia	1	Rostov State University. Institute of Applied Physics
4	Novosibirsk	Russia	1	Institute of Geophysics. Siberian Departmen of Russian Academy of Sciences
5	Tomsk	Russia	1	Siberian Institute of Physics and Technology
6	Yakutsk	Russia	1	Institute of Space Physics
3	Ashkhabad	Turkmenia	1	Turkmenian Institute of Physics and Technology
7	XinXian	China	2	Chinese Research Institute of Radio Wave Propagation

Figure 2: Europe and Asia Locations Map of Ionosonde PARUS (Version 3.0).

of ionosperic behaviour depend on reliable representation of past ionospheric data and the knowing correlation with solar activity and other states of environment.

Undoubtedly, main center of Ionospheric propagation forecasting and Data Base are in USA at National Geophysical Data Center (http://www.ngdc.noaa.gov/stp/IONO/ionogram.html.) Forecast Service of Australia presents interesting results, dealing with ionosphere: http://www.ips.gov.au. Europe server allows to use digital ionospheric data at Web-page: http://www.iono.noa.gr/DIAS.

Now Russian Ionospheric Data are available in the Interactive System SPIDR (Space Physics Interactive Data Resource). World Data System for Solar-Terrestrial Physics at Moscow is a part of World Data Center System (http://www.ngdc.noaa.gov/wdc/wdcmain.html) of the International Council of Scientific Unions.

5. CONCLUSIONS

Though there are a lot of ionospheric measurements all over the world, this information is not homogeneous, there is not enough Interactive Ionosperic Data Resource in Russia. Meanwhile, HF radio wave propagation forecast is in urgent need of Russian, Europe, World Maps of such ionosperic parameter as f_0F_2, full Common Information System of Ionosphere Monitoring.

Software of Ionosonde "Parus" didn't contain automatic data processing, but it is not so serious disadvantage. Manual data processing of single ionogram need at less than 5 minutes, but precision of all ionospheric parameters and characteristics are perfect. It is well-known, that inaccuracy of automatic data processing may reach 30%. But for scientific investigations of ionosphere high precision is more preferable than time-delay.

As regards HF radio wave propagation forecast, software of Ionosonde "Parus" contains so-called "Clearance procedure" of row ionogram. This procedure may simplify automatic finding of main ionospheric parameters of each, unique ionogram. This will be new way, different from mean square approximation to the parameters of "nearest" ionograms of Digital Ionogram DataBase, which is provided for general use at Software of "Digisonde".

During period 2002–2009 years Data Base of processed ionograms and accounts are accumulated at IZMIRAN. Now Ionospheric Data of Ionosonde "Parus" are regularly sent to World Data Centers in Moscow. There is not enough Interactive Ionospheric Data Resource in Russia. That is why nearest future plan is to add all available digital ionospheric data stored by network Ionosphere Stations "Parus" into existing Information Systems of Ionospheric Data.

REFERENCES

1. Gajdanskij, V. I., A. L. Karpenko, N. I. Manaenkova, S. V. Silvestrov, and A. A. Smirnov, "The base network digital ionospheric station "PARUS"," in *Abstracts. XXVth General Assembly of the International Union of Radio Science*, 360, Lille, France, August 1996.
2. Karpenko, A. L. and N. I. Manaenkova, "Nonlinear time series analysis of the ionospheric measurements," *Geologishe Rundshau*, Vol. 85, No. 1, 124–129, Springer-Verlag, 1996.

Active Space Experiments with the Use of the Transport Spacecraft "Progress" and Irkutsk IS Radar

Alexander P. Potekhin[1], **Vitaly V. Khakhinov**[1, 2], **Andrey V. Medvedev**[1], **Dmitry S. Kushnarev**[1], **Valentin P. Lebedev**[1], **and Boris G. Shpynev**[1]

[1]Institute of Solar-Terrestrial Physics of Siberian Branch of Russian Academy of Sciences
664033, Lermontov St. 126a, p/o Box 291, Irkutsk, Russia
[2]Irkutsk State University of Railway Engineering, Irkutsk, Russia

Abstract— A sequence of active space experiments was carried out in 2007–2009. Engine burns of orbital maneuvering subsystem of the transport spacecraft "Progress" were used for creating disturbances in the ionosphere and for changing reflecting characteristics of the spacecraft. Amount of engine exhaust products was from 2 to 11 kg. The Irkutsk Incoherent Scatter Radar was used for observing burns. Flow directions relative to the radar and amount of injected exhaust products were changed for each flight. Reflecting characteristics of "Progress" and space-time disturbances of plasma parameters were investigated during the experiments. The exhaust stream was found out to produce significant electron density depletion (20–40%) when it was directed into the radar antenna diagram. According to the estimation of ionospheric "hole" life-time, its average values are 10–15 minutes.

1. INTRODUCTION

The Institute of Solar-Terrestrial Physics of Siberian Branch of Russian Academy of Sciences (ISTP SB RAS) carried out a new "space-laboratory" experiment "Plasma-Progress" in cooperation with the Russian Rocket Cosmic Corporation "Energy" and Central Research Institute for Machine-Building during the periods of September 19–24, 2007, February 10–14, 2008, September 1–8, 2008, and February 6, 2009. The main goal of the experiment was to investigate size and dynamic of ionospheric disturbances and changes in the transport spacecraft (TSC) "Progress" radar cross-section associated with exhaust products of the orbital maneuvering subsystem (OMS). Two types of engines were used in different combinations. Eight Orientation and Mooring Engines (OME), 47 gram/sec exhaust product each, ran simultaneously, and the Approach and Correction engine (ACE) with 1 kg/sec exhaust product ran separately from OME. Directions of burn and amount of exhaust products were different for each day of the experiment.

Artificial ionospheric disturbances associated with spacecraft engine exhaust were investigated during some experiments, which were performed with the NASA Space-Shuttle programme and Incoherent Scatter Radars (ISR) (Millstone-Hill, Jicamarca and Arecibo) [1–6]. During these experiments, large portions of exhaust products injected into the ionosphere almost simultaneously and produced large area of ionization depletion. The amount of exhaust products varied from 87 kg [2] (25×10^{26} molecules) up to 830 kg (24×10^{27} molecules) [3]. These experiments, along with earlier ones [4–6], produced large disturbances observed in the ionosphere for the period of one hour or more along the Shuttle track near the F2 layer maximum.

According to [1–3], exhaust products in the ionosphere initiate two observable effects: first is the production of local peak in radar received power, with tens of second duration; second is the reaction of exhaust gases (H_2O, H_2, and CO_2) with the ambient ionospheric plasma, which make dominant atomic ions (O^+) convert to molecular ions which, in their turn, recombine rapidly with the ambient electrons to form neutral species.

The second process under consideration depends on the stream direction and can be of different duration depending on the background plasma density. As this process produces airglow emissions and formation of an ionospheric hole, it can be observed by ground-based diagnostic instruments.

Ionospheric conditions during the Plasma-Progress experiment corresponded to the low solar activity. Geomagnetic conditions were quiet; their local index K was 2–4. Quiet geomagnetic conditions were the advantage of the experiment, whereas the low solar activity producing low background electron density was the disadvantage for the radar signal/noise ratio and, hence, for experimental data quality.

TSC "Progress" flights over the Irkutsk ISR usually took place at night, so that the F2 peak density was only 0.7–$1.3 * 10^5$ el./sm^3, and points of burns were usually above the F2 peak.

All "Progress" spacecrafts were used after their mission on the International Space Station (ISS) during reduction of their orbit and destruction in the Pacific Ocean. Table 1 presents directions, running time, and values of exhaust products for different experiments. According to the table, portions of exhaust products were much smaller than those in earlier studies [1–6]; thus, they could produce relatively low electron density depletions. However, these experiments could be repeated during some the days. This repeatable feature of the experiment was a good possibility to separate artificial and natural ionospheric disturbances.

Table 1.

Date	Time UT	Burn direction	Burn time	Exhaust product
September 19, 2007	21:54:11	on braking	2.7 sec.	2.7 kg
September 20, 2007	20:39:53	toward ISR	5.1 sec	5.1 kg
September 21, 2007	21:00:13	on braking	5.4 sec.	1.9 kg
September 22, 2007	19:45:00	toward ISR	5.1 sec.	5.1 kg
September 23, 2007	20:04:18	toward ISR	6.4 sec.	2.4 kg
September 24, 2007	20:23:25	on runaway	6.4 sec.	2.4 kg
February 10, 2008	11:13:00	toward ISR	5.0 sec	5.0 kg
February 11, 2008	10:00:37	toward ISR	5.0 sec	5.0 kg
February 12, 2008	10:22:45	toward ISR	5.4 sec	1.7 kg
February 13, 2008	09:09:33	toward ISR	5.4 sec	1.7 kg
February 14, 2008	09:31:10	on braking	5.0 sec	5.0 kg
September 1, 2008	22:53:27	on braking	5.0 sec.	5.0 kg
September 2, 2008	23:17:27	toward ISR	11.0 sec	3.5 kg
September 3, 2008	22:06:01	toward ISR	10.0 sec.	10.0 kg
September 4, 2008	22:29:03	toward North	11.0 sec.	11.0 kg
September 6, 2008	21:40:10	toward North	10.0 sec.	3.2 kg
September 7, 2008	20:28:08	on runaway	11.0 sec.	11.0 kg

2. EXPERIMENT

The Irkutsk Incoherent Scatter Radar was used as diagnostic equipment for "Plasma-Progress" experiments. The Radar is located 120 km to the north-west of Irkutsk. ISR is the monostatic, pulsed, frequency scan radar unit. It is used for measuring electron densities, electron and ion temperatures, ion composition, and plasma drift velocities [7]. The Radar can be used for detecting spacecrafts and large debris, and for determining their trajectory parameters. Table 2 presents basic parameters of the Irkutsk IS radar.

Table 2.

Range of frequencies	(154–162) MHz
Peak output power	3.2 MW
Pulse duration	70–850 mcs
Type of antenna	Sectoral horn
Antenna gain	35–38 dB
Angular size of the beam	$0.5° \times 10°$
Scan sector	$\pm 30°$
Polarization	Linear

Figure 1 demonstrates typical geometry of the active Space experiment. Size of the Irkutsk ISR antenna beam (blue heavy line) at the height of 340 km is ~ 3 km in south-north direction and ~ 70 km in east-west direction. Trajectories of TSC flights (green line) were usually directed along the east-west side of antenna beam; in this case, the effect must be maximal. Radar beam was
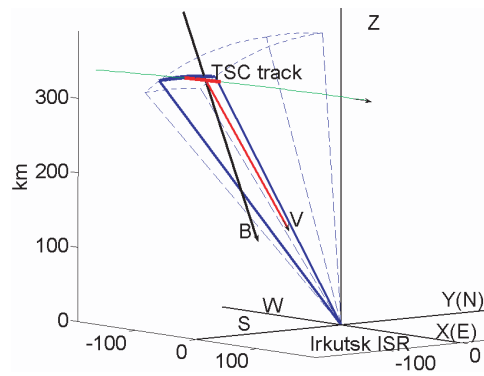
Figure 1: Geometry of the active space experiment.

usually pointed along the geomagnetic field $\vec{B}$ line (black arrow). Dominant direction of the TSC burn is presented by red arrow.

Since the width of main lobe of antenna diagram is only $\sim 3\,\mathrm{km}$ in north-south direction (Fig. 1), two important technical and management tasks were solved: aiming of radar antenna beam to the TSC track, and timeliness of engines' switching on. These tasks were solved due to development of special software of radar diagram management and operative coordination with the Mission Control Center.

Ionospheric conditions for most of experiments required 3–6 minutes data averaging, but nevertheless they produced very dispersive electron density profiles. The Irkutsk ISR operated in incoherent scatter mode [7] with 154 microseconds pulse filled by 13-elements Barker consequence for electron density measurements, and with simple 750 microseconds pulse for spectral measurements of electron and ion temperatures, and ion composition.

To measure initial undisturbed conditions and to track the process of ionosphere relaxation after each OME burn we analyzed time interval an hour before and an hour after each flight. The ISR antenna beam in most experiments was directed into the centre of area, where OME engine ran. These directions were almost parallel to geomagnetic field lines in the latitude of Irkutsk. Unfortunately, there were uncertainties in direction and values of the neutral wind, which shifted disturbed area beyond antenna diagram.

3. OBSERVATION RESULTS

In this study, we examine only electron density (Ne) changes, but we have to notice that there was no significant reaction in electron and ion temperatures, which can be associated with ionospheric hole formation. This conforms to results of [2]: exhaust products are cold relative to ambient molecules, and their small amount can not affect background temperature significantly. Experiments on September 1–8, 2008 showed remarkable changing in O^+/H^+ ratio, but we need additional information for interpretation of these changes. Electron density is the most important ionospheric parameter. Hereafter we present results observed during the September 2007 experiments.

At night, when there are no ionization sources at low altitudes of the midlatitude ionosphere, filling of the ionospheric hole can be made with outgoing flow along geomagnetic field lines. A quite long-term effect can be expected here. Figs. 2–5 show time-altitude plots of electron density during some TSC Progress flights. Black triangles on the plot show the OMS burn time. Direction of each burn and amount of exhaust products are given in Figure captures. Altitude of each flight is approximately the same and equals to $\sim 340\,\mathrm{km}$. The spacecraft intersected the antenna beam in West-East direction (Fig. 1), that was nearly perpendicular to geomagnetic field lines.

Burns directed toward the ISR were almost along the geomagnetic field line. In these cases, the pronounced effect was observed. This effect is clearly visible in Fig. 2 and Fig. 5, but is weaker in Fig. 4. On September 21, 2007 (Fig. 3), the hole was clearly manifested at all altitudes below the flight altitude, though OME ran for deceleration. Such a high degree of ionization depletion was surprising. According to the estimation of the hole life-time, its average values were 10–15 minutes. Electron density depletions varied from 12% up to 40% relative to the background level.

Some experiments in February 2008 and September 2008 showed that ionospheric holes associated with the TSC exhaust were moved rapidly beyond the radar beam by the meridianal neutral wind. The most pronounced effect was observed when burn is directed against the wind.
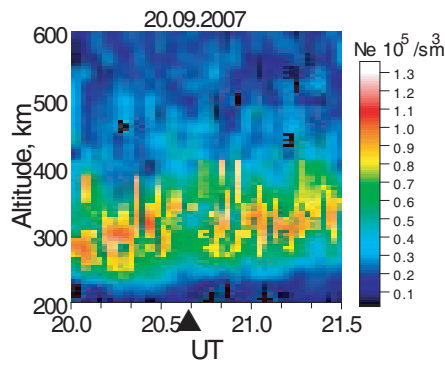
Figure 2: September 20, ACE running toward ISR for 5.1 sec (exhaust 5.1 kg).
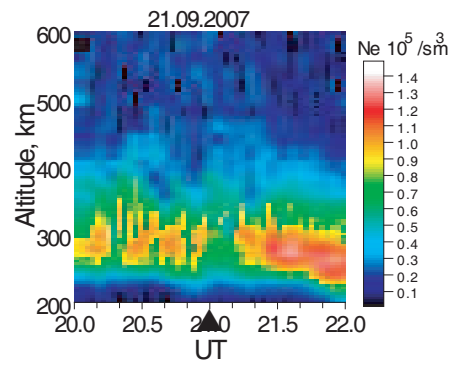
Figure 3: September 21, — 8 OME running on braking for 5.4 sec (exhaust 1.9 kg).
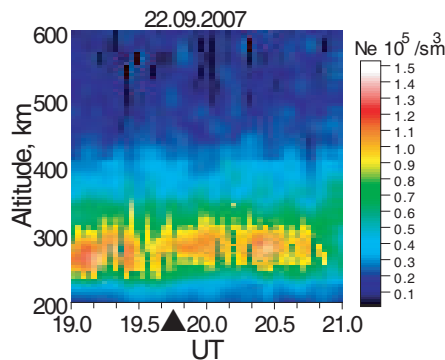
Figure 4: September 22, — ACE running toward ISR for 5.1 sec (exhaust 5.1 kg).
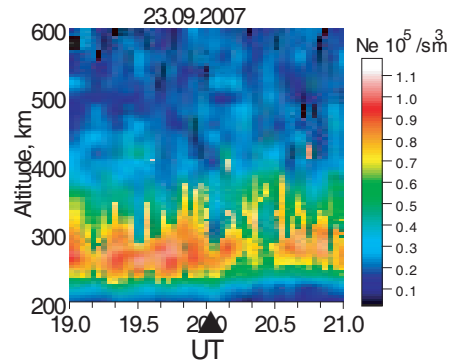
Figure 5: September 23, — 8 OME running toward ISR for 6.4 sec (exhaust 2.4 kg).

4. DISCUSSION

The experiments carried out in 2007–2009 show repeatable feature of the ionization hole formation. Even several kilograms of exhaust product can significantly affect the ionosphere in local area. Significant electron density depletions (up to 40%) were the main result of "Plasma-Progress" experiments. However, the distinctions between flights cause some questions about process of ionospheric hole formation. One of them is the reason of significant difference between flights with the similar exhaust stream direction. Comparing September 22 and September 23 data, we can see that a smaller amount of exhaust on September 23 causes a stronger ionization depletion that reaches altitude of ~ 270 km. A larger exhaust on September 22, when background N_e was 20% greater, caused a smaller relative depletion. Perhaps this difference is determined by the engine type, shapes, and velocity of streams. If we analyze data obtained on September 22 (Fig. 4), we understand that ionization depletion was short in the maximum of the N_e profile, but at the height of ~ 330 km, only ten kilometers below altitude of exhaust, it was quite long. Similar experiment on September 20 (Fig. 2 and Fig. 6) with lowest background N_e cause more than 40%-depletion. This comparison allows us to suggest that the hole shape depends on duration of exhaust gas reaction with ambient O^+ ions.

This may explain the most unexpected result when rather large ionization depletion on September 21 was formed when OMS worked with deceleration and only 1.9 kg of exhaust gases impacted the ionosphere. In this case exhaust products have no initial velocity component along the geomagnetic field line, hence the hole formation is determined only by proper atmosphere-ionosphere transport processes. As for differences between 'toward ISR' experiments, they may be caused by the neutral meridian wind, which shifts exhaust cloud from or inside the radar diagram beam.

5. CONCLUSION

Artificial ionospheric disturbances associated with the TSC Progress engine burn can produce significant changes in the ionosphere even by relatively small amount of exhaust product. The ionospheric hole shape caused by exhaust gases depends on ambient plasma transport processes

and on geometry of the exhaust cloud. At night, the depletion of ionization in the midlatitude ionosphere can cover all ionospheric altitudes along geomagnetic field lines under the region of exhaust. The exhaust stream was found out to produce significant electron density depletion (20–40%) when it was directed into the radar antenna diagram. According to the estimation of ionospheric "hole" life-time, its average values are 10–15 minutes.

ACKNOWLEDGMENT

REFERENCES

1. Bernhardt, P. T., J. D. Huba, W. E. Swartz, and M. C. Kelly "Incoherent scatter from space shuttle and rocket engine plumps in the ionosphere," *JGR*, Vol. 103, No. A2, 2239–2251, 1998.
2. Bernhardt, P. T., J. D. Huba, E. Kudeki, R. F. Woodman, L. Condori, and F. Villanueva, "Lifetime of a depression in the plasma density over Jicamarca produced by space shuttle exhaust in the ionosphere," *Radio Science*, Vol. 36, No. 5, 1209–1220, 2001.
3. Foster, J. C., J. M. Holt, and L. J. Lanzerotti, "Mid-latitude ionospheric perturbation associated with the spacelab- plasma depletion experiment at millstone hill," *Ann. Geophys.*, Vol. 18, 111–119, 2000.
4. Mendillo, M., J. Baumgardner, D. P. Allen, J. Foster, J. Holt, G. R. A. Ellis, A. Klekociuk, and G. Reber, "Spacelab-2 plasma depletion experiments for ionospheric and radio astronomical studies," *Science*, Vol. 238, 1260–1264, 1987.
5. Mendillo, M. and J. M. Forbes, "Artificially created holes in the ionosphere," *J. Geophys. Res.*, Vol. 83, 5785–5792, 1991.
6. Mendillo, M., G. S. Hawkins, and J. A. Klobuchar, "A sudden vanishing of the ionospheric F region due to the launch of Skylab," *J. Geophys. Res.*, Vol. 80, 2217–2228, 1975.
7. Shpynev, B. G., "Incoherent scatter Faraday rotation measurements on a radar with single linear polarization," *Radio Sci.*, Vol. 39, No. 3, 2004, RS3001 doi: 10.1029/2001RS002523.

Detection of Heating Effects Due to Powerful Radiowaves Propagation by Irkutsk Complex for Passive Doppler Sounding of the Ionosphere

O. I. Berngardt, **V. G. Abramov**, **V. I. Kurkin**, and **G. A. Zherebtsov**

Institute of Solar-Terrestrial Physics, SB RAS, Russia

Abstract— Irkutsk Complex for Passive Doppler Sounding of the Ionosphere (ICPDSI) was created in Institute of Solar-Terrestrial Physics SB RAS (ISTP SB RAS). The ICPDSI includes the system for simultaneous four-channel receiving of 1–30 MHz radiosignals with the ability of program frequency control and the three-position receiving system for estimating radiowaves propagation azimuth. Doppler measurements in ISTP SB RAS was started a long time ago, but solving the task of making regular measurements in continuous monitoring mode for different propagation paths becomes possible only recently due to increasing of technical abilities. In the talk we have presented the data of observations of the signals generated by the heaters SURA (Russia, October 20–22, 2008) and Tromso (Norway, March 4–12, 2009) in Irkutsk. The main peculiarities of the observations are long propagation distance almost along the latitude over the midlatitude (SURA-Irkutsk) and subpolar (Tromso-Irkutsk) paths. The source generating the radiowaves is lengthy and located at ionospheric heights (near the F2 maximum). In the talk the variations of frequency and amplitude of the received signals are presented. The observations of spectral broadening of the signals, received at the basic heating frequency, are demonstrated. The preliminary estimations of azimuthal characteristics of the received signals are presented and discussed. Numerical simulations of long propagation of radiosignals, arising as a result of propagation of powerful radiowaves in the ionosphere, are made. The estimation of the conditions for successful observations of the heater facilities signals is done. Qualitative interpretation of the observations is made. It is shown that Irkutsk Complex for Passive Doppler Sounding of the Ionosphere is an instrument effective enough for detecting the effects caused by the heating facilities functioning and for investigating the propagation conditions for radiowaves, generated during the heating of the ionosphere by powerful radiowaves.

1. INTRODUCTION

Heating facilities now are the radiosystems that able to solve a number of scientific tasks: to diagnose the near-Earth and cosmic space; to investigate radiowaves propagation in the atmosphere, the ionosphere and the Earth crust; to study the physics of plasma instabilities [1]. Nowadays, the following five such facilities are functioning: EISCAT (Tromso, Norway) [7], HAARP and HIPAS (Alaska, USA) [6], Aresibo (Puerto-Rico) [8] and SURA (N. Novgorod, Russia) [4]. One of the basic effects caused by the functioning of the heating facilities is the creation of the disturbed region (heated region) in the ionosphere, with the characteristics, substantionally different from characteristics of the neighboring media [3]. This region radiates energy in a very wide frequency range [1, 2, 5].

The basic aim of the Irkutsk Complex for Passive Doppler Sounding of the Ionosphere (ICPDSI) experiments was a detection of the creation of such a region using the Stimulated Electromagnetic Emission (SEE) generated by it in short radiowaves range. Usually, studying the SEE carried out for sufficiently short paths, having the order of about the size of the disturbed region, at long paths the investigations of SEE are rare enough [5].

ICPDSI is a system for multichannel, narrowband (up to 3 kHz) receiving of the short-wave radiosignals (1–30 MHz) with recording the full signal shape (its quadrature components), crated in Institute of Solar-Terrestrial Physics SB RAS in 2007–2009.

As preliminary calculations shows, the shortwave signals propagation in such a task is multihop one, i.e., signal for the heated region to the receiver comes not directly, but after a reflection from the ground. The problem of the detection in such a situation is not a new [1, 9], but the basic difference of these experiments are the long longitudinal length of the path, and for the Tromso-Irkutsk experiment — propagation of the radiosignals over the subpolar regions.

The most important question for detection of the SEE in the case when ICPDSI listens at heating frequency is the source of the signal received at long paths: if the source is ionospheric one [6], or the basic part of the signal is the radiowaves from the heating facility propagating in the strongly-disturbed ionosphere [3].

As a heating facilities for these experiments we have used SURA and Tromso heaters. The geometry of the experiments is shown at Fig. 1.

2. OBSERVATIONS

2.1. SURA-Irkutsk experiment

Experiment SURA-Irkutsk was made 20–22/10/2008. The SURA facility worked from 11:00 till 14:00UT in 15 minutes pulse mode: 10 minutes heating +5 minutes of a silence. The heating frequency was 4300 kHz. At ICPDSI at this very time a signal was registered at frequencies that are very close to the heating frequency. The analysis of spectrogramms (running spectrum of the received signal as a function of frequency and time, FTI-plot) (see Fig. 2) shows that the received signal repeats exactly the heating cycle. Digitizing of the low-frequency quadrature components of the received signal was made using time resolution 100 mks for bandwidth 300 Hz. This allows to fully reconstruct the received signal. The spectral estimations was made using time window about 10 seconds, which corresponds to the spectral resolution of about 0.1 Hz.
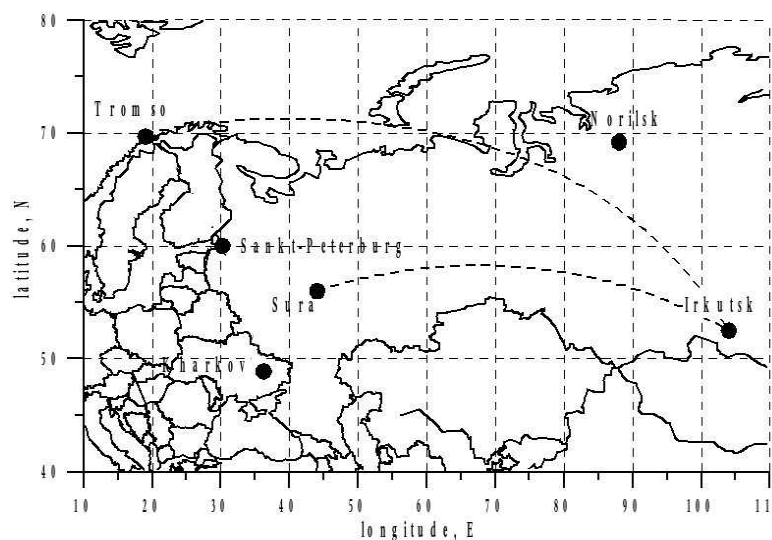
Figure 1: Geometry of the experiments.
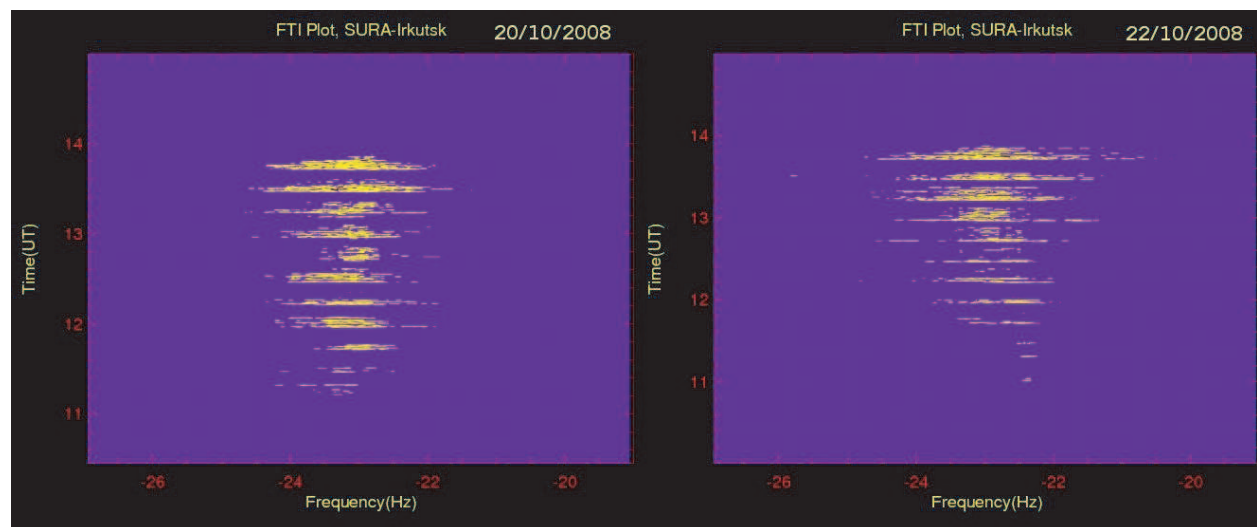
Figure 2: Frequency-time-intensity plots (as contours) for SURA-Irkutsk, during 20/10/2008 (left panel) and 22/10/2008 (right panel) experiments.

At Figs. 2–3, the FTI plots for the experiment are shown. One can see from them that:
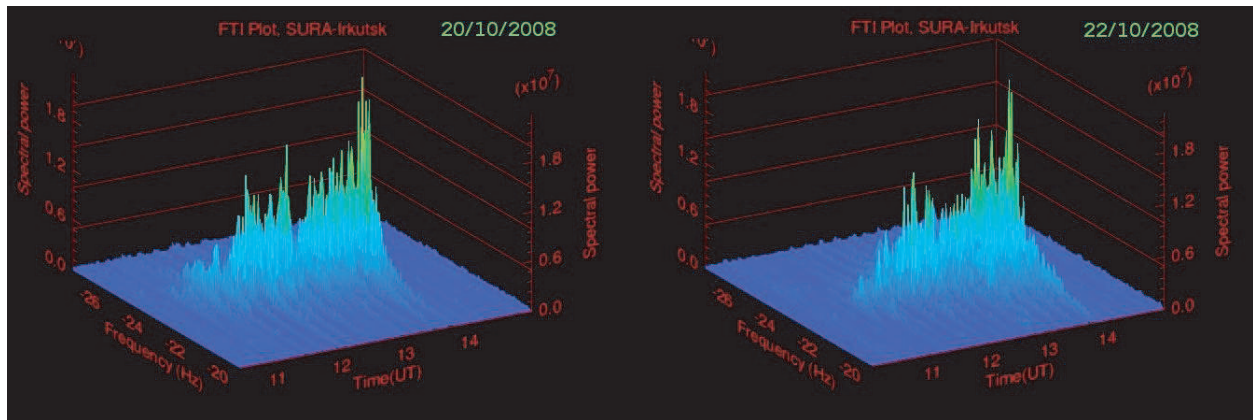
Figure 3: Frequency-time-intensity plots (as 3D plots) for SURA-Irkutsk, during 20/10/2008 (left panel) and 22/10/2008 (right panel) experiments.

1. During the heating (i.e., with increasing the time) the increase of the spectral width was observed (Fig. 2), up to 3–5 Hz per 3 hour experiment, and the spectral width monotonically growth during the heating, approximately 1 Hz/hour.

2. During the heating the amplitude of the signal grow too, this growth almost monotonic during the heating and at the end of the experiment the spectral amplitude becomes 10 times more powerful in comparison with the start of the experiment.

2.2. Experiment Tromso-Irkutsk

Experiment Tromso-Irkutsk was made 4–12/03/2009. Tromso heating facility worked at different modes. During the experiment 14:20–14:40, 05/03/2009 the heater frequency was 4040.3 kHz. At ICPDSI at this very time a signal was registered at frequencies that are very close to the heating frequency. The analysis of spectrogramms (running spectrum of the received signal as a function of frequency and time, FTI-plot) (see Fig. 4) shows that the received signal repeats the heating cycle. Digitizing of the low-frequency quadrature components of the received signal was made using time resolution 100 mks for bandwidth 300 Hz. This allows to fully reconstruct the received signal. The spectral estimations was made using time window about 10 seconds, which corresponds to the spectral resolution of about 0.1 Hz.

At Figs. 4–5, the FTI plots for the experiment are shown. One can see from them that:

1. During the heating (i.e., with increasing the time) the increase of the spectral width was observed (Fig. 4), up to 1 Hz per 20 minutes experiment, and the spectral width monotonically growth during the heating, approximately 2 Hz/hour.

2. During the heating the amplitude of the signal grow too, this growth almost monotonic
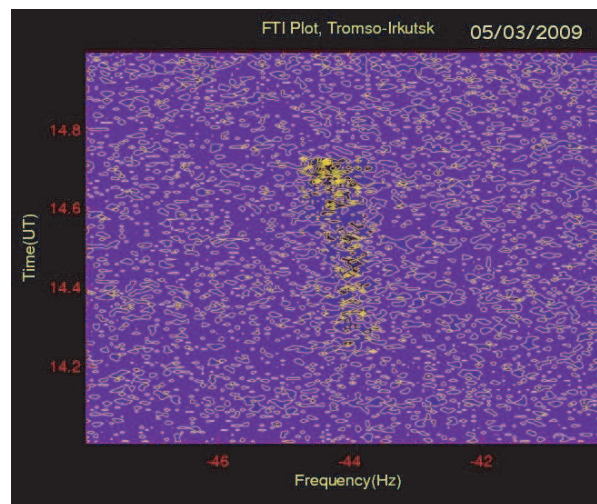
Figure 4: Frequency-time-intensity plots (as contours) for Tromso-Irkutsk during 05/03/2009 experiment.
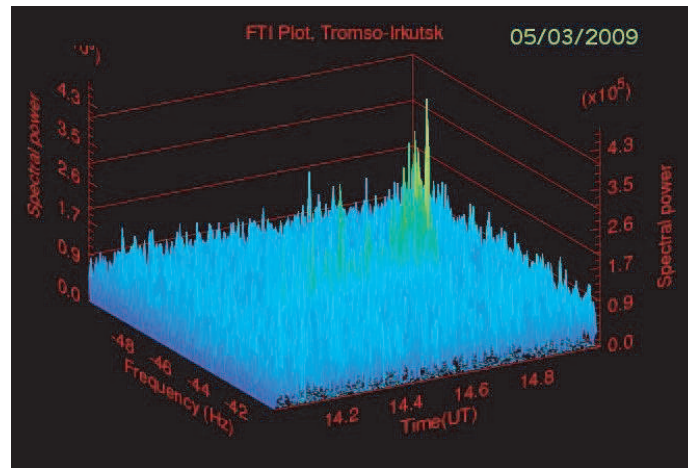
Figure 5: Frequency-time-intensity plots (as 3D plots) for Tromso-Irkutsk during 05/03/2009 experiment.

during the heating and at the end of the experiment the spectral amplitude becomes 2 times more powerful in comparison with the start of the experiment.

3. DISCUSSION

Experimental observations of the SURA and Tromso heating facilities at heating frequencies at Irkutsk show that signal spectra from both heaters have the same properties: they increase theirs amplitude and spectral width and correlates with the working cycle of the heaters. According to this, one of the possible explanations of these properties of the received signal characteristics is the interpretation of the signal as a result of the ionospheric emission due to scattering of the heater signal at the non-static irregularities, generated by the heater (SEE). The similar observations were made earlier, for example in [2, 6].

Due to geometrooptical path from ionospheric transmitter to the ICPDSI is shorter than path from the heater to ICPDSI, and decrease of radiowave amplitude due to propagating through the ionospheric layers with high damping (for example, D-layer). We could also take into account that the direct signal from heater comes from the lower sidelobes of the antenna, that are usually 40dB lower than the main beam, and that the SEE is initiated by the main beam of the heater antenna pattern. This allows us to explain that direct signal from the heater can be much lower than signal from the ionospheric source, especially for such a long paths.

The presence in the received signal at the same time the signal from the heater and signal for the disturbed region of the ionosphere at long paths was observed earlier, for example [9]. In our case the SEE power is higher than direct signal from the heater due to experimental geometry and effects of the ionospheric radiowaves propagation.

REFERENCES

1. Blagoveshenskaja, N. F., *Geophysical Effects of the Active Affects in the Near Cosmic Space*, Gidrometeoizat, 2001 (in Russian).

2. Frolov, V. L., L. M. Kagan, and E. N. Sergeev, "Review of features of stimulated electromagnetic emission (SEE): Recent results obtained at the 'SURA' facility," *Radiophysics and Quantum Electronics*, Vol. 42, No. 7, 557–561, 1999.

3. Kagan, L. M., M. J. Nicolls, M. C. Kelley, V. L. Frolov, V. V. Belikovich, N. V. Bakhme'eva, G. P. Komrakov, D. I. Nedzvetski, V. P. Uryadov, Y. M. Yampolski, A. V. Koloskov, A. V. Zalizovski, V. L. Galushko, S. B. Kasheev, N. F. Blagoveshenskaja, V. A. Kornienko, T. D. Borisova, A. V. Gurevich, G. G. Vertogradov, V. G. Vertogradov, T. S. Trondsen, and E. Donovan, "Optical and RF diagnostics of the ionosphere over the SURA facility. Review of results," *Radiofizika i Astronomia (Radiophysics and Astronomy, Ukraina)*, Vol. 11, No. 3, 221–241, 2006.

4. Karashtin, A. N., G. P. Komrakov, Y. V. Tokarev, and Y. V. Shlyugaev, "Radar studies using the 'SURA' facility," *Radiophysics and Quantum Electronics*, Vol. 42, No. 8, 674–686, 1999.

5. Leyser, T. B., "Stimulated electromagnetic emissions by high-frequency electromagnetic pumping of the ionospheric plasma," *Space Science Reviews*, Vol. 98, 223–328, 2001.

6. Tze-Ho Pau, J., "Electromagnetic wave interraction with the auroral plasma," Ph.D. thesis, University of California, 2003.

7. Thide, B., H. Derblom, A. Hedberg, H. Kopka, and P. Stubbe, "Observations of stimulated electromagnetic emissions in ionospheric heating experiments," *Radio Sci.*, Vol. 18, 851–859, 1983.

8. Thide, B., A. Hedberg, J. A. Fejer, and M. P. Sulzer, "First observations of stimulated electromagnetic emission at Aresibo," *Geophys. Res. Lett.*, Vol. 16, 369–372, 1989.

9. Zalizovski, A. V., S. B. Kashcheyev, Y. M. Yampolsky, V. G. Galushko, V. S. Beley, B. Isham, M. T. Rietveld, C. La Hoz, A. Brekke, N. F. Blagoveschenskaya, and V. A. Kornienko, "Spectral features of HF signals from the EISCAT heating facility in Europe and in Antarctica," *Radiofizika i Radioastronomiya (Radiophysics and Radio Astronomy, in Russian)*, Vol. 9, No. 3, 261–273, 2004.

Ionosphere Wave Packets Excited by the Solar Terminator: AGW or MHD Origin?

E. L. Afraimovich, **S. V. Voyeikov**, **I. K. Edemskiy**, **and Yu. V. Yasyukevich**

Institute of Solar-Terrestrial Physics SB RAS, Russia

Abstract— We analyzed the dynamic and spectral characteristics of the medium-scale travelling ionospheric disturbances (MS TID) in the form of travelling wave packets (MS TWP). We used total electron content (TEC) measurements from the global network of GPS receivers (up to 1500 stations) in 1998–2007 and the dense Japanese network GPS/GEONET (1220 stations) in 2008–2009. Diurnal, seasonal, spectral and spatial-temporal MS TWP characteristics are determined by the solar terminator (ST) dynamics and do not depend on the solar or geomagnetic activity. In the time field, TWPs are narrow-band TEC oscillations of duration of about 1–2 hours with oscillation periods of 10–20 minutes. In winter, TWPs in the northern hemisphere are observed 3–4 hours after the morning ST passage, when the TEC time derivative achieves his maximum. In summer, TWPs are recorded 1.5–2 hours before the evening ST occurrence at the point of observations, but at the moment of the evening ST passage in the magneto-conjugate area. The TWP spatial structure is of a high degree of anisotropy and coherence at the distance of more than 10 wavelengths; the TWP wavelength is about 100–300 km. Both the high Q-factor of oscillatory system and synchronization of TWP occurrence with solar terminator passage at the point of observations and in the magneto-conjugate area testify the MHD nature of ST-excited TWPs. The obtained results are the first experimental evidence for the hypothesis for the ST-generated ion sound waves.

1. INTRODUCTION

Recent investigations have shown that movement of the solar terminator (ST) causes generation of acoustic-gravity waves (AGW), turbulence and instabilities in the ionosphere plasma. Pioneering theoretical works of V. M. Somsikov ([1] and other papers) marked the beginning of numerous experimental observations of "terminator" waves with the use of different methods of ionospheric radio sounding [2–4, etc.]. However, virtually all experimental data were obtained using indirect methods for analyzing the spectrum of ionosphere parameter variations, which can result from a number of factors [5].

Recently a considerable progress has been achieved in the study of terminator waves using the new technology of GPS radio sounding and the total electron content (TEC) determination with high spatial and temporal resolution. Afraimovich [6] has obtained the first GPS-TEC evidence for the wave structure excited by the morning ST and has found ST-generated medium-scale travelling wave packets (MSTWP). However registering time dependence of ionosphere parameters is insufficient to identify ST-generated wave disturbances. It is necessary to determine the spatial structure of these disturbances. Using TEC measurements from the dense network of GPS sites GEONET, Afraimovich et al. [7] has obtained the first GPS-TEC image of the space structure of MSTWP excited by the morning ST.

The goal of this paper is to obtain the detailed information regarding the spatial, spectral and dynamic characteristics of MSTWPs excited by the ST as deduced from the dense GPS network GEONET.

2. DATA AND METHOD

We use data for 2008–2009 from the Japanese GPS network GEONET (about 1225 stations in total). Actually, it is the world's largest regional GPS network (ftp://terras.gsi.go.jp/data/GPS_products/). Procedure of TEC obtaining from GPS data is described in details in several papers [8, 9]. The geomagnetic situation on selected and analyzed days of 2008–2009 can be characterized as quiet: the Kp index varied from 1.0 to 3.0.

Primary data include series of "oblique" values of TEC $I_0(t)$, as well as the corresponding series of elevations $\theta_s(t)$ and azimuths $\alpha_s(t)$ of the line of sight (LOS) to the satellite. Series of values of elevations $\theta_s(t)$ and azimuths $\alpha_s(t)$ of LOS was used to determine coordinates of subionospheric points (SIP) for the height $h_{\max} = 300\,\mathrm{km}$ of the F_2-layer maximum and to convert the "oblique" TEC $I_o(t)$ to the corresponding value of the "vertical" TEC $I(t)$. All results in this study were obtained for elevations $\theta_s(t)$ larger than $50°$.

To eliminate variations in the regular ionosphere, as well as trends introduced by orbital motion of the satellite, we derive TEC variations $dI(t)$ by filtering from the initial $I(t)$-series over the range of periods of 2–20 min.

3. TWP SPATIAL CHARACTERISTICS

In order to study space properties and dynamics of TWPs in detail, we employ 2D-space distribution of values of filtered TEC series $dI(\varphi, \lambda)$ for each 30-sec TEC counts with spatial resolution of 0.15° in latitude and 0.15° in longitude. Similar technology was first developed by Saito et al. [10] and was used in [11]. Fig. 1(a) presents the 2D-space distribution $dI(\varphi, \lambda)$ after the evening ST passage over Japan on 13 June 2008, at 15.28 UT. The amplitude of $dI(t)$ variations is about 0.1 TECU. Line marks the wave front extension and number near line marks direction α of the MSTWP wave vector $\mathbf{K} \approx 240°$.

We have analyzed a number of similar images of MS TWP spatial structure over Japan. The MS TWP space image is characterized by pronounced anisotropy (ratio between the lengthwise and transversal scales exceeds 10) and high coherence over a long distance of about 2000 km. The MS TWP wavelength varies from 100 km to 300 km. Spatial structure of $dI(\varphi, \lambda)$ remain stable along whole Japan at the distance of up to 2000 km.

4. DYNAMIC CHARACTERISTICS OF TWPS BY THE SADM-GPS METHOD

In order to determine dynamic characteristics of TIDs, we use SADM-GPS method taking the relative motion of SIPs into account [8, 12]. A SADM-GPS method was proposed for determining the travelling ionospheric disturbance (TID) dynamics (the unambiguous $\alpha(t)$ orientation of the wave-vector $\mathbf{K}$ over the range of 0–360° and the horizontal velocity $V(t)$ at each specific instant of time). Using different sets of n GPS arrays, we managed to obtain space average values of the horizontal projection V and direction α for given time interval. A detailed description of the
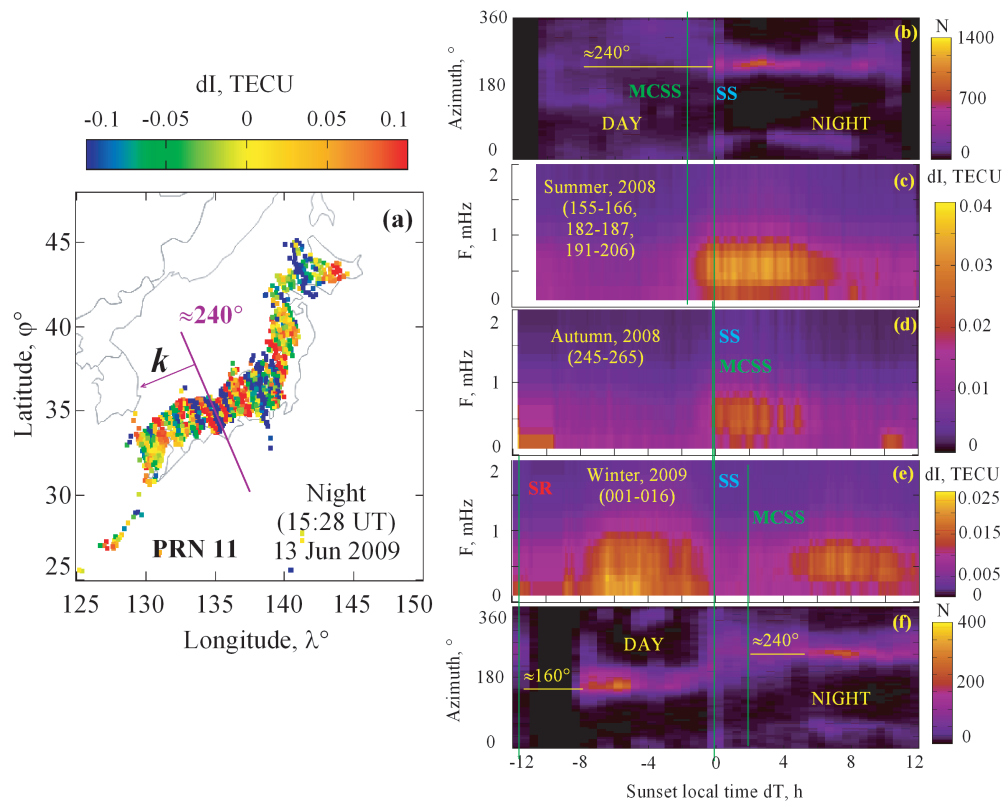
Figure 1: (a) The latitude-longitude 2D-space distribution of the filtered TEC $dI(\varphi, \lambda)$ after evening ST on 13 June 2008, 15.28 UT (b). (c), (d), (e) — the dynamic spectra of TWPs versus the local terminator time $dT = t_{obs} - t_{st}$ between the time of observation t_{obs} and the time t_{st} of sunset (SS) ST passing over the observation points. (b), (f) — similar dependencies of the azimuth α versus the local terminator time dT. Vertical lines MCSS mark the moments of SS ST passage over the magneto-conjugate points.

method is presented in [8, 12].

The hypothesis of the connection between wave packet generation and ST appearance can be tested in the terminator local time (TLT) system: $dT = t_{obs} - t_{st}$, where t_{obs} is the data point time, and t_{st} is the time of ST appearance at the altitude of H over this point [7]. Of the greatest interest is total diurnal distributions of travelling direction α for summer 2008 (Fig. 1(b)) and winter 2009 (Fig. 1(f)) versus the TLT. 2D-distributions of the azimuth α are calculated using data from $n = 492590$ GPS-arrays for whole Japan (b); and $n = 197150$ (f). The numbers on the panels mark the numbers of the analyzed days for the summer and winter. The steps on TLT and azimuth α equal 0.5 h and 5°, respectively. The scale for number of count hits N in different bins of distributions is plotted on panels (b) and (f) at the right.

The total distribution in Fig. 1(b) corresponds to the strongly directional travelling of MSTWPs at the night for full 35 summer days; the mean value and RMS of the azimuth α equal 240° and 15°, respectively. The strongly directional travelling begins immediately after the sunset (SS) ST appearance at observational points and continues for about 5 h. A similar picture is also significant for the night for full 16 winter days (Fig. 1(f)); the mean value and RMS of the azimuth α equal 240° and 10°, respectively. But in this case the strongly directional travelling begins 5 h after SS ST appearance at observation points and continues for about 5 h. For the day, the strongly directional travelling of MSTWPs corresponds to the mean value and RMS of the azimuth α equal to 160° and 28°, respectively. It starts 4 h after the sunrise (SR) ST appearance at observation points and continues for about 3–4 h. Beyond the mentioned time intervals is a total absence of directional MSTWP travelling (see also auxiliary material).

As we have found out, two types of MSTWPs (regular and chaotic ones) are observed for 24 hours. The regular MSTWPs travel with duration of some hours is synchronized with the ST passage. "Day" and "night" values of the MSTWP wave vector direction in the regular motion stage are determinate fixed and independent of a season and terminator front direction.

There are many existing and supposed sources of MSTIDs, which make a random interference field of the neutral atmosphere wave disturbance. The result is a random MS intensity distribution of electron density in the ionosphere with chaotic change of the apparent travel direction. This can be recorded some hours before the passage of the morning and evening ST over the observation point or in the magneto-conjugate area. When ST arrives, a strongly regular structure of wave disturbance can be observed. This structure overlaps the random interference field of different sources [5].

5. TWP SPECTRUM AND ST APPEARANCE OVER OBSERVATIONAL AND MAGNETO-CONJUGATE POINTS

Main characteristics of wave processes are temporal and spatial spectra. A calculation of a single spectrum of TEC variations involves continuous series of $dI(t)$ with duration of no less than 2.3 hours, thus enabling us to obtain a number of counts equal to 256 that is convenient for the algorithm of the fast Fourier transform (FFT) used in this study. To improve the statistical validity of the data, we use the method involving a regional spatial averaging of TEC disturbance spectra for all GPS/GEONET sites and PRN.

Figures. 1(c), (d), and (e) present the dynamic spectra of TWPs versus the local terminator time dT for the SS ST passing over the points of observation. The dynamic spectra are calculated using N counts for each bins of spectra (total number of $dI(t)$ data series $m = 3687173$ for (c); $m = 2059177$ for (d); $m = 1656426$ for (e)). The numbers on the panels mark the numbers of the analyzed days for the summer 2008 (c); for the autumn 2008 (d), and for the winter 2009 (e). The steps on TLT dT and variation frequency F equal 0.5 h and 0.13 mHz, respectively. The amplitude of spectral components is of about 0.02–0.1 TECU (scale for dI is plotted at the right).

According to the dynamic spectra, MSTWPs are the chain of narrow-band TEC oscillations with individual packet's duration of about 1–2 hours and oscillation periods of 10–20 minutes. Its total duration is about 4–6 hours.

The most important discovery is that MSTWPs in Japan in summer are registered 1.5–2 hours before the SS ST appearance over the registration point, when the evening ST passes over the magneto-conjugate point in Australia (c). At the equinox, those moments (SS and MCSS) contemporize (d); in winter TWPs are recorded 4–6 hours after the evening SS and MCSS moments (e).

It is very interesting to compare TLT dependencies of MSTWP spectrum with similar dependencies of the azimuth α (Fig. 1(b), (f)). The strongly directional travelling begins after MSTWP

appearance and continues over less time interval than the MSTWP appearance in spectra.

6. DISCUSSION AND CONCLUSION

The obtained results are in agreement with the theoretical indications of the ST effects [1] and agree with the experimental data on the MSTID spatial structure, dynamics and spectrum [3–5, 8–11, 13, 14].

However the question about the mechanism of the observed TEC oscillation is still unclear. MSTIDs (including those dependent on the terminator) are traditionally connected with modulation of the electron density by AGWs generated in the lower atmosphere as the terminator passes over the observation point. However, this hypothesis is not in agreement with characteristics of terminator waves we have found out (a high spatial coherence, strong anisotropy, stable directions of the wave vector azimuth). It is known that MSAGWs and MSTIDs can propagate without significant attenuation and changes in their shape or loss of their coherence no farther than 500–1000 km [14, 15].

The strongest argument against the AGW model of wave packets, at least for night conditions in summer, is our observations of TWP 1.5 hour before the terminator goes over an observation point and the explicit dependence on the instant of the terminator passage through a magneto-conjugate point. This implies that the TWP formation depends on a number of phenomena at magneto-conjugate points and in the magnetic field line joining these points.

Using a new law to the mid-latitude model Sami2 of the ionosphere, Huba et al. [16] found that ion sound waves can be generated in the topside low-latitude ionosphere at sunrise and sunset. The waves can persist ~ 1–3 h at altitudes above the O+/H+ transition altitude (~ 1000 km) with periods about 10'min. The waves result from the rapid heating and cooling of the lower ionosphere that occurs at sunrise and sunset. At sunrise, photoelectron heating produces strong upward plasma flows along the geomagnetic field. These flows lead to a local compression and heating of the plasma at the apex of the field line, which in turn generates ion sound waves. At sunset, the waves are produced by a rapid cooling of the "plasma". Our study is the first experimental proof for the correctness of the model [16].

As such oscillations are sometimes connected with the terminator passage in the ionospheric region conjugated via the geomagnetic field, their transportation by some magnetospheric MHD waves would appear reasonable. Alfven or slow magneto sonic (SMS) waves propagate along the magnetic field. The periods of the observed oscillations are far beyond the minimum periods of the proper Alfven waves at these latitudes (≈ 10 s), but correspond to the periods of the first harmonics of stationary SMS waves propagating along geomagnetic field lines [17]. In that study the authors conclude that the ionosphere plays no part in either generation or SMS wave absorption. This conclusion stems from the fact that all electromagnetic components and transverse components of plasma oscillations tend to zero in the ionosphere. But the said study also shows that the longitudinal component of the plasma oscillation velocity does not vanish in the ionosphere. It is just this oscillation component that is responsible for the electron density modulation that is detected by TEC recording.

Skewness of seasonal dependence in Japan is noteworthy (Fig. 1). In summer, wave packets appear before the sunset, but they are not registered at the winter magneto-conjugate area. This implies that the modulated plasma stream moves in the only one direction (from the winter area after sunset to the summer daytime magneto-conjugate area).

Our results are important for the development of ionosphere irregularity physics and modelling of the transionospheric radio wave propagation, for finding possible earthquakes precursors in the given range of TEC oscillation periods, for detecting ionospheric response to hurricanes and tornadoes, etc.

A new era for studying terminator waves and medium-scale ionospheric disturbances begins: this provides a better space-time resolution, global observations, and a magnetohydrodynamic conception of nature of these disturbances. Actually, we found out a NEW PHENOMENON and provided the experimental proof for a possible detection of ST-generated ion sound waves using modern methods of ionospheric diagnostics.

ACKNOWLEDGMENT

REFERENCES

1. Somsikov, V. M., "On mechanisms for the formation of atmospheric irregularities in the solar terminator region," *J. Atmos. Terr. Phys.*, Vol. 57, No. 1, 75–83, 1995.
2. Drobzhev, V. I., D. E. Zachateisky, P. E. Kozina, M. M. Konoplyanko, D. A. Kurmangaliev, and V. M. Somsikov, "Mid-latitude short-period disturbances in the ionosphere during the solar terminator passage," *Geomagn. Aeron.*, Vol. 32, 181–183, 1992.
3. Dominici, P., L. R. Cander, and B. Zolesi, "On the origin of medium-period ionospheric waves and their possible modelling: A short review," *Annali di Geofisica*, Vol. 11, No. 5, 1171–1178, 1997.
4. Galushko, G., V. V. Paznukhov, Y. M. Yampolski, and J. C. Foster, "Incoherent scatter radar observations of AGW/TID events generated by the moving solar terminator," *Ann. Geophys.*, Vol. 16, 821–827, 1998.
5. Hocke, K. and K. Schlegel, "A review of atmospheric gravity waves and traveling ionospheric disturbances: 1982–1995," *Ann. Geophys.*, Vol. 14, 917–940, 1996.
6. Afraimovich, E. L., "First GPS-TEC evidence of wave structure excited by solar terminator," *Earth, Planets and Space*, Vol. 60, 895–900, 2008.
7. Afraimovich, E. L., I. K. Edemskiy, S. V. Voeykov, Yu. V. Yasyukevich, and I. V. Zhivetiev, "The first GPS-TEC imaging of the space structure of MS wave packets excited by the solar terminator," *Ann. Geophys.*, Vol. 27, 1521–1525, 2009.
8. Afraimovich, E. L., N. P. Perevalova, and S. V. Voyeikov, "Traveling wave packets of total electron content disturbances as deduced from global GPS network data," *J. Atm. Solar-Terr. Phys.*, Vol. 65, No. 11–13, 1245–1262, 2003.
9. Hernandez-Pajares, M., J. M. Juan, and J. Sanz, "Medium-scale traveling ionospheric disturbances affcting GPS measurements: Spatial and temporal analysis," *J. Geophys. Res.*, Vol. Ill, No. A07S11, doi:10.1029/2005JA011474.
10. Saito, A., S. Fukao, and S. Miyazaki, "High resolution mapping of TEC perturbations with the GSI GPS network over Japan," *Geophys. Res. Lett.*, Vol. 25, 3079–3082, 1998.
11. Tsugawa, T., Y. Otsuka, A. J. Coster, and A. Saito, "Medium-scale traveling ionospheric disturbances detected with dense and wide TEC maps over North America," *Geophys. Res. Lett.*, Vol. 34, No. L22101, doi:10.1029/2007GL031663.
12. Afraimovich, E. L., K. S. Palamartchouk, and N. P. Perevalova, "GPS radio interferometry of travelling ionospheric disturbances," *J. Atmos. and Sol.-Terr. Phys.*, Vol. 60, 1205–1223, 1998.
13. Kotake, N., Y. Otsuka, T. Ogawa, T. Tsugawa, and A. Saito, "Statistical study of medium-scale traveling ionospheric disturbances observed with the GPS networks in Southern California," *Earth Planets Space*, Vol. 59, 95–102, 2007.
14. Drobzhev, V. I., M. Z. Kaliyev, Y. G. Litvinov, B. D. Chakenov, and A. F. Yakovets, "The spatial coherence of the field of wave disturbances of the ionosphere," *Geomagn. Aeron.*, Vol. 31, 334–336, 1991.
15. Francis, S. H., "A theory of medium-scale traveling ionospheric disturbances," *J. Geophys. Res.*, Vol. 79, 5245–5259, 1974.
16. Huba, J. D., G. Joyce, and J. A. Fedder, "Ion sound waves in the topside low latitude ionosphere," *Geophys. Res. Lett.*, Vol. 27, No. 19, 3181–3184, 2000.
17. Leonovich, A. S., D. A. Kozlov, and V. A. Pilipenko, "Magnetosonic resonance in a dipole-like magnetosphere," *Ann. Geophys*, Vol. 24, No. 8, 2277–2289, 2006.

Theoretical Investigation of the Ultrawideband FMCW Signal Propagation through Ionospheric Radiochannel

Nikolay V. Ilyin[1] and Vitaly V. Khakhinov[1, 2]

[1]Institute of Solar-Terrestrial Physics of Siberian Branch of Russian Academy of Sciences, Irkutsk, Russia
[2]Irkutsk State University of Railway Engineering, Irkutsk, Russia

Abstract— A theoretical description is given to the chirpsounder operation configuration in the mode of sounding the ionospheric radiochannel by the ultrawideband frequency-modulated continuous wave signal. A preprocessing of the received signal is carried out using the frequency-compression method. It is shown that the result de-rived from processing an individual time sample is mathematically equivalent to a sounding of the radio channel by a complex-valued narrow-band impulse signal. Analysis of both in-phase and quadrature components of received frequency-modulated continuous wave signal at the output of intermediate frequency band-pass filter of the chirpsounder demonstrates a new possibility of recovering the transfer function of the HF radiochannel within the band of operating frequencies and the interval of time delays that are de-fined by the intermediate frequency filter characteristics.

1. INTRODUCTION

The central objective in the frequency-modulated continuous wave (FMCW) theory is to solve the problem of ionospheric propagation of HF ultrawideband signals. The well known approaches to solving this problem are the following. The earlier approach was reported in [1]. The principle of the method is that the radiated FMCW signal is divided into narrow-band components using the theory of ionospheric propagation of narrow-band pulses. Another approach has been reported in [2]. The transfer function of the ionospheric radiochannel was represented as a set of transfer functions, each of which was expanded into a Taylor series in the neighborhoods of central frequencies; the passing of the transmitted signal through each transfer function was considered separately.

The approach used in this paper was suggested in [3], and differs fundamentally from those mentioned above. It is based on a consistent formal examination of the influence results exerted by the ionospheric radiochannel and the chirpsounder receiver devices on the FMCW signal. Subsequent transformations of the formal expression obtained for the recorded spectrum are carried out by using the main functional and technical characteristics of the chirpsounder receiver. It is shown that the recorded spectrum of the received signal sample is similar to the response of the ionospheric radiochannel to the narrow-band signal with the envelope, which is an exact replica of the form of the window's spectral function.

Digital methods applied to chirp signal processing considerably expand its ability to adaptively reverse signal distortion in the dispersive ionospheric radiochannels and correct the phase-frequency characteristic of the radiochannel. This paper presents a technique that analyses the FMCW signal at the output of the intermediate frequency (IF) filter to reconstruct the radiochannel transfer function of the ionospheric path.

2. WINDOW PROCESSING OF THE FMCW SIGNAL

The basic concept of the chirpsounder operations for ionospheric HF sounding is known for decades. The transmitted FMCW signal with frequencies deviation from 1 MHz to 30 MHz has duration about some minutes.

To date, several approximate theoretical methods have been developed to model the chirpsounder operations [1, 2, 4]. One of the approaches, as discussed in [3] and further developed in [5, 6], bases its methodology in systematic formal examination of the impact produced by the ionospheric radiochannel and the chirpsounder receiver circuitry on the sounding FMCW signal. We briefly describe the major points of the method below.

The transmitted FMCW signal with constant unit amplitude can be represented as:

$$e_{tr}(t) = \begin{cases} \sin \chi t^2, & t > 0 \\ 0, & t < 0 \end{cases} \tag{1}$$

where χ is the chirp sweep rate. Assuming that the characteristics of the ionospheric radiochannel are linear, signal at the input of the receiver may be written as a convolution $e_{tr}(t)$ with the impulse

response function of the radiochannel:

$$e_{rec}(t) = \int_0^\infty h(\tau) e_{tr}(t - \tau) d\tau \tag{2}$$

In the receiver, signal $e_{rec}(t)$ is mixed with the replica of transmitted signal $e_{tr}(t)$, and passed through a low-pass filter. The low-frequency signal is sampled within a particular time window $w(t)$ placed at times t_k. As the window slides with time, the samples are fed to the spectrum analyzer to obtain set of output spectra $S_k^+(F)$, corresponding to the positive values of frequency F. The set of spectra $S_k^+(F)$ is the result of one chirpsounder measurement session.

$$S_k^+(F) = \frac{1}{4} e^{iFt_k} \int_0^\infty h(\tau) W(F - 2\chi\tau) e^{i(\chi\tau^2 - 2\chi t_k \tau)} d\tau \tag{3}$$

Here W is the spectrum of the window $w(t)$. In [3] showed that processing of the individual time domain samples of the received FMCW signal is equivalent, from the mathematical point of view, to analysis of the complex narrow-band pulse signals propagating the radiochannel at the group delays determined by the peak positions in the observed spectrum $S_k^+(F)$. In [5] obtained an expression for the dispersive distortion for individual observed spectra depending on dispersion of the group time delay, time window length, and FMCW sweep rate. Calculated widths of the spectral lines due to dispersion are consistent with the experimental data obtained at the chirpsounder [7] of Institute of Solar-Terrestrial Physics, Siberian Branch, Russian Academy of Science.

3. MODELING OF THE DIGITIZED FMCW SIGNAL AT INTERMEDIATE FREQUENCY

The proposed technique for reconstructing transfer function of the ionospheric radiochannel is based on a possibility of digitizing FMCW signal at the IF. Let us analyze the IF signal shape assuming known band-pass filter properties. The sequence of transformation of the FMCW signal is shown at Figure 1.

Received FMCW signal is mixed with the signal of the reference oscillator $e_0(t)$:

$$e_o(t) = \sin\left(\omega_i t + \chi t^2\right), \tag{4}$$

where ω_i is the IF. The beat tones are transferred to the IF amplifier that amplifies the low-frequency part and cuts off the high-frequency part by a band-pass filter with the impulse response
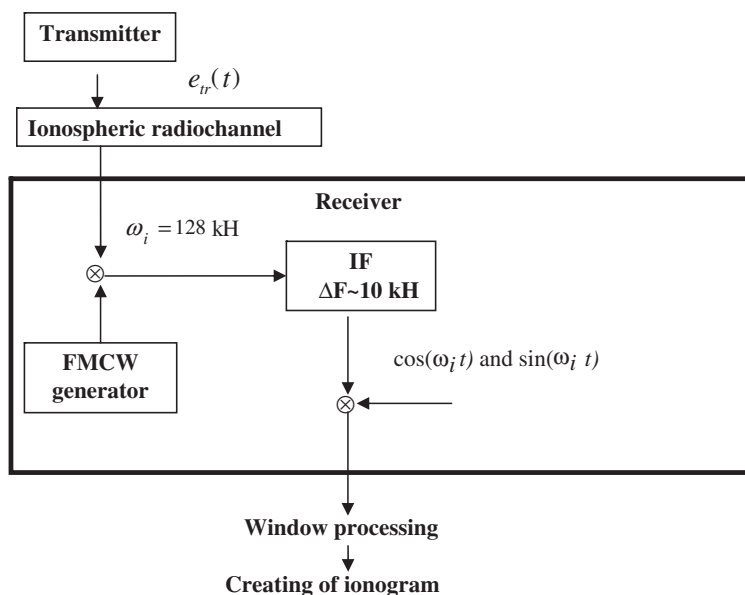
Figure 1: Processing of the FMCW signal.

function $f(t)$. Without limiting generality of our reasoning, we will assume that the IF amplifier's gain is 1. Then signal at the band filter output $e_i(t)$ has the following form:

$$e_i(t) = \frac{1}{2} \int\limits_0^\infty f(\xi) \int\limits_{-\infty}^\infty h(\tau) \cos \left[\omega_i(t - \xi) + 2\chi\tau(t - \xi) - \chi\tau^2 \right] d\xi d\tau \qquad (5)$$

The signal $e_i(t)$ can be split into its in-phase and quadrature components $e_a(t)$ and $e_b(t)$ by multiplying it by $\cos(\omega_i t)$ and $\sin(\omega_i t)$ in two different radiochannels while simultaneously suppressing the high-frequency components:

$$e_a(t) = \frac{1}{4} \int\limits_0^\infty f(\xi) \int\limits_{-\infty}^\infty h(\tau) \cos \left[\omega_i\xi - 2\chi\tau(t - \xi) + \chi\tau^2 \right] d\xi d\tau$$

$$(6)$$

$$e_b(t) = \frac{1}{4} \int\limits_0^\infty f(\xi) \int\limits_{-\infty}^\infty h(\tau) \sin \left[\omega_i\xi - 2\chi\tau(t - \xi) + \chi\tau^2 \right] d\xi d\tau$$

By the causality principle, $f(t) = 0$ when $t < 0$ and therefore the lower limit of integrals can be extended down to $-\infty$.

Under standard processing we shift the signal to low frequency where exists only one component, which is linear combination of both components. However, as it will become clear from the following discussion, the proposed method for reconstructing the radiochannel transfer function requires both quadrature components to be acquired. For convenience of further analysis, we express the signal in the complex form:

$$\tilde{e}_i(t) = e_a(t) - ie_b(t) \qquad (7)$$

Expressions (6) and (7) describe signal at the IF. Substituting (6) into (7) and interchange of integrations yields:

$$\tilde{e}_i(t) = \frac{\pi}{2} \int\limits_{-\infty}^\infty h(\tau) F(-\omega_i - 2\chi\tau) e^{-i(\chi\tau^2 - 2\chi\tau t)} d\tau \qquad (8)$$

Here $F(\omega)$ is the transfer function of band-pass filter at the IF.

By changing the integration variable in (8) and turning to $\omega = 2\chi\tau$, we can conclude that (8) is structurally analogous to a mathematical description of signal with spectrum $h(\omega/2\chi)$ passing through a band-pass filter with transfer function $\tilde{F}(\omega) = F(-\omega_i - \omega) \exp(-i\omega^2/4\chi)$. Or, in other words, signal (8) is the response of the band-pass filter with transfer function $\tilde{F}(\omega)$ to a signal with spectrum $h(\omega/2\chi)$. Dispersive properties of this filter considerably differ from the properties of the typical band-pass filter installed in a chirpsounder.

4. METHOD OF RECONSTRUCTING CHANNEL TRANSFER FUNCTION

Modern digital signals processing techniques can be used to build a corrective filter that can reverse dispersive distortion of the signal in radiochannel by modifying the transfer function $\tilde{F}(\omega)$. To that end, the circuitry for preprocessing of the received signal is proposed to include an additional corrective filter with a transfer function $F_c(\omega)$ that is related to the transfer function $F(\omega)$ of the band-pass filter, within its band $[\omega_i, \omega_i + \Omega]$, by the following expression:

$$F(\omega)F_c(\omega) = \begin{cases} e^{i\frac{(\omega_i + \omega)^2}{4\chi}}, & \omega \in [\omega_i, \omega_i + \Omega] \\ 0, & \omega \notin [\omega_i, \omega_i + \Omega] \end{cases} \qquad (9)$$

Correcting filter with such characteristics can be implemented in the digital form. Then the signal passed sequentially through the band-pass and correcting filters is equivalent to the signal passed through an "effective" filter whose transfer function is product of the transfer functions in (9). The resulting output signal can then be written as:

$$\tilde{e}(t) = \frac{\pi}{2} \int\limits_{-\infty}^\infty h(\tau) F(-\omega_i - 2\chi\tau) F_c(-\omega_i - 2\chi\tau) e^{-i(\chi\tau^2 - 2\chi\tau t)} d\tau \qquad (10)$$

Representing the impulse response function of the ionospheric radiochannel as a sum $h = h_1(\tau) + h_2(\tau)$, where $h_1(\tau)$ is not zero for $\tau = [0, \tau_1 = \Omega/2\chi]$ and zero for $\tau > \tau_1$, and $h_2(\tau)$ is not zero only for $\tau > \tau_1$, we obtain

$$\tilde{e}(t) = \frac{\pi}{2} \int\limits_{-\infty}^{\infty} h_1(\tau) e^{i2\chi t\tau} d\tau \tag{11}$$

The expression (11) is a Fourier transform of impulse function of the ionospheric radiochannel $h_1(\tau)$, which means that its transfer function is equal to

$$\tilde{e}(t) = \pi^2 H(2\chi t) \tag{12}$$

The expression obtained above signifies the following. Adding the corrective filter with characteristics described by Equation (9) to pre-processing circuitry of the chirpsounder at its IF produces signal $\tilde{e}(t)$ that is uniquely and directly determined by the part of the ionospheric radiochannel's transfer function responsible for the group time delays from 0 to τ_1. To determine the transfer function for the ionosphere's response corresponding to delays larger than τ_1, the start time of reference oscillator must be shifted up, similar to what is done in order to observe, for example, round-the-globe signals.

The restored transfer function reflects current ionosphere state. The calculation of ionosphere parameters (electron concentration profile $N_e(h)$, the place and value of maximum $N_e(h)$) by means of transfer function is the inverse problem goal and is not considered here.

5. CONCLUSION

Analysis of both in-phase and quadrature components of the FMCW signal at the IF of the chirpsounder receiver shows possibility of reconstructing the part of the ionospheric radiochannel transfer function that determines the group time delays of interest. To obtain the transfer function, a digital correcting filter can be implemented as an additional pre-processing circuit. The described method is applicable in any of the chirpsounder operating modes such as the vertical, oblique and backscatter sounding. At the same time, the method does not require other changes to the receiver, and conventional windowing operations can still be applied to the reconstructed transfer function to produce standard ionograms. The obtained expressions for FMCW signal in the receiver can be used to consider alternative ways to analyze "frequency-time" variables in order to obtain the dependence of group time delays from frequency, such as, for example, the wavelet analysis. These ways shall determine the delay and frequency resolution.

Practical implementation of the proposed method in FMCW sounding requires analysis of the noise characteristics that will affect the result of the pre-processing by the correcting filter.

The result of one chirpsounder séance under standard processing is dependence of group delay on frequency — ionogram. The practical usage of proposed technique allows us to reconstruct the part of the ionospheric radiochannel transfer function which is directly characterizes the ionosphere state.

REFERENCES

1. Phillipp, N. D., N. S. Blaunshtein, L. M. Eruhimov, V. A. Ivanov, and V. P. Uryadov, *Modern Methods Investigation of Dynamical Process in Ionosphere*, Shtiinca, Kishinev, 1991.
2. Lunborg, B. and M. Lungren, "On the spectral width of chirpsounder signals," *Journal of Atmospheric and Terrestrial Physics*, Vol. 54, 311–321, 1992.
3. Ilyin, N. V., V. V. Khakhinov, V. I. Kurkin, V. E. Nosov, I. I. Orlov, and S. N. Ponomarchuk, "The theory of chirp-signal ionospheric sounding," *Proceedings of the 1996 International Symposium on Antennas and Propagation*, Vol. 3, 689–692, Chiba, Japan, September 1996.
4. Salous, S., "On the potential applicability of auto-regressive spectral estimation to HF chirp sounders," *Journal of Atmospheric and Solar-Terrestrial Physics*, Vol. 59, 1961–1972, 1997.
5. Davydenko, M. A., N. V. Ilyin, and V. V. Khakhinov, "On the shape of measured spectra of the ionosphere sounding by an FMCW signal under dispersion case," *Journal of Atmospheric and Solar-Terrestrial Physics*, Vol. 64, 1897–1902, 2002.
6. Ivanov, V. A., V. I. Kurkin, V. E. Nosov, V. P. Uryadov, and V. V. Shumaev, "Chirp ionosonde and its application in the ionospheric researches," *Radiophysics and Quantum Electronics*, Vol. 46, No. 11, 821–851, 2003.

7. Brynko, I. G., I. A. Galkin, V. P. Grozov, N. I. Dvinskikh, S. M. Matyushonok, and V. E. Nosov, "An automatically controlled data gathering and processing system using an FMCW ionosonde," *Advances in Space Research*, Vol. 8, No. 4, 121–124, 1988.

Nongaussian Kravchenko-Rvachev Distributions in Radio Physical Applications

V. F. Kravchenko[1], **O. V. Kravchenko**[2], **and A. R. Safin**[1]

[1]Kotel'nikov Institute of Radio Engineering and Electronics of RAS, Russian Federation
[2]Bauman Moscow State Technical University, Russian Federarion

Abstract— In this paper a new class of nongaussian distributions application is considered and grounded for radio physical problems which are the solutions of functional differentional equation such kind

$$Lf(x) = \lambda \sum_{k=1}^{M} c(k) f(ax - b(k)), \ |a| > 1. \tag{1}$$

1. KRAVCHENKO-RVACHOV DISTRIBUTION AND ITS APPLICATIONS

Kravchenko-Rvachov distribution is a finite solve of Equation (1) in case of $L = \frac{d}{dx}$, $M = 2$ and it have such analytical expression [1–5]:

$$p(x) = \frac{1}{b} h_a \left(\frac{x - m}{b} \right) \tag{2}$$

where

$$h_a(x) = \frac{1}{2\pi} \int_{\mathbb{R}} \prod_{j=1}^{\infty} \operatorname{sinc} \left(\frac{t}{a^j} \right) e^{itx} dt. \tag{3}$$

The function $h_a(x)$ has the following properties [1]:

(a) $\int_{\mathbb{R}} h_a(x) dx = 1$,

(b) $h_a(x) = 0$ if $|x| > \frac{1}{a}$,

(c) $h_a(x) = \frac{a}{2}$ if $|x| \leq \frac{a-2}{a(a-1)}$, $a \geq 2$,

(d) Fourier transform of $h_a(x)$ is $F_a(p) = \prod_{k=1}^{\infty} \operatorname{sinc} \left(\frac{p}{a^k} \right)$,

(e) Moments of $h_a(x)$ are computed thus $\int_{\mathbb{R}} x^{2k} h_a(x) dx = (-1)^k F_a^{(2k)}(0)$.

In addition $F_a^{(2k)}(0) = (2k)! c_{2k}(a)$ where $c_{2k}(a)$ are computed by recurrent formulas $c_0(a) = 1$, $c_{2k}(a) = \frac{1}{a^{2k}-1} \sum_{j=0}^{k-1} \frac{(-1)^{k-j} c_{2j}(a)}{(2k-2j+1)!}$, $k = 1, 2, \ldots$. Plots of function $h_a(x)$ and its Fourier transform are illustrated in Figure 1 with $a = 2$.

2. N-DIMENSIONAL KRAVCHENKO-RVACHOV PROBABILITY DENSITY

One of N-dimensional probability densities construction methods based on $h_a(x)$ is direct product [5]. Plot of two-dimensional probability density molded shown on Figure 2.

In paper are considered some distributions generated of equation such form

$$Lf(x) = F[f(ax - b)], \ x \in \mathbb{R} \tag{4}$$

where L — differential operator (Laplace, d'Alambert, Helmholtz, etc.), $F[\cdot]$ — functional from distribution f, linearly dependent from argument and $a, b \in \mathbb{R}$.
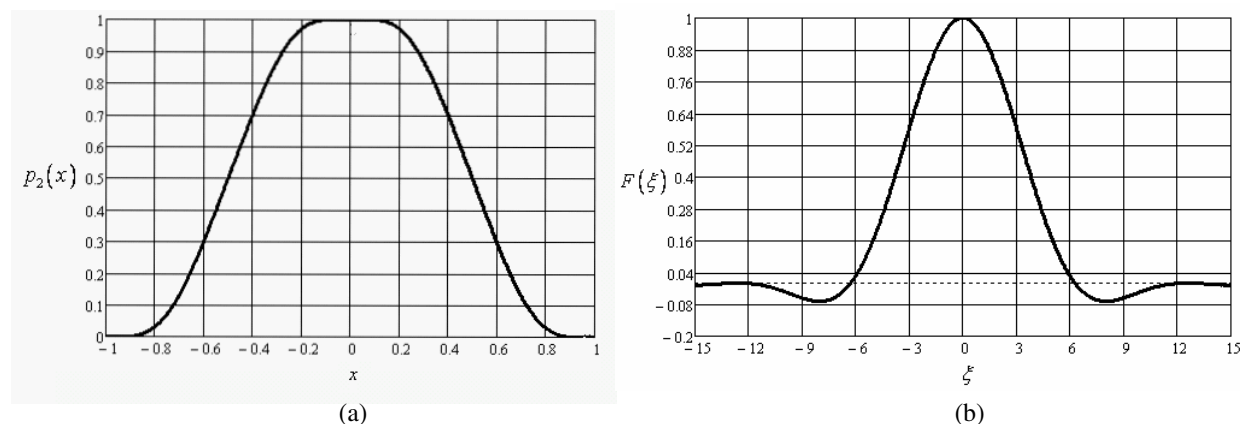
Figure 1: (a) Probability density $h_a(x)$ with $a = 2$, (b) Fourier transform of $h_a(x)$.
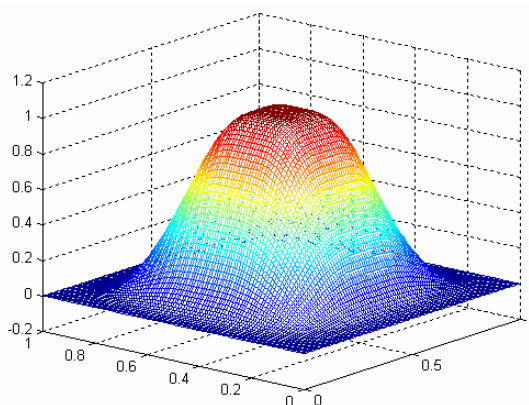
Figure 2: Two-dimensional probability density based on composition of one-dimensional distributions.

3. GENERALIZED PROBABILITY DENSITIES BASED ON KRAVCHENKO-RVACHOV DISTRIBUTION

Major computational random processes with finite distributions characteristics are analyzed based on one-dimensional probability density $up(x) = h_2(x)$ which are shown after in Table 1.

Kravchenko-Poissone probability

$$p(x) = \begin{cases} \frac{1}{c} up\left(\frac{x}{b}\right) \exp\left(-\frac{x}{a}\right), & \text{if } x \geq 0, \\ 0, & \text{if } x < 0, \end{cases} \tag{5}$$

where a, b, $c \in \mathbb{R}$.

Kravchenko-Gauss probability density

$$p(x) = \frac{1}{\sqrt{2\pi}c} e^{-\frac{x^2}{2a^2}} up\left(\frac{x}{b}\right), \quad a, b, c \in \mathbb{R}. \tag{6}$$

Kravchenko-Rayleigh probability density

$$p(x) = \begin{cases} \frac{x}{c} up\left(\frac{x}{b}\right) \exp\left(-\frac{x^2}{2 \cdot a^2}\right), & \text{if } x \geq 0, \\ 0, & \text{if } x < 0, \end{cases} \tag{7}$$
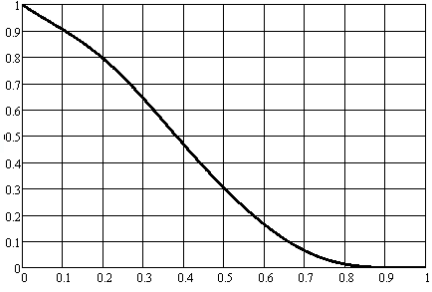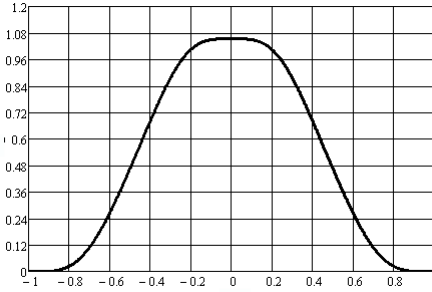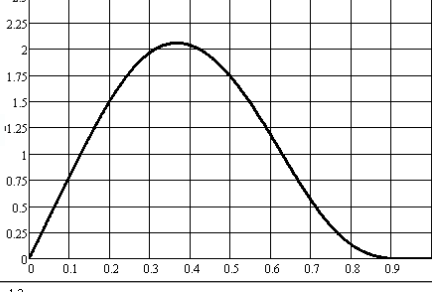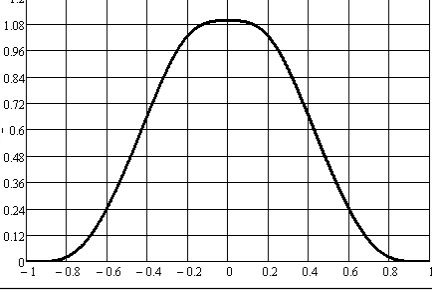
where a, b, $c \in \mathbb{R}$.

Kravchenko-Cauchy probability density

$$p(x) = \frac{1}{c} \frac{\frac{a}{\pi}}{a^2 + x^2} up\left(\frac{x}{b}\right), \quad a, b, c \in \mathbb{R}. \tag{8}$$

Constant c in Equations (5)–(8) is selected in this way $\int_{\mathbb{R}} p(x)\, dx = 1$.

Table 1: Probability densities (5)–(8).

Distributions ($a = b = 1$)	Plots $p(x)$	Moments
Kravchenko-Poisson		$m_1 = 0,095$, $m_2 = 0,035$, $m_3 = 0,016$, $m_4 = 0,008023$, $m_5 = 0,00443$.
Kravchenko-Gauss		$m_1 = 0$, $m_2 = 0.134$, $m_3 = 0$, $m_4 = 0,0013$, $m_5 = 0$.
Kravchenko-Rayleigh		$m_1 = 0,387$, $m_2 = 0,18$, $m_3 = 0,093$, $m_4 = 0,053$, $m_5 = 0,031$.
Kravchenko-Cauchy		$m_1 = 0$, $m_2 = 0,099$, $m_3 = 0$, $m_4 = 0,023$, $m_5 = 0$.

4. CONCLUSIONS

In this paper a questions of obtaining random processes which have Kravchenko-Rvachov distributions in one-dimensional and N-dimensional cases are considered [6]. An applications of its distribution are regarded in problems of digital signal and image processing, code and decode of signals in multichannel communications.

REFERENCES

1. Kravchenko, V. F., *Lectures on the Theory of Atomic Functions and Their Some Applications*, Publishing House Radio Engineering, Moscow, 2003 (in Russian).
2. *Digital Signal and Image Processing in Radio Physical Applications*, edited by V. F. Kravchenko, Fizmatlit, Moscow, 2007 (in Russian).

3. Zelkin, E. G., V. F. Kravchenko, and V. I. Gusevskiy, *Constructive Methods of Approximation in Theory of Antennas*, Science-Press, Moscow, 2005 (in Russian).

4. Volosyuk, V. K. and V. F. Kravchenko, *Statistical Theory of Radio Technical Systems of Remote Sensing and Radar*, edited by V. F. Kravchenko, Fizmatlit, Moscow, 2008 (in Russian).

5. Kravchenko, V. F., O. V. Kravchenko, and A. R. Safin, "Atomic functions in the probability theory and random processes," *Successes of Modern Radio Electronics*, No. 5, 2009.

6. Bykov, V. V., "Digital modeling in the statistical radio engineering," *Soviet Radio*, Moscow, 1971.

The Theory of Spectral Estimation of Signals and Generalized Kravchenko-Kotel'nikov-Levitan Theorems

V. F. Kravchenko and D. V. Churikov

Kotel'nikov Institute of Radio Engineering and Electronics of RAS, Russian Federatian

Abstract— In this report the theory of spectral estimation of signals on based of generalized two-dimensional (2D) Kravchenko-Kotel'nikov-Levitan theorems is considered. In the first part the 2D weight functions with support area of the complex shape on the basis of R-functions are constructed. In the second part the 2D Kravchenko-Kotel'nikov-Levitan theorems are formulated. In the third part it's application for spectral estimation, filtering and correction of 2D signals and images. As the examples the problems of noise reduction, scaling and also spectral properties improvement of images are submited. The numerical experiment and physical analysis of 2D signal processing results are show efficiency of new 2D kernels construction of sampling theorems.

1. INTRODUCTION

In communication theory the two dimensional (2D) signals are represented in the form of a linear combination of elementary functions

$$s(x,y) = \sum_{k=0}^{N-1} \sum_{l=0}^{M-1} C(k,l)\,\varphi_{k,l}(x,y). \tag{1}$$

Here, $\varphi_{k,l}(x,y)$ is an elementary signal of number (k,l), N, M are the dimensions of the elementary signals massive used in decomposition and

$$C(k,l) = \int_0^{T_1} \int_0^{T_2} s(t)\,\varphi_{k,l}(x,y)dxdy. \tag{2}$$

Thus, there is a signal decomposition on some basis. Application of the spectral analysis of signals in basis of digital functions in comparison with the spectral harmonious offers certain advantages. They are defined by the physical nature of representation of signals. Optimum digital processing in spectral area in comparison with the time possesses a number of advantages at numerical realization. It is known that spectral processing of signals possesses a high noise stability to action of the strong hindrances which own basis differs from own functions of a signal.

2. TWO-DIMENSIONAL GENERALIZED KRAVCHENKO-KOTEL'NIKOV-LEVITAN SAMPLING THEOREMS

As the basic functions it is expedient to choose kernels of the generalised Kravchenko-Kotel'nikov and Kravchenko-Levitan series. It is connected with that several factors. In the first the basis formed by these functions turns out by shifting of mother function. In the second such decomposition more naturally and also allows to apply fast transformation algorithms. Let's consider 2D signal $f(x,y) \in L_2\left(\mathbb{R}^2\right)$ with Fourier transform (FT) $\hat{f}(f_1, f_2) \in L_2\left(\mathbb{R}^2\right)$, and let $\hat{f}(f_1, f_2) = 0$, $(f_1, f_2) \notin \Omega_y$ (see the Figure 1). For simplicity we will admit that areas have the form of squares. Then

$$f(x,y) = \frac{1}{4\pi} \iint_A \hat{f}(f_1, f_2) \exp\left(j\left(f_1 x + f_2 y\right)\right)df_1 df_2. \tag{3}$$

Theorem. If $\Delta_x \le \frac{\pi}{f_{\max\,xS}}$ and $\Delta_y \le \frac{\pi}{f_{\max\,yS}}$, then

$$f(x_1, x_2) = \sum_{k_1, k_2 \in \mathbb{Z}} f(k\Delta_x, l\Delta_y)\varphi(x - k\Delta_x, y - l\Delta_y). \tag{4}$$

Here, the function spectrum $\hat{\varphi}(f_1, f_2) \in \Omega$ and $\forall (f_1, f_2) \in \Omega_y$: $\hat{\varphi}(f_1, f_2) \equiv 1$.

For simple support areas (rectangle and ellipse) probably to use constructions of one-dimensional of Kravchenko-Kotel'nikov (KK)

$$w_{KK}(t) = \prod_{j=1}^{M} \text{sinc}\left(\frac{\pi}{\Delta a^{j-1}} t\right) \tag{5}$$
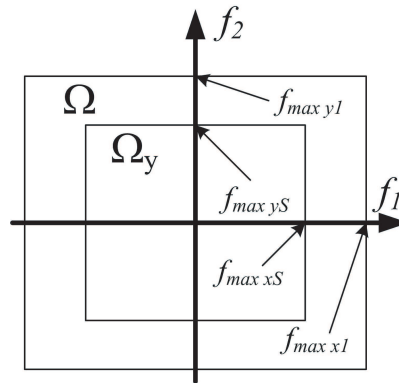
Figure 1: Geometry of spectras.
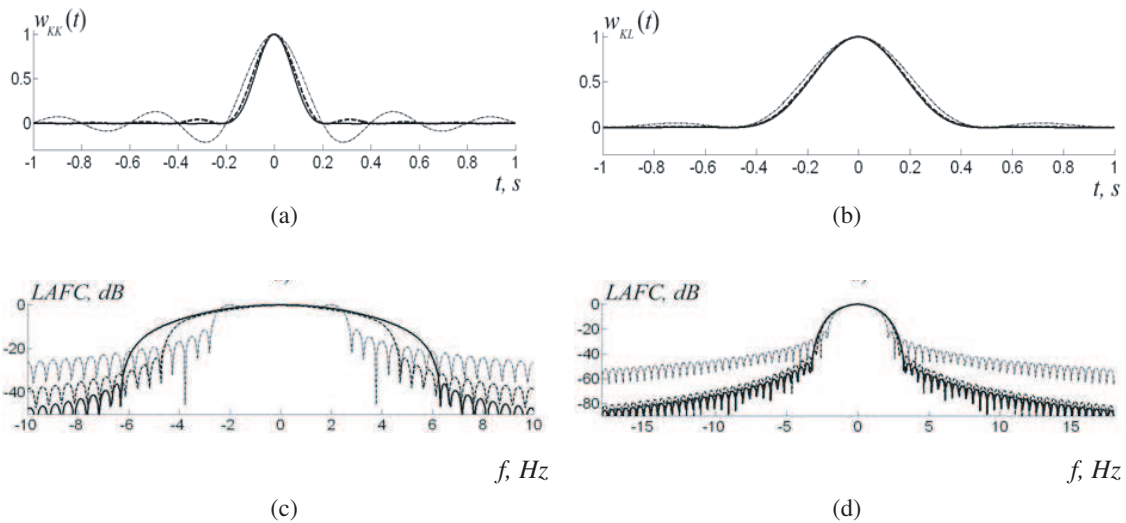
Figure 2: (a) Kravchenko-Kotel'nikov weight functions ($a = 1, 2$, $\Delta = 0, 2$ s), (c) their LAFC; (b) Kravchenko-Levitan weight functions ($r = 0$, $\Delta = 0, 5$ s), (d) their LAFC for $M = 1$ (dotted line), $M = 2$ (dot-dash line), $M = 3$ (solid line).
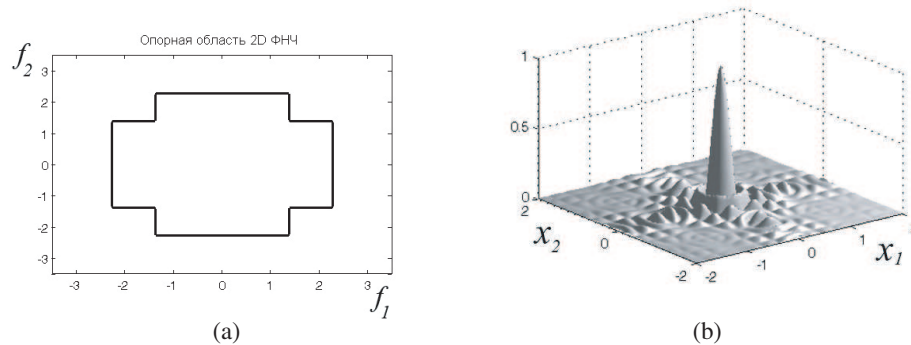
Figure 3: Support area (pass-area) (a) and function $\varphi(x, y)$ (b).

and Kravchenko-Levitan (KL)

$$w_{KL}(t) = \prod_{j=1}^{M} \left(\mathrm{sinc} \left(\frac{\pi}{\Delta 2^{j-1}} t \right) \right)^{2r+2} \tag{6}$$

kernels. Their plots are presented on Figure 5. For rectangular area it is $\varphi_{rect}(x, y) = w(x; \Delta_x) w(y; \Delta_y)$. For ellipse area we will write down so $\varphi_{\mathrm{ellipse}}(x, y) = w \left(\sqrt{(x/a)^2 + (y/b)^2} \right)$. Here $a = a(\Delta_x)$, $b = b(\Delta_y)$ are ellipse semiaxes.

3. TWO-DIMENSIONAL KRAVCHENKO KERNELS WITH SUPPORT AREA OF COMPLEX SHAPE

For construction of 2D functions with any geometry of pass-area of the spectrum we will take advantage of the theory of R-functions [4, 5]. The constructing of function $\varphi(x, y)$ is the following:

1. The spectral characteristics pass-areas which is described by function $\omega(f_1, f_2)$ such $\omega(f_1, f_2) \geq 0$, $f_1, f_2 \in \Omega$ (see the Figure 1).

2. The ideal frequency characteristic of the low-pass filter is defined so

$$H(f_1, f_2) = \begin{cases} 1, & \omega(f_1, f_2) \subset \Omega_y, \\ g(f_1, f_2), & \omega(f_1, f_2) \not\subset \Omega_y, \\ 0, & \omega(f_1, f_2) < 0. \end{cases} \tag{7}$$

   Here, the function $g(f_1, f_2)$ is choosing out so that to provide the greatest smoothness.

3. The function $\varphi(x, y)$ is calculated so

$$\varphi(x, y) = \frac{1}{4\pi^2} \int_{-\pi}^{\pi} \int_{-\pi}^{\pi} H(f_1, f_2) e^{j(f_1 x + f_2 y)} df_1 df_2. \tag{8}$$
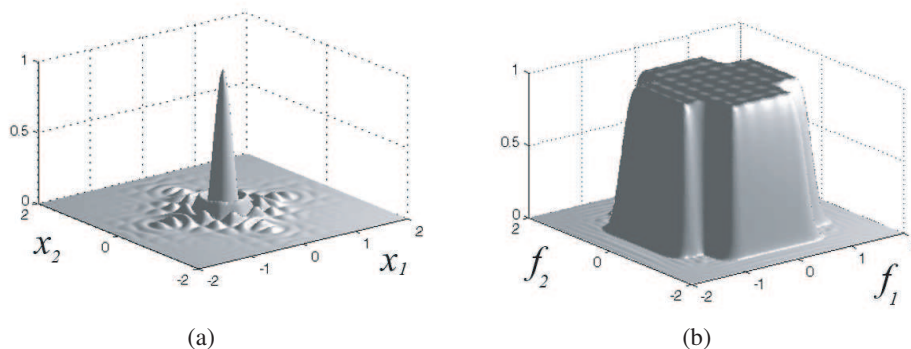
Figure 4: Function $\tilde{\varphi}(x, y)$ (a) and its spectra (b).
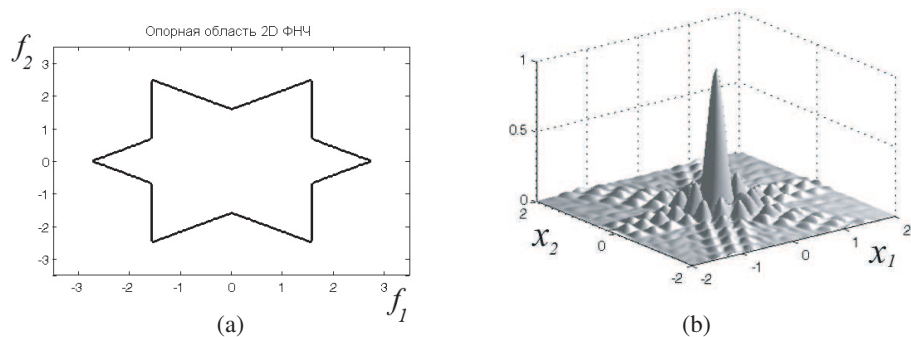
Figure 5: Support area (pass-area) (a) and function $\varphi(x, y)$ (b).

4. For convergence improvement of the series the coefficients $\varphi(x, y)$ are multiplied on finite 2D weight function (WF) $w(x, y)$: $\tilde{\varphi}(x, y) = w(x, y)\varphi(x, y)$. Weight function $w(x, x)$ defined so $w(x, y) = w_1(1 - \omega_{WF}(x, y))$ where $w_1(x)$ is a one-dimensional prototype [4] and $\omega_{WF}(x, y)$ is support area for 2D WF.

(a) (b)
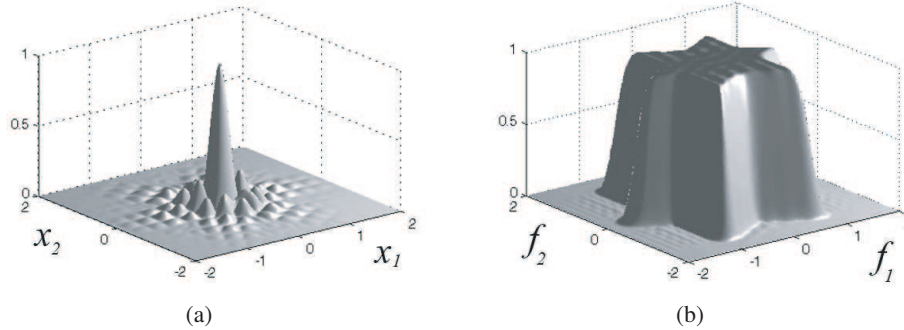
Figure 6: Function $\tilde{\varphi}(x, y)$ (a) and its spectra (b).

4. CONCLUSIONS

The numerical experiment carried out and also an analysis of physical results show potential opportunities arising from application of the suggested and proved new Kravchenko-Kotel'nikov-Levitan sampling Theorems for various problems of radio physics.

ACKNOWLEDGMENT

REFERENCES

1. Kravchenko, V. F., editor, *Digital Signal and Image Processing in Radio Physical Applications*, Fizmatlit, Moscow, 2007 (in Russian).
2. Dudgeon D. E. and R. M. Mersereau, *Multidimensional Digital Signal Processing*, Prentice-Hall, Inc, Englewood Cliffs, 1984.
3. Shirman, J. D., editor, *Radioelectronic Systems Constructing Basis and Theory Handbook*, by Publishing House Radio Engineering, Moscow, 2007 (in Russian).
4. Kravchenko, V. F., *Lectures on the Theory of Atomic Functions and Their Some Applications*, Publishing House Radio Engineering, Moscow, 2003 (in Russian).
5. Kravchenko, V. F. and V. L. Rvachov, *Boolean Algebra, Atomic Functions and Wavelets in Physical Applications*, Fizmatlit, Moscow, 2006 (in Russian).
6. Kravchenko, V. F., D. V. Churikov, and A. V. Yurin, "The analytical description of complex shape locus by means of R-operations and atomic functions. Digital signal and image processing," *Successes of Modern Radio Electronics*, No. 5, 3–64, 2008 (in Russian).
7. Kravchenko, V. F. and D. V. Churikov, "Atomic and R-functions in the synthesis of two-dimensional fir filters," *Proceedings of 11th International Conference and exhibition on Digital Signal Processing and Its Applications*, Vol. 1, 141–144, Moscow, Russia, March 25–27, 2009 (in Russian).
8. Kravchenko, V. F., O. S. Labun'ko, A. M. Lerer, and G. P. Sinyavsky, *Computing Methods in the Modern Radio Physics*, edited by V. F. Kravchenko, Fizmatlit, Moscow, 2009 (in Russian).

Application of the Theory of R-functions to the Analysis and Synthesis of Multidimensional Signals

D. V. Churikov

Kotel'nikov Institute of Radio Engineering and Electronics of RAS, Moscow, Russian Federation

Abstract— In this report application of the theory of R-functions for construction of two-dimensional digital filters is considered. It is known that two-dimensional digital filters are synthesized in time or frequency space on some support areas which geometry has significant importance. The form of support area influences physical characteristics of two-dimensional digital filter. Known methods allow to synthesize two-dimensional digital filters only on the elementary support areas. Theory of R-functions (Rvachev functions) allows to describe at analytical level the equation of support area of the complex shape. As the examples the problems of noise reduction and spectral properties improvement of images are submitted. The numerical experiment and physical analysis of two-dimensional signal processing results are show efficiency of new two-dimensional digital filters.

1. INTRODUCTION

Synthesis of two-dimensional (2D) digital filters (DF) with various geometries of support area is actual in many applied areas of physics and techniques. First of all it concerns a radar-location, communication, transfers of the digital information. Thus, special attention by developers of equipment is given to spectral properties of these devices. It is known [1–3] that the most widespread forms of support areas are following: round, rectangular and hexagonal. In connection with active development of computer facilities and specialized processors there is an interest to synthesis of filters with difficult geometry of support area. The purpose of the given work is development, substantiation and application of the theory of R-functions (Rvachev functions) [4–7] to considered problems.

2. TWO-DIMENSIONAL DIGITAL FILTERS WITH THE FINITE IMPULSE RESPONSE

For synthesis of two-dimensional (2D) digital filters (DF) with the finite impulse response (FIR) the special attention is given to their spectral and constructive properties [1–4]. Filters with round, rectangular or hexagonal form of pass-band in frequency space [2, 3] (see Figures 1(a), (b), (c) are usually synthesized.
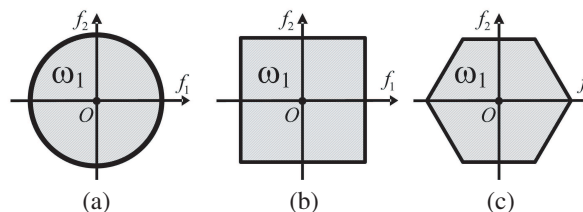
Figure 1: Examples of simple areas: round (a), rectangular (b) and hexagonal (c).

The example of difficult geometry of support area is shown on Figure 2(a). This area can be realized as superposition of simple ones (see Figure 2(b)).

The impulse responses (IR) of each of simple areas are known $h_1(f_1, f_2)$ and $h_2(f_1, f_2)$. We will notice that circumstance that in a place of interface spectral component their mutual imposing necessary to consider (area ω_E on Figure 2(b)) which leads to discrepancies of demanded IR calculation. The theory of R-functions [5] allows at analytical level without approximations to describe geometry of difficult pass-area of the ideal filter.

3. ALGORITHM OF TWO-DIMENSIONAL DIGITAL FIR FILTER SYNTHESIS

The algorithm of construction of 2D FIR filter with spectral characteristics pass-areas of complex shape [2] consists of following stages.
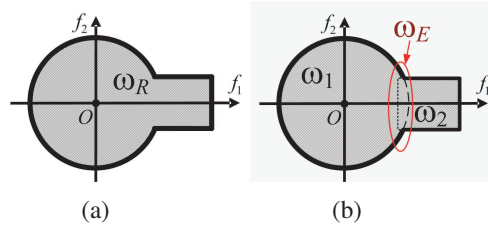
Figure 2: Geometry of complex shape (a) and its approximation in the form of a combination of two simple (b).

1. The spectral characteristics pass-areas which is described by function $\omega(f_1, f_2)$ such that $\omega(f_1, f_2) \geq 0$, $f_1, f_2 \in \Omega$ (Ω is filter pass-area).

2. The ideal frequency characteristic of the low-pass filter is defined so

$$H_0(f_1, f_2) = \begin{cases} 1, & \omega(f_1, f_2) \geq 0, \\ 0, & \omega(f_1, f_2) < 0. \end{cases} \tag{1}$$

3. The impulse response of ideal filter calculated so $h_0(x_1, x_2) = \frac{1}{4\pi^2} \int\limits_{-\pi}^{\pi} \int\limits_{-\pi}^{\pi} H_0(f_1, f_2) e^{j(f_1 x_1 + f_2 x_2)}$ $df_1 df_2$. For realization of 2D FIR-filter their IR should be finite. It leads to deterioration of convergence [1–5]. In this case characteristics of synthesized filters depend on choice of WF.

4. For convergence improvement of the series the coefficients $h_0(x_1, x_2)$ are multiplied on finite 2D WF $w(x_1, x_2)$: $h(x_1, x_2) = w(x_1, x_2) h_0(x_1, x_2)$. WF $w(x_1, x_2)$ defined so $w(x_1, x_2) = w_1(1 - \omega_{WF}(x_1, x_2))$, where $w_1(x)$ is a one-dimensional prototype [4] and $\omega_{WF}(x_1, x_2)$ is support area for 2D WF.

4. NUMERICAL REALISATION OF ALGORITHM AND THE PHYSICAL RESULTS ANALYSIS

As WF we will consider the following [4]: $w_1(x) = \text{fup}_2(2x)/\text{fup}_2(0)$, $w_2(x) = h_{3/2}(x)$, Hemming. For analysis of the synthesised filters we will use the modified physical characteristics [1, 7]. Position of the first zero and width on level $-6\,\text{dB}$ are normalized. We realize FIR-filter with the support area represented on Figure 2(a). As the WF we will choose $w_1(x) = \text{fup}_2(2x)/\text{fup}_2(0)$ [1]. Here the $\omega_{WF}(x_1, x_2)$ is represents conical surface forming a circle of radius R_{WF} at crossing with a plane $x_1 0 x_2$. By changing of R_{WF} we will vary smoothness rate of frequency response of synthesized filter and time-localization of its IR. The IR of filter realized by means of R-functions [1, 2], frequency response and their equiscalar lines are represented on Figure 3.

In Table 1, the average values of physical characteristics of the given and synthesized filters for sections by planes $f_1 = 0$, $f_2 = 0$, $f_1 = f_2$, $f_1 = -f_2$ are presented. The quality estimation was spent by the analysis of change of physical characteristics of the synthesized filters in relation to the given ones

$$b_k = 100\% \cdot (\gamma_k^* - \gamma_k)/\gamma_k^*, \tag{2}$$

where γ_k^* is given characteristics. In Table 2, the following physical characteristics are resulted: relative change of position of the first zero; width on the level $-3\,\text{dB}$; relative change of width on level $-6\,\text{dB}$; peak sidelobe; an energy share going on signal overamplification

$$P = 100\% \cdot \frac{\sum\limits_{\forall f_1, f_2: |H(f_1, f_2)| > 1} |H(f_1, f_2)| - 1}{\sum |H(f_1, f_2)|}. \tag{3}$$

Relative change of a constant of uncertainty on time

$$D_t^* = 100\% \cdot (D_t^* - D_t)/D_t^* \tag{4}$$

(characterizes improvement of the time permission).
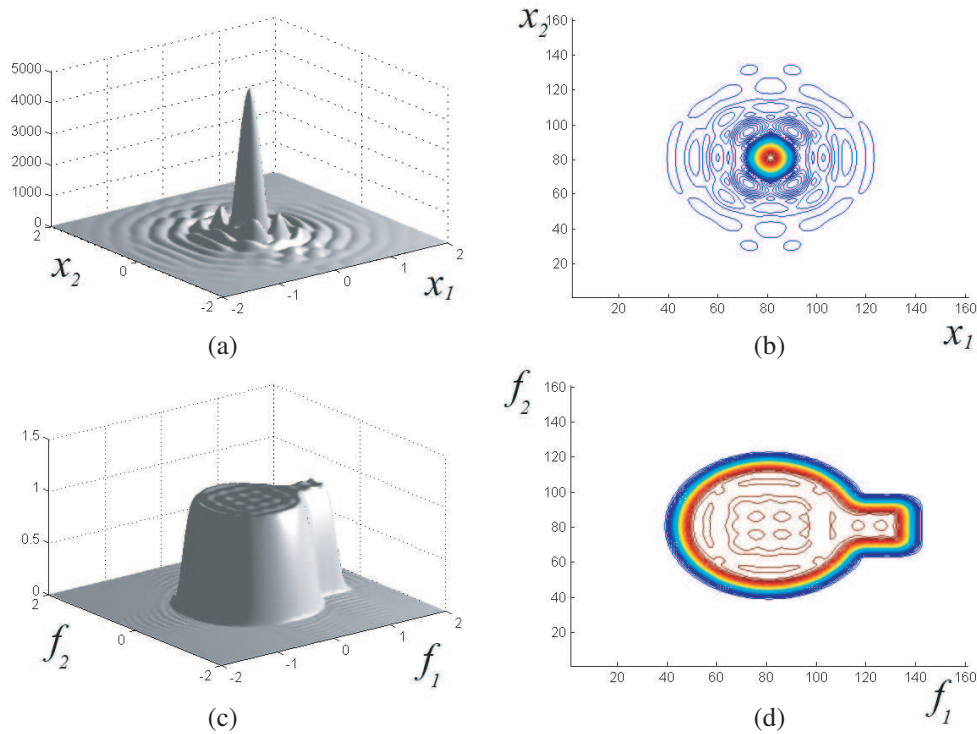
Figure 3: Impulse response (a), frequency response (c) and their equiscalar lines (b, d) of FIR-filter realized by means of R-functions.

Table 1: Physical characteristics of given and the synthesized filters.

Impulse response	R_{WF}	γ_2	γ_3	γ_4	γ_9	γ_7	D_t	γ_8	γ_{10}	γ_{11}
Given filter	6		0,444		–	0,065	0,806	5,921	0,514	8,205
$h_{12}(f_1, f_2)$	6	0,569	0,444	0,475	−54,37	0,052	0,724	7,210	0,190	**8,730**
$h_R(f_1, f_2)$	6	0,569	0,444	0,475	**−55,19**	0,051	**0,721**	7,303	0,182	8,769
Given filter	8		0,444		–	0,065	0,806	5,921	0,514	8,205
$h_{12}(f_1, f_2)$	8	**0,522**	0,444	0,469	−46,01	0,055	0,752	6,745	0,273	**8,525**
$h_R(f_1, f_2)$	8	0,528	0,444	0,469	**−47,00**	0,054	**0,747**	6,847	0,259	8,569
Given filter	10		0,444		–	0,065	0,806	5,921	0,514	8,205
$h_{12}(f_1, f_2)$	10	0,519	0,444	0,463	−39,11	0,057	0,769	6,466	0,339	**8,409**
$h_R(f_1, f_2)$	10	0,519	0,444	0,463	**−39,84**	0,056	**0,764**	6,572	0,321	8,454

Table 2: Comparison of physical characteristics of given and the synthesized filters.

Impulse response	R_{WF}	$b_2, \%$	$b_4, \%$	γ_9, dB	$P, \%$	$D_t^*, \%$
$h_{12}(f_1, f_2)$	6	−22,973	−7,042	−54,371	1,756	20,436
$h_R(f_1, f_2)$	6	−22,973	−7,042	**−55,195**	**0,054**	**21,031**
$h_{12}(f_1, f_2)$	8	**−12,838**	−5,634	−46,016	2,080	15,333
$h_R(f_1, f_2)$	8	−14,189	−5,634	**−47,003**	**0,132**	**16,372**
$h_{12}(f_1, f_2)$	10	−12,162	−4,225	−39,110	2,451	11,339
$h_R(f_1, f_2)$	10	−12,162	−4,225	**−39,839**	**0,350**	**12,812**

5. CONCLUSIONS

The universal algorithm the allowing to project the synthesized digital filters with support area of complex shape is offered and proved. It is based on constructive properties of the theory of R-functions (V. L. Rvachev functions). Filters with support area of complex shape can find wide application in problems of recognition, coding and a filtration of signals of the various physical nature. Results of work are reported at 11th international conference and an exhibition "Digital signals processing and its applications" [7].

ACKNOWLEDGMENT

REFERENCES

1. Kravchenko, V. F., editor, *Digital Signal and Image Processing in Radio Physical Applications*, Fizmatlit, Moscow, 2007 (in Russian).
2. Dudgeon, D. E. and R. M. Mersereau, *Multidimensional Digital Signal Processing*, Prentice-Hall, Inc., 1984.
3. Shirman, J. D., editor, *Radioelectronic Systems Constructing Basis and Theory Handbook*, Publishing House Radio Engineering, Moscow, 2007 (in Russian).
4. Kravchenko, V. F., *Lectures on the Theory of Atomic Functions and Their Some Applications*, Publishing House Radio Engineering, Moscow, 2003 (in Russian).
5. Kravchenko, V. F. and V. L. Rvachev, *Boolean Algebra, Atomic Functions and Wavelets in Physical Applications*, Fizmatlit, Moscow, 2006.
6. Kravchenko, V. F., D. V. Churikov, and A. V. Yurin, "The analytical description of complex shape locus by means of R-operations and atomic functions. Digital signal and image processing," *Successes of Modern Radio Electronics*, No. 5, 3–64, 2008 (in Russian).
7. Kravchenko, V. F. and D. V. Churikov, "Atomic and R-functions in the synthesis of two-dimensional fir filters," *Proceedings of 11th International Conference and exhibition on Digital Signal Processing and Its Applications*, Vol. 1, 141–144, Moscow, Russia, March 25–27, 2009 (in Russian).

An Application Generalized Kravchenko-Kotel'nikov Theorem on Atomic Functions $fup_N(t)$ to Interpolation Nonstationary Random Processes

O. V. Kravchenko[1] and A. R. Safin[2]

[1]Bauman Moscow State Technical University, Russian Federarion
[2]Kotel'nikov Institute of Radio Engineering and Electronics of RAS, Russian Federation

Abstract— In this paper considered a generalized Kravchenko-Kotel'nikov theorem application based on atomic functions $fup_N(t)$ [1–4] for interpolation of nonstationary random processes in multichannel communications.

1. INTRODUCTION

Analog-digit convertor systems (ADC) which used on practice are constructed with principles puls-code modulations (PCM). They include 2 basic blocks [5] digitizer and quantizer on Figure 1 are shown. Quantization result is binary number of quantization interval which includes analog signal sample. Obtained code is arrived in communication for transfer. Besides digitizer and quantizer scheme ADC contain also prefilter and range another elemets. On receiving end are used devises which realized converse operations. After code reception its transformation into voltage is became.

Difference estimate between the samples supported given error with descretization on time is evaluated with Whittaker-Kotel'nikov-Shannon (WKS) [4] theorem help. In practice applications desired signal is passed with disturbance (noise) therefore it is necessary to account discretization and quantization of random signal.
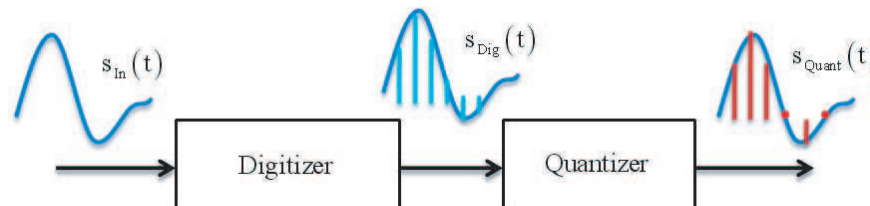
Figure 1: Digitizer and quantizer scheme.

2. SOME INFORMATION ABOUT RANDOM PROCESSES THEORY

Bring basic definitions [8] from random processes theory which will be useful for discretization.

Definition 1. A random process is called analytical in some area if nearly every all its realizations accepted analytic continuation in this area.

Definition 2. A random process $\xi(t)$ is called a random process with finite spectrum on $\left(-\omega_{\hat{A}}, \omega_{\hat{A}}\right)$ if its covariance $B(\tau) = M\overline{\xi(t+\tau)\xi(t)}$ is represented in such form

$$B(\tau) = \frac{1}{2\pi} \int\limits_{-\omega_{Up}}^{\omega_{Up}} e^{i\omega\tau} dF(\omega)$$

where $F(\omega)$ is monotonic function of bounded variation, i.e., value $B(0) = M|\xi(t)|^2$ is limited.

3. RANDOM PROCESSES SAMPLING INTERPOLATION

In multichannel communications (Figure 3) signals $a_i(t)$ are included desire signals and disturbances of different origins. Therefore apply Kravchenko-Kotel'nikov theorem to random processes interpolation.

State the following proposition [5].

Proposition. If covariance of random stationary process $B(\tau)$ is integer function of finite power less or equal β then nearly every sample functions are integer functions of finite power less or equal β. (If $\xi(t)$ is random process then $B(\tau) = M\xi(t+\tau)\xi(t)$).

State the following theorem.

Theorem. If $\xi(t), t \in \mathbb{R}$ is stationary random process with finite spectrum on $(-\beta, \beta)$ then for nearly all sampling functions (realizations) $x(t)$ is true

$$x(t) = \sum_{k \in \mathbb{Z}} x(k\Delta) \operatorname{sinc}^N \left(\frac{\alpha(t - k\Delta)}{2} \right) \prod_{j=1}^{\infty} \operatorname{sinc} \left(\frac{\alpha(t - k\Delta)}{2^{j-1}} \right). \tag{1}$$

Thus, in this paper a different applications of formula (1) are considered in radio physics applications with random processes discretization.

ACKNOWLEDGMENT

REFERENCES

1. Kravchenko, V. F., *Lectures on the Theory of Atomic Functions and Their Some Applications*, Publishing House Radio Engineering, Moscow, 2003 (in Russian).
2. Kravchenko, V. F., *Digital Signal and Image Processing in Radio Physical Applications*, Fizmatlit, Moscow, 2007 (in Russian).
3. Zelkin, E. G., V. F. Kravchenko, and V. I. Gusevskiy, *Constructive Methods of Approximation in Theory of Antennas,* Science-Press, Moscow, 2005 (in Russian).
4. Kravchenko, V. F. and A. R. Safin, "Atomic functions and N-dimensional generalized Whittaker-Kotel'nikov-Shannon," *Electromagnetic Waves and Electronic Systems*, Vol. 13, No. 12, 31–44, 2008.
5. Pilipchuk, N. I. and V. P. Yakovlev, *Adaptive Puls-Code Modulation*, Radio i Svyaz, Moscow, 1986.
6. Hurgin, Y. I. and V. P. Yakovlev, *Finite Functions in Physic and Technique*, Nauka, Moscow, 1971.

Construction of New Kravchenko-Kotel'nikov-Chebyshev-Legendre Spectral Kernels and Their Application in Digital Multidimensional Signals Processing

D. V. Churikov

Kotel'nikov Institute of Radio Engineering and Electronics of RAS, Russian Federation

Abstract— In this report the new approach based on combination of Kravchenko-Kotel'nikov weight functions (WF) (windows) with Chebyshev and Legendre polynomials as spectral kernels is proposed. Shown that obtained structures have some advantages in comparison with spectral wave analysis of multidimensional signals. The new approach based on application of spectral kernels to problems of digital signal processing is considered. The physical characteristics and analysis of numerical experiment confirm efficiency of new spectral kernels and also WA-systems on their basis in tasks of spectral estimation and digital multidimensional signal processing.

1. INTRODUCTION

Application of the spectral analysis of signals in basis of digital functions in comparison with the spectral harmonious offers certain advantages which are defined by the physical nature of representation of signals [1–6]. Signals can be set in the form of some linear combination [2]

$$s(x) = \sum_{k=0}^{N-1} C(k)\,\varphi(k, x), \tag{1}$$

where $\varphi(k, x)$ is elementary function of number k, N is quantity of the functions used in decomposition. At approximation the generalized Fourier transformation of a kind

$$C(k) = \int_0^T s(x)\,\varphi(k, x)\,dt \tag{2}$$

provides the minimum value of mean-square error. Thus, there is a signal decomposition on some basis which in many problems of digital signal processing can not be orthogonal. The work purpose consisted in showing advantages of the new combined designs of Kravchenko-Chebyshev-Legendre based on classical Chebyshev and Legendre polynomials and also atomic functions (AF) [1–8].

2. THE MODIFIED CHEBYSHEV AND LEGENDRE POLYNOMIALS

Classical orthogonal polynomials are defined as follows [1].

1. Chebyshev polynomials of the first type $\tilde{w}_{CH1}(x) = T_n(x)$ are defined by means of a recurrent parity:

$$T_0(x) = 1, \quad T_1(x) = x, \quad T_{n+1}(x) = 2xT_n(x) - T_{n-1}(x). \tag{3}$$

2. Chebyshev polynomials of the second type $\tilde{w}_{CH2}(x) = U_n(x)$ can be received by means of a following recurrent parity:

$$U_0(x) = 1, \quad U_1(x) = 2x, \quad U_{n+1}(x) = 2xU_n(x) - U_{n-1}(x). \tag{4}$$

3. Legendre polynomials are defined under the formula of Rodriga

$$P_n(x) = \frac{1}{2^n n!} \frac{d^n}{dx^n} \left(x^2 - 1\right)^n, \tag{5}$$

or by means of recurrent dependence

$$P_0(x) = 1, \quad P_1(x) = x, \quad P_{n+1}(x) = \frac{2n+1}{n+1} x P_n(x) - \frac{n}{n+1} P_{n-1}(x) \tag{6}$$

For their use as spectral kernels we will spend modification so that function on the interval ends was equal to zero and at zero value of argument was equal to unit, i.e., $w(-1) = w(1) = 0$, $w(0) = 1$. Four cases are possible: 1) $\tilde{w}(-1) = \tilde{w}(1) \neq 0$, $\tilde{w}(0) \neq \tilde{w}(1)$; 2)$\tilde{w}(-1) = \tilde{w}(1) = 0$, $\tilde{w}(0) \neq \tilde{w}(1)$; 3) $\tilde{w}(-1) = \tilde{w}(1) \neq 0$, $\tilde{w}(0) = \tilde{w}(1)$; 4) $\tilde{w}(-1) \neq \tilde{w}(1)$. For condition normalizing performance we will choose only functions of 1st and 2nd types. Then for functions of the first type we will spend transformation $w^*(x) = 1 - \tilde{w}(x)/\tilde{w}(-1)$, and then for functions of both types normalizing $w(x) = w^*(x)/w^*(0)$. Corresponding plots are resulted on Figures 1–3 and physical characteristics in Table 1.

3. CONSTRUCTING OF KRAVCHENKO-KOTEL'NIKOV-CHEBYSHEV-LEGENDRE KERNELS

New spectral kernels on the basis of orthogonal polynomials we will receive by means of operation of direct product with the Kravchenko-Kotel'nikov functions based on AF [3–6].

Kravchenko-Kotel'nikov kernels [5] are defined so

$$w_{KK}(x) = \prod_{j=1}^{M} \text{sinc}\left(\frac{\pi}{\Delta a^{j-1}}x\right). \tag{7}$$

Its behaviour is influenced by three following parametres: M, a, Δ.
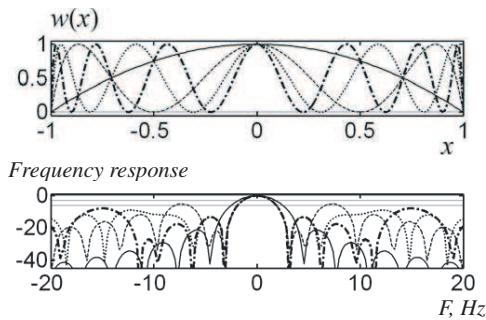
Figure 1: Plots of the normalizing Chebyshev polynomials of the first type $w_{CH1}(x)$ for various even n (continuous — 2, shaped — 6, dotted — 10, shaped-dotted — 14) and their frequency responses.
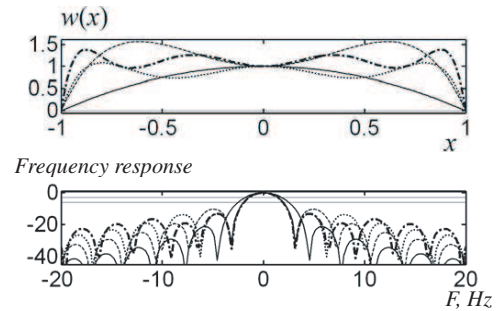
Figure 2: Plots of the normalizing Chebyshev polynomials of the second type $w_{CH2}(x)$ for various even n (continuous — 2, shaped — 4, dotted — 6, shaped-dotted — 8) and their frequency responses.

Table 1: Physical characteristics of normalizing Chebyshev and Legendre polynomials.

function	n	γ_2	γ_3	γ_4	γ_7^*	γ_8	γ_9	γ_{10}	γ_{11}
$w_{CH1}(x)$	2	**2,500**	**1**	**2,382**	**0,375**	**1,206**	**−21,298**	**2,202**	**3,015**
	6	2,444	1	1,787	0,486	1,477	−5,081	4,146	5,839
	10	2,333	1	1,787	0,495	1,499	−8,996	3,965	5,722
	14	2,333	1	1,787	0,498	1,506	−7,949	3,911	5,690
$W_{CH2}(x)$	2	**2,500**	**1**	**2,382**	**0,375**	**1,206**	**−21,298**	**2,202**	**3,015**
	4	**2,444**	**1**	**1,936**	**0,208**	**1,081**	**−10,362**	**3,505**	**3,844**
	6	**2,444**	**1**	**1,936**	**0,292**	**1,047**	**−13,471**	**3,692**	**3,890**
	8	**2,333**	**1**	**1,787**	**0,225**	**1,032**	**−13,215**	**3,768**	**3,903**
$w_L(x)$	2	**2,500**	**1**	**2,382**	**0,375**	**1,206**	**−21,298**	**2,202**	**3,015**
	4	2,250	1	1,638	0,088	1,216	−6,090	4,580	5,430
	6	2,444	1	1,787	0,405	1,209	−7,993	3,948	4,771
	8	2,333	1	1,787	0,094	1,204	−10,237	3,915	4,723

4. NUMERICAL EXPERIMENT

Consider following combinations of functions: $w_{KK}(x)w_{CH1}(x)$, $w_{KK}(x)w_{CH2}(x)$, $w_{KK}(x)w_L(x)$. Their plots for different n (continuous — 2, shaped — 4, dotted — 6, shaped-dotted — 8) are resulted on Figures 4–6, and physical characteristics in Table 2.
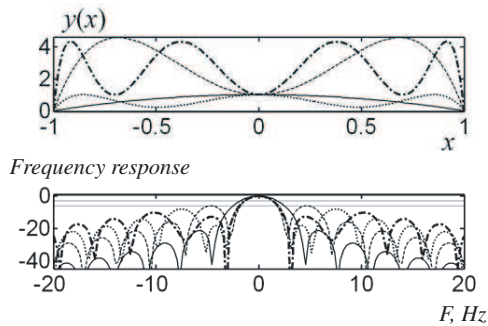
Figure 3: Plots of the normalizing Legendre polynomials $w_L(x)$ for various even n (continuous — 2, shaped — 4, dotted — 6, shaped-dotted — 8) and their frequency responses.
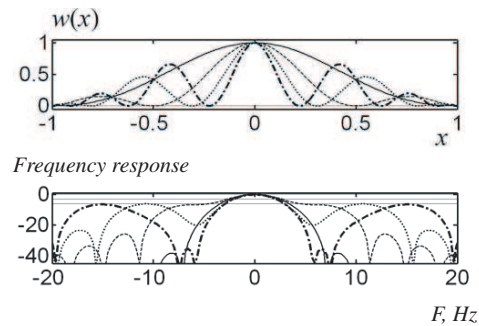
Figure 4: Plots of $w_{KK}(x)w_{CH1}(x)$ for different n (continuous — 2, shaped — 6, dotted — 10, shaped-dotted — 14) and their frequency responses.
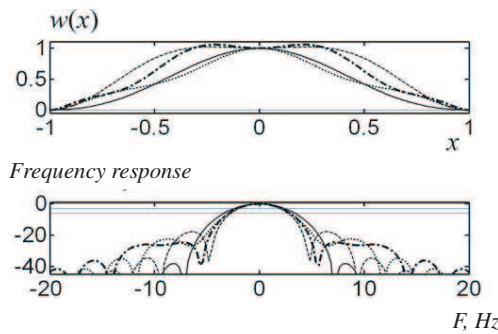
Figure 5: Plots of $w_{KK}(x)w_{CH2}(x)$ for different n (continuous — 2, shaped — 4, dotted — 6, shaped -dotted — 8) and their frequency responses.
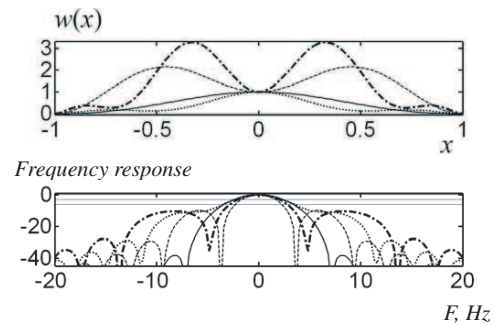
Figure 6: Plots of $w_{KK}(x)w_L(x)$ for different n and their frequency responses.

Table 2: Physical characteristics of spectral functions ($M = 3$, $a = 2$, $\Delta = 1$).

Kernels	n	γ_2	γ_3	γ_4	γ_7^*	γ_8	γ_9	γ_{10}	γ_{11}
$w_{KK}(x)w_{CH1}(x)$	2	3,000	1	3,276	0,546	1,619	$-38,100$	1,233	3,324
	2	3,000	1	3,276	0,546	1,619	$-38,100$	1,233	3,324
$w_{KK}(x)w_{CH2}(x)$	4	2,462	1	2,680	0,374	1,318	$-17,930$	1,855	3,053
	6	3,143	1	2,829	0,527	1,428	$-22,495$	1,631	3,180
	8	2,846	1	2,829	0,411	1,397	$-24,670$	1,660	3,113
	2	3,000	1	3,276	0,546	1,619	$-38,100$	1,233	3,324
$w_{KK}(x)w_L(x)$	4	2,273	1	2,233	0,191	1,264	$-9,813$	2,572	3,590
	6	5,133	1	3,424	0,739	1,848	$-28,744$	1,331	3,999
	8	2,462	1	2,680	0,174	1,610	$-10,331$	1,718	3,786

5. CONCLUSIONS

New combinations of spectral functions, which based on AF and also orthogonal Chebyshev and Legendre polynomials. New designs of functions were used with reference to time-and-frequency

digital processing signals in a class of transformations of Cohen. Numerical experiment and also the physical analysis of results confirm efficiency of new spectral functions of Kravchenko-Kotel'nikov-Chebyshev-Legendre in problems of spectral estimation and a filtration of multidimensional digital signals.

ACKNOWLEDGMENT

REFERENCES

1. Dzyadyk, V. K., *Introduction to the Theory of Uniform Approximation of Functions by Polynomials*, Nauka, Moscow, 1977 (in Russian).
2. Kravchenko, V. F., *Lectures on the Theory of Atomic Functions and Their Some Applications*, Publishing House Radio Engineering, Moscow, 2003 (in Russian).
3. Kravchenko, V. F. and V. L. Rvachov, *Boolean Algebra, Atomic Functions and Wavelets in Physical Applications*, Fizmatlit, Moscow, 2006 (in Russian).
4. Kravchenko, V. F., editor, *Digital Signal and Image Processing in Radio Physical Applications*, Fizmatlit, Moscow, 2007 (in Russian).
5. Volosyuk, V. K. and V. F. Kravchenko, *Statistical Theory of Radio Technical Systems of Remote Sensing and Radar*, Fizmatlit, Moscow, 2008 (in Russian).
6. Kravchenko, V. F. and D. V. Churikov, "Kravchenko-Kotelnikov-Levitan-Wigner distributions in radio physical applications," *Proc. Int. Conference "DAYS on DIFFRACTION"*, 79–84, St. Petersburg, Russia, June 3–6, 2008.
7. Kravchenko, V. F. and D. V. Churikov, "Analytic wavelets Kravchenko-Kotelnikov and Kravchenko-Levitan in the digital UWB signal processing," *Successes of Modern Radio Electronics*, No. 8, 3–33, 200 (in Russian).
8. Kravchenko, V. F., O. S. Labun'ko, A. M. Lerer, and G. P. Sinyavsky, *Computing Methods in the Modern Radio Physics*, Edited by V. F. Kravchenko, Fizmatlit, Moscow, 2009 (in Russian).

Short Range Radar with MIMO Antenna System and Multifrequency Sounding Signal

V. V. Chapursky, **S. I. Ivashov**, **I. A. Vasiliev**, and **A. V. Zhuravlev**

Bauman Moscow State Technical University, Russia

Abstract— Algorithms of slow moving objects allocation on a background of motionless local objects reflections in MIMO radar with radiation of orthogonal signals by transmitting elements of the multielement antenna system are offered. Results of laboratory experiments with created breadboard model of MIMO small range radar with eight-elements transmitting and receiving linear antenna arrays at radiation of sounding signals with step frequency modulation are given.

1. INTRODUCTION

The radar of MIMO (Multiple Input-Multiple Output) type [1] assumes the use of transmitting and receiving antenna systems (AS) consisting of spatially distributed elements, radiating mutually orthogonal sounding signals (SS). One of the first radars of the given class is French long range system RIAS [2]. Similar radars are studied also in Russia and China [3–5]. Application of MIMO radar principles is perspective also at creation of short range radars for detection of people behind radiotransparent obstacles since allows to apply energetically more favorable continuous multifrequency SS. At continuous radiation and the greater number of MIMO AS elements the greater signal accumulation takes place. The low level of side lobe of system signal function (SSF) on spatial coordinates is reached also. Such approach does not demand the application of a complex antenna element phase control system and allows to make the space surveillance in digital vector signals processing system fed from outputs of simple receiving elements of AS.

In the given work, some questions of the spatial resolution theory of MIMO radars are considered and breadboard model of small range MIMO radar with AS consisting of eight-element transmitting and eight-element receiving linear antenna arrays at radiation of step-frequency SS in frequency range from 1.45 GHz up to 1.75 GHz is created. Simple methods of allocation of slow moving objects on the background of motionless local objects (LO) without speed resolution are offered and checked up. Operational processing algorithms of receiving signals are developed in view of systematic errors in the microwave signal path and in MIMO AS. Results of laboratory experiments with detection of slowly moving object as a metal plate on a background of reflections from indoor LO and a penetrating signal of the transmitter are received.

2. FUNDAMENTALS OF MIMO RADAR RESOLUTION THEORY

Let AS consists of $N_t + 1$ transmitting and $N_r + 1$ receiving elements. At consecutive radiation and reception of step-frequency modulated (step-FM) SS each n_t element of transmitting antenna array radiates, and each n_r element of receiving antenna array accepts a signal consisting from $M + 1$ frequency components from the general frequency grid with uniform step $\Delta\omega = 2\pi\Delta f$,

$$\omega_m = \omega_0 + m \cdot \Delta\omega, \quad m = 0, \dots, M. \tag{1}$$

The duration of everyone frequency step is equal to $\tau_\omega = T_\omega - \tau_{\max}$, where T_ω is the time interval of reference signal existence on the same frequency in the receiver device, and $\tau_{\max} = 2R_{\max}/c$, where $R_{\max}$ is equal to the maximum (unique) radar range, c is the velocity of light.

Element pairs "n_t-n_r" work in a time division mode, and a full time working interval of the entire AS will make size

$$T_\Sigma = (N_t + 1)(N_r + 1)(M + 1)T_\omega. \tag{2}$$

The value of T_Σ was accepted equal to the radiation time period (or the information updating period), $T_r = T_\Sigma$. If all step-FM bursts of SS are not overlapped in time, the value $N_\Sigma = (N_t + 1)(N_r + 1)(M + 1)$ is equal to the total amount of orthogonal signals in the system. The average level of side lobes of the generalized ambiguity function (GAF) on spatial coordinates of MIMO radar system is estimated by value $1/\sqrt{N_\Sigma}$, but the width of GAF main lobe assesses resolution cell on spatial coordinates.

For a configuration and parameters choice of MIMO AS quantitative analysis of GAF in a horizontal coordinate's plane (x, y) at an arrangement of AS elements in a vertical plane was carried out. Formula received for GAF in [6] was used:

$$\Psi(\vec{r}_R, \vec{r}_M) = \frac{1}{(N_t + 1)(N_r + 1)(M + 1)} \left| \sum_{n_t=0}^{N_t} \sum_{n_r=0}^{N_r} \frac{\sin[\pi \Delta f (M + 1) \cdot \Delta\tau(\vec{r}_M, \vec{r}_R; n_t, n_r)]}{\sin[\pi \Delta f \cdot \Delta\tau(\vec{r}_M, \vec{r}_R; n_t, n_r)]} \right.$$
$$\left. \times \exp\{j2\pi[f_0 + \Delta f M/2]\Delta\tau(\vec{r}_M, \vec{r}_R; n_t, n_r)\} \right|, \tag{3}$$

Relative delays $\Delta\tau(\cdot)$ are calculated here as a difference of arrival times of the received signals reflected from the target with a vector of coordinates $\vec{r}_R$ and reference signals in processing system, adequate to virtual target with a vector of coordinates $\vec{r}_M$, at working of "transmitter-receiver" elements with numbers (n_t, n_r):

$$\Delta\tau(\vec{r}_M, \vec{r}_R; n_t, n_r) = \tau(\vec{r}_M; n_t, n_r) - \tau(\vec{r}_R; n_t, n_r), \quad \text{where} \quad \tau(\vec{r}; n_t, n_r) = \tau_{tn_t}(\vec{r}) + \tau_{rn_r}(\vec{r}), \tag{4}$$

$$\text{and} \quad \tau_{tn_t}(\vec{r}) = \frac{1}{c}|\vec{r} - \vec{r}_{tn_t}|, \quad \tau_{rn_r}(\vec{r}) = \frac{1}{c}|\vec{r} - \vec{r}_{rn_r}| \tag{5}$$

are accordingly propagation delays for a way from transmitting element number n_t and coordinate vector $\vec{r}_{tn_t}$ up to a point of space with coordinate vector $\vec{r}$ and for a way from this point up to receiving element with number n_r and coordinate vector $\vec{r}_{rn_r}$.

For 2D radar objects detection and coordinate measurement in a horizontal plane (x, y), it is sufficient the arrangement of transmitting and receiving elements linearly in a plane (x, z) with constant interelement distances. Transmitting and receiving antenna arrays are parallel and vertically divided in this plane (Fig. 1). Interelement distances were different in transmitting and in receiving arrays. Optimization of transmitting and receiving arrays length was carried out at a constant number of elements $N_t + 1 = N_r + 1 = 8$ by the criterion of a minimum level of the diffraction lobes remains of GAF. GAF calculations were carried out at initial frequency and frequency bandwidth of step-FM equal accordingly to $f_0 = 1.45$ GHz, $\Delta F = 300$ KHz, and $M + 1 = 64$. The optimum sizes of transmitting and receiving antenna arrays have turned out equal $L_t = 0.918$ m and $L_r = 1.2$ m, at interelement distances in them equal to $d_t = 0.131$ m and $d_r = 0.171$ m. It is more then a half of average radiation wavelength, $\lambda_{av}/2 = 0.094$ m.

A configuration of the AS and a view of GAF are given on Figs. 1(a) and 1(b). The view of an ambiguity body testifies to low levels of lateral and diffraction lobes remains in an azimuths interval $(-90°, 90°)$. It is explained by a choice of various and not multiple steps of elements in transmitting and receiving antenna arrays.

3. SIGNAL PROCESSING ALGORITHMS IN MIMO RADAR WITH STEP-FM SS

The signal processing algorithm on a single k-th full working cycle (period) of multielement AS with radiation of step-FM signals was received on the basis of generalized covariance signals processing integral in multichannel receiving system [7] in view of all pairs of transmitting and receiving

(a)   (b)
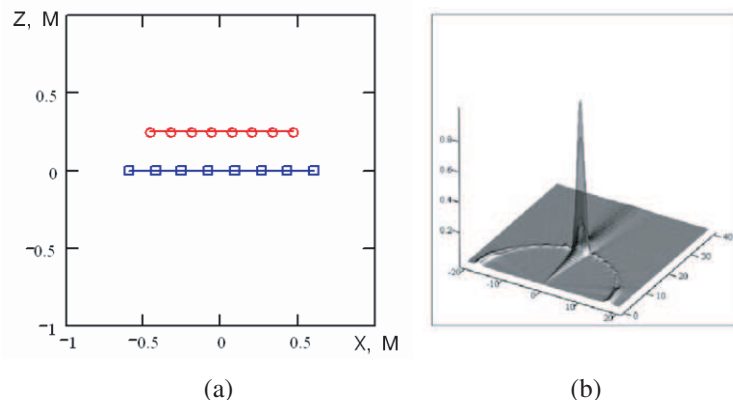
Figure 1: (a) The configuration of transmitting (top line) and receiving (bottom line) antenna arrays, (b) volumetric GAF diagram at the target coordinates $x_R = 0$ m, $y_R = 15$ m.

elements (n_t, n_r):

$$\dot{Q}_k(\vec{r}_M) = \sum_{n_r=0}^{N_r} \sum_{n_t=0}^{N_t} \sum_{m=0}^{M} \exp(j\omega_m \tau(\vec{r}_M; n_t, n_r)) \cdot \dot{V}_{m,k}(n_t, n_r), \tag{6}$$

where $\dot{V}_{m,k}(n_t, n_r)$ are complex process on a quadrature detector output at coherent processing on m-th frequency in k-th sounding period at work of pair elements (n_t, n_r). The reference delay τ in (6) is given by formulas (5) at $\vec{r} = \vec{r}_M$. Expression (6) is an algorithm of multichannel coherent space-time processing on one sounding period in MIMO radar with arbitrary arrangement of $N_t + 1$ transmitting and $N_r + 1$ receiving elements at consecutive radiation by transmitting elements of step-FM bursts. At realization of Algorithm (6) application of FFT on frequency index number m is possible.

Processing algorithm of moving target detection (MTD) with notch filters on each frequency component. As the first case we consider simple *notch* filter (NF) for complex amplitudes $\dot{V}_{m,k}(n_t, n_r)$ on each frequency component ω_m of the received signal. The elementary NF is the first order high-pass filter with a time constant τ_f rejecting steady components of intensive signals from local objects and a penetrating transmitter signal. A discrete equivalent of such NF for each frequency component is the recursive filter of the first order:

$$\dot{U}_{m,k+1} = (1 - T_r/\tau_f) \cdot \dot{U}_{m,\kappa} + \dot{V}_{m,k+1} - \dot{V}_{m,k}, \quad k = 0, 1, \ldots, K; \quad m = 0, 1, \ldots, M, \tag{7}$$

where $\dot{V}_{m,k}$ — are input sequences of complex amplitudes on filter input at frequency ω_m, $\dot{U}_{m,k}$ are output sequences. To exclude a transitive mode at coherent focusing on spatial coordinates readouts of a kind $\dot{U}_{m,k_0}$ at $\kappa_0 > 3\tau_f/T_r$ were used. Output values $\dot{U}_{m,k_0}$ are substituted further in the Algorithm (6) instead of $\dot{V}_{m,k}$.

MTD system on a basis of intersurvey subtraction. At use for MTD the variant of unitary coherent subtraction of the data focused on space at two AS radiation time periods was considered:

$$\Delta\psi(\vec{r}_M) = \left| \dot{Q}_{k+\Delta k}(\vec{r}_M) - \dot{Q}_k(\vec{r}_M) \right|. \tag{8}$$

Here $\dot{Q}_k(\vec{r}_M)$ is calculated on (6), and the value Δk meets to some number of the radiation time periods. Results of modeling for first and second MTD algorithms have shown their practically identical efficiency on a level of lateral lobes and suppression of LO signals. MTD system with subtraction is characterized by a little bigger losses of a useful signal and, probably, additional losses on signal/clutter ratio. Losses in a level of a useful signal are increased with reduction of Δk up to the values answering to time, comparable with time of correlation of movings of the slow moving target.

4. EXPERIMENTAL RESULTS

For reception of experimental results the breadboard model of small range 2-D MIMO radar was created on the basis of the stated theoretical preconditions. The breadboard model worked with step-FM SS in a frequency bandwidth of 300 MHz and in a frequency range from 1450 MHz up to 1750 MHz. In the given frequency bandwidth it was used 16 frequencies with uniform frequency step. AS has the parameters specified in Section 2. The view of a breadboard model is submitted on Fig. 2.
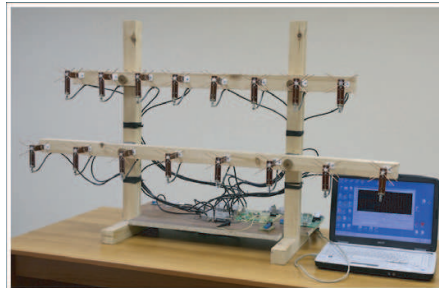
Figure 2: Experimental breadboard model of small range MIMO radar.
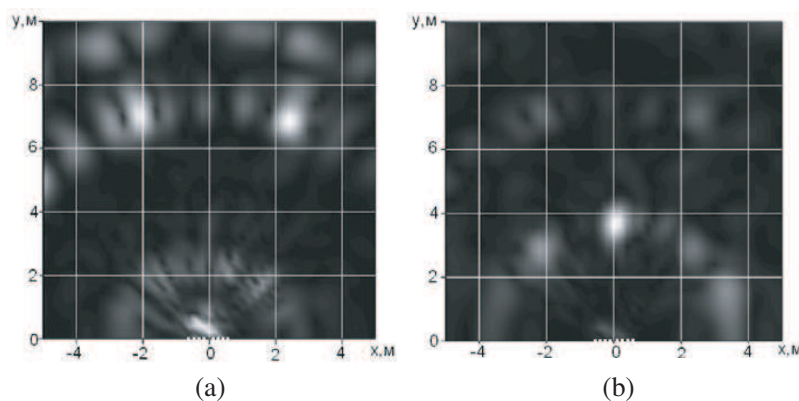
Figure 3: Topographical SSF diagrams at absence (a) and presence (b) of subtraction (experiment).
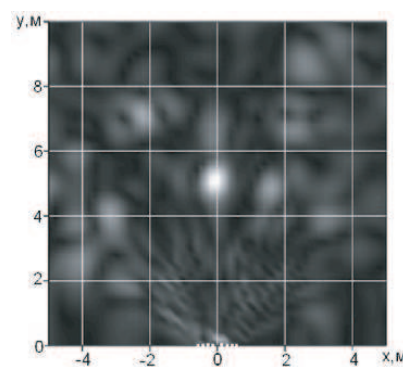
Figure 4: The same, as in Fig. 3, but range up to the target is increased by 1.4 m.

The check of the breadboard model operation was carried out in laboratory experiment at which digital registration of signal quadrature components for all 64 pairs of elements "transmitter-receiver" on each of 16 frequencies of step-FM SS was spend. As slow moving object the metal sheet in the size $25 \times 40\,cm^2$ was used. Its position changed on 1 cm on range in time interval between two full radiation time periods. During each of the periods the sheet remained motionless. Average distances from radar up to the target were equal 1.6 m and 3.0 m in different experiments. For check of the target selection on a background of motionless LO and a penetrating transmitter signal the data on two radiation time periods were registered. Then these data were focused on plane coordinates in two complex files and *the second variant of processing algorithm* on a basis of unitary coherent subtraction (8) was applied.

By results of processing presence of regular errors on delays of the signals varied with constant step on elements of the antenna arrays was revealed. The given errors were measured at adjustment of breadboard model on a motionless reflector with known angular position and taken into account in digital processing algorithm at focusing on spatial coordinates. There was also a constant additional delay for all antenna elements equivalent to 2 m on distance. Results of processing are submitted as topographical diagrams of system signal function (SSF) on Fig. 3, (a) - at absence of subtraction (Algorithm (6)) and (b) - at presence of subtraction (Algorithm (8)). On Fig. 3 the enough number of the intensive marks caused by reflections from LO and penetrating signals is visible. The target mark on equivalent range 3.6 m on Fig. 3(a) practically is not visible, since it is suppressed by powerful false signals. The result of unitary coherent subtraction (8) submitted on Fig. 3(b) shows presence of a true mark. A nature of false marks is explained by insufficient efficiency of suppression of signals from motionless LO and penetrating signals, and also presence of an interference in a room for signals from the mobile target, including an ambiguous ranges. The Fig. 4 is similar to Fig. 3(b), but corresponds to extending of target range on 1.4 m.

5. CONCLUSION

As a whole the results of the carried out researches open opportunities of the further improvement of hardware and algorithmic construction of spatially and frequency multichannel small range MIMO radars. Directions of such perfection should become the reduction of registration time of spatially multichannel multifrequency signals as due to reduction of duration of one spatial-frequency component, and so, probably, due to reduction of number of spatial channels, for example, on the basis of multiplicate processing algorithms offered in [6]. Such reduction will allow increasing efficiency of subtraction of local objects reflections owing to reduction of absolute instability of frequency grid of a multifrequency signal.

ACKNOWLEDGMENT

REFERENCES

1. Fishler, E., A. Haimovich, R. Blum, D. Chizhik, L. Cimini, and R. Valenzuela, "MIMO radar: An idea who's time has come," *Proceedings of the IEEE Radar Conference*, 71–78, Toulouse, France, April 26–29, 2004.

2. Dorey, J., G. Garnier, and G. Auvray, "RIAS, radar a impulsion et antenne syntetique," *Colloque International sur le Radar*, 556–562, Paris, France, April 1989.

3. Chapursky, V. V. and Yu. S. Kucherov, "Antenna arrays with superfast beam scanning," *Radio Engineering and Electronics*, 1562–1569, Russian, 1994.

4. Vovshin, B. M., "Ultrawideband radar-tracking systems," *Progressive Development Directions of Radio-electronic Complexes and Systems, Proceedings of 30-anniversary Conference, Devoted to Foundation of TzNIIRES Company*, Part 1, 139–149, Moscow, Russia, September 12–14, 2001.

5. Wu, J., K. Jiang, and R. He, "Researches of a new kind of advansed meter wave radar," *Proceedings of International Radar Conference*, 71–75, Beijing, China, October 2001.

6. Chapursky, V. V., "Sum and product back projection algorithms in MIMO radar-locations at radiation of step-FM signals," *The Second International Conference "Acousto-optic and Radar-tracking Methods of Measurements and Information Processings"*, 194–198, Conference Reports, Suzdal, Russia, September 25–27, 2007.

7. Shirman, Ya. D. and V. N. Manjos, "Theory and processing technique of the radar-tracking information on a noise background," *Radio and Communication*, Moscow, Russian, 1981.

A Wavelet Technique to Extract the Backscatter Signatures from SAR Images of the Sea

S. Zecchetto[1], F. De Biasio[1], and P. Trivero[2]

[1]Istituto Scienze dell'Atmosfera e del Clima, Italy
[2]Università di Alessandria, Italy

Abstract— SAR images of the sea often show backscatter patterns linked to the horizontal structure of the Marine Atmospheric Boundary Layer (MABL) at the interface with the sea surface. In general, their dimensions are spread over a wide range of length scales, presenting spatial periodicity as well as intermittence. With the aim to isolate such backscatter structures, the two-dimensional Continuous Wavelet Transform (CWT2) analysis has been applied to SAR images of the sea. The CWT2 analysis permits to highlight the backscatter cells associated to the structure of MABL, as well as to evidence the structure of the atmospheric gravity waves occurring at the lee side of islands and coast. The cells detected in the range $0.3\,\mathrm{km} \div 4\,\mathrm{km}$ are directly associated to the wind spatial structure deriving, in turns, from the turbulent characteristics of the wind flow. They have an elliptic shape, with the major axis along the (aliased) wind direction. Those with size falling inside the spatial range $4\,\mathrm{km} \div 20\,\mathrm{km}$ describe, instead, the atmospheric gravity waves structure (if present) and the structures linked to the wind shading. The technique developed is the background for several applications: it has been used to compute the wind fields without any a priori information, as well as to study the inner structure of the Langmuir atmospheric circulation. Other applications could be on the detection of sea surface oil slicks.

1. INTRODUCTION

The increased availability of satellite Synthetic Aperture Radar images over the sea and coastal areas imposes on scientists the development of methods to extract geophysical information from the detailed maps of the radar backscatter. Scientific literature about SAR images over the ocean has shown a variety of geophysical phenomena detectable by SAR [1, 7–11, 15], including the multiscale structure in the atmospheric turbulence under high winds and the structure of the convective turbulence under low wind. More recently, some effort has been devoted to evaluate the wind direction, using the backscatter signatures produced by the atmospheric wind rolls or those occurring at the lee side of islands [12] as effect of wind shielding, by computing the local gradient of the image backscatter [5, 6] or by using the two dimensional Continuous Wavelet Transform (CWT2) [13, 14].

This paper outlines the possibilities offered by the CWT2 in detecting and quantifying the backscatter structures linked to the spatial structure of the Marine Atmospheric Boundary Layer (MABL), both in the small ($0.3\,\mathrm{km} \div 4$ km) and in the intermediate (4 km $\div$ 20 km) ranges. It summarises the CWT2 methodology applied to SAR images, providing the results obtainable by showing a case study chosen among the hundreds of images analysed.

2. THE METHODOLOGY

The Continuous Wavelet Transform [2, 4] $\tilde{f}$ of a function $f(u)$ is a local transform, dependent on the parameters s and τ, defined as

$$\tilde{f}(s,\tau) = \langle \psi_{(s,\tau)}, f \rangle = \int_{-\infty}^{+\infty} du\, \psi_{(s,\tau)}^*(u) f(u) \tag{1}$$

where $\psi_{(s,\tau)}(u) = |s|^{-1}\, \psi\left(\frac{u-\tau}{s}\right)$ is the mother wavelet at a given scale (or dilation) s and location τ (the asterisk denotes complex conjugation). The quantity $|\tilde{f}(s,\tau)|^2$ plays the role of local energy density at given (s,τ). The Continuous Wavelet Transform in two dimensions (CWT2) is then,

$$\tilde{f}(s_x,\tau_x; s_y,\tau_y) = \iint_{-\infty}^{+\infty} du\, dv\, \psi_{(s_x,\tau_x)}^*(u)\, \psi_{(s_y,\tau_y)}^*(v)\, f(u,v).$$

The CWT2 has been computed using the Mexican Hat as mother wavelet, able to capture the fine scale structure of the data and suitable for the continuous wavelet transform because it is non-orthogonal.

The images must be preprocessed before the CWT2 analysis, to mask the land and to mitigate the effects introduced by the variation in range of the radar incidence angle to avoid that structures on the inner part of the image, where the radar incidence angle is smaller and the radar backscatter higher, prevail on the outer ones.

The choice of the scales range is very important because it defines the geophysical phenomena to investigate: if the wind field retrieval is of interest, the spatial range is set from 300 m to 4 km; if phenomena such as the atmospheric gravity waves are the object of study, the spatial range has to be set from 4 km up to 20 km.

A basic quantity yielded by the CWT2 is the wavelet variance map, derived from the wavelet coefficients. Providing information about the energy distribution as a function of (s_r, s_c), in the same way as the two dimensional Fourier spectrum does as a function of wavenumbers, it is used to select the scales, taken around the maximum of the wavelet variance map, to built a SAR-like map (reconstructed map). This is obtained adding the wavelet coefficient maps at the selected scales: a SAR-like image is thus obtained, representing a spatial pattern due to only the most energetic spatial scales present in the original SAR image.

The reconstructed map undergoes a thresholding process to isolate the structures from the background. The result of this procedure is a map of backscatter cells, then used as a mask on the original SAR image to get the values of the Normalised Radar Cross Section inside the detected cells, as well as to estimate their shape and size. The reconstructed map depends on the range of scales used in the analysis. Thus, the CWT2 methodology shown here acts as a filtering procedure based on energetic considerations.

3. A CASE STUDY

Among the hundreds images processed with the methodology above described, we present an Envisat ASAR Wide Swath [3] image taken in the eastern Mediterranean Sea in the Crete island area (Fig. 1). This image covers about 400 km by 400 km, with a pixel resolution of 75 m by 75 m.

While the fine structure (O(1 km)) of the radar backscatter is not well visible, masked by the tilting effect due to the change of the radar incidence angle — from 16° on the right side to 43° on the left side, larger structures such as the atmospheric gravity waves and wind sheltered areas at the islands lee side (the wind blowed from northwest) are detectable by eye.

The map reconstructed in the range 0.3 km $\div$ 4 km, shown in the left panel of Fig. 2, evidences the small scale structure of the radar backscatter, formed by elliptic cells with a major axes orientation falling into two classes, roughly 90° apart, as evidenced in the right panel of Fig. 2, which reports the frequency distribution of the orientation of the cells' major axis. The existence of these two classes is due to the texture of the SAR images, and does not represent the geophysical pattern
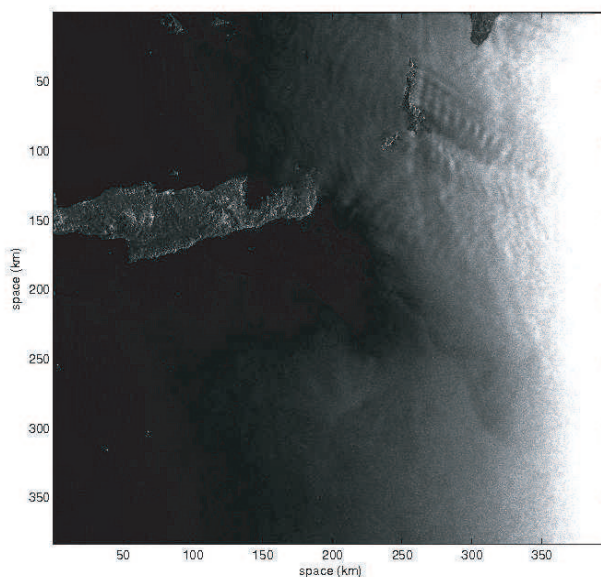
Figure 1: An Envisat ASAR WS image of the eastern Mediterranean Sea: 15-May-2008 at 08:20:47 GMT.

of the backscatter cells excited by the turbulent wind. These may be extracted considering those with directions close to the most probable one, in this case $\theta = 300°$. Thus a reconstructed map with only the cells produced by the wind can be obtained. Fig. 3 reports it for the whole image of Fig. 1 (left panel) and for a portion of it. Note the uneven spatial distribution of the cells but also the high spatial resolution of information obtained. From this map, used as a mask over the original one, it is then possible to retrieve the wind field [14] and to produce a statistics of the cell's size, which may have important implications of the study of the air-sea interaction because it can be linked to the structure of the MABL.
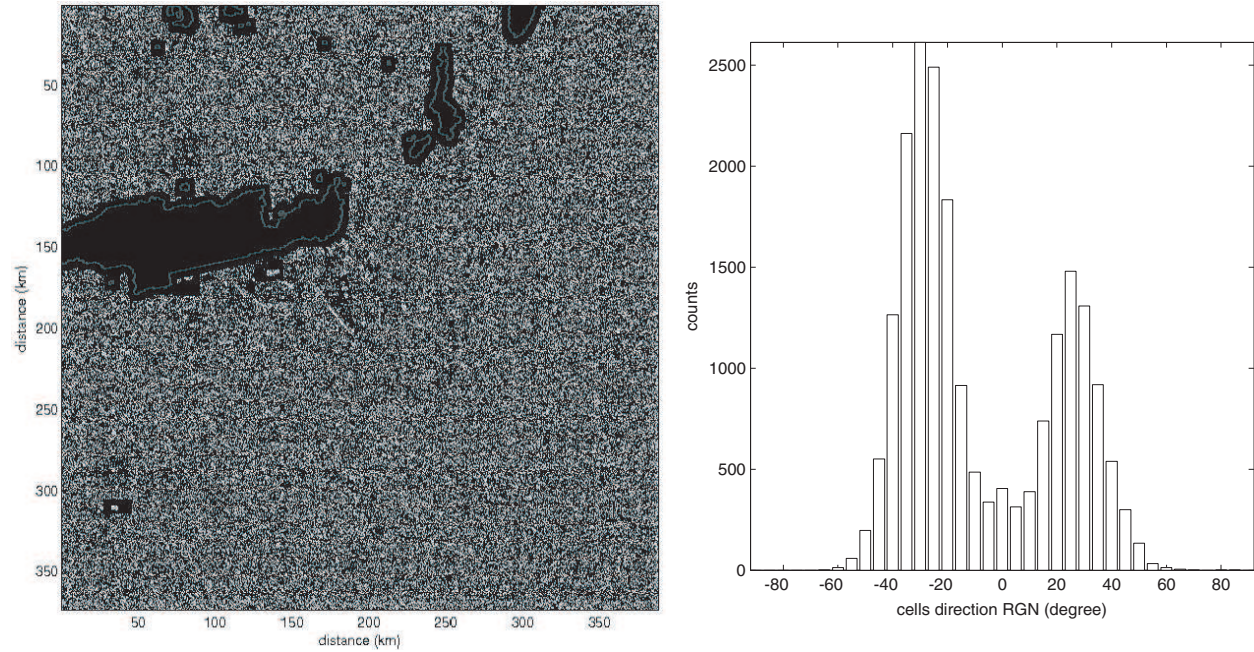
Figure 2: Map reconstruction in the spatial range $0.3\,\text{km} \div 4\,\text{km}$. Left panel: the reconstructed map. Right panel: the frequency distribution of the orientation of cells' major axis.
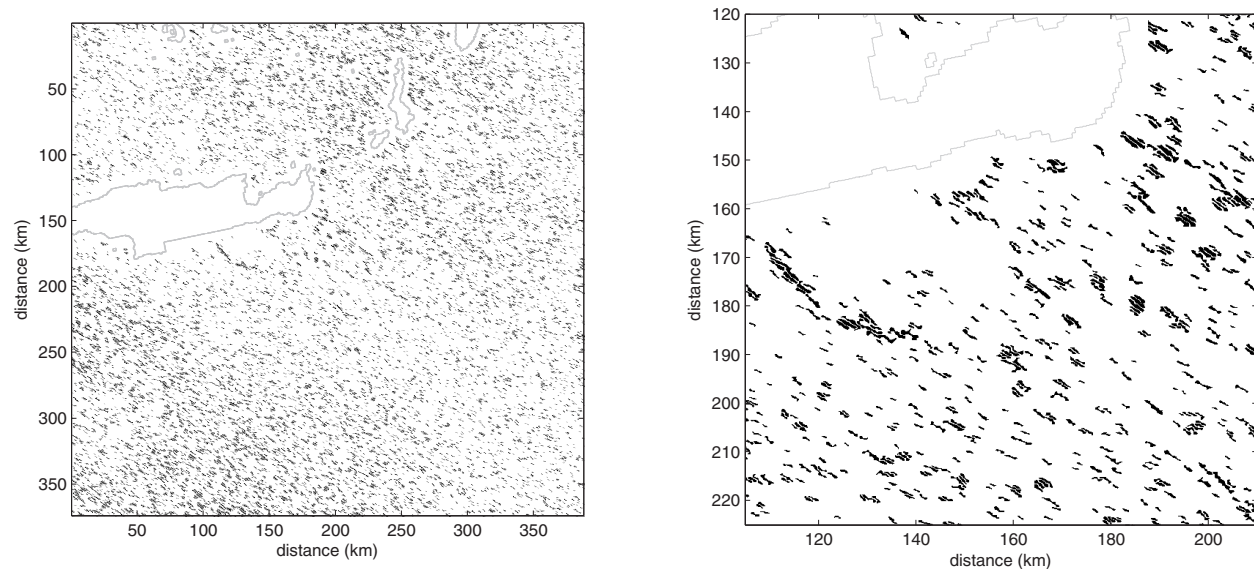
Figure 3: Reconstructed map with only the cells produced by the wind. Left panel: whole map, corresponding to Fig. 1. Right panel: a blow up of it.

The map reconstructed in the range $4\,\text{km} \div 20\,\text{km}$, reported in the left panel of Fig. 4, clearly shows the pattern of the atmospheric gravity waves in its upper right part. The two dimensional spectral analysis of this map yields the 2D spectrum shown in the right panel of Fig. 4, where

two directions are evidenced: that of the maximum energy, occurring at a peak wavelength of 8350 m and an aliased direction of propagation of 296°, and a secondary one, due to the presence of different atmospheric gravity wave trains in the image, with a peak wavelength of 16.7 km and a direction of 63°. This does not really represent a geophysical phenomenon different from that evidenced by the primary peak.

These information may be used, as in [11], to estimate the vertical thickness of the MABL.
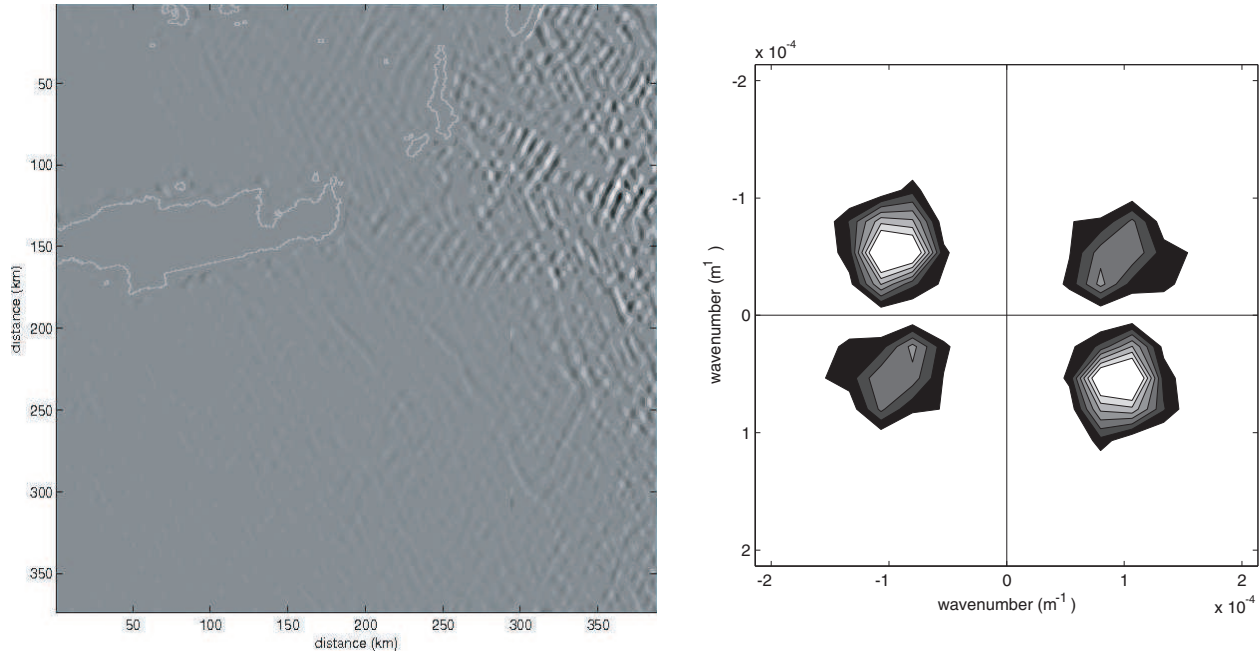
Figure 4: Map reconstruction in the spatial range $4\,km \div 20\,km$. Left panel: the reconstructed map. Right panel: the 2D power spectrum of the reconstructed map.

4. CONCLUSIONS

The described methodology has been applied over hundreds of SAR images, demonstrating its robustness and its capability to detect the most energetic backscatter signatures over the sea. These are strongly related to the horizontal structure of the MABL, roughly from 0.6 km to 10 km, where micro-scale (convection, thermals, dynamical instabilities) and meso-scale (thunderstorms, atmospheric gravity waves and orographic disturbances) atmospheric phenomena occur.

The case study shown here indicates a common feature of the radar backscatter from the sea surface: its complexity, deriving both from the complexity of the MABL and the possibility of wrong interpretation of the backscatter signatures. For instance, the secondary peak in the 2D power spectrum shown in the right panel of Fig. 4 does not represent any other atmospheric phenomenon but it is only produced by the simultaneous presence of different wave trains. This prevents of extract geophysical quantitative information directly from the SAR images, which must be deeply processed instead.

The ongoing research is aimed to derive a statistics on the performances of the model, especially for the wind speed estimations, since the possibility to compare the results with scatterometer wind fields. Future research will be devoted to derive further quantitative geophysical information from the structure of the MABL evidenced by the CWT2 analysis.

REFERENCES

1. Alpers, W. and B. Brümmer, "Atmospheric boundary layer rolls observed by the synthetic aperture radar aboard the ERS-1 satellite," *Journal of Geophysical Research*, Vol. 99, No. C6, 12613–12621, 1994.

2. Beylkin, G., R. Coifman, I. Daubechies, S. Mallat, Y. Meyer, and L. Raphael, *Wavelets and Their Applications*, Jones and Barlett Publishers, Boston, 1992.

3. ESA, *Asar Product Handbook*, Technical report, European Space Agency, Paris, France, August 2002.

4. Foufoula-Georgiou, E. and P. Kumar, *Wavelet in Geophysics, Volume 4 of Wavelet Analysis and Its Applications*, Academic Press, Inc., San Diego, CA, 1994.

5. Horstmann, J., W. Koch, and S. Lehner, "High resolution wind fields retrieved from SAR in comparison to numerical models," *Proceedings of the IEEE International Geoscience and Remote Sensing Symposium*, Toronto, Canada, June 2002.

6. Koch, W., "Directional analysis of SAR images aiming at wind direction," *IEEE Trans. Geosci. Remote Sens.*, Vol. 42, No. 4, 702–710, 2004.

7. Kravtsov, Y. A., M. I. Mityagina, V. G. Pungin, and K. D. Sabinin, "Manifestation of the wind-field fine structure ahead of an atmospheric cold front on radar imagery of the sea surface," *Earth Obs. Rem. Sens.*, Vol. 5, 513–525, 1999.

8. Mitnik, L., M. Hsu, and M. Mitnik, "Sharp gradients and organised structures in sea surface wind field in the region of polar vortex formation," *Global Atmos. Ocean Syst.*, Vol. 4, 335–361, 1996.

9. Mityagina, M. I., V. G. Pungin, and V. V. Yakovlev, "Two-polarization Ku-band radar imagery of the sea surface in presence of atmospheric boundary layer motions," *Waves Random Media*, Vol. 8, 111–118, 1998.

10. Mourad, P. D., "Inferring multiscale structure in the atmospheric turbulence using satellite-based synthetic aperture radar imagery," *J. Geophys. Res.*, Vol. 101, 18433–18449, 1996.

11. Sikora, T. D., G. S. Young, H. N. Shirer, and R. D. Chapman, "Estimating convective atmospheric boundary layer depth from microwave radar imagery of the sea surface," *J. Appl. Meteorol.*, Vol. 36, 833–845, 1997.

12. Vachon, P. W. and F. W. Dobson, "Wind retrieval from radarsat sar images: Selection of a suitable C-band HH polarization wind retrieval model," *Canadian Journal of Remote Sensing*, Vol. 24, No. 4, 306–313, 2000.

13. Zecchetto, S. and F. De Biasio, "On shape, orientation and structure of atmospheric cells inside wind rolls in SAR images," *IEEE Trans. of Geoscience and Remote Sensing*, Vol. 40, No. 10, 2257–2262, 2002.

14. Zecchetto, S. and F. De Biasio, "A wavelet based technique for sea wind extraction from SAR images," *IEEE Trans. of Geoscience and Remote Sensing*, 2008.

15. Zecchetto, S., P. Trivero, B. Fiscella, and P. Pavese, "Wind stress structure in the unstable marine surface layer detected by SAR," *Boundary Layer Meteorol*, Vol. 86, 1–28, 1998.

Orthogonal Kravchenko Wavelets in Digital Signal and Image Processing

Y. Y. Konovalov and A. V. Yurin

Bauman Moscow State Technical University, Moscow, Russia

Abstract— A new class of orthogonal Kravchenko WA-systems [1] is discussed. These wavelets are based on multiresolution analysis construction with the using of atomic functions. As there are many different classes of atomic functions, so a new class of wavelets contains a wide set of functions. Each of them has its own properties: localization both in time and frequency; decomposition and reconstruction filters; uncertainty constants. Their common properties are smoothness and symmetry. The comparison of new Kravchenko wavelets with the well known ones is presented. It demonstrates the advantage of new WA-systems. The numeric experiment shows the efficiency of new Kravchenko wavelets in model problems of digital signal and image processing.

1. INTRODUCTION

In present time the great attention is given to the wavelet theory as mathematical tool. Because of local properties in spatial and frequency domain, orthogonality, vanishing moments, multiresolution analysis, numerical algorithms based on wavelets have valuable advantages as compared to Fourier transforms. In wavelet theory various mathematical theories become closer. For example well known spline-wavelets, which use both spline and wavelet means. So construction of a new class of orthogonal Kravchenko wavelets based on atomic functions has great scientific and practical interest.

2. ATOMIC FUNCTIONS AND THEIR PROPERTIES

Atomic functions [2] are compactly supported infinite differentiable solutions of differential equations with shifted argument $Lf(x) = \lambda \sum_{k=1}^{M} f(ax - b(k))$, $|a| > 1$, where L — linear differential operator with constant coefficients; a, b — constants. In this paper $up(x)$ function will be discussed (Figure 1). Atomic function $up(x)$ is a solution of equation $f'(x) = 2f(2x + 1) - 2f(2x - 1)$. It can be presented as $up(x) = \frac{1}{2\pi} \int_{-\infty}^{\infty} \hat{up}(\omega) \exp(i\omega x) d\omega$; where $\hat{up}(\omega) = \prod_{k=1}^{\infty} \frac{\sin(\omega 2^{-k})}{\omega 2^{-k}}$ is a Fourier transform of $up(x)$. $up(x)$ function's properties [2] are: supp $up(x) = [-1; 1]$; $up(x) \in C^{\infty}[-1; 1]$; $up(x)$ is an even function $up(x) = up(-x)$; $up(x) = 1 - up(1 - x)$; sum of integer shifts $up(x)$ identically equals to one $\sum_{k=-\infty}^{k=\infty} up(x - k) \equiv 1$; $up(x)$ has a fast convergent Fourier expansion $up(x) = 0,5 + \sum_{k=1}^{\infty} \hat{up}(\pi k) \cos(\pi(2k - 1)x)$.

3. ORTHOGONAL KRAVCHENKO WAVELETS CONSTRUCTION

Constriction of wavelets is based on multiresolution analysis [3, 4] a system of closed embedded subspaces $V_j \subset L^2(R)$, $j \in Z$, with following properties: $\overline{\bigcup_{j \in Z} V_j} = L^2(R)$; $\bigcap_{j \in Z} V_j = \{0\}$; $f(x) \in V_j \Leftrightarrow f(2x) \in V_{j+1}$; scaling function $\varphi(x) \in V_0$ exists which shifts generates a Riesz basis in V_0.

Let V_0 be a subspace of $L^2(R)$, generated by shifts of function $\varphi(x)$. In order that shifts of function $\varphi_n(x) = \varphi(x - n)$ generate a Riesz basis [3] in V_0 conditions of this theorem must be satisfied:

Theorem 1. Functions $\varphi_n(x) = \varphi(x - n)$ form orthonormal basis in subspase $V_0 \subset L^2(R)$ if and only if $\sum_{n \in Z} |\hat{\varphi}(\omega + 2\pi n)|^2 = 1$ almost everywhere.

We'll look for a function $\chi(\omega) = |\hat{\varphi}(\omega)|^2$, which shifts $\chi_n(\omega) = \chi(\omega + 2\pi n)$ form partition of unity $\sum_{n \in Z} \chi(\omega + 2\pi n) = 1$, satisfying conditions: supp$(\chi(\omega)) = [-4\pi/3; 4\pi/3]$, $\chi(\omega) = 1$ if $\omega \in [-2\pi/3; 2\pi/3]$, $\chi(\pi) = 0.5$.
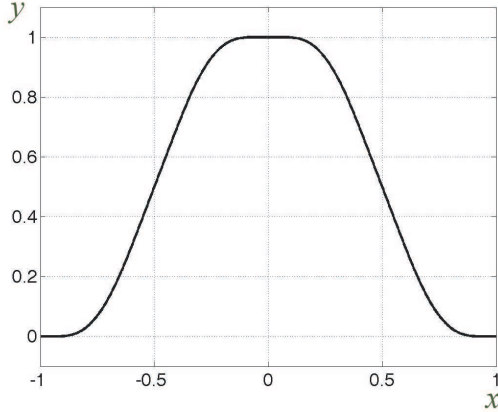
Figure 1: $up(x)$ function.
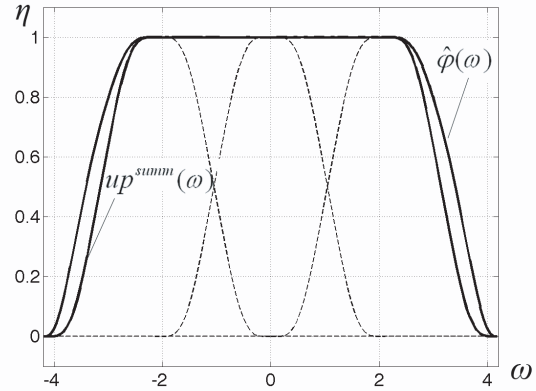
Figure 2: Sifts of $up(\omega)$, $up^{summ}(\omega)$, $\hat{\varphi}(\omega)$.

According to the properties of $up(t)$ function $\sum\limits_{n \in Z} up(x + n) \equiv 1$.

We consider the partial sum $up^{summ}(t) = up\left(\frac{3}{2\pi}t + 1\right) + up\left(\frac{3}{2\pi}t\right) + up\left(\frac{3}{2\pi}t - 1\right)$ (Figure 2). This modified atomic function meets all conditions of function $\chi(\omega)$. We define $\hat{\varphi}(\omega)$ as $\hat{\varphi}(\omega) = \sqrt{up^{summ}(\omega)}$.

To meet the third property of multiresolution analysis it is necessary to satisfy scaling equation:

$$\hat{\varphi}(\omega) = H_0\left(\omega/2\right) \Leftrightarrow \hat{\varphi}(\omega) = \prod_{k=1}^{\infty} H_0\left(\omega/2\right) \tag{1}$$

Basing on (1) we determine conjugate mirror filter $H_0(\omega)$. Since $\hat{\varphi}\left(\omega/2\right) = 1$ if $\omega \in [-4\pi/3; 4\pi/3]$ and $\hat{\varphi}(\omega)$ vanishes outside of $[-4\pi/3; 4\pi/3]$, so $H_0(\omega) = \hat{\varphi}(2\omega)$ if $\omega \in [-2\pi/3; 2\pi/3]$ and vanishes if $\omega \in [-\pi; -2\pi/3] \cup [2\pi/3; \pi]$.

Then we periodically continue it with period 2π $H_0(\omega) = \sum\limits_{n \in Z} \hat{\varphi}(2(\omega + 2\pi n))$ and using (1) we'll see that scaling equation is satisfied $H_0\left(\omega/2\right) \hat{\varphi}\left(\omega/2\right) = \sum\limits_{n \in Z} \hat{\varphi}(2(\omega + 2\pi n)) \cdot \hat{\varphi}\left(\omega/2\right) = \hat{\varphi}(\omega)$.

Then $H_0(\omega)$ meets conditions of the theorem:

Theorem 2. If shifts of scaling function $\varphi_n(x) = \varphi(x - n)$ generate an orthonormal basis in subspace V_0 then conjugate mirror filter $H_0(\omega)$ has such property:

$$|H_0(\omega)|^2 + |H_0(\omega + \pi)|^2 = 1 \quad \text{almost everywhere.} \tag{2}$$

According to [3] first two properties of multiresolution analysis are satisfied too.

Thus Fourier transform of function which products multiresolution analysis is constructed (Figure 3):

$$\varphi(x) = \frac{1}{2\pi} \int_{-\infty}^{\infty} \hat{\varphi}(\omega) \exp(i\omega x) d\omega = \frac{1}{\pi} \int_{0}^{-\frac{4\pi}{3}} \hat{\varphi}(\omega) \cos\left(\omega x\right) d\omega$$

Then we can define orthogonal basis produced by shifts and dilations of wavelet $\psi(x) \in W_0$ ($V_{j+1} = V_j \oplus W_j$, $V_j \bot W_j$, $W_j \bot W_k$, for all $j, k \in Z$, $k \neq j$), which can be constructed from $\varphi(x)$. According to [4] Fourier transform of wavelet defined as:

$$\hat{\psi}(\omega) = e^{\frac{i\omega}{2}} \overline{H_0\left(\frac{\omega}{2} + \pi\right)} \hat{\varphi}\left(\frac{\omega}{2}\right) = e^{\frac{i\omega}{2}} \left(\hat{\varphi}(\omega - 2\pi) + \hat{\varphi}(\omega + 2\pi)\right) \hat{\varphi}\left(\frac{\omega}{2}\right).$$

From (2) follows $\sum\limits_{n \in Z} \left|\hat{\psi}(\omega + 2\pi n)\right|^2 = 1$ almost everywhere. Then according to first theorem shifts $\psi_n(x) = \psi(x - n)$ generate orthonormal basis. We get wavelet function in spatial domain by
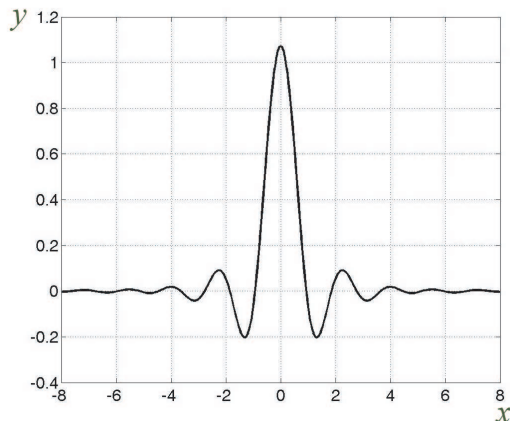
Figure 3: Scaling function $\varphi(x)$.
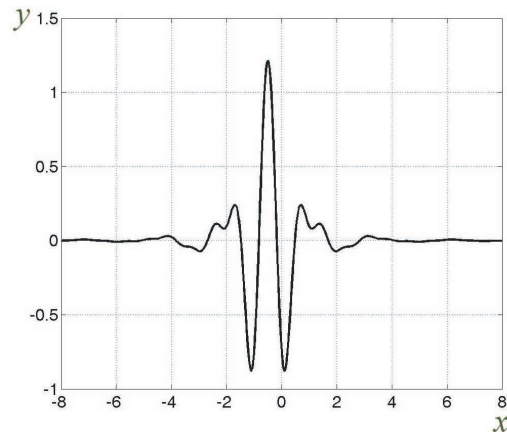
Figure 4: Wavelet $\psi(x)$.

inversing Fourier transform:

$$\psi(x) = \frac{1}{2\pi} \int\limits_{-\infty}^{\infty} e^{\frac{i\omega}{2}} \left(\hat{\varphi}(\omega - 2\pi) + \hat{\varphi}(\omega + 2\pi)\right) \hat{\varphi}\left(\frac{\omega}{2}\right) e^{i\omega x} d\omega = \frac{1}{\pi} \int\limits_{\frac{2\pi}{3}}^{-\frac{8\pi}{3}} \hat{\varphi}(\omega - 2\pi)\hat{\varphi}\left(\frac{\omega}{2}\right) \cos \omega (x + 0.5) d\omega.$$

New Kravchenko function has all properties of wavelets (Figure 4).

Functions $\varphi(x)$ and $\psi(x)$ satisfies these scaling equations:

$$\varphi(x) = \sqrt{2} \sum_{n \in Z} h_n \varphi(2x - n), \quad \psi(x) = \sqrt{2} \sum_{n \in Z} g_n \varphi(2x - n), \quad g_n = (-1)^{n+1}\overline{h}_{-n-1},$$

where $\{h_n\}$ — coefficients of the low-pass decomposition filter $H(\omega) = \sqrt{2}H_0(\omega) = \sum\limits_{n \in Z} h_n e^{-in\omega}$,

which can be found by Fourier-series expansion of the H_0 function: $h_n = \frac{\sqrt{2}}{2\pi} \int\limits_{-\pi}^{\pi} H_0(\omega)e^{in\omega}d\omega$. Other

filters $(G, \tilde{H}, \tilde{G})$ can be easily found from $H(\omega)$.

Kravchenko functions $\varphi(x)$ and $\psi(x)$ are not compactly supported but they rapidly decrease (due to infinite differentiability), then we can select an effective support from such conditions:

$$\|\varphi - \varphi_{eff}\| \cdot 100\% \leq 0.001\%, \quad \|\psi - \psi_{eff}\| \cdot 100\% \leq 0.001\%.$$

Effective supports of new Kravchenko functions are $\mathrm{supp}(\varphi_{eff}(x)) = [-8; 8]$ and $\mathrm{supp}(\psi_{eff}(x)) = [-8; 8]$. Then number of filter coefficients $\{h_n\}$ is limited to $n = -16 \ldots 16$. New Kravchenko wavelets have properties like Meyer and Kotelnikov-Shannon wavelets and have these advantages: symmetry, they decay faster then Meyer wavelet but not compactly supported. However, Fourier transforms of Kravchenko wavelets are infinite differentiable and can be presented as a single analytical expression, and localization of new Kravchenko wavelets in time and frequency domain is much better then Kotelnikov-Shannon wavelets. Further comparison with known wavelets we'll do by rate of efficient support and values of uncertainty constants $\Delta_\varphi \hat{\Delta}\hat{\varphi}$, $\Delta_\psi \hat{\Delta}\hat{\psi}$ [1]. In the Table 1, physical characteristics of new and known wavelets ere shown.

Table 1: Physical characteristics of new and known wavelets.

Wavelets	$\mathrm{supp}(\varphi_{eff}(x))$, $\mathrm{supp}(\psi_{eff}(x))$	$\Delta_\varphi \Delta_{\widehat{\varphi}}$	$\Delta_\psi \Delta_{\widehat{\psi}}$
Kravchenko	$[-8, 8]$	0,87264	2,83008
Meyer	$[-8, 8]$	1,01148	3,27802
Kotelnikov-Shannon	$[-10^4, 10^4]$	∞	∞

Thus new construction of Kravchenko wavelets theoretically substantiated and has all properties of multiresolution analysis. Scheme of wavelet construction can be expanded on other sets of atomic functions.

4. ORTHOGONAL KRAVCHENKO WAVELETS AND DIGITAL SIGNAL PROCESSING

Wavelet analysis widely applied to digital signal processing. We consider the implementation orthogonal Kravchenko wavelets for denoising signal.

We denoise one-dimensional signal $f_s(n) = \exp(x/8) \cdot \sin(x^{1,5})$, $x \in [0, 3\pi]$ with sampling frequency 108,65 Hz. Noise component is a white noise with standard deviation $\sigma = 0.4472$. Signal-to-noise ratio is 16.45.

At first step we have to do a wavelet transform, which is calculated using decomposition filters. New wavelets are not compactly supported then filters have infinite pulse characteristics. In practice we can limit number of coefficients because used basis functions decay fast.

We select threshold level using Stain's principle unbiased risk estimation for each scale of wavelet decomposition. Then we thresholding coefficients and reconstruct signal using inverted wavelet transform.

We make comparative analysis of denoising with Kravchenko wavelet and known smooth wavelets: Meyer, Daubechies 4, Coifman 4, symlet 4. In the Table 2, comparative characteristics are shown: number of filter coefficients, relative error by L_2 norm $\varepsilon = 100\% \cdot \|f_s - f_d\|_{L_2} / \|f_s\|_{L_2}$, signal-to-noise ratio.

According to Table 2, signal filtered with Kravchenko wavelet has the highest value of signal-to-noise ratio and the lowest relative error. We got these characteristics with number of coefficients of decomposition and reconstruction filters limited to 22, which less then for Meyer and Coifman 4.

We can use for filtering other Kravchenko wavelets constructed from other atomic functions with the same method. Parameters of Kravchenko wavelets filters optimized to minimize relative error ε. Physical characteristics of wavelets and filtered signals are shown in Table 2.

Analysis of characteristics of the signal filtered with different wavelet systems shows that new Kravchenko wavelets denoise signal mach better then other ones. Number of coefficients of the decomposition and reconstruction filters is more then for wavelets Daubechies 4, Coifman 4, symlet 4 and less then Meyer.

Table 2: Characteristics of denoised signals (Soft thresholding).

Wavelet		Compactly supported	Number of filter coefficients n	$j_{\max}$	ε, %	Signal-to-noise ratio
Meyer		No	102		4,882528	421,9
Daubechies	4	Yes	8		5,499327	332,2
Symlet	4	Yes	8		6,404075	249,4
Coiflet	4	Yes	24		4,708402	467,6
Kravchenko based on $up(x)$		No	22	5	4,594575	479,8
Kravchenko based on $fup_N(x)$	2	No	34		4,369962	529,8
	3		34		4,474193	502,9
	4		34		4,434180	513,3
	5		36		4,418859	518,1

5. CONCLUSIONS

New construction of Kravchenko wavelets based on atomic function theoretically substantiated. It is shown that it has all properties of multiresolution analysis. Scheme of wavelet construction can be expanded on other sets of atomic functions. Comparison of physical characteristics shows that new wavelets have better time-frequency localization then known. Application new Kravchenko wavelets to digital signal processing shows their efficiency in denoising.

REFERENCES

1. Kravchenko, V. F., O. S. Labun'ko, A. M. Lerer, and G. P. Sinyavsky, *Computing Methods in the Modern Radio Physics*, edited by V. F. Kravchenko, Fizmatlit, Moscow, 2009 (in Russian).
2. Kravchenko, V. F. and V. L. Rvachov, *Boolean Algebra, Atomic Function and Wavelet in Physical Applications*, Fizmatlit, Moscow, 2006 (in Russian).
3. Mallat, S., *A Wavelet Tour of Signal Processing*, Academic Press, 1999.
4. Daubechies, I., *Ten Lectures on Wavelets*, SIAM, 1992.

5. Kravchenko, V. F. and A. V. Yurin, "The application of the new class of wavelet-functions in signal and image processing," *Successes of Modern Radio Electronics*, Vol. 13, No. 5, 3–64, 2008 (in Russian).

Signal Processing and Time Delay Resolution of Noise Radar System Based on Retrodirective Antennas

V. V. Chapursky[1], V. A. Cherepenin[2], and V. I. Kalinin[2]

[1]Bauman Moscow State Technical University, Russia
[2]Institute of Radioengineering and Electronics, Moscow, Russia

Abstract— Theoretical comparison results of basic noise signal processing methods for one channel retrodirective noise radar system are obtained. Three methods of noise signal processing were studied: cross-correlation processing with delayed reference transmitter signal; double spectrum processing of received signal; cross-correlation processing with recirculated reference signal at various reference time delays.

1. INTRODUCTION

One of the most interesting self-steering technologies for UWB radar is application of noise sounding signals. In recent years, investigations for the target observation method using wideband noise radar with retrodirective antennas have been resumed [1–3]. The retrodirective antenna principle of sounding is based on recirculation of a noise signal in the spatial feedback loop. The loop is closed by means of combining a portion of the received radar signal with the current signal of the transmitter and radiation of the obtained sum signal toward the target. The given method theoretically allows to improve radar resolution and detection ability, including at MIMO radar surveillance [4]. At the same time in the elaboration of noise signal processing methods in radar with spatial recirculation there is a number of unresolved questions to the part of which the contents of the given work is devoted.

This report presents theoretical comparison results of basic noise signal processing methods for one channel retrodirective noise radar system: 1) cross-correlation processing with delayed reference signal of noise transmitter generator; 2) double spectrum processing of received recirculation noise signal; 3) cross-correlation processing with reference noise signal in special design recirculator based on various reference time delays.

2. CROSS CORRELATION PROCECCING WITH REFERENCE NOISE SIGNAL

A bloc diagram of the cross-correlation retrodirective noise radar system is shown in Fig. 1. A noise generator forms noise signal $s(t)$ with rectangular envelope $A(t)$ of duration T:

$$s(t) = A(t)\,\xi(t), \tag{1}$$

where $\xi(t)$ — stationary noise process with zero mean value, correlation function $k_\xi(\tau) = \mathbf{M}\{\xi(t)\xi(t+\tau)\}$ ($\mathbf{M}$ is a symbol of mean value) and correlation time τ_ξ. The recirculation of noise signal is performed in the spatial feedback loop with target time delay τ_t.
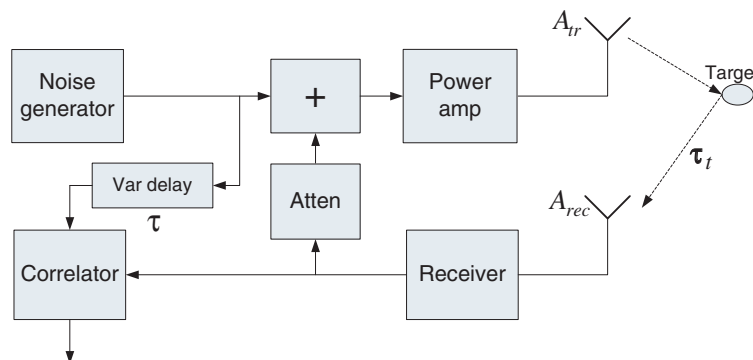
Figure 1: Bloc diagram of retrodirective noise radar with cross correlation processing.

In the case when envelope duration T and target delay τ_t are satisfied conditions $T \gg \tau_t \gg \tau_\xi$ then analysis is simplified and complex transmission coefficient of the spatial feedback loop with time delay τ_t can be calculated at stationary approximation as [3]:

$$\dot{K}(\omega) = \frac{K_\Sigma \exp(-j\omega\tau_t)}{1 - \gamma K_\Sigma \exp(-j\omega\tau_t)}, \tag{2}$$

where K_Σ is transmission coefficient of the unclosed spatial feedback loop without attenuator loss γ [5]. Total transmission coefficient of closed spatial feedback loop satisfies the important condition $K_\Sigma \gamma < 1$ when self-oscillations are not excited in closed feedback loop including transmitter and receiver amplifiers. Consequently to this assumption noise waveform $\eta(t)$ on the output of spatial feedback loop (or receiver output) can be written as

$$\eta(t) = \sum_{k=0}^{\infty} K_\Sigma^{k+1} \gamma^k \xi(t - (k+1)\tau_t), \tag{3}$$

The average value evaluation of cross-correlation function on the correlator output in Fig. 1 is expressed as

$$k_{\xi\eta}(\tau) = \mathbf{M}\{\xi(t-\tau)\eta(t)\} = \sum_{k=0}^{\infty} K_\Sigma^{k+1} \gamma^k k_\xi(\tau - (k+1)\tau_t). \tag{4}$$

The expression (4) of cross-correlation function contents a set of equidistantly components placed at multiple points $\tau_k = (k+1)\tau_t$ where $k = 0, 1, 2, 3, \ldots$. The form of each component coincides with correlation function $k_\xi(\tau)$ of initial noise signal $\xi(t)$. The level of correlation components is decreased as law $(K_\Sigma \gamma)^k$ when time delay τ_k is increased. Therefore the range (time delay) ambiguity of target detection is appeared as result of spatial recirculation of sounded signals. Analysis of correlation function (4) shown in Fig. 3 as solid curve confirms that space (time delay) resolution of retrodirective noise radar with delayed noise reference is only defined frequency bandwidth of noise signal $\xi(t)$ as well as correlation noise radar without any recirculation.

3. DOUBLE SPECTRUM PROCESSING OF RECEIVED RECIRCULATION SIGNAL

Wideband noise radar with double spectrum processing (DSP) was proposed in basic work [5] and in detail investigated on the object of signal/noise ratio in [6]. Here retrodirective antenna-based noise radar with double spectrum processing is considered. Its block diagram shown in Fig. 2 contents new elements: second linear summator, first SA1 and second SA2 spectrum analyzers unlike correlation noise radar in Fig. 1. Double spectrum processing is performed by means of successive connected the first SA1 and second SA2 spectrum analyzers. Three different radar schemes with double spectrum processing are examined: 1) received noise waveform is applied on the input of SA1 when switch is placed at position 1; 2) sum of received and noise generator waveforms are applied on the input of SA1 when switch is placed at position 2; 3) sum of received noise and inner feed-back loop reference waveforms are applied on the input of SA1 when switch is placed at position 3.

Complex transmission coefficients are determined for the three above mentioned cases as

$$\dot{K}_1(\omega) = \dot{K}(\omega) = \frac{K_\Sigma \exp(-j\omega\tau_t)}{1 - \gamma K_\Sigma \exp(-j\omega\tau_t)}, \tag{5}$$

$$\dot{K}_2(\omega) = 1 + \frac{K_\Sigma \exp(-j\omega\tau_t)}{1 - \gamma K_\Sigma \exp(-j\omega\tau_t)}, \tag{6}$$

$$\dot{K}_3(\omega) = 1 + \frac{(1+\gamma) K_\Sigma \exp(-j\omega\tau_t)}{1 - \gamma K_\Sigma \exp(-j\omega\tau_t)}. \tag{7}$$

In the first case results of double spectrum and cross correlation processing from Section 2 exactly coincide.

If power spectrum $S_\xi(\omega)$ is rectangular approximated by $S_{\xi 0}$ in a frequency bandwidth (ω_L, ω_H) then because symmetric properties of Fourier transform the output of DSP can be written as

$$k_i(\tau) = 2S_{\xi 0} \int_{\omega_L}^{\omega_H} \left|\dot{K}_i(\omega)\right|^2 \cos(\omega\tau)\, d\omega, \quad i = 1, 2, 3, \tag{8}$$

Formula (8) is used for calculation of output correlation functions in the three DSP schemes. It is let following parameters for DSP noise radar based on retrodirective antenna: $f_L = 100\,\text{MHz}$; $f_H = 500\,\text{MHz}$; $K_\Sigma = 1$; $\gamma = 0.5$. The time delay τ_t of reflected signal is established as $\tau_t = 15\,\text{ns}$. Output correlation functions simulated for all DSP schemes are presented in Fig. 3.

It can be clearly seen in this figure that all DSP schemes and cross correlation processing from Section 2 have alike correlation functions with the same width of correlation peaks. Therefore, all DSP and cross correlation schemes are characterized by the same range (time delay) resolution.

4. CROSS CORRELATION PROCESSING BASED ON RECIRCULATED REFERENCE

In this paper we present new method of retrodirective radar detection with cross-correlation processing based on recirculation noise reference. A block diagram of that noise radar is shown in Fig. 4. Radar transmitter contents additional recirculation loop with variable time delay τ and recirculation coefficient $\gamma_0 < 1$. The output of the recirculation reference loop is fed to first input of a correlator. Its second input is connected to one of the receiver output. The other output of a receiver closes the recirculation loop with the spatial feedback loop having total time delay τ_t. The proposed method has the highest theoretical and practical interest and therefore correlation signal processing is analyzed in detail here. It is assumed that noise signal $s(t) = A(t)\xi(t)$ has rectangular envelope $A(t)$ of finite duration T. Received waveforms $\eta(t, \tau_t)$ and recirculation reference $\eta_0(t, \tau_0)$ can be expressed analogically (3) as

$$\eta\left(t, \tau_t\right) = \sum_{k=0}^{\infty} K_\Sigma^{k+1} \gamma^k A\left(t - (k+1)\,\tau_t\right) \xi\left(t - (k+1)\,\tau_t\right), \tag{9}$$
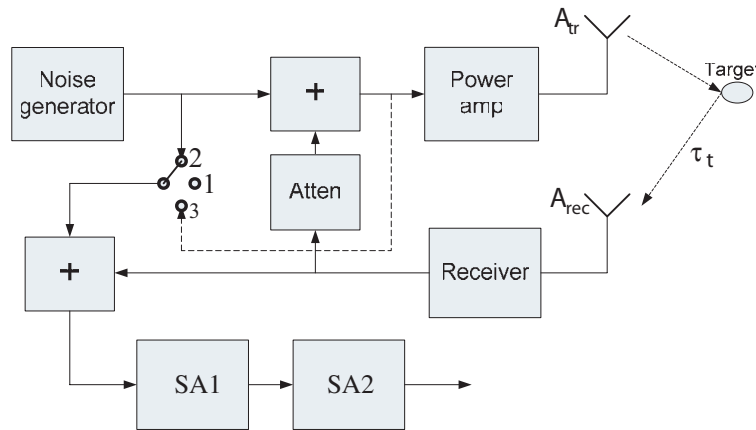
Figure 2: Bloc diagram of retrodirective noise radar with double spectral processing.
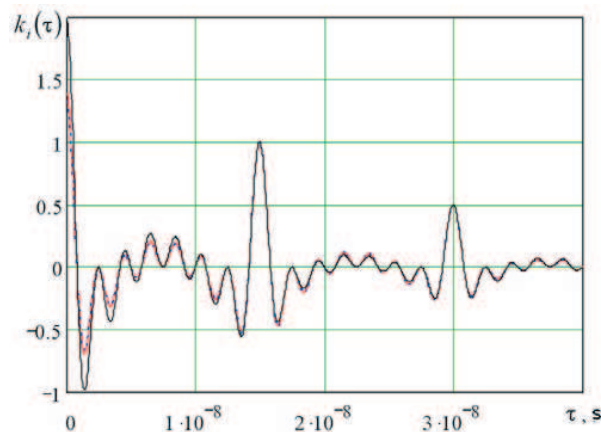
Figure 3: Simulated correlation functions for three DSP schemes.

$$\eta_0\left(t,\tau_0\right) = \sum_{k=0}^{\infty} \gamma_0^k A\left(t-(k+1)\tau_0\right)\xi\left(t-(k+1)\tau_0\right). \tag{10}$$

Mean value of correlation integral for signals (9) and (10) is defined as result of integral calculating at current time t and statistic averaging:

$$
\begin{aligned}
\bar{Q}\left(\tau_t,\tau_0\right) &= \mathbf{M}\left\{\int_{-\infty}^{\infty} \eta\left(t,\tau_t\right)\eta\left(t,\tau_0\right)dt\right\}\\
&= \sum_{k_1,k_2=0}^{\infty} K_\Sigma^{k_1+1}\gamma^{k_1}\gamma_0^{k_2}\left[b\left(\Delta_{k_1,k_2}\left(\tau_0,\tau_t\right)\right)-a\left(\Delta_{k_1,k_2}\left(\tau_0,\tau_t\right)\right)\right]\\
&\quad\times h\left(b\left(\Delta_{k_1,k_2}\left(\tau_0,\tau_t\right)\right)-a\left(\Delta_{k_1,k_2}\left(\tau_0,\tau_t\right)\right)\right)\cdot k_\xi\left(\Delta_{k_1,k_2}\left(\tau_0,\tau_t\right)\right),
\end{aligned}
\tag{11}
$$

where $\Delta_{k_1,k_2}\left(\tau_0,\tau_t\right)=(k_2+1)\tau_0-(k_1+1)\tau_t$, $a\left(\Delta\right)=\max\left(0,\Delta\right)$, $b\left(\Delta\right)=\min\left(T,T+\Delta\right)$.

Expression (11) for averaged cross-correlation functions of recirculation signals (9), (10) is general and valid for arbitrary duration T of noise impulse $s(t)=A(t)\xi(t)$. Averaged cross-correlation (11) is evaluated when large duration is assumed $T\gg\tau_t\gg\tau_\xi$ with the purpose of a comparison between previously obtained results. It is let the same parameters of wideband noise signal $f_L=100\,\mathrm{MHz}$, $f_H=500\,\mathrm{MHz}$ as in Sections 2, 3. Other parameters are equal $K_\Sigma=1$, $\gamma_0=1$, $\gamma=0.9$, $\tau_t=50\,\mathrm{ns}$. Reference delay τ_0 is varied from $40\,\mathrm{ns}$ to $60\,\mathrm{ns}$ in the time interval centered on target delay $\tau_t=50\,\mathrm{ns}$. In Fig. 5 output cross correlations are shown for noise radar based on retrodirective antennas in case with delayed convention noise reference according to
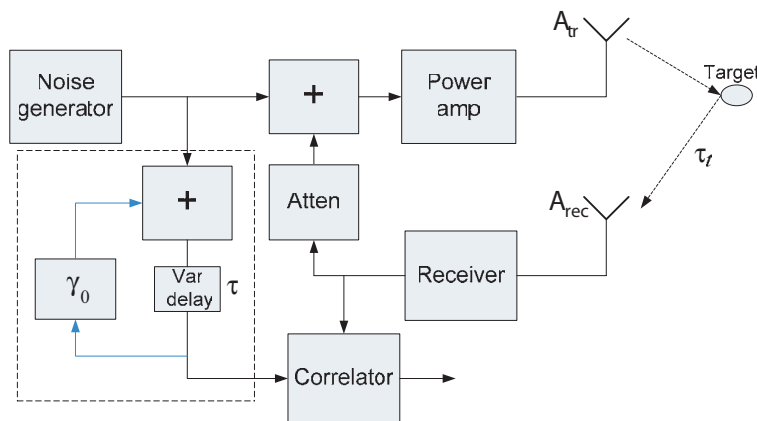
Figure 4: Bloc diagram of retrodirective noise radar based on recirculation reference.
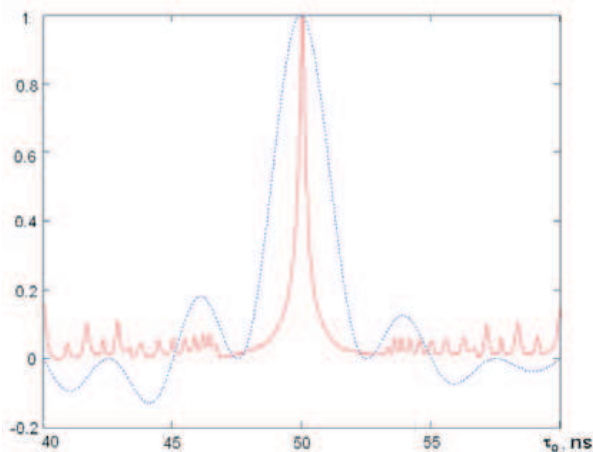
Figure 5: Comparision of classic and retrodirective noise radars resolution.
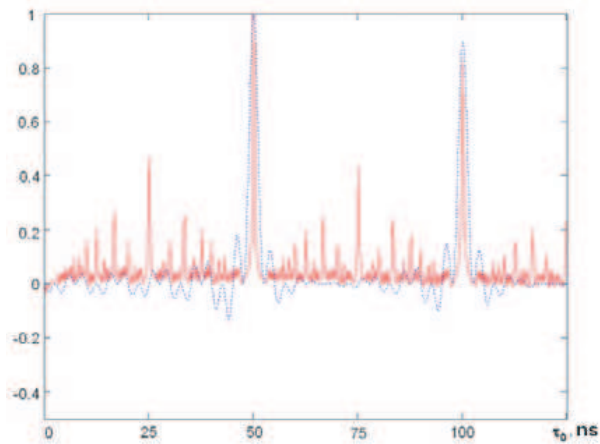
Figure 6: The view of grating and combination lobes in noise radars ambiguity function.

Section 2 (dash curve) and in case with recirculation noise reference according to Section 4 (solid curve). A comparison between solid curve and dash curve indicates that solid curve width is some times narrow as dash curve width. Consequently space resolution of retrodirective noise radar with recirculation reference exceeds some times then in case with delayed reference. Output cross correlation functions (solid and dash in Fig. 6) simulated on large time delay interval content a set of intensive combination lobes which can cause target detection ambiguity on time delays multiple of target delay $\tau_t = 50$ ns. This ambiguity can be eliminated by means of time strobing for example decreasing noise impulse duration.

5. CONCLUSION

The design principles of wideband noise radar based on retrodirective antennas are described. The correlation and double spectrum processing methods are discussed. Analytical relationships for output cross-correlations calculation are derived. Numerical results have allowed to reveal presence of recirculation maxima on delays, multiple to a basic target delay and also to estimate and to compare resolution of the considered methods on a delay (range). There was, that only in cross correlation processing with recirculated transmitter reference on an interval of reference delays it is probable an achieving resolution ability on range in some times surpassing resolution of classical noise radar and actually reaching the superresolution effect. By virtue of high resolution this method demands the further profound studying, especially regarding for the development of combinational response rejection algorithms.

REFERENCES

1. Gupta, S. and T. R. Brown, "Noice-correlating radar based on retrodirective antennas," *IEEE Transactions on Aerospace and Electronic Systems*, Vol. 43, No. 2, 472–479, April 2007.
2. Chapursky, V. V. and V. I. Kalinin, "Ultrawideband noise radiolocation on basis of retrodirective antenna arrays with signal recirculation," *Radio Engineering and Electronics*, Vol. 53, No. 10, 1266–1277, 2008 (in Russian).
3. Kalinkevich, A. A., M. S. Krylova, and M. S. Turygin, "Ultrawideband signals in a radars, communications and acoustics," *Record of All Russian Science Conf.*, 415, Murom, Russia, July 1–3, 2003 (in Russian).
4. Lesturgie, M., J. P. Eglizeaud, D. Muller, B. Olivier, and C. Delhote, "The last decades and the future of low frequency radar concepts in France," *RADAR 2004, International Conference on Radar Systems*, 1SE-PLEN-3, Toulouse, France, 2004.
5. Poirier, J. L., "Quasi-monochromatic scattering and some possible radar applications," *Radio Science*, Vol. 3, No. 9, 881–886, 1968.
6. Chapursky, V. V. and V. I. Kalinin, "Efficiency of the double spectral analysis in noise radiolocation at presence of local subjects reflections," *Radio Engineering and Electronics*, Vol. 51, No. 3, 303–313, 2006 (in Russian).

Fractal Properties, Structural Entropy and Color of Printed Circuits Boards Processed by Laser Treatment

B. Varga[1], Sz. Nagy[2], and I. Mojzes[3]

[1]Temic Telefunken Microelectronic Hungary Kft., H-1106 Budapest, Napmátka u. 6., Hungary
[2]Department of Telecommunications, Széchenyi István University, H-9026 Győr, Egyetem tér 1., Hungary
[3]Department of Electronics Technology, Budapest University of Technology and Economics
H-1111, Budapest, Goldmann Gy. tér 3., Hungary

Abstract— Printed circuits boards (PCB) are sufficient parts of electronics appliances. Mass production of these devices requires identification of these products both during the technological steps (Traceability) and the services. The most effective way for marking these plates is to form data matrix code (DMC) on the surface and/or in-depth profiling of the solder masks up to the metallization. This is the first step in the surface mounted technology. In the course of the present work different PCB's were analyzed originating from 12 manufacturers. The data matrix was formed using Nd:YAG and CO_2 lasers with different power and duration.

Two types of PCB samples were investigated. In the first group, only discoloration of the solder mask appeared, which was caused by the laser beam penetrating into the layer only down to a depth of several µs (coloring). In the second case, the solder mask is completely removed up to the copper layer, according to the pattern of data matrix code (engraving). The marking process of the first case with CO_2 laser is much different from the removal of layer with Nd:YAG laser. The different wavelength causes different marking solution. Coloring requires a low energy laser pulse in contrast to the engraving.

In our paper we present the results of laser parameter optimization for the first laser types (coloring). Different layers need different coloring method, in order to avoid or reduce soot production during the coloring process. A new coloring measure system was developed for the PCB's identification, namely measuring the coloring in XYZ-color system. The XYZ values of solder mask layers are measured, and a software was developed for calculating automatically the color coordinates x and y and the brightness value L. The solder layers were analyzed using fractal mathematics, some pictures showed fractal behavior. The line sharpness of the grains of the solder masks' electron microscope pictures were also determined by using a structural entropy based method, which is able to derive the localization type of grid distributions.

1. INTRODUCTION

The mass production of the electronical devices require printed circuits boards that are traceable during the whole production line, the commerce, at the customer, in the services and during waste procession. Mostly, the PCBs are marked with a data matrix code, which is a two-dimensional rectangular pattern consisting of light and dark dots or squares, coding up to 2000 characters of information [1] with or without error correction. The marking process is usually carried out by laser pulses because of the durability of the resulting symbols. Two methods are applied in the industry. In the first case, the enamel or paint solder mask is completely removed from the copper plate of the PCB according to the patterns of the data matrix code, engraving the matrix into the SM. If multilayer enamel or paint is applied, the removal of various layers can result in multi-colored figures. This method is mostly used in labeling the controls of the devices. Because of the high necessary pulse energy, Nd:YAG lasers are usually applied [2, 3]. In the second method, the upper, several microns thick layer of the solder mask is laser treated, causing discoloration of the surface. The reason of the color change is usually structure changing of the SM material due to photothermal heating or a photo chemical process. The required pulses need to be of lower energy, thus CO_2 lasers are used [2].

In the engraving method for some solder masks the laser beam causes the upper layer to blow off the surface resulting in bad marking shapes. In the coloring method, the thickness and the material composition of the solder mask results in different colors for different PCBs. Often soot or other, non-preferable dark discoloring occurs. For getting the ideal result, in both cases, different pulse energy or pulse length is needed, which is usually determined by sample data matrix generation with a series of laser pulse energies. However, from the electron microscope images of the various SM surfaces one can suggest the required laser parameters prior to the laser markings. Numerical

characterization of the images of the solder masks is really important, since this data makes the correct laser choice easier. The present contribution describes three different methods for characterizing the solder mask, namely measuring color coordinates, fractal dimension and localization type.

2. COLOR MEASUREMENTS

The different colors of the solder masks of various manufacturers are easy to see. This depends not only on the layer thickness of the SM, but the material composition, too. Measuring color [4] can be carried out in many ways, the most natural of which is the luminance-chrominance determination. These color coordinates are near to the color detecting method of the human eye. Twelve samples of different manufacturers with different SM layer thickness are determined by a software developed for controlling the laser pulses. The measured data are summarized in Figure 1. The thick layers have relatively small luminance, the thinner ones are lighter, whereas the thin layers are usually a bit darker again. The solder mask with almost identical average layer thickness can have really different color shade, as it can be seen in case of the first few points of the second subplot, the rate of the two color coordinates vary hectically.

3. FRACTAL DIMENSION CALCULATIONS

The solder masks are analyzed by electron microscopy, too. In Figure 2 the electron microscopy images of three different plastic SMs are summarized. The various granularity can be studied. The more granular samples have usually BaS in the grains.
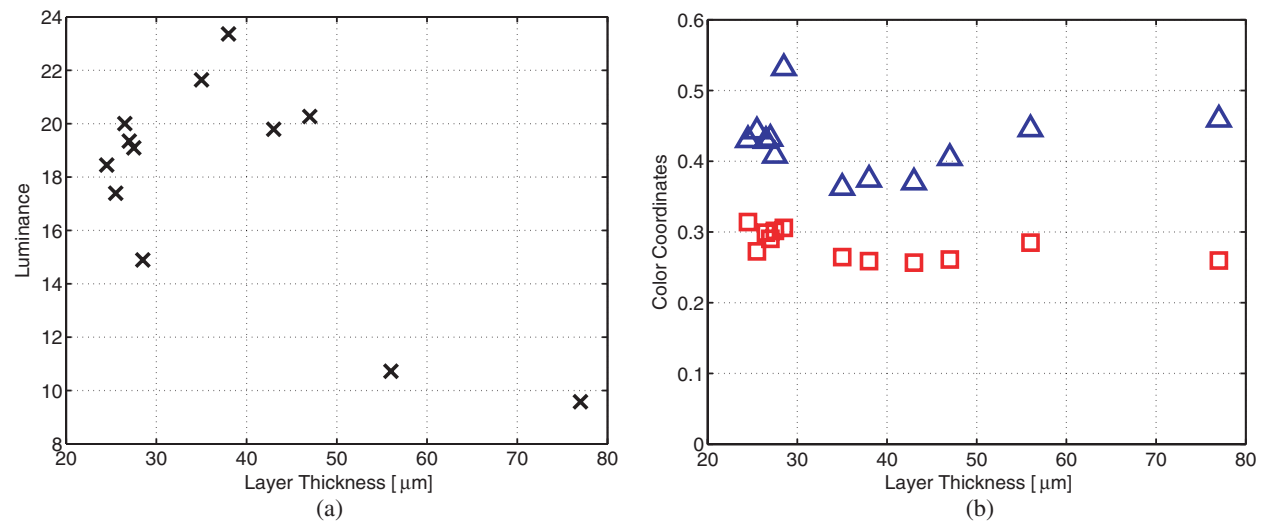
Figure 1: The luminance (a) and chrominance (b) coordinates of the printed circuits boards' solder masks of various manufacturers by means of the layer thickness.
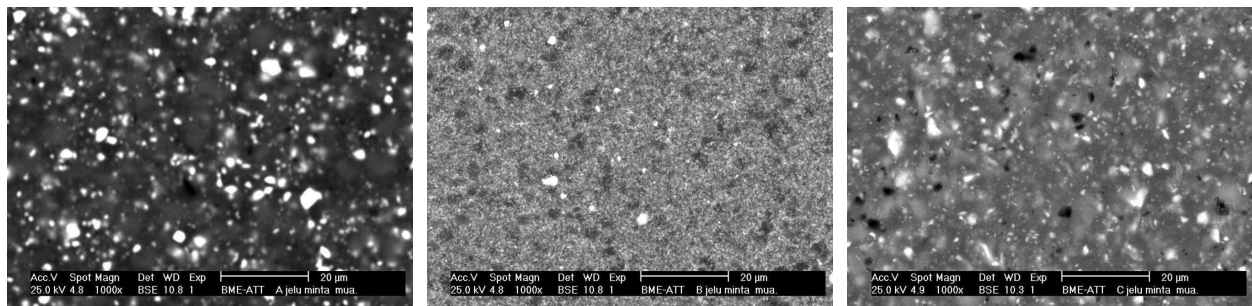
Figure 2: Electron microscopy images of various PCBs with plastic solder masks. Scale in the pictures.

In characterizing the topology of micro and nano structures, determination of the fractal dimension is a useful tool [5]. Fractal-like structures appear in many fields of science, from meteorology through chemistry to physics, e.g., thin metallic layers on compound semiconductor surfaces [6, 7].

Fractal dimension calculations were carried out by a commercial software package using standard box-counting algorithm. The resulting values are plotted in Figure 3, similarly to the luminance and color coordinates in the previous section. Most of the samples have fractal dimension about 1.8.

4. STRUCTURAL ENTROPY CALCULATIONS

Structural entropy was introduced by Pipek and Varga [8, 9] for characterizing mezoscopic electron systems modeled on a grid. Since grayscale electron microscopy images can be normalized in such a way that their sum luminance is 1, they can be treated as probability distributions on a regular grid. If the normalized intensity of the ith pixel is I_i, the following statements hold

$$I_i \geq 0, \qquad \text{for } i = 1, \ldots, N \tag{1}$$

$$\sum_{i=1}^{N} I_i = 1, \tag{2}$$

where N is the total number of pixels. Rényi entropies

$$S_n = \frac{1}{1-N} \ln \sum_{i=1}^{N} I_i^n \tag{3}$$

can be introduced for these grid distributions. The first of expressions (3) is the well known Shannon entropy.

The difference of Rényi entropies can characterize the type of localization of the distributions the following way. If the difference

$$S_{str} = S_1 - S_2 \tag{4}$$

of the first and the second Rényi entropy (the so called structural entropy) is plotted as a function of the difference of the zeroth and second entropy, all the distributions of the given localization type follow a given curve. The Gaussian localization e.g., is under the exponential localization curve, which is under the power law localization curves etc., no matter what the parameters of the distribution are. Examples of 2D distributions' localization curves can be seen as the lines in Figure 4. The method is valid for other Rényi entropy differences, too. For a detailed discussion, see [6, 10]. Figure 4 shows the localization maps of five different samples, too. Different colors and marker shapes mean different samples. The samples with mark ∘ and × match the second
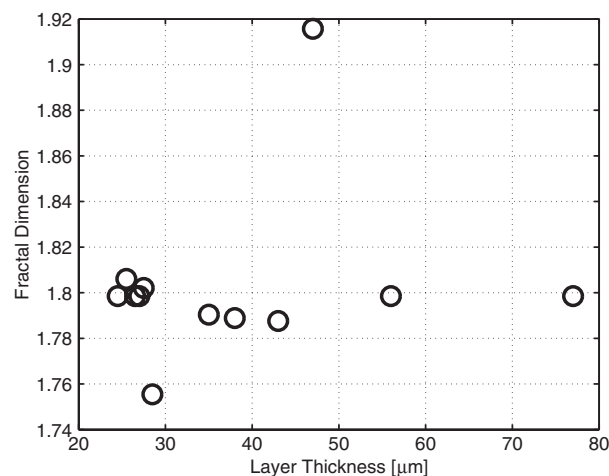
Figure 3: Fractal dimension as a function of the solder mask layer thickness of various PCB samples.
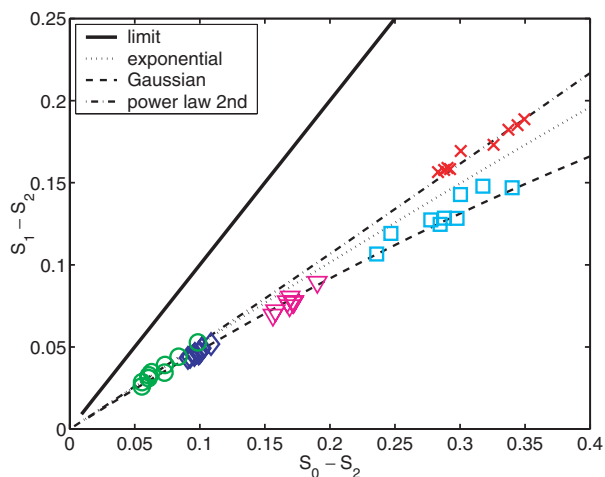
Figure 4: Localization plot of the solder mask layer thickness of 5 different PCB samples. The theoretical limiting curve of the possible points is also plotted as well as the localization curves of the Gaussian ($\sim \exp(-ar^2)$), exponential ($\sim \exp(-a|r|)$) and the second order power law ($\sim (1+ar)^{-2}$) distributions.

order power law curve very well, whereas the other samples follow Gaussian localization law: the tendency to zero of the electron microscopy images of samples with marks $\diamond$, $\triangledown$ and $\square$ is much slower than that of the other two samples.

Table 1: Fractal dimension, localization type, layer thickness, and color coordinates of printed circuits boards samples with various solder masks.

Fractal Dimension	Localization	Average Thickness [μm]	Luminance	Color x	Color y
1.7985	$\sim \exp(-|r|^3)$	77.0	9.5804	0.2596	0.4589
1.7985	$\sim \exp(-|r|^3)$	56.0	10.7230	0.2850	0.4453
1.9157	$\sim (1+r)^{-2}$	47.0	20.2676	0.2611	0.4045
1.7876	$\sim \exp(-r^2)$	43.0	19.7923	0.2567	0.3701
1.7889	$\sim \exp(-|r|^3)$	38.0	23.3601	0.2588	0.3739
1.7904	$\sim \exp(-r^2)$	35.0	21.6413	0.2645	0.3624
1.7554	$\sim \exp(-r^2)$	28.5	14.8930	0.3058	0.5316
1.8021	$\sim \exp(-r^2)$	27.5	19.0957	0.3016	0.4080
1.7985	$\sim \exp(-r^2)$	27.0	19.3463	0.2903	0.4317
1.7985	$\sim \exp(-r^2)$	26.5	20.0039	0.2990	0.4287
1.8061	$\sim \exp(-r^2)$	25.5	17.3931	0.2725	0.4423
1.7985	$\sim \exp(-|r|^3)$	24.5	18.4511	0.3140	0.4300
1.5392	$\sim (1+r)^{-2}$		21.7943	0.2716	0.4006
1.8440	$\sim \exp(-r^2)$		20.3489	0.3019	0.4385
1.7038	$\sim (1+r)^{-2}$		19.8118	0.3537	0.4874

5. CONCLUSION

The results of the measurements and calculations are summarized in Tab. 1. It can be seen, that the fractal dimension, the localization type, and the color properties are independent quantities, all three is needed for a proper characterization of the solder mask layers of the printed circuits boards. Tendencies can be recognized, the thicker samples are of darker color, the extreme fractal dimensions belong to quick, power law type localization.

ACKNOWLEDGMENT

REFERENCES

1. Standard Designation ISO/IEC 16022:2000(E), "International technology — International symbology specifiction — Data matrix," 2000.
2. Ready, J. F. and D. F. Farson, *LIA Handbook of Laser Material Processing*, Laser Institute of America Magnolia Publishing, Orlando, 2001. ISBN 0-912035-15-3.
3. Steen, W. M., *Laser Material Processing*, Springer-Verlag, London, 1998.
4. Hunt, R. W. G., *Measuring Colour*, 3rd Edition, Fountain Press, London, 1998.
5. Dávid, L., L. Dobos, B. Kovács, I. Mojzes, and B. Pécz, "Fractal character of in situ heat treated metal-compound semiconductor contacts," *J. Mater. Sci.: Mater. Electron*, Vol. 17, No. 4, 321–324, 2006.
6. Mojzes, I., C. Dominkonics, G. Harsányi, S. Nagy, J. Pipek, and L. Dobos, "Heat treatment parameters effecting the fractal dimensions of AuGe metallization on GaAs," *Appl. Phys. Lett.*, Vol. 91, No. 7, Article No. 073107, 2007.
7. Schuszter, M., L. Dobos, K. A. Nemcu, S. Nagy, and I. Mojzes, "Analysis of morphology changes of heat treated metallization of compound semiconductors by the fast wavelet-transform based on B-Spline," *J. Optelectron. Adv. Mat.*, Vol. 9, No. 7, 2241–2244, 2007.
8. Pipek, J. and I. Varga, "Universal classification scheme for the spatial localization properties of one-particle states in finite D-dimensional systems," *Phys. Rev. A*, Vol. 46, 3148–3164, 1992.

9. Pipek, J. and I. Varga, "Scaling behavior of energy functionals of highly complex distributions," *Int. J. Quantum Chem.*, Vol. 70, 125–131, 1998.

10. Varga, I. and J. Pipek, "Rényi entropies characterizing the shape and the extension of the phase space representation of quantum wave functions in disordered systems," *Phys. Rev. E*, Vol. 68, No. 026202, 2003.

Weak Signals Detection, Recovery Algorithms and Real Time Processing

Li-Ping Chen and Xiao-Juan Zhang

Institute of Electronics, Chinese Academy of Sciences, Beijing 100080, China

Abstract— The signals processing is essential and very important in weak signal detecting. In order to improve the SNR of the signals in the output of the system, digital signals processing algorithm is frequently used. In the paper, we studied some algorithms that can separate the weak signals from the noise. In the base-band of the detection system, based on a digital signal processing card and a notebook, we finished a platform that can process the signals in real time. We describe a modified single channel speech enhancement algorithm based on a spectral gain derived from MMSE-LSA and a minimum noise estimation approach. The proposed method does not need a voice activity detector to estimate the noise and renew the noise estimation in every frame to track varying level noise. Considering the properties of clean speech signal, we modified the spectral gain derived from MMSE-LSA. Extensive testing has shown that this algorithm can be implemented in real time and excellent noise suppression is achieved, while avoiding the musical residual noise phenomena and leading weak speech distortion.

1. INTRODUCTION

There are mainly two important components in the digital process algorithm: Noise power spectrum estimation and speech spectrum amplitude estimation. The algorithms described below are including mainly two methods of noise power spectrum estimation based on minimum statistic and speech spectrum amplitude estimation based on improved MMSE-LSA estimator. For post-process of the experiment data the results need storage. Meanwhile for the real time process we compose a real time process part of the weak vibration detection system using a data process card and a PC, which can translate the analog signals into digital signals, after processing and then translate it into analog signals again. Simple process algorithms are executed in PC.

In Section 2, we will present the algorithm of noise psd estimation and spectral amplitude estimator. Section 3 will present the real time process part of the weak vibration detection system. In Section 4, we will present the experiment results and post-process results using the algorithm.

2. DESCRIPTION OF ALGORITHM

The output signals represent the weak vibration excited by the speech signals and have some distortion. Here we consider the additive distortion only. The sampled signal of the microwave receiver base-band output is a sum of a speech signal $s(i)$ and a noise $w(i)$, $y(i) = s(i) + w(i)$, where i denotes the time index. We further assume that $s(i)$ and $w(i)$ are statistically independent.

2.1. Noise Estimation

R. Martin proposed a noise power spectrum estimation method [6] based on minimum statistic. The minimum statistics method rests on two observations namely that the speech and the disturbing noise are usually statistically independent and that the power of a noisy speech signal frequently decays to the power level of the disturbing noise. We consider a recursively smoothed periodogram

$$P(\lambda, k) = \alpha(\lambda, k)P(\lambda - 1, k) + (1 - \alpha(\lambda, k))\left|Y(\lambda, k)\right|^2 \tag{1}$$

The noise psd $\widehat{\sigma}_w(\lambda, k)$ is derived from the smoothed signal psd estimate $P(\lambda, k)$. A time-varying and possibly frequency dependent smoothing parameter $\alpha(\lambda, k)$ is used to make $P(\lambda, k)$ satisfy conflicting requirements. The final smoothing parameter is

$$\widehat{\alpha}(\lambda, k) = \frac{\alpha_{\max}\alpha_c(\lambda)}{1 + \left[P(\lambda - 1, k)/\widehat{\sigma}_N^2(\lambda - 1, k) - 1\right]^2} \tag{2}$$

In the time length of about 1.5 s sliding window the minimum are searched and bias compensated

$$P_{\min}(\lambda, k) = \min\left\{P(\lambda - D + 1, k), \ldots, P(\lambda - 1, k), P(\lambda, k)\right\} \tag{3}$$

The noise psd $\widehat{\sigma}_w(\lambda, k)$ is

$$\widehat{\sigma}^2_w(\lambda, k) = \frac{P_{\min}(\lambda, k)}{E\{P_{\min}(\lambda, k)\}|_{\sigma^2_w(\lambda, k)=1}} = B_{\min}(D, Q_{\text{eq}}(\lambda, k)) P_{\min}(\lambda, k) \tag{4}$$

2.2. Spectral Amplitude Estimator

The observed noisy speech signal is given by

$$y(t) = s(t) + w(t), \qquad 0 \le t \le T \tag{5}$$

where without loss of generality, we let the observation interval be $[0, T]$. Let $X_k \triangleq A_k \exp(j\alpha_k)$, D_k, $Y_k = R_k \exp(j\vartheta_k)$ denote the kth spectral component of signal $x(t)$, the noise $w(t)$, and the noisy observations $y(t)$ respectively.

Y. Ephraim and D. Malah proposed a spectral amplitude estimator [3]

$$G^{\text{LSA}}(k) = \frac{\xi_k}{1 + \xi_k} \exp\left\{\frac{1}{2} \int_{v_k}^{\infty} \frac{e^{-t}}{t} dt\right\} \tag{6}$$

Here we make some improvements based on the estimator above. Let

$$G'(k) = \left(\frac{\xi_k}{\beta + \xi_k}\right)^{\alpha} \exp\left\{\frac{1}{2} \int_{v_k}^{\infty} \frac{e^{-t}}{t} dt\right\} \tag{7}$$

where α, β can be tuned to be fit for different situation. Meanwhile the speech absent probability is involved to improve the spectral amplitude estimator.

$$G^{\text{fin}} = G_M(k) G'(k) \tag{8}$$

$G_M(k) = \left\{1 + \frac{q_k}{1-q_k}(1 + \xi_k) \exp(-v_k)\right\}^{-1}$, q_k is the priori speech absent probability.

3. REAL TIME PROCESS PART

We use a data process card that can translate both digital and analog signals into each other, a PC compose the real time process part. It can store and process the experiment data and it works on multi-thread theory. In order to deny the loss of the experiment data, we use the multi-FIFO memory method. The block diagram is as follow.
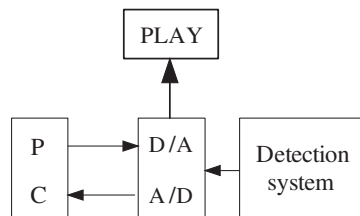
Figure 1.

4. EXPERIMENT RESULTS

Here is the original speech signal in Figure 2.

Using the weak signal detection system and the real time process part, we get the baseband signal experiment result in Figure 3.

Using the algorithm of this paper, we get the results after process in Figure 4.

There is something to announce that the detection system has its own convolution distortion so the result is needed to be further processed. That is a point we will do some improvements.
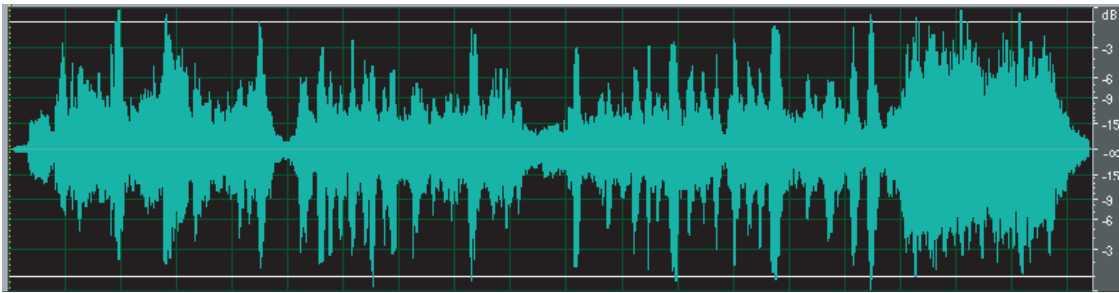
Figure 2. Original speech signal.
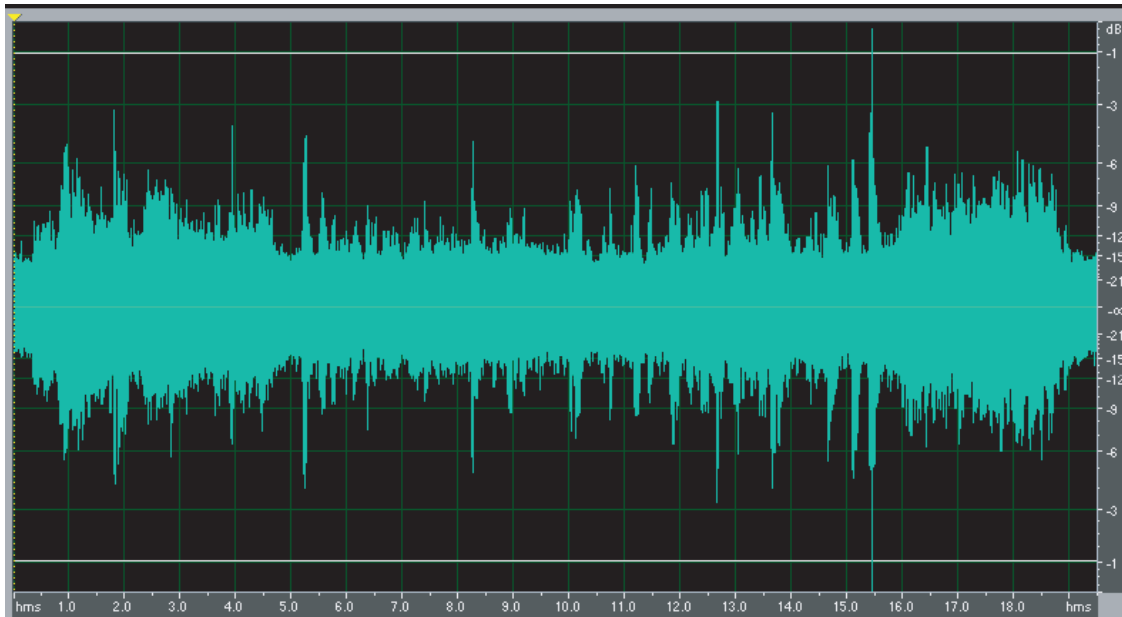
Figure 3. Experiment results.
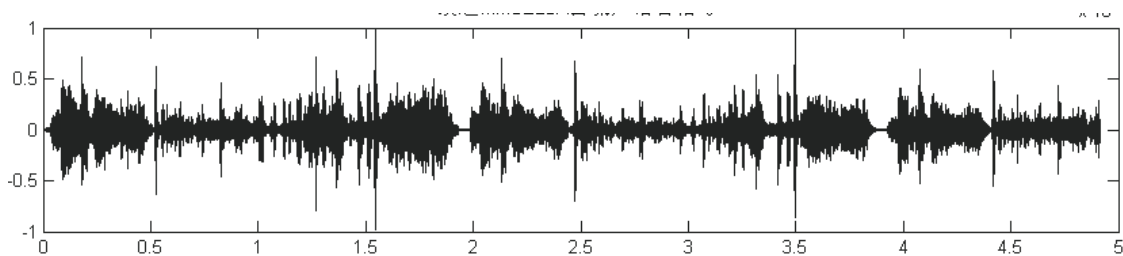
Figure 4. Results after process.

REFERENCES

1. Berouti, M., R. Schwartz, and J. Makhoul, "Enhancement of speech corrupted by acoustic noise," *Proceedings of 4th IEEE International Conference on Acoustics, Speech and Signal Processing, ICASSP-79*, 208–211, Washington DC, April 2–4, 1979.

2. Ephraim, Y. and D. Malah, "Speech enhancement using a minimum mean-square error short-time spectral amplitude estimator," *IEEE Trans. Acoust. Speech Signal Process.*, Vol. 32, No. 6, 1109–1121, December 1984.

3. Ephraim, Y. and D. Malah, "Speech enhancement using a minimum mean-square error short-time log-spectral amplitude estimator," *IEEE Trans. Acoust. Speech Signal Process.*, Vol. 33, No. 2, 443–445, April 1985.

4. Martin, R., "An efficient algorithm to estimate the instantaneous SNR of speech signals,"

Proceedings of the 2nd European Conference on Speech, Communication and Technology, EU-ROSPEECH'93, 89–792, Berlin, Germany, September 21–23, 1994.

5. Martin, R., "Spectral subtraction based on minimum statistics," *Proceedings of the 7th European Signal Processing Conference, EUSIPCO-94*, 1182–1185, Edinburgh, Scotland, September 13–16, 1944.

6. Martin, R., "Noise power spectral density estimation based on optimal smoothing and minimum statistics," *IEEE Trans. Speech Audio Process.*, Vol. 9, No. 5, 504–512, July 2001.

7. Malah, D., R. V. Cox, and A. J. Accardi, "Tracking speech-presence uncertainty to improve speech enhancement in non-stationary noise environments," *Proceedings of IEEE International Conference on Acoustics, Speech, and Signal Processing*, 789–792, 1999.

8. Martin, R., "Bias compensation methods for minimum statistics noise spectral density estimation," *Signal Processing*, Vol. 86, No. 6, 1215–1129, 2006.

Three-dimensional Views of Buried Objects from Holographic Radar Imaging

M. Inagaki[1], C. G. Windsor[2], T. Bechtel[3], E. Bechtel[3], S. Ivashov[4], and A. Zhuravlev[4]

[1]Walnut Ltd, Japan
[2]116, New Road, East Hagbourne, OX119LD, UK
[3]Enviroscan Inc, USA
[4]Remote Sensing Laboratory, Bauman Moscow State Technical University, Russia

Abstract— Holographic radars produce a plan view in a grey scale. They operate at 5 discrete frequencies of continuous waves from 3.6 to 4.0 GHz. Since the phase of the reflected wave is dependent upon target depths, the strength of the received wave varies with depth. It produces periodic stripes for a slanting flat object. The stripes correspond to the unlabelled contour lines on geographical maps. Slightly changing frequency shows the slanting direction that allows us to label the contour lines. A two-dimensional image with corresponding labeled contour lines could make a three-dimensional view of buried objects by some suitable software. It is an additional merit of holographic radar.

1. INTRODUCTION

Conventional pulsed radar produces an image along an underground vertical section. The image is a two-dimensional view. The main purpose is to locate the positions and the depths of buried objects and to delineate layer boundaries. In contrast holographic radar produces a plan view in a selected rectangular area. The image is also two-dimensional but horizontally. The main purpose is to visualize the shapes of buried objects in silhouette [2–4]. The received gain varies with the phase position of the continuous wave. If an object is large enough to include reflections from different phase positions ranging over more than one cycle, the phase effect may appear as plural black and white stripes on the image. The stripes play a role like contour lines on a geographical map. Contour lines possess the depth information. As a result the three-dimensional view could be reconstructed from a two-dimensional holographic radar image. It has been demonstrated that the stripes appearing on radar images are close to those theoretically predicted using some artificial objects.

2. PHASE PHENOMENON

Holographic radar, which is called the RASCAN system, produces a plan view in a grey scale. It operates at 5 discrete frequencies of continuous waves from 3.6 to 4.0 GHz with two receiving antennae in parallel and cross polarizations relative to the transmitter. As a result, two sets of five images are obtained.

The characteristic of the radar image is due to phase [2, 4]. The reflected wave is observed at different phase position due to target depth or signal frequency. Actually, reflections come back from wide range of directions. But usually the perpendicular direction is dominantly strong. Therefore, the distance to an object may be expressed by depth. An object appears black on the radar image if the depth coincides with close to positive max of the continuous wave, and appears white if it coincides with close to negative max. Of course there may be an unfortunate case where it coincides with zero gain position, where the object will not be recognized on the image. The schematic view is shown in Figure 1. If an object is large enough (around the size of the wavelength in the soil) and lying in the corresponding depths ranging phases more than one cycle, phase phenomenon can be seen on an image.

For instance, scans over a slanting aluminium plate using the RASCAN system produce a radar image with repeated black and white stripes [1]-dubbed the *zebra effect* (Figure 2).

The intervals of the stripes are different with the slanting angles. The larger the angle is, the smaller the intervals are. The zebra stripes similarly correspond to topographic contour lines on a map, as if a precipitous mountain has compressed contour lines on a map. The only difference is that the datum is sea level on a map and is a distance from the antenna on a radar image. This difference is nothing critical. The problem is that, similar to unlabelled topographic contour lines, the zebra stripes without independent depth information entail concavo-convex ambiguity.
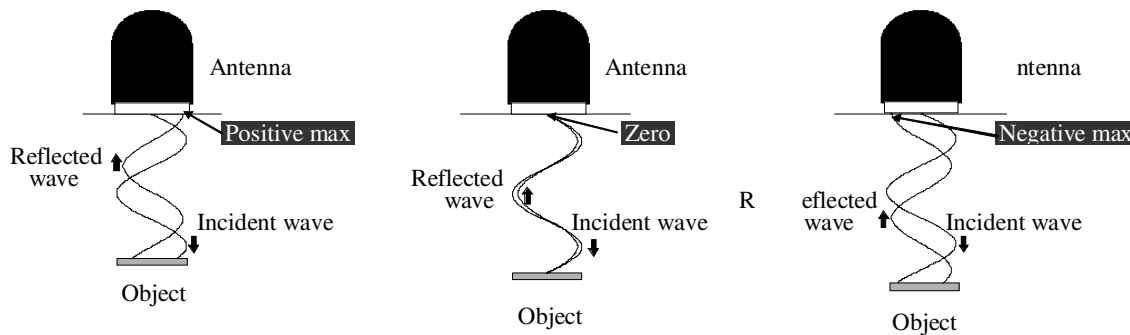
Figure 1: Strength of reflected wave that varies with the depth of an object.
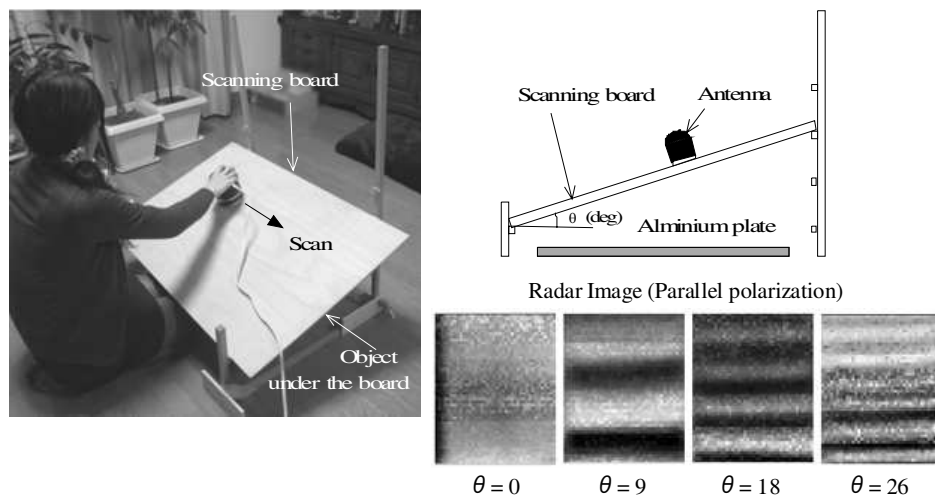
Figure 2: GPR image from aluminium plate with various angles (Showing the zebra effect).
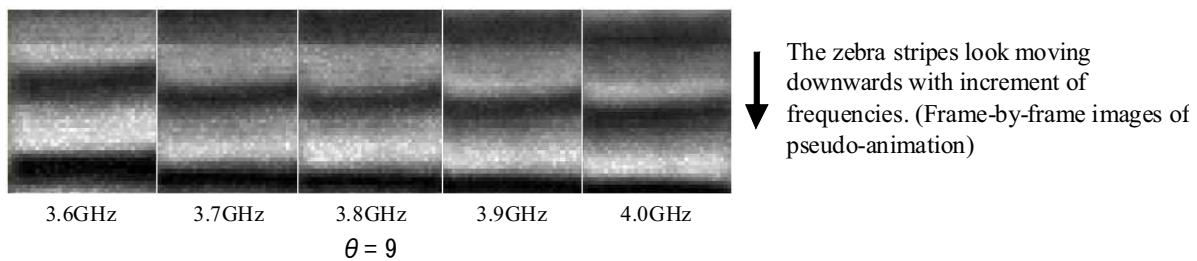
Figure 3: Holographic radar images with aluminium plate (Basic sample of the zebra shift).

When viewing the five images from differing frequencies frame-by-frame, pseudo-animated view can be seen (See Figure 3). In this animation, the widths of the stripes shorten with increasing frequency. Thus, the zebra stripes produced by the inclined aluminium plate appear to move in the animation, which creates the stripes moving to one way. The moving direction points to the position where the antenna is close to the slanting aluminium plate. This phenomenon is dubbed the *zebra shift*.

There are very obvious images showing the *zebra shift* (See Figure 4). In further testing, RAS-CAN produced concentric circle zebra stripes over a hemispherical steel bowl. From a single RAS-CAN image, the hemispherical shape can be seen, but it cannot be told whether the bowl lies concave up or down. The bowl animation reveals that if the concentric circles expand outwards, the bowl lies concave up. If the stripes shrink inwards, the bowl lies concave down. Thus, it has been found that the animation of multiple frequency images is an effective way to determine relative heights of zebra stripes on image by observing the zebra shift.

Concave down (Parallel polarization)

| Object | 3.6GHz | 3.7GHz | 3.8GHz | 3.9GHz | 4.0GHz |

Concave up (Parallel polarization)

| Object | 3.6GHz | 3.7GHz | 3.8GHz | 3.9GHz | 4.0GHz |
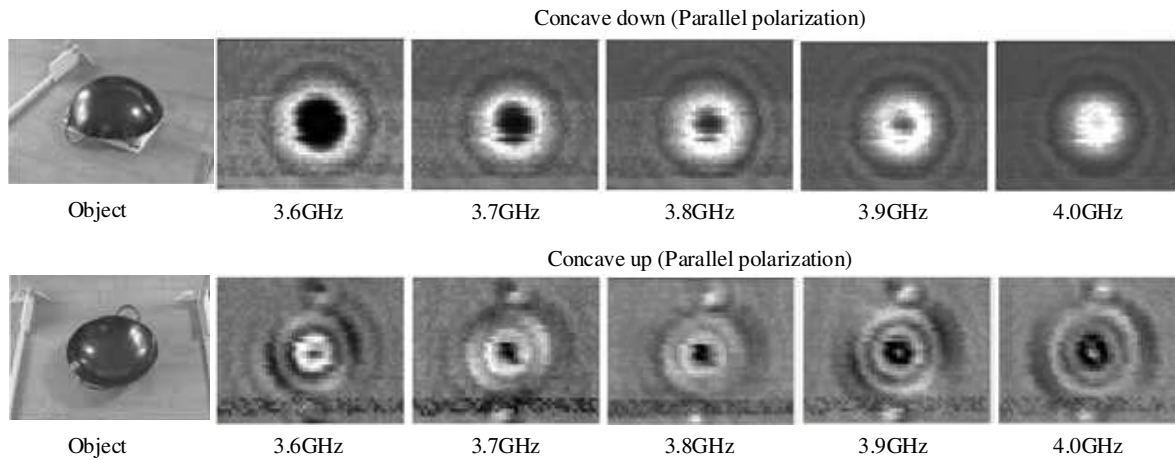
Figure 4: Radar images with hemispherical bowl (Obvious sample of the zebra shift).

$\theta = 0$ $\theta = 9$ $\theta = 18$ $\theta = 26$

Actual GPR images (4GHz, Parallel)

Object (Pyramid)
300mm square base
100mm height

Simulated images (Corresponding to 4GHz, Parallel)
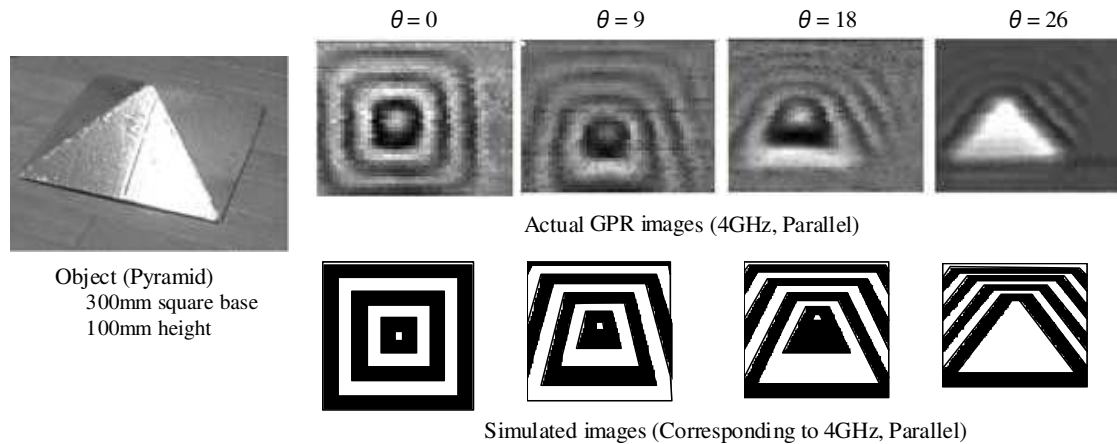
Figure 5: Comparison between actual GPR images and the simulated images.

3. EXPERIMENT

Aluminium plate and a bowl have simple shapes. If an object has a slightly more complex shape, the reflected image might be distorted. A pyramid-shaped test object, with 300 mm square base and 100 mm height was prepared (See Figure 5). A thin aluminium film was placed on the pyramid surface. Holographic images have been recorded in four different angles with the apex directly up, to 30 degrees from vertical. The resulting radar images show zebra stripes. As the distances from antenna to the reflected point on the pyramid surface are known, we produced a simulated image to show how the stripes would look for 4.0 GHz wavelength. Although the stripes are a little rounded on the images, they look very similar to the simulated contour lines in any angular position. Thus a slightly smoothed three-dimensional view of the pyramid will be able to be reconstructed by digitizing the contour lines and applying suitable geographical software.

There is another model. In order to demonstrate the identification of concavo or convex, a test object shaped like a volcanic island was prepared (See Figure 6). It is like a mountain annexed with another small hill. There is a crater on the top of the volcano. The size of the mountain is 300 mm diameter round base and 100 mm height with 180 mm diameter and 40 mm depth crater. The size of the annexed hill is 150 mm diameter round base and 30 mm height. The image is shown in Figure 6.

Several concentric circles with the top of the mountain as the center are seen. Halfway up the mountain a white contour line is smoothly connected to the hillside, and forms the shape of a bottle guard. It well expresses the continuity of the same height line. There are some remarkable points (A to C) on the image. A white circle (represented by point A) shifts rightwards with increment of frequencies. That is the direction of shrinking inwards. However, a white dot (pointed by point B) gets larger and a black dot newly appears atop the mountain. That is the direction of expanding
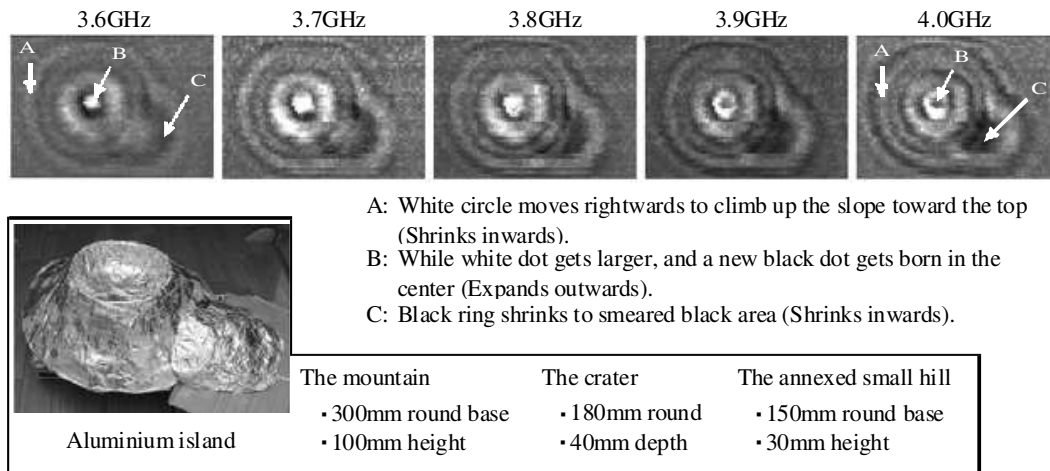
Figure 6: Holographic radar image on the artificial island with volcano.

outwards. Furthermore, a black ring (represented by point C) shrinks to an indistinct black area. All of these phenomena allow us to identify whether concentric circles shows concave up or down. Thus, the zebra stripes are labeled with the help of the zebra shift.

4. CONCLUSIONS

Holographic radar has been proven to have an additional merit. It tells not only the existence of buried objects but also three-dimensional shapes by its phase characteristic. Actual buried objects will not always provide such simple geometry, the burial medium may have differing water content, and there may be clutter objects as well. All of these could distort the zebra stripes. However, these tests demonstrate that the holographic radar images contain information, similar to topographic contour maps, which could produce a three-dimensional view of buried objects.

REFERENCES

1. Windsor, C. G., A. Bulletti, L. Capineri, P. Falorni, S. Valenini, S. Matucci, M. Inagaki, T. D. Bechtel, F. Bechtel, E. Bechtel, A. Zhuravlev, and S. Ivashov, "Depth information from holographic radar scans," *Progress In Electromagnetics Research Symposium, PIERS2009*, Moscow, Russia, August 18–21, 2009.

2. Ivashov, S. I., V. V. Razevig, I. A. Vasilyev, A. Zhuravlev, T. D. Bechtel, and L. Capineri, "The holographic principle in subsurface radar technology," *International Symposium to Commemorate the 60th Anniversary of the Invention of Holography*, 183–197, Springfield, Massachusetts USA, October 27–29, 2008.

3. Ivashov, S. I., I. A. Vasilyev, T. D. Bechtel, and C. Snapp, "Comparison between impulse and holographic subsurface radar for NDT of space vehicle structural material," *PIERS Online*, Vol. 3, No. 5, 658–661, 2007.

4. Chapursky, V. V., S. I. Ivashov, V. V. Razevig, A. P. Sheyko, and I. A. Vasilyev, "Microwave hologram reconstruction for the RASCAN type subsurface radar," *Proceedings of the Ninth International Conference on Ground Penetrating Radar, GPR'2002*, 520–526, Santa Barbara, California USA, April 29–May 2, 2002.

Diagnostics of Mediums and Line Objects, Probing with Ultra-wideband Short-pulse Signals

A. Yu. Grinev[1], A. V. Andriyanov[2], D. V. Bagno[1], V. S. Temchenko[1], E. V. Ilyin[1], and D. V. Nikishov[1]

[1]Moscow Aviation Institute (State Technical university), Russia
[2]"Tenzor" Co. Ltd., Russia

Abstract— The new multi-channel Ground Penetrating Radar (GPR) design is presented for search of metallic and dielectric objects in soil down to 1.2 meters depth. GPR parameters, its hardware and software are discussed. Computational diagnostics method is discussed for parameters restoration of subsurface objects and mediums. Experimental results are presented.

1. INTRODUCTION

Generally, Ground Penetrating Radar (GPR) technologies are used for detection, identification and diagnostics of objects through optically opaque but radio transparent medium. In particular, GPR applications include inspection of underground communication lines, soils, road coatings, airport runways, localization of fuel leakage out of underground storages, measurement of underground water level, demining, geophysical and archeological investigations, as well as search and identification of other different inhomogenities inside of the ground [1]. Substantial specifics of GPR equipment is implementation of ultra-wideband (UWB) sounding signal which propagates through extremely lossy and dispersive medium (soil).

Traditionally, procedures of interpretation of incoming data and identification of detected inhomogenities (underground objects) are accomplished by operator (the human). Considerable role of human brings down the reliability of inspection and limits inspection rate, thereby reduces GPR productivity and prevents GPR usage in variety of applications. The reliability of diagnostics and identification of subsurface mediums and objects can be enhanced by development and implementation of procedures of their geometrical and electrophysical parameters restoration. Besides other important stages, these procedures must solve inverse problem of electromagnetic wave scattering.

The organization of this paper is as follows. In Section 2, the structure and key features of designed GPR software is briefly disclosed. The software is based on Computational Diagnostics Method (CDM). The general formulation of the CDM is given in Section 3. CDM applications for plane-layered medium diagnostics and underground metallic cylinder diagnostics are discussed in Sections 4 and 5 respectively. In Section 6, experimental multi-channel GPR setup is presented. Experimental results of layered medium and underground object diagnostics are discussed in Section 7. Finally, paper is concluded with a brief summary.
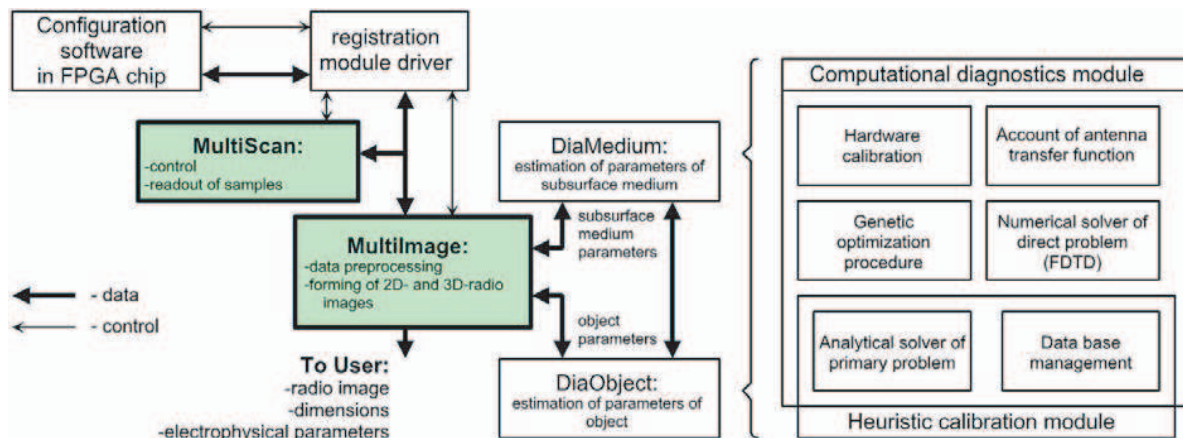
Figure 1: Structure of GPR software package "ComDia".

2. GPR SOFTWARE

The structure of "ComDia" ("Computer Diagnostics") software is shown in Fig. 1. "MultiScan" and "MultiImage" programs provide graphic user interface, control GPR transmitter/receiver and accept the data from it, visualize B- and C-scans, form 2D and 3D radio images of subsurface objects. As well, "MultiImage" launches "DiaMedium" and "DiaObject" software modules designed for estimation of geometry and electrophysical parameters of subsurface medium and objects inside of it.

The following procedures are integrated in GPR software at present time: radio images forming by use of reverse projections method and range migration method [1]; geometrical and electrophysical parameters measuring for plane-layered subsurface medium using CDM; identification of typical subsurface objects using CDM and radio images analysis [1–3].

3. COMPUTATIONAL DIAGNOSTICS METHOD (CDM)

The CDM [2] is applied for restoration of geometrical (d_i) and electrophysical (ε_i, μ_i, σ_i) parameters of subsurface mediums and objects basing on radio waves. This task belongs to a class of inverse problems of scattering. The task is formulated as the estimation of vector $\mathbf{x} = (\varepsilon_i, \mu_i, v\sigma_i, d_i)$, $i = 1 \ldots N$, where N is object count, basing on measured scattered field $\mathbf{u}$. In general case, $\mathbf{u}$ have to be measured in some frequency band and some spatial angular sector. Both $\mathbf{x}$ and $\mathbf{u}$ are related by operator equation of the first kind:

$$\mathbf{Ax} = \mathbf{u}, \quad \mathbf{x} \in \mathbf{X}, \ \mathbf{u} \in \mathbf{U}, \tag{1}$$

where $\mathbf{A}$ is totally continuous and (in general case) nonlinear operator; $\mathbf{X}$ and $\mathbf{U}$ are metric spaces.

Following CDM, the solution comes in form of global extremum search of smoothed functional

$$\Phi_\alpha(\mathbf{x}, \mathbf{A}, \mathbf{u}_\Delta) = \|\mathbf{Ax} - \mathbf{u}_\Delta\|_{\mathbf{U}}^2 + \alpha \left[\mathbf{\Omega}(\mathbf{x}) + \gamma \|\mathbf{x} - \mathbf{x}_0\|_{\mathbf{X}}^2 \right], \tag{2}$$

and the solution $\tilde{\mathbf{x}}_{\alpha\Delta}$ itself is found as a result of minimization of (2):

$$\tilde{\mathbf{x}}_{\alpha\Delta} = \{\mathbf{x}_{\alpha\Delta} : \inf \left[\Phi\alpha(\mathbf{x}, \mathbf{A}, \mathbf{u}_\Delta) \right]\}. \tag{3}$$

The first summand in the right part of (2) is the discrepancy function of measured scattered field $\mathbf{u}_\Delta$ (its space-time distribution) and result $\mathbf{Ax}$ of the direct problem solution. Always there is some difference $\|\mathbf{u} - \mathbf{u}_\Delta\| \leq \Delta$ between true ($\mathbf{u}$) and measured ($\mathbf{u}_\Delta$) distributions of scattered field which is caused by inaccuracy of measurements and approximative nature of model. Detailed form of the first summand in (2) depends on data acquisition strategy: in case of purely "spatial" data, i.e., variation of aspect angle θ at fixed frequency ω_0 during the sounding, it has a form

$$\|\mathbf{Ax} - \mathbf{u}_\Delta\|_{\mathbf{U}}^2 = \int_{\theta_1}^{\theta_2} \left\{ \mathbf{A}(\omega_0, \mathbf{x}) - \mathbf{u}(\omega_0, \theta) \right\} \cos\theta \, d\theta; \tag{4}$$

in case of "temporal" (spectrum) data, i.e., variation of radio frequency ω at fixed position θ_0, it has a form

$$\|\mathbf{Ax} - \mathbf{u}_\Delta\|_{\mathbf{U}}^2 = \int_{\omega_1}^{\omega_2} \left\{ \mathbf{A}(\theta_0, \mathbf{x}) - \mathbf{u}(\theta_0, \omega) \right\}^2 d\omega. \tag{5}$$

The second summand in the right part of (2) is stabilizing add-on, and α is regularization parameter. Positively defined functional $\Omega(\mathbf{x})$ forces a choice of the most simple solution $\tilde{\mathbf{x}}_{\alpha\Delta}$ from a set of possible solutions $\mathbf{X}_\Delta : \|\mathbf{A}\tilde{\mathbf{x}}_{\alpha\Delta} - \mathbf{u}_\Delta\|_{\mathbf{U}}^2 \leq \Delta^2$. If necessary, the second stabilizer $\gamma \|\mathbf{x} - \mathbf{x}_0\|_{\mathbf{X}}^2$ is activated. It forces a choice of that solution from a set $\mathbf{X}_\Delta$ which is mostly close to hypothetical solution $\mathbf{x}_0$ built basing on *a priori* information. Here weighting factor γ reflects amount of *a priori* information.

For arbitrary mediums and objects, the direct problem $\mathbf{Ax}$ is solved numerically on a grid of frequencies ω_n within finite frequency band $\Delta\Omega$. While choosing solution, all artifacts should be taken into account which distort both the sounding and the scattered waves. The strongest distortions are those which caused by vector effective height of transmit/receive antenna of the GPR and by radio frequency channel of the GPR. Methods of FDTD, FEM and MoM were tested for the direct problem solution depending on particular medium and object. Because the functional (2) is non-convex and multi-extremal, numerical methods of global optimization were involved for the global extremum search. We have found that Genetic algorithm and Bees algorithm are the most effective one.

4. DIAGNOSTICS OF SUBSURFACE MEDIUM

Plane-layered medium have been chosen as the basic model. Vector of parameters $\mathbf{x} = (\varepsilon_i, \mu_i, \sigma_i, d_i)$ is formed of each layer parameters ($i = 1 \dots N$, N is the number of layers in the model). Traditional methods of diagnostics of layered mediums (which are based on ray conception) have limited applicability since they are: unsuitable for "thin" layers; disuse signal information completely; totally ignore fundamental distortions caused by GPR antenna and nonflat frequency response of receiver. So other methods were considered which provide better reliability of diagnostics due to better correspondence between calculated scattering and the measured scattering. We have chosen and tested the following methods: "virtual source" [3, 4]; approximation by a set of elementary dipoles; decomposition of a field to plane waves [4].

"Virtual source" method assumes partial account of characteristics of transmit/receive antenna: the scattered field distribution is substituted by that one produced by a single elementary electric dipole. The dipole is placed above the medium at position of phase center of the real antenna (e.g., T-horn). Frequency response of the real antenna is measured and is taken into account while angular directivity of the real antenna is ignored [4].

Unlike this way, we have proposed and tested "dipole approximation" which provides more accurate account of antenna performance basing on comprehensive electromagnetic simulation. Electromagnetic field produced by real transmitting antenna is represented by a field produced by equivalent system of electric (magnetic) dipoles which is arranged on the antenna aperture plane. Parameters of the "dipole approximation" are: quantity, positions, moments (orientations, amplitudes and phases) of the dipoles. The following two approaches of finding appropriate "dipole model" parameters of the real antenna in GPR operating frequency band were considered. Following the first approach, the moments of electric (magnetic) dipoles are found basing on tangential component of electric (magnetic) field distribution on a plane located in the near zone of the real antenna. Field distribution can be found either from numerical simulation of antenna or measured [3]. The second approach is based on reciprocity theorem and uses electrical signals registered on the antenna input terminals both in transmit and receive mode. In receive mode, reflection from flat metallic screen is registered [3, 4]. Correspondence between the real antenna field and the "dipole model" is set up by implementation of either Method of moments or some of methods of global optimization.

The "dipole approximation" was numerically verified for a single electric dipole and for a "dipole model" of real antenna (T-horn). The "dipole model" of T-horn is built basing on the results of numerical calculation of T-horn field in the near zone. Further, for the purpose of finding scattered field from plane-layered medium, an incident field is decomposed to a limited combination of E- and H-waves for each frequency ω_n. During iteration procedure of finding (3), Fresnel coefficients and scattered waves are calculated for every plane wave and given $\mathbf{x}$ and ω_n. Then received signal is calculated at antenna terminals using reciprocity theorem [3]. So performance of the real GPR antenna is taken into account in the functional (2).

5. DIAGNOSTICS OF METALLIC CYLINDER IN SOIL

The measurement of diameter of subsurface long conductive cylinder (to classify a pipe or a cable) is based on *a priori* information about plane wave scattering on different polarizations. In case of cross-polarized incident wave, cylinder Radar Cross Section (RCS) or its transfer function has interference peaks and fades. The frequency f_1 of the first interference peak $f_1 = c_0/\pi D\sqrt{\varepsilon}$, where c_0 is electromagnetic wave speed in free space and ε is relative dielectric permittivity of a soil. Moderate loss of creeping wave energy is required to detect interference structure of RCS.

Both measured and calculated transfer functions of the object are used in CDM functional (2). The transfer function of object (cylinder) K_{Obj} is determined here in simplified form as a relation of spectrum densities of strengths of electric field component of scattered plane electromagnetic wave E_2 and incident plane electromagnetic wave E_1:

$$K_{Obj}(\mathbf{r}_1, \mathbf{r}_2; f) = E_2(\mathbf{r}_2; f)/E_1(\mathbf{r}_1; f), \tag{6}$$

where $\mathbf{r}_1$, $\mathbf{r}_2$ are the plane waves' propagating vectors. To apply CDM correctly, the most artifacts must be eliminated. For this, in addition to investigating object reflection s_{Obj}, the following two signals must be recorded: reflection s_{Ref} from the reference subsurface object (an object with known transfer function K_{Ref}) and reflection s_{BKGND} from the background [3]. The further processing is

made according to the equation

$$\tilde{K}_{Obj} = \frac{\widehat{\Im}\left\{ (s_{Obj} - s_{Obj.BKGND}) \cdot w_3 \right\} \cdot \widehat{\Im}\left\{ s_{Ref} \cdot w_2 \right\}}{K_{Ref} \cdot \widehat{\Im}\left\{ (s_{Ref} - s_{Ref.BKGND}) \cdot w_1 \right\} \cdot \widehat{\Im}\left\{ s_{Obj} \cdot w_4 \right\}}, \tag{7}$$

where: $\widehat{\Im}\{\ldots\}$ is discrete Fourier transform operator; w_1 and w_3 are range strobes which select reflections caused by reference and investigating objects; w_2 and w_4 are range strobes which are used for GPR long-term instability compensation (w_2 and w_4 selects some specific permanent reflecting region inside the GPR signal channel, e.g., T-horn antenna feed point).

6. EXPERIMENTAL MULTI-CHANNEL GPR SETUP

For experimental verification of proposed CDM-based approach, multi-functional GPR has been designed (Fig. 2). The GPR consists of registering module 9 (UWB short-pulse signal generator, low-noise preamplifier, stroboscopic receiver, computer interface), pin-diode antenna switch 8, seven-element antenna module 3, power supply (4, 6) and laptop computer 2 with control and processing software (see Fig. 1). All modules are mounted on four-wheel cart. In Fig. 2 also: 1 — laptop protective housing, 5 — handles, 7, 13 — fiberglass tubes, 10 — calibration channel socket, 11 — antennas, 12 — radio transparent basement.

The GPR performance parameters: outgoing waveform — a single period of sine wave, pulse width — 1 ns, repetition rate — 1 MHz, amplitude — 25 V, operating bandwidth — 1.4 GHz (0.6...2.0 GHz), controlled amplification range — 80 dB, number of samples on a time sweep — up to 1024, power budget — 100 dB. GPR antenna is array of screened T-horns with dielectric filling (WA1–WA7 in Fig. 2) arranged in staggered rows, SWR — 2 : 1 or less, power gain of a single element — 5 dBi at 1 GHz. Samples step in direction of GPR movement — 5 cm; minimal samples step in depth — 0.5 mm (for moisten sand with $\varepsilon = 3.8 \ldots 4.3$ and 25 ... 30 dB/m loss at 1 GHz). The samples step in cross direction (15 cm) was chosen as a compromise to obtain a qualitative radio image. As long as the single T-horn aperture size (25×30 cm) exceeded that value, the seven elements were combined in two lines (four elements in front line and three in rear line) and arranged in staggered rows. The mutual coupling among closely spaced elements was essentially reduced by dissipative screening of each element. Resolution in depth direction — 10 cm, in direction of GPR movement — 20 cm.

The GPR structure is based on time-domain reflectometer. The multi-channel operation is realized by sequential connection of one of seven antennas and a single calibration channel to the reflectometer port. Stroboscopic method is used for reception of UWB short-pulse signals.

7. EXPERIMENTAL VERIFICATION OF CDM-BASED APPROACH IN GPR

7.1. Restoration of Parameters of Plane-layered Medium

The following parameters were chosen for the test purposes: $d_1 = 10.0$ cm, $\varepsilon_1 = 4.0$ ("sand"); $d_2 = 10.5$ cm, $\varepsilon_2 = 1.0$ ("air"); $d_3 \to \infty$, $\varepsilon_3 = 4.0$ ("sand"); $\sigma_1 = \sigma_2 = \sigma_3 = 0$. This three-layer structure simulates an air cavity in soil. T-horn antenna of the GPR was placed in the air, above
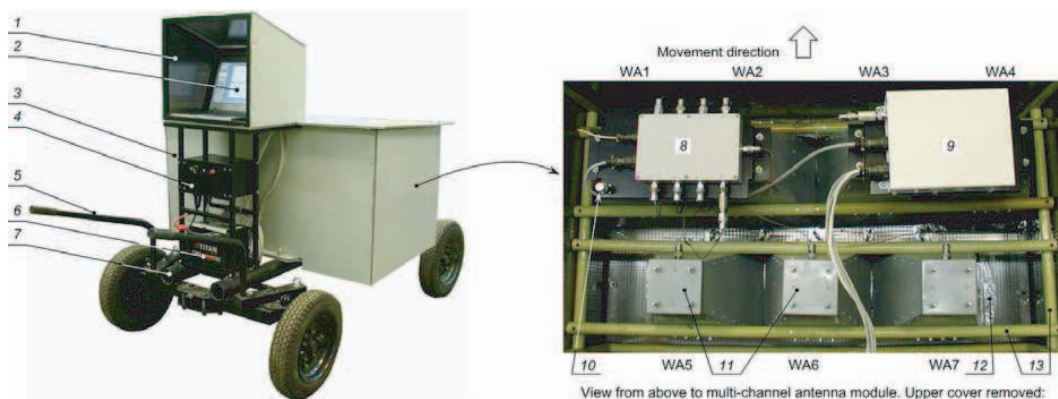
Figure 2: Experimental GPR setup.

the first layer, at 47 cm height, so the "virtual source" of antenna was at 85.0 cm above the ground. Fig. 3 shows signature of that test medium which was calculated numerically through integration in complex plane (Line 1), numerically using FDTD (2), and thorough approximation by a limited number of propagating and damping plane E- and H-waves (3). Also experimental results are shown (4).

Figure 4 shows functional (2) with discrepancy function (5) for that test medium. It was found that for this case Genetic algorithm converges and reports correct position of the global minimum if bandwidth in (5) ranges from 1500 MHz (40 discrete frequencies total) to 2000 MHz (55 frequencies). Measured parameters of test structure are the following: $d_1 = 9.6$ cm, $\varepsilon_1 = 3.8$; $d_2 = 9.9$ cm, $\varepsilon_2 = 1.0$.

7.2. Measuring Metallic Cylinder Diameter in Soil

A 2 m — long piece of communication cable with outer metallic coating of 25 mm diameter was buried into moisten sand ($\varepsilon = 4.0$) at 40 cm depth. Reflection from the same cable was used in (7) as a reference signal s_{Ref}. This reference signal was recorded using parallel polarized wave, i.e., GPR antenna was turned so electric field vector became parallel to the cable axis. The shape of amplitude spectrum of reflected signal is independent on cable diameter in this case. The background reflection signal s_{BKGND} was registered after the GPR was moved 1 m away from the cable trace.

Both received reflections from the object s_{Obj} and from the background s_{BKGND} are shown in Fig. 5(a). The following local scatterers are seen there: 1 — feed point of T-horn, 2 — T-horn throat, 3 — T-horn aperture, 4 — interface air-soil, 5 — buried cable. Result of background compensation
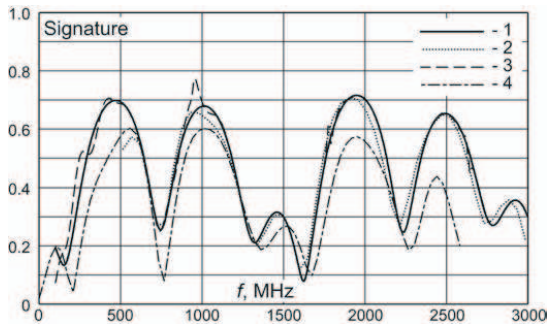
Figure 3: Normalized transfer function ("signature") of test medium.
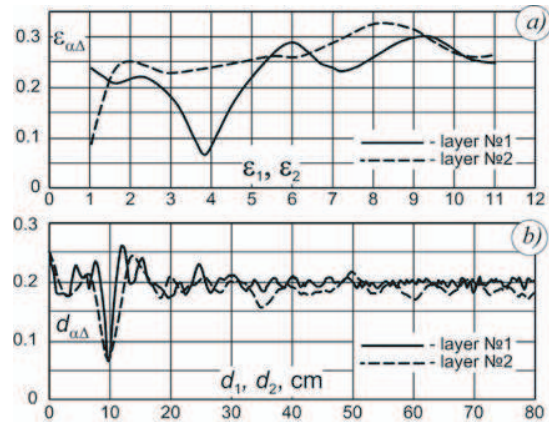
Figure 4: CDM functional for test medium.
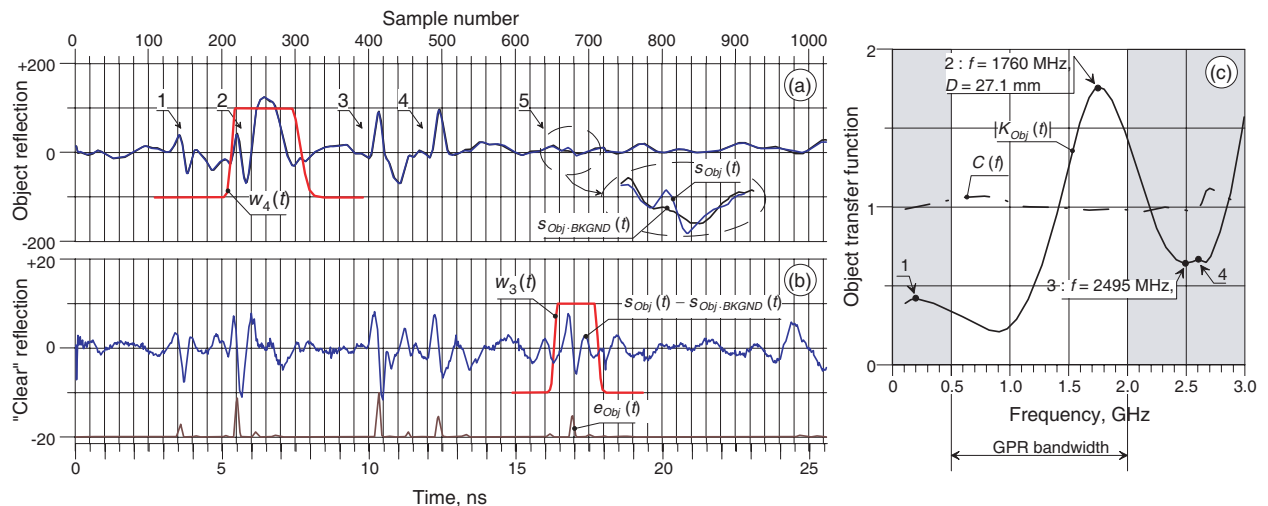
Figure 5: Experimental measurement of diameter of 25 mm thick metallic cylinder buried in moisten sand.

is shown in Fig. 5(b). The strobe $w_3(t)$ (see Fig. 5(b)) was arranged automatically to select object reflection region. For this purpose an auxiliary function $e_{Obj}(t)$ was calculated which characterize an energy distribution by time. The same procedure was applied to obtain a "clear" reflection from the reference object. The slow drift of GPR signal shape and signal channel parameters can occur between the moments of soundings of investigated and reference objects (in $1/2\ldots 10$ min or so). Correction of this kind of instability is made in frequency domain, correcting function $C(f)$ is shown by dashed curve in Fig. 5(c). The firm line in Fig. 5(c) is the transfer function $|K_{Obj}(f)|$ found using (7). Global maximum 2 is observed at 1760 MHz, this gives value 27.1 mm of cable diameter with ratio error $+8.4\%$. The proposed method of measurement of diameter of subsurface metallic cylinder for the GPR was verified on different cylinders ranging 25 to 80 mm in diameter. The ratio error did not exceed 20%.

8. CONCLUSION

The offered approach based on Computational diagnostics method can increase reliability of diagnostics and identification of subsurface mediums and objects for the GPR applications.

REFERENCES

1. Grinev, A. Yu. Ed., *Problems of Subsurface Radiolocation, Collective Monography*, Radiotechnics Publishing House, Moscow, Russia, 2005.
2. Tikhonov, A. N. Ed., *Ill-defined Problems of Natural Science*, Publishing House of Moscow State University, Moscow, Russia, 1987.
3. Grinev A. Yu., V. N. Sablin, D. V. Bagno, and V. S. Temchenko, "Multi-channel ultra-wideband short-pulse ground penetrating radar," *Proceedings of the 5th European Radar Conference*, 296–299, Amsterdam, The Netherlands, October 2008.
4. Lambot, S., E. C. Slob, and I. van den Bosch, "Modeling of GPR for accurate characterization of subsurface electric properties," *IEEE Trans. On Geoscience and Remote Sensing*, Vol. 42, 2555–2567, 2004.

Multi-frequency Full-polarized Subsurface Holographic Radar with Quadrature Receiver

A. V. Zhuravlev, **S. I. Ivashov**, **V. V. Razevig**, and **I. A. Vasiliev**

Remote Sensing Laboratory, Bauman Moscow State Technical University, Russia

Abstract— To replace the existing version of RASCAN multi-frequency radar system, its new modification is currently under development. Among improvements are quadrature detector, frequency synthesizer, and symmetric realization of polarization channels. These modifications enhance capabilities of the radar system currently in production by providing opportunities to implement hologram reconstruction algorithms, depth estimation technique, and perform measurements disregarding depolarization effects when observing elongated objects.

1. INTRODUCTION

During past several years the family of holographic radars RASCAN proved to be useful in many application cases where high plane resolution is necessary and objects of interest are situated at shallow depths. Depending on application case, three modifications of the radars were designed in the frequency bands around 2, 4, and 7 GHz [1, 2]. The plane resolution of the radars increases with frequency while penetration depth decreases. Among application cases there were mapping of heating pipes in concrete [3], detection of leaks in walls, detection of buried objects in soil, and even discovering delamination spots under Space Shuttle thermal protection tiles [4, 5]. During numerous field experiments several limitations of the radar system were revealed. This paper describes limitations of the current radar systems and reports on improvements that were made in the new modification of the radar.

2. EARLIER LIMITATIONS, CURRENT IMPROVEMENTS

The current modification of the subsurface holographic radar RASCAN features an amplitude detector and operates on five frequencies providing sufficient contrast of a buried object on at least one frequency at a maximum achievable depth. Ten grayscale images (5 frequencies × 2 polarizations) reflect phase shifts between the reference signal and the signal reflected by a buried object providing high sensitivity of the method. For many application cases when attenuation in the sounding medium is high, the interferential side lobes are barely visible and the interference pattern resembles the shape of a buried object. Such a technique gives images that allow confident identification of objects, especially when a priori information is available.

Such design of the radar system revealed certain limitations during numerous field experiments. The dependence of phase shift for the reflected wave results in the fact that the contrast of the same buried object depends on its depth. This situation forces browsing through all five frequencies and two polarizations in the search for the best representative image that is most adequate to the underlying object. Moreover, when switching through all five frequencies, certain pauses where necessary to eliminate transition effects in the circuitry, thus, limiting the maximum scanning speed to 50 cm/s approximately. Using two signal quadratures gives opportunity to use a single frequency without a chance of loosing the object. If concealed in one quadrature channel it definitely reveals itself in the other channel. Using a single frequency without switching leads to a lesser noise eliminating transient processes in the circuitry. Further noise suppression can be achieved by oversampling and signal filtering. In the single frequency mode the maximum scanning speed increases by several times.

Another limitation of the currently produced radar system is the absence of a depth estimation technique. Operation at several frequencies is necessary when relative or absolute depth information is required. The possibility to use an arbitrary frequency set was achieved by using an integral frequency synthesizer with software frequency selection. The use of a frequency synthesizer and a quadrature receiver was aimed at hologram reconstruction algorithms. The depth evaluation for a buried object by a holographic radar is feasible without providing a wide frequency band as it is usually required in impulse radars. High spatial resolution of acquired holographic images allows considering layered approximation of the sounding medium and a technique of phase measurements on two or several close frequencies to get relative in-depth positions of buried objects.

When acquiring holographic data by scanning over an area of interest, the situation where the image holds not only underlying objects but also some area without it is the rule. This area can also be of interest because it gives the opportunity to formulate the problem of recovering dielectric properties of a medium using, for example, a layered model for half space, with its simplest formulation as homogeneous half space.

The early version of the radar had one transmit and two receive mutually orthogonal stub antennas. The codirectional receive antenna gave parallel polarization channel while the orthogonal receive antenna gave cross polarization channel. Due to asymmetric antenna configuration the registered interference pattern was dependent on the orientation of the radar antenna toward an elongated buried object. The depolarization effect in cross polarization channel has significant response when underlying objects have a narrow elongated shape, or over the ridges of more extended objects. To take advantages of these effects independently on radar antenna orientation at scanning, the new modification has two orthogonal transmit and two orthogonal receive antennas spawning four channels altogether. An RF-switch allows commuting transmit-receive pairs. Such a configuration gives additional possibilities when presenting images to the user.

The described modifications of the radar system are currently under tests and only preliminary experiments on hologram registration with the new hardware are done. Figure 1(a) shows an experiment setup used at radiohologram registration produced by different objects in air. Figure 1(b) shows an example hologram of pliers at a close distance.

(a)   (b)
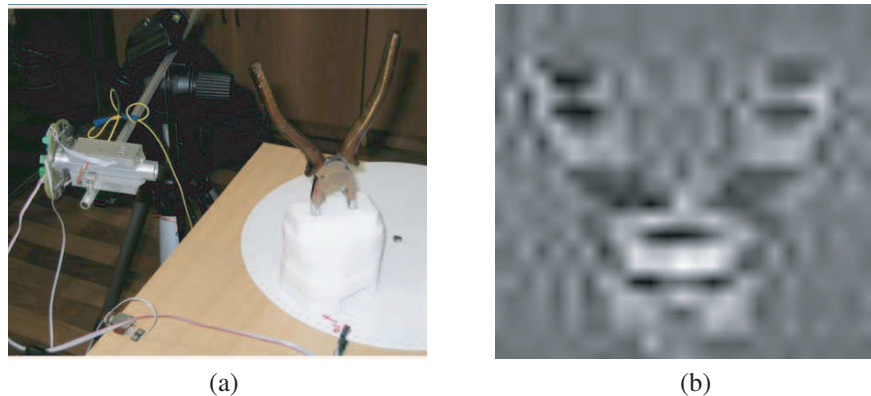
Figure 1: (a) Experimental setup. (b) Radiohologram of pliers at 15 GHz.

3. CONCLUSIONS

A new modification of the radar RASCAN features a quadrature receiver and a transmitter on an integral frequency synthesizer with software frequency selection. These modifications are aimed at implementation hologram reconstruction algorithms with acquired data. Two approaches of depth estimation are under development: relative and absolute. The latter algorithm uses an area of the scanning surface that is free from objects for the calibration purpose. The symmetric implementation of polarization channels gives an additional freedom of scanning without paying attention to a buried object possible orientation. These improvements, currently under development or tests, are planned to be included in the software package assisting the radar system.

ACKNOWLEDGMENT

REFERENCES

1. Ivashov, S., V. Razevig, I. Vasilyev, A. Zhuravlev, T. Bechtel, and L. Capineri, "The holographic principle in subsurface radar technology," *International Symposium to Commemorate the 60th Anniversary of the Invention of Holography*, 183–197, Springfield, Massachusetts, USA, October 27–29, 2008.

2. http://www.rslab.ru/?lang=english&dir=product.

3. Razevig, V. V., S. I. Ivashov, A. P. Sheyko, I. A. Vasilyev, and A. V. Zhuravlev, "An example of holographic radar using at restoration works of historical building," *Progress In Electromagnetics Research Letters*, Vol. 1, 173–179, 2008.

4. Ivashov, S. I., I. A. Vasiliev, T. D. Bechtel, and C. Snapp, "Comparison between impulse and holographic subsurface radar for NDT of space vehicle structural materials," *PIERS Online*, Vol. 3, No. 5, 658–661, 2007.

5. Lu, T., C. Snapp, T.-H. Chao, A. Thakoor, T. Bechtel, S. Ivashov, and I. Vasiliev, "Evaluation of holographic subsurface radar for NDE of space shuttle thermal protection tiles," *Sensors and Systems for Space Applications, Proceedings of SPIE*, Vol. 6555, 2007.

Testing of the Theoretical Model for a Wideband Pulse Propagation in the Oil-Gas Collector Media

V. L. Mironov and K. V. Muzalevskiy

Kirensky Institute of Physics, SB RAS, Krasnoyarsk, Russia

Abstract— Recently, there were carried out [1] experiments on propagation of a quasi plane pulse wave through the rock fluidized with oil and saline water. The results of [1] can be used to test the theoretical model [2, 3] of ultra wideband (UWB) pulses propagating through the structures used in [1]. Using the methodology of [2] and [3], the shape and analytical signal amplitude of the pulse transmitted and reflected as in [1] were calculated, with the error of theoretical simulations being estimated. The standard deviation of the simulated values from those measured appeared to be of 11.5% and 8.2%, respectively, concerning shape for the pulse transmitted, through a rock layer fluidized with oil and water, and reflected from two bordering on each other layers, one of which being fluidized with saline water and the other with both the saline water and oil. In the case of pulse propagated though the rock layer fluidized with saline water and oil, a simulation error was found to be of 3.7%, as determined for the analytical signal amplitude. The simulation errors obtained have to be limited to a short propagation distance of only 5 cm.

1. INTRODUCTION

In our paper [2], there was developed a theoretical model for propagation of a UWB pulse radiated by a point electric dipole placed in an oil-bearing rock which is bordering on a water-bearing one, both representing the media characteristic for oil-gas collectors. A spherical wave field emitted by the dipole was represented as a superposition of plane waves propagating through an absorbing and frequency dispersive medium. In the propagation model of [2], there was used the refractive mixing dielectric spectrum model earlier proposed in [3]. Recently [1], there were conducted experiments on propagation and reflection of quasi plane pulse waves in the oil-gas collector media similar to those used for simulation in [2]. The results of work [1] can be applied to testing the theoretical model proposed in [2] and estimating the errors caused by the approximations accepted in [3], regarding both the propagation theory and dielectric model.

2. THEORETICAL STATEMENT OF EXPERIMENT

A schematic view of the experimental set up used in [1] is shown in Fig. 1. A cell containing layered fluidized rocks was located at the distances of x_1 and x_2 from the transmitting, $x = 0$, and receiving, $x = L$, identical parabolic antennas. The transmitting antenna formed a pulse quasi plane wave to propagate in the range x_1 to x_2. Let us identify this set up as a transmittance scheme.

Using the set up as shown in Fig. 1, there were measured voltages of pulses at the output of the receiving antenna, with the measuring cell being in place, $S_{T_2}(t)$, or removed, $S_{T_1}(t)$, t standing for the time. Those can be used to obtain complex spectra of the respective pulses, that is, $S_2(\omega)$ and $S_1(\omega)$. If fluidized rock is removed from the measuring cell, according to [4], the spectrum of received pulse, $S_{T_1}(t)$, is expressed in the following form:

$$S_{T_1}(\omega) = E_0(\omega)e^{i\frac{\omega}{c}L}P(\omega)K(\omega), \tag{1}$$

here $E_0(\omega)$ — spectral density of electric field in the aperture plane of transmitting antenna, while $K(\omega)$ and $P(\omega)$ are a transfer function of the receiving antenna and empty measuring cell, respectively; ω is a circular wave frequency, c — is the light speed in vacuum, and i stands for the imaginary unit. The voltage spectrum $S_1(\omega)$ is measured to get information about the experimental
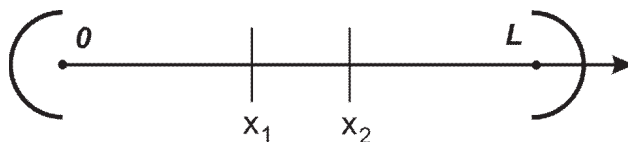
Figure 1: Schematic view of experimental set up used in [1].

set up used. To acquire information on the plane wave transmission coefficient, $T(\omega)$, regarding the rock fluidized with saline water and oil, there was applied the following formula:

$$S_{T_2}(\omega) = E_0(\omega)e^{i\frac{\omega}{c}L}T(\omega)e^{-i\frac{\omega}{c}\Delta}P(\omega)K(\omega) = T(\omega)e^{-i\frac{\omega}{c}\Delta}S_{T_1}(\omega), \tag{2}$$

where $\Delta = x_2 - x_1$, as shown in Fig. 1.

Another experimental set up was applied, when measuring a two layers rock sample consisting of the one layer, fluidized with saline water and oil, and the other, which was bordering on the first one and fluidized with only saline water. In this set up, an ideally conducting metal sheet was placed at the plane $x = x_1$, with the pulse being emitted and received with the same antenna, located at the plane $x = 0$. Let us identify this set up as a reflectance scheme. To acquire the information about the new experimental set up, the voltage spectrum of the pulse $S_{R_1}(t)$ reflected from the metal sheet, can be written in the form

$$S_{R_1}(\omega) = -E_0(\omega)e^{2i\frac{\omega}{c}x_1}K(\omega). \tag{3}$$

To acquire information on the plane wave reflection coefficient, $R(\omega)$, regarding the two layers rock sample placed in the range from x_1 to x_2, the following formula for the spectrum of pulse voltage $S_{R_2}(t)$ at the output of receiving antenna was applied:

$$S_{R_2}(\omega) = E_0(\omega)e^{2i\frac{\omega}{c}x_1}K(\omega)R(\omega) = R(\omega)S_{R_1}(\omega). \tag{4}$$

3. TESTING OF THE THEORETICAL MODEL

Using the values of transmission, $T_C(\omega)$, and reflection, $R_C(\omega)$, coefficients calculated on the basis of the theory developed in [2, 3], the simulated pulse shapes, relative to the transmittance, $S_{T_2C}(t)$, and reflectance, $S_{R_2C}(t)$, schemes of measurements, were obtained via Fourier transforms.

The simulated and measured pulse shapes are shown in Fig. 2. As seen from Fig. 2, the duration of initial pulse, marked with symbol 1, was about 100 ps.

On the basis of data shown in Fig. 2, the standard deviation between the calculated and measured pulse shapes related to the transmittance and reflectance schemes appeared to be of 11.5% and 8.2%, respectively. To estimate the attenuation measured for the transmitted pulse as a function of the sample thickness, the analytical signal amplitudes $A_{T_1}(t)$ and $A_{T_2}(t)$, related to the pulse shapes $S_{T_1}(t)$ and $S_{T_1}(t)$, respectively, were calculated, as in [5]. With the values of $A_{T_1}(t)$ and $A_{T_2}(t)$ being known, the transmitted pulse attenuation was estimated as a ratio $P = A_{T_2}(t_m)/A_{T_1}(t_m)$ where t_m designates the time corresponding to the maximum of an analytical signal amplitude. Simultaneously, on the basis of theory developed in [2] and [3], the attenuation value, P_C, was determined for the attenuation of the plane wave pulse having passed the distance Δ in the oil and water fluidized rock. The attenuations measured and calculated are given in Fig. 3.
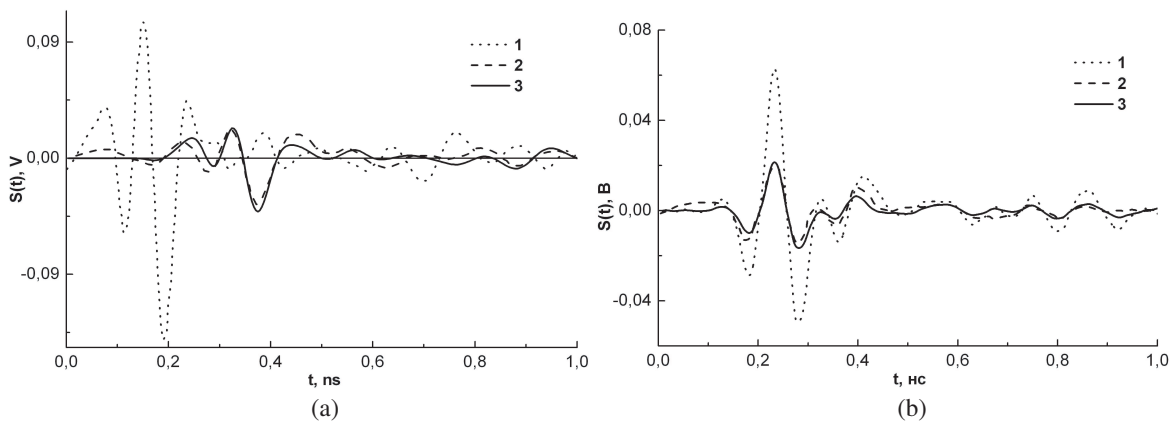
Figure 2: Pulse shapes in the cases of transmittance (a) and reflectance (b) schemes, 1, 2, and 3 stands for the measured and calculated values, respectively. $1 - S_{T_1}(t)$ and $S_{R_1}(t)$, $2 - S_{T_2}(t)$ and $S_{R_2}(t)$, $3 - S_{T_2C}(t)$, $S_{R_2C}(t)$.
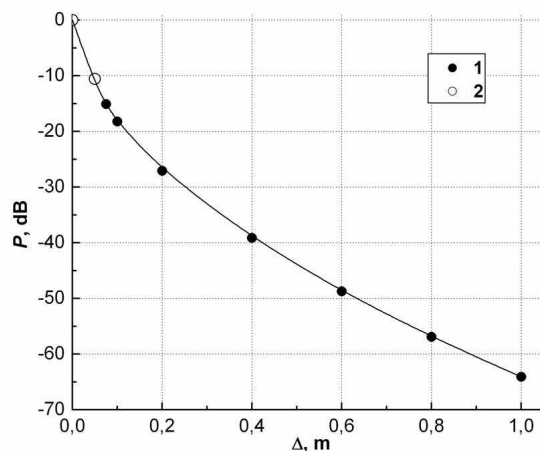
Figure 3: Attenuations P as a function of distance Δ. 1 — calculated, 2 — measured.

On the basis of data shown in Fig. 3, the calculated attenuation P_C was found to deviate from the measured one P on the order of 3.5% only, thus proving the theoretical approach applied in [2] and [3] to yield good agreement with the experiment result at the level of $-10\,\text{dB}$. Nevertheless, as the dependence on the distance of the attenuation P is nonlinear (see Fig. 3), some additional measurements at longer distances are needed to validate the theory of [2] and [3] at greater attenuations.

4. CONCLUSION

The error of theoretical simulation of the results of experiment carried out in [1] with the methods and algorithms developed in [2] and [3] was shown to be on the order of 11.5% and 8.2%, regarding the shape of a 100 ns initial pulse transmitted though the rock fluidized with saline water and oil, directly and with the use of reflecting plane, respectively. This result is limited to a short distance of 0.05 m, at which the attenuation of pulse amplitude was observed to be less then 10 dB.

REFERENCES

1. Epov, M. I., O. V. Yakubov, E. D. Telpukhovsky, V. L. Mironov, and V. P. Yakubov, "The method of ultrawideband radiowave logging horizontal wells," *Izvestiya Vuzov. Phizika*, Vol. 51, No. 9, 63–71, 2008 (in Russian).
2. Epov, M. I., V. L. Mironov, S. A. Komarov, and K. V. Muzalevskiy, "Ultrabroadband electromagnetic wave propagation in hydrocarbon reservoirs in the presence of an oil-water interface," *Russian Geology and Geophysics*, Vol. 50, No. 1, 46–52, 2009.
3. Epov, M. I., V. L. Mironov, S. A. Komarov, and K. V. Muzalevskiy, "Nanosecond electromagnetic sounding of a fluid-saturated layered formation," *Russian Geology and Geophysics*, Vol. 48, No. 12, 1054–1060, 2007.
4. Kong, J. A., *Electromagnetic Wave Theory*, EMW Publishing, Cambridge, Massachusetts, 2008.
5. Cook, C. E. and M. Bernfeld, *Radar Signal: An Introduction to Theory and Application*, Academic Press, New York, 1967.

A Single Display for RASCAN 5-frequency 2-polarisation Holographic Radar Scans

C. G. Windsor[1], **A. Bulletti**[2], **L. Capineri**[2], **P. Falorni**[2], **S. Valentini**[2], **G. Borgioli**[2], **M. Inagaki**[3], **T. Bechtel**[4], **E. Bechtel**[4], **A. Zhuravlev**[5], and **S. Ivashov**[5]

[1]116, New Road, East Hagbourne, OX11 9LD, UK
[2]Dipartimento Elettronica e Telecomunicazioni, Università di Firenze, Firenze, Italy
[3]Walnut Ltd, 4-2-54 Sakaecho Tachikawa 190, Japan
[4]Enviroscan Inc, 1051 Columbia Avenue, Lancaster, PA 17603, USA
[5]Remote Sensing Laboratory, Bauman Moscow State Technical University, Russia

Abstract— The RASCAN holographic radar system has been developed by the Remote Sensing Laboratory of Bauman Moscow Technical University. The present design uses five frequencies and two polarisations to give 10 distinct images of scan from buried objects. Because of the sinusoidal phase variation of the interference signals, all displays show a complex picture of dark and light phases which vary in a complicated way between different frequencies and polarizations. This is a preliminary investigation into the optimal presentation of the 10 images as a single composite image. The objective is to display as much as possible of the information present in the original image. The solution presented here is to sum the absolute values of the background-corrected amplitude over both the five frequencies and the two polarizations. The method is justified using an experiment in which nine US pennies, and 9 metal washers, were buried in sand at increasing depths in the range 0 to 56 mm. The method is illustrated by example images from the fields of civil engineering and mine detection.

1. INTRODUCTION

Conventional Ground Penetrating Radar uses echo sounding from a pulsed source to determine the range of buried objects [1]. A quite different radar system was developed by the Remote Sensing Laboratory of Bauman Moscow Technical University [2]. Their RASCAN system uses continuous wave unmodulated signals at several different frequencies. The signal reflected from the subsurface structure is multiplied by the original signal from the antenna to form a hologram. The amplitude and phase of the hologram is sensitive to the depth of any buried object, to its reflectivity and to the properties of the medium. The indication of depth is indicated by the phase change of the radar wave in passing through the material to the buried object. The indication of reflectivity is given by the amplitude of the reflected signal. Generally the antenna and receiver are the same, and placed close to the ground surface. The holographic amplitude and phase may be presented as a function of position (x, y) across the ground surface and scanned manually or automatically to give a holographic image $H(x, y)$ whose amplitude may be plotted as a grey scale image. In the RASCAN system five frequencies are operated simultaneously to give five different holographic images whose amplitude and phase response differs as the phase change caused by the phase difference along the path length alters. The RASCAN system also has two perpendicular polarizations so that the response may be measured both along and perpendicular to the scanning direction. The RASCAN system thus results in 10 different holographic response images. The RASCAN display software allows all 10 images to be displayed either simultaneously, or as a time-sequence set of images. Neither is completely satisfactory for use by unskilled operators and the present paper considers ways in which the 10 individual holograms may be combined into a single composite image.

2. THE CONVENTIONAL DISPLAY FROM A TYPICAL RASCAN IMAGE

As an example image, a floor scan of a concrete floor containing conduits, metal meshes and metal pan decking has been chosen. The scan was made at the Fackenthal Hall at Franklin and Marshall College, Lancaster, USA. Figure 1 shows the floor in question, with the RASCAN being manually pushed along the scan direction (x). The scan length was 500 mm with measurements every 5 mm. The scans were repeated at 20 mm intervals along the direction perpendicular to the scan (y), over 2 m. This gave 100×100 points in total although the images displayed here will only extend over only 60×60 points as much of the scan is a repetitive background. Figure 2 shows the display given by the RASCAN software.

Figure 1: The floor scan at the Fackenthal Hall in progress. The RASCAN head is being swept along the scan direction. The progress of the scan could be watched on the monitor behind.
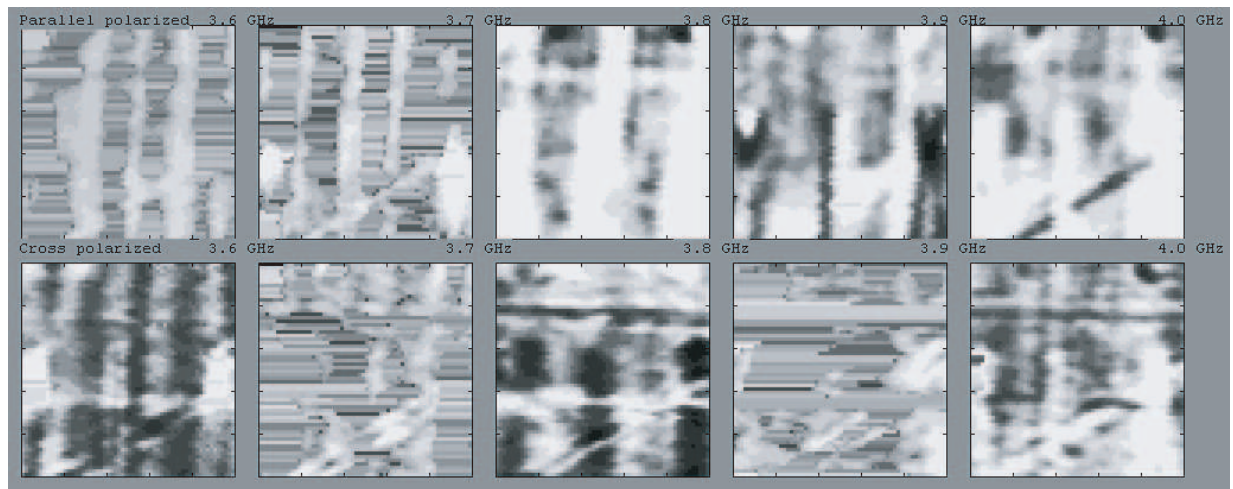
Figure 2: The display from the RASCAN software. The five frequencies from 3.6 to 4.0 GHz are displayed from left to right and the two polarisations are parallel above and cross polarised below.
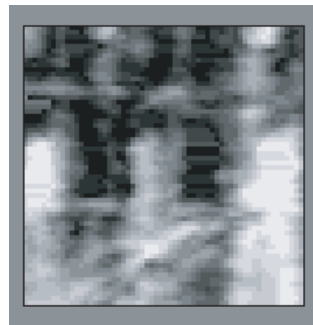
Figure 3: A single image display generated from the RASCAN scan above. The image is sum of the differences from the background level summed over all the ten images shown above. All the featues mentioned above may be seen.

Several sets of features are visible in these images. The thin vertical bands sometimes light, sometimes dark, are likely to be the vertical rebars. The broader bands seen at other frequencies are likely to be the corrugations of the pan decking. The thin horizontal bands, more clearly seen on the cross polarization are likely to be the horizontal rebars. At the lower right is clearly seen a diagonal electrical conduit that appears either light or dark in many of the images. This series of images is clearly not straightforward to understand without careful study of all the images. Can this process be simplified without loss of detail?

The RASCAN software package has one such process. An option is to display the images within each polarisation direction in sequence. It helps greatly in the process of assimilating the data together.

An example of our approach is shown in Figure 3. The method has many options and this is just one result. The method will be explored in more detail using images from a much simpler example: a series of buried pennies of different depths.

3. THE METHOD EXPLORED FOR A SIMPLE RASCAN IMAGE

Figure 4 above, shows raw RASCAN data from a scan over 9 US pennies buried in sand at increasing depths from about zero on the left to about 65 mm on the right. Only the parallel polarisation is shown. The scan length and separation were both 1 cm. These experiments are presented in more detail in reference [4] from this meeting. The lower set of circles were some other foreign coins, and are not analysed here. The scans were made along the direction of increasing depth by manually moving the RASCAN head on a glass plate over the sand surface.

An interesting feature is that the background level at each frequency is quite different. In holographic radar there is no specific "main bang" ground reflection from the surface. In this case it is an air-sand interface covered by a thin plastic sheet. Rather the amplitude and phase of the reflected wave from the surface interferes with the incident wave to give a characteristic background signal level. In this example, there was a wide region of sand without pennies that
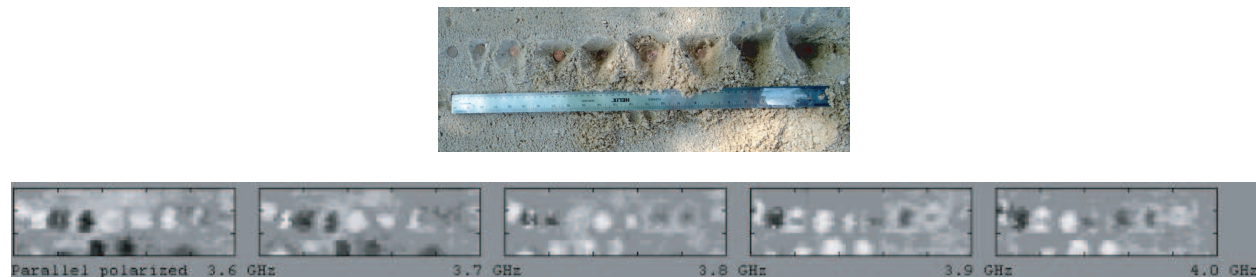
Figure 4: A set of nine US pennies buried in sand at different depths and is set of RASCAN images in the parallel polarisation.
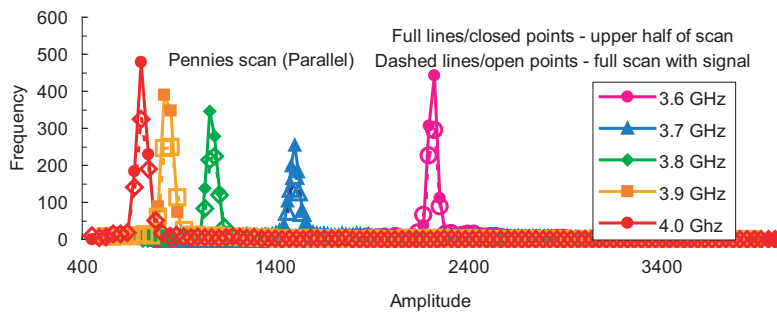
Figure 5: The histogram of signal amplitudes over the raw data from a scan over 9 US pennies buried in sand. The scan showed a larger region of background than is shown in Figure 3. Note the change in amplitude with frequency.
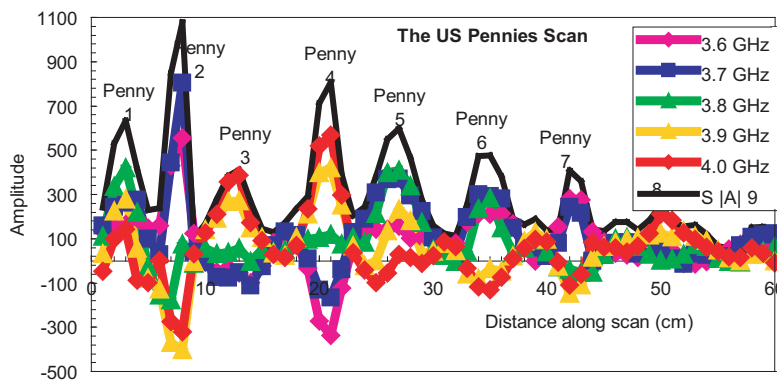
Figure 6: The amplitude along the scan of pennies for the five frequencies (coloured) and for the summed absolute amplitude (black).

could be analysed to give the background level. Figure 5 shows the histogram of the amplitudes for each of the frequencies. There is width to the peak in amplitude at each frequency and a small almost invisible "tail" to the distribution from the much larger amplitude variations present in the portion of the scan representing the pennies. This background level is important in since it enables "contrast", or deviation from background, to be identified. Positive and negative phases have at last a clear meaning. In the pennies scan that particular scan giving the largest amplitude across each penny was identified, (almost always one particular scan) and the coloured lines in Figure 6 shows this scan for each of the five frequencies. It is seen that for penny 1 all the frequencies show a positive peak. For penny 2 the 3.7 GHz peak has the largest positive amplitude and the 3.9 GHz the largest negative peak. For penny 4 the 4.0 GHz peak has the largest positive amplitude and the 3.6 GHz the largest negative amplitude. By penny 6 this situation is almost reversed. The full line in Figure 6 shows the sum of the five frequencies of the modulus of the amplitude

$$\boldsymbol{F} = \boldsymbol{\Sigma}_f |A_f(x) - B_f|$$

where the summation is over frequencies f, $A_f(x)$ is a the amplitude at frequency f and position x, and B_f is the background.

Figure 7 shows this representation for the pennies scan. The first seven pennies are clearly delineated with positive signals and there are suggestions of the remaining two deeper pennies.

Figure 7: The mean modulus of the amplitude for the pennies scan.
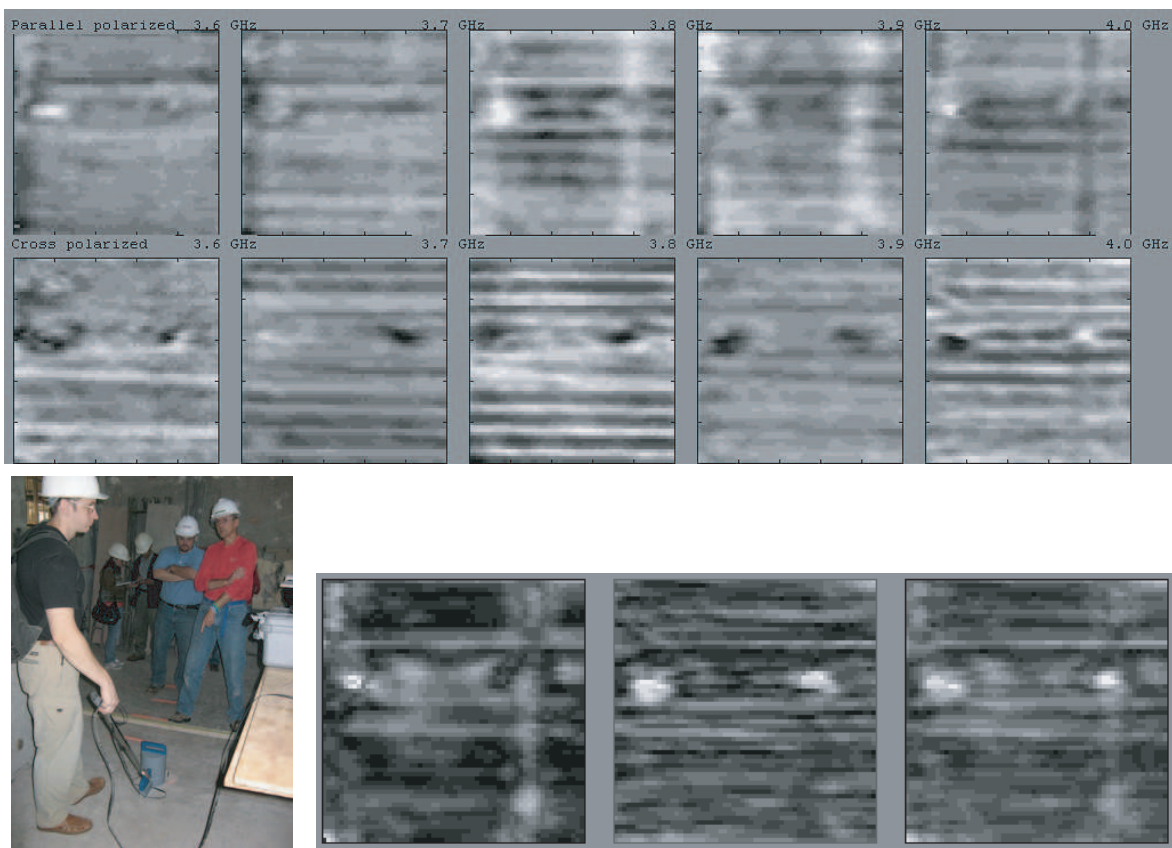
Figure 8: Above, a second RASCAN at the Fackenthal Hall over an area containing two holes and several unknown signals. On the left is shown the scene and below is shown the composite image from parallel perpendicular and combined polarisations.

4. SOME EXAMPLES OF THE COMBINED IMAGE FOR OTHER RASCAN IMAGES

Returning to the Fackenthal Hall location a second image was taken of an interesting location which showed two holes 16 cm diameter separated by 36 cm. The scans are again parallel to the corrugations. A portion of the RASCAN data collected are shown in Figure 8 with the same presentation as with the scan of Figure 2. Much is seen in this image: in particular the two holes appear with varying phases. Some scans show clear vertical lines which are probably from electrical conduit which approach the holes in both directions.

In the lower part of Figure 8 the two polarisations, parallel and perpendicular to the scan direction (left to right) are shown separately. In this case they are appreciably different with the corrugations being much clearer in the parallel direction.

A third example is RASCAN image of simulated mines and is from the published literature [3]. In Figure 9 above is shown on the left the four simulated mines. Two of the simulants were made of metal and they are easily picked up by the metal detector scan shown in the centre of the figure. On the right is shown the amplitude composite image. This is presented on a logarithmic scale and shows some noise background. However the two metal mines are also seen very clearly, as is a length of metal wire which was placed beneath the sand surface. The two plastic simulants are seen on the lower left and right. The rather conspicuous object in the lower centre of the figure is a "knee print" from one of the operators.
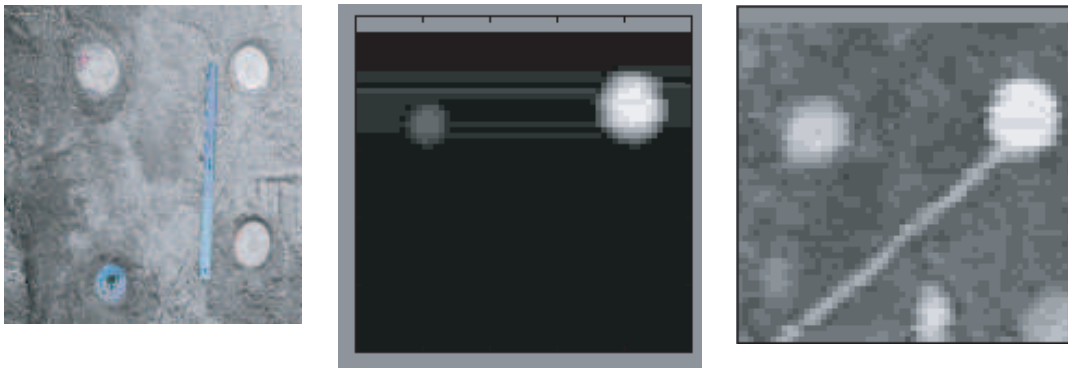
Figure 9: A scan from the garden in the University of Florence previously reported [1]. The mine simulant objects are shown on the left, the metal detector image in the centre and the composity single image on the right.

5. CONCLUSIONS

A method for combining the ten images given by the RASCAN system is proposed based on a sum of the modulus of the background-corrected amplitudes, without affecting the spatial resolution.

In the pennies experiment the summed images showed all pennies distinctly. In the Fackenthal Hall experiment the summed images showed all the expected features, including the conduit, the metal mesh and the deeper metal pan decking.

In the test bed of the University of Florence experiment with simulated mines, all four mines, two metal and two plastic were all seen satisfactorily.

The precise form of the average over background corrected amplitudes does not seem critical.

REFERENCES

1. Daniels, D. J., "Surface penetrating radar for industrial and security applications," *Microwave Journal*, 68–82, December 1994.
2. Capineri, L., S. Ivashov, T. Bechtel, A. Zhuravlev, P. Falorni, C. Windsor, G. Borgioli, I. Vasiliev, and A. Sheyko, "Comparison of GPR sensor types for landmine detection and discrimination," *12th International Conference on Ground Penetrating Radar, GPR*, Birmingham, UK, 2008.
3. Ivashov, S. I., et al., "Holographic subsurface radar technique and it applications," *12th International Conference on Ground Penetrating Radar, GPR*, Birmingham, UK, 2008.
4. Windsor, C., A. Bulletti, L. Capineri, P. Falorni, S. Valentini, M. Inagaki, T. Bechtel, E. Bechtel, A. Zhuravlev, and S. Ivashov, "Depth information from holographic radar scans," *Progress In Electromagnetics Research Symposium*, Moscow, Russia, August 18–21, 2009.

TDR Calibration for Soil Moisture Measurements Using a Spectroscopic Dielectric Model

V. L. Mironov, L. G. Kosolapova, and K. V. Muzalevskiy

Kirensky Institute of Physics, SB, RAS, Krasnoyarsk, Russia

Abstract— In this paper, a new calibration methodology for TDR moisture measurements is developed. The calibration characteristics are calculated from the theoretical modeling of pulse propagation along a TDR rod immersed in a moist soil. The rod was excited with a voltage pulse at one end, and the time forms of the electric current induced in the rod at the same end were calculated. The Hallen integral equation for the current induced in the rod were applied to determine time delays of the pulse reflected from the other end of the rod relative to a pulse driver. To ensure such calculations, there was employed the mineralogically based spectroscopic dielectric model by Mironov et al., which provided for complex dielectric permittivity spectra needed. As a result, the theoretical calibration plots in the form of time delay versus moisture were obtained, the clay content being used as a parameter. The calibration plots were calculated for the ensemble of soils and driving pulse duration used in the respective measurements conducted by Miyamoto et al., with moistures and clay contents varying from nearly dry to field capacity and from 0 to 62%, respectively. Given the measured and calculated delays of reflected pulse are known, the error, with which soil moisture is determined using the theoretical calibration plots, was estimated with regard to the ensemble of soils measured by Miyamoto. The standard deviation error was found to be of $0.016\,\text{cm}^3/\text{cm}^3$.

1. INTRODUCTION

Pulse TDR reflectometers are widely used for measurements of dielectric constant and volumetric moisture content of topsoil. For TDR measurement of soil moisture, the calibration relationship is needed to link the volumetric water content with the time delay of reflected pulse measured by TDR device. Given a certain make of the TDR device, such a calibration must be conducted for the temperatures and soil types to be involved in further moisture measurements. This approach is very laborious, if measurements are carried out for a broad set of soils and moistures varying from the air-dry soil to the field water capacity. There are some attempts [1, 2] to perform TDR calibrations with the use of empirical dielectric models of moist soils and to develop dielectric models of moist soils on the basis of TDR calibration plots measured. At that, a simple relationship, $t_{delay} = 2L\sqrt{(\varepsilon(W,\ C,\ S))}/c$, between the time delay, t_{delay}, and real dielectric constant, $\varepsilon(W,\ C,\ S)$, as a function of volumetric moisture, W. Here the following parameters of the soil and TDR device are also used: clay, C, and sand, S, percentages; length of TDR rod, L; and the light velocity in the vacuum, c. The models developed with this approach are suggested in [1, 2] to be applied to theoretical calibration of TDR devices, employed for soil moisture measurement, with regard to other soil types and TDR makes, using the same relationship, $t_{delay} = 2L\sqrt{(\varepsilon(W,\ C,\ S))}/c$, and soil texture parameters, C, S. Apparently, such a theoretical calibration is limited in terms of sounding pulse spectrum characterized by its medium frequency and width. In addition, given the same make of TDR device is supposed to be calibrated, a question remains whether the empirical dielectric models worked out in [1] and [2] on the basis of certain soil sets can be applied to other soil types. Both of this problems have never been discussed in the literature.

Therefore, the task to develop a theoretical method for calibrating TDR devices of arbitrary make, which is applicable to a large variety of soil types, is still actual. That problem was formulated and solved in this paper. Using the Hallen integral equation for the electric current induced by a voltage pulse driver in the rod immersed in the moist soil, we calculated the time delay of the pulse reflected from the end of the rod, relative to a pulse driver. The soil complex dielectric permittivity was taken in the form the mineralogy based spectral dielectric model developed in [3] to provide for dielectric spectra as a function of soil moisture and clay content. Then the theoretical calibration plots in the form of time delay versus moisture were obtained for the ensemble of soils and driving pulse duration used in the measurements conducted in [2]. With known values of the delays measured and calculated, the error of deducing soil moisture with the theoretical calibration plots, was estimated with regard to the ensemble of soils measured in [2].

2. TDR THEORETICAL MODEL

To model a TDR device, let us consider a metallic rod of length L oriented along axis x and connected at one end to a driving pulse generator, with the voltage complex spectrum being of $V(\omega)$ where ω is the circular frequency. Provided the diameter of the rod, $2a$, is much less then its length, $2a \ll L$, the current in rod induced by the driving pulse, can be determined from the integral equation of Hallen [4]:

$$\int_0^L I_x(x', \omega) K(x - x', \omega) dx' = A \cos kx + B \sin kx - \frac{1}{2} \frac{V(\omega)}{Z_0} \frac{\varepsilon(\omega, C, W)}{\sqrt{\varepsilon(\omega, C, W)}} \sin k|x| \qquad (1)$$

where $k = \sqrt{\varepsilon(\omega, C, W)} \cdot \omega/c$, Z_0 — wave impedance of vacuum, $K(x - x', \omega) = \exp(ikR)/4\pi R$, $R = \sqrt{a^2 + (x - x')^2}$, $\varepsilon(\omega, C, W)$ — complex dielectric constant of soil, A, B — unknown constant.

Let the driving pulse voltage be assigned in the form of first order derivative of the Blackmann-Harris window function with duration of 0.8 ns (see Fig. 1(a)).

This duration is equal to that of the TDR pulse drivers employed in [2]. For the complex dielectric constant $\varepsilon(W, C)$, we use the physically and mineralogy based spectroscopic dielectric model developed in [3] on the basis of the comprehensive dielectric data base over the frequency band from 0.3 to 26.5 GHz, clay contents from 0 to 76%, and moistures from air dry to the field capacity values. This data base represents the complex dielectric constants measured at the temperature of 20°C by Curtis et al. for the soils collected in the USA. The integral Equation (1) was solved with the MoM to obtain the current in the rod at the feeding point, $x = 0$. In the case of 4 soils, for which the TDR pulse delays were measured in [2], the example of the time forms for the pulses of electric current calculated from the Equation (1) are shown in Fig. 1(b). In calculations of these time forms, the diameter and length of the rod were assigned to be 0.002 m, and 0.475 m, respectively, with the volumetric soil moisture being of 20%.

As seen from Fig. 1(b), the reflected pulse delay and the pulse amplitude decrease with increasing clay content in the soil. This can be attributed to the increasing fraction of bound water in the soil, which real dielectric constant is less then that of the unbound soil water, while the imaginary dielectric constant exceeds that of the unbound water [3].

Being further based on the pulse current patterns like presented in Fig. 1(b), let us calculate the time delays for the set of 4 soils (Toyoura sand, $C = 0.3\%$, Red-yellow soil, $C = 50.0\%$, Brown forest topsoil, $C = 30.4\%$, Brown forest subsoil, $C = 61.8\%$) measured in [2] over the whole range of moistures. All the soils considered have organic matter contents less then 11.5%. The theoretical calibration plots obtained with the pulse delays calculated are presented in Fig. 2, alongside with those measured in [2].

Each theoretical calibration plot shown in Fig. 2 has a piecewise linear dependence on moisture, W, with a break of its derivative by W being located at the moisture equal to the maximum bound water fraction, W_t (see [3]). With the theoretical and measured calibration plots given in Fig. 2,
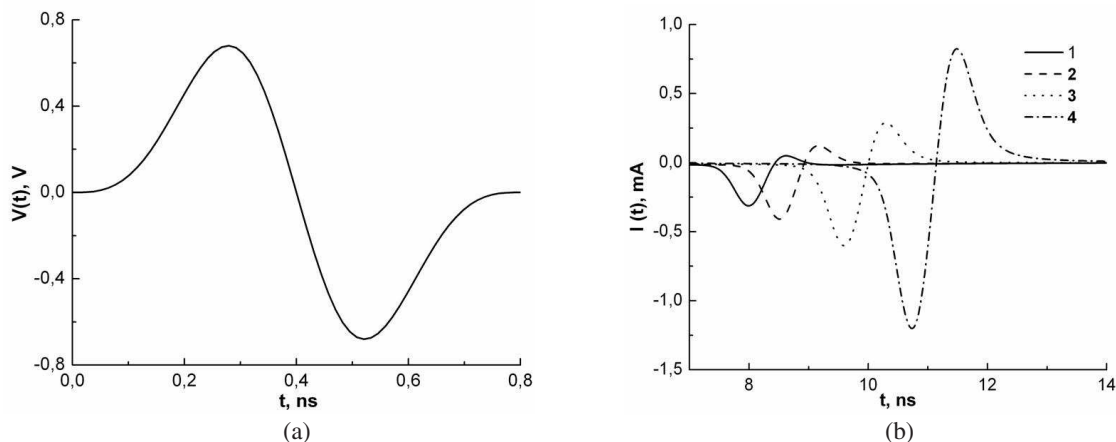
Figure 1: (a) Voltage applied to the rod at the feeding point, $x = 0$. (b) The current time forms reflected from the end of the rod as measured at the feeding point. Gravimetric content of clay, C: 1–61.8%; 2–50.0%; 3–30.4%; 4–3.0%.
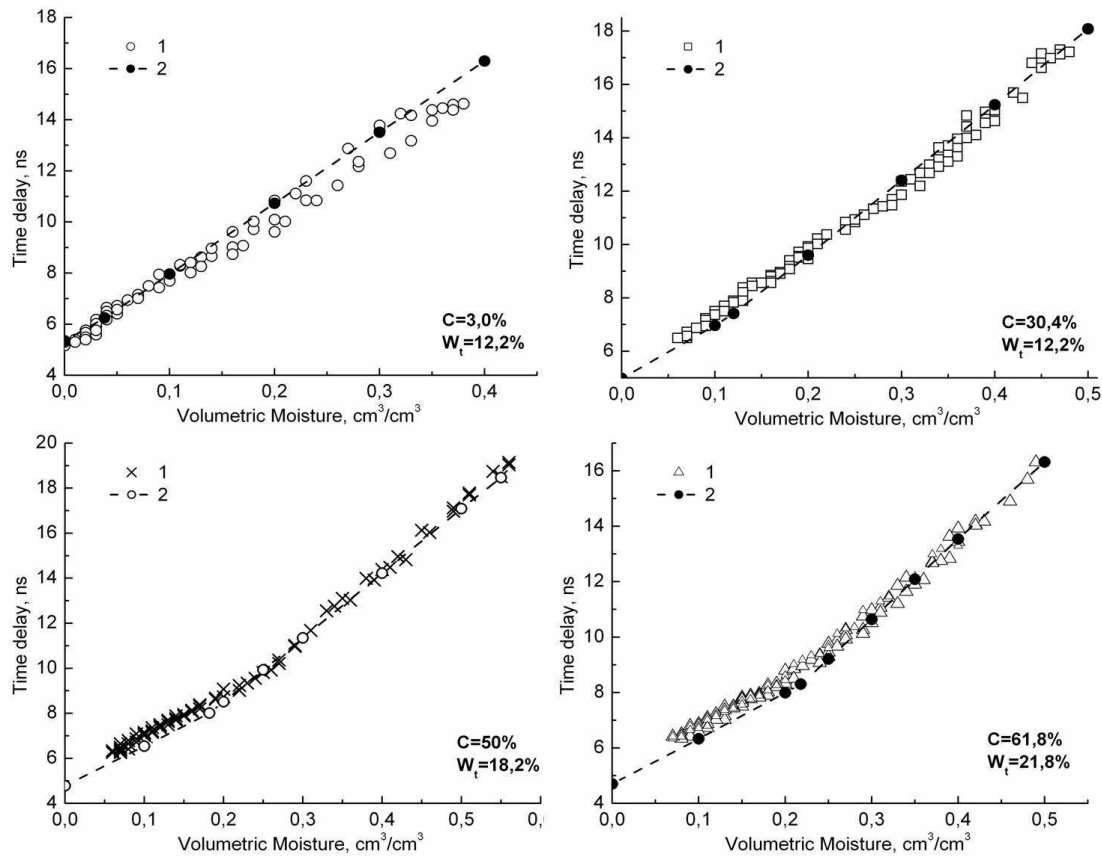
Figure 2: Calibration plots measured (1) and theoretical (2) for the set of four soils from [2]. W_t — maximum bound water fraction as determined in [3].
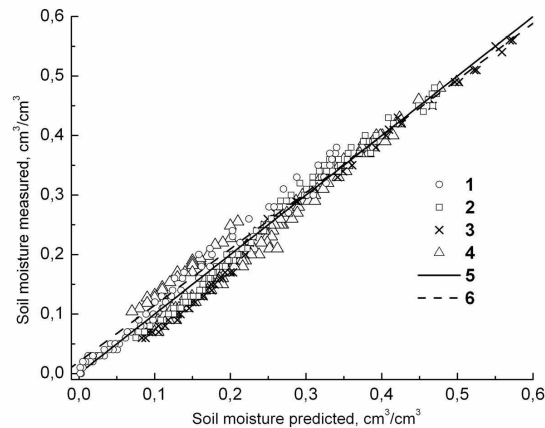
Figure 3: Correlation of the predicted soil moistures, W_p, with the measured ones, W_m. Solid and dotted lines represent the bisector (5) and linear fit (6), respectively. Soil clay content C: 1–0.3% (Toyoura Sand); 2–30.4% (Braun forest topsoil); 3–50.0% (Red yellow soil); 4–61.8% (Braun forest subsoil). Correlation coefficient, R, and standard deviation, SD, are equal to: $R_{DC} = 0.984$, $SD = 0.032$. The linear fit (6) is expressed as follows: $W_m = 0.019 + 0.95W_p$.

there were determined the moistures corresponding to the continuum of time delays, the latter being assigned to be the same for both calibration plots and equal to those measured in [2]. The moistures determined with the use of the theoretical and measured calibration plots were named as the predicted and measured ones, respectively. To allow for correlation analysis, the measured moistures are shown as a function of the predicted ones in Fig. 3.

According to the correlation analysis given in Fig. 3, the soil moistures determined with the TDR calibration characteristics measured are in good agreement with the ones derived with the

theoretical ones. The theoretical method proposed ensures the error of moisture measurements with the TDR device of $0.016 \, \text{cm}^3/\text{cm}^3$, in terms of standard deviation corresponding to the whole range of moistures and clay contents typical for the natural soils with organic matter content less then 11.5%. This method substantially simplifies the process of TDR calibration, as a clay content is the only soil parameter, needed to obtain the calibration characteristic, is often available from the soil science data bases.

3. CONCLUSIONS

In this paper, a new calibration methodology for TDR moisture measurements is developed. It is based on the theory of broadband pulse propagation through the moist soils which textures are known, thus allowing to exclude laborious calibration measurements. The standard deviation error of moisture measurements with the use of the proposed theoretical calibration, based on the comprehensive dielectric spectroscopic dielectric model, proved to be of $0.016 \, \text{cm}^3/\text{cm}^3$, which is on the same order as that obtained with the calibration characteristics measured. The error of $0.016 \, \text{cm}^3/\text{cm}^3$ also meets the requirements of the ESA Soil Moisture and Ocean Salinity sensor and can be recommended for use in validation field experiments.

ACKNOWLEDGMENT

REFERENCES

1. Ponizovsky, A. A., S. M. Chudinova, and Y. A. Pachersky "Performance of TDR calibration models as affected by soil texture," *Journal of Hydrology*, Vol. 218, 35–43, 1999.
2. Miyamoto, T. and J. Chikushi, "Time domain reflectometry calibration for typical upland soils in Kyushu," *Japan JARQ*, Vol. 40, No. 3, 225–231, 2006, http://www.jircas.affrc.go.jp.
3. Mironov, V. L., L. G. Kosolapova, and S. V. Fomin, "Soil dielectric model accounting for contribution of bound water spectra through clay content," *PIERS Online*, Vol. 4, No. 1, 31–35, 2008.
4. Hallén, E., *Electromagnetic Theory*, Wiley, New York, 1962.

Smooth Functional for Optimization of Peak to Average Ratio

D. A. Shapiro[1] and A. I. Latkin[2]

[1]Institute of Automation and Electrometry, Siberian Branch, Russian Academy of Sciences
1 Koptjug Ave, Novosibirsk 630090, Russia
[2]Novosibirsk State University, 2 Pirogov Str., Novosibirsk 630090, Russia

Abstract— A new method for the minimization of the crest factor for multi-tone signals based on the sampling functional optimization is proposed. The minimum of smooth functional is used as an initial value for the min-max search. For the number of tones the mini-max values are better than previously reported. Applications in fiber optics are discussed.

1. INTRODUCTION

Minimizing of the crest factor for multi-tone signals is an important problem known for a long time in radiophysics [1]. Optimization of optical comb filters based on fiber Bragg grating put in the forefront this problem in optics [2], too.

Let us consider the sampling functional

$$S(x; \varphi_0, \ldots, \varphi_{N-1}) = \sum_{l=0}^{N-1} \exp\left[ilx + i\varphi_l\right], \tag{1}$$

where $x = \Delta k z$ is the dimensionless coordinate z, Δk is the distance between the channels, N is the number of channels, should be minimized with respect to phases $\varphi_l, l = 0, 1, \ldots, N-1$. The aim is to find the min-max value

$$g = \min_{\vec{\varphi}} \max_{0 \le x \le 2\pi} |S(x; \vec{\varphi})| \tag{2}$$

and corresponding vector of phases $\vec{\varphi} = (\varphi_0, \varphi_1, \ldots, \varphi_{N-1})$. Phases $\varphi_0 = \varphi_1 = 0$ are arbitrary, however all the other $N-2$ variables should be scanned. It makes the problem rather complicated for $N > 10$ and stimulates the development of approximate numerical methods.

Friese [1] proposed minimization procedure by clipping method similar to Gerchberg-Saxton algorithm [3]. The starting point was complex generalized Barker sequences. Kolossovski et al. [4] suggested the functional approach. Functional $\langle |S| \rangle$ of phases is minimized, where the angle brackets denote the averaging over coordinate x. Then its minimum is exploited for numerical calculation of the mini-max value by clipping. The functional approach gives better values of g. In the present paper we propose a modified functional that gives comparable results without the clipping and even better values at some N.

2. FUNCTIONAL

The square of absolute value $|S|^2$ of the sampling functional can be expressed in terms of discrete correlation functions c_l

$$|S|^2 = N + \sum_{l=1}^{N-1} c_l e^{ilx}, \qquad c_l = \sum_{j=1}^{N-l} m_{j+l} m_j^*, \tag{3}$$

where $m_j = \exp[ij\varphi_j]$. The average value can be calculated from (3) and turns to be constant: $\langle |S|^2 \rangle = N$. Then the higher powers should be used for preliminary minimization, e.g., 4th power. At large number of channels the functional suggested in [4] is asymptotically proportional to the 4th power functional

$$X = \frac{2}{N^2} \langle |S|^4 \rangle - 1 = \frac{2}{N^2} \sum_{l=1}^{N-1} |c_l|^2. \tag{4}$$

Here we propose the 6-th power functional

$$Y = \langle |S|^6 \rangle. \tag{5}$$

The sixth-power functional can also be expressed in terms of discrete correlation functions (3)

$$Y = N^3 + 6N^2 \sum_{l=1}^{N-1} |c_l|^2 + 9N \sum_{l=1}^{N-1} \left(\sum_{m=1}^{N-l-1} c_l c_m c_{l+m}^* + \sum_{m=1}^{l-1} c_l c_m^* c_{l-m}^* \right). \tag{6}$$

It is smooth, real, its gradient vector is known, then its minimum can be easily calculated numerically. At the same time, this functional is more sensitive to the crest-factor, than fourth-power functional (4). Then its minimum is closer to desired min-max and can be applied as a starting point for some procedure of numerical minimization. Case $N = 9$ is shown in Fig. 1. Maximal value of the dotted curve is a bit greater than that of dashed curve. Both are close to the best solid curve. The difference between functionals (4) and (6) increases with the number of channels N. For example, at $N = 19$ functional X is minimal at $g = 1.160$, Y is minimal at $g = 1.109$, while the best value is $g = 1.084$.

3. NUMERICAL MINIMIZATION

For the minimization of $\max_x |S(x)|$, we use the standard Powell method [5]. The function is not smooth, then a zero-order method is necessary. Initial value of vector $\vec{\varphi}$ is being found by functional Y minimization. The initial and final plots of the sample functional are shown in Fig. 2. The azimuthal angle is coordinate x, the modulus is normalized value $|S|/\sqrt{N}$. The right picture resembles the left one. Thus, the minimum of sixth-power functional is close to the min-max value. That is why the standard minimization method is sufficient and clipping is not necessary. The
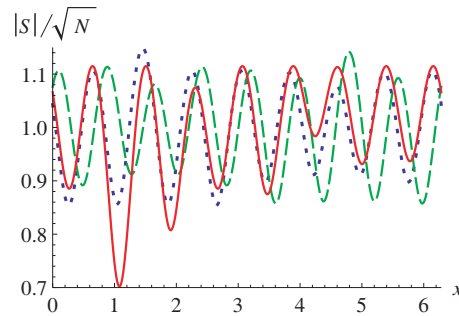
Figure 1: Absolute value of the sample functional $|S(x)|/\sqrt{N}$ as a function of coordinate x at $N = 9$. Phases are found by minimization of functional X (dotted), Y (dashed), and the best result of numerical minimization (solid). Corresponding values of min-max g are 1.1483, 1.1417, 1.1149, respectively.
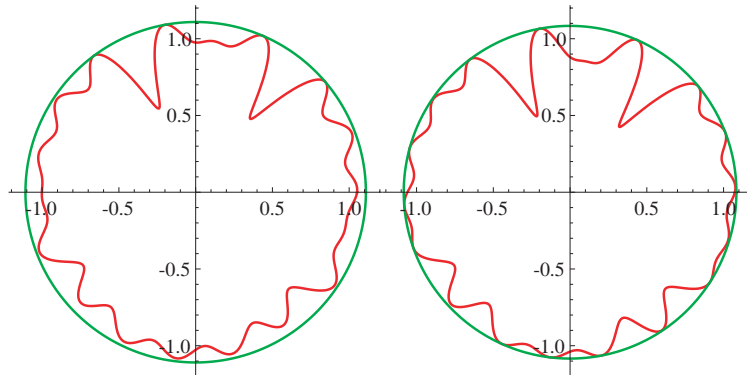
Figure 2: The sampling functional for $N = 19$ in polar coordinates: *left* — After the first stage, the minimization of Y; *right* — After the second stage, further minimization of $\max_x |S|$. Min-max values are shown by circles. The radius of the left circle is $g = 1.1089$, the right radius is $g = 1.0836$.
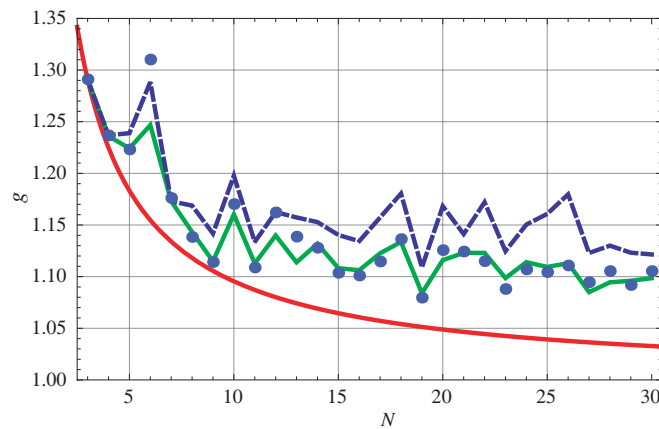
Figure 3: The achieved value of the min-max g as a function of the channel number $N = 3 \div 30$: The preliminary minimization of functional Y (dashed line), the best results found in the present calculation (broken solid line), the values reached by clipping [4] (circles), and the theoretical limit (7) (bottom smooth solid curve).
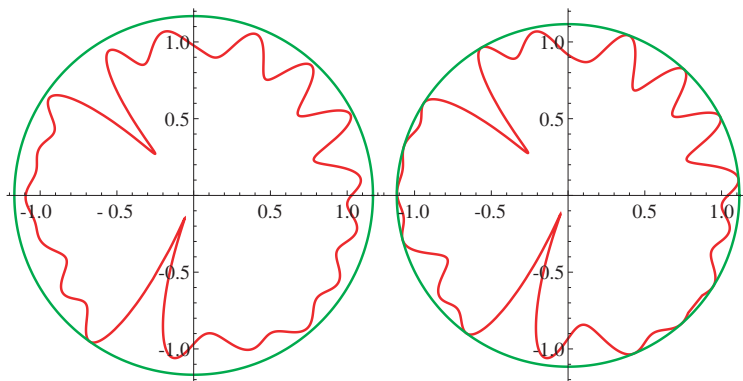
Figure 4: The sampling functional for $N = 20$: *left* — After the minimization of Y; *right* — After the minimization of $\max_x |S|$. The radii of the left and right circles are $g = 1.1682$ and $g = 1.1158$, respectively.

minimization procedure trims the peaks, but safes the symmetry of solution (the mirror plane in polar coordinates).

The results of two-stage minimization for $N = 3 \ldots 30$ are summarized in Fig. 3 by the broken line. The theoretical estimate of minimal value by Friese [1]

$$\inf g = \sqrt{1 + \frac{2}{N}} \qquad (7)$$

is shown by the smooth line. Filled circles indicate the result obtained by the clipping method. The best results do not achieve the theoretical limit, except of $N = 3, 4, 9$. The other observation is different values of g_N at odd and even N. As a rule, for odd N the value is less.

To compare profiles for even and odd numbers of channels we plot in Fig. 4 the same, as in Fig. 2, but for $N = 20$. Two differences are evident: For even number the profile has no symmetry plane, but has deep minima. This two differences are likely originate lager value of g.

4. CONCLUSIONS

Thus, the proposed functional has a number of advantages. It allows the explicit formula for the gradient with respect to phases at arbitrary number N of dephasing angles necessary for efficient numerical minimization. The functional is sensitive even to weak deviations from the homogeneous distribution. Then its minimum could be applied as a starting point for the numerical mini-max evaluation. Starting from the phases minimizing Y one could get by generic method the value of min-max none the worse than the result given by the special clipping technique while the latter started from the $\langle |S| \rangle$ functional minimum or Barker sequences.

REFERENCES

1. Friese, M., "Multitone signals with low crest factor," *IEEE Trans. on Comm.*, Vol. 45, No. 10, 1338–1244, 1997.
2. Al-Marzoug, S. M. and R. J. W. Hodgson, "Luus-Jaakola optimization procedure for phase-only sampled-fiber Bragg gratings," *Appl. Opt.*, Vol. 47, No. 13, 2275–2280, 2008.
3. Gerchberg, R. W. and W. O. Saxton, "Phase determination for image and diffraction plane pictures in the electron microscope," *Optik*, Vol. 34, 275, 1971.
4. Kolossovski, K. Y., R. A. Sammut, A. V. Buryak, and D. Y. Stepanov, "Three-step design optimization for multi-channel fibre Bragg gratings," *Optics Express*, Vol. 11, No. 9, 1029–1038, 2003.
5. Press, W. H., B. P. Flannery, S. A. Teukolsky, and W. T. Vetterling, *Numerical Pecipes in Fortran*, Cambridge University Press, Cambridge-New York, 1992.

Two-photon Autocorrelation in a MQW GaAs Laser at 1.55 μm

D. Duchesne[1], L. Razzari[1, 2], L. Halloran[1], M. Giguère[1], F. Légaré[1],
R. Morandotti[1], A. J. SpringThorpe[3], D. N. Christodoulides[4], and D. J. Moss[1, 5]

[1]INRS-EMT, Varennes, Qubec, Canada
[2]Dipartimento di Elettronica, Università di Pavia, Pavia, Italy
[3]Canadian Photonics Fabrication Centre (CPFC), National Research Council
Ottawa, Ontario, Canada
[4]College of Optics and Photonics, CREOL & FPCE, University of Central Florida
Orlando, USA
[5]IPOS/CUDOS, School of Physics, University of Sydney, Sydney, Australia

Abstract— A quadratic two-photon photocurrent is measured in a novel multiple-quantum well GaAs laser waveguide at 1550 nm. We show that this device is ideal for nonlinear detection and signal processing applications due to its large efficiency and high sensitivity. In particular, we measure the autocorrelation trace of a 100 fs pulse using sub-watt peak power levels.

1. INTRODUCTION

Two photon detectors have become increasingly important for ultrafast signal processing applications and for the characterization of ultrashort pulses [1–6]. Recently, they have been shown to be ideal for optical time division multiplexing [3], optical performance monitoring [4], switching [5], and for optical thresholding devices in code division multiple access systems [6]. They are attractive since they combine both the (near instantaneous) nonlinear response with a direct conversion to the electrical domain in a small, cost-effective package.

Integrated nonlinear detection through two-photon absorption (TPA) in semiconductor waveguides has previously been demonstrated in silicon [7] and AlGaAs [8, 9]. Despite the large amount of work dedicated to this field in the early 90's, the inclusion of quantum wells for nonlinear detection purposes has not been explored. Given the surge in activity in all-optical signal processing during the last 6 to 8 years [10], it is certainly of significant interest to see whether the enhanced performance of the linear GaAs/AlGaAs multiple quantum well (MQW) optoelectronic devices developed in the 1990s [11–14] for operation at ~ 775 nm also translate into improved performance for nonlinear (two-photon based) operation at 1550 nm (i.e., near the half-bandgap).

In this paper we report a novel GaAs MQW laser structure and demonstrate a two-photon nonlinear photocurrent at 1550 nm. This device is similar to previous [11] components developed to achieve efficient multifunctional (laser, electroabsorption modulator, photodetector) performance at 850 nm. Here, we show that our device also displays similar advantages when operated as a nonlinear photodetector near 1550 nm, such as improved quantum efficiency, high speed operation as well as a large sensitivity. Moreover, we demonstrate the practical use of this device as an integrated autocorrelator by measuring the trace of 100 fs pulses. Because these components operate efficiently both as reverse-biased EA modulators and two photon detectors, they raise the prospect of being able to electrically modulate the TPA coefficient and hence the nonlinear figure of merit (FOM) [15, 16] at 1550 nm (i.e., near half the direct bandgap, as mentioned before) via the quantum confined Stark Effect.

2. THEORY

Nonlinear absorption processes arise from the imaginary part of the odd order nonlinear susceptibilities [15], and generally occur at high optical intensities. When the photon energy is greater than half the bandgap, a two-photon process can occur whereby an electron is excited to the conduction band via a 2 step process involving a virtual state. Efficient TPA photocurrent results for photon energies comprised between the bandgap and the half-band gap, which for GaAs is typically between 0.71 EV and 1.43 eV (870 nm to 1740 nm). This photocurrent can be shown to be quadratic with the input light power (or intensity) in the device [17]:

$$J = \eta \frac{e}{2hf} \frac{\beta z}{A_{eff}} P_0^2 \tag{1}$$

Here J is the photocurrent, P_0 is the input power, A_{eff} the effective area of the mode in the waveguide, h is Planck's constant, f the frequency of the incident light, β is the TPA coefficient, z the propagation length in the waveguide and e the electronic charge. η refers to the internal quantum efficiency, namely the ratio of electron-hole pairs collected to the absorbed number of photons absorbed in the material. Several approximations are required to arrive at Equation (1), including neglecting free carrier and single photon absorption, as well as requiring moderate power levels (as the photocurrent saturates at high powers). These approximations have been justified experimentally below and theoretically elsewhere [17].

Two useful parameters in determining the efficiency of the nonlinear photocurrent process for practical applications are the external quantum efficiency and the device sensitivity, defined by:

$$\eta_{ext} = \frac{Jhf}{eP_0} \tag{2}$$

$$S_J = \frac{J}{P_{peak} \cdot P_{avg}} \quad (S = P_{peak} \cdot P_{avg}) \tag{3}$$

Equation (2) relates how much photocurrent is generated for the total light power coupled into the waveguide device (to differentiate from the internal efficiency which relates the absorbed power, a quantity hard to measure experimentally), where as Equation (3) describes the minimum photocurrent observable in the device and in parenthesis the typical efficiency for second harmonic generation autocorrelators.

3. DEVICE AND FABRICATION

The MQW waveguide structure is composed of an $Al_xGa_{1-x}As$ heterostructure, as is shown in Figure 1, which was grown via molecular beam epitaxy while precisely controlling the doping and the temperature. A p-i-n junction was formed by p-doping the top side of the device with beryllium and the bottom side (n-doped) with silicon. The active layer consists of four GaAs quantum wells of 8 nm widths separated by 3.5 nm $Al_{20}Ga_{80}As$ barriers and forms the core region of the waveguide structure. A high quality film morphology was targeted in order to produce better laser and detector performances than those in bulk GaAs/AlGaAs TPA detectors. The waveguide ridge was defined using stepper lithography and patterned with inductively coupled plasma dry etching, resulting in extremely low sidewall roughness. The device was finally metalized, annealed and then cleaved into 250 μm long bars.
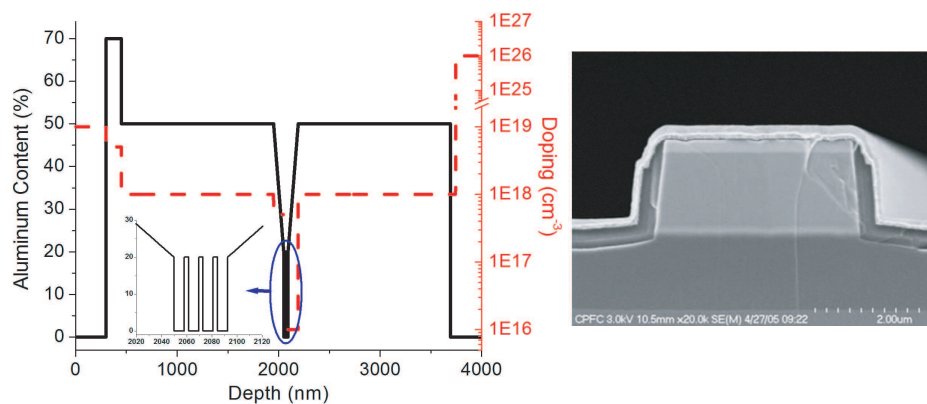
Figure 1: (Left) Doping and alloy profile and of the AlGaAs multilayer structure. Inset: Zoom of undoped quantum well region. (Right) Scanning electron microscopy picture of device after metallization.

4. QUADRATIC PHOTOCURRENT

Pulses from a mode-locked fiber laser, emitting 1 ps pulses at 5.2 MHz and centered at 1550 nm, were used to characterize the nonlinear photocurrent from the MQW device. The waveguide was placed on a three dimensional micro-positioner and 50X objectives were used to focus the light onto and out of the device. A Lock-In amplifier (in current mode) was used to measure the generated current by probing the top (p-side) of the device. Average power measurements were performed

using a photodetector, from which the peak power of our pulses were obtained from the given laser repetition rate and experimentally measured time duration of the pulse. A transverse electric mode polarization was used in all our experiments.

Characterization of the device at the bandgap (~ 850 nm) was first performed [17], which confirmed the device operation as a laser as well as the expected quantum confined Stark Effect when the device was biased [18]. Subsequently, using a variable neutral density filter and the 1550 nm source, we varied the incident power on the MQW device between 0 to 2 Watts and recorded the generated photocurrent. The photocurrent was found to be purely quadratic, confirming the TPA nature, as can be seen in Figure 2. It was found that single photon absorption was negligible which testifies to the excellent growth quality of the device. In fact, the photocurrent remained purely nonlinear for sub-Watt peak powers. Note that the absolute level of absorption of the device is quite low. This is a direct result of the short waveguide length — we estimate that > 200 W peak power would be needed to induce a 10% decrease in transmission from TPA alone, which although readily achievable with standard laser sources, would damage the structure. These results suggest that our device is ideal for telecommunication applications where low energy pulses are used, as the pulse can be sampled, monitored or characterized from the effects owing to a strong TPA, while still maintaining an excellent throughput which shows no trace of nonlinear phase or modulation.

We also determined the external efficiency as a function of input peak power (plotted in Figure 2) and obtained the expected linear relation. The external efficiency of our device was calculated according to Equation (2), from which the slope of the linear fit of Figure 2 was determined to be 8.6×10^{-5} W^{-1}, seven orders of magnitude greater than previously reported in photodiodes [19], and comparable with previously reported p-i-n waveguide devices [9]. The inclusion of quantum wells is predicted to have a large increase in the quantum efficiency, and can be theoretically close to 100% as previously shown in similar GaAs laser structures [12, 13]. By making this assumption, the TPA coefficient can also be estimated, and we obtain $\beta \sim 0.54$ cm/GW from Equation (18), agreeing very well with previous reports in non-MQW AlGaAs waveguides [20].

The minimum detectable photocurrent with our TPA photodetector, i.e., 28 pA, was obtained at a peak input peak power as low as 330 mW. Using Equation (3) we estimate the sensitivity of the device to be 0.1 nA/mW^2 (0.28 mW^2), orders of magnitude better than commercial SHG autocorrelators where $\sim 10^{-3}$ nA/mW^2 are typically observed when they are coupled to photomultiplier tubes [21]. These results compare well with recent reports of SOI and InGaAsP based waveguide autocorrelators with sensitivities of 1 mW^2 [22] and 0.08 mW^2 [23], respectively. Recent results in GaAs microcavities have shown a sensitivity of $\sim 9.3 \times 10^{-4}$ mW^2 due to the TPA enhancement [24], suggesting that a highly reflective coating on our waveguide facets would significantly increase its sensitivity.
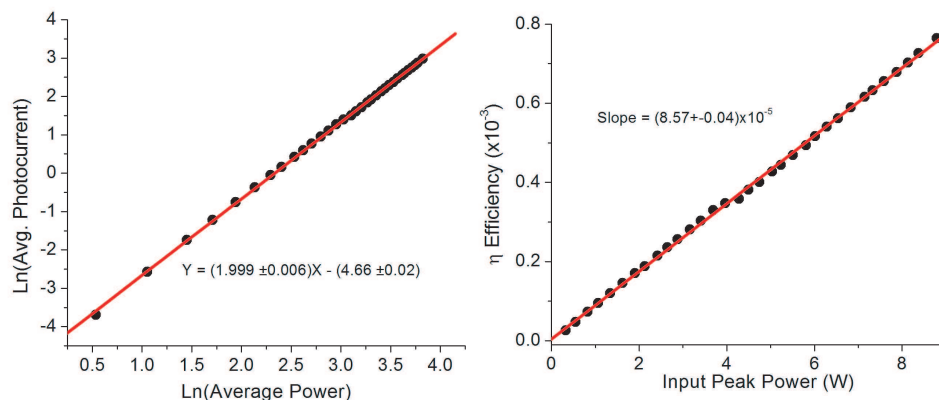
Figure 2: (Left) Average photocurrent as a function of the input power in the waveguide. A log-log plot determines that the relation is purely quadratic, and hence that the photocurrent is a result of TPA. (Right) The external efficiency as a function of the coupled input peak power.

5. AUTOCORRELATION

To demonstrate the feasibility of using the MQW waveguide device in practical applications, a pump-probe set-up was built whereupon an incident pulse was split into 2 using a 50 : 50 beam

splitter. One of the arms was temporally delayed and cross polarized with respect to the original, and then both arms were recombined by means of a second beam splitter and then sent into the waveguide via the end-fire coupling set-up described above. As the photocurrent generated is proportional to the light power squared (or intensity squared), the autocorrelation of the input pulse can be measured by simply tuning the delay.

For this experiment, 100 fs pulses from an optical parametric oscillator (OPO) at 80 MHz were used. The autocorrelation of this pulse was experimentally measured to have a FWHM of 145 fs, and can be seen in Figure 3. Assuming a Gaussian shape for the pulse, this corresponds to the expected 100 fs pulse from the OPO. An autocorrelation trace was also obtained with a standard commercial second-harmonic autocorrelator, which proves the accuracy of our waveguide device for this application. Our set-up allowed for a 1 fs resolution, although limitations from modal dispersion (between the cross-polarized pulses) and TPA process speed also need to be considered.
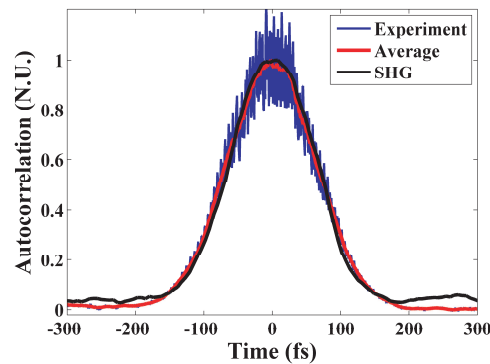
Figure 3: (Blue) Experimental autocorrelation measurement. The rapid oscillations are residual interference caused by the slightly non-orthogonal beams (delayed and non-delayed). The interference is about the mean 'non-interference' value which we obtained (red) by simply averaging the experimental data. The autocorrelation obtained with a commercial SHG autocorrelator is also shown (Black).

6. CONCLUSION

We demonstrate two-photon detection in a reverse biased GaAs MQW laser structure near 1550 nm for the first time. We observed a purely nonlinear TPA photocurrent at 1550 nm with a high sensitivity and external efficiency. Moreover, an autocorrelation trace of ultrashort 100 fs pulses was obtained. These results are extremely promising for nonlinear signal processing applications such as optical performance monitoring and pulse characterization, where the benefit of low cost and ability to combining a nonlinear optical response with direct optical to electrical conversion is extremely useful. The MQW structure also raises the prospect of several qualitatively new features for TPA detectors such as a combined nonlinear optical and ultrafast electrical response, with efficient carrier sweep-out rates greatly reducing the effects of TPA generated carrier pile-up, as well as the potential for direct electrical control of the nonlinear figure of merit via the quantum confined Stark Effect.

REFERENCES

1. Xi, P., Y. Andegeko, L. R. Weisel, V. V. Lozovoy, and M. Dantus, "Greater signal, increased depth, and less photobleaching in two-photon microscopy with 10 fs pulses," *Opt. Commun.*, Vol. 281, 1841–1849, 2008.

2. Huber, R., A. Brodschelm, F. Tauser, and A. Leitenstorfer, "Generation and field-resolved detection of femtosecond electromagnetic pulses tunable up to 41 THz," *Appl. Phys. Lett.*, Vol. 76, 3191–3193, 2000.

3. Dorrer, C., "High-speed measurements for optical telecommunication systems," *IEEE J. Sel. Top. Quantum Electron.*, Vol. 12, 843–858, 2006.

4. Wielandy, S., M. Fishteyn, and B. Zhu, "Optical performance monitoring using nonlinear detection," *J. Lightwave Technol.*, Vol. 22, 784–793, 2004.

5. Tsang, H. K., R. S. Grant, R. V. Penty, I. H. White, J. B. D. Soole, E. Colas, H. P. Leblanc, N. C. Andreadakis, M. S. Kims, and W. Sibbett, "GaAs/GaAlAs multiquantum well waveguides for all-optical switching at 1.55 μm," *Electron. Lett.*, Vol. 27, 1993–1995, 1991.

6. Zheng, Z., A. M. Weiner, J. H. Marsh, and M. M. Karkhanehchi, "Ultrafast optical thresholding based on two-photon absorption GaAs waveguide photodetectors," *IEEE Photon. Technol. Lett.*, Vol. 9, 493–495, 1997.

7. Salem, R., M. A. Foster, A. C. Turner, G. F. Geraghty, M. Lipson, and A. L. Gaeta, "Signal regeneration using low-power four-wave mixing on silicon chip," *Nature Photon*, Vol. 2, 35–38, 2008.

8. Laughton, F. R., J. H. Marsh, and A. H. Kean, "Very sensitive two-photon absorption GaAs/AlGaAs waveguide detector for an autocorrelator," *Electron. Lett.*, Vol. 28, 1663–1665, 1992.

9. Laughton, F. R., J. H. Marsh, D. A. Barrow, and E. L. Portnoi, "The two-photon absorption semiconductor waveguide autocorrelator," *IEEE J. Quantum Electron.*, Vol. 30, 838–845, 1994.

10. Radic, S., D. J. Moss, and B. J. Eggleton, "Nonlinear optics in communications: From crippling impairment to ultrafast tools," *Optical Fiber Telecommunications V: Components and Subsystems*, Academic Press, Oxford, 2008.

11. Chatenoud, F., K. Dzurko, M. Dion, D. J. Moss, R. Barber, and D. Landheer, "GaAs/AlGaAs multiple quantum well lasers for monolithic integration with optical modulators," *Can. J. Phys.*, Vol. 69, 491–496, 1991.

12. Moss, D., F. Chatenoud, S. Charbonneau, A. Delage, D. Landheer, and R. Barber, "Laser compatible waveguide modulators," *Can. J. Phys.*, Vol. 69, 497–507, 1991.

13. Moss, D. J., D. Landheer, D. Halliday, S. Charbonneau, F. Chatenoud, and D. Conn, "High speed photodetection in a reverse biased GaAs/AlGaAs GRINSCH SQW laser structure," *Photon. Technol. Lett.*, Vol. 4, 609–611, 1992.

14. Moss, D. J., D. Landheer, A. Delage, F. Chatenoud, and M. Dion, "Laser compatible waveguide electroabsorption modulator with high contrast and low operating voltage in GaAs/AlGaAs," *IEEE Photon. Technol. Lett.*, Vol. 3, 645–647, 1991.

15. Aitchison, J. S., D. C. Hutchings, J. U. Kang, G. I. Stegeman, and A. Villeneuve, "The nonlinear optical properties of AlGaAs at the half band gap," *IEEE J. Quantum Electron.*, Vol. 33, 341–348, 1997.

16. Villeneuve, A., C. C. Yang, G. I. Stegeman, C. N. Ironside, G. Scelsi, and R. M. Osgood, "Nonlinear absorption in a GaAs waveguide just above half the band gap," *IEEE J. Quantum Electron.*, Vol. 30, 1172–1175, 1994.

17. Duchesne, D., L. Razzari, L. Halloran, R. Morandotti, A. J. SpringThorpe, D. N. Christodoulides, and D. J. Moss, "Two-photon photodetector in a multiquantum well GaAs laser structure at 1.55 μm," *Opt. Expr.*, Vol. 17, 5298–5310, 2009.

18. B. Miller, D. A., D. S. Chemla, T. C. Damen, A. C. Gossard, W. Wiegmann, T. H. Wood, and C. A. Burrus, "Band-edge elecroabsorption in quantum well structures: the quantum confined stark effect," *Phys. Rev. Lett.*, Vol. 53, 2173–2176, 1984.

19. Takagi, Y., T. Kobayashi, K. Yoshihara, and S. Imamura, "Multiple-shot and single-shot sutocorrelator based on 2-photon conductivity in semiconductors," *Opt. Lett.*, Vol. 17, 658–660, 1992.

20. Villeneuve, A., C. C. Yang, G. I. Stegeman, C.-H. Lin, and H.-H. Lin, "Nonlinear refractive-index and two photon-absorption near half the band gap in AlGaAs," *Appl. Phys. Lett.*, Vol. 62, 2465–2467, 1993.

21. Reid, D. T., W. Sibbett, J. M. Dudley, L. P. Barry, B. Thomsen, and J. D. Harvey, "Commercial semiconductor devices for two photon absorption autocorrelation of ultrashort light pulses," *Opt. Photon. News*, Vol. 9, 8142–8144, 1998.

22. Liang, T. K., H. K. Tsang, I. E. Day, J. Drake, A. P. Knights, and M. Asghari, "Silicon waveguide two-photon absorption detector at 1.5 µm wavelength for autocorrelation measurements," *Appl. Phys. Lett.*, Vol. 81, 1323–1325, 2002.

23. Tsang, H. K., L. Y. Chan, J. B. D. Soole, H. P. LeBlanc, M. A. Koza, and R. Bhat, "High sensitivity autocorrelation using two-photon absorption in InGaAsP waveguides," *Electron. Lett.*, Vol. 31, 1773–1775, 1995.

24. Maguire, P. J., L. P. Barry, T. Krug, W. H. Guo, J. O'Dowd, M. Lynch, A. L. Bradley, J. F. Donegan, and H. Folliot, "Optical signal processing via two-photon absorption in a semiconductor microcavity for the next generation of high-speed optical communications network," *J. Lightwave Technol.*, Vol. 24, 2683–2692, 2006.

Light Scattering by Preferentially Oriented Ice Crystals

A. Borovoi and N. Kustova

Institute of Atmospheric Optics, Rus. Acad. Sci., Tomsk, Russia

Abstract— Scattered light for preferentially oriented ice crystals is divided into specular and diffuse components where the specular scattering is created by horizontally oriented facets of fluttering crystals. The specular component for a fluttering thin plate modeling these crystals is found analytically as a 2D convolution of a geometric optics pattern depending only on flutter and an independent diffraction function. The geometric optics pattern is explicitly expressed through the probability density for particle tilts and the diffraction function is taken in the Fraunhofer diffraction approximation. Certain possibilities to retrieve both flutter parameters and particle sizes from the specular patterns are discussed.

1. INTRODUCTION

Cirrus clouds consisting mainly of ice crystals play an important role in radiative budget of the Earth. Consequently, their radiative properties are needed to incorporate in up-to-date numerical models of climate prediction and change. These radiative properties have been calculated by a lot of authors in the assumption that the crystals are 3D randomly oriented. However, experimental data obtained from both the ground [1] and satellites [2–4] prove that the ice crystals often reveal their preferentially horizontal orientation. For such crystals, the radiative properties are poor studied yet both experimentally [1–4] and theoretically [5, 6].

Light scattered by preferentially oriented ice crystals reveals a specific property. Namely, it is divided on two qualitatively different parts called the specular and diffuse components (e.g., [7]). Therefore it is convenient to introduce the terms of specular and diffuse scattering by a crystal if the crystal obeys a sharp probability distribution over its spatial orientations. To some extend, the specular scattering is formed by reflection of light from those crystal facets that are horizontally oriented while the other facets create the diffuse component. Radiative properties of the specular component are simply expressed through the microphysical parameters of the crystals: Sizes, shapes and orientation. Such expressions are subjects of direct scattering problems. And vice versa, from the point of view of inverse scattering problems, this is the specular component that is mostly informative for retrieving the microphysical parameters from scattered light. A purpose of this paper is to present a simple and rather general theory for the specular scattering that can be effectively used for both direct and inverse scattering problems. It is worthwhile to note that such a theory can be applied not only to light scattering in the atmosphere but also to any scattering media consisting of aligned and large as compared to the incident wavelength particles. Examples of such media are special paints, biological structures and tissues, forest canopy, and so on.

Oscillations of orientation of the preferentially oriented ice crystals near the horizon are called flutter. In the atmosphere, the flutter is usually confined to a narrow cone with the maximum flutter tilt T of about a few degrees. The value T for cirrus clouds was studied from the ground by use of scanning polarization lidars [1]. Also, the value T was estimated from the data obtained for the specular scattering component by the satellite radiometer POLDER [2, 3]. We show that not only the maximum flutter tilt T, but the tilt probability density can be, in principle, retrieved from certain specular scattering patterns.

2. SPECULAR AND DIFFUSE SCATTERING BY AN ICE CRYSTAL

In the problem of light scattering by an atmospheric ice crystal, it is expedient to consider the near zone at first where a lot of analytical expressions that are valid at arbitrary distances from the particle can be written down directly without any analytical or numerical calculations (e.g., [8]). Geometric optics description of the electromagnetic field in the near zone is a rather exact approximation. It is no wonder that practically all numerical calculations of this problem are made by means of the ray-tracing method corresponding exactly to geometric optics. Within the framework of geometric optics, it is obvious that the near-zone scattered light is produced by illuminated facets of the crystal. Every facet illuminated by a plane electromagnetic wave creates two plane-parallel beams with known transversal shapes and propagation directions. One of them is the reflected beam which becomes directly a component of the near-zone scattered field desired. Another, i.e.,

refracted, beam propagates in the crystal until it meets other facets. Then every of these facets produce new components of the near-zone field because of refraction, and so on. The total near-zone scattered field consists of a lot of plane-parallel beams with different sizes, shapes, polarization, and propagation directions. It is worthwhile to note that such a facet-tracing computer code calculating scattering matrices for ice crystals was developed by us [9, 10] and it has been successfully exploring.

Let us go to horizontally oriented crystals. We say that a crystal has a perfect horizontal orientation if one or more of its facets are always horizontal when the crystal rotates about the vertical. For such a rotating crystal, a horizontal facet reflects the incident light in the same direction while non-horizontal facets smooth their reflected beams over changing propagation directions. As a result, the scattered light averaged over the crystal rotation consists of a bright dot and a fuzzy wan pattern corresponding to the specular and diffuse scattering, respectively.

In practice, every horizontally oriented crystal is exposed to the flutter or, equivalently, it reveals its preferentially horizontal orientation where the rotation axis oscillates slightly about the vertical. In this case, both the bright dot of the specular component and a fuzzy pattern of the diffuse component are expanded as compared to those of a perfectly oriented crystal. It is well known that the preferentially horizontal orientation of ice crystals in the atmosphere is inherent mainly to plate-like crystals. Here two basic facets of the plate-like crystals tend to be horizontal. Column-like crystals sometimes reveal such kind of orientation, too. In particular, the so-called Parry orientation for a hexagonal column means that the long axis of a column rotates in the horizontal plane about the vertical while two rectangular crystal facets are saved horizontally.

The split of the scattered electromagnetic field $\mathbf{E}$ into the specular and diffuse components

$$\mathbf{E} = \mathbf{E}_s + \mathbf{E}_d \tag{1}$$

is strictly defined as follows. Among the horizontally oriented facets of a crystal, it is easy to distinguish a main oriented facet that contributes directly to the specular component by reflection of the incident light. In addition to this plane-parallel beam reflected by the main oriented facet, there are a number of other beams leaving the crystal in the same direction at a given crystal orientation. By definition, superposition of all the beams leaving the crystal in the same direction as the beam reflected from the main oriented facet are called the specular component $\mathbf{E}_s$. The rest part of the total near-zone scattered field corresponds to the diffuse scattering component $\mathbf{E}_d$.

We should emphasize that the superposition of Eq. (1) is quite general. It retains its validity at arbitrary distance from the particle including the wave zone. Indeed, at any distance from the crystal each component of Eq. (1) can be obtained independently of the other by certain integral transform of the near-zone fields. By definition, the split of Eq. (1) is provided by appearance of the preferentially oriented facets of crystals. Otherwise, for example, in the case of 3D randomly oriented crystals, this split becomes meaningless.

3. SCATTERING BY A FLUTTERING PLATE

The main physical regularities inherent to the specular component can be obtained within a simplified problem of light scattering by a fluttering plate. Consider a thin plate with its orientation $\mathbf{N}$ illuminated by an incident plane electromagnetic wave propagating in the direction $\mathbf{i}$. In the near zone, the scattered field corresponding to the specular scattering is a plane-parallel beam propagating in the reflection direction $\mathbf{r}$. These three unit vectors $\mathbf{r}$, $\mathbf{i}$, and $\mathbf{N}$ are connected with each other by the following equations

$$\mathbf{r} = \mathbf{i} - 2(\mathbf{i} \cdot \mathbf{N})\mathbf{N} \qquad \mathbf{N} = (\mathbf{i} - \mathbf{r})/|\mathbf{i} - \mathbf{r}| \tag{2}$$

A dot between two vectors means their scalar product.

At large distance from the plate, the reflected plane-parallel beam spreads about the reflection direction $\mathbf{r}$ because of diffraction. In the wave zone, this beam is transformed into a spherical diverging wave. Though polarization of the scattered field can be easily taken into account, the scalar approximation is used in this paper for brevity. Then the differential cross section of the spherical scattered wave $\sigma(\mathbf{s}, \mathbf{i})$ is generally presented as

$$\sigma(\mathbf{s}, \mathbf{i}) = A \left| \mathbf{I} \cdot \mathbf{N} \right| R(\mathbf{i} \cdot \mathbf{N}) F_{\mathbf{i}, \mathbf{N}}(\mathbf{s} - \mathbf{r}) \tag{3}$$

where A is a plate area, R is the reflection coefficient that is well known for any given polarization of incident light and the dimensionless function $F_{\mathbf{i}, \mathbf{N}}$ normalized to unity describes diffraction. In

the Fraunhofer approximation [11] the function $F_{\mathbf{i},\mathbf{N}}$ is the 2D Fourier transform

$$F_{\mathbf{i},\mathbf{N}}(\mathbf{s} - \mathbf{r}) \approx \left| (k/2\pi) \int \exp\left(-ik\left[(\mathbf{s} - \mathbf{r}) \cdot \boldsymbol{\rho}'\right]\right) S'(\boldsymbol{\rho}')d\boldsymbol{\rho}' \right|^2 / A' \tag{4}$$

where $k = 2\pi/\lambda$, λ is the wavelength, and the function $S'(\boldsymbol{\rho}')$ describing a shape of the near-zone reflected beam is equal to unity inside and to zero outside the beam in the plane $\boldsymbol{\rho}'$ perpendicular to the reflection direction $\mathbf{r}$. In particular, for a circle of the radius a, we get

$$F_{\mathbf{i},\mathbf{N}}(\mathbf{s} - \mathbf{r}) = \frac{\beta(ka)^2}{4\pi} \left(\frac{2J_1\left[ka\sqrt{(w_{\|}\beta)^2 + w_{\perp}^2}\right]}{ka\sqrt{(w_{\|}\beta)^2 + w_{\perp}^2}} \right)^2 \tag{5}$$

where J_1 is the Bessel function and $\beta = (\mathbf{i} \cdot \mathbf{N})$. Here we denote a projection of the vector $\mathbf{s} - \mathbf{r}$ on the plane $\boldsymbol{\rho}'$ orthogonal to the reflection direction $\mathbf{r}$ as the vector $\mathbf{w}$ and its longitudinal and transversal components relative to the direction $[\mathbf{N} - (\mathbf{N} \cdot \mathbf{r})\mathbf{r}]/|\mathbf{N} - (\mathbf{N} \cdot \mathbf{r})\mathbf{r}|$ are denoted $w_{\|}$ and $w_{\perp}$, respectively.

We have to average the scattering differential cross-section given by Eq. (3) over a probability density of plate orientations $p(\mathbf{N})$. Denoting this averaging by angular brackets, we get finally after certain calculations

$$\langle \sigma(\mathbf{s}, \mathbf{i}) \rangle = (A/4) \int R(\mathbf{i} \cdot \mathbf{N}(\mathbf{r})) F_{\mathbf{i},\mathbf{N}(\mathbf{r})}(\mathbf{s} - \mathbf{r}) p(\mathbf{N}(\mathbf{r})) d\mathbf{r} \tag{6}$$

To clarify a physical meaning of Eq. (6), let us ignore diffraction by replacing the diffraction function $F_{\mathbf{i},\mathbf{N}}(\mathbf{s} - \mathbf{r})$ by the Dirac delta-function $\delta(\mathbf{s} - \mathbf{r})$. In this case, Eq. (6) is reduced to the geometric optics differential cross section

$$\langle \gamma(\mathbf{s}, \mathbf{i}) \rangle = (A/4) R(\mathbf{i} \cdot \mathbf{N}(\mathbf{s})) p(\mathbf{N}(\mathbf{s})) \tag{7}$$

Equation (7) reveals a remarkably simple physical meaning. It means that the differential cross section of a fluttering plate within the framework of geometric optics at any scattering direction $\mathbf{s}$ is equal (with the trivial factor of $AR/4$) to the probability density of flutter at the corresponding plate orientation $\mathbf{N}(\mathbf{s})$. Main properties of the function $\langle \gamma(\mathbf{s}, \mathbf{i}) \rangle$ are studied in our recent paper [12].

Now Eq. (11) allows us to write down Eq. (10) as the physically obvious 2D convolution:

$$\langle \sigma(\mathbf{s}, \mathbf{i}) \rangle = \int \langle \gamma(\mathbf{s}, \mathbf{i}) \rangle F_{\mathbf{i},\mathbf{N}(\mathbf{r})}(\mathbf{s} - \mathbf{r}) d\mathbf{r} \tag{8}$$

Thus, the problem of light scattering by a fluttering plate is strictly reduced to a 2D convolution of two functions. One of the functions is responsible for flutter and the other describes diffraction. If a scale of the diffraction function $F_{\mathbf{i},\mathbf{N}}$ is less than a scale of the geometric optics pattern, the total specular scattering can be treated as a smoothing of a rather sharp geometric optics pattern by diffraction. In the opposite case, we can say that a diffraction pattern is broadened by flutter.
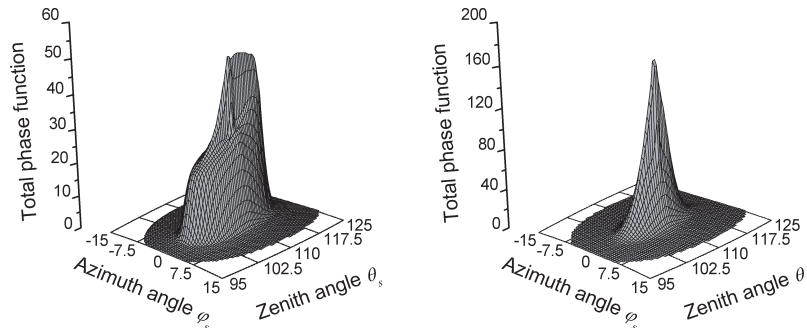
Figure 1: Phase functions of a fluttering circular disc for the uniform (left) and gaussian (right) tilt distributions.

As an illustration, Fig. 1 presents the total phase function $\langle\sigma(\mathbf{s},\mathbf{i})\rangle$ calculated numerically. Here light is incident on a circular plate of $\lambda/a = 0.027$ fluttering with the maximum zenith angle $5°$ relative to the vertical. The zenith and azimuth angles of the incident direction $\mathbf{i}$ are $\theta_i = 70°$ and $\phi_i = 0°$, respectively. The reflection coefficient R corresponds to an interface with the refraction index of 1.31 and unpolarized incident light. It is interesting to note that, in addition to trivial smoothing of contours of the geometric optics phase function, a kind of cumulative effect for the total phase functions in the center can appear as seen in Fig. 1. This cumulative effect is explained by the fact that the elongated diffraction functions $\mathbf{F_{i,N}}$ of Eq. (5) are oriented predominantly to the center.

4. CONCLUSIONS

A conception of specular scattering by ice crystals with preferential orientations proves to be efficient for both direct and inverse scattering problems of optics of cirrus clouds. It is shown that the specular scattering component is a 2D convolution of the geometric optics scattering pattern and the diffraction function. Here the geometric optics pattern is determined by only flutter parameters while the diffraction function depends only on the ratio of wavelength/(crystal size). The geometric optics specular pattern is found analytically in our recent paper [12] as a mapping of a probability density of plate orientations into scattering directions. Therefore, in the inverse scattering problems, not only a maximum tilt of fluttering crystals but the tilt probability density can be retrieved if the specular patterns are not essentially distorted by diffraction. On the other hand, a distortion of the specular patterns by diffraction can be used for retrieving sizes of crystal if the specular patterns are measured at several wavelengths. Such an opportunity has been recently demonstrated in [7]. The results obtained in this paper are rather general and they can be also applied to various scattering media with aligned and large as compared to incident wavelength particles: Special paints, biological media, forest canopy, etc.

ACKNOWLEDGMENT

REFERENCES

1. Noel, V. and K. Sassen, "Study of planar ice crystal orientations in ice clouds from scanning polarization lidar observations," *J. Appl. Meteorol.*, Vol. 44, 653–654, 2005.
2. Noel, V. and H. Chepfer, "Study of ice crystal orientation in cirrus clouds based on satellite polarized radiance measurements," *J. Atmos. Sci.*, Vol. 61, 2073–2081, 2004.
3. Breon, F.-M. and B. Dubrulle, "Horizontally oriented plated in clouds," *J. Atmos. Sci.*, Vol. 61, 2888–2898, 2004.
4. Cho, H.-M., P. Yang, G. W. Kattawar, S. L. Nasiri, Y. Hu, P. Minnis, C. Trepte, and D. Winker, "Depolarization ratio and attenuated backscatter for nine cloud types: Analysis based on collocated CALIPSO lidar and MODIS measurements," *Opt. Express*, Vol. 16, 3931–3948, 2008.
5. Noel, V., G. Ledanois, H. Chepfer, and P. H. Flamant, "Computation of a single-scattering matrix for nonspherical particles randomly or horizontally oriented in space," *Appl. Opt.*, Vol. 40, 4365–4375, 2001.
6. Lavigne, C., A. Roblin, and P. Chervet, "Solar glint from oriented crystals in cirrus clouds," *Appl. Opt.*, Vol. 47, 6266–6276, 2008.
7. Borovoi, A., V. Galileiskii, A. Morozov, and A. Cohen, "Detection of ice crystal particles preferably oriented in the atmosphere by use of the specular component of scattered light," *Opt. Express*, Vol. 16, 7625–7633, 2008.
8. Borovoi, A. G. and A. A. Kokhanovsky (Ed.), "Multiple scattering of short waves by uncorrelated and correlated scatterers," *Light Scattering Reviews*, Vol. 1, 181–252, Springer-Praxis, Chichester, 2006.
9. Borovoi, A. G. and I. A. Grishin, "Scattering matrices for large ice crystal particles," *J. Opt. Soc. Amer. A*, Vol. 20, 2071–2080, 2003.
10. Borovoi, A. G., N. V. Kustova, and U. G. Oppel, "Light backscattering by hexagonal ice crystal particles in the geometrical optics approximation," *Opt. Eng.*, Vol. 44, 071208, 2005.

11. Born, M. and E. Wolf, *Principles of Optics: Electromagnetic Theory of Propagation, Interference and Diffraction of Light*, Cambridge University, 1999.
12. Borovoi, A. and N. Kustova, "Display of ice crystal flutter in atmospheric light pillars," *Geophys. Res. Lett.*, Vol. 36, L04804, 2009.

Fast Light and Focusing in 2D Photonic Quasicrystals

Y. Neve-Oz[1], **T. Pollok**[2], **Sven Burger**[2], **Michael Golosovsky**[1], and **Dan Davidov**[1]

[1]The Racah Institute of Physics, The Hebrew University of Jerusalem
Jerusalem 91904, Israel
[2]Zuse Institute, Takustrasse 7, Berlin 14195, Germany

Abstract— We present numerical studies of the electromagnetic wave propagation in a metamaterial built from dielectric rods. The rods were arranged in a quasicrystalline lattice based on 10-fold Penrose tiling. We find wide isotropic band gaps and localized states, as expected in a quasicrystalline lattice. Our most important finding is the presence of the band gap edge states that are characterized by a very small refractive index (fast light). We use this phenomenon to design a focusing device — a plano-concave lens.

1. INTRODUCTION

Photonic crystals and metamaterials attract much interest due to their ability to manipulate light in unique ways that are impossible to achieve using uniform materials. For periodic crystals, the highest level of rotational symmetry does not exceed six, therefore it is almost impossible to avoid significant anisotropy in their electromagnetic properties. This anisotropy precludes wide omnidirectional band gaps. In contrast to periodic photonic crystals, quasicrystals have higher local rotational symmetry, hence their optical properties are more isotropic and they can exhibit wide omnidirectional band gaps [1–6]. Previous studies of photonic quasicrystals focused mostly on localized states inside the band gap since this feature is crucial for lasing [7–10].

In this work, we study electromagnetic wave propagation through planar photonic quasicrystals and focus on the band gap edge states. In distinction to previous works [11–14] that focused on the states with a low *group* velocity, we find propagating states with a very high *phase* velocity — fast light. We demonstrate how this phenomenon can be used for focusing with a plano-concave lens. So far, focusing with such device was thought to be associated with negative refraction [15–17].

2. METHODOLOGY

Our seed structure is the 10-fold Penrose tiling shown in Fig. 1. The dielectric rods are mounted in the vertices of this tiling. Fig. 1(c) shows that this arrangement indeed has 10-fold symmetry.

To simulate electromagnetic wave propagation through this array we used the software JCM-suite [18] that is based on a time-harmonic, adaptive, higher-order finite-element method. Our numerical model uses 520 dielectric rods arranged in a quasicrystalline lattice as shown in Fig. 1. The rod diameter is $d = 2.5\,\text{mm}$, the distance between the rods is $a = 5.4\,\text{mm}$, in such a way that the filling factor is 0.2. The dielectric constant of the rods is $\epsilon_r = 12$ (this corresponds to Si). The size of the array is $160\,\text{mm} \times 80\,\text{mm}$ and the plane wave impinges on the wide side of the array, whereas the electric field is parallel to the rod's axes. The model assumes transparent boundary conditions at all boundaries of the computational domain.

3. RESULTS

Figure 2 shows electromagnetic wave transmission through our array. The incident TM wave propagates from top to bottom. We considered transmission at different incident angles. To this end the direction of propagation was kept fixed and the crystalline structure was rotated around the vertical axis located in the lower left corner of the model shown in Fig. 1. The rectangular shape of the array was preserved.

Transmission plot demonstrates two band gaps: at 17–22 GHz and at 30–32.5 GHz. The band gap positions do not depend on the angle of incidence, as expected for quasicrystals. The band structure found in our work should be compared to that found in Ref. [6] who considered a quasicrystalline array of dielectric rods with almost the same sizes, symmetry and filling factor. The two works used different numerical methods: JCM software based on finite-element method (this work) as compared to direct solution of Maxwell equations using a plane wave method [6]. It is rewarding to observe that both works found a very similar band structure.

We performed field mapping for several chosen frequencies in order to determine the shape of the wave front and to calculate the phase velocity. At the high frequency edge of the second band gap
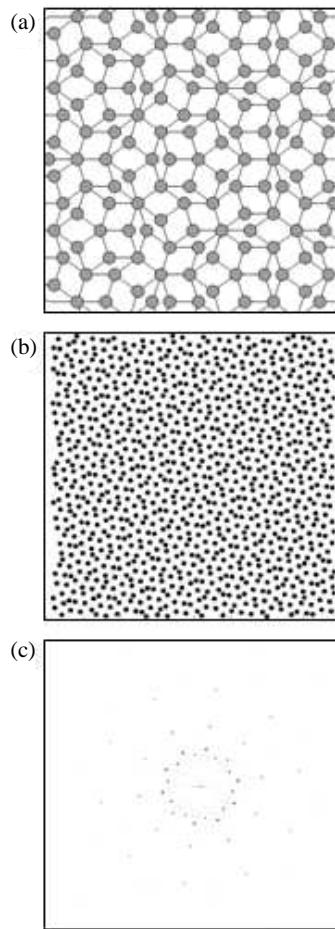
Figure 1: (a) A 10-fold Penrose tiling. The circles denote the vertices. (b) Photonic quasicrystal based on the dielectric rods mounted at the vertices of the tiling shown in (a). (c) Fourier transform of the configuration shown in (b). Note a 10-fold symmetry.
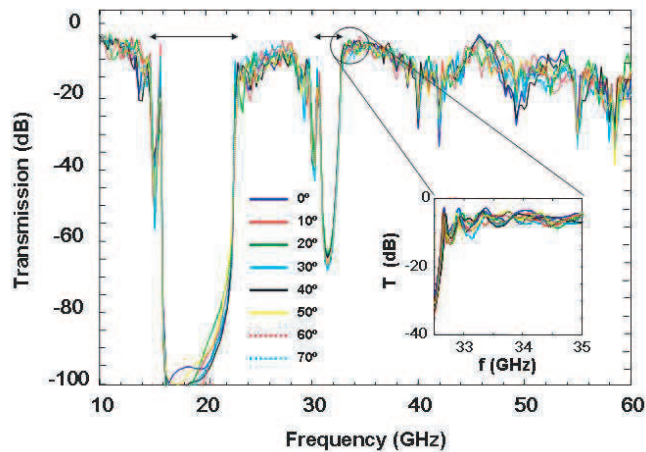
Figure 2: Millimeter-wave transmission through the photonic quasicrystal shown in Fig. 1 at different angles of incidence. Transmission spectrum is nearly independent of the incident angle. The first band gap appears at 17–22 GHz and the second band gap appears at 30–32.5 GHz. The inset shows expanded view of the frequency range where fast light appears.

(Fig. 2, inset) the electromagnetic wave propagating inside the array is characterized by especially long wave length. The long wavelength corresponds to a very high phase velocity (fast light). In what follows we studied this phenomenon in detail.

Figure 3 shows spatial distribution of the magnitude and phase of the electric field for one of the frequencies exhibiting fast light. The phase distribution in the array is nearly uniform (Fig. 3(b)), as

if it were a standing wave. Fig. 3(c) indicates that the field magnitude exhibits a strong maximum inside the array suggesting that this is a localized resonant state.

In what follows we study transmission through the array in which there is one localized state. Fig. 4 shows that the transmission has a sharp, resonant dependence on frequency. The transmission at resonance is close to -3.5 dBm and the Q-factor is about 1000. Fig. 4 shows that the maximum field magnitude inside the array closely follows the transmission curve and this is an additional indication of the resonant transmission.

Our results suggest that the fast light is associated with the resonant transmission through one or several resonance states. Similar states were found in Refs. [6, 14, 20]. In particular, the Ref. [14] showed that the propagating states at the band gap edge evolve in abrupt way when the sample size is changed — a clear indication that these states are associated with transmission through localized states. This is very similar to resonant tunnelling through tunnel barriers in electronic transport in solids [21].

The fast light phenomena can be used for device fabrication. To achieve focusing we constructed a plano-concave lens with the width 300 mm and the curvature $R = 180$ mm (Fig. 5). The plane wave impinges on the plane side of the lens. Because of the very long wavelength inside the lens, the phase of the wave at the concave exit face remains the same (Fig. 5(b)). Hence, this lens transforms the plane wave front of the incident wave to the wave front determined by the exit face of the lens. This face is curved hence the outgoing radiation is focused to a spot (Fig. 5(c)). The intensity in the focus exceeds the intensity in the incident wave by a factor of ten. To estimate focal length we
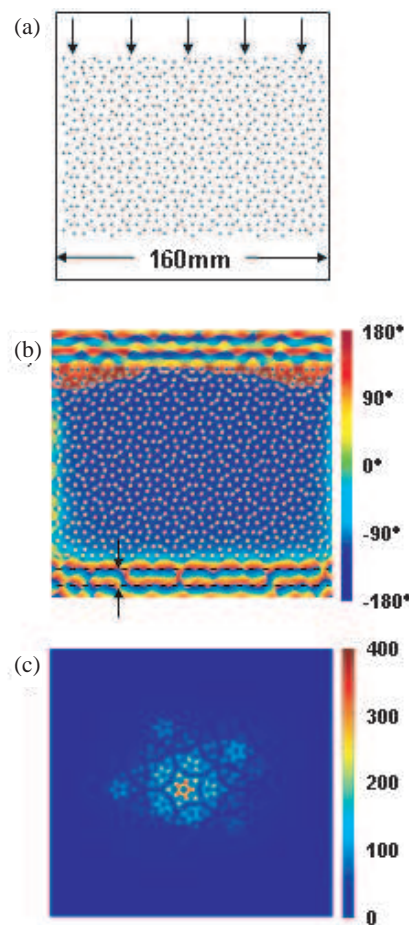
Figure 3: Plane mm-wave (32.6 GHz) propagation through the photonic quasicrystal shown in Fig. 1. (a) Numerical model. (b) Phase distribution. The wave fronts of the incident wave are clearly seen as horizontal blue lines. The wavelength is equal to the distance between subsequent horizontal lines of the same color. The color in the interior of the photonic crystal slowly changes from the dark-blue at the top to the blue at the bottom. This indicates a very small phase gradient along the sample, i.e., a very long wavelength (fast light). (c) Intensity distribution. Note increased intensity in the central part of the crystal. The intensity of the incident wave is equal to 1.
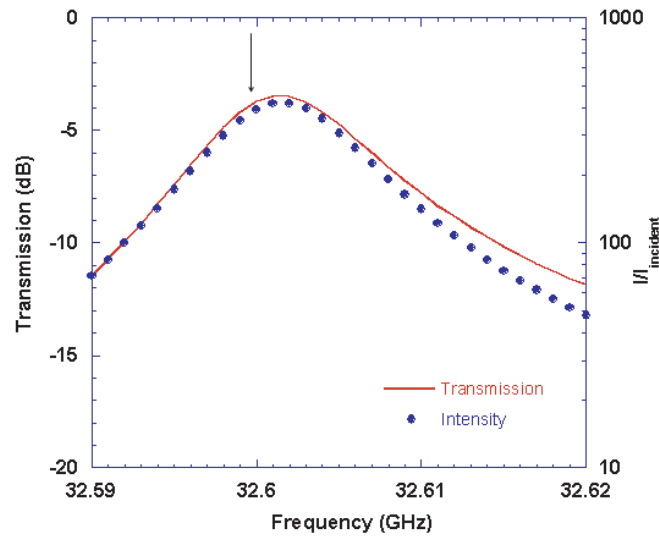
Figure 4: Transmission as a function of frequency for the photonic quasicrystal shown in Fig. 3 (red line). The arrow shows the frequency for which the field distribution in Fig. 3 has been obtained. A narrow transmission peak indicates resonant transmission. The blue circles denote the maximum field intensity inside the sample. Note the correlation between the transmission and the maximum field intensity inside the array.

(a)   (b)   (c)
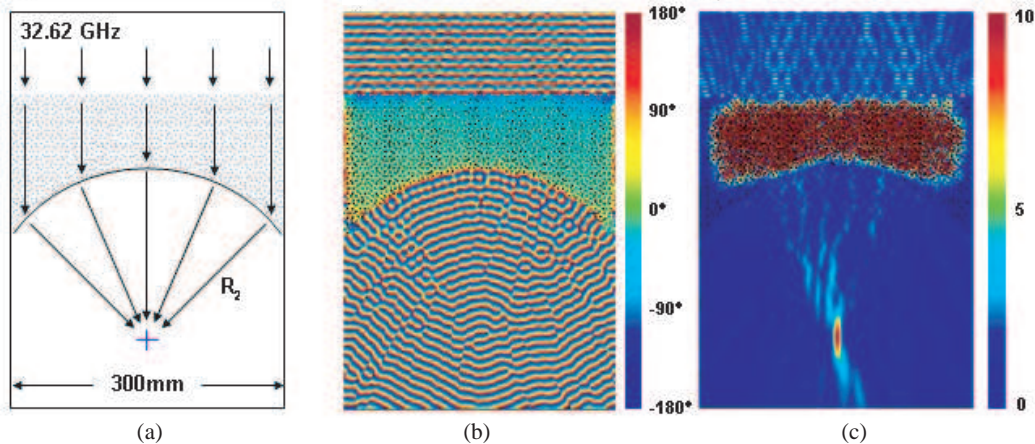
Figure 5: Focusing by a plano-concave lens made from the photonic quasicrystal shown in Fig. 1. (a) Design. The number of rods is 1272. The blue cross indicates the focus. (b) Phase distribution. Note the plane wave front in the incident wave, almost constant phase inside the lens, and a converging cylindrical wave front in the outgoing wave. (c) Intensity distribution. Note bright red spot in the outgoing wave that indicates focusing. The intensity at the focus is ten times higher than the intensity of the incident wave.

use the lens-makers equation for a plano-concave lens:

$$\frac{1}{f} = \frac{n-1}{R} \tag{1}$$

Since $n \sim 0$, $f \approx R$ (see Fig. 5(c)).

4. DISCUSSION

We observe fast light at the high frequency edge of the second band gap, but not at the edges of the first band gap. It was shown earlier [3, 6, 19] that the large omnidirectional band gap in quasicrystals is associated with the short-range electromagnetic interactions, while higher band gaps are associated with long-range interactions. Hence, it is not a surprise that the fast light (very long-range phase coherence) is observed in the second band gap and not in the first. So far, narrow beam focusing using quasicrystals was thought to be associated with negative refraction [13] although the later work [12] challenged this view and attributed focusing to short range interactions.

In this work, we clearly demonstrate plane wave focusing by a quasicrystalline lens where focusing arises from the long-range interactions.

REFERENCES

1. Chan, Y. S., C. T. Chan, and Z. Y. Liu, "Photonic band gaps in two dimensional photonic quasicrystals," *Physical Review Letters*, Vol. 80, 956–959, 1998.
2. Bayindir, M., E. Cubukcu, I. Bulu, and E. Ozbay, "Photonic band-gap effct, localization, and waveguiding in the two-dimensional Penrose lattice," *Physical Review B*, Vol. 63, 161104, 2001.
3. Della Villa, A., S. Enoch, G. Tayeb, V. Pierro, V. Galdi, and F. Capolino, "Band gap formation and multiple scattering in photonic quasicrystals with a penrose-type lattice," *Physical Review Letters*, Vol. 94, 183903, 2005.
4. Kaliteevski, M. A., S. Brand, and R. A. Abram, "Directionality of light transmission and reflection in 2D Penrose tiled photonic quasicrystals," *J. Phys. Condens. Matter*, Vol. 16, 1269, 2004.
5. David, S., A. Chelnokov, and J. M. Lourtioz, "Isotropic photonic structures: Archimedean-like tilings and quasi-crystals," *IEEE Journal of Quantum Electronics*, Vol. 37, 1427–1434, 2001.
6. Wang, K., "Structural effcts on light wave behavior in quasiperiodic regular and decagonal Penrose-tiling dielectric media: A comparative study," *Physical Review B*, Vol. 76, 085107, 2007.
7. Man, W., M. Megens, P. J. Steinhardt, and P. M. Chaikin, "Experimental measurement of the photonic properties of icosahedral quasicrystals," *Nature*, Vol. 436, 993–996, 2005.
8. Notomi, M., H. Suzuki, T. Tamamura, and K. Edagawa, "Lasing action due to the two-dimensional quasiperiodicity of photonic quasicrystals with a Penrose lattice," *Physical Review Letters*, Vol. 92, 123906, 2004.
9. Freedman, B., G. Bartal, M. Segev, R. Lifshitz, D. N. Christodoulides, and J. W. Fleischer, "Wave and defect dynamics in nonlinear photonic quasicrystals," *Nature*, Vol. 440, 1166, 2006.
10. Matsui, T., A. Agrawal, A. Nahata, and Z. Valy Vardeny, "Transmission resonances through aperiodic arrays of subwavelength apertures," *Nature*, Vol. 446, 517–512, 2007.
11. Zhang, X., Z. Li, B. Cheng, and D. Z. Zhang, "Non-near-field focus and imaging of an unpolarized electromagnetic wave through high-symmetry quasicrystals," *Optics Express*, Vol. 15, 1292, 2007.
12. Gennaro, E. D., C. Miletto, S. Savo, A. Andreone, D. Morello, V. Galdi, G. Castaldi, and V. Pierro, "Evidence of local effcts in anomalous refraction and focusing properties of dodecagonal photonic quasicrystals," *Physical Review B*, Vol. 77, 193104, 2008.
13. Feng, Z., X. Zhang, Y. Wang, Z. Y. Li, B. Cheng, and D. Z. Zhang, "Negative refraction and imaging using 12-fold-symmetry quasicrystals," *Physical Review Letters*, Vol. 94, 247402, 2005.
14. Lai, Y., Z. Q. Zhang, C. H. Chan, and L. Tsang, "Anomalous properties of the band-edge states in large two-dimensional photonic quasicrystals," *Physical Review B*, Vol. 76, 165132, 2007.
15. Parazzoli, C. G., R. B. Greegor, K. Li, B. E. C. Koltenbah, and M. Tanielian, "Experimental verification and simulation of negative index of refraction using Snell's law," *Physical Review Letters*, Vol. 90, 107401, 2003.
16. Vodo, P., P. V. Parimi, W. T. Lu, and S. Sridhar, "Focusing by planoconcave lens using negative refraction," *Applied Physics Letters*, Vol. 86, 201108, 2005.
17. Saado, Y., Y. Neve-Oz, M. Golosovsky, D. Davidov, and A. Frenkel, "Photonic crystal superlattice as a left-handed planoconcave lens," *Journal of Applied Physics*, Vol. 104, 124512, 2008.
18. JCMwave GmbH, Haarer Str. 14a, 85640 Putzbrunn, Germany.
19. Mnaymneh, K. and R. C. Gauthier, "Mode localization and band-gap formation in defect-free photonic quasicrystals," *Optics Express*, Vol. 15, 5089–5099, 2007.
20. Della-Villa, A., S. Enoch, G. Tayeb, F. Capolino, V. Pierro, and V.Galdi, "Localized modes in photonic quasicrystals with Penrose-type lattice," *Optics Express*, Vol. 14, 10021–10027, 2006.
21. Bending, S. J. and M.R. Beasley, "Transport properties via localized states in thin a-Si tunnel barriers," *Physical Review Letters*, Vol. 55, 324–327, 1985.

Global and Local Field EM Modeling and Novel GL Double Layered Electromagnetic Cloaks

Ganquan Xie, **Jianhua Li**, **Feng Xie**, and **Lee Xie**

GL Geophysical Laboratory, USA

Abstract— In this paper, we propose global and local electromagnetic (EM) field modeling in time domain and a novel GL double layered EM cloak. The GL double layered cloak (GL cloak) consists of two sphere annular layers, $R_1 \leq r \leq R_2$ and $R_2 \leq r \leq R_3$. Two type cloak materials are proposed and installed in its each layer, respectively. The outer layer of the GL cloak has the invisible function, while its inner layer has the fully absorption function. The outer layer cloaks the Local concealment from the Global exterior EM field; The inner layer cloaks the Global free space region from the Local field excited inside the concealment. The GL cloak metamaterials are weak degenerative When the source is located outside of the GL cloak, the excited EM wave field propagation is similar as that in free space, hence cannot be disturbed or disrupted by the cloak. Furthermore, the exterior EM wave does not penetrate into the inner layer, or the concealment. When local sources are located inside of the GL double cloaked concealment with normal EM materials, the excited EM wave propagates subject to Maxwells equations. It is completely absorbed by the inner layer of GL cloak and never propagate outside of the inner layer. Moreover, the EM wave-field in concealment is not disrupted by the cloak. The GL cloak is a robust, since it has complete and sufficient invisibility functions. Its concealment is the normal electromagnetic environment. Our EM GL double layered cloak is different from conventional common cloaks. The GL double layered EM cloak is proposed and developed based on a 3D GL EM modeling. Our GL modeling combines analytical and numerical approaches. There are no large matrices to solve in the GL method. Moreover, the GL method does no need artificial boundary and absorption boundary condition on it to truncate infinite domain. The 3D GL EM modeling simulations for the double layered cloak are presented. The GL method is different from the conventional methods. It has dual capabilities of the theoretical analysis and numerical simulations to study the cloak meta-materials, and field scattering problem in physical sciences.

1. INTRODUCTION

Finding and exploration is inverse problem; Hiding and cloaking is other inverse problem. They have close relationship. Based on the 3D GL EM modeling simulations [1, 2] and GL inversion [3], we propose global and local electromagnetic (EM) field modeling in time domain and a double layered EM cloak in this paper which is called, GL double layered cloak, simply labeled as the GL cloak. The single layer cloak proposed by Pendry et al. [4] is labeled, PS cloak. The GL double layered cloak consists of two sphere annular layers, $R_1 \leq r \leq R_2$ and $R_2 \leq r \leq R_3$. Two different type cloak materials are proposed and installed in its each layer, respectively. The outer layer of the GL cloak has the invisibility function, while its inner layer cloak has a fully absorption function to absorb the EM wave excited from local sources inside of the concealment. The outer layer cloaks the Local concealment from the Global exterior EM field; The inner layer cloaks the Global free space region from the Local field excited inside the concealment. That is the significance of the GL double layer cloak. When the source is located outside of the GL cloak, the excited EM wave field propagation outside of the cloak is similar to that in free space and never be disrupted by the cloak. Moreover, the exterior EM wave does not penetrate into the inner layer and concealment. When local sources are located inside the GL double cloaked concealment with the normal EM materials, the excited EM wave propagates according to Maxwells equations, and is completely absorbed by the inner layer cloak of the GL cloak, and does not propagate outside of the inner layer of the GL cloak. Finally, the EM wave-field in the concealment is not disrupted by the cloak. The GL doubled layered cloak is robust, and has complete and sufficient invisibility functions. Its concealment is the normal electromagnetic environment. Our EM GL double layered cloak is different from conventional common cloak. The GL double layered meta-materials are weakly degenerative, and dispersive.

A double layer cloth phenomenon to prevent the GILD inversion [5–7] detection has been observed in [8] in 2001 which is published in SEG online: The double cloth anti detection is obvious around the fly in Figure 12 and around the bar in Figure 13. After that year, we developed a novel and effective Global and Local field (GL) modeling and inversion to study and simulate the

meta-materials, periodic photonic crystals and condense nanometer materials etc. wide physical sciences. 3D GL EM modeling and inversion [9] and computational mirage [10] have been presented in PIERS 2005 and published in the proceeding of PIERS 2005 in Hangzhou in PIERS web. Metamaterial of the novel GL double layer cloak is proposed and simulated in this paper and eprint paper [11].

The analytical method and numerical method for physical sciences have been developed separately in history. The GL method consistently combines both analytical and numerical approaches. The GL method does not need to solve large matrix equations, it only needs to solve 3×3 and 6×6 matrix equations. Moreover, the GL method does not prescribe any artificial boundary, or a PML absorption condition necessary to truncate the infinite domain. The Finite Element Method (FEM) and Finite Difference Method (FDM) have numerical dispersions which confuse and contaminate the physical dispersion resulting from field and materials interactions. The frequency limitation is a difficulty of FEM and FDM.

The GL method is a significant scattering process which reduces the numerical dispersion and is suitable to simulate physical wave-field scattering in the materials, in particular, for dispersive materials. Born approximation is a conventional method in the quantum mechanics and solid state physics. However, it consists of one iteration only in the whole domain which may not be accurate in the high frequency and high contrast materials. The GL method divides the domain as a set of small sub-domains or sub-lattices. The Global field is updated by the local field from the interaction between the global field and local sub-domain materials successively. Once all sub-domain materials are scattered, the GL field solution obtained turn out to be more accurate than the Born approximation.

Moreover, the GL method can be mesh-less, including arbitrary geometry sub-domains, such as rectangle, cylindrical and spherical coordinate mixed coupled together. It is full parallel algorithm. The GL method advantages help overcome many historical obstacles described in detail in [1]. The theoretical foundation of the GL method is described in the paper [2]. We have used the 3D GL modeling [1, 2] and inversion technique in [3] to simulate many cloak meta-materials, nanometer materials, periodic photonic crystals etc. When the point source is located outside or inside of the various geometry cloaks, the 3D GL EM modeling simulations for the EM wave-field propagation through the cloaks have been done. These simulations show that the GL method is fast and accurate. In this paper, the 3D GL EM modeling simulations of the EM wave field propagation through the new GL double layered cloak is presented. When the local sources are located outside or inside of the outer layer cloak, EM wave propagation through outer layer cloak, do not penetrate into the inner layer and the concealment, i.e., $r \leq R_2$. The exterior EM wave-field propagation outside of GL double layered cloak is not disrupted by the cloak. The outer layer cloak has the invisibility function. When the local sources inside of the GL double layer cloaked concealment with normal materials, the excited EM wave normally propagating subject to Maxwells equations, the EM field is then completely absorbed by the inner layer cloak and can not propagate outside of the inner cloak. The EM environment in the GL double cloaked concealment is normal, in which there exist a Maxwell EM wave field excited by nonzero local sources, have no reflection from the boundary $r = R_1$, and does not propagate outside of of the boundary $r = R_2$.

By using the 3D GL EM modeling [1, 2] simulation and its theoretical analysis, we found and verified a phenomenon, that there exists no Maxwell EM wave field that can be excited by nonzero local sources inside of the single layer cloaked concealment with normal materials. Our GL double layered cloak overcomes the drawback and difficulty in the single cloak. Pendry et al. in paper [4] used a coordinate transformation and ray tracing to propose the annular cloak in which the ray being bending and re-direction around central sphere object and cannot penetrate into it. The cloak device like the vacuum and does not disturb exterior wave field. There are several other works that simulated the exterior plane wave propagation through the cloak [13–15]. Chen et al. presented the Mie analytical TEM model to simulate the plane wave through the spherical cloak [13]. Cummer et al. in paper [14] presented numerical simulations by using the COMSOL Multi-Physics finite element-based electro-magnetics solver for the 2D plane wave propagation through cylindrical cloak. Argyropoulos et al. described a dispersive finite difference method in time domain (FTFD) in [15] to simulate 2D TEM plane wave field through cylindrical cloak, in which the authors considered the difficulty of conventional FDTD scheme for dispersive materials. In papers [14] and [15], authors introduced many papers for cloak research works. Because the plane wave is excited by plane sources, it cannot be located inside of the cloak or concealment. To study the EM wave excited from local sources inside of the cloaked concealment is absent from these papers. Authors of [16]

and [17], studied the effect on invisibility of active devices inside the cloaked region. Author in [17] stated that "when these conditions are over-determined, finite energy solutions typically do not exist."

We use 3D GL method to do many simulations for studying the behavior of EM field excited inside of the single layer cloaked concealment. These simulations are divergent or become chaos when the EM wave propagates to the inner boundary of the single layer cloak. Our statement is that: There exists no Maxwell EM wave field that can be excited by nonzero local sources inside of the single layer cloaked concealment with normal materials [12]. For overcoming the weakness and difficulty of the single layer cloak, we propose the GL double layer EM cloak, which is on Eprint [11]. The detailed proof and 3D GL simulations are presented in this paper. Before the practice production of the single layered cloak, the electromagnetic field environment inside of the concealment cannot be studied in physical experiment. Our GL double layered cloak proposed in this paper overcomes the drawback and difficulty of the single layer cloak, and avoid disrupting the EM phenomenon inside of the single layered cloaked concealment with normal materials. The GL double layered EM cloak meta-materials inventive and fabrication technology right and 3D GL EM modeling software are patented by GL Geophysical Laboratory. The GL double layer cloak figures and movies are protected by GLGEO's color mapping and all right is reserved by GLGEO. We present grateful thanks to GL Geophysical Laboratory for approving the publication of the GL modeling method, GL double layered cloak material, theory, and simulations [11, 12]. If our GL double layer cloak material, method, properties, simulation results, figures and similar contents are appear in any publication by other author will be detection and identified and request the author to cite our papers as reference.

We describe this paper in the following order: The introduction is described in Section 1. In Section 2, we propose a GL double layered cloak materials. The EM integral equations are presented in Section 3. The 3D GL EM modeling are described in Section 4. The theoretical analysis of properties and functions of the GL double layered cloak are proposed in Section 5. The simulations of the EM wave propagation through the GL double layered Cloak by using the GL EM modeling are presented in Section 6. The advantages of the GL double layered cloak is presented in Section 7. In Section 8, we conclude this paper.

2. GL DOUBLE LAYERED CLOAK MATERIALS

2.1. GL Inner Layered Cloak Anisotropic Material

On the inner sphere annular domain, $\Omega_{\mathrm{GLI}} = \{r : R_1 \leq r \leq R_2\}$, by the GL EM modeling and inversion [1–3], we propose an anisotropic material as follows,

$$[D]_{\mathrm{GLI}} = \mathrm{diag}\left[\bar{\varepsilon}_i, \bar{\mu}_i\right], \quad \bar{\varepsilon}_i = \mathrm{diag}\left[\varepsilon_{r,i}, \varepsilon_{\theta,i}, \varepsilon_{\phi,i}\right]\varepsilon_0, \quad \bar{\mu}_i = \mathrm{diag}\left[\mu_{r,i}, \mu_{\theta,i}, \mu_{\phi,i}\right]\mu_0,$$

$$\varepsilon_{r,i} = \mu_{r,i} = \left(\frac{R_2^2 - R_1^2}{R_2^2}\right)\sqrt{\frac{R_2^2 - r^2}{R_2^2 - R_1^2}}, \quad \varepsilon_{\theta,i} = \varepsilon_{\phi,i} = \mu_{\theta,i} = \mu_{\phi,i} = \sqrt{\frac{R_2^2 - R_1^2}{R_2^2 - r^2}}\frac{R_2^2}{R_2^2 - r^2}. \tag{1}$$

The Ω_{GLI} is called as GL inner layered cloak, the materials, $[D]_{\mathrm{GLI}} = \mathrm{diag}[\bar{\varepsilon}_i, \bar{\mu}_i]$ in (1), are the anisotropic GL inner layered cloak materials.

2.2. GL Outer Layered Cloak Anisotropic Material

Let the outer sphere annular domain $\Omega_{\mathrm{GLO}} = \{r : R_2 \leq r \leq R_3\}$ be the GL outer layered cloak with the following anisotropic GL outer layered cloak materials,

$$[D]_{\mathrm{GLO}} = \mathrm{diag}\left[\bar{\varepsilon}_o, \bar{\mu}_o\right], \quad \bar{\varepsilon}_o = \mathrm{diag}\left[\varepsilon_{r,o}, \varepsilon_{\theta,o}, \varepsilon_{\phi,o}\right]\varepsilon_0, \quad \bar{\mu}_o = \mathrm{diag}\left[\mu_{r,o}, \mu_{\theta,o}, \mu_{\phi,o}\right]\mu_0,$$

$$\varepsilon_{r,o} = \mu_{r,o} = \frac{R_3}{r}\frac{r^2 - R_2^2}{r^2}\frac{\sqrt{r^2 - R_2^2}}{\sqrt{R_3^2 - R_2^2}}, \quad \varepsilon_{\theta,o} = \mu_{\theta,o} = \varepsilon_{\phi,o} = \mu_{\phi,o} = \frac{R_3}{\sqrt{R_3^2 - R_2^2}}\frac{r}{\sqrt{r^2 - R_2^2}}. \tag{2}$$

The GL inner cloak Ω_{GLI} domain and GL outer cloak Ω_{GLO} domain are bordering on the sphere annular surface $r = R_2$. We assemble the Ω_{GLI} as the inner sphere annular domain and Ω_{GLO} as the outer sphere annular domain and make them coupling on their interface boundary annular surface $r = R_2$ as follows,

$$\Omega_{\mathrm{GL}} = \Omega_{\mathrm{GLI}}\bigcup\Omega_{\mathrm{GLO}} = \{r : R_1 \leq r \leq R_2\}\bigcup\{r : R_2 \leq r \leq R_3\} = \{r : R_1 \leq r \leq R_3\}, \tag{3}$$

and offer the coupled anisotropic dielectric and susceptibility tensors $[D]_{\mathrm{GL}}$ on the Ω_{GL} as follows,

$$[D]_{\mathrm{GL}} = \{[D]_{\mathrm{GLI}}, \, r \in \Omega_{\mathrm{GLI}} [D]_{\mathrm{GLO}}, \, r \in \Omega_{\mathrm{GLO}}. \tag{4}$$

The GL cloak material $[D]_{\mathrm{GLI}} = \mathrm{diag}[\bar{\varepsilon}_i, \bar{\mu}_i]$ in (1) on the Ω_{GLI} and GL outer layered cloak material $[D]_{\mathrm{GLO}} = \mathrm{diag}[\bar{\varepsilon}_o, \bar{\mu}_o]$ in (2) on Ω_{GLO} are assembled into the GL anisotropic doubled layered cloak material on the domain Ω_{GL}. The domain Ω_{GL} with the metamaterial $[D]_{\mathrm{GL}}$ in (4) is called as the GL double layered cloak. The outer layer cloaks the Local concealment from the Global exterior EM field; The inner layer cloaks the Global free space region from the Local field excited inside the concealment. That is the significance of the GL double layer cloak.

3. 3D ELECTROMAGNETIC INTEGRAL EQUATION

The 3D EM integral equation in frequency domain has been proposed in authors' papers [1, 2]. In this paper, we proposed the EM integral equation in time domain as follows:

$$\begin{bmatrix} E(r,t) \\ H(r,t) \end{bmatrix} = \begin{bmatrix} E_b(r,t) \\ H_b(r,t) \end{bmatrix} + \int_\Omega G_{E,H}^{J,M}(r',r,t) *_t \delta\left[D(r')\right] \begin{bmatrix} E_b(r',t) \\ H_b(r',t) \end{bmatrix} dr', \tag{5}$$

and

$$\begin{bmatrix} E(r,t) \\ H(r,t) \end{bmatrix} = \begin{bmatrix} E_b(r,t) \\ H_b(r,t) \end{bmatrix} + \int_\Omega G_{E,H,b}^{J,M}(r',r,t) *_t \delta\left[D(r')\right] \begin{bmatrix} E(r',t) \\ H(r',t) \end{bmatrix} dr'. \tag{6}$$

In the EM integral Equation (5),

$$G_{E,H}^{J,M}\left(r',r,t\right) = \left[E^J\left(r',r,t\right) \quad H^J\left(r',r,t\right) E^M\left(r',r,t\right) \quad H^M\left(r',r,t\right)\right], \tag{7}$$

and $G_{E,H,b}^{J,M}$ is the EM Green's tensor in the background medium, where, $E(r,t)$ is the electric field, $H(r,t)$ is the magnetic field, $E_b(r,t)$ and $H_b(r,t)$ is the incident electric and magnetic field in the background medium, $E^J(r',r,t)$ is electric Green's tensor, $H^J(r',r,t)$ is magnetic Green's tensor, they are excited by the point impulse current source, $E^M(r',r,t)$ and $H^M(r',r,t)$ are electric and magnetic Green's tensor, respectively, they are excited by the point impulse magnetic moment source, $*_t$ is convolution with respect to t, $\delta[D]$ is the electromagnetic material parameter variation matrix,

$$\delta\left[D\right] = \begin{bmatrix} \delta D_{11} & 0 \\ 0 & \delta D_{22} \end{bmatrix}, \; \delta D_{11} = (\bar{\sigma}(r) - \sigma_b I) + (\bar{\varepsilon}(r) - \varepsilon_b I)\frac{\partial}{\partial t}, \; \delta D_{22} = (\bar{\mu}(r) - \mu_b I)\frac{\partial}{\partial t}, \tag{8}$$

δD_{11} and δD_{22} are a 3×3 symmetry, inhomogeneous diagonal matrix for the isotropic material, for anisotropic material, they are an inhomogeneous diagonal or full matrix, I is a 3×3 unit matrix, $\bar{\sigma}(r)$ is the conductivity tensor, $\bar{\varepsilon}(r)$ is the dielectric tensor, $\bar{\mu}(r)$ is susceptibility tensor which can be dispersive parameters depend on the angular frequency ω, σ_b is the conductivity, ε_b is the permittivity, μ_b is the permeability in the background free space, Ω is the finite domain in which the parameter variation matrix $\delta[D] \neq 0$, the $(\bar{\varepsilon}(r) - \varepsilon_b I)E$ is the electric polarization, and $(\bar{\mu}(r) - \mu_b I)H$ is the magnetization.

4. 3D GL EM MODELING

We propose the GL EM modeling based on the EM integral Equations (1) and (2) in the time space domain.

(3.1) The domain Ω is divided into a set of N sub domains, $\{\Omega_k\}$, such that $\Omega = \bigcup_{k=1}^{N} \Omega_k$. The division can be mesh or meshless.

(3.2) When $k = 0$, let $E_0(r,t)$ and $H_0(r,t)$ are the analytical global field, $E_0^J(r',r,t)$, $H_0^J(r',r,t)$, $E_0^M(r',r,t)$, and $H_0^M(r',r,t)$ are the analytical global Green's tensor in the background medium. By induction, suppose that $E_{k-1}(r,t)$, $H_{k-1}(r,t)$, $E_{k-1}^J(r',r,t)$, $H_{k-1}^J(r',r,t)$, $E_{k-1}^M(r',r,t)$, and $H_{k-1}^M(r',r,t)$ are calculated in the $(k-1)$th step in the subdomain Ω_{k-1}.

(3.3) In $\{\Omega_k\}$, upon substituting $E_{k-1}(r,t)$, $H_{k-1}(r,t)$, $E_{k-1}^J(r',r,t)$, $H_{k-1}^J(r',r,t)$, $E_{k-1}^M(r',r,t)$, and $H_{k-1}^M(r',r,t)$ into the integral Equation (1), the EM Green's tensor integral Equation (1) in Ω_k is reduced into 6×6 matrix equations. By solving the 6×6 matrix equations, we obtain the Green's tensor field $E_k^J(r',r,t)$, $H_k^J(r',r,t)$, $E_k^M(r',r,t)$, and $H_k^M(r',r,t)$.

(3.4) According to the integral Equation (1), the electromagnetic field $E_k(r,t)$ and $H_k(r,t)$ are updated by the interaction scattering field between the Green's tensor and local polarization and magnetization in the subdomain Ω_k as follows,

$$\begin{bmatrix} E_k(r,t) \\ H_k(r,t) \end{bmatrix} = \begin{bmatrix} E_{k-1}(r,t) \\ H_{k-1}(r,t) \end{bmatrix} + \int_{\Omega_k} \left\{ \begin{bmatrix} E_k^J(r',r,t) & H_k^J(r',r,t) \\ E_k^M(r',r,t) & H_k^M(r',r,t) \end{bmatrix} *_t \delta \left[D(r') \right] \begin{bmatrix} E_{k-1}(r',t) \\ H_{k-1}(r',t) \end{bmatrix} \right\} dr' \quad (9)$$

(3.5) The steps (3.2) and (3.4) form a finite iteration, $k = 1, 2, \ldots, N$, the $E_N(r,t)$ and $H_N(r,t)$ are the electromagnetic field of the GL modeling method. The GL electromagnetic field modeling in the time space domain is short named as GLT method.

The GL EM modeling in the space frequency domain is proposed in the paper [2], we call the GL modeling in frequency domain as GLF method.

5. THEORETICAL ANALYSIS OF INTERACTION OF THE EM WAVE FIELD THROUGH THE CLOAKS

5.1. Theoretical Analysis of Interaction of the EM Wave Field Through the GL Double Layered Cloaks

We propose the theoretical analysis of the interaction between the EM wave and GL cloaks in this section.

Statement 1: Let domain Ω_{GL} in (3) and the metamaterial D_{GL} in (4) be GL double layered cloak, and $\varepsilon = \varepsilon_{\text{b}}$, $\mu = \mu_b$ be basic permittivity and permeability, respectively, inside of the central sphere concealment $|\vec{r'}| < R_1$ and outside of the GL cloak $|\vec{r'}| > R_3$, we have the following statements: (1) Provide the local source is located inside of the concealment of GL double layered cloak, $|\vec{r}_s| < R_1$, the excited EM wave field inside of the concealment never be disturbed by the cloak; (2) Provide the local source is located inside of concealment or inside of the inner layer of the GL double layered cloak, $|\vec{r}_s| < R_2$, the EM wave field is vanished outside of the inner layer of GL cloak and is always propagating and going to the boundary $r = R_2$ and before $r = R_2$. (3) Provide the source is located outside of the GL double layered cloak, $|\vec{r}_s| > R_3$, the excited EM wave field propagation outside of the double layered cloak as same as in free space and never be disturbed by the double layered cloak; (4) Provide the local source is located outside of double layered cloak or located inside of the outer layer of GL cloak, $|\vec{r}_s| > R_2$, the excited EM wave field never propagate into the inner layer of GL cloak and the concealment.

5.2. There Exists No Maxwell EM Wavefield Can Be Excited by Nonzero Local Sources Inside of the Single Layered Cloaked Concealment with Normal Materials

Statement 2: Suppose that a 3D anisotropic inhomogeneous single layered cloak domain separates the whole 3D space into three sub domains, one is the single layered cloak domain Ω_{clk} with the cloak material; the second one is the cloaked concealment domain Ω_{conl} with normal EM materials; other one is the free space outside of the cloak. If the Maxwell EM wavefield excited by a point source or local sources outside of the concealment Ω_{conl} is vanished inside of the concealment Ω_{conl}, then there exists no Maxwell EM wave field can be excited by the local sources inside the cloaked concealment Ω_{conl} with normal materials.

The Statement 2 is proved by the GL method in author's paper [12].

6. THE GL EM MODELING SIMULATIONS OF THE EM WAVE FIELD THROUGH THE GL DOUBLE CLOAKS

6.1. The Simulation Model of the GL Double Layered Cloak

The simulation model: The 3D domain is $[-0.5\,\text{m}, 0.5\,\text{m}] \times [-0.5\,\text{m}, 0.5\,\text{m}] \times [-0.5\,\text{m}, 0.5\,\text{m}]$, the mesh number is $201 \times 201 \times 201$, the mesh size is $0.005\,\text{m}$. The electric current point source is defined as

$$\delta(r - r_s)\delta(t)\vec{e}, \quad (10)$$

where the r_s denotes the location of the point source, the unit vector $\vec{e}$ is the polarization direction, the time step $dt = 0.3333 \times 10^{-10}$ second, the frequency band is from $0.05\,\text{GHz}$ to $15\,\text{GHz}$, the largest frequency $f = 15\,\text{GHz}$, the shortest wave length is $0.02\,\text{m}$. The EM GL double layered cloak $\Omega_{\text{GL}} = \Omega_{\text{GLI}} \bigcup \Omega_{\text{GLO}}$ is consist of the double spherical annular Ω_{GLI} and Ω_{GLO} with the center in the origin and interir radius $R_1 = 0.22\,\text{m}$, meddle radius $R_2 = 0.3\,\text{m}$. and exterior radius $R_3 = 0.35\,\text{m}$. The cloak is divided into $90 \times 180 \times 90$ cells. The spherical coordinate is used in the sphere $r \le R_3$, the Cartesian rectangular coordinate is used in outside Ω_{GL} to mesh the domain.

6.2. Point Source in the Concealment and Other Point Source in the Free Space

The two point sources are used to excite the EM wave propagation through the GL double layered cloak. The first point current source is located inside of the center sphere concealment at $(-0.12\,\mathrm{m}, -0.12\,\mathrm{m}, 0.0)$, by which the excited EM wave is named as *First electric wave*, $E_{xx,1}$ The second current point source is located in free space at $(0.518\,\mathrm{m}, 0.518\,\mathrm{m}, 0.0)$ where is the right and top corner outside of the whole GL double layered cloak. The EM wave by the second source is named as *Second electric wave*. $E_{xx,2}$, The GL modeling simulations of the EM wave excited by above two point sources propagation through the GL double layered cloak are presented in the Figures 1–4. The two waves are propagating separately at time step $38dt$ that is shown in the Figure 1, at this moment, the most part of the front of the *First electric wave*, $E_{xx,1}$, propagates enter to the inner layer, $R_1 \le r \le R_2$, a few part of the front of the $E_{xx,1}$ is located in right and top of the concealment. The front of *Second electric wave*, $E_{xx,2}$, reaches the outer boundary $r = R_3$ of the GL double layered cloak. At the time step $58dt$, the *First electric wave*, $E_{xx,1}$, propagation has been inside of the inner layer of the GL cloak $R_1 \le r \le R_2$, its speed is smaller than the light speed. The part of the front of *Second electric wave*, $E_{xx,2}$, has been inside of outer layer of the

Figure 1: (color online) At time step $98dt$, front of *Second EM wave*, $E_{xx,2}$ inside of the outer layer of GL cloak $R_2 \le r \le R_3$ propagates more faster than light speed. The wave front of the *First electric wave*, $E_{xx,1}$, propagates inside the inner layer, $R_1 \le r \le R_2$.

Figure 2: (color online) At time step $98dt$, front of *Second EM wave*, $E_{xx,2}$ inside of the outer layer of GL cloak $R_2 \le r \le R_3$ propagates a little faster than light speed. It is slower than $E_{xx,2}$ in Figure 1. The wave front of the $E_{xx,1}$, propagates inside the inner layer, $R_1 \le r \le R_2$.

Figure 3: (color online) At the time step $21dt$, the E_{xx} excited inside outer and inner layer cloaks propagate through cloaks.

Figure 4: (color online) At the time step $48dt$, the E_{xx} excited inside outer and inner layer cloaks are propagating through the cloak.

GL double layered cloak, $R_2 \leq r \leq R_3$, and being backward bending with speed smaller than the light speed. The EM wave propagation image is presented in Figure 2. In the Figure 3, at time step $75dt$, the *Second electric wave*, $E_{xx,2}$, is propagating inside of the outer layer cloak of the GL double layered cloak, $R_2 \leq r \leq R_3$, and around the sphere annular $r = R_2$ and never penetrate into the inner layer of GL cloak and the concealment, i.e., $r \leq R_2$. It does disperse and split into the two phases around the sphere annular $r = R_2$, the front phase speed exceeds the light speed; the back phase is slower than the light speed. The *First electric wave*, $E_{xx,1}$, is propagating inside of the inner sphere annular layer of the GL double layered cloak, $R_1 \leq r \leq R_2$. In the Figure 4, at time step $98dt$, one part of front the *Second electric wave*, $E_{xx,2}$, is propagating inside of the outer layer cloak, $R_2 \leq r \leq R_3$. It has around the sphere annular $r = R_2$ and forward bending in the left of the sphere annular $r = R_2$ and never penetrate into the inner layer of GL cloak and the concealment, i.e., $r \leq R_2$ The *First electric wave*, $E_{xx,1}$, is still propagating inside of the inner sphere annular layer of the GL double layered cloak, $R_1 \leq r \leq R_2$.

7. HISTORY AND DISCUSSIONS

7.1. History

A double layer cloth phenomenon to prevent the GILD inversion [5–7] detection has been observed in paper [8] in 2001 which is published in SEG online $http://segdl.org/journals/doc/SEGLIB-home/dci/searchDCI.jsp$. The double layer cloth to cloak fly from the exterior wave GILD detection is obvious around the fly which is shown in Figure 5; the double cloth around the bar is shown in Figure 6. We developed a novel and effective Global and Local field (GL) modeling and inversion to study the meta materials, periodic photonic crystals and condense physics etc. wide physical sciences. 3D GL EM modeling and inversion [9] and computational mirage [10] have been presented in PIERS 2005 and published in proceeding of PIERS 2005 in Hangzhou, which can be downloaded from $http://piers.mit.edu/piersproceedings/piers2k5Proc.php$. We developed 3D FEM for the elastic mechanics first in China in 1972 [18] and discovered the superconvergence of the 3D cubic curve isoparameter element first in the world [18, 19]. The 3D isoparameter element can be used for making arbitrary curve cloak [18]. We deeply to know the merits and drawbacks of FEM. The GL method overcomes the drawbacks of FEM and FD methods. The history of development of FEM and GILD and GL method has been described in [2, 18]. The 3D and 2D GL parallel software is made and patented by GLGEO. The GL modeling and its inversion [1–3] and GL EM quantum field modeling are suitable to solve quantization scattering problem of the electromagnetic field in the dispersive and loss metamaterials, cloaks and more wide anisotropic materials.

7.2. The EM GL Double Layered Cloak Is Robust for Invisibility

The wave front of the First electric wave, which is excited by a point source inside of the inner layer cloak Ω_{GLI}, is always propagating inside of inner layer cloak Ω_{GLI} or concealment Ω_{conl} and never propagate outside of the interface annular S_1. Therefore, the EM GL double layered cloak is robust for invisibility.
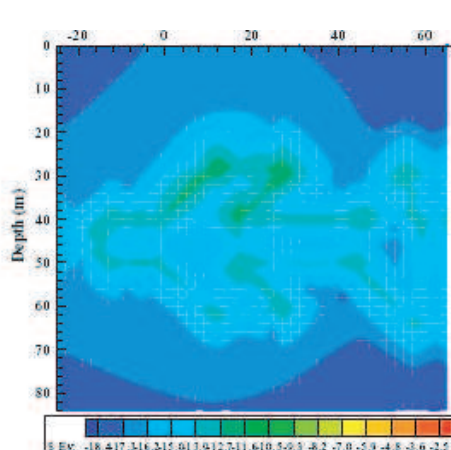
Figure 5: (color online) A double cloth anti detection is around the fly model, The Figure 5 is from the Figure 11 in paper [8] in 2001.
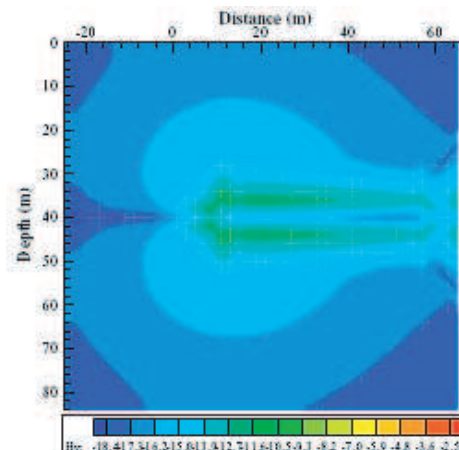
Figure 6: (color online) A double cloth anti detection is around the bar model, The Figure 6 is from the Figure 2 in paper [8] in 2001.

7.3. The EM GL Double Layered Cloak Is Complete Invisible

The Figures 1–4 clearly show that the outer layer cloak of the GL double layered cloak has the invisibility function, while the inner layer cloak has fully absorption function to absorb the EM wave excited from local sources inside of the concealment. When the source is located outside of the GL double layered cloak, the excited EM wave field propagation outside of the double layered cloak is as same as in free space and never be disturbed by the cloak; also, the exterior EM wave can not penetrate into the inner layer and concealment of the GL double layered cloak. When local sources are located inside of the GL double cloaked concealment with the normal EM materials, the excited EM wave is propagating under Maxwell equation governing, it is complete absorbed by the inner layer cloak of GL double cloak and never propagate to outside of the inner layer of the GL cloak, moreover, the EM wavefield in concealment never be disturbed by the cloak.

Provide only single outer layered cloak is adopted. The EM field excited by local sources inside of its concealment with normal materials does not satisfy the Maxwell equation. The EM chaos phenomena, which is divorced from the Maxwell equation governing, may damage devices and human inside the concealment, or may degrade the invisibility of the cloak. Invisibility function of the single layered cloak is not complete. The EM GL double layered cloak overcome the drawback of the single layered cloak. The GL double layered cloak has the complete invisibility function.

7.4. The EM GL Double Layered Cloak Can Be Double Ellipsoid Annular

The EM GL double layered cloak can be extended to have double ellipsoid annular and other geometry.

7.5. Advantages of the GL Method

The GL EM modeling is fully different from FEM and FD and Born approximation methods and overcome their difficulties. There is no big matrix equation to solve in GL method. Moreover, it does not need artificial boundary and absorption condition to truncate the infinite domain. Born Approximation is a conventional method in the quantum mechanics and solid physics, however, it is one iteration only in whole domain which is not accurate for high frequency and for high contrast materials. The GL method divides the domain as a set of small sub domains or sub lattices. The Global field is updated by the local field from the interaction between the global field and local subdomain materials successively. Once all subdomain materials are scattered, the GL field solution is obtained which is much more accurate than the Born approximation. GL method is suitable for all frequency and high contrast materials. When the size of the sub domain is going to zero, the GL method is convergent and has $O(h^2)$ if the trapezoidal integral formula is used, moreover, is has super convergence $O(h^4)$ if the Gaussian integral formula is used [18, 20] The GL method has double capabilities of the theoretical analysis and numerical simulations that has been shown in this paper.

8. CONCLUSION

Many simulations of the EM wave propagation through the GL double layered cloak by the GL modeling and theoretical analysis verify that the EM GL doubled cloak is robust cloak and has complete and sufficient invisibility functions. Its concealment is the normal electromagnetic environment. The outer layer cloak of the GL double layered cloak has the invisible function, the inner layer cloak has fully absorption function. The EM GL double layered cloak has advantages to overcome the drawback and difficulty of the single layered cloak.

The 3D GL simulations of the EM wave through the photonic crystals, single and multiple spherical cloaks show that the GLT and GLF EM modeling are accurate, stable and fast. The GL EM modeling is fully different from FEM and FD and Born Approximation methods and overcome their difficulties. There is no big matrix equation to solve in GL method. Moreover, it does not need artificial boundary and absorption condition to truncate the infinite space. The GL EM method consistent combines the analytical and numerical approaches together. GL EM quantum field modeling is useful to solve quantization scattering problem of the electromagnetic field in the dispersive and loss metamaterials, cloaks and more wide anisotropic materials. Moreover, GL time domain modeling for EM, acoustic and elastic wave field with dispersion have wide applications in nanometer materials, optical materials, dispersion engineering of photonic crystals, metamaterial Cloak, EM stirring, porous material, nondestructive testing, destructive mechanics, and geophysical exploration. The GL method is an effective physical simulation method. It has double abilities of the theoretical analysis and numerical simulations to study the cloak metamaterials and wide material and Field scattering in physical sciences.

The 3D and 2D GL parallel algorithms and software are made by authors in GL Geophysical Laboratory and are patented by GLGEO and all rights are reserved in GLGEO.

REFERENCES

1. Xie, G., F. Xie, L. Xie, and J. Li, "New GL method and its advantages for resolving historical diffculties," *Progress In Electromagnetics Research*, PIER 63, 141–152, 2006.
2. Xie, G., J. Li, L. Xie, and F. Xie, "GL method for solving equation in math-physics and engineering," *Acta Mathematicae Application Sinica*, Vol. 23, No. 2, 391–404, 2008.
3. Xie, G., J. Li, L. Xie, and F. Xie, "GL metro carlo EM inversion," *Journal of Electromagnetic Waves and Applications*, Vol. 20, No. 14, 1991–2000, 2006.
4. Pendry, J. B., D. Schurig, and D. R. Smith, "Controlling electromagnetic field," *Science Express*, Vol. 312, 1780, 2006.
5. Xie, G., J. Li, D. Zhuo, M. Enrest, and M. Oristaglio, "3-D electromagnetic modeling and nonlinear inversion," *Geophysics*, Vol. 65, No. 3, 804–822, 2000.
6. Xie, G. and J. Li, "New parallel SGILD modeling and inversion," *Physics D*, Vol. 133, 477–487, 1999.
7. Xie, G., "A new iterative method for solving the coefficient inverse problem of wave equation," *Comm. on Pure and Applied Math.*, Vol. 39, 307–322, 1986.
8. Li, J., G. Xie, C. Lin, and J. Liu, "2.5 dimensional GILD electromagnetic modeling and application," *SEG, Expanded Abstracts*, Vol. 21, No. 1, 692–695, 2002, http://www.segdl.org/journals/doc/SEGLIBhome/dci/searchDCI.jsp.
9. Xie, G., J. Li, and F. Xie, "New global and local electromagnetic field modeling and inversion," *Progress In Electromagnetics Research Symposium*, 68, Hangzhou, China, August 22–26, 2005, [ISBN: 1-933077-06-9], http://piers.mit.edu/piersproceedings/piers2k5Proc.php.
10. Xie, F. and L. Xie, "New computational mirage," *Progress In Electromagnetics Research Symposium*, 296, Hangzhou, China, August 22–26, 2005, [ISBN: 1-933077-06-9], http://piers.mit.edu/piersproceedings/piers2k5Proc.php.
11. Xie, G., J. Li, F. Xie, and L. Xie, "An electromagnetic GL double layered cloak," arXiv:0904.3168, 2009.
12. Li, J., G. Xie, F. Xie, and L. Xie, "No Maxwell electromagnetic wave field excited in cloaked concealment," arXiv:0904.3040, 2009.
13. Chen, H., B. Wu, B. Zhang, and J. A. Kong, "Electromagnetic wave interactions with a metamaterial cloak," *Physical Review Letters*, Vol. 99, 063903, 2007.
14. Cummer, S. A., B. J. Popa, D. Schurig, D. R. Smith, and J. Pendry, "Full-wave simulations of electromagnetic cloaking structures," *Physical Review E*, Vol. 74, 036621, 2006.
15. Argyropoulos, C., Y. Zhao, and Y. Hao, "A radial-dependent dispersive finite-difference time-domain method for the evaluation of electromagnetic cloaks," arXiv:0805.2050v1, 2008.
16. Zhang, B., H. Chen, B. I. Wu, and J. Kong, "Extraordinary surface voltage effect in the invisibility cloak with an active device inside," *Physical Review Letters*, Vol. 100, 063904-14, 2008.
17. Greenleaf, A., Y. Kurylev, M. Lassas, and G. Uhlmann, "Full-wave invisibility of active devices at all frequencies," *Communication Math. Phys.*, Vol. 275, 749–789, 2007.
18. Xie, G., "The 3-D finite element method in the elastic structure," *Mathematical Practice and Knowledge*, Vol. 1, 28–41, Chinese, 1975.
19. Xie, G., J. H. Li, L. Xie, and F. Xie, "A new broadband invisible GL double layer EM cloak," Technology Report of GL Geophysical Lab., Vol. 9, 11–28, 2009.
20. Brandts, J. and M. Krizek, "History and futures of superconvergence in three dimensional finite element method," *Mathematical Sciences and Applications*, Vol. 15, 24–35, 2001.

Electromagnetic Dispersion of Waveguide Based on Periodic Structures

S. Bouali and T. Aguili

National Engineering School of Tunis, ENIT, Tunisia

Abstract— This paper presents a study of electromagnetic dispersion of waveguide based on periodic structure using the transmission line approach and Floquet's theorem. The waveguide structure discussed in this paper is made of an infinite repetition of layers in one dimension. The structure is modeled as an infinite repetition of unit cell, by defining the matrix chaine of the unit cell and using Floquet's theorem. Then we obtain the equation of dispersion of the structure. This structure produce a set of allowed and forbidden frequency bands which is plotted and discussed, the width of these bands depends of many parameter of the structure; the results of this analysis are presented.

1. INTRODUCTION

Electromagnetic band gap (EBG) materials are creating new possibilities for controlling and manipulating the flow of electromagnetic waves. They are formed from dielectric structures that are periodic in one or more dimensions [1]. These periodical structures produce a set of allowed and forbidden frequency bands [2]. Many interesting properties of these structures are explored for many applications in electromagnetism like to improve the performances of antennas as in the design of the circuit. In the same perspective, this work studies the electromagnetic dispersion of rectangular waveguide based on periodic structures, this electromagnetic dispersion is examined between 2 GHz and 500 GHz, a numerically analysis is given. The following paragraph will presents a modeling of the structure. Using floquet's therem and Transmission line approach we obtain the analytical dispersion relation. Then, we present the curve dispersion simulations of this structure, and finally we will interpret the results.

2. MODELING OF THE STRUCTURE

The structure shown in Figure 1 is considered as waveguide formed by periodic variation of permittivity dielectric. By using the transmission line approach we consider the structure as a succession of transmission line. The unit cell consists of a succession of three part network one half of the transmission line ($a/2$), a transmission line (b) and another half ($a/2$) of the transmission line, the total line length is l ($l = a + b$), as shown in Figure 2.

Therefore, the matrix of the unit cell can be obtained by cascading three matrixes: First, the matrix chaine of the half ($a/2$) of the transmission line, the matrix chaine of the transmission line (b) and the matrix chaine of the half ($a/2$) of the transmission line. The transmission matrix of the transmission line ($a/2$) and (b) are given by:

$$C_1 = \begin{pmatrix} \cosh\left(\gamma\frac{a}{2}\right) & Z_{C1}\sinh\left(\gamma\frac{a}{2}\right) \\ Y_{C1}\sinh\left(\gamma\frac{a}{2}\right) & \cosh\left(\gamma\frac{a}{2}\right) \end{pmatrix} \text{ and } C_2 = \begin{pmatrix} \cosh\left(\gamma b\right) & Z_{C2}\sinh\left(\gamma b\right) \\ Y_{C2}\sinh\left(\gamma b\right) & \cosh\left(\gamma b\right) \end{pmatrix} \quad (1)$$

where Z_{C1} (Z_{C2}) is a characteristic impedance of a waveguide defined by the transmission line $a/2$ (the transmission line b). γ is the transmission line propagation constant, and a, b are the length
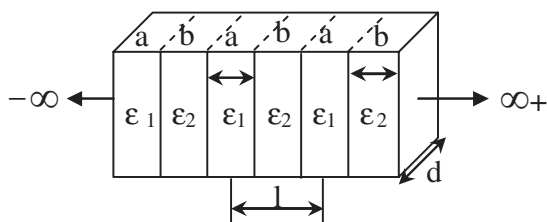
Figure 1: The structure of waveguide formed by periodic variation of permittivity.
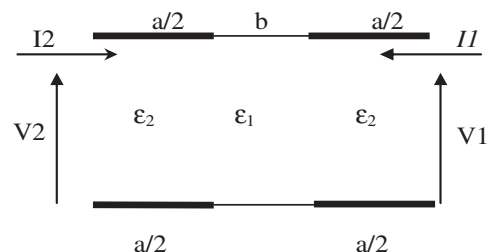
Figure 2: A unit cell, represented as a three part network.

of the transmission line. The matrix chaine of the unit cell is given by:

$$C_T = C_1 \cdot C_2 \cdot C_1 \qquad (2)$$

We suppose that a periodic structure supports the propagation wave, VN and IN are voltage and current corresponding to the propagating wave threw the n-th unit cell. $\gamma p = (\alpha p + j\beta p)$ is the complex propagation constant of the periodic structure. Using the Floquet's theorem for periodic structures, the dispersion equation obtained is given by:

$$\mathrm{Ch}\left(\alpha_p \frac{a+b}{2}\right) = \frac{\cos(\beta a)\cos(\beta b)}{\cos(\beta_p \frac{a+b}{2})} - \frac{1}{2}\left[\frac{Z_{C1}}{Z_{C2}} + \frac{Z_{C2}}{Z_{C1}}\right]\sin(\beta a)\sin(\beta b)\mathrm{avec}\beta_p \frac{a+b}{2} = n\pi \qquad (3)$$

$$\cos\left(\beta_p \frac{a+b}{2}\right) = \cos(\beta a)\cos(\beta b) - \frac{1}{2}\left[\frac{Z_{C1}}{Z_{C2}} + \frac{Z_{C2}}{Z_{C1}}\right]\sin(\beta a)\sin(\beta b)\mathrm{avec}\alpha_P = 0 \qquad (4)$$

with

$$\frac{Z_{C1}}{Z_{C2}} = \sqrt{\left(1 - \left(\frac{C}{2df\sqrt{\varepsilon_{r2}}}\right)^2\right) \Big/ \left(1 - \left(\frac{C}{2df\sqrt{\varepsilon_{r1}}}\right)^2\right)} \qquad (5)$$

We consider the function G that:

$$G(f) = \cos(\beta a)\cos(\beta b) - \frac{1}{2}\left[\frac{Z_{C1}}{Z_{C2}} + \frac{Z_{C2}}{Z_{C1}}\right]\sin(\beta a)\sin(\beta b) \qquad (6)$$

The mode of transmission in the rectangular waveguide is TE_{10}, f is the frequency and C is the speed of light. There are two equations of dispersion (3) and (4) with condition, in Equation (3), the attenuation constant αp is varying and the phase constant βp is fixed, for this equation if $\mathrm{Ch}(\alpha p(a+b)/2) > 1$, the periodic structure supports a propagation waves, else $(\mathrm{Ch}(\alpha p(a+b)/2)) < 1$ no wave can propagate along the structure. In Equation (4), the attenuation constant $\alpha p = 0$ and the phase constant is varying, for this equation if $\cos(\beta p((a+b)/2)$ is varying between -1 and $+1$ the structure supports a propagation waves, else no wave can propagate along the structure.

3. SIMULATION OF THE STRUCTURE

To simulate the structure we can vary two parameters the couple $(\varepsilon_{r1}, \varepsilon_{r2})$ or the length l of the unit cell. For this work we propose that the length of the unit cell $l = (a + b)$ is varying, and we present the results for several cases.

3.1. Visualization of the Dispersion Curve with Attenuation

We plot the function $G(f)$ for fixed values of l ($l = a + b$), the function $G(f) = \mathrm{Ch}[\alpha_p(a + b)/2]$ represented the curve of dispersion with attenuation. The frequency ranges corresponding to $G(f)$ larger than 1 indicate the pass band while the frequency regions with $G(f) < 1$ correspond to the stop band.

3.2. Visualization of the Dispersion Curve without Attenuation

We plot the function $G(f)$ for fixed values of l ($l = a + b$), the function $G(f) = \cos[\beta p(a + b)/2]$ represented the curve of dispersion without attenuation. To have propagation $G(f)$ should be between -1 and $+1$.

3.3. Visualization of the Attenuation Constant

Using Equation (3) the attenuation constant was calculated, and given by:

$$\alpha_p = \frac{2}{a+b}\mathrm{arch}(G(f)) \text{ with } \beta_p \frac{a+b}{2} = 2k\pi \qquad (7)$$

3.4. Visualization of the Phase Constant

Using Equation (4) The phase constant was calculated, and given by:

$$\beta_p = \frac{2}{a+b}\mathrm{arcos}(G(f)) \text{ with } \alpha_p = 0 \qquad (8)$$

The range of the frequency in Figure 5 (respectively Figure 6) represents propagation without attenuation agree well with Figure 7 (respectively Figure 8) that we have $\alpha = 0$ and Figure 9 (respectively Figure 10) that we have $\beta \neq 0$ it's a non attenuated propagation ($\alpha = 0$ and $\beta \neq 0$). The range of the frequency in Figure 3 represents propagation with attenuation agree well with Figure 7 that we have $\alpha \neq 0$ and Figure 9 that we have $\beta = 0$ it's an attenuated wave.
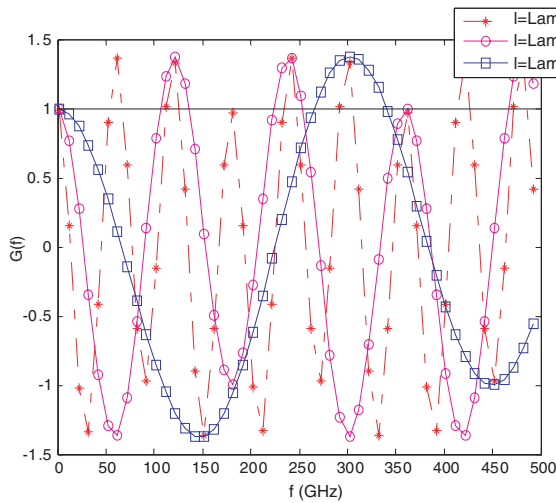
Figure 3: Dispersion curve with attenuation for three values of l ($b = a/2 = l/3$).
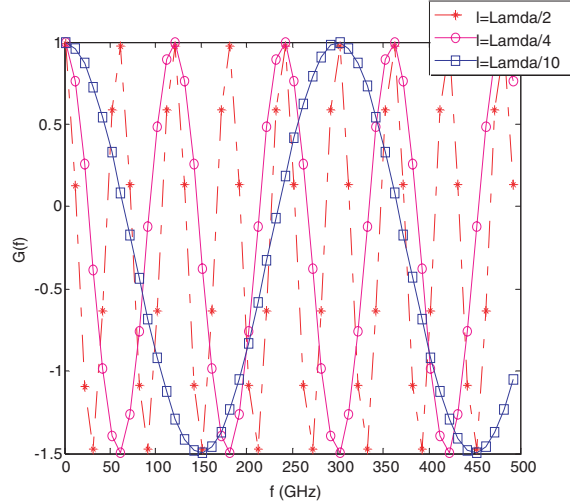
Figure 4: Dispersion curve with attenuation for three values of l ($a = b = l/2$).
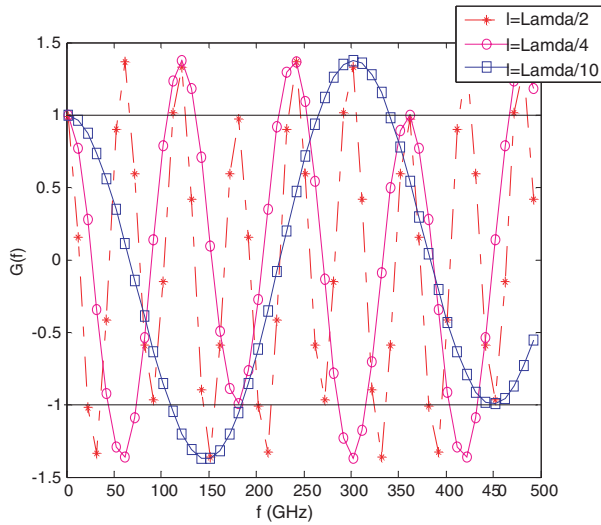
Figure 5: Dispersion curve without attenuation for three values of l ($b = a/2 = l/3$).
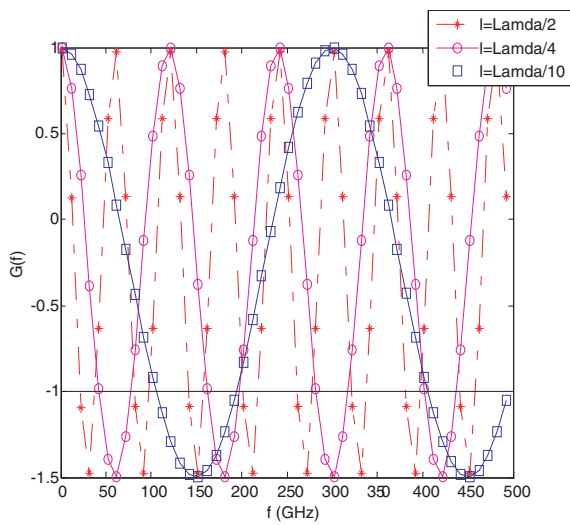
Figure 6: Dispersion curve without attenuation for three values of l ($a = b = l/2$).
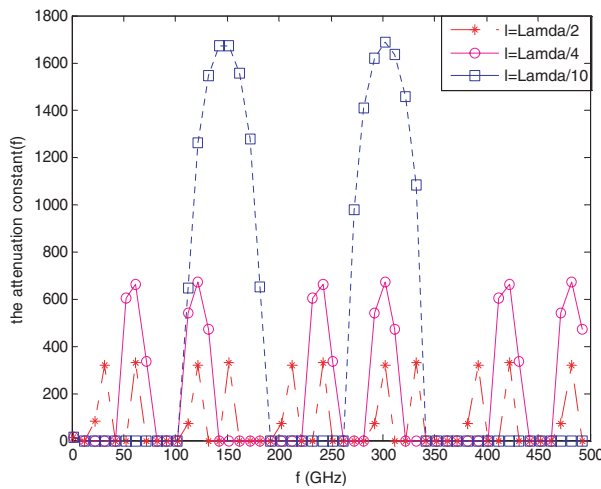
Figure 7: The attenuation constant for three values of l ($b = a/2 = l/3$).
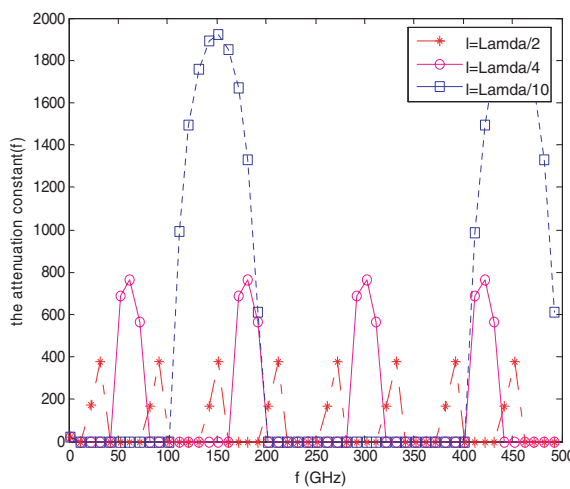
Figure 8: The attenuation constant for three values of l ($a = b = l/2$).
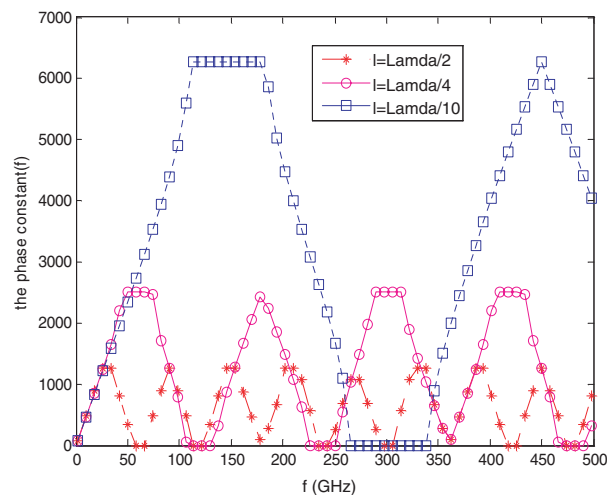
Figure 9: The phase constant for three values of l ($b = a/2 = l/3$).
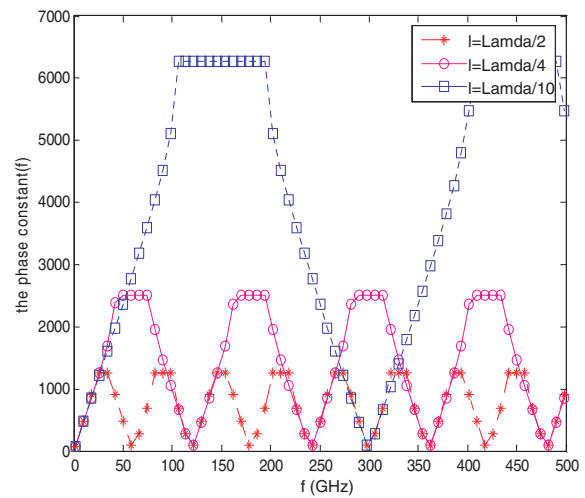
Figure 10: The phase constant for three values of l ($a = b = l/2$).

4. CONCLUSION

We have analyzed the dispersion properties of our periodic structure. The analytical dispersion relation for waveguide based on periodic transmission line has been formulated by the TL approach and has been solved with Floquet's theorem; we obtained tow equations which depend on the attenuation and phase constant. Using MATLAB we simulated these equations. The results revels the presence of stop band and pass band. The attenuation and phase constant was calculated and plotted in Figures 7 & 9 and Figures 8 & 10, which agree well with the stop and pass bands. The frequency ranges corresponding to the stop band depend on the physical configuration of the structure like the length of the periodic unit cell. By varying this length a range of frequencies where propagating modes can be fully suppressed, and we can commend the stop and the pass band.

REFERENCES

1. Joannopoulos, J. D., R. D. Meade, and J. N. Winn, *Photonic Crystals: Molding the Flow of Light*, Princeton, Princeton Univ. Press, NJ, 1995.
2. Massaoudi, S., A. Lustrac, and T. Denidni, "Study of dielectric and metallic photonic band gap material at micro-waves frequencies: calculation and experimental verification," 1-4244-0123-2/06/$20.00, IEEE, 2006.
3. Gao, J. and L. Zhu, "Guided-wave characteristics of cpw transmission line metamaterials: Effective per-unit-length parameters," 0-7803-8842-9/05/S$20.00, IEEE, 2005.
4. Gao, J. and L. Zhu, "Per-unit-length parameters of 1-D CPW metamaterials with simultaneously series C and shunt-L loading," 0-7803-9433-X05/$20.00, IEEE, 2005.
5. Bulgakov, A. A., O. V. Kostylyova, and A. V. Meruits, "Electromagnetic wave propagation in waveguide with layered-periodic walls," *MSMW'04 Symposuim Proceedings*, Kharkov, Ukraine, June 21–26, 2004.
6. Bouali, S. and T. Aguili, "Etude de la dispersion électromagnétique dans les méta matériaux," *GEI'2008 Tunisie*, March 17–19, 2008.
7. Bouali, S. and T. Aguili, "The study of electromagnetic dispersion in the periodic structures," *MMS 2008 Syria*, October 14–16, 2008.

Introduction of a New Class of Materials Called Double Zero Media Having the Real Parts of Epsilon and Mu Equal to Zero

Homayoon Oraizi[1], **Ali Abdolali**[1], **and Noushin Vaseghi**[2]

[1]Department of Electrical Engineering, Iran University of Science and Technology
Tehran 1684613114, Iran
[2]Department of Electrical Engineering, K. N. Toosi University of Technology
Tehran 16315-1355, Iran

Abstract— We introduce a new class of materials called double zero metamaterials (DZR) having the real parts of both its epsilon and mu equal to zero and investigate the electromagnetic wave propagation in them. We investigate the reflection coefficient from a PEC plate coated with DZR metamaterials. It is shown that the reflection coefficient from such structures is real quantity.

1. INTRODUCTION

Various uncommon materials such as metamaterials have been recently the subject of intensive research [1–4] which had negative real parts of permittivity and/or permeability namely double negative [DNG, $\text{Re}(\varepsilon) < 0$ and $\text{Re}(\mu) < 0$], epsilon negative [ENG $\text{Re}(\varepsilon) < 0$ and $\text{Re}(\mu) > 0$] and mu negative [MNG, $\text{Re}(\varepsilon) > 0$ and $\text{Re}(\mu) < 0$]. Metamaterials (MTMs) are mostly realized by periodically embedding conducting wires (TWs) and split ring resonators (SRRs) inside the dielectric media. We introduce a new class of materials, denoted as double zero metamaterials (DZR), characterized by $\text{Re}(\varepsilon) = 0$ and $\text{Re}(\mu) = 0$ and investigate the wave propagation in them and reflection from such media [5–7]. Such materials may also be approximated by those media characterized as epsilon near zero, [ENZ, $\text{Re}(\varepsilon) \to 0$] and mu near zero, [MNZ, $\text{Re}(\mu) \to 0$]. It should be noted that the selection of correct signs of the real and imaginary parts of ε, μ, k (wave number) and η (intrinsic impedance) of various types of metamaterials is necessary in their mathematical treatment [5, 6]. As an example, we study oblique plane wave incidence on a PEC plate coated by two layers [7–10] composed of DZR metamaterials for TM polarization. It is shown that the reflection coefficient becomes real.

2. FORMULATION AND NUMERICAL EXAMPLE

Consider a TM plane wave obliquely incident on a planar multilayer structure, as shown in Fig. 1.
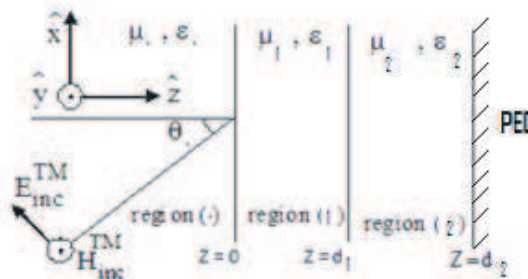
Figure 1: A TM polarized plane wave obliquely incident on a planar two-layers structure composed of DZR metamaterials backed by a PEC.

The transverse field components in layer l are [5]

$$region\ (l): \begin{cases} H_{ly} = (A_l e^{-jk_l \cos\theta_l z} + B_l e^{+jk_l \cos\theta_l z})e^{-jk_{lx}x} \\ E_{lx} = \eta_l \cos\theta_l (A_l e^{-jk_l \cos\theta_l z} - B_l e^{+jk_l \cos\theta_l z})e^{-jk_{lx}x} \end{cases} \tag{1}$$

where

$$k_l = \omega\sqrt{\mu_0 \varepsilon_0 \mu_l \varepsilon_l}$$

$$\eta_l = \sqrt{\frac{\mu_0 \mu_l}{\varepsilon_0 \varepsilon_l}} \tag{2}$$

$$k_{lx} = k_l \sin\theta_l = k_{l+1}\sin\theta_{l+1}$$

where ε, μ, k & η are its permittivity, permeability, wave number and intrinsic impedance and A_l, B_l are the forward and backward traveling waves in the l'th layer. After the imposition of boundary conditions at the plane boundaries at $Z = d_l$ for $l = 0, 1, 2$ the reflection coefficient of the structure is defined as

$$R = \frac{B_0}{A_0} \tag{3}$$

The imposition of boundary conditions at the interfaces between adjacent media, leads to a set of linear equations for the wave amplitudes, which have real parameters. Consequently, all the amplitudes are real and the imaginary part of reflection coefficient from the structure becomes zero too.

Now as an example we consider a PEC plate coated by two layers of DZR metamaterials. The first layer has thickness $1\,\mathrm{mm}$ and parameters $\varepsilon_1 = 0 - j0.4$, $\mu_1 = 0 - j0.5$ and the second layer has thickness $3\,\mathrm{mm}$ and parameters $\varepsilon_2 = 0 - j0.1$, $\mu_2 = 0 - j0.8$. A TM plane wave is obliquely incident on the structure. The real and imaginary parts of reflection coefficient are computed by Eq. (3) and drawn in Fig. 2 as a function of the angle of incidence at frequencies $f = 1, 5, 20\,\mathrm{GHz}$. Note that $\mathrm{Im}(R)$ is zero for all the angles of incidence and the specified frequencies.
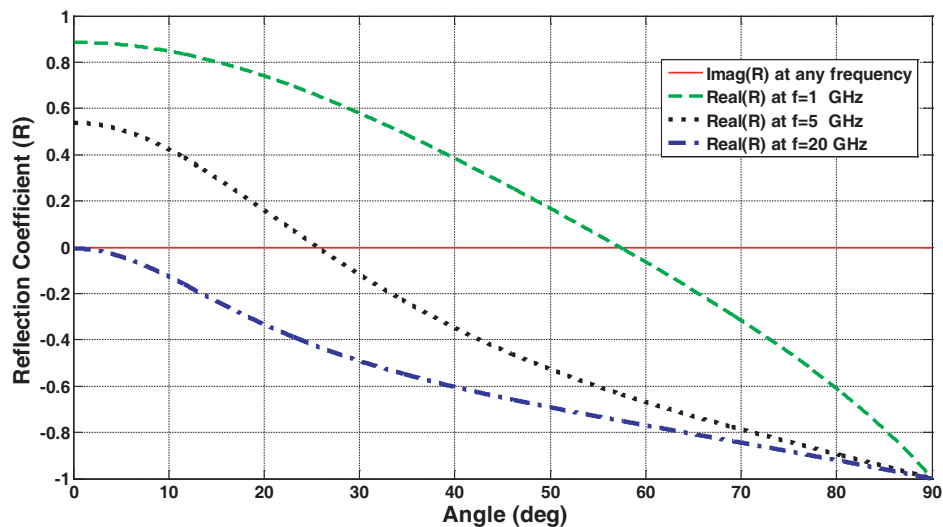
Figure 2: The real and imaginary parts of reflection coefficient versus angle of incidence from a PEC coated with two layers of DZR metamaterial at several frequencies $f = 1, 5, 20\,\mathrm{GHz}$.

3. CONCLUSION

Double zero (DZR) metamaterials are introduced where the real parts of permittivity $\mathrm{Re}(\varepsilon_r)$ and permeability $\mathrm{Re}(\mu_r)$ are zero. The media have been assumed lossy, linear, homogeneous and isotropic. A PEC plate coated by two layers made of DZR metamaterials was considered and its reflection coefficient was determined for plane wave oblique incidence at TM polarization. An example of the calculation of reflection coefficient was considered for such a structure. DZR metamaterials have potential applications in the reduction of radar cross section (RCS).

REFERENCES

1. Veselago, V. G., "The electrodynamics of substances with simultaneously negative values of ε and μ," *Soviet Physics Uspekhi*, Vol. 10, No. 4, 509–514, Jan.–Feb. 1968.

2. Caloz, C. and T. Itoh, *Electromagnetic Metamaterials, Transmission Line Theory and Microwave Applications*, Wiley-IEEE Press, Hoboken, NJ, 2005.

3. Marques, R., F. Martin, and M. Sorolla, *Metamaterials with Negative Parameters Theory, Design, and Microwave Applications*, 1st Edition, Wiley, 2008.

4. Smith, D. R., W. J. Padilla, D. C. Vier, S. C. Nemat-Nasser, and S. Schultz, "Composite medium with simultaneously negative permeability and permittivity," *Phys. Rev. Lett.*, Vol. 84, No. 18, 4184–4187, May 2000.

5. Oraizi, H. and A. Abdolali, "Design and optimization of planar multilayer antireflection metamaterial coatings at Ku band under circularly polarized oblique plane wave incidence," *Progress In Electromagnetics Research C*, Vol. 3, 1–18, 2008.

6. Oraizi, H. and A. Abdolali, "Mathematical formulation for zero reflection from multilayer metamaterial structures and their notable applications," *IET Microwaves, Antennas & Propagation Journal*, to be published.

7. Kong, J. A., "Electromagnetic wave interaction with stratified negative isotropic media," *Progress In Electromagnetics Research*, PIER 35, 1–52, 2002.

8. Cory, H. and C. Zach, "Wave propagation in metamaterial multilayered structures," *Microwave and Optical Technology Letters*, Vol. 40, No. 6, 460–465, Mar. 2004.

9. Alù, A. and N. Engheta, "Pairing an epsilon-negative slab with a mu-negative slab: Resonance, tunneling and transparency," *IEEE Trans. on Antennas and Propagation*, Vol. 51, No. 10, 2558–2571, Oct. 2003.

10. Lai, A., C. Caloz, and T. Itoh, "Composite right/left-handed transmission line metamaterials," *IEEE Microwave Magazine*, Vol. 5, No. 3, 34–50, Sep. 2004.

Ultra Wide Band Radar Absorbing Materials

Ali Abdolali[1], Homayoon Oraizi[1], and Ahad Tavakoli[2]

[1]Department of Electrical Engineering, Iran University of Science and Technology, Tehran, Iran
[2]Department of Electrical Engineering, Amirkabir University of Science and Technology, Tehran, Iran

Abstract— The reflected power from a planar multilayered structure backed by a perfect electric conductor is minimized with respect to the real and imaginary parts of ε and μ. Very deep levels of reduction of reflected powers are thus achievable by assuming arbitrary dispersion relations as opposed to the common ones.

1. INTRODUCTION

Radar absorbing materials (RAMs) have been studied for stealth technology, which have different characteristics and many applications [1]. Salisbury plates and Dallenbach layers [2] have been developed for narrow frequency band. However, multilayer structures such as Jaumann absorbers were developed for the wide frequency band reduction of radar cross section (RCS) [3, 4]. In the investigation of RAM, the dispersion properties of materials may first be ignored to acquire a general understanding of their behavior. However, available physically realizable dispersion relations may be adopted and their parameters may be determined to devise a RAM suitable for an application [5].

In this paper, we follow a procedure to obtain the permittivity ε and permeability μ of a material at several discrete frequencies in a band width. Then, any particular dispersion function may be fitted to the data to determine its parameters. This procedure of not limiting to and not assuming any particular dispersion, leads to a drastic reduction of RCS and reflected power in an ultra wide frequency band. The Genetic Algorithm [6] has been used for the optimization process and the generalized Fourier series has been used to fit a continuous function to the data.

2. PROBLEM CONFIGURATION, FORMULATION AND NUMERICAL IMPLEMENTATION

Consider a perfect electric conductor (PEC) plate covered by two layers of lossy materials as in Fig. 1.

A plane wave is normally incident on the structure. The forward and backward traveling plane waves are considered in the three regions [7]. The reflection coefficient R may be determined by imposing the boundary conditions

$$R = f\left(t_1, t_2, \varepsilon'_1, \varepsilon''_1, \mu'_1, \mu''_1, \varepsilon'_2, \varepsilon''_2, \mu'_2, \mu''_2\right) \tag{1}$$

It is a function of layer thicknesses (t_1, t_2) and the parameters of their permittivities and permeabilities. We may assume some constraints on the layer thicknesses, we fix them at some values.

$$t_1 = 2\,\text{mm}, \quad t_2 = 1.9\,\text{mm} \tag{2}$$
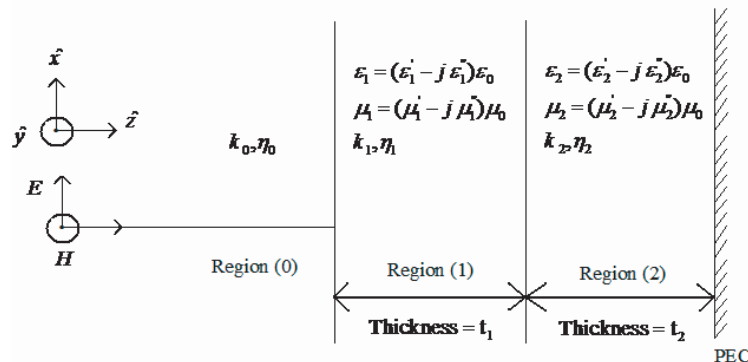
Figure 1: Problem Configuration.

We now construct an error function to minimize the reflection from this structure as [8]

$$Error = |R|^2 \qquad (3)$$

This error function is minimized with respect to the parameters of layers denoted in (2). At first the error function is minimized at single frequencies $f = 10, 20, 30, 40\,\text{GHz}$. The values of parameters for each frequency are given in Table 1.

Table 1: The optimum values of the real and imaginary parts of ε and μ for each layer at frequencies $f = 10, 20, 30, 40\,\text{GHz}$.

Frequency (GHz)	$\text{Re}\,(\varepsilon_{r1})$	$\text{Im}\,(\varepsilon_{r1})$	$\text{Re}\,(\mu_{r1})$	$\text{Im}\,(\mu_{r1})$	$\text{Re}\,(\varepsilon_{r2})$	$\text{Im}\,(\varepsilon_{r2})$	$\text{Re}\,(\mu_{r2})$	$\text{Im}\,(\mu_{r2})$
1.	0.7645	1.2817	0.8290	1.5108	0.6648	0.1866	0.5734	1.5051
2.	0.7989	0.9926	0.8311	0.9538	0.6242	0.4201	0.3318	1.5175
3.	0.8023	0.9255	0.8576	0.9420	0.5851	0.6942	0.3190	1.5537
4.	0.8485	0.8956	0.8622	0.9233	0.5547	0.8559	0.3117	1.5932
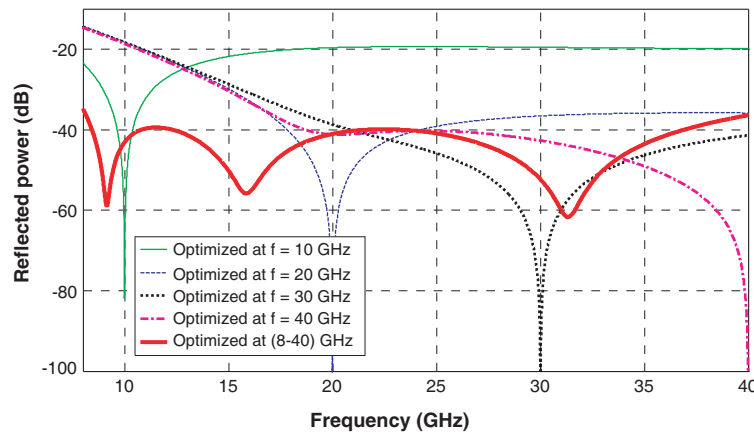
Figure 2: Reflected power (dB) versus frequency from a PEC plate coated with two layers with thicknesses $t_1 = 2\,\text{mm}$, $t_2 = 1.9\,\text{mm}$ and optimum real and imaginary parts of ε and μ after minimization at single frequencies $f = 10, 20, 30, 40\,\text{GHz}$ and in a wide frequency band width in the range 8–40 (GHz).

Then the magnitude of reflection coefficient is calculated for each case over the frequency band 8–40 (GHz) and drawn in Fig. 2. It is seen that in each case, R has a very low value at the related frequency, but its magnitude changes between 20–100 dB in the frequency range.

Then, the minimization of the error function is carried out in a wide frequency band width in the range 8–40 (GHz) at discrete frequencies at steps of 0.5 GHz. We assume dispersion relations as various functions such as $a + bf + cf^2$ and $d + \frac{e}{f} + \frac{g}{f^2}$ for the real part and the imaginary part of ε and μ. The generalized Fourier series is used to determine the constants in the dispersion relations. Then the magnitude of R is evaluated with the dispersion relations in the frequency band 8–40 (GHz) and drawn in Fig. 2. It is seen that the magnitude of reflection coefficient has actually reduced more than 40 dB. The realization of these dispersion relations should be the subject of further research.

3. CONCLUSION

The reflected power from a two layer structure backed by a PEC is minimized with respect to the values of the complex permittivities and permeabilities. The thicknesses of layers are assumed fixed. The reduction of reflected power through some synthesized dispersion relations is significantly much more than the common dispersion relations. The determination of dispersion relations for the minimization of reflected powers from multilayer structures could potentially have effective applications for absorbing boundary conditions (ABCs) and perfect matched layers (PMLs).

REFERENCES

1. Vinoy, K. J. and R. M. Jha, *Radar Absorbing Materials: From Theory to Design and Characterization*, Kluwer Academic Publishers, Norwell, Massachusetts, 1996.

2. Jaggard, D. L. and N. Engheta, "Chiroshield: A salisbury/dallenbach shield alternative," *Electron. Lett.*, Vol. 26, No. 17, 1332–1334, August 1990.

3. Berenger, J. P., "A perfectly matched layer for the absorption of electromagnetic waves," *Journal of Computational Physics*, Vol. 114, 185–200, 1994.

4. Chew, W. C., J. M. Jin, and E. Michielssen, "Complex coordinate stretching as a generalized absorbing boundary condition," *Microwave Opt. Technol. Lett.*, Vol. 15, 363–369, August 1997.

5. Oraizi, H. and A. Abdolali, "Design and optimization of planar multilayer antireflection metamaterial coatings at Ku band under circularly polarized oblique plane wave incidence," *Progress In Electromagnetics Research C*, Vol. 3, 1–18, 2008.

6. Michielssen, E., J. M. Sajer, S. Ranjithan, and R. Mittra, "Design of lightweight, broad-band microwave absorbers using genetic algorithms," *IEEE Trans. Microwave Theory Tech.*, Vol. 41, No. 67, 1024–1031, 1993.

7. Kong, J. A., *Theory of Electromagnetic Waves*, EMW Pub., New York, 2005.

8. Oraizi, H., "Application of the method of least squares to electromagnetic engineering problems," *IEEE Antenna and Propagation Magazine*, Vol. 48, No. 1, 50–75, 2006.

A Theorem for the Reflection and Transmission of Electromagnetic Waves from a Slab Made of Common Materials and Metamaterials

Homayoon Oraizi and Ali Abdolali

Department of Electrical Engineering, Iran University of Science and Technology
Tehran 1684613114, Iran

Abstract— Consider a slab made of nondispersive common materials or metamaterials situated between two half free spaces. A TM polarized plane wave is obliquely incident on it. Now each layer is filled by its dual medium according to the interchange DPS ↔ DNG. Then, the reflection and transmission coefficients from the slab become the complex conjugates of of each other. Consequently, the reflected power and transmitted power from the dual slabs are the same.

1. INTRODUCTION

Metamaterials have negative real parts of permittivity and permeability [1, 2]. They are called double negative (DNG). Common materials are called double positive (DPS). We consider a slab composed of DNG or DPS materials.Which is placed between two half free spaces. Assume that a plane wave with TM on it as shown in Fig. 1.

In this paper, we use a full-wave matrix method, whereby the field is decomposed into forward and backward travelling waves [3, 4]. We prove a theorem for the reflection and transmission coefficients of incident plane waves onto a planar DPS or DNG slab.

2. PROOF OF THE THEOREM

Consider a planar slab made of a double positive (DPS) material located between two half spaces as shown in Fig. 1.

A TM polarized plane wave is obliquely incident on the slab. The transverse field components in the three religions are [3, 4]

$$\text{region } (l) : \begin{cases} H_{ly} = \left(A_l e^{+jk_l \cos\theta_l z} + B_l e^{-jk_l \cos\theta_l z} \right) e^{-jk_{lx}x} \\ E_{lx} = \eta_l \cos\theta_l \left(A_l e^{+jk_l \cos\theta_l z} - B_l e^{-jk_l \cos\theta_l z} \right) e^{-jk_{lx}x} \end{cases} ; \quad l = 0, 1, 2 \qquad (1)$$

$$k_l = \omega\sqrt{\mu_0\varepsilon_0\mu_l\varepsilon_l}, \;\; \eta_l = \sqrt{\frac{\mu_0\mu_l}{\varepsilon_0\varepsilon_l}}, \;\; k_{lx} = k_l\sin\theta_l = k_{l+1}\sin\theta_{l+1} = k_0\sin\theta_0; \quad l = 0, 1, 2 \qquad (2)$$

where A_ℓ, B_ℓ are the amplitudes of forward and backward traveling waves. The reflection and transmission coefficients are defined as

$$R = \frac{B_0}{A_0}, \quad T = \frac{A_2}{A_0} \qquad (3)$$
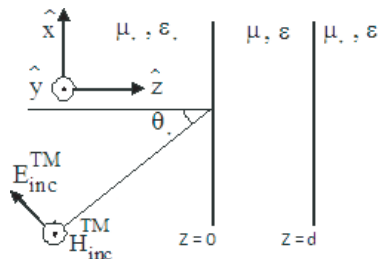
Figure 1: Geometry of the problem: Oblique TM wave interaction with one slab.

The boundary conditions at the two planes of the slab may be written in a matrix equation

$$
\begin{bmatrix}
+1 & -1 & -1 & 0 \\
p & +1 & -1 & 0 \\
0 & a & 1/a & -b \\
0 & a & -1/a & -pb
\end{bmatrix}
\begin{bmatrix}
R \\
A_1 \\
B_1 \\
T
\end{bmatrix}
=
\begin{bmatrix}
-1 \\
p \\
0 \\
0
\end{bmatrix}
\tag{4}
$$

where

$$
a = e^{-jk_1 \cos\theta_1 d}, \quad b = e^{-jk_0 \cos\theta_0 d}, \quad p = \frac{\eta_0 \cos\theta_0}{\eta_1 \cos\theta_1}
\tag{5}
$$

Then the reflection and transmission coefficients may be determined

$$
R^{\mathrm{TM}} = \frac{-1 + a^2 + p^2 - a^2 p^2}{2p + 1 + 2a^2 p - a^2 + p^2 - a^2 p^2} \quad \& \quad T^{\mathrm{TM}} = \frac{4pa}{b\left(2p + 1 + 2a^2 p - a^2 + p^2 - a^2 p^2\right)}
\tag{6}
$$

Now, the DPS media in the three regions are replaced by symmetrical double negative (DNG) media, according to the following relations [4–5]

$$
\begin{cases}
\varepsilon_{\mathrm{DPS}} = \varepsilon' - j\varepsilon'' \\
\mu_{\mathrm{DPS}} = \mu' - j\mu''
\end{cases}
\Rightarrow
\begin{cases}
\varepsilon_{\mathrm{DNG}} = -\varepsilon' - j\varepsilon'' \\
\mu_{\mathrm{DNG}} = -\mu' - j\mu''
\end{cases}
\tag{7}
$$

Consequently, the wave numbers and intrinsic impedances are obtained according to the rules given in [4–7].

$$
\begin{cases}
k_{\mathrm{DPS}} = k' - jk'' \\
\eta_{\mathrm{DPS}} = \eta' \pm j\eta''
\end{cases}
\Rightarrow
\begin{cases}
k_{\mathrm{DNG}} = -k' - jk'' = -k^*_{\mathrm{DPS}} \\
\eta_{\mathrm{DNG}} = \eta' \mp j\eta'' = \eta^*_{\mathrm{DPS}}
\end{cases}
\Rightarrow
\begin{cases}
a_{\mathrm{DNG}} = a^*_{\mathrm{DPS}} \\
b_{\mathrm{DNG}} = b^*_{\mathrm{DPS}} \\
p_{\mathrm{DNG}} = p^*_{\mathrm{DPS}}
\end{cases}
\tag{8}
$$

These relations are substituted in Eq. (5), which lead to the following relations

$$
R^{\mathrm{TM}}_{\mathrm{DNG}} = R^{\mathrm{TM}^*}_{\mathrm{DPS}}, \quad T^{\mathrm{TM}}_{\mathrm{DNG}} = T^{\mathrm{TM}^*}_{\mathrm{DPS}}
\tag{9}
$$

Therefore, the reflected powers, $P_r = RR^* = |R|^2$ and the transmitted powers $P_t = TT^* = |T|^2$ in the two cases are equal.

Now in a practical situation that the half spaces in the two cases are filled with the same media, but the material in the slab is interchanged (DPS $\leftrightarrow$ DNG), then only the reflection coefficients become complex conjugates of each other, but the transmissions coefficients are not and do not have a simple relationship.
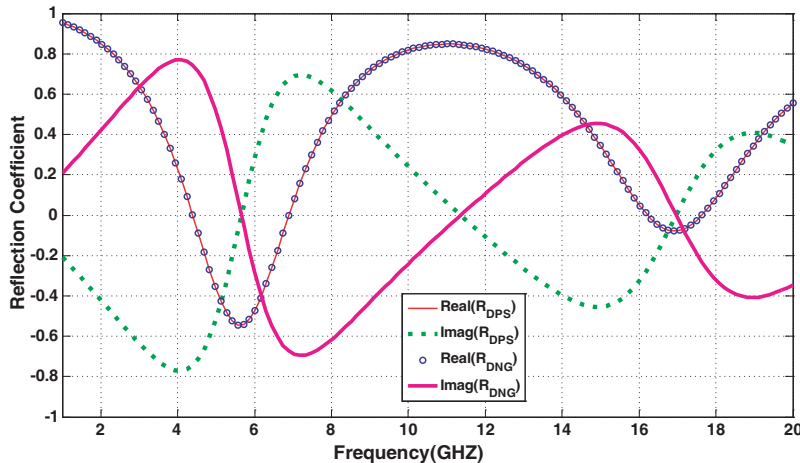
Figure 2: The real and imaginary parts of reflection coefficients from a DPS and DNG layer in free space with parameters specified in the text.

3. NUMERICAL EXAMPLE

As an example, consider a slab of thickness $d = 5$ mm composed of DPS material with characteristics $\varepsilon = 7 - j0.3$ and $\mu = 1 - j0.1$, which is placed in free space Then consider this slab to be composed of a dual DNG metamaterial with symmetrical characteristics $\varepsilon = -7 - j0.3$ and $\mu = -1 - j0.1$. A plane wave is obliquely incident on these two dual slabs. The real and imaginary parts of the reflection coefficients are computed and drawn as a function of frequency in Fig. 2. It is observed that $\mathrm{Re}(R)$ for the two dual cases are equal but $\mathrm{Im}(R)$ are symmetrical. This example verifies the above theorems.

4. CONCLUSION

A theorem has been proved for the plane wave oblique incidence on slabs composed of a DPS common materials or DNG metamaterials, where the slabs are placed between two half free spaces. The interchange DPS $\leftrightarrow$ DNG, leads to the reflection coefficients being complex conjugates of each other, similarly for the transmission coefficient. Here, common materials and metamaterials are assumed nondispersive. This theorem reveals some type of duality between DPS and DNG media.

REFERENCES

1. Veselago, V. G., "The electrodynamics of substances with simultaneously negative values of ε and μ," *Soviet Physics Uspekhi*, Vol. 10, No. 4, 509–514, Jan.–Feb. 1968.
2. Smith, D. R., W. J. Padilla, D. C. Vier, S. C. Nemat-Nasser, and S. Schultz, "Composite medium with simultaneously negative permeability and permittivity," *Phys. Rev. Lett.*, Vol. 84, No. 18, 4184–4187, May 2000.
3. Kong, J. A., *Theory of Electromagnetic Waves*, EMW Publishing, 2005.
4. Oraizi, H. and A. Abdolali, "Design and optimization of planar multilayer antireflection metamaterial coatings at Ku band under circularly polarized oblique plane wave incidence," *Progress In Electromagnetics Research C*, Vol. 3, 1–18, 2008.
5. Ziolkowski, R. W. and E. Heyman, "Wave propagation in media having negative permittivity and permeability," *Phys. Rev. E, tat. Phys. Plasmas Fluids Relat.*, Vol. 64, No. 5, 617–625, 2001.
6. Kong, J. A., "Electromagnetic wave interaction with stratified negative isotropic media," *Progress In Electromagnetics Research*, PIER 35, 1–52, 2002.
7. Oraizi, H. and A. Abdolali, "Mathematical formulation for zero reflection from multilayer metamaterial structures and their notable applications," *IET Microwaves, Antennas & Propagation*.

High Reflection Coatings with Negative and Positive Refractive Indexes

C. Sabah[1] and S. Uckun[2]

[1]Johann Wolfgang Goethe-University, Physikalisches Institut
D-60438, Frankfurt am Main, Germany
[2]Electrical and Electronics Engineering Department
University of Gaziantep, Gaziantep, Turkey

Abstract— In this paper, we intend to create a stratified coatings comprised of negative and positive refractive indexes, NRI and PRI, to achieve high reflection. Generally, quarter wave length longs of high and low refractive index media are applied to the substrate to form NRI-PRI multilayer stacks. By choosing the proper indexes, the various reflected wave fronts can be made to interfere gainfully to generate a well-organized reflector. The coatings and computations are performed and determined using the theory of transfer matrix method. Numerical results of this work show that the coatings are effective for both parallel and perpendicular polarization components, and can be designed for a wide frequency range. In addition, this paper also provides to be able to decrease/increase the frequency range to the desired band and to make size reduction in the layer number.

1. INTRODUCTION

Recently, there have been many studies on metamaterials having simultaneously negative permittivity and permeability which yields negative refractive index over a certain frequency ranges. These metamaterials are generally known as left-handed (LH) or negative refractive index (NRI) materials and theoretically started by Veselago in 1968 [1]. In his paper, the possibility of negative refractive index is discussed in detail. In addition, wave propagation in NRI materials was also given in his paper. His predictions were confirmed approximately thirty years later when Pendry and his colleagues presented their studies on the possibility of the realization of the negative permittivity and the negative permeability [2, 3]. Next, Smith and his collaborators created and tested a composite NRI material by inspiring the studies of Veselago and Pendry et al. in 2000 [4]. In 2001, Ziolkowski and Heyman presented their analytical and numerical study on the propagation of electromagnetic waves in NRI media [5]. Then, Kong provided an extensive study on the electromagnetic wave interaction with NRI media by starting to analyze the oblique wave incidence from semi-infinite free space upon a semi-infinite NRI medium and continuing with the detail analysis of the plane wave incident on a stratified isotropic NRI media [6]. After that, a brief overview of electromagnetic properties of NRI media and some ideas for potential applications of NRI materials were discussed by Engheta in 2002 [7]. Afterward, Chew studied the energy conservation property and loss condition of a NRI material in 2005 [8]. Additionally, the numerical study on the propagation and refraction of a cylindrical wave through a NRI slab [9], the investigation of the time-domain electric and magnetic energy stored in a frequency dispersive NRI medium [10], the analysis of the reflection and transmission characteristics of a multilayered structure consisting of NRI material and dielectric slabs [11], and some interesting applications of NRI materials [12] can be given as additional references to the NRI material works and their potential applications. Furthermore, Sabah et al. have been also studied the wave propagation through NRI media, scattering features of some constructions including NRI materials, and reflection and transmission characteristics of various configurations for particular applications [13–21]. In addition to all mentioned studies, many researchers continue to study the NRI materials and their future applications to build new constructions such as multilayer structures for special purposes.

In this study, it is intended to create a stratified structure comprised of NRI and PRI layers to obtain high reflection for microwave frequency range. High reflection coatings are formed from N pieces of NRI and PRI slabs with different material properties and thicknesses. By selecting the materials of appropriate refractive indexes, the various reflected wave fronts can be made to interfere constructively to produce a highly efficient reflector. The peak reflectance value is dependent upon the ratio of the refractive indexes of the two materials, as well as the number of layer pairs. Increasing either increases the reflectance. The larger the ratio is, the wider the high

reflectance region will be. Furthermore, the coatings are effective for both parallel and perpendicular polarizations, and can be designed for a wide angle of incidence range. In the theory, the incident electric field is assumed a plane wave with any arbitrary polarization. Transfer matrix method is used in the analysis. Simply, the electric and magnetic fields both inside and outside the multilayer structure are obtained by imposing the boundary conditions and then the transfer matrix is obtained. Note that, the elements of the transfer matrix are expressed as a function of the incidence angle, structure parameters, thickness of each slab, and frequency. All computations are based on the mentioned theoretical analysis. Propagation properties in multilayered structures consisting of metamaterial and dielectric layers are studied in [11]. A structure containing several identical pairs of alternating dielectric and metamaterial slabs is demonstrated to maximize the reflection for the high frequency range. It was found that for these metamaterial-dielectric high reflection structures the pass band is larger and the effects of angle of incidence and polarization were less dominant as compared to all dielectric structures. Moreover, these structures show no ripples and a monotonous quasi symmetric rise in their transmittance to the left and to the right of central frequency was observed. This kind of structures is further studied in our work to decrease the frequency range and to reduce the number of layers.

2. NUMERICAL RESULTS

In the computations, the incident electric field is assumed as the plane electromagnetic wave with the perpendicular polarization ($E_{\parallel} = 0$). The operation frequency is selected arbitrarily as $f_o = 10$ GHz. The thicknesses are arranged to become quarter wave length long at the operation frequency. In our configuration, seven NRI and PRI layers embedded in air are considered.

First of all, the frequency response of all dielectric structure with the high and low refractive indexes is shown. The permittivity and permeability of are selected 12.2500 and 1.0 (silicon-Si) for high index layers; and 1.8225 and 1.0 (cryolite-Na_3AlF_6) for low index layers [22]. Figure 1 presents the reflectance and transmittance for all dielectric layers as a function of the frequency for incidence angles of $0°$, $20°$, and $40°$. Solid lines correspond to $0°$, dotted lines to $20°$, and dashed lines to $40°$. As it is seen from the figure, the reflectance becomes unity and the transmittance becomes zero at and around the central frequency. The symmetry shifts in frequency to the right side when the incident angle increased. The reflectance region is wider than the coating investigated in [11]. In addition, there are more ripples in the frequency behavior of the reflectance and transmittance. Secondly, the frequency response of seven NRI and PRI layers is presented. The permittivity and permeability are -12.2500 and -1.0 for NRI layers and 1.8225 and 1.0 for PRI layers, respectively. Figure 2 shows the reflectance and transmittance for the combination of NRI and PRI layers versus frequency for the incidence angles of $0°$, $20°$, and $40°$. Solid lines correspond to $0°$, dotted lines to $20°$, and dashed lines to $40°$. It is found that, for this NRI-PRI high reflection structures the pass band is wider and the effect of the incident angle is less dominant as compared to the all dielectric structures. In addition, these structures have no ripples and no sharp shifts and therefore they can be used as high reflection coatings. Furthermore, the reflectance band achieved here is wider than the region obtained for the coating investigated in [11].
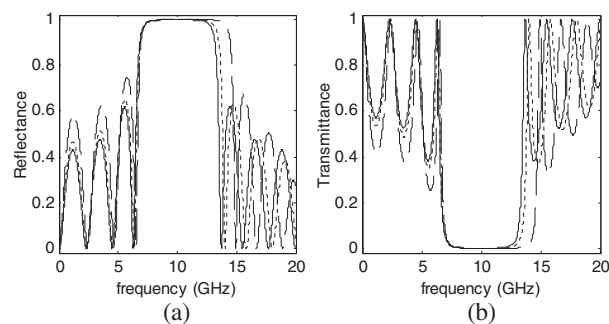
Figure 1: Reflectance and transmittance for all dielectric layers as a function of the frequency for the incidence angles of $0°$, $20°$, and $40°$. Solid lines correspond to $0°$, dotted lines to $20°$, and dashed lines to $40°$.
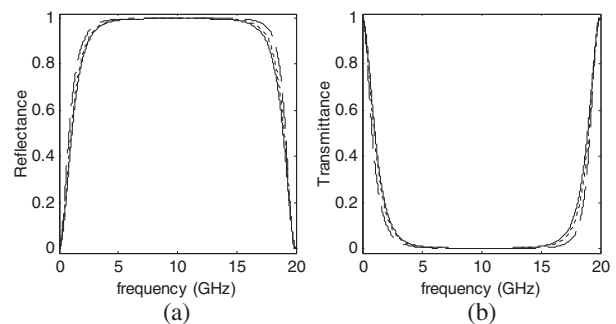
Figure 2: Reflectance and transmittance for NRI and PRI layers versus frequency for the incidence angles of $0°$, $20°$, and $40°$. Solid lines correspond to $0°$, dotted lines to $20°$, and dashed lines to $40°$.

The reflectance and transmittance for stratified structures consisting of half wavelength long NRI

and PRI layers are also computed to show the effect of the layer thickness. The same parameters are used as in the previous example except the thicknesses. The computed results are presented in Figure 3. From the figure, the frequency band for high reflectance is narrow and split into two parts in this example. Also, there is high transmission at the operation frequency. Figure 3 recommends creating high transmission coatings using NRI and PRI layers. Using the results of the previous example, we tried to create high transmission coatings using NRI and PRI layers. After proper combination of seven NRI and PRI layers, a high transmission coating can be created. To do this, NRI layers is selected to be a quarter wavelengths long while PRI layers are a half wavelengths long. The permittivity and permeability of are selected -5.0625 and -1.0 for high index layers and 2.1025 and 1.0 for low index layers. The results are shown in Figure 4. According to the figure, high transmission occurs in many frequency bands. At this band, transmittance sometimes becomes unity while the reflectance vanishes. At some bands shown in the figure, the reflectance becomes greater than the transmittance. Thus, the structure can be utilized as high and partially transmission coatings. Note that, the numerical computations obtained here can easily be extended for the incident wave with the parallel polarization.
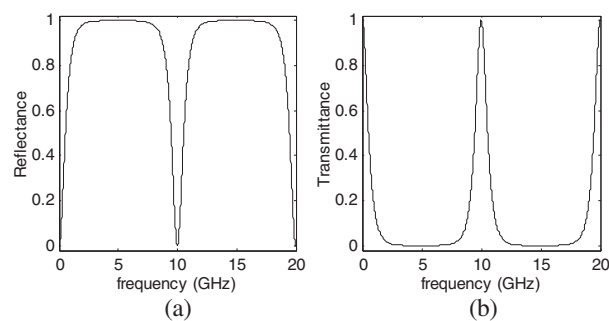
Figure 3: Reflectance and transmittance for half wavelength long seven NRI and PRI layers against the frequency.
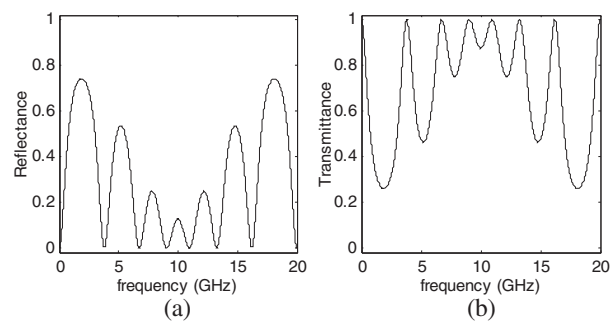
Figure 4: Reflectance and transmittance for half wavelength long NRI and quarter wavelength long PRI layers versus the frequency.

3. CONCLUSIONS

A coating containing several identical pairs of NRI-PRI stacks is demonstrated to maximize the reflection for the microwave frequency range. It is found that for NRI-PRI high reflection coatings, the pass band is larger and the effect of angle of incidence and polarization is less dominant as compared to the all PRI structures. Furthermore, these structures display no ripples but a monotonous quasi symmetric rise in the transmittance to the left and to the right of operation frequency is observed. Moreover, a high transmission coating comprised of NRI and PRI layers can be created using the results obtained in this paper. A numerical example is already presented in the previous section. The mentioned high transmission coating can be further studied and it can be considered for future studies.

REFERENCES

1. Veselago, V. G., "The electrodynamics of substances with simultaneously negative values of ε and μ," *Soviet Physics Uspekhi*, Vol. 10, 509–514, 1968.
2. Pendry, J. B., A. J. Holden, W. J. Stewart, and I. Youngs, "Extremely low frequency plasmons in metallic mesostructures," *Physical Review Letters*, Vol. 76, 4773–4776, 1996.
3. Pendry, J. B., A. J. Holden, D. J. Robbins, and W. J. Stewart, "Magnetism from conductors and enhanced nonlinear phenomena," *IEEE Trans. on Microwave Theory and Techniques*, Vol. 47, 2075–2084, 1999.
4. Smith, D. R., W. J. Padilla, D. C. Vier, S. C. Nemat-Nasser, and S. Schultz, "Composite medium with simultaneously negative permeability and permittivity," *Physical Review Letters*, Vol. 84, 4184–4187, 2000.
5. Ziolkowsky, R. W. and E. Heyman, "Wave propagation in media having negative permittivity and permeability," *Physical Review E*, Vol. 64, 056625.1–056625.15, 2001.
6. Kong, J. A., "Electromagnetic wave interaction with stratified negative isotropic media," *Progress In Electromagnetics Research*, PIER 35, 1–52, 2002.

7. Engheta, N., "Ideas for potential application of metamaterials with negative permittivity and permeability," A chapter in *Advances in Electromagnetics of Complex Media and Metamaterials, NATO Science Series, the Proceedings of NATO Advanced Research Workshop in Marrakech (Bianisotropics'2002)*, (S. Zouhdi, A. H. Sihvola, and M. Arsalane, editors), Kluwer Academic Publishers, Inc., 19–37, 2002.

8. Chew, W. C., "Some reflections on double negative materials," *Progress In Electromagnetics Research*, PIER 51, 1–26, 2005.

9. Karkkainen, M. K., "Numerical study of wave propagation in uniaxially anisotropic Lorentzian backward-wave slabs," *Physical Review E*, Vol. 68, 026602.1–026602.6, 2003.

10. Cui, T. J. and J. A. Kong, "Time-domain electromagnetic energy in a frequency-dispersive left-handed medium," *Physical Review B*, Vol. 70, 205106.1–205106.7, 2004.

11. Cory, H. and C. Zach, "Wave propagation in metamaterial multi-layered structures," *Microwave and Optical Technology Letters*, Vol. 40, 460–465, 2004.

12. Engheta, N. and R. W. Ziolkowski, "A positive future for double-negative metamaterials," *IEEE Transactions on Microwave Theory and Techniques*, Vol. 4, 1535–1556, 2005.

13. Sabah, C., G. Ögücü, and S. Uckun, "Reflected and transmitted powers of electromagnetic wave through a double-negative slab," *Journal of Optoelectronics and Advanced Materials*, Vol. 8, 1925–1930, 2006.

14. Sabah, C., "Theoretical and numerical analysis of double-negative slab," *Optica Applicata*, Vol. 37, 123–131, 2007.

15. Sabah, C. and S. Uckun, "Electromagnetic wave propagation through the frequency-dispersive and lossy double-negative slab," *Opto-Electronics Review*, Vol. 15, 133–143, 2007.

16. Sabah, C. and G. Ögücü, "Reflection from and transmission through the double-negative slab," *Journal of Optoelectronics and Advanced Materials* (*JOAM*), Vol. 9, 1861–1864, 2007.

17. Sabah, C., "Effects of loss factor on plane wave propagation through a left-handed material slab," *Acta Physica Polonica A*, Vol. 113, 1589–1597, 2008.

18. Sabah, C. and S. Uckun, "Physical features of left-handed mirrors in millimeter wave band," *Journal of Optoelectronics and Advanced Materials* (*JOAM*), Vol. 9, 2480–2484, 2007.

19. Sabah, C. and S. Uckun, "Scattering characteristics of the stratified double-negative stacks using the frequency dispersive cold plasma medium," *Zeitschrift für Naturforschung A* (*A Journal of Physical Sciences*), Vol. 62a, 247–253, 2007.

20. Sabah, C. and S. Uckun, "Frequency response of multilayer media comprised of double-negative and double-positive slabs," *Chinese Physics Letters*, Vol. 24, 1242–1244, 2007.

21. Sabah, C., "Left-handed chiral metamaterial," *Central European Journal of Physics*, Vol. 6, 872–878, 2008.

22. Orfanidis, S. J., *Electromagnetic Waves and Antennas*, online text book. www.ece.rutgers.edu/~orfanidi/ewa, 2004.

Electromagnetic Forces on Charged Particles

Zi-Hua Weng

School of Physics and Mechanical & Electrical Engineering
Xiamen University, Xiamen 361005, China

Abstract— The paper presents a theoretical method with the quaternion algebra to define the electromagnetic force from the linear momentum. It predicts that a new force of electromagnetic field will cause a test charge to move along the magnetic force line. In a constant magnetic field, the test charge will do uniform circular motion in the direction perpendicular to the magnetic force line, and do uniform variable rectilinear motion along the magnetic force line. The resulting track of the test charge is a helix with variable screw-pitch. The deduction can explain why the solar wind varies velocity along the magnetic force line in the solar system.

1. INTRODUCTION

The force is one of important physical quantities for electromagnetic field. There is only Lorentz force in the electromagnetic field described by the vectorial quantity. But this viewpoint can not explain why the solar wind varies velocity along the magnetic force line in the interplanetary space or the coronal hole on the sun [1].

One of J. C. Maxwell's research characteristics is to demonstrate the electromagnetic property with two methods simultaneously, the vectorial quantity and quaternion algebra [2]. The quaternion was invented by W. R. Hamilton in 1843. Subsequently the quaternion was decomposed as the scalar quantity and vectorial quantity. J. C. Maxwell mixed two methods to expatiate upon the electromagnetic properties. Nowadays, it is found that there are a few discrepancies between two descriptions with the vectorial quantity and quaternion algebra respectively [3, 4]. The discrepancy has being become an attentive focus [5, 6].

The electromagnetic theory described by the quaternion asserts that there are a few new forces besides Lorentz force [7]. One of them can cause a test charge to move along the magnetic force line. This consequence does not violate any principle of physics, but it must be validated experimentally. In the electromagnetic theory with the vector, it does not deal with the charge's force along the magnetic force line, and we were used to suppose the force to be zero. However, the deduction has never been validated before. Currently, this question leaves the blank theoretically, and is not validated experimentally. The prediction about new forces has become an emergent and key question to be broke through in the researching of electromagnetic field.

The paper presents a theoretical method with quaternions to define the electromagnetic force from the linear momentum. It attains a result that a new one of electromagnetic forces will cause the charge to move along the magnetic force line.

2. ELECTROMAGNETIC FORCE

The gravitational field and electromagnetic field both can be illustrated by the quaternion, and their quaternion spaces will be combined together to become the octonion space. In other words, the characteristics of gravitational field and electromagnetic field can be described with the octonion space at the same time.

In the quaternion space for the gravitational field, the basis vector $\mathbb{E}_g = (1, i_1, i_2, i_3)$, and the radius vector $\mathbb{R}_g = (r_0, r_1, r_2, r_3)$, with the velocity $\mathbb{V}_g = (v_0, v_1, v_2, v_3)$. For the electromagnetic field, the basis vector $\mathbb{E}_e = (I_0, I_1, I_2, I_3)$, the radius vector $\mathbb{R}_e = (R_0, R_1, R_2, R_3)$, and the velocity $\mathbb{V}_e = (V_0, V_1, V_2, V_3)$, with $\mathbb{E}_e = \mathbb{E}_g \circ I_0$.

The $\mathbb{E}_e$ is independent of the $\mathbb{E}_g$. Both of them can be combined together to become the basis vector $\mathbb{E}$ of the octonion space.

$$\mathbb{E} = (1, i_1, i_2, i_3, I_0, I_1, I_2, I_3) \tag{1}$$

The radius vector $\mathbb{R}(r_0, r_1, r_2, r_3, R_0, R_1, R_2, R_3)$ in the octonion space is

$$\mathbb{R} = r_0 + i_1 r_1 + i_2 r_2 + i_3 r_3 + I_0 R_0 + I_1 R_1 + I_2 R_2 + I_3 R_3 \tag{2}$$

and the velocity $\mathbb{V}(v_0, v_1, v_2, v_3, V_0, V_1, V_2, V_3)$ is

$$\mathbb{V} = v_0 + i_1 v_1 + i_2 v_2 + i_3 v_3 + I_0 V_0 + I_1 V_1 + I_2 V_2 + I_3 V_3 \tag{3}$$

where, $r_0 = v_0 t$; v_0 is the speed of light; t is the time; the $\circ$ denotes the octonion multiplication.

When the electric charge is combined with the mass to become the electron or the proton etc., we obtain the $R_i I_i = r_i i_i \circ I_0$ and $V_i I_i = v_i i_i \circ I_0$, with $i_0 = 1$. $i = 0, 1, 2, 3$; $j = 1, 2, 3$.

Table 1: The octonion multiplication table.

	1	i_1	i_2	i_3	I_0	I_1	I_2	I_3
1	1	i_1	i_2	i_3	I_0	I_1	I_2	I_3
i_1	i_1	-1	i_3	$-i_2$	I_1	$-I_0$	$-I_3$	I_2
i_2	i_2	$-i_3$	-1	i_1	I_2	I_3	$-I_0$	$-I_1$
i_3	i_3	i_2	$-i_1$	-1	I_3	$-I_2$	I_1	$-I_0$
I_0	I_0	$-I_1$	$-I_2$	$-I_3$	-1	i_1	i_2	i_3
I_1	I_1	I_0	$-I_3$	I_2	$-i_1$	-1	$-i_3$	i_2
I_2	I_2	I_3	I_0	$-I_1$	$-i_2$	i_3	-1	$-i_1$
I_3	I_3	$-I_2$	I_1	I_0	$-i_3$	$-i_2$	i_1	-1

In the electromagnetic field theory, the Aharonov-Bohm effect states that the field potential is more essential than the field strength. As a result, we can define the field strength and field source successively from the electromagnetic field potential by means of the quaternion operator.

The potential of the gravitational and electromagnetic fields are $\mathbb{A}_g = (a_0, a_1, a_2, a_3)$ and $\mathbb{A}_e = (A_0, A_1, A_2, A_3)$ respectively. They are combined together to become the potential $\mathbb{A} = \mathbb{A}_g + k_{eg}\mathbb{A}_e$, with k_{eg} being the coefficient.

The strength $\mathbb{B}(b_0, b_1, b_2, b_3, B_0, B_1, B_2, B_3)$ consists of the gravitational strength $\mathbb{B}_g$ and the electromagnetic strength $\mathbb{B}_e$. The gauge equations satisfy $b_0 = 0$ and $B_0 = 0$.

$$\mathbb{B} = \lozenge \circ \mathbb{A} = \mathbb{B}_g + k_{eg}\mathbb{B}_e \tag{4}$$

where, the quaternion operator $\lozenge = \partial_0 + \Sigma(i_j \partial_j)$; $\partial_i = \partial/\partial r_i$; $\nabla = \Sigma(i_j \partial_j)$.

The gravitational strength $\mathbb{B}_g$ includes two components, $\mathbf{g}/v_0 = \partial_0 \mathbf{a} + \nabla a_0$ and $\mathbf{b} = \nabla \times \mathbf{a}$.

$$\mathbf{g}/v_0 = i_1(\partial_0 a_1 + \partial_1 a_0) + i_2(\partial_0 a_2 + \partial_2 a_0) + i_3(\partial_0 a_3 + \partial_3 a_0) \tag{5}$$
$$\mathbf{b} = i_1(\partial_2 a_3 - \partial_3 a_2) + i_2(\partial_3 a_1 - \partial_1 a_3) + i_3(\partial_1 a_2 - \partial_2 a_1) \tag{6}$$

where, $\mathbf{a} = \Sigma(a_j i_j)$. $\mathbf{a} = 0$ and $\mathbf{b} = 0$ in the Newtonian gravity.

At the same time, the electromagnetic strength $\mathbb{B}_e$ involves two parts, $\mathbf{E}/v_0 = (B_{01}, B_{02}, B_{03})$ and $\mathbf{B} = (B_{23}, B_{31}, B_{12})$.

$$\mathbf{E}/v_0 = I_1(\partial_0 A_1 + \partial_1 A_0) + I_2(\partial_0 A_2 + \partial_2 A_0) + I_3(\partial_0 A_3 + \partial_3 A_0) \tag{7}$$
$$\mathbf{B} = I_1(\partial_3 A_2 - \partial_2 A_3) + I_2(\partial_1 A_3 - \partial_3 A_1) + I_3(\partial_2 A_1 - \partial_1 A_2) \tag{8}$$

In the electromagnetic field theory with the quaternion, some invariants are the same as them with vectors respectively, including the definition of field strength, Maxwell's equations, d'Alembert equation, and continuity equation. But some are different, such as the definition of gauge equation, direction of displacement current, and electromagnetic force.

The electric current density $\mathbb{S}_e = q\mathbb{V}_g \circ I_0$ is the source for the electromagnetic field, and the linear momentum density $\mathbb{S}_g = m\mathbb{V}_g$ for the gravitational field. The source $\mathbb{S}$ satisfies,

$$\mu\mathbb{S} = (\mathbb{B}/v_0 + \lozenge)^* \circ \mathbb{B} = \mu_g^g \mathbb{S}_g + k_{eg}\mu_e^g \mathbb{S}_e + \mathbb{B}^* \circ \mathbb{B}/v_0 \tag{9}$$

where, m is the mass density; q is the electric charge density; μ, μ_g^g, and μ_e^g are the constants; $*$ denotes the conjugate of octonion; $k_{eg}^2 = \mu_g^g/\mu_e^g$; $\mathbb{B}^* \circ \mathbb{B}/(2\mu_g^g)$ is the field energy density.

$$\mathbb{B}^* \circ \mathbb{B}/\mu_g^g = \mathbb{B}_g^* \circ \mathbb{B}_g/\mu_g^g + \mathbb{B}_e^* \circ \mathbb{B}_e/\mu_e^g \tag{10}$$

In the electromagnetic field, the linear momentum is defined as one function of field source. The electromagnetic force is defined from the linear momentum by the quaternion operator, and includes the Lorentz force with a few new forces. When the quaternion is decomposed to the scalar quantity and vectorial quantity, a few differences will exist in two descriptions.

The force density $\mathbb{F}$ is defined from $\mathbb{P} = \mu\mathbb{S}/\mu_g^g$, which is the extension of the $\mathbb{S}_g$.

$$\mathbb{F} = v_0(\mathbb{B}/v_0 + \Diamond)^* \circ \mathbb{P} \tag{11}$$

where, the force density includes the gravity density, inertial force density, Lorentz force density, and interacting force density between electromagnetic strength with magnetic moment, etc.

In case of the gravitational field and the electric field both can be neglected, the above can be decomposed in the basis vector (i_1, i_2, i_3) further. Besides the inertial force, we can obtain the electromagnetic forces as follows.

$$\mathbf{f}_e = q\mathbf{B} \times \mathbf{V} - q\mathbf{B} \circ \mathbf{V}_0 \tag{12}$$

where, $\mathbf{B} = \Sigma(B_j I_j)$, $\mathbf{V} = \Sigma(\mathbf{V}_j I_j)$, $\mathbf{V}_0 = V_0 I_0$.

In the above, the first term is Lorentz force, and the second term is a new force. This new force of electromagnetic field will cause a test charge to move along the magnetic force line, but the phenomena was used to be attributed to other factors. In a constant magnetic field, the charge will do uniform circular motion in the direction perpendicular to the magnetic force line, and do uniform variable rectilinear motion along the magnetic force line. And then the resulting track of the test charge is a helix with variable screw-pitch.

3. CONCLUSION

In a constant magnetic field, the test charge will vary velocity along the magnetic force line, and has a deviation from the uniform rectilinear motion. This states that it will violate the prediction of Lorentz force along the magnetic force line. The deduction can explain why the solar wind varies velocity along the magnetic force line in the solar system.

In theoretical analysis, Maxwell's equations can not contain electromagnetic forces. Describing the electromagnetic force with the quaternion algebra can deduce a few new forces. In experimental investigation, the charge's force along the magnetic force line has never been validated before. At present, some related validating trials have been brought forward. This research improves our knowledge about the electromagnetic force.

It should be noted that the investigation for the electromagnetic force has examined only one simple case, of which one new force causes a test charge to move along the magnetic force line. Despite its preliminary character, this study can clearly indicate that the test charge does uniform variable motion along the magnetic force line. For the future studies, the research will concentrate on only the predictions about new forces in the vast bulk and constant magnetic field.

REFERENCES

1. Tu, C.-Y., C. Zhou, E. Marsch, L.-D. Xia, L. Zhao, J.-X. Wang, and K. Wilhelm, "Solar wind origin in coronal funnels," *Science*, Vol. 308, No. 5721, 519–523, 2005.
2. Maxwell, J. C., *A Treatise on Electricity and Magnetism*, Dover Publications Inc., New York, 1954.
3. Adler, S. L., *Quaternionic Quantum Mechanics and Quantum Fields*, Oxford University Press, New York, 1995.
4. Morita, K., "Quaternions, lorentz group and the dirac theory," *Progress of Theoretical Physics*, Vol. 117, No. 3, 501–532, 2007.
5. Grusky, S. M., K. V. Khmelnytskaya, and V. V. Kravchenko, "On a quaternionic Maxwell equation for the time-dependent electromagnetic field in a chiral medium," *Journal of Physics A: Math. and General*, Vol. 37, No. 16, 4641–4647, 2004.
6. Rawat, S. and O. P. S. Negi, "Quaternionic formulation of supersymmetric quantum mechanics," *International Journal of Theoretical Physics*, Vol. 48, No. 2, 305–314, 2009.
7. Weng, Z.-H. and Y. Weng, "Variation of gravitational mass in electromagnetic field," *PIERS Proceedings*, 105–107, Beijing, China, March 23–27, 2009.

TM-Electromagnetic Guided Waves in a (Kerr-) Nonlinear Three-layer Structure

K. A. Yuskaeva[1], **V. S. Serov**[2], **and H. W. Schürmann**[1]

[1]University of Osnabrück, Germany
[2]University of Oulu, Finland

Abstract— The propagation of TM- (transverse-magnetic) guided waves in a lossless and nonmagnetic three-layer structure, consisting of a film, characterized by a local Kerr-like tensorial nonlinearity, situated between two semi-infinite linear and isotropic media is considered. Maxwell's equations are reduced to an exact differential equation leading to a first integral that relates the two field components so that one component can be eliminated. Hence the other one can be found by integration. The resulting integral combined with the boundary conditions is used to derive the exact dispersion relation establishing a link between the parameters of the problem (in particular between the thickness of the film, the propagation constant, and the field intensity at the interface between the substrate and the film). Numerical results for focusing and de-focusing Kerr-nonlinearity are presented.

1. INTRODUCTION

The exact analytical solution of Maxwell's equations for a lossless nonlinear three-layer dielectric waveguide is a basic problem of classical electrodynamics. Compared with the mathematical treatment of TE-polarized waves the analysis in the case of TM-polarized guided waves is more difficult. In this case, the magnetic field **H** is the appropriate quantity but the nonlinear dielectric function ε is simple if expressed in terms of the electric field **E**. If expressed by the magnetic field, ε is determined by a complicated equation that contains **H** and derivative of **H** [1]. The investigation is further complicated because, for TM-polarized waves, the occurrence of two field components in general leads to a dielectric tensor even for an isotropic film [2].

2. STATEMENT OF THE PROBLEM

We consider electromagnetic waves guided by a homogeneous, anisotropic, nonmagnetic layer filled with a Kerr-type nonlinear dielectric medium situated between two linear semi-infinite half-spaces $x < 0$ and $x > h$ consisting of isotropic, nonmagnetic media without sources and having constant permittivities ε_1 and ε_3, respectively. Fig. 1 shows the geometry of the problem.

The (real) electrical field

$$E(x, y, z, t) = E_+(x, y, z) \cos \omega t + E_-(x, y, z) \sin \omega t \tag{1}$$

satisfies Maxwell's equations

$$rot\mathbf{H} = -i\omega\varepsilon\mathbf{E} \tag{2}$$
$$rot\mathbf{E} = -i\omega\mu\mathbf{H}, \tag{3}$$

where

$$\mathbf{E}(x, y, z) = E_+(x, y, z) + iE_-(x, y, z) \tag{4}$$
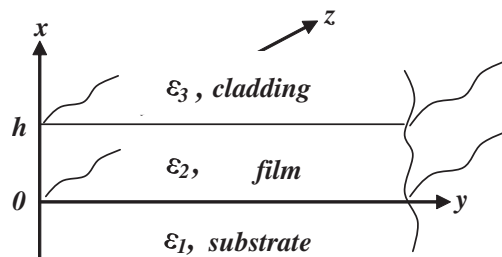
Figure 1: Geometry of the problem.

is a complex amplitude. The permittivity inside the film is described by the Kerr law

$$\varepsilon_2 = \begin{pmatrix} \varepsilon_{21} + a|E_x|^2 + b|E_z|^2 & 0 & 0 \\ 0 & 0 & 0 \\ 0 & 0 & \varepsilon_{22} + b|E_x|^2 + a|E_z|^2 \end{pmatrix}, \tag{5}$$

where ε_{21}, ε_{22}, a, b are constants.

Electromagnetic waves must satisfy Maxwell's Equations (2) and (3), the continuity conditions of the tangential field components at the interfaces, and the radiation condition at infinity.

For the TM-polarization $\mathbf{E} = (E_x, 0, E_z)$, $\mathbf{H} = (0, H_y, 0)$ Equations (2) and (3) can be evaluated to yield $E_x = E_x(x, z)$ and $E_z = E_z(x, z)$ independent on y. Since H_y is expressed in terms of E_x and E_z, H_y is also independent on y.

Assuming $H_y = H_y(x)e^{i\gamma z}$, $E_x = E_x(x)e^{i\gamma z}$, $E_z = E_z(x)e^{i\gamma z}$, after some algebra, we obtain the system

$$\begin{cases} \gamma \frac{d(iE_x(x))}{dx} - \frac{d^2 E_z(x)}{dx^2} = \omega^2 \varepsilon_z \mu E_z(x) \\ \gamma^2 (iE_x(x)) - \gamma \frac{dE_z(x)}{dx} = \omega^2 \varepsilon_x \mu (iE_x(x)). \end{cases} \tag{6}$$

Introducing the notations $k^2 = \omega^2 \mu \varepsilon_0$, normalizing according to

$$\tilde{x} = kx, \quad \frac{d}{dx} = k\frac{d}{d\tilde{x}}, \quad \tilde{\gamma} = \frac{\gamma}{k}, \quad \tilde{\varepsilon}_j = \frac{\varepsilon_j}{\varepsilon_0} \quad (j = 1, 2, 3), \quad \tilde{a} = \frac{a}{\varepsilon_0}, \quad \tilde{b} = \frac{b}{\varepsilon_0}, \tag{7}$$

we set $Z(\tilde{x}) \equiv E_z$ and $X(\tilde{x}) \equiv iE_x$. Omitting the tilde signs, system (6) in the normalized form reads

$$\begin{cases} -\frac{d^2 Z}{dx^2} + \gamma \frac{dX}{dx} = \varepsilon_z Z \\ -\frac{dZ}{dx} + \gamma X = \frac{\varepsilon_x}{\gamma} X. \end{cases} \tag{8}$$

We are looking for real solutions X, Z to (8) subject to real γ, where

$$\varepsilon_x = \begin{cases} \varepsilon_1, & x < 0 \\ \varepsilon_{21} + aX^2 + bZ^2, & 0 < x < h \\ \varepsilon_3, & x > h \end{cases}$$

$$\varepsilon_z = \begin{cases} \varepsilon_1, & x < 0 \\ \varepsilon_{22} + bX^2 + aZ^2, & 0 < x < h \\ \varepsilon_3, & x > h. \end{cases} \tag{9}$$

3. FORMAL SOLUTION

To find a solution of system (8) for $0 < x < h$ it is useful to combine both Equation (8). Hence one gets

$$-\left(X\frac{\partial \varepsilon_x}{\partial X} + \varepsilon_x \right) \frac{dX}{dZ} = \frac{\gamma^2 \varepsilon_z Z}{(\varepsilon_x - \gamma^2) X} + X\frac{\partial \varepsilon_x}{\partial Z}. \tag{10}$$

Since the permittivity tensor ε_2 satisfies the integrability condition $X\frac{\partial \varepsilon_x}{\partial Z} = \frac{\partial \varepsilon_z}{\partial X} Z$, Equation (10) is an exact differential equation with the solution

$$G(X, Z) := \left(\frac{\varepsilon_x}{2} - \gamma^2 \right) \varepsilon_x X^2 + \gamma^2 \left(\int_{Z_0}^{Z} \varepsilon_z (X_0, \zeta) \zeta d\zeta + \int_{X_0}^{X} \varepsilon_x(\xi, Z)\xi d\xi \right) - C_0 = 0, \tag{11}$$

where

$$C_0 = \left(\frac{\varepsilon_x(X_0, Z_0)}{2} - \gamma^2 \right) \varepsilon_x(X_0, Z_0)X_0^2, \tag{12}$$

with constants X_0 and Z_0.

Using (9), Equation (11) (cf. Ref. [3]) can be written as

$$
\begin{aligned}
G(X, Z) : = & \ C_1 + \frac{1}{4} \left(2\varepsilon_{21} \left(\varepsilon_{21} + 2 \left(aX^2 + bZ^2 \right) - \gamma^2 \right) X^2 + 2 \left(aX^3 + bXZ^2 \right)^2 \right. \\
& \left. - \gamma^2 \left(3aX^4 + 2bX^2Z^2 - aZ^4 - 2\varepsilon_{22}Z^2 \right) \right) = 0,
\end{aligned}
\tag{13}
$$

with

$$
\begin{aligned}
C_1 \ = \ & -\frac{1}{2} \left(aX_0^2 + bZ_0^2 + \varepsilon_{21} \right) \left(aX_0^2 + bZ_0^2 + \varepsilon_{21} - 2\gamma^2 \right) X_0^2 \\
& -\frac{\gamma^2}{4} \left(2bX_0^2Z_0^2 + aX_0^4 + aZ_0^4 + 2\varepsilon_{21}X_0^2 + 2\varepsilon_{21} \right) Z_0^2.
\end{aligned}
\tag{14}
$$

Equation (13) is of degree three with respect to X^2. Hence a real root of Equation (13) exists. Inserting the real root $X(Z^2)$ into the second Equation (8) yields

$$
\gamma \int_{Z_0}^{Z(x,\gamma,Z_0)} \frac{d\xi}{\left(\gamma^2 - \varepsilon_{21} - aX^2(\xi) - b\xi^2 \right) X(\xi)} = x - x_0,
\tag{15}
$$

where $Z_0 = Z(x_0)$. Thus, if the propagation constant γ is known in dependence on h, Z_0 and on the parameters of the problem a, b, ε_1, ε_{21}, ε_{22}, ε_3, the function $Z(x,\gamma,Z_0)$ can formally be obtained by integration and inversion according to Equation (15). Hence the function $X(x,\gamma,Z_0)$ can be evaluated by Equation (13).

It seems that $Z(x,\gamma,Z_0)$ cannot be obtained analytically from Equation (15). For the linear case ($a = b = 0$) it yields the well-known result [5].

4. DISPERSION RELATION

If combined with the boundary conditions, Equation (15) is suitable to determine the propagation constant γ.

The boundary conditions for $\mathbf{E}$ and $\mathbf{H}$ imply that $Z(x)$ and $\gamma X(x) - \frac{dZ(x)}{dx}$ are continuous at the boundaries $x = 0$ and $x = h$ Hence one obtains

$$
\varepsilon_x \left(X\left(0+0,\gamma,Z(0)\right), Z(0) \right) X\left(0+0,\gamma,Z(0)\right) = Z(0)\frac{\gamma\varepsilon_1}{\sqrt{\gamma^2 - \varepsilon_3}},
\tag{16}
$$

and

$$
\varepsilon_x \left(X\left(h-0,\gamma,Z(0)\right), Z\left(h,\gamma,Z(0)\right) \right) X\left(h-0,\gamma,Z(0)\right) = -Z(h,\gamma,Z(0)) \frac{\gamma\varepsilon_3}{\sqrt{\gamma^2 - \varepsilon_1}},
\tag{17}
$$

respectively.

Subject to certain constraints (sign of the discriminant) Equation (16) has real solutions $X(0+0,\gamma,Z(0))$. With $X_0 = X(0+0,\gamma,Z(0))$ in Equation (14) the "constant" $C_1(\gamma)$ is determined.

For $x = h$ Equation (15) reads

$$
DR(h,\gamma,Z(0)) := \gamma \int_{Z(0)}^{Z(h,\gamma,Z(0))} \frac{d\xi}{\left(\gamma^2 - \varepsilon_{21} - aX^2(\xi) - b\xi^2 \right) X(\xi)} - h = 0.
\tag{18}
$$

Function $X^2(h-0,\gamma,Z(0))$ as a solution of (13) is real and can be expressed by $Z(h,\gamma,Z(0))$. Inserting $X(h-0,\gamma,Z(0))$ into (17) $Z(h,\gamma,Z(0))$ can be determined (due to (17) it does not depend on h). Thus, Equation (18) can be evaluated by integration only. It relates $h, \gamma, Z(0)$ and the parameters $a, b, \varepsilon_{21}, \varepsilon_{22}, \varepsilon_3$ (dispersion relation).

Adding multiples of the period of the integral on the left-hand side of (18) yields higher modes.

5. APPLICATIONS

To illustrate the foregoing approach the material parameters are chosen as $\varepsilon_1 = 1$, $\varepsilon_3 = 4$, $\varepsilon_{21} = 9$, $\varepsilon_{22} = 6$, $a = 0.2$, $b = 0.1$. Fig. 2 represents the first integral $G(X, Z) = 0$ according to Equation (13) for $Z(0) = 1$: (a) shows the dependence on γ, (b) and (c) show the relation $G(X, Z) = 0$ for the first three modes (with $\gamma = 2.5$, $h_1 = 1.76$, $h_2 = 3.98$, $h_3 = 6.2$ as solutions of the dispersion relation).

(a)   (b)   (c)
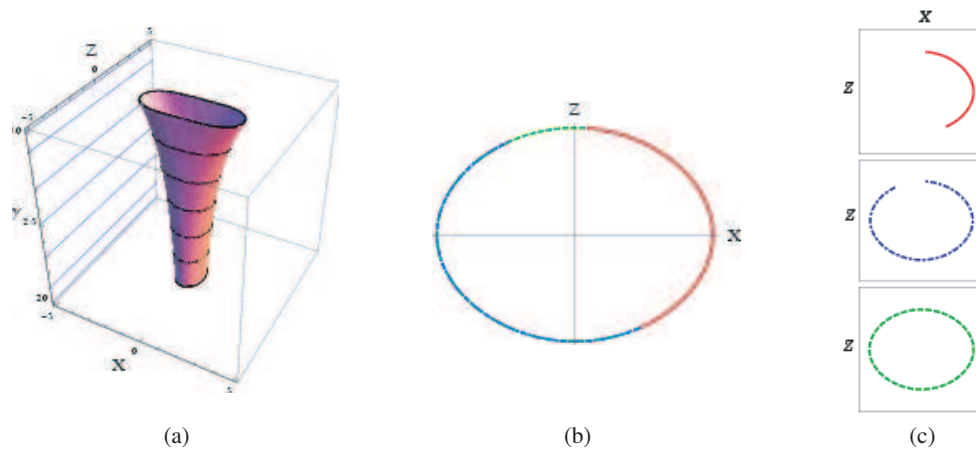
Figure 2: (a) $G(X, Z, \gamma) = 0$; (b) $G(X, Z, 2.5)$; (c) Modes $G(X_i, Z_i, 2.5) = 0$, $i = 1, 2, 3$.

(a)   (b)   (c)
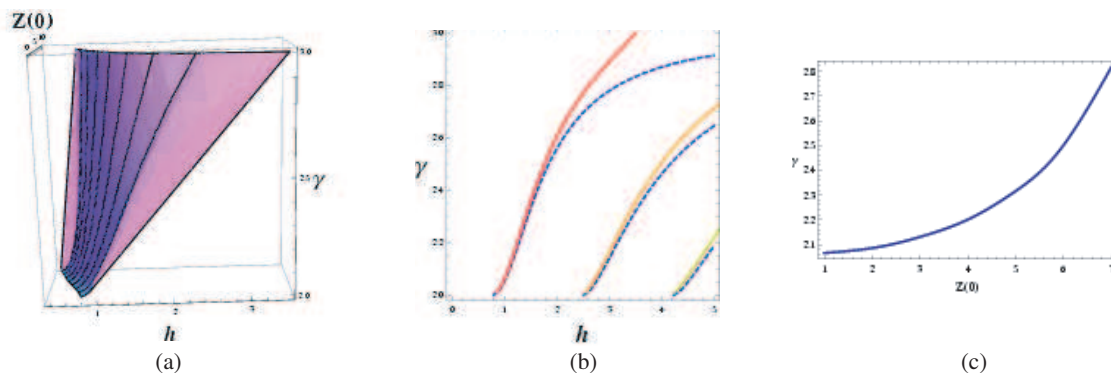
Figure 3: (a) $DR(h, \gamma, Z(0)) = 0$; (b) $DR(h, \gamma, 1) = 0$; (c) $DR(1, \gamma, Z(0)) = 0$; parameters cf. text.

(a)   (b)   (c)   (d)
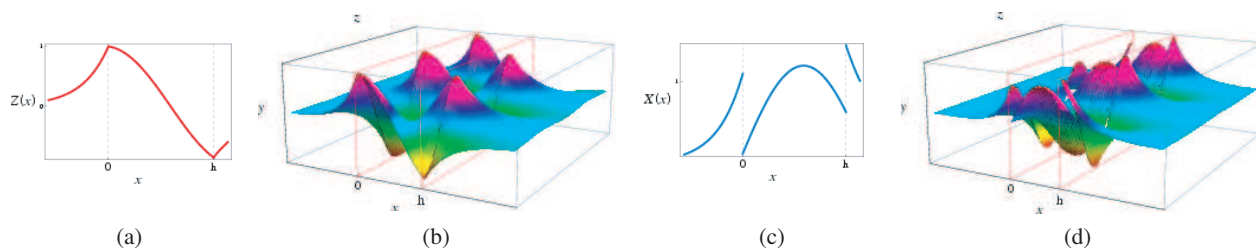
Figure 4: (a) $Z(x, 0)$; (b) $Z(x, z)$; (c) $X(x, 0)$; (d) $X(x, z)$.

Evaluation of (17) and (18) yields results depicted in Fig. 3: (a) shows the "general" relation between $h, \gamma, Z(0)$. Cuts are shown in (b) (dashed curve corresponds to the linear dispersion relation) and (c) ($Z(0) = 1$ in (b), $h = 1$ in (c)). Results are consistent with those of a recent paper [4].

Figure 4 depicts the fields $Z(x, z)$, $X(x, z)$ for the first mode with the propagation constant $\gamma = 2.5$ and the thickness of the film $h_1 = 1.76$.

The same parameters as for the focusing case are chosen for the defocusing nonlinearity, but with $a = -0.2$, $b = -0.1$. Fig. 5 shows the first integral $G(X, Z) = 0$.

Figure 6(a) presents the solution of the dispersion Equation (18) (black points) and its comparison with those of the focusing (solid lines) and linear case (dashed curves). Figs. 6(b) and (c) show field patterns for the linear (dot-dashed), focusing (solid) and defocusing (dashed) cases. The thickness of the film is $h = 2$, the propagation constants are $\gamma_{linear} = 2.56$, $\gamma_{focus} = 2.61$, $\gamma_{defocus} = 2.38$.

Figure 7 shows the field components $Z(x), X(x)$ for the first three modes (with $\gamma = 2.5$) and their corresponding solution in the space (X, Z). The normalized width of the slab for the first three modes is $h_1 = 1.97$, $h_2 = 4.42$ and $h_3 = 6.87$, respectively.

Figure 5: $G(X, Z, \gamma) = 0$.

(a)   (b)   (c)
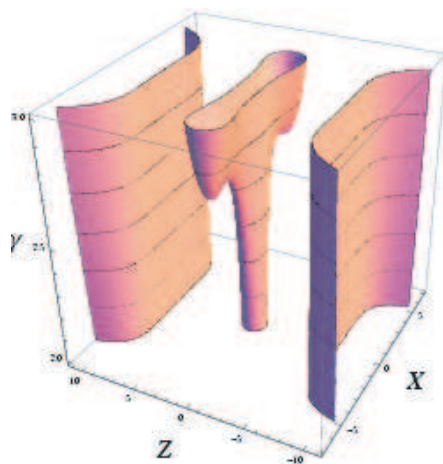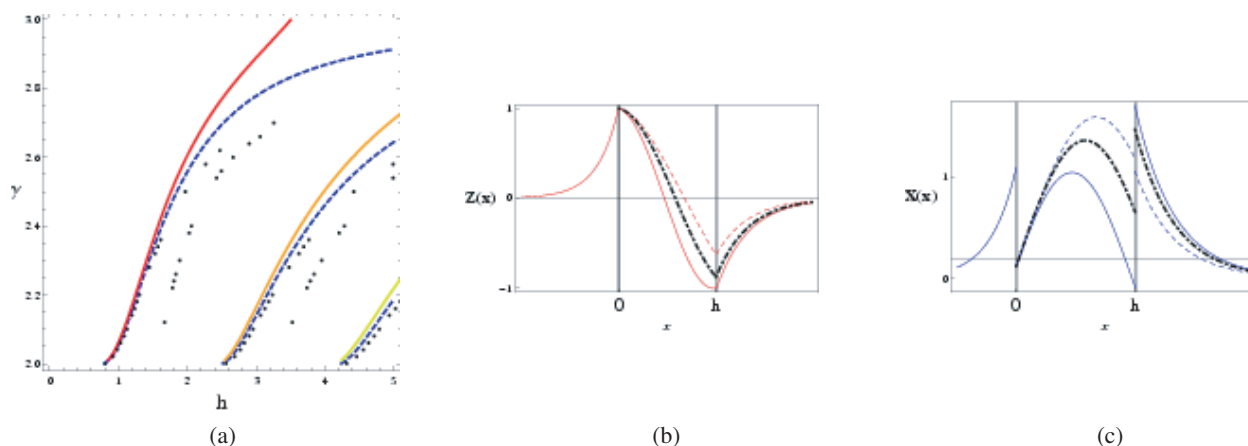
Figure 6: (a) $DR(h, \gamma, 1) = 0$; (b) Field patterns $Z(x)$; (c) Field patterns $X(x)$ (cf. text).

(a)   (b)

(c)
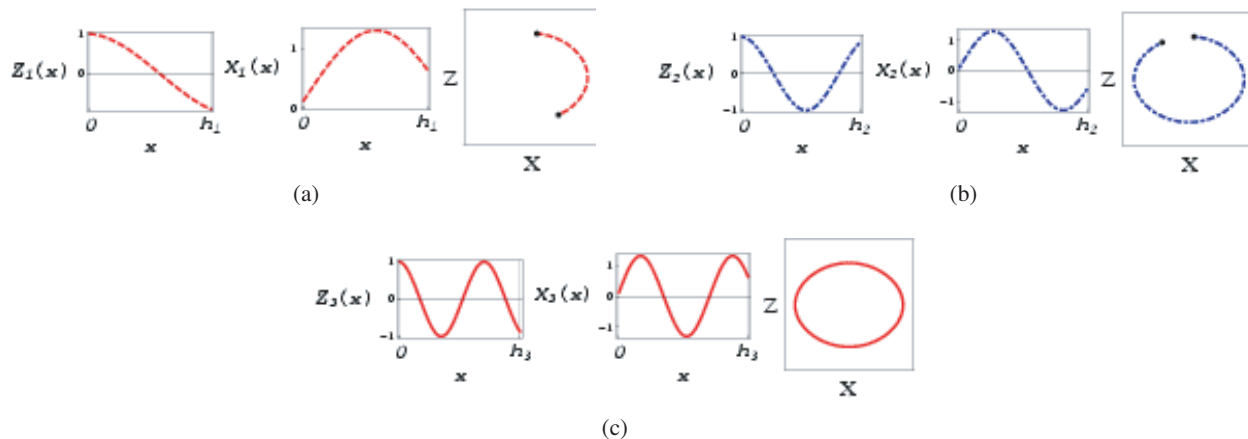
Figure 7: (a) $Z_1(x)$, $X_1(x)$, $G(X_1, Z_1, 2.5) = 0$; (b) $Z_z(x)$, $X_2(x)$, $G(X_2, Z_2, 2.5) = 0$; (c) $Z_3(x)$, $X_3(x)$, $G(X_3, Z_3, 2.5) = 0$.

6. CONCLUSION

TM-polarized guided waves in a (Kerr-like) nonlinear three-layer structure have been investigated. An exact dispersion relation has been obtained relating the propagation constant γ to the (normalized) thickness and to the intensity $Z(0)$. Formulas for the field components $Z(x), X(x)$ are presented and evaluated. In principle, there are no constrains for the parameters $\varepsilon_1, \varepsilon_3, \varepsilon_{21}, \varepsilon_{22}, a, b$ (cf. Ref. [4]).

Unsolved problems refer to an absorbing film and a stability analysis of the guided waves.

ACKNOWLEDGMENT

REFERENCES

1. Leung, K. M., "P-polarized nonlinear surface polaritons in materials with intensity-dependent dielectric functions," *Phys. Rev. B*, Vol. 32, No. 8, 5093–5101, 1985.
2. Seaton, C. T., J. D. Valera, B. Svenson, and G. I. Stegeman, "Comparison of solutions for TM-polarized nonlinear guided waves," *Optics Letters*, Vol. 10, No. 3, 149–150, 1985.
3. Joseph, R. I. and D. N. Christodoulides, "Exact field decomposition for TM-waves in nonlinear media," *Optics Letters*, Vol. 12, No. 10, 826–828, 1987.
4. Valovik, D. V. and Yu. G. Smirnov, "Calculation of the propagation constants of TM electromagnetic waves in a nonlinear layer," *Journal of Communications Technology and Electronics*, Vol. 53, No. 8, 883–889, 2008.
5. Marcuse, D., *Theory of Dielectric Optical Waveguides*, 2nd edition, Academic Press, San Diego, 1991.

A Generalized Signals and Systems Theory Scheme and Its Applications in the Description of Electromagnetic Problems

E. Gago-Ribas and A. Serroukh

Electrical Engineering Department, University of Oviedo, Spain

Abstract— Signals and systems theory plays a fundamental role in electrical engineering as well as in other scientific areas but the usual way of presenting this theory avoids treating some important concepts that may lead to later conceptual and practical problems. A generalization of the signals and systems theory is required to clarify the connection between this theory and the mathematical representation of physical problems, for instance those concerned with electromagnetic theory. A summary of this generalization is presented in this work. First, infinite dimensional function vector spaces of arbitrary variable will become a fundamental step in all the scheme, in particular the definition of an algebra structure on these spaces. Also, the systems will be characterized by keeping in mind operator theory. Based on these concepts, a representation in terms of a general linear combination operator is introduced leading to a general interpretation of a transformation and the corresponding analysis of a system under a particular transform — spectral analysis of a system —. The connection of this scheme with the theory of distributions will become a fundamental point in order to provide with a general structure capable of unifying the regular function analysis and the generalized function theory. This point becomes extremely important to clearly understand the Green's function theory, for instance. An important extension of this generalized scheme is concerned with the possibility of its extension to study complex variable signal spaces — complex signal theory — which is connected with the analysis of electromagnetic radiation and scattering problems when time and/or space coordinates are continued into complex ones. This scheme is currently being reviewed under the Rigged Hilbert Spaces (RHS) theory and its utility in the representation of electromagnetic problems.

1. INTRODUCTION

Signals and systems theory plays a fundamental role in the educational and professional background of electrical engineers. There are many references which cover this topic and they usually follow schemes similar to those presented in [1, 2], for instance. This way of analysis avoids to treat some important concepts that may lead to later conceptual and practical problems: from the simple problem of considering only time domain to the most important problem of not considering the theory of distributions to understand the Dirac delta function and other related signals. These lacks become more important when relating signal theory to the mathematical representation of physical problems defined by differential equations plus some boundary conditions; in particular, those in electromagnetic radiation and scattering theory. In this sense, a number of works have contributed to avoid this situation — refer to [3] and [4] as an example — but, up to author's knowledge, there is no generalized work involving the basic signal theory connected to the representation of physical problems. With this considerations in mind, a general scheme based on the algebra of infinite dimensional vector and operator spaces together with the theory of distributions will be summarized in the present work. This scheme is being used nowadays in both undergraduate and postgraduate courses, specially to introduce important concepts in electromagnetic theory such as integral representations of Maxwell equations as well as Green's function theory. Also, many research activities are directly involved with this scheme, specially those involving Rigged Hilbert Spaces, [5], and the continuation of real time-space radiation/scattering EM problems to their complex time-space version [6–8].

2. SUMMARY OF THE GENERAL SCHEME

The proposed signals and systems theory generalized scheme may be summarized as follows — Fig. 1 —. It is important to detach that all the mathematical details will be avoided with the exception of some representations that may facilitate the understanding of this summary.

i) The theory is constructed considering an initial vector space $\mathcal{F}_\mathcal{K}$ of general signals denoted by $a(\tau)$. The independent variable may represent any discrete or continuous ($\tau = n$ or x) variable; in practical problems, they will represent time, space, or any other variable of interest. Usually, the infinite dimension of $\mathcal{F}_\mathcal{K}$ requires to introduce some important mathematical remarks which make the differences with respect to the regular finite dimensional case. The definition of an algebra
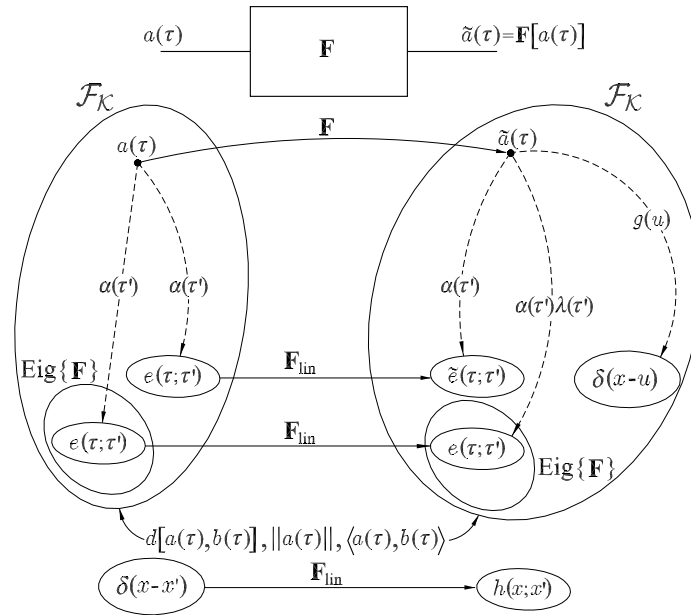
Figure 1: Scheme which summarizes the most important concepts in the signals and systems generalization procedure described in this work. Dashed lines indicate $\mathbf{LC}_{(\tau')}$ operators whose coefficients are those crossed by the lines.

structure on this space is determined by the distance, norm and scalar product, $d[a(\tau), b(\tau)]$, $\|a(\tau)\|$ and $\langle a(\tau), b(\tau) \rangle$ as well as the composition laws required to generate the vector space — sum and scalar scaling —. All of them become now fundamental concepts recalled throughout the scheme, something that is usually lost in the regular signals and systems schemes. These definitions determine not only the way of measuring within the space, but also might have later influence in certain definitions such as for the Dirac delta distribution.

ii) A generalized way to describe subspaces of signals — which may contain a finite, countable-infinite or continuous-infinite number of elements — is also introduced by using the general notation $u(\tau; \tau')$. Notice that the space elements, signals within $\mathcal{F}_{\mathcal{K}}$, depend only on τ and the variable τ' is introduced to "identify" the elements in the subspace; in many practical cases this variable corresponds to the so-called "spectral variable" and its initial meaning use to get lost. This fact is emphasized by the semicolon notation recalling the fact that the "visualization" of the subspace of elements seen as two-dimensional signals may be convenient to understand particular interpretations — refer to Fig. 2 for a particular example —. This notation also involves the usual representation $u_n(\tau)$ for the particular countable case $\tau' = n$.

iii) The concepts associated to transformations are generalized based on the description of the elements of $\mathcal{F}_{\mathcal{K}}$: (a) in terms of sets of basis functions $e(\tau; \tau') \in \mathcal{F}_{\mathcal{K}}$ together with the initial algebra defined on the space, and (b) by introducing a generalized linear combination operator $\mathbf{LC}_{(\tau')}$. This leads to a general representation of any transformation in the form,

$$\begin{cases} a(\tau) = \mathbf{LC}_{(\tau')} \left[\alpha(\tau') e(\tau; \tau') \right], \\ \\ d\left\{ a(\tau), \mathbf{LC}_{(\tau')} \left[\alpha(\tau') e(\tau; \tau') \right] \right\} \to 0 \quad \Rightarrow \quad \alpha(\tau'). \end{cases} \tag{1}$$

The pair of equations in (1) constitutes a generalized form of the *analysis and synthesis equations* usually associated to a particular transform. This representation lets to describe not only the usual Fourier series and Fourier transforms for both continuous, $\tau = x$, and discrete, $\tau = n$, variable signals (in those cases, $e(\tau; \tau')$ are orthogonal sets with respect to the usual definitions of the scalar product on the corresponding spaces and the coefficients reduce to $\alpha(\tau') = \langle a(\tau), e(\tau; \tau') \rangle$), but also takes into account the initial algebra defined on the space; notice that the analysis of the distance in (1) takes care of the existence criteria of the coefficients $\alpha(\tau')$ and also that the way to understand the linear combination depends on the definition established under the vector space composition laws. In fact, this representation also provides a suitable background to discuss the form taken by the $\mathbf{LC}_{(\tau')}$ operator related to a specific problem: in the usual cases the $\mathbf{LC}_{(\tau')}$ operator is identified with a finite or infinite sum or with different representations of a continuous

sum — Riemman or Lebesgue integrations —. This generalization is also able to qualify for the fundamental concepts required to understand other transformations different from the usual ones.
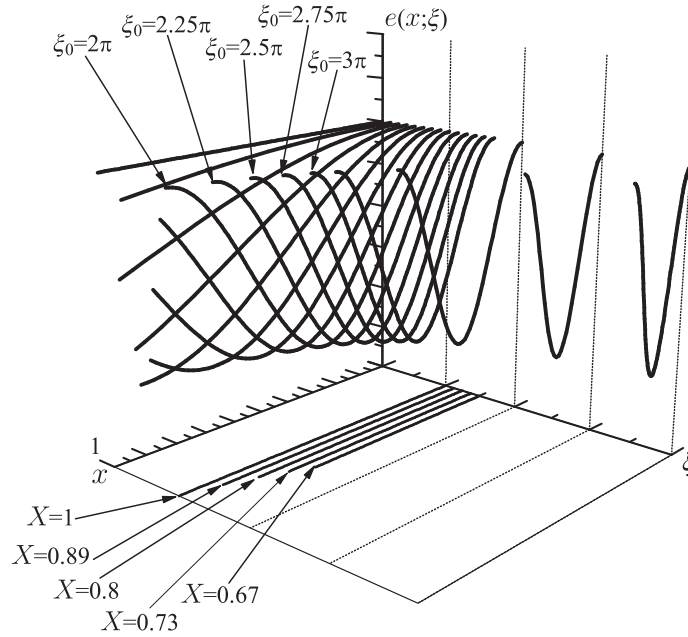
Figure 2: Example of the subspace of x-continuous variable signals $e(\tau; \tau') = e(x; \xi) = \cos(\xi x)$ with $\xi = 2\pi/X$ within the vector space $\mathcal{F}_\mathcal{K} = L^2(-\infty, \infty)$; subspace which identifies the typical basis functions under the Fourier transform.

iv) The analysis of a system is also tackled in terms of the transformation produced by an operator $\mathbf{F}$ acting over signals belonging to $\mathcal{F}_\mathcal{K}$ that are being represented in the generalized form indicated in (1), that is,

$$\tilde{a}(\tau) = \mathbf{F}[a(\tau)] = \mathbf{F}\left\{\mathbf{LC}_{(\tau')}\left[\alpha(\tau')e(\tau; \tau')\right]\right\}. \tag{2}$$

This transformation is usually described by means of how the operator acts over a concrete set of functions; in particular, the importance of the linearity property — which characterizes linear systems — is explained by means of its capability to transform elements of $\mathcal{F}_\mathcal{K}$ represented in terms of a certain set of basis functions; the effect of a linear system on the domain of $\mathcal{F}_\mathcal{K}$ may be then characterized by the transformation of the set of basis functions under consideration,

$$\tilde{e}(\tau; \tau') = \mathbf{F_{lin}}[e(\tau; \tau')] \to \tilde{a}(\tau) = \mathbf{F_{lin}}[a(\tau)] = \mathbf{LC}_{(\tau')}\left[\alpha(\tau')\tilde{e}(\tau; \tau')\right]. \tag{3}$$

Also, if $e(\tau; \tau')$ belongs to the subspace of eigenfunctions of $\mathbf{F_{lin}}$, $\tilde{e}(\tau; \tau') = \lambda(\tau')e(\tau; \tau')$ and Eq. (3) reduces to,

$$e(\tau; \tau') \in \mathrm{Eig}\{\mathbf{F_{lin}}\} \subset \mathcal{F}_\mathcal{K} \to \tilde{a}(\tau) = \mathbf{F_{lin}}[a(\tau)] = \mathbf{LC}_{(\tau')}\left[\alpha(\tau')\lambda(\tau')e(\tau; \tau')\right]. \tag{4}$$

Equation (1) together with (4) provides a generalized way to describe what is usually referred as the *spectral analysis* of a system, $\mathbf{F_{lin},\tau'}$, in the "identification" variable τ'; the set of eigenvalues $\lambda(\tau')$ associated to $e(\tau; \tau')$ are usually called the *spectrum* of the operator,

$$\alpha(\tau') \to \mathbf{F_{lin},\tau'}\left[\alpha(\tau')\right] = \alpha(\tau')\lambda(\tau'). \tag{5}$$

The characterization of the system in this particular case reduces then to identify the subspace of eigenvalues $\lambda(\tau')$ described also by a discrete or continuous function depending on the nature of τ'. For instance, in the usual Fourier analysis for discrete or continuous variable signals under *linear invariant* operators, the function $\lambda(\tau')$ turns to be the so-called *transfer function* of the system. With the present scheme in mind, this concept may be generalized under any transformation different from the usual ones. Also, when $e(\tau; \tau') \notin \mathrm{Eig}\{\mathbf{F_{lin}}\}$ a more general concept associated to the spectral characterization of a system may be introduced; it is important to recall that this is the usual case for *linear non invariant* systems under Fourier transform expansion which is usually avoided in the specialized literature; an example based on this scheme may be found in [9, 10].

v) In the particular case of continuous variable problems, $\tau = x$, the *theory of distributions*, [11], is also taken into account in this scheme not only to better understand the Dirac delta function and other related signals, but also to characterize operators in the *real domain*, that is in the original variable x. The representation of a signal $a(x)$ in terms of Dirac delta functions may be reinterpreted in the form of (1) leading to $a(x) = \mathbf{LC}_{(x')} [a(x')\delta(x - x')]$, assuming the appropriate interpretations of the set $e(x; x') = \delta(x - x')$ and the continuous $\mathbf{LC}_{(x')}$ operator both under the theory of distributions. In this case, the variable τ' turns to be the usual real variable x'. This leads to the *integral characterization* of a *linear operator* in terms of the transformation of the set $\delta(x - x')$, that is, $h(x; x') = \mathbf{F_{lin}}[\delta(x - x')]$; the well-known result for *linear invariant operators* found in the specialized literature can be perfectly understood as a particular case of these results. This generalization becomes a fundamental point in the connection between signal theory and the Green's function theory, for instance. Of course, the particular case for discrete variable problems, $\tau = n$, can be seen also within this generalized scheme avoiding all the distribution theory required for the continuous variable case. This procedure also facilitates the comparison between the discrete variable and the continuous variable cases.

vi) Finally, the generalization of the concept of a transformation in step (ii) together with the analyses in steps (iii) and (iv) lead to a scheme which is capable to explain the concepts associated to the analysis of linear systems in real and spectral domains in a generalized way. In particular, the analysis of linear non invariant systems turns to be very important because of its practical application in the mathematical representation of physical problems as those concerning EM theory; notice that invariance is a usual property in time domain, $\tau = t$, but not in space domain, $\tau = \vec{r}$, with $\vec{r}$ denoting the extension to a 3D vector space of signals, $a(\vec{r})$.

3. A PARTICULAR EXAMPLE

Let us exemplify the general scheme by considering the Green's function theory; the mathematical details will be avoided again and only the general representation will be summarized. In first place, we will consider a physical problem in such a way that it is defined by a linear differential equation represented by an operator $\mathcal{L}_d \subset \mathbf{F_{lin}}$ together with some boundary conditions BCs (for instance, the 3D variable operators $\mathcal{L}_d = \nabla^2$ or $\mathcal{L}_d = \nabla^2 + k^2$ in EM problems). Its representation is schematized in Fig. 3 and its definition given by

$$\begin{cases} \mathcal{L}_d[f(x)] = g(x) \\ \qquad + \\ \text{BCs for } f(x) \end{cases} \tag{6}$$

with $f(x)$ denoting the unknown function — usually the response to a particular physical source — and $g(x)$ representing the known function — source of $f(x)$ —. By recalling that (a) the general solution to the problem $\mathcal{L}_d^{-1}$ is an infinite subspace of functions $f(x; \kappa) = f_h(x; \kappa) + f_p(x)$, where $f_h(x; \kappa)$ represents the subspace Ker$\{\mathcal{L}_d\}$, and (b) the imposition of the BCs leads to the unique solution $f(x) = f(x; \kappa_0) \in f(x; \kappa)$, it is possible to identify the inversion problem and the unique solution to it by the following general scheme,

$$\begin{cases} \mathcal{L}_d^{-1}[g(x)] = f(x; \kappa) \\ \qquad + \\ \text{BCs for } f(x; \kappa) \end{cases} \Bigg\} \rightarrow \kappa = \kappa_0 \rightarrow \mathcal{L}_{d,\text{BCs}}^{-1}[g(x)] = f(x; \kappa_0) = f(x). \tag{7}$$
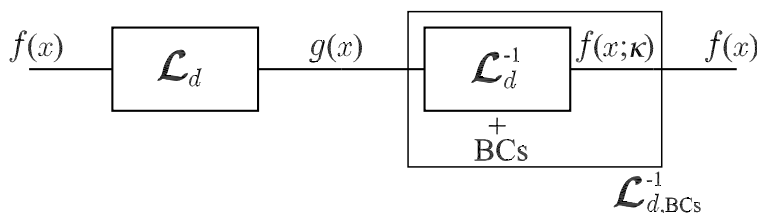
Figure 3: Generalized signals and systems scheme for the Green's function theory.

By taking into account the generalized scheme summarized in this paper, it will be possible to schematize the Green's function theory as,

$$
\begin{array}{ccccc}
\text{Linear problem} & & \text{Green's problem} & & \text{Green's functions} \\[4pt]
\begin{cases} \mathcal{L}_d[f(x)] = g(x) \\ \quad + \\ \text{BCs for } f(x) \end{cases}
& \rightarrow &
\begin{cases} \mathcal{L}_d[\mathcal{G}(x;x')] = \delta(x - x') \\ \quad + \\ \text{BCs for } \mathcal{G}(x;x') \end{cases}
& \rightarrow &
\mathcal{G}(x;x') = \mathcal{L}_{d,\mathrm{BCs}}^{-1}[\delta(x - x')]
\\[16pt]
\text{Linear invariant problem} & & \text{Green's problem} & & \text{Green's function} \\[4pt]
\begin{cases} \mathcal{L}_d[f(x)] = g(x) \\ \quad + \\ \text{BCs for } f(x) \end{cases}
& \rightarrow &
\begin{cases} \mathcal{L}_d[\mathcal{G}(x)] = \delta(x) \\ \quad + \\ \text{BCs for } \mathcal{G}(x) \end{cases}
& \rightarrow &
\mathcal{G}(x) = \mathcal{L}_{d,\mathrm{BCs}}^{-1}[\delta(x)]
\end{array}
\tag{8}
$$

4. CONCLUSIONS

This paper presents a summary of a generalized signals and systems scheme that can be applied not only to the usual practical cases but also to describe the solution to physical problems; a multidimensional version of this scheme has to be applied for this cases, that is, $\tau \equiv \vec{r}$. These analyses directly connect with Green's function theory and also with its spectral representation, a fundamental tool in the formulation and resolution of physical problems (the authors are particularly involved with the analysis of EM problems). Another important extension of this generalized scheme is concerned with the possibility of its application to generalize the study to complex variable signal spaces with $\tau \equiv \mathbf{z} = x + jy$. The practical application of these results is connected to the generalization of the analysis of radiation and scattering problems in EM when time and/or space coordinates are continued into complex ones — complex signal theory, [8] —. Although real/complex parameterizations constitute the initial aim to obtain the general scheme presented in this work, the actual scheme is being used also to successfully present the signals and systems theory to undergraduate and postgraduate students.

REFERENCES

1. Oppenheim, A. V., A. S. Willsky, and I. T. Young, *Signals and Systems (2nd Ed)*, Prentice-Hall International, 1997.
2. Lindner, D. K., *Introduction to Signals and Systems*, McGraw-Hill, 1999.
3. Poularikas, A. D. and S. Seely, *Signals and Systems*, Krieger Publishing Company, 1994.
4. Skinner, R. and J. A. Weil, "An introduction to generalized functions and their application to static electromagnetic point dipoles, including hyperfine interactions," *Am. J. Phys.*, Vol. 57, 777–791, 1989.
5. Madrid, R., et al., "The rigged hilbert space approach to the Lippmann-Schwinger Equation I," *J. Phys. A*, Vol. 39, 3949, 2006.
6. Hansen, T. and G. Kaiser, "Generalized huygens principle with pulsed-beam wavelets," http://arxiv.org/abs/0904.0683. Submitted to *J. Physics A*, 2009.
7. Gago-Ribas, E., M. J. González, and C. Dehesa, "Analytical parameterization of a 2D real propagation space in terms of complex electromagnetic beams," *IEICE Trans. on Electronics*, Vol. E80-C, No. 11, 1997.
8. Gago-Ribas, E., M. J. González, and C. Dehesa, "Challenges and perspectives of complex spaces and complex signal theory analysis in electromagnetics: First steps," *Electromagnetics in a Complex World: Challenges and Perspectives, Springer Proceedings in Physics*, Vol. 96, 175–188, (Pinto, Galdi, Felsen), Springer-Verlag, 2003.
9. Gago-Ribas, E. and F. Varona, "Real and fourier-spectral characterization of linear non invariant systems," *ENMA International Conference on Engineering and Mathematics*, 269–276, Bilbao, 2008.
10. Gago-Ribas, E., "About real and fourier-spectral characterization of general linear systems," in preparation for *PIERS Journal*.
11. Gel'fand, I. B. and G. E. Shilov, *Generalized Functions*, Academic Press, 1964.

Matrix Converter Output Voltage Control with Overmodulation

J. Lettl and S. Fligl

Department of Electric Drives and Traction, Faculty of Electrical Engineering
Czech Technical University in Prague, Czech Republic

Abstract— The matrix converter is a very popular topic today. Many papers about matrix converter deal with modulation strategies and control algorithms. In this paper, special attention is paid to the indirect space vector modulation, which is based on the virtual dc link concept. The entire converter is interpreted as a series connection of two matrix converters (rectifying and inverting virtual matrix converter). Thanks to this insight, it is possible to compose the modulation strategy for the entire matrix converter from the inverter and rectifier part modulations. The main goal is to achieve the maximal possible output voltage by overmodulation employment. The overmodulation method based on the indirect vector modulation is presented. By means of the square wave modulation the voltage transfer ratio can be increased from 0.866 up to 0.955. Moreover, together with control of the current modulation index, a linear and continuous adjustment of the output voltage can be achieved.

1. INTRODUCTION

The maximum achievable voltage transfer ratio is mentioned in papers concerning matrix converters much more frequently than in the case of any other converter

$$A_{u\max} = \frac{|\underline{u}_{out}|_{\max}}{|\underline{u}_{in}|} \tag{1}$$

This is mainly historical in nature since early methods achieved rather small output voltages ($A_{u\max} = 0.5$) and even today the matrix converter is still disadvantageous from this point of view in comparison with indirect frequency converters. It is very important to obtain a voltage of value close to the mains voltage. There is a whole gamut of devices designed in conform with the mains parameters (e.g., 230/400 Vac and 50 Hz in Europe, 120/210 Vac and 60 Hz in the USA). Often a device connected to a voltage source of lower than rated amplitude must be de-rated or it would not work at all. For example, the maximum mechanical torque of an induction machine depends on a factor of $(u_{out}/f_{out})^2$. Then for a voltage ratio of 0.5 the motor delivers a maximum torque of about 1/4 at nominal frequency in comparison with the case that it is supplied with a nominal voltage. The motor could be redesigned or re-wound or a step-up transformer could be put between mains and the converter, but additional costs would be connected with it. The handicap of authors of the first modulation methods lies in the situation of phase-voltages depicted in Fig. 1. If the output phase-voltage waveform is deformed in a proper way so that the line-voltage remains sinusoidal as shown in Fig. 2, the voltage transfer ratio can be improved to 0.866. This can be done, since the common mode voltage (one third of the phase-voltage sum) ideally does not influence the machine behaviour when the neutral line is disconnected. The ratio of 0.866 is the same ratio, which we obtained implicitly from the indirect space vector modulation. Nowadays, the number 0.866 has become a more or less obligatory part of any article relating to the matrix converter.

2. INDIRECT SPACE VECTOR MODULATION

This method strives to generate a desired output voltage vector (in a harmonic steady state with a constant amplitude $|\underline{u}_{out}|$ rotating with a constant angular speed ω_{out}) and simultaneously to take from the mains current space vector that keeps a constant angle φ_{in} towards the rotating filter output voltage space vector at $\omega_{in} = \omega_{\mathrm{mains}}$ (i.e., a constant input displacement factor of $\cos\varphi_{in}$). The indirect space vector modulation is based on the idea of the virtual dc-link. The converter can be seen as a combination of a rectifier and inverter part (see Fig. 3).

The space vector theory applied to the rectifier and inverter parts leads to the well known formulas that determine necessary switching times

$$\begin{pmatrix} d_{\underline{\alpha}} \\ d_{\underline{\beta}} \end{pmatrix} = \sqrt{2}\frac{|\underline{u}_{out}|}{(u_{P\alpha} - u_{N\beta})}\begin{pmatrix} \sin\left(\frac{\pi}{3} - \theta_{S-U}\right) \\ \sin\theta_{S-U} \end{pmatrix} \quad \begin{pmatrix} d_{\underline{\gamma}} \\ d_{\underline{\delta}} \end{pmatrix} = \sqrt{6}/3\frac{|\underline{i}_{in}|}{i_{P\alpha}}\begin{pmatrix} \sin\left(\pi/3 - \theta_{S-I}\right) \\ \sin\left(\theta_{S-I}\right) \end{pmatrix} \tag{2}$$
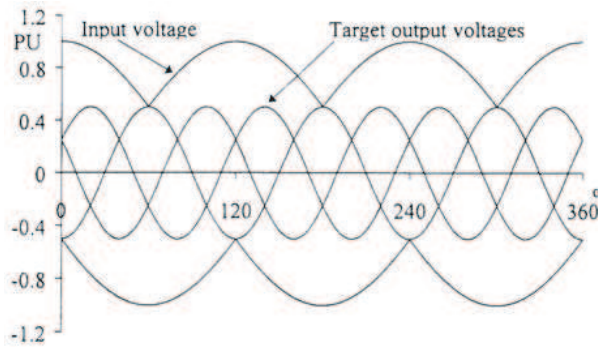
Figure 1: Input and output phase voltage waveforms ($A_{u\max} = 0.5$).
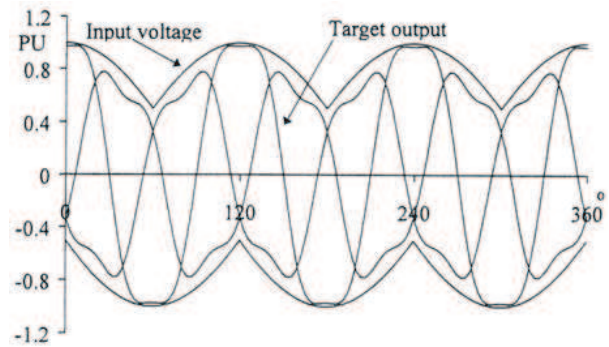
Figure 2: Input and output phase voltage waveforms ($A_{u\max} = 0.866$).
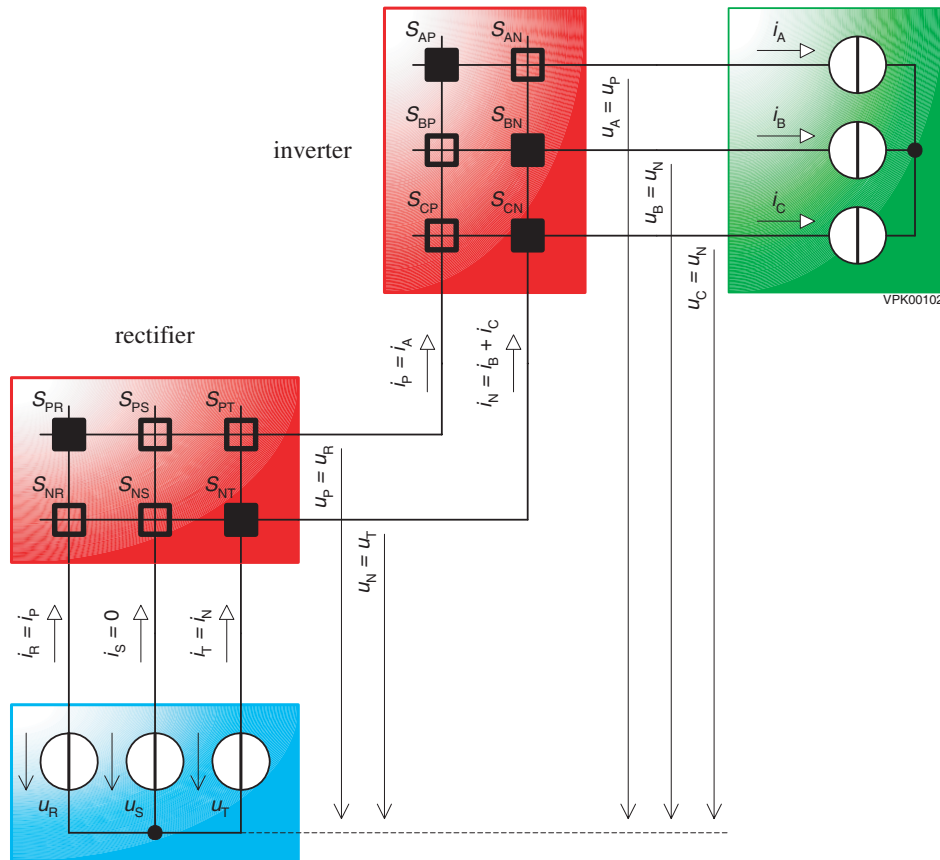
Figure 3: The concept of two virtual matrix converters.

The current modulation index

$$m_{C\alpha} = \frac{|\underline{i}_{in}|}{i_{P\alpha}} \tag{3}$$

is proposed to be kept constant by most authors. The output voltage can be then adjusted by means of d_α and d_β. But, the current modulation index influences the virtual DC-link voltage and subsequently the output voltage

$$u_{P\alpha} - u_{N\beta} = |\underline{u}_{in}| \cdot \frac{|\underline{i}_{in}|}{i_{P\alpha}} \cdot \cos \varphi_{in} \tag{4}$$

3. OVERMODULATION

From the area of indirect converters, it is known that a motor can be fed from a non-sinusoidal voltage source. The decisive parameter to the motor is then the first harmonic component of

the delivered voltage. In the next considerations, we assume the input displacement factor to be equal to one. Then when indirect space vector modulation is employed, the voltage in the virtual DC-link is constant and can be regulated from zero to 0.866 of the input voltage maximum value. The amplitude of the output line-voltage can be regulated from zero up to the voltage value in the virtual DC-link. In an indirect converter with the included energy storage of huge capacity and with a diode rectifier on the input side, the DC-link voltage can be very close to the input line-voltage amplitude. However, it would be connected with a very deformed input current waveform.

Let us depict the situation from the DC-link voltage point of view which is given by input phase-to-phase voltages (see Fig. 6).

From the theory of inverters, it is known that the maximum output voltage can be achieved when a square waveform is employed (see Fig. 7).

The amplitude of the first harmonic component can be determined by means of Fourier transformation which from an algebraic point of view is simply scalar multiplication of the analyzed function with the basis component divided by scalar multiplication of the basis component with itself. The situation is depicted in Fig. 8.

$$\text{From} \qquad \frac{u_{\text{SQ1}}}{u_{\text{SQ}}} = \frac{\int_{\pi/6}^{5\pi/6} 1 \cdot \sin\vartheta \cdot d\vartheta}{\int_{0}^{\pi} \sin^2\vartheta \cdot d\vartheta} = \frac{2 \cdot \sqrt{3}}{\pi} \cong 1.103 \qquad (5)$$

$$\text{we can express} \qquad A_{u\max,MC\textbf{square}} = \frac{3}{\pi} \cong 0.955 \qquad (6)$$

Such modulation can be easily achieved by a modification of the indirect space vector modulation. If in each step we compare $d_{\underline{\alpha}}$ with $d_{\underline{\beta}}$ and set the larger one to unity and the smaller one to zero, the output voltage vector will move with steps of 60° which correspond to generating a square waveform of output voltage. Moreover, in contrast to an indirect converter equipped with a diode rectifier, here the virtual DC-link voltage can be adjusted in any regulation step by means of current modulation ratio and thus a continuous regulation of the output voltage amplitude up to the limit is trouble-free. As far as the indirect converters are concerned, different switching patterns synchronized with the first harmonic component and similar to square wave modulation have been introduced because of this reason and the reason of power loss minimization as well (star modulation, hexagon combination with zero vectors, etc).
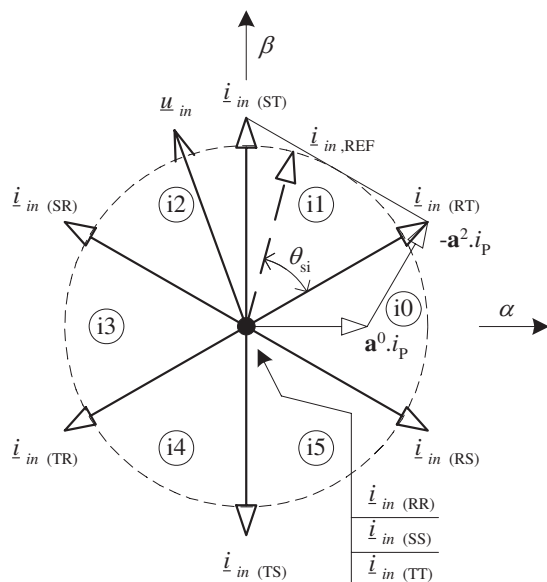
Figure 4: Current vectors.
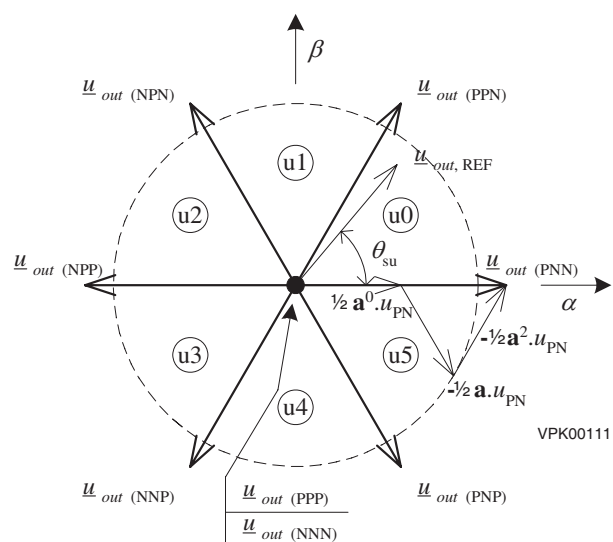
Figure 5: Voltage vectors.
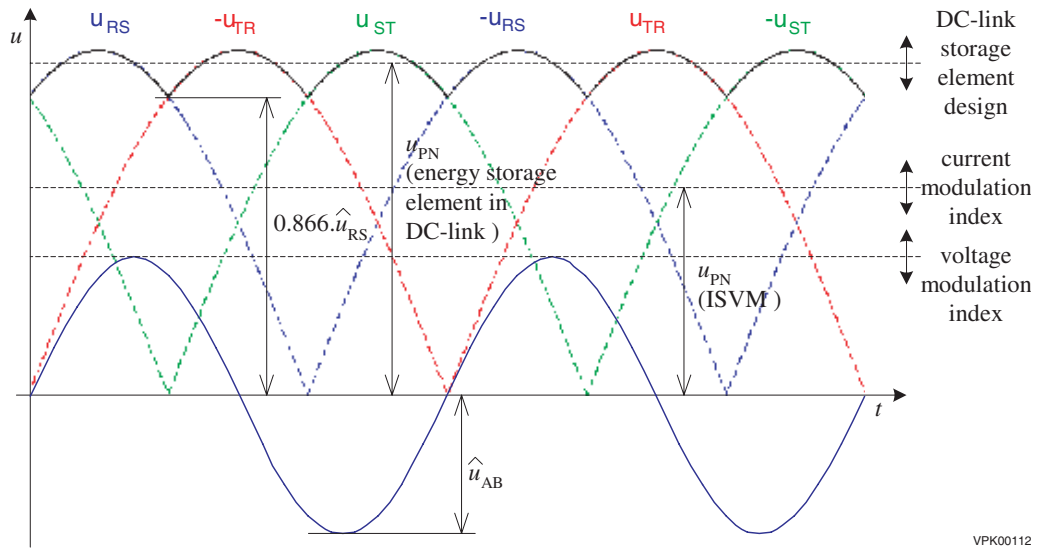
Figure 6: Input line-voltage, DC-link voltage, and generated output line-voltages.
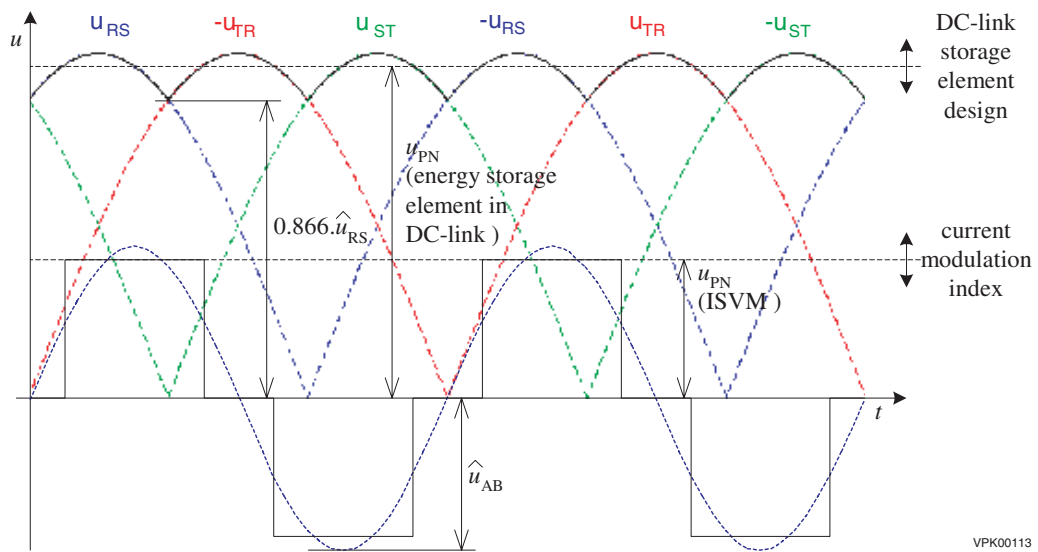
Figure 7: Input line-voltage, DC-link voltage, and generated square wave voltages.
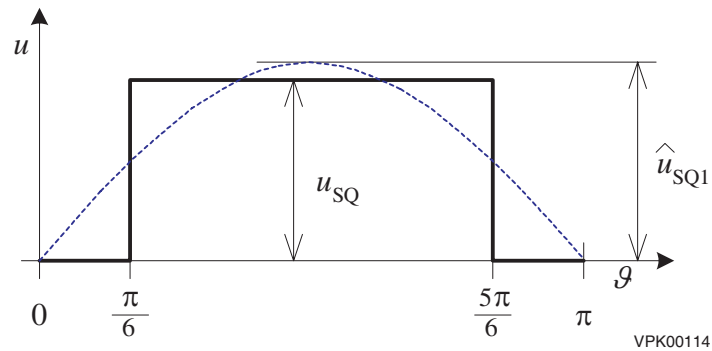
Figure 8: The first harmonic component calculation.

4. CONCLUSION

Achievement of the maximum available output voltage was defined as the main goal. Based on the indirect space vector modulation, an overmodulation with square wave output is introduced. It enables to increase the transfer ratio from the common 0.866 to the value of 0.955. The output voltage level can be adjusted continuously in an easy way, even in overmodulation. The obtained waveforms were presented in [3] and the other important results have been published in [2] and [1].

REFERENCES

1. Lettl, J. and S. Fligl, "Matrix converter control system," *PIERS Online*, Vol. 1, No. 4, 395–398, Hangzhou, China, August 2005.
2. Lettl, J., "Matrix converter induction motor drive," *Proceedings of International Conference EPE-PEMC 2006*, 787–792, Portoroz, Slovenia, August–September 2006.
3. Lettl, J. and S. Fligl, "PWM strategy applied to realized matrix converter system," *PIERS Proceedings*, 122–125, Prague, Czech Republic, August 27–30, 2007.

A Passivity-Based Control for Power Electronics Converter in a DFIG Wind Turbine

Y. B. Qu and H. H. Song

Department of Electrical Engineering and Automation, Harbin Institute of Technology, China

Abstract— Utilization of the power electronics converter in a doubly-fed induction generator wind turbine, thus decoupling mechanical and electrical frequencies and making variable-speed operation possible, can vary the electrical rotor frequency. This paper addresses the circumstances of no matter either capacitor voltage or inductor current is chosen as the output in a converter, the zero dynamics is not both stable for two power flow direction cases. A passivity-based controller for back-to-back converter is presented to avoid this problem in wind power generation. Based on the port-controlled hamiltonian model of the converter, the structure matrix and the damping matrix are collocated and the desired equilibrium is approached rapidly. Simulation studies are carried out in Matlab/Simulink and the results show that the new control method enables to avoid instability for a bidirectional use of the power converter in DFIG wind turbine.

1. INTRODUCTION

Presently, doubly-fed induction generator (DFIG) is widely employed in modern wind power industry [1]. The advantages in using DFIG are the abilities to transfer maximum power over a wide speed range in both sub- and super-synchronous modes and to reduce converter power rating which only equals to a fraction of the total power to achieve the full control of the system. The two working modes benefit form a back to back converter which often adopts the configuration of two PWM voltage source converters, a machine-side converter (MSC) and a grid-side converter (GSC), with an intermediate DC voltage link. However, no matter either voltage or current is chosen as the output of the converter, the zero dynamics [2] is not both stable for bidirectional power flow which occurs frequently in a DFIG wind turbine. This paper investigates primarily on the GSC control aiming at the problem of the power converter's instability during the current commutation, so that we take the MSC as a load and our control target is to keep intermediate DC-bus voltage of the converter at a constant value, irrespective of any sign the current may have.

The paper is organized as follows. Section 2 presents the PCH model of the three-phase PWM converter. Based on the model, a passivity-based controller is designed to handle the instable status in Section 3. Section 4 shows simulation results obtained from the control law to verify the robustness when current direction changes. Finally, conclusions are drawn in Section 5.

2. PCH MODELING OF CONVERTERS

To apply the PBC method to the converter, a port-controlled Hamiltonian model is deducted basing on the d-q model. This PCH [3] form also called energy canonical form which generates equations with structures that establishes physical relationships between system and environment through the port variables.

In this paper, we choose inductor flux and capacitor charge as state variables, then the state vector of the system is:

$$x = (x_1, x_2, x_3) = (\phi_d(t), \phi_q(t), q(t)) \tag{1}$$

and the total energy stored in the system is:

$$H(t) = \frac{1}{2} x^T M^{-1} x \tag{2}$$

which

$$M = \begin{pmatrix} L & 0 & 0 \\ 0 & L & 0 \\ 0 & 0 & C \end{pmatrix} \tag{3}$$

From the Equation (2), derivative of energy function will be

$$\dot{H}(x) = M^{-1} x \tag{4}$$

Finally, the system can be rewritten in the PCH form

$$
\begin{pmatrix} \frac{dx_1}{dt} \\ \frac{dx_2}{dt} \\ \frac{dx_3}{dt} \end{pmatrix} = \left(\begin{bmatrix} 0 & \omega L & -u_1 \\ -\omega L & 0 & -u_2 \\ u_1 & u_2 & 0 \end{bmatrix} - \begin{bmatrix} R & 0 & 0 \\ 0 & R & 0 \\ 0 & 0 & \frac{1}{R_L} \end{bmatrix} \right) \frac{\partial H}{\partial x} + \begin{pmatrix} v_d \\ v_q \\ 0 \end{pmatrix} \tag{5}
$$

with the structure matrices and the non-negative symmetric damp matrix

$$
J(x, u) = \begin{pmatrix} 0 & \omega L & -u_1 \\ -\omega L & 0 & -u_2 \\ u_1 & u_2 & 0 \end{pmatrix}, \quad g = \begin{pmatrix} v_d \\ v_q \\ 0 \end{pmatrix}, \quad R = \begin{pmatrix} R & 0 & 0 \\ 0 & R & 0 \\ 0 & 0 & \frac{1}{R_L} \end{pmatrix} \tag{6}
$$

3. CONTROLLER DESIGN

In this section, the main result of the paper is presented, namely, a passivity based controller that guarantees unity power factor and constant dc voltage is exhibited by exploiting the PCH model.

Above all, we remind the machine-side PWM ac/dc converter's control objectives [4] which are as follows:

1) The dc-component of the output x_3 should be driven to some constant desired value, which means $q(t) = q^*$.

2) To enhance the efficiency in the converter, the power factor of it should be equal to one, i.e., $I_q^* = 0$.

3.1. Controller Design

The purpose of the passivity-based control approach is to design a feedback control $u = \alpha(x)$ so that the desired target dynamics is a Hamiltonian system of the form

$$
\dot{x} = [J_d(x) - R_d(x)] \frac{\partial H_d(x)}{\partial x} \tag{7}
$$

where $J_d(x) = -J_d^T(x)$ and $R_d(x) = R_d^T(x) \geq 0$ are targeted interconnection and damping matrices. We define $H_a(x)$ is the energy applied by the controller, thereby, $H_d(x) = H(x) + H_a(x)$ is the new total energy function which has a strict local minimum at the desired equilibrium, namely, $x^* = \arg\min H_d(x)$. Here, x^* is the desired equilibrium point we impose. The matching objective is achieved if and only if

$$
[J(x) - R(x)] \frac{\partial H(x)}{\partial x} + g = [J_d(x) - R_d(x)] \frac{\partial H_d(x)}{\partial x} \tag{8}
$$

is satisfied, where $J_d(x) = J(x) + J_a(x) = -(J(x) + J_a(x))^T$ and $R_d(x) = R(x) + R_a(x) = (R(x) + R_a(x))^T \geq 0$.

Basing on the aforementioned procedure for the controller defining, we fix the interconnection and damping matrices as $J_d(x) = J(x, u)$, $R_d(x) = R(x)$, i.e., $J_a(x) = 0$ and $R_a(x) = 0$.

Let $K(x) = \frac{\partial H_a(x)}{\partial x} = (k_1, k_2, k_3)^T$, Equation (8) can be simplified to

$$
-[J - R] \frac{\partial H_a}{\partial x} + g = 0 \tag{9}
$$

Equation (9) can be solved for the controls

$$
u_1 = \frac{-v_d - k_1 R + k_2 \omega L}{k_3}, \quad u_2 = \frac{-v_q - k_2 R - k_1 \omega L}{k_3}
$$

$$
R(k_1^2 + k_2^2) + v_d k_1 + v_q k_2 + \frac{k_3^2}{R_L} = 0 \tag{10}
$$

3.2. Equilibrium Assignment

Since the equilibrium condition is the desired steady state response of the system, we let the anticipant state variables as follows:

$$\partial H_d \mid_{x=x^*} = (\partial H + \partial H_a) \mid_{x=x^*} = 0 \tag{11}$$

Following the relationship showed in (10), the controls can be deduced.

$$u_1 = \frac{-v_d + \phi_d^* R/L}{k_3} \quad u_2 = \frac{-v_q + \phi_d^* \omega}{k_3} \tag{12}$$

$$(\phi_d^*)^2 - \frac{L v_d \phi_d^*}{R} + \frac{(L q^*)^2 \, i_L}{R C q} = 0 \tag{13}$$

Finally, the control law can be expressed as:

$$u_1 = \frac{C L v_d - R C \phi_d^*}{L q^*}, u_2 = \frac{C v_q - \omega C \phi_d^*}{q^*}$$

$$\phi_d^* = \frac{L v_d}{2R} - L \sqrt{\frac{v_d^2}{4R^2} - \frac{i_L \, (q^*)^2}{R C q}} \tag{14}$$

4. SIMULATION RESULTS

Simulations were carried out by Matlab/Simulink to confirm the theoretical design. The experiment aimed at exhibiting the behavior of the controller with respect to direction and amplitude changes in load current. The following parameters are used for simulation purposes, which are the same values used in 2 MW DFIG wind power generation system. $E = 690\,\text{V}$, $f = 50\,\text{Hz}$, $C = 2200\,\mu\text{F}$, $L = 2\,\text{mH}$, $R = 2.2\,\Omega$, $v_{dc}^* = 1200\,\text{V}$; the initial value $v_{dc0} = 800\,\text{V}$. At first, v_a, v_b, v_c are converted to v_d, v_q which are depicted in Fig. 1. Our desired voltage is fixed at $v_{dc}^* = 1200\,\text{V}$, i.e., $q^* = 2.64\,\text{C}$. The load current varies from $i_L = -1\,\text{A}$ to $i_L = 2\,\text{A}$ at $t = 1\,\text{s}$, and changes to $i_L = -0.5\,\text{A}$ at $t = 2\,\text{s}$. Notice that when $i_L > 0$, current i is in the same phase with voltage v_i and power flows to the MSC; when $i_L < 0$, i is in opposite phase with v_i and power flows to the GSC.

Figure 2 shows the changes of the electric quantity q_{dc} with time. It starts at $q_{dc} = v_{dc0} \times C = 1.76\,\text{C}$ and then goes to the desired value $q^* = 2.64\,\text{C}$. The direction changes of the current are not going to obviously disturb the stable status we get. In Fig. 3, DC bus voltage which is proportional
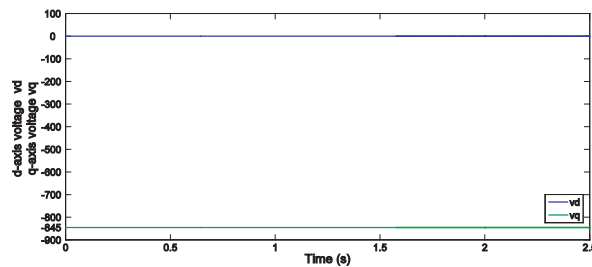
Figure 1: *d-q* axis voltage.
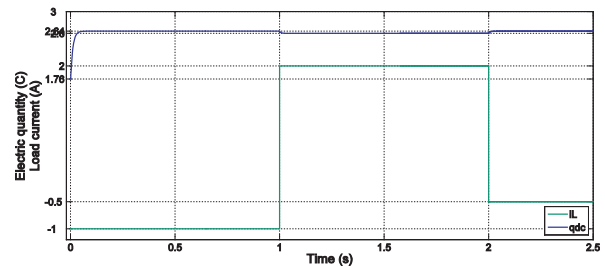
Figure 2: DC electric quantity and load current.
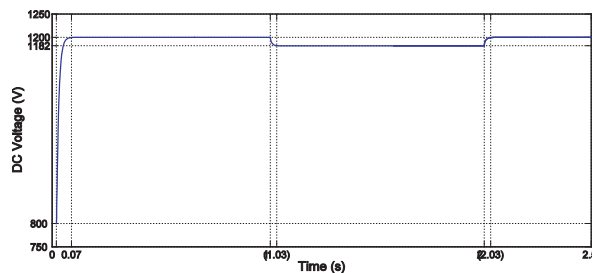
Figure 3: Output DC voltage.
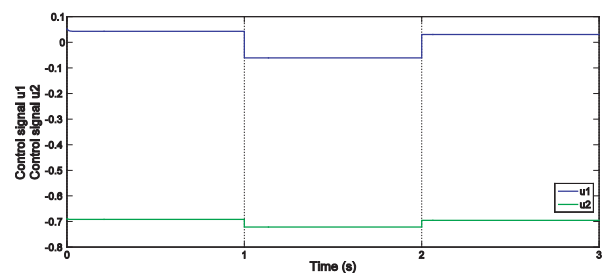
Figure 4: *d-q* axis control signal.

to the electric quantity is also exhibited. It costs only 0.07 s to get the expect value 1200 V from the initial value 800 V. When load current direction reverses at $t = 1$ s and $t = 2$ s, the voltage curve has small movements, but it gets fast dynamic response in 0.03 s to retain stability.

Figure 4 shows our d axis control signal u_1 and q axis control signal u_2 which are derived by our new PBC scheme. When load currents changes, they regulate accordingly to make the system comes back to equilibrium point.

Finally, Fig. 5 shows the control actions of abc axis. We can observe from the waveforms that the control signals u_a, u_b and u_c are all in $[-1, 1]$, which allows their discrete experimental implementation using a PWM scheme.
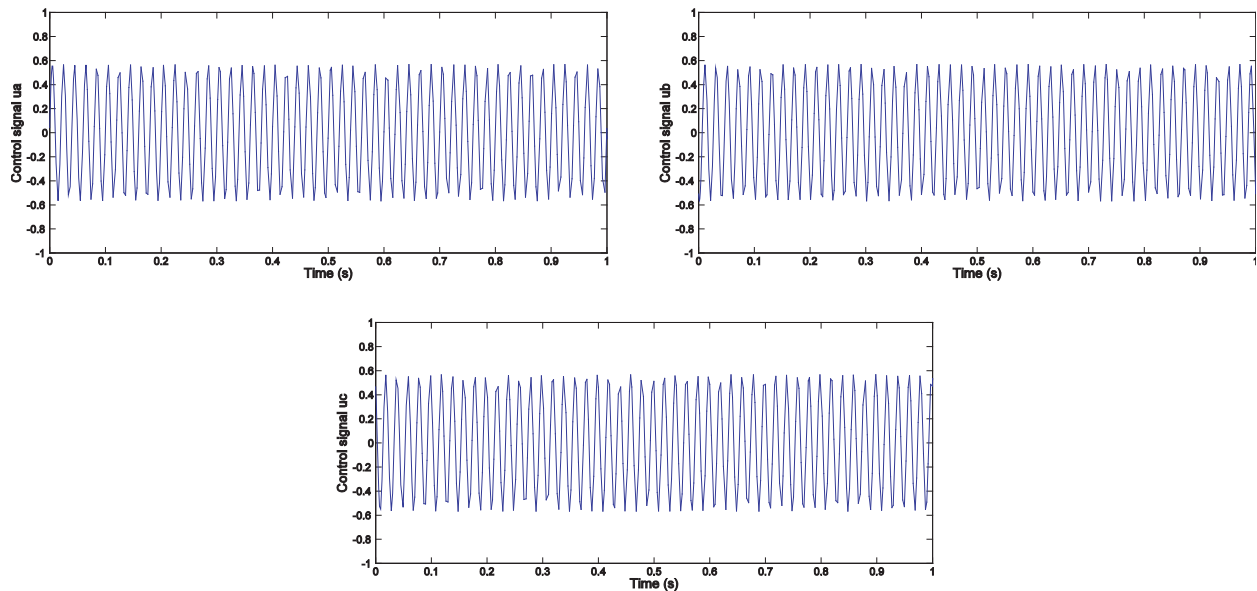
Figure 5: abc axis control signal.

5. CONCLUSIONS

Based on the theory of energy-shaping and port-controlled Hamilton, the modeling and the control of the three-phase PWM ac/dc converters which are applied to DFIG wind turbine's grid side converters are investigated in this paper. A novel control scheme is presented. This passivity based control, when used on PCH models, can assign the interconnection and damping matrices and internal energy of a closed loop by changing the matrices J, R and the storage function H. The significant advantage of this controller is its fast dynamic response to system's instability which is caused by power bidirectional flow between a back-to-back PWM converter with a simple structure. The experimental results are illustrated via simulation in Matlab showing the feasibility of the designed controller.

REFERENCES

1. Muller, S., M. Deicke, and R. W. De Doncker, "Doubly fed induction generator systems for wind turbines," *IEEE Ind. Appl. Mag.*, Vol. 8, No. 3, 26–33, 2002.
2. Batlle, C., A. Doria-Cerezo, and R. Ortega, "Power flow control of a doubly-fed induction machine coupled to a flywheel," *Proceedings of the 2004 IEEE International Conference on Control Applications*, 1645–1650, Taipei, Tawan, September 2004.
3. Ortega R., A. J. van der Schaft, and B. Maschke, "Interconnection and damping assignment passivity-based control of port-controlled Hamiltonian systems," *Automatica*, Vol. 38, No. 4, 585–596, 2002.
4. Gaviria, C., E. Fossas, and R. Grino, "Robust controller for a full-bridge rectifier using the IDA approach and GSSA modeling," *IEEE Trans. Circuits Syst. I*, Vol. 52, No. 3, 609–616, March 2005.

Computerized Calculation of Leakage Inductance Values of Transformers

R. Doebbelin, **C. Teichert**, **M. Benecke**, and **A. Lindemann**

Institute of Electric Power Systems, Otto-von-Guericke-University Magdeburg, Germany

Abstract— A low-effort prediction of leakage inductance values of transformers is required in a lot of transformer applications in various fields of electrical engineering. The article describes given approximation methods enabling leakage inductance calculation which have been implemented in MATLAB® based computer programs. Application range and accuracy of computerized leakage inductance calculation are illustrated. Further possibilities of computerized transformer investigation are considered.

1. INTRODUCTION

Power transfer and its limitation caused by internal losses or voltage drops are important aspects in all applications of power transformers. This is true in the case of mains-frequency operated transformers and is even more relevant in medium or high-frequency transformers. As is well-known, the design of a transformer with special focus on the windings has a big impact on internal losses and voltage drops of the transformer. Copper losses are influenced by the cross-section and (because of the skin and proximity effect with influences of frequency and field distribution) also by the arrangement of windings. Imperfect magnetic coupling occurring in each real transformer is expressed by the term "leakage" and represented by leakage inductances in equivalent circuits of transformers. This way, the operation of electrical equipment including transformers can be investigated by means of calculation and simulation. Whereas in most power transformer applications particularly low leakage inductance values are desirable, there are certain power electronic arrangements (e.g., resonant topologies and power sources for laser beam generation [1]), which require first of all a defined leakage inductance value of the applied transformer.

In the case of existing transformers, leakage inductance can be determined by measurements. However, more often it is necessary to predict the leakage inductance of a transformer in the design phase, especially if circuit simulation is intended [2]. This can be done applying certain approximation methods in which geometry parameters of the transformer are used to calculate its leakage inductance. Which approximation method has to be applied depends on the given arrangement of windings. If the couple of coils, whose leakage inductance is to be calculated, is arranged on the same leg of a transformer, the method of ROGOWSKI [3] and the method of PETROV [4] can be used considering further aspects, which are explained in the following paragraph. If the coils are arranged on different legs, the method of LEBEDEV [5] can be applied for leakage inductance calculation.

Concerning the used terms "winding" and "coil", the term "winding" is considered to be of higher grade, in general. Windings are realized as coils. However, in the case of fundamental transformer versions with one primary and one secondary winding, both terms can be used synonymously. In the case of transformers with interleaving of windings the primary winding and/or the secondary winding consist of a certain number of single coils.

2. LEAKAGE INDUCTANCE CALCULATION FOR COILS ARRANGED ON THE SAME LEG

If a couple of coils is arranged on the same leg (e.g., in the case of shell-type transformers with all windings on the center leg, Fig. 1, left), prediction of leakage inductance can be obtained using the approximation methods of ROGOWSKI and PETROV which have been established in the first half of the last century. The most common method is the method of ROGOWSKI which is based on the consideration of the energy of the leakage magnetic field. The formulas for leakage inductance calculation which are given in contemporary technical literature are usually predicated on this method but often slightly simplified resulting in a decrease of accuracy. As a precondition for the application of the method of ROGOWSKI [3] the coils of the considered transformer should have the same height in the case of concentric windings and the same width in the case of pie windings.
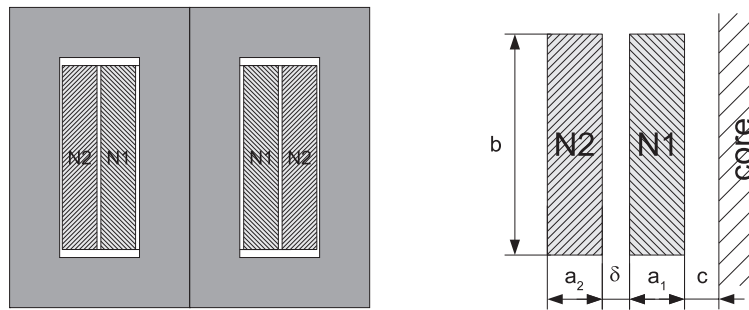
Figure 1. Transformer design enabling leakage inductance calculation using the method of ROGOWSKI left: shell-type transformer, right: dimensions for calculation of the relative leakage conductance λ according to formula (2).

According to deviations in these dimensions, inaccuracies of the calculation results occur. The leakage inductance (related to the primary side of the transformer) is calculated using the formula

$$L_L = \mu_0 \cdot w_1^2 \cdot l_m \cdot \lambda \cdot k_\sigma \tag{1}$$

with L_L — leakage inductance, μ_0 — absolute permeability, w_1 — number of primary turns, l_m — mean length per turn for whole arrangement of coils, λ — relative leakage conductance, k_σ — Rogowski factor. The relative leakage conductance has to be calculated related to the specific arrangement of coils (see Fig. 1, right) using formula (2). The Rogowski factor represents a correction factor concerning the length of leakage flux lines which is also geometry dependent and has to be calculated as described in [3]. In most cases its value is between 0.9 and 1.

$$\lambda = \frac{1}{b} \left(\delta + \frac{a_1 + a_2}{3} \right) \tag{2}$$

The method of PETROV [4], which alternatively can be used, is even suitable if the dimensions concerning height and width of the coils are different, what makes the method more universal. According to the following formula, two leakage inductance constituents have to be calculated, which have to be summed up to the final leakage inductance (what here is related to the primary side of the transformer again).

$$L_{L_x} = \frac{\mu_0}{2\pi} \cdot w_1^2 \cdot l_{m_x} \cdot \ln \left(K_{C_x} \cdot \frac{g_{12}^2}{g_1 \cdot g_2} \right) \tag{3}$$

$x = in$ — for portion inside core window

$x = out$ — for portion outside core window

L_{L_x} — leakage inductance portion

K_{C_x} — correction factor for consideration of core influence on leakage inductance

g_{12} — mean geometric distance between the cross-sections of the coils 1 and 2

g_1, g_2 — mean geometric distance of the cross-section of a coil to itself

To determine the K_C-factors related to the portions of the coils inside and outside the core window, the cross-sections of the coils have to be reflected at the adjacent or surrounding core surface lines. The calculation of the K_C-factors is based on the method of mean geometric distances (established by J. C. Maxwell [6]) considering the cross-sections of the coils and their mirror images (Fig. 2).

The methods of ROGOWSKI and PETROV are explained in some more detail in [7].

Leakage inductance calculation is a complex procedure which can be very time consuming. Therefore, the algorithms of both methods have been implemented into a MATLAB® based calculation program. Using this program it is possible to determine the leakage inductance between transformer coils within the short computational time of a PC. In Fig. 3 a template of the realized computer program is displayed as an example. It shows input parameter fields for core dimensions and parameters describing the position of the coils as well as calculated values according to the method of PETROV. At the bottom of the figure the position of the coils within the core window is displayed together with the mirror images of the coils.
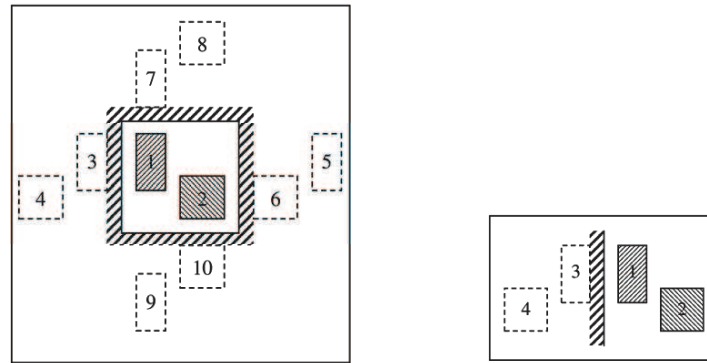
Figure 2. Formation of mirror images of the windings required for determination of the correction factor K_C for the leakage inductance portion inside core window (left) and for the leakage inductance portion outside core window (right).

Figure 3. Template of the realized computer program for leakage induction calculation (example for calculation using method of PETROV).

3. LEAKAGE INDUCTANCE CALCULATION FOR COILS ARRANGED ON DIFFERENT LEGS

Though shell-type transformers are very widespread, in certain cases the core-type transformer design (Fig. 4) has an advantage over the shell-type design of transformers. If coils are arranged on different legs, like in the case of core-type transformers, leakage inductance can be calculated by means of an approximation method which has been established by LEBEDEV [5]. As a basic assumption of this method, the leakage field can be considered to consist of three leakage flux components (Fig. 4). Resulting from this, the leakage inductance is assumed to be the sum of three parts which are related to the single flux components

$$L_L = L_{L_{in}} + L_{L_y} + L_{L_{eq}} \tag{4}$$

with inner leakage inductance $L_{L_{in}}$ related to the leakage flux $\Phi_{L_{in}}$ belonging to the section of the perimeter of the coils which is located within the core window (calculated using method of ROGOWSKI or method of PETROV), leakage inductance component L_{L_y} which is related to the
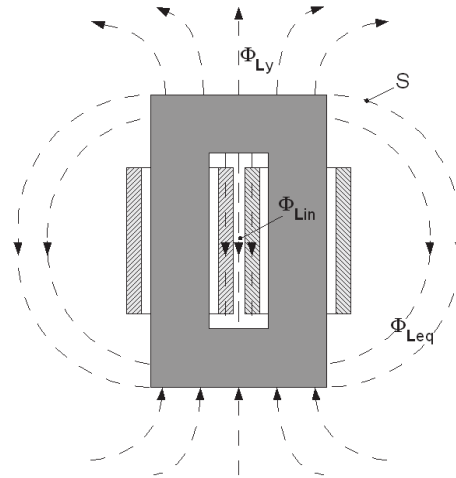
Figure 4. Components of leakage flux of a core-type transformer.

yoke leakage flux Φ_{L_y} and the so-called leakage inductance of the equivalent transformer $L_{L_{eq}}$ related to the flux component $\Phi_{L_{eq}}$.

The calculation of the single leakage inductance components and further aspects of the application of the method of LEBEDEV are explained in [8]. As well as the methods of ROGOWSKI and PETROV, also the method of LEBEDEV has been implemented into a MATLAB® based computer program.

4. APPLICATION EXAMPLES

The mentioned approximation methods enable the direct calculation of the leakage inductance related to one couple of coils of a transformer. In the case of transformers with a complex design of interleaved windings, which is often used to minimize the total leakage inductance, generally the leakage inductance values of the respective couples of single coils have to be merged together into the total transformer leakage inductance using certain combination formulas, e.g.,

$$L_{L_{total}} = \frac{w_1^2}{w_{ref}^2} \cdot \left(\frac{w_{11}}{w_1} \cdot L_{11/2} + \frac{w_{12}}{w_1} \cdot L_{12/2} - \frac{w_{11} \cdot w_{12}}{w_1^2} L_{11/12} \right) \tag{5}$$

for one of the simplest transformer versions with interleaving of windings (primary winding divided into two series-connected coils with — usually equal — number of turns w_{11} and w_{12} and the secondary winding arranged between these primary coils). Further quantities: w_1 — total number of primary turns, $L_{x/y}$ — leakage inductance values of the respective couples of coils, w_{ref} — number of turns to which the leakage inductance values of the couples of coils refer. The setup of such combination formulas for transformers with interleaving of windings is described in [9]. In the case of transformer versions with a higher degree of interleaving of windings and therefore a higher number of single coils, the combination formulas are more complex and much more leakage inductance values of couples of coils have to be determined increasing the demand for computerized calculation.

In the performed investigation the application of combination formulas was necessary to enable the comparison of the results of leakage inductance calculation with measurements concerning transformer versions with different degree of interleaving of windings.

Concerning leakage inductance determination in the case of arrangements with all coils on the same leg, shell-type transformer versions based on an identical core design but differing in the realization of windings have been considered. If the windings are interleaved, the primary coils are connected in series and the secondary coils in parallel. As an example, a transformer variant with 4 primary and 3 secondary coils (degree of interleaving shortly described as 4-3) is displayed in Fig. 5.

Beside computerized calculation due to the considered approximation methods, computer-based numerical finite elements method (FEM) calculations can be used for leakage inductance determination. Especially in the case of shell-type transformers a rotation-symmetric FEM model with

identical parameters of core area and mean length per turn compared to the real transformer can be used. Despite the simplifications of this model characterized by a reduction of the effort for the input of the geometry as well as the calculation expenditure [10], the performed FEM simulations yielded a relatively good coincidence of their results with the leakage inductance values obtained from measurement. Concerning the approximation calculation methods, it can be stated that the method of PETROV shows a higher accuracy only in the case of the initial (magnetically asymmetric) 1-1 variant whereas the method of ROGOWSKI gives results which are closer to the measurements in the considered variants with interleaving of windings which are magnetically symmetric because the width of the outer (primary) coils is half of the width of the inner (primary) coils (Fig. 6).

In addition to the comparison between the predicted and measured values, Fig. 6 illustrates the leakage inductance decreasing effect of interleaving of windings. So, in the case of the 5-4 variant, the leakage inductance is reduced to about 4% of the initial 1-1 variant.

Concerning leakage inductance determination in the case of arrangements with coils on different legs, several core-type transformer versions have been considered. The example in Fig. 7 with two coils on each leg represents a 2-2 variant regarding interleaving of windings, if two coils are connected in series which are arranged on different legs to form the primary and the secondary winding, respectively. Arrangements with a connection of the coils on the same leg are not considered in Fig. 8, because in these cases no real interleaving of windings exists.
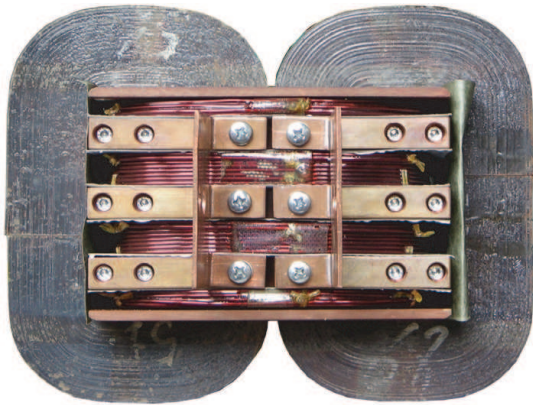
Figure 5. Shell-type transformer example with pie windings, degree of interleaving of windings 4-3, ($w_2 = 1$).
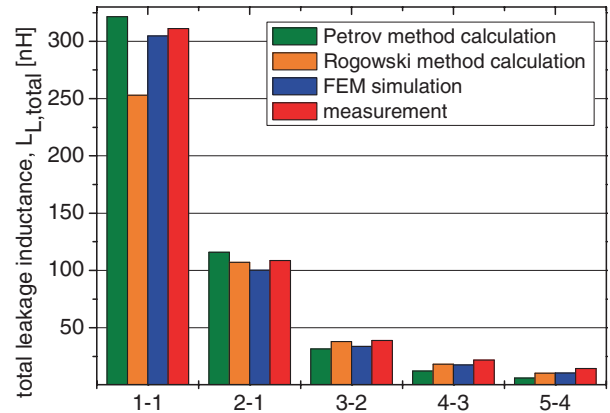
Figure 6. Predicted and measured total leakage inductance values of shell-type transformers with different degree of interleaving of windings ($w_{ref} = 1$).
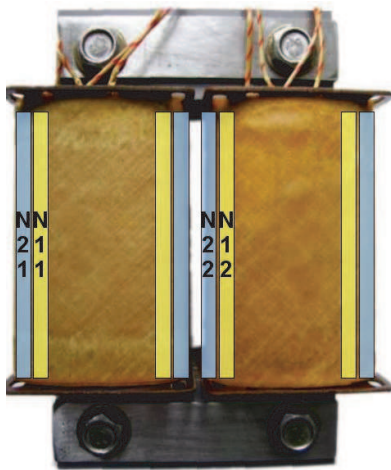
Figure 7. Core-type transformer example with concentric windings.
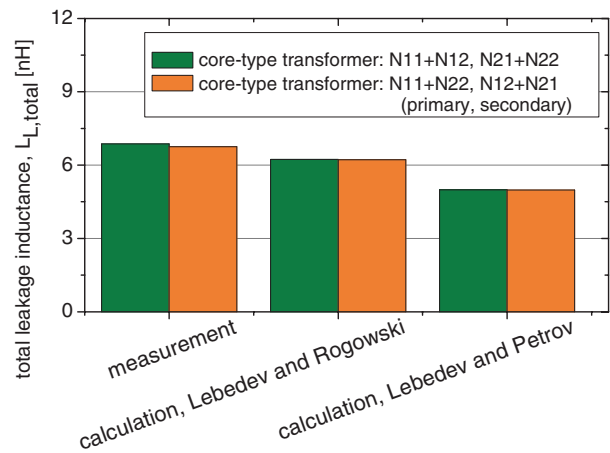
Figure 8. Predicted and measured total leakage inductance values of the considered core-type transformer ($w_{ref} = 1$).

Without interleaving of windings, leakage inductance is about 50 times higher than the values in Fig. 8, because of weak magnetic coupling between the coils of different legs of a core-type transformer.

To predict the total leakage inductance of a core-type transformer with interleaving of windings, leakage inductance values have to be merged together, which belong to couples of coils which are localized on different legs (leakage inductance to be calculated due to the method of LEBEDEV) and other couples of coils which are arranged on the same leg. Concerning the last-mentioned case, alternatively the method of ROGOWSKI or the method of PETROV can be used. As it can be seen in Fig. 8, the application of the method of ROGOWSKI results in a higher degree of coincidence with measured values.

5. CONCLUSIONS

The leakage inductance of transformers can be predicted applying approximation methods relating to the respective transformer design. Using computerized calculation after implementing the algorithms of the approximation methods into appropriate calculation software (e.g., MATLAB$^{\circledR}$), it is possible to determine the relevant leakage inductance values of a transformer within the short computational time of a PC. Thus, efficient investigations of transformer concepts with different geometry of windings can be performed. Furthermore, FEM simulation can be used for the determination of leakage inductance values of transformers. Regarding the considered transformer versions both the results of approximate calculation methods and FEM simulation are comparable to measurements. Beyond the determination of leakage inductance, FEM simulation is a useful investigation tool for transformers to clarify certain aspects of magnetic field distribution concerning core and leakage paths and current density distribution within the conductors of the windings.

REFERENCES

1. Stadler, A., M. Albach, and S. Chromy, "The optimization of high frequency operated transformers for resonant converters," *Proceedings of 11th European Conference on Power Electronics and Applications (EPE2005)*, 77, Dresden, Germany, Sept. 2005.
2. Njiende, H., H. Wetzel, N. Froehleke, and W. A. Cronje, "Models of integrated magnetic components for simulation based design of SMPS with simplorer," *Proceedings of 10th European Conference on Power Electronics and Applications (EPE 2003)*, 750, Toulouse, France, Sept. 2003.
3. Rogowski, W., *Ueber das Streufeld und den Streuinduktionskoeffizienten eines Transformators mit Scheibenwicklung und geteilten Endspulen, (Dissertation)*, VdI, Mitteilung ueber Forschungsarbeiten auf dem Gebiet des Ingenieurwesens, 1909.
4. Petrov, G. N., "Calculation of leakage of transformers (russ.)," *Električestvo*, No. 8, 3–8, 1935.
5. Lebedev, V. K., "Calculation of the short-circuit resistance of welding transformers with yoke leakage (russ.)," *Automatic Welding [Avtomatičeskaja Svarka]*, Kiev, Vol. 11, No. 4, 37–44, 1958.
6. Maxwell, J. C., *Lehrbuch der Elektrizitaet und des Magnetismus*, Vol. 2, Springer-Verlag, Berlin, 1883.
7. Doebbelin, R., T. Winkler, A. Lindemann, and C. Teichert, "Design of pulsed power transformers for capacitor discharge resistance welding machines," *International Conference Power Electronics, Intelligent Motion, Power Quality (PCIM 2006)*, 205–210, Nuernberg, May 30–June 1, 2006.
8. Doebbelin, R., M. Benecke, and A. Lindemann, "Calculation of leakage inductance of core-type transformers for power electronic circuits," *Proceedings of 13th International Power Electronics & Motion Control Conference EPE-PEMC*, Poznan, Poland, September 1–3, 2008.
9. Petrov, G. N., "Allgemeine Methode der Berechnung der Streuung von Transformatoren," *Elektrotechnik und Maschinenbau*, Vol. 51, No. 25, 345–350, 1933.
10. Schaetzing, W., *FEM fuer Praktiker: Elektrotechnik*, Vol. 4, Expert-Verlag, 2003.

The Simplifying for PEEC Model of DC Bus Based on Parameter Sensitivity Analysis

Fangzheng Li, **Xudong Sun**, **Lipei Huang**, **and Jianguo Jiang**

Country State Key Lab of Power Systems, Department of Electrical Engineering
Tsinghua University, Beijing, China

Abstract— Partial element equivalent circuit (PEEC) method is an effective way to model large, complex DC bus in converters. However the model is always composed of many passive components with complicated topology. Based on the parameter sensitivity analysis, the PEEC model of an H-bridge IGBT power unit was simplified. Taking the positive variation rate of bus current as specification, sensitivities to all partial parameters are calculated using software Pspice. The simplified model was gotten by ignoring the non-sensitive components. The transient process simulation demonstrates the accuracy of the simplified model. Further two-port network analysis illustrate that the circuit character of the simplified model agree well with the original one.

1. INTRODUCTION

Power DC bus is the predominant component of EMI propagation path and can significantly influence the EMI character of converters [1–3]. In general, lumped-circuit inductor is utilized to represent DC bus in EMI analysis [1]. However, it may be difficult even impossible to extract the lumped-circuit parameter of DC buses, especially large size bus with complex structure in high capacity converters. Partial element equivalent circuit (PEEC) technology is one of the methods to solve the problem. Recently, PEEC technique has been applied to compute impedance-frequency characteristics of large scale grounding net [4] and model low capacity converters [5].

Our former paper [6] had constructed the DC bus PEEC model of an H-bridge IGBT power unit. The structure of the DC bus is shown in Figure 1, where A and B are the positive and negative terminal of the capacitor tank, C, D and E, F are designed to fix IGBT modules respectively. The equivalent circuit is composed of more than 20 resistor components, more than 50 capacitor components and more than 20 inductor components with complicated circuit topology, as shown in Figure 2 (the mutual inductances are not shown).

Based on the simulation circuit shown in Figure 3(a), the bus current was simulated with the AC component of bridge voltage $\sim U_{CD}$ as excitation. The simulated and experimental results of the bus current and the excitation voltage were shown in Figure 3(b). Simulation results agree well with the experiment current, which illustrates that the equivalent circuit is accurate and effective.

However, the model is too complicated to express legible relationship between the mechanical structure and the circuit topology. In this paper, the complex PEEC model of the bus is simplified based on parameter sensitivity analysis. The simplified model is verified by transient process simulation and two-port network analysis.
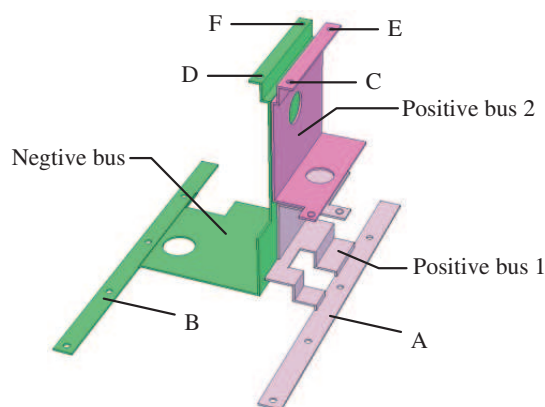
Figure 1: DC busbar structure of the H-bridge unit.
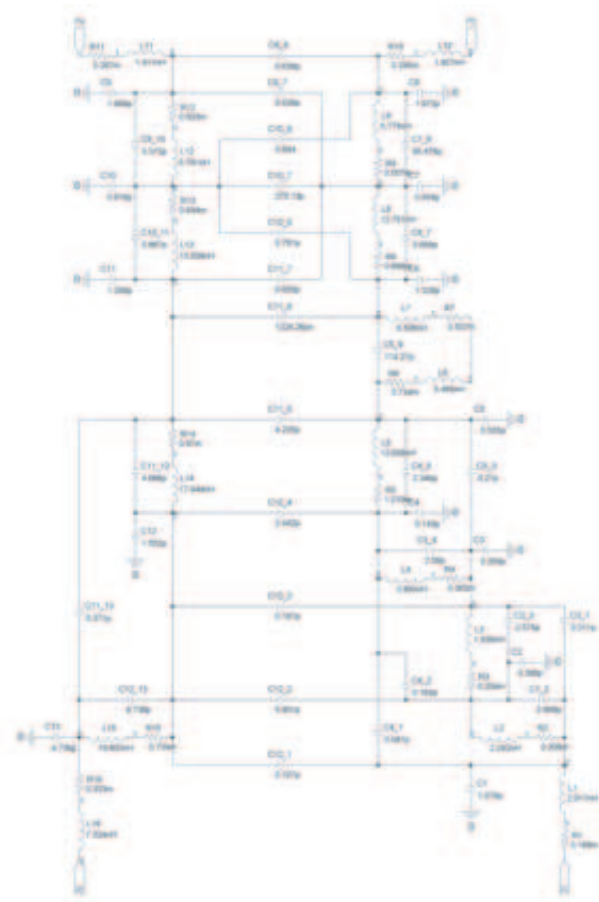
Figure 2: PEEC model of the DC bus.

(a)

(b)
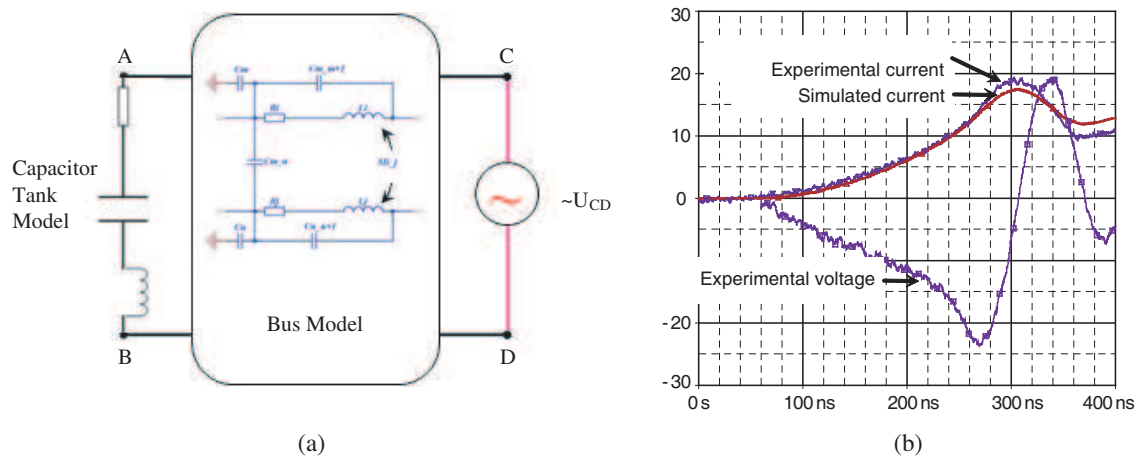
Figure 3: Schemetic of simulation circuit and the simulation results.

2. MODEL SIMPLIFYING BASED ON SENSITIVITY

Sensitivity identifies which components in a circuit have parameters critical to specified goals. From the view of EMI, the variation of current and voltage are the sources of interferes. Therefore, the variation rate of the bus current was selected as the specification for sensitivity analysis to find out the contribution of parameters of the bus model to the transient process. The variation rate of the simulated bus current was simply defined as the maximum value $i_{\max}$ divided by the rise time t_r of the current, that is

$$VR \triangleq \frac{i_{\max}}{t_r} \qquad (1)$$

(a)   (b)
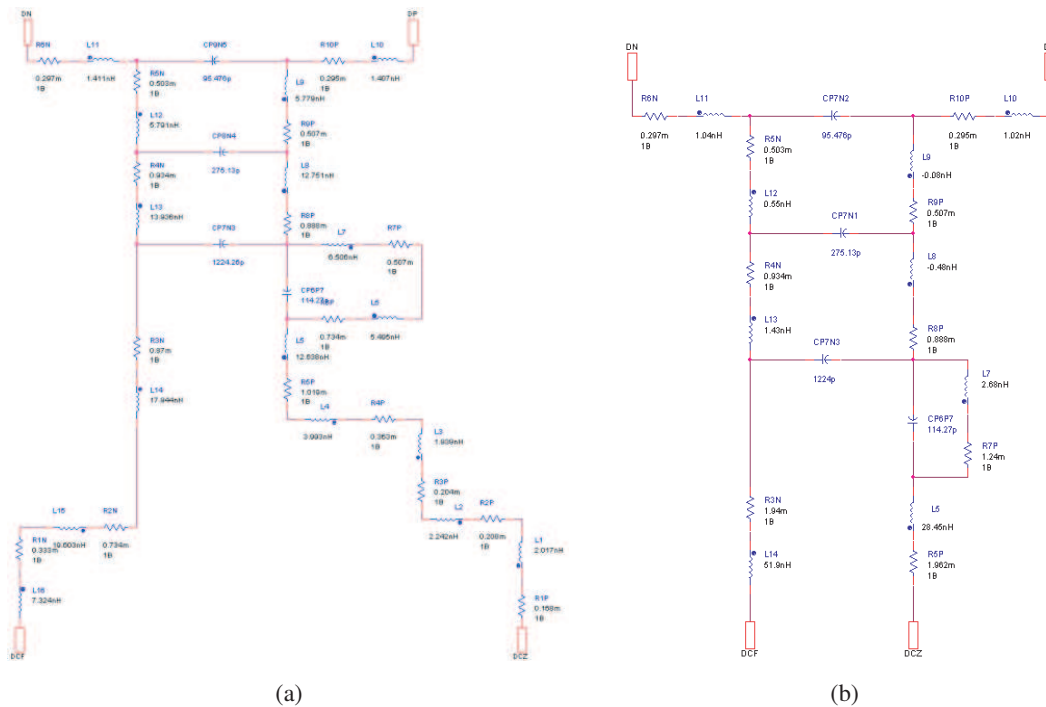
Figure 4: Simplified model of the bus.

With the sensitivity analysis tool of the circuit simulation software Pspice, it is very convenient to examine how much each component affects circuit behavior and in comparison to the other components. Running the sensitivity analysis tool, the relative sensitivity of the bus current variation rate to the parameters of bus model can be calculated. It can be conclude from the results that the predominant components of the model are

(1) Partial inductance,
(2) Mutual capacitance between neighborhood partial elements where the effective area is paralleled to the current direction,
(3) Mutual capacitance closed to the switch devices.

And the non-sensitive parameters include

(1) Partial resistance,
(2) Self-capacitance of partial elements
(3) Other mutual capacitance.

The resistance components are reserved because conductor is always modeled as inductor series with resistance. The other functionless components are removed from the PEEC model. The simplified model is composed of resistance, inductance and several important mutual capacitances between busses, as shown in Figure 4(a). The circuit will be more simple if all the mutual inductance replace by self inductance, and combine all inductances (resistances) in one branch to one component, as shown in Figure 4(b).

It should be noticed that there are some negative inductances in the circuit and this is immaterial if the only desire is a mathematical analysis.

3. VERIFICATION FOR THE SIMPLIFIED MODEL

The simulation currents of the original model and the simplified one under the same voltage excitation are almost the same, as shown in Figure 5. It illustrate that the simplified model has almost the same effect as the original model in transient process simulation.

In fact, the equivalent circuit of the bus can be regarded as a two-port network. In order to investigate the difference between the original circuit and the simplified one, the admittance parameters (Y Parameters) of the two-port network was analyzed with frequency from 100 kHz to

30 MHz, where the terminal connected to switch devices defined as input terminal and the port connected to capacitance tank as output terminal. The Y-frequency characteristics of the two models are almost the same, as shown in Figure 6(a) and (b).

The admittance parameters of the two models in several key frequencies are shown in Table 1. The resonance frequency of short-circuit admittance parameters Y11 of the two models is shown in Table 2. It can be seen that the difference between these parameters is very small. The circuit character of the simplified model agrees well with the original model.

Table 1: Admittance parameters of the models.

Admittance parameter		Frequency/Hz			
		100 kHz	1 MHz	10 MHz	30 MHz
Y11	Original	$18.61\angle - 80.83°$	$1.882\angle - 89.07°$	$0.1525\angle - 89.89°$	$0.055\angle 89.97°$
	Simplified	$18.16\angle - 83.09°$	$1.825\angle - 89.31°$	$0.1478\angle - 89.92°$	$0.0501\angle 89.97°$
Y11 (Y21)	Original	$18.61\angle - 80.83°$	$1.885\angle - 89.08°$	$0.1898\angle - 89.91°$	$0.0667\angle - 89.98$
	Simplified	$18.16\angle - 83.10°$	$1.829\angle - 89.31°$	$0.1841\angle - 89.93°$	$0.0646\angle - 89.98°$
Y22	Original	$18.61\angle - 80.83°$	$1.885\angle - 89.07°$	$0.1884\angle - 89.91°$	$0.0623\angle - 89.97°$
	Simplified	$18.16\angle - 83.09°$	$1.829\angle - 89.31°$	$0.1828\angle - 89.93°$	$0.0607\angle - 89.98°$
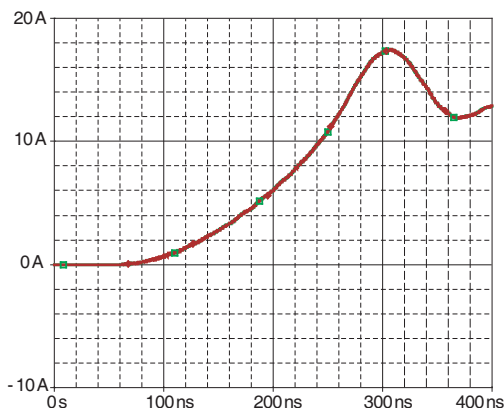
Figure 5: Simplified model of the bus.

(a) Original model
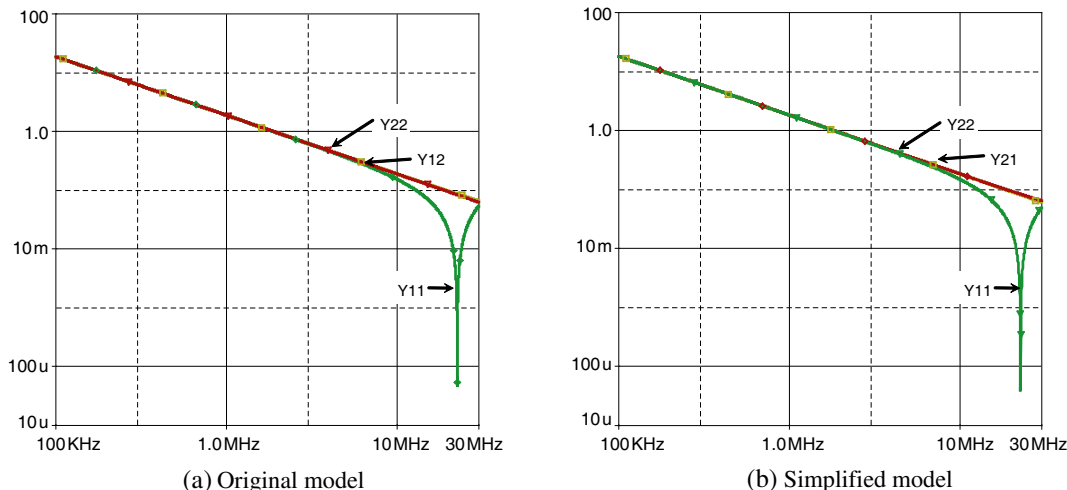
(b) Simplified model

Figure 6: Admittance-frequency characteristics of the models.

Table 2: Resonance frequency of the models.

	Frequency/MHz	Y11/uS
Original	22.412	39.132
Simplified	22.544	37.946

4. CONCLUSION

According to the sensitivity for di/dt of the bus, the complex PEEC model is simplified. Transient process analysis and two-port network analysis proved that the simplified model has almost the same character with the complex one and can used to analyze the transient process of the converter.

ACKNOWLEDGMENT

REFERENCES

1. Caponet, M. C., F. Profumo, R. W. De Doncker, and A. Tenconi, "Low stray inductance bus bar design and construction for good EMC performance in power electronic circuits," *IEEE Transactions on Power Electronics*, Vol. 17, No. 2, 225–231, 2002.
2. Huang, X. D., E. Pepa, J. S. Lai, A. R. Jr. Hefner, D. W. Berning, et al., "EMI characterization with parasitic modeling for a permanent magnet motor drive," in *IAS Annual Meeting*, Vol. 1, 416–423, 2003.
3. Yuan, L. Q., Z. M. Zhao, J. Z. Liu, and B. Li, "Experiment and analysis for single IGCT equipped in MV three-level inverter," in *Proceedings IEEE IAS*, 825–829, 2005.
4. Zhong, Y. L., Z. L. Xian, X. D. Sun, J. G. Jiang, and W. M. Ma, "HF circuit model of conducted EMI of ground net based on PEEC," *Proceedings of the CSEE*, Vol. 25, No. 17, 37–41, 149, 2005.
5. Zhang, W., M. T. Zhang, and F. C. Lee, "Conducted EMI analysis of a boost PFC circuit," in *Proceedings IEEE APEC*, 223–229, 1997.
6. Li, F. Z., L. P. Huang, X. D. Sun, and J. G. Jiang, "PEEC modeling of complex DC buses in high power converters," *J. Tsinghua Univ. (Sci. & Tech.)*, Vol. 49, No. 8, 2009.

ICI Suppression Method for the DFT-spread OFDM Communication System with Phase Noise

Sang Burm Ryu and Heung-Gyoon Ryu

Chungbuk National University

12 Kaesin-dong, Chungbuk 361-763, Korea

Abstract— The SC-FDMA (single carrier-frequency division multiple access) using DFT spread OFDM was adopted as the uplink standard of the 3GPP LTE (3rd generation partnership project long term evolution). SC-FDMA has very low PAPR (peak to average power ratio) but is sensitive to the ICI (inter carrier interference) by phase noise. In this paper, we analyze the effect of phase noise considering the back-off amount of HPA (high power amplifier). And we propose the equalizer of advanced PNS (phase noise suppressing) algorithm to remove the ICI component effectively. This equalizer has similar form of SD-FDE (frequency domain equalization) and the equalization process is based on PNS algorithm, which removes the ICI component by phase noise.

1. INTRODUCTION

SC-FDMA based on DFT-spread method was adopted for the standard technique of LTE for the uplink. SC-FDMA is to resolve the PAPR problem for the uplink [1]. And it has received more attention as a solution to reduce PAPR for the uplink. DFT-Spread OFDM has the properties of low PAPR, good spectral efficiency, commonality in design and coexistence with OFDM technique [2]. However, DFT-Spread OFDM produces more interference components of ICI and SCI (self channel interference) than ordinary OFDM because of the DFT (Discrete Fourier Transform) spreading effect and phase offset mismatch caused by random phase noise. Furthermore, much cost is required to solve these problems for high speed data in uplink data transmission. In OFDM system, it is important to reduce ICI by phase noise and many researches has studied [3, 4]. Most of previous works removed only CPE component and under assumption that CPE is removed, ICI component is compensated. So, using pilot symbol, another approach that estimates the phase noise and removes the CPE and ICI simultaneously was proposed in [4] and [5]. Moreover, signal distortion by performance loss of HPA gives an effect to system [6]. We can improve the performance by the equalizer. In previous equalizer of SC-FDE method, MMSE (minimum mean square error) is better than ZF (zero forcing) method [7]. In this paper, we propose an improved PNS algorithm to remove ICI, which is based on FDE method. To demonstrate the extraction and compensation, we confirm the BER performance according to back-off of HPA and show improvement degree of proposed algorithm considering phase noise at the same time. We show that nonlinear distorted signal at HPA in transmitter of DFT-spread OFDM system will increase the ICI component and cause the performance loss of equalizer.

2. PHASE NOISE IN DFT-SPREAD OFDM

Suppose $\tilde{S}$ data symbols are

$$C = [d_0,\, d_1, \ldots, d_{\tilde{s}-1}] \tag{1}$$

When DFT spreading block is defined as follows,

$$Q = \begin{bmatrix} 1 & 1 & \cdots & 1 \\ 1 & W^1 & \cdots & W^{(\tilde{S}-1)} \\ \vdots & \vdots & \ddots & \vdots \\ 1 & W^{(\tilde{S}-1)} & \cdots & W^{(\tilde{S}-1)(\tilde{S}-1)} \end{bmatrix}_{\tilde{S} \times \tilde{S}} \tag{2}$$

where $W = e^{-j\frac{2\pi}{\tilde{S}}}$ and DFT-spread OFDM signal is given by

$$X'_{\tilde{S}} = C \cdot Q = \sum_{\tilde{l}=0}^{\tilde{S}-1} d_{\tilde{l}} \cdot e^{-j2\pi\tilde{s}\tilde{l}/\tilde{S}}. \tag{3}$$

The DFT-spread OFDM signal is following as

$$x(n) = \sum_{k=0}^{N-1} X_k \cdot e^{j2\pi kn/N} = \sum_{k=0}^{N-1} X'_k \cdot e^{j2\pi kn/N} \tag{4}$$

where

$$X_k = X'_{\tilde{k}} = \sum_{\tilde{l}=0}^{\tilde{S}-1} d_{\tilde{l}} \cdot e^{-j2\pi \tilde{s}\tilde{l}/\tilde{S}}.$$

The received signal is

$$r(n) = x(n) \otimes h(n) + v(n). \tag{5}$$

For the simplicity, we suppose $h(n)=1$. the recovered output for the kth sub-carrier is as follows

$$Y_k = \frac{1}{N} \sum_{n \in S} r[n] \cdot e^{-j\frac{2\pi}{N}nk} = \sum_{\tilde{i}=0}^{\tilde{S}-1} d_{\tilde{l}} \cdot p_{\tilde{k},\tilde{l}} + N \tag{6}$$

DFT-spread OFDM demodulation for the transmitted symbol $d_{\tilde{k}}$ is as follows.

$$\hat{d}_{\tilde{k}} = \sum_{\tilde{s}=0}^{\tilde{S}-1} \tilde{Y}'_{\tilde{s}} \cdot e^{j2\pi \tilde{k}\tilde{s}/\tilde{S}} = d_{\tilde{k}} + N, \quad \tilde{k} = 0, \ldots, \tilde{S}-1. \tag{7}$$

When phase noise is inserted from frequency synthesizer of the transceiver, received signal is as follows.

$$r(n) = [x(n) \otimes h(n) + v(n)] \cdot e^{j\Phi(n)} \tag{8}$$

Then, after removing cyclic prefix, after FFT, the recovered output for the kth sub-carrier is given by

$$Y_k = \frac{1}{N} \sum_{n \in S} r[n] \cdot e^{-j\frac{2\pi}{N}nk} = \sum_{i \in S} X_i \cdot H_i \cdot Q_{i-k} + N_k. \tag{9}$$

where $i, k \in S$ and X_i is the frequency domain expression of $x(n)$. Finally, DFT-spread OFDM demodulation for the transmitted symbol $d_{\tilde{k}}$ is as follows.

$$\hat{d}_{\tilde{k}} = \sum_{\tilde{v}=0}^{\tilde{S}-1} Y'_{\tilde{s}} \cdot e^{j2\pi \tilde{k}\tilde{s}/\tilde{S}} = \frac{1}{N \cdot \tilde{S}} \sum_{n \in S} \sum_{i \in S} \sum_{\tilde{s}=0}^{\tilde{S}-1} \sum_{\tilde{v}=0}^{\tilde{S}-1} d_{\tilde{v}} \cdot e^{l\left\{2\pi\left[\frac{(i-s)n}{N} + \frac{(\tilde{k}\tilde{s}-\tilde{i}\tilde{v})}{\tilde{S}}\right] + \Phi[n]\right\}} + N_{\tilde{k}} \tag{10}$$
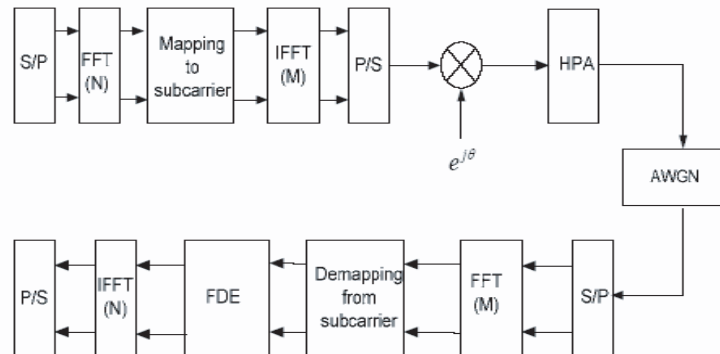
Figure 1: DFT-spread OFDM system suppressing ICI.

3. SYSTEM ANALYSIS

Here, we consider that clipped signal is randomly generated by non-linear distortion according to back-off of HPA in transmitter and coefficient of clipped signal is α.

$$r(n) = \{\alpha \cdot x(n) \otimes h(n) + v(n)\} \cdot e^{j\theta(n)} \tag{11}$$

The recovered signal at kth sub-carrier is given by

$$Y_k = \frac{1}{N} \sum_{n=0}^{N-1} [\alpha \cdot x(n) \otimes h(n) + v(n)] \cdot e^{j\theta(n)} \cdot e^{-j\frac{2\pi}{N}kn} \tag{12}$$

To analyze the effect of phase noise, channel response is 1 (i.e., $H = 1$) and signal with phase noise is approximated as follows.

$$Y_k = \sum_{i=0}^{N-1} \alpha \cdot X_i \cdot H_i \cdot Q_{i-k} + N_k = Y_{k1} + Y_{k2} + N_k \tag{13}$$

where X_k and H_i the frequency domain expression of $x(n)$, $h(n)$ corresponding to kth sub-carrier. Q is expression of phase noise in frequency domain.

4. COMPENSATION OF ICI

After FFT, compensation processing is following as

$$Y_k = \alpha \cdot X_k \cdot Q_0 + \sum_{i=0, i \neq k}^{N-1} \alpha \cdot X_i \cdot Q_{i-k} + N_k \tag{14}$$

where the first term is CPE component and second term is ICI component.

To estimate CPE component, we use the pilot symbol and estimated signal is expressed by

$$CPE_k = \frac{Y_k}{X_k} = \alpha \cdot X_k Q_0 + \frac{ICI + N_k}{X_k} = \alpha \cdot X_k Q_0 + W_k.$$
$$r_{cpe} = \frac{1}{N_p} \sum_{k \in s_p} CPE_k = \alpha \cdot X_k Q_0 + 1/4 \sum_{k \in s_p} W_k. \tag{15}$$

Here, N_p is the number of pilot symbol and 4, S_p is pilot symbol and W_k is total interference component due to ICI and AWGN.

$$\tilde{Y}_k = \alpha \cdot X_k \cdot Q_0 / r_{cpe} + \sum_{i=0, i \neq k}^{N-1} \alpha \cdot X_i \cdot Q_{i-k} / r_{cpe} + N / r_{cpe} = \sum_{i=0, i \neq k}^{N-1} \alpha \cdot X_i \tilde{Q}_{i-k} + W_{ICI+AWGN}. \tag{16}$$

We can know that CPE component is removed and ICI by non-linear distortion error, phase noise and AWGN exist. In previous work, to remove phase noise, received signal of (10) estimates
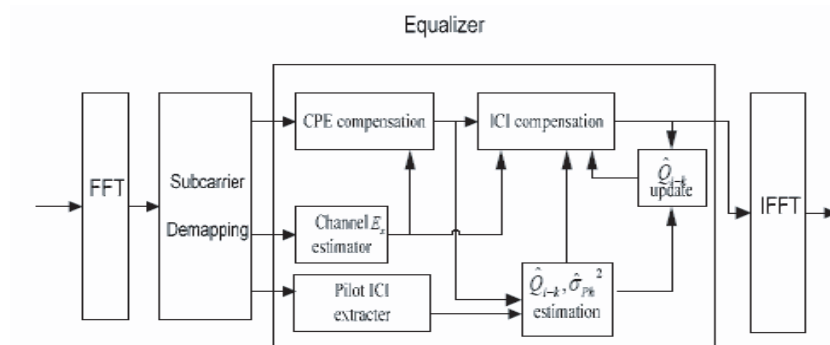
Figure 2: Compensation block diagram.

according to MMSE equalization and final recovered data sample (i.e., transmitted data sample) is following as

$$\hat{X}_k = Y_k \otimes C_k. \tag{17}$$

$$C_k = \frac{\tilde{Q}^*_{i-k} \cdot H^*_k}{\left|\tilde{Q}^*_{i-k} \cdot H^*_k\right|^2 + \frac{\tilde{\sigma}^2_x}{E_x}}. \tag{18}$$

where $(\cdot)^*$ means conjugate process, $\tilde{\sigma}^2_x$ is variance of $W_{ICI+AWGN}$ and E_x is useful signal power. Suppose that channel impulse response is much smaller than ICI effect (i.e., $H_k \ll \tilde{Q}_{i-k}$), $\tilde{Q}_{i-k} \cdot H_k \cong \hat{Q}^*_{i-k}$ and coefficient of equalizer is as follows.

$$C_k = \frac{\hat{Q}^*_{i-k}}{\left|\hat{Q}^*_{i-k}\right|^2 + \frac{\tilde{\sigma}^2_x}{E_x}}. \tag{19}$$

$$\tilde{Q}_h = \left(\frac{1}{N_P}\sum_{k \in s_p}\left|\left(Y_p - \tilde{Y}_k\right)\right|\right)^2$$

$$\min_{Q_0, k \in s_p} \sum \left|\tilde{Y}_k - X_k\tilde{Q}_h\tilde{Q}_{i-k}\right|^2 \tag{20}$$

$$\tilde{Q}_h\tilde{Q}_{i-k} = \frac{\displaystyle\sum_{Q_0, k \in s_p}\tilde{Y}_k X^*_k}{\displaystyle\sum_{k \in s_p}\left|X_k\right|^2} \tag{21}$$

5. SIMULATION RESULTS AND DISCUSSION

At 10^{-4} of Fig. 3, cases of back-off 7 dB and 5 dB show the performance improvement about 0.8 dB and 2.5 dB, respectively. As we can know this, we can achieve the improvement of performance if it removes only ICI by HPA.

Figure 4 is BER comparison of compensation in case of phase noise change. Here, we consider the back-off of 5.5 dB and control the phase noise to 0.005, 0.01, 0.06 rad^2. From 0.005 rad^2 of phase noise, this system causes the error floor at 10^{-4} without compensation. When phase noise is removed, we know that system performance is satisfied under 14 dB of SNR. However, compensation of phase noise must need to satisfy the SNR under 14 dB without phase noise.
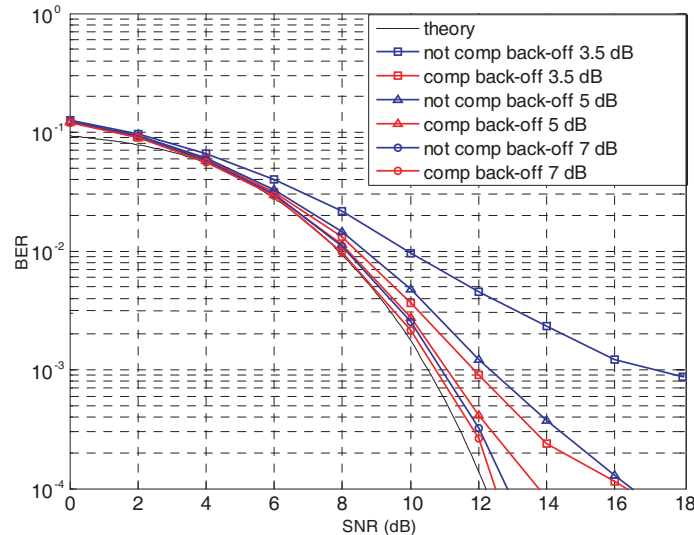
Figure 3: BER comparison of compensation in case of increasing back-off.
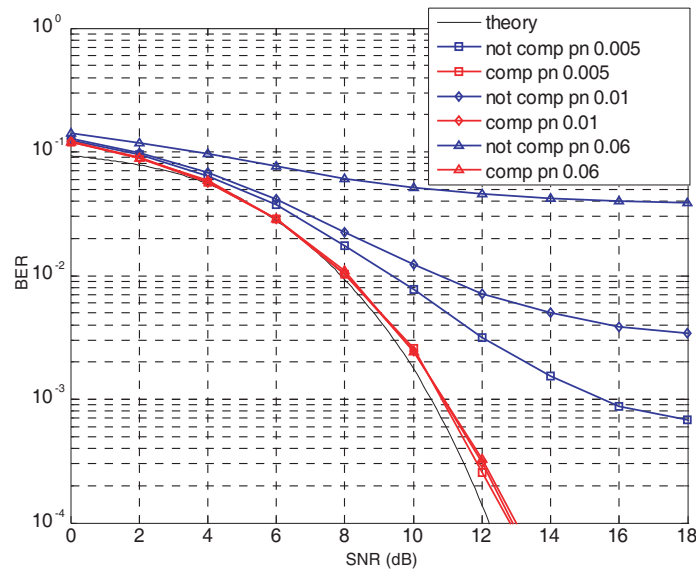
Figure 4: BER comparison of compensation in case increase phase noise.

6. CONCLUSION

We proposed the equalizer of advanced PNS algorithm to remove the ICI component effectively. When ICI component by phase noise and HPA exists in system simultaneously, propose method applies method updating reference value and tap weighting coefficient from conventional PNS algorithm, extracts the error by phase noise and HPA from pilot symbol at once and this component uses to forgetting factor. Through the result of simulation, proposed method can be achieved about 2.5 dB back-off gain comparing the performance with 7 dB back-off due to remove the ICI using proposed equalization algorithm. And we know that system has satisfied the desired SNR about 14 dB at 10^{-4}.

REFERENCES

1. 3GPP, TR 25.814, "Physical layer aspects for evolved UTRA," www.3gpp.org.
2. Ryu, H. G. and Y. S. Li, "Phase noise analysis of the OFDM communication system by the standard frequency deviation," *IEEE Transactions on Consumer Electronics*, Vol. 49, No. 1, 41–47, Feb. 2003.
3. Ryu, H. G. and H. S. Lee, "Analysis and minimization of phase noise of the digital hybrid PLL frequency synthesizer," *IEEE Transactions on Consumer Electronics*, Vol. 48, No. 2, May 2002.
4. Wu, B., S. Cheng, and H. Wang, "Clipping effects on channel estimation and signal detection in OFDM," *Personal, Indoor and Mobile Radio Communications, 14th IEEE Proceedings*, Vol. 1, 531–534, Sep. 7–10, 2003.
5. Wu, S. and Y. Bar-Ness, "A phase noise suppression algorithm for OFDM-based WLANs," *IEEE Communications Letters*, Vol. 6, No. 12, 535–537, Dec. 2002.
6. Wu, S. and Y. Bar-Ness, "OFDM systems in the presence of phase noise: Consequences and solutions," *IEEE International Conference on Communications*, Vol. 52, No. 11, 1988–1996, Nov. 2004.
7. Witschnig, H., H. Reich, K. Stallinger, H. Weigel, and R. Springer, "Performance versus effort for decision feedback equalization — An analysis based on SC/FDE adapted to IEEE 802.11a," *IEEE International Conference on Communications*, Vol. 6, 3455–3459, Jun. 2004.
8. Gholami, M. R., S. Nader-Esfahani, and A. A. Eftekhar, "A new method of phase noise compensation in OFDM," *ICC'03, IEEE International Conference on Communications*, Vol. 5, 3443–3446, May 11-15, 2003.
9. Priyanto, B. E., T. B. Sørensen, O. K. Jensen, T. Larsen, T. Kolding, and P. Mogensen, "Assessing and modelling the effect of RF impairments on UTRA LTE uplink performance," *2007 IEEE 66th Vehicular Technology Conference, VTC-2007 Fall,*, 1213–1217, Sep. 30–Oct. 3, 2007.

Comparison of Wideband Channel Sounding Techniques

Xiao Hong Mao, **Yee Hui Lee**, and **Boon Chong Ng**

School of Electrical and Electronic Engineering, Nanyang Technological University, Singapore

Abstract— This paper compares time-domain and frequency-domain wideband channel sounding techniques by using measurement results. These techniques are compared based on the received power, the multipath resolution, and the RMS delay spread. Similar conclusions can be drawn for both sounding techniques for the measurement environment. In general, both sounding techniques have their own advantages and constrains; the choice of sounding technique heavily depends on the experiment environment.

1. INTRODUCTION

Research progress in the area of wireless communication has been rapid. Over the past three decades, there has been a number of research works on wideband channel characterization by using different sounding techniques [2–8]. In general, wideband channel measurements can be classified as direct pulse measurements spread spectrum sliding correlator measurements and swept frequency measurements [1]. The first two are usually referred to time-domain sounding technique whereas the last one is referred to as a frequency-domain sounding technique.

The channel sounding in frequency domain is generally implemented by using the vector network analyzer (VNA). In [6], channel characteristics of an underground mine was studied using VNA sounding technique at UHF frequency 2.4 GHz with a bandwidth of 200 MHz. The same sounding technique was used in [7], where the feasibility of WLAN usage at frequency 2 GHz and 5 GHz was tested onboard a warship by using a VNA. In [8], ultra-wideband (UWB) channel sounding using VNA was performed inside a rectangular metal cavity in frequency band 3 GHz to 10 GHz. From all the research works mentioned above, although they cover different frequency bands and different environments, only one wideband channel sounding technique was applied for each paper. As a result, no comparisons on results obtained from different sounding techniques are available.

There are also some research works purely focusing on the sounding techniques. Authors of [9] provided a review on time domain sounding techniques for wideband mobile radio channel; it was concluded that spread spectrum technique was the optimum choice, while [10] studied the direct-sequence spread-spectrum (DSSS) communications for multipath channels theoretically. For frequency domain sounding technique, the performance of a VNA-based sounding technique has been investigated in [11]. However, none of the three papers provided comparisons between wideband channel sounding techniques in time-domain and that in the frequency-domain. As is well-known, the spread spectrum technique has advantages of low power-spectral density operation [10], controllable processing gain, controllable multipath resolution, high privacy, ability to provide bit error rate (BER) information and immunity to the noise. It has disadvantage of relatively complex system. For a VNA sounding technique, it has advantages of simple implementation requirements, relative flexible system, ability to track system error and ability to provide absolute delay to power delay profile. However, the VNA systems suffer from a relatively slow measurement time and slow update rates. Moreover, it requires a wired link to carry the transmitted reference [11], which limits the VNA sounding technique to short distance measurements if a single VNA is used. Sarabandi et al. [12] has made the effort to extend the sounding distance to 1000 m by using two VNAs. These VNAs have to be synchronized through two rubidium atomic clocks. Therefore, the whole sounding system becomes very costly.

In this paper, both spread spectrum technique (time-domain technique) and VNA technique (frequency-domain technique) are applied in wideband channel measurements along a lift shaft in a university environment. For the measurements, a 1023-bit pseudorandom noise sequence spreading over a bandwidth of 20 MHz is applied for the spread spectrum sliding correlator sounding technique (PN Sounding). A 1601 tones are transmitted over a 300 MHz bandwidth using the VNA for the frequency domain channel sounding (VNA Sounding). If a channel is assumed to be wide-sense stationary uncorrelated scattering (WSSUS), the impulse response can be expressed as (1). For PN Sounding, the channel impulse response can be obtained by correlating the received sequences with the original one. While for VNA sounding, samples of S_{21} which is directly proportional to channel transfer function $H(\omega)$ as shown in (2) are recorded and IFFT is applied to obtain the

impulse response in time domain as shown in (3). The two channel sounding techniques are studies by comparing the received power, RMS delay spread, as well as multipath resolution.

$$h_b(n, \tau) = \sum_{i=0}^{N-1} a_i \exp(j\theta_i)\delta(\tau - \tau_i) \tag{1}$$

$$S_{21}(\omega) \propto H(\omega) = \frac{Rx(\omega)}{Tx(\omega)} \tag{2}$$

$$h(t) = FT^{-1}[H(\omega)] \tag{3}$$

2. MEASUREMENT RESULTS AND DISCUSSIONS

The two sounding techniques is compared by using measurement results in this section. They are compared in terms of the 1st cluster power difference between two consecutive transmitter level, RMS delay spread, their trends with respect to Tx-Rx separation, and multipath resolution.

Figure 2 displays the mean power delay profiles (PDPs) averaged over 50 frames obtained by PN sounding. The transmitter level varies from level B3 to level B6, while both the receiver and the lift car are fixed at level B2 as shown in Figure 1. As is shown, the 1st peak in PDP of transmitter level B3 contains 2 or 3 peaks in PDPs of other transmitter levels, and the common area (0–0.25 μs) is identified as the 1st cluster. The same cluster is also indentified in Figure 3, which shows mean PDPs averaged over 50 files obtained by VNA sounding.
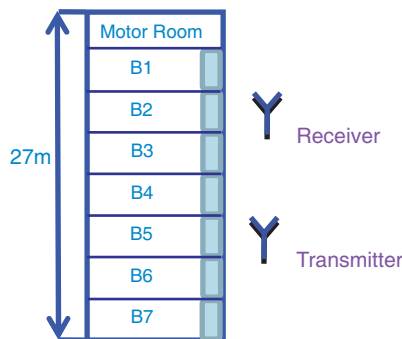
Figure 1: The schematic diagram of the measurement setup.
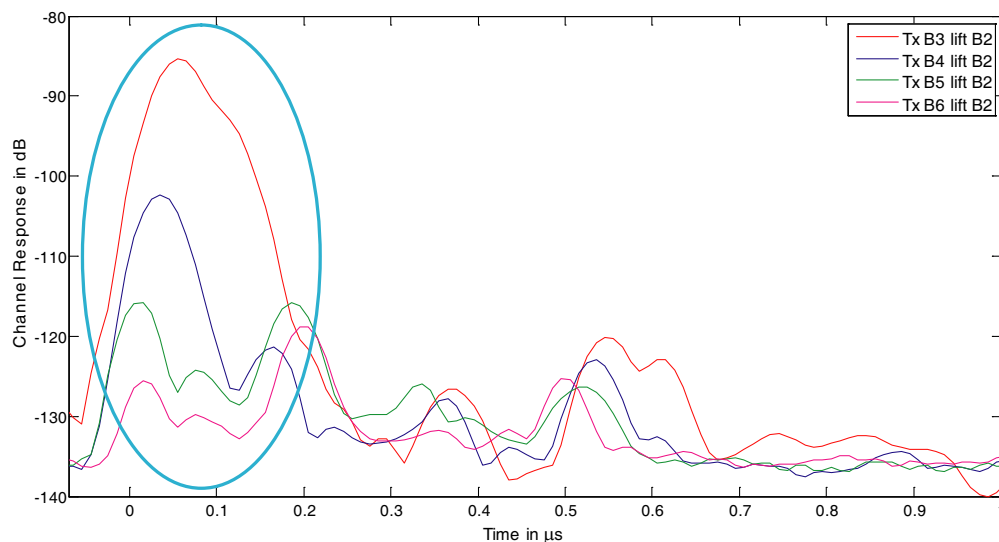
Figure 2: PDPs for different transmitter levels (PN).
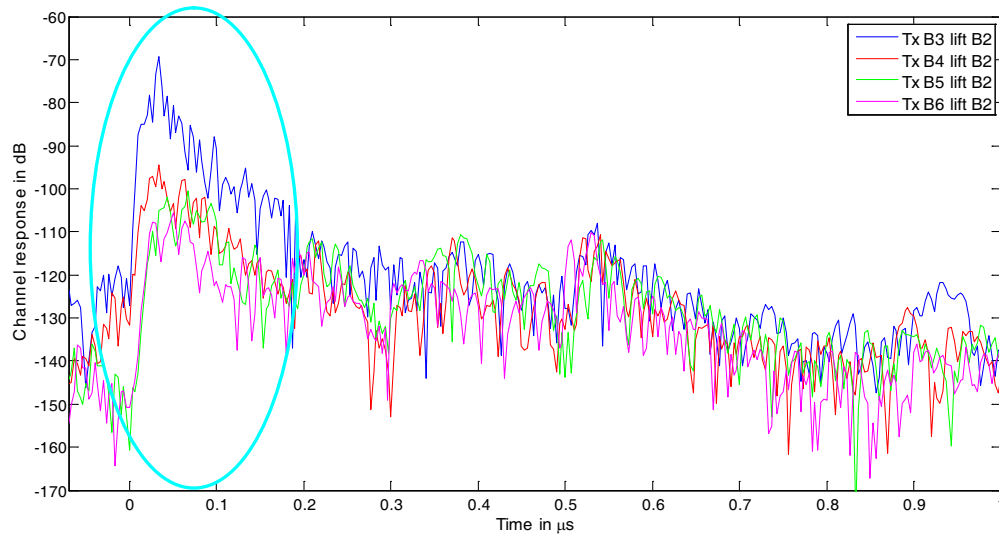
Figure 3: PDPs for different transmitter levels (VNA).

2.1. The 1st Cluster Power Difference

It is shown in both Figure 2 and Figure 3 that the amplitude of peaks in the 1st cluster decreases as the Tx-Rx separation increases. The average power in the 1st cluster is obtained by integrating PDP over the time 0 to $0.25\,\mu s$. And the power differences between two consecutive transmitter levels are listed in Table 1. From Table 1, it is observed that the decreases in power difference when transmitter moves away from the receiver are nearly the same for both sounding techniques. Moreover, they follow the same trend that the power difference decreases as the Tx-Rx separation increases.

Table 1: Power difference between levels for the 1st cluster.

Transmitter Levels	Power difference (PN)	Power difference (VNA)
B3 minus B4	20.9 dBm	20.6 dBm
B4 minus B5	9.8 dBm	6.5 dBm
B5 minus B6	5.3 dBm	4.5 dBm

2.2. RMS Delay Spread

In wideband channel sounding, time dispersion parameter such as RMS delay spread is important for channel estimation. The RMS delay spread listed in Table 2 is calculated for PDPs in Figure 2 and Figure 3. In the each of the two figures, the common peaks among PDPs are identified as signals and accounted for RMS delay spread calculation. It is shown in Table 2 that the RMS delay spreads obtained from different sounding techniques do not have significant difference even different spread bandwidths are used for different sounding techniques. Moreover, the finding that RMS delay spread increases as the Tx-Rx separation increases is consistent for both techniques.

Table 2: RMS delay spread for different transmitter level.

Transmitter Level	RMS Delay Spread (PN)	RMS Delay Spread (VNA)
B3	11.8 ns	16.7 ns
B4	52.2 ns	80.6 ns
B5	123.8 ns	128.6 ns
B6	138.9 ns	176.0 ns

2.3. Multipath Resolution

The multipath resolution capacity includes two parties: spatial resolution and maximum echo-path time delay resolution. Spatial resolution is a measure of the minimum discernible path difference

between two echo signals. For both PN and VNA sounding techniques, a larger spread bandwidth provides a finer spatial resolution. In this measurement, the spatial resolution of PN sounding (20 MHz spread bandwidth) is 15 m while that of VNA sounding (300 MHz spread bandwidth) is 1 m. The resolution difference can be observed from Figure 4, which is obtained when the transmitter is fixed at level B3. It can be observed that one peak in PDP of PN contains several peaks in that of VNA due the different spatial resolution. In general, VNA sounding technique can provide a good spatial resolution, and it is often used for ultra-wideband application. However, the PN sounding technique is not able to achieve a very high spatial resolution unless a digitizer card with very high sampling rate and broader bandwidth is provided. The maximum echo-path time delays in this measurement are 51.15 μs and 5.34 μs for PN sounding and VNA sounding respectively. It can be improved by using more bits in PN sounding technique and sending more tones for VNA sounding technique.
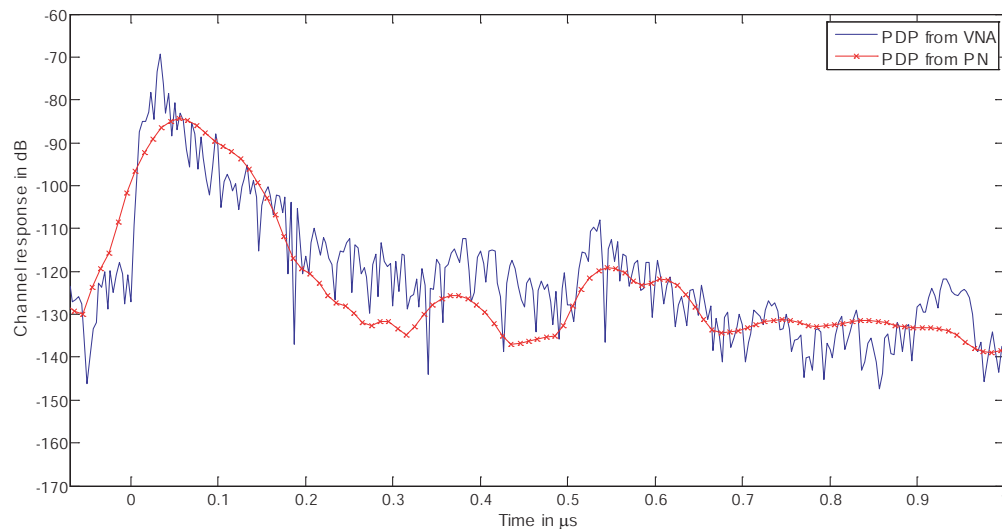
Figure 4: PDPs obtained from different sounding techniques.

3. CONCLUSIONS

The paper compares wideband measurement results obtained along a lift shaft in a university environment by using different sounding techniques. For the two sounding techniques, the amounts of decrease in power difference between two consecutive transmitter levels are similar and they follow the same trend. It is also concluded that the RMS delay spread increases as the Tx-Rx separation increases and the obtained values are close for two sounding techniques. So, in this particular environment, both techniques provide almost the same channel information, and either of them can be applied. In general, for a relatively simple environment with big obstacles where high resolution is not required, the spread spectrum sliding correlator technique is recommended. For a relatively complex environment where the distance between the transmitter and the receiver is not very long, the frequency domain channel sounding is recommended. However, each method has their own constrains to be taken care of.

REFERENCES

1. Rappaport, T. S., *Wireless Communications: Principles and Practice*, Prentice Hall, 2002.

2. Muqaibel, A., A. Saffaai., A. Attiya, B. Woerner, and S. Riad, "Path-loss and time dispersion parameters for indoor UWB propagation," *IEEE Trans. Wireless Communication*, Vol. 5, No. 10, 550–559, 2006.

3. Mao, X. H., Y. H. Lee, and B. C. Ng, "Wideband channel modelling in UHF band for urban area," *IEEE International Conference on Wireless Communication Systems*, 240–244, Reykjavik, Iceland, October 2008.

4. Oestges, C., D. V. Janvier, and B. Clerckx, "Channel characterization of indoor wireless personal area networks," *IEEE Trans. on Ant. and Prop.*, Vol. 54, No. 11, 3143–3150, 2006.

5. Ghoraishi, M., J. Takada, and T. Imai, "Identification of scattering objects in microcell urban mobile propagation channel," *IEEE Trans. on Ant. and Prop.*, Vol. 54, No. 11, 3473–3480, 2006.

6. Nerguizian, C., C. L. Despins, S. Affes, and M. Djadel, "Radio-channel characterization of an underground mine at 2.4 GHz," *IEEE Trans. on Wireless Comm.*, Vol. 4, No. 5, 2441–2453, 2005.

7. Nobels, P. and L. R. Scott, "Wideband propagation measurements onboard HMS BRISTOL," *Military Communications Conference*, 1412–1415, 2003.

8. Singh, D., H. Zhen, and R. Qiu., "UWB channel sounding and channel characteristics in rectangular metal cavity," *IEEE Southeaston*, 323–328, April 2008.

9. Parsons, J. D., D. A. Demery and A. M. D. Turkmanil, Sounding techniques for wideband mobile radio channels: a review, IEE Processings communication, speech and vision., Vol. 138, No. 5, 437-446, 1991.

10. Pursley, M. B., Direct-Sequence Spread-Spectrum Communications for Multipath Channels, IEEE Trans. On Microwave Theory and Technique, Vol. 50, No. 3, 653-661, 2002.

11. Street, A. M., L. Lukama and D. J. Edwardsl, Use of VNAs for wideband propagation measurements, IEE Proceedings on Communication, Vol. 148, No. 6, 411-415, 2001.

12. K. Sarabandi, N. Behdad, A. Nashashibi, M. Casciato, L. Pierce, and F. Wang, A measurement system for ultrawide-band communication channel characterization, IEEE Trans. Antennas Propag., vol. 53, pp. 2146-2155, July 2005.

T-DVB Services Coexistence with IMT-advanced Service

Z. A. Shamsan and T. A. Rahman

Wireless Communication Centre, Universiti Teknologi Malaysia (UTM), Malaysia

Abstract— Due to spectrum scarcity and emerging various wireless applications, coexistence and sharing between wireless systems becomes a recently critical issue. At WRC-07, 790–862 MHz is allocated for the coming fourth generation (4G) or IMT-Advanced on a co-primary basis along with existing Terrestrial-Digital Video Broadcasting (T-DVB). Therefore, coexistence and sharing requirements such as separation distance and frequency separation coordination must be achieved in terms of both co-channel and adjacent channel frequencies. The two coexisted systems are analyzed by Spectral Emission Mask (SEM) model and interference to noise ratio (I/N) of -6 dB as a standard coexistence criterion for the interference coming from broadcasting base station into base station of IMT-Advanced represented by mobile WiMAX as a candidate technology for 4G. Finally, possible intersystem interference mitigation techniques are suggested.

1. INTRODUCTION

The new capabilities of these International Mobile Telecommunications (IMT)-Advanced systems are envisioned to handle a wide range of supported Carrier bandwidth: 20 MHz up to 100 MHz and data rates with target peak data rates of up to approximately 100 Mbps for high mobility such as mobile access and up to say 1 Gbps for low mobility such as nomadic/local wireless access [1, 2]. 790–862 MHz band is one of the bands which are allocated by ITU-R (At WRC-07) for IMT-Advanced service in several countries in Asia with regulatory and technical constraints [3], meanwhile, this frequency band is currently used by broadcasting services in most of the world countries including Malaysia. This means that interference probability due to frequency sharing between these two systems is bound to happen if the two systems operate in adjacent areas with same carrier frequency (co-channel frequency) or in the same area with an adjacent carrier frequency. A few studies were done between terrestrial systems in the said band and some of them are under way. In our study the concept of SEM is presented such that the effect of T-DVB transmitter on IMT-Advanced will be addressed.

The reminder of this paper is organized as follows. In Sections 2 and 3, IMT-Advanced and DVB-T services parameters, Spectral emission mask, are described. Protection criteria, propagation models, coexistence scenarios and interference analysis methods are detailed in Section 4. Section 5 is devoted to the coexistence results, analysis and compatibility between the services. Finally, the conclusion is presented in Section 6.

2. IMT-ADVANCED AND DVB-T SERVICES PARAMETERS AND SIMULATION

In order to study and examine coexisting and sharing issues, it is necessary to clarify the parameters of both IMT-Advanced and broadcasting that will affect the interference level and criterion. These parameters are shown in Table 1.

3. SPECTRAL EMISSION MASK (SEM)

SEM is a graphical representation of a set of rules that apply to the spectral emissions of radio transmitters. Such rules are set forward by regulatory bodies such as FCC and ETIS. It is defined as the spectral power density mask, within $\pm 250\%$ of the relevant channel separation (ChS), which is not exceeded under any combination of service types and any loading. The masks vary with the type of radio equipment, their frequency band of operation and the channel spacing for which they are to be authorized [4, 5]. The SEM is considered in this study because it may be used to generate a "worst case" power spectral density for worst case interference analysis purposes. SEM is an essential parameter for adjacent frequency sharing analysis to evaluate the attenuation of interference signal power in the band of the victim receiver. To carry out this study the DVB-T SEM in the Fig. 1 is applied for coming interference from DVB-T into WiMAX BS.

4. INTERFERENCE ASSESSMENT FROM DVB-T INTO IMT-ADVANCED BS IN DENSE URBAN AREA

The method consists in calculating the I/N ratio and then comparing it with the necessary I/N (-6 dB) at the victim receiver. Firstly, the interference level I (dBm) at the victim receiver is

Table 1: IMT-Advanced and DVB-T services parameters.

Parameter	Value	
	IMT-Advanced	DVB-T
Frequency of operation (MHz)	800	800
EIRB (dBm)	43	72.15
Base station antenna gain (dBi)	15	------
Base station antenna height (m)	20	100
Interference limit power (dBm)	−109	------
Channel bandwidth (MHz)	5, 20	8
Spectral Emission Mask	Not Available	DVB-T GE06
Interference to noise ratio I/N (dB)	−6	------
Noise Figure dB	4	7
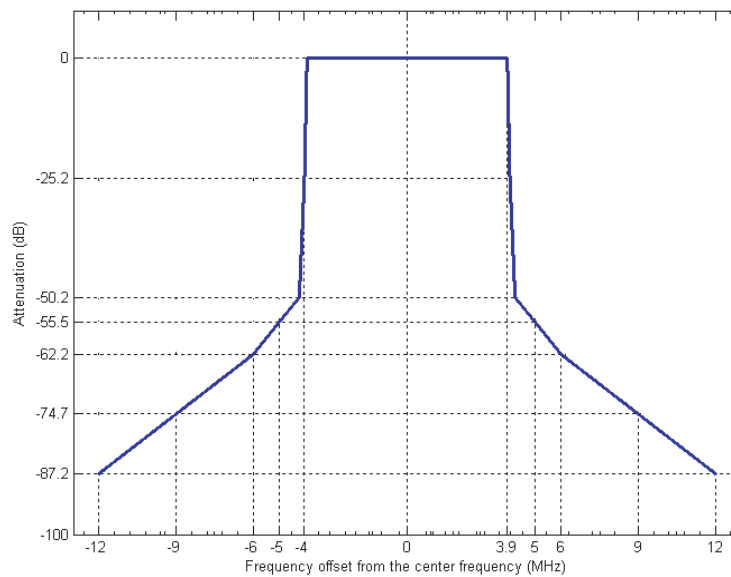
Figure 1: Critical spectrum mask of T-DVB 8 MHz (GE06 final acts, Section 3.6.2).

evaluated by assessing the level of emissions from the interferer falling within the victim receiver bandwidth for both co-channel frequency and adjacent frequency situations according to [6]:

$$I\left(\Delta f\right) = Pt + Gt + Gr + \text{Mask}\left(\Delta f\right) + \text{Corr\_band} - Att \tag{1}$$

where Pt is the transmitted power of the interferer in dBm, Gt and Gr are the gain of the interferer transmitter and the victim receiver antennas in dBi, Mask(Δf) represents attenuation of adjacent frequency due to mask where Δf is the difference between the carriers of interferer and the victim. Corr_band denotes correction factor of band ratio, Att represents attenuation due to the propagation model (model ITU-R P.452 includes free space loss and clutter loss is used [7, 8]). Secondly, to determine the thermal noise floor of victim receiver the following equation is used [9]:

$$N = -114 + NF + 10\log_{10}\left(BW_{\text{victim}}\right) \tag{2}$$

where NF is noise figure of receiver in dB and BW_{victim} represents victim receiver bandwidth in MHz. Finally, by dividing I over N as a ratio, sharing and coexistence feasibility between the two systems can be determined.

5. THE RESULTS AND DISCUSSIONS

As seen from Figs 2 and 3, the interference from T-DVB Transmitter into 5 MHz and 20 MHz WiMAX BS, respectively, as a victim receiver is applied, where the minimum separation distance

and frequency separation for the minimum I/N ratio of -6 dB are analyzed in the dense urban area. For adjacent channel coexistence it can be observed that the minimum separation distance between the two services must be greater than 5.5 km and 3.5 km for bandwidth of 5 MHz and 20 MHz, respectively, with frequency separation of 12 MHz from the carrier frequency. For deploying the two systems with a null guard band, the separation distances must be greater than 57 km for WiMAX bandwidth of 5 MHz and the two systems can be overlapping with coexisting operation if the distance is more than 3.5 km at 20 MHz WiMAX channel bandwidth. Zero (null) guard band is represented by a vertical line in the graphs.

Sharing the same channel (co-channel) is not feasible between the two systems under assumed scenario because huge and impractical separation distances are of the order of 120,000 km for 5 MHz and 80,000 km for 20 MHz WiMAX channel bandwidth, respectively, are required. The entire requirements are summarized in Table 2. Fig. 4 clarifies the relationship between minimum separation distances and how the frequency offset from the center frequency, required guard band or overlapping in spectrum to get safe sharing and coexistence. It is also clear from the results that as the bandwidth increases the noise also increases therefore the separation distance between T-DVB and WiMAX decreases.

Co-existence of IMT with T-DVB reception will require the application of the same available mitigation techniques and careful network planning. Possible ways to mitigate the interference may include limiting the maximum transmit power of the IMT terminal as well as improving the characteristics of future T-DVB receiver including T-DVB rejection performance at the image channel.

Table 2: Minimum separation distance and frequency offset to achieve coexistence (IMT-Advanced is victim).

IMT-Advanced Bandwidth	The Minimum distance	Frequency Offset	Guard Band	Overlapping band
	km	MHz	MHz	MHz
	5.5	12	5.5	-6.5
5 MHz	7.5	6.5	0.0	0.0
	120,000	0.0	-6.5	8
	3.5	12	-2	2
20 MHz	100	5.5	-8.5	8.5
	80,000	0.0	-8.1	20
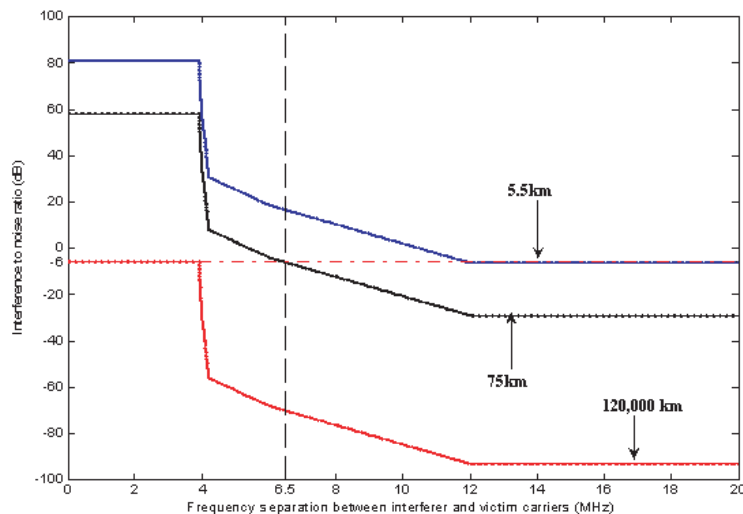
Figure 2: The interference from 8 MHz T-DVB into 5 MHz WiMAX BS.
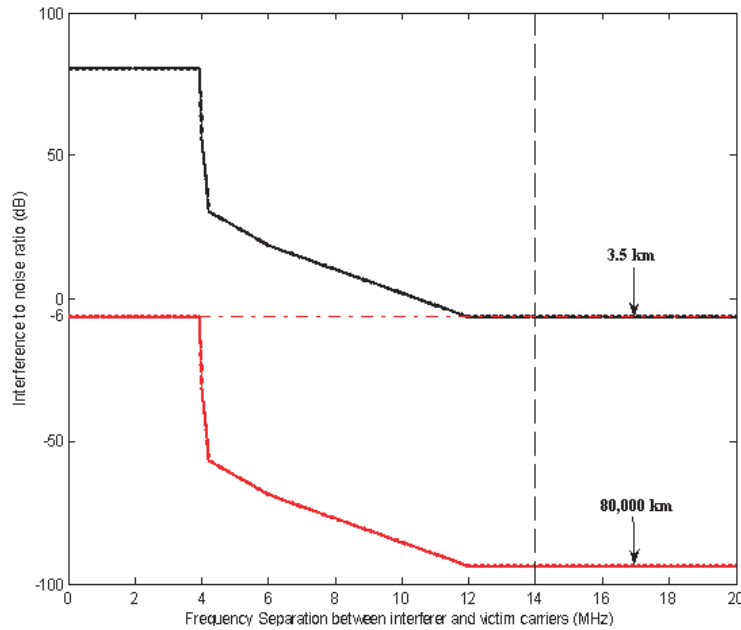
Figure 3: The interference from 8 MHz T-DVB into 20 MHz WiMAX BS.
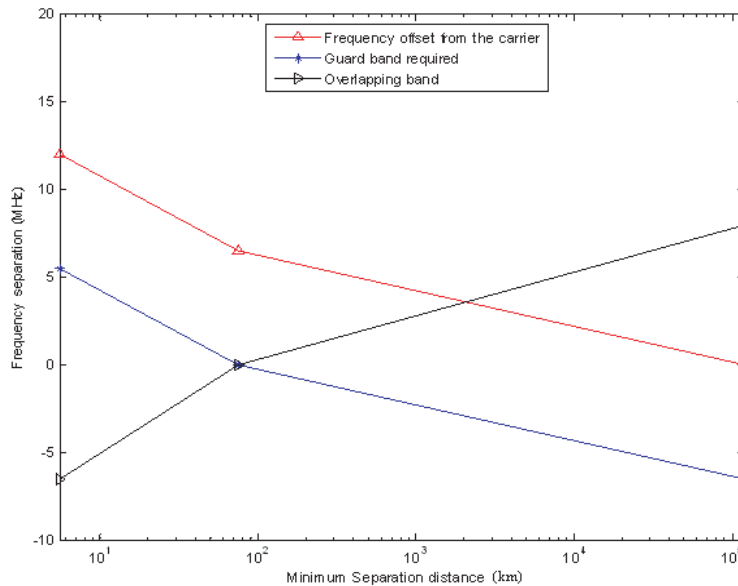
Figure 4: The minimum separation distance versus frequency separation (WiMAX $BW = 5\,\text{MHz}$).

6. CONCLUSION

It is difficult to share the same frequency channel between IMT-Advanced and T-DVB services without mitigation techniques due to high separation distance (which is considered impractical) required to satisfy coexistence requirements. Methods for enabling the coexistence of both systems would be inevitable especially at small geographical offset between two systems and at co-channel, 1st and 2nd adjacent channels frequencies. More coexistence studies between mobile and T-DVB services at 790–862 MHz are recommended.

REFERENCES

1. ITU-R M.1645, Framework and Overall Objectives of the Future Development of IMT 2000 and Systems Beyond IMT 2000, 2003.

2. Mihovska, A. and R. Prasad, "Secure personal networks for IMT-advanced connectivity," *Wireless Personal Communications*, Vol. 45, No. 4, 445–463, Springer, 2008.

3. IST-4-027756 WINNER II D 5.10.1. "The WINNER role in the ITU process towards IMT-advanced and newly identified spectrum," Vol. 1.0, Nov. 2007.
4. Shamsan, Z. A., L. Faisal, and T. A. Rahman, "On coexistence and spectrum sharing analysis between IMT-advanced and FWA systems," *WSEAS Transaction on Communication*, Vol. 7, No. 5, 505–515, May 2008.
5. Shamsan, Z. A., L. Faisal, S. K. Syed-Yusof, and T. A. Rahman, "Spectrum emission mask for coexistence between future WiMAX and existing fixed wireless access systems," *WSEAS Transaction on Communication*, Vol. 7, No. 6, 627–636, Jun. 2008.
6. Shamsan, Z. A., A. M. Al-Hetar, and T. A. Rahman, "Spectrum sharing studies of IMT-advanced and FWA services under different clutter loss and channel bandwidths effects," *Progress In Electromagnetics Research*, PIER 87, 331–344, 2008.
7. ITU-R Recommendation P.452-12, "Prediction procedure for the evaluation of microwave interference between stations on the surface of the earth at frequencies above about 0.7 GHz," 2005.
8. Shamsan, Z. A., L. F. Abdulrazak, and T. A. Rahman, "Co-channel and adjacent channel interference evaluation for IMT-advanced coexistence with existing fixed system," *Proceedings of 2008 IEEE International RF and Microwave Conference (RFM 2008)*, Kuala Lumpur, Malaysia, Dec. 2008.
9. Shamsan, Z. A. and T. A. Rahman, "Simulation model for compatibility of co-sited IMT-advanced and point to multipoint services," *Progress In Electromagnetics Research C*, Vol. 6, 127–144, 2009.

Wireless Tiny Mass Sensor System Based on FBAR

W. W. Cheng, **Y. Han**, **S. R. Dong**, **X. X. Han**, **S. H. Zhao**, and **H. J. Zhang**

Department of Information Science and Electronic Engineering
Zhejiang University, Hangzhou, Zhejiang 310027, China

Abstract— A new-type wireless tiny mass sensor circuit based on film bulk acoustic resonators (FBARs) with dual-path and a receiver to test the sensor circuit are designed, fabricated and tested. A pair of differential inputs of the sensor circuit, one is for sensing and the other is for reference, sense the increase of mass loading respectively and simultaneously in the same environment. Therefore, the sensor circuit can measure tiny mass on the FBAR accurately without effect of temperature. Further, the measuring results are sent to a receiver wirelessly to display a visual value to remote users.

1. INTRODUCTION

Film bulk acoustic resonator (FBAR) is generally composed of a piezoelectric thin-film-layer and two electrode-layers [1]. Because of its high Q factor, FBAR is used in wireless communication field for higher frequencies as a duplexer or a filter [2, 3], and in sensing system for high mass sensitivity and accuracy as a sensor with a proper oscillator [4, 5]. For the latter application, some novel circuits involved FBAR have been presented, which are based on printed circuit board [6], CMOS integrated circuit [2, 7], BiCMOS integrated circuit [8], even monolithical integrated circuit [4, 9]. And all of them mean that FBAR is competitive to the traditional devices.

Considering other aspects, accuracy and stabilization of measurement are disturbed by the temperature, humidity, pressure and other factors of environment, so dual-path architecture and application of programmable logic circuit compensate the error and process the data of measurement results precisely and in high speed. Moreover, the radio frequency transmitter sends the data to a receiver wirelessly and the receiver displays a visual value which represents the resonant frequency of FBAR which correspond to the mass to be measured to remote users.

2. THEORY AND MODEL

The MBVD (Modified Butterworth Van Dyke) equivalent circuit of FBAR is shown in Fig. 1, which includes a static capacitor C_0 and its loss R_0, mechanically dynamic capacitor C_m, dynamic inductor L_m, and dynamic loss R_m [10]. So FBAR has two resonant frequencies as the serial resonant frequency f_s which is set by Equation (1) and the parallel resonant frequency f_p which is determined by Equation (2) [4],

$$f_s = \frac{1}{2\pi\sqrt{L_m C_m}} \tag{1}$$

$$f_p = \frac{1}{2\pi\sqrt{L_m \frac{C_m C_0}{C_m + C_0}}} \tag{2}$$

where L_m is the motional inductance, C_m is the motional capacitance, C_0 is the clamped capacitance, and R_m is the motional resistance of FBAR. And the L_m and C_m account for f_s, whereas L_m, C_m, and C_0 account for f_p.

Then it is a narrow frequency band between f_s and f_p, in which the FBAR behaves like an inductor with high Q factor. Thus, this characteristic leads to the function of tiny mass sensing. When mass loading on FBAR sensor increases, f_s and f_p decrease, and this corresponding relationship is the base of mass measurement; furthermore, a typical FBAR studied in this work resonates in its fundamental thickness shear mode at around 2 GHz with the small size, and this means a high mass sensitivity in order to detect tiny mass change [11].

3. FABRICATION

The FBAR consists of a thin piezoelectric film sandwiched by two metal electrodes. For its fabrication process being compatible with standard CMOS technology, there are two main structures shown in Fig. 2, which are back-etching bulk silicon structure [12] and air gap structure [13]. In

practice, the resonance characteristics of FBAR device are similar to quartz crystals with one series resonant frequency and one parallel resonant frequency. Its Q factor is mainly determined by the electrode material and the thickness, area, surface roughness, stress, and crystal orientation of the piezoelectric material [13–17].

FBAR based on air bag reflector is fabricated on the silicon wafer, shown in Fig. 3(a). FBAR resonator curve is measured and shown in Fig. 3(b). Its resonating frequency is not very located at the designed range. Owing to no equipment to adjust resonating frequency and according process, we can not finish FBAR oscillator as design, and we extracted FBAR parameters in the model MBVD.

4. CIRCUITS DESIGN

On account of the advantages above, a novel wireless tiny mass sensor circuit based on film bulk acoustic resonators is designed, which is shown in Fig. 4. There are two FBAR oscillator circuits; the upper one for sensing varies its resonant frequency with mass loading change and the factors of environment, while the nether one for reference varies its resonant frequency only with the factors of the same environment. After the signals from FBAR oscillator circuits are amplified and divided in frequency, they come into the programmable logic circuit and subtract to get the difference between sensing value and reference value. Then this difference signal demonstrating the increase or the decrease of mass loading is modulated by radio frequency transmitter and sent to receiver through the antenna.

Thus, a receiver is designed, in Fig. 5, to receive the modulated difference signal to be demodulated by radio frequency receiver and to be processed by the programmable logic circuit. Finally, the value of frequency representing the mass loading is displayed to the remote users. Fig. 6 is the photo of the wireless sensor circuit and receiver system.

5. TESTING RESULTS

See the wireless sensor circuit and receiver system in Fig. 6, and the testing results are shown in Table 1. In fact, the minimum shifting frequency can decrease to the level below $1\,\mathrm{kHz}$, and it
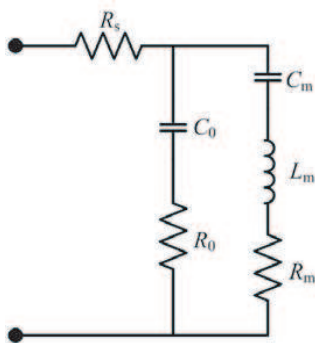
Figure 1: MBVD model.
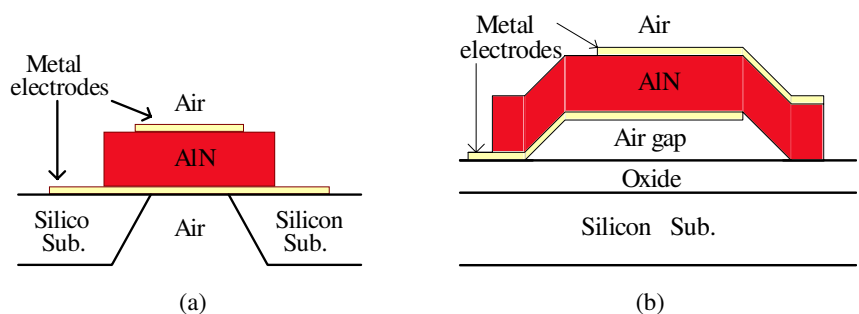
Figure 2: Cross-section of the FBAR. (a) Bottom etching structure. (b) Air gap structure.
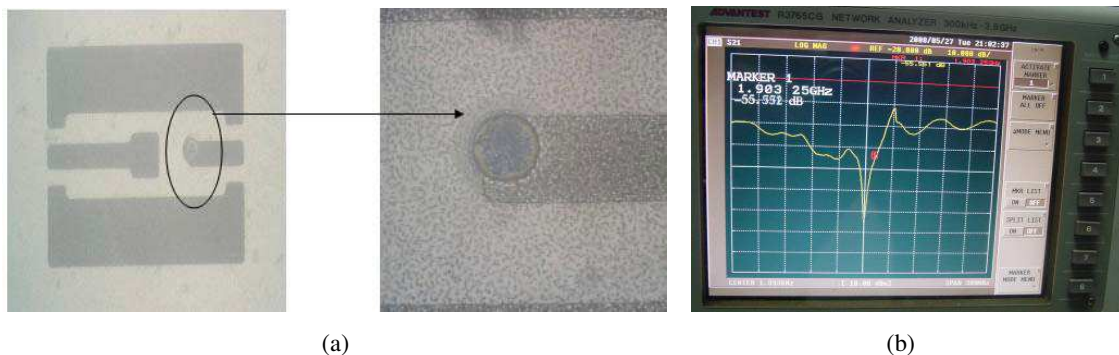
Figure 3: Chip-photo and measured resonator frequency of FBAR.
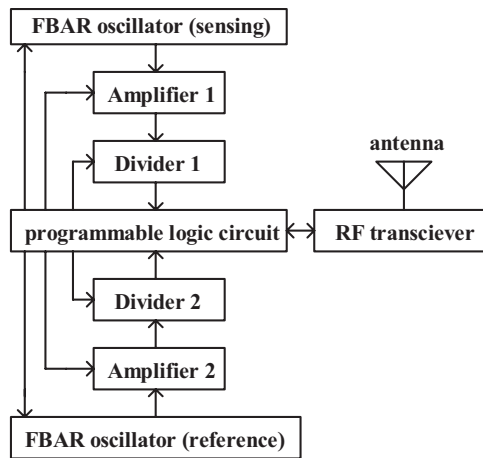
Figure 4: Wireless sensor circuit.
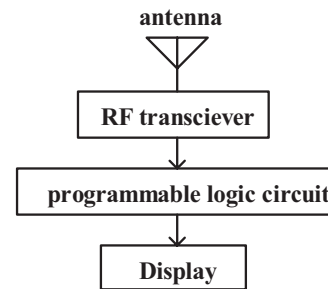
Figure 5: Receiver.
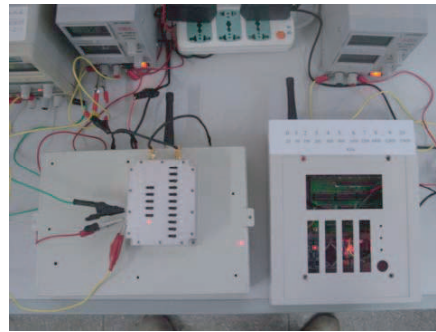
Figure 6: Wireless sensor circuit and receiver system photo.

Table 1: Specifications of the wireless tiny mass sensor system.

Parameter	Typical	Absolute Maximum	Absolute Minimum	Unit
Input Frequency		2.4		GHz
Input Amplitude	0	5.5	−4	dBm
Supply Voltage	5	7	4	V
Distance between Transmitter and Receiver		100 (indoor without block) 800 (outdoor without block)		m
Resolution of Display			3	kHz
Range of Error of Display		2		kHz
Range of Display	0∼2.4			GHz
Time of Response		0.75	0.3	s

owes to the high Q factor of FBAR and the dual-path structure which avoids the error of the mass measurement effectively.

6. CONCLUSIONS

A new wireless tiny mass sensor system has been designed, and the dual-path architecture with dividers compensates the interference of environment. In fact, comparing with previous dual-path architecture with mixers, this one with dividers and programmable logic circuits has realized that the sensing data is processed in number field instead of frequency field avoiding the effect of the harmonic frequencies produced in mixers.

Moreover, the wireless sensor circuit and the receiver can be developed to wireless sensor net-

works for greater application.

REFERENCES

1. Benes, E., M. Groschl, W. Burger, et al., "Sensors based on piezoelectric resonators," *Sensors and Actuators A-Physical*, Vol. 48, No. 1, 1–21, 1995.

2. Fang, C. M., P. Y. Chen, Y. C. Chin, et al., "Design and microfabrication of innovated FBAW filters based on an OOK receiver using 0.18 μm CMOS technology," *IEEE International Conference of Nano/Micro Engineered and Molecular Systems*, 100–105, Bangkok, Thailand, Jan. 2007.

3. Satoh, Y., T. Nishihara, T. Yokoyama, et al., "Development of piezoelectric thin film resonator and its impact on future wireless communication systems," *Japanese Journal of Applied Physics Part 1-Regular Papers Brief Communications & Review Papers*, Vol. 44, No. 5A, 2883–2894, 2005.

4. Zhang, H. and E. S. Kim, "Micromachined acoustic resonant mass sensor," *Journal of Micro-electromechanical Systems*, Vol. 14, No. 4, 699–706, 2005.

5. Norling, M., J. Enlund, I. Katardjiev, et al., "Oscillators based on monolithically integrated AlN TFBARs," *IEEE Transactions on Microwave Theory and Techniques*, Vol. 56, No. 12, 3209–3216, 2008.

6. Zhang, H., J. Kim, W. Pang, et al., "5 GHz low-phase-noise oscillator based on FBAR with low TCF," *13th International Conference on Solid-State Sensors, Actuators and Microsystems*, 1100–101, Seoul, South Korea, Jun. 2005.

7. Aberg, M., M. Yimaula, M. Ylilammi, et al., "A low noise 0.9 GHz FBAR clock," *23rd Norchip Conference*, 29–37, Oulu, Finland, Nov. 2005.

8. Aissi, M., E. Tournier, M. A. Dubois, et al., "A 5 GHz above-IC FBAR low phase noise balanced oscillator," *IEEE Radio Frequency Integrated Circuits Symposium (RFIC)*, 37–40, San Francisco, CA, USA, Jun 2006.

9. Norling, M., J. Enlund, I. Katardjiev, et al., "A 2 GHz oscillator using a monolithically integrated AlN TFBAR," *2008 IEEE MTT-S International Microwave Symposium Digest*, 1105–1108, Atlanta, GA, USA, Jun. 2008.

10. Larson, J. D., P. D. Bradley, S. Wartenberg, et al., "Modified Butterworth-Van Dyke circuit for FBAR resonators and automated measurement system," *Proceedings 2000 IEEE Ultrasonics Symposium*, 863–868, San Juan, Puerto Rico, USA, Oct. 2000.

11. Wingqvist, G., V. Yantchev, and I. Katardjiev, "Mass sensitivity of multilayer thin film resonant BAW sensors," *Sensors and Actuators A-Physical*, Vol. 148, No. 1, 88–95, 2008.

12. Chee, Y. H., A. M. Niknejad, and J. Rabaey, "A sub-100 μW 1.9 GHz CMOS oscillator using FBAR resonator," *Digest of Papers, 2005 Radio Frequency Integrated Circuits Symposium (RFIC)*, 123–126, Long Beach, California, Jun. 2005.

13. Ostman, K. B., S. T. Sipila, I. S. Uzunov, et al., "Novel VCO architecture using series above-IC FBAR and parallel LC resonance," *IEEE Journal of Solid-State Circuits*, Vol. 41, No. 10, 2248–2256, 2006.

14. Lin, A., H. Yu, M. S. Waters, et al., "Explosive trace detection with FBAR-based sensor," *21st IEEE International Conference on Micro Electro Mechanical Systems (MEMS 2008)*, 208–211, Tucson, AZ, Jan. 2008.

15. Yu, Y., T.-L. Ren, and L.-T. Liu, "High quality silicon-based ALN thin films for MEMS application," *Integrated Ferroelectrics*, Vol. 69, 367–374, 2005.

16. Park, Y., E. K. Kim, T. Y. Lee, et al., "The modeling and fabricating of film bulk acoustic resonators using sputtered PZT films with various thickness," *Integrated Ferroelectrics*, Vol. 66, No. 12, 187–194, 2004.

17. Dubois, M.-A., J.-F. Carpentier, P. Vincent, et al., "Monolithic above-IC resonator technology for integrated architectures in mobile and wireless communication," *IEEE Journal of Solid-state Circuits*, Vol. 41, No. 1, 7–16, 2006.

Investigation of Low Altitude Air-to-Ground Channel over a Tropical Sea Surface at C Band

Yee Hui Lee and Yu Song Meng

School of Electrical and Electronic Engineering, Nanyang Technological University, Singapore

Abstract— This paper investigate a low altitude air-to-ground channel over a sea surface in the tropical region at C band. It is found that, compared to a high altitude air-to-ground channel where a free space propagation condition can be assumed, the sea surface reflection and other multipath propagation phenomena for lower altitude air-to-ground channel can readily be observed. Therefore, for low altitude flight paths, spatial diversity at the ground station can be used to overcome signal degradation.

1. INTRODUCTION

Due to the rapid increase in aircraft density, the current air traffic control (ATC) system that operates at VHF band is fast becoming saturated. Therefore, an alternative frequency band is introduced for traffic control communication systems in order to satisfy this increasing demand. At present, C band is assigned for Microwave Landing System (MLS) in aviation navigation. In order to optimize the MLS performance at C band, thorough air-to-ground channel measurement in order to perform characterization is important.

Matolak et al. [1] started an interesting piece of research work on wireless channel characterization for the 5 GHz MLS system in 2007. They covered the characterization of both small and large size airports, mainly using wideband characterization. In addition to this work, Tu et al. [2] conducted a comparative study of the conventional VHF system and the MLS C band system. The focus of both studies [1, 2] concentrates on the propagation over land environments. However, little research work is done on the study of the air-to-ground link over a sea surface at C band. The evaporation duct is a well recognized form of propagation mechanism that can result in a substantial increase in signal strength when signals of frequencies above 3 GHz propagate over-water paths [3]. Therefore, there is interest in the investigation of the air-to-ground link near to a tropical ocean. These results are important to modern military and commercial applications for a seashore country such as Singapore.

As a continued work of our previous studies [4, 5]; C band channel characterization at a small airport [4], and air-to-ground channel investigation over a sea surface at high airborne altitude (20 kft to 40 kft) [5], in this study, a series of air-to-ground channel measurements at low airborne altitudes (1.2 kft to 6 kft) are conducted over the sea surface in the tropical region. The main objective of this paper is to report on the preliminary study of the spatial diversity at the ground station for the improvement of signal quality of the communication links. This is helpful for future research work in this area.

2. MEASUREMENT CAMPAIGNS

Wideband channel measurements with low airborne altitudes were conducted at 5.69 GHz over the South China Sea in February, 2009. The system hardware is upgraded and improved as compared to the previous one in [4, 5]. A vertically polarized, omni-directional blade antenna is mounted on an aircraft. The Effective Radiated Power (ERP) from the blade antenna is 40 dBm. One of popular spread spectrum techniques, maximal-length pseudo-noise (PN) sequences ("m-sequences") is implemented at the transmitter as in [1] and [6]. In our measurement, a 511-bit PN sequence is transmitted at 20 Mchips/s data rate and modulated with Binary Phase Shift keying (BPSK). This allows for a spatial resolution of 15 m and a high processing gain relative to the sounding in [1, 6]. During the flight, GPS data was logged continuously through GPS modem installed on the aircraft throughout the experiment so as to obtain instantaneous altitude, longitude, latitude, pitch and roll coordinates of the moving aircraft.

At the receiver, two identical directional antennas with a beamwidth of 20° in azimuth and 25° in elevation as shown in Figure 1(a) are used to create diverse receptor as shown in Figure 1(b). The received signals are amplified and down-converted to an intermediate frequency (IF) of 22 MHz, and then recorded by a GPS time-stamped data logger at 100 Msample/s. Details of the data logger and its performance can be obtained in [7]. The total gain of each front end of the receiver

is 84.5 dB. All the data recorded are time stamped with the GPS time in order to synchronize the data collected with the aircraft location.

The reception site (1°20'07"N, 104°01'16"E), as shown in Figure 1(c) is directly at the coast. The site is selected in order to ensure that the propagation is mainly over the sea surface and there is no blockage of the propagation signal. During the measurements, the on-site weather condition is recorded by a portable weather station, WeatherHawk, as shown in Figure 1(d).

(a) Close view of the antenna

(b) Far view of the spatial diversity

(c) Landscape in front of antennas

(d) Portable weather station, WeatherHawk
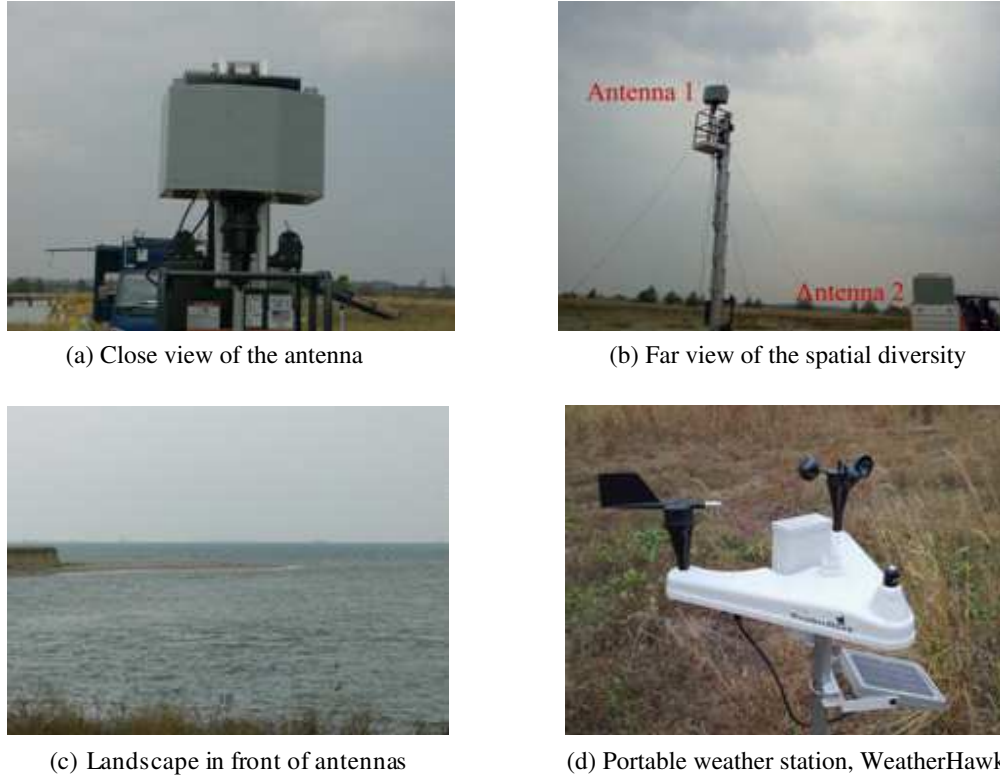
Figure 1: View of the directional antenna, spatial diversity, and environment.

3. RESULTS ANALYSIS

3.1. Sea Surface Reflection

The measured signal is down-converted to its baseband signal via a software program. The baseband signal then undergoes cross-correlation with a copy of the known original 511-bit PN sequence. This will produce the complex channel impulse response $h(\tau)$ as

$$h(\tau) = \sum_{k=0}^{M} a_k \exp(j\varphi_k)\delta(\tau - \tau_k) \tag{1}$$

where a_k, τ_k, and φ_k are the signal strength, the propagation delay and the phase shift of the kth multipath component. M is the number of multipath clusters. The power delay profile is the envelope of the received power and is proportional to $|h(\tau)|^2$. Examples of the measured power delay profile are shown in Figure 2.

From Figure 2, there is several multipath components in the air-to-ground channel at lower flight altitude (1.2 kft) as compared to results at the higher flight altitude (10 kft). This might be due to the sea surface induced reflection. Our experimental results show that, as the flight altitude is low, there is a higher probability for the appearance of multipath components. This multipath component can degrade the signal quality.

3.2. Diversity at Reception

In order to improve the quality of the communication link for the air-to-ground channel, spatial diversity at the reception as in Figure 1(b) is examined. Figure 3(a) shows the typical results for the synchronized signal to noise ratio (SNR) at the two branches when the flight altitude is about

(a) Power delay profile at 10 kft (Calibration altitude)   (b) Power delay profile at 1.2 kft
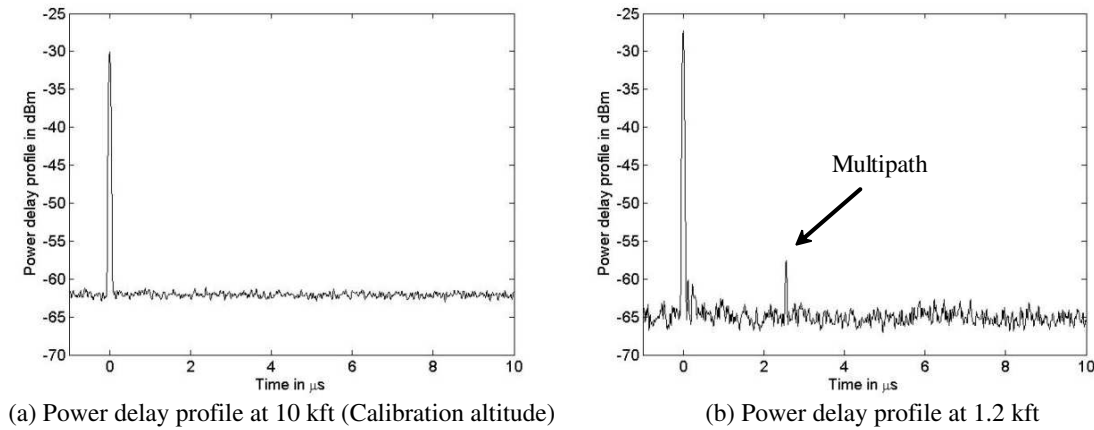
Figure 2: Examples of the power delay profile at different altitudes over sea surface.

1.2 kft, where there is a high probability of the signal degradation due to the multipath component. The results in Figure 3(a) show that the diversity effect is obvious at the diverse receptors. A selective combining is implemented and the results shown in Figure 3(b). As shown in Figure 3(b), selective combination can improve the link performance for the air-to-ground channel at lower flight altitude.

(a) Received signal to noise ratio at two branches   (b) CDF
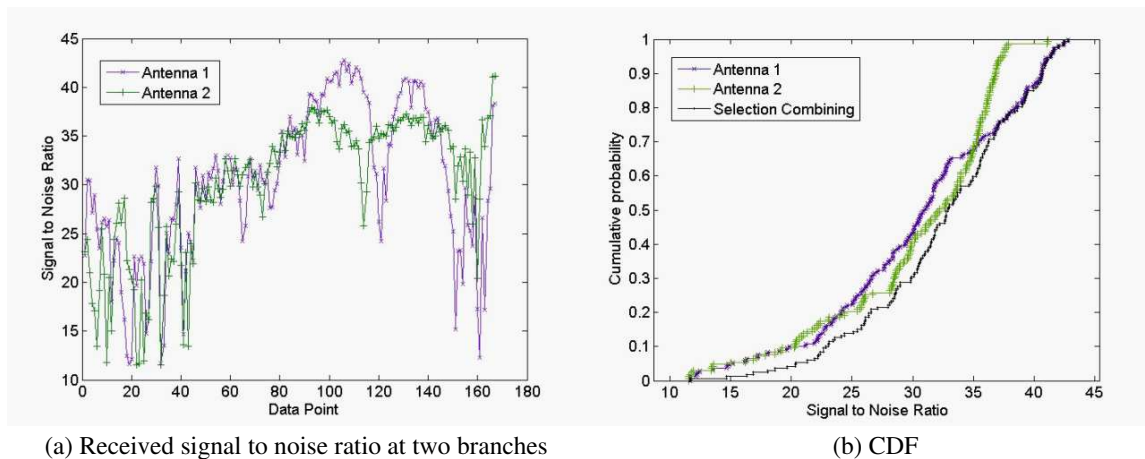
Figure 3: Examples of the signal to noise ratio for the two branches at 1.2 kft, and with selection combining scheme applied.

4. CONCLUSIONS

This paper presents a preliminary study of the air-to-ground channel over the sea surface at low flight altitude. A measurement campaign conducted in February 2009 over the South China Sea is presented. From the results, it is observed that, sea surface reflection can occur especially when the flight altitude is low. This multipath component can degrade the quality of the propagating signal. Therefore, a popular fading mitigation technique, spatial diversity is applied at the receiver side, and found to improve the communication link significantly.

REFERENCES

1. Matolak, D. W., "Wireless channel characterization in the 5 GHz microwave landing system extension band for airport surface areas," Final Project Report, NASA CR-2007-214456, May 2007.

2. Tu, H. D, S. Shimamoto, and J. Kitaori, "A proposal of a wide band for air traffic control communications," *Proceedings of IEEE Wireless Communications and Networking Conference*, 1950–1955, Las Vegas, USA, March–April 2008.

3. Hitney, H. V. and L. R. Hitney, "Frequency diversity effects of evaporation duct propagation," *IEEE Trans. Antennas and Propagation*, Vol. 38, No. 10, 1694–1700, October 1990.

4. Meng, Y. S., Y. H. Lee, and Y. H. Heng, "Channel characterization and modeling in C band for a small airport," *Proceedings of Eleventh URSI Commission F Triennial Open Symposium on Radio Wave Propagation and Remote Sensing*, 113–117, Rio de Janeiro, Brazil, October–November 2007.

5. Lee, Y. H., Y. S. Meng, and Y. H. Heng, "Experimental characterizations of an air to land channel over sea surface in C band," *Proceedings of XXIXth URSI General Assembly*, Chicago, USA, August 2008.

6. Rice, M., A. Davis, and C. Bettweiser, "Wideband channel model for aeronautical telemetry," *IEEE Trans. Aerospace and Electronic Systems*, Vol. 40, No. 1, 57–69, January 2004.

7. Meng, Y. S. and Y. H. Lee, "Practical wideband channel sounding system for air-to-ground measurements at C band," *Proceedings of IEEE International Instrumentation and Measurement Technology Conference*, Singapore, May 2009.

Realization of Ramp and Stair-step Patterns from the Rectangular Wave-guide Arrays

A. Sudhakar[1] and Y. V. Narayana[2]

[1]Department of ECE, RVR & JC College of Engineering, Chowdavaram, Guntur-522019
Andhra Pradesh, India
[2]Tirumala Engineering College, Jonnalagadda (PO), Narasaraopet-522601, Guntur (Dist)
Andhra Pradesh, India

Abstract— Antenna arrays are highly useful for the generation of narrow beams and other desired beam shapes. Any pattern obtained from antenna array consists of one major lobe followed by number of minor lobes. When an array is sufficiently large enough, the width of main beam becomes very small and is useful in point to point communication. However, it is required to design such arrays to produce the shaped beams in terms of beam width, side lobe levels. Different approaches like space distribution, amplitude control and phase excitations are employed in order to obtain the desired beam shapes. The amplitude control method can be used to produce desired beam shapes but it is not found to be suitable for fast scanning applications. Although, Fourier transform method, Chebyshev and Woodward methods are common techniques, they yield only approximate patterns. The space controlled technique also used to produce the same but it is not possible to obtain precise space functions. The phase only controlled technique is found to be the most suitable to produce optimized beam shapes and for scanning purposes with digital phase shifters. In view of the above considerations, the phase only control method is proposed to be used in the present work for obtaining any desired beam shape. In the present technique, a low side lobe narrow beam is converted into a ramp and stair-step patterns by introducing additional non-linear phase distribution which allows a fast scanning of the beam without moving antenna structure. Pencil beams are widely used for point to point communications as well as high resolution radars. Ramp patterns have the applications similar to those of pencil beams. Stair-step patterns are popularly used to identify more than one target moving in different altitudes and different angular regions. In this paper, ramp and stair-step patterns are generated from arrays of rectangular waveguides. The data on the variation of field strength as a function of $u(\sin\theta)$ for both small and large arrays over specified angular sectors is computed.

1. INTRODUCTION

A very popular and common radiator is a rectangular wave-guide which can be used to produce linearly polarized electromagnetic fields. For the synthesis of shaped beams from arrays of such wave-guides [1–5], it is also desirable to obtain a pattern of individual element. The element pattern of wave-guide is a function of wall dimensions. The formulations made in this paper are valid at any operating frequency. The optimized beam shapes particularly ramp and stair-step patterns are generated from array of rectangular wave guides. The approach adopted is phase only control technique. When the phase shift is progressive for each element in the array, it is very difficult to obtain the desired beam shape. It results in only tilting the beam which is not of our present interest. In view of this, analytical and numerical techniques are applied for realization of ramp and stair-step patterns. This technique is universal in the sense that the array of any length of any number of elements can be designed effortlessly for specified beam shape over desired angular region. The method consists of the use of stationary phase concept and energy relations [6, 7] between excitation domain and far field domain. These concepts are used to design the phase distribution function for fixed amplitude distributions.

2. ELEMENT PATTERN OF THE OPEN-ENDED WAVE-GUIDE

Consider an open ended rectangular wave-guide with its coordinate system as shown in Fig. 1. It is assumed that the dimensions a and b are chosen so that only TE_{10} mode will propagate.

The linear current densities on the surface are given by

$$\hat{K} = \hat{a}_z \times \hat{H} \tag{1}$$

and

$$\hat{K}_m = \frac{-1}{\mu_o} \left(\hat{a}_z \times \hat{E} \right) \tag{2}$$
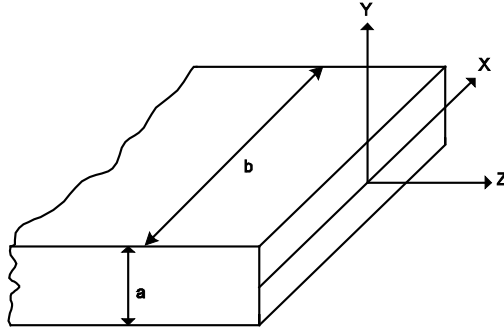
Figure 1: Open ended rectangular wave-guide.

with the present of a hole free infinite ground plane, the method of images can be invoked. It is obvious that the image of $\hat{K} = \hat{a}_z \times \hat{H}$ is counter directed and the image of $\hat{K}_m = \frac{-1}{\mu_o}(\hat{a}_z \times \hat{E})$ is co directed. As a result, the radiation pattern in $Z > 0$ can be deduced solely from the magnetic linear current distribution $(\frac{-2}{\mu_o})(\hat{a}_z \times \hat{E})$ in the mouth of the waveguide.

When the origin of coordinates are taken at the middle of a transverse cross section rather than at a corner, the electric field of the incident TE_{10} mode is expressed in the form

$$E_y^i = c \cos\left(\frac{\pi x}{b}\right) e^{j(\omega t - \beta_{10} z)} \tag{3}$$

If Γ is the reflection coefficient for the TE_{10}, the back scattered wave is given by

$$E^r = \Gamma c \cos\left(\frac{\pi x}{b}\right) e^{j(\omega t + \beta_{10} z)} \tag{4}$$

The total field in the waveguide mouth is

$$E_T = \hat{a}_y c' \cos\left(\frac{\pi \xi}{b}\right) \tag{5}$$

at a source point (ξ, η, o). Here $c' = c(1 + \Gamma)$.

From the above relations, we have

$$\hat{K}_m = \left(\frac{2ax}{\mu_0}\right) c' \cos\left(\frac{\pi \xi}{b}\right) \tag{6}$$

From the generic integral forms [2], after simplification we get

$$F_\theta(\theta, \phi) = \frac{4\pi abc' \cos\theta \cos\phi}{\mu_0} \frac{\cos(\pi x)\sin(\pi y)}{(\pi^2 - 4(\pi x)^2)\pi y} \tag{7}$$

$$F_\phi(\theta, \phi) = \frac{-4\pi abc' \sin\phi}{\mu_0} \frac{\cos(\pi x)\sin(\pi y)}{(\pi^2 - 4(\pi x)^2)\pi y} \tag{8}$$

In which

$$x = \left(\frac{b}{\lambda}\right) \sin\theta \cos\phi \tag{9}$$

$$y = \left(\frac{a}{\lambda}\right) \sin\theta \sin\phi \tag{10}$$

Making use of the relation between E and electrical vector potential F

$$E = -\nabla \times F \tag{11}$$

The radiated field, the normalized ϕ component of the electric field is reduced in the following form

$$E_\phi(\theta) = \pi^2 \cos\theta \frac{\cos\left[(\pi b/\lambda)\sin\theta\right]}{\pi^2 - 4\left[(\pi b/\lambda)\sin\theta\right]^2} \tag{12}$$

On the other hand, in the YZ plane, where $\phi = 90°$, the normalized θ component is given by

$$E_\phi(\theta) = \frac{\sin\left[(\pi a/\lambda)\sin\theta\right]}{(\pi a/\lambda)\sin\theta} \tag{13}$$

3. SYNTHESIS OF PHASE FUNCTION FOR DESIRED BEAM SHAPES

For the linear array of discrete radiators under consideration, the radiation pattern is given by

$$E(u) = \sum_{n=1}^{N} a(x) e^{\frac{j2\pi L}{\lambda}(ux+\phi(x))} \tag{14}$$

where $x = \frac{2n-1-N}{N}$; $\phi(x) = $ Phase function.

Let the pattern function be represented by

$$E_d(u) = K e_d(u) \tag{15}$$

For linear array of rectangular waveguides, the expression for resultant pattern $E_r(u)$ assumes the following form.

$$E_r(u) = K f(u) e_d(u) \tag{16}$$

$f(u)$ is the element pattern formulated in Section 2.

Using the above expression and energy relations involving definite integrals the constant K is obtained.

The energy relation equation is given by

$$\frac{L}{\lambda} \int_{u_1}^{u} \left| E(u)^2 \right| du = \int_{x_1}^{x} a^2(x) dx \tag{17}$$

By using the concept of stationary phase [6, 7], we get

$$\frac{\partial}{\partial x} \left[ux + \phi(x) \right] = 0 \tag{18}$$

This gives

$$u = -\frac{\partial \phi}{\partial x} \tag{19}$$

Using the value of the constant K and the expressions (16) and (17), the relation between u and x is obtained.

The evaluation involves the determination of integral on the right hand side of Equation (17) for a particular value of x and then varying the upper limit u of the left side integral of the same equation till the equation is satisfied. This method is repeated for different values of x in order to obtain u as a function of x.

From Equation (18), the first order differential equation is solved for finding out $\phi(x)$ for a specified pattern shape.
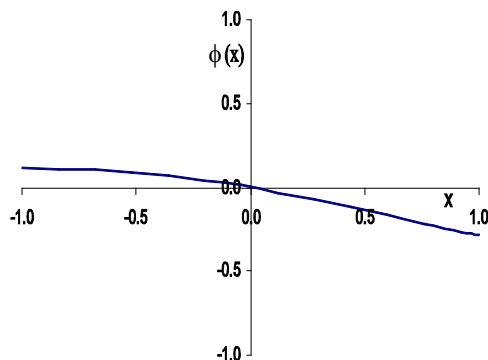
Figure 2: Phase function variation for positive ramp pattern.
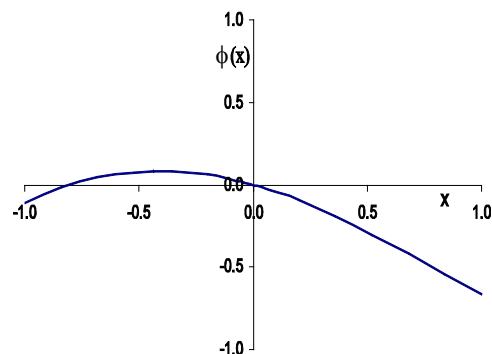
Figure 3: Phase function variation for stair-step pattern.
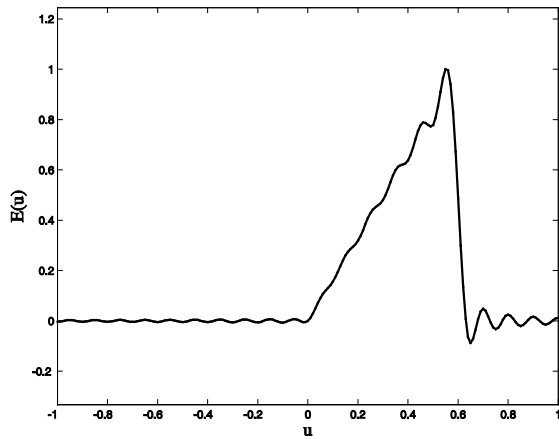
Figure 4: Normalized radiation ramp pattern for array length 20.
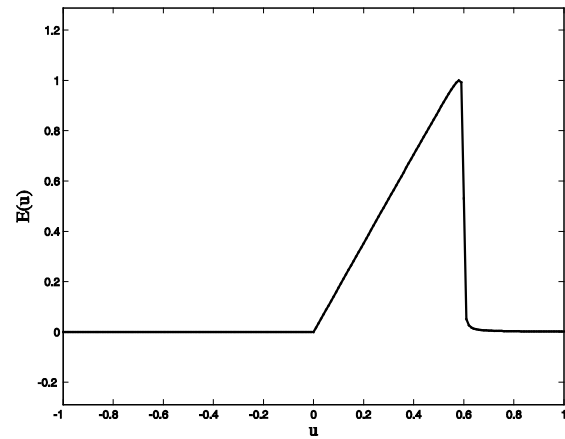
Figure 5: Normalized radiation ramp pattern for array length 200.
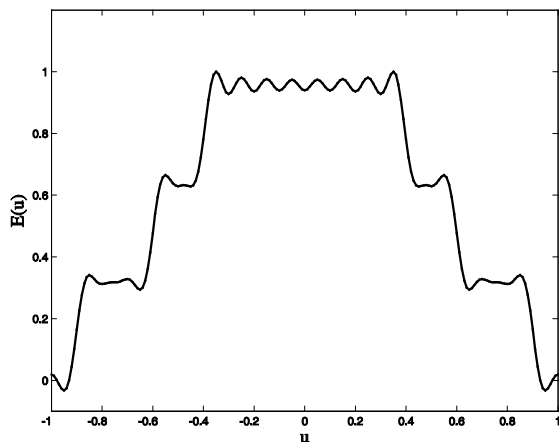
Figure 6: Normalized radiation stair-step pattern for array length 20.
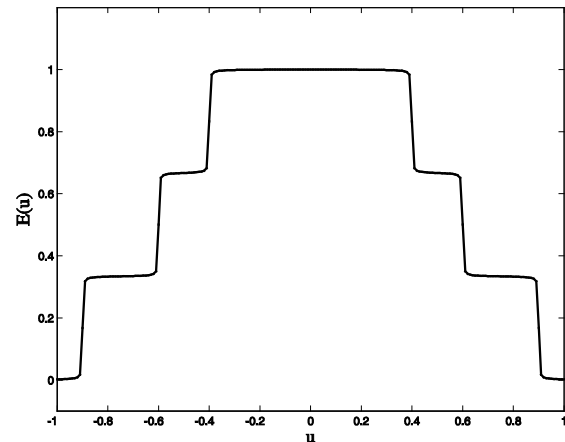
Figure 7: Normalized radiation stair-step pattern for array length 200.

4. RESULTS AND CONCLUSIONS

Using the procedure in above section, the variations of normalized phase function for ramp and stair step patterns over desired angular sectors are evaluated and presented in Figs. 2 and 3. Introducing the respective phase distribution for a fixed cosine on pedestal amplitude distribution, the resultant radiation patterns realized from elements of rectangular waveguides are shown in Figs. 4–7.

The resultant phase distribution is found to be non-linear and the nature of non linearity is different for ramps and stair steps. Moreover, they are also non symmetric to the center of the array. It is obvious from the results phase only control method considered in the present work becomes exact for larger arrays and there exists a deviation from the desired shape from small arrays. The patterns of very small arrays have some ripple components in the desired angular sectors and also in the trade off region. On the other hand they are found to be smoothened out in larger arrays.

REFERENCES

1. Ma, M. T., *Theory and Applications of Antenna Arrays*, John Wiely and Sons, NY, 1974.

2. Knittel, G. H., A. Hessel, and A. A. Oliner, "Element pattern nulls in phased arrays and their relation to guided waves," *Proc. IEEE*, Vol. 56, 1822–1836, 1968.
3. Balanis, V. C. A., *Antenna Theory: Analysis and Design*, 2nd Edition, John Wiley and Sons, 1997.
4. Pozar, D. M., *Microwave and RF Design of Wireless Systems*, John Wiley and Sons, 2001.
5. Stutzman, W. L. and G. A. Thiele, *Antenna Theory and Design*, John Wiley and Sons, 1981.
6. Olver, F. N. J., *Asymptotic and Special Functions*, Tata McGraw-Hill, New Delhi, 1974.
7. Cook, C. E. and M. Bern Field, *Radar Signals*, Academic Press, NY, 1967.

On the Design of CPW-fed Appollian Gasket Fractal Antenna

Anupam Tiwari[1] and Raj Kumar[2]

[1]Department of Applied Mathematics, Defence Institute of Advanced Technology (DU)
Girinagar, Pune-411 025, India
[2]Microwave and MM Wave Antenna Lab., Department of Electronics Engineering
Defence Institute of Advanced Technology (DU), Girinagar, Pune-411 025, India

Abstract— This paper presents Apollonian gasket CPW-fed monopole fractal antenna. The Antenna has been designed on FR4 substrate $\varepsilon_r = 4.3$ and thickness 1.53 mm. Antenna has been fabricated and tested using VNA. The experimental result shows the multiband behavior with the centre frequencies of 1.12 GHz, 4.65 GHz and 7.75 GHz with bandwidth of 50%, 19.5% and 15% respectively. The experimental radiation pattern of antenna is omni-directional at lower frequency and like electric dipole at higher frequency. This antenna can be useful for Cellular, GSM, LAN, WAN and Micro air vehicular Radar applications.

1. INTRODUCTION

The progress in wireless and dramatic development of a variety of wireless applications have remarkably increases the demand of multiband/wideband antennas with smaller dimensions than conventionally possible. Conventional microstrip antennas have attracted feature like light weight, low profile, low cost, simple to manufacture, easy to integrate with RF devices. Microstrip Patch Antenna suffers from disadvantage of narrow bandwidth, low efficiency and size. It has been reported in literature that if the size of planar antenna decreases less than $\lambda/2$, the efficiency, bandwidth, gain and polarization purity deteriorate. With growing development of small devices, the research for compact, wide bandwidth antenna has attracted researchers. Fractal, owing to their geometrical properties, has been reported in literature for miniaturization of antenna as well as for multiband and wider bandwidth [1–5]. Fractal's property of self-symmetry is utilized for multi-band and ultra wide band antennas. Puente et. al. has reported the Sierpinski gasket multiband fractal monopole antenna with probe feed [4, 5]. In this, the matching of second and third band is better than first band because current does not reach properly at the top of Sierpinski gasket. Spacing filling properties of fractal has been reported to miniaturize the antenna size [6, 7]. This paper reports the Apollonian gasket fractal antenna of small size with CPW-fed. In result, CPW-fed improves the matching at the first band with wider bandwidth in comparison to convention.

2. MATHEMATICAL MODELING

The Apollonian Gasket is probably the best known of the circle inversion fractals. It is created by iteratively carrying out circle inversions on three mutually tangent circles of the same radius. Apollonian Gasket Fractal is made by three mutually tangent circles, and draw the inner Soddy circle (red). Then draw the inner Soddy circle of this circle with each pair of the original three, and continue iteratively. Surrounding the three initial circles by an outer Soddy circle and filling the additional gaps with inner Soddy circles forms the Apollonian gasket. In this, the fractal dimension is approximately 1.3058. Intersection area of three circles leads to Apollonian zero iteration. Removing Soddy circle from zero iteration leads to Apollonian first iteration is shown as Figure 2.

3. GEOMETRY AND FABRICATION

Apollonian Gasket concept with keeping fabrication constrains, pression and connectivity factor has designed. Physical Model of Apollonian Gasket pre fractal with third iteration is made. The zero iteration is formed by intersection of three 90 mm circles and tip to tip dimension of Apollonian ideally is 45 mm bur with truncation 42 mm. First iteration is made by slotting 14 mm diameter circle from zero iteration. In the second iteration there is three circles of 4 mm diameter along with six circles of 3 mm in tangent to first circle. In the third iteration, three circles of diameter 1.5 mm and six circles of 1 mm diameter in tangent to second iteration have slotted. The antenna has been fabricated by Photolithography process on FR4 substrate of height 1.53 mm and $\varepsilon_r = 4.3$. Antenna is fed by coplanar feed of dimension 2 mm width, length of 25 mm and the gap of 0.5 mm between coplanar grounds. The advantages of CPW-fed are that radiating element and ground plane are
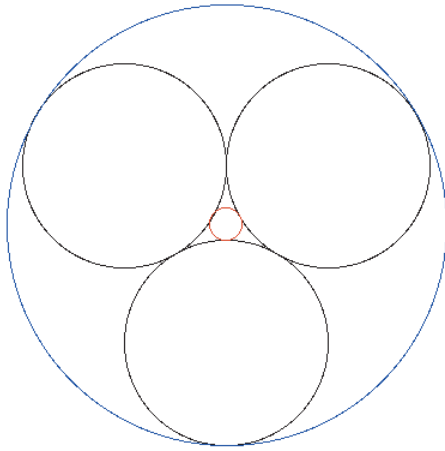
Figure 1: Ideal first iteration (centre part).
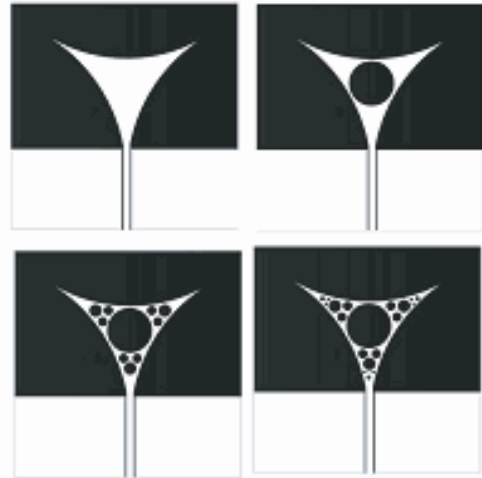
Figure 2: Apollonian Gasket 0th iteration to 3rd iteration fractal antenna.
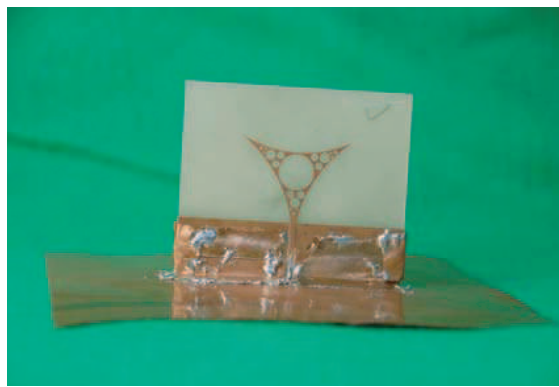
Figure 3: The photograph of apollonian Gasket CPW-fed monopole Fractal antenna.
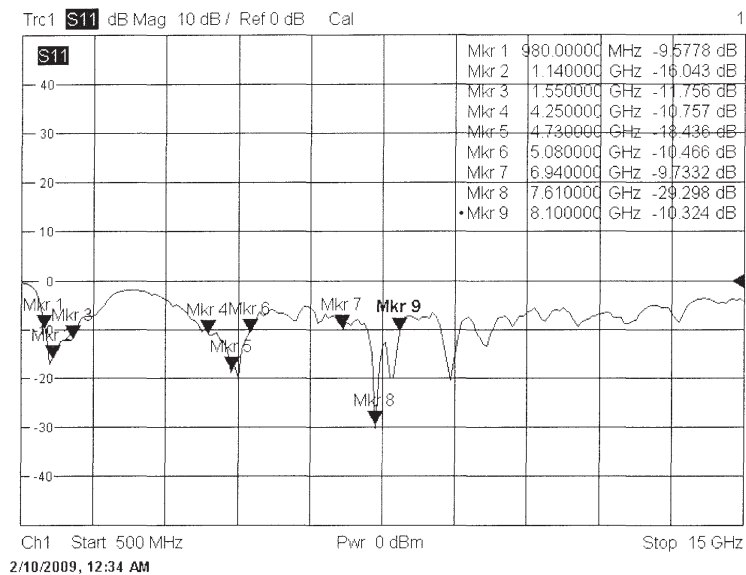
Figure 4: Experimental results of apollonian gasket fractal antenna.

at same side, no need for PTH. Dimension of one tip to another is 42 mm and height 32 mm. Apollonian Gasket CPW fed monopole antenna with various iteration are shown in Figure 3.

4. DISCUSSION AND EXPERIMENTAL RESULTS

Apollonian Gasket fractal antenna has been designed on FR4 substrate of height 1.53 mm and $\varepsilon_r = 4.3$. The photograph of Apollonian Gasket Fractal antenna with CPW-fed has been shown in Figure 3. The antenna has been fabricated and tested using VNA. The experimental result of antenna, i.e., return loss versus frequency reveals the multiband with centre frequencies of 1.265 GHz,

Table 1: Center frequency, impedance bandwidth and % fractal BW for apollonian gasket fractal antenna.

Centre Frequency	Absolute BW	% BW
1.14 GHz	570 MHz	50
4.25 GHz	830 MHz	19.5
7.6 GHz	1.1 GHZ	15
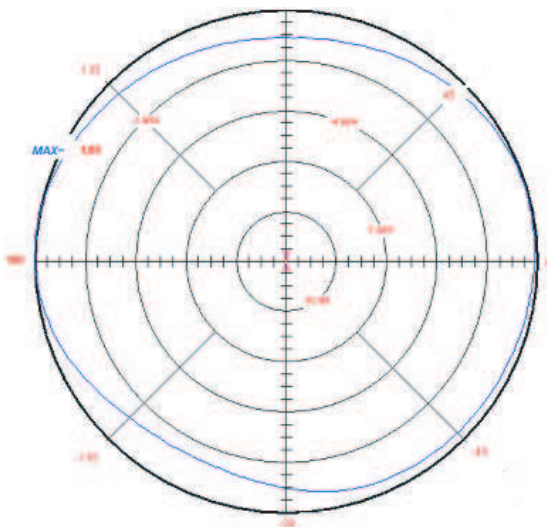
Figure 5: Experimental radiation pattern of apollonian gasket fractal antenna at 1.07 GHz.
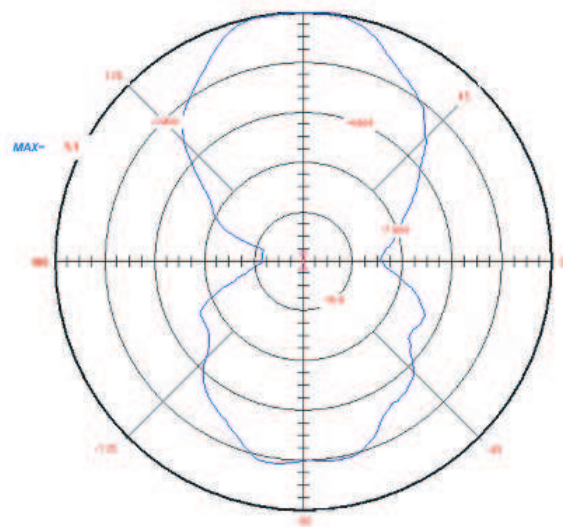
Figure 6: Experimental radiation pattern of apollonian gasket fractal antenna at 5.14 GHz.
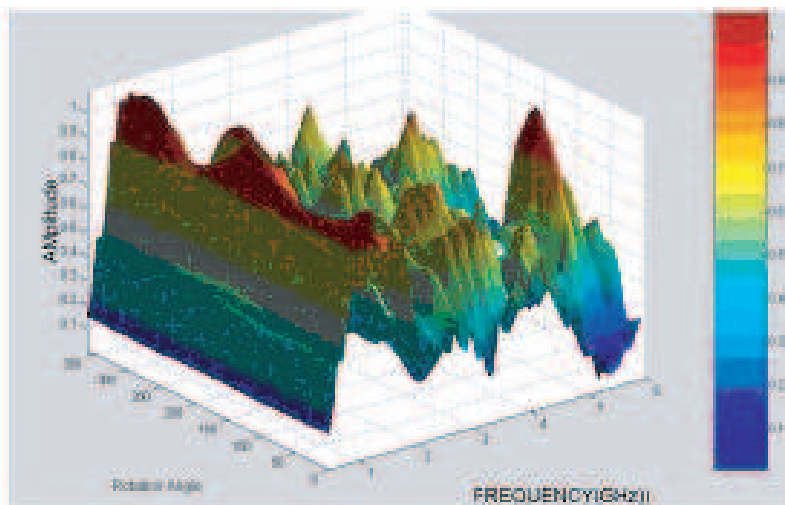
Figure 7: Experimental 3D radiation pattern Azimuth vs frequency vs. Gain amplitude from 500 MHz to 6 GHz.

4.66 GHz and 7.8 GHz respectively as shown in Figure 4. The shift in lower end frequency of first band in comparison to same dimension simple Apollonian Gasket resonant frequency 1.38 GHz indicates the size reduction. The bandwidth of the first, second and third band is 570 MHz, 830 MHz and 1100 MHz respectively. This antenna also exhibits the wider bandwidth from 4.25 to 14 GHz with return loss of better than −5 dB. Table 1 tabulates the absolute impedance bandwidth and % fractional bandwidth of Apollonian gasket fractal antenna. Such type of antenna can be useful Cellular and LAN applications.

5. EXPERIMENTAL RADIATION PATTERN

Radiation pattern of Apollonian gasket fractal antenna has been measured in anechoic chamber with antenna measurement system DC-40 GHz [8]. It has been observed that first band 980 MHz to 1.55 GHz. with a absolute impedance bandwidth of 570 MHz. The experimental radiation pattern in this band has been observed nearly omni-directional. The radiation pattern at 1.07 GHz has been shown Figure 5. The radiation pattern at higher frequency has been shown in Figure 6 at 5.14 GHz which similar to the radiation pattern of electric dipole. 3-D radiation pattern Azimuth versus frequency versus amplitude gain is shown in Figure 7.

6. CONCLUSION

Apollonian gasket fractal antenna of compact size with multi-band has been successfully demonstrated. Apollonian gasket was constructed with third iteration. The measurement results show good radiation and impedance matching characteristics at all three bands. The multi-band response of this antenna occurs in L-band, C-band to X band. The experimental radiation of the antenna is omni-direction at lower frequency and like an electric dipole at higher frequency. This antenna is compact, simple to design and easy to fabricate. Antennas of this type are attractive for GPS, PCS, imaging System and Vehicular radar.

REFERENCES

1. Werner, D. H. and R. Mittra, *Frontiers in Electromagnetics*, IEEE Press, New York, 2000.
2. Vinoy, K. J., "Fractal shaped antenna elements for wide and multi-band wireless applications," Thesis, Pennsylvania, Aug. 2002.
3. Puente, C., J. Romeu, R. Pous, and A. Cardama, "On the behaviour of the Sierpinski multi-band fractal antenna," *IEEE Transactions on Antennas and Propagation*, Vol. 46, 517–524,1998.
4. Puente, C., J. Romeu, R. Pous, and R. Bartoleme, "Perturbation of the Sierpinski antenna to allocate operating bands," *Electron. Lett.*, Vol. 32, 2186–2188, 1996.
5. Puente, C., J. Romeu, and A. Cardama, "The Koch monopole a small fractal antenna," *IEEE Transactions on Antennas and Propagation*, Nov. 2000.
6. Gianviffwb, J. P. and Y. Rahmat-Samii, "Fractal antennas: A novel antenna miniaturization technique, and applications," *Antennas Propagation Mag.*, Vol. 44, 20–36, 2002.
7. Liu, J.-C., C.-Y. Wu, D.-C. Chang, and C.-Y. Liu "Relationship between Sierpinski gasket and Apollonian packing monopole antennas," *Electronics Letter*, Vol. 42, No. 15, July 20, 2006.
8. Diamond Engineering, USA, DAMS7000, Antenna measurement System DC-40 GHz on Desk top.

A Y-Y-shaped Slot Antenna Design for an RFID Tag Designed for Metallic Tag Applications

Sung-Lin Chen and Ken-Huang Lin

Department of Electrical Engineering, National Sun Yat-Sen University, Taiwan

Abstract— This paper proposes a slot antenna for UHF RFID applications which use the metallic substrate as label carrier. The proposed metallic RFID tag directly presses out a Y-Y shape slot on the metallic foil to form an RFID tag antenna. The design methodology, simulation and measurement results of the proposed metallic RFID tag antenna are also presented in this paper. The maximum read range of the prototype metallic RFID tag can reach about 4.7 m measured with 2.0 W EIRP radiation power of RFID reader system. The low profile and low cost features make the design more suitable and applicable to metallic tag labeling system which RFID technology needs to be integrated.

1. INTRODUCTION

Radio Frequency Identification (RFID) is a technology used for objects identification and has been applied to various walks of life, such as retail, transportation, manufacturing and supply chain. An RFID solution is composed of tags, readers and information management systems. However, RFID tag is directly attached to the object or package that may make it function poorly. Particularly, when the dipole-type RFID tags adhere to metallic objects without any gap or substrate, the RFID tags do not work as usual and just exist in name only. Hence, the success of the RFID solution mainly depends on RFID tag antenna design.

In the past few years, several papers on RFID tag antenna design have been published. The dipole-type RFID tag antenna design is more common and simpler for the beginners [1–3], but it cannot be used on metallic objects. For the metallic object applications, inverted-F antenna (IFA), planar inverted-F antenna (PIFA), and patch-type antenna can all be designed for RFID applications on metallic objects [4–6]. However, the required thickness of these antenna structures all are larger than 3 mm. This fact renders these antenna structures useless on metallic tags.

In this paper, we propose a Y-Y shape slot antenna design for metallic RFID tag applications. The antenna structure and characteristics will be explained in Section 2 and Section 3 will demonstrate the simulation and measurement results of the proposed Y-Y shape slot antenna. A practical metallic RFID tag design and application that is based on the proposed design method is also presented in Section 3. Finally, we will give the conclusions in Section 4.

2. ANTENNA STRUCTURE AND CHARACTERISTICS

The proposed metallic RFID tag design is based on a Y-Y shape slot antenna that the slot can be directly pressed out on the original metallic tag. The configuration of the proposed RFID tag antenna is shown in Figure 1(a). The antenna impedance, chip impedance, and power transmission coefficient (PTC) are functions of frequency for the proposed Y-Y shape slot antenna [7]. All of them are shown in Figure 2. The antenna self-resonance frequency, f_{cAnt}, is mainly controlled by the perimeter of the Y-Y shape slot that is approximate to one wavelength. However, the RFID tag operating frequency, f_{cTag}, is determined by the frequency at which the maximum PTC occurs and it is much lower than f_{cAnt}. In the RFID tag design, not only conjugate impedance match condition between RFID chip and antenna can affect the RFID tag performance, but the gain of RFID tag antenna can also play an important role. The antenna gain of the proposed Y-Y shape slot antenna is controlled by the area of the metal tag and the width of the slot. The larger area or wider width of the slot, the higher gain we can obtain. Figures 3(a) and 3(b) show the simulation results of the antenna gain for the different metal tag areas and slot widths, respectively.

The physical dimension of the proposed Y-Y shape slot antenna is adjusted to provide sufficient impedance to match conjugate impedance of Alien RFID strap with input impedance of $(22 - j124)\,\Omega$ and sensitivity about -14 dBm at 925 MHz. For the characteristic study, a Y-Y shape slot antenna has been implemented on an FR4 substrate with thickness of 0.75 mm, relative permittivity of 4.2 and dielectric loss tangent of 0.02. The dimensional parameters of implemented slot antenna are as follows: $L = 80$ mm, $W = 50$ mm, $H = 0.75$ mm, $S_0 = 32$ mm, $S_1 = 14$ mm, $S_2 = 12$ mm, and $p = 4$ mm. A photograph of the proposed metallic RFID tag is shown in Figure 1(b).
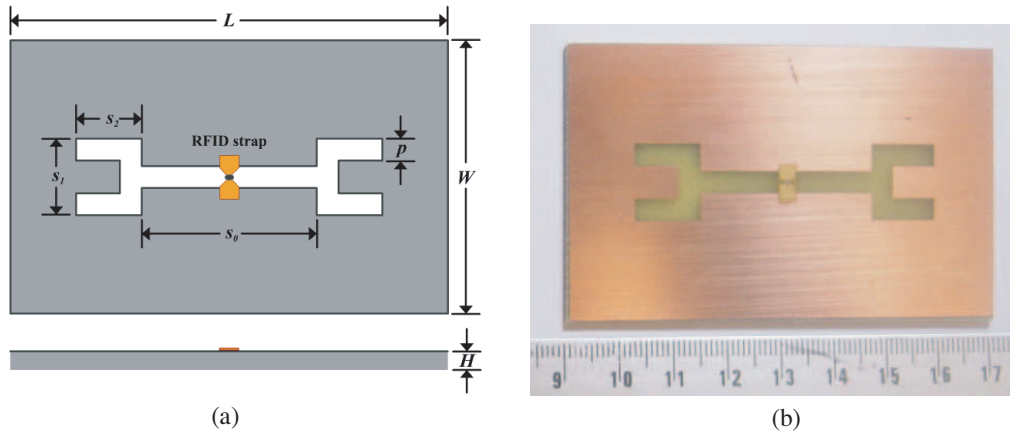
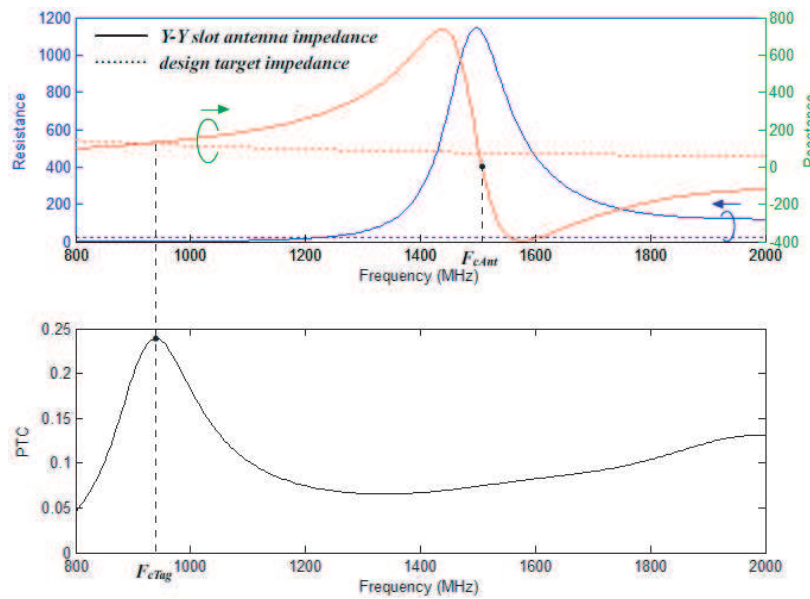Figure 1: The proposed Y-Y slot antenna. (a) Configuration, (b) prototype.

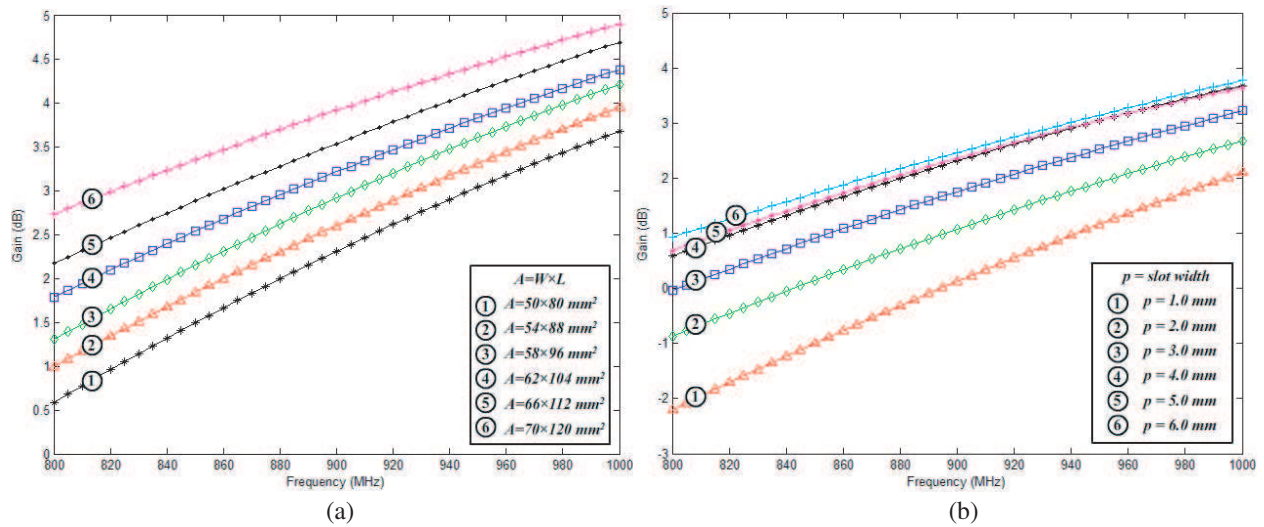Figure 2: The characteristics of the implemented Y-Y shape slot antenna.

Figure 3: The relationship between antenna gain and different parameters. (a) Metal tag area, (b) slot width.
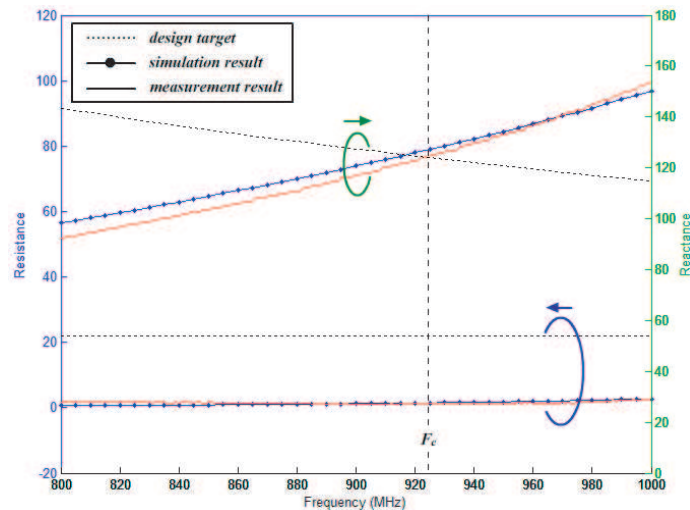
Figure 4: The relationship between antenna gain and (a) different metal tag area, (b) different slot width.

Figure 5: The photographs of a metallic RFID tag and a practical application for steel wire-rod tracking.

3. SIMULATION AND MEASUREMENT RESULTS

The antenna design is modeled and simulated using Ansoft HFSS software which allows designers to analyze antenna performance with calculated antenna impedance, gain and radiation pattern. The antenna impedance measurement was performed by using Agilent vector network analyzer ENA 5071B and the measurement platform for measuring impedance of RFID tag antenna.

The simulation and measurement results of the implemented Y-Y shape slot RFID tag antenna are shown in Figure 4 and both of them are in good agreement. In the figure, it is clear that the reactance part of the implemented antenna is close to the design target, but the resistance part is smaller than the design target. In this case, the PTC value of the implemented RFID tag is not quite satisfactory. However, the antenna gain of the implemented antenna is higher; this can redeem the low PTC condition and achieve the long read range requirement.

To verify the read range performance of the implemented RFID tag, an Impinj RFID reader system was set up with operating frequencies of 922–928 MHz, radiation power of 27.0 dBm and a circularly polarized antenna gain of 6.0 dBi. Therefore, the total transmitted power is approximately 2.0 W EIRP (Effective Isotropic Radiated Power). The maximum read range of the implemented RFID tag is about 4.7 m.

The proposed Y-Y shape slot can directly press out on the metallic foil to form a metallic RFID tag antenna. Figure 5 shows a practical application for wire-rod products tracking in steel industry that Y-Y shape slot is directly pressed out on the metallic label. In this application, the proposed metallic RFID tag design method can achieve the low profile and low cost requirements and make it more suitable and applicable to metallic RFID tag labeling system applications.

4. CONCLUSION

In this paper, we proposed a metallic RFID tag design method based on a Y-Y shape slot antenna design concept. In addition to implementing the prototype for characteristics study and verification,

a practical application for wire-rod products tracking in steel industry is also presented in this paper. The Y-Y shape slot can be directly pressed out on the original metallic foil tag, which is then mounted on the RFID chip. Hence, the requirements for low profile, low cost and easy fabrication can be achieved.

REFERENCES

1. Marrocco, G., "The art of UHF RFID antenna design: Impedance-matching and size-reduction techniques," *IEEE Antennas and Propag. Magazine*, Vol. 50, No. 1, 66–79, Feb. 2008.
2. Jeon, S. Y. Yu, and J. Choi, "Dual-band slot-coupled dipole antenna for 900 MHz and 2.45 GHz RFID tag application," *Electron. Lett.*, Vol. 42, No. 22, 1259–1260, 2006.
3. Fang, Z., R. Jin, and J. Geng, "Asymmetric dipole antenna suitable for active RFID tags," *Electron. Lett.*, Vol. 44, No. 2, 71–72, 2008.
4. Son, H. W. and G. Y. Choi, "Orthogonally proximity-coupled patch antenna for a passive RFID tag on metallic surfaces," *Microw. Opt. Technol. Lett.*, Vol. 49, No. 3, 715–717, 2007.
5. Kim, K. H., J. G. Song, D. H. Kim, H. S. Hu, and J. H. Park, "Fork-shaped RFID tag antenna mountable on metallic surfaces," *Electron. Lett.*, Vol. 43, No. 25, 1400–1402, 2007.
6. Kwon H. and B. Lee, "Compact slotted planar inverted-F RFID tag mountable on metallic objects," *Electron. Lett.*, Vol. 41, No. 24, 1308–1310, 2005.
7. Rao, K. V. S., P. V. Nikitin, and S. F. Lam, "Antenna design for UHF RFID tags: A review and a practical application," *IEEE Trans. Antennas Propag.*, Vol. 53, No. 12, 3870–3876, Dec. 2005.

On the Problem of Dielectric Coated Thin Wire Antenna

A. Adekola[1], A. I. Mowete[1], and A. Ogunsola[1, 2]

[1]Department of Electrical and Electronics Engineering, Faculty of Engineering, University of Lagos
Lagos, Nigeria
[2]Parsons Group International, Rail Treansit Divison, London, United Kingdom

Abstract— This paper addresses the problem of thin-wire antennas coated with thin layers of dielectric material, using a moment-method approach. First, it establishes that implicit in certain other moment-method solutions published in the literature is the assumption that the coated wire may be regarded as being essentially infinite in extent; and then further shows that another earlier solution, which removes this restriction, is limited by a related assumption, concerning the model for the dielectric insulation. The paper then reformulates the problem, using a quasi-static moment-method model, in which the two assumptions alluded to in the foregoing are eliminated. Computational data obtained for the input impedance and admittance of a reactively-loaded, coated thin-wire dipole, display features that are consistent with those reported in the literature, as being characteristic of this antenna type.

1. INTRODUCTION

Thin wire antennas are often coated with dielectric materials to avoid direct contact between the metallic wire and the surrounding medium. They were first proposed for use in highly conducting media, exemplified by the utilisation of coated loops as low-frequency communication antennas mounted on submarines in sea water environments [1]. Dielectric coating is also useful as a means of electrically lengthening an antenna while maintaining the frequency characteristics and physical length [2, 3]; and in addition, they find applications in the determination of the equivalent cylindrical antennas for antennas whose cross-sections are non-circular [4], as well as in the treatment of cancer with microwave hyperthermia [1].

Numerous researchers have expended efforts in developing theoretical and experimental understanding of the physics underlying the electromagnetic behavior of dielectric coated thin wire antennas and scatterers. Bretones et al. [5], for example, utilised an existing DOTIG3 computer code for a time-domain investigation of the response of coated wire antennas to excitation by electromagnetic pulses. Their formulation suggested that for thin coatings with materials characterised by relatively low permittivities, a quasi-static model consisting of a radially directed polarisation current within the dielectric, and two layers of polarization charges, one each on the inner and outer cylindrical surfaces of the coating, becomes applicable. Further analytical development discarded contributions from the polarization current, to obtain a time-domain electric field integral equation, in which the effects of the coating were taken into account by the polarisation charges only. Moore and West [3], following the earlier treatment of the problem by Popovic and Nesic [4], developed a quasi-static approximation, through which electrically-thin coatings of either the dielectric or mixed dielectric-ferrite varieties, are transformed into equivalent magnetic coatings. In the moment-method solution provided by Richmond and Newman [6], the dielectric layer is modeled by an electric volume polarisation current, which derives from a radially directed electric field in the dielectric region, due to the distribution of current along the axis of the bare-wire antenna. Lee and Balmain [8], extended Richmond and Newman's formulation, by introducing a magnetic volume polarisation current to include cases for which the insulating layer's material has both electric and magnetic losses.

Adekola and Mowete [7], pointed out that the expressions employed in [6] and [8], as approximations for the electromagnetic field in the dielectric region, are the same as those for static charge and steady current distributions of infinite extents, respectively. Based on that physical interpretation, they reformulated the approach suggested by Richmond and Newman [6], by modeling the dielectric insulation with an electric volume polarisation current, described in terms of the electric field of a uniform static charge distribution of the same extent as the physical length of the bare wire: that reformulation however, implicitly suggested that only the radial component of the volume polarization current need be considered.

This paper also follows the earlier approach adopted by Adekola and Mowete [7], but advances arguments to suggest that not only is the contribution of the axial component of the electric

polarisation current dominant, but also that its radial component, as indicated by Bretones et al. [5], may be neglected. Numerical results obtained and described in graphical formats, for the input impedance and admittance of a coated dipole antenna display features, which have been reported in the literature [2, 6, 8], as being characteristic of coated thin-wire dipole antennas.

2. THEORITICAL FORMULATION

The starting point of our moment-method formulation and solution of the coated thin-wire antenna problem is the proposal by [6] that the dielectric coating on the thin-wire structure may be modeled by a volume distribution of polarisation current, denoted by $\mathbf{J}$ and given by:

$$\mathbf{J} = j\omega \left(\varepsilon_d - \varepsilon_0 \right) \mathbf{E}, \tag{1}$$

in which ε_d represents the permittivity of the dielectric material, and $\mathbf{E}$, the electric field in the dielectric region. This electric field, according to [6], admits the approximate representation, in terms of the filamentary current distribution $I(l)$ along the axis of the bare wire, given as:

$$j\omega \mathbf{E} = - \left[\frac{\partial I(l)/\partial l}{2\pi\varepsilon_d} \right] \hat{\mathbf{u}}_\rho, \tag{2}$$

which, as pointed out by Adekola and Mowete [7], describes the electrostatic field of a uniform line charge distribution $\sigma(l)$, of infinite extent, when it is recognised that the equation of continuity specifies that

$$-\frac{\partial I(l)}{\partial l} = j\omega\sigma(l) \tag{3}$$

It is a matter of interest to observe that Lee and Balmain [8], arrived at the same expression as (2), by suggesting that the dielectric coating may be modeled by

$$\mathbf{H} = \frac{I(l)}{2\pi\rho}\hat{\mathbf{u}}_\phi, \tag{4}$$

an expression, which as pointed out elsewhere [7], describes the static magnetic field of a uniformly distributed steady electric current carried by a conductor of infinite extent.

In this analysis, we adopt a modification of the solution proposed in [6], by suggesting that the electric field of (2) derives from a filamentary charge distributed over the finite extent of the bare wire, and related to the filamentary current carried by the wire through (3), the equation of continuity; that is:

$$\mathbf{E} = \frac{1}{4\pi\varepsilon_d} \int\limits_L \left(\frac{\sigma\left(l'\right)\rho dl'}{\left(l'^2 + \rho^2\right)^{3/2}}\hat{\mathbf{u}}_\rho - \frac{\sigma\left(l'\right)l'dl'}{\left(l'^2 + \rho^2\right)^{3/2}}\hat{\mathbf{u}}_{l'} \right) \tag{5}$$

Because $I(l')$ is an unknown, so is $\sigma(l')$; but the method of moments [9] offers an approximate solution to $I(l')$ in a technique that starts with its series expansion in terms of known functions $G_k(l)$, and unknown expansion coefficients α_k according to

$$I(l) = \sum_{k=1}^{N} \alpha_k G_k(l) \tag{6}$$

In this analysis, we choose the piece-wise linear functions described by Kuo and Strait [10], for which the nth member of the series expansion of (6) is given by:

$$G_n(l) = \begin{cases} \frac{l - l_{2n-1}}{l_{2n+1} - l_{2n-1}}, & l_{2n-1} \leq l \leq l_{2n+1} \\ \frac{l_{2n+3} - l}{l_{2n+3} - l_{2n+1}}, & l_{2n+1} \leq l \leq l_{2n+3} \end{cases} \tag{7a}$$

so that we may then describe the charge distribution of (5) in terms of the piece-wise uniform functions given by

$$G'_n(l) \equiv \frac{\partial G_n(l)}{\partial l} = \begin{cases} \frac{1}{l_{2n+1} - l_{2n-1}}, & l_{2n-1} \leq l \leq l_{2n+1} \\ \frac{-1}{l_{2n+3} - l_{2n+1}}, & l_{2n+1} \leq l \leq l_{2n+3} \end{cases} \tag{7b}$$

A substitution of (7b) for G_n into (5) then yields:

$$
\mathbf{E}_n = \frac{-1}{j\omega} \frac{1}{4\pi\varepsilon_d}
\begin{bmatrix}
\left(\frac{1}{l_{2n+1}-l_{2n-1}} \int_{l_{2n-1}}^{l_{2n+1}} \frac{\rho dl'}{(l'^2+\rho^2)^{3/2}} - \frac{1}{l_{2n+3}-l_{2n+1}} \int_{l_{2n+1}}^{l_{2n+3}} \frac{\rho dl'}{(l'^2+\rho^2)^{3/2}} \right) \hat{\mathbf{u}}_\rho \\
+ \left(\frac{-1}{l_{2n+1}-l_{2n-1}} \int_{l_{2n-1}}^{l_{2n+1}} \frac{l' dl'}{(l'^2+\rho^2)^{3/2}} + \frac{1}{l_{2n+3}-l_{2n+1}} \int_{l_{2n+1}}^{l_{2n+3}} \frac{l' dl'}{(l'^2+\rho^2)^{3/2}} \right) \hat{\mathbf{u}}_l
\end{bmatrix}
\tag{8}
$$

so that with (1), we find that:

$$
\mathbf{J}_n = \frac{-(\varepsilon_d-\varepsilon_0)}{2\varepsilon_d}
\begin{bmatrix}
\left\{
\begin{array}{l}
\left(\frac{1}{(l_{2n+1}-l_{2n-1})} \right) \left(\frac{l_{2n+1}}{(l_{2n+1}^2+\rho^2)^{1/2}} - \frac{l_{2n-1}}{(l_{2n-1}^2+\rho^2)^{1/2}} \right) - \\
\left(\frac{1}{(l_{2n+3}-l_{2n+1})} \right) \left(\frac{l_{2n+3}}{(l_{2n+3}^2+\rho^2)^{1/2}} - \frac{l_{2n+1}}{(l_{2n+1}^2+\rho^2)^{1/2}} \right)
\end{array}
\right\} \frac{\hat{\mathbf{u}}_\rho}{\rho} \\[2em]
+ \left\{
\begin{array}{l}
\left(\frac{1}{l_{2n+1}-l_{2n-1}} \right) \left(\frac{1}{(l_{2n+1}^2+\rho^2)^{1/2}} - \frac{1}{(l_{2n-1}^2+\rho^2)^{1/2}} \right) \\
\left(\frac{-1}{l_{2n+3}-l_{2n+1}} \right) \left(\frac{1}{(l_{2n+3}^2+\rho^2)^{1/2}} - \frac{1}{(l_{2n+1}^2+\rho^2)^{1/2}} \right)
\end{array}
\right\} \hat{\mathbf{u}}_l
\end{bmatrix}
\tag{9}
$$

According to Harrington and Mautz [11], for a thin dielectric shell with a large dielectric constant, the polarization current's normal component may be neglected and the tangential component expressed in terms of a net surface current. Also, the quasi-static solution described by Bretones et al. [5], indicate that the normal (radial) component of the polarization current is negligible. Accordingly, for each expansion function, G_{nw}, defined for the bare wire by (7a), we define a model for the dielectric insulation, a corresponding expansion function, G_{nd}, given as $\mathbf{G}_{nd} = \hat{\mathbf{u}}_l \iint_s J_l \rho d\rho d\phi$, so that from (9), we find that

$$
G_{nd} = \frac{(\varepsilon_0-\varepsilon_d)}{2\varepsilon_d}
\begin{bmatrix}
\zeta_n \left\{ \begin{array}{l} (b^2+l_{2n+1}^2)^{1/2} - (a^2+l_{2n-1}^2)^{1/2} \\ -(b^2+l_{2n-1}^2) + (a^2+l_{2n-1}^2) \end{array} \right\} \\
+\zeta_{n+1} \left\{ \begin{array}{l} (b^2+l_{2n+3}^2)^{1/2} - (a^2+l_{2n+3}^2)^{1/2} \\ -(b^2+l_{2n+1}^2)^{1/2} + (a^2+l_{2n-1}^2)^{1/2} \end{array} \right\}
\end{bmatrix} G'_n(l')
\tag{10}
$$

in which the Neumann functional symbolised by ζ is defined by:

$$
\zeta_n = \begin{cases} 1, & l_{2n-1} \le l' \le l_{2n+1} \\ 0, & \text{elsewhere} \end{cases}
\tag{11}
$$
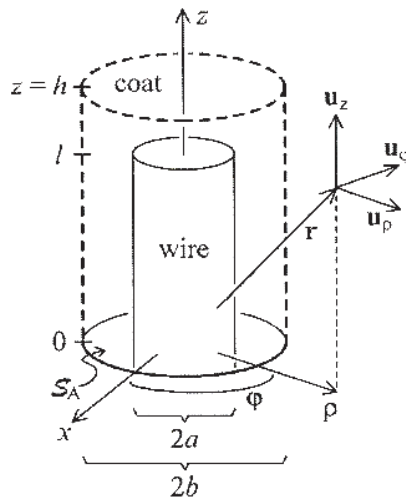
Figure 1: Dielectric coated thin wire.

so that

$$\zeta_{n+1} = \begin{cases} 1, & l_{2n+1} \leq l' \leq l_{2n+3} \\ 0, & \text{elsewhere} \end{cases} \tag{12}$$

where "a" and "b" in (10) represents the radii of the thin wire and dielectric shell, respectively, as shown in the problem geometry of Fig. 1.

For the composite coated-wire structure therefore, we define the total current in terms of the series expansion

$$I_T = I_{wn} + I_{dn} = \sum_n G_{wn} + G_{dn}, \tag{13}$$

with the subscripts "w" and "d" referring to bare wire and dielectric insulation, respectively, and in which G_{wn} and G_{dn} are given, respectively, by (7) and (10). Hence, the moment-method solution [9] to the problem emerges as:

$$[I_T] = \begin{pmatrix} Z_{mn}^{ww} & \Delta Z_{mn}^{wd} \\ \Delta Z_{mn}^{dw} & \Delta Z_{mn}^{dd} \end{pmatrix}^{-1} [V_n] \tag{14}$$

where

$$Z_{mn}^{ww} = \int\limits_{\mathbf{axis}} dl' \int\limits_{\mathbf{C}} dl \left[j\omega\mu G_{mw}(l) G_{nw}(l') + \frac{1}{j\omega\varepsilon} \frac{dG_{mw}(l)}{dl} \frac{dG_{nw}(l')}{dl'} \right] \frac{e^{-jk|\mathbf{r}-\mathbf{r}'|}}{4\pi |\mathbf{r}-\mathbf{r}'|} \tag{15}$$

and

$$\Delta Z_{mn}^{wd} = \int\limits_{\mathbf{axis}} dl' \int\limits_{\mathbf{C}} dl \left[j\omega\mu G_{mw}(l) G_{nd}(l') \right] \frac{e^{-jk|\mathbf{r}-\mathbf{r}'|}}{4\pi |\mathbf{r}-\mathbf{r}'|} \tag{16}$$

provided that "c" is a line on the surface of the bare wire parallel to the wire's axis [10].
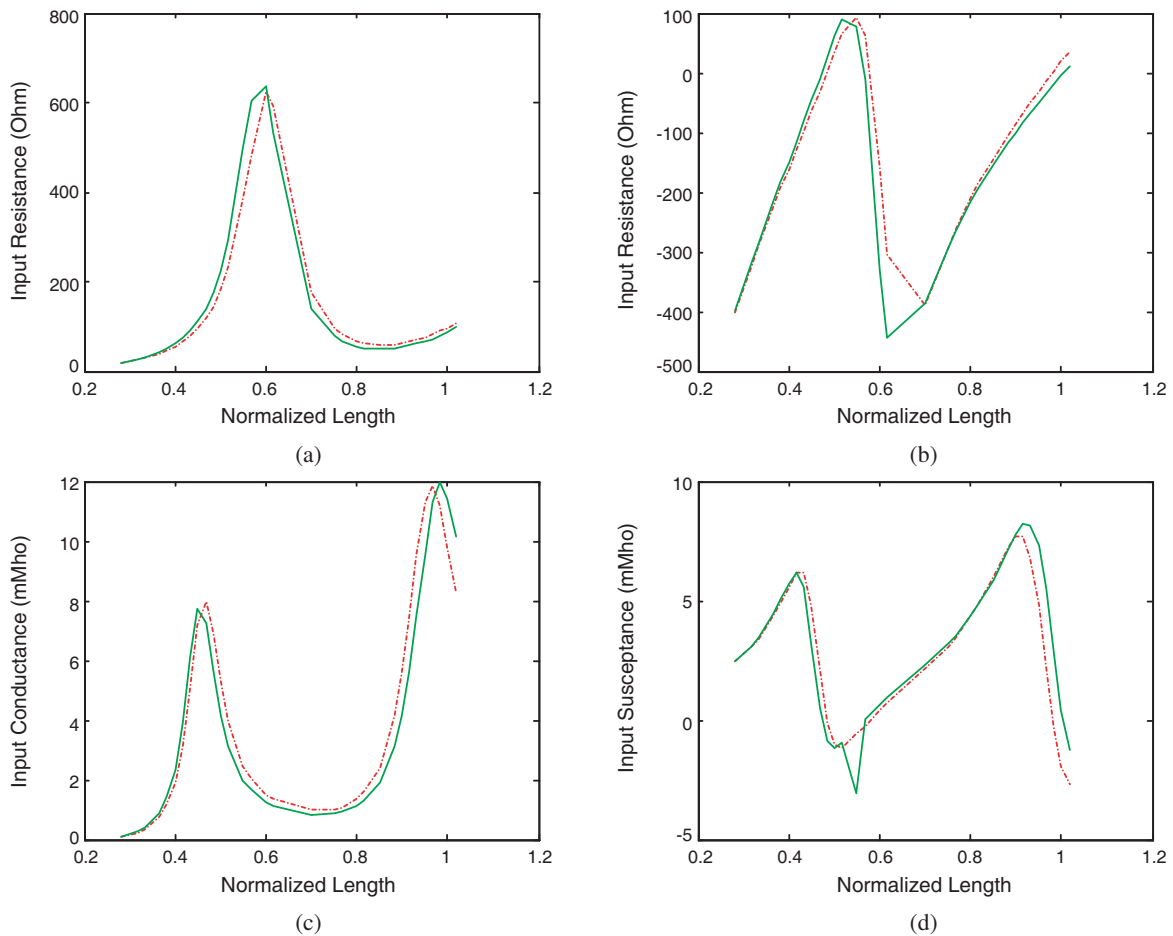
Figure 2: Comparison of the input impedance and admittance characteristics of the thin wire dipole antenna and its dielectric coated version (- - - bare wire, — coated wire).

3. RESULTS AND DISCUSSSIONS

For the computation of numerical results, we used an adaptation of the FORTRAN computer program described by Kuo and Strait [10], for a bare reactively loaded thin-wire of length $0.5\,\mathrm{m}$ and radius $3.37\,\mathrm{mm}$. The numerical results described in the ensuing discussions are for this same wire, when uniformly coated by a homogeneous, electrically lossy dielectric, of varying thickness.

Displayed in Fig. 2 below are graphical representations of computation data obtained for the input impedance and admittance of the coated wire, for a dielectric material of relative permittivity $\varepsilon_r = (4.6 - j4.7)$, and whose coating thickness $b = 6a$.

It is readily observed from Fig. 2(a) that the input resistance values for the bare wire are less than those for the coated wire below first resonance. In addition, peak resistance value for the bare wire is less than that for the coated wire, and since the latter occurs before the former, it may be said that one effect of the coating is to lower resonant frequency, and these observations are consistent with those reported elsewhere [6, 8]. The input reactance curves of Fig. 2(b) also exhibit the same general behavior as those described in the foregoing, for input resistance. In this case, however, we observe that the difference between values of reactance for the coated and bare dipoles differ sharply for values of normalized length (l/λ) between 0.6 and 0.7. Input conductance characteristics for the bare and insulated dipole antennas are displayed in Fig. 2(c) from which we find, as noted by Richmond and Newman [6], that the effect of insulation is to shift conductance, such that it is between that of a bare wire in free space and a bare wire in a homogeneous medium, whose permittivity is the same as that of the insulating material. The curves of Fig. 2(d) for input susceptance exhibit the same general features as those for input reactance. Unlike input reactance, however, the sharp difference in input susceptance values for the bare and coated dipole antennas.

The numerical results obtained for the reactively loaded coated thin-wire are displayed in the response curves of Fig. 3.
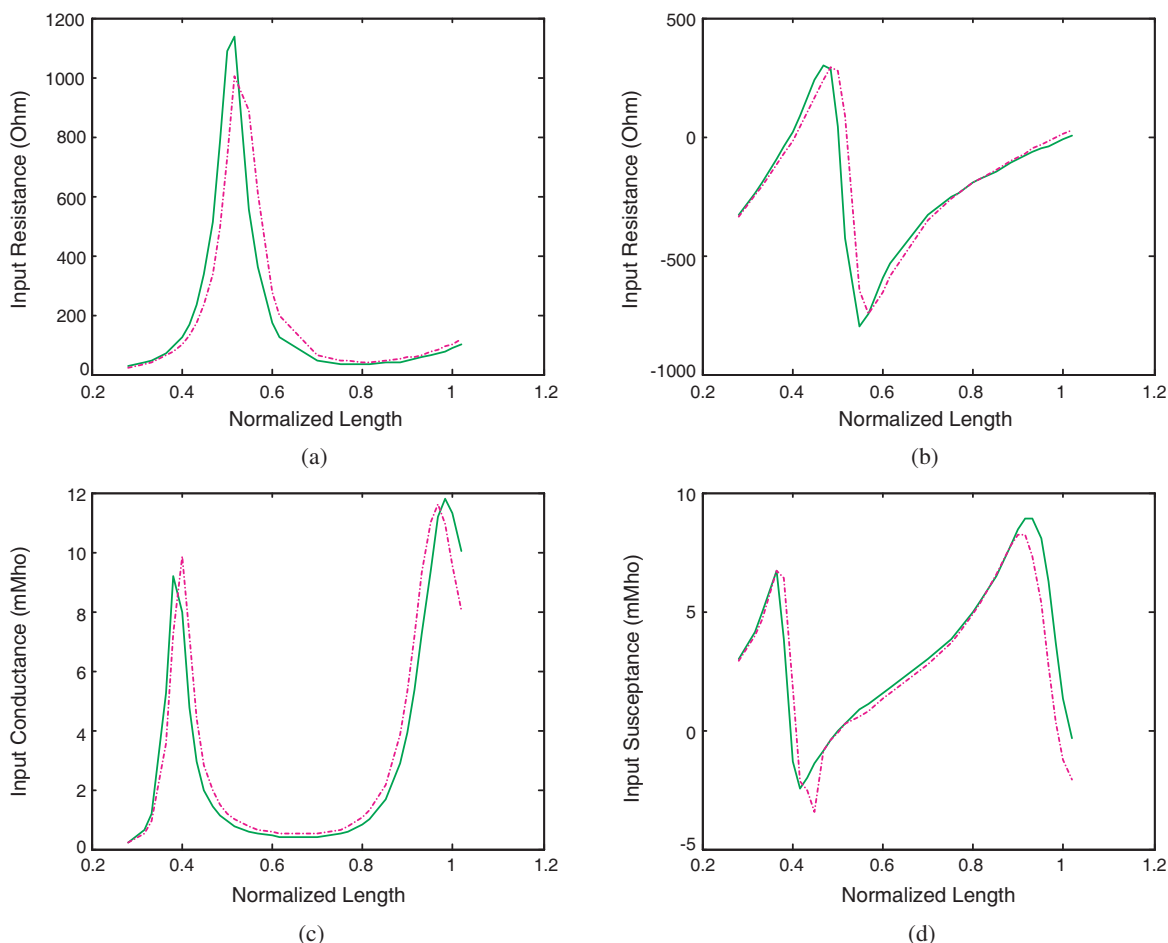
Figure 3: Comparison of the input impedance and input admittance characteristics of a reactively loaded thin wire dipole antenna and its dielectric coated version (- - - bare wire, — coated wire).

The dimensions of the wire and coating thickness remain the same as before, but in this case, the antenna was loaded with an inductive load of $1 \, k\Omega$, as described by Kuo and Strait [10]. It is clear from the curves that the effects of dielectric insulation are more pronounced in this case of the reactively loaded dipole that was the case with the unloaded dipole. A comparison of Figs. 2(a)–2(d) and 3(a)–3(d), for example, suggests that bandwidth is significantly reduced, when the antenna carries an inductive load. From Fig. 3(a), we find that apart from the reduced bandwidth, peak input resistance for the coated wire is now significantly much larger than peak input resistance for the bare wire. A similar observation is true for peak input conductance, which as seen from Fig. 3(c), has significantly larger values for the bare wire than for the insulated wire. Input reactance characteristics share certain features with input resistance characteristics including the fact that peak reactance at first resonance is larger for the bare wire than for the coated wire. After the first resonance, when reactance may be said to be capacitive, we find that reactance varies more smoothly in the case of reactive loading, than for the case of the unloaded antenna. And it is also of interest to observe that peak capacitive reactance values in Fig. (3b) occur at much closer values of normalized length (and hence frequency of operation) than was the case with Fig. 2(b).

In order to examine the effects of coating thickness on input impedance and admittance characteristics, the numerical results displayed in Fig. 4 were compiled for the reactively loaded dipole, using three different values ($b = 6a$, $b = 4a$, and $b = 2a$) of coating thickness.

Figure 4(a) reveals that before first resonance, input resistance increases with increasing coating thickness, or equivalently, increasing coating thickness shifts the input resistance curve to the left. It is noteworthy to observe that values of peak input resistance for $b = 6a$ and $b = 4a$ are close; and that they are both significantly greater than the value of peak input resistance for $b = 2a$. The input reactance response curves of Fig. 4(b) also indicate an increase in values with increase in coating thickness, before first resonance; though the differences are not as large as those recorded for input
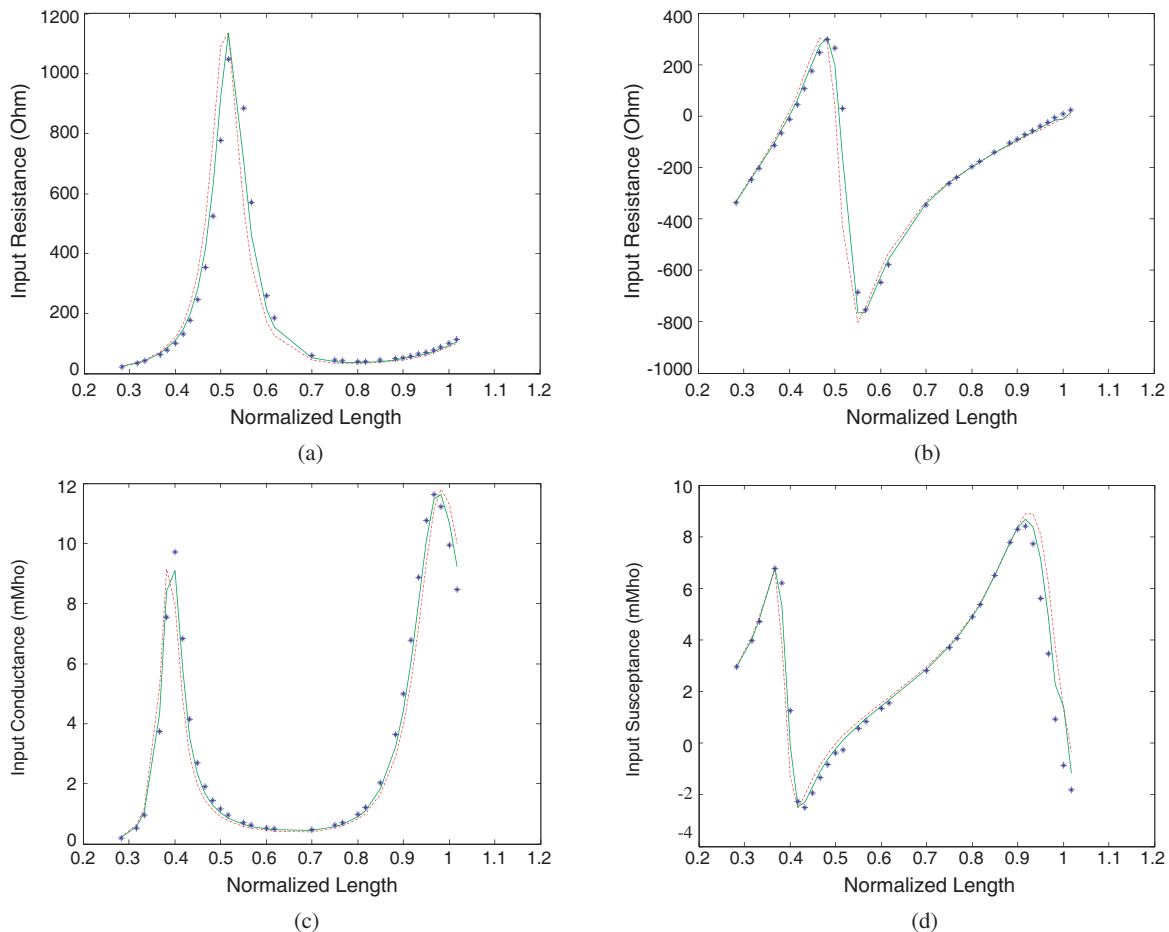
Figure 4: Variation of input impedance and input admittance with coating thickness (*** $b = 2a$; — $b = 4a$; --- $b = 6a$).

resistance, possibly because of the $1\,\mathrm{k\Omega}$ inductive load carried by the dipole. It is interesting to observe from the input conductance curve of Fig. 4(c) that whereas the general behavior is similar to that described in the foregoing for input resistance and reactance, peak input conductance for $b = 2a$ is significantly larger than peak input resistance for both $b = 4a$ and $b = 6a$, at first resonance. On the other hand, we find from Fig. 4(d) that peak input susceptance is virtually the same at first resonance for all three values of coating thickness considered in this paper.

4. CONCLUSION

This concludes our analysis of the problem of coated thin-wire antennas. It has been shown in the paper that certain published frequency-domain (Moment-Method) and time-domain solutions of the problem indicate that it admits a quasi-static solution in terms of a charge distribution that serves as model for the coated wire's dielectric insulation. By giving a physical interpretation to the analytical frequency-domain solutions alluded to above, this paper reformulated the problem to suggest that the solution should be in terms of a quasi-static charge distribution, which derives directly from the approximate current distribution utilized for the bare wire, and whose extent is the same as the wire's physical length.

Numerical results were obtained for the input impedance and input admittance characteristics of a reactively loaded thin-wire dipole antennas, and the results were in agreement with findings in the open literature, that the effects of insulating a thin-wire antenna include lowering resonant frequency, increasing peak admittance, and narrowing bandwidth. Our paper also examined the effects of varying coating thickness, and the results obtained indicate that in general, whereas peak input resistance, reactance, and susceptance decrease with increase in coating thickness, peak input conductance increases with decrease in coating thickness.

REFERENCES

1. Hertel, T. W. and G. S. Smith, "The insulated linear antenna-revisited," *IEEE Trans. Antennas Propag.*, Vol. 48, No. 6, 914–919, June 2000.
2. Lamensdorf, D., "An experimental investigation of dielectric coated antennas," *IEEE Trans. Antennas Propag.*, Vol. 15, No. 6, 767–771, 1967.
3. Moore, J. and M. A. West, "Simplified analysis of coated wire antennas and scatterers," *Proc. IEE Microw. Antennas Propag.*, Vol. 142, No. 1, 14–18, February 1995.
4. Popovic, B. D. and A. Nesic, "Generalisation of the concept of equivalent radius of thin cylindrical antenna," *IEE Proc.*, Vol. 131, No. 3, 153–158, 1984.
5. Bretones, A. R., A. Martin, R. Gomez, A. Salinas, and I. Sanchez, "Time domain analysis of dielectric coated wire antennas and scatterers," *IEEE Trans. Antennas Propag.*, Vol. 42, No. 6, 815–819, June 1994.
6. Richmond, J. H. and E. H. Newman, "Dielectric coated wire antenna," *Radio Science,* Vol. 11, 13–20, 1976.
7. Adekola, S. A. and A. I. Mowete, "A quasi-static moment-method analysis of dielectric coated thin-wire antennas," *Proc. SATCAM 2000*, Paper 14 AP/BEM, University of Stellenbosch, Cape Town, South Africa, September 2000.
8. Lee, J. P. Y. and K. G. Balmain, "Wire antennas coated with magnetically and electrically lossy material," *Radio Science*, Vol. 14, No. 3, 437–445, May–June 1979.
9. Harrington, R. F., "Matrix methods for field problems," *Proc. IEEE*, Vol. 55, No. 2, 136–149, February 1967.
10. Kuo, D.-C. and B. J. Strait, "Computer programs for radiation and scattering by arbitrary configurations of bent wires," *Interaction Notes (Note 191)*, Electrical Engineering Department, Syracuse University, New York, September 1970.
11. Harrington, R. F. and J. R. Mautz, "An impedance sheet approximation for thin dielectric shells," *IEEE Trans. Antennas Propag.*, 531–534, July 1975.

Leaky-wave Antenna Based of EBG Structures

S. E. Bankov

Institute of Radio Engineering and Electronics of Russian Academy of Science, Russian Federation

Abstract— A leaky-wave flat antenna on the base of EBG structures is considered. The antenna contains a system of coupled EBG waveguides with array of radiating slots and an exciter that feeds this array. The exciter is considered in two variants: planar double layered EBG mirror with a planar horn and EBG waveguide with leaky wave. Radiating array and EBG waveguide with leaky wave are simulated with help of compensating sources technique combined with transversal resonance method. Finite elements method is applied for planar mirror modeling. Output characteristics of the antenna including frequency dependence of angle of radiation, gain, bandwidth etc. are evaluated numerically.

1. INTRODUCTION

Electromagnetic bandgap (EBG) structures are intensively investigated now in different aspects. Complex waveguide circuits may be formed inside EBG structure inserting special defects in regular EBG array [1]. Applying this way one may construct antenna that contains radiating array and feeding circuit. Our purpose is to study such antenna theoretically and numerically.

An important step of our investigation is a choice of EBG structure. In microwave range good perspectives has array of metal cylinders located inside parallel plate waveguide (PPW) (see Fig. 1).

We should note that previously was proposed and investigated so-called post wall waveguide [2] and antenna arrays on its base. These structures are close to presented below but not identical because in our case posts (cylinders) form media while in [2] they form only wall. Sometimes this difference is sufficient. However we may consider this work also as a development of ideas presented in [2].

The antenna structure is shown in Fig. 2. It consists of radiating array and exciter. There are many ways to realize these devices. We will consider system of coupled EBG waveguides with continuous longitudinal slots (see Fig. 3) as a radiating array. Also two types of exciters will be studied. First of them is EBG waveguide with leaky wave. Dominant wave of the waveguide slowly radiates energy inside PPW forming wide wave beam that in its turn excites array (see Fig. 2). The second exciter transforms cylindrical wave of a planar horn located at a down layer (down PPW) to plane wave at an upper layer (upper PPW). First function is performed due to shape of EBG structure forming planar mirror (see Fig. 4). The second one is performed due to coupling slot.

2. LEAKY-WAVE EBG WAVEGUIDE

Model of leaky-wave EBG waveguide shown in Fig. 5 consists of two parts: semi-infinite EBG structure and EBG structure with a finite number of layers along $0y$ axis. Numerically was shown that for intensive radiation of energy from waveguide structure with one layer shown in Fig. 5 should be applied. Next we will consider only this case.

Analysis of eigen modes of the waveguide may be performed with help of transversal resonance method (TRM) [3]. To apply TRM we should solve two key problems. First of them is diffraction of plane T-wave PPW at semi-infinite EBG structure (Fig. 6). The second problem is plane T-wave
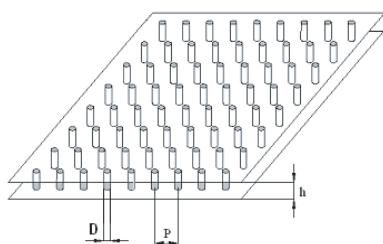
Figure 1: EBG structure.   Figure 2: Antenna structure.   Figure 3: Radiating array.
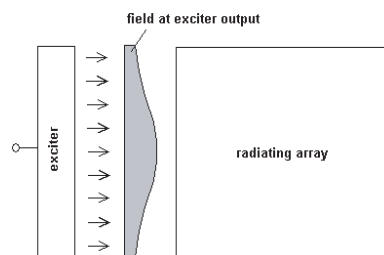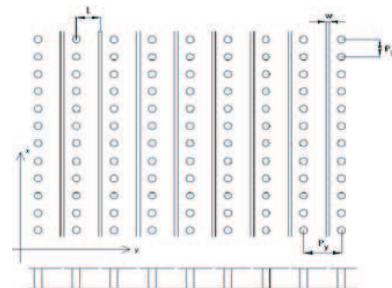
scattering by the layer of cylinders (Fig. 7). In both cases T-wave incidences at an arbitrary angle that is described by an arbitrary wave number γ.

Scattered field in both problems is presented as a series of spatial Floquet harmonics. They are characterized by number $n = \ldots - 1, 0, 1, \ldots$. Next we will consider structures that have so small periods (P_{ex}, P_c) that only zero number harmonics propagates in free space. We suppose that media inside PPW is vacuum. In addition let us suppose that distance between semi-infinite structure and layer L is enough large to negligee interaction between these structures through all harmonics except dominant zero number harmonic. Thus we may describe T-wave scattering with help of S-parameters that are reflection coefficient $R_e(\gamma)$ for semi-infinite structure and reflection and transmission coefficients $R_c(\gamma)$, $T_c(\gamma)$ for layer.

Propagation of wave in EBG waveguide may be presented as a process of series reflections as it is shown in Fig. 6. TRM gives conditions of field self-matching in waveguide. It may be written as follows:

$$1 - R_e(\gamma)R_c(\gamma)\exp(-2i\kappa L) = 0, \quad \kappa = (k^2 - \gamma^2)^{1/2}, \tag{1}$$

where k is free space wave number. Condition (1) should be solved relatively unknown γ that is a complex propagation constant of wave in leaky-wave waveguide: $\gamma = \beta - i\alpha$, β, α are propagation and attenuation constants.

Solutions of formulated above key problems were obtained with help of CST (see [4]). Thus our problem is only solution of Equation (1). This equation has complex roots because layer is partially transparent and therefore modulus of $R_c(\gamma)$ is not equal to unit. Modulus of $R_e(\gamma)$ is exactly equal to unit because EBG structure without dissipative loss in stop band completely reflects all incident waves.

Frequency dependencies of real and imaginary parts of γ are shown in Fig. 8. They are obtained for the following parameters: diameter of cylinders in semi-infinite structure 5, diameter of cylinders in layer 3, $P_{ex} = 12.5$, $P_{ey} = 12.5$, $P_c = 13.5$, $L = 19.5$. All dimensions here and below are presented in millimeters.
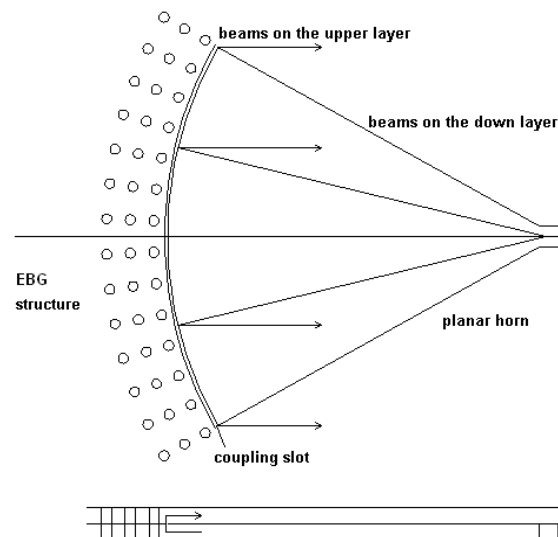
Figure 4: Planar mirror — interlayer connector.
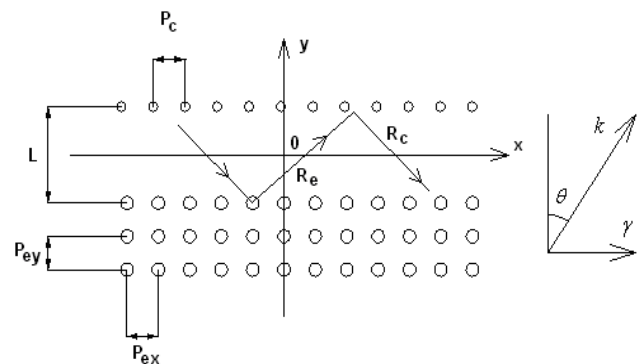
Figure 5: Leaky — wave waveguide.
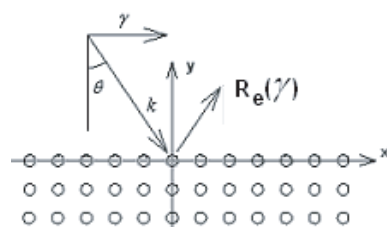
Figure 6: Semi-infinite structure.
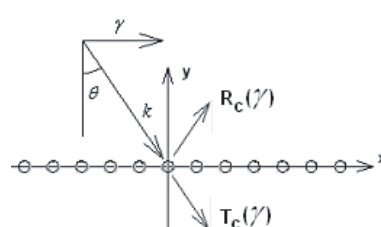
Figure 7: Single layer.
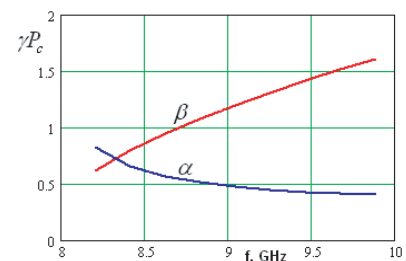
Figure 8: Complex propagation constant.

3. PLANAR MIRROR

Planar mirror was analyzed in two steps. First and the main step is analysis of a straight mirror. The second step is analysis of a low curved mirror.

Analysis of a key structure shown in Fig. 9 allows us to find parameters providing good matching and to find dependence of transmission coefficient S_{12} phase on angle of incidence φ. This dependence is required for synthesis of mirror profile.

Finite elements method (FEM) was applied for analysis of key structure. Its periodicity along $0y$ axis allows one to reduce solution in infinite space to analysis of one period as it is shown in Fig. 10. In this case the following periodical conditions should be satisfied in planes $y = \pm P_y/2$:

$$E(P_y/2) = E(-P_y/2) \exp(-ikP_y \sin \varphi). \tag{2}$$

Thus we obtain a waveguide junction that has four ports (see Fig. 10). Ports 3, 4 describe radiation of energy through EBG structure. Output waveguides are Floquet channels.

Theoretical and numerical investigation shows that planar mirror has two strongly different regimes: static and dynamic. Their existence depends on height of PPW in region of coupling slot — $2h + t$. Dominant T-mode of PPW propagates at any frequency. However the first higher order mode has cutoff frequency. Thus it may propagate or not dependently on height $2h + t$. In the first case one has static regime in the second case dynamic one. Well matching may be obtained in both regimes but bandwidth in them is sufficiently different. Dependencies of planar mirror S-parameters in static regime on frequency f are shown in Fig. 11. Curves 1–4 correspond to $S_{1,1-4}$. Numerical results were obtained for the following parameters: $P_x = P_y = 12.5$, $2R = 5$, $t = 0.5$, $w = 2.9$, $a = 2.5$, $h = 5$. Shown in Fig. 11 plots correspond to normal incidence of T-mode.

S-parameters in dynamic regime for normal T-mode incidence are presented in Fig. 12. They were obtained for $P_x = P_y = 12.5$, $2R = 5$, $t = 3$, $w = 32$, $a = 2.5$, $h = 10$. It is seen that width of coupling slot is sufficiently greater now and also mirror is well matched in more narrow range than in static regime.

Dependence of coefficient S_{12} phase — $\tilde{\varphi}_{21}$ on angle of incidence φ plays an important role in planar mirror design because it describes an additional phase shift that should be compensated by a choice of mirror profile. Phase of S-parameter depends on choice of reference plane position. We may optimize it to obtain minimal dependence of phase on angle φ. In Fig. 13 phase-angle dependence is shown. Curves 1–3 correspond to mirror with parameters presented above in static regime at frequencies $f = 9.75$, 10.35, 10.975 GHz. For every frequency position of reference plane was selected thus to have minimal variations of S_{12} phase. One may see that these variations in range 0–50 degrees are very small. Therefore curved mirror has classic parabolic shape.

4. RADIATING ARRAY

Radiating array was also modeled with help of TRM. Array is schematically shown in Fig. 3. Let array be excited periodically thus that phase shift between neighboring channels is βP_y. We may consider under this condition one period of the array. Let us suppose as it was done in Section 2 that layers of cylinders and slots interact with each other only through dominant T-mode of PPW. This suggestion restricts height of PPW that should be not only single mode but enough thin and period
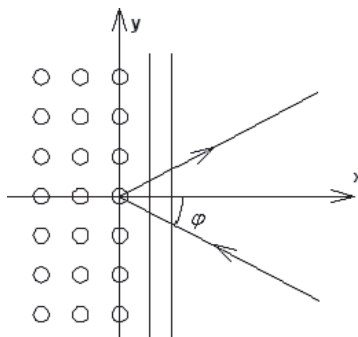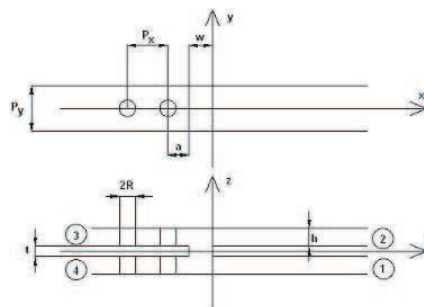

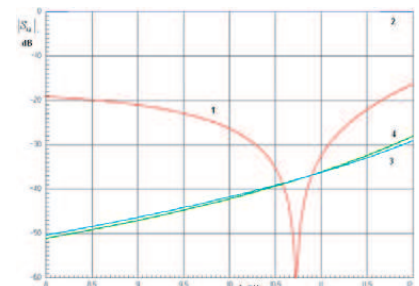Figure 9: Key structure.   Figure 10: Period of key structure.   Figure 11: S-parameters versus f.

P_x that should be enough small. If it is so we may characterize period by its S-parameters: R_{p11} — reflection coefficient from left port 1, R_{p22} — reflection coefficient from right port 2, $T_{p12} = T_{p21}$ — transmission coefficient through period. Periodical conditions connect amplitudes of incident and reflected waves at ports 1 and 2. Applying them we obtain the following equation relatively unknown propagation constant γ along $0x$ axis.

$$1 - T_{p12}\cos(\beta P_y) + (T_{p12}^2 - R_{p11}R_{p22}) = 0. \tag{3}$$

Constant γ is a complex propagation constant of array mode that depends on parameter β. Theory of microwave circuits allows one to express S-parameters of period through S-parameters of layer and slot. Parameters of layer were discussed in Section 2. Reflection and transmission coefficient of slot R_s and T_s were found in [5]. Solution of Equation (4) has real and imaginary parts — propagation and attenuation constants.

5. ANTENNA ANALYSIS

Antenna analysis was performed for mirror and leaky-wave exciters. More simple case corresponds to mirror exciter. Its simplicity is caused by fixed angle of incidence under which beam formed by exciter incidents on radiating array. It is equal to zero independently on frequency. Thus the main beam of antenna radiation pattern (RP) is situated in XOZ plane (see Fig. 3). Angle θ between main beam of RP and $0z$ axis is angle of radiation. It depends on frequency as it is shown in Fig. 14. Plots in Figs. 14, 15 were obtained for the following parameters of radiating array: $w = 2$, $h = 6$, $P_x = 12.5$. Curves 1–3 in Fig. 14 correspond to $P_y = 21, 22, 23$. Array size is 300×300. Curve 1 in Fig. 15 is antenna gain in direction defined by angle $\theta_0 = 45°$. Curve 2 is gain of a perfect aperture with uniform amplitude distribution which radiates at angle θ_0. Analyzing antenna gain we took into account that some part of energy is not radiated into free space and dissipated in matched loads.

Plots in Figs. 16, 17 were obtained for antenna with leaky-wave exciter. In this case, there are
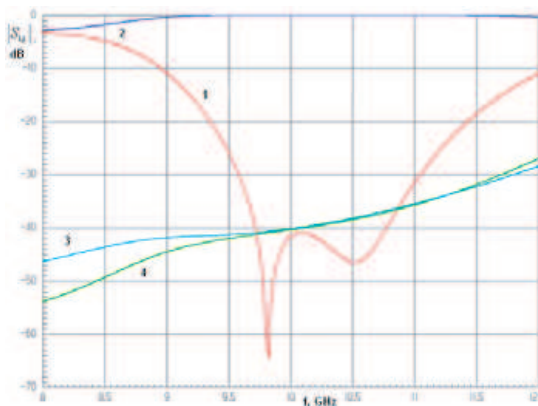
Figure 12: S-parameters.
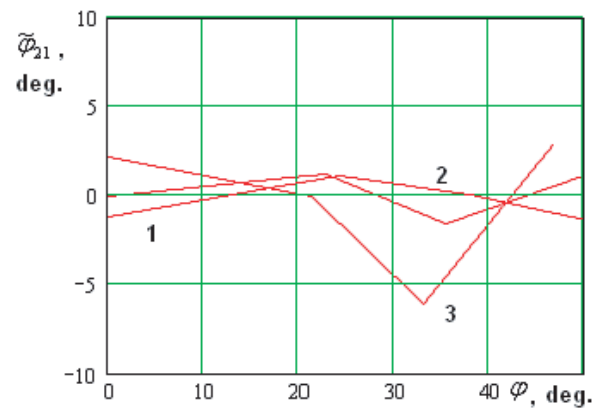
Figure 13: Phase versus angle of incidence.
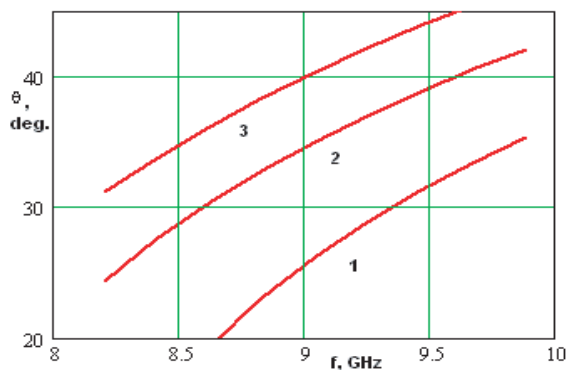
Figure 14: Angle of radiation.
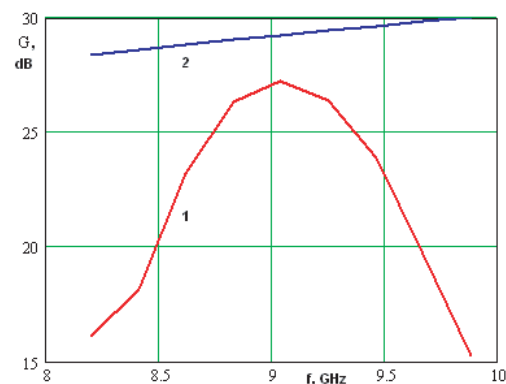
Figure 15: Antenna gain.

Figure 16: Angles of radiation.
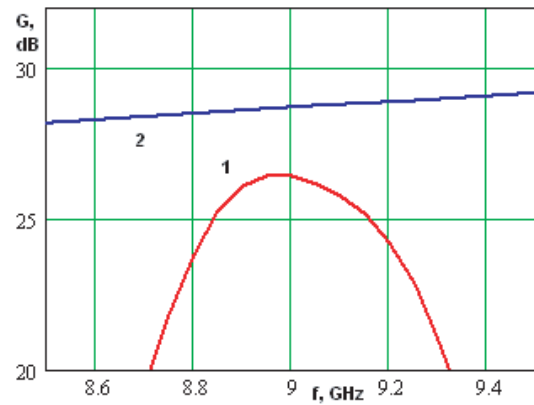
Figure 17: Antenna gain.

two angles of radiation depending on frequency as it is seen from Fig. 16. Curves 1 and 2 correspond to elevation and azimuth angles. Parameters of antenna were selected thus to have main beam in diagonal plane $x = y$ (azimuth angle is equal to 45 degrees) at frequency 9 GHz. Numerically was shown that efficiency of antenna depends on its shape and rectangular shape is not optimal. Better results gives sector shape. Gain of such antenna ($R = 300$) is presented in Fig. 17. Curves 1, 2 correspond to the same parameters as in Fig. 15.

REFERENCES

1. Mosallaei, H. and Y. Rahmat-Samii, "Periodic bandgap and effective dielectric materials in electromagnetics," *IEEE Trans. AP*, Vol. 51, No. 3, 549–563, 2003.
2. Hirokawa, J. and M. Ando, "Single-layer feed waveguide consisting of posts for plane TEM wave excitation in parallel plates," *IEEE Trans. AP*, Vol. 46, No. 5, 625–630, 1998.
3. Zucker, F. J., "The guiding and radiation of surface waves," *Proc. Symp. Mod. Advan. Microwave Tech.*, 403–436, New York, USA, Nov. 1954.
4. Bankov, S. E., "Diffraction of electromagnetic waves by the boundary of a semi-infinite metamaterial," *Journal of Comm. Tech. and Electr.*, Vol. 53, No. 1, 15–25, 2008.
5. Nefedov, E. I. and A. T. Fialkovsky, *Strip Transmission Lines*, Nauka, Moscow, 1980.

Beam Forming Networks on the Base of Coupled Waveguides for Multi-beam Hybrid Antennas

S. E. Bankov, **V. A. Kaloshin**, and **E. V. Frolova**

Institute of Radio Engineering and Electronics of Russian Academy of Science, Russian Federation

Abstract— Proposed and investigated theoretically, numerically and experimentally a new class of beam forming networks for multi-beam hybrid antennas. The main part of the beam-forming network is a system of coupled waveguides. The following types of beam-forming networks are considered: one-dimensional (linear) with identical coupled waveguides and fixed phase shifters, linear with different coupled waveguides without phase shifters, two-dimensional with rectangular grid, identical waveguides and phase shifters, two-dimensional with rectangular grid and different waveguides, two-dimensional with hexagonal grid, identical waveguides and phase shifters. All the devices have several input ports and form in free space several sector type radiation patterns which are optimal for illumination of optical system.

1. INTRODUCTION

Multi-beam antennas (MBA) are widely used in different radio systems particularly in radio vision systems (RVS). Typical configuration of hybrid MBA includes an optical system (OS) that may be realized as a system of mirrors or lens and a beam-forming network (BFN). The OS together with BFN form in free space a system of narrow beams as it is schematically shown in Fig. 1. Every n-th beam may be characterized by its radiation pattern (RP).

The BFN is an N-channel array which illuminates OS. It is a known fact that ports of BFN may be matched and isolated only if its RP are orthogonal to each other [1]. Typical system of orthogonal RP may be produced if BFN excited from each port forms in OS aperture uniform amplitude distributions with linear phase dependence on coordinates. At the same time BFN should illuminate OS thus to minimize loss of energy. One may see that these requirements are satisfied if BFN forms a system of sector type RP with shifted phase centers. Such RP may not be formed by BFN with isolated channels. Channels of BFN should be coupled to distribute energy from input port to several outputs.

Coupling between waveguides of BFN may be arranged in different ways. In papers [2, 3] authors propose to use directional couplers. Alternative way is presented in [4] where authors considered one-dimensional system of coupled waveguides. Our work develops this idea.

2. LINEAR BEAM-FORMING NETWORKS

One dimensional (linear) BFN of two types are considered in this section. First of them is BFN with identical waveguides and phase shifters and the second one is BFN with non-identical waveguides. They are shown in Figs. 2 and 3. We will analyze BFN with identical waveguides in terms of coupled waves theory. Next variants including two-dimensional (2D) BFN may be considered analogously.
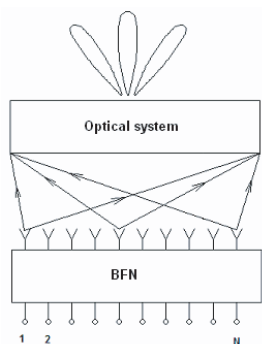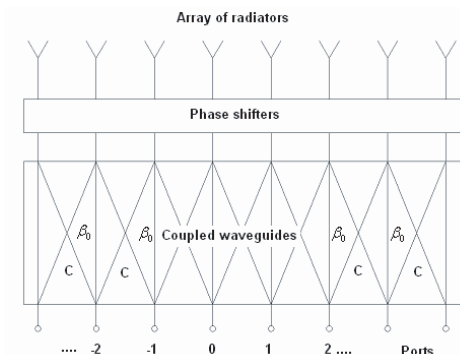

Figure 1: MBA structure.

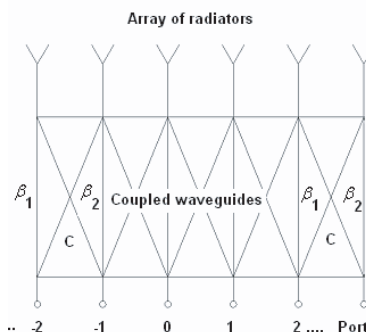Figure 2: Linear BFN with phase shifters.

Figure 3: BFN with different waveguides.

In terms of this theory propagation of waves in coupled waveguides is described by the following system of differential equations:

$$dU_n/dz + i\beta_0 U_n + iCU_{n-1} + iCU_{n+1} = 0, \quad n = \ldots - 1, 0, 1, \ldots \tag{1}$$

where $U_n(z)$ — amplitude of wave in the n-th waveguide, C — linear coupling coefficient (LCC) between waveguides, β_0 — propagation constant of wave in uncoupled waveguide, z — coordinate directed along waveguide axis, n — number of waveguide in array. System (1) corresponds to an infinite along $0z$ axis array. We also suppose that only neighboring waveguides are coupled with each other. In case of periodical regime amplitudes $U_n(z)$ are connected by the following relation: $U_n(z) = U_0(z) \exp(-i\beta nP)$. Constant β defines phase shift between waveguides, P is a period of the array. Substituting this relation to (1) we reduce system of equations to one differential equation which may be simply solved. The solution has the following form:

$$U_0(z) = A(\beta) \exp(-i\gamma z), \quad \gamma = \beta_0 + 2C\cos(\beta P). \tag{2}$$

Next we consider array of a finite length L ($0 < z < L$) that is excited from port number 0 by a wave with unit amplitude. In plane $z = 0$ amplitudes of waves should be continuous:

$$U_n = 1 \quad \text{for} \quad n = 0 \quad \text{and} \quad U_n = 0 \quad \text{for} \quad n \neq 0. \tag{3}$$

Solution for non-periodical excitation may be presented as an integral over variable β with integrand (2) [4]. Applying integral presentation and relation (3) we find function $A(\beta)$ and amplitudes of waves in the output plane $z = L$:

$$A(\beta) = P/2\pi \quad \text{for} \quad |\beta| < \pi/P \quad \text{and} \quad A(\beta) = 0 \quad \text{for} \quad |\beta| > \pi/P. \tag{4}$$

$$U_n = (-i)^n J_n(2CL) \exp(-i\beta_0 z). \tag{5}$$

One may see that these amplitudes have incorrect phase shifts $\pm\pi/2$. Phase shifters in waveguides (see Fig. 2) improve phase distribution thus that it has only phase shifts $\pm\pi$. They have transmission coefficients Φ_n:

$$\Phi_n = 1 - (1 + i)\cos^2(\pi n/2). \tag{6}$$

Formulas (5), (6) allow one to calculate RP $F_b(\theta)$ of BFN applying known elementary theory of arrays. Angle θ is count off from normal to array plane. Coefficient of rectangularity K defined below characterizes quality of BFN:

$$K = \left| \int_{-\theta_s/2}^{\theta_s/2} F_b(\theta)d\theta \right|^2 \Bigg/ \theta_s \int_{-\pi}^{\pi} |F_b(\theta)|^2 \, d\theta. \tag{7}$$

Briefly presented above analysis with small changes may be done for BFN shown in Fig. 3. We should note that non-identical waveguides are used instead of phase shifters. Waveguides with different propagation constants $\beta_{1,2}$ correct phase distribution produced by array of identical waveguides.

Some numerical results obtained for linear BFN are shown in Figs. 4–6. Curves 1 correspond to BFN with identical waveguides and curves 2 to non-identical one. Normalized amplitude and phase
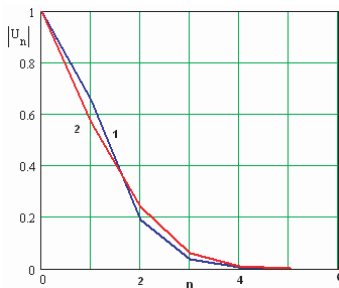

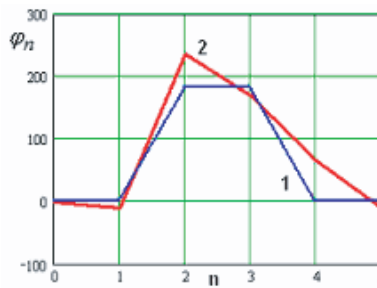
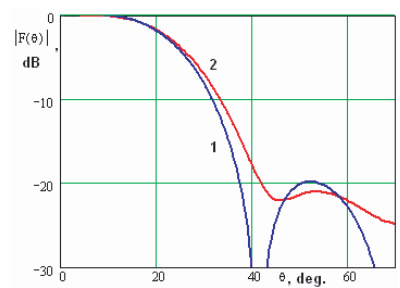Figure 4: Amplitude distribution. 　　　 Figure 5: Phase distribution. 　　　 Figure 6: Radiation pattern.

distributions in BFN output plane are shown in Figs. 4 and 5. Fig. 6 demonstrates RP of BFN of two types. Curves 1 correspond to parameter $CL = 0.5$, curves 2 to $CL = 0.6$ and $\Delta\beta = 1.15$, $\Delta\beta = \beta_1 - \beta_2$. Phase distribution in case of identical waveguides is close to perfect one because it has only phase shifts equal to $\pm\pi$. In case of BFN with non-identical waveguides it has phase errors. As a result RP shown in Fig. 6 (curve 2) is less rectangular than RP corresponding to curve 1. However errors in phase distribution do not strongly decrease coefficient K that is equal to $-0.2\,\mathrm{dB}$ in case of identical waveguides and to $-0.5\,\mathrm{dB}$ in another case. RP shown in Fig. 6 were obtained for array of metal rectangular waveguides in H-plane ($a = P = 25\,\mathrm{mm}$, $f = 8\,\mathrm{GHz}$).

3. TWO-DIMENSIONAL BEAM-FORMING NETWORKS

Considered two-dimensional BFN have systems of coupled waveguides shown in Figs. 7–9. BFN with identical waveguides also have phase shifters. These shifters have the following transmission coefficients:

$$\Phi_{n,m} = 1 - (1+i)\cos^2(\pi n/2)\cos^2(\pi m/2) - (1-i)\sin^2(\pi n/2)\sin^2(\pi m/2), \tag{8}$$

$$\Phi_{n,m} = \cos^2(\pi n/2)\cos^2(\pi m/2) + T_\psi\left(1 - \cos^2(\pi n/2)\cos^2(\pi m/2)\right), \quad T_\psi = \exp(i\psi), \tag{9}$$

where ψ — parameter that is selected numerically. Relation (8) corresponds to array with rectangular grid (Fig. 7) and (9) to hexagonal grid (Fig. 9).

Typical examples of RP of two-dimensional BFN are shown in Fig. 10. Plots in Figs. 10(a)–(c) correspond to BFN shown in Figs. 7–9. All curves 1 are obtained for plane $x = 0$. Curves 2 in Figs. 10(a) and 10(b) correspond to RP in diagonal plane $x = y$. Curve 2 in Fig. 10(c) is RP in plane $x = 3^{-1/2}y$. Presented RP have different level of rectangularity. Coefficient K varies from $-0.5\,\mathrm{dB}$ to $-1\,\mathrm{dB}$ for BFN shown in Figs. 7–9. Plots in Fig. 10 were calculated for array of square waveguides: $a = 20\,\mathrm{mm}$, $f = 8\,\mathrm{GHz}$.
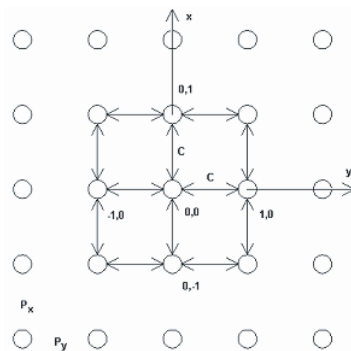

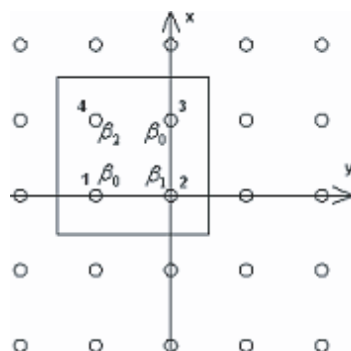Figure 7: 2D BFN with identical waveguides and rectangular grid.
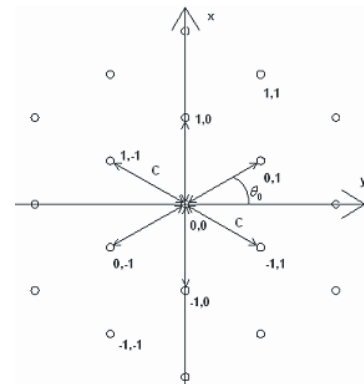
Figure 8: 2D BFN with non-identical waveguides and rectangular grid.

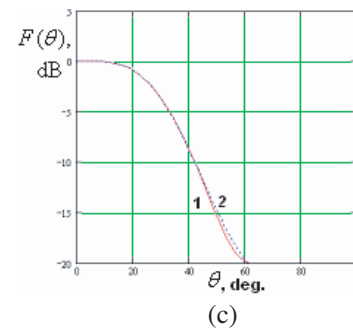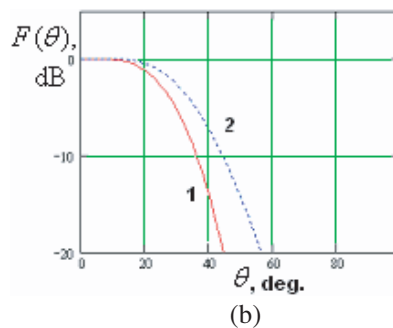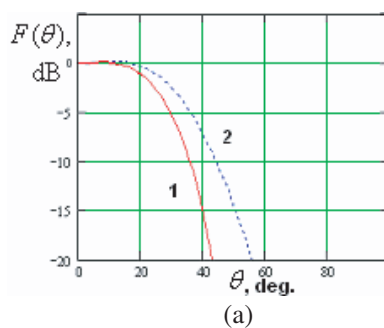Figure 9: 2D BFN with identical waveguides and hexagonal grid.

(a)

(b)

(c)

Figure 10: Radiation patterns.

4. BEAM-FORMING NETWORK ON THE BASE OF EBG WAVEGUIDES

Theory of coupled waves operates with generalized parameter LCC. Dependence of LCC on geometrical parameters of coupled waveguides may be obtained only with help of electromagnetic analysis. Such analysis was performed for so-called electromagnetic bandgap (EBG) waveguides [5]. Analyzed structure is shown in Fig. 11. It is formed by array of metal cylinders located inside parallel plate waveguide. EBG waveguides have different widths $a_{1,2}$ along $0x$ axis and therefore different propagation constants $\beta_{1,2}$ in accordance with scheme shown in Fig. 3. EBG waveguides are coupled because arrays of cylinders separating them are partially transparent.

Finite elements method was applied for electromagnetic analysis and optimization of BFN. Distance between cylinders, widths $a_{1,2}$ and number of periods along $0z$ axis were varied during numerical optimization. Coefficient K was applied as a goal function.

BFN RP's are shown in Fig. 12. They were obtained for BFN with the following parameters: $a_1 = 25.6$, $a_2 = 24.4$, cylinder diameter — 5, height of cylinders — 10, period along $0z$ axis — 14, number of periods — 14, $f = 8$ GHz, all dimensions are in mm, curves 1–4 in Fig. 12 correspond to $f = 7.5, 8, 8.5, 9$ GHz.

Numerically optimized device was fabricated (see Fig. 13) and experimentally tested. Experimentally was shown that ports of BFN are well matched and isolated. Return loss and isolation are better than -20 dB. Measured and calculated at frequency $f = 8.15$ GHz RP are shown in Fig. 14.

5. BEAM-FORMING NETWORK APPLICATION IN RADIO VISION SYSTEM

Operation of presented in Section 4 BFN in RVS was numerically simulated. The system contains BFN and three-dimensional elliptical mirror in which focal plane F_1 is located BFN. Mirror concentrates energy around its second focus F_2.
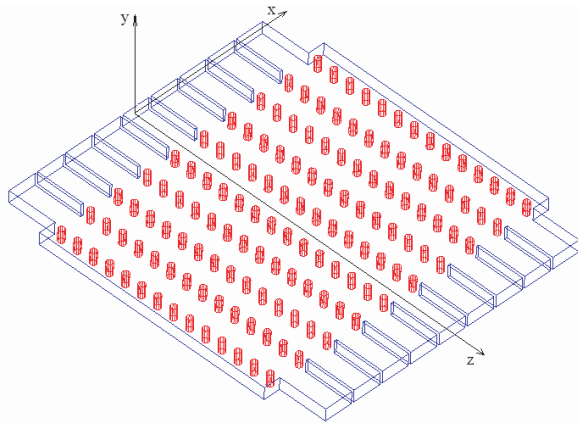

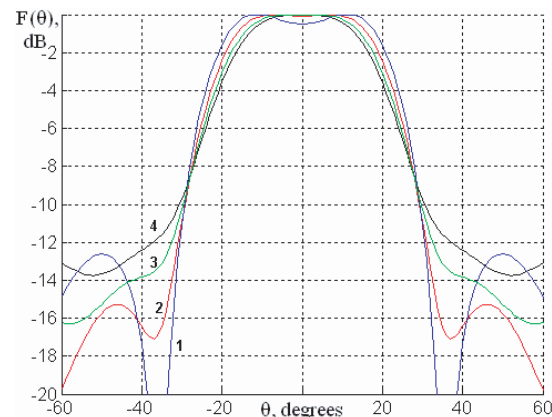Figure 11: Coupled EBG waveguides.

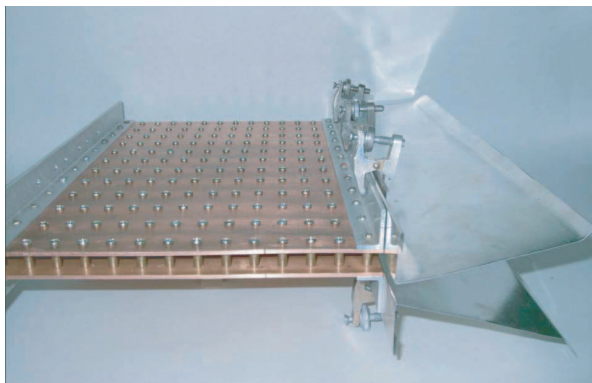Figure 12: BFN radiation pattern.
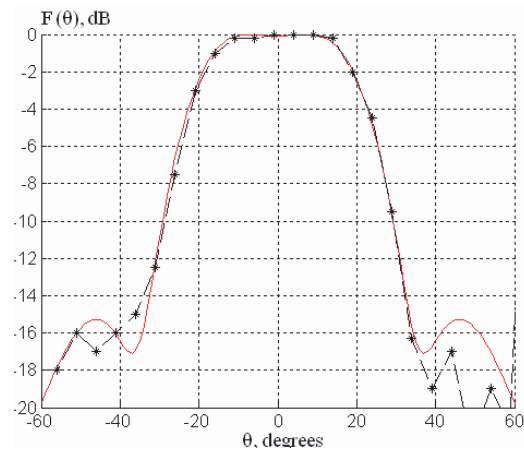

Figure 13: Experimental sample.
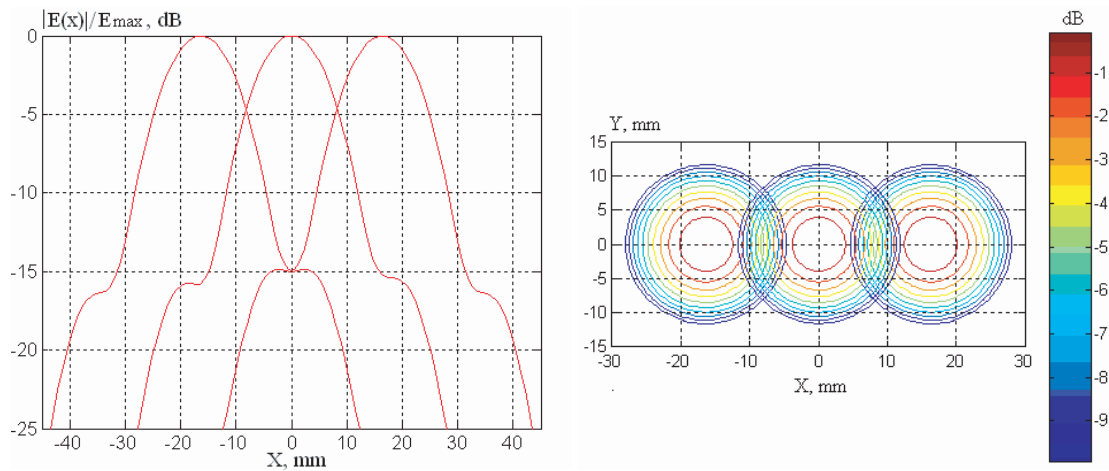

Figure 14: Radiation pattern.

Figure 15: Field distribution near focus F_2.

Physical optics approach was applied for numerical analysis of RVS. Normalized field distribution produced by BFN at frequency $f = 90\,\text{GHz}$ with three excited neighboring ports near focus F_2 is shown in Fig. 15. It is seen that application of the BFN allows one to obtain with minimal loss of energy a plurality of closely located spots without blind zones.

ACKNOWLEDGMENT

REFERENCES

1. Sazonov, D. M., "Fundamentals of matrix theory of antenna arrays," *Sbornik Nauchno-Metodicheskih Statey Po Prikladnoy Elektrodinamike*, No. 6, 111–162, 1983 (in Russian).
2. Skobelev, S. P., "Analysis and synthesis of antenna array with sector radiation pattern," *Radiotehnika*, No. 10, 44–47, 1990 (in Russian).
3. Skobelev, S. P. and A. S. Vyazigin, "Forming flat-topped element patterns in antenna arrays of two-mode waveguides," *Elect. Lett.*, Vol. 29, No. 15, 1326–1327, 1993.
4. Bankov, S. E. and T. I. Bugrova, "Analysis of a millimeter wave integrated beamforming network for quasioptical multibeam antennas," *Microwave and Opt. Tech. Lett.*, No. 6, 782–786, 1993.
5. Bankov, S. E., "Mathematical modeling of photonic bandgap crystals with defects by the method of compensating sources," *Journal of Comm. Tech. and Elect.*, Vol 50, No. 9, 968–979, 2005.

Application of Imbedding Method to the Problem of Nanosecond Impulses Distortion

P. V. Filonov and V. L. Kuznetsov

Moscow State Technical University of Civil Aviation, Moscow, Russia

Abstract— Some problems of distortion of nanosecond impulse radiated by antenna are considered. As a main reason we propose a dispersion of signal connected with Woods's resonances. On basis of embedding method the equations for coefficients for horn array antenna were built. The solution of basic subproblem of diffraction on ideal conductive lattice is shown. The results of numerical experiments are presented.

1. INTRODUCTION

In recent time there are a lot of interest in science works to nanosecond radiolocation. Characteristics of hypershort impulses allow to improve efficient of radiolocation systems. However, the modern models of antennas didn't provide full description of processes witch takes place in radiation of nanoseconds impulses. The hypershort impulses characterized by ultra wide spectrum and it is important to save phase interconnections between the components of spectrum. Misphasing of spectrum elements could bring to signal distortion. In this way we could lose all advantages of nanosecond radiolocation. To describe negative effects we must provide recommendations to form of signals and antenna system geometry. To solve such problem we need easy in use mathematical model of antenna witch could sufficiently describes the misphasing of spectrum elements of radiated signals.

By our opinion, the main reason of distortion could be nonlinear dependence of phase shift in spectrum of radiated signal. This could be caused by Wood's resonances concerning with crossradiation of antenna elements. We consider transformation of signal as a filter with could be represented as a operator $T(\omega) = A(\omega) e^{i\Phi(\omega)}$ (Fig. 1), there $\Phi(\omega)$ — phase shift for different components of signal spectrum.

If $\Phi(\omega) \sim \omega$ then signal keeps it form and could only shift in time domain. But, if $\Phi(\omega)$ has nonlinear dependence then the form of signal could change [1]. Schematically this could be considered as nonlinear dependence near points of resonance (Fig. 2). We propose that nonlinear regions of $\Phi(\omega)$ have periodic character. The description of these anomalies looks naturally in embedding method.
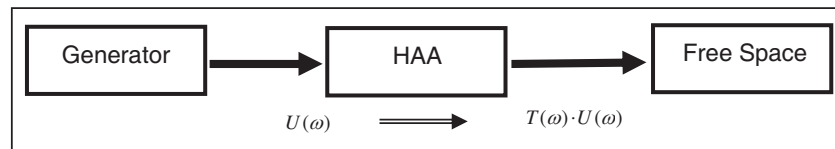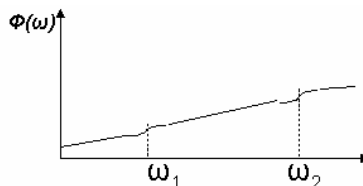

Figure 1: Transformations of impulse.

Figure 2: Nonlinear regions of $\Phi(\omega)$.

2. HORN ARRAY ANTENNAS AS A MATCHING LAYER. EMBEDDING METHOD

Let's consider the problem of impulse radiated by horn array antenna (Fig. 3) [2]. Such geometry provides more efficient of radiation by better matching of filed in feeding waveguides with free space.

For description of transparency coefficient $T(\omega, q, q')$ we will use technique of periodic prolongation of antenna. Such representation allows us to represent filed in free space as a discrete set of plane waves. In this way operator $T(\omega, q, q')$ takes view of matrix operator $T(\omega, q, q') \rightarrow T_{qq'}(\omega)$.
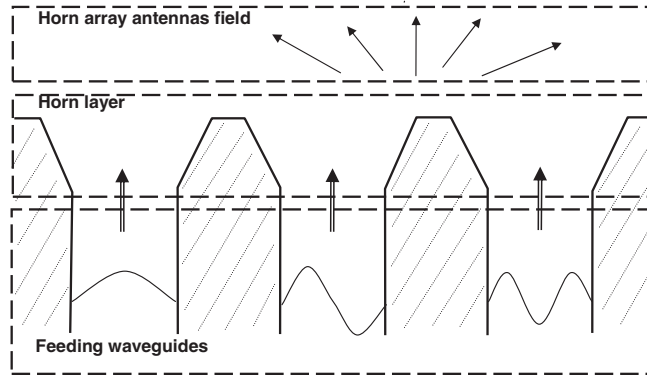

Figure 3: Horn array antenna.

According to ideology of embedding method [2–4] we could reduce boundary problem to *Cauchy* problem. As a initial condition we will consider the system of truncated waveguides. As a embedding parameter we will take height of horn layer $h \in [0, H]$. To obtain embedding equations we must build dependence of $T(z + \Delta z)$ from $T(z)$. Since evolution of $T(z)$ depended on reflection coefficient of horn layer $R(z)$, further we will consider evolution of this parameters together.

As it was shown in [2, 4] embedding equations takes following form:

$$
\begin{aligned}
T(z + \Delta z) &= t(\Delta z) \left(\sum_{k=0}^{\infty} (R(z) r(\Delta z))^k \right) T(z) \\
R(z + \Delta z) &= r(\Delta z) + t(\Delta z) \left(\sum_{k=0}^{\infty} (R(z) r(\Delta z))^k \right) R(z) t(\Delta z)
\end{aligned}
\tag{1}
$$

where series

$$
\sum_{k=0}^{\infty} (R(z) r(\Delta z))^k
\tag{2}
$$

Describes multiply scattering of filed in virtual resonator consisted of semitransparent mirrors. Lower mirror of resonator is a truncated horn layer and upper is a elementary layer with coefficient of reflection and transparency r, t. In previous woks, series (2) excludes from system and considered single equation for $T(z)$

$$
T(z + \Delta z) = [R(z + \Delta z) - r(\Delta z)] t^{-1}(\Delta z) R^{-1}(z) T(z)
\tag{3}
$$

For $R(z)$ the additionally Ruccati equation were used [2, 3].

In new approach we propose to represent series (2) as sum of geometric progression with coefficient $R(z) r(\Delta z)$. It could be shown [5] that such operator's series converge if spectrum radius is less then one $(\lambda(R \cdot r) < 1)$. In this case following equation takes place:

$$
\sum_{k=0}^{\infty} (R \cdot r)^k = [I - R \cdot r]^{-1}
\tag{4}
$$

Let's mark new operator as $M = I - R \cdot r$ and rewrite system (1) marking elements connected with layer z by index n and with layer $z + \Delta z$ by index $n + 1$:

$$
\begin{cases}
T_{n+1} = t_{n+1} \cdot M_{n+1}^{-1} \cdot T_n \\
R_{n+1} = r_{n+1} + t_{n+1} \cdot M_{n+1}^{-1} \cdot R_n \cdot t_{n+1} \\
M_{n+1} = I - R_n \cdot r_{n+1}
\end{cases}
\tag{5}
$$

System (5) represents recurrent equations witch allows us to observer the evolution of antenna parameters with increasing height of horn layer. Such system is also could be used with more complexity antenna geometry. In way that Δz is little enough — elementary layer could be represented as a lattice of ideal conductive bars with small height. By choosing the difference of bars parameters from layer to layer we could get different geometries of horn layer including inhomogeneous dielectric permittivity.

Since system (5) describes iteration procedure the error if calculation of r and t could accumulate. This situation provides more complexity requirements to accuracy of calculating t_n and r_n witch describes diffraction of plane wave (homogeneous and inhomogeneous) on elementary layer.

3. THE RESULTS OF NUMERICAL EXPERIMENTS

Equations (4) were tested on following problem. We take the lattice of bars and try to grow it by embedding method using system (4). We made test with different quantity of iterations $m = 2, 10, 100$ and compare results with etalon solution. It could be shown (Fig. 4) that we have good accuracy to etalon solutions. And only on higher modes we see the growing of errors.

Checking of Pointing's theorem for this problem show us that errors grows slowly from quantity of iterations (Fig. 5) and in worst case ($m = 100$) makes 2% near the point of resonance. To reduce errors we must choose criteria for value of elementary layer height (h) and increase number of modes considering in equations.
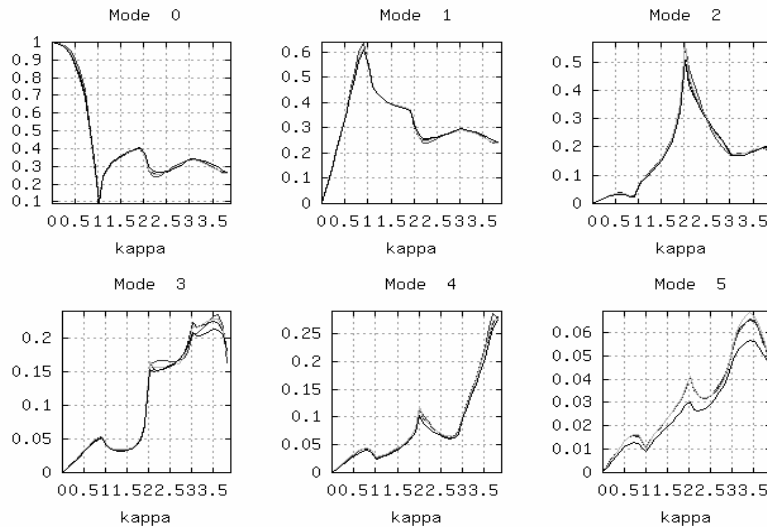

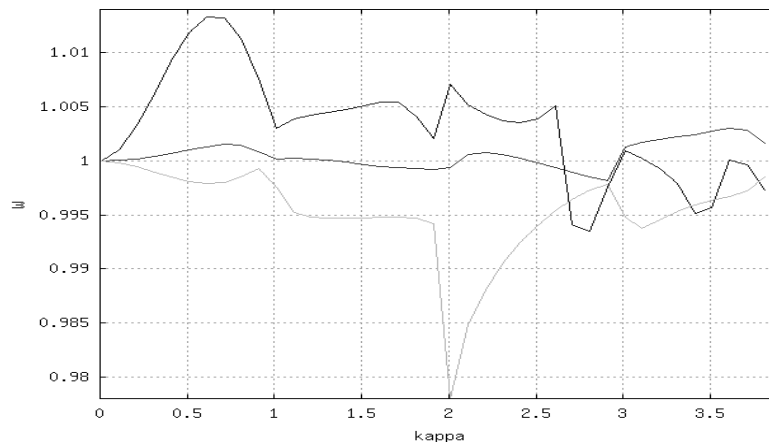Figure 4: Solution of etalon and testing system.

Figure 5: Pointing theorem.

4. CONCLUSION

The problems of nanosecond radiolocation considered. Proposed reason of distortion of UWB signals. New model for horn array antenna are proposed. Numerical experiments confirm possibility of implementation of new model to problem of horn array antenna radiation process.

REFERENCES

1. Wainshtein, L. A., *Electromagnetic Waves*, 1957.
2. Bakhrakh, L. D., V. L. Kuznetsov, and I. I. Vizgina, "The theory of HAA (embedding method)," *Telecommunications and Radio Engineering*, No. 8–9, 2004.
3. Bakhrakh, L. D., A. I. Kozlov, and V. L. Kuznetsov, "Ideology of embedding method in theory of HAA-antennas," *Telecommunications and Radio Engineering*, No. 2, 48, 2001.
4. Filonov, P. V. and V. L. Kuznetsov, "The new approach of computing transparency of horn layer of linear antenna lattice," *Progress In Electromagnetics Research Symposium Abstracts*, Beijing, China, March 26–30, 2007.
5. Kantorovich, L. V. and G. P. Akulov, *Functional Analyses*, 1984.

Electric and Magnetic Spinor Particles — The Electromagnetic Source of Gravitation, Theory and Experiments

Robert Sizov

Individual researcher, Moscow, Russia

Abstract— The universally known gravitational field is electromagnetic in its nature and, under natural conditions, is generated by EM atomic and nucleonic shells. Immediate elementary sources of GF are provided by eddy EM quasi-particles (*s*-gravitons) which contain electric and magnetic fundamental particles, both material and physical-vacuum ones.

The *s*-gravitons constitute the so-called compensated EM density and populate atomic or nucleonic orbits in accordance with the refined Pauli principle for EM shells (see the entry for Pauli principle in the Glossary).

The existing theoretical contention that atoms in the normal (unexcited) state do not emit., anything is profoundly erroneous. Atoms in any state continuously generate a gravitational EM fields constitutive, for example, the Earth gravity field. As to excited atoms, they emit photons (known from spectra of atomic emission) in the pulsed mode in addition to atomic gravitational radiation. Note that the emission of photons appears to be, generally speaking, exotic against the background of steady generation of GF by atoms.

It is worthy of note that the gravitational field, which is simple to perceive, as well as to technically implement, remains an unrealizable dream and a cause for endless theoretical variations until the magnetic particles are recognized by scientists and engineers and until controlled MC currents are involved in experiments and technical projects.

Atomic gravitational fields may be both vector (axially vector) and tensor ones. Condensed media (liquids and solids) for the most part radiate a tensor GF field. In particular, the Earth gravity field is a tensor one. Mutual repulsion or displacement of one film by the other takes place between the vector and tensor gravitational fields. Such interactions manifest themselves in the effects of volatility of light atoms (molecules) of gases, for example, gaseous hydrogen.

Continuous generation (radiation) of gravitational field by atomic EM shell made up of electrons and magnetons presumes the mandatory existence of the World fundamental field medium; in the processes of interaction with this medium, the fundamental particles show their "capacity" to generate fields which correspond to their nature. Regarded as such medium in the present book are fields of physical vacuum (PV). Under conditions of interaction of electrons and magnetons with PV field medium, they "act" as continuously operating converters of initial PV fields into electric or magnetic fields corresponding to these particles. The very capacity of electrons and magnetons for such transformations is perceived as their charge.

The geometric direction of flow of transformation of PV field medium by fundamental particles may apparently serve as explanation for a sacramental notion such as spin vector of particles. If the fundamental particles involved in the processes of foregoing transformations perform a rotational motion and, in so doing, the rotation axis coincides with the direction of flow of transformation of PV into respective fields, the word *spin* will correspond to the universally accepted opinion of spin as intrinsic rotational moment of movement of particles. However, in this case, the notion of spin of fundamental particles acquires a physical content which shows up as its correlation with the processes of transformation of initial PV fields into electric and magnetic fields.

The part played by the spin of fundamental particles is not limited to defining the direction of flow of transformation of PV fields. The modulus of the spin vector $|\mathbf{S}|$, which corresponds to the angular rotational velocity of particle, defines the rate of efflux of the flow of fields being transformed, i.e., the rate of propagation of intensity of electric and magnetic fields and, in the end, the velocity of light in the medium.

Given in the book is the author's assumption as to the nature of the charge of fundamental particles (electric or magnetic), which may be defined by the direction of rotation of particles (counterclockwise or clockwise). These directions of rotation may be introduced into electrons and magnetons during their production by respective left or right neutrinos.

The processes, of transformation of initial PV fields into excited fields such as electric and magnetic ones are performed exclusively by material fundamental particles, namely, electrons and

magnetons. The negative charge of material particles always corresponds to this pattern (directionality) of the process of transformations. At the same time, processes of inverse directionality are realized under conditions of spinor system (compositions of physical mass), i.e., transformation of excited fields into initial PV fields. The fundamental PV particles, which always realize the latter transformations, are charged positively. Hence follows that the positive charge of any elementary particles is always defined by positively charged fundamental PV particles, and the negative charge — by negatively charged material fundamental particles. For example, the positive charge of proton is defined by its component PV particles.

The atomic gravitational field, which is formed by both nucleons and EM density of atomic shells, manifests itself beyond the limits of atoms and constitutes fields of gravity of bodies. However, in addition to this, forces of interatomic gravitational attraction act between atoms as individual sources of natural GF. These forces are estimated as very significant for interatomic spacmgs of $< 10^{-8}$ cm; they are universal and may quite serve as the basic forces in the formation of condensed states of substance (solids, liquids). The universally known interatomic bonding forces (metallic, covalent, hydrogen etc.) are specific and define the individual features of the physical and mechanical properties of condensed formations. The effects of interatomic gravitational attraction mentioned above were previously overlooked by theory, because the erroneous concept of purely electron shell of atom ruled out any possibilities of even assumptions of the existence of these so significant classical bonding forces.

The author's inference that it is the atom-like structure (nucleus and EM shell) of any elementary particle that defines its ability to generate intrinsic GF. Hence follows that our ordinary substance, which is formed by atom-like elements (nucleons, atoms), is a gravitation-generating medium (GGM) or a variety of physical mass. Note that, in addition to generation of GF, the physical mass is further characterized by photon emission; therefore, gravitation-generating media may be referred to as "light media". However, phase states may quite possibly exist, which are on a lower stage of structural organization and do not contain atom-like elements in their medium. The structural formations of such phases are incapable of generating intrinsic gravitational fields, while these formations proper (which came to be referred to as gravitation-non-generating media — GNGM) drop out of gravitational interactions defined by the law of gravitation. In addition, by virtue of the low structural organization of constituent elements, media of the type of GNGM are most likely devoid of any capabilities of photon emission either. Therefore, media of the type of GNGM may well be referred to as "dark matter". Media of the type of GNGM ("dark matter") apparently make up the major part of material Universe. For example, in [25] noted that our ordinary "light media" or GGM makes up 20% or less of the material part of the Universe.

Because nucleons generate intrinsic gravitational field, i.e., their structure is atom-like, they are involved, as components of nuclei, in internucleon gravitational interactions which show up in their mutual attraction. Therefore, the forces of internucleon gravitational attraction are active in atomic nuclei in addition to the forces of universally known Coulomb repulsion of protons and forces of compression of nucleons by atomic gravitational pole (see Section 2.8 of the book). For internucleon spacings in nuclei of $< 10^{-13}$ cm, these forces are estimated as very significant. Most probably, it is these bonding forces between nucleons as sources of intrinsic gravitational fields that define the possibility of existence of stable atomic nuclei devoid of EM shells.

An example of manifestation of forces of internucleon gravitational attraction may be provided by α-particles which remain stable even after the EM shell is "stripped off" them. It is believed that the forces of internucleon gravitational attraction in nuclei, may exceed the forces of Coulomb repulsion of protons. Note that the protons in nuclei are likewise involved in internucleon gravitational attractions.

In view of the author's contention that nucleons are miniatoms with EM shell of their own and a nucleus, it is logical to infer the possible existence in nucleons of electric and magnetic particles with charges smaller than those of electron and magneton. By analogy with atomic structure, minielectrons and minimagnetons must be present in the composition of EM shell, on its orbits, and miniprotons and minineutrons — in the composition of nucleonic nuclei. It is known that electric quarks with charges of 1/3 and 2/3 of electron ones, which are charged both positively and negatively, are adopted in the physics of elementary particles. The negatively charged quarks, along with minimagnetons, may well form EM shells of nucleons, and the positively charged quarks may enter the composition of nucleonic nuclei as miniprotons. The author made an assumption that miniproton in nucleonic nuclei may well be provided by universally known positron.

The discovery of magnetic particles and their introduction into the physical concepts made it possible to more accurately define the structure of atom, as well as to clarify the principle of structural arrangement of nucleons. It is demonstrated in this book that nucleons are miniatoms

with EM shell and nucleonic nucleus. Owing to their atom-like structural organization, nucleons are direct sources (generators) of tensor gravitational field which manifests itself in their mutual gravitational attraction. For internucleon spacings in atomic nuclei ($< 10^{-13}$ cm), these forces are estimated to be very significant. In the author's opinion, it is these forces of mutual attraction of nucleons that make up strong interaction. Because the gravitational field is an electromagnetic field, the strong interaction is likewise electromagnetic by nature, at least, in atomic nuclei. Therefore, according to the results of investigations performed by the author, three interactions out of the known four are electromagnetic by nature. The true nature of weak interaction is still to be clarified.

Effective Experiments:

1. **Attempts at Experimental Generation of a Gravitational Field Using Rotating Superconductors**
2. **Experiments in Determining the Sign of Interaction between Natural (Tensor) and Artificial (Vector) Gravitational Fields**
3. **Experiments in Clarifying the Nature of Volatility of Atoms (Molecules) of Gases Using the Manifestation of Volatility of Gaseous Hydrogen as an Example**

1. SOME OF REFINED PHYSICAL TERMS

Atom is a variety of physical mass, which is formed by spinor (material and physical-vacuum) particles incorporating a nucleonic nucleus and EM shell. The latter largely consists of *s*-gravitons, i.e., dynamic spinor quasi-particles formed by eddy electric and magnetic bispinors. The stable functioning of atoms is defined exclusively by interactions between spinor particles, which are accomplished via spinor fields. Atoms form atomic GF which make up the gravitational fields of all bodies, including the GF of the Earth. In addition, excited atoms emit diverse photons. Determining interactions in stationary atoms are gravitational interactions of *s*-gravitons with nuclei and other *s*-gravitons. The interactions of the former type manifest themselves as the repulsion of *s*-gravitons from the nucleus, and the latter ones — as both the repulsion and attraction of *s*-gravitons from and to one another. The electric Coulomb interaction between atomic electrons and nucleus show up in full measure only in the formation of atoms; in normal atoms, the Coulomb attraction between orbital electrons and nucleus is most likely absent. Also absent in stationary atoms is the interelectron repulsion. The reason for these absences is the fact that electrons, similar to magnetons, in an EM atomic shell are included in the structures of quasi-particles such as *s*-gravitons which emit exclusively GF. It is to the composition of GF that the orbital electrons and magnetons "deliver" their fields as its electric and magnetic components.

The shells of magnetic atoms (Fe, Co, Ni, and others) further emit the magnetic spinor field rot $\mathbf{H}^\circ$. The sources of atomic magnetic fields are provided by magnetic bispinors which are unpaired with electric bispinors and are moving as a rule in outer atomic orbits.

Gravitational Field is a spinor EM field with close (circular) lines of force, whose intensities at any point are defined by the axial vector rot $[\mathbf{E}^\circ - \mathbf{H}^\circ]$. The elementary source of GF is the spinor dynamic EM quasi-particle, discovered by the present author and given the name of *s*-graviton. The *s*-graviton consists of electron and magneton plus the respective antiparticles (antispinor PV particles). The *s*-graviton may be represented as the electric and magnetic currents which are in phase with each other, are simultaneously realized in a very small closed conductor turn, and are defined by the expression rot $[J_e^\circ - J_g^\circ]$ The gravitational field formed by a single *s*-graviton is a vector (axial-vector) field. The gravitational fields emitted by atoms, in whose shells numerous *s*-gravitons exist, as well as by condensed substances, are tensor fields defined by tensors of rank two and corresponding at each point to the vector condition $\langle \text{rot}\,[\mathbf{E}^\circ - \mathbf{H}^\circ] \rangle = 0$. However, in practice, the foregoing axial-vector compensation of GF at any point does not result in the compensation of the force effect of GF. The tensor GF may also be referred to as quasi-scalar field, which is characterized by the density gradient of gravitational lines of force.

Mutual rejection or displacement of one field by the other shows up between the tensor and vector gravitational fields. It is this interaction between the tensor gravitational field of the Earth and the vector gravitational field of atoms of light gases, for example, of hydrogen, that defines the effect of volatility of these light gases.

The GF waves are plane and sinusoidal and are characterized by the oscillation of the vectors of dynamic intensities $\mathbf{E}^\circ$ and $\mathbf{H}^\circ$ with antiparallel orientation.

The capacity for the formation of gravitational field is the basic property of the physical category such as mass; therefore, the *s*-gravitons must be further recognized as the elementary "brick" of physical mass.

Mass (physical) is a spinor material-and-physical-vacuum formation which emits both gravitational field and photons. Classed with the category of physical mass (PM) must be everything that is structured within the spinor system starting with s-graviton (see the entry for s-graviton in this Glossary) and on to nucleons, atoms, and substance. Apparently, the varieties of mass include elementary particles such as positron, muon, and heavy lepton. Note that the material particle such as neutrino is massless. Also massless are the components of mass such as electron and magneton. The initial elementary "brick" of mass is provided by s-graviton. The mass may further be referred to as "light" formation, in view of the fact that it is only the mass that is capable of emitting photons. Matter in the form of electric and magnetic fundamental particles, for example, electrons and magnetons, enters into the compositions of physical mass; however, it is important to emphasize that the mass and matter are, in principle, entirely different physical categories and cannot be confused. The mass exhibits inertial properties; however, these properties are introduced exclusively by matter, i.e., by material particles in its compositions. As was already mentioned, electrons and magnetons as purely material particles are not mass. The universally known principle of equivalence of gravitational and inertial forces is valid strictly within physical mass, though not in all of its varieties. Outside of the limits of mass, this principle makes no sense whatsoever, because there is nothing in this case that may produce a gravitational field. For example, the material particles such as electron, magneton, or neutrino exhibit only inertial properties and are absolutely incapable of exhibiting gravitational properties. The violation of equivalence principle is obvious here. In view of the foregoing, the generally accepted terms of "inert mass" or "electron mass" present absolute physical absurdity.

Matter: in the most general sense, matter in pure form is everything that is not mass or field. An exclusive property of matter is its capacity for exhibiting inertia. In addition, matter in pure form involves the complete absence of the capacity for emission of both gravitational and photon EM fields. It must be emphasized that matter is just a part of mass, its material filling. The fact that the mass is likewise characterized by the capacity for inertia is defined by the presence in its compositions of material particles, for example, electrons and magnetons. Material fundamental particles, which exist outside of mass, make up the so-called "dark matter". The interaction between matter and PV fields is accomplished by means of material fundamental particles, for example, electrons and magnetons which, owing to their charge and spins, are capable of transforming initial PV fields into electric and magnetic fields. In addition, material fundamental particles along with PV particles form physical mass (nucleons, atoms, substance etc.).

s-Gravitons are spinor electromagnetic dynamic quasi-particles. They are elementary sources of all gravitational fields, as well as basic "bricks" of physical mass. The letter s stands for source. Two dynamic bispinors (electric and magnetic ones) enter into the composition of s-gravitons; the bispinors proper are bound pairs of spinor particles, for example, electron and PV antielectron. All four fundamental particles (two material and two physical-vacuum ones) in the composition of quasi-particle such as s-graviton produce eddy (circular) EM current which shows up in the ambient space as axial-vector GF. The EM current produced by a single s-graviton is defined by the expression rot $[J_e^\circ - J_g^\circ]$, where J_e° and J_g° are the density vectors of circular electric and magnetic currents, respectively. The minus sign in the foregoing expression corresponds to the phase angle of $180°$ between the electric and magnetic currents.

Each atomic orbit in the composition of EM shell is populated by a single s-graviton rather than by a single electron, as is generally believed. The pole particles in the composition of s-gravitons "deliver" their fields strictly into the composition of gravitational field which is a spinor or, to be more precise, dibispinor EM field. Therefore, under natural conditions, s-gravitons are realized in EM shells of atoms or nucleons and show up as atomic or nucleonic gravitational fields.

The universally known Pauli principle was refined in this book in application to EM shell and, in this case, consists in the following: only one s-graviton may be located on one atomic or nucleonic orbit. Note that the so-called minielectrons and minimagnetons enter into the compositions of nucleonic s-gravitons. It is further significant that electron- and magneton-based s-gravitons were artificially produced by the author by way of pairing linear currents of electric and magnetic charges in superconductor

Pauli Principle (refined) consists in that only one s-graviton may be located on one atomic orbit in EM shells of atoms. Another, possibly easier to perceive, definition of refined Pauli principle for the case of EM shells of atoms is as follows: only two spinor material particles, namely, electron and magneton, may be located in one and the same atomic orbit or in one and the same quantum state. Note that the latter definition is not exhaustive, because it implies "carrying" PV particles

without which no spinor electron and magneton are possible.

REFERENCES

1. Sizov, R. A., *Electric, and Magnetic Spinor Particle — Structure-forming Component Mass and Electromagnetic Source of Gravitation*, Moscow, 2008.

Generation of the Microwave Chaotic Oscillations by CMOS Structure

Artem Yu. Nikishov[1, 2]

[1]Moscow Institute of Physics and Technology, Russia
[2]Kotel'nikov Institute of Radioengineering and Electronics of RAS, Russia

Abstract— In the report CMOS-structure, representing self-oscillation system and capable to generate ultrawideband microwave chaotic signal with uniform power spectral density, is proposed. Results of the simulations of the oscillator circuit, its topology and its experimental realization as an integrated microcircuit on 180 nm CMOS process are presented. Basic dynamics of the oscillation modes is described. The fact of the chaotic oscillations generation is shown. Bifurcation phenomena are analyzed. It is proved that chaotic oscillations are excited on the basis of mechanism of double-frequency oscillations mode destruction. Proposed CMOS-structure oscillator can be used in different wireless communication applications as a compact device for ultrawideband microwave chaotic signal generation.

1. INTRODUCTION

Chaotic oscillations have certain advantages which make them attractive to use in ultrawideband (UWB) applications. Among these are: ultra wide bandwidth (naturally spread spectrum), large variety of chaotic modes in oscillators and possibility of their control, relative simplicity of oscillators structure, self-synchronization, stability to fading in multipath environment, etc.

A promising approach to UWB communications is direct chaotic communication (DCC) scheme. The basic idea of DCC is that generation of chaotic carrier, its modulation and demodulation by information signal are performed in microwave band [1–3].

Effective sources of UWB chaotic signals are necessary for implementation of such systems. These sources must have a simple structure, form a chaotic signal in a necessary frequency band and provide uniform power spectral density. The main requirements to the sources are: low weight and size, reliability, low power consumption, etc. One of types of such sources is ring chaotic oscillation system based on the lumped elements and used RFIC amplifiers as active elements [4]. This oscillator allows generating UWB microwave chaotic signal with uniform power spectral density in bandwidth from 3 to 5 GHz and output power is about 0.5 mW.

Distinctive feature of this oscillator is absence of any microstrip lines and presence only lumped elements, such as resistance, inductance, capacity and RFIC amplifiers which in experimental realization can be simply presented as surface mounting device (SMD). Possibility of chaotic oscillator realization on the lumped elements gives a chance to implement such type of oscillator as an integrated microcircuit.

In this report CMOS-structure, capable to generate UWB microwave chaotic signal with uniform power spectral density, is proposed. This CMOS-structure actually representing ring self-oscillation system that realized as an integrated microcircuit on 180 nm CMOS process and consists of three microwave amplifiers and a frequency selective circuit (on which parameters the range and bandwidth of oscillations frequencies depends) connected in series in a closed loop. Results of the simulations of the oscillator circuit, its topology and its experimental realization are presented. Basic dynamics of the oscillation modes is described. The fact of the chaotic oscillations generation is shown. Bifurcation phenomena are analyzed. It is proved that chaotic oscillations are excited on the basis of mechanism of double-frequency oscillations mode destruction. Proposed CMOS-structure oscillator can be used in different wireless communication applications as a compact device for UWB microwave chaotic signal generation.

2. SCHEME OF THE PROPOSED CMOS STRUCTURE

The block-scheme of the proposed CMOS-structure is presented in the Figure 1. The main parts of the system are three microwave amplifiers (AMPs) and a frequency selective circuit (FSC) connected in series in a closed loop. All of them are matched on 50 Ohm and implemented on the 180 nm CMOS process libraries.

The FSC has one RC-, and some LC-sections. In this paper oscillator with two LC-sections in the feedback loop is considered (Figure 2). The similar set of sections is chosen because it is
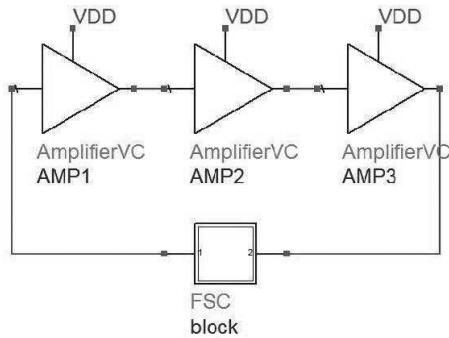
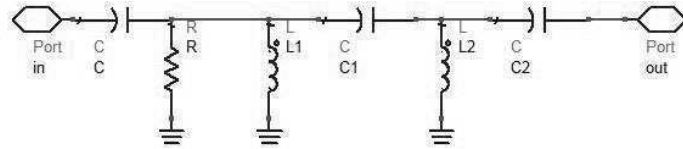Figure 1: Block-scheme of the ring CMOS-structure.

Figure 2: Block diagram of the FSC.

minimum set for chaotic oscillations generating on the basis of mechanism of double-frequency oscillations mode destruction. This RC- and LC-sections are high-pass filters and it is distinctive feature of the oscillator. Therefore using given sections and microwave amplifiers it is possible to generate ultrawideband microwave chaotic oscillations.

Amplifiers (AMPs) represent especial interest because they have very simple structure but form a system that is very steady against various fluctuations of values of elements of which it consists. The AMPs are small-signal microwave amplifiers with amplification gain from 10 to 2 dB in frequency band from 1 to 10 GHz. Each AMPs used in oscillator consists of two cascades. The first cascade is an inverter (common-source circuit) with negative feedback. The second cascade is a buffer (common-drain circuit). The important property of the proposed ring self-oscillation system is absence of necessity for additional adjustment of the device after its manufacturing in integrated circuit form because it is supposed that oscillator supply voltage will be the unique adjustable parameter capable to influence on the device work.

3. SIMULATION

Ring chaotic self-oscillation system (proposed CMOS-structure) dynamics is investigated by means of considering the following questions: establishment of the fact of chaotic oscillations generation at certain parameters of the system; analysis of spectral characteristics; studying the bifurcation phenomena; determining the scenario of the chaotic oscillations evolution. This research can be most effectively carried out by means of oscillator simulation in some CAD system.

For such simulation, model and topology of the CMOS-structure integrated microcircuit based on active and passive elements of the 180 nm CMOS process was designed according to block-scheme represented in the Figure 1.

An analysis of the oscillator model spectral characteristics has shown that at different the supply voltage various oscillation modes, including chaotic, are observed. For instance, single-mode oscillations are excited at a frequency close to 4 GHz at supply voltage 1.4 V (Figure 3(a)). The supply voltage increase up to 1.6 V (Figure 3(b)) leads to excitation of oscillations on the second frequency (0.7 GHz). Then double-frequency oscillations mode is replaced by the multifrequency mode (Figure 3(c)) and, at last, oscillations become chaotic at voltage 1.8 V (Figure 3(d)).

As follows from the bifurcation diagram analysis (Figure 4), single-mode oscillations are excited at first time, when supply voltage is sufficiently small. Then supply voltage increase leads to excitation of double-frequency oscillations mode and invariant torus is formed in oscillations phase space. The further voltage increase leads to structural reorganization of the resonances on the torus which finally comes to its subsequent destruction and transition to chaos. Such structural reorganization of the resonances is reflected in an increase of the number of spectral components of the output signal. Thus, in this case chaotic oscillations are excited on the basis of destruction of double-frequency oscillations mode. The described process illustrates a general principle of UWB chaotic oscillations generation in considered self-oscillation system. Frequency range and bandwidth of the generated signal utterly corresponds to those of AMPs used and the cutoff frequency of the FSC.

Possibility of double-frequency oscillations mode in the system is explained by the following circumstance. As follows from the phase-frequency response (PFR) represented in the Figure 5,
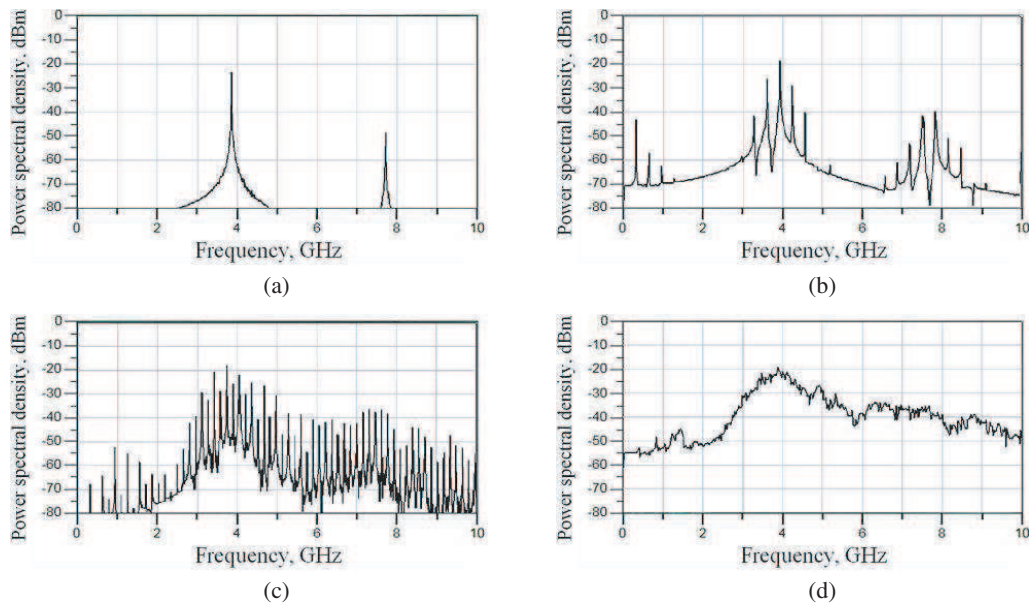
(a)

(b)

(c)

(d)

Figure 3: Oscillations power spectral density for supply voltage: (a) 1.4 V; (b) 1.6 V; (c) 1.65 V; (d) 1.8 V.
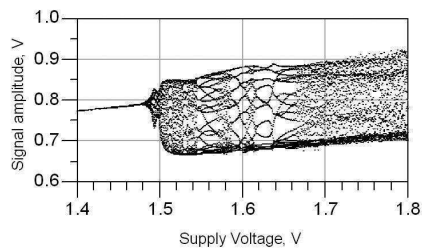

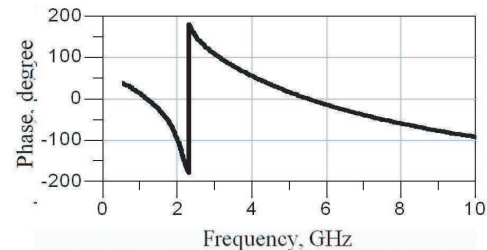Figure 4: Bifurcation diagram as a function of supply voltage.

Figure 5: PFR of the proposed ring CMOS-structure feedback loop.

in the range from 0 to 10 GHz two frequencies have phase incursion $2\pi n$, where n is an integer. According to Nyquist-Mihaylov criterion, self-sustaining oscillations can excite on each of these frequencies in case the amplitude balance is fulfilled (feedback loop gain is above unity). Analysis of the amplitude-frequency response (AFR) shows that at supply voltage 1.4 V the feedback loop gain becomes more than unity at a frequency close to 4 GHz. So, at this frequency a first self-sustaining oscillation mode appears. Then, at supply voltage 1.6 V, oscillations at second 0.7 GHz frequency occur, thus, double-frequency oscillations mode is observed.

According to the simulations results the basic power of the oscillations contains in the frequency band from 3.6 to 4.6 GHz and it is about -4 dBm. Consumed current is 25 mA.

4. EXPERIMENT

Using positive simulation results, an experimental realization of the proposed ring CMOS-structure as an integrated CMOS microcircuit was made. Microcircuit topology size is about $0.8 \times 0.9 \, \text{mm}^2$ (microcircuit in QFN package represented in the Figure 6). Frequency modes were adjusted by varying supply voltage in the range from 0 V to 3.5 V.

Experimental investigation showed that single-mode oscillations excite at the frequency close to 3.3 GHz at supply voltage 1.5 V (Figure 7(a)). With an increase of supply voltage double-frequency oscillations mode (second frequency is about 500 MHz) that are then replaced by multifrequency mode (Figures 7(b) and 7(c)) appear. At supply voltage about 2.5 V chaotic oscillations with uniform power-density spectrum and integrated power of about -6 dBm occur in frequency band 2.8–3.8 GHz (7(d)).
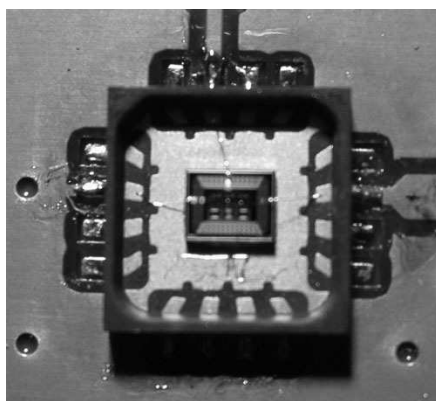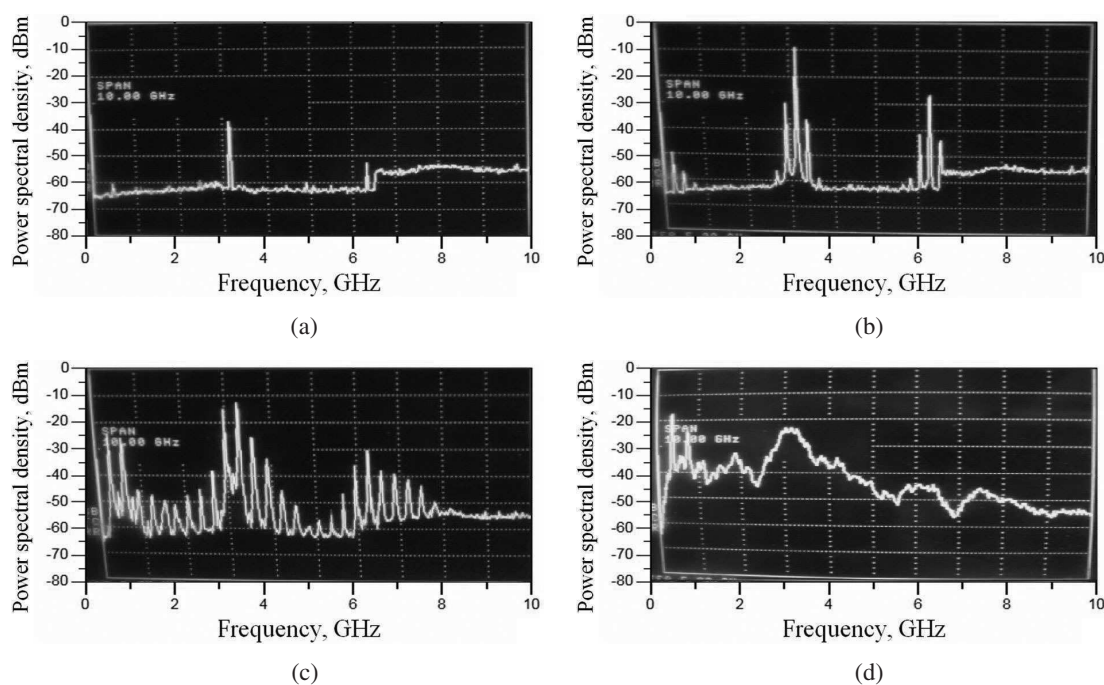
Figure 6: Microcircuit in QFN package.

Figure 7: Oscillations power spectral density for supply voltage: (a) 1.5 V; (b) 2 V; (c) 2.3 V; (d) 2.5 V.

5. CONCLUSION

In the report CMOS-structure, representing self-oscillation system and capable to generate ultra-wideband microwave chaotic signal with uniform power spectral density, is proposed. The basic result of work is realization of the CMOS-structure as an integrated microcircuit on technology 180 nm with the topology area less than $1 \, \text{mm}^2$ and demonstration of its activity in experiment.

Experimental realization of the device has confirmed simulation results. Chaotic oscillations have uniform power spectral density in frequency band from 2.8 GHz to 3.8 GHz and integrated output power reaches about −6 dBm.

It is possible to draw following conclusions by the results of simulations and experimental researches. At first, oscillation modes which were observed in experiment qualitatively identical to oscillation modes which were observed at simulation. It means that theoretical conclusions about bifurcation phenomena based on the simulation are experimentally proved.

At second, chaotic oscillations are really excited on the basis of mechanism of double-frequency oscillations mode destruction.

At third chaotic modes can be controlled using only external supply voltage of the device that does its very convenient from the point of view that there is no necessity for additional adjustment of fabricating microcircuit samples.

Quantitative discrepancies between model and experiment are certainly observed. However it is explained by technological errors arising at microcircuits fabrication. But at simulations this errors were not considered because qualitative acknowledgements of theoretical assumptions (the scientific component) was important.

Thus, proposed ring CMOS-structure oscillator can be used in different wireless communication applications as a compact device for UWB microwave chaotic signal generation.

Merits of the considered oscillator are:

- simplicity;
- tuning by supply voltage;
- represent as CMOS integrated microcircuit;
- stability (reproducibility) of chaotic modes;
- compatible with other integrated circuits and UWB devices;
- low-consumption device.

ACKNOWLEDGMENT

REFERENCES

1. Dmitriev, A., B. Kyarginsky, A. Panas, and S. Starkov, "Experiments on ultra-wideband direct chaotic information transmission in microwave band," *Int. J. Bifurcation and Chaos*, Vol. 13, No. 6, 1495–1507, 2003.
2. Dmitriev, A., M. Hasler, A. Panas, and K. Zakharchenko, "Basic principles of direct chaotic communications," *Nonlinear Phenomena in Complex Systems*, Vol. 6, No. 1, 488–501, 2003.
3. Dmitriev, A. S., A. V. Kletsov, L. V. Kuzmin, A. M. Laktushkin, A. I. Panas, and V. Y. Sinyakin, "Ultrawideband transceiver platform based on chaotic signals," *Proceedings of International Symposium NOLTA'2006*, Bologna, Italy, 2006.
4. Nikishov, A. Y. and A. I. Panas, "Generation of UWB microwave chaotic oscillations by ring-structure oscillation system composed of microchip amplifiers," *Proceedings of International Conference XXIX URSI General Assembly*, Chicago, USA, August 2008.

Forest Fire Localization Using Distributed Algorithms in Wireless Sensor Networks

A. Khadivi, **L. Georgopoulos**, and **M. Hasler**

School of Computer and Communication Sciences
Ecole Polytechnique Fédérale de Lausanne (EPFL), Switzerland

Abstract— The fire localization using a distributed consensus finding algorithm in a wireless sensor network is described. The fire is circumscribed by a circle. The information is available at all sensor nodes that are alive, which makes it robust against failures and losses. Minimizing energy consumption is crucial for sensor nodes that have to function autonomously as long as possible. Therefore, the speed of convergence of the consensus finding algorithm has to be optimized. We argue that optimizing, as is customary, the asymptotic speed of convergence is not the best method when a consensus value of low precision is sufficient.

1. INTRODUCTION

Wireless sensor networks are a new technology that starts being deployed for various applications, in particular for environmental monitoring. In this paper we are in particular addressing the monitoring of forest fires. Wireless sensor networks potentially can alert the fire brigades very shortly after the outbreak of a forest fire and give continuously information about its localization, even if the outbreak is in a very remote area. The main challenges are:

- The sensor and the wireless communication module at a node of the network should consume as little energy as possible. Therefore, as long as no fire has been detected, the communication module should be in a "sleep" mode. Nevertheless, it should be able to wake up in a very short time, either when its sensor detects a fire outbreak in its vicinity, or when it receives an order to wake up from a neighboring node.

- Again for energy conservation purposes, a communication module is restricted to communicate only with its neighbors. Thus, direct communication with a central base station is for most nodes in the network impossible. Therefore, a multi-hop protocol has to be adapted and/or information has to be elaborated locally.

- The fire will destroy part of the network as it progresses.

We suppose that at each network node, a temperature sensor is located that periodically takes measurements and makes them available for the communication module. The nodes are location aware, which can be achieved at network deployment time. Through iterated information exchange with its neighbors and processing, every node has all the information about the fire available. This information can thus be extracted by fixed or mobile means from any node of the network that is alive and communicated to the fire brigades. This makes the network robust against local failures.

The distributed computing approach in sensor networks has recently been described in the literature [1, 2]. The contribution of this paper is twofold:

- To enhance the speed of convergence of the algorithm in its initial phase.
- To show how the fire can be localized with distributed algorithms.

Here, the ideas are spelled out, but the details will be given elsewhere [3, 4].

2. SPEEDING UP CONSENSUS FINDING

As will be explained later, the basic mathematical operation to be performed is the computation of a mean value (also called consensus value) of a scalar quantity (e.g., temperature) over the whole or over part of the network. This cannot be done in one step since the various nodes can communicate only with their neighbors. However, a simple iterative algorithm allows reaching consensus, in theory only asymptotically in time, but in practice after a certain number of iterations. At each node and at each time step, taking the mean value of the current estimation of the quantity among the node and its neighbors is the simplest approach. Replacing the mean by a weighted mean [1] allows speeding up the convergence, which is important for energy conservation.

We suppose the network is obtained by randomly placing n sensor nodes in a finite area (the forest) according to a uniform probability density (they might be dropped by an airplane). Sensor nodes within wireless communication range are linked by an edge. We suppose that the resulting graph is connected. Let $x_i(t)$, $t = 0, 1, 2, \ldots$ be the state of node i at time t. It is initialized at $x_i(0)$, typically the unprocessed sensor measurement. For the linear consensus finding algorithm the update equation is

$$x_i(t+1) = \sum_{j=1}^{n} w_{ij} x_j(t) \tag{1}$$

or in vector form

$$\mathbf{x}(t+1) = \mathbf{W}\mathbf{x}(t) \tag{2}$$

The interaction weights w_{ij} are only different from zero if nodes i and j are within wireless communication range, i.e., joined by an edge of the graph. We suppose that the matrix $\mathbf{W}$ satisfies in addition the following conditions:

$$w_{ij} \geq 0 \text{ for } i \neq j, \quad \sum_{j=1}^{n} w_{ij} = 1 \text{ for all } i, \quad \mathbf{W} = \mathbf{W}^T, \quad \mathbf{W}\mathbf{1} = \mathbf{1}, \quad \rho\left(\mathbf{W} - \frac{1}{n}\mathbf{1}\mathbf{1}^T\right) < 1 \tag{3}$$

where "T" denotes the transpose and ρ the spectral radius of a matrix and 1 is the column vector composed of all 1's. These conditions guarantee that consensus is always reached:

$$\mathbf{x}(t) \xrightarrow[t \to \infty]{} \left[\frac{1}{n}\sum_{i=1}^{n} x_i(0)\right] \cdot \mathbf{1} \tag{4}$$

Furthermore, the speed of convergence to consensus can be deduced from [2]

$$\mathbf{x}(t) - \left[\frac{1}{n}\sum_{i=1}^{n} x_i(0)\right] \cdot \mathbf{1} = \left(\mathbf{W} - \frac{1}{n}\mathbf{1}\mathbf{1}^T\right)^t \mathbf{x}(0) \tag{5}$$

The question is now how to choose the nonzero interaction coefficients such that convergence is as fast as possible. For this purpose, it is useful to remark that $\mathbf{W} = \mathbf{I} - \mathbf{L}$ where $\mathbf{I}$ is the identity matrix and $\mathbf{L}$ is the weighted graph Laplacian. Since the eigenvalues of $\mathbf{L}$ are nonnegative, the eigenvalues of $\mathbf{W}$ satisfy $1 = \lambda_1 > \lambda_2 \geq \ldots \geq \lambda_n$. The eigenvector for eigenvalue 1 is 1. Therefore, the eigenvalues of $\mathbf{W} - \frac{1}{n}\mathbf{1}\mathbf{1}^T$ are 0 and $1 > \lambda_2 \geq \ldots \geq \lambda_n > -1$. The first and the last inequalities are strict, because of the condition on the spectral radius in (3). Clearly, due to (5) the asymptotic exponential convergence rate is given by $\min\{|\ln(1 - \lambda_2)|, |\ln(\lambda_n + 1)|\}$. In [2], it is shown that the matrix $\mathbf{W}$ that maximizes the asymptotic convergence rate can be found by convex optimization.

In Fig. 1, the error

$$Err(t) = \sqrt{\frac{1}{n}\sum_{k=1}^{n}\left[x_k(t) - \frac{1}{n}\sum_{i=1}^{n} x_i(0)\right]^2} \tag{6}$$

as a function of the iteration t is represented, averaged over 100 instances of Gaussian distributed random initial vectors $\mathbf{x}(0)$. The upper curve corresponds to weights obtained by convex optimization and the lower curve by the Metropolis-Hastings weights

$$w_{ij} = 1/\max\{d_i, d_j\} \text{ for } i \neq j, \qquad w_{ii} = 1 - \sum_{i \neq j} w_{ij} \tag{7}$$

where d_i is the number of edges connected to node i. The asymptotic rate of convergence is higher for the optimized weights, as it should be. However, if a precision of only about 0.1 is desired, the algorithm with the Metropolis-Hastings weights needs only about half as many iterations to reach this goal. In [3], it is shown that a nonlinear algorithm is able to combine both fast transient and optimal asymptotic convergence.
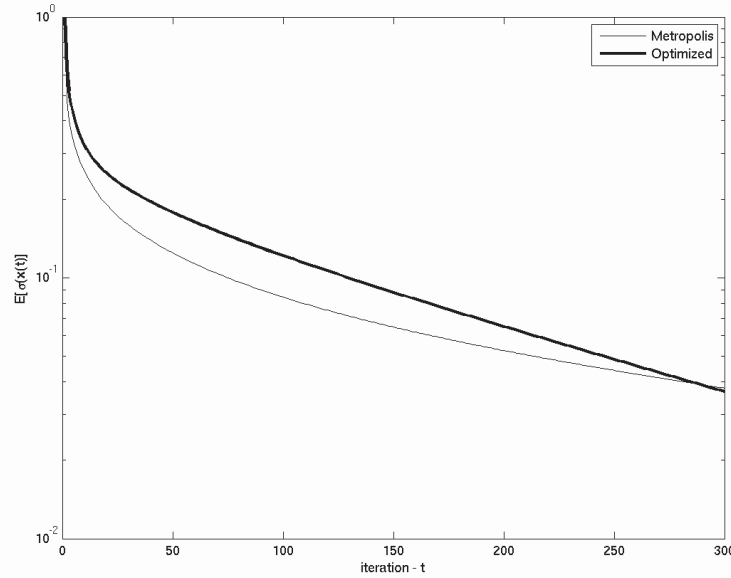
Figure 1: Evolution of the $Err(t)$ defined in (6) as a function of time. Bold: Connection weights obtained by convex optimization. Clearly the error has a faster asymptotic convergence rate Normal: Metropolis Hastings connection weights. The error decreases faster in the transient phase.

3. FIRE LOCALIZATION

Various distributed algorithms of the cellular automata type can be designed for fire alert. An example where all nodes of the network after a short time are alerted is described in [4]. We shall concentrate on the subsequent processing action of the sensor network, namely to localize the fire within a circle, because it is entirely based on consensus finding as described above.

At regular intervals, a consensus algorithm is run that approximates the perimeter of the fire by a circle. It is initialized by determining all sensor nodes that show an intermediate temperature (e.g., between 30°C and 150°C). The consensus algorithm is only run among these nodes. Denote their indices by $i_1, \ldots, i_m$, and suppose their geographical positions are $(x_{i_1}, y_{i_1}), \ldots, (x_{i_m}, y_{i_m})$. Then, we determine a circle of radius r and center (u, v) such that the mean square error of the radius

$$D(u, v, r) \quad = \quad \frac{1}{m} \sum_{k=1}^{m} \left[\sqrt{(x_{i_k} - u)^2 + (y_{i_k} - v)^2} - r \right]^2 \tag{8}$$

is minimal. This is a nonlinear least squares problem that can be solved by a sequence of linear least squares problems. It can be shown [4] that the linear least squares problem is solved, using some simplifying assumption, by computing the following three mean values

$$\frac{2}{m} \sum_{k=1}^{m} \frac{x_{i_k} - u}{\sqrt{(x_{i_k} - u)^2 + (y_{i_k} - v)^2}} \cdot \left(\sqrt{(x_{i_k} - u)^2 + (y_{i_k} - v)^2} - r \right)$$

$$\frac{2}{m} \sum_{k=1}^{m} \frac{y_{i_k} - v}{\sqrt{(x_{i_k} - u)^2 + (y_{i_k} - v)^2}} \cdot \left(\sqrt{(x_{i_k} - u)^2 + (y_{i_k} - v)^2} - r \right) \tag{9}$$

$$\frac{2}{m} \sum_{k=1}^{m} \left(\sqrt{(x_{i_k} - u)^2 + (y_{i_k} - v)^2} - r \right)$$

which is achieved by a consensus algorithm. The result, i.d. the center (u,v) and the radius r of the circle is communicated to all alive sensor nodes by multi-hop communication. The sensor nodes whose temperature is above a certain threshold (e.g., 200°C) are supposed to be dead. This neither disturbs the consensus algorithm among the nodes at the border of the fire nor the spreading of the information to all other alive sensor nodes.

In Fig. 2, the efficiency of the fire localization algorithm is shown. The evolution of the fire is simulated by the FARSITE fire simulation software [5]. The nodes in the border of the fire are
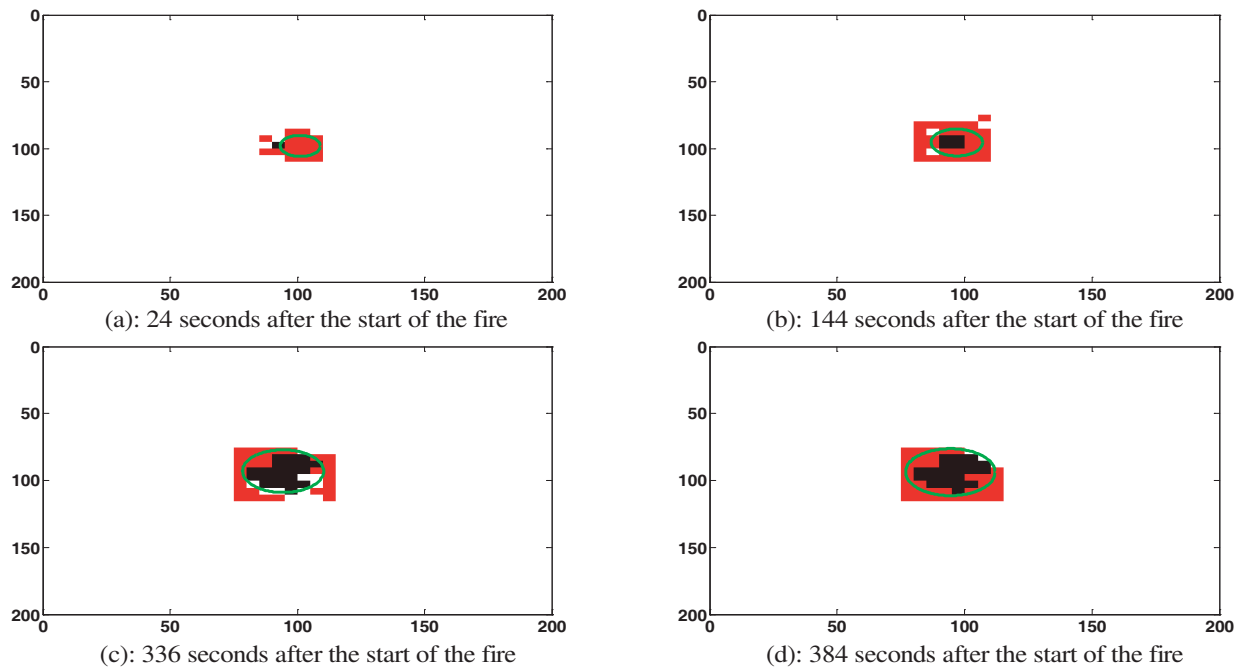
(a): 24 seconds after the start of the fire

(b): 144 seconds after the start of the fire

(c): 336 seconds after the start of the fire

(d): 384 seconds after the start of the fire

Figure 2: Sensor network deployed in a $200\,\text{m} \times 200\,\text{m}$ area. Each $5\,\text{m} \times 5\,\text{m}$ cell contains one sensor, placed in a random location. In the figure, the state of a sensor node is indicated by a color filling out the whole cell. Evolution of the border (red) of the fire (temperature between $30°\text{C}$ and $150°\text{C}$) in time, and the circle approximating it (green), computed by a consensus algorithm among the nodes in the border. The black sensor nodes are dead. The other sensors that are alive without being in the border of the fire are colored in white.

marked by dark read, the dead nodes and the computed circle is green. Clearly, the circle is a good approximation of the border of the fire.

4. CONCLUSIONS

We have shown how to use a consensus algorithm for fire localization by circumscribing it by a circle. The center and the radius of the circle are determined by repeated application of a distributed consensus algorithm. The information is made available at all sensor nodes that are still alive, which makes it robust against failures and losses. For energy conservation purposes, it is important to speed up the consensus finding algorithm. It is well known that this can be done by suitably weighting the edges of the network graph. However, we point out that the usual solution that optimizes the asymptotic convergence rate may not be optimal when a low precision of the result is sufficient.

ACKNOWLEDGMENT

REFERENCES

1. Olfati-Saber, R. and R. M. Murray, "Consensus problems in networks of agents with switching topology and time-delays," *IEEE Trans. Automat. Control*, Vol. 49, No. 9, 1520–1533, 2004.
2. Xiao, L., S. Boyd, and S.-J. Kim, "Distributed average consensus with least-mean-square deviation," *J. Parallel Distrib. Comput.*, Vol. 67, 33–46, 2007.
3. Georgopoulos, L. and M. Hasler, "Nonlinear average consensus," submitted.
4. Khadivi, A. and M. Hasler, "Fire localization and detection using wireless sensor networks," submitted.
5. FARSITE: http://www.firemodels.org.

Information Transmission between Neuron-like Elements

A. S. Dmitriev[1] and A. I. Ryzhov[2]

[1]Institute of Radio Engineering and Electronics of RAS, Mokhovaya st., 11/7, Moscow 125009, Russia
[2]Moscow Institute of Physics and Technology, Institutskiy pereulok, 9, Dolgopruniy 141700, Russia

Abstract— The problem of information transmission in neural networks is a key question in understanding how human and animal brains operate. At present there is still a lack of satisfactory models revealing this process. In this report information transmission between two neurons is considered in terms of classic communication theory. By means of mathematical modeling of neuron-like elements it is shown how binary information can be transferred from one neuron to the other.

1. INTRODUCTION

Serious efforts were produced to research neurons and neuron-like systems, which gave an opportunity to understand the foundations of separate neuron dynamics and neuron nets to some degree [1–4]. However, nowadays the question of data transmission in neuron systems at information level is not as clear as at signal level.

In this report we do not try to answer this question directly, but we reformulate it from pragmatic point of view: what does neuron represent if treated like information transmitter or receiver in general theory of communications? How can information flow be organized with neuron-like elements in the form of conventional bit streams? What is the performance of communication channel between neurons and what does it depend on?

2. INFORMATION TRANSMISSION MODEL

To solve this task we use a mathematical model of a neuron as information transmitter and the same model for a neuron-receiver. In addition, this model of data transmission includes a former of the stream of rectangular pulses (source of transmitted information) which feeds its data to the input of neuron-transmitter. This pulse stream is related to a certain encoding method, e.g., on-off keying (OOK) modulation in case of binary information transmission: pulse transmission corresponds to "1", and pulse absence stands for "0". The next communication element is a "channel" which is responsible for the further signal propagation. Spike stream from the output of neuron-transmitter arrives at the input of neuron-receiver after passing through the channel. At the output of neuron-receiver there is a decoding device.

If this decoding device restores correctly the bit sequence generated by the pulse former, then the information bit stream is considered successfully transmitted with the use of "neuron communication channel".

Thereby, in first approximation the method of encoding transmitted information is not crucial because the main goal is to restore pulse sequence without mistakes. However, note that immunity in noisy environment depends on encoding method. Fig. 1 shows block diagram of the discussed communication system.
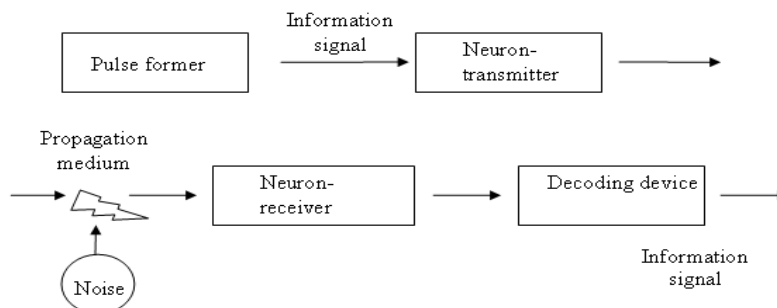

Figure 1: Scheme of information transmission using neuron-like elements.

It is reasonable to take a simple neuron model for our purpose, able to represent main neuron features connected with its reaction to external stimulus and with spike generation. Here, Hodgkin-Huxley system is used, described by the following differential equations:

$$C_m \dot{V} = I_{ion}(V, m, h, n), \quad \dot{m} = \alpha_m(V)(1 - m) - \beta_m(V)m,$$
$$\dot{h} = \alpha_h(V)(1 - h) - \beta_h(V)h, \quad \dot{n} = \alpha_n(V)(1 - n) - \beta_n(V)n, \tag{1}$$

where V is membrane potential; m, n and h characterize membrane conductance; current is:

$$I_{ion}(V, m, h, n) = -G_k n^4 (V - V_k) - G_{na} m^3 h (V - V_{na}) - G_L(V - V_L) \tag{2}$$

and constants α_m, β_m, α_n, β_n, α_h, β_h, represent the conductance in both directions and vary with membrane potential V, they are calculated from these empiric expressions:

$$\alpha_m = 0.1 \frac{25 - V}{\exp\left(\frac{25-V}{10}\right) - 1}, \quad \beta_m = 4 \exp\left(\frac{-V}{18}\right),$$

$$\alpha_h = 0.07 \exp\left(\frac{-V}{20}\right), \quad \beta_h = \frac{1}{\exp\left(\frac{30-V}{10}\right) + 1}, \tag{3}$$

$$\alpha_n = 0.01 \frac{10 - V}{\exp\left(\frac{10-V}{10}\right) - 1}, \quad \beta_n = 0.125 \exp\left(\frac{-V}{80}\right).$$

In further simulation the parameters in (1) are set at: C_m (membrane capacity) $= 1\,\mu\mathrm{F/cm^2}$, G_{Na} (maximum Na^+ conductance) $= 120\,\mathrm{mS/cm^2}$, G_K (maximum K^+ conductance) $= 36\,\mathrm{mS/cm^2}$, G_L (conductance that characterizes leakage current) $= 0.3\,\mathrm{mS/cm^2}$, V_{Na} (displacement for resting potential for Na) $= 110\,\mathrm{mV}$, V_K (displacement for the resting potential for K) $= -12\,\mathrm{mV}$, V_L (displacement for the resting potential for leakage current) $= 10.6\,\mathrm{mV}$.

3. TRANSMITTING NEURON

Neuron under external influence is described with Eq. (1) with additional member I_{ext}. Neuron reaction to positive pulse signal with $4\,\mu\mathrm{A/cm^2}$ amplitude is plotted in Fig. 2(a). With an increase of the input signal amplitude, the spike amplitude remains nearly the same and it reaches approximately $100\,\mathrm{mV}$.

As far as information transmission is produced by spike generation, communication channel characteristics are determined by conditions under which such spike generation is possible in case of external pulse signal.

First of all, let us find out the values of amplitude and width of input pulses which allow the neuron to respond to this pulse sequence. Assume that a spike appears in the system if neuron output impulse (membrane potential V) exceeds $50\,\mathrm{mV}$. For each amplitude value of input impulse
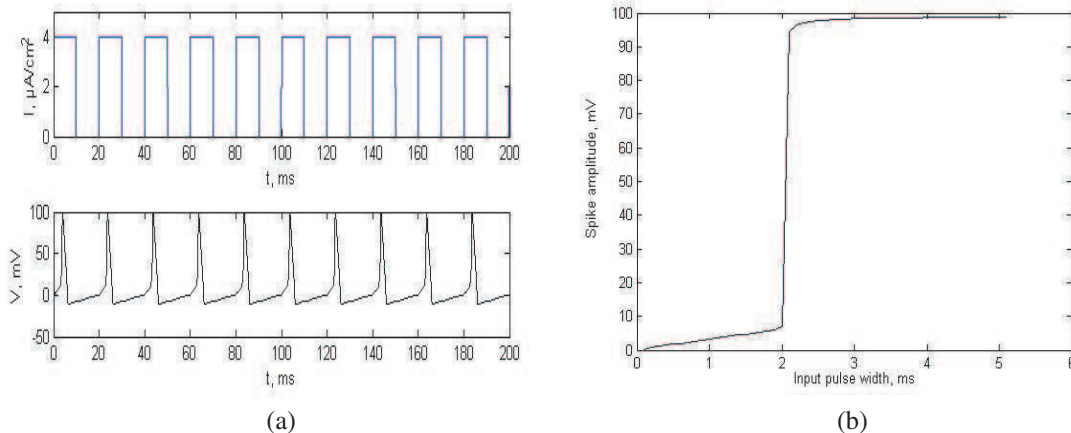

(a)   (b)

Figure 2: Neuron reaction to pulses with $I = 4\,\mu\mathrm{A/cm^2}$ and T (pulse width) $= 10\,\mathrm{ms}$ (a); Maximum output amplitude versus input pulse width ($I = 4\,\mu\mathrm{A/cm^2}$) (b).

we gradually increase its width and watch if there is an above-mentioned exceeding that leads to spike generation. Simulation results show that there is a critical input pulse width $T = 2$ ms for amplitude $I = 4 \, \mu\text{A/cm}^2$. If input pulse width is less than 2 ms, then no spikes can be observed. If it is necessary to work with shorter pulses (e.g., to increase transfer rate) input pulse amplitude must be enlarged.

Maximum output signal amplitude as a function of input pulse width (input pulse amplitude is fixed at $I = 4 \, \mu\text{A/cm}^2$) is plotted in Fig. 2(b).

As follows from figure, for the given current the minimum input pulse width is 2 ms (this pulse width is sufficient for spike generation), whereas spike duration is ~ 10 ms.

The discussed neuron model is characterized by the presence of refractory period, a period of time when neuron is not able to generate a spike after previous generation, so the neuron cannot respond to external influence during this time. Simulation shows that refractory period for this neuron model and given parameters values is about 10 ms.

4. RECEIVING NEURON

Let us consider now the neuron as receiver, the main property of which is to register spikes coming to its input through communication channel from neuron-transmitter. Assume that the source of information signals transmits 20-ms rectangular pulses. As can be seen in Fig. 3, such a signal is successfully received by neuron-receiver, which is verified with stable spikes.

Thus, communication channel correctly transmits information with spikes in the absence of signal distortions. However, in communication channel the signal can attenuate. Therefore, the system was simulated in the case of attenuation of the signal from neuron-transmitter (components of this system are: neuron-transmitter, communication channel and neuron-receiver). As was found, spike amplitude at the output of neuron-receiver drops abruptly if signal in communication channel is attenuated by a factor of 10.

According to restrictions on transmitted information signal described in Section 3 (especially, refractory period), the success of signal reception is determined by incoming spike amplitude. For example, the refractory period in neuron-receiver does not affect the signal reception because neuron-transmitter cannot send two very close to each other spikes. Fig. 4 illustrates a case when neuron-receiver "loses" some bits due to too small time interval between rectangular pulses produced by pulse former so that neuron-transmitter can not send them all.

It is quite natural that there is some noise in communication channel; so it is reasonable to consider the effect of noise on neuron-receiver. The response of neuron-receiver on external noise is as follows: for low-amplitude noise the output neuron signal is also slightly noisy. When input
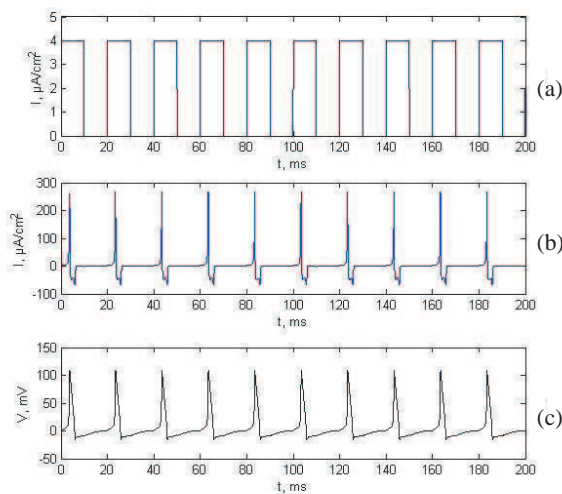

Figure 3: Neuron-receiver response (c) to external stimulus (b) when input pulses with T (pulse period) $= 20$ ms and $I = 4 \, \mu\text{A/cm}^2$ are used in the pulse former (a).
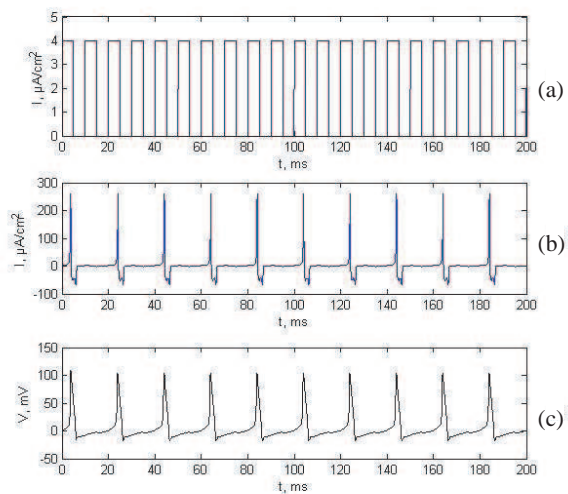
Figure 4: Neuron-receiver response (c) to external stimulus (b) when input pulses with T (pulse period) $= 10$ ms are used in the pulse former.

noise amplitude is increased, spikes appear at random moments in the system, first rare, then more and more frequent. Neuron reaction to Gaussian noise with amplitude 100 μA/cm^2 is shown in Figs. 5(a) and (b).

Finally, let us consider a mixture of the required signal and zero-mean Gaussian noise in communication channel. Signal reception quality as function of the noise level in the channel is to be investigated. Let us use OOK modulation in our combined system of neuron-like elements to fix the idea. Bit error ratio of the received signal is to be calculated to estimate the quality of signal reception. We utilize threshold device to detect presence or absence of spike in a certain time interval in our model. The threshold level is selected to minimize error probability of signal reception. So in our model it is taken at 80 mV. Spike width at this threshold level is approximately 2 ms; during modeling it was found that if there is a high noise level, then the spike delay appears and equals 2–3 ms, also it is caused by inherent neuron inertia.

Thereby, the time interval, where the spike can be located, stretches from 2 to 7 ms from the beginning of each period. It is this period of time where algorithm detects whether there is spike or no. As a result of modeling, bit error ratio as function of the signal-to-noise ratio is obtained (Fig. 5(c)). This figure illustrates that neuron-receiver recognizes the transmitted information with error probability near 10^{-3} if signal-to-noise ratio is 13 dB, and this result is comparable to probability characteristics of conventional incoherent receivers.
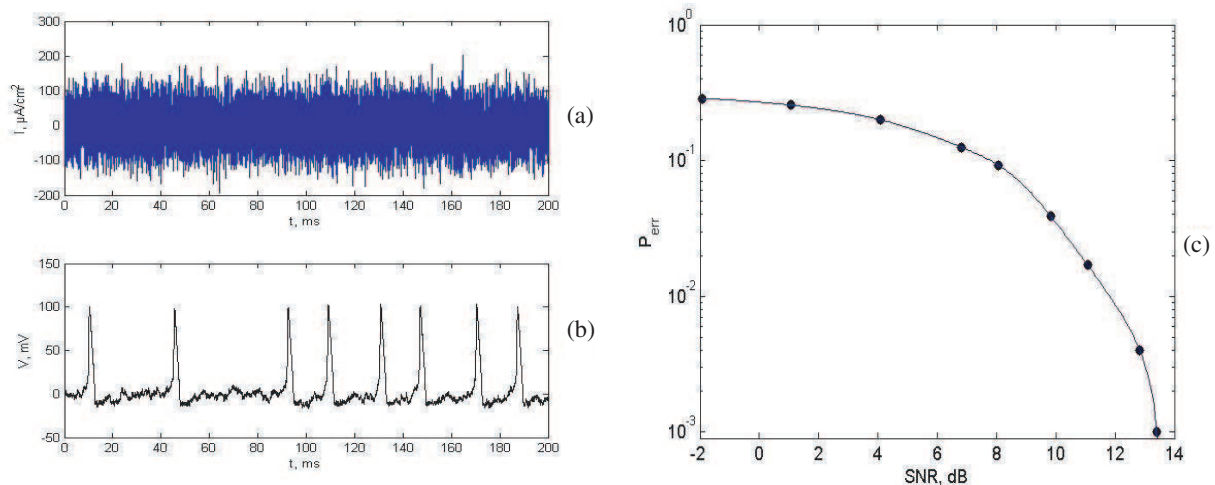

Figure 5: Neuron-receiver reaction (b) to Gaussian noise with 100 μA/cm^2 amplitude (a); Bit error ratio versus signal-to-noise ratio graph (c).

5. CONCLUSIONS

Digital communication system based on neuron-like elements used as transmitter and receiver is considered. It is shown that such a system is able to transmit binary information and it has got a certain noise immunity. The transfer rate in this system with values of parameters used in this report is 100 bit/s. It can be interpreted like an estimation of information transfer rate in live neuron systems.

REFERENCES

1. Hodgkin, A. L. and A. F. Huxley, "A quantitative description of membrane current and its application conduction and excitation in nerve," *J. Physiology*, Vol. 117, 500–544, 1952.
2. Hindmarsh, J. L. and R. M. Rose, "A model of neuronal bursting using three coupled first order differential equations," *Proc. R. Soc. Lond.*, Vol. B221, 87–102, 1984.
3. Fitzhugh, R., "Impulses and physiological states in theoretical models of nerve membrane," *Biophys. J.*, Vol. 1, 445–466, 1961.
4. Abarbanel, H. D. I., "The synchronization of neural assemblies," *Uspekhi Fizicheskih Nauk*, Vol. 166, No. 4, 1–28, 1996.

A Novel Compact Thru-silicon-via On-chip Passive MMW Bandpass Filter for 77GHz Applications

W. Woods[1], **G. Wang**[1], **J. Xu**[1], **H. Ding**[1],
Shurong Dong[2], **Wei Wei Cheng**[2], **and A. Bavisi**[3]

[1]IBM Microelectronics, USA
[2]Zhejiang University, China
[3]Freescale Semiconductor, USA

Abstract— This paper presents a novel on-chip passive bandpass filter for millimeter-wave (MMW) applications that utilizes a pair of electrically-coupled thru-silicon vias (TSV). The presented TSV bandpass filter can be used in MMW applications such as radar, medical imaging, and communication. The TSV bandpass filter uses two TSVs to extend two electrically-coupled conductors into the silicon substrate in the z-direction instead of horizontally in the x-y plane. There is a metal layer on the bottom side of the silicon substrate that shorts the ends of the two TSVs to ground. Using TSVs in the bandpass filter design reduces the silicon area required to implement the filter compared to the silicon area required for the equivalent conventional filter in the above-silicon metal-dielectric interconnect stack. The operating performance of the bandpass filter is controlled at the design stage by choosing the separation distance between the TSVs. In this work, the two TSVs were 145 μm in height (z-direction) and 3 μm × 50 μm in the x-y plane. The long edges of the TSVs (50 μm long edges) faced each other to maximize capacitance coupling between the TSV pair. The TSVs were separated by a distance of 5 μm. Full-wave electromagnetic simulations of a TSV filter designed in an IBM SiGe technology that included TSVs show a minimum pass-band insertion loss of −3.9 dB at 77 GHz with a usable pass band from 75–85 GHz is possible. The simulated operating range of the TSV bandpass filter design presented in this paper show that it is well suited for automotive radar applications.

1. INTRODUCTION

MMW circuits and systems often require on-chip filters. Passive filters often take up large amounts of silicon area to deliver adequate circuit performance. This paper addresses on-chip MMW bandpass filter design. Several designs of on-chip integrated bandpass filters have been reported in the literature. The reported on-chip MMW bandpass filter designs strive to minimize filter size while maintaining adequate electrical performance. A folded loop resonator design is presented in [1] that reduces size and achieves acceptable bandpass performance. Computer-optimized on-chip bend elements have also been used to reduce size and improve filter performance [2]. At sub-millimeter wave frequencies, a bandpass filter design using on-chip spiral inductors and active CMOS devices for tuning has been reported [3]. In [4], a novel compact bandpass design using high slow-wave factor waveguides using MIM capacitors greatly reduced size relative to a non slow wave approach. A novel on-chip balun bandpass filter design was presented in [5] based on a double parallel strip lines with an inserted conductor plane achieved high performance and size reduction. Excellent size and adequate performance results have been achieved in on-chip bandpass filter designs using MIM capacitors and lumped element spiral inductors at 77 GHz [6]. Size reductions have also been shown using capacitively loaded CPW resonators without MIM capacitors [7]. These previously reported bandpass filter design approaches optimized performance and size using elements commonly available in CMOS or BiCMOS technologies. MIM capacitors, CMOS device tuning elements, spiral inductors, capacitively loaded waveguides, folded resonators, and metal planes were all fabricated from available on-chip devices and wiring elements. Now, another on-chip element is available for use in MMW bandpass filter design: the TSV. TSVs have recently become available in some technologies for use in reducing system size by stacking chips or improving analog design performance through the use of TSV ground routing from a grounded metal plane on the bottom of a silicon die. TSVs offer inherent size reduction to MMW filter designs by making use of the z-direction on-chip. This paper presents the concept of using TSVs in MMW bandpass filter designs. TSVs do not require a large on-chip area footprint in the top-side of the chip because they extend deep into the silicon. The bandpass filter described here is intended for MMW circuits and the operation range explored for two different TSV filter designs is between 65–85 GHz. This frequency can be tuned by changing the dimensions of the coupled TSV geometry, for example, by making the coupled

TSVs farther apart or wider. It is desirable to be able to design different TSV bandpass filters that include the 60 GHz frequency node for electronic wireless communication applications such as short distance HD TV home broadcasting, the 77 GHz frequency node for automobile collision avoidance radar applications, and the 94 GHz frequency node for medical imaging applications. In this work, we demonstrate a TSV bandpass filter which includes the 77 GHz frequency node.

2. TSV MMW BANDPASS FILTER STRUCTURE

The design of a 77 GHz TSV bandpass filter is shown in Figure 1. The filter design is entirely passive. It is designed in an IBM SiGe BiCMOS technology enabled with TSVs. The TSVs in this technology are 145 µm in height and measure 50 µm by 3 µm in the x-y plane of the silicon surface. In conventional applications, often multiple TSVs are used together to form a single connection between the top and bottom sides of the silicon die. For this technology, there is no patterning of the metal on the bottom side of the silicon and the entire bottom side of the silicon is metallized and connected to system ground. In Figure 1, the two TSVs can be seen to be attached to a large grounded metal plane on the bottom side of the silicon. Also, it can be seen in Figure 1, that only two TSVs are used to construct the bandpass filter. It may also be possible to construct TSV bandpass filters which make use of more than two TSVs. However, as a proof of concept, the simplest configuration was used in this design. On the top-side of the silicon substrate, conventional x-y plane metallization is used to route signals to and from the two coupled TSV. For this design, the conventional top-side metal routing is the same width as the TSVs: 50 µm. The conventionally routed metal is capacitively coupled to the input and output of the filter across gaps as shown in Figure 1. The metal layer used for top-side routing is a 4 µm thick aluminum layer, and the thick metal layer allows good capacitive coupling across the input and output gaps. The gaps are located a distance L_{TOP} from the TSVs, and the separation distance between the TSVs is 5 µm. Notice that the signal routing on the top-side of the silicon is straight and does not include any additional capacitive loading such as MIM capacitors or slow wave structures. The purpose here was not to try to produce the smallest possible TSV bandpass filter design, but to show that TSVs can be used in MMW bandpass filter designs. It is expected that additional reductions in size is possible through the use of slow wave structures on the front-side of the silicon surface.

Figure 2 shows an equivalent circuit schematic representing the coupled TSV bandpass filter design. It shows the relevant electrical elements that are present. The capacitance of the gaps in the top-side metal at the input and output of the filter is depicted as C_{gap} and it is controlled by the spacing and width of the gap, but since the width is picked to be equal to the TSV width, the spacing is the only free design parameter. The parasitic resistance, capacitance and inductance of the top-side metal routing are depicted by the R_{front}, L_{front}, and C_{front} circuit elements. The values of these elements are controlled by the length of the metal routing, L_{top}, and the width of the metal routing, which is fixed at 50 µm here. The capacitance between the TSVs is controlled by the width, height, and separation of the TSVs. In this technology, the height and the width of the TSVs is fixed at 145 µm and 50 µm respectively. The separation distance of the TSV is the only design parameter relative to the TSVs that can be controlled in this design. For this work, the TSV separation distance was chosen to be 5 µm based on HFSS simulations that showed it to be well suited to the frequency ranges of interest. The resistance, capacitance, and inductance of each
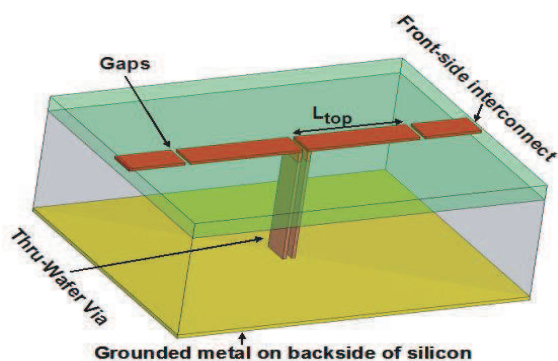

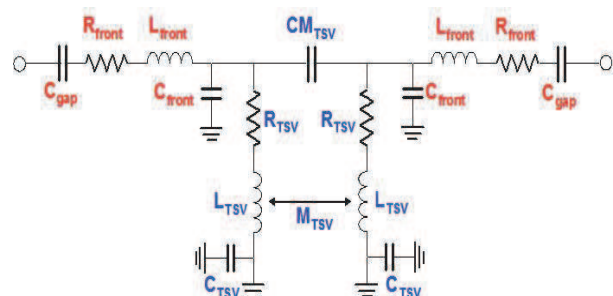Figure 1: TSV bandpass filter structure using two TSVs.

Figure 2: Circuit diagram of TSV bandpass filter.

TSV are shown in Figure 2 as the R_{TSV}, C_{TSV}, and L_{TSV} circuit elements. The values of these elements are controlled by the dimensions of the TSVs which are not controllable in this design. Note also that there is capacitive and inductive coupling, CM_{TSV} and M_{TSV}, between the TSVs that is controlled based on the separation distance between the TSVs.

The result of HFSS simulations of the electrical performance of two TSV bandpass filter designs is shown in Figure 3 and Figure 4. The only difference in the designs simulated is the length of the top-side metal interconnect used to route the signal to and from the TSVs. Figure 3 shows the HFSS results when $L_{top} = 150\,\mu\text{m}$ and Figure 4 shows the HFSS results when $L_{top} = 200\,\mu\text{m}$. Figure 3 shows a minimum insertion loss of 3.9 dB at 77 GHz with a usable 10 GHz passband from 75 GHz to 85 GHz. Here a usable frequency is considered to be one with an insertion loss less than 5 dB (S_{12} above the horizontal dashed line) and a return loss better than -15 dB. Figure 4 shows a minimum insertion loss of 4 dB at 68 GHz with a 10 GHz passband from 65 GHz to 75 GHz. These HFSS results show the TSV bandpass filter design can be practically used in on-chip MMW designs. The two TSV bandpass filter designs simulated had silicon footprints of $\sim (300 \times 50\,\mu\text{m}^2)$ and $(400 \times 50\,\mu\text{m}^2)$ respectively. When compared with the size of two other previously reported bandpass filter designs in a similar frequency range ($650 \times 670\,\mu\text{m}^2$ for 70 GHz) [1] and ($110 \times 60\,\mu\text{m}^2$ for 77 GHz) [7], it is seen that these two TSV designs have a size somewhere between the two previously reported designs. However, when compared to the smaller previously reported design [7], the HFSS results of the 77 GHz TSV bandpass filter design shows better insertions loss performance: 3.9 dB compared to 6.5 dB. Also, as mentioned, no effort was made in the TSV designs to reduce to dimensions of the top-side interconnect with, for example, slow wave structures, multiple metal layers, or serpentine metal routing. The size and electrical performance of the TSV bandpass filter design presented
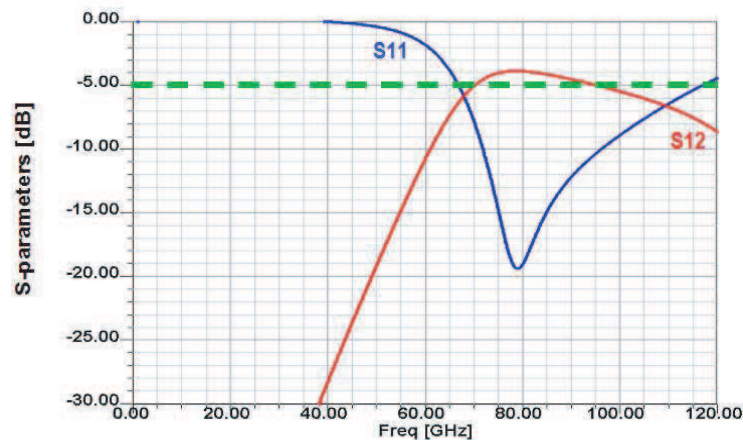

Figure 3: Simulated HFSS results of TSV bandpass filter structure using two TSVs ($L_{top} = 150\,\mu\text{m}$).
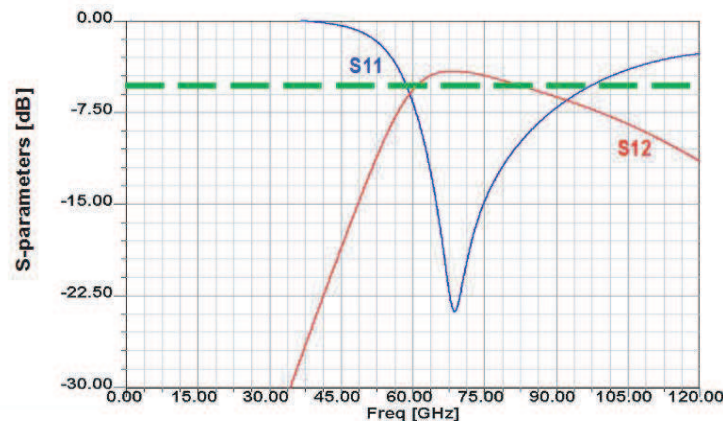

Figure 4: Simulated HFSS results of TSV bandpass filter structure using two TSVs ($L_{top} = 200\,\mu\text{m}$).

here is compares favorably against the previously reported approaches in either size or electrical performance. This is an excellent result considering that no attempts have been made to optimize the structure for either size or electrical performance. These designs were chosen for simplicity and to prove the concept of using TSVs in MMW bandpass filter designs. Future work should focus on design optimization. The performance presented here shows that TSVs can be practically used in MMW bandpass filter designs.

3. CONCLUSION

A TSV MMW bandpass filter design was presented in this paper that makes use of the z-direction on-chip to reduce overall bandpass filter size. The area requirements of the non-optimized 77 GHz TSV bandpass filter design presented was shown to be competitive with optimized bandpass filter designs presented previously. By optimizing the top-side metal of these TSV bandpass filter designs, the total filter size should be able to be greatly reduced. HFSS simulations of two TSV bandpass filter designs show that TSVs can practically be incorporated as design elements in on-chip MMW systems. The 77 GHz TSV bandpass design had a simulated insertion loss of 3.9 dB at 77GHz with a 10 GHz passband from 75 GHz to 85 GHz. The HFSS results of the TSV filters presented show that TSVs offer great promise and design flexibility for future high-performance MMW applications.

REFERENCES

1. Hsa, C. Y., C. Y. Chen, and H. R. Chuang, "70 GHz folded loop dual-mode bandpass filter fabricated using 0.18 µm standard CMOS technology," *IEEE Microwave and Wireless Components Letters*, Vol. 18, No. 9, 587–589, Sep. 2008.

2. Yang, H., H. Sun, and X. Lu, "A novel MMW bandpass filter fitting the waveguide bend structure," in *Asia-Pacific Radio Science Conference*, 275–277, Chintao, China, Aug. 2004.

3. Gao, Z., M. Yu, and Y. Ye, "A RF high-Q on-chip bandpass filter for aerospace wireless applications," *International Symposium on Systems and Control in Aerospace and Astronautics*, 559–563, Harbin, China, Jan. 2006.

4. Tso, H. T. and C. N. Kuo, "40 GHz miniature bandpass filter design in a standard CMOS process," *Digest of Papers of Silicon Monolithic Integrated Circuits in RF Systems*, 239–242, Atlanta, USA, Sep. 2004.

5. Chen, J. X., C. Y. Cheung, and Q. Xue, "Integrated bandpass filter based on double-sided parallel line with an integrated conductor plane," *Asian Pacific Microwave Conference*, Bangkok, Thailand, Dec. 2007.

6. Dehlink, B., M. Engl, K. Aufinger, and H. Knapp, "Integrated bandpass filter at 77 GHz in SiGe technology," *IEEE Microwave and Wireless Components Letters*, Vol. 17, No. 5, 346–348, May 2007.

7. Aryanfar, F. and K. Sarabandi, "Compact millimeter-wave filters using distributed capacitively loaded CPW resonators," *IEEE Transactions on Microwave Theory and Techniques*, Vol. 54, No. 3, 1161–1165, Mar. 2006.

Bandstop Filter Using Slow-wave CPW Resonator with Defected Ground Structure

A. Görür[1], C. Karpuz[2], and Ö. Akgün[3]

[1]Department of Electrical and Electronics Engineering
Nigde University, Nigde 51245, Turkey
[2]Department of Electrical and Electronics Engineering
Pamukkale University, Denizli 20100, Turkey
[3]Department of Electrical and Electronics Engineering
Aksaray University, Aksaray 68100, Turkey

Abstract— A novel slow-wave CPW resonator with defected ground structures (DGSs) in rectangular spacing-like shapes is investigated. This structure has an extremely compact size. Simulations and experimental results have verified that the structure provides a size reduction of about 33% against a conventional CPW resonator. Two bandstop filter examples are demonstrated. The bandstop filter realized with a fractional 20-dB bandwidth of 25% at 1.575 GHz includes a slow-wave CPW with DGS loaded periodically by four spiral-shaped resonators.

1. INTRODUCTION

In MICs and MMICs designs, the circuit size has always been the center of attention due to circuit miniaturization and material cost reduction. For this propose, slow-wave structures such as metal-insulator-semiconductor (MIS) planar lines and capacitive or inductive loaded transmission lines have been widely examined [1–3], which are compatible with monolithic circuit technology. Also, in order to create the slow wave effect to reduce the circuit size as well as wide and deep stopbands to reject unwanted frequencies, many periodic structures including photonic bandgap (PBG) and defected ground structure (DGS) have been extensively investigated [4–8]. In order to construct such structures in planar technology, these approaches require only partial etching of the ground plane or signal strip of a microstrip line or coplanar waveguide (CPW). In microstrip, due to etching of the ground plane, the dielectric substrate must be suspended so that the circuits cannot be located on a metal support to attain mechanic robustness and to make easy heat removal.

The loaded planar structures on its signal strip are inappropriate for high power applications because of its great discontinuities and very thin line within the main signal path. On the other hand, the etched pattern on the signal strip is restricted to the dimension on the strip itself and excessive loss is generated because of the discontinuities created on the signal strip. MIS structures also are not suitable for applications at high frequencies. Therefore, the structuring of the ground plane may technologically be much easier and more suitable than processing of the signal strip for practical use in microwave applications.

Coplanar waveguides (CPWs) can be a solution to problems mentioned above because they provide a single metal level for signal strip and ground plane. For planar circuit applications, slow-wave CPW structures can be realized by removing some conductor parts in the ground planes of CPW. The one of the important properties of such a structure with defected ground structure (DGS) is the slow-wave effect. Hence, circuit size can be reduced using this property. However, reduction in the size provided utilizing such a structure is insufficient for practical use in many microwave applications. Consequently, we have proposed a new slow-wave CPW resonator using DGS. The proposed type of DGS is realized by etching rectangular spacing on both ground planes of a conventional CPW without any dimensional changes, as illustrated in Fig. 1(b). Also, its bandstop filter applications are designed, realized and measured.

Table 1: Electrical and geometrical parameters of the proposed DGS.

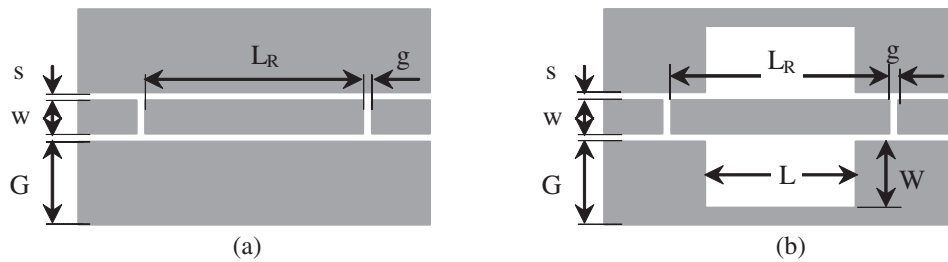| Symbol	ε_r	h (mm)	s (mm)	w (mm)	Z_0 (ohm)
Group I	2.33	1.575	0.25	4.0	60.5
Group II	6.15	1.270	0.25	2.0	49.1
Group III	10.2	1.270	0.50	1.5	50.4

Figure 1: (a) Conventional half-wavelength CPW resonator. (b) Slow-wave CPW resonator with DGS etched in ground planes.
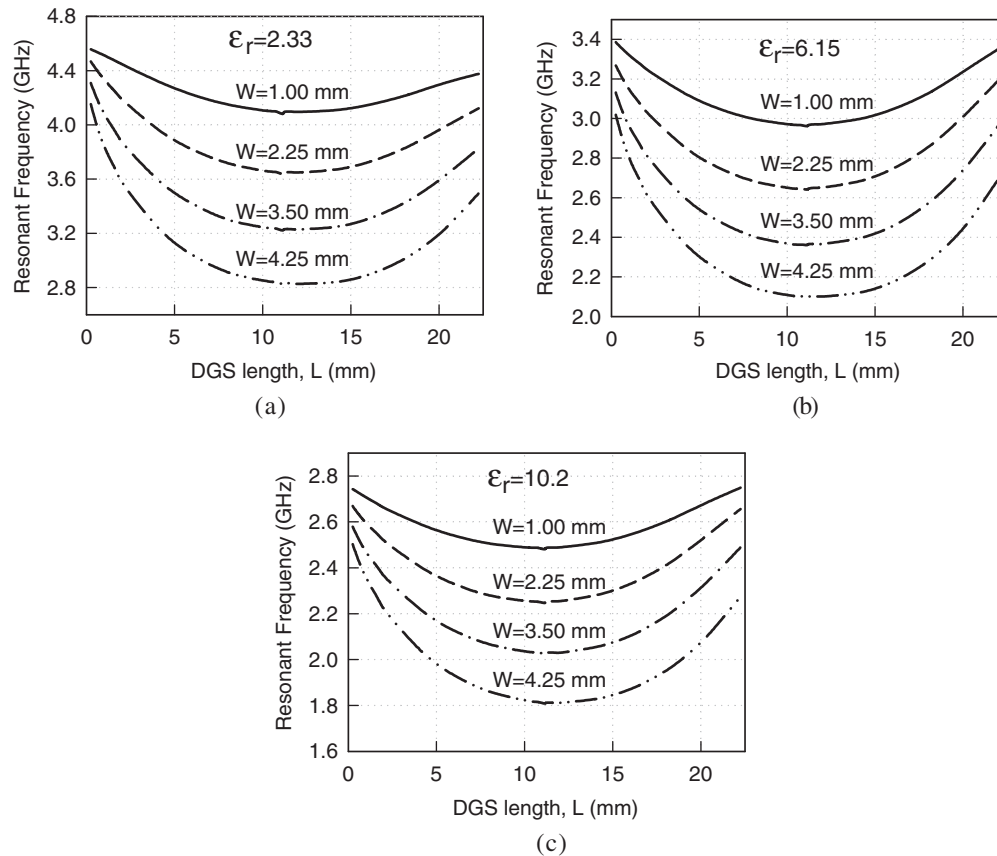

Figure 2: Resonant frequency of slow-wave CPW resonator with DGS etched in ground planes as a function ofDGS dimensions for three dielectric substrates.

2. DEVELOPMENT OF THE PROPOSED DGS

The proposed slow-wave CPW resonators with DGS are shown in Fig. 1 as well as a conventional half-wavelength CPW resonator. The DGS has been created in the ground planes of a conventional CPW for three substrate materials. Table 1 summarizes the electrical and geometrical parameters of these CPW structures. The finite ground planes of the proposed CPW have a width of $G = 4.5$ mm for all circuits. DGS has two variable dimensions such as the length and the width. The length and width of DGS are denoted as L and W, respectively. The length L for the proposed CPW resonator is varied from 0.25 mm to 22.25 mm, while the width W is varied from 0 mm (conventional finite ground CPW) to 4.25 mm. The structure becomes a CPW loaded with a narrow slit [9], when the length L is 0.25 mm. The resonant frequency of such a structure can be calculated as described in [9]. The resonant frequency of the proposed slow-wave CPW resonator can be adjusted to desired values by changing the dimensions L and W. The structure has been simulated with the use of the full-wave Sonnet EM simulator [10]. The simulation results have shown that the length L and
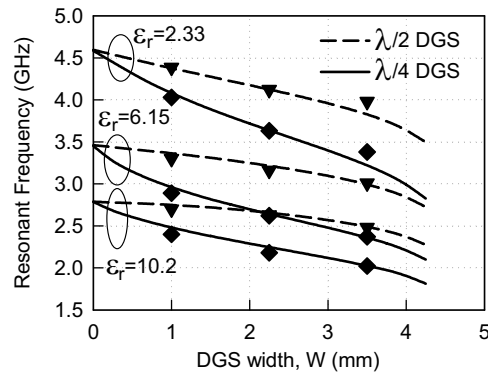
Figure 3: Comparison of resonant frequencies of slow-wave CPW resonators with $\lambda/4$ DGS and $\lambda/2$ DGS created in ground planes as a function of DGS dimensions for three dielectric substrates. Symbols show measured resonant frequencies.

width W of the DGS significantly affect the resonant characteristics of the proposed slow-wave CPW resonator. Their effects are investigated in the following.

In order to see the effect of the length L on the frequency characteristics of the proposed slow-wave CPW resonator, the half-wavelength CPW resonator circuits have been simulated with different values of the length L by keeping the occupied area the same. It is seen from the simulation results in Fig. 2 that the resonant frequency decreases as the length L increases from 0 mm (conventional CPW) to 11.125 mm. If the length L is further increased, then it increases again. It should be noted that the point $L = 11.125 \ (= \lambda/4)$ mm is a half length of the half-wavelength CPW resonator (where the length of $\lambda/2$ CPW resonator is $L_R = 22.25$ mm). Variation of the resonant frequency against the length L of the DGS has form of a parabola that opens upward. The parabola is almost symmetric about a line parallel to the frequency-axis and its vertex is at about the point $(L_{\max}/2, f_{0\min})$, where $L_{\max} = L_R$ is maximum length of the DGS and $f_{0\min}$ is minimum resonant frequency for the interested width W. The line of symmetry intersects the parabola at its vertex. As a result, the resonant frequency is the highest at the edges of the parabolic curve, while it is the lowest at the vertex of the parabola where the length L is $\lambda/4 = 11.125$ mm. Briefly, the value of $\lambda/4$ of the length of the DGS created in the ground planes leads to maximum decrease in the resonant frequency regardless of the width W.

On the other hand, the resonant frequency moves to the lower as the width W increases, as illustrated in Fig. 3. Since the slow-wave CPW resonator with DGS has the lowest resonant frequency at a DGS length of $L = \lambda/4$, the half-wavelength CPW resonator have also been simulated for various values of the DGS width W when the DGS length is $L = \lambda/4$ (namely, $\lambda/4$ DGS). In Fig. 3, the simulated and measured results are compared with the results of the CPW resonator having DGS length of $L = \lambda/2$ (namely, $\lambda/2$ DGS). It can be seen from the figure that the $\lambda/4$ DGS supports not only lower resonant frequency as compared to $\lambda/2$ DGS, but also changes faster the resonant frequency of slow-wave CPW resonator than the $\lambda/2$ DGS, depending on increasing of DGS width W. As a result, a DGS length of $\lambda/4$ instead of the DGS length of $\lambda/2$ is sufficient to obtain minimum resonant frequency and hence, maximum miniaturization. It is seen that the dimensions L and W of the DGS etched in ground planes affect directly and significantly the resonant frequency because these geometrical dimensions change the input impedance of the structure. By using of a suitable combination of the length L and width W of the proposed DGS, a size reduction of about 33% with respect to the conventional CPW structure can be obtained.

3. BANDSTOP FILTER APLICATION

Bandstop circuits are ones of the most important parts of many passive and active microwave and millimeter-wave devices employed to suppress the harmonics. It is possible to realize and design two bandstop filters using rectangular spacing shaped DGS. First, a bandstop filter with two spiral-shaped stubs is designed and simulated using a full-wave EM simulator [10], as shown in Fig. 4(a). Two spiral-shaped stubs are inserted into the rectangular spacing shaped DGS etched on the ground planes of CPW resonator. The CPW bandstop filter was fabricated on an RT/Duroid substrate having a thickness of 1.27 mm and a relative dielectric constant of 10.2. The filter dimensions are $G = 5.125$ mm, $w = 1.5$ mm, $w_1 = 0.25$ mm, $s = 0.5$ mm, $s_1 = 0.25$ mm, $s_2 = 0.125$ mm,

$s_3 = 0.25$ mm, $g = 1.0$ mm, $d_1 = 6.75$ mm, and $d_2 = d_3 = 3.25$ mm. During testing, the filter circuit was connected to an HP 8720C Network Analyzer, which is calibrated from 0.5 to 4 GHz. Standard SMA connectors were used in measurements. Fig. 5(a) illustrates the measured and simulated results. The filter has a fractional 3-dB rejection bandwidth of about 30% at about 1.565 GHz and 10-dB rejection bandwidth of 21% at the same center frequency with insertion loss better than 10-dB. The maximum return loss in the stopband was measured as 0.45 dB. The measured responses present a good agreement with simulated responses.

A second bandstop filter is designed and realized utilizing four spiral-shaped resonators. Fig. 4(b) shows the transmission line loaded periodically by four spiral-shaped resonators. The filter employs the same geometrical parameters as the filter using two spiral-shaped stubs in Fig. 4(a). The total surface area of the bandstop filter is 20.5×12.75 mm^2. Fig. 5(b) illustrates the measured and simulated results. The filter has a fractional 3-dB rejection bandwidth of 32% at 1.575 GHz and 20-dB rejection bandwidth of 25% at the same center frequency. The maximum return loss and minimum insertion loss in the stopband was measured as 0.38 dB and 18 dB, respectively. The maximum insertion losses in the lower passband and the upper passband were measured as 0.57 and 0.72 dB, respectively. The loss is due to circuit loss, including conductor and dielectric losses. The discrepancies between the measured and simulated results are due to simulation, fabrication, and measurement tolerances.
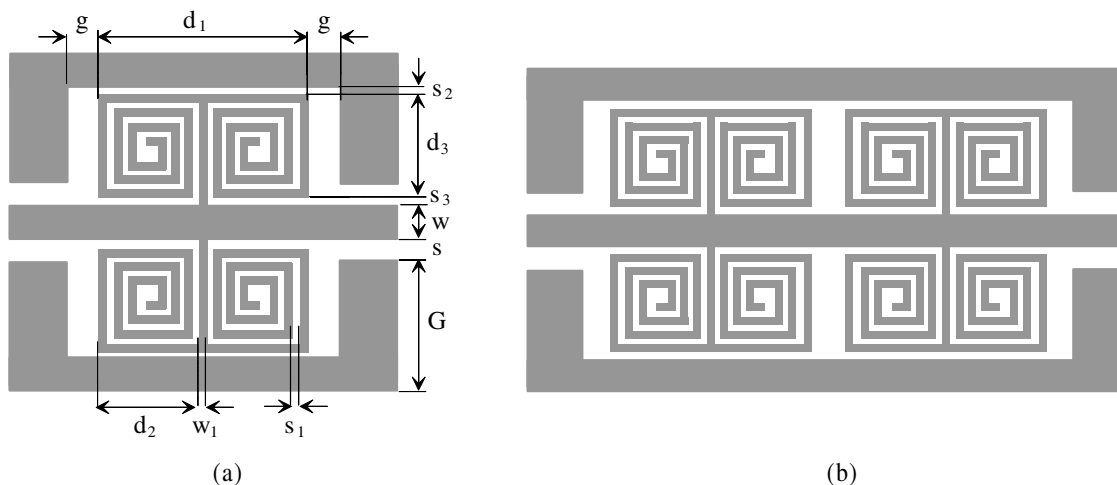

Figure 4: (a) Bandstop filter using two spiral-shaped stubs and (b) Bandstop filter using four spiral-shaped stubs.
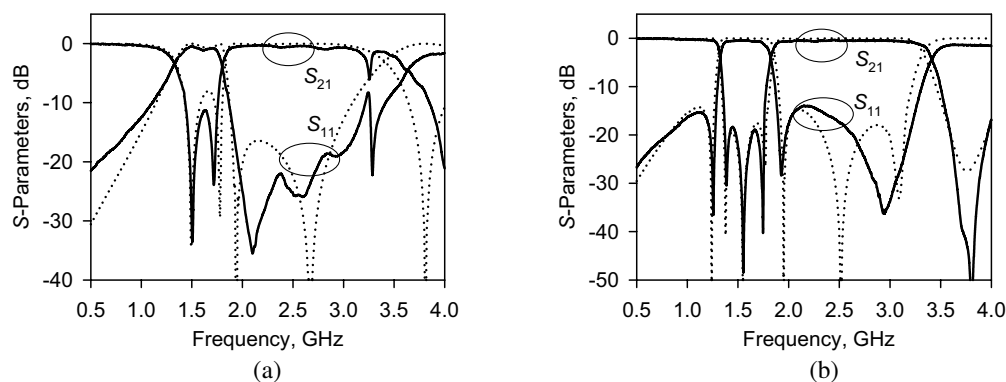

Figure 5: Simulated (dotted line) and measured (solid line) responses of bandstop filter using (a) two spiral-shaped stubs, (b) four spiral-shaped stubs.

4. CONCLUSIONS

For uniplanar circuit applications, slow-wave CPW structures have been realized by etching rectangular spacing and open-loop shaped patterns on both ground planes of a conventional CPW without

any dimensional changes. It has been shown that a size reduction of about 33% using slow-wave effect of such a structure with defected ground structure (DGS) can be obtained. For demonstration, a bandstop filter with 20-dB rejection bandwidth of 25% at 1.575 GHz was designed and realized. The filter has a low-loss due to both uniplanar circuit structure and realization in ground planes of etching processes. Moreover, there is no necessity of an additional space since all processes are realized in ground planes. Another advantage of this new type of bandstop filter based on CPW resonator is that it facilitates the practical realization at the desired center frequency adjusting the dimensions of the DGS.

REFERENCES

1. Williams, D. F., "Metal-insulator-semiconductor transmission lines," *IEEE Trans. Microwave Theory Tech.*, Vol. 47, No. 2, 176–181, 1999.
2. Hasegawa, H. and H. Okizaki, "MIS and Schottky slow wave coplanar stripline on GaAs substrate," *Electron. Lett.*, Vol. 13, 663–664, 1977.
3. Görür, A., C. Karpuz, and M. Alkan, "Characteristics of capacitively loaded CPW structures," *IEEE Microwave Guided Wave Lett.,* Vol. 8, No. 8, 278–280, 1998.
4. Yang, F. R., K. P. Ma, Y. Qian, and T. Itoh, "A novel TEM waveguide using uniplanar compact photonic-bandgap (UC-PBG) structure," *IEEE Trans. Microwave Theory Tech.*, Vol. 47, 2092–2098, 1999.
5. Ahn, D., J.-S. Park, C.-S. Kim, J. Kim, Y. Qian, and T. Itoh, "A design of the low-pass filter using the novel microstrip defected ground structure," *IEEE Trans. Microwave Theory Tech.*, Vol. 49, 86–93, 2001.
6. Lim, J.-S., J.-S. Park, Y.-T. Lee, D. Ahn, and S. Nam, "Application of defected ground structure in reducing the size of amplifiers," *IEEE Microwave Wireless Compon. Lett.*, Vol. 12, No. 7, 261–263, 2002.
7. Mao, S. G. and M. Y. Chen, "A novel periodic electromagnetic bandgap structure for finite-width conductor-backed coplanar waveguides," *IEEE Microwave Wireless Compon. Lett.,* Vol. 11, No. 6, 261–263, 2001.
8. Xue, Q., K. M. Shum, and C. H. Chan, "Novel 1-D microstrip PBG cells," *IEEE Microwave Wireless Compon. Lett.*, Vol. 10, No. 10, 403–405, 2000.
9. Görür, A. and C. Karpuz, "Influence of narrow transverse slit in CPW resonator on its resonance characteristics," *Electron. Lett.*, Vol. 36, No. 1, 49–50, 2000.
10. EM User's Manual, Sonnet Software, Inc., Version 6.0, Liverpool, NY, 1999.

An Analytical Method for Optimization of RF MEMS Wafer Level Packaging with CPW Detuning Consideration

Zheng Wang and Zewen Liu

Institute of Microelectronics, Tsinghua University, Beijing, China

Abstract— An analytical solution for detuning effect of CPW with cap wafer by applying the conformal mapping method is presented in the paper. A wafer level packaging structure for RF MEMS devices is optimized with the developed analytical formulas. The cavity depth of 40 μm is adequate to reduce the detuning of the MEMS circuit to an acceptable level for the 50 Ω CPW on the glass substrate for the glass cap wafer.

1. INTRODUCTION

With the rapid development of MEMS technology, the prominent RF performance of RF MEMS devices such as varactors [1], switches [2], and resonators has been attained. Considering that the movable friable parts of RF MEMS devices must be protected and packaged in a clean and invariable environment. These packages are required to exhibit minimum insertion loss as well as excellent match and should be manufacturable at a reasonable cost since packaging is generally the most costly step in the fabrication process. High-performance wafer-level packaging has been demonstrated as an almost best choice according to many research groups [3–5].

However, the performance of MEMS devices and the coplanar waveguide (CPW) lines will detune due to the close proximity of the wafer-level package to the MEMS surface. While the detuning effect can be diminished by providing an etched cavity in the cap wafer as shown in Figure 1, the quantitative method for detuning effect with different cap wafer materials and different lateral dimensions of CPW has not been demystified yet, which is very important for the efficient packaging structure optimization.

In this paper the conformal mapping method is applied to derive the analytical approximation for detuning effect of CPW with a wafer cap, based on the extension of the partial capacitance technique. With the developed formulas a wafer level packaging structure for RF MEMS devices is optimized considering both effects of the cap wafer and the sealing ring.

2. ANALYTICAL FORMULA

The conformal mapping method is applied to derive the analytical approximation, which assumes a quasi-TEM mode of propagation along the line. Additionally, the partial capacitance technique in which the line capacitance of CPW is presented as a sum of partial capacitances is applied. As the capacitance per unit length is known, the basic characteristics of CPW, the wave impedance and the propagation constant can be derived in the quasi-TEM limit. The cross section of CPW with a wafer cap is shown in Figure 2 where ε_{r1}, ε_{r2} and ε_{r3} are relative permittivities of substrate, air and cap wafer respectively.

The total capacitance C_{CPW} of the packaged CPW is the sum of the partial capacitances C_a and C_b. That is

$$C_{CPW} = C_a + C_b, \tag{1}$$

where C_a and C_b are the partial capacitances of the packaged CPW for the region only above metal and only below metal, respectively.
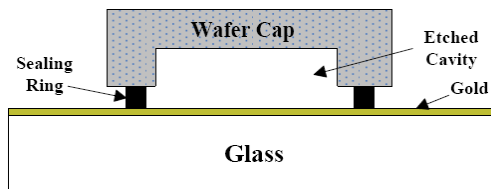

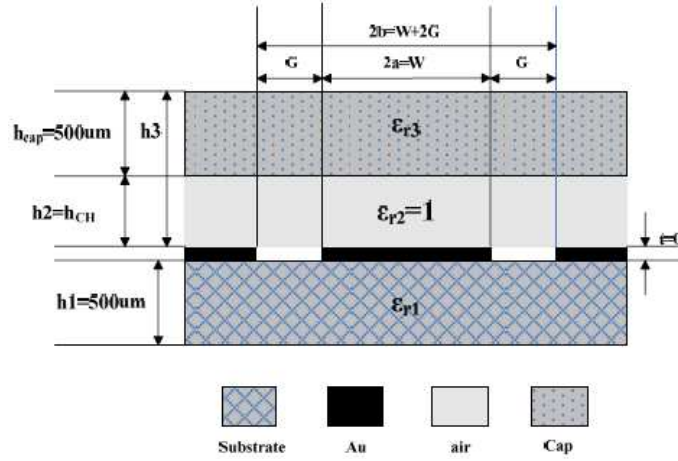Figure 1: The wafer level packaging for RF MEMS.

Figure 2: Cross section of the packaged CPW with cap wafer.

The region below CPW line is usually considered as the superposition of two parts with an air layer and a dielectric layer with equivalent relative permittivity $\varepsilon_{r1} - 1$. The partial capacitance C_1 of the substrate dielectric region is given by [6]

$$C_1 = 2\varepsilon_0(\varepsilon_{r1} - 1)\frac{K(k_1)}{K(k_1')}, \tag{2}$$

where the modulus of the complete elliptic integrals $K(k_1)$ and $K(k_1')$ are [6]

$$k_1 = \frac{\sinh(\pi S/4h_1)}{\sinh[\pi(S+2G)/4h_1]} \tag{3}$$

$$k_1' = \sqrt{1 - k_1^2}. \tag{4}$$

As the thickness of air layer below substrate is supposed to be infinite, the partial capacitance C_{air_b} of the air region is given by [6]

$$C_{air\_b} = 2\varepsilon_0\frac{K(k_0)}{K(k_0')}, \tag{5}$$

where

$$k_0 = \frac{S}{S+2G} \tag{6}$$

$$k_0' = \sqrt{1 - k_0^2}. \tag{7}$$

Thus the partial capacitance C_b is given by

$$C_b = C_1 + C_{air\_b} \tag{8}$$

The same method is extended to the region above CPW line in this paper. For the packaged CPW, the air between metal and cap can be regarded as a common dielectric layer with relative permittivity ε_{r2} equaled to 1. So the region above CPW line is considered as the superposition of three parts with different relative permittivities, $\varepsilon_{r2} - \varepsilon_{r3}$, $\varepsilon_{r3} - 1$ and 1 respectively as shown in Figures 3(a) to 3(c). Here $\varepsilon_{r2} - \varepsilon_{r3}$ has a negative value but this will not lead to invalidation as it is just equivalent relative permittivity.

So the partial capacitance C_2 of the region in Figure 3(a) is given by

$$C_2 = 2\varepsilon_0(\varepsilon_{r2} - \varepsilon_{r3})\frac{K(k_2)}{K(k_2')}, \tag{9}$$
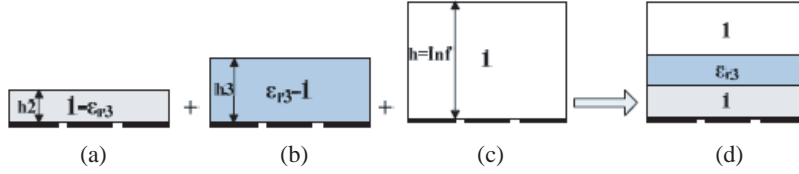
Figure 3: Configuration for partial capacitances for region above CPW.

where $k_2' = \sqrt{1 - k_2^2}$,

$$k_2 = \frac{\sinh{(\pi S/4h_2)}}{\sinh{[\pi(S + 2G)/4h_2]}}. \tag{10}$$

The partial capacitance C_3 of the region in Figure 3(b) is given by

$$C_3 = 2\varepsilon_0(\varepsilon_{r3} - 1)\frac{K(k_3)}{K(k_3')}, \tag{11}$$

where $k_3' = \sqrt{1 - k_3^2}$,

$$k_3 = \frac{\sinh{(\pi S/4h_3)}}{\sinh{[\pi(S + 2G)/4h_3]}}. \tag{12}$$

The partial capacitance C_{air_a} of the region in Figure 3(c) is equaled to C_{air_b}. Thus the partial capacitance C_a is given by

$$C_a = C_2 + C_3 + C_{air\_a} \tag{13}$$

Substituting Eqs. (2), (5), (8), (9), (11) and (13) into Eq. (1), under quasi-static approximation ε_{eff} is expressed as

$$\varepsilon_{eff} = \frac{C_{CPW}}{C_{air}} = \frac{(C_1 + C_{air\_b}) + (C_2 + C_3 + C_{air\_a})}{C_{air\_b} + C_{air\_a}} = 1 + q_1(\varepsilon_{r1} - 1) + q_2(\varepsilon_{r2} - \varepsilon_{r3}) + q_3(\varepsilon_{r3} - 1) \tag{14}$$

where

$$q_1 = \frac{1}{2}\frac{K(k_1)}{K(k_1')}\frac{K(k_0')}{K(k_0)} \tag{15}$$

$$q_2 = \frac{1}{2}\frac{K(k_2)}{K(k_2')}\frac{K(k_0')}{K(k_0)} \tag{16}$$

$$q_3 = \frac{1}{2}\frac{K(k_3)}{K(k_3')}\frac{K(k_0')}{K(k_0)} \tag{17}$$

Then we can obtain the characteristic impedance of the packaged CPW:

$$Z_0 = \frac{1}{cC_{air}\sqrt{\varepsilon_{eff}}} = \frac{c\mu_0}{4\sqrt{\varepsilon_{eff}}}\frac{K(k_0')}{K(k_0)} \tag{18}$$

Furthermore, we can realize the detuning effect of CPW with cap wafer by comparing the characteristic impedance of packaged CPW and that of unpackaged CPW.

3. PACKAGING STRUCTURE OPTIMIZATION

The performance of CPW under the cap wafer will detune due to the close proximity of the cap to the MEMS surface. Besides, the CPW line under the sealing ring will also detune as the characteristic impedance will decrease. Formula developed above is applied to minimize the loss due to package in the packaging structure optimization. The fine element numerical simulation results show close agreement with the analytical results.

3.1. The Cavity Depth

In our design, a $50\,\Omega$ CPW line ($18/120/18\,\mu m$) is designed on glass substrate. A cavity is etched in order to diminish the detuning effect of glass wafer cap for CPW lines. Applying the formulas in Section 2 the impedance variation for a $50\,\Omega$ CPW line is computed as shown in Figure 4.

The results show close agreement with the fine element numerical simulation results. A cavity depth in the order of $40\,\mu m$ is adequate to reduce the detuning of the MEMS circuit to an acceptable level for glass cap.
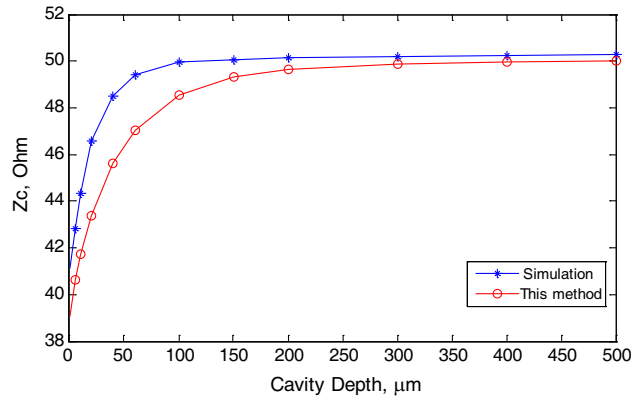
Figure 4: The comparison of the characteristic impedance of the packaged CPW with simulated results.

3.2. The CPW under the Sealing Ring

The CPW under the sealing ring can be redesigned in order to obtain uniform impedance of $50\,\Omega$. Compared with the former situation, the dielectric layer between the metal and cap is the material of sealing ring instead of air. Therefore, the formulas in Section 2 can also be helpful by substituting the corresponding relate permittivity of seal material into the parameter ε_{r2}.

As its excellent RF performance, BCB is a good candidate of the bonding and the sealing material for RF MEMS [7]. For different thickness of sealing ring, the CPW dimensions need to be optimized to achieve lower loss. The fine element numerical simulation results validate the analytical formulas as shown in Table 1.

Table 1: The comparison of the Z_C of the redesigned CPW with simulated results for seal material of BCB ($\varepsilon_{r2} = 2.65$).

Thickness of Sealing Ring	Redesigned Dimension	Z_C (simulated)	Z_C (calculated)
$2\,\mu m$	$31.6/92.9/31.6\,\mu m$	$49.3\,\Omega$	$50\,\Omega$
$5\,\mu m$	$30.6/94.8/30.6\,\mu m$	$49.7\,\Omega$	$50\,\Omega$
$10\,\mu m$	$29.8/96.5/29.8\,\mu m$	$49.8\,\Omega$	$50\,\Omega$

4. CONCLUSIONS

An analytical method for optimization of RF MEMS wafer level packaging with CPW detuning consideration is presented in the paper. A wafer level packaging structure for RF MEMS devices is optimized considering both effects of the cap wafer and the sealing ring with the developed formulas. This developed analytical method works well through the comparison with the fine element numerical simulation. A cavity depth in the order of $40\,\mu m$ is adequate to reduce the detuning of the MEMS circuit to an acceptable level for glass cap.

ACKNOWLEDGMENT

REFERENCES

1. Lakshminarayanan, B. and G. Rebeiz, "High-power high-reliability sub-microsecond RF MEMS switched capacitors," *IEEE MTT-S International Microwave Symposium Digest*, 1801–1804, 2007.

2. Hou, Z., Z. Liu, and Z. Li, "Al/Au composite membrane bridge DC-contact series RF MEMS switch," *Proceedings of the 2008 9th Conference on Solid-State and Integrated Circuit Technology*, 2488–2491, 2008.

3. Min B., K. Entesari, and G. Rebeiz, "DC-50 GHz low-loss wafer-scale package for RF MEMS," *Proceedings of the 34th European Microwave Conference*, Vol. 3, 1289–1291, 2004.

4. Schobel, J., T. Buck, M. Reimann, M. Ulm, and M. Schneider, "W-band RF-MEMS subsystems for smart antennas in automotive radar sensors," *Proceedings of European Microwave Conference*, 1305–1308, Amsterdam, Netherlands, 2004.

5. Jourdain A., K. Vaesen, J. M. Scheer, J. W. Weekamp, J. T. M. Van Beek, and H. A. C. Tilmans, "From zero to second level packaging of RF-MEMS devices," *Proceedings of International Conference on MEMS*, 36–39, Miami, FL, Jan. 2005.

6. Gevorgian, L. S., J. P. Linner, and E. L. Kollberg, "CAD models for shielded multilayered CPW," *IEEE Trans. Microwave Theory Tech.*, Vol. 43, No. 4, 772–779, 1995.

7. Jourdain A., P. De Moor, S. Pamidighantam, and H. A. C. Tilmans, "Investigation of the hermeticity of BCB-sealed cavities for housing (RF-)MEMS devices," *Proceedings of the IEEE Micro Electro Mechanical Systems (MEMS)*, 677–680, 2002.

Compact UWB L and C-shaped Resonator of PCML Bandpass Filter

J. Marimuthu and M. Esa

Faculty of Electrical Engineering, Universiti Teknologi Malaysia, UTM Skudai, Johor 81310, Malaysia

Abstract— A novel ultra-wideband (UWB) bandpass filter with four resonant modes is proposed based on parallel coupled microstrip line (PCML) with L and C-shaped resonators. The coupling factor of PCML structure depends on impedance of feeding network. PCML coupling factor can be enhanced by using feeding network with smaller characteristics impedance. With an L-shaped feeding network and C-shaped middle microstrip line a non-uniform resonator is constructed with the first two resonant modes falling within the UWB. The other two resonant modes within UWB can be obtained by adjusting the width of both L and C-shaped resonators. Overall the designed filter exhibits good UWB passband behavior with insertion loss $< -0.2\,\mathrm{dB}$ and group delay $< 0.15\,\mathrm{ns}$.

1. INTRODUCTION

In recent years, significant research activities using ultra-wideband (3.1–10.6 GHz) related applications have been carried out. UWB is a radio communications technology that promises very high data rates over short distances. Ultra wideband radar and high data-rate communication systems require RF/Microwave circuits of operating over wide frequency ranges. Although the concept has been around since the early 1970s, recent advances in semiconductor and radio communication technology have made UWB devices a reality. UWB bandpass filter is one of the key passive components in UWB radio communication system. Various type of UWB bandpass filter [1–4] has been reported with 110% fractional bandwidth at the center frequency of 6.85 GHz. In [1], a kind of UWB bandpass filter was proposed based on a non-uniform transmission line resonator. The filter is composed of three distinct sections of high impedance in the two sides and low impedance with an aperture-backed PCML with five transmission poles. Despite the structure being simple, the proposed aperture-backed PCML still required a tedious design and fabrication process.

In this paper, we proposed an improved and reduced size of UWB bandpass filter based on PCML structure with L and C-shaped resonator. Similar with [1, 5, 6], a non-uniform transmission line resonator was designed with three different sections. The filter is composed of a pair of non-aperture-backed tight PCML structure, high impedance C-shaped resonator between the PCML structure as a middle resonator and two sides of low impedance L-shaped resonator as a feeding network. We found that, the PCML coupling factor not only depend on the strips and slots width but also to the finishing impedance of the network. PCML structure with strips of broader width and slots of narrower width can produce almost constant coupling factor over broader bandwidth. The respective coupling factor can be further enhanced by using a C-shaped resonator with low impedance. By selecting a proper tight PCML structure with L and C-shaped resonator a UWB bandpass filter with good passband response over wide band can be achieved. Details of the UWB filter design are presented and measured results are given to demonstrate the performance of the proposed filter.

2. PROPOSED UWB FILTER DESIGN

The prototype layout of proposed UWB filter is shown in Figure 1(a). A C-shaped microstrip resonator of width $w_1 = r_2 - r_1$ with inner radius of r_1 and outer radius of r_2 connectcd end to end between two identical non-aperture-backed [1] highly coupled PCML structure. Comparing to the filter structure presented in [1], the highly coupled PCML structure can be used without ground plane aperture and the middle resonator between the PCML structure can be replaced with a C-shaped miscrostrip resonator with specific width. The protype filter was constructed on a substrate with the relative permitivity $\varepsilon_r = 6.15$ and the thickness $h = 1.27\,\mathrm{mm}$. The design consist of input and out feeding network of width w_o (50 Ω at 6.85 GHz) and length l_o ($\approx \lambda/4$ at 6.85 GHz) separated a distance L. The middle C-shaped resonator design with inner radius r_1 and outer radius r_2 accordingly ensures the overall length of the resonator is slightly greater than $\lambda/4$ at 6.85 GHz. The specific length was chosen to ensure the first and second resonant frequency of the C-shaped resonator occupied the UWB region. Furthermore, the width of the C-shaped resonator
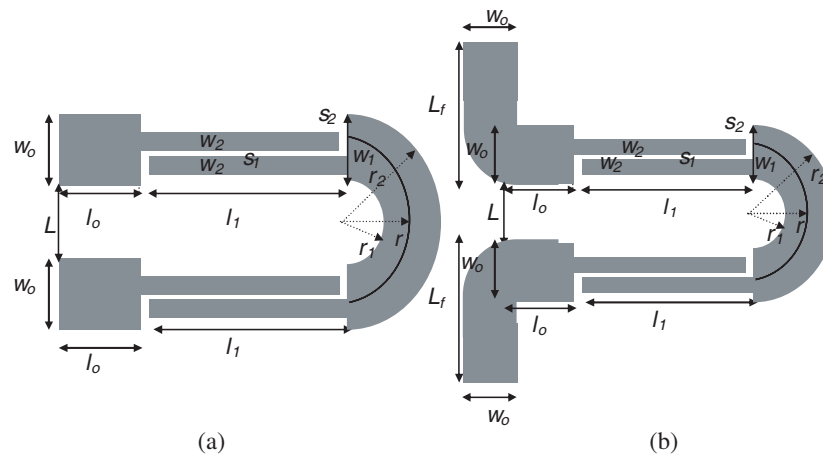
Figure 1: Proposed UWB bandpass filter: (a) with C-shaped resonator; (b) with C and L-shaped resonator.
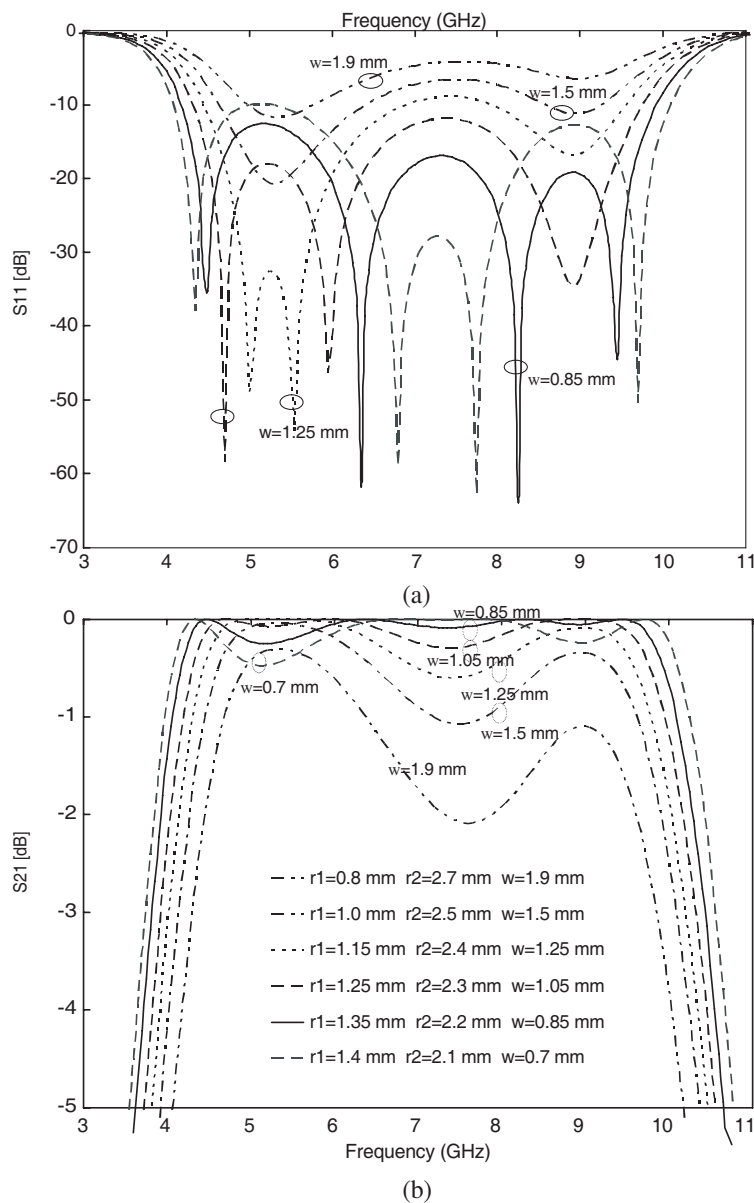

Figure 2: Predicted S-parameters results: (a) S_{11}-magnitude; (b) S_{21}-magnitude.

adjusted accordingly to achieve appropriate impedance in order to improve the coupling factor of PCML structure to excite the third and forth resonant modes of PCML structure within the first and second resonant modes of C-shaped resonator respectively. The insertion loss within UWB passband region also depends on C-shaped resonator impedance. Overall it can be concluded that a wide passband covering the whole UWB band can be achieved with four transmission poles if the non-aperture-backed PCML with tighten coupling degree are suitably coupled with the above C-shaped resonator.

In the prototype design, the PCML strip and slot widths are set $w_2 = 0.6\,\text{mm}$, $s_1 = 0.1\,\text{mm}$, $s_2 = 0.1\,\text{mm}$ and the length $l_2 = 5\,\text{mm}$ ($\approx \lambda/4$ at $6.85\,\text{GHz}$) in order to achieve a broad bandwidth of tight coupling degree and a relaxed fabrication tolerance. Meanwhile, the C-shaped middle resonator is formed with r_1, r_2 and w_1 in order to achieve a length of slightly greater $\lambda/4$ at $6.85\,\text{GHz}$. The feeding network of width $w_o = 1.9\,\text{mm}$ ($50\,\Omega$ at $6.85\,\text{GHz}$) and length $l_o = 5\,\text{mm}$ for the input and output port separated a distance $L = 1.6\,\text{mm}$ is design to accommodate the C-shaped resonator. Figure 2 shows the simulated results of S_{11} and S_{21} of a UWB filter over the wide frequency range (3.0–$11.0\,\text{GHz}$) with respect to the five different C-shaped resonator widths ($w_1 = 0.7\,\text{mm}$–$1.9\,\text{mm}$) under the fixed length of the resonator ($5.57\,\text{mm}$) and middle radius ($1.75\,\text{mm}$). At $w_1 = 1.9$ and $1.5\,\text{mm}$ with very high coupling, the all four resonant frequencies cannot be seen clearly. As the w_1 reduce with low coupling factor, the resonance frequencies tend to separate and can be seen. When $w_1 = 0.85\,\text{mm}$ ($60\,\Omega$ at $6.85\,\text{GHz}$) ($r_1 = 1.35\,\text{mm}$ and $r_2 = 2.2\,\text{mm}$) the resonant frequencies are equally spaced. It produces S_{21} — magnitude with an almost flat frequency response near the $0\,\text{dB}$ line over the desired UWB.

3. IMPROVED UWB FILTER DESIGN

The filter is further improved by introducing an L-shaped resonator as a feeding network for input and output port because the existing input and output port for the feeding network is very close to each other, thus, the SMA connectors cannot be fixed. The L-shaped resonators introduced are shown in Figure 1(b). The L-shaped resonator of width w_o and length $L_f + l_o$ as input and output port for feeding network was designed to produce an impedance of $50\,\Omega$ with length $\approx \lambda/4$ at $6.85\,\text{GHz}$. Several design of UWB filter with L-shaped resonator designed and simulated. By comparing the performances of the filters with different dimensions of L-shaped resonator, the dimensions of the L-shaped resonator with a relative good performance of filter were determined, in which the width $w_o = 1.4\,\text{mm}$ ($50\,\Omega$ at $6.85\,\text{GHz}$) and length $L_f + l_o = 6\,\text{mm}$ ($\approx \lambda/4$ at $6.85\,\text{GHz}$). Figure 3 shows the simulated results of optimized filter of Figure 1(a) and Figure 1(b) for insertion loss, return loss and group delay. It shows clearly by placing the L-shaped resonator the insertion, return loss and group delay maximum variation of the filter improves within UWB passband response. The simulated group delay of UWB filter Figure 1(a) produced a maximum variation of $0.178\,\text{ns}$, while group delay of UWB filter Figure 1(b) produced a maximum variation of $0.129\,\text{ns}$. The optimized UWB filter with L and C-shaped resonators as shown in Figure 1(b), was fabricated on a rectangular substrate of $14 \times 11.7\,\text{mm}$, which determined the overall dimension of the filter.

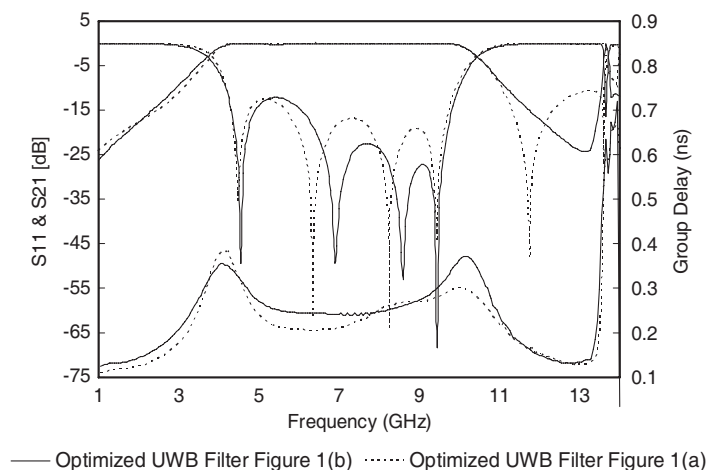—— Optimized UWB Filter Figure 1(b)   ······ Optimized UWB Filter Figure 1(a)

Figure 3: Predicted S-parameters and group delay of optimized UWB filter Figure 1(a) and Figure 1(b).
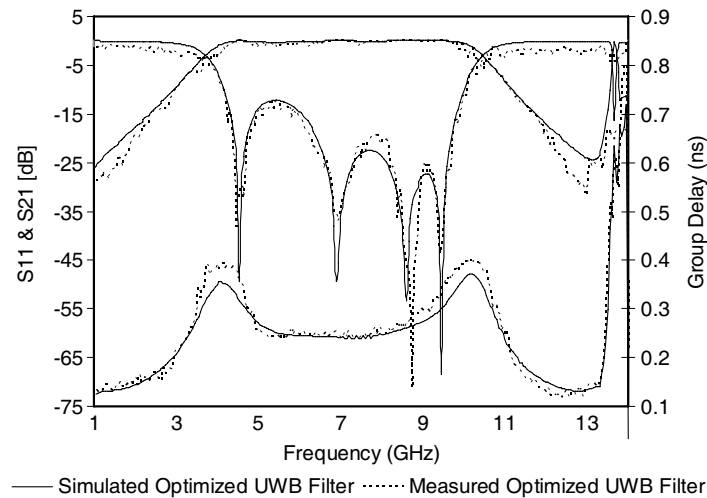
Figure 4: Predicted and Measured S-parameters and group delay of optimized UWB filter Figure 1(b).

Figure 4 illustrates the simulated and measured two-port S-parameters and group delay of the optimized L and C-shaped resonator of UWB filter. Both the measured and simulated results are found to have reasonably good agreement with each other. The measured result shows that in-band performance of the proposed filter stays almost same as predicted results, including small insertion loss and group delay variation. The measured group delay within the realized UWB passband varies between 0.25 ns and 0.4 ns with a maximum variation of 0.15 ns over its whole passband, showing good linearity of the proposed UWB filter. The maximum variation of group delay is much lesser than reported in [1].

4. CONCLUSION

A novel UWB bandpass filter based on normal tight PCML structure with L and C-shaped resonator has been proposed. The filter is composed of a pair of identical non-aperture-backed tight PCML structure, a C-shaped middle multiple-mode resonator and L-shaped input, output port feeding network. The filter shows good in-band performance, including a low insertion loss and a small group delay variation within whole passband. Overall this filter shows lowest maximum variation of group delay which is < 0.15 ns and reduced size of UWB bandpass filter of dimension 14.0×11.7 mm.

ACKNOWLEDGMENT

REFERENCES

1. Zhu, L. and H. Wang, "Ultra-wideband bandpass filter on aperture-backed microstrip line," *Electron. Lett.*, Vol. 41, No. 18, 2005.
2. Wang, H., L. Zhu, and W. Menzel, "Ultra-wideband bandpass filter with hybrid microstrip/CPW structure," *IEEE Microw. Wireless Compon. Lett.*, Vol. 15, No. 12, 844–846, 2005.
3. Li, K., D. Kurita, and T. Matsui, "An ultra-wideband bandpass filter using broadside-coupled microstrip-coplanar waveguide structure," *IEEE MTT-S Int. Dig.*, 675–678, 2005.
4. Chen, H. and Y. Zhang, "A novel and compact UWB bandpass filter using microstrip fork-form resonators," *Progress In Electromagnetic Research*, PIER 77, 273–280, 2007.
5. Marimuthu, J. and M. Esa, "Three element compact broadband parallel-coupled microstrip bandpass filter of simple configuration," *Proceedings of IEEE 2007 Asia-Pacific Conference on Applied Electromagnetics*, December 04–06, 2007.
6. Esa, M., J. Marimuthu, and S. K. Syed-Yusof, "Broadband compact simple ladder PCML filter with rectangular centre resonator," *Proceedings of IEEE International Symposium on Antennas and Propagations ISAP'08*, October 27–30, 2008.

Compact Dual Broadband Ladder PCML Filter with Rectangular Resonators

J. Marimuthu and M. Esa

Faculty of Electrical Engineering, Universiti Teknologi Malaysia, UTM Skudai, Johor 81310, Malaysia

Abstract— A simple configuration of dual broadband parallel coupled microstrip line (PCML) bandpass filter operating at 2.65 GHz and 7.85 GHz frequency bands with wide stopband design is presented. The proposed filter is composed of a pair of high coupling factor PCML structure, low impedance middle resonator and feeding network. Overall the simulated and measured results of insertion and return loss show good agreement with BW = 1.8 GHz (85%), $|S_{11}| < -12$ dB, $|S_{21}| > -0.3$ dB at 2.65 GHz and BW = 1.8 GHz (25%), $|S_{11}| < -10$ dB, $|S_{21}| - 0.5$ dB at 7.85 GHz with overall stopband of 5.2 GHz.

1. INTRODUCTION

In recent years, with the advent of communications systems, the designs of passive circuits are facing new design challenges including compact in size, wide bandwidth and multi-band operations. The current and future wireless communication systems, such as worldwide interoperability for microwave access (WiMAX) and wireless local area network (WLAN) for indoor and outdoor applications, require wide bandwidth up to several hundred of megahertz and flexibility of operating in multiple frequency bands. Planar bandpass filters fabricated on printed circuit board (PCB) are attractive for filter application because their low fabrication cost. The multi-band microwave components, when realized, can lead to both the size and cost reduction in the circuits [1–9].

In this paper, a dual broadband bandpass filter is proposed based on Stepped impedance resonators (SIRs) structure [2, 9]. The proposed filter is composed of a pair of high coupling factor PCML structure, low impedance middle resonator and feeding network. The middle resonator and feeding network width and length was adjusted accordingly to improve the insertion loss, return loss and harmonic suppression at both operating frequency in order to achieve dual band. The middle resonator and input output feeding network width was adjusted to improve the insertion loss and return loss performance of dual passband response. The length of the middle resonator was adjusted for harmonic cancellation by transmission zero frequency. Details of the dual broadband filter design are presented and measured results are given to demonstrate the performance of the proposed filter.

2. SIMPLE PCML STRUCTURE

A simple PCML structure was designed as shown in Figure 1(a), to investigate the dual band performance with respect to feeding network width. The physical parameters of PCML as strip and slots widths $w_1 = 0.6$ mm, $s_1 = 0.2$ mm and the length $l_1 = 14$ mm ($\approx \lambda/4$ at 2.65 GHz). The PCML feeding network of fixed length $l_o = 4$ mm, width was adjusted accordingly to investigate the overall coupling factor at both band. The design was constructed on a substrate with the relative permitivity $\varepsilon_r = 6.15$ and the thickness $h = 1.27$ mm. The two-port admittance Y-matrix of PCML structure can be effectively extracted using full-wave analysis of commercially available *em* tools.
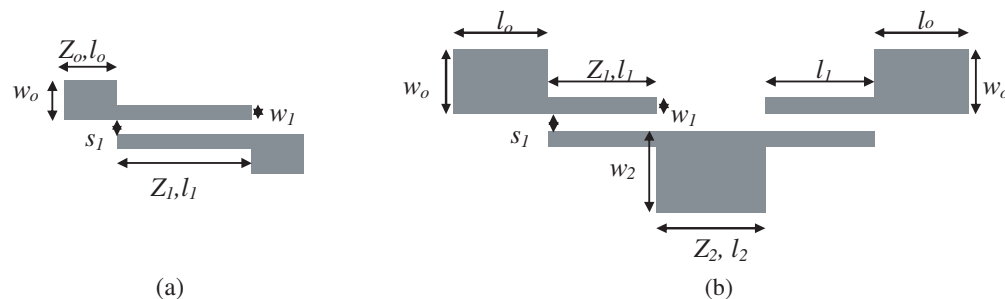

(a)　　　　　　　　　　　　　(b)

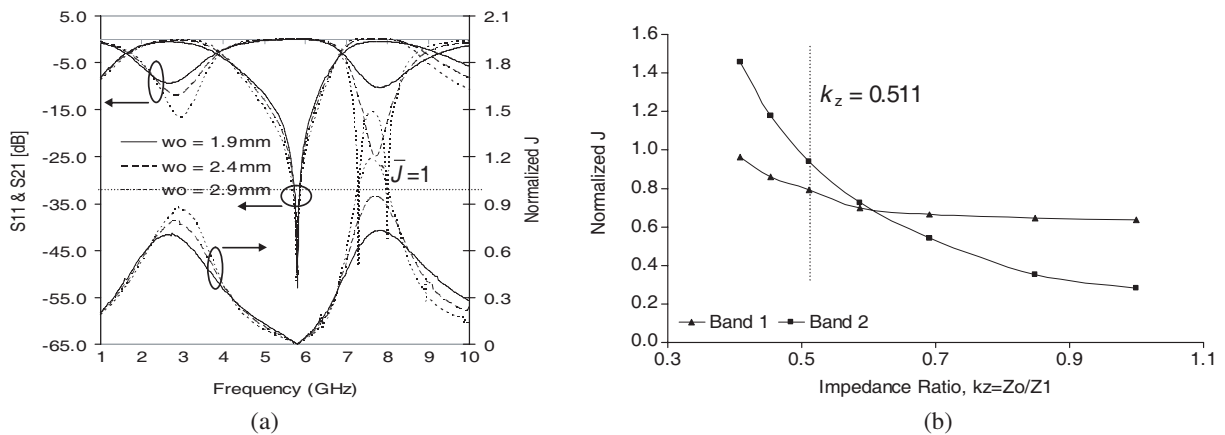Figure 1: Proposed design: (a) Simple PCML structure; (b) Dual broadband bandpass filter.

Figure 2: Predicted Simple PCML performance: (a) S-parameters and normalized J susceptance; (b) Normalized J susceptance vs impedance ratio.

The equivalent normalized $\bar{J}$-susceptance of PCML structure is calculated based on [10, 11] by using the extracted Y-parameters.

Figure 2(a) shows the normalized J-inverter susceptance $\bar{J}$ and S-parameters of a PCML structure, with various feeding network width. It shows that as the w_o increases from 1.9 mm to 2.9 mm, the $\bar{J}$ peak value for both bands increases as well. The second band centered at 7.85 GHz ($\bar{J}$ peak value 0.73 to 1.18) increased at a higher rate compared to the first band centered at 2.65 GHz ($\bar{J}$ peak value 0.71 to 0.88). Figure 2(a) also shows that the S_{11} pole appears when $\bar{J} = 1$. For PCML with $w_o = 2.9$ mm, the corresponding S_{11} pole frequency at second band is as same as the frequency for $\bar{J} = 1$. Figure 2(b) shows that the $\bar{J}$ peak value for the first and second band respect to impedance ratio $k_z = Z_o/Z_1$, Z_o is the impedance of feeding network of width w_o and Z_1 is the impedance of coupling arm at PCML structure of width w_1. Its shows clearly that the $\bar{J}$ peak value depends on k_z and both band decreases at a different of rate as k_z increases. For $k_z < 0.6$, the coupling factor of Band 2 is greater than Band 1 and is suitable for dual band design. For dual band design, PCML structure with the $k_z = 0.511$ and selected $w_o = 2.4$ mm is preferred.

3. DUAL BROADBAND FILTER STRUCTURE

The prototype layout of the proposed dual broadband filter is shown in Figure 1(b), PCML strip and slot widths are set as given above in order to achieve a dual broad bandwidth of tight coupling degree and a relaxed fabrication tolerance. Meanwhile, the middle resonator is formed with length l_2 and width w_2 in order to achieve a length of slightly greater $\lambda/4$ at 2.65 GHz. The feeding network of width $w_o = 2.4$ mm and length $l_o = 4$ mm for the input and output port is designed. Figure 3 shows the simulated results of S_{11} and S_{21} of a dual broadband filter over the wide frequency range (1.0–10.0 GHz) with respect to the different middle resonator widths (Figure 3(a)) and lengths (Figure 3(b)). Its shows that six resonant frequencies are present within 1.0 GHz to 10 GHz. The first (f_1) and second (f_2) resonant frequencies can be grouped together to form first operation band (Band 1). Meanwhile the forth (f_4) and fifth (f_5) resonant frequencies can be grouped together to form the second operation band (Band 2). The third (f_3) and sixth (f_6) resonant frequencies can be classified as first and second harmonic frequencies. The position of resonant frequencies and insertion as well return loss within passband of Bands 1 and 2 depend on middle resonator length and width. The middle resonator width is used as a main component to improve the insertion as well as to return loss at passband response and the length is used as a main component to shift the frequencies.

Figure 4(a) shows the effect of various resonance frequencies with respect to impedance ratio $k_z = Z_1/Z_2$, Z_1 is the impedance of coupling arm at PCML structure of width w_1 and Z_2 is the impedance of middle resonator of width w_2. It shows that as k_z increases, the first and second band component resonant frequencies getting closer to each other and the overall operating bandwidth is reduced. When the first and second harmonics frequencies is further reduced to smaller frequencies and brought nearer to the operating band no sign of suppression by transmission zero frequency (f_{zo}). For better dual band operation $k_z = 2.7$ selected with $w_2 = 3.9$ mm. Figure 4(b) shows the effect of various resonance frequencies with respect to resonator length ratio $k_l = l_1/l_2$, l_1 is

the length of coupling arm at PCML structure and l_2 is the length of middle resonator. It shows that as k_l increases the first and second band component resonant frequencies are further separated from each other and the overall operating bandwidth is improved. The first and second harmonics frequencies increased and first harmonic frequency suppressed by transmission zero frequency (f_{zo}) when $k_l = 1.4$ and the second harmonic frequency shifted away from the operating band. For better dual band operation with harmonic suppression $k_l = 1.4$ selected with $l_2 = 10\,\text{mm}$. The final design with $w_o = 2.4\,\text{mm}$, $w_2 = 3.9\,\text{mm}$ and $l_2 = 10\,\text{mm}$ is designed a and simulated as shown in Figure 3(b). It shows that the Band 2 insertion loss decreased, slight modification was introduced by changing $w_o = 2.3\,\text{mm}$. Figure 4 shows enhancement on passband response at both band with $w_o = 2.3\,\text{mm}$.

Figure 5 illustrates the simulated and measured two-port S-parameters of the optimized dual broadband filter. Both the measured and simulated results are found to have reasonably good agreement with each other. The measured result shows that the in-band performance for both band of the proposed filter stays almost same as the predicted results, including the small insertion loss and return loss variation. It shows that at a low cost a dual broadband PCML bandpass filter with excellent passband response can be designed and fabricated.
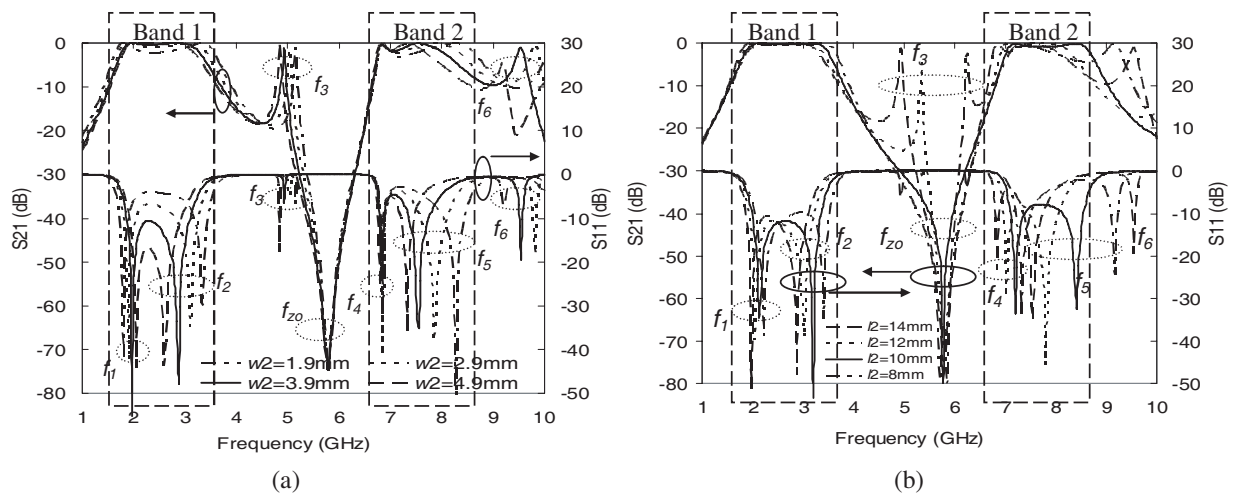

Figure 3: Predicted S-parameters: (a) for various widths; (b) for various lengths.
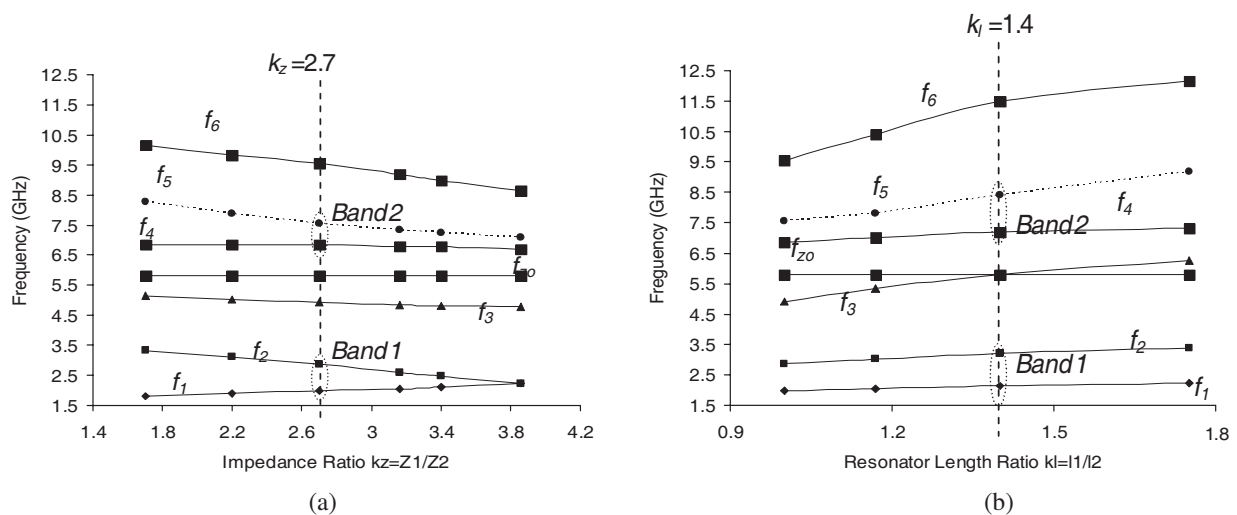

Figure 4: Predicted dual broadband bandpass filter performance: (a) Resonant frequency vs Impedance Ratio; (b) Resonant frequency vs length ratio.
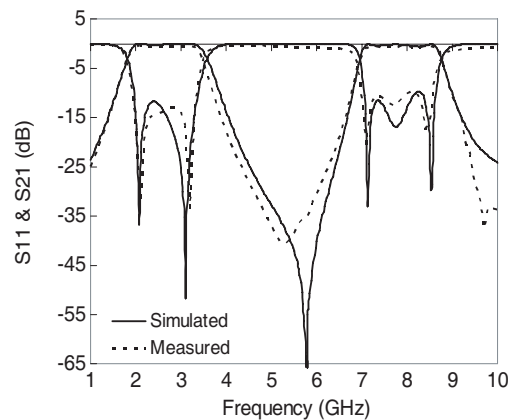
Figure 5: Predicted and measured S-parameters of optimized broadband filter Figure 1(b).

4. CONCLUSION

A simple dual broadband bandpass filter is proposed. The proposed filter uses a simple PCML structure with low impedance input output feeding network and middle resonator. A simple PCML structure shows dual band in nature. The coupling factor of both bands can be enhanced by using a low impedance input output feeding network. This idea leads to the designing of an improved version of PCML dual broadband bandpass filter. By modifying the middle resonator width and length an improved dual broadband PCML bandpass filter can be designed. The technique proposed in this study is the easiest and simplest approach for designing a dual broadband PCML bandpass filter. The optimized design shows excellent dual broadband characteristics with bandwidth BW = 1.8 GHz (85%), $|S_{11}| < -12$ dB, $|S_{21}| > -0.3$ dB at 2.65 GHz and BW = 1.8 GHz (25%), $|S_{11}| < -10$ dB, $|S_{21}| > -0.5$ dB at 7.85 GHz with overall stopband of 5.2 GHz. Overall the proposed filter exhibited excellent dual broadband bandpass performance in operation band. The experiment results are in good agreement with the simulated responses and validate the theory and design method.

ACKNOWLEDGMENT

REFERENCES

1. Wang, L., Y.-X. Guo, B.-Z. Wang, L. C. Ong, and S. Xiao, "High-selectivity dual-band stepped-impedance bandpass filter," *Electron. Lett.*, Vol. 42, No. 9, 538–540, 2006.
2. Marimuthu, J. and M. Esa, "Three element compact broadband parallel-coupled microstrip bandpass filter of simple configuration," *Proceedings of IEEE 2007 Asia-Pacific Conference on Applied Electromagnetics*, December 04–06, 2007.
3. Wang, X.-H., B.-Z. Wang, and K. J. Chen, "Compact broadband Dual-Band bandpass filters using slotted ground structures," *Progress In Electromagnetic Research*, PIER 82, 151–166, 2008.
4. Xiao, J.-K., Q.-X. Chu, and S. Zhang, "Novel microstrip triangular resonator bandpass filter with transmission zeros and wide bands using fractal-shaped defection," *Progress In Electromagnetic Research*, PIER 77, 343–356, 2007.
5. Hassan, A. and A. E. Nadeem, "Novel microstrip hairpinline narraowband bandpass filter using via ground holes," *Progress In Electromagnetic Research*, PIER 78, 393–419, 2008.
6. Chen, H. and Y. Zhang, "A novel and compact UWB bandpass filter using microstrip fork-form resonator," *Progress In Electromagnetic Research*, PIER 77, 273–280, 2007.
7. Zhu, Y.-Z. and Y.-J. Xie, "Novel microstrip bandpass filters with transmission zeros," *Progress In Electromagnetic Research*, PIER 77, 29–41, 2007.
8. Wu, G.-L., W. Mu, X.-W. Dai, and Y.-C. Jiao, "Design of novel dual-band bandpass filter with microstrip meander-loop resonator and CSRR DGS," *Progress In Electromagnetic Research*, PIER 78, 17–24, 2008.

9. Esa, M., J. Marimuthu, and S. K. Syed-Yusof, "Broadband compact simple ladder PCML filter with rectangular centre resonator," *Proceedings of IEEE International Symposium on Antennas and Propagations ISAP'08*, October 27–30, 2008.

10. Marimuthu, J. and M. Esa, "Experimental performance of harmonic suppressed bandpass filter," *Proceedings of IEEE 2007 Asia-Pacific Conference on Applied Electromagnetics*, December 04–06, 2007.

11. Marimuthu, J. and M. Esa, "Experimental performance of harmonic suppressed bandpass filter," *Proceedings of IEEE 2007 Asia-Pacific Conference on Applied Electromagnetics*, December 04–06, 2007.

Effective Constitutive Model of Grain-oriented Fe-Si Laminations Core under Orthogonal Magnetization

Zhengrong Jiang[1, 2], Zhengxi Li[1], and Dehui Sun[1]

[1]Department of Electric & Machinery Engineering
North China University of Technology, Beijing 100041, China
[2]State Key Lab of Power Systems, Department of Electrical Engineering
Tsinghua University, Beijing, China

Abstract— The mechanism of variable inductor based on orthogonal magnetization was discussed. The experiment and simulation showed that the dc bias field makes the hysteresis loop "shearing" and reduces the enclosed area. Hence the effective permeability decreases with increasing dc bias field. By comparing the shearing hysteresis caused by orthogonal magnetization with escalator, an effective anisotropic energy has been incorporated into the existing isotropic model equations. It has proved that effective constitutive model can adequately described the hysteresis and harmonic characteristic caused by orthogonal magnetization.

1. INTRODUCTION

An experimental variable inductor based on orthogonal magnetization showed many virtues such as maintaining linear permeability, safe structure under high voltage applications and lower loss. Most of these virtues derived from the orthogonal magnetization mechanism. Kenji Nakamura studied EIE-core model considering magnetic hysteresis [1]. Bernardo Tellini et al. presented the energetic behavior of hysteretic magnetic materials and obtained a series of linear nonhomogeneous diffusion equations [2]. Yi Bi investigated the effect of orthogonal bias field on magnetic flux distribution by modeling a circuit board embedded ferrite inductor (BEFI) using finite element method [3]. However, the accurate knowledge of the orthogonal magnetization mechanism was essential for improving the design of novel inductors. In the present study, B-H loops of grain-oriented silicon lamination core under the action of an orthogonal bias field were investigated first experimentally, and then the hysteresis was modeled by comparing the performance of the magnetic material under the orthogonal fields with the action of compressive stress.

2. CONSTRUCTION AND EXPERIMENTAL METHOD

Figure 1 shows the configuration of the experimental variable inductor based on the orthogonal magnetization, which consists of a vacant winding with an outer diameter of 120 mm, an inner diameter of 80 mm, a length of 150 mm, and a toriodal core winding with an outer diameter of 75 mm, an inner diameter of 72 mm and a length of 150 mm. The former is used as main coil connected with network which creates the ac exciting field along the axial direction of the toriod winding, the later winding is placed in the former and connected with dc power to create orthogonal bias field along the circumferential direction. The two field are orthogonal each other in the core. The torildal core is made up of grain-oriented silicon laminations and the hysteresis loops were measured using specific designed integral circuit and demoed by TECK power oscillograph [4].

3. B-H LOOP EXPERIMENAL RESULTS

When the grain oriented core is subjected to the orthogonal bias field, the hysteresis loop rotated clockwise on the B-H plane, and the area of the hysteresis loop decreased as well as remanence and coercivity decreased, as shown in Fig. 2.

It appears that with higher field strengths the elongation of the hysteresis curve along the H-axis consisted entirely of reversible magnetization processes, which are hysteresis free. When dc bias current reached to 5 A, the B-H loop became a straight line and the enclosed area nearly decreased up to zero, the magnetization curve has no noticeable hysteresis, as shown in Fig. 2(c). However, in the case of open path, even if the ac exciting and dc bias field are enough amplitudes, the hysteresis loop at the loop tips was not completed by fully reversible magnetization processes, although the effective permeability and hysteresis loss of the specimen still decreased with increasing orthogonal field. The reason is that there is a strong demagnetization effect along the axial direction of the core, which leads to the effective internal field was only a small fraction of the external field. In
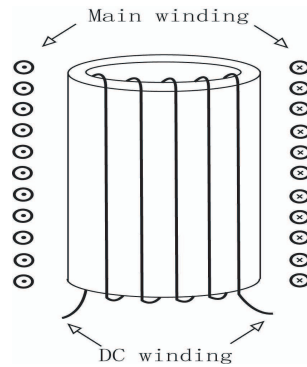
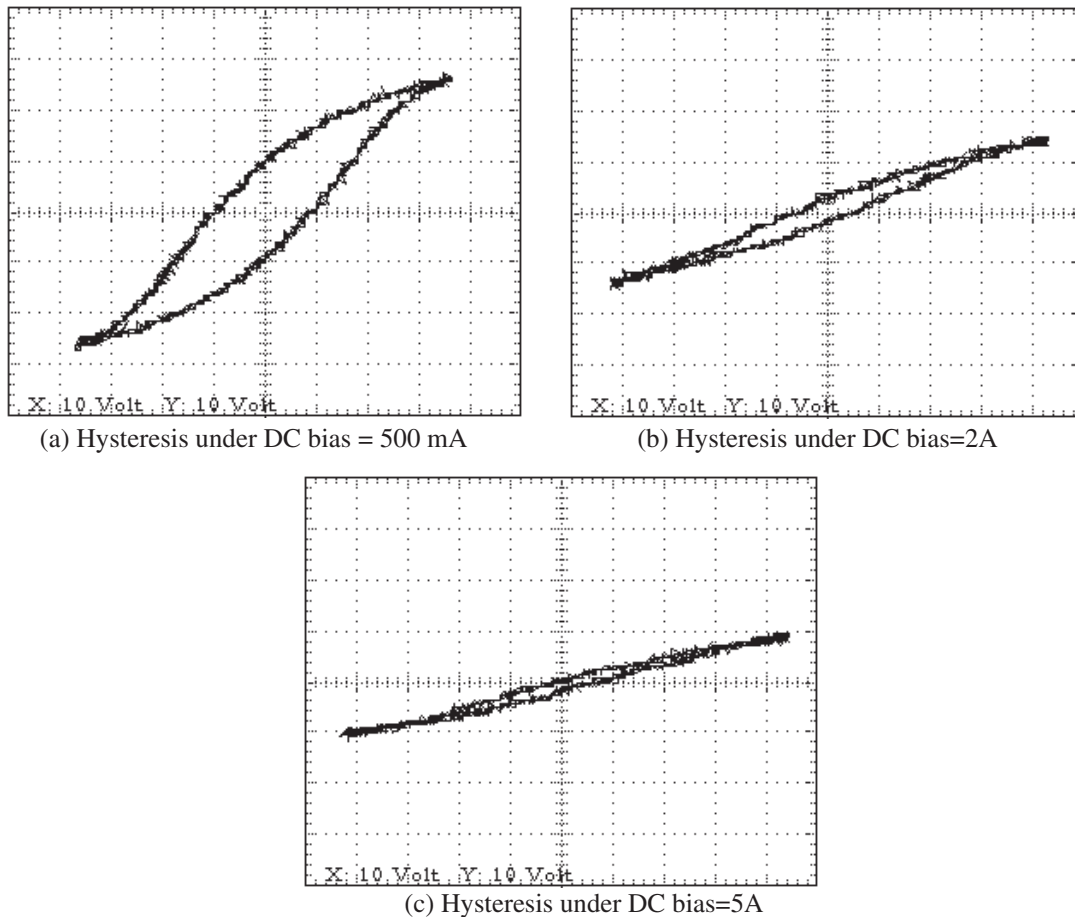Figure 1. The configuration of the experimental inductor.

(a) Hysteresis under DC bias = 500 mA

(b) Hysteresis under DC bias=2A

(c) Hysteresis under DC bias=5A

Figure 2. Hysteresis "shearing" with DC bias.

this case the orthogonal field can be used to adjust the inductance of reactor with this kind of core by altering the effective internal ac field, the variable range became more pronounced when the air path is shorter. For semi core variable inductor, the inductance is as

$$L = \frac{\overline{\mu} n^2 D \delta}{l} \tag{1}$$

where n is the number of main windings turns, D is the out diameter of the core, δ is the core net thickness and l is the core length. $\overline{\mu}$ is determined by DC bias current while main current is constant.

Orthogonal magnetization also brings about a linear permeability characteristic. This is due to two facts, one is the bias winding independent with the main winding, so there is no inductance

between the two windings. The other reason is that during the orthogonal magnetization process, the domain wall motion is the main mechanism in the low magnetization region, while domain rotation is the main in the high magnetization region. It is contra for the magnetization in axis direction. Hence the orthogonal bias field enhances the reversibility in axis direction because it magnetizes the material into fewer, larger domains and therefore there are fewer domain walls to move. The grain oriented laminations can be magnetized into a single domain along the ac exciting field none but the inner field is strong enough, and then the orthogonal field effect on the ac direction is not longer pronounced even if the orthogonal field is much more high.

4. ORTHOGONAL MAGNETIZATION MODELING

Verhoeven studied that domain rotated toward a perpendicular direction when a press strain worked on magnetic material [5]. The effect on hystersis of magnetic material is similar with that of orthogonal field. So the orthogonal magnetization modeling can be derived referring to the effect caused by compressive stress.
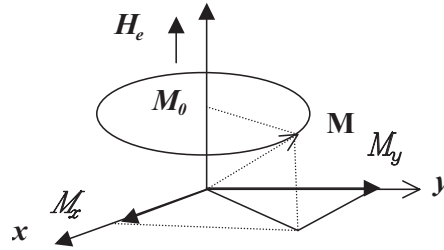

Figure 3. The magnetization movement in Descartes Coordinate.

The magnetization movement in Descartes Coordinate is as Fig. 3. In the presence of the orthogonal bias field, an additional anisotropy energy and elastic energy can be effectively calculated and included into the generalized anhysteretic function described previously [6], so the energy E of a magnetic moment can be expressed as

$$E = -\mu_0 m \cdot (H_\parallel + H_\perp + \alpha M) + \widetilde{E_{aniso}} + \widetilde{E_\sigma} \tag{2}$$

From mini energy theory, the magnetic material will get elastic distortion when the magnetization changed, so the modeling of domain rotating can be used for descript the system energy changing [7]. All this phenomena were connected with magneto mechanical field, it can be described as following:

$$E_{total} = E_H + \widetilde{E_{an}} + \widetilde{E_\sigma}$$

$$\widetilde{E_{an}} = E_0 + K_1(\cos^2\theta_1\cos^2\theta_2 + \cos^2\theta_2\cos^2\theta_3 + \cos^2\theta_3\cos^2\theta_1) \tag{3}$$

$$E_H = -\mu_0 M_s H(\cos\theta_1\cos\phi_1 + \cos\theta_2\cos\phi_2 + \cos\theta_3\cos\phi_3) \tag{4}$$

$$\widetilde{E_\sigma} = -\frac{3}{2}\lambda_{100}\sigma(\cos^2\theta_1\cos^2\beta_1 + \cos^2\theta_2\cos^2\beta_2 + \cos^2\theta_3\cos^2\beta_3)$$

$$-3\lambda_{111}\sigma(\cos\theta_1\cos\theta_2\cos\beta_1\cos\beta_2 + \cos\theta_2\cos\theta_3\cos\beta_2\cos\beta_3 + \cos\theta_3\cos\theta_1\cos\beta_3\cos\beta_1) \tag{5}$$

$$\overline{\mu_{ij}} = \frac{1}{8\pi^2}\int_0^\pi\int_0^{2\pi}\int_0^{2\pi}\mu_{ij}(\theta,\varphi,\psi)\sin\theta d\psi d\varphi d\theta \tag{6}$$

where, $\widetilde{E_{an}}$ is the effective anisotripic energy, E_H is the exciting field energy, $\widetilde{E_\sigma}$ is the effective magnetostrictive energy, θ_1, ϕ_1, β_1 is the angle between M, H, effective strain force and grain axial direction respectively.

The total energy is

$$E_{total} = E_H + \widetilde{E_{an}} + \widetilde{E_\sigma} \tag{7}$$

The effective constitutive equation can be decided as

$$B_i = q_{ijk}\sigma_{kl} + \mu_{ij}H_j + J_i^r \tag{8}$$

where q_{ijk} is magnetostrictive coefficient, σ_{kl} is stress tensor, μ_{ij} is permeability tensor, J_i^r is remanent magnetization.

Due to the hysteresis of the grain oriented lamination, the direction of M is no actually along the direction of the vector sum of two H fields. As the analysis mentioned above, the orthogonal field is similar to an additional anisotropy and a magnetostrictive energy, thus it is more effective to use a perturbation of the original hysteresis model equations to describe the magnetization along the excitation field direction in the presence of an orthogonal bias field.

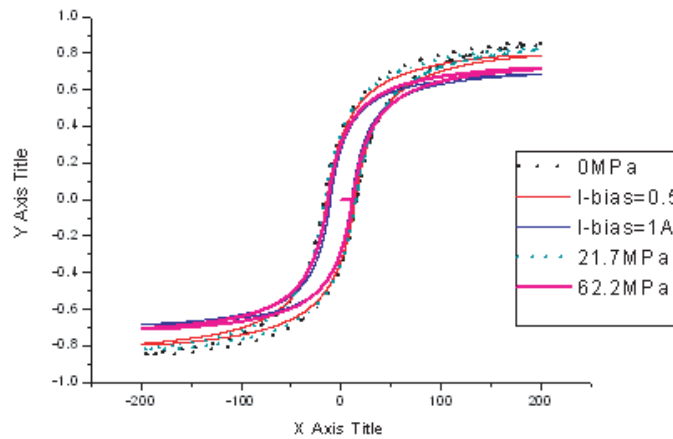

Figure 4. Cmparison of measured and modeled hysteresis curves.

(a) Voltage and current waveform when Idc=500mA, THD=4%

(b) Voltage and current waveform when Idc=6A, THD=2.8%

(c) Voltage and current waveform when Idc=10A, THD=2.5%
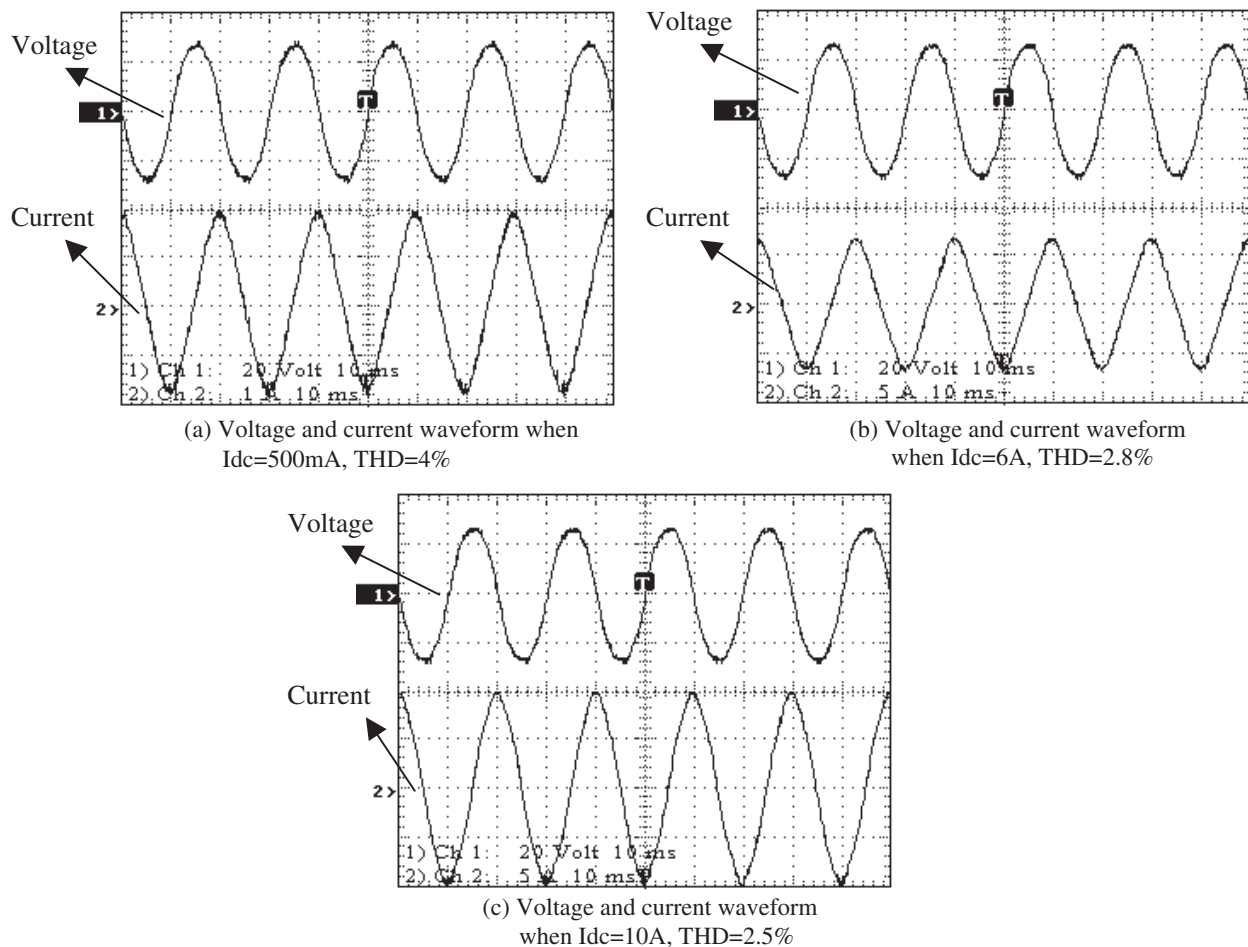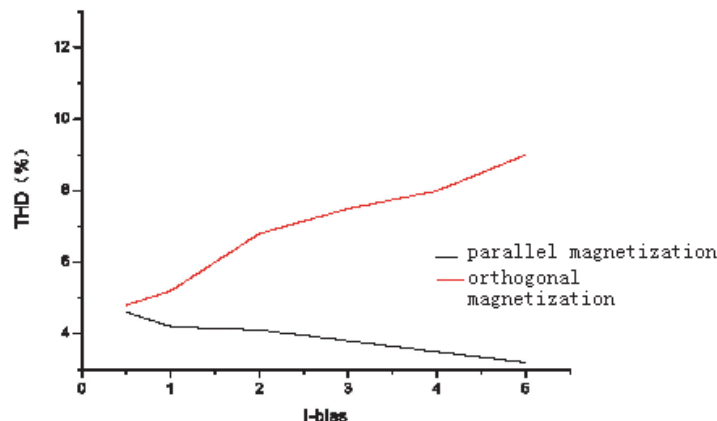
Figure 5.

Figure 6. The compare of harmonic characteristics between parallel magnetization and orthogonal magnetization.

The anhysteretic function can be quoted as

$$M_{aniso} = M_s \frac{\sum\limits_{\text{all-moments}} e^{-E/k_B T} \cos\theta}{\sum\limits_{\text{all-moments}} e^{-E/k_B T}} \quad M_{aniso} = M_s \frac{\sum\limits_{\text{all-moments}} e^{-E/k_B T} \cos\theta}{\sum\limits_{\text{all-moments}} e^{-E/k_B T}} \tag{9}$$

When orthogonal bias field was increased, according to Equation (2), the change of E makes B-H hysteresis "shearing", which is equivalent with a stress along with the axis. The calculate quantitative agreement with experimental result. The comparison of measurement and model is as Fig. 4.

The corresponding result dates are shown as Table 1.

Table 1. Calculate and experiment results.

	Saturated field (T)	Stress calculation (MPa)	Stress experiment (MPa)	Erro
$I_{\text{DC-bias}} = 0\,\text{A}$	0.95	0	0	0%
$I_{\text{DC-bias}} = 0.5\,\text{A}$	0.88	23.82	27.1	12.1%
$I_{\text{DC-bias}} = 1\,\text{A}$	0.67	55.17	62.2	11.3%
$I_{\text{DC-bias}} = 2\,\text{A}$	0.62	65.2	74.6	12.6%

Experimental results showed that the reversible magnetization component increased with increasing orthogonal field. Hence, the linearity of the permeability was improved, so the harmonic characteristic of the inductor became better with the increasing orthogonal field.

5. CONCLUSION

The effective constitutive of the grain oriented lamination core presented here is capable of representing the response of the core subject to orthogonal magnetization. Considering the dc bias field as an additional anisotropy and magnetostrictive energy, the effective constitutive is satisfactory for describing the effect on hysteresis loop caused by dc orthogonal bias current. Thus it is anticipated that the method will provide a helpful base for designing of such kind of inductors.

REFERENCES

1. Nakamura, K., S. Hayakawa, S. Akatsuka, et al., "Three-dimensional reluctance network analysis considering an iron loss characteristic for eie-core variable inductor," *IEEE Transactions on Magnetics*, Vol. 41, No. 10, Octorber 2005.
2. Tellini, B., M. Bologna, and D. Pelliccia, "A new analytic approach for dealing with hysteretic materials," *IEEE Transactions on Magnetics*, Vol. 41, No. 1, January 2005.
3. Bi, Y. and D. C. Jiles, "Finite element modeling of an electrically variable inductor," *IEEE Transactions on Magnetics*, Vol. 35, No. 5, September 1999.

4. Liu, S. and J. Yu, "Measuring alternating current magnetization curve and magnetic parameters of the ferromagnetic material," *Physics Experimentation*, Vol. 25, No. 1, January 2005.

5. Verhoeven, J. D., J. E. Ostenson, and E. D. Gibson, "The effect of composition and magnetic heat treatment on the magnetostriction of TbDyFe twinned single crystals," *J. Appl. Phys.*, Vol. 66, No. 2, 772–779, 1989.

6. Ramesh, A., D. C. Jiles, and J. Roderick, "A model of anisotropic anhysteretic magnetization," *IEEE Transactions on Magnetics*, Vol. 32, 4234, 1996.

7. Feng, X., "Studies on the constitutive theory and experiment of ferromagnetic materials," Ph.D. Thesis, Tsinghua University, 2002.

Prototype Design, Hardware and Construction of Compact and Tuneable X-band Pre-bunched Free Electron Maser

Fareq Malek[1], **James Lucas**[2], **Yi Huang**[2], **R. Badlishah Ahmad**[1],
Badr Muhammad Abdullah[3], **and Azlan Awang**[4]

[1]Universiti Malaysia Perlis (UniMAP), Malaysia
[2]The University of Liverpool, United Kingdom
[3]King Fahd University of Petroleum and Minerals (KFUPM), Kingdom of Saudi Arabia
[4]TELECOM Bretagne, France

Abstract— We are developing prototype free electron maser (FEM) that is compact, tuneable and efficient for potential industrial use. Therefore we define the characteristics for the construction of a novel X-band rectangular waveguide pre-bunched free electron maser (PFEM). Our device operates at 10 GHz and employs two rectangular waveguide cavities (one for velocity modulation and the other for energy extraction). The electron beam used in this experiment is produced by thermionic electron gun which can operate at 3 kV and up to 50 μA. The resonant cavity consists of a thin gap section of height 1.5 mm which reduces the beam energy required for beam wave interaction. The prototype design, hardware and construction process are reported in this paper.

1. INTRODUCTION

The free electron maser (FEM) is a source of microwave power which makes use of the interaction between the electron beam and electromagnetic radiation [1]. The purpose of this research is to produce a low cost FEM mainly for industrial processing, medical and communication fields for which the FEM offers the prospect of a microwave source with a broad tuning range, high power and reasonable efficiency which is higher than other conventional FEL or microwave devices.

We are developing a novel pre-bunched free electron maser (PFEM) operating at a relatively low voltage of 3 kV at a frequency of 10 GHz, using available and affordable technology. This results in a compact, powerful, efficient and low cost device potential for industrial applications, such as plasma welding torch, pollution control, microwave processing of materials and detection of shallow buried non-metallic landmine [2, 3]. The system, shown in Figure 1, consists of an input rectangular cavity (for velocity modulation of the electron beams) and an output rectangular cavity (for energy extraction). The experiment demonstrated coherent emission and gain with a beam current of up to 50 μA [4].

A novel design scheme allows the PFEM to operate at a low current and accelerating voltage, maintaining a compact design. The acceleration voltage is applied directly between the electron gun filament and input cavity. The same X-band microwave source is fed into both the cavities. The phase between this output cavity and the input cavity can be tuned by employing a phase shifter. The velocity modulated electron beam from the input cavity interacts with the microwave E-field in the output cavity, which emits strong coherent radiation, as a result, enlarged microwave power can be obtained [5, 6].

All other FEM or FEL research at universities or defence institutions either operates at very high voltage or current, or both. In all cases, the FEL cost is very expensive. This research project is unique because the PFEM uses low voltage and low current. Due to the low voltage, the output frequencies are in the microwave frequency range, where monitoring equipment are more readily available and cheaper. The equipment breakdowns are rare, and the ionizing (X-ray) radiation is not dangerous. Due to the low current, it is easy to maintain the high vacuum condition. Due to both (low voltage and low current), the PFEM system can be operated (powered) from the mains socket (240 Volts and 13 A).

The PFEM is tuneable, which means the operating frequency can be tuned by simply adjusting the acceleration voltage. The PFEM also requires minimal labour for design and construction. This means that the PFEM can be made at a cost cheaper than the currently available microwave source. The next sections will show a possible way forward in the design of a compact, low voltage and low current PFEM which has great potential for industrial applications.
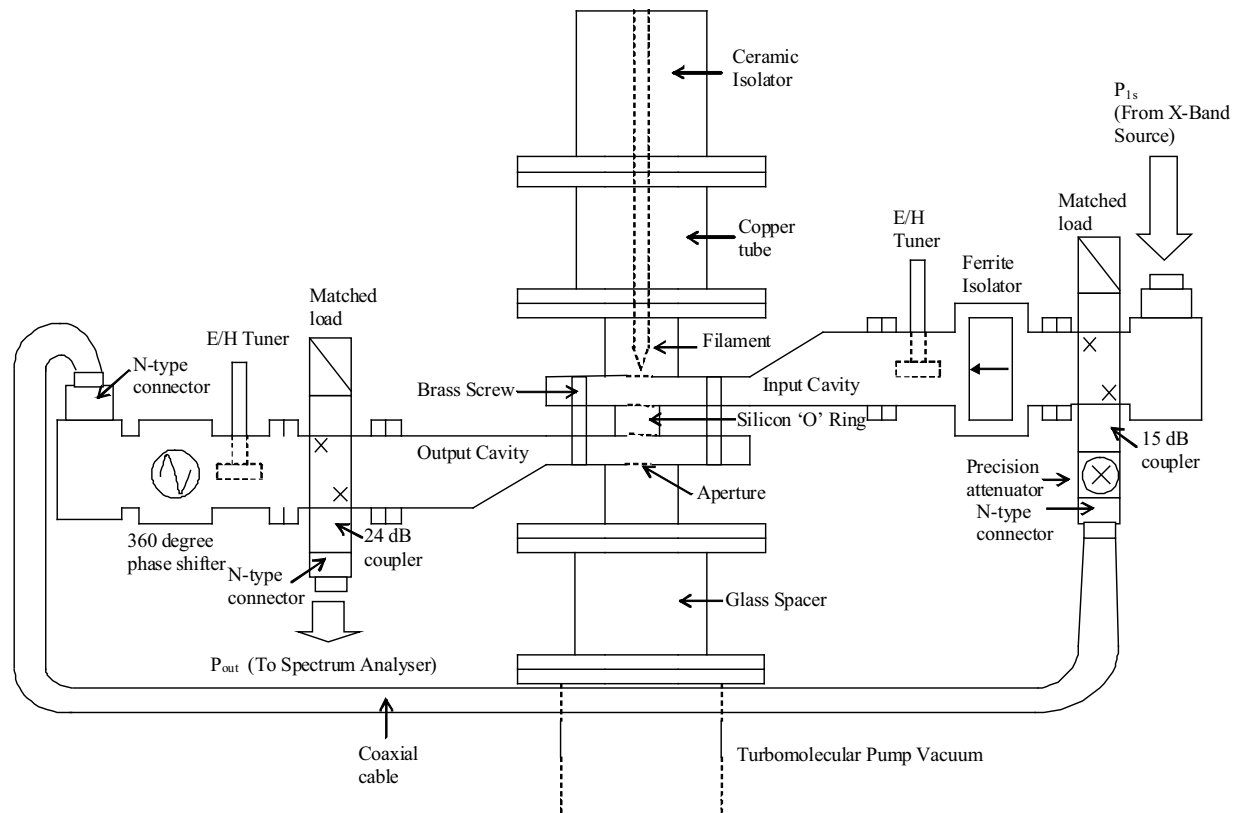
Figure 1: Diagram of Pre-Bunched Free Electron Maser (PFEM) system. The electron gun and high voltage circuits are omitted for simplicity purpose.

2. PFEM SYSTEM ARRANGEMENT

The PFEM system set-up, shown in Figure 1, consists of four main components: the electron gun, the input cavity (electron velocity modulator), the output cavity (energy extractor) and the turbo-molecular vacuum pump system. This section describes briefly these components. A simple electron gun arrangement has been used, which incorporates a cathode and an anode. The cathode is designed from tungsten filament (operated up to $50\,\mu A$). The input cavity acts as an anode. The gun is operated at voltages up to $3\,kV$. The supply polarity is negative [7]. The tungsten filament is powered using a VARIAC (variable auto transformer) and a step down filament transformer. The output lines of the transformer are connected to the tungsten filament.

The input cavity is placed directly below the electron gun. The output cavity is placed directly below the input cavity, separated by silicon 'O' ring for insulation purpose. This insulation is to allow the current flowing through the apertures to be measured. This input cavity is designed using a standard X-band waveguide, WR90/WG16, with internal broad dimension of 22.86 mm, and narrow dimension of 10.16 mm. As can be seen in Figure 1, each cavity consists of three main sections: the standard X-band section, the tapered section and the thin gap section.

The length of the standard X-band section is one waveguide wavelength (λ_g) which is calculated at 10 GHz for the TE_{10} mode. Similarly, a tapered section of one waveguide wavelength (λ_g) is placed next to this standard X-band section. In such waveguide taper, power may be lost to reflection and radiation. The taper should be designed to keep radiation reflection loss at a minimum [8]. Simulation using Vector Fields CONCERTO shows that the return loss of RF power is minimized when the taper length is designed to be equal to 1* waveguide wavelength. A thin gap section of height 1.5 mm and length 2.5* waveguide wavelength $(2.5 * \lambda_g)$ is connected to the tapered section. Apertures of 4 mm diameter are drilled in the centre of the thin gap section to allow electrons to flow through.

The microwave power (up to 10 dBm) from the Marconi signal generator is fed into the input of the X-band section of the input cavity. The same microwave power is fed into the output cavity using the 15 dB coupler, via a coaxial cable. The two cavities are fully tuned to get the best resonance by using E-H tuners, and the frequency is fixed at 10 GHz. A 360 degree phase

shifter is placed at the output cavity, and this can be adjusted to ensure the correct phase between the bunched electron beams and the microwave E-field in the output cavity. Velocity modulated electron beams will flow across the apertures of the input cavity into the apertures of the output cavity. These bunched beams will strongly interact with the microwave E-field in the output cavity. At the output cavity, a 24 dB coupler is used to extract microwave signal from the cavity to the spectrum analyzer. In the vacuum system, the pump is isolated from the output cavity by a glass spacer, for the purpose of current measurement flowing across the apertures of the cavities.

3. THE CONSTRUCTION OF PFEM

The resonant cavities of the PFEM are constructed from the WR90 rectangular waveguide (X-band frequency region). Rectangular waveguide was chosen in this project to overcome overmoding problems. The constructions of various PFEM components are described in this chapter.

3.1. Main Body of the PFEM

The main body of the PFEM device is constructed from a long X-band rectangular waveguide. The diagram of the long X-band rectangular waveguide is shown in Figure 2, where the dotted line shows the section of this waveguide to be cut using the milling cutter. The horizontal length of the thin gap section is designed to be $2.5 * \lambda_g$, while the horizontal lengths of the taper section and the standard X-band section are λ_g respectively. After cutting this waveguide, if one is to view the end result from the top (aerial view), the thin gap section and the taper section are now 'topless'. In order to cover these two 'topless' sections, copper plates will be placed on top of the respective sections. These copper plates were aluminum soldered along the edges. It is shown that leaks occurred along the edges when this aluminum soldering was used.

As a solution, soft soldering (60% tin / 40% lead) was used and no leaks occurred. The soft soldering procedure was performed at about 2000 Celsius. Due to cost reasons, the soldering method was used in constructing the cavity instead of the welding method. After covering the two sections (taper section and thin gap section) with thin copper plates, there still left an open air at the end of the thin gap section. In order to resonate, the cavity requires "mirror" at each end. These mirrors are needed to reflect the microwave radiation. In microwave frequencies, this can be provided by the short circuit wall at one end and an isolator at the other end which allows microwave in one direction and not the opposite direction.

Therefore, another thin copper plate was cut from an existing X-band waveguide, and this copper plate (1.5 mm width and 22.86 mm length) was soft soldered onto the end (open air) of the thin gap section. Apertures of 4 mm diameter are required to be placed at the centre of the thin gap section at both cavities. These 4 mm diameter apertures were drilled at the centre of the thin gap section of both cavities.

3.2. Filament Housing

The filament would need to be placed just before the aperture of the input cavity. The filament needed to be housed by a suitable material component to preserve the vacuum condition for the filament to operate in optimum condition. A copper tube is used to house the filament. The outer diameter of this copper tube was measured at 22 mm. The diameter of the copper tube was larger than the aperture diameter (4 mm) on the thin gap section, but smaller than the wide dimension of the X-band rectangular waveguide (22.86 mm). This copper tube was cut from the available long copper tube. It was cut at the centre. One copper tube was for the input cavity (for filament housing), and another copper tube was for the output cavity (for connection to glass spacer).

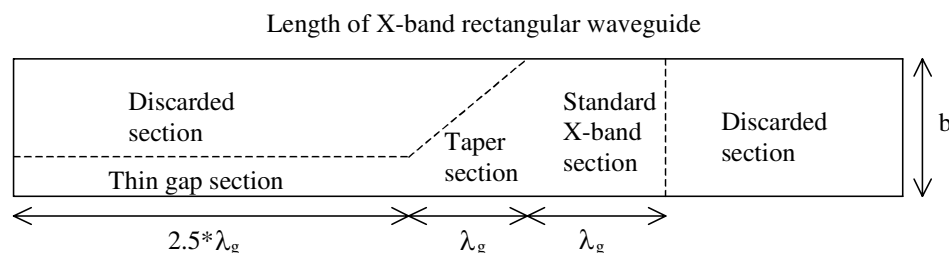Length of X-band rectangular waveguide

Figure 2: Diagram (side view) of a long X-band rectangular waveguide where the PFEM waveguide cavity will be constructed from it.

The cut length of the copper tube was measured appropriately so that the length of the filament and its copper wires can be placed comfortably in it. One end of the copper tube is silver soldered to a 70 mm diameter standard vacuum flange (DN40CF). Silver solder was used for soldering copper to steel material such as the vacuum flange. The temperature used for silver soldering was at 6000 Celsius, which was much higher than that of soft soldering. The other end of the copper tube was soft soldered on top of the thin gap section surface, encircling the aperture of the input cavity. The total distance from the vacuum flange of the copper tube to the surface of the thin gap section is measured at 48 mm.

3.3. The Silica Windows

In the input cavity, microwave EM wave enters through an aperture on one side of the cavity. The waveguide feeding the cavity from the microwave source is not evacuated. Hence, a silica window is bonded to the cavity to seal the input power aperture. The silica does not affect the microwave transmission significantly due to its low-loss dielectric characteristic. The output cavity also has a silica window seals on the output power aperture side. One end of the input cavity and output cavity was soft soldered to standard UBR100 waveguide flanges respectively, which can be seen in Figure 3. A 2 mm gap was left before the end of the waveguide cavity. This space is designated for the silica window that will terminate the waveguide cavity. These windows allow transition from the vacuum system of the resonant cavity to standard waveguide components in atmosphere.

The UV fused silica window is of 40 mm diameter and 2 mm thickness. Two rectangular shapes, with 24.5 mm length and 12 mm width each, as shown in Figure 4 were cut at the glass workshop. Epoxy Araldyte adhesive was placed along the ridge of the waveguide cavity. The silica window was then placed on top of the waveguide ridge. The silica window was left for overnight for drying. The same procedure was applied to the other waveguide cavity. The windows are now secured to the respective waveguide flanges using the epoxy Araldyte adhesives. It should be noted that the use of soft-soldering or epoxy adhesives are not recommended for high vacuum components as both soldering resin residues and epoxy out-gas quite badly. However, this is compensated by the high capacity of the vacuum pumping system.

Figure 3: UBR100 standard waveguide flange.

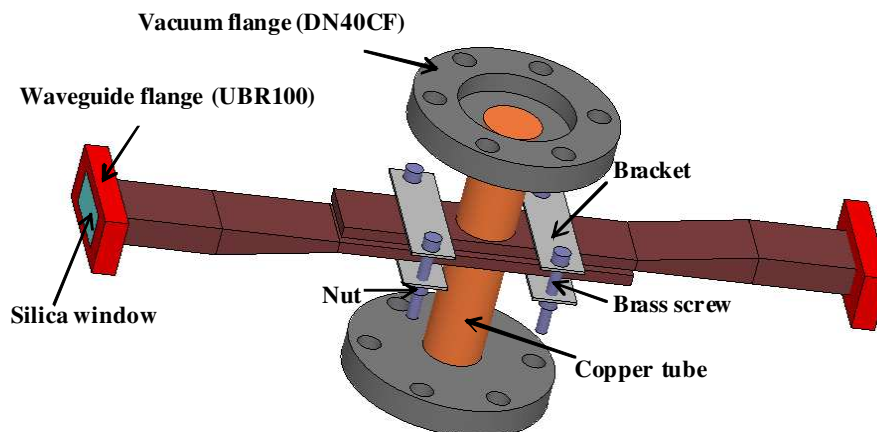Figure 4: Two rectangular shapes cut from a circular UV fused silica window.

Figure 5: Completed PFEM consisting of input and output cavities, clamped by brackets, brass screws and nuts.

3.4. The Tightening of the Two Cavities

The now completed waveguide cavities (input cavity and output cavity) can be placed on top of each other. For monitoring the current flow across the apertures, a PTFE layer is placed in between the two cavities. Silicon 'O' ring was placed in between the two cavities for vacuum sealing purpose. Two brackets and four brass screws and nuts were used to clamp the two cavities together. The length of each bracket is 5 mm and its width is 1.5 mm. The length of each brass screw is 4.1 mm. Two holes were drilled at each bracket near to each end of the bracket. The brass screw could then be slotted into the hole of one bracket, and to the hole of another bracket located below the first bracket. The holes on the two brackets were aligned with each other, so that the brass screws could be slotted perfectly into the two brackets. Nut was used to tighten the two brackets. The same procedure is applied to the other two brackets. The completed construction of the input and output cavities is shown in Figure 5.

3.5. The Filament Circuit Housing

Section 3.2 describes the cavity construction for housing the filament which is placed just before the aperture of the input cavity. A method is also needed to house the copper wires, the copper base and stanchions from the flange base. As a summary, these components can be called the filament circuit elements. The detail structure of the electron gun is not discussed in this paper. A 70 mm diameter copper tube is used to house the filament circuit housing. This copper tube was cut to 73 mm length. The copper tube was then silver soldered to two 70 mm diameter vacuum flanges (DN40CF) at both of its ends. Test performed indicated that the vacuum pressured was lowered to a satisfactory level (1×10^{-7} mbar). Hence no leakages were found in the constructed copper tube with vacuum flanges.

4. CONCLUSION AND FUTURE WORK

The design and analysis of pre-bunched free electron maser have been performed. Simulation results showed that the PFEM structure allows intense E-field strength to accumulate in the thin gap section of the cavity [4]. The resonant cavities are fine tuned using a phase shifter so that the electrons arriving at the output cavity will be in phase with the EM wave. The height of the thin gap section has been designed in such a way that the transit time of the electrons across the height of the thin gap section will be less than half of the EM wavelength. The strong E-field is expected to intersect with the in-phase electrons in the beam. Optimum energy exchange will occur and hence the output EM wave is expected to be significantly amplified.

The construction phase is now complete. Each of the main components has been evaluated as a separate module and testing of each component is now completed. The testing of the electron gun current emission has been performed, where the current flow across the apertures of the output cavity was measured. Results showed that around 50% of the total filament current will flow across the apertures of the output cavity. The PFEM cavity construction was an important process of the research. The PFEM was constructed from scratch using affordable and available technologies and components readily available in the laboratory. The construction of the main body of the PFEM was discussed, followed by the filament housing, the silica windows and the filament circuit housing. Methods used to tighten the two cavities were also presented.

The high vacuum system will be discussed in a future paper. Due to the compactness of the PFEM system, a small vacuum system was used for pumping down the system to reach a vacuum condition. The next major component of PFEM is the electron gun. The design of electron gun will be discussed in a future paper, together with the electron gun circuit. The use of Thoria coated iridium filament will also discussed. In the next step, a 'Pierce' type electron gun will be proposed for the PFEM system. The 'Pierce' type electron gun used by previous Free Electron Laser researcher produced a maximum emission current of 285 mA [9]. Hence, with the acceleration voltage of 3 kV, and the beam current of 142 mA (assuming 50% of the 285 mA current flow across the apertures of the output cavity), the resultant cavity PFEM output power will be significantly increased. In addition to that if a higher output power X-band source (23 dBm) will be used in the future, this will significantly further the cavity PFEM output power. However, emission at higher beam currents will also mean that space-charge spreading of the beam must be taken into consideration.

REFERENCES

1. Sabry, R. and S. K. Chaudhuri, "Formulation of emission from relativistic free electrons in a ring structure for electro-optical applications," *Progress In Electromagnetic Research*, PIER 50, 135–161, 2005.
2. Ku, H. S. and T. Yusaf, "Processing of composites using variable and fixed frequency microwave facilities," *Progress In Electromagnetics Research B*, Vol. 5, 185–205, 2008.
3. Tiwari, K. C., D. Singh, and M. K. Arora, "Development of a model for detection and estimation of depth of shallow buried non-metallic landmine at microwave X-band frequency," *Progress In Electromagnetics Research*, PIER 79, 225–250, 2008.
4. Malek, F., J. Lucas, and Y. Huang, "Prototype design of compact and tuneable X-band pre-bunched free electron maser," *Progress In Electromagnetic Research*, PIER 85, 1–23, 2008.
5. Gholami, M., "Analysis of output power delay in coaxial vircator," *Progress In Electromagnetics Research B*, Vol. 4, 1–12, 2008.
6. Li, Z., T. J. Cui, and J. F. Zhang, "TM wave coupling for high power generation and transmission in parallelplate waveguide," *Journal of Electromagnetic Waves and Applications*, Vol. 21, No. 7, 947–961, 2007.
7. Al-Shamma'a, A. I., A. Shaw, R. A. Stuart, and J. Lucas, "Enhancement of an electron beam buncher for a CW FEM," *Nuclear Instruments and Methods in Physics Research*, Vol. A429, 304–309, 1994.
8. Dwari, S. A., A. Chakraborty, and S. Sanyal, "Analysis of linear tapered waveguide by two approaches," *Progress In Electromagnetics Research*, PIER 64, 219–238, 2006.
9. Wright, C. C., "Development of a free electron maser for industrial applications," Department of Electrical Engineering and Electronics, The University of Liverpool, Ph.D. Thesis, 2000.